WOODHEAD PUBLISHING SERIES IN ELECTRONIC AND OPTICAL MATERIALS

Nitride semiconductor light-emitting diodes (LEDs)

Materials, technologies and applications

Edited by JianJang Huang, Hao-Chung Kuo
and Shyh-Chiang Shen

WP
WOODHEAD
PUBLISHING

VISIT…

LANZAROTE
Caliente.com

Nitride semiconductor light-emitting diodes (LEDs)

Related titles:

Organic light-emitting diodes (OLEDs)
(ISBN 978-0-85709-425-4)

Thin film growth
(ISBN 978-1-84569-736-5)

Printed films
(ISBN 978-1-84569-988-8)

Details of these books and a complete list of titles from Woodhead Publishing can be obtained by:

- visiting our web site at www.woodheadpublishing.com
- contacting Customer Services (e-mail: sales@woodheadpublishing.com; fax: +44 (0) 1223 832819; tel.: +44 (0) 1223 499140 ext. 130; address: Woodhead Publishing Limited, 80, High Street, Sawston, Cambridge CB22 3HJ, UK)
- in North America, contacting our US office (e-mail: usmarketing@woodheadpublishing.com; tel.: (215) 928 9112; address: Woodhead Publishing, 1518 Walnut Street, Suite 1100, Philadelphia, PA 19102-3406, USA)

If you would like e-versions of our content, please visit our online platform: www.woodheadpublishingonline.com. Please recommend it to your librarian so that everyone in your institution can benefit from the wealth of content on the site.

We are always happy to receive suggestions for new books from potential editors. To enquire about contributing to our Electronic and optical materials series, please send your name, contact address and details of the topic/s you are interested in to laura.pugh@woodheadpublishing.com. We look forward to hearing from you.

The team responsible for publishing this book:

Commissioning Editor: Laura Pugh
Publications Coordinator: Steven Mathews
Project Editor: Kate Hardcastle
Editorial and Production Manager: Mary Campbell
Production Editor: Richard Fairclough
Project Manager: Annette Wiseman, RCL
Copyeditor: Jonathan Webley
Proofreader: Annette Wiseman
Cover Designer: Terry Callanan

Woodhead Publishing Series in Electronic and Optical Materials:
Number 54

Nitride semiconductor light-emitting diodes (LEDs)

Materials, technologies and applications

Edited by

JianJang Huang, Hao-Chung Kuo and
Shyh-Chiang Shen

WOODHEAD
PUBLISHING

Oxford Cambridge Philadelphia New Delhi

Published by Woodhead Publishing Limited,
80 High Street, Sawston, Cambridge CB22 3HJ, UK
www.woodheadpublishing.com
www.woodheadpublishingonline.com

Woodhead Publishing, 1518 Walnut Street, Suite 1100, Philadelphia,
PA 19102-3406, USA

Woodhead Publishing India Private Limited, 303, Vardaan House,
7/28 Ansari Road, Daryaganj, New Delhi – 110002, India
www.woodheadpublishingindia.com

First published 2014, Woodhead Publishing Limited
© Woodhead Publishing Limited, 2014. The publisher has made every effort to ensure that permission for copyright material has been obtained by authors wishing to use such material. The authors and the publisher will be glad to hear from any copyright holder it has not been possible to contact.
The authors have asserted their moral rights.

This book contains information obtained from authentic and highly regarded sources. Reprinted material is quoted with permission, and sources are indicated. Reasonable efforts have been made to publish reliable data and information, but the authors and the publisher cannot assume responsibility for the validity of all materials. Neither the authors nor the publisher, nor anyone else associated with this publication, shall be liable for any loss, damage or liability directly or indirectly caused or alleged to be caused by this book.

Neither this book nor any part may be reproduced or transmitted in any form or by any means, electronic or mechanical, including photocopying, microfilming and recording, or by any information storage or retrieval system, without permission in writing from Woodhead Publishing Limited.

The consent of Woodhead Publishing Limited does not extend to copying for general distribution, for promotion, for creating new works, or for resale. Specific permission must be obtained in writing from Woodhead Publishing Limited for such copying.

Trademark notice: Product or corporate names may be trademarks or registered trademarks, and are used only for identification and explanation, without intent to infringe.

British Library Cataloguing in Publication Data
A catalogue record for this book is available from the British Library.

Library of Congress Control Number: 2013955412

ISBN 978-0-85709-507-7 (print)
ISBN 978-0-85709-930-3 (online)
ISSN 2050-1501 Woodhead Publishing Series in Electronic and Optical Materials (print)
ISSN 2050-151X Woodhead Publishing Series in Electronic and Optical Materials (online)

The publisher's policy is to use permanent paper from mills that operate a sustainable forestry policy, and which has been manufactured from pulp which is processed using acid-free and elemental chlorine-free practices. Furthermore, the publisher ensures that the text paper and cover board used have met acceptable environmental accreditation standards.

Typeset by RefineCatch Limited, Bungay, Suffolk
Printed by Lightning Source

Contents

Contributor contact details *xiii*
Woodhead Publishing Series in Electronic and Optical Materials *xvii*
Preface *xxiii*

Part I Materials and fabrication 1

1 Molecular beam epitaxy (MBE) growth of nitride semiconductors 3
Q.-D. Zhuang, Lancaster University, UK

1.1 Introduction 3
1.2 Molecular beam epitaxial (MBE) growth techniques 4
1.3 Plasma-assisted MBE (PAMBE) growth of nitride epilayers and quantum structures 5
1.4 Nitride nanocolumn (NC) materials 12
1.5 Nitride nanostructures based on NCs 17
1.6 Conclusion 21
1.7 References 21

2 Modern metal-organic chemical vapor deposition (MOCVD) reactors and growing nitride-based materials 27
F. H. Yang, AIXTRON Taiwan Co Ltd, Taiwan

2.1 Introduction 27
2.2 MOCVD systems 28
2.3 Planetary reactors 35
2.4 Close-coupled showerhead (CCS) reactors 45
2.5 *In situ* monitoring systems and growing nitride-based materials 54
2.6 Acknowledgements 65
2.7 References 65

3 Gallium nitride (GaN) on sapphire substrates for visible LEDs 66
J.-H. Ryou, University of Houston, USA

3.1 Introduction 66
3.2 Sapphire substrates 69
3.3 Strained heteroepitaxial growth on sapphire substrates 77
3.4 Epitaxial overgrowth of GaN on sapphire substrates 81
3.5 GaN growth on non-polar and semi-polar surfaces 86
3.6 Future trends 88
3.7 References 89

4 Gallium nitride (GaN) on silicon substrates for LEDs 99
M. H. Kane, Texas A & M University at Galveston, USA and
N. Arefin, University of Oklahoma, USA

4.1 Introduction 99
4.2 An overview of gallium nitride (GaN) on silicon substrates 100
4.3 Silicon overview 101
4.4 Challenges for the growth of GaN on silicon substrates 104
4.5 Buffer-layer strategies 105
4.6 Device technologies 113
4.7 Conclusion 139
4.8 References 139

5 Phosphors for white LEDs 144
H. Yamamoto, formerly of Tokyo University of Technology, Japan
and T. Yamamoto, Ajinomoto Pharmaceuticals Co, Ltd, Japan

5.1 Introduction 144
5.2 Optical transitions of Ce^{3+} and Eu^{2+} 146
5.3 Chemical composition of representative nitride and oxynitride phosphors 149
5.4 Compounds activated by Eu^{2+} 150
5.5 Compounds activated by Ce^{3+} 165
5.6 Features of the crystal structure of nitride and oxynitride phosphors 168
5.7 Features of optical transitions of nitride and oxynitride phosphors 171
5.8 Conclusion and future trends 175
5.9 Acknowledgements 176
5.10 References 176

6 Fabrication of nitride LEDs 181
R.-H. Horng, D.-S. Wuu and C.-F. Lin, National Chung Hsing
University, Taiwan and C.-F. Lai, Feng-Chia University, Taiwan

6.1 Introduction 181

6.2 GaN-based flip-chip LEDs and flip-chip technology 183
6.3 GaN FCLEDs with textured micro-pillar arrays 185
6.4 GaN FCLEDs with a geometric sapphire shaping structure 191
6.5 GaN thin-film photonic crystal (PC) LEDs 198
6.6 PC nano-structures and PC LEDs 200
6.7 Light emission characteristics of GaN PC TFLEDs 205
6.8 Conclusion 211
6.9 References 212

7 Nanostructured LEDs 216
C.-C. Lin, D. W. Lin, C.-H. Chiu, Z. Y. Li and Y. P. Lan, National Chiao Tung University, Taiwan, J. J. Huang, National Taiwan University, Taiwan and H.-C. Kuo, National Chiao Tung University, Taiwan

7.1 Introduction 216
7.2 General mechanisms for growth of gallium nitride (GaN) related materials 218
7.3 General characterization method 223
7.4 Top-down technique for nanostructured LEDs 225
7.5 Bottom-up technique for GaN nanopillar substrates prepared by molecular beam epitaxy 240
7.6 Conclusion 245
7.7 References 245

8 Nonpolar and semipolar LEDs 250
Y.-R. Wu, National Taiwan University, Taiwan, C.-Y. Huang, TSMC Solid State Lighting, Ltd, Taiwan, and Y. Zhao and J. S. Speck, University of California, Santa Barbara, USA

8.1 Motivation: limitations of conventional c-plane LEDs 250
8.2 Introduction to selected nonpolar and semipolar planes 255
8.3 Challenges in nonpolar and semipolar epitaxial growth 263
8.4 Light extraction for nonpolar and semipolar LEDs 267
8.5 References 270

Part II Performance of nitride LEDs 277

9 Efficiency droop in gallium indium nitride (GaInN)/gallium nitride (GaN) LEDs 279
D. S. Meyaard, G.-B. Lin, J. Cho and E. F. Schubert, Rensselaer Polytechnic Institute, USA

9.1 Introduction 279
9.2 Recombination models in LEDs 281
9.3 Thermal roll-over in gallium indium nitride (GaInN) LEDs 282
9.4 Auger recombination 284

9.5 High-level injection and the asymmetry of carrier concentration and mobility 286
9.6 Non-capture of carriers 290
9.7 Polarization fields 291
9.8 Carrier delocalization 291
9.9 Discussion and comparison of droop mechanisms 293
9.10 Methods for overcoming droop 294
9.11 References 298

10 Photonic crystal nitride LEDs 301
M. D. B. Charlton, University of Southampton, UK

10.1 Introduction 301
10.2 Photonic crystal (PC) technology 310
10.3 Improving LED extraction efficiency through PC surface patterning 318
10.4 PC-enhanced light extraction in P-side up LEDs 322
10.5 Modelling PC-LEDs 326
10.6 P-side up PC-LED performance 335
10.7 PC-enhanced light extraction in N-side up LEDs 342
10.8 Summary 350
10.9 Conclusions 352
10.10 References 353

11 Surface plasmon enhanced LEDs 355
Q. Hao and T. Qiu, Southeast University, China and P. K. Chu, City University of Hong Kong, China

11.1 Introduction 355
11.2 Mechanism for plasmon-coupled emission 356
11.3 Fabrication of plasmon-coupled nanostructures 358
11.4 Performance and outlook 363
11.5 Acknowledgements 365
11.6 References 365

12 Nitride LEDs based on quantum wells and quantum dots 368
J. Verma, A. Verma, V. Protasenko, S. M. Islam and D. Jena, University of Notre Dame, USA
12.1 Light-emitting diodes (LEDs) 368
12.2 Polarization effects in III-nitride LEDs 379
12.3 Current status of III-nitride LEDs 390
12.4 Modern LED designs and enhancements 399
12.5 References 400

13 Color tunable LEDs 409
Y. F. Cheung, Z. Ma and H. W. Choi, The University of Hong Kong, People's Republic of China

13.1 Introduction 409
13.2 Initial idea for stacked LEDs 410
13.3 Second-generation LED stack with inclined sidewalls 412
13.4 Third-generation tightly-integrated chip-stacking approach 417
13.5 Group-addressable pixelated micro-LED arrays 423
13.6 Conclusions 426
13.7 References 427

14 Reliability of nitride LEDs 428
T.-T. Chen, C.-F. Dai, C.-P. Wang, H.-K. Fu, P.-T. Chou and W. Y. Yeh, Industrial Technology Research Institute (ITRI), Taiwan

14.1 Introduction 428
14.2 Reliability testing of nitride LEDs 428
14.3 Evaluation of LED degradation 431
14.4 Degradation mechanisms 434
14.5 Conclusion 439
14.6 References 440

15 Chip packaging: encapsulation of nitride LEDs 441
X. Luo and R. Hu, Huazhong University of Science and Technology, People's Republic of China

15.1 Functions of LED chip packaging 441
15.2 Basic structure of LED packaging modules 446
15.3 Processes used in LED packaging 449
15.4 Optical effects of gold wire bonding 453
15.5 Optical effects of phosphor coating 456
15.6 Optical effects of freeform lenses 463
15.7 Thermal design and processing of LED packaging 468
15.8 Conclusion 476
15.9 References 476

Part III Applications of nitride LEDs 483

16 White LEDs for lighting applications: the role of standards 485
R. Kotschenreuther, OSRAM GmbH, Germany

16.1 General lighting applications 485
16.2 LED terminology 487
16.3 Copying traditional lamps? 490

16.4 Freedom of choice 491
16.5 Current and future trends 494
16.6 References 495

17 Ultraviolet LEDs 497
H. Hirayama, RIKEN, Japan

17.1 Research background of deep ultraviolet (DUV) LEDs 497
17.2 Growth of low threading dislocation density (TDD) AlN layers on sapphire 502
17.3 Marked increases in internal quantum efficiency (IQE) 507
17.4 Aluminum gallium nitride (AlGaN)-based DUV-LEDs fabricated on high-quality aluminum nitride (AlN) 513
17.5 Increase in electron injection efficiency (EIE) and light extraction efficiency (LEE) 521
17.6 Conclusions and future trends 528
17.7 References 530

18 Infrared emitters made from III-nitride semiconductors 533
Y. Kotsar and E. Monroy, CEA-Grenoble, INAC/SP2M/NPSC, France

18.1 Introduction 533
18.2 High indium (In) content alloys for infrared emitters 534
18.3 Rare-earth (RE) doped gallium nitride (GaN) emitters 536
18.4 III-nitride materials for intersubband (ISB) optoelectronics 538
18.5 ISB devices 549
18.6 Conclusions 556
18.7 Acknowledgements 557
18.8 References 557

19 LEDs for liquid crystal display (LCD) backlighting 566
C.-F. Chen, National Central University, Taiwan

19.1 Introduction 566
19.2 Types of LED LCD backlighting units (BLUs) 567
19.3 Technical considerations for optical films and plates 571
19.4 Requirements for LCD BLUs 572
19.5 Advantages and history of LED BLUs 574
19.6 Market trends and technological developments 577
19.7 Optical design 583
19.8 References 593

20 LEDs in automotive lighting 595
J. D. Bullough, Rensselaer Polytechnic Institute, USA

20.1 Introduction 595

20.2 Forward lighting 595
20.3 Signal lighting 599
20.4 Human factor issues with LEDs 599
20.5 Energy and environmental issues 603
20.6 Future trends 603
20.7 Sources of further information and advice 604
20.8 Acknowledgments 604
20.9 References 604

Index *607*

Contributor contact details

(* = main contact)

Editors

J. J. Huang
Graduate Institute of Photonics and Optoelectronics
National Taiwan University
1 Roosevelt Road, Sec. 4
Taipei 106, Taiwan

E-mail: jjhuang@cc.ee.ntu.edu.tw

H.-C. Kuo
Department of Photonics & Institute of Electro-Optical Engineering
National Chiao-Tung University
1001 University Road
Hsinchu 30010, Taiwan

E-mail: hckuo@faculty.nctu.edu.tw

S.-C. Shen
Georgia Institute of Technology
Atlanta, GA 30332, USA

E-mail: shyh.shen@ece.gatech.edu

Chapter 1

Q.-D. Zhuang
Physics Department
Lancaster University
Lancaster LA1 4YB, UK

E-mail: q.zhuang@lancaster.ac.uk

Chapter 2

F. H. Yang
AIXTRON Taiwan Co Ltd, 2F,
No 5 Lane 91, DongMei Road
Hsinchu City, Taiwan

E-mail: j.yang@aixtron.com

Chapter 3

J.-H. Ryou
Department of Mechanical Engineering
Cullen College of Engineering
University of Houston
N207 Engineering Building 1, MC-H4006
University of Houston
Houston, TX 77204-4006, USA

E-mail: jryou@uh.edu

Chapter 4

M. H. Kane*
Engineering Department
Massachusetts Maritime Academy
101 Academy Drive
Buzzards Bay, MA 02532, USA

E-mail: mhkane@maritime.edu

N. Arefin
University of Oklahoma
Norman, OK 73019, USA

Chapter 5

T. Yamamoto
3-23-3 Eifuku
Suginami-ku
Tokyo, Japan, 168-0064

E-mail: ygen29@gmail.com

Chapter 6

R.-H. Horng
Institute of Precision Engineering
National Chung Hsing University
250 Kuo Kuang Road
Taichung 402, Taiwan

E-mail: huahorng@dragon.nchu.edu.tw

D.-S. Wuu and C.-F. Lin
Department of Materials Science and Engineering
National Chung Hsing University
250 Kuo Kuang Road
Taichung 402, Taiwan

E-mail: dsw@dragon.nchu.edu.tw; cflin@dragon.nchu.edu.tw

C.-F. Lai*
Department of Photonics
Feng-Chia University
100 Wenhwa Road Seatwen
Taichung 40724, Taiwan

E-mail: chunflai@fcu.edu.tw; lai.chunfeng@gmail.com

Chapter 7

C.-C. Lin*
Institute of Photonic System
College of Photonics
National Chiao Tung University
Tainan 711, Taiwan

E-mail: chienchunglin@faculty.nctu.edu.tw

D. W. Lin, C.-H. Chiu, Z. Y. Li and Y. P. Lan
Department of Photonics & Institute of Electro-Optical Engineering
National Chiao Tung University
Hsinchu 30010, Taiwan
J. J. Huang
Graduate Institute of Photonics and Optoelectronics
National Taiwan University
1 Roosevelt Road, Sec 4
Taipei 106, Taiwan

E-mail: jjhuang@cc.ee.ntu.edu.tw

H.-C. Kuo
Department of Photonics & Institute of Electro-Optical Engineering
National Chiao-Tung University
1001 University Road
Hsinchu 30010, Taiwan

Chapter 8

Y.-R. Wu*
National Taiwan University
1 Roosevelt Road, Sec 4
Taipei 106, Taiwan

E-mail: yrwu@cc.ee.ntu.edu.tw

C.-Y. Huang
TSMC Solid State Lighting, Ltd
Epitaxy Technology Development Department
9 Li-Hsin 4th Road
Hsinchu Science Park
Hsinchu City, Taiwan 300-78, ROC

Y. Zhao and J. S. Speck
University of California, Santa Barbara
Santa Barbara, CA 93106, USA

Chapter 9

D. S. Meyaard, G.-B. Lin, J. Cho and E. F. Schubert*
Rensselaer Polytechnic Institute
Troy, NY 12180, USA

E-mail: efschubert@rpi.edu

Chapter 10

M. D. B. Charlton
Electronics and Computer Science (ECS)
Faculty of Physical and Applied Sciences
University of Southampton
Southampton SO17 1BJ, UK

E-mail: mdbc@ecs.soton.ac.uk

Chapter 11

Q. Hao and T. Qiu*
Department of Physics
Southeast University
Nanjing 211189, China

E-mail: tqiu@seu.edu.cn

P. K. Chu
Department of Physics and Materials Science
City University of Hong Kong
Hong Kong, China

Chapter 12

J. Verma,* A. Verma, V. Protasenko, S. M. Islam and D. Jena
University of Notre Dame
Notre Dame, IN 46556, USA

E-mail: jverma@nd.edu; djena@nd.edu

Chapter 13

Y. F. Cheung, Z. Ma and H. W. Choi*
Department of Electrical and Electronic Engineering
The University of Hong Kong
Hong Kong, People's Republic of China

E-mail: hwchoi@hku.hk

Chapter 14

T.-T. Chen,* C.-F. Dai, C.-P. Wang, H.-K. Fu, P.-T. Chou and W. Y. Yeh
Electronics and Optoelectronics Research Laboratories
Industrial Technology Research Institute (ITRI)
Hsinchu 310, Taiwan

E-mail: ttchen@itri.org.tw; CF_Dai@itri.org.tw; cpwang@itri.org.tw; hkfu@itri.org.tw; PTChou@itri.org.tw; WenYungYeh@itri.org.tw

Chapter 15

X. Luo* and R. Hu
Thermal Packaging Laboratory
School of Energy and Power Engineering
Huazhong University of Science and Technology
Wuhan 430074, People's Republic of China

E-mail: luoxb@mail.hust.edu.cn

Chapter 16

R. Kotschenreuther
OSRAM GmbH
D-80807 Munich, Germany

E-mail: r.kotschenreuther@osram.com

Chapter 17

H. Hirayama
RIKEN
2-1 Hirosawa
Wako, Saitama 351-0198, Japan

E-mail: hirayama@postman.riken.go.jp

Chapter 18

Y. Kotsar and E. Monroy*
CEA-Grenoble, INAC/SP2M/NPSC
17 rue des Martyrs
38054 Grenoble, France

E-mail: eva.monroy@cea.fr

Chapter 19

C.-F. Chen
Mechanical Engineering and Institute of Opto-Mechatronics Engineering
National Central University
No. 300, Jhongda Road
Jhongli City, Taoyuan County 32001, Taiwan

E-mail: ccf@cc.ncu.edu.tw

Chapter 20

J. D. Bullough
Lighting Research Center
Rensselaer Polytechnic Institute
21 Union Street
Troy, NY 12180, USA

E-mail: bulloj@rpi.edu

Woodhead Publishing Series in Electronic and Optical Materials

1 **Circuit analysis**
J. E. Whitehouse
2 **Signal processing in electronic communications: For engineers and mathematicians**
M. J. Chapman, D. P. Goodall and N. C. Steele
3 **Pattern recognition and image processing**
D. Luo
4 **Digital filters and signal processing in electronic engineering: Theory, applications, architecture, code**
S. M. Bozic and R. J. Chance
5 **Cable engineering for local area networks**
B. J. Elliott
6 **Designing a structured cabling system to ISO 11801: Cross-referenced to European CENELEC and American Standards**
Second edition
B. J. Elliott
7 **Microscopy techniques for materials science**
A. Clarke and C. Eberhardt
8 **Materials for energy conversion devices**
Edited by C. C. Sorrell, J. Nowotny and S. Sugihara
9 **Digital image processing: Mathematical and computational methods**
Second edition
J. M. Blackledge
10 **Nanolithography and patterning techniques in microelectronics**
Edited by D. Bucknall
11 **Digital signal processing: Mathematical and computational methods, software development and applications**
Second edition
J. M. Blackledge
12 **Handbook of advanced dielectric, piezoelectric and ferroelectric materials: Synthesis, properties and applications**
Edited by Z.-G. Ye
13 **Materials for fuel cells**
Edited by M. Gasik

14 **Solid-state hydrogen storage: Materials and chemistry**
Edited by G. Walker
15 **Laser cooling of solids**
S. V. Petrushkin and V. V. Samartsev
16 **Polymer electrolytes: Fundamentals and applications**
Edited by C. A. C. Sequeira and D. A. F. Santos
17 **Advanced piezoelectric materials: Science and technology**
Edited by K. Uchino
18 **Optical switches: Materials and design**
Edited by S. J. Chua and B. Li
19 **Advanced adhesives in electronics: Materials, properties and applications**
Edited by M. O. Alam and C. Bailey
20 **Thin film growth: Physics, materials science and applications**
Edited by Z. Cao
21 **Electromigration in thin films and electronic devices: Materials and reliability**
Edited by C.-U. Kim
22 ***In situ* characterization of thin film growth**
Edited by G. Koster and G. Rijnders
23 **Silicon-germanium (SiGe) nanostructures: Production, properties and applications in electronics**
Edited by Y. Shiraki and N. Usami
24 **High-temperature superconductors**
Edited by X. G. Qiu
25 **Introduction to the physics of nanoelectronics**
S. G. Tan and M. B. A. Jalil
26 **Printed films: Materials science and applications in sensors, electronics and photonics**
Edited by M. Prudenziati and J. Hormadaly
27 **Laser growth and processing of photonic devices**
Edited by N. A. Vainos
28 **Quantum optics with semiconductor nanostructures**
Edited by F. Jahnke
29 **Ultrasonic transducers: Materials and design for sensors, actuators and medical applications**
Edited by K. Nakamura
30 **Waste electrical and electronic equipment (WEEE) handbook**
Edited by V. Goodship and A. Stevels
31 **Applications of ATILA FEM software to smart materials: Case studies in designing devices**
Edited by K. Uchino and J.-C. Debus
32 **MEMS for automotive and aerospace applications**
Edited by M. Kraft and N. M. White
33 **Semiconductor lasers: Fundamentals and applications**
Edited by A. Baranov and E. Tournie
34 **Handbook of terahertz technology for imaging, sensing and communications**
Edited by D. Saeedkia
35 **Handbook of solid-state lasers: Materials, systems and applications**
Edited by B. Denker and E. Shklovsky

36 **Organic light-emitting diodes (OLEDs): Materials, devices and applications**
Edited by A. Buckley
37 **Lasers for medical applications: Diagnostics, therapy and surgery**
Edited by H. Jelínková
38 **Semiconductor gas sensors**
Edited by R. Jaaniso and O. K. Tan
39 **Handbook of organic materials for optical and (opto)electronic devices: Properties and applications**
Edited by O. Ostroverkhova
40 **Metallic films for electronic, optical and magnetic applications: Structure, processing and properties**
Edited by K. Barmak and K. Coffey
41 **Handbook of laser welding technologies**
Edited by S. Katayama
42 **Nanolithography: The art of fabricating nanoelectronic and nanophotonic devices and systems**
Edited by M. Feldman
43 **Laser spectroscopy for sensing: Fundamentals, techniques and applications**
Edited by M. Baudelet
44 **Chalcogenide glasses: Preparation, properties and applications**
Edited by J.-L. Adam and X. Zhang
45 **Handbook of MEMS for wireless and mobile applications**
Edited by D. Uttamchandani
46 **Subsea optics and imaging**
Edited by J. Watson and O. Zielinski
47 **Carbon nanotubes and graphene for photonic applications**
Edited by S. Yamashita, Y. Saito and J. H. Choi
48 **Optical biomimetics: Materials and applications**
Edited by M. Large
49 **Optical thin films and coatings**
Edited by A. Piegari and F. Flory
50 **Computer design of diffractive optics**
Edited by V. A. Soifer
51 **Smart sensors and MEMS: Intelligent devices and microsystems for industrial applications**
Edited by S. Nihtianov and A. Luque
52 **Fundamentals of femtosecond optics**
S. A. Kozlov and V. V. Samartsev
53 **Nanostructured semiconductor oxides for the next generation of electronics and functional devices: Production, properties and applications**
S. Zhuiykov
54 **Nitride semiconductor light-emitting diodes (LEDs): Materials, technologies and applications**
Edited by J. J. Huang, H. C. Kuo and S. C. Shen
55 **Sensor technologies for civil infrastructures**
Volume 1: Sensing hardware and data collection methods for performance assessment
Edited by M. Wang, J. Lynch and H. Sohn

56 Sensor technologies for civil infrastructures
Volume 2: Applications in structural health monitoring
Edited by M. Wang, J. Lynch and H. Sohn
57 Graphene: Properties, preparation, characterisation and devices
Edited by V. Skákalová and A. B. Kaiser
58 Handbook of silicon-on-insulator (SOI) technology
Edited by O. Kononchuk and B.-Y. Nguyen
59 Biological identification: DNA amplification and sequencing, optical sensing, lab-on-chip and portable systems
Edited by P. Schaudies
60 High performance silicon imaging: Fundamentals and applications of CMOS and CCD sensors
Edited by D. Durini
61 Nanosensors for chemical and biological applications: Sensing with nanotubes, nanowires and nanoparticles
Edited by K. C. Honeychurch
62 Composite magnetoelectrics: Materials, structures, and applications
G. Srinivasan, S. Priya, and N. Sun
63 Quantum information processing with diamond: Principles and applications
Edited by S. Prawer and I. Aharonovich
64 Advances in nonvolatile memory and storage technology
Edited by Y. Nishi
65 Laser surface engineering: Processes and applications
Edited by J. Lawrence, C. Dowding, D. Waugh, J. Griffiths
66 Power ultrasonics: A handbook of materials, design and applications of high power ultrasound transducers
Edited by J. A. Gallego-Juárez
67 Advances in delay-tolerant networks (DTNs): Architectures, routing and challenges
Edited by J. Rodrigues
68 Handbook of flexible organic electronics: Materials, manufacturing and applications
Edited by S. Logothetidis
69 Machine-to-machine (M2M) communications: Architecture, performance and applications
Edited by C. Anton-Haro and M. Dohler
70 Ecological design of smart home networks: Technologies, social impact and sustainability
Edited by N. Saito and D. Menga
71 Industrial tomography: Systems and applications
Edited by M. Wang
72 Vehicular communications and networks: Architectures, protocols, operation and deployment
Edited by W. Chen
73 Modeling, characterization, and production of nanomaterials: Electronics, photonics and energy applications
Edited by V. Tewary and Y. Zhang
74 Reliability characterisation of electrical and electronic systems
Edited by J. Swingler

75 Handbook of industrial wireless sensor networks: Monitoring, control and automation
Edited by R. Budampati S. Kolavennu

76 Epitaxial growth of complex metal oxides: Techniques, properties and applications
Edited by G. Koster and G. Rijnders

77 Semiconductor nanowires: Materials, synthesis, characterization and applications
Edited by J. Arbiol and Q. Xiong

Professor Hajime Yamamoto, a contributing co-author of this book, sadly passed away on 19 June 2013 before publication. The editors and the book's co-authors (many of them acquainted with him) offer their sympathies to his family.

Preface

Light-emitting diodes (LEDs) have extended their presence from being dim indicators on instrument panels and children's toys to highly efficient solid-state lighting (SSL) of daily life. This beautifully engineered technology, pioneered by Professor Holonyak in 1962 and enabled by numerous bright scientists and engineers with fifty-plus years of active research and development, is transforming the way electric energy is utilized in the creation of artificial lighting in the future. As LEDs in SSL have reached a peak efficiency of greater than 250 lm/W with a lifetime of greater than 60 000 hours (approximately three to five times longer lifetime than today's fluorescent lamps!), we can see the realization of 'the ultimate lamp' in these innovative devices that are currently produced using III-nitride (III-N) semiconductors.

Undoubtedly, constant improvements in SSL device technology along with a wider acceptance of SSL around the world will lead to eventual economies of scale for III-N LED technologies. SSL sales reached $US 19.5 billion in 2012 and will reach a projected market size of $US 31.4 billion in 2017 with a compound annual growth rate of 9.9% between 2012 and 2017 (http://www.electronics.ca/presscenter/articles/1855/1/Global-Market-for-Light-Emitting-Diodes-to-Reach-314-in-2017/Page1.html). According to the Department of Energy of the United States, the switch from incandescent light bulbs to SSL sources over the next 20 years could save $US 250 billion of energy costs over that period of time with a reduction in electricity consumption for lighting of nearly one-half (http://www1.eere.energy.gov/buildings/ssl/sslbasics_market.html). Better energy utilization in these ultimate lamps also promises a significant reduction in the carbon footprint. It is highly likely that LEDs are poised to replace the incandescent light bulbs that were brilliantly invented more than a century ago.

The ubiquitous presence of LED technology is evident in all aspects of today's consumer electronics and infrastructure, which require efficient and environmentally friendly photon emission to safeguard and enrich human life: traffic signal lights, pedestrian signage and backlight sources for displays, just to name a few. For example, the replacement of compact cathode fluorescent lamps with eco-friendly mercury-free LEDs has enabled new generations of liquid crystal displays with lower power consumption, richer color reproduction and improved response times in a highly compact form. Engineering the bandgap energy of III-N materials to emit ultraviolet (UV) photons has helped the development of compact UV light sources for efficient water sanitation and in the detection of bacteria. These novel UV LED technologies will also play a pivotal role in enhancing quality of life in the future.

There are, however, several technological roadblocks and market challenges to be overcome before LED technology can substantially impact the future world. Today, an LED lamp is much more expensive than a fluorescent lamp per lumen. The cost is associated with the economies of scale as well as the supply-and-demand dynamics of the market, which could dominate the prognosis of this new technology's success. Although government subsidies could boost the initial adoption of SSL LED technology, a sustainable SSL industry also depends on the successful development of low-cost manufacturing and device innovation.

SSL technology is, in essence, a subset of III-N device technology. In the context of III-N LED technology development, the indispensable elements for a full-fledged SSL industry infrastructure of high-quality material growth technology, robust device fabrication methodologies, low-cost package techniques and efficient thermal management. III-N material technology is a relatively new field with just a tad over twenty years of research and development. The quality of epitaxial materials still leaves much room for improvement. The lack of native substrates for III-N materials may become a fundamental impediment to improving LED efficiency and ultimately affects manufacturing costs. The design and optimization of the quantum mechanical structures needed for the manipulation and control of electron-photon interactions significantly affect the performance of III-N LEDs. These designs also need to work around the pronounced polarization charges in these polar semiconductors. In addition, the inevitable thermal effect and 'mysterious' efficiency droop phenomena have to be dealt with theoretically and experimentally before highly efficient solid-state light sources can be realized. Packaging and thermal management issues for III-N LEDs are also important. The human factor is also an intricate but interesting topic in SSL LED. The requirements for color rendering and the need to retrofit conventional lighting standards have led to many important LED developments that utilize phosphor-based wavelength conversion techniques and voltage regulation circuits.

These intertwined scientific and technological issues in III-N LED development have sparked tremendous research, development and commercialization efforts around the world over the past decade. This book aims to capture the essence of key development topics in contemporary III-N LED technology and to provide its readers with an overview of the state of current technology.

There are three parts to this book: materials and fabrication, performance of nitride LEDs and applications of nitride LEDs. Although metal-organic chemical vapor deposition (MOCVD) (Chapter 2) is the major growth technology for contemporary commercial III-N LED manufacturing, we also include a discussion on molecular beam epitaxy (MBE) (Chapter 1) to provide interested readers with the necessary background for other aspects of the advanced LED research discussed in this book. The choice of substrate for III-N LEDs has a direct impact on epitaxial quality and the subsequent cost of the LEDs. Currently, the available substrates for III-N LEDs range from (patterned) sapphire, silicon carbide, silicon and free-standing or native GaN substrates. We will discuss III-N LEDs produced using sapphire substrates (Chapter 3) and silicon substrates (Chapter 4) in this book. The electrical injection efficiency and light extraction efficiency can be optimized in III-N LED fabrication using different surface modification strategies and effective packaging approaches. Chapters 6, 14 and 15 showcase device fabrication, packaging technology and reliability developments for III-N LEDs. Along with the discussion on fabrication and material growth challenges, readers may find it useful to review the fundamental III-N quantum well design issues (Chapter 12) and efficiency droop issues (Chapter 9) to better grasp the theoretical background and to gain an understanding of III-N LED performance limitations arising from the polarization charges, as well as approaches to mitigate the impact of these issues. This book will also feature a few advanced nanoscale III-N LEDs and the use of new materials such as nanorods (Chapter 7), plasmon-assisted LEDs (Chapter 11) and photonic crystal LEDs (Chapter 10). New crystal orientations (Chapter 8) and new growth and fabrication technologies to realize ultraviolet (Chapter 17) and infrared (Chapter 18) LEDs have also been addressed. As discussed earlier, III-N LED technology developments and research into wider bandgap materials have produced solid-state light sources for various applications. Readers may find it interesting to learn about the concepts and approaches of SSL for general lighting (Chapter 16), flat-panel displays (Chapter 19) and automotive lighting (Chapter 20). The color quality of light sources is a critical issue. Chapter 13 considers color tunable LEDs. Chapter 5, written by the late Professor Yamamoto, overviews the general features of phosphors.

We were privileged to be the editors of this book and to be able to invite distinguished researchers and technologists as chapter contributors share their expertise and insights into this emerging technology. We are grateful for the time and energy they invested in this book and are excited about the advent of the ultimate lamps using III-N LEDs in the years to come. We hope this book may facilitate a wider dissemination of III-N LED technology among engineering students studying solid-state optoelectronic devices.

Finally, the editors would like to express their immense gratitude to Professor N. Holonyak, Jr, of the University of Illinois at Urbana-Champaign (UIUC), the late Professor Gregory Stillman of UIUC, Professor Russell D. Dupuis of Georgia Tech and Professor Milton Feng of UIUC for their pioneering work in compound semiconductor materials and device research, for their constant support for a younger generation of engineers and for being our academic role models with their relentless pursuit of engineering perfection through integrity, hard work and unsurpassed perseverance in insisting on doing the right and important things.

Professor JianJang Huang, Professor Hao-Chung Kuo
and Professor Shyh-Chiang Shen

1

Molecular beam epitaxy (MBE) growth of nitride semiconductors

Q.-D. ZHUANG, Lancaster University, UK

DOI: 10.1533/9780857099303.1.3

Abstract: This chapter reviews the recent progress in growing nitride alloys and nanostructures using molecular beam epitaxy (MBE). The chapter first discusses the growth mechanisms and growth optimization for nitride thin films and nanocolumns (NCs). The chapter then focuses on the recent development of nitride NCs and related quantum structures, which have great potential for various devices.

Key words: nitride, light-emitting diode (LED), laser diode (LD), metal-organic chemical vapour deposition (MOCVD), molecular beam epitaxy (MBE), quantum well, nanocolumn, electroluminescence, photoluminescence.

1.1 Introduction

It is well known that the only successful growth technique for the production of commercial nitrides for visible light sources is metal-organic chemical vapour deposition (MOCVD). Although molecular beam epitaxy (MBE) has many advantages with the epitaxial growth of various compound semiconductors and quantum structures, including the production of abrupt interfaces and sharp doping profiles and superior *in situ* growth monitoring, it was not considered a promising alternative to MOCVD for producing nitride devices until the demonstration of the first pulsed laser diodes (LDs) with a 400 nm emission wavelength grown by MBE.[1] Since then, there has been significant progress in MBE-grown nitride materials, nanostructures and related devices. This emerging growth technique has been used to create light sources operating at a wider spectral range and has generated new advanced devices. Two MBE growth technologies have been developed for nitride epitaxy: ammonia MBE and plasma-assisted MBE (PAMBE). The former MBE growth technique uses ammonia as the nitrogen precursor, while the latter uses plasma to atomize nitrogen gas. Significant progress in MBE-grown nitride devices has been demonstrated, but many challenges exist in the growth of nitrides using MBE for high-performance devices, including high-quality buffer layers, high-quality indium-rich InGaN alloys and their p-doping as well as n-doping aluminium-rich AlGaN alloys. This chapter will review recent progress in the growth of nitride materials and nanostructures using MBE and the potential solutions to circumvent the challenges.

1.2 Molecular beam epitaxial (MBE) growth techniques

Ammonia MBE can be used to grow GaN at a high growth rate (over ~1 μm/h) with a full width at half maximum (FWHM) of 540 arcseconds as measured by X-ray diffraction.[2] The GaN epilayers were initiated on a buffer layer grown by plasma-assisted MBE at a growth temperature of 500 °C. Typical ammonia MBE growth requires a high ammonia flow of ~200 sccm, a high V/III flux ratio (of up to 10^3) that is NH_3-rich and a high growth temperature of 800–900 °C, which is close to that of MOCVD. Hooper *et al.*[1] produced the first room-temperature pulsed InGaN LD using ammonia MBE with an emission wavelength of 400 nm and a threshold current of 30 kA/cm^2. Since then this group has continued to develop these lasers, producing the best lasers using ammonia MBE, which emit at 405 nm and have a continuous-wave (CW) operation at room temperature with a threshold current of 3.6 kA/cm^2, with a maximum CW output power of 45 mW per facet and a lifetime of 42 h.[3] Although ammonia MBE was used to produce the first nitride LD, it is not used by the majority of the nitride MBE community due to the large consumption of ammonia, the high growth temperature, the corrosive nature of ammonia and the high hydrogen background during the epitaxial process, which limit its extensive use for nitride growth. Sharp Laboratories of Europe Ltd is, perhaps, the only research group that is active in using ammonia MBE. PAMBE has become the technique that is used by the majority of the MBE community in nitride epitaxy.

Two plasma sources are used for PAMBE: electron-cyclotron resonance (ECR)[4] and radio-frequency (RF) plasma.[5] Molecular nitrogen is inert in MBE, but it can be effectively cracked into reactive nitrogen species, that is neutral and charged molecular nitrogen (N_2, N_2^+) and neutral and ionic atomic nitrogen (N, N^+), and free electrons. RF plasma sources are generally preferred to ECR plasma sources since they produce more neutral atomic nitrogen, which is favourable to the incorporation of nitrogen during the epitaxial process. In addition, it has been shown that high quality nitride materials are obtained from the metal-rich condition, with much lower growth temperatures compared to ammonia MBE. This growth behaviour has been extensively investigated theoretically and experimentally to understand the growth mechanisms. Theoretical work based on density-functional theory revealed the existence of an efficient lateral diffusion channel for adatoms on a semiconductor surface just below the thin metallic film.[6] In particular, the activation energy of this so-called adlayer-enhanced lateral diffusion (AELD) is small and hence enables high-quality step-flow epitaxy at temperatures much lower than estimates based on the melting point of the material. Because of the low growth temperature, PAMBE has been identified as the main MBE growth technique for nitride materials.

1.3 Plasma-assisted MBE (PAMBE) growth of nitride epilayers and quantum structures

There has been a worldwide effort to develop nitride materials, including InGaN and AlGaN alloys, and their quantum structures to produce LEDs and LDs operating at different wavelengths, especially deep ultraviolet (d-UV), UV, visible light and white light. Such devices require aluminium-rich AlGaN or indium-rich InGaN alloys, relevant quantum structures and doping for the contacts. However, there are a number of challenges including the degradation of materials with increasing indium content in InGaN alloys and the difficulty in obtaining p-doping, and the difficulty in obtaining n-doping in aluminium-rich AlGaN alloys as well as the high strain for specific wavelengths. Enormous efforts have been made in growing nitrides using PAMBE to understand the growth mechanisms, to optimize the growth conditions and to create new structures, which have resulted in various high-performance devices.

1.3.1 Gallium nitride (GaN) epilayers

MBE growth diagrams, also referred to as surface phase diagrams, are instrumental in producing device-quality thin films. The GaN epilayers are generally grown on 1–2 μm thick GaN templates grown by MOCVD on c-plane sapphire, which have an estimated dislocation density of 5×10^8 to $5 \times 10^9\,\text{cm}^{-2}$. The growth of GaN epilayers using PAMBE for different growth conditions has been studied using various technologies, such as reflective high-energy electron diffraction (RHEED).[7] RHEED patterns have been produced from the hexagonal GaN (0001) surfaces under different gallium fluxes, where a high gallium flux is considered to be a gallium-rich condition, and a low one a nitrogen-rich condition. Figure 1.1 shows

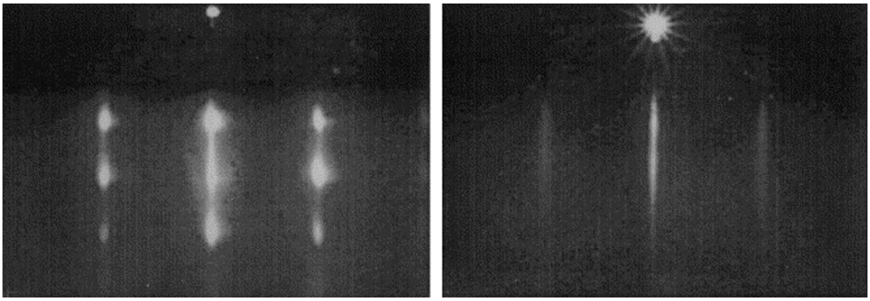
(a) (b)

1.1 RHEED patterns for GaN epilayers under: (a) a nitrogen-rich condition (gallium flux ~4×10^{-7} Torr) and (b) a gallium-rich condition (gallium flux ~5×10^{-7} Torr). The substrate temperature, N_2 flow and RF power were 800 °C, 1.5 sccm and 400 W respectively.[7]

typical RHEED patterns for GaN grown on c-plane sapphire under different conditions. The gallium-rich condition produced a streaky pattern suggesting two-dimensional (2D) growth, while the nitrogen-rich condition resulted in a spotty pattern indicating three-dimensional (3D) growth. This difference is explained by the different migration of excess species on the surface between the nitrogen-rich and gallium-rich conditions. For the growth with a spotty RHEED pattern, the rough morphology can be recovered after the gallium shutter is closed. If the gallium flux is too high, then gallium droplets form on the surface, and the surface recovery takes a longer time compared to nitrogen-rich growth, mainly due to the slow re-evaporation of excess gallium. Due to the similar atomic arrangement between cubic (111) and hexagonal (0001) crystals, it is possible to grow cubic crystalline epilayers on hexagonal substrates. This was demonstrated by Okumura and co-workers at a low growth temperature, which was far from the equilibrium growth conditions.[7] The growth temperature is dependent on the gallium flux; at a typical gallium flux of 5×10^{-7} mbar, a growth temperature less than 640 °C will lead to the growth of cubic GaN. A lower gallium flux requires a lower growth temperature.

Surface reconstruction was also studied to identify the optimal PAMBE growth conditions for GaN materials.[8] The transition of 1 × 1 and 2 × 2 at different growth temperatures and fluxes follows a curve as plotted in Fig. 1.2. It shows that a higher gallium flux or lower growth temperature (upper left of a curve) yields the 1 × 1 pattern, whereas a lower gallium flux or higher growth temperature gives rise to the 2 × 2 pattern. This transition curve can be as a reference to determine the optimal growth conditions. GaN epilayers grown at conditions close to the transition curve (on the 2 × 2 side) have good carrier mobility, while epilayers grown in the regime of 1 × 1 pattern yield gallium droplets.

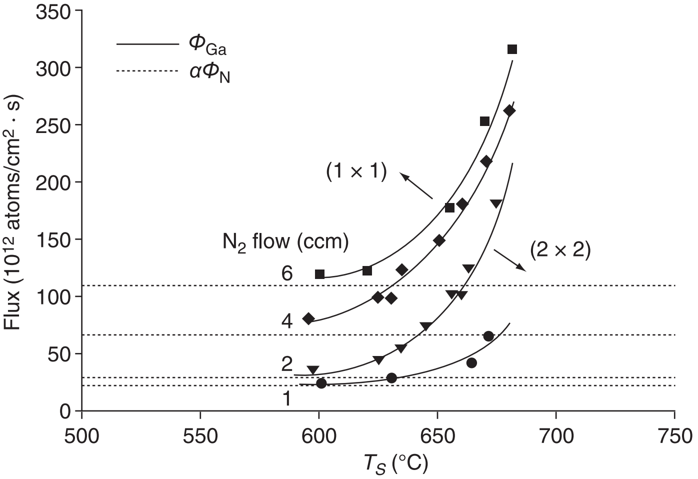

1.2 Plot of Ga flux Φ_{Ga} vs growth temperature T_s showing the transition curves for differing N_2 flow rates.[8]

Furthermore, atomic force microscopy (AFM)[9–11] has been used to figure out the dependence of the morphology of the GaN epilayers on growth parameters. It was concluded that the gallium-rich condition is necessary for a smooth surface and results in strong photoluminescence (PL).[9] Heying and co-workers[12] established a detailed growth diagram for GaN using AFM and cross-sectional transmission electron microscopy (TEM). Three growth regimes are shown in Fig. 1.3, and Fig. 1.4 shows AFM images of the surface morphology of the resulting GaN epilayers. They concluded that growth within the nitrogen-stable regime results in a surface composed entirely of inverted, pyramid-shaped pits initiated at threading dislocations (TDs). Epilayers grown within the intermediate regime have flat surfaces between large pit features stabilized by low-angle grain boundaries. Films grown within the gallium droplet regime have atomically flat surfaces with no pit features. The reduction of the pit density was attributed to the change in the growth kinetics due to the increasing coverage of the surface by metallic gallium.[11]

Due to the shortage of suitable substrates for nitride growth, nitride devices are normally grown on free-standing GaN wafers, or sapphire or silicon substrates using a thin layer of AlN as a nucleation layer to relax the strain (caused by lattice mismatch). A two-step growth procedure produces high-quality AlN epilayers with excellent crystalline quality and a smooth surface.[13] This procedure starts with a nitrogen-rich growth condition then switches to aluminium-rich growth conditions. Faleev and co-workers developed the procedure for the growth of this buffer layer, which has a low threading dislocation density of $1.75 \times 10^5\,\mathrm{cm}^{-2}$, on sapphire.[14] Lee and co-workers developed a novel buffer technique to produce

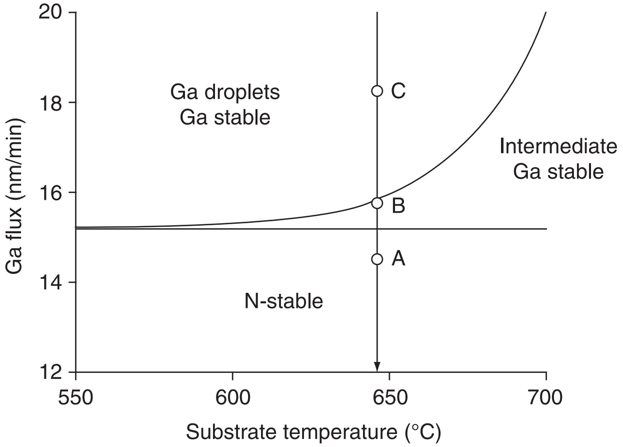

1.3 Growth diagram showing gallium flux vs substrate temperature for the gallium-droplet, intermediate and nitrogen-stable growth regimes at a constant nitrogen flux of 2.8 nm/min.[12]

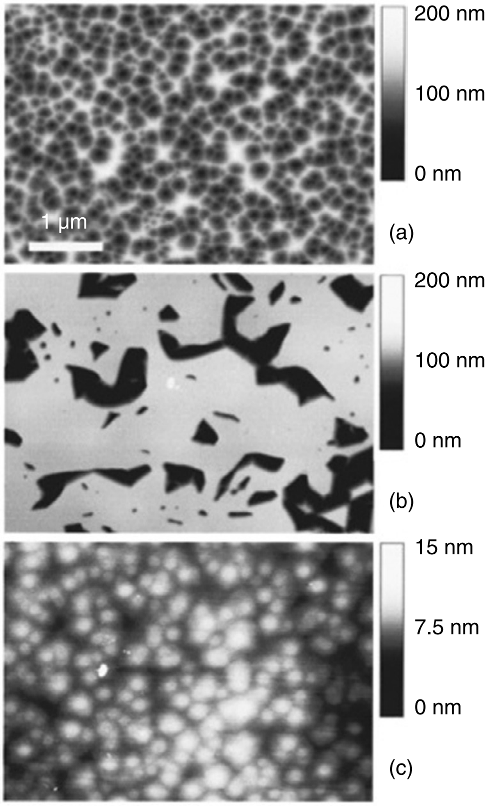

1.4 AFM images of GaN grown within (a) the nitrogen-stable regime (gallium flux: 14.5 nm/min), (b) the intermediate regime (gallium flux: 15.8 nm/min) and (c) the gallium-droplet regime (gallium flux: 18.2 nm/min).[12]

free-standing GaN using a thin MBE-grown zinc-polar ZnO layer on sapphire.[15] This buffer layer was used to produce a strain-free GaN epilayer with extensive photoluminescence indicating the promising potential of nitrides grown on sapphire by MBE for advanced devices.

1.3.2 Aluminium nitride (AlN) epilayers

High-quality AlN epilayers grown by PAMBE have been obtained after a comprehensive study of growth.[16] It was found that the III/V flux ratio and the growth temperature are the critical parameters to achieve high-quality AlN layers in terms of morphology and crystalline quality. A III/V ratio close to stoichiometry and high growth temperatures (≥900 °C) lead to optimal AlN epilayers, which exhibit a FWHM of 10 arcmin in X-ray diffraction and an average surface roughness of 48 Å. High-quality AlGaN alloys with an aluminium content ranging from 10% to 76% were also obtained at an optimal growth temperature of 770 °C.[17] The aluminium mole fraction has a linear dependence on the aluminium flux, indicating the ease of controlling of the AlGaN alloy compositions with PAMBE.

1.3.3 Indium gallium nitride (InGaN) and indium nitride (InN) epilayers

InGaN alloys have attracted increasing interest due to their large tunability of bandgap energy, high carrier mobility, superior light absorption and radiation resistance. However, it is still challenging to obtain high-quality InGaN alloys due to the large differences in bond energies and bond lengths, the large lattice mismatch as well as the different thermal dissociation temperatures of GaN and InN. Since InGaN alloys have a low thermal dissociation temperature, PAMBE is a good technique for growing indium-rich InGaN alloys. Kraus and co-workers investigated the incorporation of indium during the PAMBE growth of InGaN.[18] They found that the incorporation of indium is linearly dependent on the indium flux but inversely dependent on the growth temperature. It was thought that these behaviours were due to the different sticking coefficients of gallium and indium, thermal desorption and the segregation of indium. They also found that indium incorporation is dependent on the growth regime. For the near stoichiometric regime, indium desorption is the dominant process. For the metal-rich regime, the effect of indium segregation is severe and produces a higher indium content phase. This was observed in the growth of InGaN with an indium content of 25%. Extensive PL was observed for an InGaN epilayer grown at 520 °C with an indium content of 18.6%. InGaN epilayers with a higher indium content (>70%) were also obtained on InN templates using PAMBE at an optimal growth temperature of 550 °C. It was found that the quality of the materials is dependent on the InN template, so a specific process to nitridate sapphire substrates was developed to produce an optimal InN buffer layer.[19]

1.3.4 Nitride-based InGaN/GaN multi-quantum wells (MQWs)

The growth of InGaN/GaN MQWs using MBE has been extensively studied for applications for LEDs and LDs. Exceptional efficiency was achieved in InGaN/GaN MQW-based light-emitting devices despite a very high density of threading dislocations. This was attributed to the carriers' localization at the in-plane potential fluctuation due to compositional inhomogeneities in the MQWs.[20] The width of the quantum well, indium composition and growth temperature can affect the distribution of the indium composition in the wells, which modifies the optical properties of the InGaN/GaN QWs.[21–23] In addition, the intrinsic electric field in InGaN/GaN MQWs also plays an important role in emission efficiency and energy and was optimized for the emitting devices. However, realizing highly efficient long-wavelength visible LEDs and LDs remains very challenging due to the significant drop of the internal quantum efficiency if the indium content is increased in the InGaN QWs.[24] For instance, the performance of green LEDs is much lower than that of blue LEDs. This was attributed to several factors, including indium segregation in the QWs, a piezoelectric field owing to the quantum confined Stark effect, the generation of dislocations and the decomposition of the QWs in the doping layer during growth or post-growth annealing. Due to these challenges, the longest visible wavelength obtained for LDs is around 485 nm. The LD used was grown by MOCVD with an indium content of 30% in the QWs.[25] To overcome these problems, an attempt was made to grow InGaN/InGaN MQWs using PAMBE. Siekacz *et al.* produced MQWs exhibiting PL at a wavelength of 510 nm.[83] Furthermore, InN/InGaN MQWs have been obtained using PAMBE, and the PL was successfully extended into the near infrared, which is very important for telecoms. For instance, PL at wavelengths of 1.55 μm[26] and 1.75 μm[27] have been demonstrated for these MQWs. On the other hand, GaN/AlGaN MQWs have been developed and LEDs operating at a deep ultraviolet wavelength of 273 nm have been obtained.[28]

1.3.5 Doping in nitride materials

When fabricating devices, it is essential to be able to introduce p-type and n-type materials. Silicon and magnesium are typical dopants used widely for n-type and p-type GaN, respectively, and GaN-based devices, including LEDs and lasers, have been produced. However, doping is challenging for structures that require aluminium-rich AlGaN and indium-rich InGaN alloys. It is difficult to obtain p-type doping InGaN with an indium content above 30% using magnesium.[29] Recently carbon has received considerable interest as an acceptor because it has a similar atomic radius and electronegativity as nitrogen. CBr_4 has been shown to be an effective carbon source for GaN grown by PAMBE[30,31] and a doping level up to 10^{19} cm^{-3} was reported in PAMBE-grown GaN.[32] The calculation of the ionization energy of carbon as an acceptor (substituting for nitrogen) and as a donor (substituting for gallium or indium) in InGaN alloys across the entire range of indium compositions revealed that carbon incorporation is more favourable when it acts as an acceptor (substituting for nitrogen) leading to p-type doping.[33] This theoretical study combined with experimental work indicates the great potential of carbon as a dopant for realizing p-doping indium-rich InGaN alloys. For AlGaN alloys, silicon has difficulty in producing n-type doping if the aluminium content is above 49%, which is mainly due to the increased ionization energy as shown in Fig. 1.5.[34] A higher electron concentration can be obtained using MBE compared with MOCVD, and a doping concentration of 8×10^{18} cm^{-3} in AlGaN with 50% aluminium has been demonstrated;[35] however, AlN doping is still a challenge, which impedes progress in producing deep ultraviolet AlN LEDs.

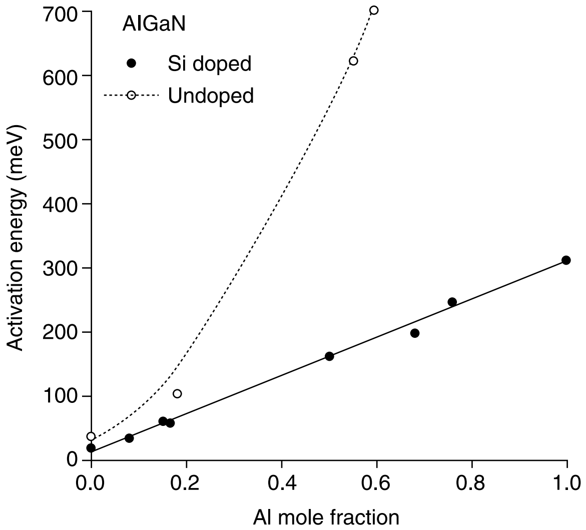

1.5 Activation energies of silicon-doped (full circles) and nominally undoped (open circles) $Al_xGa_{1-x}N$. The lines are drawn as guides.[34]

1.3.6 Light emitters based on nitride MQWs

These impressive research efforts in the development of MBE-grown III-nitride materials have resulted in LEDs and LDs with a wide spectral range from 273–480 nm (see Table 1.1). Grandjean *et al.* reported UV LEDs grown by ammonia MBE operating at a wavelength of 390 nm in 1998.[36] In 2004, Waltereit *et al.* produced LEDs operating at 480 nm with an external efficiency >1.5%, which is close to that for LEDs grown by MOCVD.[37] Skierbiszewski and co-workers have made a considerable contribution to nitride LDs. In 2004, they produced blue-violet InGaN/GaN MQWs LDs operating at 408 nm, room temperature and pulsed operation with a threshold current of 12 kA/cm^2 and a high output power of 0.83 W;[38] in 2006, they achieved room temperature InGaN/GaN MQW LDs operating at a wavelength of 411 nm with a threshold current of 4.2 kA/cm^2 and a high output power of 60 mW.[39] Liao and co-workers produced LEDs operating at sub-300 nm wavelengths (275 nm) in 2011.[28] In addition, white light LEDs have been proposed by monolithically stacking blue and yellow nitride MQWs; they have a reduced cost and increased efficiency compared with phosphor-based LEDs. Although such LEDs have been produced by MOCVD, the drawback of this structure is that the chromaticity coordinates strongly depend on the injection current. Damilano *et al.* produced PAMBE-grown white LEDs using a yellow converter of five-period $In_{0.2}Ga_{0.8}N$ (4 nm)/GaN (7.5 nm) MQWs followed by monolithic-grown blue light MQWs.[40] The InGaN and GaN were grown at temperatures of 550 °C and 800 °C, respectively. However, optimal light mixing conditions are still not obtainable in such conventional MQW structures.

Table 1.1 Some of the key developments and milestones achieved during the development of MBE-grown LEDs and LDs

Device	Group, year
390 nm LEDs	Grandjean *et al.*, 1998 [36]
480 nm LEDs	Waltereit *et al.*, 2004 [37]
408 nm LDs	Skierbiszewski *et al.*, 2004 [38]
411 nm LDs	Skierbiszewski *et al.*, 2006 [39]
White light LEDs	Damilano *et al.*, 2008 [40]
273 nm LEDs	Liao *et al.*, 2011 [28]

1.4 Nitride nanocolumn (NC) materials

One-dimensional nanocolumns (NCs) are newly emerging materials and have attracted increasing attention in the last few years due to a number of advantages. NC materials have large aspect ratios and 3D stress relief mechanisms leading to dislocation-free structures.[41] Their small footprint helps to release strain and thermal expansion. In light-emitting device applications, these structures have a high light extraction efficiency. The light emission colours can be tuned from blue to red by modifying the NC diameter.[42] Furthermore, core-shell NC structures are obtainable, which supress the strong surface recombination and improve the efficiency of the light-emitting devices.[43] Consequently, nitride NC materials are a promising candidate for a breakthrough development in light-emitting devices.

1.4.1 Self-catalyst growth of GaN NCs using MBE

Nitride NCs can be grown by MBE using catalytic or self-catalytic (catalyst-free) methods. The growth method using a catalyst is called the vapour-liquid-solid (VLS) mechanism and is generally adopted in chemical vapour deposition (CVD). Metals such as gold,[44] nickel[45] and molybdenum[46] have been used as the catalyst. In MBE, nitride NCs are more generally grown without a metal catalyst. The earliest report of the growth of GaN NCs using PAMBE was from Sophia University, Tokyo,[47] and then a group from Ciudad University, Madrid, also produced GaN NCs grown by PAMBE.[48] Both groups reported that the nitrogen-rich growth condition leads to the formation of GaN NCs in PAMBE. Since then the best growth conditions for GaN NCs have been explored and optimized to achieve high-quality NCs with controllable geometry, aspect ratio and area density. The V/III flux ratio is the crucial factor for producing NCs of GaN,[48] AlN[49] as well as InN.[50] Figure 1.6 shows the typical morphology of GaN NC materials grown under nitrogen-rich condition (a) and a GaN compact epilayer grown under gallium-rich condition (b). These observations were interpreted as being due to a mechanism where the high V/III flux ratio reduces the diffusion

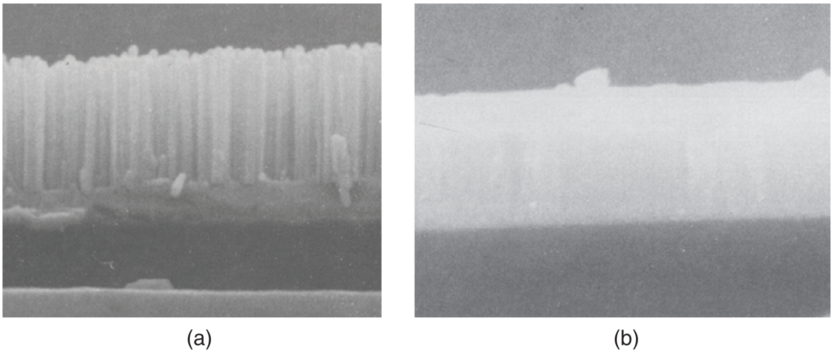
(a) (b)

1.6 Scanning electron micrographs (SEMs) of GaN NCs grown directly on Si (111) substrates under (a) nitrogen-rich and (b) gallium-rich conditions.[48]

distance of gallium adatoms and supresses the coalescence of nucleation sites.[51] It was consequently concluded that VLS is not the growth mechanism in PAMBE-grown NCs, instead, the growth of NCs is driven by a process that involves nucleation and the diffusion of adatoms on the surface:

1. GaN precursor islands nucleate on the surface. Such islands are plastically relaxed and result from different growth modes. For GaN NCs grown on an AlN buffer layer, the nucleation of GaN islands is driven by the Stranski–Krastanow (SK) growth mode; for GaN NCs grown on a different substrate, such as bare oxidized[52] or nitridated[51] silicon substrates, the islands form due to the Volmer–Weber (VW) growth mode.
2. GaN islands develop with further deposition and then initiate the growth of NCs when they reach a critical size.
3. The growth of NCs strongly depends on two contributions: one is growth due to the direct impinging of atoms on a NC apex. The other contribution occurs when adatoms arrive on the surface. They diffuse to the base of a NC then climb up along the lateral sidewalls of the NC to the apex and become incorporated into the crystal.

Figure 1.7 shows these growth processes. Furthermore, Debnath *et al.*[53] suggested that adsorption at the tip of a NC would have a significant effect on a NC with a thick diameter, and this was used to interpret the observation that an ensemble of NCs is normally a mixture of short and thick NCs with long and thin ones.

High-quality GaN NCs have been successfully grown on a few different substrates including silicon (111),[54] sapphire (0001)[55] and silicon (001).[56] Although there is a big lattice mismatch, the PAMBE-grown NCs on these substrates demonstrate fully relaxed epitaxial growth resulting in *strain-free*, *dislocation-free* and *extended defect-free* high-quality single crystals, which have excellent optical properties.[57–59] For the NCs grown on silicon substrates, there is a standard

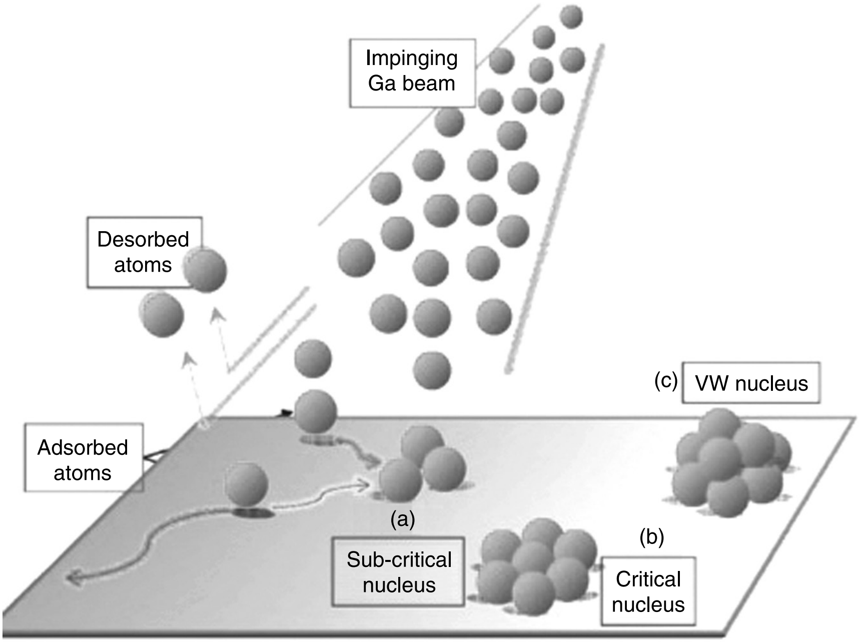

1.7 Growth of NCs from stable nuclei including direct incorporation from the impinging gallium flux (*j*(L)), and growth where gallium diffuses on the substrate (*j*(D)) to the base of a NC and up to the apex.[51]

procedure to desorb the native oxide:[54] the silicon substrate is first etched by diluted HF, then it is transferred into the MBE system followed by thermal treatment in a vacuum at 800 °C, which ensures an excellent surface condition and a 7 × 7 RHEED pattern is visible. Three different procedures have been used to start the growth of NCs: on a buffer layer of GaN grown at low temperatures of 500–600 °C,[54] on a buffer layer of AlN[17] and the direct growth of NCs on a bare silicon substrate.[57,60] The growth of the GaN NCs follows at a typical temperature of 720 °C. The influence of the growth conditions on NC geometry, such as lateral dimension, height and number density, has been comprehensively investigated. It was reported that the tuneable range can be from <20 nm to ~800 nm for the lateral dimension, from 50 nm to 3 μm for the height, and of the order of $\sim 10^6$ to $10^7\,\mathrm{cm}^{-2}$ for the area number density.[54] Uniform GaN NCs with a narrow lateral dimension variation of 20–40 nm on silicon (001) have been produced;[56] these NCs are strain-free and exhibit intense narrow excitonic PL indicating the high quality.

Besides these hexagonal GaN (h-GaN) NCs, cubic GaN (c-GaN) NCs have also been obtained by PAMBE on a silicon (111) substrate.[61] After the thermal de-oxidization of silicon, a thin AlN layer was grown to improve the orientation of the GaN NCs. h-GaN NCs were then grown in a nitrogen-rich condition at a growth temperature of 850 °C. The substrate temperature was then reduced to 580 °C to grow a c-GaN NC section using the same nitrogen and gallium fluxes. A PL emission peak at 3.27 eV was observed and attributed to the band-edge transition from the c-GaN NC section. Due to the high homogeneity of c-GaN, this PL linewidth is narrow and makes the donor-bound exciton visible. The realization of a high quality c-GaN section on h-GaN NCs could lead to novel devices.

1.4.2 Aluminium gallium nitride (AlGaN) NCs

In addition to the success in growing GaN NC materials using PAMBE, wide bandgap AlGaN NCs have been attempted. Landré *et al.* grew AlN NCs using catalyst-free PAMBE and described the structural and optical properties.[62] The AlN NCs were grown on a substrate of silicon (100) covered with a thin layer of a few monolayers of SiO_2. The aluminium/nitrogen flux ratio was fixed to about 1/6, to ensure nitrogen-rich conditions. The growth temperature was in the range 900–950 °C, which is higher than that for GaN NCs to compensate for the low diffusion rate of aluminium compared to gallium. The resulting AlN NCs were assessed by high-resolution TEM, Raman spectroscopy and PL measurements. It was observed that the NCs were completely strain relaxed, which is thought to be because they match the SiO_2/Si. PL with an energy of 6.04 eV at 10 K was observed, dominated by near-band edge emission. It was also found that there was no wetting layer at the base of the NCs, suggesting that the growth obeys a VW mode. AlGaN NCs with an aluminium content up to 30% have been produced.[63,64] It was found that the incorporation of aluminium increases the diameter of the resulting NCs. In addition, it was observed that beryllium-doping led to large vertical GaN ribbons or GaN NCs with a slightly conical shape.[63] These observations indicated that surface diffusion has a strong effect on the growth of NCs.

1.4.3 InN and InGaN NCs

Due to the narrow bandgap energy of InN (0.6 eV) and the high carrier mobility, the growth of InN NCs by PAMBE has been extensively studied and optimized.[65,66] The growth temperature and the V/III flux ratio are the major factors that determine the resulting InN structures. Hsiao *et al.* grew InN structures on an InN buffer layer and an AlN buffer layer. A fixed indium flux of 2.5×10^{-7} Torr was used with various nitrogen/indium flux ratios at various growth temperatures.[65] They found that materials grown at a temperature above 530 °C and nitrogen/indium flux ratio of 40 were grain-like InN, but a lower temperature (450–500 °C) led to InN NCs, while InN grown at temperatures of 450 °C with a nitrogen/indium flux ratio of 20 produced an epilayer. Chang *et al.*[67] developed a new PAMBE technique for growing high-quality InN NCs on a silicon (111) substrate using an *in situ* indium seeding layer. This growth technique produced well-separated and uniform InN NCs, which were nearly defect free and not tapered, as shown in Fig. 1.8. The PL has a narrow spectral linewidth of 13 meV. In addition, a low residual carrier concentration of $\sim 1 \times 10^{16}\,\text{cm}^{-3}$ was achieved in such InN NCs. These achievements indicate the great potential of this technique for device-quality InN NCs. The growth temperature is also a major factor for modifying the morphology of InN materials grown with this technique. Figure 1.9 shows InN materials grown in a nitrogen-rich condition at different temperatures. X-ray diffraction measurements indicate that the resulting materials are mono-crystalline.

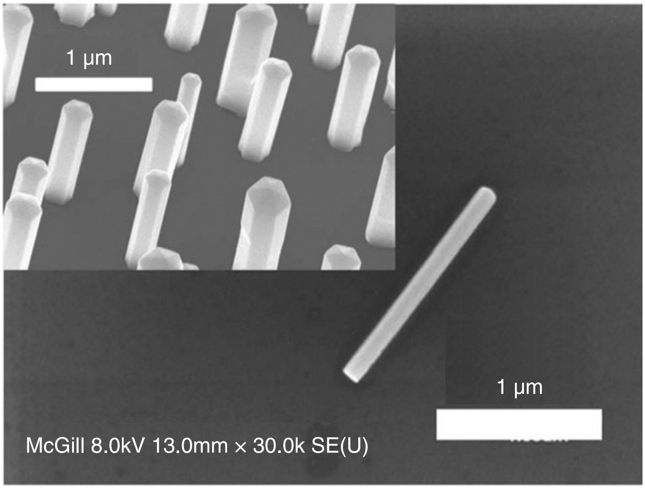
1 µm
1 µm
McGill 8.0kV 13.0mm × 30.0k SE(U)

1.8 SEM image of a single non-tapered InN NC and an InN NC ensemble grown on an Si (111) substrate (inset).[67]

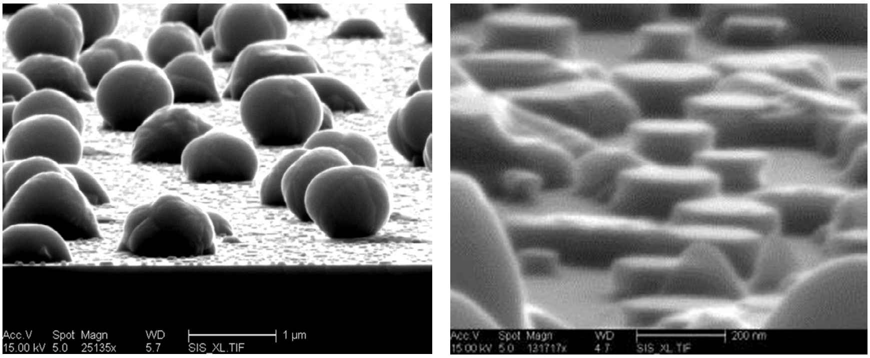
Acc.V Spot Magn WD 1 µm
15.00 kV 5.0 25135x 5.7 SIS_XL.TIF
Acc.V Spot Magn WD 200 nm
15.00 kV 5.0 131717x 4.7 SIS_XL.TIF

(a) (b)

1.9 SEM images of InN grown at different temperatures: (a) InN grains grown at 550 °C and (b) short InN NCs grown at 450 °C.

1.4.4 Overgrowth of nitride NCs

The overgrowth of high-quality nitride epilayers on GaN NCs has been achieved. In particular, these overgrown epilayers were reported to be *strain free* and *dislocation free* as discovered for a 2.7-μm-thick overgrown GaN epilayer on GaN NCs.[68] A sapphire substrate was etched by a mixture of H_2SO_4 and H_3PO_4 at 110 °C for 30 min followed by the deposition of titanium onto the back, then it was loaded into the MBE system and thermally cleaned at 950 °C for 30 min. Growth started after nitridation at 750 °C for 20 min. An AlN buffer layer was grown at 850 °C with a nitrogen flow of 5.3 sccm and RF power of 450 W. After this, the GaN NCs started to grow at a growth rate of 2.3 um/h under a nitrogen-rich condition. Then the growth condition was changed to a gallium-rich regime, leading to the direct growth of a GaN epilayer on the NCs. Figure 1.10 shows a scanning electron micrograph of the resulting free-standing GaN epilayer grown on the GaN NCs on a sapphire substrate. This method is a new route for fabricating high-quality *dislocation-free* GaN epilayers on foreign substrates, and is very important to the nitride community.

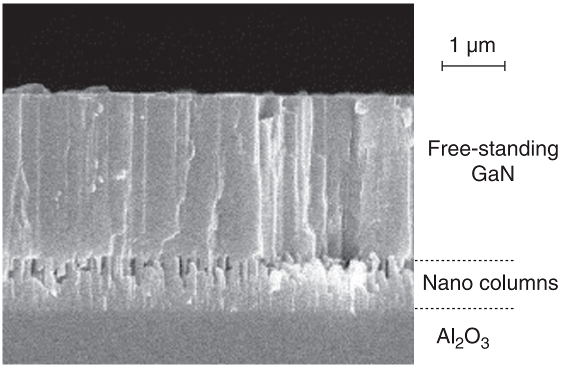

1.10 A cross-sectional SEM image of overgrown GaN on NCs on a sapphire substrate.[68s]

1.5 Nitride nanostructures based on NCs

1.5.1 Quantum disks embedded in NCs

GaN quantum disks embedded in AlGaN NCs and AlN/GaN Bragg reflectors were produced by Ristić *et al.*[69] Such structures are extremely attractive for single photon sources. The nanocavities formed in these NCs are crack free and defect free, which was attributed to relaxation at the silicon interface and the high aspect ratio. The PL was tuned by modifying the thickness of the GaN quantum disks and the aluminium content of the AlGaN. PL emissions at peak energy varied from 3.4 to 4.0 eV.

Recently, InGaN/GaN dots-in-NCs have attracted increasing attention due to a number of unique properties including significantly reduced threading dislocation densities, suppressed polarization fields, enhanced light extraction efficiency, the capability of accommodating InGaN dots with a larger indium content, as well as the capacity for monolithic integration with large area and low-cost silicon substrates. Consequently such nanostructures have great potential in producing advanced LEDs compared with conventional thin-film MQWs. It has been a big challenge to realize GaN-based LEDs operating in the red spectral range due to the huge lattice mismatch. Mi *et al* explored the growth of such nanostructures using PAMBE. Red LEDs based on such nanostructures operating at room temperature were obtained with an internal efficiency of up to 30%.[70] They are very important for realizing phosphor-free solid-state lighting and full colour displays. Full-colour white light InGaN/GaN dots-in-NCs LEDs with an internal efficiency of 56.8% have been produced.[71–73] Figure 1.11 is a schematic of a core-shell NC (CSNC) white light LED. The emission of white light is realized by a stack of InGaN nanodisks (NDs) embedded in a GaN nanorod p-n junction. To optimize the light mixing effect, different thicknesses (10–25 nm) and indium content in the InGaN nanodisks were obtained through varying the growth temperature and indium/gallium flux ratio.[73] The number and positions of the nanodisks are important for obtaining the appropriate light mixing conditions. Additionally, in such LED devices, an indium content up to 50% has been obtained

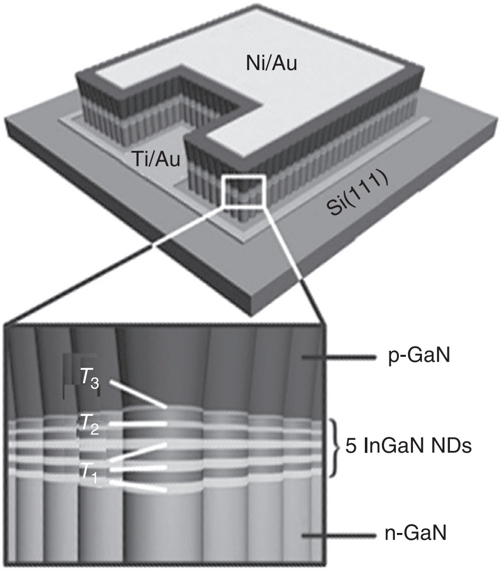

1.11 InGaN/GaN CSNC white light LED: the active regions contain multiple InGaN nanodisks with various thicknesses and indium content.[73]

in the InGaN dots. These results clearly indicate the advantages of 1D NC materials for realizing optimal light mixing conditions.

1.5.2 Core-shell NCs

It is well known that NC materials have a large number of surface states leading to significant surface recombination, which reduces carrier mobility and radiative recombination efficiency in NCs. Consequently, reducing the number of surface states is needed before the advantages of NCs can be exploited to produce highly efficient NC devices. Core-shell NCs (CSNCs) are a promising class of semiconductor nanostructures. The effect of surface states is suppressed resulting in a significant potential for optoelectronic device applications. Hestroffer *et al.* produced GaN/AlN CSNCs using PAMBE.[74] Growth started from GaN NCs under a nitrogen-rich condition and a growth temperature of ~850 °C followed by deposition of AlN onto the top, which resulted in the formation of AlN shell layers around the GaN core NCs. Growth was attributed to the significant lateral growth of AlN due to the limited diffusion of aluminium on the NW facets (see references in Nguyen *et al.*[74]). GaN/AlGaN CSNCs have been produced with a wide tuneable emission spectral range of 280–400 nm.[75] To obtain such CSNCs, 200 nm-high GaN core NCs were first grown at a temperature of 750 °C and a growth rate of 3 nm/min, then AlGaN shells were grown at a temperature of 800 °C and a growth rate of 1.5 nm/min. The aluminium content in the AlGaN shell layers was controlled by varying the aluminium/gallium flux ratio. The nitrogen plasma was maintained in a nitrogen-rich condition: an N_2 flow of 1 sccm and a RF power of 350 W. A high internal efficiency up to 58% from such CSNCs has been realized. In addition, InN/InGaN CSNCs have also been produced.[76] InN core NCs were first grown at a growth temperature of 470 °C and a growth rate of 3.3 nm/min (a 0.5 nm-thick indium seeding layer was used to initiate NCs growth), then the InGaN shell layers were produced at a growth temperature of 500 °C and gallium and indium beam equivalent pressure fluxes of 6.4×10^{-8} and 1×10^{-8} Torr, respectively. A high internal quantum efficiency of 62% for PL at room temperature was obtained and attributed to strong carrier confinement and the nearly intrinsic InN core NCs. These studies reveal the advantages for LED and other optoelectronic device applications.

1.5.3 Selective area growth of NCs

Although there has been significant progress in PAMBE-grown nitride NCs in the last few years, controlling the size, position and geometry of NCs as well as the composition of the alloys still remains a significant challenge. This causes difficulties in the control of emission wavelengths and material processing of NC devices. Consequently, producing controllable NCs with uniform height is highly demanding. Selective area growth on patterned substrates has been proposed for circumventing the difficulties to produce ordered and uniform NCs. In this approach, NCs only grow on regions of the patterned substrate with pores. Various mask materials have been considered including SiO_2/GaN,[77] Ti/GaN[78–80] and SiN_x/AlN.[81] The first selective area growth of GaN NCs was demonstrated by Kishino and co-workers on Ti/GaN/sapphire templates.[78,80] The effect of the growth parameters on the morphologies of the resulting materials has been studied. Growth temperature is a critical factor for NCs: a growth temperature in the range 880–900 °C produced NCs. There was no selective area growth at lower temperatures because there is insufficient diffusion; however, higher temperatures increased the inhomogeneity of the geometry of the NCs and decreased the diameter of the NCs due to enhanced gallium desorption and diffusion.[80] They also reported that the V/III flux ratio dramatically affected the geometry of the resulting NCs. A high flux ratio, i.e., a nitrogen-rich condition, increased the height and diameter of the NCs.[78] The effect of the aperture diameter of the pattern on the geometry of the resulting NCs was systematically investigated on NCs grown on SiN_x/AlN templates.[81] Single NCs were obtained for a pattern with an aperture diameter ≤500 nm. A larger opening produced coalesced nanostructures with rough and faceted tops.

Regularly aligned NCs in a 2D array leads to the photonic crystal effect, which can be used to enhance and tune the light emission from an NC ensemble. Kouno *et al.*[82] produced a rectangular array of GaN NCs consisting of eight-period InGaN/GaN MQWs. The 2D array had a horizontal lattice constant of 230 nm and a vertical lattice constant of 245 nm. The emission of a specific wavelength was enhanced in such 2D NCs array as shown in Fig. 1.12. The figure clearly

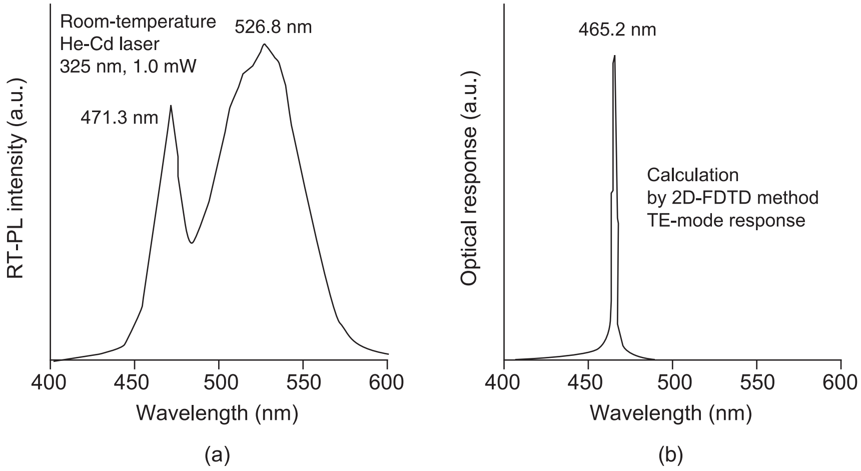

1.12 (a) Low-excitation room-temperature PL (RT-PL) spectra of eight-period InGaN/GaN MQWs embedded on top of GaN rectangular-lattice NCs, and (b) light response spectrum calculated by a 2D-FDTD method.[82]

shows that the experimental specific peak emission at a wavelength of 471 nm coincides with the calculated spectrum based on a 2D finite-difference time domain (2D-FDTD) method using the assumption of a refractive index dispersion of GaN. This observation opens a new route for tuning the light emitted from NC arrays.

1.6 Conclusion

In summary, MBE has demonstrated its capacity for producing high-quality nitride materials. A variety of devices have been realized with performances comparable to those grown by MOCVD. This growth technique has also exhibited its advantages in producing ultraviolet and near infrared LEDs. These achievements indicate the great potential of MBE for producing commercial devices. More importantly, the NC materials grown by MBE have seen significant progress in the last few years. It is proposed that MBE is a very promising route for producing high-performance solid-state light-emitting devices.

1.7 References

1 S. E. Hooper, M. Kauer, V. Bousquet, K. Johnson, J. M. Barnes, *et al.*, InGaN multi quantum well laser diodes grown by moleculor beam epitaxy, *Electrn. Lett.* 40, 33–34 (2004).

2 Z. Yang, L. K. Li and W. Wang, GaN growth by molecular beam epitaxy at high growth temperature rates using ammonia as the nitrogen source, *Appl. Phys. Lett.* 67, 1686–1688 (1995).

3 W. S. Tan, M. Kauer, S. E. Hooper, J. M. Barnes, M. Rossetti, *et al.*, High-power and long-lifetime InGaN blue–violet laser diodes grown by molecular beam epitaxy, *Electron. Lett.* 44, 351–352 (2008).

4 A. Ohtani, K. S. Stevens and R. Beresford, Microstructure and photoluminescence of GaN grown on Si(111) by plasma-assisted moecular beam epitaxy, *Appl. Phys. Lett.* 65, 61–63 (1994).

5 Z. Yang, F. Guarin, I. W. Tao, W. I. Wang and S. S. Iyer, Approach to obtain high quality GaN on Si and SiC-on-silicon-on-insulator compliant substrate by molecular-beam epitaxy, *J. Vac. Sci. Technol. B* 13, 789–791 (1995).

6 J. Neugebauer, T. K. Zywietz, M. Scheffler, J. E. Northrup, H. Chen, *et al.*, Adatom kinetics on and below the surface: the existence of a new diffusion channel, *Phys. Rev. Lett.* 90, 056101 (2003).

7 H. Okumura, K. Balakrishnan, H. Hamaguchi, T. Koizumi, S. Chichibu, *et al.*, Analysis of MBE growth mode for GaN epilayers by RHEED, *J. Crys. Grow.* 189/190, 364–369 (1998).

8 P. Hacke, G. Feuillet, H. Okumura and S. Yoshida, Monitoring surface stoichiometry with the (2 × 2) reconstruction during growth of hexagonal-phase GaN by molecular beam epitaxy, *Appl. Phys. Lett.* 69, 2507 (1996).

9 Z. Yu, S. K. Buczkowski, N. C. Giles, T. H. Myers and M. R. Richards-Babb, The effect of atomic hydrogen on the growth of gallium nitride by molecular beam epitaxy, *Appl. Phys. Lett.* 69, 2731 (1996).

10 E. J. Tarsa, B. Heying, X. H. Wu, P. Fini, S. P. DenBaars, *et al.*, Homoepitaxial growth of GaN under Ga-stable and N-stable conditions by plasma-assisted molecular beam epitaxy, *J. Appl. Phys.* 82, 5472 (1997).

11 B. Heying, E. J. Tarsa, C. R. Elsass, P. Fini, S. P. DenBaars, *et al.*, Dislocation mediated surface morphology of GaN, *J. Appl. Phys.* 85, 6470 (1999).

12 B. Heying, R. Averbeck, L. F. Chen, E. Haus, H. Riechert, *et al.*, Control of GaN surface morphologies using plasma-assisted molecular beam epitaxy, *J. Appl. Phys.* 88, 1855 (2000).

13 J. F. Falth, S. K. Davidsson, X. Y. Liu and T. G. Anderson, Influence of Al/N flux ratio during nucleation layer growth on the structural properties of AlN grown on sapphire by molecular beam epitaxy, *Appl. Phys. Lett.* 87, 161901 (2005).

14 N. Faleev, H. Li and W. J. Schaff, Low density of threading dislocations in AlN grown on sapphire, *J. Appl. Phys.* 101, 093516 (2007).

15 S. W. Lee, T. Minegishi, W. H. Lee, H. Goto, H. J. Lee, *et al.*, Strain-free GaN thick films grown on single crystalline ZnO buffer layer with *in situ* lift-off technique, *Appl. Phys. Lett.* 90, 061907 (2007).

16 E. Calleja, M. A. Sanchez-Garcia, E. Monroy, F. J. Sanchez, E. Munoz, *et al.*, Growth kinetics and morphology of high quality AlN grown on Si(111) by plasma-assisted molecular beam epitaxy, *J. Appl. Phys.* 82, 4681 (1997).

17 E. Calleja, *et al.*, Growth of III-nitrides on Si(111) by molecular bema epitaxy doping, optical, and electrical properties, *J. Crys. Grow.* 201/202, 296 (1999).

18 A. Kraus, S. Hammadi, J. Hisek, R. Bub, H. Jonen, *et al.*, Growth and characterization of InGaN by RF-MBE, *J. Cryst. Grow.* 323, 72 (2011).

19 H. Naoi, M. Kurouchi, D. Muto, T. Araki, T. Miyajima, *et al.*, Growth of high quality In-rich InGaN alloys by RF-MBE for the fabrication of InN-based quantum well structures, *J. Cryst. Grow.* 288, 283 (2006).

20 S. Chichibu, T. Azuhata, T. Sota and S. Nakamura, Spontaneous emission of localized excitons in InGaN single and multiquantum well structures, *Appl. Phys. Lett.* 69, 4188 (1996).

21 M. Stevens, A. Bell, M. R. McCartney, F. A. Ponce, H. Marui, *et al.*, Effect of layer thickness on the electrostatic potential in InGaN quantum wells, *Appl. Phys. Lett.* 85, 4651 (2004).

22 Y.-S. Lin, K.-J. Ma, C. Hsu, S.-W. Feng, Y.-C. Cheng, *et al.*, Dependence of composition fluctuation on indium content in InGaN/GaN multiple quantum wells, *Appl. Phys. Lett.* 77, 2988 (2000).

23 F. Schulze, J. Blasing, A. Dadgar and A. Krost, Time-delayed indium incorporation in ultrathin (In_xGa_{1-x} N/GaN) multiple quantum wells grown by metaorganic vapor phase epitaxy, *Appl. Phys. Lett.* 82, 4558 (2003).

24 C. Wetzel and T. Detchprom, Development of high power green light emitting diode chips, *MRS Internet J. Nitride Semicond. Res.* 10(2) (2005).

25 K. S. Kim, J. K. Son, S. N. Lee, Y. J. Sung, H. S. Paek, *et al.*, Characteristics of long wavelength InGaN quantum well laser diodes, *Appl. Phys. Lett.* 92, 101103 (2008).

26 J. Grandal, J. Pereiro, A. Bengoechea-Encabo, S. Fernández-Garrido, M. A. Sánchez-García, *et al.*, InN/InGaN multiple quantum wells emitting at 1.5 μm grown by molecular beam epitaxy, *Appl. Phys. Lett.* 98, 061901 (2011).

27 S.-B. Che, W. T. Y. Ishitani, A. Yoshikawa, T. Matsuda, *et al.*, Fine-structure N-polarity InN/InGaN multiple quantum wells grown on GaN underlayer by molecular beam epitaxy, *Appl. Phys. Lett.* 86, 261903 (2005).

28 Y. Liao, C. Thomidis, C. Kao and T. D. Moustakas, AlGaN based deep ultraviolet light emitting diodes with high internal quantum efficiency grown by molecular beam epitaxy, *Appl. Phys. Lett.* 98, 081110 (2011).

29 R. Dahal, B. Pantha, J. Li, J. Y. Lin and H. X. Jiang, InGaN/GaN multiple quantum well solar cells with long operating wavelengths, *Appl. Phys. Lett.* 94, 063505 (2009).

30 D. S. Green, U. K. Mishra and J. S. Speck, Carbon doping of GaN with CBr_4 in radio-frequency plasma-assisted molecular beam epitaxy, *J. Appl. Phys.* 95, 8456 (2004).

31 C. Poblenz, P. Waltereit, S. Rajan, S. Heikman, U. K. Mishra, *et al.*, Effect of carbon doping on buffer leakage in AlGaN/GaN high electron mobility transistors, *J. Vac. Sci. Technol. B* 22(3), 1145 (2004).

32 A. Zado, E. Tschumak, J. W. Gerlach, K. Lischka and D. J. As, Carbon as an acceptor in cubic GaN/3C-SiC, *J. Cryst. Grow.* 323, 88 (2011).

33 C. Tablero, Ionization energy levels in C-doped $In_xGa_{1-x}N$ alloys, *Appl. Phys. Lett.* 97, 192102 (2010).

34 R. Zeisel, M. W. Bayerl, S. T. B. Goennenwein, R. Dimitrov, O. Ambacher, *et al.*, DX-behavior of Si in AlN, *Phys. Rev. B* 61, R16283 (2000).

35 M. Ahoujja, J. L. McFall, Y. K. Yeo, R. L. Hengehold and J. E. Van Nostrand, Electrical and optical investigation of MBE grown Si-doped $Al_xGa_{1-x}N$ as a function of Al mole fraction up to 0.5, *Mater. Sci. Engineering* B91–92, 285 (2002).

36 N. Grandjean, J. Massies, M. Leroux and P. Lorenzini, Ultraviolet GaN light-emitting diodes grown by molecular beam epitaxy using NH_3, *Appl. Phys. Lett.* 72, 82 (1998).

37 P. Waltereit, H. Sato, C. Poblenz, D. S. Green, J. S. Brown, *et al.*, Blue GaN-based light-emitting diodes grown by molecular-beam epitaxy with external quantum efficiency greater than 1.5%, *Appl. Phys. Lett.* 84, 2748 (2004).

38 C. Skierbiszewski, Z. R. Wasilewski, M. Siekacz, A. Feduniewicz, P. Perlin, *et al.*, Blue-violet InGaN laser diodes grown on bulk GaN substrates by plasma-assisted molecular-beam epitaxy, *Appl. Phys. Lett.* 86, 011114–011116 (2004).

39 C. Skierbiszewski, P. Wiśniewski, M. Siekacz, P. Perlin, A. Feduniewicz-Zmuda, *et al.*, 60 mW continuous-wave operation of InGaN laser diodes made by plasma-assisted molecular-beam epitaxy, *Appl. Phys. Lett.* 88, 221108 (2006).

40 B. Damilano, A. Dussaigne, J. Brault, T. Huault, F. Natali, *et al.*, Monolithic white light emitting diodes using a (Ga,In)N/GaN multiple quantum well light converter, *Appl. Phys. Lett.* 93, 101117 (2008).

41 D. Zubia and S. D. Hersee, Nanoheteroepitaxy: the application of nanostructuring and substrate compliance to the heteroepitaxy of mismatched semiconductor materials, *J. Appl. Phys.* 85, 6492 (1999).

42 I. Sekiguchi, K. Kishino and A. Kikuchi, Emission color control from blue to red with nanocolumn diameter of InGaN/GaN nanocolumn arrays grown on same substrate, *Appl. Phys. Lett.* 96, 231104 (2010).

43 A. Waag, X. Wang, S. Fündling, J. Ledig, M. Erenburg, *et al.*, The nanorod approach: GaN NanoLEDs for solid state lighting, *Phys. Status Solidi C* 8, 2296 (2011).

44 B. Liu, Y. Bando, C. Tang, F. Xu and D. Golberg, Quasi-aligned single-crystalline GaN nanowire arrays, *Appl. Phys. Lett.* 87, 073106 (2005).

45 Q. Li and G. T. Wang, Improvement in aligned GaN nanowires growth using submonolayer Ni catalyst films, *Appl. Phys. Lett.* 93, 043119 (2008).

46 F. Shi, H. Li and C. Xue, GaN nanorods catalyzed with Mo: effect of ammoniating time on microstructure, morphology, and optical properties, *J. Mater Sci. Mater. Electron.* 21, 1249 (2010).

47 M. Yoshizawa, A. Kikuchi, M. Mori, N. Fujita and K. Kishino, Growth of self-organized GaN nanostructures on Al_2O_3(0001) by RF-radical source molecular beam epitaxy, *Jpn. J. Appl. Phys. Part 2* 36, L459 (1997).
48 M. Sanchez-Garcia, E. Calleja, E. Monroy, F. J. Sanchez, F. Calle, *et al.*, The effect of the III/V ratio and substrate temperature on the morphology and properties of GaN- and AlN-layers grown by molecular beam epitaxy on Si(111), *J. Cryst. Growth* 183, 23 (1998).
49 S. Karmann, H. P. D. Schenk, U. Kaiser, A. Fissel and Wo Richter, Growth of columnar aluminum nitride layers on Si(111) by molecular beam epitaxy, *Mater. Sci. Engineering B* 50, 228 (1997).
50 T. Stoica, R. Meijers, R. Calarco, T. Richter and H. Lüth, MBE growth optimization of InN nanowires, *J. Cryst. Growth* 290, 241 (2006).
51 J. Ristic, E. Calleja, S. Fernández-Garrido, L. Cerutti, A. Trampert, *et al.*, On the mechanisms of spontaneous growth of III-nitride nanocolumns by plasma-assisted molecular beam epitaxy, *J. Cryst. Growth* 310, 4035 (2008).
52 T. Stoica, E. Sutter, R. J. Meijers, R. K. Debnath, R. Calarco, *et al.*, Interface and wetting layer effect on the catalyst-free nucleation and growth of GaN nanowires, *Small* 4, 751 (2008).
53 R. K. Debnath, R. Meijers, T. Richter, T. Stoica, R. Calarco, *et al.*, Mechanism of molecular beam epitaxy growth of GaN nanowires on Si(111), *Appl. Phys. Lett.* 90, 123117 (2007).
54 L. W. Tu, C. L. Hsiao, T. W. Chi, I. Lo and K. Y. Hsieh, Self-assembled vertical GaN nanorods grown by molecular beam epitaxy, *Appl. Phys. Lett.* 82, 1601 (2003).
55 E. Calleja, M. A. Sanchez-Garcia, F. J. Sanchez, F. Calle, F. B. Naranjo, *et al.*, Luminescence properties and defects in GaN nanocolumns grown by molecular beam epitaxy, *Phys. Rev. B* 62, 16826 (2000).
56 L. Cerutti, J. Risti, S. Fernández-Garrido, E. Calleja, A. Trampert, *et al.*, Wurtzite GaN nanocolumns grown on Si(001) by molecular beam epitaxy, *Appl. Phys. Lett.* 88, 213114 (2006).
57 Y. S. Park, C. M. Park, D. J. Fu, T. W. Kang and J. E. Oh, Photoluminescence studies of GaN nanorods on Si (111) substrates grown by molecular-beam epitaxy, *Appl. Phys. Lett.* 85, 5718 (2004).
58 S. N. Yi, J. H. Na, K. H. Lee, A. F. Jarjour, R. A. Taylor, *et al.*, Photoluminescence properties of a single GaN nanorod with GaN/AlGaN multilayer quantum disk, *Appl. Phys. Lett.* 90, 101901 (2007).
59 H.-Y. Chen, H.-W. Lin, C.-H. Shen and S. Gwo, Structure and photoluminescence properties of epitaxially oriented GaN nanorods grown on Si(111) by plasma-assisted molecular-beam epitaxy, *Appl. Phys. Lett.* 89, 243105 (2006).
60 R. Calarco, R. J. Meijers, R. K. Debnath, T. Stoica, E. Sutter, *et al.*, Nucleation and growth of GaN nanowires on Si(111) performed by molecular beam epitaxy, *Nano Lett.* 7, 2248 (2007).
61 J. Renard, G. Tourbot, D. Sam-Giao, C. Bougerol, B. Daudin, *et al.*, Optical spectroscopy of cubic GaN in nanowires, *Appl. Phys. Lett.* 97, 081910 (2010).
62 O. Landré, V. Fellmann, P. Jaffrennou, C. Bougerol, H. Renevier, *et al.*, Molecular beam epitaxy growth and optical properties of AlN nanowires, *Appl. Phys. Lett.* 96, 061912 (2010).
63 K. A. Bertness, A. Roshko, N. A. Sanford, J. M. Barker and A. V. Davydov, Spontaneously grown GaN and AlGaN nanowires, *J. Crystal Growth* 287, 522 (2006).

64 J. Ristić, M. A. Sánchez-García, E. Calleja, J. Sanchez-Páramo, J. M. Calleja, *et al.*, AlGaN Nanocolumns grown by molecular beam epitaxy: optical and structural characterization, *Physica Status Solidi (a)*, 192, 60 (2002).

65 C.-L. Hsiao, L.-W. Tu, M. Chen, Z.-W. Jiang, N.-W. Fan, *et al.*, Polycrystalline to single-crystalline InN grown on Si(111) substrates by plasma-assisted molecular-beam epitaxy, *Jpn. J. Appl. Phys. Part 2* 44, L1076 (2005).

66 Y.-L. Chang, F. Li and Z. Mi, Optimization of the structural and optical quality of InN nanowires on Si(111) by molecular beam epitaxy, *J. Vac. Sci. Technol. B* 28, C3B7 (2010).

67 Y.-L. Chang, Z. Mi and F. Li, Photoluminescence properties of a nearly intrinsic single InN nanowire, *Adv. Funct. Mater.* 20, 4146–4151 (2010).

68 K. Kusakabel, A. Kikuchi and K. Kishino, Overgrowth of GaN layer on GaN nanocolumns by RF-molecular beam epitaxy, *J. Cryst. Growth* 237–239, 988 (2002).

69 J. Ristić, E. Calleja, A. Trampert, S. Fernández-Garrido, C. Rivera, *et al.*, Columnar AlGaN/GaN nanocavities with AlN/GaN Bragg reflectors grown by molecular beam epitaxy on Si(111), *Phys. Rev. Lett.* 94, 146102 (2005).

70 H. P. T. Nguyen, S. Zhang, K. Cui, A. Korinek, G. A. Botton, *et al.*, High efficiency InGaN/GaN dot-in-a-wire red light emitting diodes, *IEEE Photon. Tech. Lett.* 24, 321 (2012).

71 H. P. T. Nguyen, K. Cui, S. Zhang, S. Fathololoumi and Z. Mi, Full-color InGaN/GaN dot-in-a-wire light emitting diodes on silicon, *Nanotechnol.* 22, 445202 (2011).

72 H. P. T. Nguyen, S. Zhang, K. Cui, X. Han, S. Fathololoumi, *et al.*, p-type modulation doped InGaN/GaN dot-in-a-wire white light emitting diodes monolithically grown on Si(111), *Nano Lett.* 11, 1919 (2011).

73 H.-W. Lin, Y.-J. Lu, H.-Y. Chen, H.-M. Lee and S. Gwo, InGaN/GaN nanorod array white light-emitting diode, *Appl. Phys. Lett.* 97, 073101 (2010).

74 K. Hestroffer, R. Mata, D. Camacho, C. Leclere, G. Tourbot, *et al.*, The structural properties of GaN/AlN core–shell nanocolumn heterostructures, *Nanotechnol.* 21, 415702 (2010).

75 Q. Wang, H. P. T. Nguyen, K. Cui and Z. Mi, High efficiency ultraviolet emission from $Al_xGa_{1-x}N$ core-shell nanowire heterostructures grown on Si (111) by molecular beam epitaxy, *Appl. Phys. Lett.* 101, 043115 (2012).

76 K. Cui, S. Fathololoumi, M. Golam Kibria, G. A. Botton and Z. Mi, Molecular beam epitaxial growth and characterization of $InN/In_xGa_{1-x}N$ core/shell nanowire heterostructures on Si(111) substrates, *Nanotechnol.* 23, 085205 (2012).

77 S. D. Hersee, X. Y. Sun and X. Wang, The controlled growth of GaN nanowires, *Nano Lett.* 6, 1808 (2006).

78 K. Kishino, S. Sekiguchi and A. Kikuchi, Improved Ti-mask selective-area growth (SAG) by rf-plasma assisted molecular beam epitaxy demonstrating extremely uniform GaN nanocolumn arrays, *J. Cryst. Growth* 311, 2063 (2009).

79 A. Bengoechea-Encabo, F. Barbagini, S. Fernandez-Garrido, J. Grandal, J. Ristic, *et al.*, Understanding the selective area growth of GaN nanocolumns by MBE using Ti nanomasks, *J. Cryst. Growth* 325, 89 (2011).

80 H. Sekiguchi, K. Kishino and A. Kikuchi, Ti-mask selective-area growth of GaN by RF-plasma-assisted molecular-beam epitaxy for fabricating regularly arranged InGaN/GaN nanocolumns, *Appl. Phys. Express* 1, 124002 (2008).

81 K. A. Bertness, A. W. Sanders, D. M. Rourke, T. E. Harvey, A. Roshko, *et al.*, Controlled nucleation of GaN nanowires grown with molecular beam epitaxy, *Adv. Funct. Mater.* 20, 2911 (2010).

82 T. Kouno, K. Kishino, K. Yamano and A. Kikuchi, Two-dimensional light confinement in periodic InGaN/GaN nanocolumn arrays and optically pumped blue stimulated emission, *Optics Express* 17, 20440 (2009).

83 M. Siekacz, M. Sawicka, H. Turski, G. Cywinski, A. Khachapuridze, *et al.*, Optically pumped 500 nm InGaN green lasers grown by plasma-assisted molecular beam epitaxy, *J. Appl. Phys.* 110, 063110 (2011).

2

Modern metal-organic chemical vapor deposition (MOCVD) reactors and growing nitride-based materials

F. H. YANG, AIXTRON Taiwan Co Ltd, Taiwan

DOI: 10.1533/9780857099303.1.27

Abstract: Modern metal-organic chemical vapor deposition (MOCVD) systems have evolved to meet the demands for GaN-based light-emitting diodes (LEDs) and electronic devices. Growth mechanisms in MOCVD will be reviewed. Requirements for throughput, uniformity and reproducibility in modern MOCVD system will be discussed. The flow dynamics and thermal management of the two major types of reactor, the horizontal planetary reactor and the vertical close-coupled showerhead (CCS) reactor, will be introduced. The throughput, uniformity and reproducibility in state-of-the-art planetary and CCS reactors will be described. *In situ* monitoring systems in process control can aid understanding of the growth mechanism in a MOCVD reactor and enhance performance. Some methods, their principles and their application to the growth of nitride-based materials will be discussed.

Key words: MOCVD, GaN, planetary reactor, close-coupled showerhead, boundary layer, gas phase reaction, *in situ* monitoring, reflectance measurement, temperature measurement, curvature measurement, strain management.

2.1 Introduction

The development of metal-organic chemical vapor deposition (MOCVD) systems for the production of group III–V based devices in the last decade is impressive. Today's large-scale production MOCVD systems provide excellent controllability of growth parameters to give good uniformity of the growth rate and doping levels, and sharp layer interfaces. All of these properties are important in achieving good device properties at high yields. The argument that a competing technology – molecular beam epitaxy (MBE) – provides better uniformity and controllability compared to MOCVD is no longer valid. MOCVD has become the most popular system for the production of GaN- and GaAs-based optoelectronic devices, such as light-emitting diodes (LEDs), laser diodes, hetero-bipolar junction transistors (HBTs), high electron mobility transistors (HEMTs), solar cells and photodetectors. However, for general lighting in the future, the lumens per dollar cost for an LED light bulb is still too high for the consumer market. A further reduction in the cost of ownership of MOCVD systems is still necessary to drive down the overall cost of an LED bulb. This can be realized by increasing capacity, using larger reactors with more wafers per run, improving wafer uniformity and yield, improving system-to-system reproducibility, automating wafer loading and unloading to reduce the effect of human factors, etc.

In this chapter, the principles of MOCVD will be reviewed and state-of-the-art MOCVD systems will be introduced. Readers will be given an overview of MOCVD technology and an idea of future trends in development. Section 2.2 introduces the fundamentals of epitaxial growth by MOCVD. Sections 2.3 and 2.4 describe the principles of horizontal and vertical reactors. Finally, Section 2.5 discusses *in situ* monitoring systems and the growth mechanism for GaN-based materials.

It is recommended that readers refer to the book by Stringfellow, 1989,[1] and the book edited by Hurle, 1994,[2] for an in-depth overview of MOCVD technology and growth mechanisms. For GaN-based materials and LEDs, readers should refer to the book by Nakamura *et al.*, 2000,[3] which provides an overview of the growth mechanism for nitride-based materials and GaN-based devices. This chapter will mainly focus on modern MOCVD reactor technology.

2.2 MOCVD systems

2.2.1 Basic principles of MOCVD systems

Figure 2.1 is a basic diagram of a MOCVD system. Typical growth pressures for nitride-based devices range from 50 to 1000 mbar due to the requirements for material properties and the limitations of reactor design. The left side of the figure is the gas blending system, which controls and mixes the carrier gas (hydrogen or nitrogen), group III precursors and group V reactant gases. In the reactor, wafers are

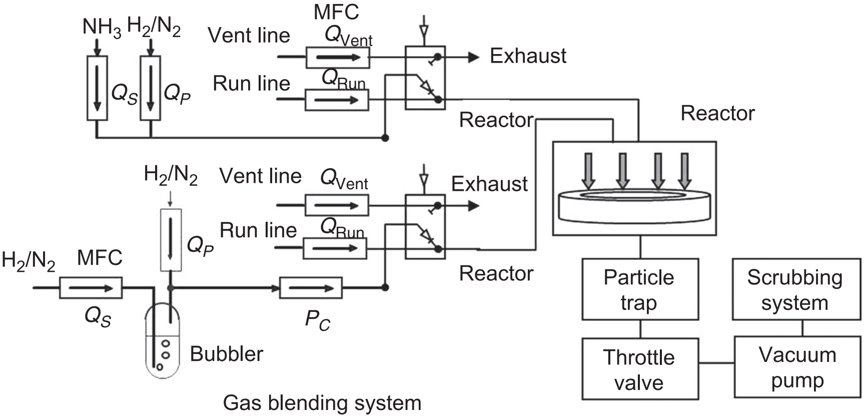

NH_3
H_2/N_2
Q_S
Q_P
MFC
Vent line
Q_{Vent}
Run line
Q_{Run}
Exhaust
Reactor
Reactor
H_2/N_2
Vent line
Q_{Vent}
Exhaust
Q_P
Run line
Q_{Run}
H_2/N_2
MFC
Q_S
P_C
Reactor
Bubbler
Gas blending system
Particle trap
Scrubbing system
Throttle valve
Vacuum pump

2.1 MOCVD system with a gas blending system, reactor, particle trap, throttle valve, vacuum pump and scrubbing system.

placed onto a wafer carrier, called the susceptor, which will be resistively or inductively heated to the process temperature. The metal-organic (MO) precursors evaporate in the bubbler and are transported by the carrier gas into the reactor, where they heat up and decompose gradually as they approach the hot susceptor. The susceptor rotates to average out any non-uniform process conditions along the circumference direction. The unused gas and the products of the reaction will pass through the particle trap all the way to the scrubbing system. The throttle valve is used to control the reactor pressure by changing the cross section of the exhaust tube.

Typical group III MO precursors used to grow an AlGaInN LED are trimethylgallium (TMGa), triethylgallium (TEGa), trimethylaluminum (TMAl) and trimethylindium (TMIn). The source of the nitrogen atoms is typically ammonia (NH_3), which is not really an ideal source due to its strong N–H bond and thus low cracking efficiency at the typical growth temperature for AlGaInN.[4] However, it is available in large quantities and it has electronic purity and a low price. Other nitrogen sources, such as hydrazine (NH_2–NH_2) and hydrogen azide (HN–N_2), have been considered as alternatives to replace NH_3 due to the lower bond strength of NH_2–NH_2 and HN–N_2 compared to the N–H bond in NH_3.[5] However, these nitrogen precursors are toxic, flammable or explosive, which has hindered their application in production systems. The n-type dopant for GaN is silane (SiH_4) or di-silane (Si_2H_6) and the only effective p-type dopant is bis-cyclopentadienylmagnesium (Cp_2Mg).

In an MOCVD system, the reactant is controlled and distributed into the reactor through an electronic controller and valves. The lower left of Fig. 2.1 shows an example of an MO source configuration. The carrier gas, H_2 or N_2, is metered through the mass flow controller (MFC) and then flows into the MO bubbler. The carrier gas transports the vaporized MO precursor out of the bubbler. The bubbler is placed in a thermal bath to control and stabilize the temperature and thus the vapor pressure of the precursor. The pressure in the bubbler is controlled by a pressure controller. The molar flow rate of the MO precursor X_{MO} is determined by the vapor pressure P_{MO}, the bubbler pressure P_C and the carrier gas flow rate from the source MFC Q_S:

$$X_{\mathrm{MO}}\ [\mathrm{mol/min}] = Q_S\ [\mathrm{sccm}]/22400\ [\mathrm{scc/mol}] \times \{P_{\mathrm{MO}}/(P_C - P_{\mathrm{MO}})\} \qquad [2.1]$$

There is another push MFC Q_P, downstream of the bubbler, to give the mixed gas sufficient velocity, but it does not affect the molar flow rate. The run line and vent line are used to ensure there is a sharp transition in the growth interface. Before the growth step starts, the gas flows to the vent line and then to the exhaust. When the growth step starts, the valve switches to the run line and the reactant goes into the reactor. The run/vent valves are placed as close to the reactor as possible to shorten the gas switching transition. The pressures in the run and vent lines are set at the same level to prevent flow oscillation after the valve is switched. This reactor design creates a smooth flow field and MOCVD can grow very thin layer-like superlattices with very sharp interfaces.

The molar flow rate of MO precursors into the reactor can change if there is a shift in the thermal bath temperature, the pressure from the controller or the filling of the bubbler. To monitor and control the molar flow rate of MO precursors, a gas concentration monitoring system[6] is used to measure the concentration of MO precursors in the piping, as shown in Fig. 2.2. The system uses an ultrasonic transceiver to determine the travel time Δt of the ultrasonic wave. With a known distance d between the emitter and receiver, the speed of the ultrasonic wave V can be calculated and it is also related to the gas properties:

$$V = d/\Delta t = (\gamma RT/M)^{1/2}, \qquad [2.2]$$

where γ is the specific heat of the gas mixture, R is the universal gas constant ($R = 8.3143\,\text{JK}^{-1}\,\text{mol}^{-1}$), T is the absolute temperature (K) of the cell and M is the molecular weight of the gas mixture. Assuming the MO precursor has a concentration x, specific heat γ_{MO} and molecular weight M_{MO}, and that for carrier gas these are γ_C and M_C, we have the following relation:

$$\gamma = x\gamma_{\text{MO}} + (1-x)\gamma_C \quad \text{and} \quad M = xM_{\text{MO}} + (1-x)M_C \qquad [2.3]$$

By solving the two equations, 2.2 and 2.3, we can deduce the MO concentration. Since the MO concentration at the typical temperature of the thermal bath is relatively low, the accuracy of the measurements depends on the difference between the molecular weights. Using a closed-loop control mode, the flow rates of the source MFC Q_S and push MFC Q_P are adjusted automatically to deliver the intended MO concentration.

For example, the TMIn precursor is a solid at room temperature and has a very low vapor pressure (about 0.85 Torr at 17 °C). Two kinds of TMIn bubbler are used in the LED industry. One uses TMIn powder dissolved in an oily organic solution. The advantage is the surface area of the TMIn powder is large enough to keep the vapor pressure saturated in the bubbler even with a high flow rate of

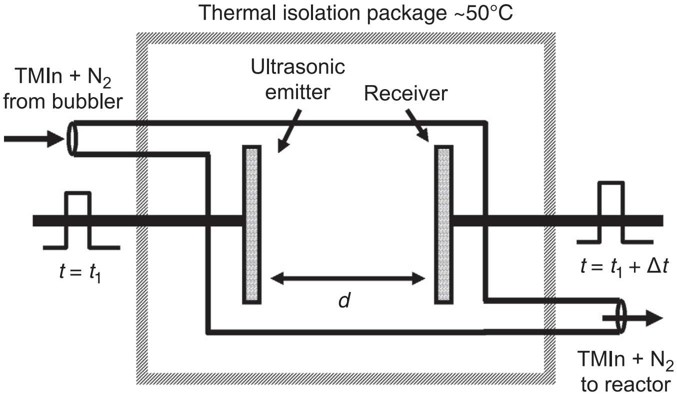

2.2 Gas concentration monitoring system.

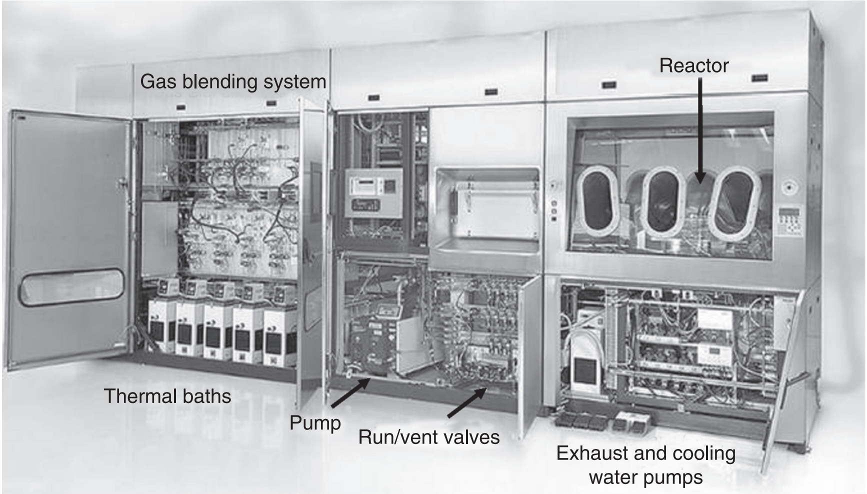

2.3 Modern MOCVD system. The reactor chamber is located inside a glovebox. The stack of run/vent valves is placed next to the reactor. The footprint of the system is 1.2 m × 6 m.

carrier gas. However, the oily organic solution can vaporize and can also be transported by the carrier gas even though its vapor pressure is extremely low compared to TMIn. The other bubbler design uses solid TMIn with a porous structure to increase the surface area and increase the sublimation rate. However, with a large flow rate of carrier gas, the molar flow rate of TMIn will start to saturate since the sublimation rate is not sufficient to supply enough vapor because of the limited surface area. Another issue with this design is that some channels in the porous structure might become larger with time and merge together. The surface area will then reduce and the bubbler's efficiency will degrade with time. Thus it is more reliable to monitor the concentration of TMIn going into the reactor and to use closed-loop control to produce an InGaN quantum well with a stable composition and emission wavelength.

Figure 2.3 shows a modern MOCVD system. The reactor, on the right, is located inside a N_2-purged glovebox to prevent contamination by moisture or oxygen. The middle part of the system is the pump and the stack of run/vent valves, which is placed as close to the reactor as possible to shorten the transition time. The left side is the gas mixing system and the thermal baths of the MO bubbler.

2.2.2 Growth mechanisms of MOCVD

Figure 2.4 shows the simplified growth mechanism of MOCVD. In a typical GaN-based MOCVD reactor, the major gas species are H_2 and N_2 but the NH_3 fraction might be as high as 50% in some cases. The MO precursors will diffuse through

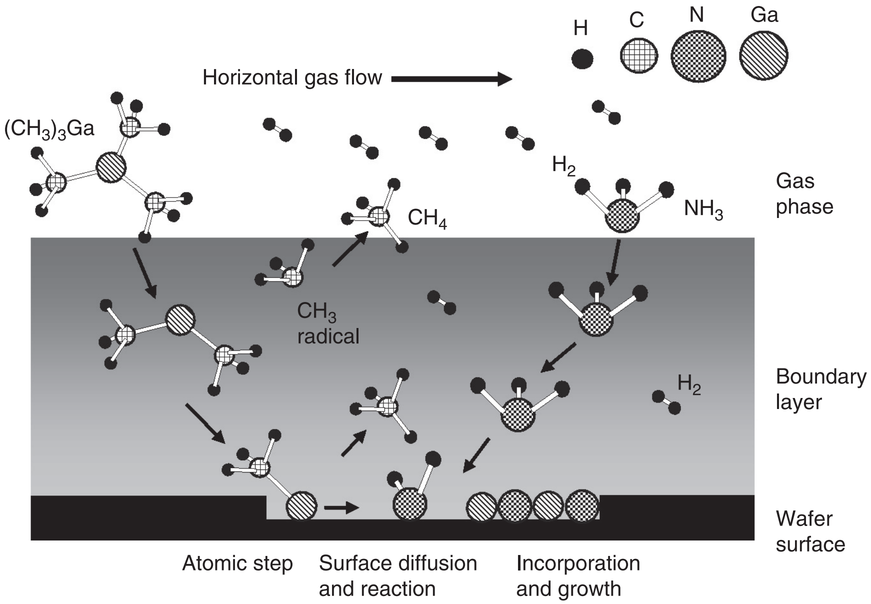

2.4 Simplified growth mechanism in a GaN MOCVD system.

the mixed atmosphere to reach the wafer surface. On the way to the wafer surface, the MO precursors will be heated up and start to decompose into various species. After reaching the surface, the MO species will diffuse laterally on the surface until they reach a suitable crystal site where they become incorporated. Typically, NH_3 is oversupplied so that the growth rate only depends on the supply of the MO precursors to the wafer surface. The surface reaction rate can be assumed to be large enough that the vapor pressure of the MO precursors is zero on the wafer surface. This will result in a gradient of MO concentration from the gas phase to the wafer surface and generate a diffusion force of MO species from the high-concentration region toward the low-concentration region at the wafer surface. Another driving force for the MO precursors is the convection force of the total reactor gas flow, which pushes the MO precursors from the high-pressure side (the gas inlet) toward the low-pressure side (the exhaust). The layer of gas with the MO concentration gradient is called the boundary layer. The thinner the boundary layer, the larger the gradient and diffusion flux onto the wafer.

With a low growth temperature, the growth rate is limited by the surface reaction rate. For example, the GaN nucleation layer is grown at a low temperature of around 500 °C to relax the strain. By increasing the growth temperature, the growth rate of the nucleation layer will increase significantly for the same amount of TMGa and the same NH_3 flow rate. When the growth temperature increases further, the surface reaction rate will be high enough that the growth rate becomes limited by the diffusion rate of the reactant species onto the wafer surface.

To grow a GaN epitaxial layer, the temperature range is in the transportation limited regime. In this regime, the growth rate R_g is

$$R_g \sim \rho D\,(Y_{\text{Max}} - Y_{\text{surface}})/\delta, \qquad [2.4]$$

$$\rho \sim PT^{-1} \text{ and } D \sim T^{1.7}\,P^{-1} \qquad [2.5]$$

where ρ is the gas density, D is the diffusion coefficient of the MO species, Y_{Max} is the maximum MO concentration above the surface, Y_{surface} is the MO concentration on the surface, δ is the thickness of the boundary layer, P is the reactor pressure and T is the gas temperature. The opposite dependence of the density and the diffusion coefficient on the pressure cancels out the pressure. Therefore, ideally the growth rate is independent of the reactor pressure in the mass-transport-limited growth regime. The impression that the growth rate depends on the reactor pressure is due to the parasitic gas phase reaction, which depletes the MO species. A significant change in the growth rate and the on-wafer uniformity will be observed at an elevated pressure if the reactor design is poor so that the growth condition favors the gas phase reaction. At even higher growth temperatures, the growth rate starts to drop due to the onset of the gas phase reaction, increased deposition on the reactor wall, layer decomposition and desorption of reactant species from the wafer surface.

Table 2.1 summarizes the major properties of the N_2 and H_2 carrier gases that have a strong impact on the growth mechanism of MOCVD. The density of N_2 is 14 times higher than that of H_2 due to the molecular weights. N_2 will have a higher flux momentum than H_2 for the same flow velocity after injection into the reactor, so that N_2 will penetrate deeper into the reactor. The Reynolds number is the ratio between convection and diffusion. N_2 has a higher Reynolds number than H_2 so that N_2 has a more pronounced jetting phenomenon. H_2 has a much higher thermal conductivity than N_2. This difference is used in reactors for temperature control. Increasing the N_2 fraction in the carrier gas reduces the gas temperature and delays

Table 2.1 Comparison of gas properties of N_2 and H_2

Property	Comparison[a]	Impact on process
Density	$\rho(N_2) = 14\,\rho(H_2)$	N_2 has higher flow momentum
Reynolds number	$\text{Re}(N_2) \sim 8\,\text{Re}(H_2)$	N_2 has more pronounced jetting phenomenon
Thermal conductivity	$K(N_2) \sim 0.1\,K(H_2)$	N_2 can delay the decomposition of the MO precursor
Diffusion of MO species	$D(N_2) \sim 0.2\,D(H_2)$	Smaller diffusion coefficient for MO in N_2 results in lower growth rate

Note: [a] $D(N_2)$ is the diffusion coefficient of the MO species in an N_2 atmosphere, etc.

the decomposition of MO precursors. The N_2 and H_2 mixing ratio is also used to control the thermal boundary of the reactor. The diffusion coefficient of MO species through an N_2 atmosphere is also much lower than for H_2. The following example illustrates how this can affect the growth of a nitride-based material. H_2 gas cannot be used to grow InGaN alloys because a small amount of H_2 greatly hinders the incorporation of indium into the InGaN layer. Therefore, N_2 carrier gas is used to grow InGaN in a MOCVD reactor. Compared to the growth rate of GaN in H_2 carrier gas, the growth rate of InGaN is relatively low because of the smaller diffusion coefficient of MO species in the N_2 atmosphere.

Since GaN MOCVD typically operates at a pressure around 50–1000 mbar, the mean free path of the reactant gas is quite short so that interactions in the reactant gas before it arrives on the wafer surface are unavoidable. A widely accepted model of the gas phase reaction between $M(CH_3)_3$ and NH_3 was proposed by Creighton *et al.*[7] Two pathways were proposed for gas phase nucleation and particle formation, as shown in Fig. 2.5. According to this model, TMGa and TMIn tend to take the upper pathway, where the decomposition of methyl ligands results in mono-methyl-gallium or mono-methyl-indium, which react with NH_3 to form GaN or InN nuclei of 10–100 atoms. TMAl takes the lower pathway to form the nuclei. The difference is, in the lower pathway there is no methyl ligand to decompose so the reactions happen at a lower reactor temperature than that in the upper pathway. This can explain why it is more difficult to grow AlGaN alloys with a high aluminum concentration in a MOCVD reactor.

The nuclei might diffuse toward the wafer surface and contribute to the growth of the layer. They will also accumulate into bigger nanoparticles with a size of

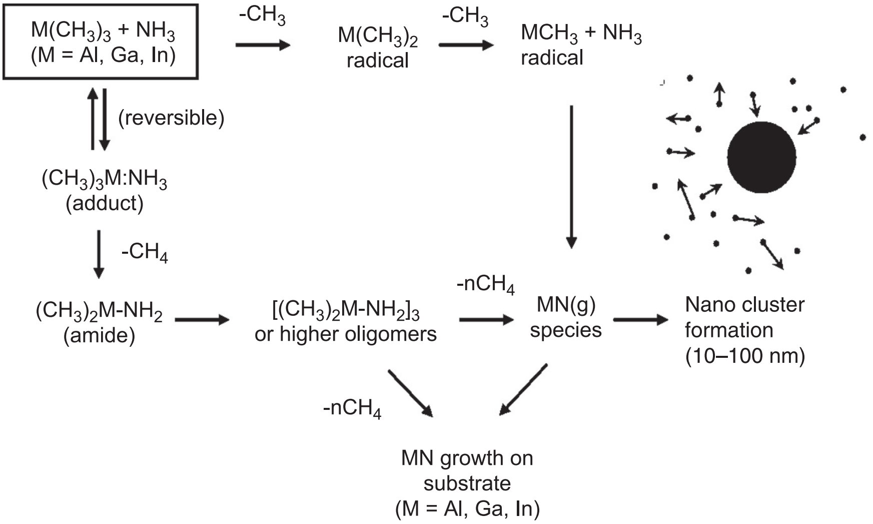
M(CH3)3 + NH3
(M = Al, Ga, In)
-CH3
M(CH3)2 radical
-CH3
MCH3 + NH3 radical
(reversible)
(CH3)3M:NH3 (adduct)
-CH4
(CH3)2M-NH2 (amide)
[(CH3)2M-NH2]3 or higher oligomers
-nCH4
MN(g) species
Nano cluster formation (10–100 nm)
-nCH4
MN growth on substrate (M = Al, Ga, In)

2.5 Pathways for the gas phase reaction.

10–100 nm. When the particle size is around 10–100 nm, the thermophoretic force will push the particles out from the hot region to the cold region and they will not contribute to the growth rate. The nanoparticles will deposit on the cold reactor wall or flow with the gas streamline to the exhaust. This will decrease the growth rate and also affect the doping uniformity and efficiency. The radius of a nanoparticle increases linearly with the residence time so that the volume of a nanoparticle then increases with the cubic power of the residence time. Assuming a 1 s residence time, the estimated growth rate of a nanoparticle is several magnitudes of order higher than the diffusion limited growth rate on the wafer surface. This indicates that MO precursors will be depleted completely from the gas phase if the residence time is too long or there is a vortex in the flow field. Thus, for high MO growth efficiency, it is very important that the reactor geometry creates a laminar flow field. The gas phase chemistry of dopant precursors such as Cp_2Mg and silane is not well known due to a lack of research. From the experimental evidence, the doping efficiency of magnesium and the on-wafer uniformity will be affected by the flow condition, pressure and temperature. This indicates that Cp_2Mg has a different (higher) depletion rate compared to TMGa.

To prevent the gas phase reaction, the lower the pressure the better. However, it is preferable to grow GaN-based LEDs at elevated pressure to give a higher NH_3 partial pressure, which can suppress the formation of nitrogen vacancies and give better crystal quality. Another factor is reducing the residence time of the gas in the reactor. This can be achieved with a higher total flow velocity and preventing recirculation in the reactor. Modern computational fluid dynamics is very useful in designing a reactor to ensure that there is no recirculation in the reactor even at an elevated pressure of 800 mbar.

The thermal distribution in the reactor is important for the flow field as well as the epitaxial growth on the wafer surface. The emission wavelength of an InGaN/GaN multiple quantum well (MQW) will shift 2–4 nm/°C due to desorption of indium atoms from the surface and less indium incorporation at the higher surface temperature. Another reason is that the gas phase reaction of TMIn with NH_3 differs with local variations of surface temperature. Therefore, the design of a reactor needs significant effort to produce a stable and uniform surface temperature across the susceptor and wafer to give good wavelength uniformity.

2.3 Planetary reactors

2.3.1 Introduction to the principles of a planetary reactor

A planetary reactor, as shown in Fig. 2.6, is a type of horizontal reactor where the reactant gases are injected into the center of the reactor and flow radially to the exhaust on the reactor's edge. The group III precursors and group V hydride are separated in different injectors to prevent pre-reactions. The injector shown in the figure is called a triple injector: the group III precursors are in the middle injector and the group V hydride is in the top and bottom injectors. The wafers are

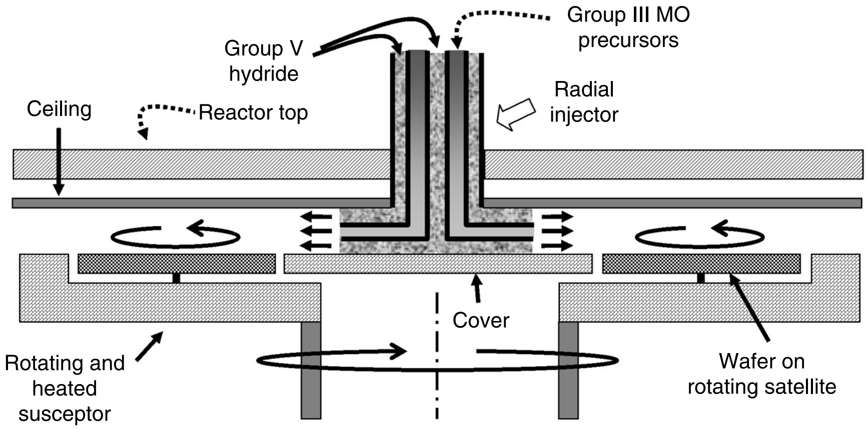

2.6 Planetary reactor.

loaded into the pocket of a rotating disk and the disks are carried by a graphite susceptor. The graphite susceptor is inductively heated and transfers the heat to the disk and the wafer. The ceiling of the reactor is controlled at specific temperatures during the growth of different layers. The growth rate along the radius of susceptor will decrease gradually due to depletion of reactant species. Thus the disk needs to spin to average out the growth rate to give good on-wafer uniformity. The susceptor will also rotate around the axis of the reactor's center to average out any deviations along the circumference direction. The whole system looks like spinning planets orbiting around the sun; hence, the name planetary reactor.

Figure 2.7 shows how to achieve a uniform growth rate in a planetary reactor. TMGa is injected into the reactor and thermally decomposes to form monomethyl gallium (MMGa) after losing two methyl ligands. The distribution of the MMGa concentration in the figure was calculated by computational fluid dynamics. The maximum is in front of the edge of the susceptor where almost all of the TMGa decomposes. MMGa is transported horizontally by forced convection of the total flow toward the exhaust. On the interface of the susceptor, the concentration of MMGa can be assumed to be zero due to the high reaction rate in the mass-transport limited growth regime. The MMGa concentration gradient means that MMGa diffuses vertically toward the susceptor and the ceiling to participate in reactions. The growth rate on the susceptor is proportional to the MMGa concentration gradient as indicated by Eq. 2.4. That is why the growth rate curve along the radius of the susceptor matches the distribution of MMGa concentration. The curve has a peak in front of the hot susceptor and declines toward the exhaust due to depletion of MMGa; this curve is called the depletion curve.

Changing the total flow rate will shift the maximal position and affect the shape of the depletion curve. Changing the mixing ratio of gas species, such as H_2, N_2

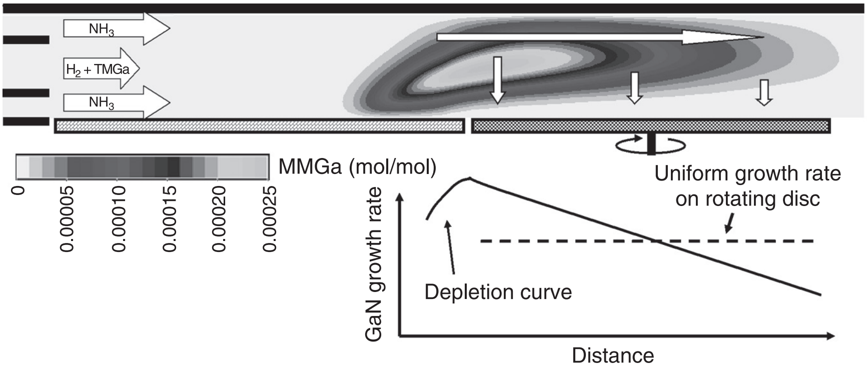

2.7 Depletion curve for a planetary reactor. MMGa is transported horizontally by the total flow convection force and vertically by the diffusion force of the concentration gradient. The growth rate on the rotating disc can be made uniform by averaging out the depletion curve.

and NH_3, will change the diffusion coefficient of MMGa in the gas mixture, resulting in a change in the distribution of MMGa. When the diffusion coefficient for MMGa increases, the growth rate for GaN will increase and MMGa will deplete earlier so that the maximal position of the depletion curve will shift toward the injector and the depletion curve will sag, and vice versa. These are the two parameters used to tune the uniformity in a planetary reactor. Combined with a spinning disk, very uniform growth on the wafer can be achieved.

In MOCVD, the reactants will not only deposit on the wafer but also on the chamber walls and ceiling, so that the reactor needs to be cleaned after a number of growth runs. The ceiling of a planetary reactor acts as a liner, which can be replaced easily for maintenance. Its other important function is to provide an upper thermal boundary in the reactor. The ceiling's temperature will affect the coating on it and the growth rate on the wafer. It will also affect the thermal gradient between the susceptor and the ceiling, which is important for achieving a stable flow field. Figure 2.8(a) shows how the ceiling temperature can be controlled by adjusting the thermal conductivity of the purging gas in the gap between the ceiling and the reactor top. The heat flux from the susceptor is transported vertically through the process gap, the ceiling and the ceiling gap to the reactor top. Inside the reactor top, cooling water flows at a fixed temperature to carry the heat away. The average thermal gradient from the susceptor to the reactor top is fixed by the process condition, but the local temperature of the ceiling and the temperature gradient in the ceiling gap will change due to the thermal conductivity of the gas. The following describes how the ceiling temperature is controlled:

$$\text{Heat flux} = K(H_2,N_2) \times (T_{\text{ceiling}} - T_{\text{water}})/d, \qquad [2.6]$$

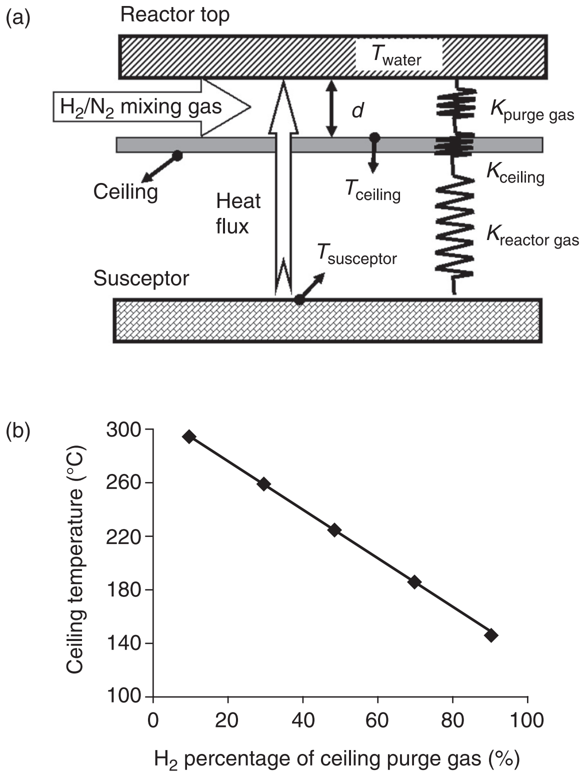

2.8 Ceiling temperature control. (a) The heat flux through the ceiling to the water-cooled reactor top. (b) An example of how the ceiling temperature can be controlled by changing the H_2 fraction.

where $K(H_2,N_2)$ is the thermal conductivity of the mixture of H_2 and N_2 gases, $T_{ceiling}$ is the ceiling temperature, T_{water} is the temperature of the cooling water and d is the ceiling gap. The mixing gas is purged in the ceiling gap from the center toward the edge of the ceiling. H_2 has, by a factor of 10, a higher thermal conductivity than N_2. If there is a higher H_2 fraction in the mixture, the thermal conductivity increases and the ceiling temperature will decrease and vice versa. The flow rate of the purge gas will not affect the ceiling temperature due to the relatively small specific heat of the gas compared to the cooling water: the heat carried away by the ceiling purge gas is negligible. Figure 2.8(b) is an example of a graph of ceiling temperature versus H_2 fraction. A wide range of ceiling temperatures can be achieved by changing the H_2 fraction. In the above formula, the ceiling gap is another parameter used to control the ceiling temperature. We will see an application of this later in this section.

In a planetary reactor, the susceptor is inductively heated up by a radio-frequency (RF) electromagnetic (EM) field as shown in Fig. 2.9. The EM field is

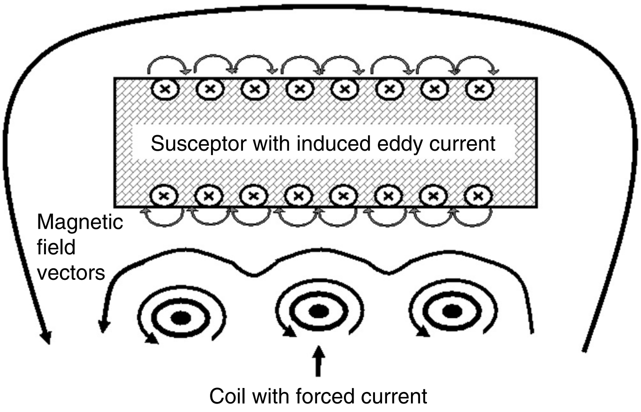

2.9 The RF coil electrically heats the conductive graphite susceptor. The RF magnetic field induces an eddy current on the surface of the susceptor. The power dissipates and heats the susceptor. Parts made of insulators, like quartz, will not be heated by the RF power.

fed into the reactor through a conducting coil. The coil is made from a copper tube with cooling water flow inside and with gold plating on the surface to reflect thermal radiation. The advantage of using an RF coil compared to a resistive heater is that the temperature of the coil can be kept cold and the lifetime and reliability of the RF coil are much better. The EM field will penetrate to a depth called the skin depth, and induce a local eddy current on the surface of the conducting susceptor, which is usually made of graphite. The power of the eddy current will dissipate and heat up the susceptor. Adjusting the distance between the RF coils and the susceptor and the gap between the RF coils will change the distribution of the electromagnetic field and affect the temperature distribution in the susceptor. These two factors can be used in a computational simulation to optimize the design of an RF coil. In addition, the rotating disk will average out the temperature deviation of the susceptor to give good temperature uniformity for growth.

From the discussion above, it can be seen that the rotating disk is essential for good uniformity of the growth rate and the process temperature. The growth temperature of GaN-based materials is too high for any mechanically rotating design to stay reliable. In addition, a mechanically rotating disk will have physical contact with the other parts and this will most likely leave particles on the wafer. Figure 2.10 shows how the gas-foil rotation of a satellite disk used in a planetary reactor works. H_2 or N_2 gas is injected under the disk through the channel inside the susceptor. The disk is supported by a molybdenum pin, which is the only point of contact with the susceptor. The convection force of the gas will lift up the disk and form a gas foil, which reduces the friction force between the disk and susceptor.

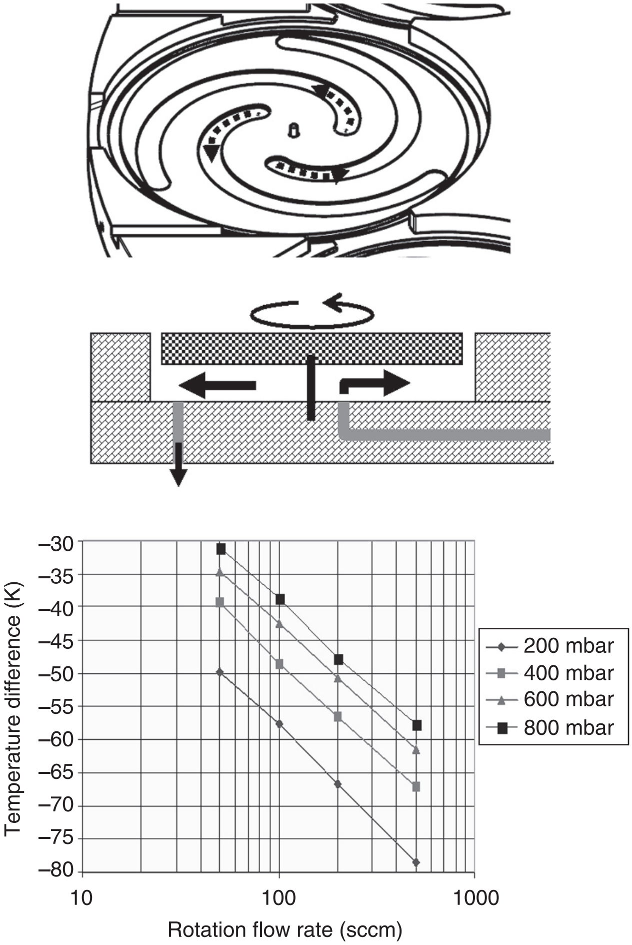

2.10 Gas-foil rotation of a satellite disc. The susceptor body has channels for the rotation gas. The upper side of the susceptor has spiral grooves, which guide the rotation gas. The graph shows the change of surface temperature of a satellite disc vs the flow rate of N_2 rotation gas.

The gas is then pushed out laterally through the spiral grooves on the upper surface of the susceptor. The viscous force of the gas will make the disk rotate. The lift-up distance, the so-called flying height and the rotation speed of the satellite disk can be controlled by the flow rate and whether the gas is N_2, H_2 or a mixture. If the reactor pressure decreases, the velocity of the rotation gas will increase and so will the flying height and rotation speed of the disk. The thermal conductivity of the gas foil and the flying height are different for H_2 and N_2, so that the surface temperature of the disk can be actively controlled. The graph shown in Fig. 2.10 is the surface temperature change of the disk with N_2 rotation gas. With a constant flow rate, the surface temperature decreases as the reactor pressure decreases.

2.3.2 Design of a modern planetary reactor

Figure 2.11 shows a state-of-the-art planetary reactor. The reactor height is 25 mm and the diameter of the reactor is 740 mm. The wafer configuration can be changed from 56 × 2″ to 14 × 4″, 8 × 6″ or 5 × 8″ by changing the susceptor, satellite disks and a few other parts.

The details of the design of a reactor including the flow dynamics and thermal management are shown in Fig. 2.12. Inside the reactor top there are two cooling water loops (A in the figure) with the water flowing in opposite directions. The water temperature in the outlet on one side of reactor will be higher than in the inlet on the other side during growth. This design can compensate for the heating of the cooling water. The lower side of the reactor top, which is curved (B in the

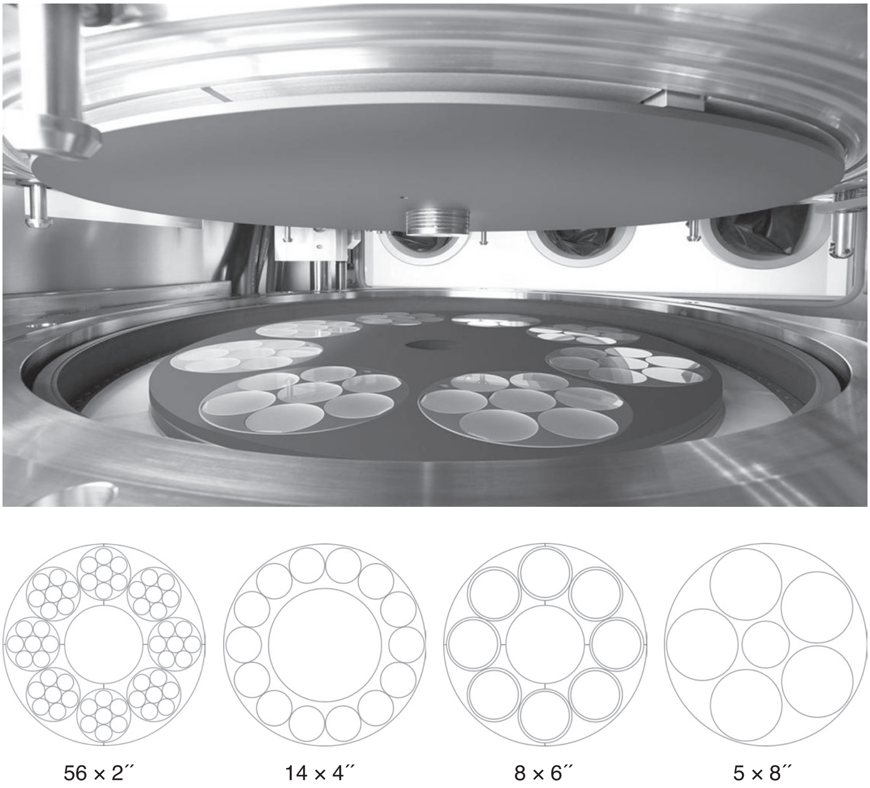

2.11 State-of-the-art planetary reactor with 56 × 2″ wafers. The wafer configuration can be easily swapped to take 14 × 4″, 8 × 6″ or 5 × 8″ wafers by changing a few reactor parts.

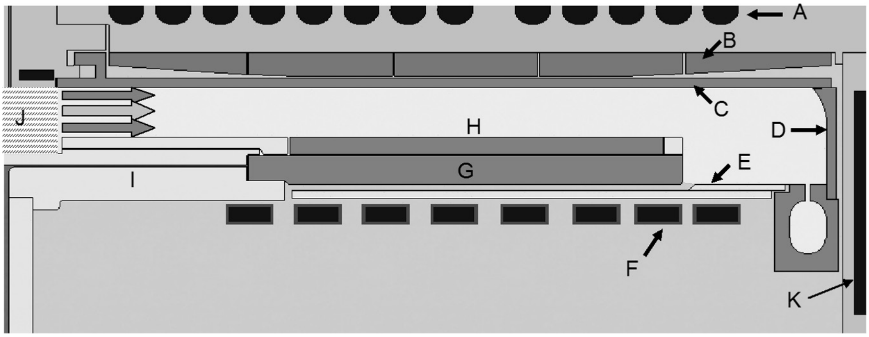

2.12 Cross section of a state-of-the-art planetary reactor with 56×2″ wafers. A: cooling water loop, B: shaped reactor top, C: graphite ceiling, D: graphite liner and exhaust collector, E: quartz diffusion barrier, F: RF coil, G: graphite susceptor, H: graphite satellite disk, I: susceptor support plate, J: triple injector, K: reactor wall with cooling water.

figure), together with the SiC-coated graphite ceiling, are designed to give a uniform ceiling temperature. The inner part of the ceiling (nearest the injector) and the outer part (nearest the outer wall) are farther from the hot susceptor so that they receive less thermal radiation than the middle part of the ceiling. Because the reactor top is curved, there is a larger gap between it and the parts of the ceiling away from the middle of the ceiling, which increases the thermal resistance and therefore the temperature of these two areas. Graphite is used for the ceiling because it has a similar thermal expansion coefficient as GaN. The GaN coating on the ceiling, which accumulates with each growth run, is stable during the thermal cycles of an LED growth run. This means a reactor can operate without frequent maintenance of the ceiling.

The liner and exhaust collector are also made of graphite. The gap between the liner and the reactor sidewall is purged with N_2 gas to provide a stable thermal boundary. The gap between each RF coil on the susceptor edge is smaller to increase the heating of the susceptor edge, which produces a more uniform temperature across the susceptor. A quartz diffusion barrier is used to insulate the coil and the susceptor and to prevent reactant gas from diffusing into the heater chamber. Quartz is also a good thermal insulator and it reduces the heat loss to the water-cooled RF coils. Each satellite disk has a gas channel, and rotation gas is fed all the way from the reactor bottom, to the susceptor support plate and then to the susceptor body. Each channel is controlled by an MFC, which adjusts the rotation flow and compensates for temperature deviations in large-diameter susceptors. This design can achieve excellent wavelength uniformity from wafer to wafer.

The triple gas injector is the heart of the reactor. The geometry of the injector was designed with the aid of computer modeling, which simulated the flow field in order to achieve a smooth flow in the reactor. Computer modeling provides insights into the flow dynamics and greatly improves the design, which takes less

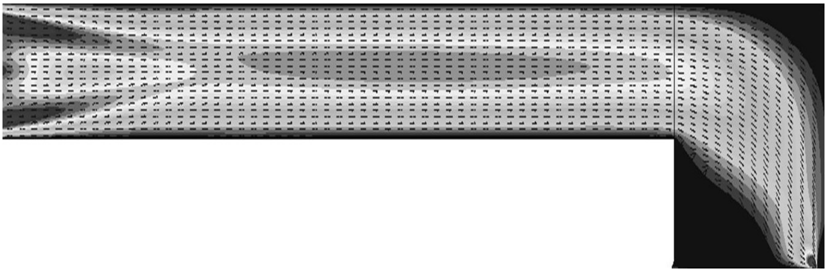

2.13 Laminar flow field of a 56×2″ planetary reactor at a pressure of 600 mbar and a total flow rate of 400 slm.

time since there is no tedious process of trial and error. The upper and lower injectors are for NH_3, the middle injector is for MO precursors and dopants. The design of an injector is very important; it must allow a high total flow rate without recirculation when the gas is injected into the reactor. This can reduce the residence time and enable a high growth rate at high reactor pressure with minimal gas phase reactions. The exhaust is intentionally located away from the edge of a satellite disk and down to the lower side of the reactor. This makes the streamlines of the gas flow very smooth across the whole susceptor and improves the uniformity of the growth rate. Figure 2.13 shows the laminar flow field of a 56 × 2″ reactor at a pressure of 600 mbar with a flow rate up to 400 slm generated by a computer model. The typical operating flow rate of this reactor is around 200 slm, which works well for the various layers of a GaN-based device. This injector design has enabled the operation of a large-scale MOCVD reactor at a sub-atmosphere pressure with an excellent uniform growth rate.

Figure 2.14 shows the growth rate versus the TMGa molar flow rate for various reactor pressures from 200 up to 800 mbar in a 56 × 2″ planetary reactor.

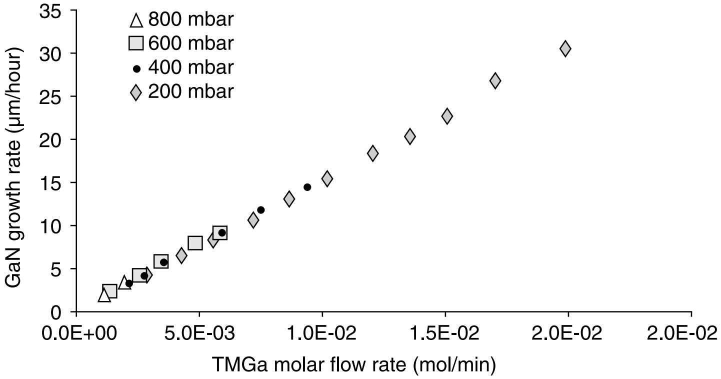

2.14 Growth rate vs TMGa molar flow rate for different reactor pressures in a 56×2″ planetary reactor.

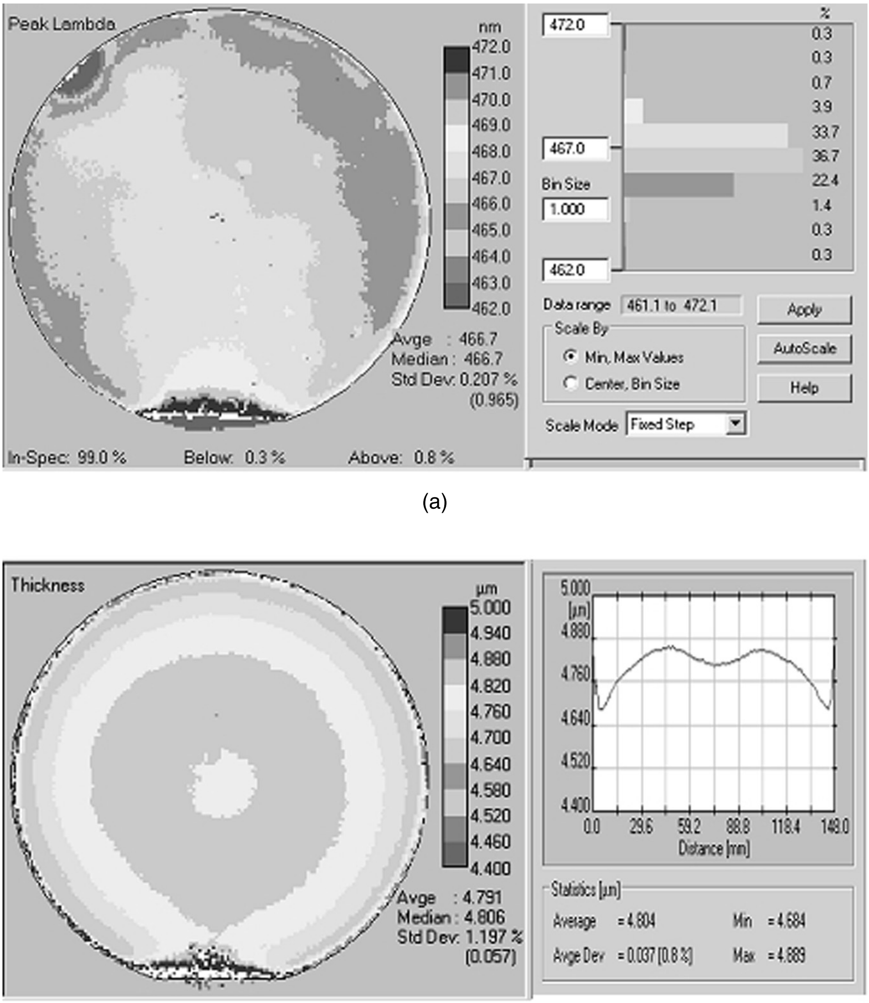
Peak Lambda
nm
472.0
471.0
470.0
469.0
468.0
467.0
466.0
465.0
464.0
463.0
462.0
%
0.3
0.3
0.7
3.9
33.7
36.7
22.4
1.4
0.3
0.3
Apply
AutoScale
Help
Thickness
µm
5.000
4.940
4.880
4.820
4.760
4.700
4.640
4.580
4.520
4.460
4.400
5.000 [µm]
4.880
4.760
4.640
4.520
4.400
0.0
29.6
59.2
88.8
118.4
148.0
Distance [mm]

Avge : 466.7
Median : 466.7
Std Dev: 0.207 % (0.965)
In-Spec: 99.0 % Below: 0.3 % Above: 0.8 %
472.0
467.0
Bin Size 1.000
462.0
Data range 461.1 to 472.1
Scale By
● Min, Max Values
○ Center, Bin Size
Scale Mode Fixed Step

(a)

Avge : 4.791
Median : 4.806
Std Dev: 1.197 % (0.057)
Statistics [µm]
Average = 4.804 Min = 4.684
Avge Dev = 0.037 [0.8 %] Max = 4.889

(b)

2.15 (a) MQW photoluminescence wavelength and (b) n-GaN thickness mapping of 6″ wafers grown in an 8×6″ planetary reactor.

The growth rate can reach 10 µm/h at 600 mbar without saturation and is still as high as 3 µm/h at 800 mbar. Figure 2.15 shows the on-wafer uniformity of the GaN growth rate and LED wavelength for the 8 × 6″ configuration. A standard deviation of thickness of about 1.2% and wavelength of about 1 nm can be achieved in a large-scale MOCVD system.

2.4 Close-coupled showerhead (CCS) reactors

2.4.1 Introduction to the principles of a CCS reactor

A vertical reactor is shown in Fig. 2.16. The gas is injected vertically into the reactor, impinges on the susceptor and then flows horizontally to the exhaust on the edge of the reactor. On the way to the exhaust, the flow becomes laminar. There is a stagnation point in the center of the reactor where the gas velocity is zero. The wafer at this point will have a different growth rate than in other part of the susceptor. In a vertical reactor, the initiation of buoyancy-induced recirculation can be determined from the Grashof number, which is the ratio of the buoyancy force and the viscous force:

$$\mathrm{Gr} = \rho^2 g H^3 (T_s - T_0)/(T_0 \mu^2) \qquad [2.7]$$

where g is the acceleration due to gravity, ρ is the gas density, H is the reactor height, T_s is the susceptor temperature, T_0 is the temperature at the top of the reactor and μ is the gas dynamic viscosity. With a square power dependence on gas density and a cubic power dependence on reactor height, it is better to operate a reactor at low pressure and have a small reactor height.

One type of vertical reactor, the rotating disk reactor (RDR), uses a high rotation speed around 500–1500 rpm to further suppress the recirculation of the flow. The high rotation speed of the susceptor has two effects. One is to average out the reactor deviation along the circumference direction. The other is that the rotating susceptor surface will drag the viscous gas in the horizontal direction and push it out radially along the susceptor. The rotating susceptor acts like a pump and enhances the downward force convection. This can suppress the buoyancy force, reduce the thickness of the boundary layer and improve the uniformity of the

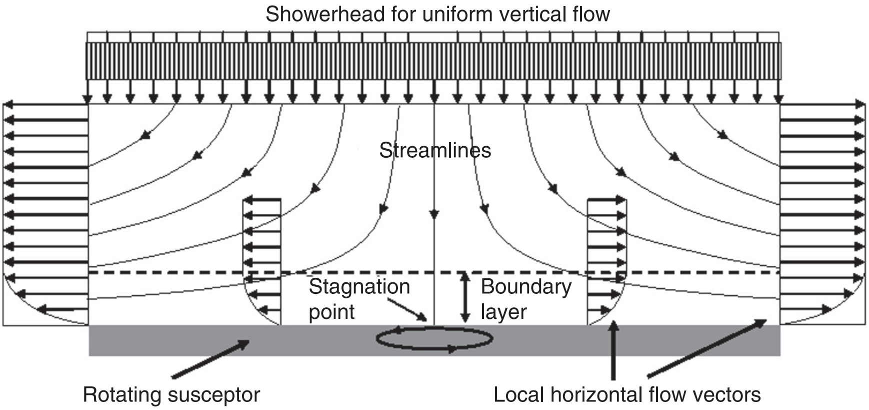
Showerhead for uniform vertical flow
Streamlines
Stagnation point
Boundary layer
Rotating susceptor
Local horizontal flow vectors

2.16 A vertical flow reactor with a showerhead to give a uniform flow distribution.

growth rate. The relation between rotation speed, reactor pressure and a stable flow field has been well studied.[8,9] We will not discuss it further in this chapter.

The close-coupled showerhead (CCS) reactor is another type of vertical reactor where the reactant gas is uniformly injected from the top of the reactor into the whole susceptor through tubes with a relatively small diameter compared to the reactor diameter. Since the Grashof number has a cubic dependence on the reactor height, the most effective way to suppress recirculation is to reduce the chamber height. This is the basic principle behind a CCS reactor and the standard reactor height is set at 11 mm. A cross section of a CCS reactor is shown in Fig. 2.17. The showerhead contains two plenums to separate the group III MO precursors and group V hydride gas in order to minimize the pre-reaction of the reactant gases. Tubes are used to deliver the gas from the upper and lower plenums to the reactor. The susceptor is placed on a quartz support and heated by a resistive heater. The quartz support carries the susceptor, which rotates at a rate of 50–100 rpm to average out any deviations in heating to give a more uniform temperature along the circumference direction. The rotation rate of the susceptor is kept low enough so that it does not affect the flow field. Substrates are located in recessed pockets on the susceptor. The heater is made of a hard metal such as tungsten and has different zones, which are fed in parallel with electrical power from separate power supply units. In a large production reactor, one heater has four heater zones. The dissipation of heat on the susceptor's edge is higher than that at the susceptor's center due to the larger surface area and increased thermal radiation. Therefore, the highest power is fed into the heater zone on the edge to achieve a uniform temperature distribution across the whole susceptor. There is a thermocouple underneath the susceptor to control the process temperature. As the bottom of the showerhead is only 11 mm away from the hot susceptor surface, there is a loop of cooling water inside the wall between the susceptor and the bottom of the plenum. The temperature of the cooling water in the showerhead is set at a constant value (typically 60 °C). There is also a separate loop of cooling water at 20 °C inside the chamber's sidewall. Both loops of cooling water produce

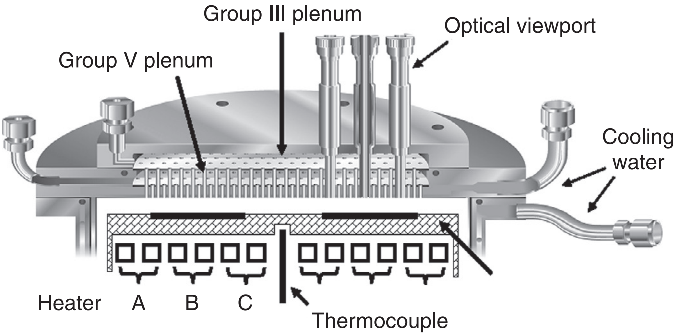

2.17 Close-coupled showerhead reactor.

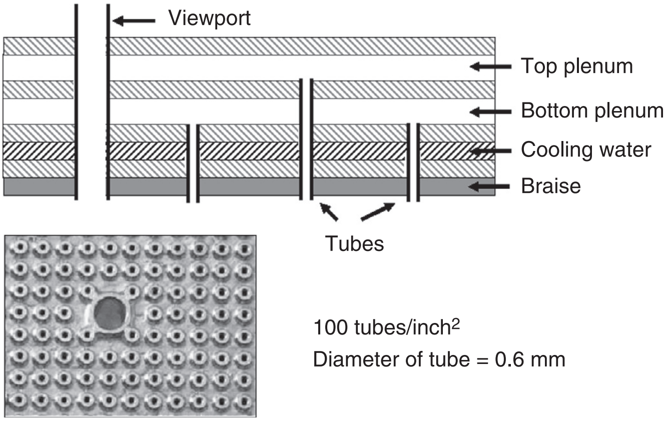

2.18 Cross section of a showerhead (upper) and its surface on the reactor side (lower).

a stable thermal boundary, which is extremely critical for the stability of the process. MO precursors are easier to crack thermally than hydride, so they are distributed in the top plenum where they are kept as cold as possible.

Figure 2.18 shows the detailed arrangement of the showerhead plenums, tubes and optical viewports. The injection tubes are arranged so that basically one group III tube is surrounded by four group V tubes and vice versa to ensure good mixing of the reactant gases. The diameter of an injection tube is only 0.6 mm and there are 100 tubes per square inch. The diameter and density of the tubes satisfy the criterion that the pressure drop inside a tube has to be much higher than the pressure drop across the whole plenum. This is important to ensure that the gas delivered into certain location of the plenum can be uniformly injected through all the tubes. The bigger tubes are viewports for the *in situ* monitoring system, which is above the showerhead. These viewport tubes are also purged with gas to prevent coating during growth. The *in situ* monitoring system will be introduced in Section 2.5.

Figure 2.19 shows a simulation of the flow field of the gas injected from the group III and group V plenums, which was used to optimize the showerhead design. The reactor height is 11 mm and the diameter of the susceptor is 300 mm with a $19 \times 2''$ wafer configuration. The flow conditions are: H_2 total flow is 20 slm, NH_3 total flow is 20 slm, pressure is 130 mbar and the susceptor surface temperature is 1030 °C. In total, the showerhead has about 10 000 tubes for gas injection. The carrier gas H_2 from the group III tubes has a lower momentum than the NH_3 gas from the group V tubes so the NH_3 penetrates deeper into the reactor than the H_2. The jets are fully expanded a few millimeters from the tubes and a smooth flow field develops without recirculation. Even with the sudden geometry change from the narrow tube to the wide-open reactor, the closely distributed injection tubes ensure there is no dead volume or vortices between the tubes. Hence the

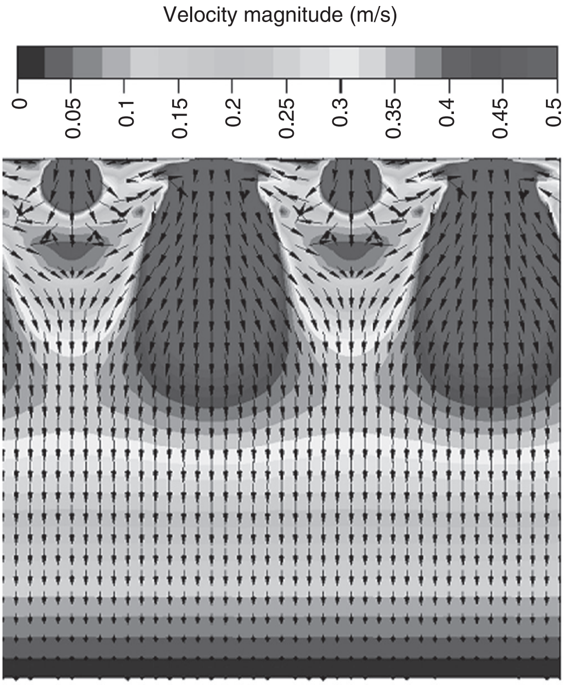

2.19 Flow field in a CCS reactor of height 11 mm. The two tubes with stronger jetting deliver NH_3 from the group V plenum and the other two tubes deliver H_2 from the group III plenum.

showerhead is close coupled. The challenge in scaling up a reactor for mass production is the manufacturing of the large-diameter showerhead with a high tube density. However, the CCS reactor design greatly increases the window for stable flow fields so that there is no risk of recirculation in most flow conditions, especially at an elevated reactor pressure. The residence time of the reactant gas is short due to the low reactor height and adduct formation can be suppressed to facilitate a high growth rate.

Figure 2.20 shows a calculated distribution of TMGa and MMGa. After being injected into the reactor, the TMGa diffuses laterally and distributes uniformly within the upper third of the reactor. It decomposes to MMGa, which has a maximum concentration around halfway up the reactor, and the layer from the middle of the reactor to the susceptor is defined as the boundary layer. The thickness of the boundary layer (δ) in a CCS reactor is inversely proportional to the square root of the Reynolds number (Re), which is the ratio between the momentum fluxes for convection and for diffusion:[10]

$$\mathrm{Re} = \frac{\rho v(d^2/H)}{\mu} \qquad [2.8]$$

$$\delta \sim 1/(\mathrm{Re})^{0.5} \qquad [2.9]$$

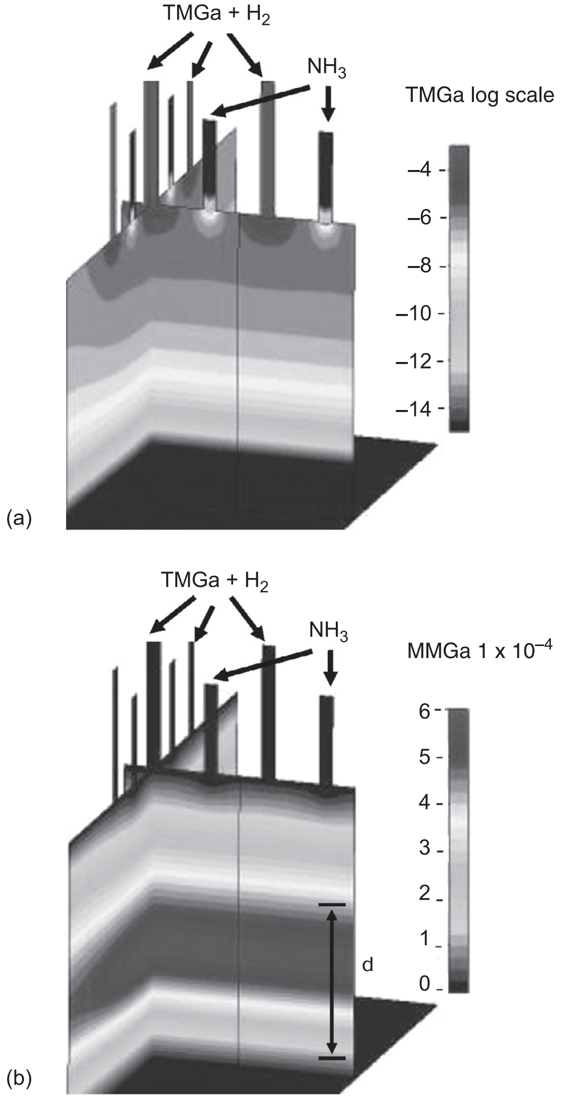
TMGa + H2
NH3
TMGa log scale
–4
–6
–8
–10
–12
–14
(a)
TMGa + H2
NH3
MMGa 1 x 10–4
6
5
4
3
2
1
0
d
(b)

2.20 Distribution of TMGa and MMGa in a CCS reactor.

where ρ is the gas density, v is the flow velocity, d is the chamber diameter, H is the reactor height and μ is the dynamic viscosity. As a rule of thumb, the boundary layer becomes thinner for a higher total flow rate and thus higher flow velocity. The boundary layer is also thinner with N_2 than H_2 carrier gas due to the higher density of N_2. The growth rate in the mass-transport limited growth regime is inversely related to the thickness of the boundary layer. Therefore, the growth rate

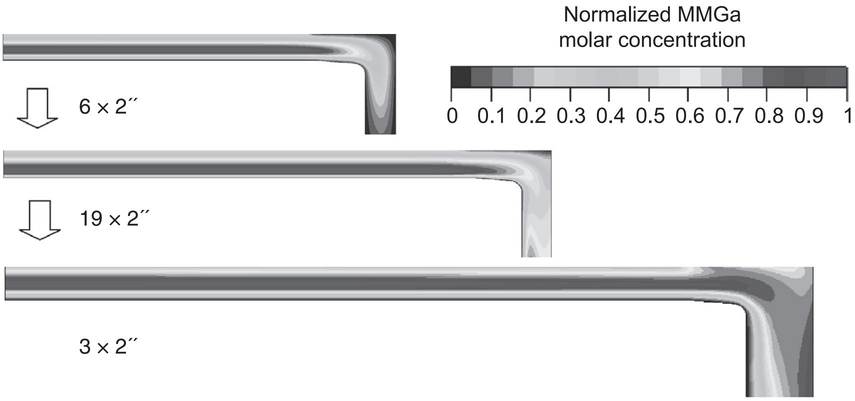

2.21 Calculated distribution of MMGa for different sizes of CCS reactor. The boundary layer thicknesses are very similar and thus the growth rates are similar in the different reactors. Thus it is easy to transfer a process from a small reactor to a larger reactor.

will increase with an increase in total flow. However, with N_2 carrier gas, the diffusion coefficient of MO species is lower than with H_2. The growth rate might not increase with N_2 carrier gas. The growth rate is independent of reactor pressure because ρv is constant when the pressure changes for the same total flow rate. The computer simulation shows that the thickness of the boundary layer is uniform across the whole susceptor so that a uniform growth rate is an intrinsic property of a CCS reactor. For a larger diameter of CCS reactor, the growth rate can be kept the same by scaling up the total flow rate and the molar flow of the MO precursor by the ratio of the area as shown in Fig. 2.21. This makes scaling up CCS reactors very straightforward and the process can be transferred from a small reactor to a larger reactor.

2.4.2 Design of a modern CCS reactor

Figure 2.22(a) shows a state-of-the-art CCS reactor with a wafer configuration of 55 × 2″. The configuration can be changed just by swapping the susceptors. The default reactor height is 11 mm and the diameter of the susceptor is 490 mm. In Fig. 2.22(b) the reactor height is larger compared to Fig. 2.22(a). One of the advanced features of this CCS reactor is that the reactor height can be adjusted in the range 5–25 mm and there is precise control using a step motor. This can be done dynamically during the growth run through electronic control to optimize the growth conditions for different materials or device structures. For example, it is better to grow a GaN layer at an elevated reactor pressure because this improves the quality of the crystal. However, the gas phase reactions of TMGa and NH_3 will also increase at elevated pressure. Reducing the reactor height during GaN growth at an elevated pressure can increase the growth rate.

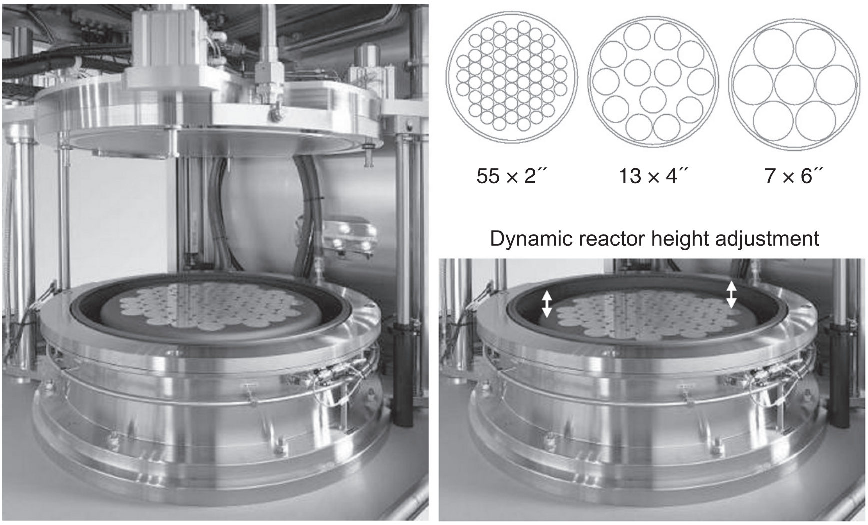
55 × 2″
13 × 4″
7 × 6″
Dynamic reactor height adjustment

2.22 State-of-the-art 55 × 2″ CCS reactor. The wafer configuration can be changed to 13 × 4″ and 7 × 6″ by swapping the susceptor. In the photograph on the right, the susceptor has moved down to increase the reactor height.

Figure 2.23(a) shows the tungsten heater for this 55 × 2″ CCS reactor. The heater has three zones, which are controlled separately. As the diameter of the susceptor becomes larger and larger, it is more and more difficult to maintain a uniform temperature across the whole susceptor. A computer model of the thermal management is very helpful and saves time and costs in heater design. Figure 2.23(b) shows the temperature distribution at the susceptor's edge, which

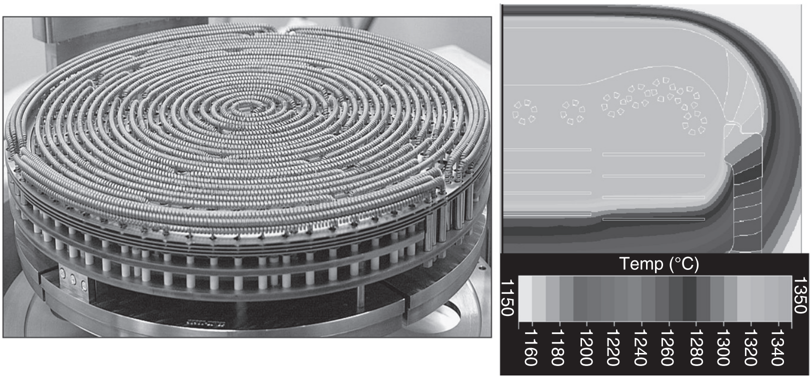
Temp (°C)
1150
1350
1160
1180
1200
1220
1240
1260
1280
1300
1320
1340

(a)

(b)

2.23 Heater for a 55 × 2″ CCS reactor. (a) Tungsten heater with three zones. (b) Computer model for heater optimization.

needs special care due to its higher heat loss through thermal radiation. The tungsten filaments in the heater zone on the edge have a higher density and are elevated to be closer to the susceptor. There are four molybdenum plates underneath the tungsten filaments, which reflect the thermal radiation up to the susceptor. With this design, the edge of the susceptor can be heated more efficiently to give a uniform susceptor temperature.

Figure 2.24(a) shows the growth rate of GaN versus reactor pressure for various reactor heights with a fixed TMGa molar flow. At the standard height of 11 mm, the growth rate drops from 2.5 μm/h at 200 mbar to 1.3 μm/h at 800 mbar, which is about a 50% reduction of the growth efficiency. At the reduced heights of 9 and

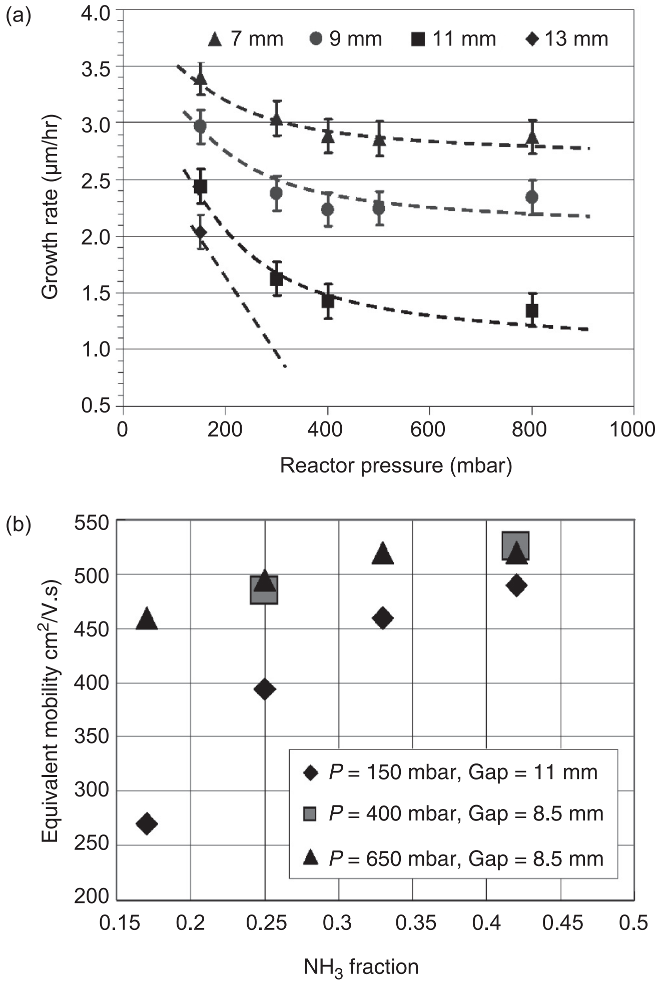

2.24 n-GaN growth for different reactor heights: (a) growth rate vs reactor pressure; (b) electron mobility vs NH_3 fraction.

7 mm, the growth rate at 200 mbar is 3.0 μm/h and 3.4 μm/h and only drops to 2.3 μm/h and 2.8 μm/h at 800 mbar, respectively. There is only about a 20% reduction of the growth rate from 200 mbar to 800 mbar. There are two reasons for the increase in growth rate with reduced reactor height. One is the reduced thickness of the boundary layer, which is inversely proportional to the square root of the reactor height. The other reason is that the residence time of the reactant gases is reduced with reduced height, which decreases the chances of the gas phase reaction occurring between the reactant gases. Figure 2.24(b) shows the electron mobility of the n-GaN layer versus NH_3 fraction for various pressures. Since the growth rate of the n-GaN layer depends on pressure, the reactor height was adjusted to give the same growth rate with the same TMGa molar flow rate. The target doping level for the n-GaN layer was 2×10^{17} cm^{-3}. However, there is a slight shift in the doping level of the n-GaN samples for different growth conditions. The empirical trend of the electron mobility versus carrier concentration in a CCS reactor was used to calibrate the mobility of the n-GaN samples at 2×10^{17} cm^{-3}. At 150 mbar pressure with 11 mm height, the electron mobility has a strong dependence on the NH_3 fraction. However, the electron mobility of n-GaN grown at 400 mbar and 650 mbar with 8.5 mm height is almost the same and for both conditions there is a weaker dependence on the NH_3 fraction than at 150 mbar. For all fractions of NH_3, a higher pressure improves electron mobility.

Figure 2.25 shows the GaN growth rate in the 55 × 2″ reactor for elevated pressures up to 900 mbar. The growth conditions, such as total flow rate and reactor height, were optimized to give the maximum growth rate for each pressure. A growth rate of up to 30 μm/h can be achieved at 200 mbar in such a large-scale

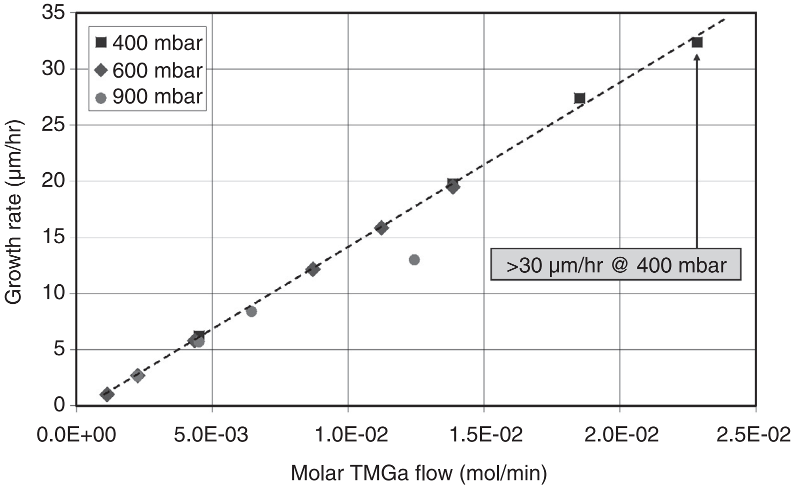

2.25 GaN growth rate vs TMGa molar flow for elevated reactor pressures up to 900 mbar.

reactor. The linearity of growth rate versus TMGa molar flow indicates that there are no gas phase reactions, which would reduce the growth efficiency. The growth rate at 900 mbar can reach 10 μm/h before saturation starts due to the gas phase reaction.

2.5 *In situ* monitoring systems and growing nitride-based materials

The requirements for LEDs are increasing in applications such as back-lighting units for liquid crystal displays and solid-state lighting. To increase production yields and therefore to reduce costs, it is very beneficial to use an *in situ* monitoring system during the epitaxial growth of LED wafers. A state-of-the-art *in situ* monitoring system for GaN-based materials can measure the reflectance, temperature and curvature of the wafer, which are used for analysis and to control the growth parameters.

2.5.1 Measuring reflectance

Light radiates through the viewport of the reactor onto the wafer and is reflected by the wafer back to the photodetector. The intensity of reflectance depends on the refractive index of the layer, interference at interfaces, absorption of light by material and scattering at the layer surface, which depends on the morphology of the layer. The refractive index of a material is a function of temperature so that changing the temperature can change the refractive index and therefore the reflectance signal. By interrupting the growth and observing the surface morphology using a scanning electron microscope (SEM) and an atomic force microscope (AFM), data were collected, which show that there is quite good correlation between the reflectance curve and surface morphology or crystal quality of the epitaxial layer.

A GaN-based LED epiwafer grown on a sapphire substrate is transparent to the typical wavelengths of the light sources used for reflectance measurement, such as 950 nm, 880 nm and 633 nm. There are more than two interfaces that reflect the incident light and this results in Fabry–Pérot (FP) oscillations.[11] Figure 2.26 shows an FP oscillation. When the optical path of the reflected light is an integer multiple of the wavelength in the material ($m\lambda/n_1$), there is constructive interference and the strong intensity of the reflected light can be measured. If the optical path is $(m+1/2)\lambda/n_1$ there is destructive interference, which reduces the intensity of the reflected light. As the thickness of the layer increases during growth, the light undergoes alternating constructive and destructive interference, which results in peaks and valleys in the reflectance curve. Assuming that the light is incident normal to the surface, which is the typical set-up in MOCVD systems, constructive interference happens when

$$2d_1 = m\lambda/n_1 \text{ and } 2d_2 = (m+1)\lambda/n_1 \qquad [2.10]$$

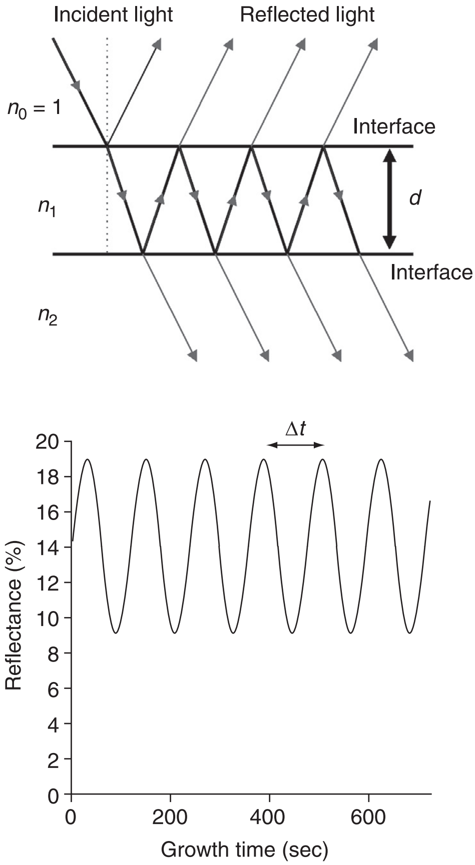

2.26 Fabry–Pérot oscillation of the reflectance signal during GaN growth on a sapphire substrate. n_1 and n_2 are the refractive indices of GaN and sapphire, respectively.

where d_1 and d_2 are the thicknesses at the start and end of the growth of duration Δt, λ is the wavelength of the light source and m is an integer. Hence the growth rate is given by

$$R_g = (d_2 - d_1)/\Delta t = \lambda/(2n_1\Delta t) \qquad [2.11]$$

The change of thickness for one oscillation cycle is $\lambda/(2n_1)$, which means the shorter the wavelength, the thinner the layer needed for one full oscillation cycle required for the growth rate calculation. Various wavelengths are used to measure reflectance. Therefore it is more beneficial to use a shorter wavelength such as 633 nm and 405 nm to calculate the growth rate of a thin layer in the structure of an LED or other device.

The amplitude of an oscillation between a peak and a valley and the average reflectance level will decrease if the light source has a broad bandwidth or there is

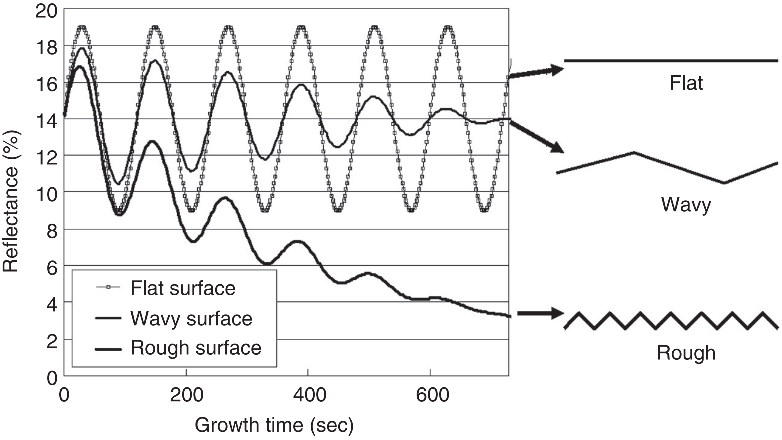

2.27 Reflectance signal for three surface morphologies of a GaN layer grown on a sapphire substrate.

absorption by material and they also depend on the surface morphology of the layer. Figure 2.27 shows the reflectance for three typical surface morphologies – flat, wavy and rough – that are found in GaN epitaxial growth. For a wavy surface, the incident light will follow paths of different lengths inside the layer and this will reduce the coherence of the reflected light and the amplitude of the interference will shrink gradually as the total thickness increases. For a rough surface, the coherence of the reflected light will be reduced further and the intensity of the reflected light will decrease due to scattering by the rough surface. The difference between a wavy surface and a rough surface is down to the dimensions of the feature. When the period of the feature L is much larger than the wavelength λ, the surface is described as wavy. If L is close to the wavelength λ, the surface is described as rough.

Figure 2.28 shows a typical reflectance curve of GaN grown on a sapphire substrate measured by *in situ* monitoring system using a 950 nm light source. The reflectance of the bare sapphire substrate for the 950 nm wavelength is 7.8%. The thickness of the low-temperature GaN nucleation layer can be deduced from the increase in the reflectance, which acts as an indirect tuning parameter for the nucleation thickness. The recrystallization of the nucleation layer at an elevated temperature changes the smooth surface of the amorphous GaN nucleation layer into 3D GaN polycrystalline islands, which scatter the light and reduce the reflectance. When the TMGa precursor is introduced into the reactor, the GaN islands grow three dimensionally and scatter the light further and this results in almost zero reflectance. Then the islands start to coalesce with each other to form a quasi 2D layer. The reflectance curve starts to increase periodically until the islands fully coalesce into a smooth surface. The periodic oscillation comes from the FP interference of the truncated pyramids. The growth time for the reflectance

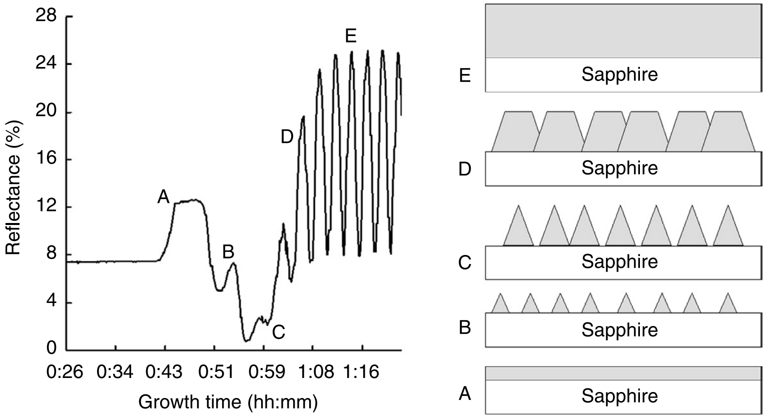

2.28 The shape of the reflectance curve correlates to the surface morphology. A: nucleation growth, B: recrystallization, C: 3D island growth, D: 3D coalescence to 2D, E: fully coalesced layer.

curve to reach a saturated level is an indicator of the thickness of the 3D layer. This layer can relax the strain between the GaN epilayer and the sapphire substrate and reduce the dislocation density. The thicker the layer the better.

Figure 2.29 shows the reflectance curve at 950 nm and the reactor temperature for the growth of the full LED structure. The growth rates of the strain-relaxation

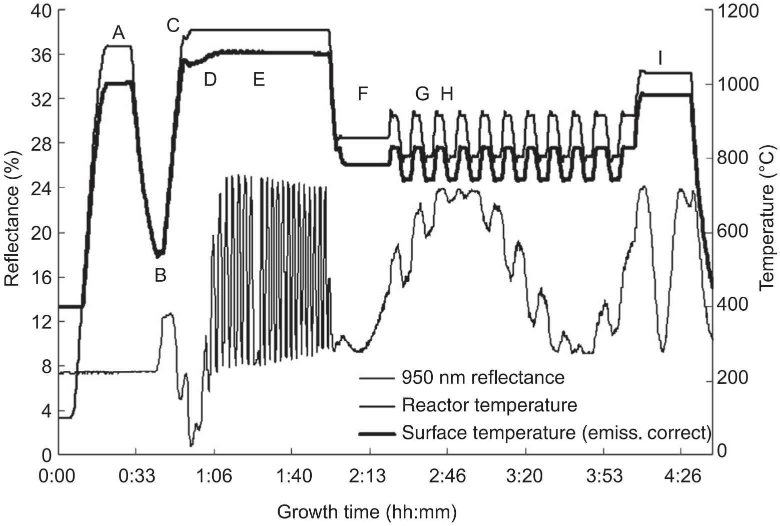

2.29 The reflectance curve, reactor temperature and emissivity-corrected surface temperature of a generic LED growth run.
A: desorption, B: nucleation, C: recrystallization, D: 3D → 2D recovery,
E: undoped GaN and n-doped GaN, F: strain-relaxation layer,
G: barrier, H: quantum well, I: p-doped GaN.

layer and the MQW are quite low so that the oscillation of the reflectance is slow. The reflectance of the MQW is modulated by temperature ramping between the barrier and the quantum well because the refractive index of the material is modulated by temperature ramps. The p-doped GaN layer is about 0.2 μm thick, which produces one full oscillation of the reflectance curve. If the reflectance were measured using a 633 nm or 405 nm light source, the increased number of oscillations would make it easier to calculate the growth rate and monitor the growth.

2.5.2 Measuring temperature

The incorporation of indium atoms into an InGaN layer and therefore the emission wavelength of InGaN/GaN MQWs are strongly related to the surface temperature of the wafer. Depending on the thickness and the indium composition of the quantum well, the emission wavelength can shift 2–4 nm/°C. In a MOCVD reactor, the surface temperature of the wafer needs to be uniform and stable because any temperature variation has a strong impact on the yield, given a typical LED wavelength bin of 2.5 nm. Precise measurement and closed-loop control of the surface temperature will help to keep the surface temperature of the wafer more uniform and stable.

The principle of temperature measurement using a pyrometer is based on Planck's law. Planck's formula for the intensity of black-body radiation as a function of absolute temperature is:

$$B_\lambda(T) = \frac{2hc^2}{\lambda^5} \cdot \frac{1}{e^{hc/\lambda kT} - 1} \qquad [2.12]$$

where h is Planck's constant, c is the speed of light, λ is the wavelength of the black-body radiation, k is the Boltzmann constant and T is the temperature in kelvin. By measuring the intensity of the radiation at certain wavelengths, one can deduce the temperature of the object. In reality, different materials have different emissivities (ε), which affects the intensity of the radiation. Figure 2.30 shows spectra of black-body radiation at 800 K, 1000 K and 1400 K, which are the typical growth temperatures for a low-temperature GaN nucleation layer, a quantum well and n-GaN, respectively. The intensity at the typical wavelength of 950 nm used by pyrometers is indicated on the right of Fig. 2.30(b).

Figure 2.31 shows the emissivity-corrected surface temperature of a GaN wafer measured with a 950 nm pyrometer. Because GaN on sapphire is transparent to 950 nm radiation, the 950 nm wavelength radiation measured by the photodetector mainly comes from the surface of the susceptor. Thus, the surface temperature of the susceptor is measured, instead of the surface temperature of the wafer. Some of the radiation will be reflected by the wafer interfaces or scattered by the rough underside of the substrate so that the detector will measure a reduced intensity and a lower surface temperature for the susceptor. Moreover, the reflectance will

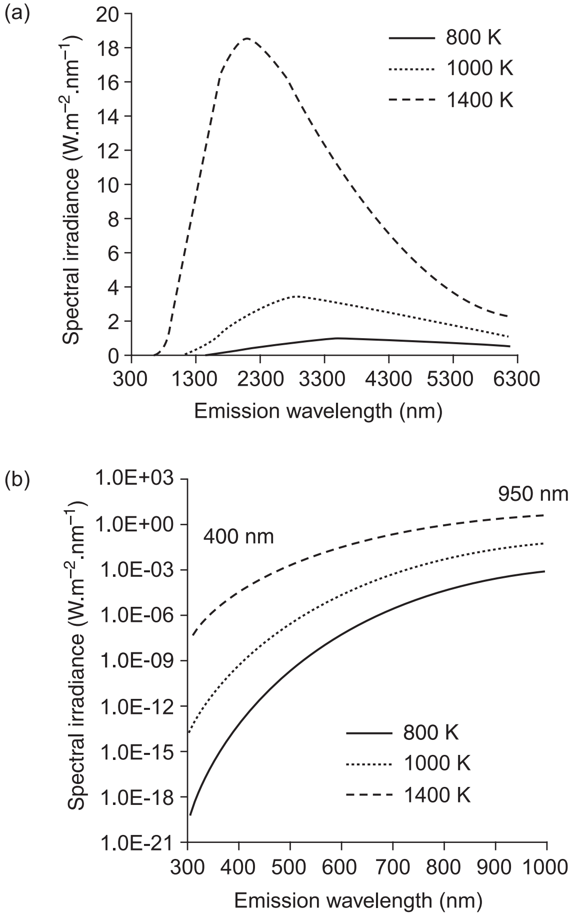

2.30 Spectra of black-body radiation at 800 K, 1000 K and 1400 K. (a) Full spectra with intensity in a linear scale. (b) Spectra from 300 nm to 1000 nm with intensity in a logarithmic scale.

oscillate due to FP interference. The surface temperature will also oscillate with the same period as the reflectance curve. To get a reliable temperature measurement, the reflectance of the GaN wafer at 950 nm is measured to recover the original intensity of the radiation. The scattering loss due to the unpolished underside of the substrate is also calibrated. The resulting calculated temperature is called the emissivity-corrected surface temperature of the susceptor. In the recovery step indicated in the chart, the surface of the GaN layer is rough due to 3D growth. This increases the loss by scattering of the thermal radiation so that the temperature measured in the recovery step is much lower than that in the fully coalesced step, even though the reactor temperature is the same. This is an artifact of the temperature measurement.

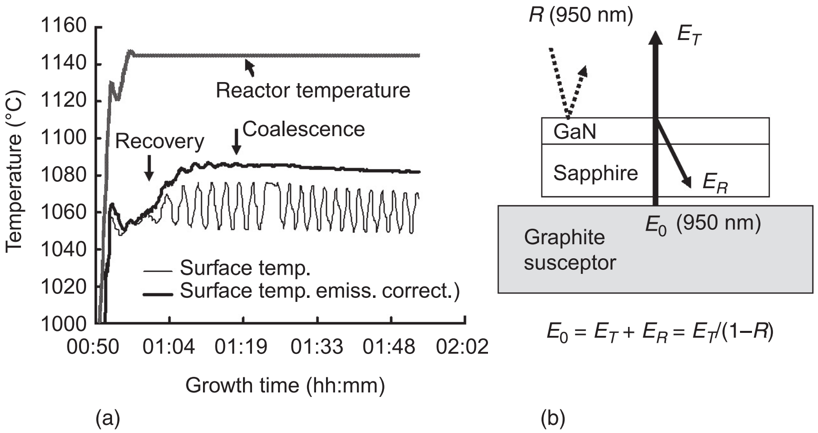

2.31 (a) Surface temperature and emissivity-corrected surface temperature vs growth time during GaN growth on a sapphire substrate. The emissivity-corrected surface temperature is much lower in the recovery step than in the fully coalesced step, even though the reactor temperature is the same. (b) Measurement of the surface temperature of a graphite susceptor. E_0 is the radiation from the susceptor surface. E_R is the radiation lost in the air/GaN/sapphire interface. E_T is the radiation received by the photodetector.

For a vertical MOCVD reactor, an optical viewport can only cover the area of the susceptor passing under it by the main rotation of the susceptor and it only provides temperature information for a few single points in the radial direction. This is not good enough to control the temperature uniformly over the whole susceptor. A linear detector array is designed to provide 2D mapping of the surface temperature of the susceptor in a CCS system, as shown in Fig. 2.32. The linear detector array is mounted on the viewport of the group III upper plenum of the showerhead and each detector is aligned with an injection tube for the group III plenum. The thermal radiation from the susceptor will penetrate through the very narrow injection tubes, which act as spatial collimators and filter the incident radiation. Only radiation from a small area under a tube is collected by a detector. Therefore, it can provide a high spatial resolution of the susceptor temperature. The detector array is distributed radially from the center to the edge of the susceptor and one revolution of the susceptor provides a full scan over the entire susceptor to create a 2D map of the surface temperature. Each detector has two diodes packed together; they are made of Si and InGaAs and they detect two different wavelengths. The emissivity change of the radiation through the wafer and the injection tube can be simultaneously calibrated for each measurement to generate a reliable emissivity-corrected surface temperature. In Fig. 2.32(b), the position of the wafer pockets can be clearly identified from the 2D map since the temperature in a pocket is slightly higher than at the edge of a pocket. This is because the thickness of the susceptor is slightly thinner under a pocket than it is

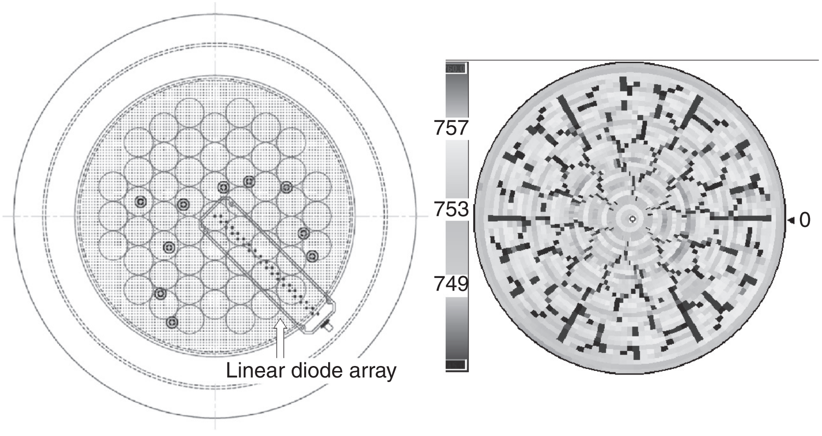

(a) (b)

2.32 (a) Linear diode array for 2D mapping of the surface temperature in a CCS reactor. (b) 2D map of surface temperature.

on the pocket edge and because the surface is closer to the heater. By *in situ* adjustment of the feeding ratio of the three-zone heater power, the temperature deviation over the entire susceptor can be controlled within 1 °C.

Measuring the surface temperature of the susceptor can give a quite good indication for how to adjust the growth temperature because the temperature gradient from the susceptor to the wafer surface is more or less fixed and predictable. However, this is not precise enough to meet the high yield requirement of LED production nowadays. Figure 2.33(a) shows the surface temperature of a GaN wafer made by the latest 400 nm pyrometer. In the typical growth temperature of 700–800 °C for a InGaN/GaN MQW or 1000–1100 °C for a GaN bulk layer, the GaN bandgap will fall from 3.39 eV at room temperature to around 3.0 eV at 700 °C.[12] Therefore, the GaN layer becomes opaque to the 400 nm wavelength thermal radiation (with photon energy 3.1 eV) from the susceptor and the radiation will not penetrate through the GaN layer to the photodetector. The 400 nm wavelength thermal radiation collected by the detector will only come from the GaN surface and there will be no FP interference to affect the intensity of the thermal radiation. As shown in the figure, the surface temperature of the GaN layer measured by a 400 nm pyrometer is lower than that measured by a 950 nm pyrometer. Because of the concave bowing, there is a deviation of the GaN surface temperature from the center to the edge of about 8 °C, which cannot be seen by a traditional 950 nm pyrometer. A pyrometer operating at 400 nm can provide a precise measurement of the surface temperature of a wafer during InGaN/GaN MQW growth and can be used to stabilize the MQW wavelength through closed-loop control. However, as indicated in Fig. 2.30, the thermal radiation at 400 nm for typical growth temperatures of 700–1100 °C for a GaN-based LED is three to

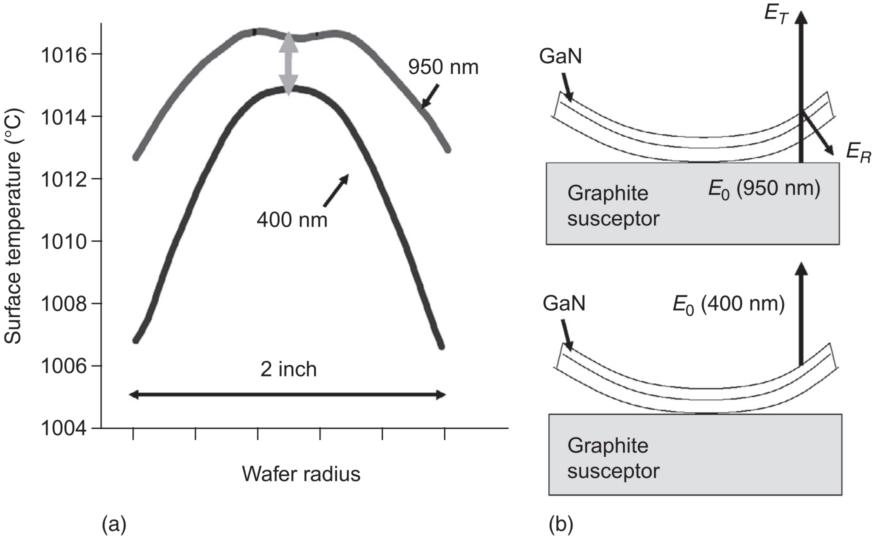

2.33 (a) Comparison of the surface temperature of GaN on sapphire measured with a pyrometer using 400 nm or 950 nm light. (b) Measurement of radiation from the GaN surface.

seven orders of magnitude lower than at 950 nm. The measurement system needs to have a high signal-to-noise ratio to deal with the very low intensity of radiation to get reliable data.

2.5.3 Measuring curvature

As discussed in the previous section for the 400 nm pyrometer, bowing of the wafer will change the thermal contact between the wafer and the susceptor and significantly change the surface temperature of the wafer. Therefore, it is beneficial to measure and control wafer bowing during LED growth, especially in an MQW growth step, which is very sensitive to the surface temperature. Figure 2.34 shows the optical set-up for curvature measurement. A laser beam from a semiconductor laser diode is passed through a beam splitter, which generates two parallel laser beams. The two parallel laser beams will have different angles of incidence on the curved wafer surface. A charge-coupled-device (CCD) camera is used to detect the two laser beams. *In situ* software fitting of the CCD image is used to determine the distance between the laser spots. An increase in the distance means convex bowing and a decrease means concave bowing. Based on Euclidean geometry, the curvature of the wafer surface and the gap (Δz) between the wafer and the susceptor can be deduced from the distance between the spots:

$$\Delta z = R_C \cdot \left(1 - \cos\frac{r}{R_C}\right) \qquad [2.13]$$

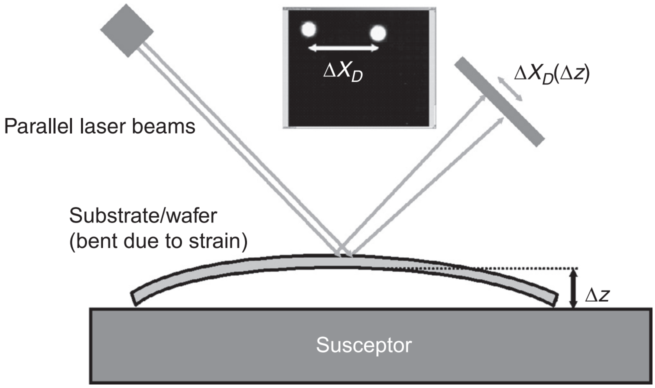

2.34 Optical set-up for wafer curvature measurement (courtesy of Laytec).

where R_C is the radius of curvature of the wafer, which is the inverse of curvature, and r is the radius of the wafer. For a 4″ wafer with a curvature of $+100\,\text{km}^{-1}$ (concave), the gap at the edge of the wafer will be as large as 130 μm, which will cause a significant drop of the surface temperature on the wafer's edge.

Table 2.2 shows the lattice constant and coefficient of thermal expansion (CTE) of nitride-based materials and substrates. At the typical growth temperature, the thermal gradient will cause concave bowing of a wafer because there is a higher temperature at the susceptor and wafer bottom than at the wafer surface. In a GaN-based device, a tensile strain in the upper layer applied to the lower layer due to the mismatch of both lattice constant and CTE will cause convex bowing of the wafer, while a compressive strain in the upper layer applied to the lower layer will cause concave bowing of the wafer. Sometimes, a defective layer grown at a low temperature is used as a strain-relaxation layer to decouple the upper and lower

Table 2.2 Material properties of III nitrides and substrates[13]

Material	Axis	Lattice constant (Å)	Thermal expansion coefficient (10^{-6}/K)
AlN	a	3.11	5.72
	c	4.978	4.77
GaN	a	3.189	5.59
	c	5.185	7.75
InN	a	3.54	5.7
	c	5.705	3.7
Sapphire	a	4.758	7.5
	c	12.991	8.5
Si (111)	a	3.84	2.6

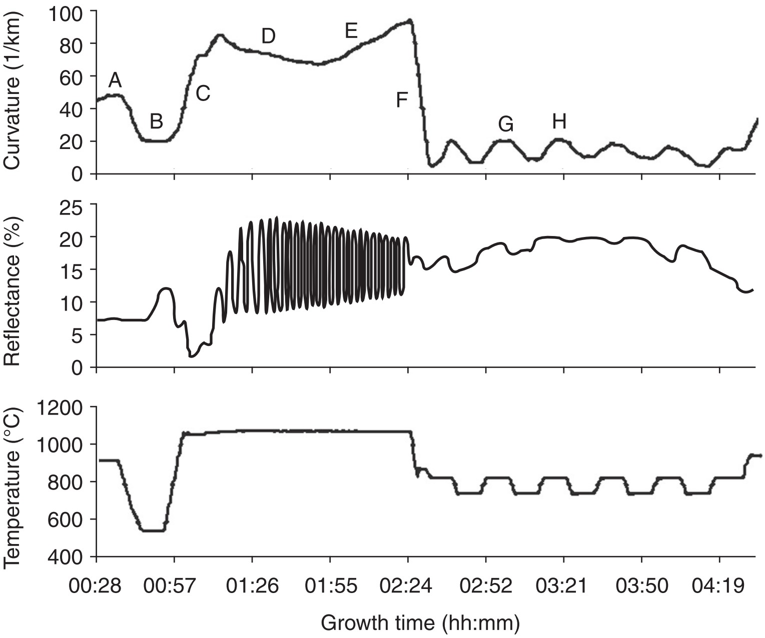

2.35 Curvature measurement during an LED run (until the MQW step). Positive curvature is defined as concave bowing. A: desorption, B: nucleation, C: temperature-related curvature change, D: undoped GaN, E: n-doped GaN, F: temperature-related curvature change, G: barrier, H: quantum well.

layers. Inserting different nitride-based materials into the device structure is basically the way to manage the strain and wafer bowing. Figure 2.35 shows the curvature for a typical GaN-based LED growth run using a low-temperature GaN nucleation layer.

In the high-temperature desorption step with bare sapphire, the concave bowing of the wafer is due to the thermal gradient through the thickness of the substrate. The curvature in the nucleation step drops due to the lower growth temperature and lower thermal gradient. The growth of GaN nucleation does not change the curvature as it is too thin to apply a strain to the substrate. In the recrystallization and coalescence steps, the reactor temperature rises again and the curvature increases accordingly. The conditions in the nucleation, recrystallization and coalescence steps will determine how much the strain between the GaN epitaxial layer and the sapphire substrate is released and affect the curvature of the wafer during the growth of the upper layers. In this case, during the growth of undoped GaN, the curvature decreases, which is a result of strain relaxation during the 3D to 2D coalescence. However, the curvature increases during the growth of n-doped GaN because the silicon atoms are smaller than the gallium atoms they replace and a compressive strain is applied to the undoped GaN layer. When the temperature cools down for MQW growth, the curvature decreases dramatically to nearly zero due to the larger CTE of the sapphire substrate compared to the nitride-based materials in the LED. This means the wafer on the susceptor is flat during the growth of a quantum well. The surface temperature of the wafer will be uniform and so will be the emission wavelength of the MQW. It is more efficient to determine which layer causes curvature using *in situ* monitoring of curvature during the whole growth process than a complex experiment to identify the root cause by measuring a wafer after the growth run has finished.

2.6 Acknowledgements

The author would like to thank Dr Martin Dauelsberg, Dr Rainer Beccard, Thomas Korst and Dr Olivier Feron of AIXTRON SE for contributing graphs and photographs for this chapter.

2.7 References

1. Stringfellow, G.B. (1989) *Organometallic Vapor-Phase Epitaxy: Theory and Practice*, San Diego, Academic Press.
2. Hurle, D.T.J. (1994) *Hand Book of Crystal Growth Volume 3: Thin Films and Epitaxy*, Amsterdam, Elsevier.
3. Nakamura, S., Pearton, S. and Fasol, G. (2000) *The Blue Laser Diode: The Complete Story*, Berlin, Springer.
4. Mesrine, M., Grandjean, N. and Massies, J. (1998) 'Efficiency of NH_3 as nitrogen source for GaN molecular beam epitaxy', *Appl. Phys. Lett.* 72, 350.
5. Neumayer, D.A. and Ekerdt, J.G. (1996) 'Growth of group III nitrides: a review of precursors and techniques', *Chem. Mater.* 8, 9.
6. Stagg, J.P., Christer, J., Thrush, E.J. and Crawley J. (1992) 'Measurement and control of reagent concentrations in MOCVD reactor using ultrasonics', *J. Crystal Growth* 120, 98.
7. Creighton, J.R., Wang, G.T., Breiland, W.G. and Coltrin, M.E. (2004) 'Nature of the parasitic chemistry during AlGaInN OMVPE', *J. Crystal Growth* 261, 204.
8. Mitrovic, B., Gurary, A. and Quinn, W. (2007) 'Process conditions optimization for the maximum deposition rate and uniformity in vertical rotating disc MOCVD reactors based on CFD modeling', *J. Crystal Growth* 303, 323–29.
9. Mihopoulos, T.G., Hummel, S.G. and Jensen, K.F. (1998) 'Simulation of flow and growth phenomena in a close-spaced reactor', *J. Crystal Growth* 195, 725–32.
10. Schlichting, H. (1979) *Boundary-Layer Theory*, 7th ed., New York, McGraw-Hill.
11. Yariv, A. (1991) *Optical Electronics*, 4th ed., Orlando, Saunders College, Ch. 4.
12. Teisseyre, H., Perlin, P., Suski, T., Grzegory, I., Porowski S., *et al.* (1994) 'Temperature dependence of the energy gap in GaN bulk single crystals and epitaxial layer', *J. Appl. Phys.* 76(4), 2429–34.
13. Edgar, J.H. (1994) *Properties of Group III Nitrides*, London, INSPEC, Ch. 1.

3

Gallium nitride (GaN) on sapphire substrates for visible LEDs

J.-H. RYOU, University of Houston, USA

DOI: 10.1533/9780857099303.1.66

Abstract: This chapter describes GaN epitaxial materials grown on sapphire substrates since they are a very important technological platform for visible light-emitting diodes (LEDs) and solid-state lighting technology. The chapter begins with the historical background of GaN material development and describes the fundamental properties of sapphire as a substrate for the epitaxial growth of GaN. The chapter then discusses fundamental, technical and economic aspects of GaN on sapphire, relevant for LEDs, including strained heteroepitaxial growth, epitaxial overgrowth and non-polar and semi-polar GaN growth, followed by a brief outlook of LEDs based on GaN on sapphire.

Key words: light-emitting diode (LED), GaN (gallium nitride), sapphire substrate, strained heteroepitaxial growth, epitaxial overgrowth.

3.1 Introduction

The III-nitride (III-N)-based visible blue and green light-emitting diodes (LEDs) currently in production are predominantly (more than 90% as of the time of writing) manufactured on sapphire substrates with a gallium nitride (GaN) buffer layer. Therefore, GaN on sapphire is the most important technology currently in use for LEDs and LED-based solid-state lighting (SSL) applications. The epitaxial growth of GaN materials has a longer history than is generally perceived – only slightly shorter than gallium arsenide (GaAs) and indium phosphide (InP) (~10 years after the epitaxial growth of GaAs) (Dupuis and Krames, 2008), even though the successful development of epitaxial growth technology followed by device development came approximately 30 years later. This section gives an overview of the history of the synthesis and epitaxy technology for GaN materials as recorded in the literature.

As already mentioned, sapphire substrates are an important and currently the dominant technological platform for the epitaxial growth of III-N-based photonic and electronic devices (Davis *et al.*, 2003; DenBaars, 1997; Pearton and Ren, 2000; Mishra *et al.*, 2002). Using sapphire substrates for the epitaxy of III-V semiconductor materials (including III-N semiconductor materials) also has a long history. The first epitaxial single-crystal GaN films were grown on sapphire substrates (Kosicki and Kahng, 1969; Maruska and Tietjen, 1969). Manasevit, who is acknowledged as the inventor of the metalorganic chemical vapor deposition (MOCVD) process (Manasevit, 1981, 1983), used sapphire substrates along with other substrates such as spinel ($MgAl_2O_4$), beryllium oxide (BeO) and thorium oxide (ThO_2), for the epitaxial growth of III-V and II-VI materials (Manasevit, 1968, 1972).

3.1.1 The history of epitaxial GaN on sapphire substrates for device-quality materials

The history of GaN material technology can be divided into several phases by technological maturity, including the early development, powder GaN, thin-film GaN and device-quality epitaxial GaN.

Early development

In the early development stage, GaN materials were powder forms prepared mostly by chemists. Research was focused on the synthesis of nitrides of various metallic compounds, including boron nitride (BN) and aluminum nitride (AlN), and their fundamental properties. The synthesis of GaN materials can be traced back to the 1930s. Johnson *et al.* (1932) described the formation of a GaN material using metallic gallium (Ga) and ammonia (NH_3) gas, which are similar to the sources currently used in gas-source molecular beam epitaxy (MBE). The reaction occurred after passing NH_3 gas over metallic gallium at 900–1000 °C following the proposed reaction:

$$2Ga + 2NH_3 \rightarrow 2GaN + 3H_2 \qquad [3.1]$$

In the same report, they also described an unsuccessful attempt to react metallic gallium with nitrogen gas (N_2). In addition, the exceedingly stable thermal and chemical properties of GaN in solutions of HCl, HF, HNO_3 and hot aqua regia were reported (Johnson *et al.*, 1932). Hahn and Juza (1940) also prepared GaN by thermal decomposition of ammonium hexafluorogallate ($(NH_4)_3GaF_6$). Later, Renner (1959) prepared GaN by a van Arkel–de Boer process (a crystal bar process) with the following reaction using sources similar to those currently used in hydride vapor phase epitaxy (VPE):

$$GaCl_3 + NH_3 \rightarrow GaN + 3HCl \qquad [3.2]$$

Powder GaN

In the 1960s, as one of the wide-bandgap semiconductors, GaN started to find applications, especially as a phosphor in cathode-ray tubes. The GaN materials, however, were still powder forms, unlike the thin-film epitaxial materials on specific substrates currently used for active devices (in contrast to passive device). For example, Addamiano (1961) used powders of gallium phosphide (GaP) or GaAs in a stream of NH_3 gas at 1000–1100 °C, such as in the following reaction:

$$GaP+NH_3 \rightarrow GaN+\frac{1}{4}P_4+\frac{3}{2}H_2 \qquad [3.3]$$

In the same study, AlN was also synthesized and the AlN and GaN powders were mixed in a heated and sealed quartz container in an attempt to prepare ternary AlGaN materials. Even though it was not successful, this was the first attempt at the synthesis of ternary III-N materials recorded in the literature. Lorenz and Binkowski (1962) used reduction and nitridation of gallium trioxide (Ga_2O_3) to prepare GaN powder using NH_3 through the proposed reaction:

$$Ga_2O_3+2NH_3 \rightarrow 2GaN+3H_2O \qquad [3.4]$$

Thin-film GaN

Thin-film GaN materials were later prepared by gas discharge on a quartz plate by Pasternak and Souckova (1963) but the deposited film appeared to be polycrystalline:

$$2GaCl_3+N_2 \rightarrow 2GaN+3Cl_2 \qquad [3.5]$$

The first single-crystal epitaxial GaN films were described by Kosicki and Kahng (1969) and Maruska and Tietjen (1969), and both were grown on sapphire (0001) substrates. Kosicki and Kahng (1969) used a remote gaseous discharge to dissociate molecular N_2 into atomic nitrogen (N) and elemental gallium, which was similar to the method used by Pasternak and Souckova (1963) to obtain a single-crystal epitaxial GaN layer at temperatures above 550 °C. This paper was the first to identify the 30° rotation of basal GaN hexagons along the *c*-axis with respect to sapphire to minimize the mismatch between them:

$$(0001)_{GaN} //(0001)_{Al_2O_3} \text{ and } [\bar{1}2\bar{1}0]_{GaN} //[\bar{1}100]_{Al_2O_3}.$$

Maruska and Tietjen (1969) deposited the film by hydride VPE using HCl and NH_3 through these typical simplified reactions:

$$Ga+HCl \rightarrow GaCl+\frac{1}{2}H_2 \text{ and } GaCl+NH_3 \rightarrow GaN+HCl+H_2 \qquad [3.6]$$

Structural and electronic properties including lattice constants $a=3.189$ Å and $c=5.185$ Å and a bandgap energy of $E_g=3.39$ eV at room temperature, which are very close to currently accepted values, were measured. A high electron concentration of $n=1-5\times10^{19}\,cm^{-3}$ and a mobility of $\mu=125-150\,cm^2.V^{-1}.s^{-1}$ were obtained, possibly due to rather high densities of defects such as point defects (vacancies and impurities), line defects (dislocations) and even planar defects (grain boundaries). However, there was no description of the surface morphology in this report, which was suspected to be very rough, not specular.

Since the first demonstration of single-crystal thin-film GaN layers, many studies followed, which further investigated the quality of the films using various synthesis methods. Faulkner *et al.* (1970) prepared thin-film GaN layers using vapor deposition by reacting $GaCl_3$ and NH_3 on silicon carbide (SiC) substrates. Manasevit *et al.* (1971) described the MOCVD growth of GaN and AlN on sapphire and SiC substrates in a series of publications on growth using metalorganics via the following simplified chemical reaction:

$$Ga(CH_3)_3 + NH_3 \rightarrow GaN + 3CH_4 \qquad [3.7]$$

This paper described the surface morphology of a GaN layer on a sapphire substrate. The rough surfaces had whiskers, which are essentially the same as the nanorods used in contemporary nanotechnology. Wickenden *et al.* (1971) also described the epitaxial growth of GaN on both sapphire and SiC substrates using both hydride VPE and trichloride VPE. In particular, this study compared the growth of GaN on sapphire substrates with various orientations including (0001), $(10\bar{1}0)$ and $(11\bar{2}0)$, which is a similar approach to the current non-polar and semi-polar growth of GaN. The surfaces were not smooth on the (0001) sapphire substrates in this research, either. In parallel with the development of epitaxial growth to produce high-quality GaN thin-film materials (Hashimoto *et al.*, 1984), the optical, chemical and electrical properties of the newly developed GaN layers were investigated (Ilegems *et al.*, 1972; Monemar and Lagerstedt, 1979; Khan *et al.*, 1983). In particular, Pankove *et al.* (1971) were the first to describe electroluminescence (EL) in GaN. They observed blue emission from spots near a negative electrode at ~2.6 eV ($\lambda \sim 475$ nm) for a zinc-doped GaN layer on a sapphire substrate.

Besides the development of the growth of thin-film GaN, Zetterstrom (1970) synthesized single-crystal GaN needles up to 1 mm thick and 5 mm in length from a specially treated GaN powder in a stream of NH_3.

Device-quality GaN epitaxial growth

While there had been extensive studies on GaN materials and their properties for potential applications as visible light-emitting devices, progress in producing a 'device-quality' GaN epitaxial layer was slow, until the development of buffer layer concepts for heteroepitaxial growth. Yoshida *et al.* (1983) and Amano *et al.* (1986) were the first to report the growth of device-quality GaN epitaxial layers on sapphire substrates employing a 'buffer' layer. This buffer layer in strained heteroepitaxial growth was arguably the most important aspect of the development of III-N-based materials and device technology, which will be further described in Section 3.3.

3.2 Sapphire substrates

Synthetic sapphire, whose chemical formula is Al_2O_3, can be distinguished from alumina (aluminum (III) oxide), which has the same chemical formula, because sapphire is a single-crystalline material whereas alumina is generally a polycrystalline material. Single-crystalline sapphire substrates are the platforms most commonly used in the growth of GaN buffer layers to produce LED heteroepitaxial structures. Besides being used as a substrate for III-N LEDs, sapphire is a popular choice in comparison with other synthetic single crystals for various semiconductor, electronics and optics applications, due to the combination of favorable chemical, electrical, mechanical, optical and thermal properties including the following (Dobrovinskaya *et al.*, 2009):

- resistance to chemical attack by a wide range of chemicals
- high electrical resistivity even at elevated temperatures, for example, typically $>10^{11}$ Ω.cm at ~300 K – this property along with low thermal conductivity (thermal conductivity coefficient of $<30\,W.m^{-1}.K^{-1}$ near room temperature) is not necessarily beneficial in the application as a substrate for LEDs
- high dielectric strength with a dielectric constant of 11.5 and 9.3 in the directions parallel with (//*c*) and perpendicular to ($\perp c$) the *c*-axis, respectively, at 298 K in the frequency range of $10^3 - 10^9$ Hz
- high compression strength of ~2 GPa ($\sim 3 \times 10^5$ psi), not necessarily high tensile strength (275–400 MPa) and high bending strength (~1.03 GPa and ~758 MPa in directions //*c* and $\perp c$, respectively)
- high hardness of ~9 on the Mohs hardness scale; Knoop hardness is 1900 and $2200\,kg.mm^{-2}$ in directions //*c* and $\perp c$, respectively
- high degree of refractoriness.

Besides these properties, in this section the properties of sapphire that are relevant for a foreign substrate for III-N strained heteroepitaxial growth are described.

3.2.1 Properties of sapphire for substrates of III-N materials

Structural properties

Unlike gemstone sapphires, which have characteristic colors because of trace amounts of other elements (i.e., impurities), the synthetic sapphire used in electronics applications is the purest form of single-crystalline Al_2O_3, with no porosity or grain boundaries. The final form of crystalline Al_2O_3 is also called α-alumina or corundum. α-alumina (α-Al_2O_3) is one of the phases, along with metastable and transitional phases (β, γ, η, θ, κ, χ, etc.), of aluminum oxide and is the most thermodynamically stable phase. Corundum is also a representative name for the crystalline structure of α-Al_2O_3. In the corundum structure, the O^{2-} anions form layers of a hexagonal closest-packed plane in parallel with a relative rotation angle of ~64.3° (not the ideal 60°); the Al^{3+} cations are located in two-thirds of the octahedral sites between the adjacent O^{2-} layers. The coordination number of Al^{3+} is six, with three neighboring O^{2-} in the upper layer and three O^{2-} in the lower layer; hence, an Al^{3+} ion fills a hollow in an octahedron consisting of six O^{2-} anions. The Al^{3+} ions and remaining octahedral hollows also compose a hexagonal closest-packed plane. Corundum has a rhombohedral lattice structure ($a=b=c$ and $\alpha=\beta=\gamma\neq 90°$), if a primitive unit cell is considered (with ten atoms in a cell); however, an equivalent hexagonal lattice unit cell, which contains three primitive cells (30 atoms), is more widely used and is more convenient for describing the epitaxial growth of hexagonal GaN along the *c*-axis [0001], which is currently the dominant technology in the development of LEDs. This hexagonal geometry of the atomic configuration of the basal plane of sapphire is similar to that of the *c*-plane of a thermodynamically stable GaN single crystal, which has a wurtzite structure.

Chemical and thermal properties

This hexagonal atomic arrangement makes sapphire the natural preferred choice as a foreign substrate in GaN heteroepitaxy. However, the hexagonal geometry is not the only reason that sapphire is such a popular choice for the epitaxy of III-N materials and visible LEDs. In fact, there are many single-crystal materials with hexagonal lattices, which can also serve as substrates for III-N epitaxy (and some of them have a smaller lattice mismatch with GaN), as will be further described in Section 3.2.2. In addition to the advantages of having a similar crystalline structure, sapphire is a chemically and thermally very stable material. With a melting temperature of 2323 K (2050 °C) and boiling temperature of 3253 K (2980 °C), sapphire maintains its stability at the very high temperatures used in GaN buffer epitaxial growth, which are higher than 1000 °C. In particular, sapphire is very resistant to chemical attack by a wide range of chemicals even at elevated temperatures. In typical GaN epitaxy using MOCVD, hydrogen (H_2) is commonly introduced as a carrier gas and it is a by-product of hydride cracking. H_2 can also be generated in some MBE techniques using NH_3. H_2 at elevated temperatures enhances the 'thermal' etching of materials, resulting in decomposition of the substrate surface. Therefore, in the growth of GaN on a foreign substrate, maintaining the thermal and chemical stability of the substrate at a high temperature in ambient H_2 is the first requirement for a viable platform for epitaxial growth. In fact, a minor degree of surface decomposition is suspected to occur even for a sapphire substrate, and this releases oxygen from the sapphire surface during heating. This released oxygen is reincorporated during the initial stage of GaN epitaxy, until it is depleted from the growth chamber; a thin GaN layer that is auto-doped with oxygen forms near the sapphire substrate. An impurity and dopant depth profile of GaN layers on a sapphire substrate measured by secondary-ion mass spectrometry showed the oxygen concentration [O] tailing off from a peak $[O] \sim 1\times10^{18}\,cm^{-3}$ and decreasing to the detection limit of $[O] < 1\times10^{16}\,cm^{-3}$ over a thickness range of ~0.5 μm (Lee *et al.*, 2007a).

In summary, the important material properties of sapphire together with the GaN semiconductor are listed in Table 3.1.

Table 3.1 Material properties of sapphire and GaN

	Sapphire (α-Al_2O_3)	GaN (hexagonal)
Crystal structure	Rhombohedral	Wurtzite
Lattice parameter, *a*	4.758 Å	3.189 Å
Lattice parameter, *c*	12.99 Å	5.185 Å
Thermal expansion coefficient $\alpha_{//}$	$8.1 \times 10^{-6} K^{-1}$ [a]	$5.59 \times 10^{-6} K^{-1}$ [b]
Thermal expansion coefficient $\alpha_{\perp}$	$7.3 \times 10^{-6} K^{-1}$ [a]	$3.17 \times 10^{-6} K^{-1}$ [c] $7.75 \times 10^{-6} K^{-1}$ [d]
Thermal conductivity	$0.3 W.cm^{-1}.K^{-1}$	$2.3 W.cm^{-1}.K^{-1}$

Notes:

[a] Mean thermal expansion coefficients in the range 200–800 °C

[b] Mean thermal expansion coefficients in the range 27–627 °C

[c] Mean thermal expansion coefficients in the range 27–427 °C

[d] Mean thermal expansion coefficients in the range 427–627 °C

Source: Maruska and Tietjen, 1969; Yim and Paff, 1974

3.2.2 Comparison with other substrates

Bulk GaN substrates (Kelly *et al.*, 1999; Denis *et al.*, 2006) are not readily available at reasonable cost; hence, research, development and manufacturing of GaN-based materials and structures have been focused on the heteroepitaxy of GaN on different materials that can be prepared in the form of high-quality single-crystalline substrates with a reasonably large surface area. When selecting a foreign substrate for the heteroepitaxial growth of GaN, several properties and conditions are generally considered, such as the similarity in crystalline structure, in-plane lattice mismatch of the growth surface, thermal expansion coefficient mismatch, chemical and thermal stability at elevated temperatures of the GaN epitaxial growth, maturity of the substrate technology, manufacturability and scalability of the substrates considering the maximum wafer size, production volume and price (and also the intellectual property rights of the technology).

In this section, several alternative substrates to sapphire in the epitaxy of GaN and LED heterostructures are described with a focus on the aforementioned characteristics. We will limit the description to substrates for wurtzite GaN and III-N materials (and not cubic III-N materials), with potential applications as LEDs (not to transistors or other applications).

Silicon carbide (SiC) substrates

SiC substrates are currently the second most popular substrate (~10% of LED production), next to sapphire, in III-N-based heterostructures and devices, especially for visible blue, green and white LEDs (Cree, 2013) and heterostructure field-effect transistors (HFETs or high-electron mobility transistors, HEMTs). Of the many polytypes of SiC materials, 4H-and 6H-SiC, mostly on a silicon-face surface, are used as substrates in the heteroepitaxy of wurtzite GaN. They have hexagonal crystal structures (the same space group as wurtzite) and their in-plane lattice constants are closer to GaN ($a = 3.073$ Å and $a = 3.081$ Å for 4H- and 6H-SiC, respectively) than those of sapphire. These lattice constants make the in-plane lattice mismatch between GaN and SiC significantly smaller (~ −3.5%) than that between GaN and sapphire (~14%). This lattice mismatch is even further mitigated by using an AlN buffer layer between the GaN layer and the SiC substrate, which is typical in the growth of GaN on SiC (Lin *et al.*, 1993; Weeks *et al.*, 1995), as the lattice constant of AlN is between those of GaN and SiC. For GaN on 6H-SiC with an AlN buffer layer, the lattice mismatch is split into −0.96% and −2.45% for AlN on 6H-SiC and GaN on AlN, respectively. Achieving layer-by-layer two-dimensional growth is difficult for GaN directly grown on an SiC substrate, possibly due to the difficulty of wetting GaN on SiC or the onset of the Stranski–Krastanow growth mode (Waltereit *et al.*, 1999; Jeganathan *et al.*, 2005).

A GaN epitaxial film grown on hexagonal SiC using an AlN buffer layer maintains the simple crystallographic relations of the parallel basal planes and parallel faces of the hexagons (Ponce *et al.*, 1995), unlike those of GaN and sapphire:

$$(0001)_{\mathrm{GaN}} \,//\, (0001)_{\mathrm{AlN}} \,//\, (0001)_{\mathrm{SiC}}$$

$$[10\bar{1}0]_{\mathrm{GaN}} \,//\, [10\bar{1}0]_{\mathrm{AlN}} \,//\, [10\bar{1}0]_{\mathrm{SiC}} \text{ or } [11\bar{2}0]_{\mathrm{GaN}} \,//\, [11\bar{2}0]_{\mathrm{AlN}} \,//\, [11\bar{2}0]_{\mathrm{SiC}}$$

For high-quality GaN materials on SiC, the growth condition and the quality of the AlN buffer layer (Fan *et al.*, 2000; Koleske *et al.*, 2002) and the surface treatment of the SiC substrate (Torres *et al.*, 1999; Kawasuso *et al.*, 2000; Losurdo *et al.*, 2005) have been reported to be important. The dislocation density of GaN films grown under optimized growth conditions was estimated to be slightly lower (as low as $10^7\,\mathrm{cm}^{-2}$) than that on sapphire substrates (Bassim *et al.*, 2005). The thermal expansion coefficient of SiC is generally smaller than those of AlN and GaN. This difference in thermal expansion coefficient between III-N and SiC makes the lattice mismatch at the growth temperature larger, which is in addition to the lattice mismatch at room temperature. A GaN or AlN film grown at a higher temperature will be under a higher biaxial compressive stress. An AlN layer grown on SiC at a temperature higher than 1400 °C was reported to have peeled off from the substrate mainly by the mismatch of the thermal expansion coefficients (Balakrishnan *et al.*, 2006). The strain status of GaN layers with various thicknesses on an SiC substrate employing an AlN buffer layer is very complicated (Edwards *et al.*, 1998), possibly because of the growth mode and strain relaxation mechanism associated with the buffer layer (Waltereit *et al.*, 1999).

SiC materials have significantly higher thermal conductivities than sapphire. This property gives the critical advantage of better heat dissipation; hence, there is improved thermal management especially for high-power devices. In addition, unlike sapphire, which is an insulator, 4H- and 6H-SiC are wide bandgap semiconductors, allowing effective doping of both conductive and semi-insulating substrates. These conductive substrates allow the implementation of a backside contact on the substrate for vertical geometry devices such as LEDs and laser diodes. However, the AlN buffer layer commonly used in GaN heteroepitaxy on SiC is quite resistive, if not insulating, even with controlled doping for n-type conductivity. In order to avoid this resistive layer in a vertical device, a conducting silicon-doped $Al_{0.1}Ga_{0.9}N$ layer between the n-SiC substrate and n-GaN layer has been developed (Yoo *et al.*, 2006).

As described, SiC substrates have many advantageous characteristics and properties over sapphire substrates; however, in terms of substrate economy, SiC substrates have significant drawbacks compared to sapphire substrates. SiC substrates are commercially available only from a few manufacturers at relatively high prices. The maximum size of the available substrates, at the time of writing, is 6″ in diameter, but mainstream substrates are still limited to 4″.

Silicon (Si) substrates

Regarding substrate economy and the maturity of substrate technology – not the maturity of the epitaxial growth of GaN on the silicon (Si) substrate – silicon is the best choice for a substrate for III-N heteroepitaxy. Silicon substrates with a very large size (larger than 12″ to a maximum size of 18″) are available at very low cost. Their quality, in terms of crystalline perfection and surface condition, is better than any other substrate material used with III-V materials and structures due to the mature development of the technology. As silicon has a diamond crystal structure, which is a face-centered cubic lattice in the Bravais lattice system, (111) is a preferred plane for the epitaxy of wurtzite-structure materials as it provides a hexagonal closest-packed plane on the growing surface. However, the crystalline quality of GaN epitaxial layers and the performance characteristics of LEDs on silicon substrates are still inferior to those on sapphire substrates, though extensive efforts are being made to grow high-quality GaN films and to fabricate high-brightness LEDs on Si (111) substrates.

Other foreign substrates based on oxides, sulfides and metals

Several single-crystalline oxide materials other than sapphire have been considered for III-N heteroepitaxy. Some of them, such as ZnO and $LiGaO_2$, have a smaller lattice mismatch with GaN, which was the compelling motivation for their investigation. First, ZnO is a prime candidate for a substrate (Matsuoka *et al.*, 1992; Hellman *et al.*, 1996) as well as a compliant buffer layer (Detchprohm *et al.*, 1993; Johnson *et al.*, 1996) and as a visible LED material (Ozgur *et al.*, 1995). Wurtzite-ZnO has the same crystalline structure as GaN, and with a lattice constant of $a = 3.250$ Å, its lattice mismatch (~1.9%) is significantly smaller than those of the substrates described above (Morkoc and Ozgur, 2009). The additional mismatch induced by the difference in thermal expansion coefficient is smaller than that of SiC substrates (Hamdani *et al.*, 1998) and this thermal mismatch induces compressive strain, compensating for the tensile strain from the lattice mismatch at room temperature. Bulk ZnO substrates with a large area (>3″ diameter) from mass production are currently not readily available; however, this may not pose a real barrier to the development of GaN and LEDs on ZnO substrates because of the rapid development of bulk ZnO to cope with the increasing demands of the optoelectronics and electronics industries (Avrutin *et al.*, 2010a). Possibly the biggest challenge for ZnO substrates for LEDs is its chemical and thermal stability. The decomposition of ZnO in the temperature range used for typical GaN epitaxy by MOCVD and MBE is very severe, and zinc and oxygen impurities can form in the subsequent GaN and LED structures (Hellman *et al.*, 1996). Also, many ZnO bulk substrates contain a high concentration of impurities, which generally have high diffusion coefficients. After reincorporation and diffusion during the growth of the LED structure, these impurities in the heterostructure of LEDs are suspected of creating a high concentration of non-radiative recombination centers, which limits the internal quantum efficiency of III-N visible LEDs on ZnO substrates.

Another oxide substrate, $LiGaO_2$ (Ishii *et al.*, 1998; Doolittle *et al.*, 1998), shares similar advantages (i.e., small lattice match with $\Delta a = 1.9\%$ and $\Delta b = -0.19\%$) (Doolittle *et al.*, 2000) and problems (i.e., substrate economy and chemical and thermal stability) (Kung *et al.*, 1996). Other oxide, sulfide and even metallic substrates, including $LiTaO_3$ (Tsuchiya *et al.*, 2006), $LiAlO_2$ (Xu *et al.*, 1999), $LaAlO_3$ (Lee *et al.*, 2000), $(La,Sr)(Al,Ta)O_3$ (Sumiya *et al.*, 2002), $NdGaO_3$ (Mamutin *et al.*, 1999), $Ca_8La_2(PO_4)_6O_2$ (Yoshikawa *et al.*, 1999), $(Mn, Zn)Fe_2O_4$ (Ohta *et al.*, 2001), $MgAl_2O_4$ (Kuramata *et al.*, 1995), MoS_2 (Yamada *et al.*, 1999), hafnium (Beresford *et al.*, 1997), copper (Inoue *et al.*, 2006), silver (Inoue *et al.*, 2007), etc., have been investigated in attempts to find an alternative substrate, which has a better lattice and thermal match, is more economical and has better thermal dissipation, higher reflectivity and so on. However, most studies have failed to make a breakthrough by finding a technologically viable substrate. No studies have found an efficient light emitter except one study of laser diodes (LDs) on a spinel ($MgAl_2O_4$) substrate (Nakamura *et al.*, 1996).

Native substrates

For 'traditional' III-V semiconductors such as GaAs- and InP-based materials, epitaxial growth generally begins with a homoepitaxial buffer layer grown on a native (hence, lattice-matched) substrate prepared from a single-crystal boule,

Table 3.2 Comparison of various foreign and native substrates for wurtzite III-N semiconductors for the applications to LEDs

	Crystal structure	In-plane lattice mismatch with GaN[a]	Thermal expansion coefficient, $\alpha_{//}$[b]	Thermal and chemical stability	Substrate economy[c]
Sapphire (0001)	Rhombohedral		8.1×10^{-6} K^{-1}	Excellent	Currently 3–4″ diameter; 6″ and 8″ development in progress
4H-SiC (0001)	Hexagonal	–3.6%		Excellent	High price; up to 4″ (or 6″) diameter; potential intellectual property rights issues
6H-SiC (0001)	Hexagonal	–3.4%		Excellent	
Si (111)	Diamond			Medium	Low price; large substrate (>12″ diameter)
w-ZnO (0001)	Wurtzite	1.9%	6.5×10^{-6} K^{-1}	Problematic	N/A (currently in research)
$LiGaO_2$ (001)	Orthorhombic	1.9% (*a*-direction) –0.19% (*b*-direction)		Problematic	N/A (currently in research)
$MgAl_2O_4$ (111)	Spinel	–10.3%			N/A (currently in research)
GaN (0001)	Wurtzite	0%	Same as GaN layer	Excellent	Very high price; up to 3″ diameter

[a] The in-plane lattice mismatch is calculated using the basal-plane lattice parameter *a* (for the hexagonal closest-packed plane) from $(a_S - a_L)/a_L$, where a_S and a_L are the bulk lattice parameters of the substrate and layer (before epitaxial growth), respectively. This formula yields negative values for biaxial in-plane compressive strain ($a_L > a_S$) and positive values for biaxial in-plane tensile strain ($a_S > a_L$) applied in the epitaxial layer.

[b] The mean thermal expansion coefficients are in the range 200–800 °C.

[c] Substrate economy includes the maximum wafer size, production volume, price and intellectual property rights.

Source: Doolittle *et al.*, 2000; Kuramata *et al.*, 1995; Norton *et al.*, 2004; Tsuchiya *et al.*, 2006 which is a bulk material grown from a melt via either the vertical gradient freeze (VGF) technique (Gault *et al.*, 1986) or the liquid-encapsulated Czochralski (LEC) technique (Mullin *et al.*, 1965). In contrast, GaN-based materials are generally not grown on native GaN substrates. The bulk growth of GaN crystals in the same way as for other III-V semiconductors (i.e., from a liquid melt) is extremely difficult due to the very high vapor pressure of nitrogen at the melting temperature of GaN (Grzegory, 2001). Alternate methods of GaN bulk crystal growth have been investigated, such as the ammonothermal crystal growth technique and the sodium flux method (Denis *et al.*, 2006; Avrutin *et al.*, 2010b; Ehrentraut and Fukuda, 2010). An alternative method of preparing GaN substrates has also been developed: a thick GaN layer is grown on a foreign substrate by hydride VPE (Xu *et al.*, 2002) followed by removal of the foreign substrate and wafering processes (Kelly *et al.*, 1999). The GaN substrates prepared in this way are called 'free-standing' substrates to distinguish them from GaN substrates prepared by more traditional melt-growth technologies. Free-standing GaN substrates have relatively large diameters (~3″ diameter) and threading dislocation densities as low as about $10^5\,\text{cm}^{-2}$ (Paskova *et al.*, 2010). They have become a dominant technology platform for the development of visible LDs in Blu-ray players. 'True bulk' GaN substrates from bulk GaN crystals grown using an ammonothermal process have recently been commercially developed with a wafer diameter up to 1.5″. However, the current price and available wafer size are not favorable for adoption as a platform for LED technology, in spite of the significantly reduced dislocation densities. While the reduced dislocation density must be beneficial for the performance characteristics of LEDs (Dai *et al.*, 2009), the degree of the beneficial effect on the internal quantum efficiency and the efficiency droop for visible LEDs are still controversial (Akita *et al.*, 2007; Cao *et al.*, 2004; Kyono *et al.*, 2005; Liu *et al.*, 2009, 2011; Rozhansky and Zakheim, 2007; Schubert *et al.*, 2007), even without considering substrate economy.

In summary, the various foreign and native substrates used for GaN semiconductor materials for LEDs are compared in Table 3.2.

3.3 Strained heteroepitaxial growth on sapphire substrates

This section describes a growth technique that overcomes one of the serious technical challenges in the epitaxial growth of GaN-based materials due to the large lattice mismatch between the GaN epitaxial layer and the sapphire substrate. Strained heteroepitaxy by two-step growth employing a buffer layer is probably the most important technological development for III-N-based materials and device technology. The section begins with the history of strained heteroepitaxial growth developed by tenacious Japanese researchers (Akasaki, 2007), and then discusses a mechanism for growth evolution.

3.3.1 Concept development and demonstration of strained heteroepitaxial growth

As briefly described in Section 3.1.1, the first 'device-quality' GaN materials on sapphire substrates were developed by Japanese research groups using both the MBE and MOCVD growth techniques (Yoshida *et al.*, 1983; Amano *et al.*, 1986). For growth by reactive MBE using aluminum and gallium molecular beams and NH_3, a single-crystalline AlN layer was grown at ~1100 °C between a GaN epitaxial layer and a sapphire (0001) substrate, instead of growing the GaN layer directly on the sapphire surface (Yoshida *et al.*, 1983). While this AlN layer can function as a buffer layer, Yoshida *et al.* (1983) did not use the term 'buffer', instead, they described the material as 'AlN-deposited' sapphire. They focused on the lattice mismatch and thermal expansion coefficient differences of the sapphire, AlN and GaN. From their previous experiments on AlN grown on sapphire substrates (Yoshida *et al.*, 1975, 1979), they were able to produce single-crystalline AlN film with a smooth surface without cracks or hillocks, even with rather large in-plane lattice mismatch and thermal expansion coefficient differences. This AlN layer (thickness ~300 nm), having a smaller lattice mismatch with GaN than sapphire with GaN, was used as a buffer layer between the sapphire substrate and the GaN epitaxial layer to reduce the strain applied to the GaN layer – as described in Section 3.2. The in-plane lattice mismatch on the (0001) plane is ~2.4% and ~13.9% for GaN on AlN and on sapphire, respectively. In the same study, they reported significantly improved Hall mobility and a luminescence peak from band-to-band transitions (at $\lambda \sim 360$ nm) by cathodoluminescence for the GaN on AlN/sapphire compared to GaN on sapphire, which suggests the improved crystalline quality of GaN because of the AlN buffer layer.

Amano *et al.* (1986) were the first to report an 'optically flat' and 'crack-free' GaN epitaxial layer grown by MOCVD on a sapphire substrate employing an AlN 'buffer' layer between the substrate and the GaN epitaxial layer in order to improve the crystalline quality of the GaN layer. Amano and Akasaki were the first to use the term 'buffer' layer in III-N epitaxial growth and they are credited with the development of strained heteroepitaxy for growing a high-quality GaN layer on foreign substrates (Akasaki, 2007). While this AlN buffer layer appears to be similar to that reported by Yoshida *et al.* (1983), which was produced using reactive MBE, it is different in several aspects besides the different growth technology. This AlN buffer layer was grown at a relatively low temperature and is a fine crystallite and amorphous material in contrast to the single-crystalline material of AlN grown at high temperatures as in reactive MBE. This low-temperature (LT) buffer layer is believed to be of critical importance for producing a smooth, specular and crack-free GaN surface layer (Amano and Akasaki, 2001; Amano *et al.*, 2002). In addition, its thickness (20–50 nm) was significantly thinner than the AlN produced by Yoshida *et al.* (1983). In particular, there was direct evidence of crystalline quality improvement with a narrow full width at half maximum (FWHM) of the peak measured from symmetric and asymmetric X-ray rocking curves and an optically smooth surface measured by scanning electron microscopy. The strained heteroepitaxy on sapphire substrates consists of two steps: growing a thin LT buffer, followed by growing a rather thick (>1 μm) high-temperature (HT) GaN layer typically at 1000–1060 °C; hence, it is often called two-step strained heteroepitaxy.

Subsequently, Nakamura (1991a) was the first to produce an LT GaN buffer layer (instead of LT AlN buffer layer), which was grown between 450 and 600 °C with a thickness of 10–120 nm and which has a similar role to an LT-AlN buffer layer. The study also reported that the GaN layer was of high-quality with smooth surfaces, high Hall mobility and improved crystalline quality. This development of two-step strained heteroepitaxial growth of a GaN 'template', consisting of an LT buffer (GaN or AlN) and a HT GaN layer, paved the way for further development of photonic and electronic heterostructures and devices based on III-N semiconductors, as these high-quality templates can be used as a platform for epitaxial layer structures for operational devices.

3.3.2 Growth mechanism in GaN strained heteroepitaxy

Since the first experimental demonstration of a GaN layer grown on a sapphire substrate using an LT buffer layer, the growth mechanism in two-step strained heteroepitaxy has been studied in comparison to that of GaN grown directly on a sapphire substrate. In direct GaN growth, many hexagonal columns of crystalline GaN with different sizes and heights form and grow three-dimensionally, resulting in a rough surface with many pits at the column boundaries. In contrast, the AlN (or GaN) LT buffer layer produced in strain heteroepitaxial growth consists of fine hexagonal crystallites, amorphous-like structures or zinc-blende crystallites with <111> direction, depending on the deposition condition of the LT buffer, which can be measured by reflection high-energy electron diffraction and cross-sectional transmission electron microscopy (Akasaki *et al.*, 1989; Kuznia *et al.*, 1993; Wickenden *et al.*, 1994; Kapolnek *et al.*, 1995). The zinc-blende crystallites have a high density of stacking faults and can be partially converted to hexagonal crystallites during the heating for HT GaN growth (Wu *et al.*, 1996). At the same time, this LT buffer layer promotes uniform surface coverage during the subsequent film growth. In the initial stage of GaN growth on the AlN LT buffer, many truncated hexagonal pyramidal mesas of GaN are formed. These mesas then grow quasi-laterally, eventually resulting in a flat GaN surface (Akasaki *et al.*, 1989). Therefore, the role of the AlN buffer layer is to decrease the interfacial free energy between the substrate and the epitaxial GaN layer, and to supply nucleation sites for GaN with the same crystal orientation as the substrate (Amano *et al.*, 1988). GaN heteroepitaxial growth on a sapphire substrate using an LT buffer layer proceeds with the following steps: (1) nucleation of high-density GaN, (2)

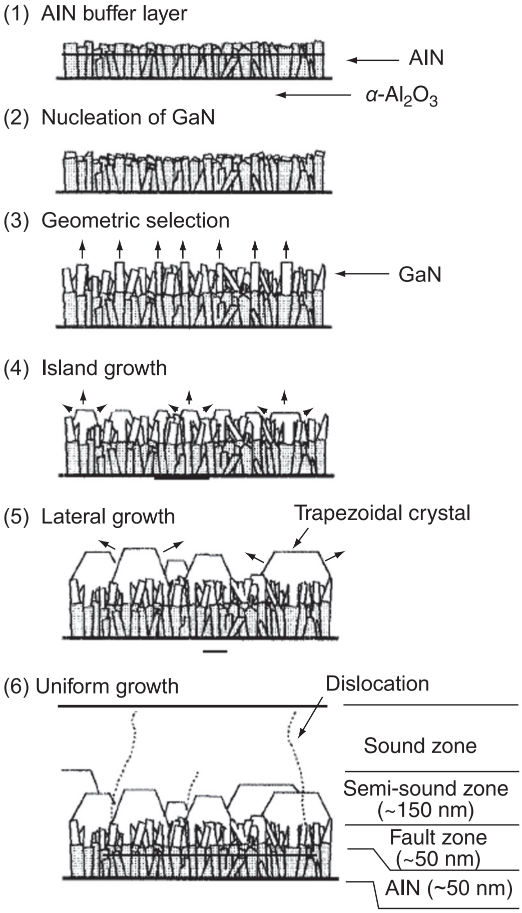
(1) AlN buffer layer
AlN
α-Al2O3
(2) Nucleation of GaN
(3) Geometric selection
GaN
(4) Island growth
(5) Lateral growth
Trapezoidal crystal
(6) Uniform growth
Dislocation
Sound zone
Semi-sound zone (~150 nm)
Fault zone (~50 nm)
AlN (~50 nm)

3.1 Strained heteroepitaxial growth of GaN on a sapphire substrate using a low-temperature buffer layer (Hiramatsu *et al.*, 1991, with permission from Elsevier).

geometric selection of the crystallographic direction of the GaN columnar crystals and (3) highly lateral growth of the trapezoidal islands with the *c*-face on top, as shown in Fig. 3.1. This non-uniform growth of GaN on AlN plays an important role in the realization of form growth and in obtaining high-quality GaN layers with few defects even for the epitaxial growth of a layer on a substrate with a large lattice mismatch (Hiramatsu *et al.*, 1991). This growth mechanism has been experimentally confirmed by *in situ* measurement of the growing surface, which avoids any possible effects on surface morphology caused by cooling down, which would be seen in an *ex situ* measurement (Nakamura, 1991b).

3.4 Epitaxial overgrowth of GaN on sapphire substrates

As described in Sections 3.1 and 3.2, the epitaxial growth of GaN is generally not carried out on native GaN substrates, unlike other semiconductors, the epitaxial growth of which generally begins with a homoepitaxial buffer layer grown on a lattice-matched same-material substrate. Instead, GaN-based epitaxial structures are grown on a GaN buffer layer that is grown on a foreign substrate (sapphire or SiC) by strained heteroepitaxial growth (Amano *et al.*, 1986; Weeks *et al.*, 1995), which causes transformational changes in the GaN-based materials and devices. However, even with this buffer layer, the dislocation density in the epitaxial materials is from mid-10^8 to low-$10^9\,\text{cm}^{-2}$ due to both lattice constant and thermal expansion mismatches, which are significantly higher than those of other semiconductors with values of the order of $10^5\,\text{cm}^{-2}$ and lower. This suggests that typical LED devices of dimensions $300 \times 300\,\mu\text{m}^2$ and $1 \times 1\,\text{mm}^2$ should contain more than 90 000 and 1 000 000 dislocations per device, respectively, assuming that the dislocation density is higher than $1 \times 10^8\,\text{cm}^{-2}$. While the high dislocation density of a III-N epitaxial structure does not prevent the device from working as a photon emitter, it limits its full potential, as these defects act as current leakage paths and carrier traps, limiting the performance characteristics of the transistors (Hinoki *et al.*, 2008; Lochner *et al.*, 2011) and providing avenues for the non-radiative recombination of light emitters (Rozhansky and Zakheim, 2006; Schubert *et al.*, 2007).

In order to further improve the crystalline quality of GaN-based epitaxial structures, a reduction in dislocation density is required. Several growth techniques mainly using epitaxial overgrowth schemes to reduce the dislocation density are described in this section, including epitaxial lateral overgrowth (ELOG), pendeo-epitaxy and the patterned sapphire substrate (PSS) technique.

3.4.1 Selective-area growth and epitaxial lateral overgrowth

The selective-area epitaxial growth technique has been actively used for many material structures and device applications based on traditional (GaAs- and InP-based) III-V semiconductors (Jastrzebski, 1983; Caenegem *et al.*, 1997). For instance, higher-order quantum-confined structures (more than one-dimensionally confined quantum-well structures), such as quantum wires, quantum dots and nanorods, can be fabricated using epitaxial growth in a selected defined area. Buried heterostructures employing the regrowth of lateral cladding layers on an etched surface to define a mesa are commonly used for LDs. They are commonly referred to as buried heterostructure LDs and have enhanced confinement of currents, photons and carriers (Coldren *et al.*, 2012).

The terms used in this section need to be clarified. Selective-area growth (SAG), which is also called selective growth (SG), selective epitaxy (SE), selective-area epitaxial growth (SAEG) and selective epitaxial growth (SEG), involves the epitaxial growth of materials on a non-masked region (a window) but does not necessarily include lateral growth over the masked region. When there is lateral overgrowth over the masked region, the process is termed lateral epitaxial overgrowth (LEO), lateral epitaxial growth (LEG), lateral overgrowth (LOG), epitaxial lateral overgrowth (ELOG or ELO) or selective-area lateral epitaxial overgrowth (SALEO).

For III-N materials, Kato *et al.* (1994) and Kitamura *et al.* (1995) were the first group to demonstrate the SAEG of GaN and AlGaN on stripe-patterned and dot-patterned windows using an SiO_2 mask. They demonstrated the excellent selectivity of GaN growth only on the GaN surface in the window region (not on the SiO_2 surface) and the self-limited stable formation of $\{10\bar{1}1\}$ facets for selectively grown GaN materials. The growth selectivity of GaN (unlike AlGaN) is due to a difference in the sticking coefficient, s, between gallium adatoms (or its species) on the GaN surface ($s \sim 1$) and the SiO_2 surface ($s \sim 0$). This difference in the sticking coefficient is related to bonding energy differences in the Si-O (799.6 kJ/mol), Ga-O (353.6 kJ/mol) and Si-N (439 kJ/mol) bonds. Therefore, a nucleation of GaN on the SiO_2 surface, replacing silicon with gallium (or oxygen with nitrogen), is not energetically favorable; thus, it is not likely to occur. However, these reports focused on SAG and there was no *lateral* epitaxial overgrowth.

Zheleva *et al.* (1997) and Nam *et al.* (1997) are credited with the first demonstration of the dislocation reduction effect by LEO in III-N materials by MOCVD. They were the first to demonstrate that lateral epitaxial growth occurs over the SiO_2 mask after the initial vertical growth in the window region, as GaN growth proceeds. While threading dislocations in the underlying GaN in the window region keep propagating through the vertical growth area, the lateral overgrowth region has a very low density of dislocations. Dislocations underneath the SiO_2 are blocked by the mask due to the termination of the epitaxial. In particular, Nam *et al.* (1997) investigated the effect of the orientation of a stripe-patterned mask for the $\langle 11\bar{2}0\rangle$ (*a*-direction) and the $\langle 1\bar{1}00\rangle$ (*m*-direction) on a (0001) *c*-plane GaN surface and grew a rectangular GaN stripe having a (0001) top facet and $\{11\bar{2}0\}$ side facets for the mask opening oriented along the $\langle 1\bar{1}00\rangle$ direction. These rectangular GaN stripes can be coalesced into a GaN layer by merging two lateral growth fronts (with $\{11\bar{2}0\}$ side facets) from two adjacent rectangular GaN stripes, as schematically shown in Fig. 3.2(a). This coalesced layer has a flat GaN surface with a reduced dislocation density in certain (laterally grown) areas; it can be used as a high-quality template for the subsequent growth of heteroepitaxial structures for devices. In separate research, Usui *et al.* (1997) also reported the reduction of dislocations in a thick GaN layer (>140 μm) that had overgrown an SiO_2 mask using hydride VPE. The density of dislocations was as low as $6 \times 10^7\,\text{cm}^{-2}$ in this film. However, the researchers failed to elucidate the mechanism for the dislocation reduction by LEO, and the reduction in dislocation density might have been due to the thick layer grown by hydride VPE.

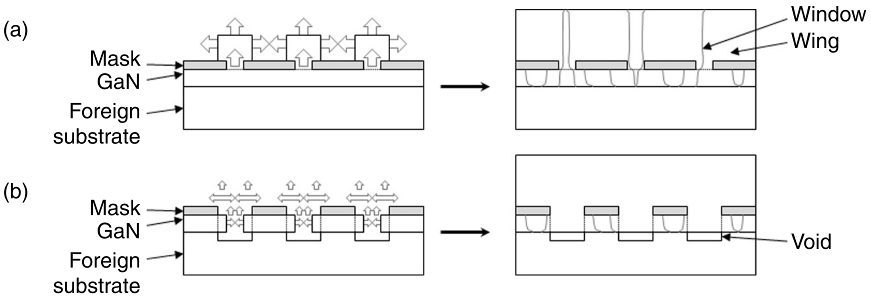
(a)
Mask
GaN
Foreign substrate
Window
Wing
(b)
Mask
GaN
Foreign substrate
Void

3.2 (a) Lateral epitaxial overgrowth and (b) pendeo-epitaxy of GaN.

GaN layers overgrown using SAG and/or ELOG can have different structures depending on the growth parameters and pattern geometries. As described earlier, a striped mask pattern results in stripes with different stable facets. The different structures originate from the different growth rates of the different planes, which depends on the orientation of the masks (Kapolnek *et al.*, 1997; Park *et al.*, 1998). The growth rate of each facet also depends on the growth temperature and pressure, as schematically shown in Fig. 3.3 (Hiramatsu *et al.*, 1999; Hiramatsu, 2001). For striped masks oriented along the $\langle 11\bar{2}0\rangle$ direction, triangular cross-sectional GaN stripes with stable $\{10\bar{1}1\}$ facets are formed independent of growth pressure and temperature, which suggest that the growth rates on the $\{10\bar{1}1\}$ planes are almost constant and are not a function of pressure or temperature. However, for striped masks oriented along the $\langle 1\bar{1}00\rangle$ direction, the formation of several facets, $\{0001\}$, $\{11\bar{2}0\}$ and $\{11\bar{2}2\}$, and their resulting structures strongly depends on growth pressure and temperature. Triangular cross-sectional stripes with $\{11\bar{2}2\}$ facets are more stable at higher pressure and lower temperature,

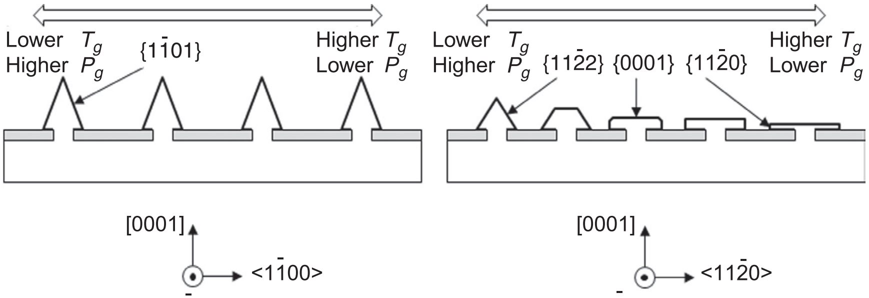
Lower T_g
Higher P_g
{1$\bar{1}$01}
Higher T_g
Lower P_g
Lower T_g
Higher P_g
{11$\bar{2}$2}
{0001}
{11$\bar{2}$0}
Higher T_g
Lower P_g
[0001]
<1$\bar{1}$00>
<11$\bar{2}$0>
[0001]
<11$\bar{2}$0>
<1$\bar{1}$00>

3.3 Evolution of selective area and lateral epitaxial overgrowth depending on the orientation of striped masks.

while rectangular cross-sectional stripes with $\{0001\}$ and $\{11\bar{2}0\}$ facets are more stable at lower pressures and higher temperatures. These different structures are the result of the different growth rates of different facets.

3.4.2 Pendeo-epitaxy

While the ELOG technique brought innovative changes in reducing the dislocation density of GaN templates grown on foreign substrates, the beneficial effect of the reduction of dislocations is not uniform, but localized in selected areas. This areal dependence of dislocation density confines the placement of devices only to laterally overgrown regions. To overcome this limitation of ELOG, a new approach for selective growth was proposed, which would give a more uniform and large-area dislocation reduction. Pendeo-epitaxy ('pendeo' is from the Latin, meaning 'hangs on' or 'suspends from'), a term coined by Zheleva *et al.* (1999) and Linthicum *et al.* (1999) to describe lateral growth without contact with a mask or substrate, is an extension of ELOG, which uses the substrate itself as a 'pseudo-mask'. This approach, however, differs from ELOG in that growth does not initiate through open windows but begins on sidewalls etched in the GaN layer, which acts as a seed layer for pendeo-epitaxy.

The first demonstration of pendeo-epitaxy used a maskless approach and only relied on the preferred growth of certain facets of GaN (Zheleva *et al.*, 1999). A GaN layer grown by strained heteroepitaxy was given a striped pattern along the $\langle 1\bar{1}00\rangle$ direction by etching through the GaN layer into the foreign substrate to form a seed GaN layer; the stripes had a top surface of the $\{0001\}$ facet and sidewalls of $\{11\bar{2}0\}$ facets. Pendeo-epitaxy was carried out at high temperature (1080 °C) and low pressure (45 Torr) to facilitate the growth of the preferred facets. The pendeo-epitaxial materials grow laterally as well as vertically and coalesce. During pendeo-epitaxial growth, nucleation and the subsequent growth of GaN on the surface of the foreign substrate do not occur, which confirms that the foreign substrate can act as a pseudo-mask. This lateral growth in combination with no growth on the foreign substrate results in a 'free-standing' (since it is not bound to the substrate) and dislocation-reduced (as dislocations do not propagate laterally) layer. The dislocation density of the lateral growth region is lower by $10^4-10^5\,\text{cm}^{-2}$. However, the dislocation density of the vertical growth region is the same as a typical GaN layer on a foreign substrate ($\sim 10^9\,\text{cm}^{-2}$), which indicates that areal non-uniformity of the dislocation density still exists.

To overcome the problem of the remaining high dislocation density region, for the second pendeo-epitaxy demonstration, an Si_xN_{1-x} mask was deposited by plasma-enhanced chemical vapor deposition (PE-CVD) onto the $\{0001\}$ face of the GaN seed (Linthicum *et al.*, 1999; Gehrke, 2008). No growth occurred on the Si_xN_{1-x} mask and on the exposed foreign substrate. Figure 3.2(b) schematically shows the structural development of GaN during pendeo-epitaxy. In the initial stage of pendeo-epitaxy, a high growth temperature and low pressure were used to enhance lateral growth. In combination with the Si_xN_{1-x} mask and the foreign substrate pseudo-mask, only lateral growth on the $\{11\bar{2}0\}$ facets was forced, so that the GaN grown by pendeo-epitaxy was suspended from the sidewalls of the GaN seed layer. The suspended GaN has exposed $\{0001\}$ facets, which are not covered by the mask and vertical growth of GaN occurs together with lateral growth. During pendeo-epitaxy, the relative growth rates are controlled by the growth parameters. When the height of the GaN exceeds the thickness of the Si_xN_{1-x} mask, ELOG occurs over the mask and there is eventual coalescence of the pendeo-epitaxial-grown GaN over the mask, which completes the epitaxial growth. The material has a flat continuous surface with a uniformly reduced dislocation density. The dislocations are buried under the mask.

3.4.3 Patterned sapphire substrates

Of the many growth techniques described in these sections, the patterned sapphire substrate (PSS) technique is a far more popular approach for LEDs. The PSS technique, which is an inherently mask-free process (hence the process is free of potential contamination and epitaxial growth interruption), produces LED epitaxial structures with a lower threading dislocation density and, more importantly, with a higher light extraction efficiency. Many different types of PSS technology have been studied and successfully employed in the fabrication of high-brightness and high-power LEDs.

The patterning of a sapphire substrate that was used to grow a GaN buffer layer was reported by Ashby *et al.* (2000) and Detchprohm *et al.* (2001). They used stripe-patterned deep trenches on sapphire substrates, mainly to reduce the density of dislocations in the GaN film. The PSS technique for LEDs was first implemented with stripe patterns, possibly by extending ELO and pendeo-epitaxy using stripe patterns (Tadatomo *et al.*, 2001). *c*-plane sapphire substrates were patterned with parallel groves either along the $\langle 11\bar{2}0\rangle_{\text{sapphire}}$ direction or the $\langle 1\bar{1}00\rangle_{\text{sapphire}}$ direction. Because of the crystallographic relation between the GaN layer and the planar sapphire substrate, described in Section 3.2, GaN stripes along the $\langle 1\bar{1}00\rangle_{\text{GaN}}$ and $\langle 11\bar{2}0\rangle_{\text{GaN}}$ directions were formed along the PSS for the $\langle 11\bar{2}0\rangle_{\text{sapphire}}$ and $\langle 1\bar{1}00\rangle_{\text{sapphire}}$ grooves, respectively. The evolution of the overgrowth of GaN stripes along the different directions is very similar to ELOG, shown in Fig. 3.2. Tadatomo *et al.* (2001) also reported that the material had a reduced density of dislocations ($1.5\times10^8\,\text{cm}^{-2}$ compared to $4\times10^8\,\text{cm}^{-2}$ for conventional planar sapphire substrates) and increased light output power of near-UV LEDs.

Yamada *et al.* (2002) used a two-dimensional hexagonal pattern (as opposed to a one-dimensional array of stripes), which resembled a honeycomb. One side of a hexagon was parallel with the $\langle 11\bar{2}0\rangle_{\text{sapphire}}$ *a*-axis of the sapphire to improve the planarization of the GaN overgrowth buffer layer. There was a moderate reduction of the dislocation density ($4.8\times10^8\,\text{cm}^{-2}$ compared to $1\times10^9\,\text{cm}^{-2}$ for conventional planar sapphire substrates) and a significant improvement in the external quantum efficiency by ~35% when the PSS technique was combined with a mesh p-electrode in the LED device structures.

Following these reports, various patterns and fabrication processes for PSS technology have been studied, including patterns of stripes (Feng and Lau, 2005), holes (Wuu *et al.*, 2005), microlenses (Choi *et al.*, 2004) and pyramidal shapes (Lee *et al.*, 2007b), and using dry etching (Park *et al.*, 2001) and wet etching (Cuong *et al.*, 2007). The shape, periodicity and aspect ratio of a pattern significantly affect the light extraction efficiency depending on the LED device geometry and this will be further discussed in Chapter 6, in the context of LED fabrication and characterization.

3.5 GaN growth on non-polar and semi-polar surfaces

The epitaxial growth of III-N films on the (0001) *c*-plane of sapphire substrates has produced layers and structures that grow in the polar direction $\langle 0001 \rangle$. Because of the polar nature of wurtzite GaN, the *c*-direction from the nitrogen-face to the gallium-face is called the [0001] direction. The top surface of a film grown in the [0001] direction is the (0001) c^+-plane (a gallium-face plane). The top surface of a film grown in the $[000\bar{1}]$ direction is a c^--plane (a nitrogen-face plane). It is relatively easier to achieve better surface morphology and a reduction in crystalline defects for the GaN film with a gallium face using strained heteroepitaxy on a foreign substrate. As a result, ever since the first successful demonstration of strained heteroepitaxy employing a buffer layer, the GaN buffer layers on foreign substrates that are used as universal platforms for the heterostructures of III-N light emitters and transistors are mostly the gallium-face GaN layers grown in the [0001] direction.

These III-N heterostructures grown in the polar direction, however, induce polarization charges near the interfaces by spontaneous and/or piezoelectric polarization (Bernardini *et al.*, 1997). The charges modify the electronic band structure profile in the III-N heterostructures by inducing internal fields, which result in the formation of a two-dimensional electron gas in AlGaN/GaN heterostructures without introducing modulation doping (this is sometimes called the 'self-doping' effect) (Ambacher *et al.*, 1999) and the quantum-confined Stark effect (QCSE) (Miller *et al.*, 1984) in the quantum wells (Takeuchi *et al.*, 1997). For III-N visible LEDs, the QCSE in the InGaN/GaN multiple-quantum-well active region results in a narrowing of the effective bandgap of the quantum wells (QWs), a blue-shift of the photoluminescence and EL peaks with increasing injections, and the spatial separation of electron and hole wave functions (Ryou *et al.*, 2009). In particular, the spatial separation of the wave functions leads to a reduced overlap between the wave functions of the two charge carriers, which, in turn, reduces the oscillator strength for the recombination of the carriers (Bernardini and Fiorentini, 1998; Im *et al.*, 1998). In order to improve the transition probability for radiative recombination, and, hence, internal quantum efficiency, a III-N QW has to be thinner than the non-polar QWs of GaAs- and InP-based materials. Even with thinner QWs, wave function separation cannot be completely suppressed and these thinner QWs may have other problems, such as a lower capture rate of electrons in combination with polarization-induced electronic band bending (Schubert and Schubert, 2010) and a higher carrier density, which could enhance non-radiative Auger recombination rates in the QWs (Shen *et al.*, 2007).

In order to address the technical challenges associated with the QCSE in InGaN QWs, non-polar and semi-polar heterostructures have been proposed for LEDs and LDs (Waltereit *et al.*, 2000), which requires the development of non-polar and semi-polar GaN. This section describes the growth of non-polar and semi-polar GaN on a sapphire substrate on surfaces other than the *c*-plane, in relation to the polarization field and device performance characteristics.

In a wurtzite structure, the $\{10\bar{1}0\}$, $\{11\bar{2}0\}$ and $\{10\bar{1}2\}$ planes are non-polar or semi-polar planes, and are designated the *m*-, *a*- and *r*-planes, respectively. The epitaxial growth along those directions is becoming important especially for light emitter applications with the compelling motivation as described above. Interestingly, in an attempt to improve the crystalline quality of a GaN film on a foreign substrate (Sasaki and Zembutsu, 1987), though not necessarily to mitigate the electrostatic fields in the QWs, epitaxial growth in non-polar directions was attempted almost at the same time as the development of strained heteroepitaxial growth. The effect of crystal orientation on the piezoelectric field and electronic properties of III-N materials and QWs (Park and Chuang, 1999; Park, 2002) suggests that the polarization-induced internal field should be absent or mitigated depending on the plane to be grown. Driven by the importance of these expected beneficial effects, the growth of GaN, InGaN/GaN MQWs and LED structures with non-polar and semi-polar orientations of the wurtzite crystals was explored by growing III-N films on various foreign substrates.

The non-polar $(11\bar{2}0)$ GaN *a*-plane has been grown on $(1\bar{1}02)$ *r*-plane sapphire substrates (Ng, 2002; Craven *et al.*, 2002) and on *a*-plane sapphire (Paskova *et al.*, 2003) and SiC (Craven *et al.*, 2004) substrates. The non-polar $(10\bar{1}0)$ GaN *m*-plane has been grown on *m*-plane sapphire (Matsuoka and Hagiwara, 2001) and SiC (Gardner *et al.*, 2005) substrates. For *a*-plane GaN on sapphire substrates, two-dimensional layer-by-layer growth was obtained with the following crystallographic relations:

$$(11\bar{2}0)_{\mathrm{GaN}} \mathbin{//} (1\bar{1}02)_{\mathrm{sapphire}} \text{ and } [0001]_{\mathrm{GaN}} \mathbin{//} [\bar{1}101]_{\mathrm{sapphire}} \text{ (or } [\bar{1}100]_{\mathrm{GaN}} \mathbin{//} [11\bar{2}0]_{\mathrm{sapphire}}).$$

However, the epitaxial film had a high density of crystalline defects including not only a high threading dislocation density of $>2\times10^{10}\,\mathrm{cm}^{-2}$ but also a high density of stacking faults of $4\times10^{5}\,\mathrm{cm}^{-1}$ (Haskell *et al.*, 2003a). The higher density of crystalline defects in a film grown on a non-polar surface compared to a polar surface is due to the anisotropic in-plane strain in the films (Darakchieva *et al.*, 2003). LEO (Haskell *et al.*, 2003b), the insertion of a metal interlayer (Tavernier *et al.*, 2004), sidewall epitaxial overgrowth (Imer *et al.*, 2006), *in situ* SiN nanomasks (Chakraborty *et al.*, 2006) and two-stage epitaxial lateral overgrowth (Ni *et al.*, 2006) have been employed to reduce the density of crystalline defects.

In general, however, the non-polar growth of GaN and InGaN materials via strained heteroepitaxy on sapphire substrates suffers from poor crystalline quality and the layers have high densities of threading dislocations and stacking faults and rough surface morphologies. A reduction in threading dislocation densities has been reported for LEO materials; however, stacking faults cannot be eliminated (Haskell *et al.*, 2005). As a result, meaningful device data (with reasonable quantum efficiency) from LEDs grown on non-polar sapphire substrates have not been reported. LED structures have been grown on non-polar and semi-polar free-standing native GaN substrates. Stable peak positions (i.e., with no blue-shift) of EL with increasing current has been demonstrated for non-polar visible LEDs (Schmidt *et al.*, 2007; Liu *et al.*, 2008). This low defect density substrate was a breakthrough for creating device-quality epitaxial materials by non-polar growth. External quantum efficiencies of non-polar LEDs grown on *m*-plane native GaN substrates have been reported and the peak external quantum efficiency of an LED operating at $\lambda \sim 407$ nm was reported to be ~40% (Kim *et al.*, 2007). There may be a real benefit in using non-polar or semi-polar structures for LDs. Long wavelength continuous-wave lasing actions at $\lambda \sim 481$ nm (blue-green) and $\lambda \sim 520$ nm (green) were achieved at room temperature with non-polar and semi-polar GaN substrates (Okamoto *et al.*, 2008; Yoshizumi *et al.*, 2010).

The results from LEDs and LDs grown on native non-polar and semi-polar GaN substrates are encouraging, but there are technical and economic issues to be resolved before these devices are successful in the market. Even though quantum efficiency has been improved significantly, the reported state-of-the-art values of quantum efficiency for non-polar and semi-polar LEDs are still lower than those of the well-developed polar LEDs. In addition, the biggest hurdle in the commercialization of useful SSL devices, especially LEDs, grown on native non-polar substrates is the extremely high cost and tiny size (e.g., they have an area of less than 1 cm^2) of the substrates available.

3.6 Future trends

As described so far, GaN on a sapphire platform has been dominant for LED components and modules and this will continue thanks to their optimized characteristics, technological maturity (compared to GaN on a silicon platform) and advantages in volume and cost (compared to GaN on alternative substrates including native GaN substrates). The size of sapphire substrates has increased from the 2″ diameter, while the price has decreased. Currently (as at the time of writing), a successful transition to 3″ and 4″ diameters has been made by many

LED manufacturers and the trend for larger wafer sizes, such as 6″ and 8″ diameters, will continue to maintain the price competitiveness of LEDs by reducing manufacturing costs. At the same time, the dominance of GaN on a sapphire platform for LEDs may face serious challenges from alternative substrates, especially GaN on a silicon platform.

3.7 References

Addamiano, A. (1961) 'On the preparation of the nitrides of aluminum and gallium', *J Electrochem Soc* 108, 1072.

Akasaki, I. (2007) 'Lifetime of research on nitrides – alone in the wilderness', in Takahashi, K., Yoshikawa, A. and Sandhu, A., *Wide Bandgap Semiconductors, Fundamental Properties and Modern Photonic and Electronic Devices*, Berlin, Springer, pp. IX–XVII.

Akasaki, I., Amano, H., Koide, N., Hiramatsu, K. and Sawaki, N. (1989) 'Effect of AlN buffer layer on crystallographic structure and on electrical and optical properties of GaN and $Ga_{1-x}Al_xN$ ($0<x\leq 0.4$) films grown on sapphire substrate by MOVPE', *J Crystal Growth* 98, 209–219.

Akita, K., Kyono, T., Yoshizumi, Y., Kitabayashi, H. and Katayama, K. (2007) 'Improvements of external quantum efficiency of InGaN-based blue light emitting diodes at high current density using GaN substrates', *J Appl Phys* 101, 033104-1–033104-5.

Amano, H. and Akasaki, I. (2001) 'Novel aspects of the growth of nitrides by MOVPE', *J Phys: Condens Matter* 13, 6935–6944.

Amano, H., Sawaki, N., Akasaki, I. and Toyoda, Y. (1986) 'Metalorganic vapor phase epitaxial growth of a high quality GaN film using an AlN buffer layer', *Appl Phys Lett* 48, 353–355.

Amano, H., Akasaki, I., Hiramatsu, K., Koide, N. and Sawaki, N. (1988) 'Effect of buffer layer in metalorganic vapor phase epitaxy of GaN on sapphire substrate', *Thin Solid Film* 163, 415–420.

Amano, H., Kamiyama, S. and Akasaki, I. (2002) 'Impact of low-temperature buffer layers on nitride-based optoelectronics', *Proc IEEE* 90, 1015–1021.

Ambacher, O., Smart, J., Shealy, J.R., Weimann, N.G., Chu, K., *et al.* (1999) 'Two-dimensional electron gases induced by spontaneous and piezoelectric polarization charges in N- and Ga-face AlGaN/GaN heterostructures', *J Appl Phys* 85, 3222–3233.

Ashby, C.I.H., Mitchell, C.C., Han, J., Missert, N.A., Provencio, P.P., *et al.* (2000) 'Low-dislocation-density GaN from a single growth on a textured substrate', *Appl Phys Lett* 77, 3233–3235.

Avrutin, V., Cantwell, G., Zhang, J., Song, J.J., Silversmith, D.J. and Morkoc, H. (2010a) 'Bulk ZnO: current status, challenges, and prospects', *Proc IEEE* 98, 1339–1350.

Avrutin, V., Silversmith, D.J., Mori Y., Jawamura, F., Jitaoka, Y., *et al.* (2010b) 'Growth of bulk GaN and AlN: progress and challenges', *Proc IEEE* 98, 1302–1315.

Balakrishnan, K., Fujimoto, N., Kitano, T., Bandoh, A., Imura, M., *et al.* (2006) 'Critical aspects of high temperature MOCVD growth of AlN epilayers on 6H-SiC substrates', *Phys Stat Sol (c)* 3, 1392–1395.

Bassim, N.D., Twigg, M.E., Eddy, Jr, C.R., Culbertson, J.C., Mastro, M.A., *et al.* (2005) 'Lowered dislocation densities in uniform GaN layers grown on step-free (0001) 4H-SiC mesa surfaces', *Appl Phys Lett* 86, 021902-1–021902-3.

Beresford, R., Paine, D.C. and Briant, C.L. (1997) ‘Group IVB refractory metal crystals as lattice-matched substrates for growth of III nitrides by plasma-source molecular beam epitaxy’, *J Crystal Growth* 178, 189–200.

Bernardini, F. and Fiorentini, V. (1998) ‘Macroscopic polarization and band offsets at nitride heterojunction’, *Phys Rev B* 57, R9427–R9430.

Bernardini, F., Fiorentini, V. and Vanderbilt, D. (1997) ‘Spontaneous polarization and piezoelectric constants of III-V nitrides’, *Phys Rev B* 56, R10024–R10027.

Caenegem, T.V., Moerman, I. and Demeester, P. (1997) ‘Selective area growth on planar masked InP substrates by metal organic vapour phase epitaxy (MOVPE)’, *Prog Crystal Growth Charact* 35, 263–288.

Cao, X.A., LeBoeuf, S.F., D’Evelyn, M.P., Arthur, S.D., Kretchmer, J., *et al.* (2004) ‘Blue and near-ultraviolet light-emitting diodes on free-standing GaN substrates’, *Appl Phys Lett* 84, 4313–4315.

Chakraborty, A., Kim, K.C., Wu, F., Speck, J.S., DenBaars, S.P., *et al.* (2006) ‘Defect reduction in nonpolar *a*-plane GaN films using *in situ* SiN_x nanomask’, *Appl Phys Lett* 89, 041903-1–041903-3.

Choi, H.W., Liu, C., Gu, E., McConnell, G., Girkin, J.M., *et al.* (2004) ‘GaN micro-light-emitting diode arrays with monolithically integrated sapphire microlenses’, *Appl Phys Lett* 84, 2253–2255.

Coldren, L.A., Corzine, S.W. and Mashanovitch, M.L. (2012) *Diode Lasers and Photonic Integrated Circuits*, Hoboken, John Wiley & Sons.

Craven, M.D., Lim, S.H., Wu, F., Speck, J.S. and DenBaars, S.P. (2002) ‘Structural characterization of nonpolar $(11\bar{2}0)$ *a*-plane GaN thin films grown on $(1\bar{1}02)$ *r*-plane sapphire’, *Appl Phys Lett* 81, 469–471.

Craven, M.D., Wu, F., Chakraborty, A., Imer, B., Mishra, U.K., *et al.* (2004) ‘Microstructural evolution of *a*-plane GaN grown on *a*-plane SiC by metalorganic chemical vapor deposition’, *Appl Phys Lett* 84, 1281–1283.

Cree (2013) *LED Components and Modules*. Available online at: http://www.cree.com/led-components-and-modules

Cuong, T.V., Cheong, H.S., Kim, H.G., Kim, H.Y., Hong, C.-H., *et al.* (2007) ‘Enhanced light output from aligned micropit InGaN-based light emitting diodes using wet-etch sapphire patterning’, *Appl Phys Lett* 90, 131107-1–131107-3.

Dai, Q., Schubert, M.F., Kim, M.H., Kim, J.K., Schubert, E.F., *et al.* (2009) ‘Internal quantum efficiency and nonradiative recombination coefficient of GaInN/GaN multiple quantum wells with different dislocation densities’, *Appl Phys Lett* 94, 111109-1–111109-3.

Darakchieva, V., Paskov, P.P., Paskova, T., Valcheva, E., Monemar, B., *et al.* (2003) ‘Lattice parameters of GaN layers grown on *a*-plane sapphire: effect of in-plane strain anisotropy’, *Appl Phys Lett* 82, 703–705.

Davis, R.F., Einfeldt, S., Preble, E.A., Roskowski, A.M., Reitmeier, Z.J., *et al.* (2003) ‘Gallium nitride and related materials: challenges in materials processing’, *Acta Mater* 51, 5961–5979.

DenBaars, S.P. (1997) ‘Gallium-nitride-based materials for blue to ultraviolet optoelectronics devices’, *Proc IEEE* 85, 1740–1749.

Denis, A., Goglio, G. and Demazeau, G. (2006) ‘Gallium nitride bulk crystal growth processes: a review’, *Mater Sci Eng Report* 50, 167–194.

Detchprohm, T., Amano, H., Hiramatsu, K. and Akasaki, I. (1993) ‘The growth of thick GaN film on sapphire substrate by using ZnO buffer layer’, *J Crystal Growth* 128, 384–390.

Detchprohm, T., Yano, M., Sano, S., Nakamura, R., Mochiduki, S., *et al.* (2001) 'Heteroepitaxial lateral overgrowth of GaN on periodically grooved substrates: a new approach for growing low-dislocation-density GaN single crystals', *Jpn J Appl Phys* 40, L16–L19.

Dobrovinskaya, E.R., Lytvynov, L.A. and Pishchik, V. (2009) *Sapphire: Material, Manufacturing, Applications*, New York, Springer.

Doolittle, W.A., Kropewnicki, T., Carter-Coman, C., Stock, S., Koh, P., *et al.* (1998) 'Growth of GaN on lithium gallate substrates for development of a GaN thin compliant substrate', *J Vac Sic Technol B* 16, 1300–1304.

Doolittle, W.A., Kang, S. and Brown, A. (2000) 'MBE growth of high quality GaN on $LiGaO_2$ for high frequency, high power electronic applications', *Solid State Electron* 44, 229–238.

Dupuis, R.D. and Krames, M.R. (2008) 'History, development, and applications of high-brightness visible light-emitting diodes', *J Lightwave Technol* 26, 1154–1171.

Edwards, N.V., Bremser, M.D., Davis, R.F., Batchelor, A.D., Yoo, S.D., *et al.* (1998) 'Trends in residual stress for GaN/AlN/6H-SiC heterostructures', *Appl Phys Lett* 73, 2808–2811.

Ehrentraut, D. and Fukuda, T. (2010) 'The ammonothermal crystal growth of gallium nitride – a technique on the up rise', *Proc IEEE*, 98, 1316–1323.

Fan, J.Y., Rong, G., Newman, N. and Smith, D.J. (2000) 'Defect annihilation in AlN thin films by ultrahigh temperature processing', *Appl Phys Lett* 76, 1839–2841.

Faulkner, K.R., Wickenden, D.K., Isherwood, B.J., Richards, B.P. and Scobey, I.H. (1970) 'Gallium nitride formed by vapour deposition and by conversion from gallium arsenide', *J Mater Sci* 5, 308–313.

Feng, Z.H. and Lau, K.M. (2005) 'Enhanced luminescence from GaN-based blue LEDs grown on grooved sapphire substrates', *IEEE Photon Technol Lett* 17, 1812–1814.

Gardner, N.F., Kim, J.C., Wierer, J.J., Shen, Y.C. and Krames, M.R. (2005) 'Polarization anisotropy in the electroluminescence of *m*-plane InGaN–GaN multiple-quantum-well light-emitting diodes', *Appl Phys Lett* 86, 111101-1–111101-3.

Gault, W.A., Monberg, E.M. and Clemans, J.E. (1986) 'A novel application of the vertical gradient freeze methods to the growth of high quality III-V crystals', *J Crystal Growth* 74, 491–506.

Gehrke, T. (2008) 'Review of structured thin films in wide bandgap semiconductors: pendeo-epitaxy of GaN and AlGaN', *J Nanophotonic* 2, 021990-1–021990-12.

Grzegory, I. (2001) 'High pressure growth of bulk GaN from solutions in gallium', *J Phys: Condens Matter* 13, 6875–6892.

Hahn, H. and Juza, R. (1940) 'Untersuchungen über die nitride von cadmium, gallium, indium und germanium metallamide und metalinitride', *Z Anorg Allgem Chem* 244, 111–124.

Hamdani, F., Yeadon, M., Smith, D.J., Tang, H., Kim, W., *et al.* (1998) 'Microstructure and optical properties of epitaxial GaN on ZnO (0001) grown by reactive molecular beam epitaxy,' *J Appl Phys* 83, 983–990.

Hashimoto, M., Amano, H., Sawaki, N. and Akasaki, I. (1984) 'Effects of hydrogen in an ambient on the crystal growth of GaN using $Ga(CH_3)_3$ and NH_3', *J Crystal Growth* 68, 163–168.

Haskell, B.A., Wu, F., Matsuda, S., Craven, M.D., Fini, P.T., *et al.* (2003a) 'Structural and morphological characteristics of planar nonpolar ($11\bar{2}0$) *a*-plane gallium nitride grown by hydride vapor phase epitaxy', *Appl Phys Lett* 83, 1554–1556.

Haskell, B.A., Wu, F., Craven, M.D., Matsuda, S., Fini, P.T., *et al.* (2003b) 'Defect reduction in $(11\bar{2}0)$ *a*-plane gallium nitride via lateral epitaxial overgrowth by hydride vapor phase epitaxy', *Appl Phys Lett* 83, 644–646.

Haskell, B.A., Baker, T.J., McLaurin, M.B., Wu, F., Fini, P.T., *et al.* (2005) 'Defect reduction in $(1\bar{1}00)$ *m*-plane gallium nitride via lateral epitaxial overgrowth by hydride vapor phase epitaxy', *Appl Phys Lett* 86, 111917-1–111917-3.

Hellman, E.S., Buchanan, D.N.E., Wiesmann, D. and Brener, I. (1996) 'Growth of Ga-face and N-face GaN films using ZnO substrates', *MRS Internet J Nitride Semicond Res* 1, 16.

Hinoki, A., Kikawa, J., Yamada, T., Tsuchiya, T., Kamiya, S., *et al.* (2008) 'Effects of traps formed by threading dislocations on off-state breakdown characteristics in GaN buffer layer in AlGaN/GaN heterostructure field-effect transistors', *Appl Phys Express* 1, 011030-1–011030-3.

Hiramatsu, K. (2001) 'Epitaxial lateral overgrowth techniques used in group III nitride epitaxy', *J Phys: Condens Matter* 13, 6961–6975.

Hiramatsu, K., Itoh, S., Amano, H., Akasaki, I., Kuwano, N., *et al.* (1991) 'Growth mechanism of GaN growth on sapphire with AlN buffer layer by MOVPE', *J Crystal Growth* 115, 628–633.

Hiramatsu, K., Nishiyama, K., Motogaito, A., Miyake, H., Iyechika, Y., *et al.* (1999) 'Recent progress in selective area growth and epitaxial lateral overgrowth of III-nitrides: effects of reactor pressure in MOVPE growth', *Phys Stat Sol (a)* 176, 535–543.

Ilegems, M., Dingle, R. and Logan, R.A. (1972) 'Luminescence of Zn- and Cd-doped GaN', *J Appl Phys* 43, 3797–3800.

Im, J.S., Kollmer, H., Off, J., Sohmer, A., Scholz, F., *et al.* (1998) 'Reduction of oscillator strength due to piezoelectric fields in GaN/$Al_xGa_{1-x}N$ quantum wells', *Phys Rev B* 57, R9435–R9438.

Imer, B.M., Wu, F., DenBaars, S.P. and Speck, J.S. (2006) 'Improved quality $(11\bar{2}0)$ *a*-plane GaN with sidewall lateral epitaxial overgrowth', *Appl Phys Lett* 88, 061908-1–061908-3.

Inoue, S., Okamoto, K., Matsuki, N., Kim, T.-W. and Fujiokaa, H. (2006) 'Epitaxial growth of GaN on copper substrates', *Appl Phys Lett* 88, 261910-1–261910-3.

Inoue, S., Okamoto, K., Nakano, T. Ohta, J. and Fujiokaa, H. (2007) 'Growth of single crystalline GaN on silver mirrors', *Appl Phys Lett* 91, 201920-1–201920-3.

Ishii, T., Tazoh, Y. and Miyazawa, S. (1998) 'Single-crystal growth of $LiGaO_2$ for a substrate of GaN thin films', *J Crystal Growth* 186, 409–419.

Jastrzebski, L. (1983) 'SOI by CVD: epitaxial lateral overgrowth (ELO) process – review', *J Crystal Growth* 63, 493–526.

Jeganathan, K., Shimizu, M. and Okumura, H. (2005) 'High-density self-assembled GaN nanoislands on SiC (0001) by molecular-beam epitaxy', *Appl Phys Lett* 86, 073106-1–073106-3.

Johnson, M.A.L., Fujita, S., Rowland, Jr, W.H., Hughes, W.C., Cook, Jr, J.W., *et al.* (1996) 'MBE growth and properties of ZnO on sapphire and SiC substrates', *J Electron Mater* 25, 855–862.

Johnson, W.C., Parsons, J.B., and Crew, M.C. (1932) 'Nitrogen compounds of gallium III. gallic nitride', *J Phys Chem* 36, 2651–2654.

Kapolnek, D., Wu, X.H., Heying, B., Keller, S., Keller, B.P., *et al.* (1995) 'Structural evolution in epitaxial metalorganic chemical vapor deposition grown GaN films on sapphire', *Appl Phys Lett* 67, 1541–1543.

Kapolnek, D., Keller, S., Vetury, R., Underwood, R.D., Kozodoy, P., *et al.* (1997) ‘Anisotropic epitaxial lateral growth in GaN selective area epitaxy’, *Appl Phys Lett* 71, 1204–1206.

Kato, Y., Kitamura, S., Hiramatsu, K. and Sawaki, N. (1994) ‘Selective growth of wurtzite GaN and AlGaN on GaN/sapphire substrates by metalorganic chemical vapor deposition’, *J Crystal Growth* 144, 133–140.

Kawasuso, A., Kojima, K., Yoshikawa, M., Itoh, H. and Narumi, K. (2000) ‘Effect of hydrogen etching on 6H SiC surface morphology studied by reflection high-energy positron diffraction and atomic force microscopy’, *Appl Phys Lett* 76, 1119–1121.

Kelly, M.K., Vaudo, R.P., Phanse, V.M., Gorgens, L., Ambacher, O., *et al.* (1999) ‘Large free-standing GaN substrates by hydride vapor phase epitaxy and laser-induced liftoff’, *Jpn J Appl Phys* 38, L217–L219.

Khan, M.A., Skogman, R.A., Schulze, R.G. and Gershenzon, M. (1983) ‘Electrical properties and ion implantation of epitaxial GaN grown by low-pressure metalorganic chemical vapor deposition’, *Appl Phys Lett* 48, 35–37.

Kim, K.-C., Schmidt, M.C., Sato, H., Wu, F., Fellows, N., *et al.* (2007) ‘Improved electroluminescence on nonpolar *m*-plane InGaN/GaN quantum wells LEDs’, *Phys Stat Sol (RRL)* 1, 125–127.

Kitamura, S., Hiramatsu, K. and Sawaki, N. (1995) ‘Fabrication of GaN hexagonal pyramids on dot-patterned GaN/sapphire substrates via selective metalorganic vapor phase epitaxy’, *Jpn J Appl Phys* 34, L1184–L1186.

Koleske, D.D., Henry, R.L., Twigg, M.E., Culbertson, J.C., Binari, S.C., *et al.* (2002) ‘Influence of AlN nucleation layer temperature on GaN electronic properties grown on SiC’, *Appl Phys Lett* 80, 4372–4374.

Kosicki, B.B. and Kahng, D. (1969) ‘Preparation and structural properties of GaN thin film’, *J Vac Sci Technol* 6, 593–596.

Kung, P., Saxler, A., Zhang, X., Walker, D., Lavado, R., *et al.* (1996) ‘Metalorganic chemical vapor deposition of monocrystalline GaN thin films on β-$LiGaO_2$ substrates’, *Appl Phys Lett* 69, 2116–2118.

Kuramata, A., Horino, K., Domen, K., Shinohara, K. and Tanahashi, T. (1995) ‘High-quality GaN epitaxial layer grown by metalorganic vapor phase epitaxy on (111) $MgAl_2O_4$ substrate’, *Appl Phys Lett* 67, 2521–2523.

Kuznia, J.N., Khan, M.A., Olson, D.T., Kaplan, R. and Freitas, J. (1993) ‘Influence of buffer layers on the deposition of high quality single crystal GaN over sapphire substrates’, *J Appl Phys* 73, 4700–4702.

Kyono, T., Hirayama, H., Akita, K., Nakamura, T. and Ishibashi, K. (2005) ‘Effects of In composition on ultraviolet emission efficiency in quaternary InAlGaN light-emitting diodes on freestanding GaN substrates and sapphire substrates’, *J Appl Phys* 98, 113514-1–113514-8.

Lee, J.J., Park, Y.S., Yang, C.S., Kim, H.S., Kim, K.H., *et al.* (2000) ‘MBE growth of wurtzite GaN on $LaAlO_3$ (100) substrate’, *J Crystal Growth* 213, 33–39.

Lee, T.-X., Gao, K.-F., Chien, W.-T. and Sun, C.-C. (2007b) ‘Light extraction analysis of GaN-based light-emitting diodes with surface texture and/or patterned substrate’, *Opt Express* 15, 6670–6676.

Lee, W., Ryou, J.-H., Yoo, D., Limb, J., Dupuis, R.D., *et al.* (2007a) ‘Optimization of Fe doping at the regrowth interface of GaN for applications to III-nitride-based heterostructure field-effect transistors’, *Appl Phys Lett* 90, 093509-1–093509-3.

Lin, M.E., Strite, S., Agarwal, A., Salvador, A., Zhou, G.L., *et al.* (1993) ‘GaN grown on hydrogen plasma cleaned 6H-SiC substrates’, *Appl Phys Lett* 62, 702–704.

Linthicum, K., Gehrke, T., Thomson, D., Carlson, E., Rajagopal, P., *et al.* (1999) 'Pendeoepitaxy of gallium nitride thin films', *Appl Phys Lett* 75, 196–198.

Liu, J.P., Limb, J., Ryou, J.-H., Yoo, D., Horne, C.A., *et al.* (2008) 'Blue light emitting diodes grown on free standing $(11\bar{2}0)$ *a*-plane GaN substrates', *Appl Phys Lett* 92, 011123-1–011123-3.

Liu, J.P., Limb, J., Lochner, Z., Yoo, D., Ryou, J.-H., *et al.* (2009) 'Green light-emitting diodes with p-InGaN:Mg grown on *c*-plane sapphire and GaN substrates', *Phys Stat Sol (a)* 206, 750–753.

Liu, Z., Wei, T., Guo, E., Yi, X., Wang, L., *et al.* (2011) 'Efficiency droop in InGaN/GaN multiple-quantum-well blue light-emitting diodes grown on free-standing GaN substrate', *Appl Phys Lett* 99, 091104-1–091104-3.

Lochner, Z., Kim, H.J., Lee, Y.C., Zhang, Y., Choi, S., *et al.* (2011) 'NpN-GaN/$In_xGa_{1-x}N$/GaN heterojunction bipolar transistor on free-standing GaN substrate', *Appl Phys Lett* 99, 193501-1–193501-3.

Lorenz, M.R. and Binkowski, B.B. (1962) 'Preparation, stability, and luminescence of gallium nitride', *J Electrochem Soc* 109, 24–26.

Losurdo, M., Capezzuto, P., Bruno, G., Brown, A., Kim, T.-H., *et al.* (2005) 'Interfacial reactions during GaN and AiN epitaxy on 4H-and 6H-SiC (0001)', *Appl Phys Lett* 86, 021920-1–021920-3.

Mamutin, V.V., Sorokin, S.V., Jmerik, V.N., Shubina, T.V., Ratnikov, V.V., *et al.* (1999) 'Plasma-assisted MBE growth of GaN and InGaN on different substrates', *J Crystal Growth* 201/202, 346–350.

Manasevit, H.M. (1968) 'Single-crystal gallium arsenide on insulating substrates', *Appl Phys Lett* 12, 156–159.

Manasevit, H.M. (1972) 'The use of metalorganics in the preparation of semiconductor materials: growth on insulating substrates', *J Crystal Growth* 13/14, 306–314.

Manasevit, H.M. (1981) 'Recollections and reflections of MO-CVD', *J Crystal Growth* 55, 1–9.

Manasevit, H.M. (1983) *Epitaxial Composite and Method of Making*, US patent 4368098C, 11 January 1983.

Manasevit, H.M., Erdmann, F.M. and Simpson, W.I. (1971) 'The use of metalorganics in the preparation of semiconductor materials: IV. The nitrides of aluminum and gallium', *J Electrochem Soc: Solid State Science* 118, 1864–1868.

Maruska, H.P. and Tietjen, J.J. (1969) 'The preparation and properties of vapor-deposited single-crystalline GaN', *Appl Phys Lett* 15, 327–329.

Matsuoka, T. and Hagiwara, E. (2001) 'GaN growth on novel lattice-matching substrate: tilted *m*-plane sapphire', *Phys Stat Sol (a)* 188, 485–489.

Matsuoka, T., Yoshimoto, N., Sasaki, T. and Katsui, A. (1992) 'Wide-gap semiconductor InGaN and InGaAlN grown by MOVPE', *J Electron Mater* 21, 157–163.

Miller, D.A.B., Chemla, D.S., Damen, T.C., Gossard, A.C., Wiegmann, W., *et al.* (1984) 'Band-edge electroabsorption in quantum well structures: the quantum-confined Stark effect', *Phys Rev Lett* 53, 2173–2176.

Mishra, U.K., Parikh, P. and Wu, Y.-F. (2002) 'AlGaN/GaN HEMTs – an overview of device operation and applications', *Proc IEEE* 90, 1022–1031.

Monemar, B. and Lagerstedt, O. (1979) 'Properties of VPE-grown GaN doped with Al and some iron group metals', *J Appl Phys* 50, 6480–6491.

Morkoc, H. and Ozgur, U. (2009) *Zinc Oxide: Fundamentals, Materials and Device Technology*, Weinheim, Germany, Wiley-VCH Verlag.

Mullin, J.B., Straughan, B.W. and Brickell, W.S. (1965) ‘Liquid encapsulation techniques: the use of an inert liquid in suppressing dissociation during the melt-growth of InAs and GaAs crystals’, *J Phys Chem Solids* 26, 782–784.

Nakamura, S. (1991a) ‘GaN growth using GaN buffer layer’, *Jpn J Appl Phys* 30, L1705–L1707.

Nakamura, S. (1991b) ‘*In-situ* monitoring of GaN growth using interference effects’, *Jpn J Appl Phys* 30, 1620–1627.

Nakamura, S., Senoh, M., Nagahama, S.-I., Iwasa, N., Yamada, T., *et al.* (1996) ‘InGaN multi-quantum-well structure laser diodes grown on $MgAl_2O_4$ substrates’, *Appl Phys Lett* 68, 2105–2107.

Nam, O.-H., Bremser, M.D., Zheleva, T.S. and Davis, R.F. (1997) ‘Lateral epitaxy of low density defect GaN layers via organometallic vapor phase epitaxy’, *Appl Phys Lett* 71, 2638–2640.

Ng, H.M. (2002) ‘Molecular-beam epitaxy of GaN/$Al_xGa_{1-x}N$ multiple quantum wells on *r*-plane $(10\bar{1}2)$ sapphire substrates’, *Appl Phys Lett* 80, 4369–4371.

Ni, X., Ozgur, U., Fu, Y., Biyikli, N., Xie, J., *et al.* (2006) ‘Defect reduction in $(11\bar{2}0)$ *a*-plane GaN by two-stage epitaxial lateral overgrowth’, *Appl Phys Lett* 89, 262105-1–262105-3.

Norton, D.P., Heo, Y.W., Ivill, M.P., Ip, K., Pearton, S.J., *et al.* (2004) ‘ZnO: growth, doping and processing’, *Materials Today* 7, 34–40.

Ohta, J., Fujioka, H., Takahashi, H. and Oshima, M. (2001) ‘Crystal growth of GaN on $(Mn,Zn)Fe_2O_4$ substrates’, *Phys Stat Sol (a)* 188, 497–500.

Okamoto, K., Tanaka, T. and Kubota, M. (2008) ‘High-efficiency continuous wave operation of blue-green laser diodes based on nonpolar *m*-plane gallium nitride’, *Appl Phys Express* 1, 072201-1–072201-3.

Ozgur, U., Alivov, Y.I., Liu, C., Teke, A., Reshchikov, M.A., *et al.* (1995) ‘A comprehensive review of ZnO materials and devices’, *J Appl Phys* 98, 041301-1–041301-103.

Pankove, J.I., Miller, E.A., Richman, D. and Berkeyheiser, J.E. (1971) ‘Electroluminescence in GaN’, *J Luminescence* 4, 63–66.

Park, J., Grudowski, P.A., Eiting, C.J. and Dupuis, R.D. (1998) ‘Selective-area and lateral epitaxial overgrowth of III-N materials by metalorganic chemical vapor deposition’, *Appl Phys Lett* 73, 333–335.

Park, S.-H. (2002) ‘Crystal-orientation effects on electronic properties of wurtzite InGaN/GaN quantum wells’, *J Appl Phys* 91, 9904–9908.

Park, S.-H. and Chuang, S.L. (1999) ‘Crystal-orientation effects on the piezoelectric field and electronic properties of strained wurtzite semiconductors’, *Phys Rev B* 59, 4725–4737.

Park, S.-H., Jeon, H., Sung, Y.-J. and Yeom, G.-Y. (2001) ‘Refractive sapphire microlenses fabricated by chlorine-based inductively coupled plasma etching’, *Appl Optics* 40, 3698–3702.

Paskova, T., Darakchieva, V., Valcheva, E., Paskov, P.P., Monemar, B., *et al.* (2003) ‘Growth of GaN on *a*-plane sapphire: in-plane epitaxial relationships and lattice parameters’, *Phys Stat Sol (b)* 240, 318–321.

Paskova, T., Hanser, D.A. and Evans, K.R. (2010) ‘GaN substrates for III-nitride devices’, *Proc IEEE* 98, 1324–1338.

Pasternak, J. and Souckova, L. (1963) ‘Herstellung dünner schichten von aluminium-, gallium, sowie indiumnitrid unter einer gasentladung’, *Phys Stat Sol* 3, K71–K74.

Pearton, S.J. and Ren, F. (2000) ‘GaN electronics’, *Adv Mater* 12, 1571–1580.

Ponce, F.A., Krusor, B.S., Major, Jr, J.S., Plano, W.E. and Welch, D.F. (1995) 'Microstructure of GaN epitaxy on SiC using AlN buffer layers', *Appl Phys Lett* 67, 410–412.

Renner, T. (1959) 'Herstellung der nitride von bor, aluminium, gallium und indium nach dem aufwachsverfahren', *Z Anorg Allgem Chem* 298, 22–33.

Rozhansky, I.V. and Zakheim, D.A. (2006) 'Analysis of the causes of the decrease in the electroluminescence efficiency of AlGaInN light-emitting-diode heterostructures at high pumping density', *Semiconductors* 40, 839–845.

Rozhansky, I.V. and Zakheim, D.A. (2007) 'Analysis of processes limiting quantum efficiency of AlGaInN LEDs at high pumping', *Phys Stat Sol (a)* 204, 227–230.

Ryou, J.H., Yoder, P.D., Liu, J.P., Lochner, Z., Kim, H.S., *et al.* (2009) 'Control of quantum-confined Stark effect in InGaN-based quantum wells', *IEEE J Select Topic Quantum Electron* 15, 1080–1091.

Sasaki, T. and Zembutsu, S. (1987) 'Substrate orientation dependence of GaN single crystal films grown by metalorganic chemical vapor phase epitaxy', *J Appl Phys* 61, 2533–2540.

Schmidt, M.C., Kim, K.-C., Sato, H., Fellows, N., Masui, H., *et al.* (2007) 'High power and high external efficiency *m*-plane InGaN light emitting diodes', *Jpn J Appl Phys* 46, L126–L128.

Schubert, M.F. and Schubert, E.F. (2010) 'Effect of heterointerface polarization charges and well width upon capture and dwell time for electrons and holes above GaInN/GaN quantum wells', *Appl Phys Lett* 96, 131102-1–131102-3.

Schubert, M.F., Chhajed, S., Kim, J.K., Schubert, E.F., Koleske, D.D., *et al.* (2007) 'Effect of dislocation density on efficiency droop in InGaN/GaN light-emitting diodes', *Appl Phys Lett* 91, 231114-1–231114-3.

Shen, Y.C., Mueller, G.O., Watanabe, S., Gardner, N.F., Munkholm, A., *et al.* (2007) 'Auger recombination in InGaN measured by photoluminescence', *Appl Phys Lett* 91, 141101-1–141101-3.

Sumiya, M., Chikyow, T., Sasahara, T., Yoshimura, K., Ohta, J., *et al.* (2002) 'Epitaxial growth of GaN film on (La,Sr)(Al,Ta)O_3 (111) substrate by metalorganic chemical vapor deposition', *Jpn J Appl Phys* 41, 5038–5041.

Tadatomo, K., Okagawa, H., Ohuchi, Y., Tsunekawa, T., Imada, Y., *et al.* (2001) 'High output power InGaN ultraviolet light-emitting diodes fabricated on patterned sapphire substrates using metalorganic vapor phase epitaxy', *Jpn J Appl Phys* 40, L583–L585.

Takeuchi, T., Sota, S., Katsuragawa, M., Komori, M., Takeuchi, H., *et al.* (1997) 'Quantum-confined Stark effect due to piezoelectric fields in GaInN strained quantum wells', *Jpn J Appl Phys* 36, L382–L385.

Tavernier, P.R., Imer, B., DenBaars, S.P. and Clarke, D.R. (2004) 'Growth of thick $(11\bar{2}0)$ GaN using a metal interlayer', *Appl Phys Lett* 85, 4630–4632.

Torres, V.M., Edwards, J.L., Wilkens, B.J., Smith, D.J., Doak, R.B., *et al.* (1999) 'Influence of 6H-SiC (0001) substrate surface morphology on the growth of AlN epitaxial layers', *Appl Phys Lett* 74, 985–987.

Tsuchiya, Y., Kobayashi, A., Ohta, J., Fujioka, H. and Oshima, M. (2006) 'Heteroepitaxial growth of GaN on atomically flat $LiTaO_3$ (0001) using low-temperature AIN buffer layers', *J Crystal Growth* 293, 22–26.

Usui, A., Sunakawa, H., Sakai, A. and Yamaguchi, A.A. (1997) 'Thick GaN epitaxial growth with low dislocation density by hydride vapor phase epitaxy', *Jpn J Appl Phys* 36, L899–L902.

Waltereit, P., Brandt, O., Trampert, A., Ramsteiner, M., Reiche, M., *et al.* (1999) 'Influence of AlN nucleation layers on growth mode and strain relief of GaN grown on 6H-SiC (0001)', *Appl Phys Lett* 74, 3660–3662.

Waltereit, P., Brandt, O., Trampert, A., Grahn, H.T., Menniger, J., *et al.* (2000) 'Nitride semiconductors free of electrostatic fields for efficient white light-emitting diodes', *Nature* 406, 865–868.

Weeks, Jr, T.W., Bremser, M.D., Ailey, K.S., Carlson, E., Perry, W.G., *et al.* (1995) 'GaN thin films deposited via organometallic vapor phase epitaxy on α(6H)-SiC (0001) using high-temperature monocrystalline AlN buffer layers', *Appl Phys Lett* 67, 401–403.

Wickenden, A.E., Wickenden, D.K. and Kistenmacher, T.J. (1994) 'The effect of thermal annealing on GaN nucleation layers deposited on (0001) sapphire by metalorganic chemical vapor deposition', *J Appl Phys* 75, 5367–5371.

Wickenden, D.K., Faulkner, K.R., Brander, R.W. and Isherwood, B.J. (1971) 'Growth of epitaxial layers of gallium nitride on silicon carbide and corundum substrates', *J Crystal Growth* 9, 158–164.

Wu, X.H., Kapolnek, D., Tarsa, E.J., Heying, B., Keller, S. Keller, *et al.* (1996) 'Nucleation layer evolution in metal-organic chemical vapor deposition grown GaN', *Appl Phys Lett* 68, 1371–1373.

Wuu, D.S., Wang, W.K., Shih, W.C., Horng, R.H., Lee, C.E., *et al.* (2005) 'Enhanced output power of near-ultraviolet InGaN–GaN LEDs grown on patterned sapphire substrates', *IEEE Photon Technol Lett* 17, 288–290.

Xu, K., Xu, J., Deng, P., Qiu, R. and Fang, F. (1999) 'MOCVD growth of GaN on $LiAlO_2$ (100) substrates', *Phys Stat Sol (a)* 176, 589–593.

Xu, X., Vaudoa, R.P., Loria, C., Salanta, A., Brandesa, *et al.* (2002) 'Growth and characterization of low defect GaN by hydride vapor phase epitaxy', *J Crystal Growth* 246, 223–229.

Yamada, A., Ho, K.P., Akaogi, T., Maruyama, T. and Akimoto, K. (1999) 'Layered compound substrates for GaN growth', *J Crystal Growth* 201/202, 332–335.

Yamada, M., Mitani, T., Narukawa, W., Shioji, S., Niki, I., *et al.* (2002) 'InGaN-based near-ultraviolet and blue-light-emitting diodes with high external quantum efficiency using a patterned sapphire substrate and a mesh electrode', *Jpn J Appl Phys* 41, L1431–L1433.

Yim, W.M. and Paff, R.J. (1974) 'Thermal expansion of AlN, sapphire, and silicon', *J Appl Phys* 45, 1456–1457.

Yoo, D., Limb, J., Ryou, J.-H., Lee, W. and Dupuis, R.D. (2006) 'GaN full-vertical p-i-n rectifiers employing AlGaN:Si conducting buffer layers on n-SiC substrates', *Appl Phys Lett* 88, 193503-1–193503-3.

Yoshida, S., Misawa, S. and Itoh, A. (1975) 'Epitaxial growth of aluminum nitride films on sapphire by reactive evaporation', *Appl Phys Lett* 26, 461–462.

Yoshida, S., Misawa, S., Fujii, Y., Takada, S., Hayakawa, H., *et al.* (1979) 'Reactive molecular beam epitaxy of aluminium nitride', *J Vac Sci Technol* 16, 990–993.

Yoshida, S., Misawa, S. and Gonda, S. (1983) 'Improvement on the electrical and luminescent properties of reactive molecular beam epitaxially grown GaN films using AlN-coated sapphire substrates', *Appl Phys Lett* 42, 427–429.

Yoshikawa, A., Kochurikhin, V.V., Futagawa, N., Shimamura, K. and Fukuda, T. (1999) 'Growth of $Ca_8La_2(PO_4)_6O_2$ single crystals as substrates for GaN epitaxial growth', *J Crystal Growth* 204, 302–306.

Yoshizumi, Y., Adachi, M., Enya, Y., Kyono, T., Tokuyama, S., *et al.* (2010) 'Continuous-wave operation of 520 nm green InGaN-based laser diodes on semi-polar $(20\bar{2}1)$ GaN substrates', *Appl Phys Express* 2, 092101-1–092101-3.

Zetterstrom, R.B. (1970) ‘Synthesis and growth of single crystals of gallium nitride’, *J Mater Sci* 5, 1102–1104.

Zheleva, T.S., Nam, O.-H., Bremser, M.D. and Davis, R.F. (1997) ‘Dislocation density reduction via lateral epitaxy in selectively grown GaN structures’, *Appl Phys Lett* 71, 2472–2474.

Zheleva, T.S., Smith, S.A., Thomson, D.N., Linthicum, K.J., Rajagopal, P., *et al.* (1999) ‘Pendeo-epitaxy: a new approach for lateral growth of gallium nitride films’, *J Electron Mater* 28, L5–L8.

4

Gallium nitride (GaN) on silicon substrates for LEDs

M. H. KANE, Texas A & M University at Galveston, USA
and N. AREFIN, University of Oklahoma, USA

DOI: 10.1533/9780857099303.1.99

Abstract: Widespread implementation of light-emitting diodes for solid-state lighting applications has been hindered by the high cost of the traditionally used heteroepitaxial substrates, sapphire and silicon carbide. The growth of GaN LEDs on silicon substrates would give significant cost savings. This chapter will summarize some of the challenges associated with the growth of GaN on silicon, discuss various strategies for alleviating the lattice mismatch and tensile strain imparted during the growth, and review efforts for the growth of light-emitting diodes on silicon substrates.

Key words: large-area substrates, GaN on silicon, heteroepitaxy, LEDs.

4.1 Introduction

III-nitride materials possess a number of properties that are simply not accessible in any other semiconductors, which will continue to make them an active area of scientific and technological development. The unique capabilities of the III-nitrides include a high dielectric breakdown voltage and a bandgap that spans from the infrared to the deep ultraviolet. However, there are some unique processing challenges related to the crystal structure and bonding. They have long been of interest for implementation in applications ranging from high-power transistors to a solid-state replacement for traditional lighting. Widespread market implementation of solid-state lighting sources would result in at least a twofold reduction in current energy consumption for lighting (roughly 10% of overall energy demand) worldwide (Craford, 2005), with a corresponding drop in demand for foreign petroleum and a fall in greenhouse gas emissions.

The consumer implementation of these sources has been hindered by cost barriers from the initial material growth steps, which ultimately are related to the lack of a thermally conductive, lattice-matched substrate. The implementation of GaN-based LEDs has been extraordinarily successful, though GaN devices differ from other III-V semiconductors in that there are no suitable lattice-matched substrates for their growth. The best substrates, silicon carbide and sapphire, were selected for their chemical stability in the aggressive metal-organic chemical vapor deposition (MOCVD) growth environment. One continuing issue for widespread solid-state lighting is the need to lower the cost per lumen of solid-state lighting devices. Silicon is an extremely attractive option in this regard because of the ready availability of cheap large-area substrates, but it has some unique challenges in the growth of GaN-based devices. These challenges have only recently been addressed successfully.

4.2 An overview of gallium nitride (GaN) on silicon substrates

A key problem has been the lack of a suitable lattice-matched substrate for the III-nitrides, as homoepitaxial substrates are not readily available and are extremely expensive. The most commonly used substrates for GaN growth are sapphire and silicon carbide, but this choice is driven by the need for chemical stability under the aggressive conditions for nitride growth rather than lattice mismatch concerns. The use of sapphire as a substrate presents a number of complications for the implementation of devices. One problem is that sapphire is an electrical insulator – instead of being able to put contacts on the backside surface of the substrate, the electrical contacts must all be placed on the topside of the structure. In addition to complicating the device processing, this results in the devices being dependent on a significant amount of lateral transport, even in nominally vertical devices. Given the high dislocation densities present in III-nitride devices ($\sim 10^9$ cm^{-2}), this lateral transport can result in a considerable amount of resistive heating within the material. The geometric considerations associated with contact placement of the *p*- and *n*-contacts can also result in severe problems with current crowding in the devices. This effect is compounded by the thermally insulating nature of sapphire. Excessive heating within the material reduces device lifetimes. Moreover, the inability to remove heat effectively from a device limits the drive current and emission power from high-power visible and ultraviolet light-emitting diodes (LEDs).

The development of novel substrates for the III-nitrides has been explored since the inception of these devices. Though initial reports focused on sapphire as the substrate of choice, efforts focusing on exploring substrates with better lattice matches were conducted in parallel. In order to understand the possible routes towards improved device performance in heteroepitaxial systems, it is useful to examine what has previously been reported for other techniques. Table 4.1 lists the materials parameters of several heteroepitaxial substrates that have been explored for GaN growth. In general, the most suitable materials for heteroepitaxial growth are oxides with close-packed oxygen sublattices. Most of these crystals, in contrast to GaN, can be readily grown by the Czochralski method. Of the Czochralski-grown crystals, silicon has achieved the highest level of perfection and lowest cost due to the ubiquitous implementation of silicon-based devices.

Table 4.1 Possible substrates for the epitaxial growth of GaN

Substrate	Crystal structure	Orientation	Lattice parameter			Lattice mismatch	Polar/ nonpolar
			a (Å)	*b* (Å)	*c* (Å)		
Al_2O_3	Corundum	(0001)	4.758	4.758	12.988	16%	Polar
6H-SiC	Hexagonal	(0001)	3.081	3.081	15.17	–3.4%	Polar
γ-$LiAlO_2$	Tetragonal	(100)	5.169	5.169	6.268	–1.4%	Both
$LiGaO_2$	Orthorhombic	(001)	5.403	6.372	5.007	1.9; 0.2%	Both
ZnO	Wurtzite	(0001), (11.0)	3.249	3.249	5.207	1.8; 0.4%	Both
LSAT	Perovskite	(111)	7.735	7.735	7.735	<1%	Polar
$MnAl_2O_4$	Spinel	(111)	~8	~8	~8	10.4%	Polar
$LiNbO_3$	Perovskite	(111)	5.147	5.147	5.147	7.1%	Polar
Si	Diamond	(111)	5.431	5.431	5.431	–16.9%	Polar
Ge	Diamond	(111)	5.646	5.646	5.646	–	Polar
$ScMgAlO_4$	Rhombohedral	(111)	3.236	3.236	3.236	1.8%	Polar
$LiTaO_3$	Perovskite	(111)	5.154	5.154	–	7.2%	Polar
$MnAl_6O_{10}$	Perovskite	(111)	7.984	7.984	7.984	–11.5%	Polar
GaN	Wurtzite	All	3.189	3.189	5.186	0%	Both

4.3 Silicon overview

4.3.1 Advantages of silicon

One key parameter needed to drive solid-state lighting further into the marketplace is lowering the cost per lumen. The luminous efficacy of these devices has increased to well over the performance found in fluorescent and incandescent light bulbs and the color quality has improved to render these devices suitable for most applications. Thus, the chief remaining hurdle has been the cost of GaN-based LED devices. The high cost of GaN LEDs is driven somewhat by the initial costs of the metal-organic precursors and the process expense of heating them to the growth temperatures. Another significant cost is the price of the substrates traditionally used for the growth of GaN-based materials. Silicon carbide and sapphire are both tremendously expensive, and though they share some crystallographic similarities with GaN, they are still not ideal for growth. Homoepitaxial growth of large-area GaN is still several years away. Switching to silicon instead of one of these other substrates could offer significant cost benefits, provided equivalent crystalline quality can be maintained.

There are several advantages in using silicon as a substrate for the growth of GaN LEDs, the most important of which is the low cost and high area of the available silicon substrates. The growth of silicon substrates has matured extensively over the past 50 years enabling modern silicon technology. Silicon substrates of greater than 12″ are routinely available, whereas sapphire and silicon carbide substrates are typically used in 2″ or 4″ sizes. Moreover, the cost of silicon is an order of magnitude lower than sapphire, and two to three orders of magnitude lower than silicon carbide of the same size. Thus, as efforts continue to lower the costs of solid-state lighting sources, the reduction of substrate costs can have a significant impact on the overall cost of a device. Substrate costs can be of the order of 80% (Zhu *et al.*, 2012) of the total processing cost. In addition, silicon is still the leading material for microelectronic applications; thus if the growth of gallium nitride on silicon can be achieved, it would be possible to monolithically integrate gallium nitride lighting devices with silicon microelectronics. Another advantage of silicon as a substrate is that it can be very easily wet-etched, unlike sapphire or silicon carbide. Thus it should be possible to have different device configurations such as vertical light-emitting diodes, and to remove the substrate completely and place the device on a high thermal conductivity heat sink; the latter can increase the lifetimes of GaN LEDs when operated at the high powers needed for general illumination applications. Patterning of silicon is also easier because wet etching processes can be used, unlike sapphire, which requires a dry etch process.

4.3.2 Crystallography

Most of the effort spent on developing the growth of GaN on silicon has been for *c*-axis growth on Si (111) substrates. Gallium nitride has a wurtzite structure with an *a*-axis lattice parameter of 3.189 Å and a *c*-axis lattice parameter of 5.185 Å. Silicon, on the other hand, crystallizes to a cubic diamond structure with a lattice parameter of 5.430 Å. Thus, in order to match the symmetry of the gallium nitride layer with the silicon substrate, most efforts to grow gallium nitride on silicon have been performed on the silicon (111) face. This results in an effective lattice parameter of 3.84 Å, which gives a lattice mismatch of 16.9%. Thus, the critical thickness of the gallium nitride layer on silicon is of the order of a few nanometers. However, this is not all that problematic because a typical sapphire substrate has a lattice mismatch of 16%. Moreover, gallium nitride LEDs are known to work with dislocation densities of the order of 10^{10} per cubic centimeter.

Gallium nitride grows on the silicon (111) surface with the following crystallographic orientation: *GaN*(0001)//*Si*(111), *GaN*[11–20]//*Si*[1–10]. In contrast, for GaN grow on sapphire there is a 30° rotation of the epilayer, yielding a 16% lattice mismatch on sapphire. Thus, the magnitudes of the lattice mismatch between silicon and sapphire are similar; however, the layers end up in tensile strain on silicon and compressive strain on sapphire, which has a huge impact on the necessary interlayer growth schemes. The same issues that are found for *c*-axis-grown gallium nitride on sapphire substrates will also be found in GaN on silicon substrates, such as the quantum-confined Stark effect. More recent attempts (Dadgar *et al.*, 2007) have focused on the nonpolar growth of gallium nitride on the Si (111) face by MOCVD, which has a lattice mismatch of 0.8% and 19% in the in-plane directions for basal plane growth (Reiher *et al.*, 2009). Figure 4.1 shows the relative orientation of heteroepitaxial aluminum nitride on underlying atoms in the silicon layer.

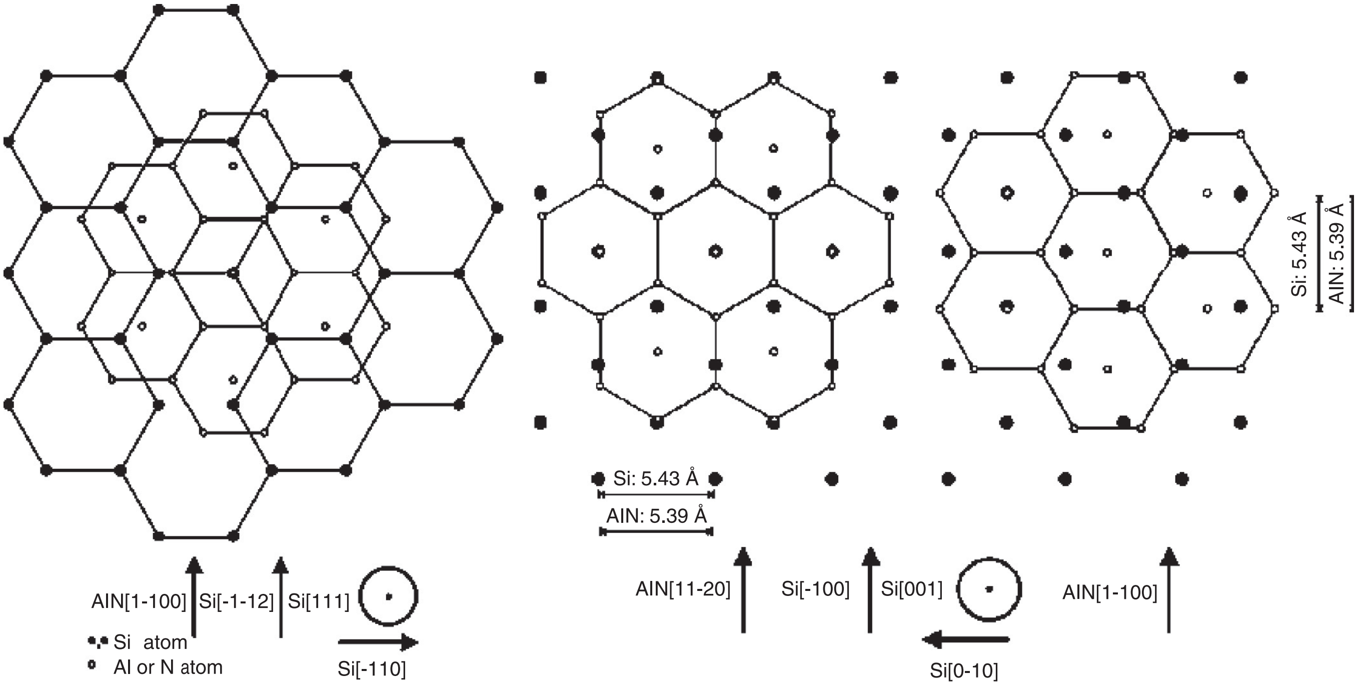
AlN[1-100]
Si[-1-12]
Si[111]
Si[-110]
Si atom
Al or N atom
Si: 5.43 Å
AlN: 5.39 Å
AlN[11-20]
Si[-100]
Si[001]
Si[0-10]
AlN[1-100]
Si: 5.43 Å
AlN: 5.39 Å

4.1 Atomic orientation of AlN on Si (111) and Si (100) substrates (Dadgar *et al.*, 2007).

4.4 Challenges for the growth of GaN on silicon substrates

In addition to the crystallographic concerns, several challenges exist for the growth of gallium nitride on a silicon substrate. First of all, the aggressive growth conditions and particularly the hydrogen atmosphere used for MOCVD growth can cause severe problems at the growth interface because chemical reactions occur at the surface of the silicon substrate. Meltback etching of the substrate can also occur, which results in a significant increase in the surface roughness and difficulty in nucleating layers (Ishikawa *et al.*, 1998). In addition, silicon is a fast diffuser, which results in the formation of impurities in the subsequently grown gallium nitride layers; gas phase diffusion of silicon can also occur.

4.4.1 Thermal expansion mismatch between GaN and silicon

Another severe problem with the growth of GaN materials is the thermal expansion mismatch between GaN and silicon, which can be as high as 54%. The thermal expansion coefficient of gallium nitride is 5.59×10^{-6}/K for gallium nitride in the *a*-axis direction, but only 3.59×10^{-6}/K for silicon. Thus, at normal growth temperatures the GaN and silicon layers may grow appropriately, but as the sample cools the gallium nitride layer contracts significantly more than the silicon layer. This places the gallium nitride layer in tensile strain, which can result in cracking if the tensile stress is high enough. Images of such cracking are shown in Fig. 4.2. In addition, this strain in the growth process can cause bowing of the silicon substrates at the growth temperature; this has a significant impact on sample and device uniformity, particularly for large-area substrates.

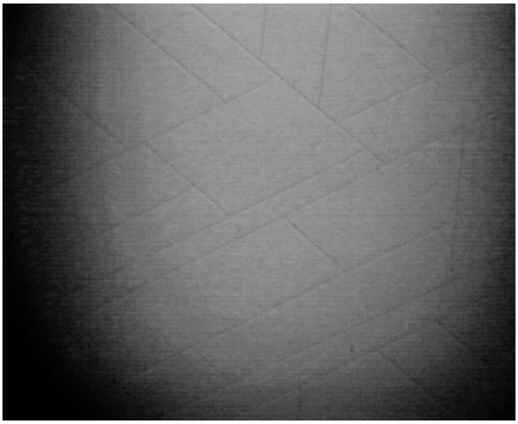

4.2 Optical micrograph of a GaN layer grown directly on a Si (111) substrate showing cracking.

Though a film can be grown at elevated temperatures with relatively low dislocation densities, when the film cools the difference between the thermal expansion coefficients of the film and the substrate causes the gallium nitride layer to be placed in tensile strain. Because gallium nitride is a tough ceramic material, this can often result in severe cracking in the gallium nitride layers, rendering them useless for devices. The difference in lattice parameters can also result in bowing of a wafer, which can have deleterious effects on the uniformity of an as-grown crystal (Krost *et al.*, 2005).

Thus strategies for growing gallium nitride on silicon must not only lower the dislocation densities to allow the growth, they must also take into account the tensile strain that tends to result from the thermal expansion difference. Therefore, the most common strategies involve placing either an aluminum nitride structure or aluminum nitride superlattice within a buffer layer to compensate for this thermal strain upon cooling down. As the lattice constant of aluminum nitride is lower than that of gallium nitride, the will cause the gallium nitride layer to be in compressive strain; if this residual compressive strain can be maintained, then it is possible to grow crack-free layers as discussed in the following pages.

4.4.2 Thermal management

Another problem with the use of traditional substrates is the low thermal conductivity of sapphire. Thus, when light-emitting diodes are produced from layers grown on sapphire, resistive heating causes premature failure. As the need for solid-state illumination and higher-bandgap materials for extreme ultraviolet applications increases, the problem with low thermal conductivity is exacerbated. Several failure mechanisms have been proposed for GaN-based devices when the heat generated in the device is not properly dissipated, ranging from local structural modifications in the material (Meneghesso *et al.*, 2002), to depassivation and reaction of the dopant states in the *p*-type material (Meneghini *et al.*, 2006). In order to control the junction temperature of the active region, several strategies have been applied. One method is to use substrates with a higher thermal conductivity than sapphire, such as diamond (Song *et al.*, 2007; May *et al.*, 2006); this is cost-prohibitive for solid-state lighting applications where cost-competitiveness with traditional lighting applications is essential. Silicon has more than three times the thermal conductivity of sapphire, which would be beneficial for high-brightness diodes.

4.5 Buffer-layer strategies

4.5.1 Zinc oxide (ZnO), aluminum arsenide (AlAs) and other materials

The search for suitable buffer layers has not been limited to just the more traditional AlN-based buffers and superlattice structures. GaN layers on silicon have also been grown with GaAs, AlAs, BP and ZnO buffer layers. The results of these studies and the advantages of each of these buffer layers will be discussed below.

GaAs was used in early studies on the growth of GaN on silicon through a two-step process of molecular beam epitaxy (MBE) growth and nitridation (Nakamura *et al.*, 1998). This allowed for the growth of layers, but it is not economical and limits the growth at high temperatures. In response, Strittmatter *et al.* (1999) attempted to grow AlAs layers using MOCVD in series with the growth process. These AlAs layers were thought to be more thermally stable, conductive and yet still epitaxial to the underlying Si (111) substrate. X-ray diffraction (XRD) scans of these layers showed linewidths of 290 arcsec for the $\theta - z\theta$ scan. Secondary ion mass spectrometry (SIMS) revealed no significant diffusion of either arsenic or silicon into a layer, but there was a pronounced yellow band emission in the photoluminescence (PL), as seen in Fig. 4.3.

Another different buffer layer grown on silicon is ZnO. Park *et al.* (1999) demonstrated that enhanced photoluminescence emission could be observed in GaN films grown on ZnO buffers on Si (0001); however, the films were polycrystalline and not device quality. Films were heavily textured in the (0001) direction.

Boron phosphide (BP) was used as buffer layer by Nishimura *et al.* (2004). This material has a good lattice match with GaN and had been successfully grown on silicon. Moreover, it opens up the possibility for the growth of cubic GaN. They used MOCVD to grow 0.1-μm layers of BP on silicon, prior to the growth of GaN. Scanning electron microscopy (SEM) images of the GaN layer show a smooth interface. The XRD spectra of GaN layers grown on (100) surfaces have cubic

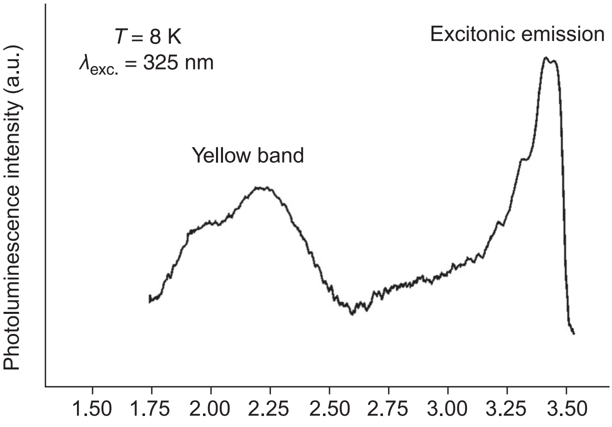

4.3 PL spectra of GaN on an AlAs buffer on silicon (Strittmatter *et al.*, 1999).

diffraction peaks. However, significant amounts of impurities were found in the GaN layer, as evidenced by ultraviolet illumination.

Silicon nitride has also been used as a buffer layer in the growth of GaN films. Liu *et al.* (2000) used *in situ* nitridation of the silicon surface. After cleaning, they thermally etched the silicon passivation layer and used a 5×10^{-4} Torr pressure to nitridate the surface, and followed that with an overgrowth of a GaN buffer layer. X-ray photoelectron spectroscopy (XPS) showed peaks characteristic of silicon and Si_3N_4. More importantly, yellow luminescence was suppressed in the photoluminescence spectrum. Huang *et al.* (2002) also used a similar pre-nitridation process to grow GaN on silicon. They observed a similar reduction in the yellow luminescence in the PL spectrum, and attributed this to a reduction in the substitutional oxygen and silicon impurities in the substrate. Limiting the diffusion of gas phase silicon through passivation of the silicon surface can also be an important method for limiting diffusion. This is another novel buffer-layer scheme.

4.5.2 Aluminum nitride (AlN) buffer layer

As other growth buffer layers are unsuitable for long-term integration into large-area GaN LEDs, the focus for the buffer layers quickly shifted to AlN. Due to a significant amount of lattice mismatch (17%) between *c*-plane GaN and Si (111), a buffer layer has to be applied to reduce the strain on the epitaxial GaN layer. Although SiC has the best match in terms of lattice constant, SiC is expensive; hence, a comparatively cheaper buffer layer has been sought for a long time. Watanabe *et al.* (1993) first proposed that a thin AlN buffer layer could be grown over the silicon before GaN deposition, after Takeuchi *et al.* (1991) suggested using SiC as a buffer-layer material. They used metal-organic vapor phase epitaxy (MOVPE) as the growth process under atmospheric pressure.

As a buffer layer, AlN has several advantages: (i) it possesses a similar wurtzite structure as the GaN crystal structure, (ii) when the AlN buffer layer is grown on Si (111), the tensile strain between GaN and silicon is converted to compressive strain and (iii) AlN prevents the direct contact of Ga atoms with the silicon atoms, as this causes an SiN layer to grow on top of the silicon substrate as a result of nitridation. There have been reports of growing high-temperature AlN (HT-AlN) and low-temperature AlN (LT-AlN), both of which have their own advantages. For example, when AlN is grown on Si (111), the AlN layer suffers from tensile strain from the silicon layer. This can be reduced through decreasing the AlN growth temperature (Blasing *et al.*, 2002), which results in GaN growth on LT-AlN under compressive interlayer-induced strain. On the other hand, better crystalline quality of the grown GaN layers is observed when HT-AlN is used as the buffer layer (Gong *et al.*, 2003) (Fig. 4.4).

Thus it appears from the research that LT-AlN helps to prevent cracking of the epitaxial GaN layer, while a HT-AlN buffer layer results in better crystalline

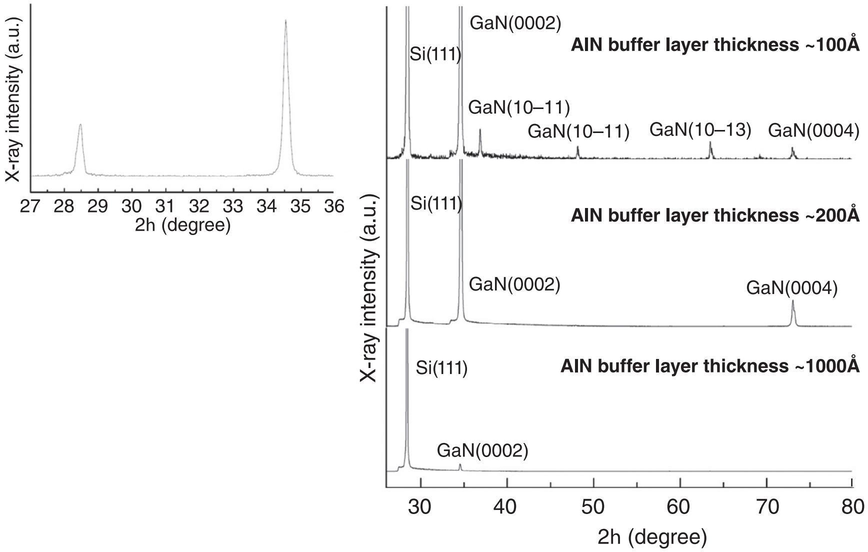

4.4 Θ-to-2Θ XRD patterns for (top left) a HT-GaN film grown on an LT-AlN coated Si (111) and (right) HT-GaN films grown on HT-AlN coated Si (111) with AlN buffer layer thickness of 100 Å, 200 Å and 1000 Å (Gong *et al.*, 2003).

quality of the GaN epilayer. Arslan *et al.* (2008) used the advantages of both these techniques, with LT-AlN sandwiched between two HT-AlN layers, followed by a graded $Al_xGa_{1-x}N$ layer before the desired GaN epilayer was deposited. This graded $Al_xGa_{1-x}N$ layer was introduced to further reduce cracking in the GaN layer, which occurred even though the AlN stack was thicker than 400 nm. The $Al_xGa_{1-x}N$ composition was reduced from $x=0.64$ to 0.22 (in seven steps) to match well with the GaN layer on top.

4.5.3 Superlattice structures

A superlattice (SL) is a structure where two different materials are grown to a specific thickness in alternating layers. In addition to LT-AlN and HT-AlN buffer layers, superlattice structures are also very popular among researchers for engineering the strain in the GaN epilayer. In addition, a superlattice helps to reduce the dislocation glide significantly. A very common approach for growing a GaN epilayer that is smoother and free of strain-induced defects is to grow a GaN/AlN superlattice right on top of the AlN buffer layer and then grow the GaN epilayer on top of the superlattice (Kim *et al.*, 2007). The researchers used ten to 20 periods of SL before the MOCVD growth of GaN (300 nm) on AlN nucleated silicon, keeping the other growth conditions constant. From Raman spectral analysis of the GaN films grown on different numbers of SL pairs (Fig. 4.5, top), it was concluded that the GaN epilayer with a 15-pair GaN/AlN SL had significantly reduced in-plane stress in comparison to the ten and 20-pair SLs. In addition, a high-resolution x-ray diffraction (HRXRD) scan (Fig. 4.5, bottom) showed that crystal quality is better for the 15-pair SL structure as the full width at half maximum (FWHM) of the 15-pair SL structure was the lowest among the tested samples. Optical microscope images did not show any cracks in the

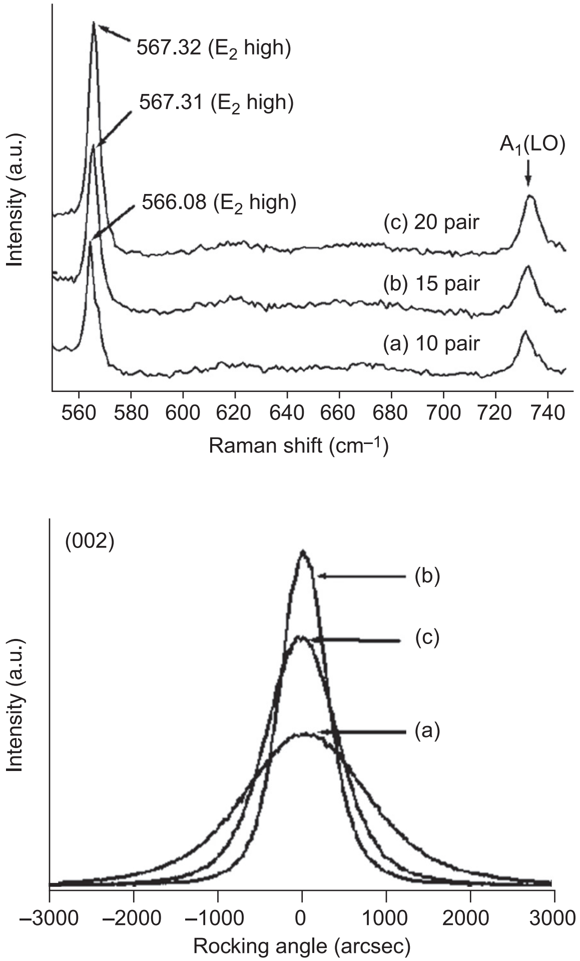

4.5 Top: Raman spectra for GaN epilayers grown on Si (111) substrates with (a) 10-pair, (b) 15-pair and (c) 20-pair GaN/AlN SLs. Bottom: HRXRD rocking curves of GaN epilayers grown on Si (111) substrates with (a) 10-pair, (b) 15-pair and (c) 20-pair GaN/AlN SLs (Kim *et al.*, 2007).

structures with ten to 15-pair SLs, while cracks were clearly visible in a 20-pair SL structure. Ma *et al.* (2012) fabricated an improved GaN-based LED on Si (111) using AlN/GaN SLs and compared its performance with LT-AlN band and MT-AlN interlayer based devices. In terms of dislocation density reduction, PL intensity, output power and crystalline quality of the active region, the LED devices fabricated using AlN/GaN SLs showed much better performance than the other two technologies.

Dadgar *et al.* (2001c) used a superlattice structure of AlN/AlGaN and achieved a ten times lower dislocation density than a 'traditional' GaN on silicon sample. They used a 15-fold SL structure of 0.9 μm thickness. Lin *et al.* (2007) used a multilayer buffer of AlN (HT-AlN/LT-AlN/HT-AlN) on Si (111), growing the GaN on top of it to reduce crack formation on the edges of a 150 mm silicon wafer. The LT-AlN layer (grown at 800 °C) helped to reduce the propagation of dislocations from the first HT-AlN layer (grown at 1050 °C); it was also used to reduce the formation of Si_xN_y. The third layer (HT-AlN at 1050 °C) helped in growing a more relaxed AlN layer on top. Later Saengkaew *et al.* (2009) adopted a similar HT-AlN/LT-AlN method to grow $Al_xGa_{1-x}N$ layers for ultraviolet lighting applications. Another SL approach was followed by Xi *et al.* (2007), who grew AlGaN using an $Al_xGa_{1-x}N/Al_yGa_{1-y}N$ SL structure and compared it to AlGaN with an LT-AlN interlayer. Their atomic force microscopy (AFM) scans showed that samples grown with a $Al_xGa_{1-x}N/Al_yGa_{1-y}N$ SL had a lower root mean square (RMS) roughness (0.4 nm) than the samples grown with an LT-AlN interlayer (0.5 nm) (Fig. 4.6). The AFM scans also revealed the reduced dislocation density in the $Al_xGa_{1-x}N/Al_yGa_{1-y}N$ SL structure samples; these samples also had better electron mobility.

4.5.4 Atomic layer deposition (ALD) of Al_2O_3

A novel approach for GaN growth on large-area silicon has been to grow a thin Al_2O_3 barrier layer by MOCVD to help alleviate the strain mismatch and chemical diffusivity issue of the silicon. Atomic layer deposition gives precise control of the thickness of layers through self-limiting surface reactions. Although the growth rates are slow due to the atomically controlled layer-by-layer growth, it has been used in industrial processes where precise atomic-level thickness control is needed. A schematic of the ALD process is shown in Fig. 4.7. Self-limiting surface reactions allow for the control of the aluminum oxide layers through sequential pulses of trimethylaluminum and water, at a temperature below the pyrolytic temperature of trimethylaluminum.

Fenwick *et al.* (2009) performed the initial studies of ALD-grown interlayers. They systematically investigated the growth and annealing process for the as-grown layers. Following substrate cleaning, ALD layers from 5 nm to 100 nm were grown and subsequently annealed at temperatures ranging from 1000 °C to 1300 °C in either an air or nitrogen atmosphere. Amorphous alumina layers

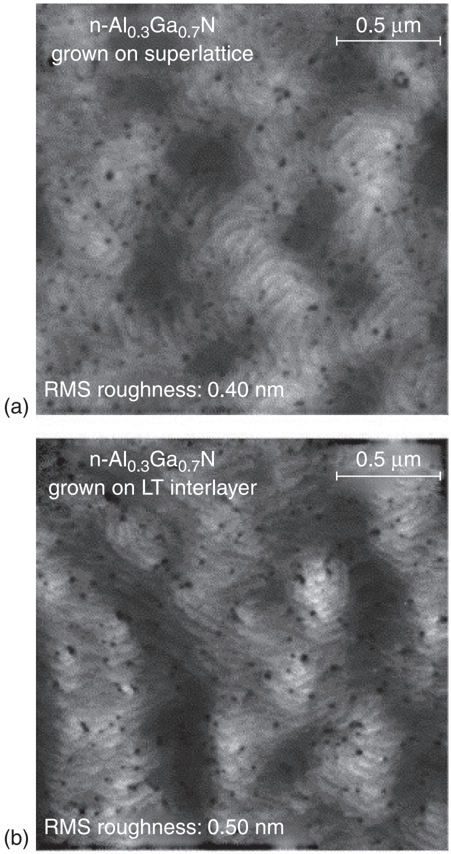
n-$Al_{0.3}Ga_{0.7}N$
grown on superlattice
0.5 μm
RMS roughness: 0.40 nm
(a)
n-$Al_{0.3}Ga_{0.7}N$
grown on LT interlayer
0.5 μm
RMS roughness: 0.50 nm
(b)

4.6 AFM images of samples: (a) grown on an AlGaN(AlN)/AlGaN SL, showing lower dislocation density; (b) grown on an LT AlN interlayer, showing the higher dislocation density (Xi *et al.*, 2007).

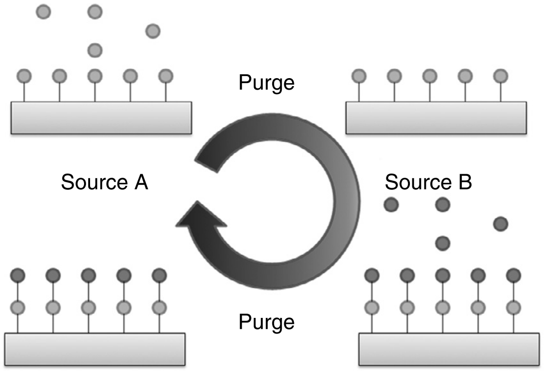
Purge
Source A
Source B
Purge

4.7 Series of reactant and purge pulses used for single layer control in atomic layer deposition.

were observed on the surface upon growth, which then crystallized during annealing. The layers became mirror-like upon annealing, but the thicker layers had surface pits, as shown in Fig. 4.8. Following the optimization of the growth process, GaN layers were grown on the thinner layers using either a high-temperature AlN layer (Fig 4.8) or a low-temperature GaN buffer layer. Layers grown with the LT-GaN layer were found to have relatively large linewidths (14 720 arcsec for the GaN (0002) reflection), while the linewidths of the HT-AL were around 4000 arcsec. Further optimization of the process resulted in

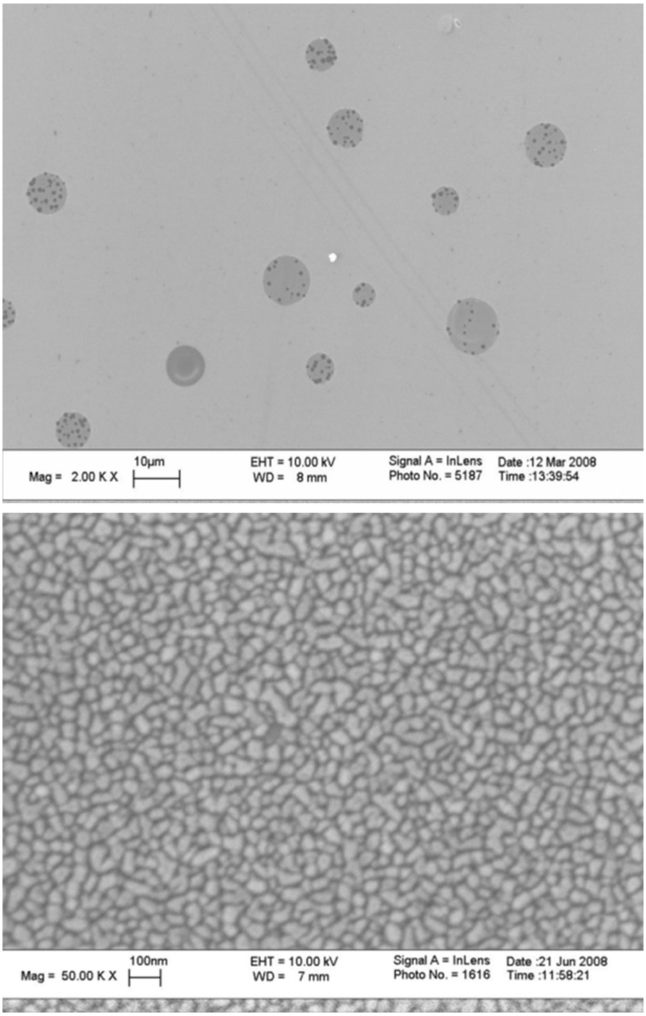
10µm
Mag = 2.00 K X
EHT = 10.00 kV
WD = 8 mm
Signal A = InLens
Photo No. = 5187
Date :12 Mar 2008
Time :13:39:54
100nm
Mag = 50.00 K X
EHT = 10.00 kV
WD = 7 mm
Signal A = InLens
Photo No. = 1616
Date :21 Jun 2008
Time :11:58:21

4.8 (Top) Surface pits in GaN grown on 100 nm ALD Al_2O_3. (Bottom) SEM image of HT-AlN interlayer on ALD Al_2O_3 (Fenwick *et al.*, 2009).

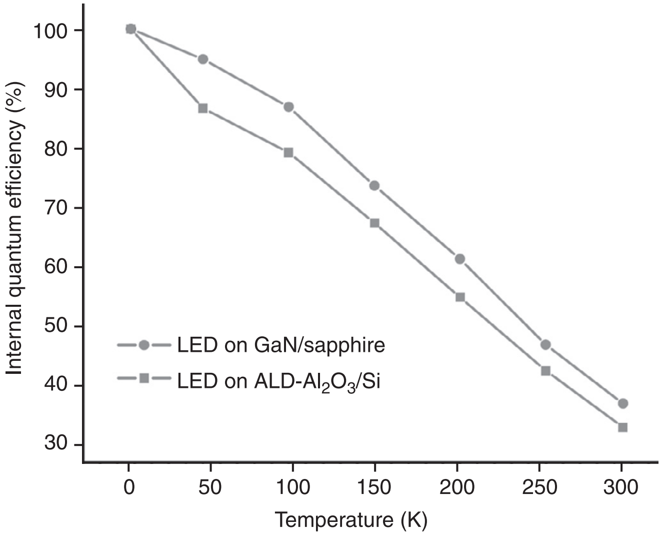

4.9 IQE data for LEDs grown on sapphire and ALD-coated silicon substrates (Jamil *et al.*, 2010).

improvements to the XRD (002) and (102) GaN reflections to 380 arcsec and 740 arcsec, respectively.

Jamil *et al.* (2010) further improved the growth of these layers and implemented them into LEDs. Using the same atomic layer deposition on silicon described above, they grew free-standing GaN LEDs and removed the substrate. Figure 4.9 shows a plot of the internal quantum efficiency (IQE) of gallium nitride LEDs on sapphire and ALD substrates. Figure 4.10 shows electroluminescence (EL) spectra of these two substrates; similarities can be observed and there are Fabry–Pérot oscillations for the ALD substrate. This work is promising for the future growth on large-area substrates.

4.6 Device technologies

4.6.1 Early device efforts

The previous sections discussed the advantages of silicon, the challenges involved in attaining the objectives and the buffer-layer approaches used to resolve the issues. This section will focus on the LED technologies that have influenced the research arena the most in the last 15 years. Sapphire and SiC continue to be the most dominant substrate materials in LED chip fabrication. In 1998, Guha and Bojarczuk (1998a, 1998b) produced double heterostructure LEDs grown using MBE on Si (111) substrates with an AlN nucleation layer and AlGaN buffer layers. Their samples had high threading ($\sim 5 \times 10^9$ cm^{-2}) and planar defects

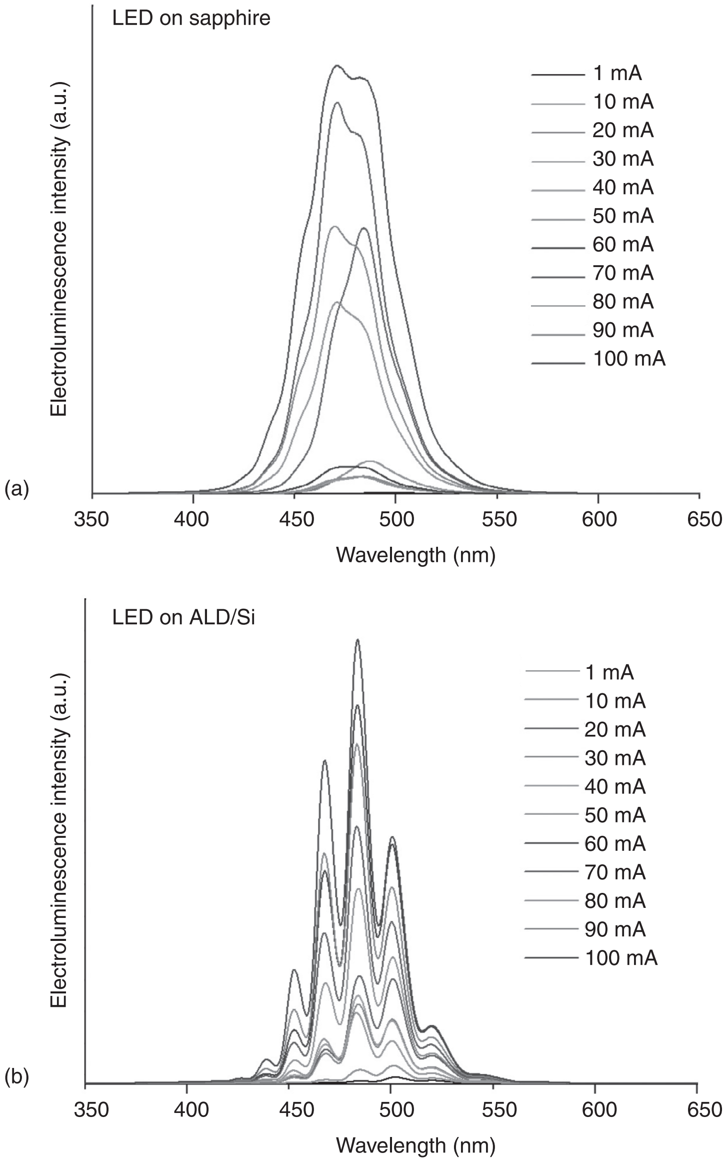

4.10 EL spectra for LEDs grown (a) on sapphire and (b) on Si/ALD-Al_2O_3 (Jamil *et al.*, 2010).

(towards the 0001 growth direction). They also demonstrated that *p*-type doping is possible for AlGaN/GaN quantum well (QW) devices on silicon.

Later Zhang *et al.* (2001) and Dadgar *et al.* (2001c) fabricated blue LED chips on Si (111) using MOCVD, but these samples made during the late 1990s produced poor brightness compared to those made on sapphire or SiC substrates. Zhang *et al.* used an AlGaN/AlN buffer layer with InGaN/GaN QWs as the active region. They were influenced by Guha and Bojarczuk (1998a, 1998b) to use an AlGaN/AlN buffer layer to reduce the strain-induced cracks from the thermal mismatch. Dadgar *et al.* (2001a), on the other hand, used a patterned Si (111) substrate (with a Si_xN_y mask). Both these device technologies yielded LEDs with microwatt output, which was very low compared to the more mature sapphire and SiC substrate devices and was not suitable for general illumination applications. The use of superlattice structures also became popular (Tran *et al.*, 1999; Dadgar *et al.*, 1999; Egawa *et al.*, 2005) to reduce the strain-induced cracks in the epilayers grown on a bare nucleation layer. The devices with a superlattice had improved cracking and hence luminescence similar to LEDs on sapphire, but the output efficiency was very low as they required 150 A/cm^2 input current for an output of 400 μW (Fig. 4.11). Although the efficiency was not very impressive, the devices maintained a stable performance during aging tests.

4.6.2 Progress in large-area substrates

It is useful to grow LEDs on large-area silicon substrates, i.e., of size 150 mm, 200 mm or 300 mm, as these are the standard sizes employed in the current silicon device industry, and using these sizes obviously reduces costs.

As demonstrated by CamGaN Ltd, a University of Cambridge spin-off, the cost of high brightness GaN LEDs can be reduced by 80% if 150-mm silicon wafers are used as substrates (Zhu *et al.*, 2012). The cost of a 6″ Si (111) wafer is around USD 25, while a 6″ sapphire wafer costs at least USD 650. In addition, a 6″ wafer has 40% more usable area compared to a 2″ wafer, and the wafer processing cost for a 6″ wafer is very close to that of a 2″ wafer but it can be used to make ten times as many LED chips. Li *et al.* (2006) showed that the growth of an AlN/Si template followed by a thin graded AlGaN (~50 nm) layer ultimately facilitates the growth of an LED on a large-area silicon wafer. The AlGaN layer helps to reduce cracking and bowing of the wafer due to the thermal mismatch. A 2-μm *n*-doped GaN layer was grown on top of an AlGaN layer, followed by eight periods of an InGaN/GaN multiple quantum well (MQW), with a magnesium-doped *p*-type GaN layer on top. Characterization of the LEDs (Li *et al.*, 2006) showed a forward bias of 4.1 V with a reverse leakage current of 20 μA (at −20 V). Figure 4.12 shows the *I-V* and *L-I* characteristics of the devices along with the EL spectrum of the blue LEDs grown on a 6″ silicon wafer. The devices (Li *et al.*,

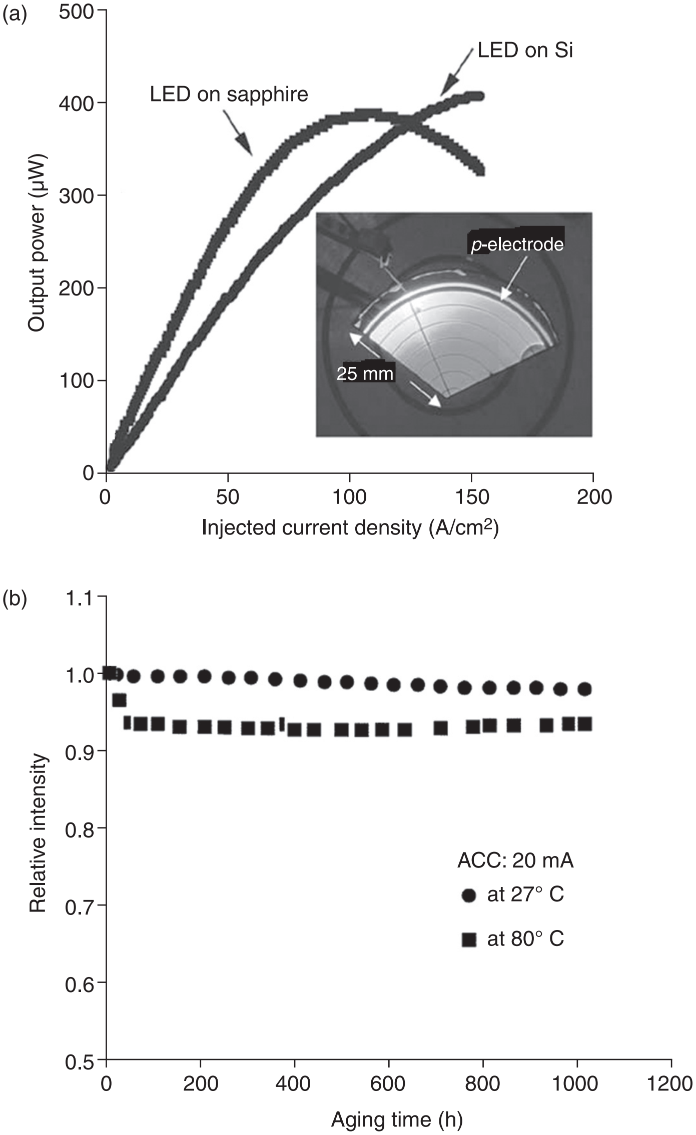

4.11 (a) Comparison of *L-I* characteristics of blue LEDs on sapphire and silicon substrates; (b) variation of relative intensity with aging time (Egawa *et al.*, 2005).

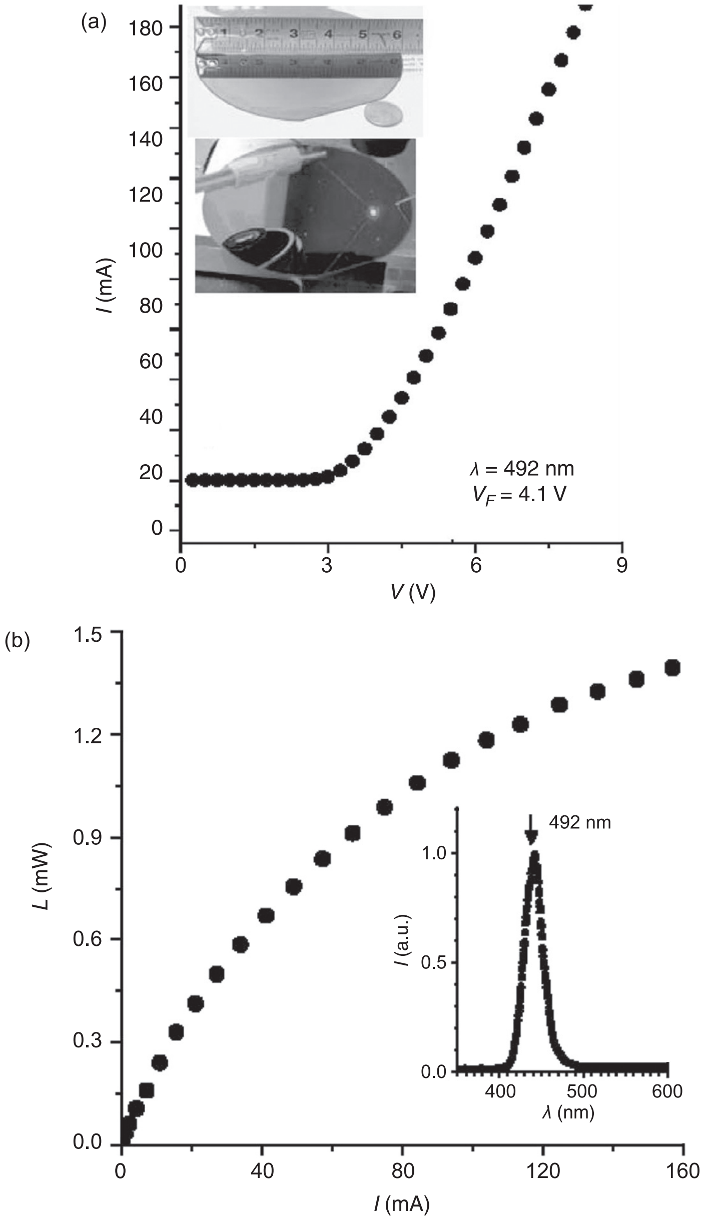

4.12 (a) *I-V* and (b) *L-I* curves for an InGaN/GaN MQW blue LED. Inset: (a) Optical microscope image of the LED. Inset: (b) EL spectrum showing the dominant emission at λ=492 nm (Li *et al.*, 2006).

2006) had an output power in the milliwatt range with input current injection in the milliampere region, which is a significant improvement compared to devices produced by Egawa *et al.* (2005).

Tripathy *et al.* (2007) used nanoscale silicon-on-insulator (SOI) substrates for InGaN/GaN blue LEDs. The SOI technique is useful for growing LEDs that can be easily lifted off through sacrificial etching of the SiO_2 and the silicon overlayer. Also, a very thin SOI helps to produce more blue-green light (which is absorbed in the silicon substrate of a vertical LED). SOI (111) substrates were prepared using the SIMOX (separation by implantation of oxygen) process. The rest of the LED structure is the same as that produced by Li *et al.* (2006). SOI substrates prepared using SIMOX appear to have a highly reflective mirror-like surface beneath the AlN buffer layer, due to the high contrast of the refractive indices in the interface. This results in multiple interference peaks, yielding an increase in the aggregated EL intensity compared to LEDs grown on an Si (111) substrate (Plate I, see colour section between pages 330 and 331). This shows that the energetic maxima of the EL interference peaks of LEDs on a SOI (111) are significantly stronger than those on Si (111).

Zhu *et al.* (2011) inserted (without an Si_xN_y layer) a 100-pair *n*-AlN/GaN (5/20 nm) strained layer superlattice (SLS) on top of the buffer layer, before the *n*-GaN epilayer. They increased the *n*-GaN epilayer thickness, while keeping the other layers the same; this boosts the external quantum efficiency (EQE) and light output power of the LEDs, as shown in Fig. 4.13. In addition, the increase in the *n*-GaN epilayer thickness results in an improved crystalline quality of the GaN layer, as shown in the HRXRD scan of the two samples. The EQE of the thicker GaN layer (2 μm) LED appeared to be almost double that of the LED with the 1-μm GaN epilayer, and had a higher input current value – 325 mA, compared to 200 mA for the thinner GaN layer.

A big improvement in the IQE of LEDs occurs with the insertion of an Si_xN_y layer on top of the buffer layer. Initially, the growth of GaN on Si (111) suffered from bowing and hence crack-generation due to the large thermal expansion coefficient mismatch (46%) between GaN and Si (111). Phillips and Zhu (2009) and Zhu *et al.* (2010) reported that Si (111) itself has a slight convex bow, which switches to a concave bow after heating and *in situ* annealing (due to the positive temperature gradient between the top and bottom of the wafer).

Although deposition of an AlN nucleation layer increases concave bowing, there is convex bowing after the growth of the buffer layers and the *n*-GaN epilayer, increasing the compressive stress. After the growth of the MQWs, barrier layers and ultimately the *p*-GaN layer on top, there is still significant convex bowing. It was found that with temperature optimization in the growth chamber, bowing can be controlled to yield a flat wafer.

The LEDs grown had higher dislocation densities, but Zhu *et al.* (2010) deposited a SiN_x layer on of top of the AlGaN/AlN buffer layer before the GaN epilayers were grown onto it. This layer helped the GaN epilayer to bend over the generated defects and annihilate them, and thus reduced the threading dislocation

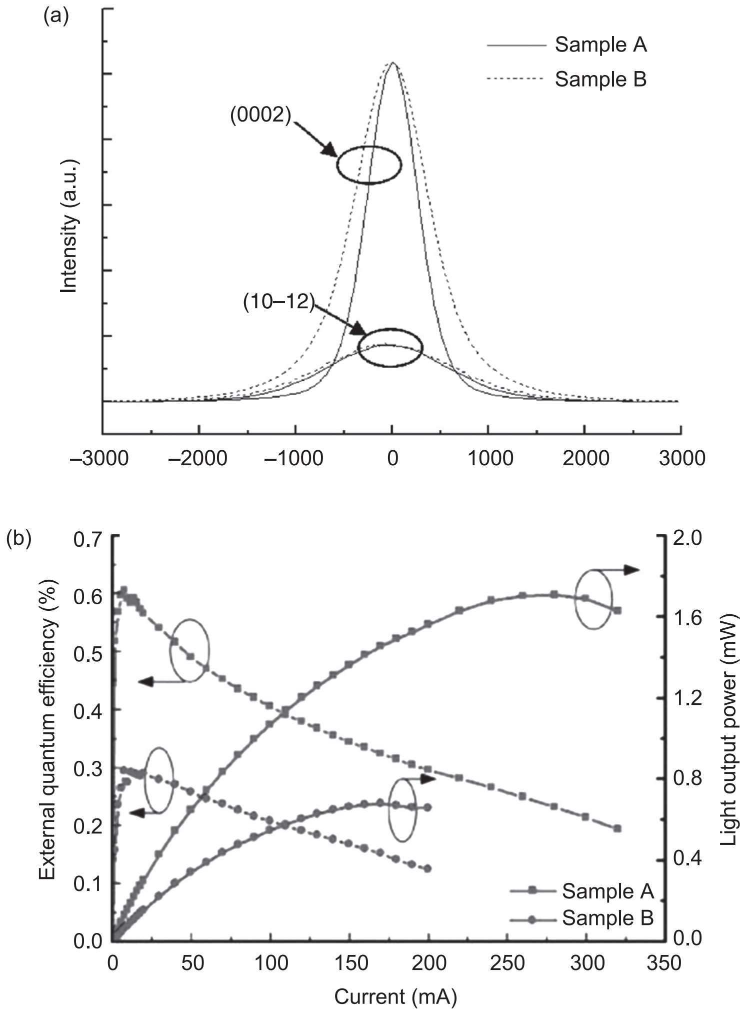

4.13 (a) HRXRD rocking curves for GaN (0002) and (10–12) ω-scans of samples A (n-GaN thickness 2 μm) and B (n-GaN thickness 1 μm), (b) EQE and light output power of the samples (Zhu *et al.*, 2011).

density. Figure 4.14 is a transmission electron microscope (TEM) image of a GaN/SiN_x/AlGaN/AlN/Si structure. It was demonstrated that the bending of the dislocations at the interfaces was due to the compressive stress caused by the larger in-plane *a* lattice parameter of GaN compared with AlN. It was also suggested that the AlGaN buffer layers filter the crystal disorientation arising from the AlN nucleation layer, thus improving the crystal quality of the GaN layer grown on top. Zhu *et al.* (2012) produced GaN LEDs on large-area Si (111)

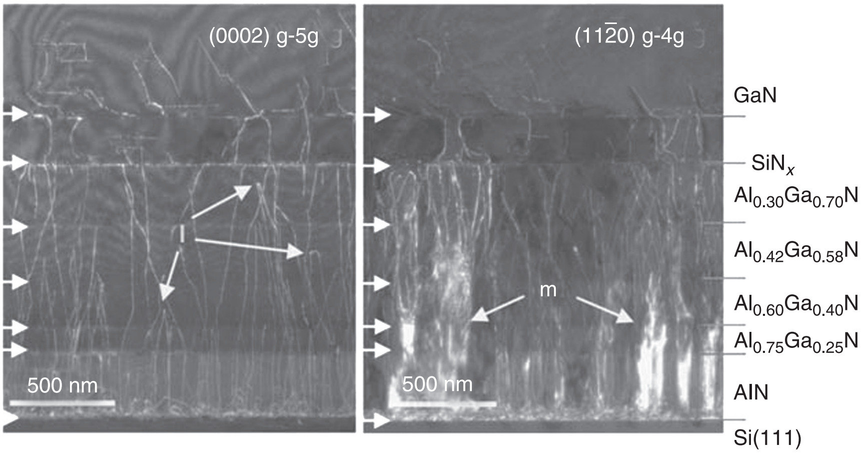

4.14 Weak-beam dark-field TEM images of GaN/SiN$_x$/AlGaN/AlN/Si structures. The position of each interface is indicated by a horizontal arrow. Pure screw/mixed type dislocations are visible in the TEM image to the left, with loops labeled with 'l', while pure edge/mixed type dislocations and disorientated grains ('m') are visible in the TEM image to the right (Zhu *et al.*, 2010).

substrates. They reported 58% IQE (at the blue 460 nm wavelength) for the MQW GaN LEDs on a 6″ Si (111) wafer (a similar design as Zhu *et al.*, 2010), and this is the highest reported IQE so far. In terms of dislocation densities, very high numbers of threading dislocations (TDs) have been reported ($8–9 \times 10^8/\mathrm{cm}^2$); this is strong enough to limit the IQE, in comparison to that for GaN LEDs grown on sapphire (IQE = 70%). Their observation of the TDs using AFM and the PL spectra are shown in Fig. 4.15.

Thus, temperature optimization during the MOCVD growth of epilayers and the insertion of Si_xN_y as a TD blocking layer facilitate the growth of GaN LEDs on large-area silicon wafers. Zhu *et al.* (2010, 2012) produced *n*-GaN layers of thickness 1–1.5 μm. Zhu *et al.* (2011) showed that there should be improvements through increasing the thickness of the layer. The opposite of what was reported by Zhu *et al.* (2011) applies, as the use of Si_xN_y is strongly capable of reducing the TDs in devices and hence helping to increase the EQE to attain a value than that reported.

4.6.3 Layer transfer

Layer transfer, which is commonly achieved using the laser lift-off process, has been used extensively recently in the industrial production of light-emitting diodes. The method is used in transferring a prefabricated device from the growth substrate onto a new host substrate for final active device processing. This

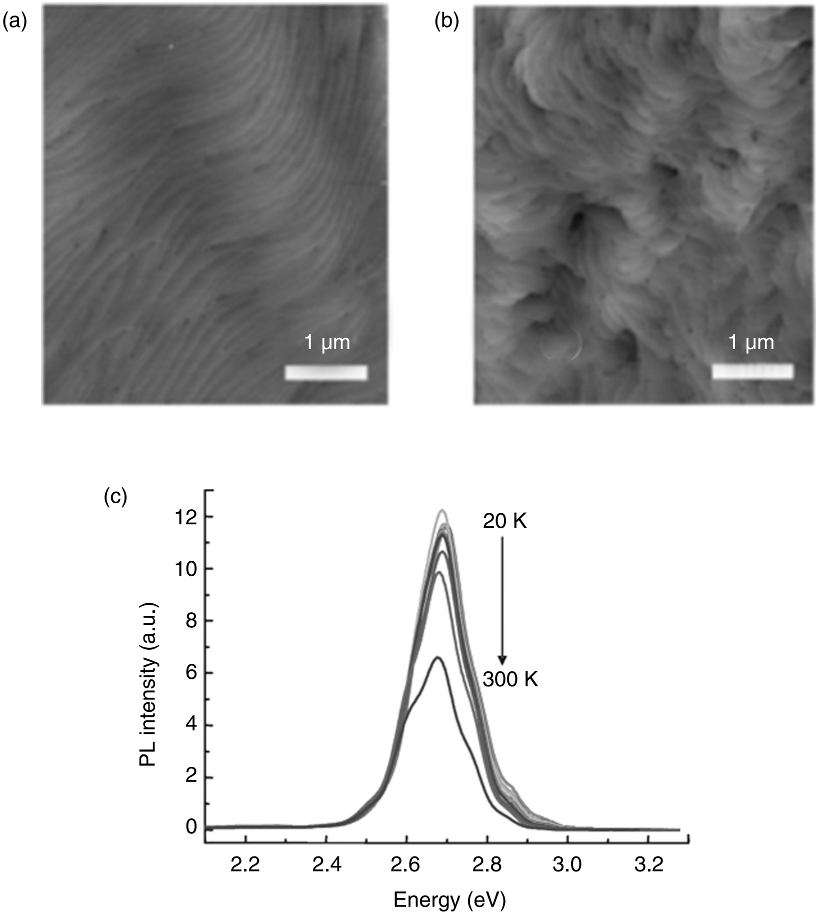

4.15 Large-area AFM images of GaN films on Si (111): (a) with an Si_xN_y interlayer, (b) without an Si_xN_y interlayer. (c) Temperature-dependent PL of a 460 nm MQW structure (Zhu *et al.*, 2012).

ultimately integrates the better quality material to create a monolithically optimized system. In the laser lift-off process, high energy (more than the bandgap of GaN) excimer laser (KrF) light is applied to the back of the substrate wafer; the laser is focused on the seed layer beneath the GaN epilayer. This evaporates nitrogen from the back of the epilayer; a thin layer of liquid gallium remains on the epilayer, which is cleaned by a wet chemical etching process. The sapphire substrate is removed following post-growth treatment using an excimer laser.

Once the growth layer has been removed, it can be rebonded to another material with a higher thermal conductivity, which acts as a heat sink and lowers the junction temperature of the device under bias. This is a relatively specialized process and requires an additional treatment step with high-power lasers. Moreover, this process results in significant local heating of the sample at the places where the laser ablation removes the substrate; this damage can be detrimental to the performance of certain devices. The lift-off process has also been used to improve the efficiency of III-nitride-based laser diodes (Wong *et al.*, 2001).

Ideally, there should be a process that can remove a substrate without the post-processing laser lift-off step. Wet chemistry is commonly used to form a release layer for III-V (van Niftrik *et al.*, 2008; Kyono *et al.*, 1994), II-VI (Chou *et al.*, 1996) and IV-VI (Li *et al.*, 2005) electronic devices. For GaN on silicon, a strong etchant like $HNO_3 + HF + CH_3COOH + H_2O$ is used for etching Si (111) in a chemical lift-off process. However, it is hard to control the etchant without affecting the GaN epilayer.

Although silicon is considered to be a very economical substrate for vertically grown GaN LEDs, the large lattice and thermal expansion coefficient mismatches do not support good GaN crystal growth on silicon. This can be resolved using an AlN buffer layer on Si (111) prior to GaN growth, as mentioned in Section 4.5.2. However, the large band offset between the AlN buffer layer and the Si (111) substrate obstructs the current-voltage characteristics of vertically conducting LEDs (Guha and Bojarczuk, 1998a; Ishikawa *et al.*, 2003). In addition, Si (111) substrates absorb vertically emitted visible light. To eliminate these two drawbacks, Zhang *et al.* (2005) devised an approach to transfer vertically grown InGaN multiple QW LEDs, using a selective chemical lift-off process, onto a copper carrier. This selective lift-off (SLO) approach helps to reduce the probability of crack generation from strain relaxation, which originates with the complete etching of a silicon substrate using conventional wet etching. In SLO, the InGaN MQW LED structure grown on silicon is bonded onto a copper carrier via metal-to-metal bonding. Then, the SLO process is used to remove the silicon substrate. The complete process is shown in Fig. 4.16.

Prior to SLO, first the *p*-type ohmic contacts are formed on the epilayer surface using a 10 nm thick nickel layer and annealed at 600 °C for 3 minutes in ambient air. Next, a highly reflective Al/Au layer is deposited onto the annealed nickel surface. The InGaN LED epiwafer is then bonded onto a gold-coated copper carrier at 200 °C using indium as the adhesive. Then the silicon substrate is mechanically polished down to 60 μm. Next, the silicon substrate is selectively removed using a HNA solution ($HF{:}HNO_3{:}CH_3COOH = 1{:}1{:}1$) and polyimide as the mask. Finally, the exposed region of the buffer layers is subjected to reactive ion etching (RIE) and Ti/Au contacts are deposited to complete the fabrication of the LED. The reported device performance is shown in Fig. 4.17.

A double flip process was demonstrated by Wong *et al.* (2010) and Lau *et al.* (2011): the first flip was used to bond the LEDs on silicon to a temporary substrate, followed by a second flip where the devices were removed from the silicon and transferred to a copper substrate by electroplating. This results in LEDs where the

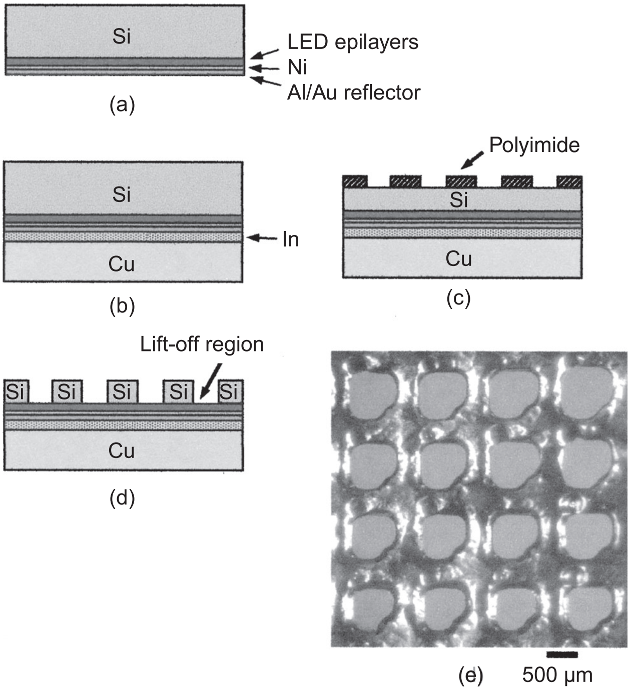

4.16 Selective lift-off process flow: (a) A *p*-type ohmic contact is formed and a high-reflectivity metal reflector (Al/Au) is deposited onto the epitaxial surface of the LED epiwafer. (b) The metal/InGaN MQW LED/silicon is bonded onto a copper carrier. (c) The silicon substrate is thinned by mechanical polishing. (d) The silicon substrate is selectively removed by wet-chemical etching. (e) An image of the device after the SLO process (Zhang *et al.*, 2005).

p-side layer is on top, maintaining the as-grown order of the epilayers. In this process, after an LED is grown onto a silicon substrate, the entire front device surface is spin-coated with a polyimide layer and baked up to 180 °C for 4 hours. This protects the LEDs during wet etching of the silicon. Next, the device side of the wafer is bonded temporarily to a sapphire wafer using wax. The bonded structure is then put into a HNA solution ($HF:HNO_3:CH_3COOH = 1:2:3$) for 40 minutes, which completely removes the silicon substrate. Following etching, Ti (5 nm)/Al (100 nm)/Ti (10 nm)/Au (100 nm) are deposited onto the backside of the LEDs using e-beam evaporation. Of these metal layers, aluminum serves as a reflective mirror and gold acts as a seed layer for the subsequent copper electroplating. The second flip now takes place where the LED is flipped from the temporary sapphire wafer to a copper substrate. An 80 μm thick copper layer is electrodeposited as the new substrate for the LEDs. Then the temporary sapphire layer is debonded from the LEDs on a hot plate, and the wax is removed using

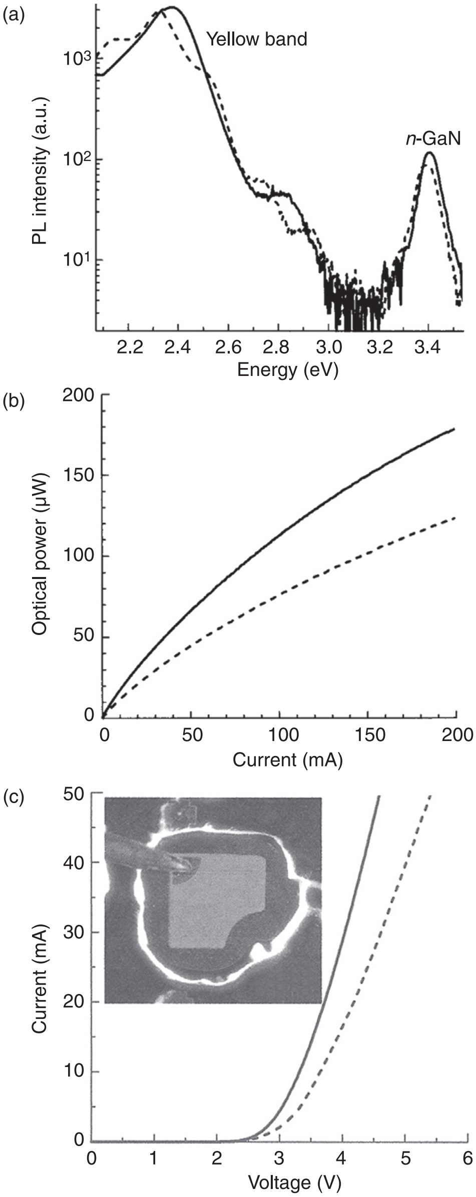

4.17 (a) *n*-GaN PL spectra at room temperature, (b) *L-I* characteristics and (c) *I-V* characteristics of the LED before (dashed lines) and after (solid lines) substrate removal. The inset in (c) shows an emission image of the LED fabricated on the substrate removal region. The image was taken at 0.5 mA under room light and microscope light conditions. The emission wavelength is about 518 nm (Zhang *et al.*, 2005).

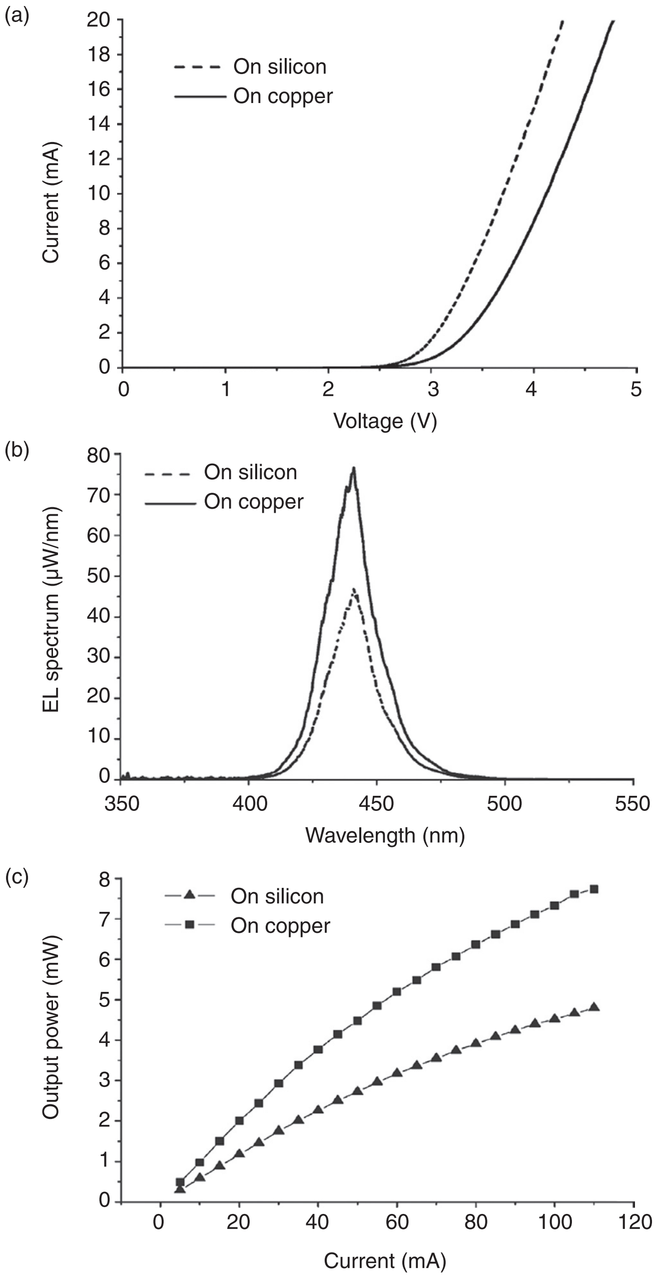

4.18 (a) *I-V* characteristics, (b) EL spectra at 20 mA and (c) *L-I* characteristics of LEDs on silicon and a copper wafer (Wong *et al.*, 2010).

trichloroethylene (TCE) cleaning. The polyimide is removed using an organic resist stripper at 70 °C. Figure 4.18 shows the improvement of devices transferred onto copper after being grown on silicon (Wong *et al.*, 2010). It can be concluded that this layer transfer approach is very helpful for fabricating high-power LEDs, for large-area LED arrays subject to repeated high thermal operation cycles, for the hybrid integration of GaN devices on silicon and for flip-chip bonding of LEDs.

4.6.4 GaN LEDs on patterned silicon substrates

Patterned silicon substrates were first used by Kawaguchi *et al.* (1998) to grow a few micron-sized GaN dots. However, Yang *et al.* (2000) were the first to use this idea to fabricate LEDs on silicon, although their devices had cracks. Dadgar *et al.* (2001a, 2001b, 2003) and Strittmatter *et al.* (2001) produced GaN LEDs on silicon without cracks using silicon substrate patterning. SEM images of the sample are shown in Fig. 4.19.

In this research, an AlGaN/GaN buffer layer was used to reduce the tensile strain. However, all the LEDs mentioned here have poor brightness compared to conventional sapphire substrate devices. Zhang *et al.* (2007) produced patterned silicon substrate LEDs where they used a HT-AlN nucleation layer as a dislocation filter, especially for edge and mixed dislocations (Fig. 4.20). The device output was significantly lower (0.7 mW at 20 mA) compared to that of sapphire substrate devices (2.2 mW at 20 mA) at that time. In later research, Lau *et al.* (2011) grew the same device on patterned silicon, transferred it onto copper and showed that the PL intensity and the output light power were significantly higher.

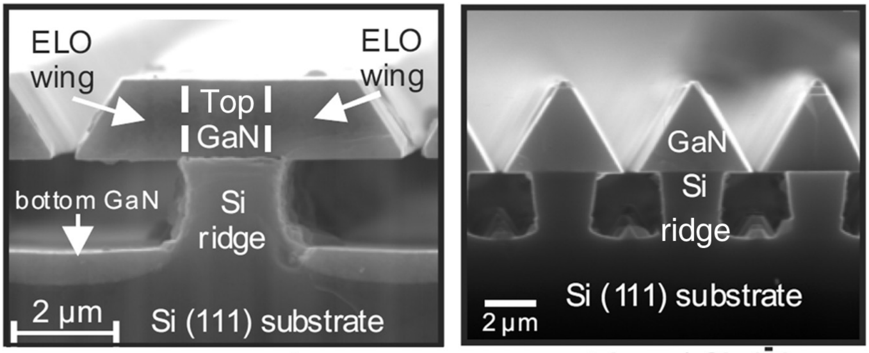

stripes || Si<1$\bar{1}$0> **stripes ⊥ Si<1$\bar{1}$0>**

4.19 SEM cross sections of GaN grown on a structured Si (111) substrate with different stripe orientations (Dadgar *et al.*, 2003).

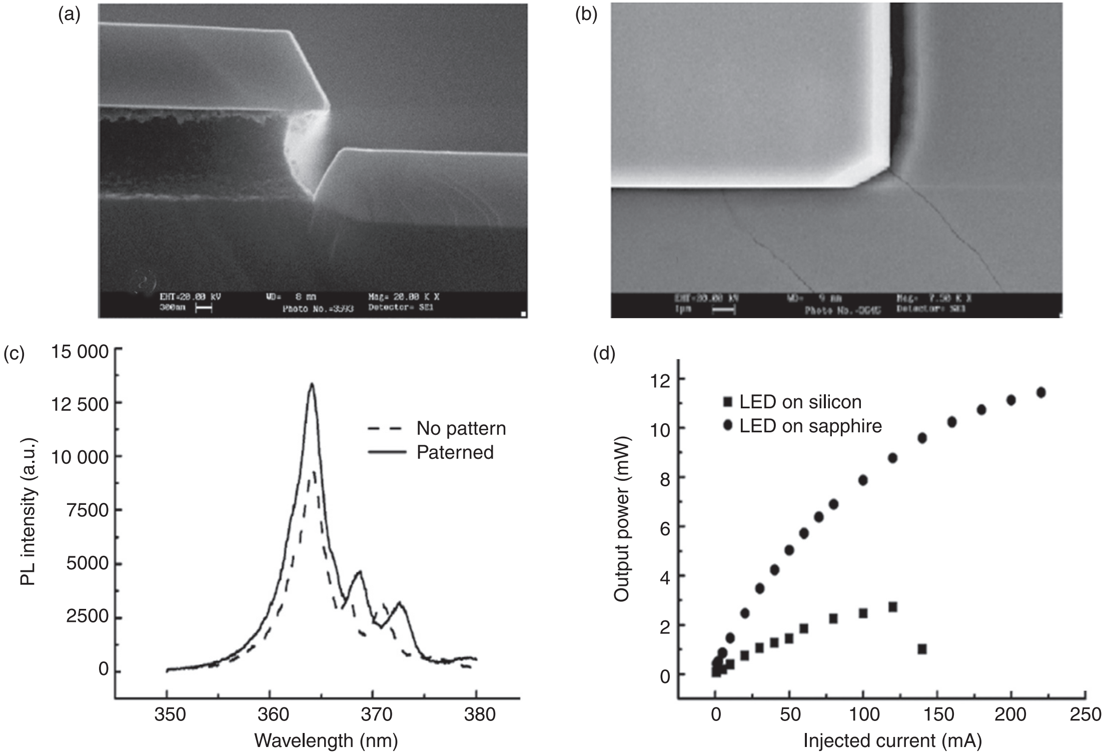

4.20 (a) Cross section and (b) top view of GaN on patterned Si (111). (c) PL spectra of GaN samples with a pattern and without a pattern on the silicon substrate. (d) *L-I* characteristics of InGaN/GaN LEDs on a silicon substrate and a sapphire substrate (before being packaged) (Zhang *et al.*, 2007).

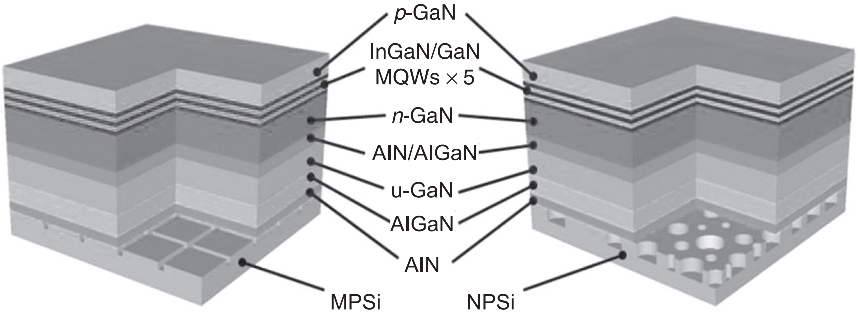

4.21 Left: MPLED; right: NPLED (Chiu *et al.*, 2011a).

Chiu *et al.* (2011a) reduced the pattern size on the silicon wafer and showed that this significantly improved the LED device performance. They prepared 340 μm × 340 μm sized islands on a silicon wafer to create a micro-patterned silicon (MPSi) substrate and 200 nm diameter islands to create a nano-patterned silicon (NPSi) wafer. Figure 4.21 shows the LED's schematics and Fig. 4.22 shows the variation in PL intensity and EQE with output light power of the MPLED (an LED grown on MPSi) and NPLED (an LED grown on NPSi) devices. They reported also that the NPSi devices showed a significant improvement in terms of TDs, and better surface morphology and light emission resulting from better carrier confinement and a higher radiative recombination rate. In addition, a higher injection current (100 mA) was observed for NPSi devices with 20% less droop in EQE.

4.6.5 Semipolar and nonpolar GaN LEDs on silicon

The quantum-confined Stark effect (QCSE) causes strong polarization in InGaN MQWs when the active GaN layers are grown in the *c*-axis direction and are thicker than 3 nm. This reduces the efficiency of the LEDs and was the motivation behind the search for semipolar or nonpolar GaN LEDs. Since the devices are grown in the semipolar or nonpolar direction, the QCSE-induced polarization field acts laterally through the active region and does not create any lack of carrier confinement in the QW. The semipolar or nonpolar growth of LEDs on a silicon substrate involves selective-area growth and patterning of silicon wafers. Figure 4.23 shows the different planes in a GaN wurtzite structure (Masui *et al.*, 2010). Figure 4.24 shows the results from a theoretical simulation, which demonstrates the benefit of using the nonpolar directions for growing GaN LEDs (because it reduces the QCSE in the vertical device direction) (Chichibu *et al.*, 2006; Masui *et al.*, 2010).

Hikosaka *et al.* (2008) fabricated an InGaN/GaN active-region LED using (i) GaN (1–101) growth on Si (001) and (ii) GaN (11–22) growth on Si (113)

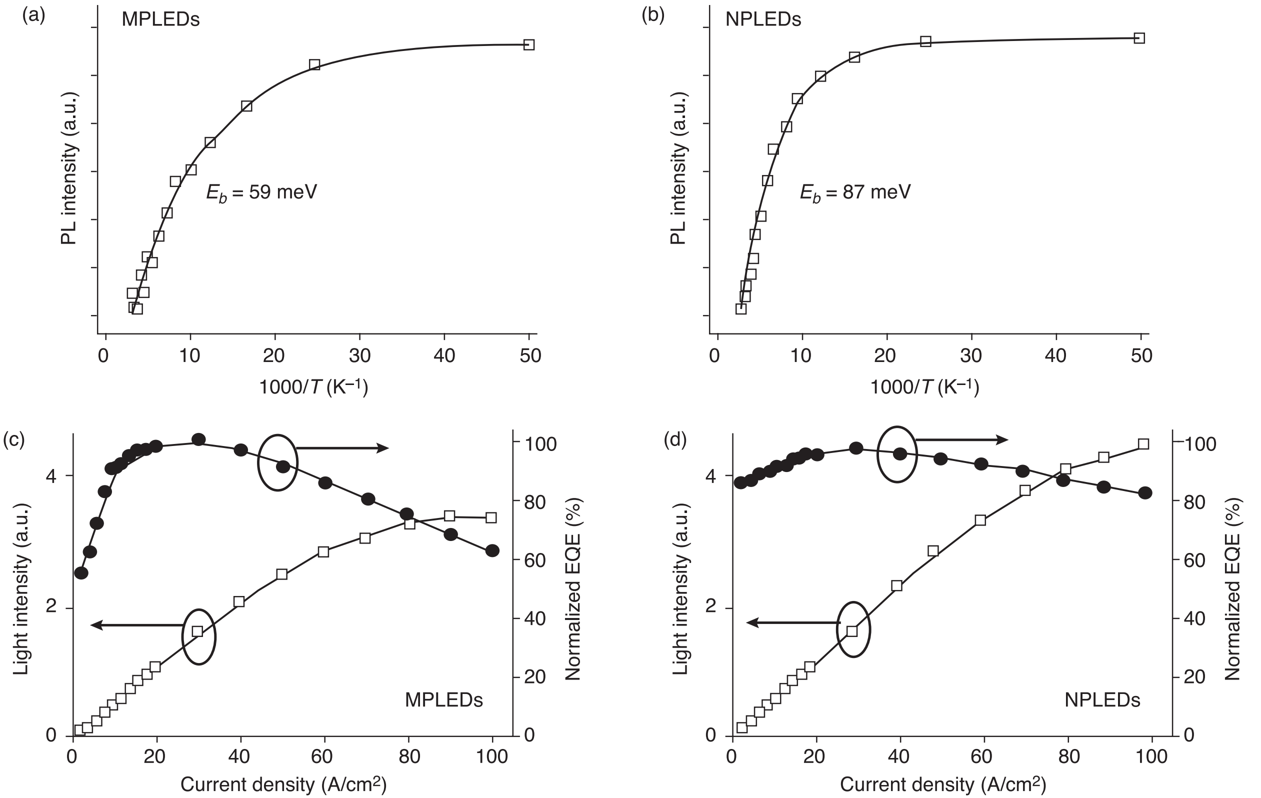

4.22 PL intensity of (a) MPLEDs, (b) NPLEDs. Light intensity and EQE of (c) MPLEDs and (d) NPLEDs (Chiu *et al.*, 2011a).

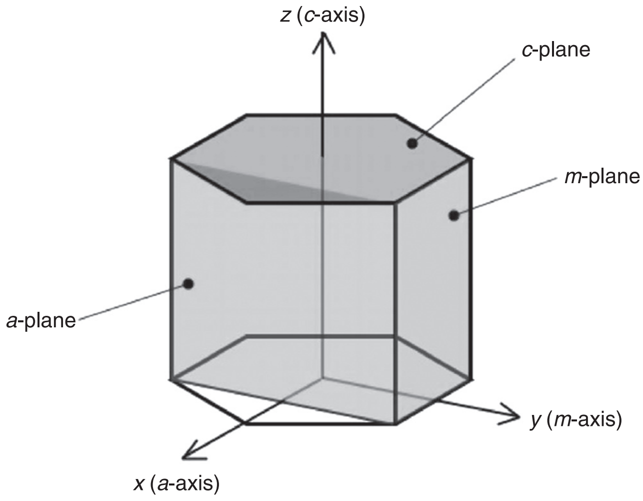

4.23 Hexagonal prism representing a GaN crystal unit cell with nonpolar (*a* and *m*) and polar (*c*) planes (Masui *et al.*, 2010).

(Hikosaka *et al.*, 2008; Tanikawa *et al.*, 2008). Previously, they had grown nonpolar GaN via selective-area growth (SAG) (Hikosaka *et al.*, 2004). Now they used the SAG epitaxial lateral overgrowth (SAG-ELO) technique. In this process, for example, a (111) face is opened on a (001) silicon wafer using KOH anisotropic etching and the other opened faces ((001) and (-1-11)) are covered using an SiO_2 film. This silicon substrate is placed in a growth chamber to grow GaN by SAG on the open face. *c*-plane GaN grows on the cleaved open face (normal to <111>) but at an inclined angle to the original silicon wafer plane (001). Thus, a different plane of GaN (1–101) is observed as normal to the original silicon wafer. The process is shown in Fig. 4.25 (Hikosaka *et al.*, 2008). They also demonstrated that to get a better quality GaN film, a deep groove followed by a narrow facet opening is helpful.

Ni *et al.* (2009) used a similar SAG-ELO growth process to grow *m*-plane (1–100) InGaN/GaN QW LEDs on a Si (112) wafer. They also showed that the TDs, by nature, propagate along the *c*-direction, and thus have a lesser impact on the device epilayers grown along the *m*-direction. A schematic of their device, along with XRD scans, is shown in Fig. 4.26. To compare the *m*-plane and *c*-plane LEDs, the PL intensities of the devices were examined: the *m*-plane LED did not show any blue-shift compared to the *c*-plane device. Additionally, it had a better IQE than the *c*-plane device, as shown in Fig. 4.27 (Ni *et al.*, 2009): the IQE was 65% at a steady-state carrier density of $1.2 \times 10^{18}/\text{cm}^3$, which appears to be almost twice that of the *c*-plane LED. Chiu *et al.* (2011b) grew a (1–101) semipolar GaN LED on Si (001) achieving a low TD density along the growth direction, as did Ni *et al.* (2009). They also reported that semipolar GaN LEDs show less efficiency droop compared to polar (*c*-plane) LEDs at a high injection current (Chiu *et al.*,

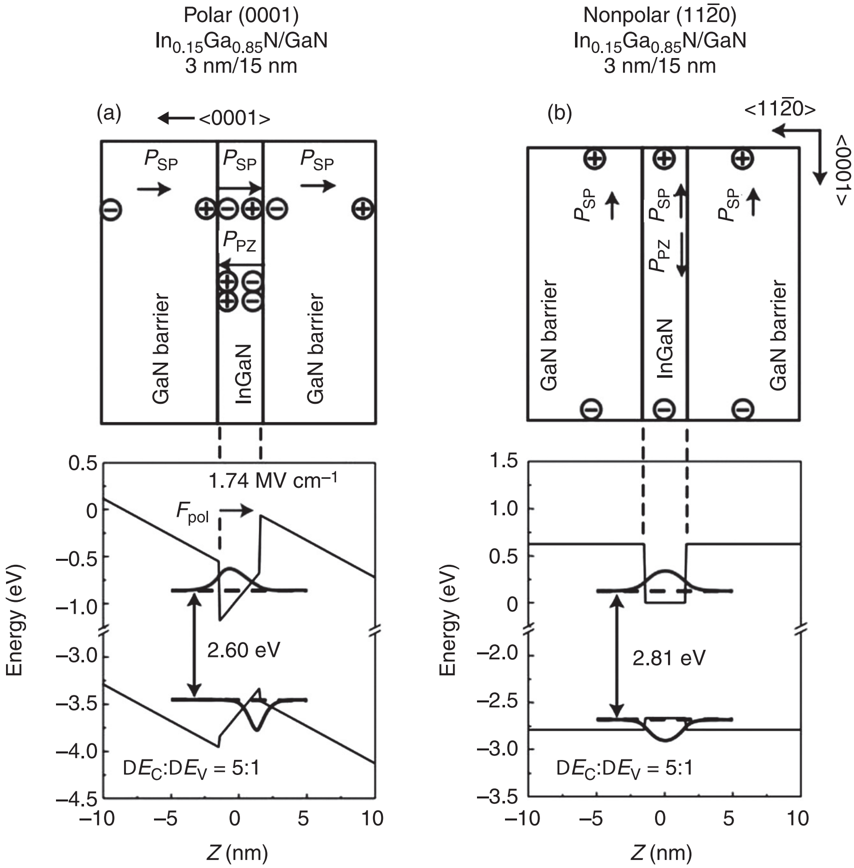
Polar (0001)
In0.15Ga0.85N/GaN
3 nm/15 nm
Nonpolar (112̄0)
In0.15Ga0.85N/GaN
3 nm/15 nm
(a)
<0001>
PSP
PPZ
GaN barrier
InGaN
GaN barrier
(b)
<112̄0>
<0001>
1.74 MV cm−1
Fpol
2.60 eV
2.81 eV
DEC:DEV = 5:1
Energy (eV)
Z (nm)

4.24 QW structures on (a) polar and (b) nonpolar orientations and their band diagrams. Polarization charges appear at the interfaces of the polar-oriented QW and induce electric fields that spatially separate electrons and holes in the QW. In nonpolar orientations, polarization charges do not affect the band structure. Because of the internal electric fields in a polar-oriented QW, the transition energy is lower than that of a nonpolar-oriented QW (due to the QCSE). When a QW is embedded in a common +*c*-oriented LED structure, the internal electric fields increase as the LED positive bias increases (Chichibu *et al.*, 2006; Masui *et al.*, 2010).

2011b). However, they also reported that there was a small blue shift in the PL spectrum of a semipolar LED.

4.6.6 GaN nanowires and nanorods on silicon

For growing better GaN-based LEDs, only the epitaxial growth of GaN films has so far been discussed. It is also possible to grow 3D wire-like GaN entities on

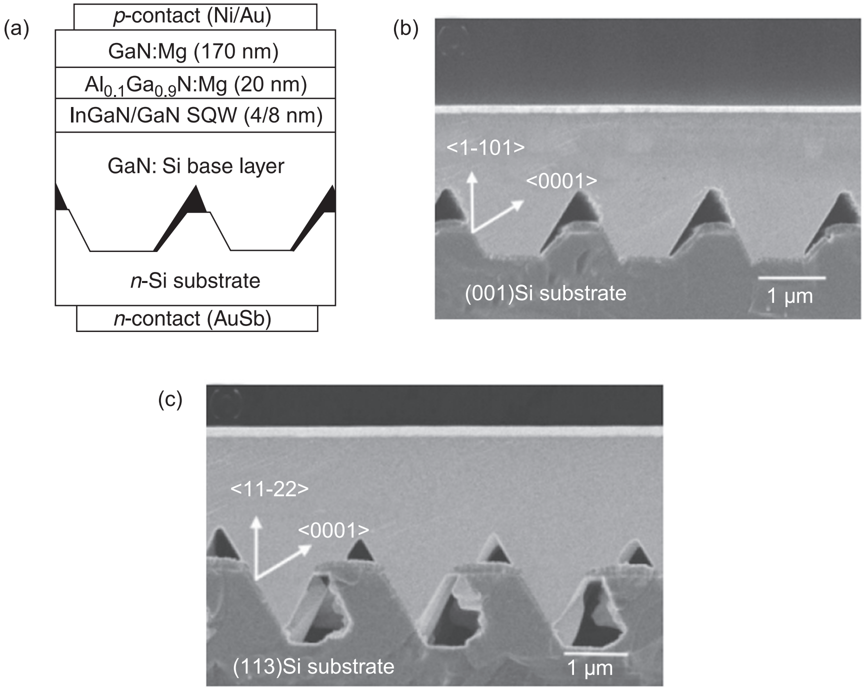
(a)
p-contact (Ni/Au)
GaN:Mg (170 nm)
Al0.1Ga0.9N:Mg (20 nm)
InGaN/GaN SQW (4/8 nm)
GaN: Si base layer
n-Si substrate
n-contact (AuSb)
(b)
<1-101>
<0001>
(001)Si substrate
1 μm
(c)
<11-22>
<0001>
(113)Si substrate
1 μm

4.25 (a) (1–101) LED device structure. (b), (c) Cross-sectional SEM images of a (1–101) LED and a (11–22) LED (Hikosaka *et al*, 2008). (SQW: single quantum well)

silicon substrates, which are called nanorods, nanowires or nanocolumns. These structures have significant advantages over a traditional epilayer grown on silicon: (i) nanorods have zero or very few dislocations, (ii) the larger surface area helps to outcouple light to give a brighter LED, (iii) nanorods have very high quality crystallinity along with a strong ability to manage the strain induced during growth and (iv) nanorods do not cause bowing of the wafer on large-area substrates (Waag *et al.*, 2011). On the other hand, they are not free of constraints: (i) the growth method is more complicated than conventional epilayer growth and (ii) the large surface area is subject to the detrimental effects of surface states and possible surface degradation. In general, successful GaN nanorod devices on silicon were initially produced using radio-frequency (RF) plasma-assisted MBE on *n*-type Si (111) (Kikuchi *et al.*, 2004; Chen *et al.*, 2006) or bulk Si (111) (Park *et al.*, 2004). However, because of the possibility of forming Si_xN_y at the GaN-Si interface, Chen *et al.* (2006) and Calleja *et al.* (2007) grew ultrathin Si_3N_4 buffer layers using plasma nitridation on clean Si (111) 7 × 7 surfaces, and then grew AlN, to avoid the possible loss of epitaxial orientation.

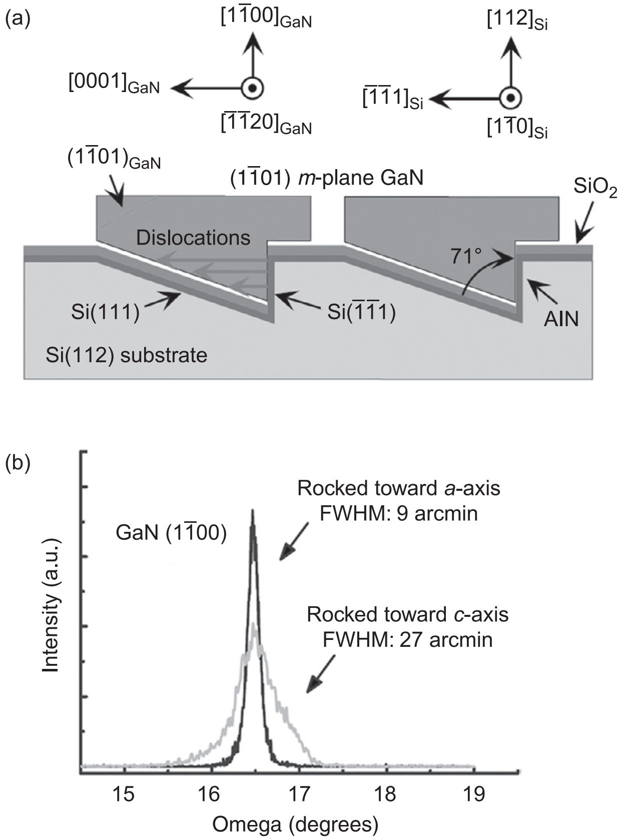
(a)
$[1\bar{1}00]_{GaN}$
$[0001]_{GaN}$
$[\bar{1}\bar{1}20]_{GaN}$
$[112]_{Si}$
$[\bar{1}\bar{1}1]_{Si}$
$[1\bar{1}0]_{Si}$
$(1\bar{1}01)_{GaN}$
$(1\bar{1}01)$ m-plane GaN
SiO_2
Dislocations
71°
Si(111)
$Si(\bar{1}\bar{1}1)$
AlN
Si(112) substrate
(b)
Intensity (a.u.)
GaN $(1\bar{1}00)$
Rocked toward a-axis
FWHM: 9 arcmin
Rocked toward c-axis
FWHM: 27 arcmin
15
16
17
18
19
Omega (degrees)

4.26 (a) Growth of selective area *m*-plane GaN on patterned Si (112). (b) X-ray rocking curves of a GaN film grown toward the *m*-plane showing broadening due to tilting during lateral growth in both +*c* and −*c* directions (Ni *et al.*, 2009).

Kikuchi *et al.* (2004) grew GaN-based nanorods using an RF-MBE process. They fabricated *p-n* junction nanocolumn LEDs with InGaN/GaN multiple quantum disk (MQD) active layers. They increased the growth diameter of the nanorod LEDs in the upper *p*-type GaN region, and ultimately all the nanorods were connected together in that region. This coalescence on top of the nanorods helped to form a continuous layer. This was an ELO process and the LEDs required only a simple contact formation on top. Figure 4.28 shows an SEM cross section of the device (Kikuchi *et al.*, 2004) and the schematic of the device. Chen *et al.* (2006) used a similar growth process to that of Kikuchi *et al.* (2004), but they used *n*-type Si (111) on which, prior to GaN nanorod growth, an ultrathin β-Si_3N_4 buffer layer was formed by plasma nitridation; this prevented the silicon surface from reacting with the nitrogen atoms. They grew two different lengths of

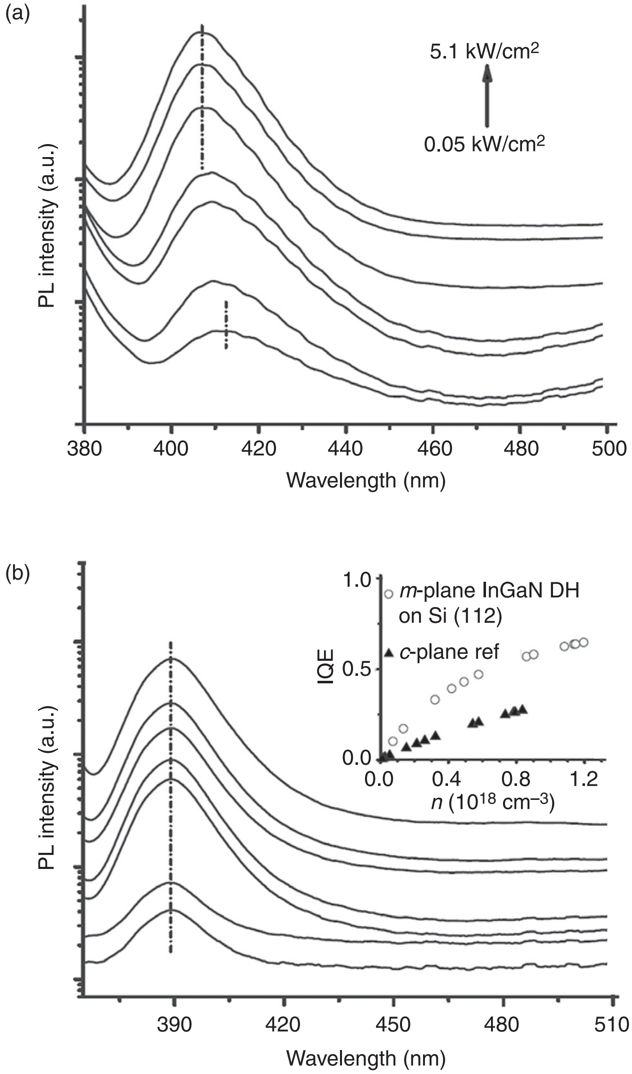

4.27 Room-temperature PL spectra (measured with a HeCd laser at different excitation densities) for 6 nm thick InGaN double heterostructure LED active layers on (a) *c*-GaN on sapphire and (b) *m*-GaN on Si (112). The excitation power densities in both plots were 0.05, 0.15, 0.52, 1.0, 2.0, 2.5 and 5.1 kW/cm^2. The inset in (b) shows the IQEs of both samples extracted from the excitation dependence of the PL intensity using a titanium-sapphire laser (370 nm) (Ni *et al.*, 2009). (DH: double heterostructure)

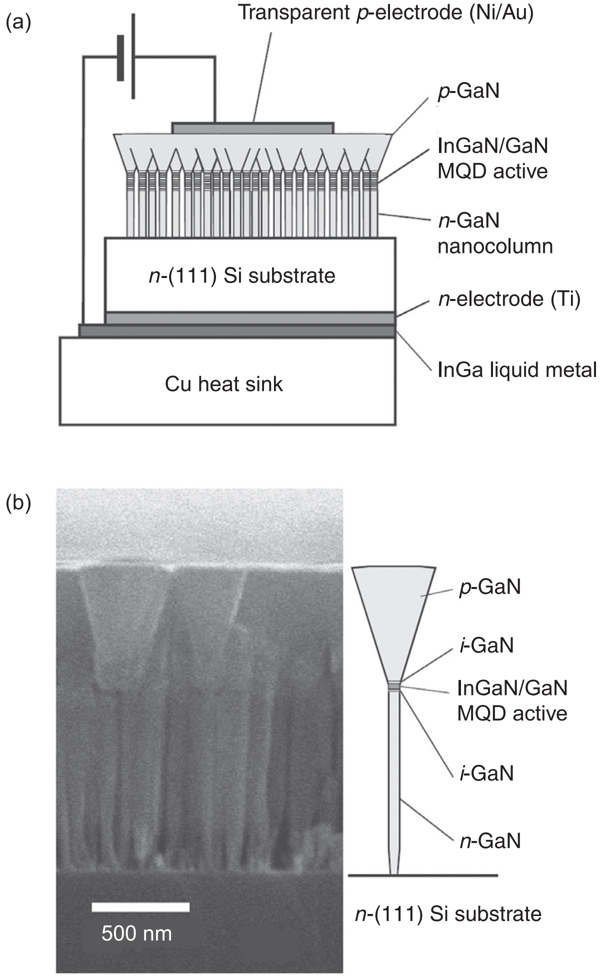
(a)
Transparent *p*-electrode (Ni/Au)
p-GaN
InGaN/GaN MQD active
n-GaN nanocolumn
n-(111) Si substrate
n-electrode (Ti)
InGa liquid metal
Cu heat sink
(b)
p-GaN
i-GaN
InGaN/GaN MQD active
i-GaN
n-GaN
n-(111) Si substrate
500 nm

4.28 (a) InGaN/GaN nanorod LEDs on Si (111); (b) SEM of a device cross section with a single nanorod (Kikuchi *et al.*, 2004).

nanorods: 0.4 μm and 1.0 μm. A field emission scanning electron microscope (FE-SEM) scan and room-temperature (RT) PL spectra of a 1.0 μm GaN nanorod sample (Chen *et al.*, 2006) are shown in Fig. 4.29. From the RT-PL spectral analysis, Chen *et al.* (2006) reported that the device has strong near-band-edge ultraviolet photoluminescence at 3.40 eV with an FWHM of 50 meV. No defect-related emissions except for a very weak broadband yellow emission were observed at room temperature, as the GaN nanorods grown under the optimized conditions efficiently suppress yellow luminescence; this is an important step toward obtaining pure green LEDs.

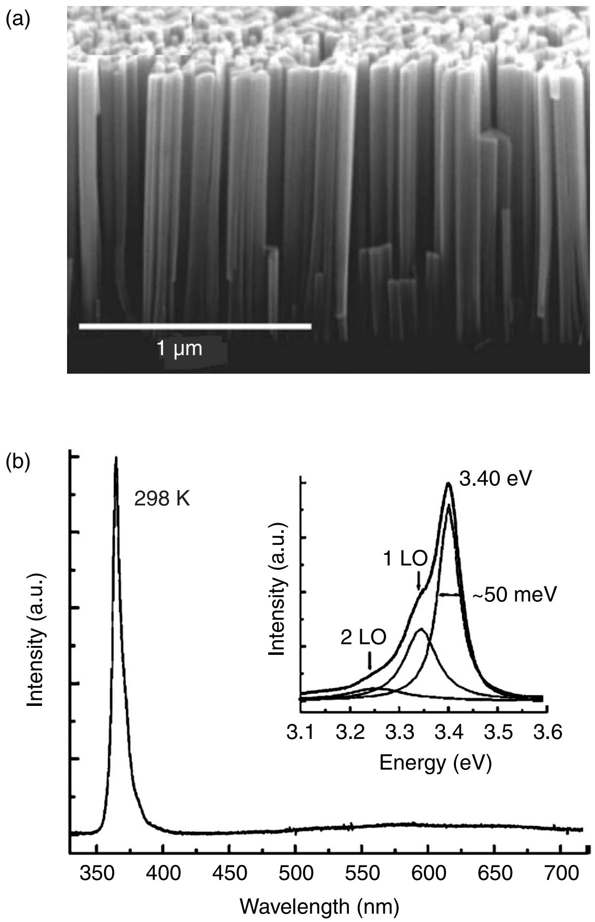

4.29 (a) FE-SEM (cross-section view) and (b) RT-PL spectra of 1.0 μm GaN nanorod sample (Chen *et al.*, 2006).

The MOCVD growth of GaN nanorods was demonstrated by Fündling *et al.* (2009) using a pre-patterned Si (111) substrate. They grew hexagonal silicon pillars via lithography (e-beam or photo). The LED structures were grown on 3D silicon micro-structures (5 μm × 5 μm) and nano-structures (700 nm × 700 nm), which were patterned with hexagonal columns. Figure 4.30 shows a schematic of the LED on silicon pillars. Fündling *et al.* (2009) also reported that the funnel-type growth of *p*-GaN, as shown in Fig. 4.31, is highly influenced by the incorporation of magnesium ions during the growth of the *p*-GaN layer. This results in enhanced lateral growth of the ELO GaN layer. They also found additional growth in the {1–101} planes, which ultimately created a 3D pyramidal structure in the LED with a hexagonal top facet, as seen in the cathodoluminescence

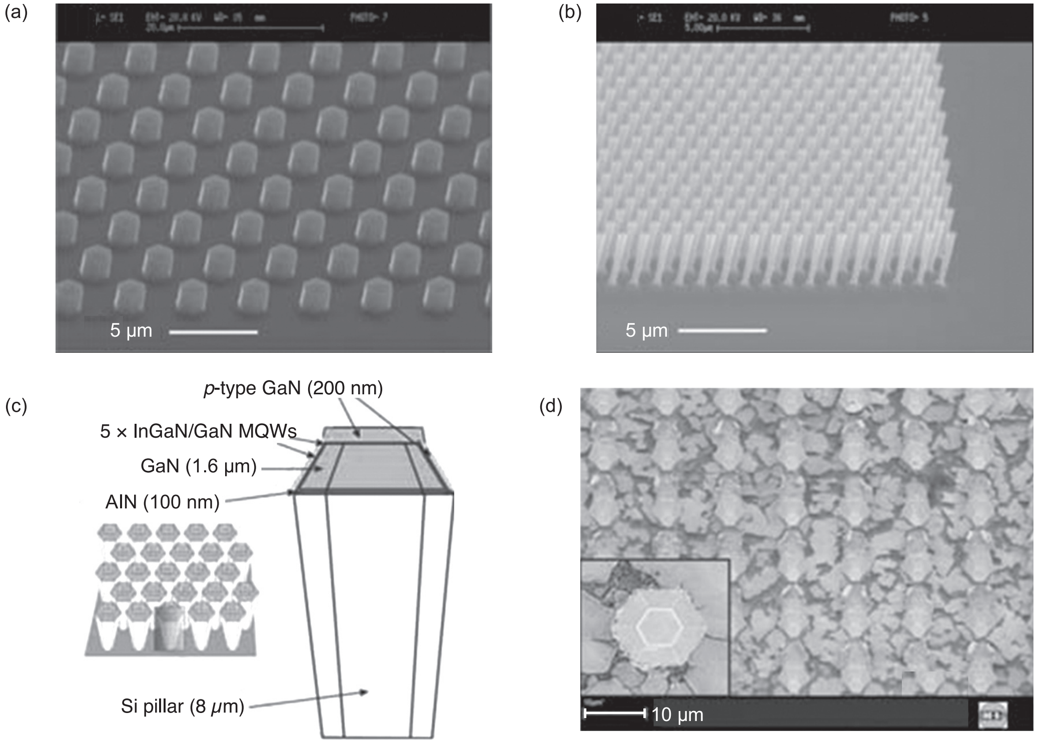
(a)
5 μm
(b)
5 μm
(c)
p-type GaN (200 nm)
5 × InGaN/GaN MQWs
GaN (1.6 μm)
AlN (100 nm)
Si pillar (8 μm)
(d)
10 μm

4.30 SEM images of Si (111) pillars after dry etching: (a) 5 μm × 5 μm (nominal diameter × distance) array, (b) 700 nm × 700 nm array, without a photoresist mask on the top (0001) plane. (c) Cross section of the silicon/GaN 3D LED structure. (d) FE-SEM image of GaN structures grown on a patterned silicon substrate showing a 5 μm × 5 μm array (Fündling *et al.*, 2009).

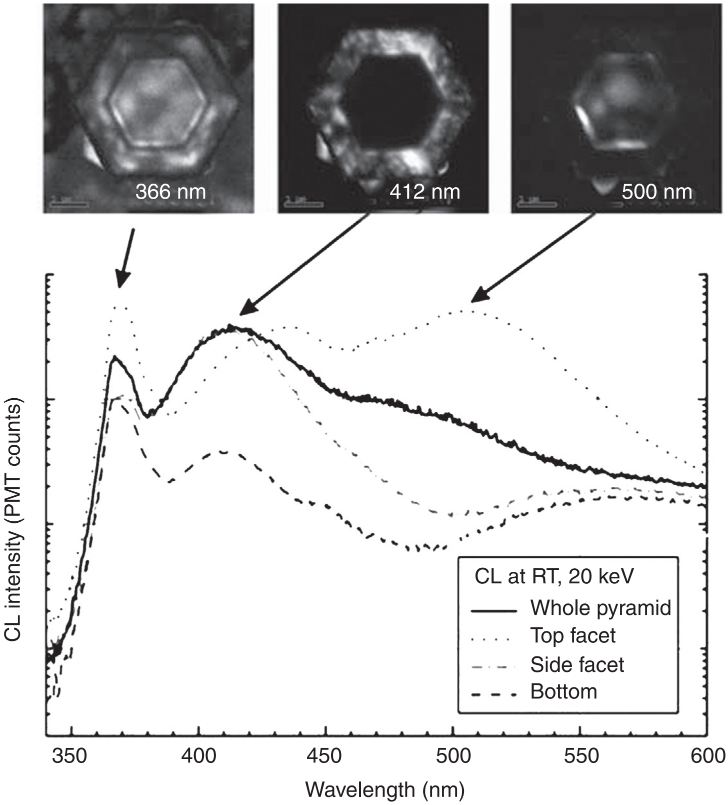

4.31 Room-temperature CL spectrum of a GaN LED structure made by exciting the whole pyramid compared with those made by exciting its top facet, one of its side facets and the deposition on the bottom substrate. The upper CL images were taken at the peak wavelengths of 366 nm, 412 nm and 500 nm (Fündling *et al.*, 2009).

(CL) images. Figure 4.31 shows the CL intensity due to luminescence from different facets, top, side and bottom. As the CL peaks are different when different facets are illuminated, it was estimated that this was due to changes in indium content and/or growth rates in the {1–101} or (0001) planes. When CL measurements were taken at both room temperature and cryogenic temperature, a blue shift was observed. When the bottom layer was illuminated, it output a broad luminescence around 570 nm (the yellow band) with a low intensity, indicating there was a high defect density in the bottom layer. In another report, Hasegawa *et al.* (2009) observed a more vertical and uniform growth of GaN nanorods on Si (001) when SiO_2 was grown as an intermediate layer between a GaN nanorod and the Si (001) surface. This also assists in preventing the formation of Si_3N_4.

4.7 Conclusion

The development of solid-state lighting technologies for the immediate future will focus on methods for reducing the cost of the solid-state lighting sources. One of the quickest ways to reduce the cost of these devices is to reduce the cost of the substrate by switching from sapphire to silicon. Provided that the same quality of light can be achieved and the same output levels and efficiency are realized, this will present a very promising avenue for future research and industrial development. This chapter has briefly described some of the methods used to grow GaN on silicon substrates and the challenges associated with this growth. The latter half of this chapter focused on some of the recent developments for LED devices on silicon. Future efforts are sure to push the boundaries in this rapidly developing field.

4.8 References

Arslan E, Ozturk M, Teke A, Ozcelik S and Ozbay E, 2008, Buffer optimization for crack-free GaN epitaxial layers grown on Si(1 1 1) substrate by MOCVD, *J. Phys. D. Appl. Phys.*, 41, 155317.

Blasing J, Reiher A, Dadgar A, Diez A and Krost A, 2002, The origin of stress reduction by low-temperature AlN interlayers, *Appl. Phys. Lett.*, 81, 15, 2722–2724.

Calleja E, Ristic J, Fernandez-Garrido S, Cerutti L, Sanchez-Garcia M, *et al.*, 2007, Growth, morphology, and structural properties of group-III-nitride nanocolumns and nanodisks, *Phys. Stat. Sol. (b)*, 244, 2816–2837.

Chen H, Lin H, Shen C and Gwo S, 2006, Structure and photoluminescence properties of epitaxially oriented GaN nanorods grown on Si(111) by plasma-assisted molecular-beam epitaxy, *Appl. Phys. Lett.*, 89, 243105.

Chichibu SF, Uedono A, Onuma T, Haskell B A, Chakraborty A, *et al.*, 2006, Origin of defect-insensitive emission probability in In-containing (Al,In,Ga)N alloy semiconductors, *Nature Materials*, 5, 810–816.

Chiu C, Lin C, Deng D, Lin D, Li J, *et al.*, 2011a, Optical and electrical properties of GaN-based light emitting diodes grown on micro- and nano-scale patterned Si substrate, *IEEE J. Quan. Elec.*, 47(7), 899–906.

Chiu C, Lin D, Lin C, Li Z, Chang W, *et al.*, 2011b, Reduction of efficiency droop in semipolar (1101) InGaN/GaN light emitting diodes grown on patterned silicon substrates, *Appl. Phys. Exp.*, 4, 012105.

Chou HC, Rohatgi A, Jokerst NM, Kamra S, Stock SR, *et al.*, 1996, Approach toward high efficiency CdTe/CdS heterojunction solar cells, *Mat. Chem. Phys.*, 43, 178–182.

Craford MG, 2005, LEDs for solid state lighting and other emerging applications: status, trends, and challenges, *Proc. SPIE*, 5941, 594101.

Dadgar A, Poschenrieder M, Blasing J, Fehse K, Diez A, *et al.*, 1999, Thick, crack-free blue light-emitting diodes on Si(111) using low-temperature AlN interlayers and *in situ* Si_xN_y masking, *Appl. Phys. Lett.*, 80, 3670–3672.

Dadgar A, Alam A, Riemann T, Blasing J, Diez A, *et al.*, 2001a, Crack-free InGaN/GaN light emitters on Si(111), *Phys. Stat. Sol. (a)*, 188(1), 155–158.

Dadgar A, Poschenrieder M, Blasing J, Fehse K, Riemann T, *et al.*, 2001b, *MRS Fall Meeting*, Vol. 14.7, Boston, MA.

Dadgar A, Christen J, Riemann T, Richter S, Blasing J, *et al.*, 2001c, Bright blue electroluminescence from an InGaN/GaN multiquantum-well diode on Si(111): impact of an AlGaN/GaN multilayer, *Appl. Phys. Lett.*, 78, 2211.

Dadgar A, Strittmatter A, Bläsing J, Poschenrieder M, Contreras O, *et al.*, 2003, Metalorganic chemical vapor phase epitaxy of gallium-nitride on silicon, *Phys. Stat. Sol. (c)*, 0(6), 1583–1606.

Dadgar A, Schulze F, Wienecke M, Gadanecz A, Bläsing J, *et al.*, 2007, Epitaxy of GaN on silicon – impact of symmetry and surface reconstruction, *New J. Phys.*, 9, 389.

Egawa T, Zhang B and Ishikawa H, 2005, High performance of InGaN LEDs on (111) silicon substrates grown by MOCVD, *IEEE Elec. Dev. Lett.*, 26(3), 169–171.

Fenwick W, Melton A, Xu T, Li N, Summers C, *et al.*, 2009, Metal organic chemical vapor deposition of crack-free GaN-based light emitting diodes on Si (111) using a thin Al_2O_3 interlayer, *Appl. Phys. Lett.*, 94, 222105.

Fündling S, Li S, Sökmen Ü, Merzsch S, Hinze P, *et al.*, 2009, Three-dimensionally structured silicon as a substrate for the MOVPE growth of GaN nanoLEDs, *Phys. Stat. Sol. (a)*, 206(6), 1194–1198.

Gong J, Yeh M and Wang C, 2003, Growth and characterization of GaN and AlN films on (111) and (001) Si substrates, *J. Crystal Growth*, 247, 261–268.

Guha S and Bojarczuk NA, 1998a, Ultraviolet and violet GaN light emitting diodes on silicon, *Appl. Phys. Lett.*, 72, 415–417.

Guha S and Bojarczuk NA, 1998b, Multicolored light emitters on silicon substrates, *Appl. Phys. Lett.*, 73, 1487–1489.

Hasegawa S, Seo J, Uchida K, Tambo H, Kameoka H, *et al.*, 2009, Influence of native silicon oxides on the growth of GaN nanorods on Si (001), *Phys. Stat. Sol. (c)*, 6(S2), S570–S573.

Hikosaka T, Narita T, Honda Y, Yamaguchi M and Sawaki N, 2004, Optical and electrical properties of (1–101)GaN grown on a 7 off-axis (001)Si substrate, *Appl. Phys. Lett.*, 84, 4717.

Hikosaka T, Tanikawa T, Honda Y, Yamaguchi M and Sawaki N, 2008, Fabrication and properties of semi-polar (1–101) and (11–22) InGaN/GaN light emitting diodes on patterned Si substrates, *Phys. Stat. Sol. (c)*, 5(6), 2234–2237.

Huang J, Ye Z, Wang L, Yuan J, Zhao B, *et al.*, 2002, Comparison of GaN epitaxial films on silicon nitride buffer and Si(111), *Solid-State Electronics*, 46(8), 1231–1234.

Ishikawa H, Yamamoto K, Egawa T, Soga T, Jimbo T, *et al.*, 1998, Thermal stability of GaN on (1 1 1) Si substrate, *J. Crystal Growth*, 189/190, 178–182.

Ishikawa H, Zhang B, Egawa T and Jimbo T, 2003, Valence-band discontinuity at the AlN/Si Interface, *Jpn. J. Appl. Phys.*, 42, 6413–6414.

Jamil M, Xu T, Melton A, Jampana B, Zaidi T, Liu S, *et al.*, 2010, Free-standing GaN-based LEDs with ALD-Al_2O_3/Si substrate removed by wet etching, *Proceedings of SPIE 7784, Tenth International Conference on Solid State Lighting, 77840E* (18 August 2010).

Kawaguchi Y, Honda Y, Matsushima H, Yamaguchi M, Hiramatsu K, *et al.*, 1998, Selective area growth of GaN on Si substrate using SiO_2 mask by metalorganic vapor phase epitaxy, *Jap. J. Appl. Phys.*, 37, L966–L969.

Kikuchi A, Kawai M, Tada M and Kishino K, 2004, InGaN/GaN multiple quantum disk nanocolumn light-emitting diodes grown on (111) Si substrate, *Jap. J. Appl. Phys.*, 43(12A), L1524–L1526.

Kim T, Yang S, Son J, Hong Y and Yang G, 2007, Growth of a GaN epilayer on a Si (111) substrate by using and AlN/GaN superlattice and application to a GaN microcavity structure with dielectric-distributed Bragg reflector, *J. Kor. Phys. Soc.*, 50(3), 801–805.

Krost A, Schulze F, Dadgar A, Strassburger G, Haberland K, *et al.*, 2005, Simultaneous measurement of wafer curvature and true temperature during metalorganic growth of group-III nitrides on silicon and sapphire, *Phys. Stat. Sol. (b)*, 242(13), 2570–2574.

Kyono CS, Ikossi-Anastasiou K, Rabinovich WS, Bowman SR, Katzer DS, *et al.*, 1994, GaAs/AlGaAs multiquantum well resonant photorefractive devices fabricated using epitaxial lift-off, *Appl. Phys. Lett.*, 64, 2244–2246.

Lau KM, Wong K, Zuo X and Chen P, 2011, Performance improvement of GaN-based light-emitting diodes grown on patterned Si substrate transferred to copper, *Optics Exp.*, 19, A956–A961.

Li J, Lin J and Jiang H, 2006, Growth of III-nitride photonic structures on large area silicon substrates, *Appl. Phys. Lett.*, 88, 171909.

Li YF, Sow A, Yao C and McCann PJ, 2005, Transfer of IV-VI multiple quantum well structures grown by molecular beam epitaxy from Si substrates to copper, *Thin Solid Films*, 488, 178–184.

Lin K, Chang E, Hsiao Y, Huang W, Li T, *et al.*, 2007, Growth of GaN film on 150 mm Si (111) using multilayer AlN/AlGaN buffer by metal-organic vapor phase epitaxy method, *Appl. Phys. Lett.*, 91, 222111.

Liu H, Ye Z, Zhang H and Zhao B, 2000, Wurtzite GaN epitaxial growth on Si(111) using SiN as an initial layer, *Mat. Res. Bull.*, 35, 1837.

Ma J, Zhu X, Wong K, Zou X and Lau KM, 2012, Improved GaN-based LED grown on silicon (111) substrates using stress/dislocation-engineered interlayers, *J. Crystal Growth*, 370, 265–268.

Masui S, Nakamura S, DenBaars S and Mishra U, 2010, Nonpolar and semipolar III-nitride light-emitting diodes: achievements and challenges, *IEEE Trans. Elec. Dev.*, 57(1), 88–100.

May PW, Tsai HY, Wang WN and Smith JA, 2006, Deposition of CVD diamond onto GaN, *Diamond Related Mat.*, 15, 526–530.

Meneghesso G, Levada S, Zanoni E, Podda S, Mura G, *et al.*, 2002, Failure modes and mechanisms of DC-aged GaN LEDs, *Phys. Stat. Sol. (c)*, 194, 389–392.

Meneghini M, Trevisanello L, Meneghesso G, Zanoni E, Rossi F, *et al.*, 2006, High-temperature failure of GaN LEDs related with passivation, *Superlattices Microstructures*, 40, 405–411.

Nakamura S, Senoh M, Nagahama S, Iwasa N, Yamada T, *et al.*, 1998, InGaN/GaN/AlGaN-based laser diodes with modulation-doped strained-layer superlattices grown on an epitaxially laterally overgrown GaN substrate, *Appl. Phys. Lett.*, 72, 211.

Ni X, Wu M, Lee J, Li X, Baski A, *et al.*, 2009, Nonpolar *m*-plane GaN on patterned Si(112) substrates by metalorganic chemical vapor deposition, *Appl. Phys. Lett.*, 95, 111102.

Nishimura S, Matsumoto S and Terashima K, 2004, GaN on Si for LED and LD applications, *Phys. Stat. Sol. (c)*, 1, 238.

Park DC, Fujita S and Fujita S, 1999, Growth of polycrystalline GaN on silicon (001) substrates by RF plasma chemical vapor deposition with ZnO buffer layer, *Phys. Stat. Sol. (a)*, 176, 579.

Park Y, Park C, Fu D, Kang T and Oh J, 2004, Photoluminescence studies of GaN nanorods on Si (111) substrates grown by molecular-beam epitaxy, *Appl. Phys. Lett.*, 85, 5718–5720.

Phillips A and Zhu D, 2009, UK cracks GaN-on-silicon LEDs, *Compound Semiconductor*, 19.

Reiher F, Dadgar A, Blasing J, Wieneke M, Muller M, *et al.*, 2009, InGaN/GaN light-emitting diodes on Si(1 1 0) substrates grown by metal–organic vapour phase epitaxy, *J. Phys. D: Appl. Phys.*, 42, 055107.

Saengkaew P, Dadgar A, Blasing J, Hempel T, Veit P, *et al.*, 2009, Low-temperature/high-temperature AlN superlattice buffer layers for high-quality $Al_xGa_{1-x}N$ on Si(111), *J. Crystal Growth*, 311, 3742–3748.

Song JH, Huang JL, Lu HH and Sung JC, 2007, Investigation of wurtzite (B,Al)N films prepared on polycrystalline diamond, *Thin Solid Films*, 516, 223–227.

Strittmatter A, Krost A, Strassburg M, Türck V, Bimberg D, *et al.*, 1999, Low-pressure metal organic chemical vapor deposition of GaN on silicon(111) substrates using an AlAs nucleation layer, *Appl. Phys. Lett.*, 74, 1242.

Strittmatter A, Rodt S, Reissmann L, Bimberg D, Schröder H, *et al.*, 2001, Maskless epitaxial lateral overgrowth of GaN layers on structured Si(111) substrates, *Appl. Phys. Lett.*, 78, 727–729.

Takeuchi T, Amano H, Hiramatsu K, Sawaki N and Akasaki I, 1991, Growth of single crystalline GaN film on Si substrate using 3C-SiC as an intermediate layer, *J. Crystal Growth*, 115, 634.

Tanikawa T, Hikosaka T, Honda Y, Yamaguchi M and Sawaki N, 2008, Growth of semi-polar (11–22)GaN on a (113)Si substrate by selective MOVPE, *Phys. Stat. Sol. (c)*, 5(9), 2966–2968.

Tran CA, Osinski A, Karlicek Jr RF and Berishev I, 1999, Growth of InGaN/GaN multiple-quantum-well blue light-emitting diodes on silicon by metalorganic vapor phase epitaxy, *Appl. Phys. Lett.*, 75, 1494–1496.

Tripathy S, Lin V, Teo S, Dadgar A, Diez A, *et al.*, 2007, InGaN/GaN light emitting diodes on nanoscale silicon on insulator, *Appl. Phys. Lett.*, 91, 231109.

van Niftrik ATJ, Schermer JJ, Bauhuis GJ, Mulder P, Larsen PK, *et al.*, 2008, HF species and dissolved oxygen on the epitaxial lift-off process of GaAs using AlAsP release layers, *J. Electrochem. Soc.*, 155, 35–39.

Waag A, Wang X, Fündling S, Ledig J, Erenburg M, *et al.*, 2011, The nanorod approach: GaN nanoLEDs for solid state lighting, *Phys. Stat. Sol. (c)*, 8(7–8), 2296–2301.

Watanabe A, Takeuchi T, Hirosawa K, Amano H, Hiramatsu K, *et al.*, 1993, The growth of single crystalline GaN on a Si substrate using AlN as an intermediate layer, *J. Crystal Growth*, 128, 391–396.

Wong K, Zuo X, Chen P and Lau KM, 2010, Transfer of GaN-based light-emitting diodes from silicon growth substrate to copper, *IEEE Elec. Dev. Lett.*, 31(2), 132–134.

Wong WS, Kneissl M, Mei M, Treat DW, Teepe M, *et al.*, 2001, Integration of $In_xGa_{1-x}N$ laser diodes with dissimilar substrates by laser lift-off, *MRS Proc.*, 639, 12–2.

Xi Y, Chen K, Mont F, Kim J, Schubert E, *et al.*, 2007, Comparative study of *n*-type AlGaN grown on sapphire by using a superlattice layer and a low-temperature AlN interlayer, *J. Crystal Growth*, 299, 59–62.

Yang J, Lunev A, Simin G, Chitnis A, Shatalov M, *et al.*, 2000, Selective area deposited blue GaN–InGaN multiple-quantum well light emitting diodes over silicon substrates, *Appl. Phys. Lett.*, 76, 273–275.

Zhang B, Egawa T, Ishikawa H, Liu Y and Jimbo T, 2005, Thin-film InGaN multiple-quantum-well light-emitting diodes transferred from Si (111) substrate onto copper carrier by selective lift-off, *Appl. Phys. Lett.*, 86, 071113.

Zhang B, Liang H, Wang Y, Feng Z, Ng KW, *et al.*, 2007, High-performance III-nitride blue LEDs grown and fabricated on patterned Si substrates, *J. Crystal Growth*, 298, 725–730.

Zhang BJ, Egawa T, Ishikawa H, Nishikawa N, Jimbo T, *et al.*, 2001, InGaN multiple-quantum-well light emitting diodes on Si(111) substrates, *Phys. Stat. Sol. (a)*, 188(1), 151–154.

Zhu D, McAleese C, Häberlen M, Salcianu C, Thrush T, *et al.*, 2010, InGaN/GaN LEDs grown on Si(111): dependence of device performance on threading dislocation density and emission wavelength, *Phys. Stat. Sol. (c)*, 7(7–8), 2168–2170.

Zhu D, McAleese C, Haberlen M, Kappers M J, Hylton N, *et al.*, 2012, High-efficiency InGaN/GaN quantum well structures on large area silicon substrates, *Phys. Stat. Sol. (a)*, 209(1), 13–16.

Zhu Y, Watanabe A, Lu L, Chen Z and Egawa T, 2011, High performance of GaN-based light emitting diodes grown on 4-in. Si(111) substrate, *Jap. J. Appl. Phys.*, 50, 04DG08.

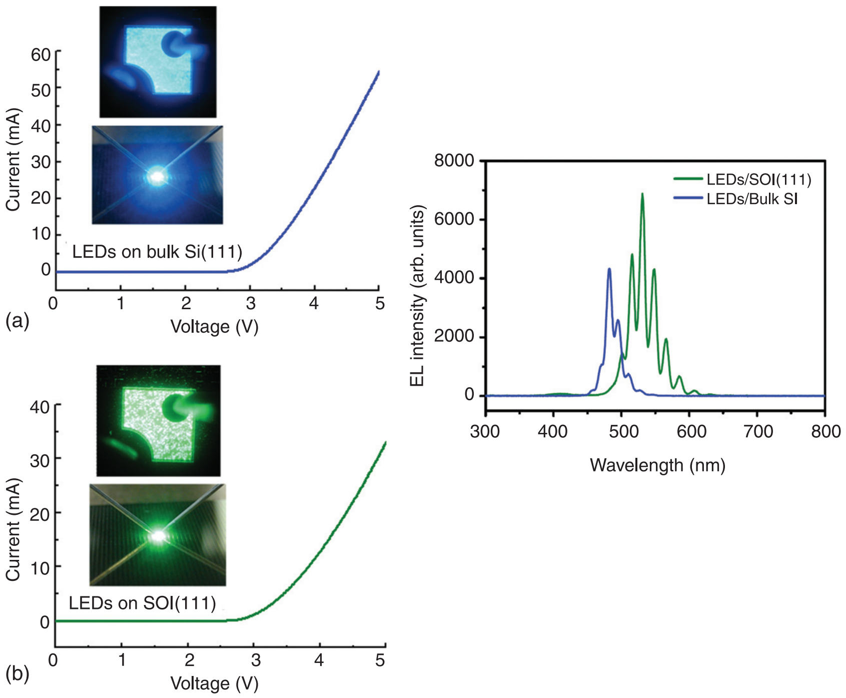

Plate I (Chapter 4) (a) Optical microscope image of green LEDs grown on SOI (111) under electrical probing and the *I-V* curve of an LED; (b) EL spectra of LEDs grown on Si (111) and SOI (111) under 100 mA current injection (Tripathy *et al.*, 2007).

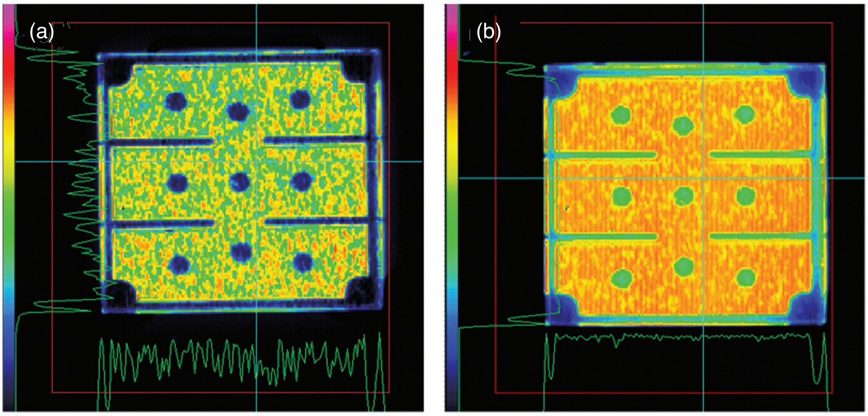

Plate II (Chapter 6) Photons from (a) a conventional flat-surface FCLED and (b) a MPA-FCLED for a dc injection current of 350 mA.

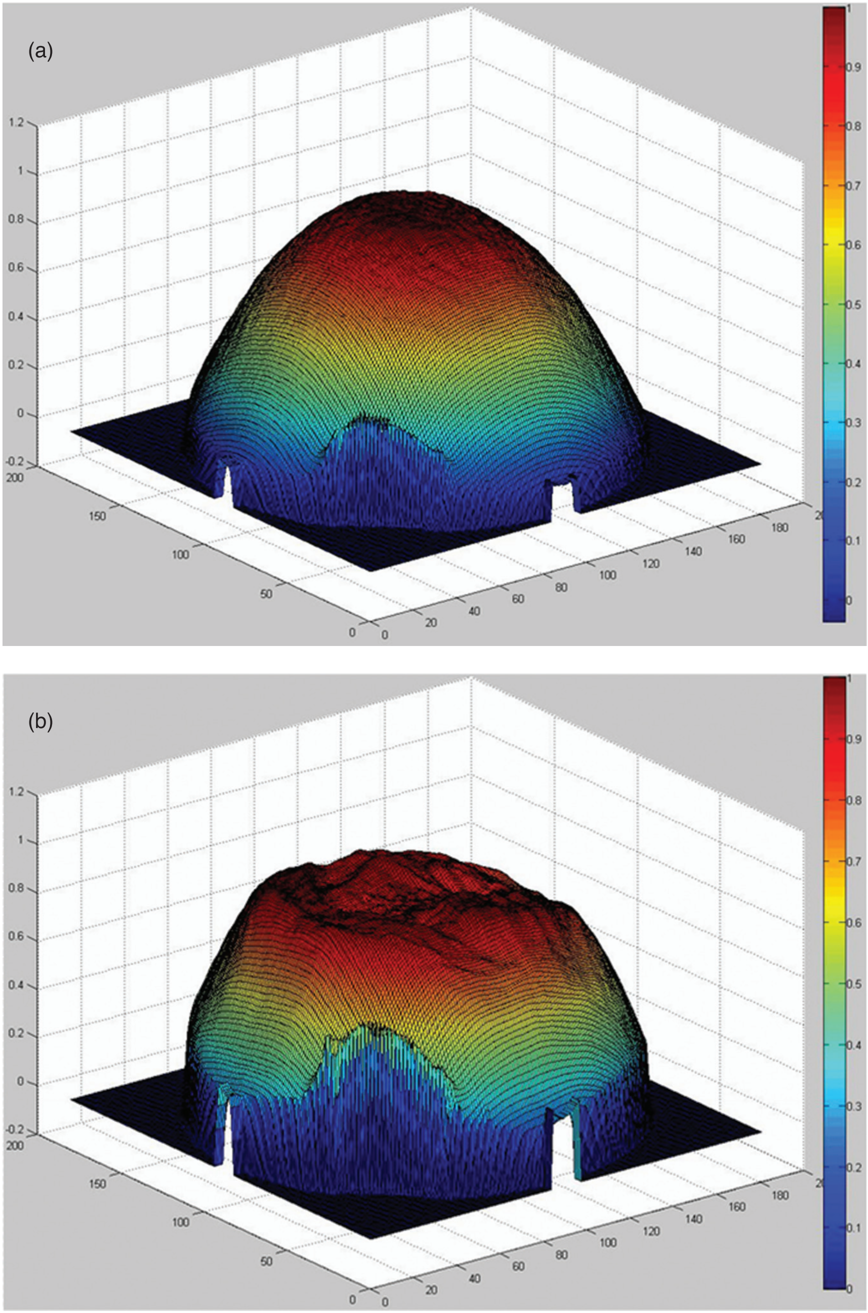

Plate III (Chapter 6) Normalized three-dimensional far-field patterns for (a) C-FCLEDs and (b) SS-FCLEDs.

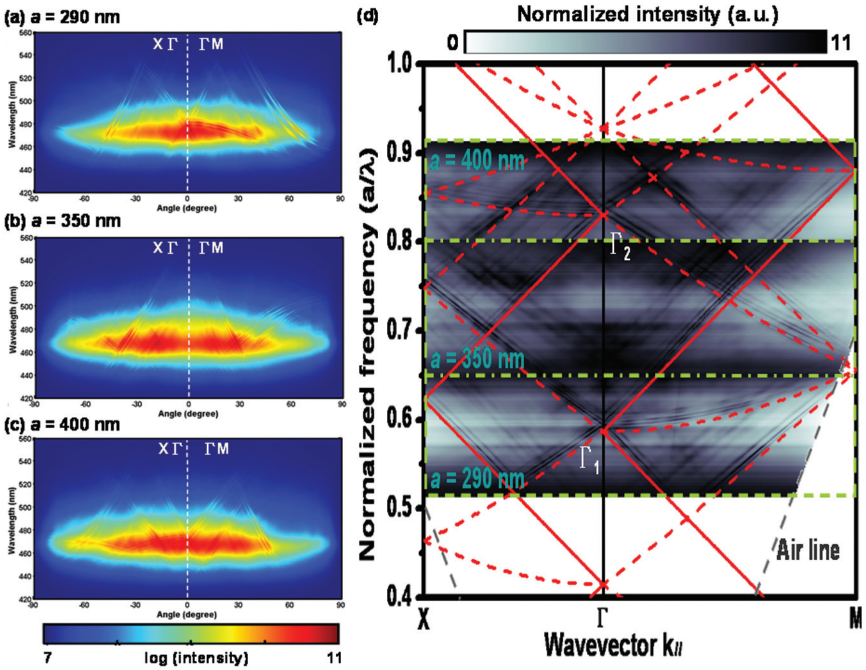

Plate IV (Chapter 6) Angular-resolved spectra for lattice constant (a) *a* = 290 nm, (b) *a* = 350 nm and (c) *a* = 400 nm, where ΓX direction points to the left and the ΓM direction points to the right. (d) Free-photon band structure calculated with *n* = 2.42 for the transverse electric modes. The red thick lines are the collinear coupled modes. The red dashed lines are the non-collinear coupled bands. The boxes show the experimental regions for *a* = 290 nm, 350 nm and 400 nm. The insets in the boxes are the calculated band structures.

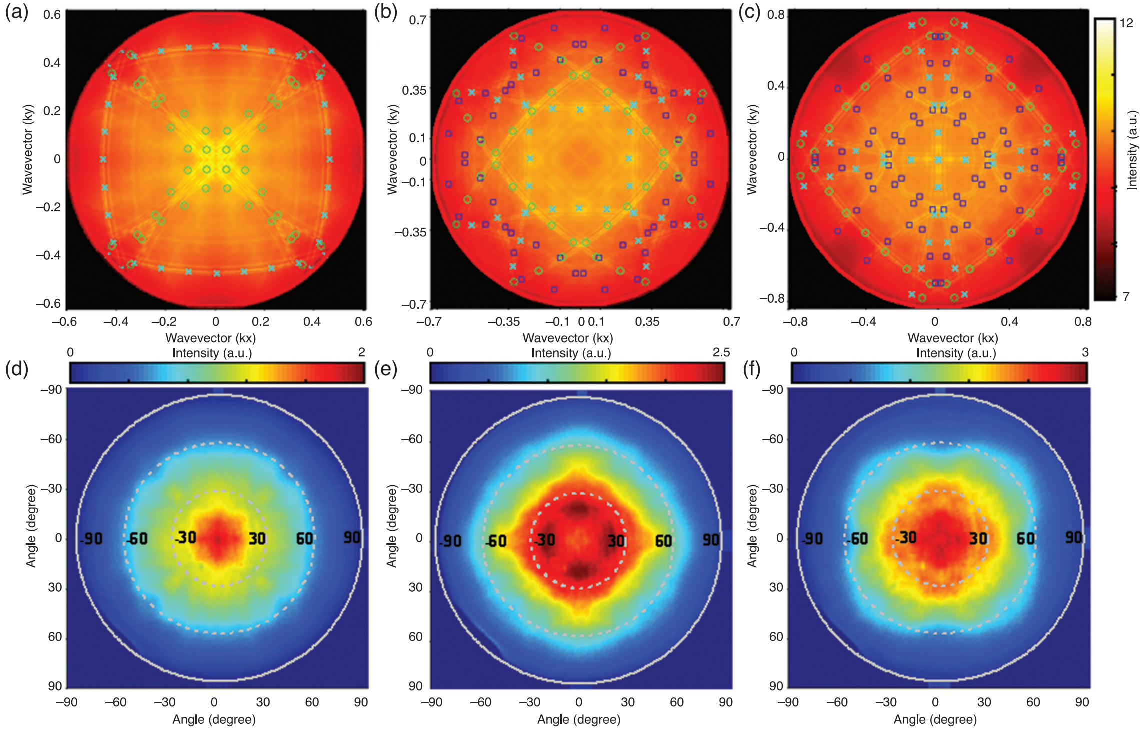

Plate V (Chapter 6) Intensity map of the extracted light at a fixed wavelength $\lambda = 470$ nm for (a) $a = 290$ nm, (b) $a = 350$ nm and (c) $a = 400$ nm. Symbols show values calculated using Bragg's diffraction theory fitted with effective refractive index $n_{\mathrm{eff}} = 2.414$ (cyan crosses for the ΓX direction, green circles for the ΓM direction and blue squares for the ΓXΓM direction). Top view of 3D far-field pattern for (d) $a = 290$ nm, (e) $a = 350$ nm and (f) $a = 400$ nm.

5

Phosphors for white LEDs

H. YAMAMOTO, formerly of Tokyo University
of Technology, Japan and T. YAMAMOTO,
Ajinomoto Pharmaceuticals Co, Ltd, Japan

DOI: 10.1533/9780857099303.1.144

Abstract: White light-emitting diodes (LEDs) are an innovative light source composed of a blue- or violet-emitting diode covered with a phosphor, which converts blue or violet light to yellow or other visible light. They are more efficient than conventional light sources. This chapter reviews the structure of white LEDs and the properties required for the phosphor. The optical transitions of Ce^{3+} and Eu^{2+} and the compounds activated by them are discussed. The chemical composition, crystal structure and optical transitions of some nitride and oxynitride phosphors are described.

Key words: white LED, phosphor, cerium, europium, nitride, oxynitride.

5.1 Introduction

5.1.1 Impact of white LEDs on society

The white light-emitting diode (LED) was an innovative light source composed of a blue- or violet-emitting diode covered with a phosphor, which converts blue or violet light to yellow or other visible light. The most popular type is a combination of a blue LED and a yellow phosphor, which is usually a compound based on $Y_3Al_5O_{12}:Ce^{3+}$. Since they were invented in the 1990s, white LEDs have made remarkable progress in luminescence efficiency, particularly in producing more light from blue LEDs. The highest luminous efficiency so far reported is 197 lm/W for laboratory samples (Bando, 2010) and 150 lm/W for manufactured products. These values are by far higher than the 30 lm/W for incandescent lamps, and are even higher than the 80–100 lm/W for fluorescent lamps. The all-solid-state structure of white LEDs means they last much longer than any conventional lamp bulbs. In addition, in contrast to fluorescent lamps, which use a mercury vapour discharge, white LEDs contain no toxic elements. These advantages enable us to save some of the energy used for lighting, which contributes to a reduction of CO_2 emissions, while keeping our environment clean and safe.

The use of white LEDs has expanded into various fields. Initially, they were used as point light sources such as for a flash lamp or a spotlight. Their compact size soon meant they were used in large numbers as liquid crystal backlighting for cellular phones. Medical applications of LEDs have utilized their light weight and compact size, first as head-mounted lamps for doctors and then as small light sources for endoscopes. An increase in the efficiency and input power has made it possible to use white LEDs for high-brightness light sources, e.g. street lighting or automobile headlamps. As fishing lamps, they do not need the oil traditionally used. Because they are compatible with incandescent lamps and fluorescent lamps, 'LED lamps' are easily used in homes and offices. In the last few years, white LEDs have been widely used as backlighting for liquid crystal TV displays in place of cold cathode fluorescent lamps. Currently, this application has the largest share of the whole market for white LEDs.

As mentioned above, white LEDs will play a more important role in the future. The phosphors are a key material in this new light source. In the last decade, nitride and oxynitride phosphors have emerged as a new group of materials that are suitable for white LEDs. This chapter describes the present status of these interesting and useful materials in comparison with conventional oxide or sulphide phosphors.

5.1.2 Structure of white LEDs

In most cases, a white LED is made from a blue LED covered with yellow phosphor powder dispersed in epoxy or silicone resin (Fig. 5.1). The most popular yellow phosphor is $(Y,Gd)_3Al_5O_{12}:Ce^{3+}$, because the partial substitution of yttrium with gadolinium shifts the luminescence band of Ce^{3+} to longer wavelengths and improves the colour rendering index compared with $Y_3Al_5O_{12}:Ce^{3+}$.

In spite of these improvements, the combination of blue and yellow emissions produces a cool white colour sometimes called 'pseudo-white', because its correlated colour temperature (CCT) is as high as 11 000–4600 K. To provide warm white emissions with a CCT of around 2500 K, a red or orange phosphor is added to the combination of blue and yellow. Sometimes another phosphor emitting green luminescence is added to improve the colour rendering.

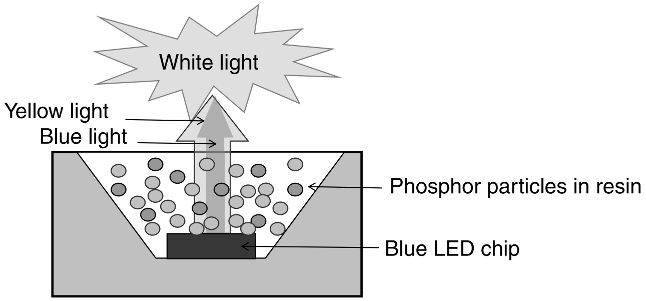

5.1 Cross section of a typical white LED.

5.1.3 Requirements for white-LED phosphors

Here we briefly describe the properties required for white-LED phosphors by considering the blue-light excitation at 450–460 nm. Needless to say, the first requirement for a phosphor is the strong absorption of blue light and subsequent emission of visible light at longer wavelengths from green to red. Not many conventional phosphors satisfy this requirement, because conventional applications of phosphors use an excitation energy much higher than blue light, e.g. from X-rays, cathode rays or UV light. We cannot use the fundamental absorption of a host crystal to absorb blue light, because a compound with a narrow band gap must include a toxic heavy element as one of its constituent elements. Instead, we can use an activator ion that absorbs blue light. We need an ion that has an allowed electronic transition in the blue region and efficiently emits luminescence by a reverse process. Eu^{2+} and Ce^{3+} are the only activator ions that have found practical use so far, though others, e.g. Eu^{3+}, Mn^{2+} and Mn^{4+}, have been investigated.

Preferably the absorption or excitation spectrum of the activator should be as flat as possible around the centre of the blue-LED emission, which is at 450–460 nm. This is because the emission spectrum of a blue LED may vary from lot to lot, if only slightly. If an activator has a narrow absorption band, its luminescence intensity will also depend on the wavelength of the blue-emission peak. If the variation in luminescence intensity is large, it will degrade the reproducibility of the white-light output. In this respect, Eu^{2+} is superior to Ce^{3+}, because the number of excited states is much larger for Eu^{2+} than for Ce^{3+}. The shape of the absorption band will broaden when an activator ion occupies more than one lattice site.

The temperature dependence of the luminescence efficiency is also important, because the temperature of an LED increases to up to 150 °C under operation. The heating of an LED occurs because a relatively high current, e.g. 0.3 mA, flows through a small emitting area, typically about 0.3 mm in diameter. The temperature is particularly high for high-power LEDs. Accordingly it is necessary for a phosphor to maintain high luminescence efficiency at temperatures as high as 150 °C or even higher.

Degradation of the luminescence intensity under operation can be a serious issue. Some phosphors react with moisture from the air that penetrates through the resin in which the phosphor is embedded. This results in a decrease in the luminescence efficiency of the surface layer. Typical examples are $CaS{:}Eu^{2+}$ and other sulphides, and $Ba_3SiO_5{:}Eu^{2+}$ and other silicates. Under intense light irradiation and at a high operating temperature, photoionization of Eu^{2+} can occur, reducing the concentration of Eu^{2+} ions. Materials resistant to such severe conditions are required for heavy-loading LEDs.

5.2 Optical transitions of Ce^{3+} and Eu^{2+}

To help in explaining luminescence properties, here we describe the electronic transitions for the most important activators for white-LED phosphors: Ce^{3+} and

Eu^{2+}. Both ions absorb light by the promotion of a 4 f electron to a 5 d state and emit light by a reverse process, as the electron returns from the lowest 5 d state to a 4 f energy level. These are allowed transitions with strong light absorption and a fast decay time. The strong absorption leads to high luminescence output. The fast decay time, a few nanoseconds for Ce^{3+} and a few microseconds for Eu^{2+}, keeps the luminescence efficiency high, even at high excitation density, without saturation.

5.2.1 Physical factors in a host crystal affecting the optical transition energies of Ce^{3+}

We will discuss mainly Ce^{3+}, because Ce^{3+} has a single 4 f electron and simple 5 d energy levels, as shown schematically in Fig. 5.2. A Ce^{3+} ion has two 4 f levels, denoted as $^2F_{5/2}$ and $^2F_{7/2}$, corresponding to whether the orbital and spin angular momenta are anti-parallel or parallel, respectively. The two levels are separated in energy by 0.27 eV or 2.2×10^3 cm^{-1}. This separation is inherent to a 4 f electron in Ce^{3+} and does not change because of the electrostatic forces from other ions in a crystal, because a 4 f electron is fully shielded from external forces by the outer $(5\,s)^2(5\,p)^6$ closed shell.

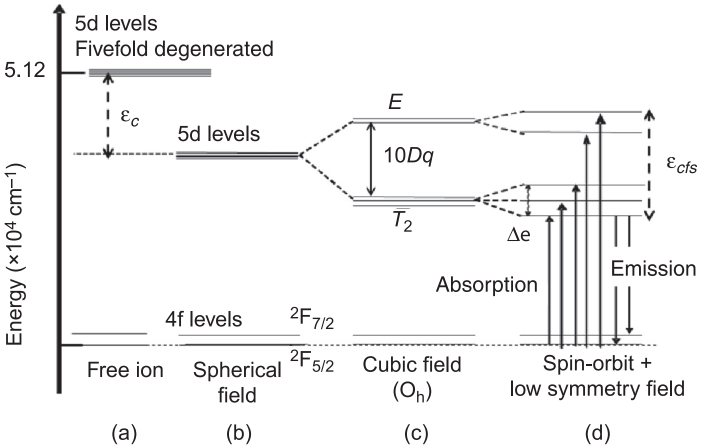
5d levels
Fivefold degenerated
5.12
ε_c
5d levels
E
10Dq
T_2
ε_{cfs}
Δe
Absorption
Emission
Energy (×10^4 cm^{-1})
4f levels
$^2F_{7/2}$
$^2F_{5/2}$
Free ion
Spherical field
Cubic field (O_h)
Spin-orbit + low symmetry field
(a)
(b)
(c)
(d)

5.2 Energy level diagram for Ce^{3+}: (a) as a free ion, (b) at a lattice site with a hypothetical spherical field, (c) at a lattice site with a cubic field and (d) in a crystal field with a cubic field perturbed by an axial field and a spin-orbit interaction. The notation 10*Dq* represents the energy splitting of the fivefold degenerate 5 d levels by the cubic crystal-field potential. $\Delta\varepsilon$ is the energy splitting of the threefold degenerate levels by the axial crystal-field and the spin-orbit interaction. The difference in the energy between the 5 d levels in the spherical field (b) and the free-ion state (a) is ε_c. The energy width of the 5 d levels in (d) is ε_{cfs}.

The energy levels of Ce^{3+} in $Y_3Al_5O_{12}$ were discussed by Blasse and Bril in 1967 and a unified understanding of the Ce^{3+} energy levels in different crystals was presented by Dorenbos (2002). The five 5 d orbitals are degenerate when a Ce^{3+} ion is not affected by any external forces or it is in a gas state, as shown in Fig. 5.2(a). When Ce^{3+} is incorporated into a crystal (Fig 5.2(b)), the energy of the 5 d levels is lowered as a result of the total electrostatic forces from all the ions other than Ce^{3+}. The decrease in the energy, known as the centroid (barycentre) shift, is shown as ε_c in Fig. 5.2 (Dorenbos, 2000). This is due to the stabilization of a Ce^{3+} ion doped in a host crystal. When the chemical bond between a Ce^{3+} ion and an anion has high covalency, the 5 d orbital is spatially expanded. In other words, the charge density of the 5 d electron is lower and the electrostatic interaction with the anions reduces. It is thought that this expansion of the electron cloud decreases the 5 d barycenter energy, and allows optical transitions at low photon energy. This 'nephelauxetic effect' is believed to work in nitride and oxynitride phosphors, which absorb in the blue region.

In contrast to the gas sate, a crystal imposes electrostatic forces on Ce^{3+}. There is some symmetry because of the atomic arrangement around Ce^{3+}. A non-spherical distribution of the electrostatic potential lifts the degeneracy of the 5 d levels. Under the highest symmetry, the cubic symmetry O_h, the 5 d energy levels split into two components; the lower are threefold and the upper are twofold degenerate as shown in Fig. 5.2(c). The weighted barycenter of the 5 d levels is constant if the electrostatic potential of the ions around Ce^{3+} or the crystal field is approximated as a perturbation to the original potential of a 5 d electron. The energy difference between the two components is called the crystal-field splitting and is denoted as $10Dq$. Here q is a constant proportional to the electron charge e and is independent of the cation-anion distance R. For a cation coordinated with six anions of atomic number Z in the form of an octahedron (point symmetry O_h), D is defined as follows within the framework of the point-charge model:

$$D = 35Ze/4R^5 \qquad [5.1]$$

This expression shows that the crystal-field splitting depends primarily on the cation-anion distance R. Decreasing the bond length leads to a decrease in the energy of the lowest 5 d level. When the symmetry is lowered by an additional, weaker potential with an axial or distorted form, the degeneracy is further lifted giving rise to a maximum of five levels. The energy splitting of the three 5 d levels caused by the additional potential is shown as ε in Fig. 5.2(d). Spin-orbit coupling also perturbs the potential of a 5 d electron, slightly splitting the energy levels.

Light is absorbed by transitions from the lowest energy level, $^2F_{5/2}$, to all the 5 d levels. In many host crystals, the energy of a photon absorbed by Ce^{3+} is in the UV region. An exceptional case is $Y_3Al_5O_{12}$ and other oxides with the garnet-type structure, which can absorb blue light. The reason for the absorption and emission red-shift of Ce^{3+} in the garnet-type crystals is still being debated, but it has been experimentally shown that the lowest 5 d level is lowered by the distorted oxygen

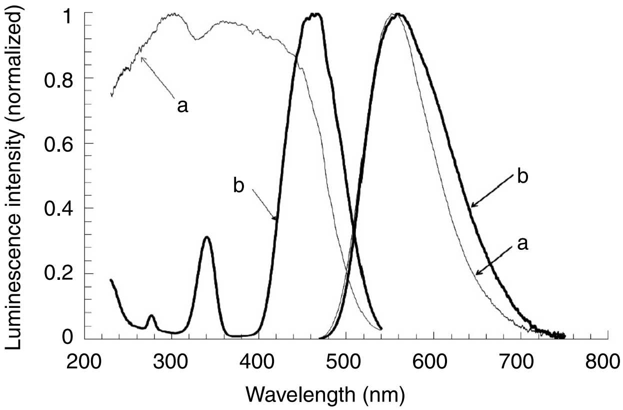

5.3 Luminescence and excitation spectra of (a) $(Sr_{0.75}Ba_{0.25})_2SiO_4:Eu^{2+}$ and (b) $(Y_{0.75}Gd_{0.25})_3Al_5O_{12}:Ce^{3+}$ at room temperature. The luminescence was excited by 460 nm light and the excitation spectrum was monitored at the wavelength for the maximum luminescence intensity.

arrangement around the Y^{3+} site where Ce^{3+} is situated (Wu *et al.*, 2007). This means that the energy splitting, ε, is large.

Luminescence occurs from the lowest excited state to the two ground state levels, $^2F_{5/2}$ and $^2F_{7/2}$. Accordingly a luminescence spectrum is composed of two bands separated in energy by 0.27 eV. These electronic transitions are associated with phonon emission processes, which enhance the intensity at lower photon energy or at the long wavelength side. Luminescence and excitation spectra of $Y_3Al_5O_{12}:Ce^{3+}$ are shown in Fig. 5.3 together with those of $(Sr,Ba)_2SiO_4:Eu^{2+}$, an example of an Eu^{2+}-activated phosphor.

5.2.2 Optical transitions of Eu^{2+}

In an Eu^{2+} ion, the 5 d state can be split at most into five levels, as is the case with Ce^{3+}, but each excited state is further split into many sublevels, because each ^7F_J state of the $4f^6$ configuration, which remains after one of the seven 4 f electrons is promoted, has $2J+1$ components with different orbital angular momenta. There are 49 sublevels, given by the summation of $2J+1$ for $J=0, 1, \ldots, 6$. Such a large number of states causes broadening of each absorption band compared with Ce^{3+}. Detailed energy levels were given by Weakliem (1972).

5.3 Chemical composition of representative nitride and oxynitride phosphors

Binary nitrides, AlN, GaN and InN, and their solid solutions have been used widely for light-emitting diodes and semiconductor lasers. One might expect that these binary nitrides could work also as phosphors for photon or cathode-ray excitation. In fact, GaN:Zn was investigated as a blue-emitting phosphor for low-energy electron excitation (Sato *et al.*, 2002; Li *et al.*, 2008a). It is preferable, however, to incorporate an activator ion, such as a rare-earth or a transition-metal ion, into a host crystal to provide a variety of emission colours with high efficiency and high reliability. Materials with such a chemical composition, i.e. multinary nitrides or oxynitrides having a cation or a vacant site, which accommodates an activator ion, have proved to be excellent phosphors for white LED applications. In the subsequent sections, we explain the performance of these compounds by presenting the chemical compositions, crystal structures and luminescence properties.

The nitride phosphors so far developed are based on Si_3N_4 and/or AlN in combination with nitrides of alkaline-earth elements or yttrium, lanthanum or gadolinium atoms. They are formally known as imido-(alumina-)silicates or oxoimido-(alumino)silicates. A zinc imido-silicate phosphor, $ZnSiN_2$:Mn^{2+}, was also reported (Uheda *et al.*, 2001). The long expression ‘imido-silicates and oxoimido-silicates’ will be abbreviated as ‘(oxo)imido-silicates’.

In some cases, an oxoimido-silicate can be derived from an aluminate by cross-substitution of an (Al,O) pair with (Si,N) or from an imido-silicate by cross-substitution of a (Si,N) pair with (Al,O). An example of the former is the conversion of $SrAl_2O_4$:Eu^{2+} to $SrAl_{2+x}O_{4-x}N_x$:Eu^{2+} (Li *et al.*, 2006a). An example of the latter is the formation of β-sialon or $Si_{6-x}Al_xO_xN_{8-x}$ from β-Si_3N_4.

There is considered to be significant potential in a combination of cations and nitrogen/oxygen. Accordingly, (oxo)imido-silicates form a rich group of new compounds. Here we tentatively classify them by focusing on an ion hosting an activator as listed below. Unless otherwise stated, the phosphors shown below can be excited by blue light. In this section, we give an overview of representative materials so far developed. Several good reviews have been published on (oxo) imido-silicate phosphors or phosphors for solid-state lighting (van Krevel, 2000; Xie and Hirosaki, 2007; Smet *et al.*, 2011; Xie *et al.*, 2011).

5.4 Compounds activated by Eu^{2+}

5.4.1 AE-Si-N (AE = Ca, Sr, Ba) compounds

$AESiN_2$ and $AE_2Si_5N_8$ in the AE_3N_2-Si_3N_4 system were described in the earliest period of nitride phosphor research. $AESiN_2$:Eu^{2+} produces orange to red luminescence with a peak around 630 nm for AE = Ca, 670–685 nm for AE = Sr and 600–630 nm for AE = Ba. A quantum efficiency of 40% and 25% relative to the efficiency of $Y_3Al_5O_{12}$:Ce^{3+} was reported for AE = Ba and Sr, respectively (Duan *et al.*, 2008).

Crystals of $Ca_2Si_5N_8$ have a monoclinic structure and belong to the space group Cc (No. 9) (Schlieper and Schnick, 1995), while those of $Sr_2Si_5N_8$ and $Ba_2Si_5N_8$

are orthorhombic with an identical space group of Pmn2_1 (No. 31) (Schlieper *et al.*, 1995). These compounds have two non-equivalent sites for alkaline-earth atoms. Since Eu^{2+} ions are located at the alkaline-earth sites, they show two luminescence bands, which overlap each other.

Luminescence and excitation spectra of $AE_2Si_5N_8:Eu^{2+}$ (AE = Ca, Sr or Ba) with europium concentration of 5 at% per AE site are shown in Fig. 5.4 (Li *et al.*, 2006b; Li and Hintzen, 2008). The luminescence spectra have peaks at 618, 628 and 638 nm for AE = Ca, Sr and Ba, respectively, and they have side bands at 678, 687 and 694 nm. Probably these two bands can be ascribed to the two europium sites. The luminescence colour is yellow to orange for AE = Ca and red to deep red for AE = Sr or Ba, depending on the europium concentration. The excitation spectra cover a broad range from 600 nm to UV with a broad maximum in the blue region. A phosphor based on $Sr_2Si_5N_8:Eu^{2+}$ has been used as a red component of white LEDs with high colour rendering. This phosphor has, however, the disadvantage that thermal quenching is larger than another red phosphor, $CaAlSiN_3:Eu^{2+}$. Note that, in most host crystals, the peak wavelength shifts to a longer wavelength with europium concentration.

In $SrSi_6N_8$, Eu^{2+} shows blue luminescence and excitation bands peak in the UV region. The luminescence and excitation spectra are at wavelengths shorter than

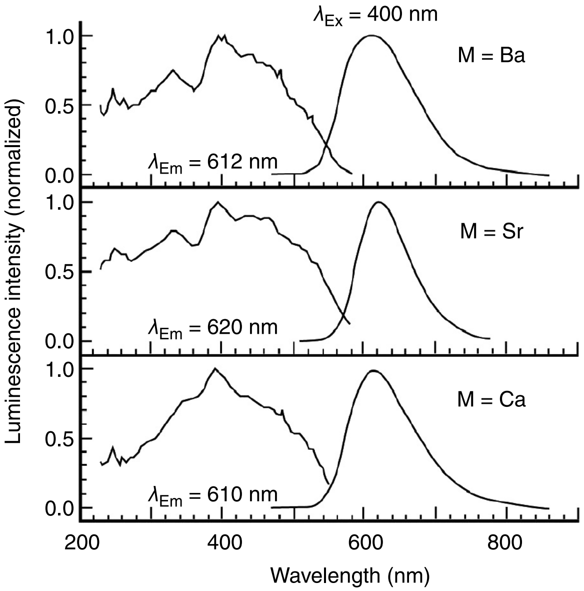

5.4 Luminescence and excitation spectra of $AE_2Si_5N_8:Eu^{2+}$ (AE = Ca, Sr or Ba) at room temperature. The europium concentration is 5 at.% per AE site. (Reproduced from Li and Hintzen (2008) by permission of the Illuminating Engineering Institute of Japan.)

those in other imido-silicates because of the weak crystal field at the strontium site, which is due to the relatively long bond lengths with nitrogen atoms. The strontium site in $SrSi_6N_8$ is tenfold coordinated by nitrogen atoms with an average bond length of 0.303 nm, which is longer than the average distance in Ca-α-sialon (0.2606 nm) or in $Ca_2Si_5N_8$ (0.2652–0.2708 nm) (Shioi *et al.*, 2008). The cyan luminescence of Eu^{2+} in $BaSi_7N_{10}$ is also considered to be due to the weak crystal field (Li *et al.*, 2009, 2010).

5.4.2 AE-Al-Si-N (AE = Ca, Sr) compounds

The synthesis and structure determination of $CaAlSiN_3$ were performed first by Ottinger (2004). The refinement of the lattice parameters was performed by Uheda *et al.* (2009) on a phase containing a small amount of oxygen.

Uheda *et al.* (2006) found that $CaAlSiN_3$:Eu^{2+} emits deep red luminescence efficiently by blue light excitation. The luminescence band shifts to longer wavelengths with an increase in europium concentration, but at the optimum concentration of about 1 at%, it has a peak at 650 nm. Typical luminescence and excitation spectra are shown in Fig. 5.5. It has high quantum efficiency (internal quantum efficiency ≈90%), low thermal quenching and high chemical stability. These advantages have made it almost the standard material both for general lighting and liquid-crystal backlighting.

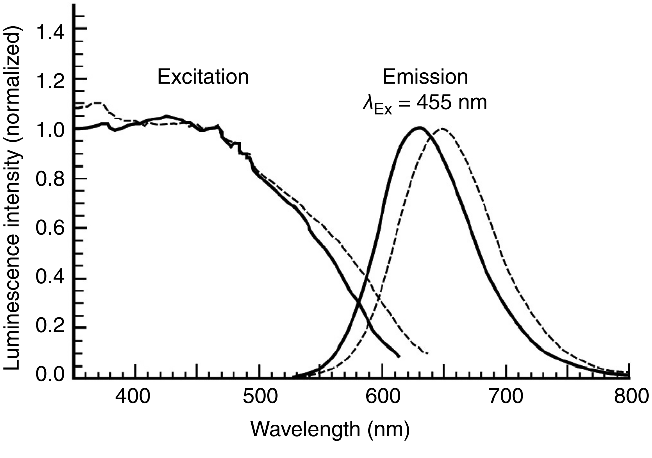

5.5 Luminescence and excitation spectra of $CaAlSiN_3$:Eu^{2+} (solid line) and $Sr_{0.8}Ca_{0.2}AlSiN_3$:Eu^{2+} (dotted line) at room temperature. The europium concentration is 0.8 at.% per calcium and strontium sites. The luminescence intensity is normalized at the maximum and the excitation intensity is normalized at 455 nm. (Reproduced from Watanabe *et al.* (2008) by permission of the Electrochemical Society.)

One can derive $CaAlSiN_3$ from AlN by replacing two-thirds of the aluminium with calcium and silicon. The crystal structure is distorted wurtzite, into which Ca^{2+} ions are stuffed (Fig. 5.6(a)). Tetrahedra of $(Al,Si)N_4$ form six-membered rings by sharing a vertex and the rings combine to form a plane, as illustrated in Fig. 5.6(b). A second plane that is a 180° rotation of the first plane is overlaid onto the first plane and the rings form channels. The channels formed in this way accommodate Ca^{2+} ions, which are partly replaced by Eu^{2+} ions. Silicon and aluminium atoms are distributed randomly at a single crystallographic site. Two-thirds of the nitrogen atoms are bonded to three silicon atoms, whereas the remaining one-third is coordinated with two silicon atoms. The network made by the three-coordinated nitrogen atoms forms a rigid structure, giving rise to mechanical hardness and the low thermal quenching of the luminescence. The Ca^{2+} site is coordinated by four nitrogen atoms at the first nearest neighbour and another nitrogen atom is located slightly further away, as shown in Fig. 5.7 (Uheda *et al.*, 2006, 2009). This low-symmetry coordination around Eu^{2+} is unusual, because Eu^{2+} ions are sixfold coordinated in many crystals.

The luminescence band of $CaAlSiN_3$:Eu^{2+} extends to the infrared region. As a result, its luminous efficiency is decreased, though the light output power is high. Substitution of calcium with strontium shifts the luminescence band to shorter wavelengths, improving the luminous efficiency. Unfortunately, under the synthesis conditions for $CaAlSiN_3$:Eu^{2+}, i.e. 0.9 MPa N_2 at 1800 °C, the solubility of strontium is limited to about 50%. Above this strontium fraction, the

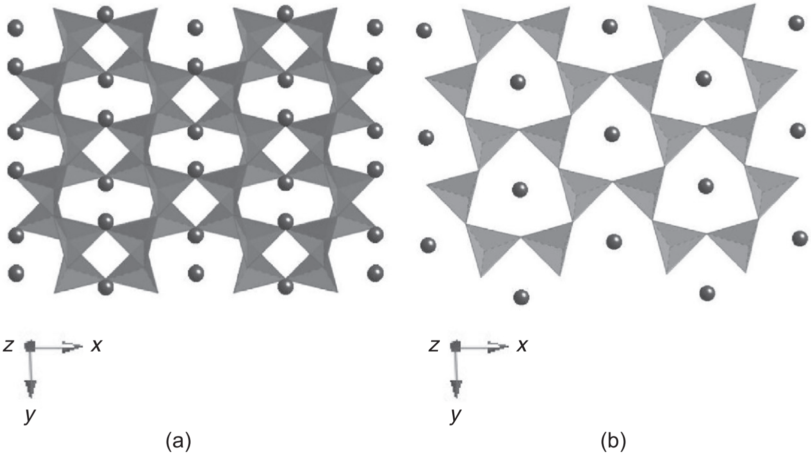

5.6 The crystal structure of $CaAlSiN_3$. The dark tetrahedra are [(Al,Si) N_4] and the small balls are calcium atoms. (a) Projection onto the *xy* plane and (b) the [(Al,Si)N_4] tetrahedra form six-membered rings on a plane parallel to the *xy* plane. (Reproduced from Uheda *et al.* (2006) by permission of the Electrochemical Society.)

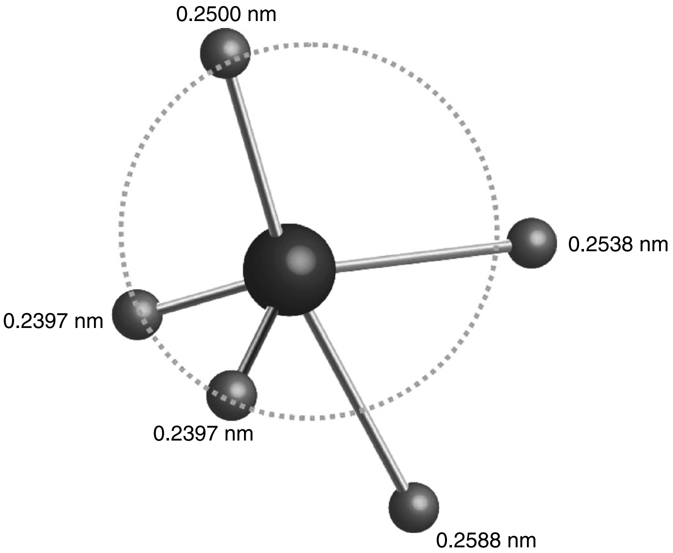

5.7 Local coordination around calcium atom in $CaAlSiN_3$.

$(Ca,Sr)_2Si_5N_8$ phase forms as a secondary phase and near a strontium fraction of 1.0, only the $Sr_2Si_5N_8$ phase forms. In other words, $SrAlSiN_3$ is less stable than $Sr_2Si_5N_8$. To overcome this difficulty, Watanabe *et al.* (2008) developed a new synthesis method starting from alloys of calcium, strontium, silicon and europium metals. The synthesis temperature and pressure are elevated, up to 1900 °C and 190 MPa. The obtained samples of $(Ca,Sr)AlSiN_3:Eu^{2+}$ indeed show a luminescence band shifted to shorter wavelengths. Figure 5.5 compares the luminescence spectrum of $(Ca_{0.2},Sr_{0.792}Eu_{0.008})AlSiN_3$ with that of $(Ca_{0.992}Eu_{0.008})AlSiN_3$. The luminescence peak becomes shifted from 648 nm to 627 nm by strontium substitution of nearly 80 mol%. The luminescence intensity has the same magnitude for both materials, but a portion at wavelengths longer than 700 nm is smaller for $(Ca_{0.2},Sr_{0.792}Eu_{0.008})AlSiN_3$. Accordingly, a luminous efficiency nearly twice that of $(Ca_{0.992}Eu_{0.008})AlSiN_3$ was obtained. The CIE colour coordinates shift from $x=0.66$, $y=0.33$ for a strontium fraction of 0.2 to $x=0.61$, $y=0.38$ for a strontium fraction of 0.9. Compared with $(Ca_{0.992}Eu_{0.008})AlSiN_3$, the excitation spectrum of $(Ca_{0.2},Sr_{0.792}Eu_{0.008})AlSiN_3$ is similar in shape in the blue region, but the tail above 500 nm shifts to shorter wavelengths with increasing strontium fraction (Fig. 5.5).

Other members of the Ca_3N_2-AlN-Si_3N_4 system are shown in Fig. 5.8, together with AE-Si-N compounds. Interestingly, new red-emitting materials beside $CaAlSiN_3:Eu^{2+}$ were discovered in this group and also in analogous strontium compounds. $SrAlSi_4N_7:Eu^{2+}$ emits red luminescence with a peak at 640 nm. It has

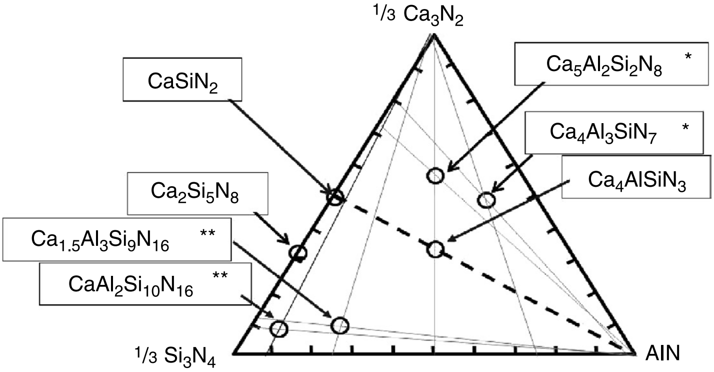

5.8 Reported phases in the Ca_3N_2-AlN-Si_3N_4 system. The symbols * and ** mean that the compounds were reported by Ottinger (2004) and van Krevel *et al.* (2002), respectively.

a highly condensed network of [SiN_4] tetrahedra, because some of the tetrahedra are connected by edge-sharing (Hecht *et al.*, 2009). Another red phosphor, $Sr_2Al_3Si_7ON_{13}$:Eu^{2+} (Fukuda and Matsuda, 2010) is derived from $SrAlSi_4N_7$:Eu^{2+} by cross-substitution of 1/2(Si,N) by 1/2(Al,O).

Li *et al.* (2004) determined the crystal structure of $SrYSi_4N_7$ and the luminescence properties of this material when activated by Eu^{2+} or Ce^{3+}. The luminescence band of Eu^{2+} has a peak around 550 nm at the optimum europium concentration of 5 at%. The excitation spectrum covers a broad range from 230 to 450 nm. The Ce^{3+}-activated material shows blue luminescence with a peak at 450 nm composed of double bands characteristic of Ce^{3+} energy levels. It shows an excitation spectrum from 230 to 380 nm. In $SrRSi_4N_7$ (R = Y, Yb), some nitrogen atoms are coordinated with four silicon atoms. In other words, four [SiN_4] tetrahedra are joined together at a single vertex (Fig. 5.9). This unique coordination makes it possible to carbonize this compound. Duan *et al.* (2011) formed $RE_2Si_4N_6C$ (RE = Lu, Y or Gd) activated by Ce^{3+}, Tb^{3+} and their combination.

$Ba_2AlSi_5N_9$:Eu^{2+} has a luminescence band, which peaks at 584 nm. The full width at half maximum (FWHM) is as large as 100 nm, because Eu^{2+} ions substitute eight non-equivalent barium sites (Kechele *et al.*, 2009a).

5.4.3 Si-Al-O-N compounds – Ca-α-sialon:Eu^{2+} and β-sialon:Eu^{2+}

The host crystals of new and important phosphors, α- and β-sialon, are derived by cross-substitution of (Si,N) with (Al,O) in α- and β-Si_3N_4, respectively. The chemical formula of β-sialon is $Si_{6-z}Al_zO_zN_{8-z}$ with $0<z<4.2$. Although it is

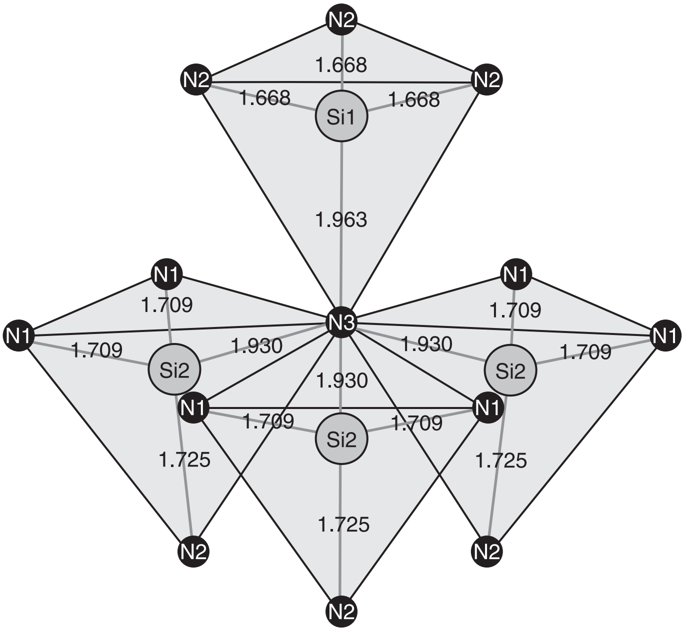

5.9 Nitrogen atom coordinated with four silicon atoms in $SrYSi_4N_7$. (Reproduced from Li *et al.* (2004) by permission of Elsevier BV.)

difficult to incorporate foreign cations into β-sialon, Hirosaki *et al.* (2005) found that addition of Eu^{2+} leads to bright green luminescence. By Rietveld refinement of X-ray diffraction analysis, Li *et al.* (2008b) predicted that Eu^{2+} ions are located at interstitial sites in the open channels running along the *c*-axis of the hexagonal lattice of β-sialon. This was supported by direct observation of the atomic arrangement by scanning transmission electron microscopy (Kimoto *et al.*, 2009). Figure 5.10 shows the crystal structure viewed along the *c*- axis of β-sialon. The interstitial positions, where Eu^{2+} can be incorporated are shown by dark spheres. Li writing in Xie *et al.* (2011:220) estimated the Eu^{2+} position along the *c*-axis using a total energy calculation and concluded that the (0,0,0) or (0,0,0.5) site in the β-Si_3N_4 lattice is most favourable. The channel widens at these positions, since it is formed by six-membered rings of $[(Al,Si)N_4]$ tetrahedra. Since Eu^{2+} ions are squeezed into the narrow channels, the solubility limit of europium is low and depends on the composition. The optimum europium concentration is about 0.3 mol%. The excess positive charge of Eu^{2+} is balanced by a decrease in the aluminium content and an increase in the oxygen content. Accordingly, the general formula of europium-doped β-sialon is $Eu_xSi_{6-z}Al_{z-x}O_{z+x}N_{8-z-x}$.

Excitation and luminescence spectra of β-sialon:Eu^{2+} are shown in Fig. 5.11. The peak of the luminescence band ranges from 527 to 550 nm for $z = 0.1$ to 2.0

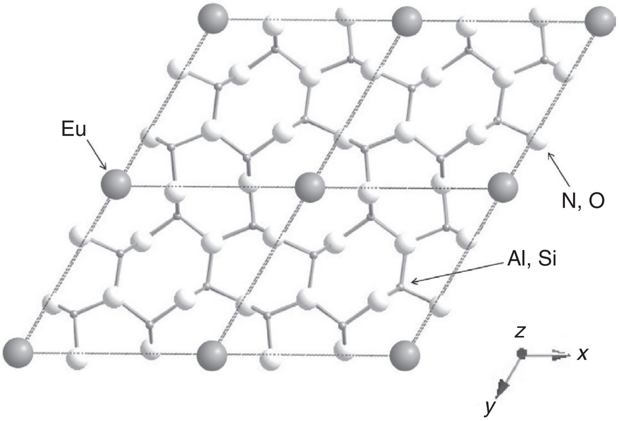

5.10 Crystal structure of β-sialon viewed along the *c*-axis. Europium atoms are located at interstitial positions in the channels. Not all the positions shown are occupied by Eu^{2+}.

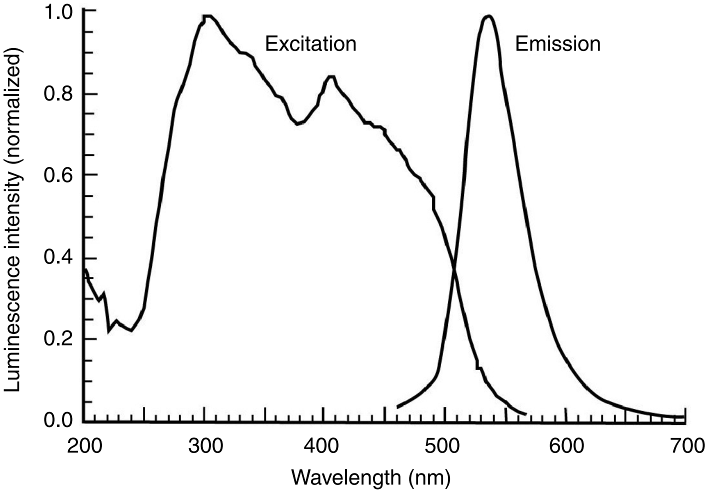

5.11 Typical excitation and luminescence spectra of β-sialon:Eu^{2+} at room temperature. The fraction of oxygen $z=0.5$ and the Eu^{2+} concentration is 0.3 at.%. The luminescence band has a peak at 538 nm. (Reproduced from Xie and Hirosaki (2007) by permission of Elsevier BV.)

(Xie *et al.*, 2007b). The luminescence band has an asymmetric shape with a tail at long wavelengths. Recently Hirosaki *et al.* (2012) improved the colour purity of the luminescence by decreasing this tail, which was achieved by reducing the oxygen content to $z=0.025$. They found that some of the oxygen was introduced

Table 5.1 Green phosphors with narrow bandwidth

Phosphors	Luminescence peak wavelength (nm)	Bandwidth (nm, (eV))	External quantum efficiency[a]	References
β-sialon:Eu^{2+}	527–550	55 (0.24)	50	Xie and Hirosaki, 2007b
$Ba_3Si_6O_{12}N_2$:Eu^{2+}	525	67 (0.31)	64	Uheda *et al.*, 2007
$Sr_3Si_{13}Al_3O_2N_{21}$:Eu^{2+}	515–520	66 (0.31)	67	Fukuda *et al.*, 2009
Zn_2SiO_4:Mn^{2+} (UV excitation)	525	42 (0.19)	67	Ohkubo and Shigeta, 1999

Note: [a] Under 450–460 nm excitation except for Zn_2SiO_4:Mn^{2+}, which was excited by 254 nm light.

through oxygen impurities in Si_3N_4, one of the starting materials, and replaced it by metallic silicon. Compared with other green-emitting phosphors, which can be excited by blue light, the luminescence spectrum has a relatively narrow bandwidth. This luminescence spectrum is favourable for the backlighting for liquid crystal displays, because absorption loss can be minimized using a green colour filter with a band-shaped transmission spectrum. The luminescence properties of three oxynitride phosphors are shown in Table 5.1, together with Zn_2SiO_4:Mn^{2+}, which is used for fluorescent lamps. Possible reasons for the narrow bandwidth of β-sialon:Eu^{2+} may be the low concentration of europium incorporated into the β-sialon lattice and the weak electron–phonon interaction. The narrow bandwidth of the Mn^{2+} emission in Zn_2SiO_4:Mn^{2+} is necessary for the green phosphors used for backlighting. The phosphor β-sialon:Eu^{2+} has another advantage that thermal quenching is low because of its rigid crystal lattice.

The crystal structure of α-sialon has a relatively large cage formed by the network of $[(Al,Si)(N,O)_4]$ tetrahedra. Many investigations on sintering agents for α-sialon ceramics have shown that the cage can accommodate cations with a small ionic radius, i.e. Li^+, Mg^{2+}, Ca^{2+}, Y^{3+} and other lanthanide ions except for La^{3+} and Ce^{3+}. The unit cell of α-sialon projected along the c-axis is shown in Fig. 5.12. The cage accommodates two Ca^{2+} ions. The general formula of α-sialon is given by $Me_xSi_{12-m-n}Al_{m+n}O_nN_{16-n}$, where the solubility of the metal Me is given by $x = m/v$ with v being the valence of the metal. There are two interstitial sites per unit cell with coordinates $(1/3, 2/3, z)$ and $(2/3, 1/3, z + 1/2)$ where $z = 0.228$, which limits the solubility of the metal. For Me = Ca, the occupancy factor for each site was found to be 0.339. An activator, Eu^{2+}, substitutes for some of the Ca^{2+} ions and emits bright yellow luminescence. The luminescence intensity depends on the

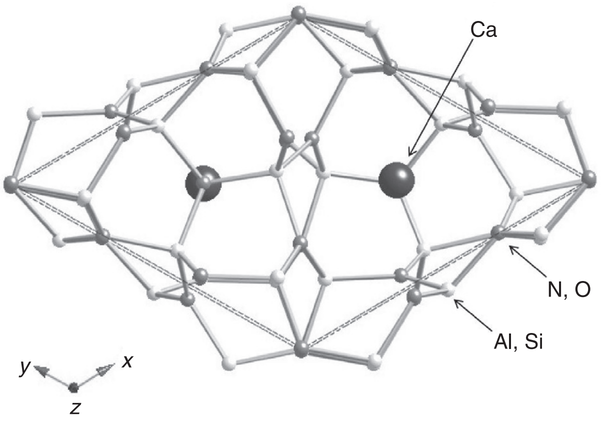

5.12 Crystal structure of Ca-α-sialon viewed along the *c*-axis. Calcium atoms are located at interstitial positions in the channels.

solubility of calcium, *m*, and the europium concentration. The optimum value is $m = 2$ with a europium concentration per calcium ion of 7.5 at%.

The excitation and luminescence spectra of α-sialon:Eu^{2+} are shown in Fig. 5.13. As seen in the excitation spectrum, this phosphor has high luminescence output by 450–460 nm light excitation. Its yellow luminescence has high

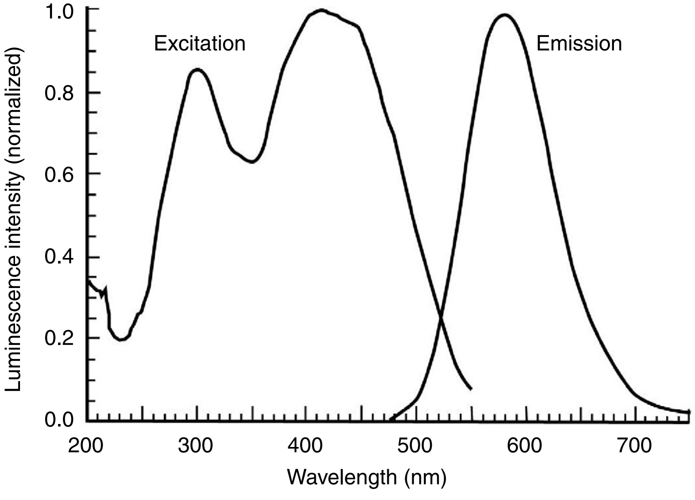

5.13 Typical excitation and luminescence spectra of Ca-α-sialon:Eu^{2+} at room temperature. The composition of the sample was $Ca_{0.925}Eu_{0.075}Si_9Al_3ON_{15}$. The excitation spectrum was measured at a monitoring wavelength of 581 nm and the luminescence was excited by 420 nm light. (Reproduced from Xie and Hirosaki (2007) by permission of Elsevier BV.)

efficiency, which is comparable to the $Y_3Al_5O_{12}$:Ce^{3+} system and maintains high intensity at temperatures above room temperature.

5.4.4 Sr-sialon or $SrSi_{10-x}Al_{18+x}N_{32-x}O_x$ ($x \approx 0$)

As described above, the Sr^{2+} ion has a large ionic radius, 0.118 nm for six-coordination, and so it cannot be incorporated into an α- or β-sialon lattice. However, strontium-containing polytypoid phases with the general formula $SrSi_{10-x}Al_{18+x}N_{32-x}O_x$ ($x \approx 0$) have been found in the Sr-Si-Al-O-N system. They are called Sr-sialon. The structural model elucidated by high-resolution transmission electron microscopy (HRTEM) is shown in Fig. 5.14 (Grins *et al.*, 1999). Sr^{2+} ions are located at open spaces created by two $[SiX_4]$ layers (X = O, N) with inverse polarity, which are connected at oxygen vertices. These layers are alternately interleaved normally between eight AlN-type layers, which change polarity at the middle of the block. Based on this model, such phases form a homologous series represented by $(SrM_4X_5)(M_6X_9)(M_3X_3)_{n-2}$, where M = Si or Al, X = N or O and *n* is the number of layers between the SrM_4X_5 regions. An activator

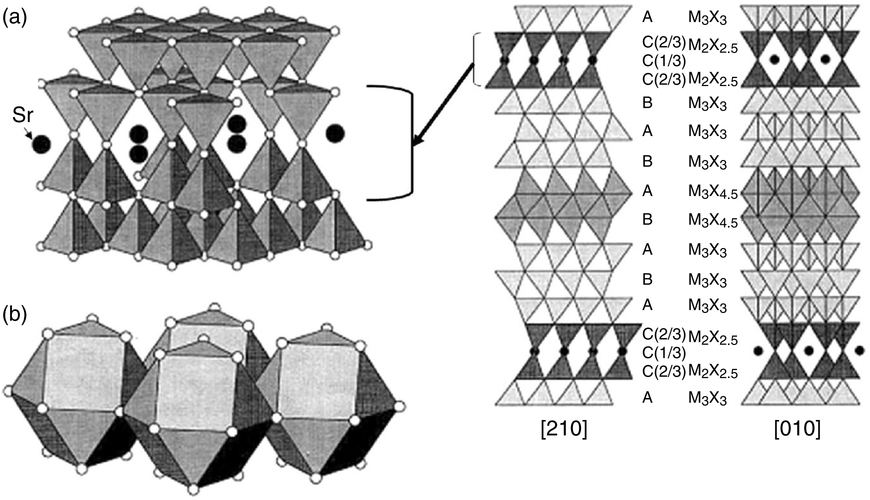

5.14 Right: crystal structure of Sr-containing sialon viewed along the [210] and [010] directions. The strontium atoms are shown by filled circles. M = Si or Al and X = N or O atoms. Left: The three-layer ($Si_2X_{2.5}$–SrX–$Si_2X_{2.5}$) region containing strontium is magnified in (a). The polarity of $[SiX_4]$ tetrahedra is reversed at the vertices occupied by oxygen atoms and forms a space. Strontium atoms are accommodated in this space. The anion atoms directly coordinated with strontium form cubo-octahedra as illustrated in (b). (Reproduced from Grins *et al.* (1999) by permission of Elsevier BV.)

Eu^{2+} substitutes for Sr^{2+} giving rise to blue luminescence under UV or cathode-ray excitation (Fukuda *et al.*, 2006).

Hirosaki *et al.* (2007) found that $AlN:Eu^{2+}$ has a blue luminescence band characteristic of divalent europium, which peaks at 461–465 nm, under UV or cathode-ray excitation. The internal quantum efficiency, external quantum efficiency and absorption efficiency are 76%, 46% and 63%, respectively, under 365 nm excitation (Inoue *et al.*, 2009). The introduction of as much as 2.2 mol% silicon is essential to the solid solution of Eu^{2+} ions, the formation of phase-pure $AlN:Eu^{2+}$ and the increased blue luminescence (Inoue *et al.*, 2009). A chemical composition determined by chemical analysis shows a low concentration of europium and silicon, e.g. $Eu_{0.0028}Si_{0.0308}Al_{0.958}O_{0.0020}N_{1.06}$ (Hirosaki *et al.*, 2007). For this reason, the formula is also written as $AlN:Eu^{2+},Si$. Transmission electron microscopy–energy dispersion X-ray spectroscopy (TEM-EDS) and high angle annular dark field scanning electron microscopy (HAADF-STEM) analysis revealed the distribution of the elements in the samples. It was directly observed that europium ions stay in a single layer with silicon precipitation. This structure is similar to the model of Sr-sialon proposed by Grins *et al.* (1999), though the spacing of the layers containing europium and silicon is not regular in $AlN:Eu^{2+},Si$ (Takeda *et al.*, 2010). In most Eu^{2+}-activated nitrides, luminescence appears at wavelengths longer than blue as a consequence of the covalency or nephelauxetic effect. Regarding the blue luminescence of $AlN:Eu^{2+},Si$, the bond between an Eu^{2+} ion and the nearest-neighbour anions is as long as 0.315(8) nm. As with $SrSi_6N_8$ and $BaSi_7N_{10}$, the long bond distance will decrease the crystal-field strength around Eu^{2+}. Another possible reason may be selective coordination of oxygen impurities with Eu^{2+}, so that the Eu^{2+} bonds have a more ionic character. The role of oxygen atoms is not clear yet, however.

Fukuda *et al.* (2009) produced a green-emitting phosphor, $Sr_3Si_{13}Al_3O_2N_{21}:Eu^{2+}$, which does not belong to the Sr-sialon polytypoid group described above. This material has a layered orthorhombic structure having ten-coordinated Sr^{2+} sites with an average bond distance of 0.30 nm. It has an excitation spectrum covering the blue region and a narrow luminescence band peaking at 515 nm at 8 mol% europium. It has a high internal quantum efficiency of 75%. With such high performance, this green phosphor is suitable for the backlighting for liquid crystal displays.

5.4.5 AE-Si-O-N (AE = Ca, Sr, Ba) compounds

This group includes $AESi_2O_2N_2$ (AE = Ca, Sr, Ba), $Ba_3Si_6O_9N_4$ and $Ba_3Si_6O_{12}N_2$ activated by Eu^{2+}. They have in common an AE/Si atomic ratio of 1/2 and are expressed by the general formula: $AE_3Si_6O_{(3+3n)}N_{(8-2n)}:Eu^{2+}$ with $n = 1, 2$ or 3. All of them have layered crystal structures built of sheets formed by corner-shared $[Si(N,O)]_4$ tetrahedra, which are intervened by AE atoms. The crystal structures are, however, slightly different from each other as shown in Table 5.2 and Table 5.3.

Table 5.2 Crystal structures of $AESi_2O_2N_2$ (AE = Ca, Sr or Ba)

Composition	$CaSi_2O_2N_2$	$SrSi_2O_2N_2$	$BaSi_2O_2N_2$
Crystal system	Monoclinic	Triclinic	Orthorhombic
Space group	$P2_1$ (No. 40)	P1 (No. 1)	Cmcm (No. 63)
Reference	Höppe *et al.*, 2004	Oeckler *et al.*, 2007	Kechele *et al.*, 2009b

Table 5.3 Crystal structures of $Ba_3Si_6O_9N_4$ and $Ba_3Si_6O_{12}N_2$

Composition	$Ba_3Si_6O_9N_4$	$Ba_3Si_6O_{12}N_2$
Crystal system	Trigonal	Trigonal
Space group	P-3 (No. 143)	P-3 (No. 147)
Reference	Stadler and Schnick, 2006	Uheda *et al.*, 2007

The imido-silicate layers in $Ba_3Si_6O_9N_4$ ($n = 2$) and $Ba_3Si_6O_{12}N_2$ ($n = 3$) contain bridging oxygen atoms, $O^{[2]}$, while the layers in $AESi_2O_2N_2$ ($n = 1$) compounds are more condensed, because they are made only by the sharing of three-coordinated nitrogen atoms, $N^{[3]}$. The oxygen atoms terminate the bonds with silicon at one side and are coordinated to AE atoms on the other side. The arrangement of layers and AE atoms in $AESi_2O_2N_2$ crystals is shown in Fig. 5.15, with the local coordination around AE atoms.

$Ba_3Si_6O_{12}N_2:Eu^{2+}$ is a green phosphor with a narrow luminescence bandwidth, which matches well with the transmittance spectrum of a green filter for LCD backlighting (Uheda *et al.*, 2007). It is one of the competitors of β-sialon:Eu^{2+} (Table 5.1). Excitation and luminescence spectra are shown in Fig. 5.16. In spite of its similar chemical composition and crystal structure, $Ba_3Si_6O_9N_4:Eu^{2+}$ has very low luminescence efficiency even at low temperatures.

The compounds, $AESi_2O_2N_2:Eu^{2+}$, show efficient luminescence: in yellow for calcium, in green for strontium and in blue-green for barium. Excitation and luminescence spectra of calcium, strontium and barium compounds are shown in Fig. 5.17 (Schmidt *et al*, 2008). Schmidt *et al.* (2008) produced a green LED using a green phosphor, $SrSi_2O_2N_2:Eu^{2+}$(2%), in combination with a violet LED emitting at 414 nm over $1 \times 1\ mm^2$. The performance of this LED was very stable over a wide range of drive current, up to 1 A, and temperature, up to 200 °C. For $SrSi_2O_2N_2:Eu^{2+}$(2%), a very high and stable internal quantum efficiency of 0.95 at 25 °C and 0.94 at 200 °C was reported.

The luminescence colour can be tuned by forming a solid solution between different AE compounds. Bachman *et al.* (2009a) systematically investigated colour tuning in $SrSi_2O_2N_2:Eu^{2+}$ (2 at%) by substitution of strontium with calcium or barium. One of their results is shown in Fig. 5.18. In either case, the emission colour shifts from green to yellowish with increased fraction of calcium or barium. This cannot be explained by the simple idea that expansion of the lattice causes a

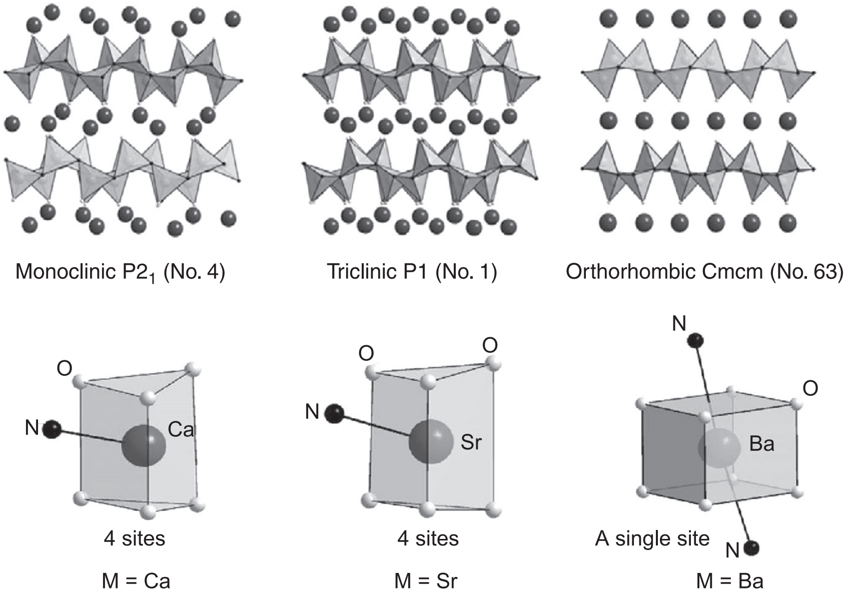
Monoclinic P2$_1$ (No. 4)
Triclinic P1 (No. 1)
Orthorhombic Cmcm (No. 63)
O
N
Ca
4 sites
M = Ca
O
O
N
Sr
4 sites
M = Sr
N
O
Ba
A single site
N
M = Ba

5.15 Layered structures of $AESi_2O_2N_2$ (AE = Ca, Sr or Ba) and the coordination arrangement around AE atoms. The large circles represent AE atoms and the tetrahedra are the $[SiN_3O]$ groups. The nearest-neighbours of AE atoms are oxygen atoms as shown in the local arrangements. Calcium and strontium atoms form corrugated planes, while barium atoms are arranged on planar layers. (Reproduced from Schmidt *et al.* (2008) by permission of SPIE.)

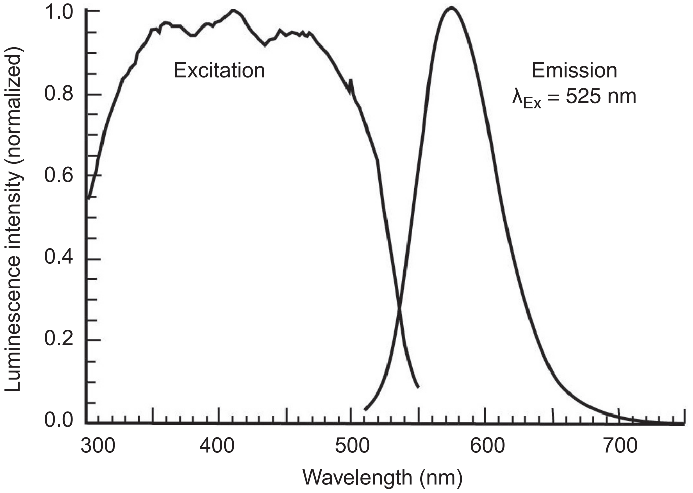

5.16 Excitation and luminescence spectra of $Ba_3Si_6O_{12}N_2:Eu^{2+}$ at room temperature. (Reproduced from Mikami *et al.* (2009) by permission of Elsevier BV.)

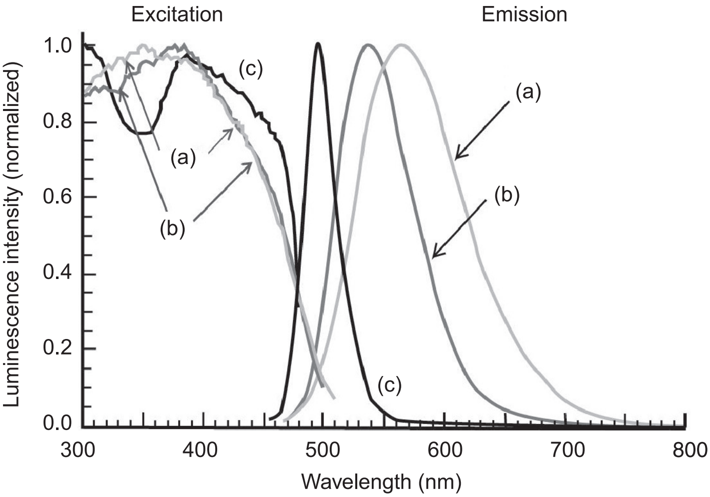

5.17 Excitation and luminescence spectra of AE$Si_2O_2N_2$:Eu^{2+} (2 at.%), where AE = (a) Ca, (b) Sr and (c) Ba. The measurement was made at 25 °C. (Reproduced from Schmidt *et al.* (2008) by permission of SPIE.)

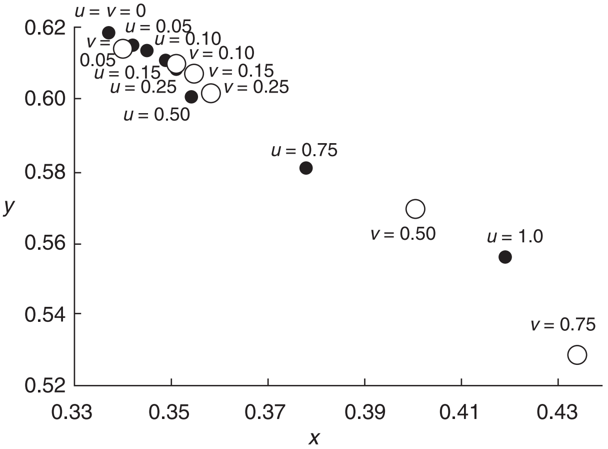

5.18 The CIE colour coordinates of $(Sr_{1-u}Ca_u)Si_2O_2N_2$:Eu^{2+} (2 at.%; filled circles) and $(Sr_{1-v}Ba_v)Si_2O_2N_2$:Eu^{2+} (2 at.%; open circles) as a function of calcium fraction *u* and barium fraction *v*. Excitation was made by 450 nm light. (Data are from Tables 3 and 4 of Bachmann *et al.* (2009a) by permission of ACS Publications.)

blue shift of the luminescence as a result of decreased crystal-field potential. Between a barium fraction of 1.00 for $BaSi_2O_2N_2$:Eu^{2+} and 0.75, there is a discontinuous change in the colour coordinates from $x = 0.076$, $y = 0.440$ to $x = 0.434$, $y = 0.528$. Such anomalous phenomena probably result from distorted local arrangements of coordinated anions around Eu^{2+}. An internal quantum efficiency as high as 90% was found for compositions near $SrSi_2O_2N_2:Eu^{2+}$ (2 at%). The luminescence of $(Sr,Ca)Si_2O_2N_2:Eu^{2+}$ has, however, a lower quenching temperature. For compositions up to 50% Ba^{2+}, the high quantum efficiency and a high quenching temperature are maintained for Eu^{2+} luminescence.

Yun *et al.* (2007) reported that $(Sr_{1-v}Ba_v)_{1-x}Eu_xSi_2O_2N_2$ $(0 \leq v \leq 0.75)$ has a broad optimum concentration of europium of 10–15 at% for luminescence intensity under 460 nm excitation. For $v = 0.25$, the internal quantum efficiency was found to be 61%, much lower than the value reported for 2 at% europium (Bachman *et al.*, 2009a), but the absorption efficiency was 81% as a consequence of the high europium concentration. The high optimum concentration or small concentration quenching presumably results from a weak interaction between Eu^{2+} ions in the layered structure. The composition, $(Sr_{0.58}Ba_{0.34}Eu_{0.08})Si_2O_2N_2$, shows yellow luminescence with a colour close to that of $(Y,Gd)_3Al_5O_{12}:Ce^{3+}$. It could, therefore, be used to substitute for $(Y,Gd)_3Al_5O_{12}:Ce^{3+}$.

Unlike many other nitrides and oxynitrides, $AESi_2O_2N_2:Eu^{2+}$ can be prepared at atmospheric pressure and at temperatures that are not extremely high, e.g. 1300 °C, though reduced gas is required. Yun *et al.* (2007) developed a new synthesis route using $AE_2SiO_4:Eu^{2+}$ as a precursor, which produces a single-phase material with high luminescence efficiency.

5.5 Compounds activated by Ce^{3+}

5.5.1 La-Si-N compounds

Two Ce^{3+}-activated phosphors have been found in this group. $LaSi_3N_5:Ce^{3+}$ has blue luminescence with a peak at 440 nm. The first excitation band appears at about 360 nm. This phosphor is, therefore, suitable for UV excitation rather than blue excitation. Meanwhile, another phase $La_3Si_6N_{11}:Ce^{3+}$ has yellow luminescence, which can be excited by blue light. Excitation and luminescence spectra are shown in Fig. 5.19. It was reported that $La_3Si_6N_{11}:Ce^{3+}$ shows smaller thermal quenching than yellow-emitting $(Y,Gd)_3Al_5O_{12}:Ce^{3+}$ (Seto *et al.*, 2009). This phosphor is expected to be a substitute for the $Y_3Al_5O_{12}:Ce^{3+}$ system. When contaminated with oxygen impurities, for example by using CeO_2 as a starting material, the fired product includes $LaSi_3N_5:Ce^{3+}$ as an impurity phase resulting in a degraded luminescence hue.

5.5.2 Ln-Si-O-N:Ce^{3+} or Tb^{3+} (Ln = Y, La) compounds

Cations with a small ionic radius, such as Li^+, Mg^{2+} and Ca^{2+}, can be incorporated into the lattice of α-Si_3N_4 and help in the sintering of α-Si_3N_4 ceramics. Larger cations, such as Y^{3+} or other rare-earth ions, form a new phase with Si_3N_4. Figure 5.20 shows the quaternary phases in the Y_2O_3-YN-Si_3N_4-SiO_2 system

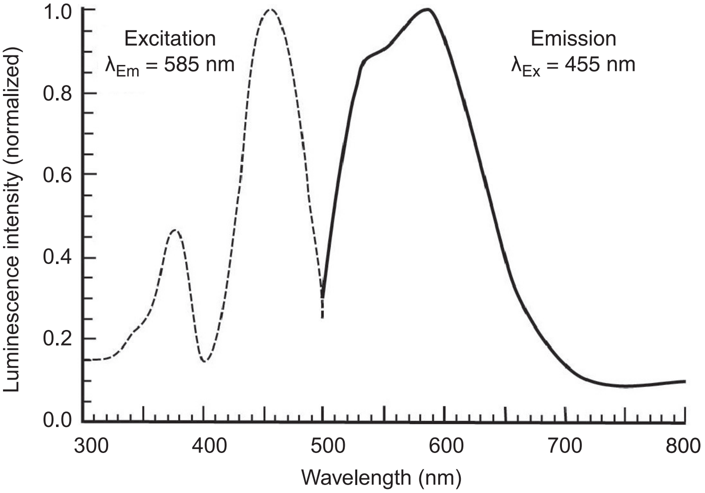

5.19 Excitation and luminescence spectra of $La_{2.94}Ce_{0.06}Si_6N_{11}$ at room temperature. (Reproduced from Seto *et al.* (2009) by permission of the Electrochemical Society.)

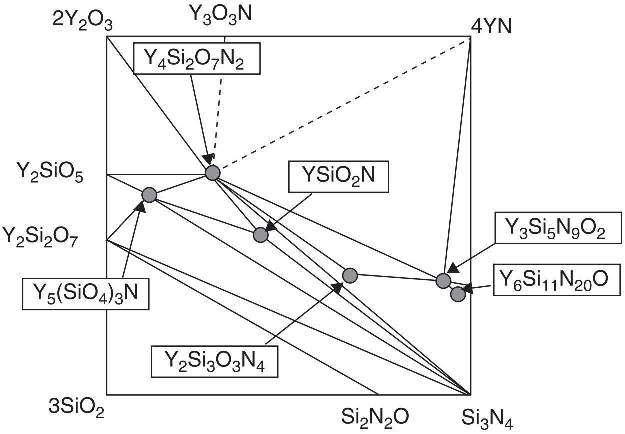
$2Y_2O_3$
Y_3O_3N
4YN
$Y_4Si_2O_7N_2$
Y_2SiO_5
$YSiO_2N$
$Y_2Si_2O_7$
$Y_3Si_5N_9O_2$
$Y_6Si_{11}N_{20}O$
$Y_5(SiO_4)_3N$
$Y_2Si_3O_3N_4$
$3SiO_2$
Si_2N_2O
Si_3N_4

5.20 Quaternary phases of Y_2O_3-YN-Si_3N_4-SiO_2 system. (Reproduced from Liddell and Thompson (2001) by permission of the Royal Society of Chemistry.)

(Liddell and Thompson, 2001). They were discovered through investigating sintering agents to improve the high-temperature strength of Si_3N_4 ceramics.

The luminescence properties of the following oxynitrides activated by Ce^{3+} or Tb^{3+} were reported by van Krevel *et al.* (1998):

- $Y_5(SiO_4)_3N$ (H phase or N-apatite). Though this formula has been published many times, it was thought to be $Y_{10}Si_7O_{23}N_4$ by Lange *et al.*, (1977). It is formally made of Y_2O_3, Si_3N_4 and SiO_2 in a molar ratio of 5:1:4.
- $Y_4Si_2O_7N_2$ (J phase or N-YAM), which is made of Y_2O_3 and Si_2N_2O in a molar ratio of 2:1.
- $YSiO_2N$ (K phase or N-wollastonite), which is made of Y_2O_3 and Si_2N_2O in a molar ratio of 1:1.
- $Y_2Si_3O_3N_4$ (N-melilite), which is made of Y_2O_3 and Si_3N_4 in a molar ratio of 1:1.

In these oxynitrides, Ce^{3+} has blue luminescence with double emission bands and Tb^{3+} has green luminescence characteristic of its 4 f–4 f emission lines. Excitation and luminescence spectra of Ce^{3+}-activated compounds are shown in Fig. 5.21 (van Krevel *et al.*, 1998). As seen in this figure, these materials are not excited by blue light but by violet or UV light. An increase in the Stokes shift with higher N/O ratios was found and was interpreted as a result of increasing stiffness with a larger content of nitrogen. A trend of a red shift of the luminescence was also observed, though $Y_4Si_2O_7N_2:Ce^{3+}$ has an irregular red shift compared with the other members.

Phases of lanthanum analogous to the yttrium compounds, the H, J and K phases, are known, but the fourth phase is unstable in the lanthanum system. Instead, $La_3Si_8N_{11}O_4$, or $3LaN\text{-}4Si_2N_2O$, is believed to exist. Blue luminescence of Ce^{3+} in a series of lanthanum phases was reported by Dierre *et al.* (2007).

5.5.3 Ln-Si-Al-O-N:Ce^{3+} (Ln = La, Ce) compounds

Xie *et al.* (2004) synthesized cerium-doped α-sialon materials using powder mixtures of α-Si_3N_4, AlN and $CeO_2 + Y_2O_3$ or $CeO_2 + CaO$. The dual doping of cerium as well as yttrium or calcium is essential to obtain α-sialon:Ce^{3+}. When prepared only with CeO_2 in addition to α-Si_3N_4 and AlN, $CeAl(Si_{6-z}Al_z)(N_{10-z}O_z)$ or the JEM phase is formed. The crystal structure of the JEM phase was determined by Grins *et al.* (1995) to be orthorhombic with the space group of Pbcn. The JEM phases of lanthanum and cerium are isostructural and form complete solid solutions. The compound expressed as $LaN\text{–}AlN\text{–}2(Si,Al)_3(N,O)_4$ or $LaAl(Si_{6-z}Al_z)(N_{10-z}O_z)$ is closely related to $LaSi_3N_5$, because substitution of AlN with LaN and $(Si,Al)_3(N,O)_4$ with Si_3N_4 gives $LaSi_3N_5$.

Ce^{3+}-doped α-sialon has a broad luminescence band peaking at 500 nm and Ce^{3+}-doped $LaAl(Si_{6-z}Al_z)(N_{10-z}O_z)$ or the JEM phase has a blue luminescence peaking at 490 nm at 2.75 at% cerium (Xie *et al.*, 2004). Both compounds have a broad excitation band from 200 to 450 nm with a peak around 380 nm. Accordingly, they are not suited to blue light excitation, but are excited by UV light. Takahashi *et al.* (2007) reported that both the luminescence and excitation spectra are shifted to longer wavelengths with an increase in cerium concentration. At 5 at% cerium, the phosphor has an excitation intensity strong enough to be excited by a violet LED emitting at 405 nm. At this composition, the luminescence peak was at 500 nm and the external quantum efficiency was 48% under 405 nm light excitation.

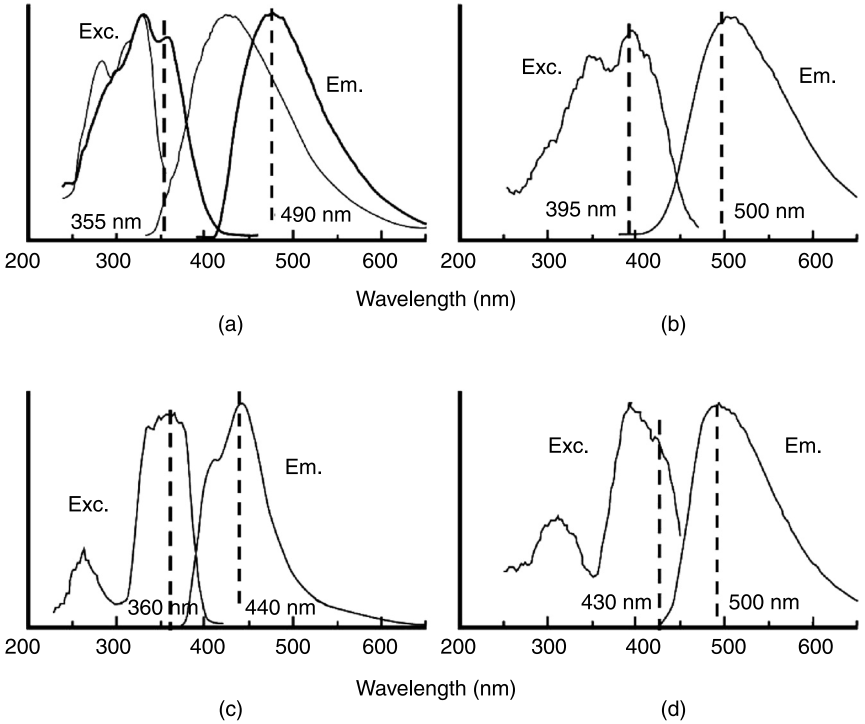

5.21 Excitation and luminescence spectra of Ce^{3+}-activated yttrium oxoimido-silicates: (a) $Y_5(SiO_4)_3N$, (b) $Y_4Si_2O_7N_2$, (c) $YSiO_2N$ and (d) $Y_2Si_3O_3N_4$. The Ce concentration was 5 at.% for all samples. For (a) $Y_5(SiO_4)_3N:Ce^{3+}$, thick lines show the spectra at longer wavelengths; the excitation spectrum was monitored at 490 nm and the luminescence was spectrum excited by 380 nm light. Thin lines show the spectra at shorter wavelengths; the excitation spectrum was monitored at 380 nm and the luminescence spectrum was excited by 285 nm light. For the other compounds, the monitored and excitation wavelengths are (b) 500 and 390 nm, (c) 440 and 350 nm and (d) 500 and 390 nm. The wavelength of an excitation peak or a shoulder at the longest wavelength and the wavelength of the luminescence peak are indicated by broken lines to give an approximation of the Stokes shift. (Reproduced from van Krevel *et al.* (1998) by permission of Elsevier BV.)

5.6 Features of the crystal structure of nitride and oxynitride phosphors

Compared with conventional oxide or sulphide phosphors, the (oxo)imido-silicate phosphors have uncommon features in their crystal structures. This difference partly results from covalent bonding of nitrogen with silicon or aluminium atoms and also from the multinary chemical compositions. Besides their practical importance, it is interesting to look at such a variety of structures, which are not seen in conventional phosphor materials. In this section, we focus on these features by looking at the phosphors discussed above.

5.6.1 Location of the activator ion in a host crystal

The (oxo)imido-silicate phosphors have a network made of [(Al,Si)N_4] and/or [(Al,Si)O_4] tetrahedra connected to each other by sharing vertices or edges. The crystal structures of these phosphors are, therefore, closely related to the structures of Si_3N_4 or SiO_2. In addition to this network, they contain other elements to accommodate activator ions; i.e. alkaline-earth atoms for Eu^{2+} or Ce^{3+} and Y^{3+}, La^{3+}, Gd^{3+} or Lu^{3+} for trivalent rare earth ions. In many (oxo)imido-silicate crystals, the ions to be replaced by activators are located in openings or channels of the network. For example, the network of [(Al,Si)N_4] in the $CaAlSiN_3$ crystal (Fig. 5.6) has channels running along (001). Ca^{2+} and Eu^{2+} ions are stuffed into these open channels. The channels are wide enough to incorporate Mg^{2+} and Ca^{2+} ions, but are not large enough to accommodate a high concentration of Sr^{2+} ions.

In other cases, the alkaline-earth ions hosting Eu^{2+} ions form thin planes in a layered structure. Examples of this type are $AESi_2O_2N_2$ (AE = Ca, Sr, Ba), $Ba_3Si_6O_9N_4$ and $Ba_3Si_6O_{12}N_2$, as shown in Fig. 5.15. Thin planes containing Sr^{2+} or Eu^{2+} are found also in the crystal structures of Sr-sialon and AlN:Eu,Si crystals (Fig. 5.14).

The location of Eu^{2+} ions in α- and β-sialon is particularly uncommon. In most phosphors, an activator ion substitutes for a cation of the host crystal. Eu^{2+} occupies an interstitial vacant site in β-sialon or an interstitial Ca^{2+} site in α-sialon, which is quite exceptional.

The local atomic arrangement around an activator has a direct influence on the absorption and luminescence spectra. The crystal-field splitting, $10Dq$, is very strongly affected by the bond length between the activator and coordinated anions (Eq. 5.1, Section 5.2.1). There is also a general trend that the bond length is longer and the crystal-field splitting is smaller when the coordination number is larger. An example is $SrSi_6N_8$, in which a Eu^{2+} ion coordinated with ten nitrogen atoms emits blue luminescence (Section 5.4.1). It was also observed that the site symmetry of Eu^{2+} is low in many (oxo)imido-silicate hosts. A distorted local structure splits the degenerate 5 d levels, resulting in a low-energy emitting state.

5.6.2 Condensation of [(Al,Si)N_4] and [(Al,Si)O_4] tetrahedra

In every oxo-silicate lattice, two [SiO_4] tetrahedra are connected at a vertex, because an oxygen atom has two chemical bonds. Although three-coordinated oxide atoms are found in some aluminates, e.g. $Sr_4Al_{14}O_{25}$, even in such compounds they share only a small proportion of the oxide atoms. The situation is different for (oxo)imido-silicate lattices, because nitrogen, which is more electronegative than oxygen, can be coordinated with three or four silicon or aluminium atoms as well as two. As a consequence, in many imido-silicates, not just two but three $[SiN_4]$ tetrahedra are connected, as for $CaAlSiN_3$ (Fig. 5.6), and four are joined at a single vertex (Fig. 5.9) in $(AE)(RE)Si_4N_7$, where AE = Ca, Sr, Ba, Eu and RE = Y, Yb (Huppertz and Schnick, 1996). It was also found that two $[SiN_4]$ tetrahedra share edges in $AESiN_2$ (AE = Sr, Ba), $AESi_7N_{10}$ (AE = Sr, Ba) and $SrAlSi_4N_7$:Eu^{2+} (Hecht *et al.*, 2009). Such condensed tetrahedra build a rigid structure, which is mechanically rugged and resistant to temperature.

The degree of condensation for $[SiN_4]$ tetrahedra can be measured by the atomic ratio of $N^{[3]}$ or $N^{[4]}$ against the total number of nitrogen atoms. (The number of nitrogen atoms coordinated to n cations is indicated as $N^{[n]}$.) For example, $N^{[3]}/(N^{[2]}+N^{[3]})=0$ for $CaSiN_2$, 1/2 for $Ca_2Si_5N_8$ and 2/3 for $CaAlSiN_3$, showing that $CaAlSiN_3$ has a crystal structure more condensed than the other imido-silicates.

5.6.3 Lattice defects

Since the (oxo)imido-silicate phosphors are multinary compounds with complicated structures, there is a high probability that they contain defects. In addition, a high synthesis temperature possibly creates a high concentration of imperfections. One of the confirmed defects is the disordered distribution of N/O and Si/Al atoms at the same sites. For example, aluminium and silicon atoms randomly share the same site in $CaAlSiN_3$ and sialon lattices. There is a random distribution of nitrogen and oxygen atoms in sialon and oxynitrides derived from aluminates such as $SrAl_{2+x}O_{4-x}N_x$:Eu^{2+} and the Ln-Si-O-N:Ce^{3+} system. Conversely, the distribution of nitrogen and oxygen atoms is generally ordered in the layered structures of $AESi_2O_2N_2$ (AE = alkaline-earth atoms). It is difficult to confirm the distribution of light elements using X-ray diffraction analysis, but neutron diffraction and thermodynamic considerations for each distribution support the disordered distribution of nitrogen and oxygen atoms in $CaAlSiN_3$ (Mikami *et al.*, 2006).

In a $SrSi_2O_2N_2$ lattice, twins and dislocations of a nanometre-scale dimension were clearly imaged by electron diffraction and HRTEM (Oeckler *et al.*, 2007). Similar line and planar defects may also be found in other (oxo)imido-silicate lattices, if such fine observations are made.

The presence of a high number of defects is also indicated through an afterglow or thermoluminescence, which arises through the thermal release of electrons captured by traps and subsequent recombination with a hole at an activator. A long afterglow is observed in many Eu^{2+}-activated oxides, oxysulphides and sulphides, typically $SrAl_2O_4$:Eu^{2+}, in which, most probably, Eu^{2+} captures a hole. An afterglow has been observed also in some nitride phosphors, e.g. $Ba_2Si_5N_8$:Eu^{2+} (Höppe *et al.*, 2000), $Ca_2Si_5N_8$:Eu^{2+} (Miyamoto *et al.*, 2009) and $CaAlSiN_3$:Eu^{2+}. Codoping of Tm^{3+} ions to $Ca_2Si_5N_8$:Eu^{2+} remarkably increases the afterglow intensity and persistence. This material, $Ca_2Si_5N_8$:Eu^{2+},Tm^{3+}, has been reported to be a promising orange-emitting long-persistent phosphor (Miyamoto *et al.*, 2009; Van den Eeckhout *et al.*, 2009). In addition to native defects in $Ca_2Si_5N_8$, apparently Tm^{3+} ions at Ca^{2+} sites work as electron traps.

Defects in a host lattice have a more or less negative effect on luminescence efficiency, because the excitation energy of an activator can be dissipated by phonon creation or infrared emission at defects. In ZnS phosphors, where excited carriers migrate in a relatively long path, the efficiency is sensitive to a trace amount of defects or impurities. (Oxo)imido-silicate phosphors, which have high quantum efficiency under blue-light excitation, do not show high efficiency under cathode-ray or UV excitation. And even under localized excitation by blue light, a sample with poor crystallinity has poor efficiency. This is probably caused by the migration of energy among activator ions, before the energy eventually arrives at a defect. Energy migration is where excitation energy moves over the host lattice of a phosphor. Energy migration in the phosphor causes non-radiative transitions, concentration-quenching, thermal-quenching and so on.

5.7 Features of optical transitions of nitride and oxynitride phosphors

5.7.1 Excitation and luminescence transitions at long wavelength

The main reason that (oxo)imido-silicate phosphors have attracted significant attention is that they can be excited by blue light and emit green, yellow or red luminescence. Possible factors for inducing long-wavelength transitions include the low barycenter of 5 d levels, large crystal-field splitting and large splitting of degenerate energy levels by the distorted crystal-field potential, which are denoted as ε_c, $10Dq$ and ε in Fig. 5.2 (Section 5.2.1). Each of these factors is considered to be responsible, though their quantitative contribution is not clear.

It is known that absorption and emission occur at long wavelengths also in sulphide phosphors. Similarities between the sulphide and (oxo)imido-silicate phosphors suggests that the low electronegativity of sulphur and nitrogen atoms (2.58 and 3.04, respectively, against 3.44 for oxygen) or the high covalency is the key factor. It is accepted that the ‘nephelauxetic effect’ works more strongly in bonds with nitrogen than in oxide bonds. Regarding the covalency effect, it is interesting that a dense condensation of $[(Al,Si)N_4]$ tetrahedra tends to shift the luminescence peak of Eu^{2+} in imido-silicates to longer wavelengths (Hintzen, 2010). For example, $CaAlSiN_3$:Eu^{2+} with $N^{[3]}/(N^{[2]}+N^{[3]})=2/3$ has a luminescence peak at 650 nm at 1 at% europium and Ca_4SiN_4:Eu^{2+}, which has a unit of four $[SiN_4]$ tetrahedra joined at a single vertex, has a peak at 725 nm. This effect is due to the high framework density in a crystal structure built by nitrogen ($N^{[3]}$), which is coordinated to a maximum of three silicon in $[(Si\text{ or }Al)N_4]$ tetrahedra.

AEX:Eu^{2+} (AE=Mg, Ca or Sr, X=O, S or Se) compounds have a deep red luminescence peak at around 650 nm. For these compounds with a rock-salt structure, there is no reason to assume that a strong crystal-field potential or a distorted potential creates large $10Dq$ or ε. The most plausible explanation is that the 5 d electron orbitals of Eu^{2+} are hybridized with 3 d or 4 d orbitals of AE atoms, which form the X point of the conduction-band bottom (Kaneko and Koda, 1988). What is essential in lowering the 5 d emitting state is delocalization or polarization of the 5 d orbitals, for whatever reason. Mikami and Kijima (2010) pointed out that the dielectric constant directly related to the polarizability of a host crystal is correlated to the luminescence red shift. They explained a difference in luminescence colour between blue-emitting $LaSi_3N_5$:Ce^{3+} and yellow-emitting $La_3Si_6N_{11}$:Ce^{3+} using the difference in their average dielectric constants, which were 5.32 and 5.46, respectively.

5.7.2 Small thermal quenching

Another advantage of the (oxo)imido-silicate phosphors was found soon after the discovery of their long-wavelength luminescence. Some phosphors have a remarkably low thermal quenching of the luminescence intensity, e.g. $CaAlSiN_3$:Eu^{2+}, Ca-α-sialon:Eu^{2+}, β-sialon:Eu^{2+} and $La_3Si_6N_{11}$:Ce^{3+} (Seto *et al.*, 2009). When the degree of thermal quenching is compared for three imido-silicates, $CaSiN_2$:Eu^{2+}, $Ca_2Si_5N_8$:Eu^{2+} and $CaAlSiN_3$:Eu^{2+}, it is reduced more in the order of higher degree of [(Al,Si)N_4] condensation (Fig. 5.22). This result seems to suggest that low thermal quenching occurs in rigid crystal structures. In the configuration coordinate model, the low thermal quenching of these compounds

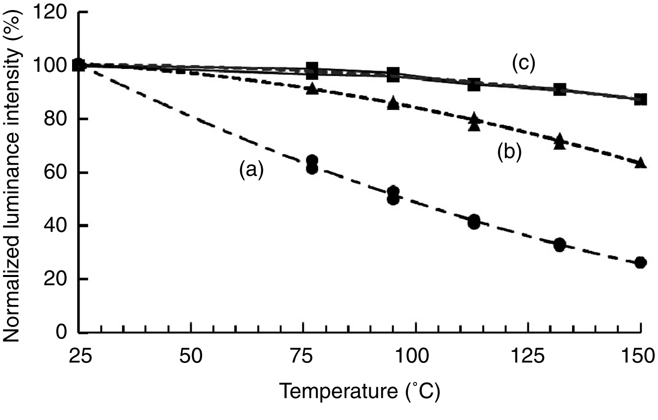

5.22 Comparison of thermal quenching of luminescence intensity under 450 nm light excitation for (a) $CaSiN_2$:Eu^{2+}, (b) $Ca_2Si_5N_8$:Eu^{2+} and (c) $CaAlSiN_3$:Eu^{2+}. Eu concentration is 1 at.%.

is related to the large force constant of a chemical bond or a large curvature of an excited-state parabola.

The strong quenching observed for $Ba_3Si_6O_9N_4:Eu^{2+}$ has been explained by photoionization (Mikami *et al.*, 2009), as schematically shown in Fig. 5.23. Knowing the band-gap energy and the location of the 5 d levels will clarify more examples of the thermal quenching caused by photoionization.

The above discussion did not include the interaction between activator ions. Actually, energy transfer between activator ions is possible through an overlap of the absorption and luminescence spectra. Energy migration more or less leads to non-radiative processes at defects and impurities, resulting in decreased efficiency. The migration rate increases with an increase in temperature, because both absorption and luminescence spectrum are broadened. As a consequence, the quenching of luminescence is accelerated at higher temperatures. A good example of such concentration-dependent quenching was presented for $Y_3Al_5O_{12}:Ce^{3+}$ by Bachman *et al.* (2009b). For an increase in temperature from 300 K to 500 K, the luminescence decay time is shortened by 80% at 3 at% cerium, but it scarcely changed at 0.3 at% or 0.03 at%. Although $CaAlSiN_3:Eu^{2+}$ has low thermal quenching at the optimum europium concentration of 1 at%, there is large quenching of the luminescence intensity at higher europium concentrations, as shown in Fig. 5.24. These results indicate that the degree of quenching at a given temperature and activator concentration will depend on the concentration of non-radiative centres in a host crystal. A sample with poor purity or crystallinity has potential to suffer from this type of quenching.

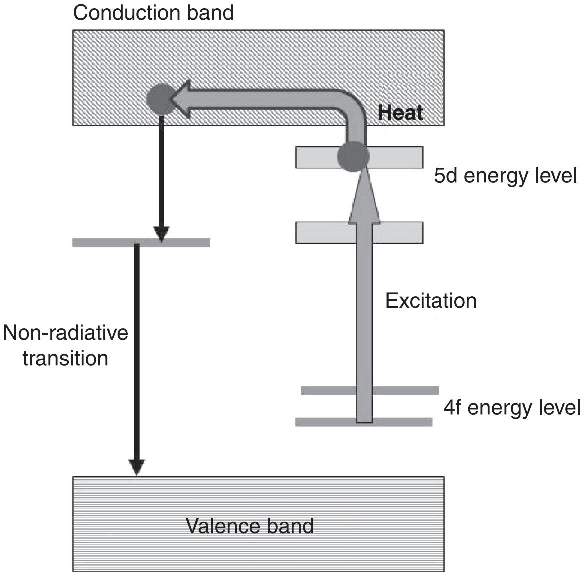

5.23 Photoionization (or autoionization) processes.

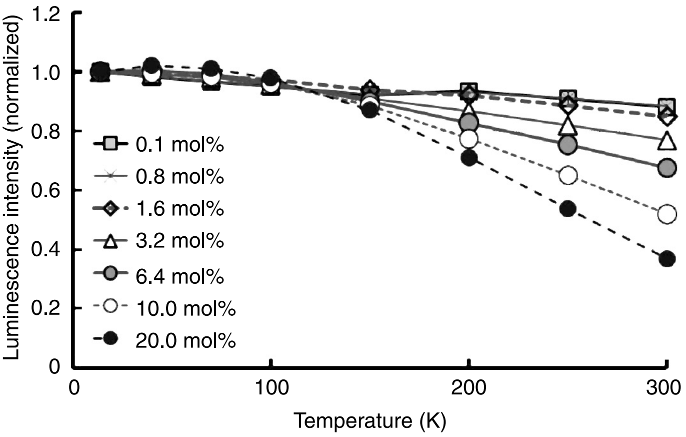

5.24 Variation of thermal quenching (below room temperature) of $CaAlSiN_3:Eu^{2+}$ with europium concentration.

5.7.3 Quantum efficiency

The luminescence quantum efficiency can be high when excitation and emission processes occur within a localized ion. Table 5.4 shows the quantum efficiency of typical white LED phosphors. It gives the exact composition of a measured sample when it is reported in the reference. The efficiencies were measured by excitation of 450 or 455 nm light. The internal quantum efficiencies of the

Table 5.4 Quantum efficiency of typical white LED phosphors

Chemical formula	Internal quantum efficiency (%)	Emission colour (peak wavelength)	Reference
$Y_3Al_5O_{12}:Ce^{3+}$	>90	Yellow (580 nm)	Ohshio, 2005
$Ca_{m/2}Si_{12\text{-}m\text{-}n}Al_{m+n}O_{n\mathrm{N}16\text{-}n}:Eu^{2+}$ $m=1.4$, $n=0.7$, [Eu] = 7.5% (Ca-α-sialon:Eu^{2+})	69	Yellow (580 nm)	Hirosaki and Xie, 2006
$Si_{6-z}Al_zO_zN_{8-z}:Eu^{2+}$ (β-sialon:Eu^{2+})	73	Green (538 nm)	Yamada *et al.*, 2010
$SrSi_2O_2N_2:Eu^{2+}$[Eu] = 2%	95	Green (544 nm)	Schmidt *et al.*, 2008
$Sr_2Si_5N_8:Eu^{2+}$ [Eu] = 2%	82	Red (628 nm)	Xie *et al.*, 2011
$CaS:Eu^{2+}$[Eu] = 1%	62	Deep red (650 nm)	Xia *et al.*, 2010
$CaAlSiN_3:Eu^{2+}$ [Eu] = 1%	87	Deep red (650 nm)	Hirosaki and Xie, 2006

phosphors studied by Xia *et al.* (2010) were calculated using the given absorption and external quantum efficiencies. In fact, the phosphors listed in Table 5.4 have fairly high internal quantum efficiencies, if we take into account that the efficiency at room temperature already suffers from some degree of quenching. It is to be noticed that the efficiency values in Table 5.4 are published data. The highest efficiency actually attained may be higher, because efficiency depends on synthesis conditions or sample purity. Smet *et al.* (2011) list quantum efficiency data for oxides, sulphides and (oxo)imido-silicates. To improve efficiency further, we must find out how we can reduce thermal quenching and concentration quenching by improving the crystallinity and purity of samples.

5.8 Conclusion and future trends

As described above, many (oxo)imido-silicates activated with Eu^{2+} or Ce^{3+} have high performance suitable for white LED applications. At present, red-emitting $(Ca,Sr)AlSiN_3:Eu^{2+}$ is used for backlighting liquid crystal displays (LCDs) and high colour-rendering illumination. Green-emitting β-sialon has been commercialized mainly for LCD backlighting and yellow- or orange-emitting α-sialon is used for illumination. In addition, more phosphors are being tested or sold on the market. The new group of phosphors is already an indispensable material in the expanding new industry of white LEDs.

Although the rate of finding new materials has slowed down, there are still significant opportunities for developing new promising phosphors, because nitride and oxynitride phosphors can be produced with many combinations of elements. Compared with Ca-α-sialon, strontium-containing sialon compounds have more potential for research at present. Expanding the number of compositions by introducing boron or carbon atoms has been attempted and further progress can be expected.

There are still many problems in the use of the established phosphors. Particles synthesized at temperatures as high as 1900 °C and at pressures as high as 1 MPa or higher are more or less sintered. After being pulverized, the particles have a damaged surface and irregular shapes, because hard milling is required to break the coagulated mechanically strong (oxo)imido-silicates. This particle morphology may reduce efficiency or stability. It may be unfavourable for the deposition process on an LED chip. Fluxes are often used to control particle size and shape in conventional synthesis methods, but they cannot be used at very high temperatures. This problem can be solved using a new synthesis process such as the gas-reduction nitridation method (for example, see Suehiro *et al.*, 2005), which is used to synthesize (oxo)imido-silicates at much lower temperatures and at atmospheric pressure. This process will also contribute to reducing the cost of (oxo)imido-silicate phosphors, which is practically quite important to successful application.

(Oxo)imido-silicate phosphors have many defects generated by multinary compositions and high-temperature synthesis. If the defect concentration can be decreased, luminescence quenching at high activator concentrations and at high temperatures may be reduced and in some cases the luminescence band may be narrower to some extent. Secondary phases, oxygen impurity, inhomogeneous diffusion of activator ions and stacking faults are all possible defects in addition to point defects. Controlling oxygen contamination during synthesis and lower firing temperatures will improve crystallinity and the performance of the phosphors.

Research and development along two lines – surveying new materials and improving the important phosphors – will lead to higher quality (oxo)imidosilicate phosphors.

5.9 Acknowledgements

The author and his family thank Dr Kyota Ueda and Ms Yoriko Suda for helping to complete this chapter.

5.10 References

Bachmann, V., Ronda, C., Oeckler, O., Schnick, W. and Meijerink, A., ‘Color point tuning for (Sr,Ca,Ba)$Si_2O_2N_2$:Eu^{2+} for white light LEDs’, *Chem. Mater.*, 2009a, 21, 316–325.

Bachmann, V., Ronda, C. and Meijerink, A., ‘Temperature quenching of yellow Ce^{3+} luminescence in YAG:Ce’, *Chem. Mater.*, 2009b, 21, 2077–2084.

Bando, K., ‘Performance of high-luminous efficacy white LEDs’, *Proceedings of LS12-WLED3*, 2010, 333–337.

Blasse, B. and Bril, A., ‘Investigation of some Ce^{3+}-activated phosphors’, *J. Chem. Phys.*, 1967, 47, 5139–5146.

Dierre, B., Xie, R.-J., Hirosaki, N. and Sekiguchi, T., ‘Blue emission of Ce^{3+} in lanthanide silicon oxynitride phosphors’, *J. Mater. Res.*, 2007, 22, 1933–1941.

Dorenbos, P., ‘5*d*-level energies of Ce^{3+} and the crystalline environment. I. Fluoride compounds’, *Phys. Rev. B*, 2000, 62, 15640–15649.

Dorenbos, P., ‘Relating the energy of the [Xe]$5d^1$ configuration of Ce^{3+} in inorganic compounds with anion polarizability and cation electronegativity’, *Phys. Rev. B*, 2002, 65, 235110-1–235110-6.

Duan, C. J., Wang, X. J., Otten, W. M., Delsing, A. C. A., Zhao, J. T., *et al.*, ‘Preparation, electronic structure, and photoluminescence properties of Eu^{2+}- and Ce^{3+}/Li^+-activated alkaline earth silicon nitride $MSiN_2$ (M = Sr, Ba)’, *Chem. Mater.*, 2008, 20, 1597–1605.

Duan, C. J., Zhang, Z., Rösler, S., Rösler, S., Delsing, A., *et al.*, ‘Preparation, characterization, and photoluminescence properties of Tb^{3+}-, Ce^{3+}-, and Ce^{3+}/Tb^{3+}-activated $RE_2Si_4N_6C$ (RE = Lu, Y, and Gd) phosphors’, *Chem. Mater.*, 2011, 23, 1851–1861.

Fukuda, Y. and Matsuda, M., ‘Red fluorescent substance and light-emitting device employing the same’, US patent application, 2010, US2010/0102707A1 (29 April 2010).

Fukuda, Y., Tamatani, M., Hiramatsu, R., Asai, H., Tatami, J., *et al.*, 2006, ‘Luminescence properties of Eu-activated Sr-SiAlON’, *Proceedings of 315th Meeting on Phosphor Research Society*, Phosphor Research Society, Tokyo (in Japanese), 2006, 1–9.

Fukuda, Y., Ishida, K., Mitsuishi, I. and Nunoue, S., ‘Luminescence properties of Eu^{2+}-doped green-emitting Sr-sialon phosphor and its application to white light-emitting diodes’, *Appl. Phys. Express*, 2009, 2, 012401.

Grins, J., Shen, Z., Nygren, M. and Ekstrom, T., 'Preparation and crystal structure of $LaAl(Si_{6-z}Al_z)N_{10-z}O_z$', *J. Mater. Chem.*, 1995, 5, 2001–2006.

Grins, J., Esmaeilzadeh, S., Svensson, G. and Shen, Z. J., 'High-resolution electron microscopy of a Sr-containing sialon polytypoid phase', *J. Euro. Ceram. Soc.*, 1999, 19, 2723–2730.

Hecht, C., Stadler, F., Schmidt, P. J., auf der Gunne, S. J., Baumann, V., *et al.*, '$SrAlSi_4N_7:Eu^{2+}$ – A nitridoalumosilicate phosphor for warm white light (pc)LEDs with edge-sharing tetrahedra', *Chem. Mater.*, 2009, 21, 1595–1601.

Hintzen, H. T., 'Nitride-based phosphor materials: science and applications', Abstract #2365, *218th ECS Meeting*, The Electrochemical Society, Las Vegas, October 2010.

Hirosaki, H. and Xie, R.-J., 'Quantum efficiencies of SiAlON phosphors', *Japan Society of Applied Physics and Related Societies, 53rd Spring Meeting, Abstract, 2006*, Musashi University of Technology, Tokyo (in Japanese), 2006, Vol. 3, 1557.

Hirosaki, H., Xie, R.-J., Kimoto, K., Sekiguchi, T., Yamamoto, Y., *et al.*, 'Characterization and properties of green-emitting β-SiAlON:Eu^{2+} powder phosphors for white light-emitting diodes', *Appl. Phys. Lett.*, 2005, 86, 211905-1–211905-3.

Hirosaki, N., Xie, R.-J. and Inoue, K., 'Blue-emitting AlN:Eu phosphor for field emission displays', *Appl. Phys. Lett.*, 2007, 91, 061101-1–061101-3.

Hirosaki, N., Xie, R.-J. and Takahashi, K., 'Improvement of emission colour purity of β-SaAlON phosphors by reduction of oxygen concentration', *Japan Society of Applied Physics and Related Societies, 59th Spring Meeting, Abstract No.16-E2-1*, Waseda University, Tokyo (in Japanese), 2012.

Höppe, H. A., Lutz, H., Mory, P., Schnick, W. and Seilmeier, A., 'Luminescence in Eu^{2+}-doped $Ba_2Si_5N_8$: fluorescence, thermoluminescence, and upconversion', *J. Phys. Chem. Solids*, 2000, 61, 2001–2006.

Höppe, H. A., Stadler, F., Oeckler, O. and Schnick, W., '$Ca[Si_2O_2N_2]$ – ein neuartiges Schichtsilicat', *Angew. Chem.*, 2004, 116, 5656–5659.

Huppertz, H. and Schnick, W., '$BaYbSi_4N_7$ – überraschende strukturelle Möglichkeiten in Nitridosilicaten', *Angew. Chem.*, 1996, 108(17), 2115–2116.

Inoue, K., Hirosaki, N., Xie, R.-J. and Takeda, T., 'Highly efficient and thermally stable blue-emitting AlN:Eu^{2+} phosphor for ultraviolet white light-emitting diodes', *J. Phys. Chem. C*, 2009, 113, 9392–9397.

Kaneko, Y. and Koda, T., 'New development in IIa-VIb (Alkaline-earth chalcogenide) binary semiconductors', *J. Crystal Growth*, 1988, 86, 72–78.

Kechele, J. A., Hecht, C., Oeckler, O., Schmedt auf der Günne, J., Schmidt, P. J., *et al.*, '$Ba_2AlSi_5N_9$ – A new host lattice for Eu^{2+}-doped luminescent materials comprising a nitridoalumosilicate framework with corner- and edge-sharing tetrahedra', *Chem. Mater.*, 2009a, 21, 1288–1295.

Kechele, J. A., Oeckler, O., Stadler, F. and Schnick, W., 'Structure elucidation of $BaSi_2O_2N_2$ – A host lattice for rare earth doped luminescent materials in phosphor-converted (pc)-LEDs', *Solid State Sci.*, 2009b, 11, 537–543.

Kimoto, K., Xie, R.-J., Matsui, Y., Ishizuka, K. and Hirosaki, N., 'Direct observation of single dopant atom in light-emitting phosphor of β-sialon Eu^{2+}', *Appl. Phys. Lett.*, 2009, 94, 041908.

Lange, F. F., Singhal, S. C. and Kuznicki, R. C., 'Phase relations and stability studies in the system Si_3N_4-SiO_2-Y_2O_3 pseudoternary system', *J. Am. Ceram. Soc.*, 1977, 60, 249–252.

Li, H. L., Xie, R.-J., Hirosaki, N., Dierre, B., Sekiguchi, T. and Yajima, Y., 'Preparation and cathodoluminescence of Mg-doped and Zn-doped GaN powders', *J. Am. Cer. Soc.*, 2008a, 91, 1171–1174.

Li, H. L., Xie, R.-J., Zhou, G. H., Hirosaki, N. and Sun, Z., 'A cyan-emitting $BaSi_7N_{10}$:Eu^{2+} phosphor prepared by gas reduction and nitridation for UV-pumping white LEDs', *J. Electrochem. Soc.*, 2010, 157, J251–J255.

Li, Y. Q. and Hintzen, H. T., 'High efficiency nitride based phosphors for white LEDs', *J. Light Vis. Env.*, 2008, 32, 129–134.

Li, Y. Q., Fang, C. M., de With, G. and Hintzen, H. T., 'Preparation, structure and photoluminescence properties of Eu^{2+} and Ce^{3+}-doped $SrYSi_4N_7$', *J. Solid State Chem.*, 2004, 177, 4687–4694.

Li, Y. Q., de With, G. and Hintzen, H. T., 'Luminescence properties of Eu^{2+}-doped $MAl_{2-x}Si_xO_{4-x}N_x$ (M = Ca, Sr, Ba). Conversion phosphor for white LED applications', *J. Electrochem. Soc.*, 2006a, 153, G278–G282.

Li, Y. Q., van Steen, J. E. J., van Krevel, J. W. H., Botty, G., Delsing, A. C. A., *et al.*, 'Luminescence properties of red-emitting $M_2Si_5N_8$:Eu^{2+} (M = Ca, Sr, Ba) LED conversion phosphors', *J. Solid State Compd.*, 2006b, 417, 273–279.

Li, Y. Q., Hirosaki, N., Xie, R.-J., Takeda, T. and Mitomo, M., 'Crystal and electronic structures, luminescence properties of Eu^{2+}-doped $Si_{6-z}Al_zO_zN_{8-z}$ and $M_ySi_{6-z}Al_{z-y}O_{z+y}N_{8-z-y}$ (M = 2Li, Mg, Ca, Sr, Ba)', *J. Solid State Chem.*, 2008b, 181, 3200–3210.

Li, Y. Q., Delsing, A. C. A., Metslaar, R., de With, G. and Hintezen, H. T., 'Photoluminescence properties of rare-earth activated BaSi7N10', *J. Alloys Compds.*, 2009, 487, 28–33.

Liddell, K. and Thompson, D. P., 'The crystal structure of $Y_3Si_5N_9O$ and revision of the compositions of some high nitrogen-containing M-Si-O-N (M = Y, La) phases', *J. Mater. Chem.*, 2001, 507–512.

Mikami, M. and Kijima, N., '5 d levels of rare-earth ions in oxynitride/nitride phosphors: to what extent is the idea *covalency* reliable?', *Opt. Mater.*, 2010, 33, 145–148.

Mikami, M., Uheda, K. and Kijima, N., 'First-principles study of nitridoaluminosilicate $CaAlSiN_3$', *Phys. Stat. Sol.*, 2006, 203, 2705–2711.

Mikami, M., Watanabe, H., Uheda, K., Shimooka, S., Shimomura, Y., *et al.*, 'New phosphors for white LEDs: material design concepts', *Mater. Sci. Eng.*, 2009, 1, 012002.

Miyamoto, Y., Kato, H., Honna, Y., Yamamoto, H. and Ohmi, K., 'An orange-emitting, long-persistent phosphor, $Ca_2Si_5N_8$:Eu^{2+},Tm^{3+}', *J. Electrochem. Soc.*, 2009, 156, J235–J241.

Oeckler, O., Stadler, F., Rosenthal, T. and Schnick, W., 'Real structure of $SrSi_2O_2N_2$', *Solid State Sci.*, 2007, 9, 205–212.

Ohkubo, K. and Shigeta, T., 'Absolute quantum efficiency of NBS phosphor standard samples', *J. Illum. Inst. Jpn.*, 1999, 83, 87–93.

Ohshio, S., 'A trend of phosphor technology for developing light sources', *Tech. Digest 310th Phosphor Res. Soc. Meeting*, 2005, 7–16.

Ottinger, F., 'Synthese, Struktur und analytische Detailstudien neuer stickstoffhaltiger Silicate und Aluminosilicate', PhD thesis, 2004, Technische Hochshule Zürich.

Sato, Y., Takahashi H., Tamaki, H. and Kameshima M., 'Luminescence properties of a blue phosphor, GaN:Zn for VFDs', *Proceedings of 9th IDW*, Hiroshima, 2002, 951–954.

Schlieper, T. and Schnick, W., 'Nitrido silicates. I. High temperature synthesis and crystal structure of $Ca_2Si_5N_8$', *Z. Anorg. Allg. Chem.*, 1995, 621, 1037–1041.

Schlieper, T., Milius, W. and Schnick, W., 'Nitrido silicates. II. High temperature synthesis and crystal structure of $Sr_2Si_5N_8$ and $Ba_2Si_5N_8$', *Z. Anorg. Allg. Chem.*, 1995, 621, 1380–1384.

Schmidt, P., Tuecks, A., Bechtel, H., Wiechert, D., Mueller-Mach, R., *et al.*, 'Layered oxonitrido silicate (SiON) phosphors for high power LEDs', *Proc. SPIE*, 2008, 7058, 70580L-1-7.

Seto, T., Kijima, N. and Hirosaki, N., 'A new yellow phosphor $La_3Si_6N_{11}$:Ce^{3+} for white LEDs', *ECS Trans.*, 2009, 25, 247–252.

Shioi, K., Hirosaki, N., Xie, R.-J., Takeda, T. and Li, Y. Q., 'Luminescence properties of $SrSi_6N_8$:Eu^{2+}', *J. Mater. Sci.*, 2008, 43, 5659–5661.

Smet, P. F., Parmentier, A. B. and Poelman, D., 'Selecting conversion phosphors for white light-emitting diodes', *J. Electrochem. Soc.*, 2011, 158, R37–R54.

Stadler, F. and Schnick, W., 'Die neuen Schichtsilicate $Ba_3Si_6O_9N_4$ und $Eu_3Si_6O_9N_4$', *Z. Anorg. Allg. Chem.*, 2006, 632, 949–954.

Suehiro, T., Hirosaki, N., Xie, R.-J. and Mitomo, M., 'Powder synthesis of Ca-a'-SiAlON as a host material for phosphors', *Chem. Mater.*, 2005, 17, 308–314.

Takahashi, K., Hirosaki, N., Xie, R.-J., Harada, M., Yoshimura, K., *et al.*, 'Luminescence properties of blue $La_{1-x}Ce_xAl(Si_{6-z}Al_z)(N_{10-z}O_z)(z\sim 1)$ oxynitride phosphors and their application in white light-emitting diode', *Appl. Phys. Lett.*, 2007, 91, 091923.

Takeda, T., Hirosaki, N., Xie, R.-J., Kimoto, K. and Saito, M., 'Anomalous Eu layer doping in Eu, Si co-doped aluminium nitride based phosphor and its direct observation', *J. Mater. Chem.*, 2010, 20, 9807–10042.

Uheda, K., Takizawa, H., Endo, T., Miura, C., Shimomura, Y., *et al.*, 'Photo- and thermoluminescence of zinc silicon nitride doped with divalent manganese', *J. Mater. Sci. Lett.*, 2001, 20, 1753–1755.

Uheda, K., Hirosaki, N., Yamamoto, Y., Naito, A., Nakajima, T., *et al.*, 'Luminescence properties of a red phosphor, $CaAlSiN_3$:Eu^{2+}, for white light-emitting diodes', *Electrochem. Solid State Lett.*, 2006, 9, H22–H25.

Uheda, K., Shimooka, S., Mikami, M., Imura, H. and Kijima, N., 'Synthesis and characterization of new green phosphor for white LED', *Proceedings of IDW '07*, Sapporo, 2007, 899–902.

Uheda, K., Yamamoto, H., Yamane, H., Inami, W., Tsuda, K., *et al.*, 'An analysis of crystal structure of Ca-deficient oxonitridoaluminosilicate, $Ca_{0.88}Al_{0.91}Si_{1.09}N_{2.85}O_{0.15}$', *J. Cer. Soc. Jpn.*, 2009, 117, 94–98.

Van den Eeckhout, K., Smet, P. F. and Poelman, D., 'Persistent luminescence in rare-earth codoped $Ca_2Si_5N_8$:Eu^{2+}', *J. Lumin.*, 2009, 129, 1140–1143.

van Krevel, J. W. H., Hintzen H. T., Metselaar, R. and Meijerink, A., 'Long wavelength Ce emission in Y–Si–O–N materials', *J. Alloys. Compd.*, 1998, 268, 272–277.

van Krevel, J. W. H., 'On new rare-earth doped M-Si-Al-O-N materials: luminescence properties and oxidation resistance', PhD thesis, 2000, Technische Universiteit Eindhoven.

Van Krevel, J. W. T., van Rutten, J. W. H., Mandal, H., Hintzen, H. T. and Metselaar, R., 'Luminescence properties of terbium-, cerium-, or europium-doped α-sialon materials', *J. Solid State Chem.*, 2002, 165, 19–24.

Watanabe, H., Wada, H., Seki, K., Itou, M. and Kijima, N., 'Synthetic method and luminescence properties of $Sr_xCa_{1-x}AlSiN_3$:Eu^{2+} mixed nitride phosphors', *J. Electrochem. Soc.*, 2008, 155, F31–F36.

Weakliem, H. A., 'Electronic interactions in the $4f^65d$ configuration of Eu^{2+} in crystals', *Phys. Rev.*, 1972, B6, 2743–2748.

Wu, J. L., Gundiah, G. and Cheetham, A. K., 'Structure-property correlations in Ce-doped garnet phosphors for use in solid state lighting', *Chem. Phys. Lett.*, 2007, 441, 250–254.

Xia, Q., Batentschuk, M., Osvet, A., Winnacker, A. and Schneider, J., 'Quantum yield of Eu^{2+} emission in $(Ca_{1-x}Sr_x)$S:Eu light emitting diode converter at 20–420 K', *Radiat. Meas.*, 2010, 45, 350–352.

Xie, R.-J. and Hirosaki, N., 'Silicon-based oxynitride and nitride phosphors for white LEDs – A review', *Sci. Tech. Adv. Mater.*, 2007, 8, 588–600.

Xie, R.-J., Hirosaki, N., Mitomo, M., Yamamoto, Y., Suehiro, T., *et al.*, 'Photoluminescence of cerium-doped α-sialon material', *J. Am. Ceram. Soc.*, 2004, 87, 1368–1370.

Xie, R.-J., Hirosaki, N., Li, H.-L., Li, Y. Q. and Mitomo, M., 'Synthesis and photoluminescence properties of β-sialon:Eu^{2+} ($Si_{6-z}Al_zO_zN_{8-z}$:Eu^{2+}). A promising green oxynitride phosphor for white light-emitting diodes', *J. Electrochem. Soc.*, 2007, 154, J314–J319.

Xie, R.-J., Li, Y. Q., Hirosaki, N. and Yamamoto, H., *Nitride Luminescent Materials and Solid State Lighting*, CRC Press, Boca Raton, 2011.

Yamada, S., Emoto, H., Ibukiyama, M. and Hirosaki, N., 'Properties of a and b-SiAlON:Eu^{2+} powder phosphors for white LEDs', *Tech. Digest, Phosphor Res. Soc. 335th Meeting*, 2010, 9–14.

Yun, B.-G., Miyamoto, Y. and Yamamoto, H., 'Luminescence properties of ($Sr_{1-u}Ba_u$) $Si_2O_2N_2$:Eu^{2+}, yellow or orange phosphors for white LEDs, synthesized with $(Sr_{1-u}Ba_u)_2SiO_4$:Eu^{2+} as a precursor', *J. Electrochem. Soc.*, 2007, 154, J320–J325.

6

Fabrication of nitride LEDs

R.-H. HORNG, D.-S. WUU and C.-F. LIN,
National Chung Hsing University, Taiwan and
C.-F. LAI, Feng-Chia University, Taiwan

DOI: 10.1533/9780857099303.1.181

Abstract: In this chapter, we discuss the flip-chip and thin-film types of GaN-based light-emitting diode (LED), which are used to produce devices with better light extraction efficiency and far-field distribution. Flip-chip LEDs (FCLEDs) with a micro-pillar array structure and FCLEDs with a geometric oblique sapphire structure are investigated. Thin-film LEDs (TFLEDs) are fabricated by a combination of wafer bonding and the laser lift-off technique, which are used to transfer the GaN epilayer to a more conductive substrate to give better thermal dissipation. GaN TFLEDs with a photonic crystal (PC) surface structure are demonstrated. This study examines the light extraction efficiency, directional far-field patterns and polarization properties of GaN PC TFLEDs.

Key words: Gallium nitride (GaN), light-emitting diode (LED), flip-chip LED (FCLED), thin-film LED (TFLED), photonic crystal (PC).

6.1 Introduction

Gallium nitride (GaN)-based materials have attracted a great deal of attention because the direct wide bandgap gives a range of optical emission wavelengths from red to ultraviolet (UV) when alloyed with indium or aluminum. Therefore, their ternary and quaternary alloys have been used for optoelectronic devices over the past ten years,[1–2] such as light-emitting diodes (LEDs) and laser diodes (LDs). Recently, high-brightness (HB) GaN-based LEDs have attracted significant interest; this is a highly energy-efficient lighting technology[3] with advantages such as small size and a long lifespan. Above all, GaN-based LEDs emit short wavelength light in the blue or UV region, which can be used to excite a yellow phosphor. This produces white light and the devices are used for solid-state lighting. The development of solid-state lighting has unlocked a number of niche markets, for example the automotive market (LEDs are now integrated into the headlamps in a number of car models), backlighting of display screens (including TVs), display projectors, street signs and, most recently, the important market of cell phones (screens, keyboards and camera flashes). It should be noted that general lighting is a major market: according to the United States (US) Department of Energy (DOE), the total sales of lighting products are $60 billion each year worldwide. Besides the economic potential of this market, the opportunities are also huge in terms of energy savings. Indeed, in the US lighting represents 8% of the total energy consumption and 22% of the electrical energy consumption. Inefficient incandescent bulbs remain the most widespread sources: they consume 40% of the lighting energy to produce only 15% of the light output. A 50% penetration of LEDs into the general lighting market would yield considerable energy savings of more than 350 TWh. Currently, the LED market is worth $3.7 billion each year globally, of which 58% is the cell phone market, while illumination only represents 5% of the market.

At present, the efficiency of GaN-based LEDs is still lower than that of fluorescent lamps in general lighting applications. Therefore, the optimization of all aspects of LED efficiency is necessary for solid-state lighting. In general, the performance of a GaN-based LED is characterized by its external quantum efficiency (EQE) or wall-plug efficiency (η), defined as the ratio of emitted optical power (P_{opt}) to injected electrical power (P_{el}) so that $\eta = P_{opt}/P_{el}$. The wall-plug efficiency η of GaN-based LEDs is limited by several factors,[2] which may be broken down as follows: $\eta = \eta_{inj} \times \eta_{int} \times \eta_f \times \eta_{extract}$. The injection efficiency η_{inj} is the fraction of electron-hole pairs injected into the LED that reaches the p-n junction. This value is, for instance, limited by leakage of the current in the LED and by Joule losses in the electrical contacts of the LED. The internal quantum efficiency (IQE) η_{int} is the fraction of electron-hole pairs reaching the p-n junction that recombines radiatively. It is limited by the non-radiative recombination of electron-hole pairs. The feeding efficiency η_f is the ratio of the energy of an emitted photon $\hbar\omega$ to the energy of an electron-hole pair injected into the LED: $\eta_f = \hbar\omega/qV$, where V is the voltage drop across the LED and q the elementary charge. In general, part of an electron's energy can be lost to phonons and $\eta_f < 1$. Finally, the light extraction efficiency $\eta_{extract}$ is the fraction of the photons emitted at the p-n junction that actually escape the LED. Its value is limited by light reflections, which trap photons inside the LED where they are eventually absorbed.

One may think that the main limiting factor would be the internal light generation and the IQE. Nevertheless, this is not the case in a variety of materials where the conversion from carriers to photons reaches 50% to 90% if the material's quality is high enough. In GaN-based LEDs, the main limiting factor is the light extraction efficiency $\eta_{extract}$, i.e. the ability of photons generated inside the semiconductor material to escape into the air. Unfortunately, most of the light emitted inside an LED is trapped by total internal reflection (TIR) at the material's interface with air as the refractive indexes of GaN and air are $n_{GaN} = 2.5$ and $n_{air} = 1.0$, respectively. Thus, the critical angle at which light generated in the InGaN/GaN active region can escape is approximately $\theta_c = \sin^{-1}(n_{air}/n_{GaN}) \sim 23°$, which limits the EQE of conventional GaN-based LEDs to only a few percent.[4] Although many efficient light extraction strategies have already been applied, they are mostly based on the principle of randomizing the paths followed by the light and this gives poor control of the far-field emission distribution in

GaN-based LEDs. The next generation of applications of GaN HB-LEDs in projectors, automobile headlights and general lighting requires further improvements in light extraction efficiency and the directional far-field emission distribution. In this chapter, the objective is to achieve high extraction efficiency and to control the directionality of the emitted light.

6.2 GaN-based flip-chip LEDs and flip-chip technology

6.2.1 Background to flip-chip LEDs

Recently, as GaN-based HB-LEDs have improved, applications such as traffic signals, backlights for cell phones and LCD televisions have become possible. However, before conventional fluorescent lighting can be replaced with solid-state lighting, the light extraction efficiency and the internal quantum efficiency of LEDs must be significantly improved. Conventional LEDs are inherently inefficient because photons are generated through a spontaneous emission process and emitted in all directions. A large fraction of the light emitted downward and toward the substrate does not contribute to the useable light output. In addition, there is an inherent problem associated with conventional nitride LEDs, i.e., the poor thermal conductivity of the sapphire substrate. Flip-chip (FC) techniques are an effective way to enhance light extraction and heat dissipation.[5] Therefore, flip-chip LEDs (FCLEDs) have always been used in high current and high power operations to alleviate the thermal budget problem. The FCLED configuration has high extraction efficiency compared to a conventional LED due to the thicker light extraction window layer and the smaller difference between the refractive index of the sapphire substrate ($n_{sapphire} = 1.76$) and air ($n_{air} = 1.0$). The critical angle of the output light is larger and TIR is reduced. Furthermore, a metal contact, including the n- and p-metal in FCLEDs, does not baffle the light output and can serve as a reflective mirror to reflect the light back through the transparent sapphire substrate.[6–8] However, in FCLEDs there is still the TIR effect between the sapphire substrate and air, which reduces the extraction efficiency of the transparent window layer. The surface roughness technique can enhance the light output; it works by scattering the photons from the textured semiconductor surface and the probability of photons escaping from the semiconductor can be increased.[9–11] A combination of conductive omnidirectional reflectors (ODRs) and a micro-pillar array sapphire surface has been developed.[12] A conductive ODR[13] serves as an ohmic contact layer and also a highly reflective mirror. Highly reflective ODRs will reflect radiated light with any incident angle to the top surface of the device.[14–16] The formation of micro-pillar arrays on the bottom side of the sapphire surface can increase the probability for photons to escape through the textured sapphire surface. FCLED performance for different micro-pillar depths and shapes will be discussed.

6.2.2 FC technology

Flip-chip (FC) technology has been developed by IBM to provide connections between the bonding pads of chips and the metallization on the substrates since 1960. The first technique was called controlled collapse chip connection (C4) and it displaced wire bonding, giving increased input/output density at a lower cost.[15] The C4 process starts by depositing under bump metallurgy (UBM) onto the bonding pads of the chips to supply good adhesion between the bonding pads and the bumps. The UBM usually consists of three layers: an adhesion and/or barrier layer, a wetting layer and an oxidation barrier layer. After that, solder bumps are formed on the UBM and reflow to become a solder ball. The next step is to put down the top surface metallurgy (TSM) onto the substrate. The chips are aligned and joined to the substrate. Subsequently, many methods of connecting the bonding pads of the chips to the metallization on the substrates have been developed, such as solder bump, tape-automated bonding (TAB), conductive adhesives, anisotropic conductive adhesives, wire bonding, metal bump, polymer bump and composite bump.

FC technology is a method for interconnecting semiconductor devices to external circuitry with flux-less solder bumps that have been deposited onto the chip pads. The LED chips are mounted onto a substrate with interconnects produced using various materials and methods. FC technology has been used for LEDs due to the better electrical and thermal dissipation. Figure 6.1 shows the structure of a conventional GaN-based LED. Sapphire is a common substrate used to grow a GaN film, but it is an insulator and a poor thermal material. Therefore, the n- and p-pads must be on the same side and lead to bonding pads that baffle the light output and decrease light extraction efficiency. Figure 6.2 shows the structure of a GaN-based FCLED. The n- and p-pads of FCLEDs do not baffle the light output and they can be used as a highly reflective mirror on the sub-mount to direct downward traveling light back to the sapphire substrate. The FC technique can enhance the light output power by 1.5 to 1.7 times compared to conventional

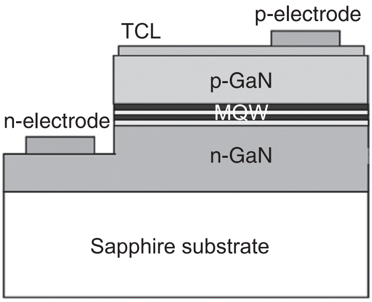

6.1 Structure of a conventional GaN-based LED. (MQW: multiple quantum well; TCL: transparent conductive layer)

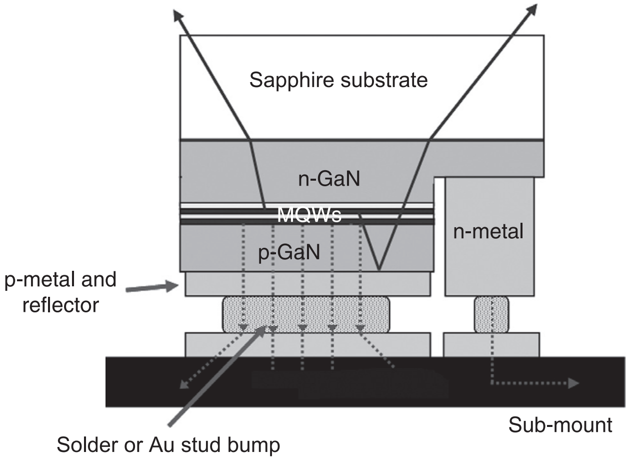

6.2 Structure of a GaN-based FCLED.

GaN-based LEDs.[16,17] Finally, heat can be conducted away by using a high thermal conductivity sub-mount bonded to metal, which gives better thermal dissipation. This is an important advantage for high-power LED applications.

6.3 GaN FCLEDs with textured micro-pillar arrays

The GaN LED structures with a dominant wavelength at 460 nm used in this study were grown by metal-organic chemical vapor deposition (MOCVD) on *c*-plane sapphire substrates. The LED structure consists of a 2-μm-thick undoped GaN layer, a 2-μm-thick highly conductive n-type GaN layer, a 0.2-μm-thick InGaN/GaN multiple quantum well (MQW), a 0.2-μm-thick p-type GaN layer and InGaN/GaN short-period superlattice (SPS) tunneling contact layers with indium-tin-oxide (ITO). Figure 6.3 shows the fabrication steps of a GaN FCLED with micro-pillar arrays (MPAs). Top-emitting LEDs with a size of 1000 μm × 1000 μm were fabricated using standard photolithography and BCl_3/Cl_2 inductively coupled plasma (ICP) etching for current isolation purposes. The p-GaN and active layers were partially etched by an ICP etcher to expose an n-GaN layer for an electrode. An indium-tin-oxide layer of 250 nm was deposited onto the p-GaN layer as a transparent conductive layer (TCL). The samples were then annealed at 500 °C for 10 minutes in air. A layer of Cr/Pt/Au metals (50 nm/50 nm/2500 nm) was deposited for the p- and n-contact pads. After completing the conventional face-up LED structure, the sapphire was ground down to a thickness of 100 μm. A 500-nm layer of nickel metal was deposited onto the bottom of the sapphire substrate as a dry-etching mask. The sample was then subjected to the ICP process using Cl_2/BCl_3 (10 sccm/30 sccm) plasma with an ICP power of 850 W and radio-frequency power of 400 W to form MPAs for light extraction. The ICP etching rate for the

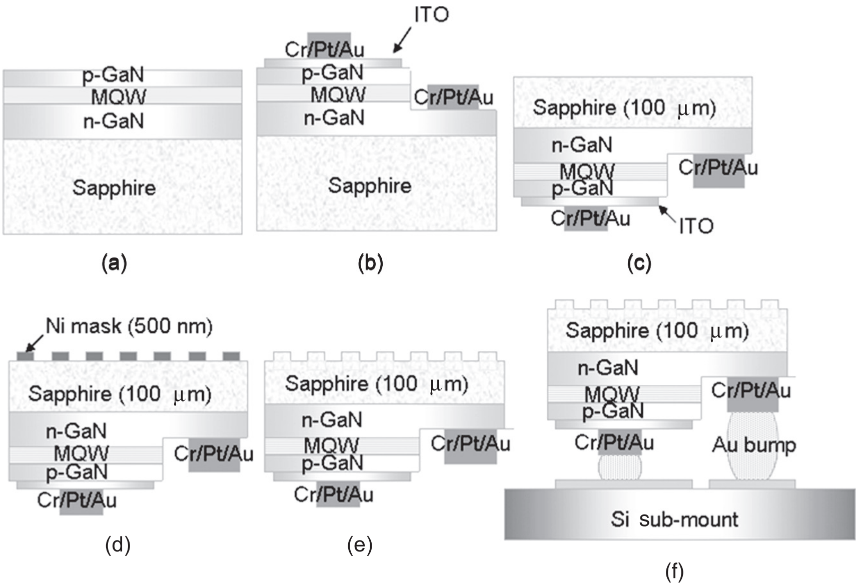
p-GaN
MQW
n-GaN
Sapphire
(a)
ITO
Cr/Pt/Au
p-GaN
MQW
Cr/Pt/Au
n-GaN
Sapphire
(b)
Sapphire (100 μm)
n-GaN
MQW
Cr/Pt/Au
p-GaN
Cr/Pt/Au
ITO
(c)
Ni mask (500 nm)
Sapphire (100 μm)
n-GaN
MQW
Cr/Pt/Au
p-GaN
Cr/Pt/Au
(d)
Sapphire (100 μm)
n-GaN
MQW
Cr/Pt/Au
p-GaN
Cr/Pt/Au
(e)
Sapphire (100 μm)
n-GaN
MQW
Cr/Pt/Au
p-GaN
Cr/Pt/Au
Au bump
Si sub-mount
(f)

6.3 Fabrication steps for GaN FCLEDs with MPAs: (a) before process, (b) normal process, (c) polishing, (d) mask layer, (e) ICP etching, (f) flip-chip bonding.

sapphire was approximately 800 Å/min. The processed LED wafer was broken into 1000 μm × 1000 μm chips using a laser scriber.

A layer of Ti/Al metals (500 Å/2000 Å) was deposited onto the silicon sub-mount as a mirror. A SiO_2 film of 800 Å was deposited onto it for passivation. A 2-μm layer of gold metal was deposited for the n- and p-bonding pads. The silicon sub-mount was then subjected to the stud bump process. Figure 6.4 shows the top view of a silicon sub-mount before FC bonding. Finally, the chips were FC bonded to the silicon sub-mount using a Panasonic ultrasonic FC bonder for electrical and optical measurement, as shown in Fig. 6.5.

In an attempt to verify the effect of the MPA surface on light extraction efficiency, pillars with various depths and bevel angles were formed for comparison. The surface morphology of the GaN FCLEDs with MPA sapphire surfaces were examined by scanning electron microscope (SEM) as shown in Fig. 6.6. The periodic distance for the pillar array was about 5.5 μm and the depth of the pillars was between ~1.1 μm and 3.2 μm. Furthermore, the bevel angle of the pillars changed from 8° to 35° with increasing dry-etching time. Figures 6.6(a) and 6.6(b) show pillars with a smooth top surface and sidewall. On increasing the dry-etching time, the surface of the micro-pillars becomes rougher and there is a larger bevel angle as shown in Fig. 6.6(c). Figure 6.6(d) shows pillars with a pineapple-like textured surface. The results may be ascribed to the uniformity of

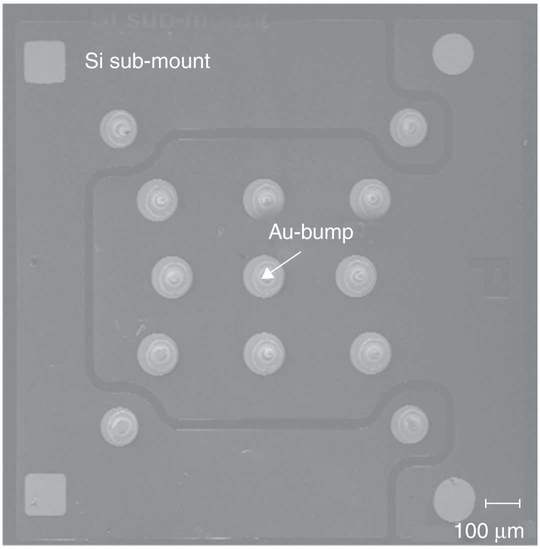
Si sub-mount
Au-bump
100 µm

6.4 SEM image of silicon sub-mount before FC bonding.

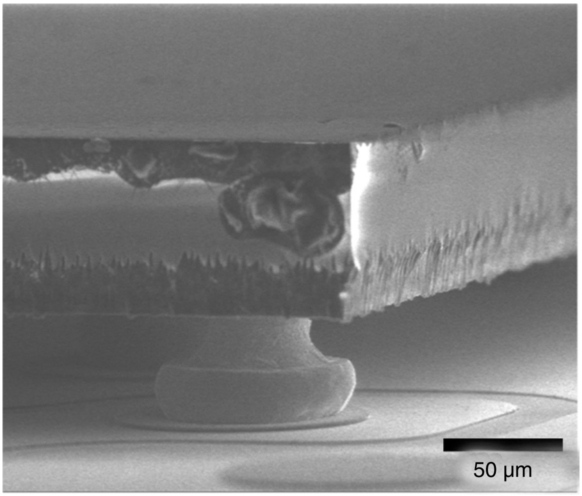

6.5 SEM image of a chip bonded to the silicon sub-mount.

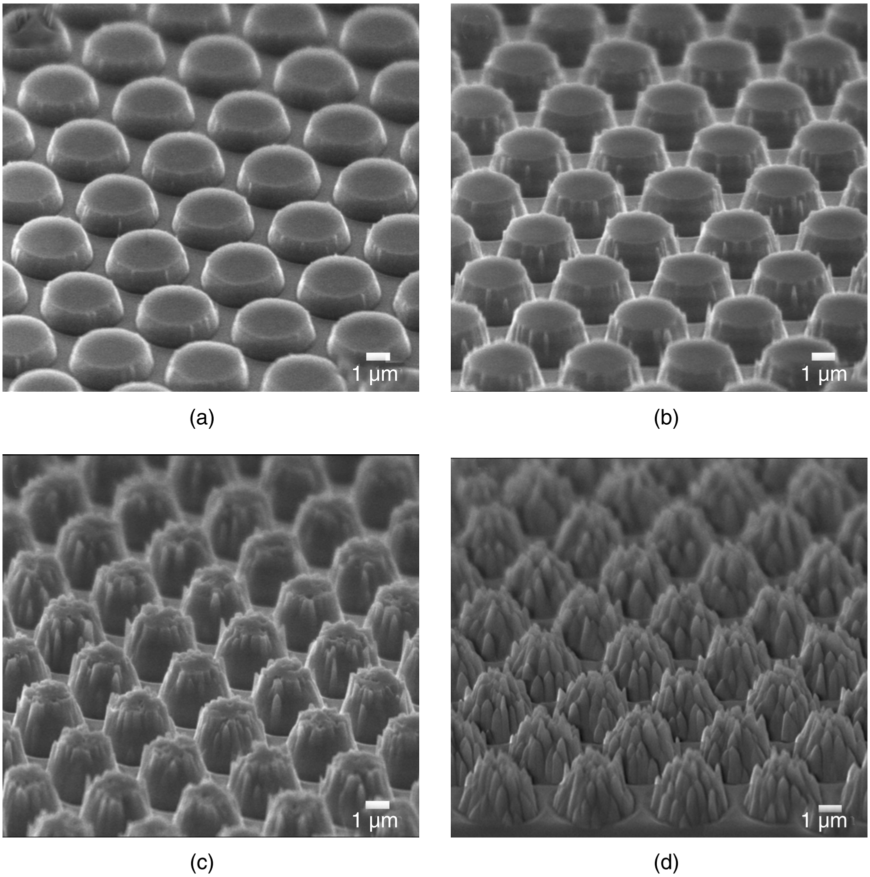

(a) (b) (c) (d)

6.6 SEM images of the MPA surfaces of a sapphire backside with various depths and bevel angles: (a) 1.1 µm MPA, (b) 1.8 µm MPA, (c) 2.7 µm MPA and (d) 3.2 µm MPA.

the hard nickel mask, which results in partial over-etching and an uneven pillar surface.

The GaN FCLED chips were packaged into a TO can without epoxy resin for subsequent measurement. The light-current-voltage (*L-I-V*) characteristics were measured using a high-current measurement instrument (Keithley-240). The light output power of the GaN FCLEDs was measured using an integrated sphere with a calibrated power meter. The *I-V* characteristics of flat-surface FCLEDs and MPA-FCLEDs were also measured as shown in Fig. 6.7. The *I-V* curves of MPA-FCLEDs show normal p-n diode behavior with a forward voltage of 3.4 V (at 350 mA), indicating that there was no heating or charging damage during the fabrication of the MPAs by the ICP etching process. The light output

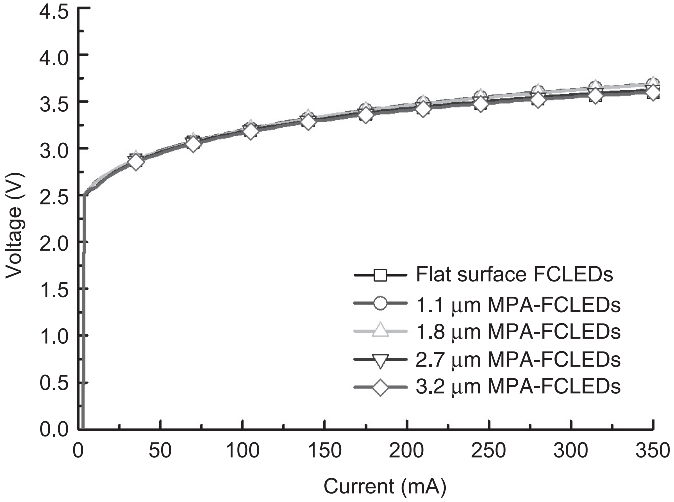

6.7 Current-voltage (*I-V*) characteristics of flat-surface FCLEDs and MPA-FCLEDs.

power-current characteristics of the flat FCLEDs and MPA-FCLEDs are shown in Fig. 6.8. We clearly observed that the output power of the MPA-FCLEDs is larger than for the flat FCLEDs. At an injection current of 350 mA, it was found that the MQW emission peaks of those devices were located at about 460 nm, and the light output power of the flat FCLEDs and MPA-FCLEDs with depths of 1.1 μm, 1.8 μm, 2.7 μm and 3.2 μm were about 151 mW, 165 mW, 179 mW, 227 mW and 252 mW, respectively. Figure 6.9 shows that the enhancement of the light extraction efficiency for MPA-FCLEDs with various pillar depths ranges from 10% to 68% at 350 mA current injection compared to a conventional flat-surface FCLED. This indicates that the textured sapphire surface reduces TIR and increases the probability that photons will escape from the semiconductor to the air. Furthermore, with the increase of pillar depth (from 1.1 μm to 3.2 μm) and bevel angle (from 8° to 35°), the light output power of the MPA-FCLED increased by 55% under 350 mA current injection. These results can be attributed to the increase of the effective surface area on increasing the depth and bevel angle of the micro-disk. Plate II (see colour section between pages 330 and 331) shows images of a conventional flat-surface FCLED and a MPA-FCLED under 350 mA current injection. The intensity distributions are also shown. The electroluminescence (EL) intensities for the MPA-FCLED clearly exceeded those from the conventional flat FCLED under the same current injection, especially on the FCLED top surface. The improved light extraction efficiency was further supported by beam view analysis results.

Obviously, the results indicate that a sapphire substrate with an MPA surface reduces the internal light reflection and increases the light extraction efficiency.

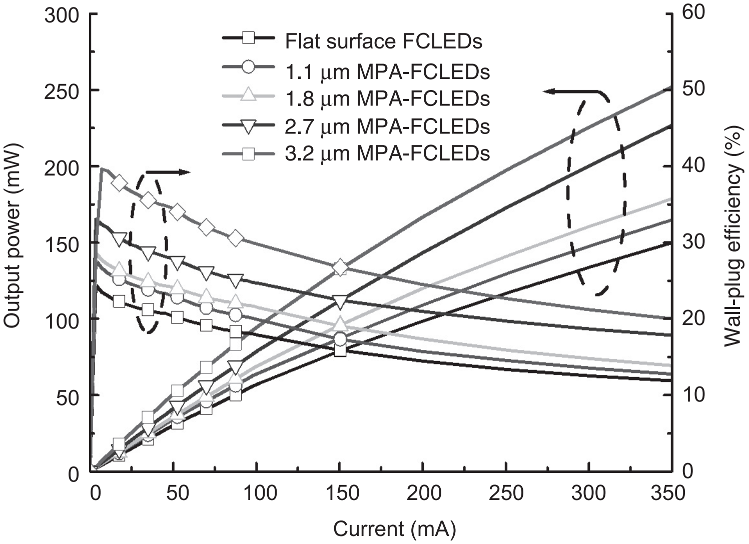

6.8 Light output power-current (*L-I*) curves of flat-surface FCLEDs and MPA-FCLEDs.

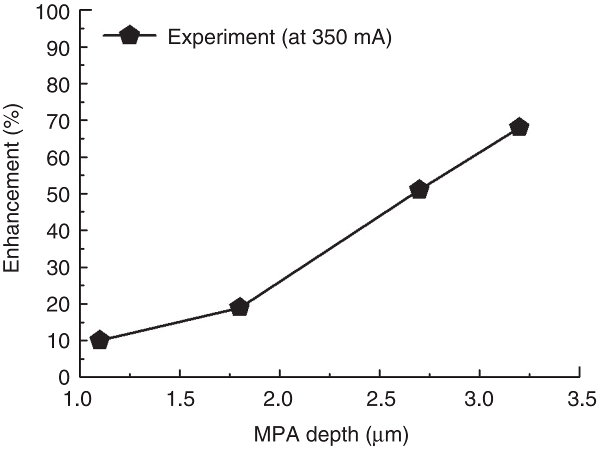

6.9 Light extraction enhancement versus MPA depth.

The probability of light escaping from the sapphire to air is increased due to the increase of the escape cone by the MPA structure. This enhancement can be attributed to the roughness of the top surface and because photons are more likely to be emitted from a surface-roughened device, resulting in an increase of the light output power of the MPA-FCLED.

6.4 GaN FCLEDs with a geometric sapphire shaping structure

There has been intensive research into improving the light extraction efficiency and enhancing the brightness of LEDs. The effect of a geometric chip structure on the light extraction efficiency has been discussed in many papers.[18–21] Krames *et al.* reported the enhancement of the extraction efficiency for truncated-inverted-pyramid AlGaInP-based LEDs.[18] Eisert and Harle described their experimental and simulated results that showed enhanced light extraction efficiency of GaN-based LEDs chip with an undercut SiC substrate.[19] Chang *et al.* reported a 10% output power enhancement from InGaN/GaN MQW LEDs with wave-like textured sidewalls.[20] Kao *et al.* described a light output enhancement for a nitride-based LED with 22° undercut sidewalls.[21] All these methods have one thing in common, which is that photons generated within the LEDs have multiple opportunities of finding the escape cone. As a result, the light extraction efficiency and the LED output intensity could both be enhanced significantly. A simple method of fabricating oblique sidewalls will help in increasing the brightness of GaN-based LEDs. GaN-based FCLEDs with a geometric sapphire shaping structure have been developed.[22] The formation of oblique sapphire sidewalls on the bottom side of the sapphire surface could be a better way to improve the probability that the photons will escape. The electrical and optical properties of the sapphire shaped FCLEDs were reported.[23]

The GaN LED structures used in this study were grown in the same way as those with textured micro-pillar arrays (Section 6.3) and had the same dominant wavelength (460 nm) and LED structure. Figure 6.10 shows the fabrication steps of GaN FCLEDs with a geometric sapphire shaping structure (SS-FCLEDs). First, an SiO_2 film of size of 1000 μm × 1000 μm was deposited onto the backside of a sapphire substrate by plasma-enhanced chemical vapor deposition and defined using standard photolithography to serve as the wet-etching hard mask. To avoid damaging the epitaxial layer, an SiO_2 film was also deposited onto the epitaxial layer as a sheathing. The sapphire substrate was then immersed in a H_2SO_4:H_3PO_4 (3:1) solution at an etching temperature of 330 °C for 70 minutes. The sapphire wet-etching rate was about 1.4 μm/min, which is related to the H_3PO_4 composition and the etching temperature. After finishing the sapphire shaping process, top-emitting LEDs with a size of 1000 μm × 1000 μm were fabricated using the standard photolithography process. They were aligned with the backside sapphire shaping pattern and were partially etched using an inductively coupled plasma etcher to expose an n-GaN layer for the electrode. An ITO layer (250 nm) was deposited onto the p-GaN layer as a transparent conductive layer. The samples were then annealed at 500 °C for 10 minutes in air. A layer of Cr/Pt/Au metals (50 nm/50 nm/2500 nm) was deposited for the p- and n-contact pads. After conventional LEDs processes, the processed LED wafer was broken into 1000 μm × 1000 μm chips using a laser scriber. A layer of Ti/Al metals

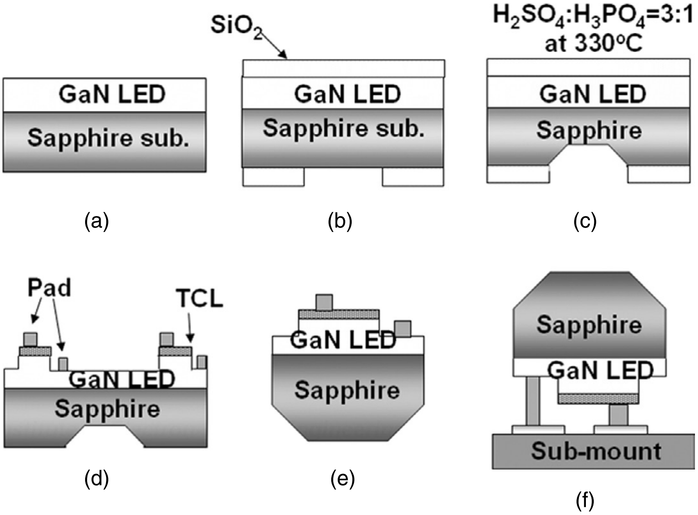

6.10 Fabrication steps for SS-FCLEDs: (a) MOCVD growth of GaN LED epilayer, (b) growth of SiO_2 passivation layer, (c) wet etching of sapphire substrate, (d) normal process, (e) laser cutting and dicing, (f) flip-chip bonding.

(500 Å/2000 Å) metals was deposited onto the silicon sub-mount as a mirror. A SiO_2 film of 800 Å was deposited onto it for passivation. A 2-μm layer of gold metal was deposited for n- and p-bonding pads. The silicon sub-mount was then subjected to stud bump process. Finally, the LED chips with an oblique sapphire shaping sidewall were FC bonded to the silicon sub-mount using a Panasonic ultrasonic FC bonder for electrical and optical measurement. Figure 6.11 is a schematic drawing of a GaN SS-FCLED and a sketch indicating how light can exit from the oblique sapphire sidewall.

Figure 6.12 shows SEM images of the sapphire shaping structure. The sapphire was etched for 70 minutes with an etching rate of about 1.4 μm/min. The etching depth was about 100 μm, as shown in Fig. 6.12(b). The crystallography facets are the (1–102), (1–106) and (11–25) planes against the (0001) c-axis and their angles against the (0001) c-axis are 60°, 30° and 50°, respectively, as shown in Fig. 6.13. Furthermore, the etching structures are all V-grooves. The V-shaped structure can be used to form a cleaving line to break the thick (~450 μm) sapphire substrate. SEM images of a conventional FCLED (C-FCLED) and a SS-FCLED are shown in Fig. 6.14. The sapphire shaping area and the much thicker window layer are clearly visible on the SS-FCLED structure compared with the C-FCLED. The oblique sapphire geometry improves light extraction by reducing the number of totally internally reflected photons from the sidewall interfaces, and the photons can escape through the oblique sidewall. In addition, the thicker sapphire window

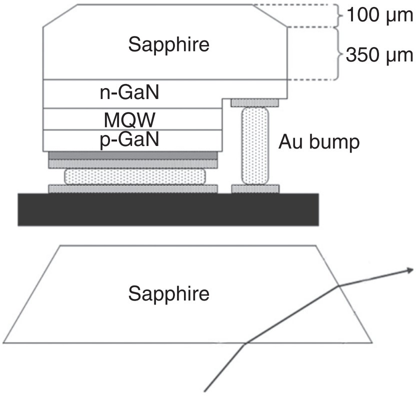
100 µm
350 µm
Sapphire
n-GaN
MQW
p-GaN
Au bump
Sapphire

6.11 Upper: GaN SS-FCLED. Lower: Light can exit from the oblique sapphire sidewall.

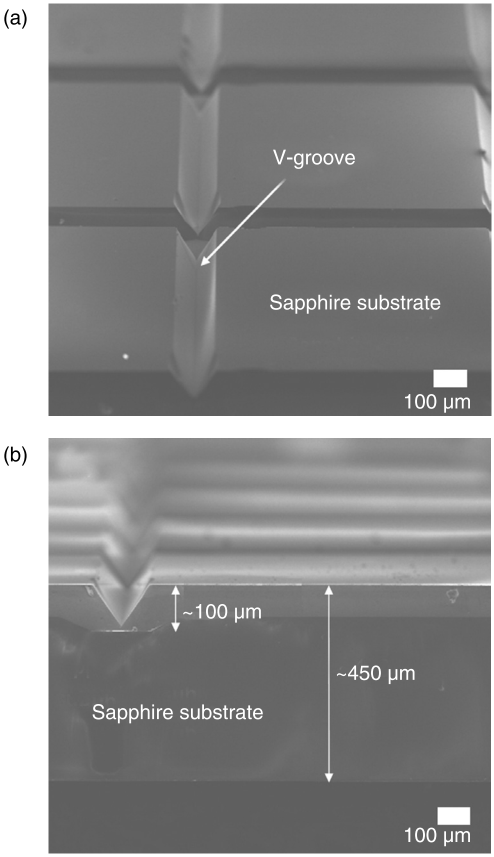
(a)
V-groove
Sapphire substrate
100 µm
(b)
~100 µm
~450 µm
Sapphire substrate
100 µm

6.12 SEM images of sapphire shaping structure: (a) top and (b) cross-sectional views.

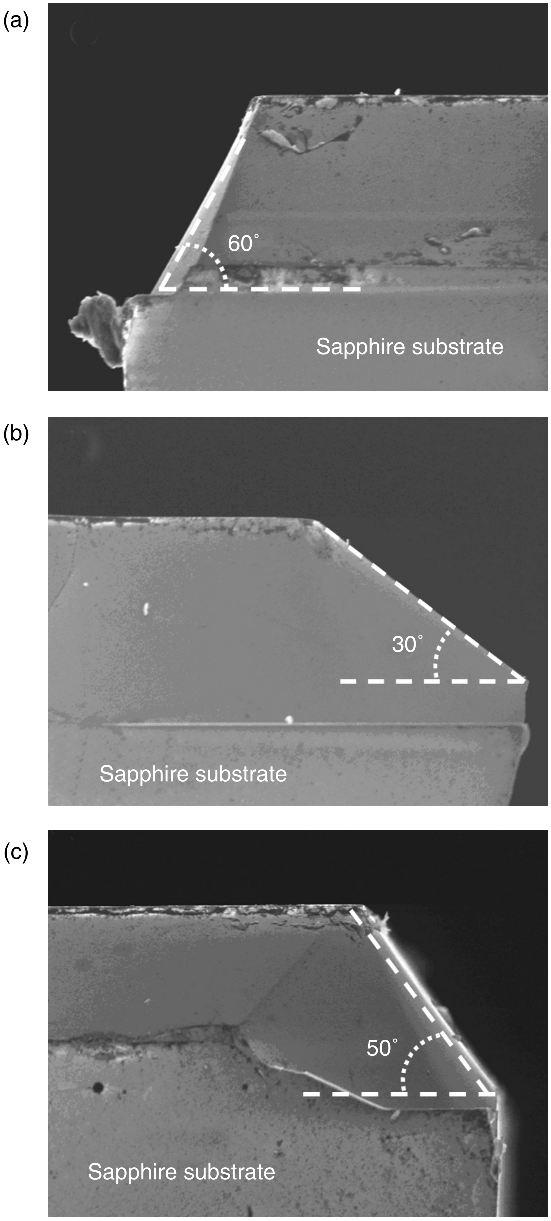
(a)
60˚
Sapphire substrate
(b)
30˚
Sapphire substrate
(c)
50˚
Sapphire substrate

6.13 SEM images of the crystallography facets of (a) R-plane (60°), (b) A-plane (30°) and (c) M-plane (50°) against (0001) c-axis.

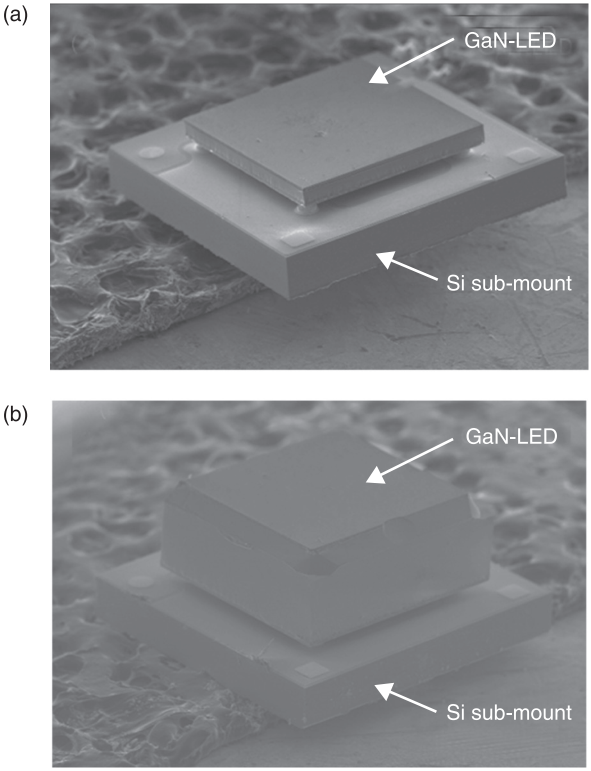

6.14 SEM images of (a) C-FCLED and (b) SS-FCLED devices.

layer has significant advantages over a conventional thin sapphire window layer because it facilitates light emission from the edges of the chip. These two processes significantly reduce the photon path length for extraction in a SS-FCLED device compared to a conventional chip. The benefits are visible in the photomicrographs in Fig. 6.15. Note that light appears to radiate evenly from the thicker window layer and oblique sidewall of the SS-FCLED compared with the C-FCLED, indicating that the light extraction efficiency was improved due to the oblique sapphire geometry and thicker window layer.

The LED chips were packaged into a TO can without epoxy resin for the subsequent measurement. The corresponding *I-V* characteristics of SS-FCLEDs and C-FCLEDs were measured, as shown in Fig. 6.16. The *I-V* curve for SS-FCLEDs exhibits a normal p-n diode behavior with a forward voltage of 3.5 V (at 350 mA), indicating that the high-temperature sapphire wet-etching process does not appear to adversely affect the *I-V* characteristics of these devices. Figure 6.17 shows the light output power and wall-plug efficiency as a function of injection current for $\lambda_p \sim 460$ nm SS-FCLEDs and C-FCLEDs. The light output power of the SS-FCLEDs is larger than for the C-FCLEDs. Under a current

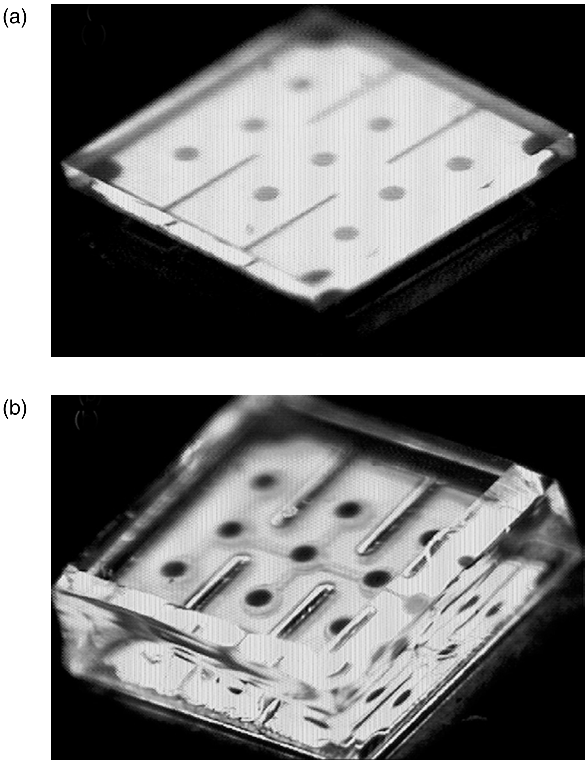

6.15 Photomicrographs of (a) C-FCLED and (b) SS-FCLED chips ($40 \times 40\,\mathrm{mm}^2$) operating at 20 mA (dc) with an emission wavelength of $\lambda_p \sim 460$ nm.

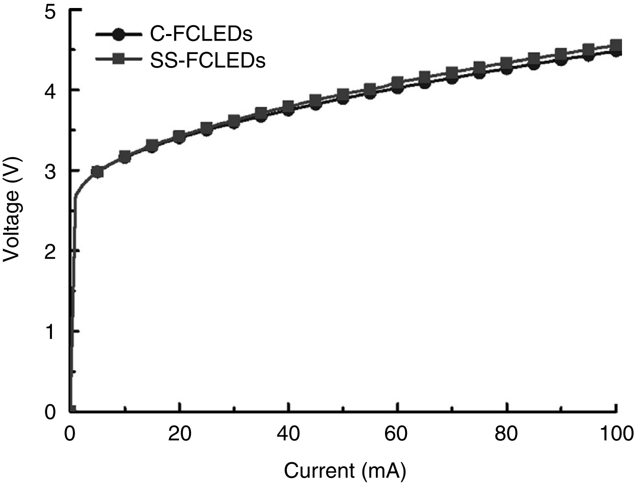

6.16 Current-voltage (*I-V*) characteristics of SS-FCLEDs and C-FCLEDs.

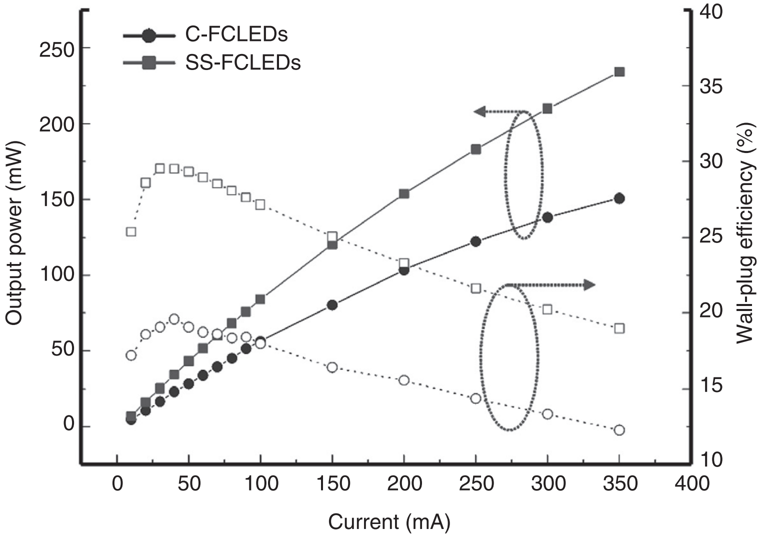

6.17 Light output power and wall-plug efficiency as a function of injection current for λ_p~460 nm SS-FCLEDs and C-FCLEDs.

injection of 350 mA, the light output power of the SS-FCLEDs compared to the C-FCLEDs was significantly raised from 150 mW to 234 mW and the wall-plug efficiency was increased from 12.26% to 18.98%. We note that bare SS-FCLEDs (without encapsulating an epoxy lens) have a 55% enhancement of light extraction efficiency under a current injection of 350 mA compared to the C-FCLEDs. This indicates that the geometric sapphire sidewall reduces TIR and increases the probability that photons will escape from the semiconductor to the air. Furthermore, the thicker sapphire window layer has a significant advantage over a conventional thin sapphire window layer because it facilitates light emission from the edges of the chip.

Figure 6.18 shows normalized far-field patterns for SS-FCLEDs and C-FCLEDs under A current injection of 20 mA. For a detailed comparison, the normalized far-field patterns in two directions – the X axis ((1–106) plane to (1–102) plane) and the Y axis ((11–25) plane to (11–25) plane) – were measured. The experiment results show the electroluminescence (EL) intensities of C-FCLEDs are concentrated on the near vertical direction. In contrast, EL intensities observed from the SS-FCLED are concentrated on the near horizontal direction (i.e. larger than 120°). Plate III (see colour section between pages 330 and 331) shows normalized three-dimensional far-field patterns of SS-FCLEDs and C-FCLEDs, which confirm that the oblique sidewall changes the far-field pattern and increases the viewing angle by 50%. This enhancement is attributed to the oblique sidewall and the thicker window layer so that the probability of photons being emitted from the device in the near horizontal directions has increased.

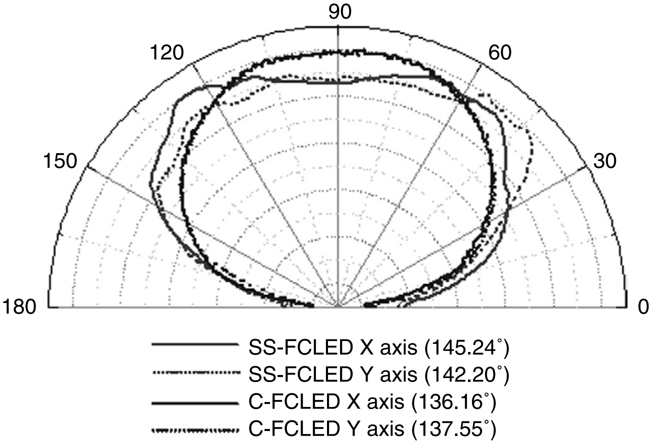

6.18 Normalized far-field patterns for SS-FCLEDs and C-FCLEDs for two directions. X axis: (1–106) plane to (1–102) plane; Y axis: (11–25) plane to (11–25) plane. The intensity is shown with arbitrary units.

6.5 GaN thin-film photonic crystal (PC) LEDs

The GaN sapphire-based LED approach is limited by several factors. First, the sapphire substrate causes substrate losses, which are difficult to avoid, other than by introducing an efficient distributed Bragg reflector (DBR), ODR, etc. Second, because thick GaN epilayers have been grown, multiple guided modes propagate and some of the lower-order guided modes tend to ignore the photonic crystal (PC) interaction. A stronger photonic interaction is desirable but this can only be obtained if the GaN layer is thin enough. Third, the question of efficient p-contacts is still unsolved. One may consider using a semitransparent metallic contact over the PC or even using a transparent injector such as ITO, but both of these present drawbacks: there is still absorption and ITO tends to lose its transparency over time. Finally, other crucial aspects for an efficient LED have been ignored, such as thermal management and mounting into a package. Sapphire is a poor thermal conductor, which limits the maximum electrical power in GaN LEDs with a sapphire substrate. Unfortunately, most of the work on GaN LEDs is directed at obtaining good high-power LEDs, which certainly require high current densities.

For all these reasons, the solution is usually to use GaN epifilm-transferred technology to obtain high-powered LEDs. The metal substrate also provides enhanced thermal dissipation. Here, the sapphire substrate is removed and the GaN epilayer thinned down. Thus, reducing the number of guided modes in a GaN waveguide LED by reducing the GaN thickness is of interest, to produce thin-film LEDs (TFLED). A GaN TFLED is actually a GaN microcavity LED composed of a GaN epifilm placed between the top air/GaN interface and the bottom metallic reflector mirror. A GaN-based TFLED combined with PC has been reported for the blue wavelength range.[24–26] Recently, an AlInGaP TFLED combined with PC and a DBR was reported to have enhanced light extraction efficiency and temperature stability in the red wavelength range.[27] GaN PC TFLEDs emitting blue wavelengths have been fabricated and the guided modes extraction behavior and the far-field emission distribution characteristics were studied in detail.[26]

6.5.1 Semiconductor wafer bonding

In the past, many approaches have been proposed and demonstrated for joining dissimilar systems onto one platform for monolithic integration. For example, in the early and mid-1980s, extensive work in integrating GaAs thin films with silicon substrates aimed to combine the optoelectronic functionality of GaAs with the processing power of complementary metal-oxide-semiconductor silicon integrated circuit technology.[28] The union of GaAs devices with silicon substrates would have created new possibilities for high-speed communications. However, the direct heteroepitaxial growth of GaAs thin films on a silicon substrate with a low density of dislocations is difficult. Wafer-bonding technology is an alternative approach to this problem. In wafer bonding, two highly polished, flat and clean wafers of almost any material, when brought into contact at room temperature, are locally attracted to each other by van der Waals forces and adhere or bond to each other. Standard direct wafer bonding is attributed to relatively weak van der Waals forces and subsequent annealing at high temperature is required to achieve a strong bond. This phenomenon has been known for a long time for optically polished pieces of material and was first investigated for polished pieces of quartz glass by Rayleigh in 1936.[29] A variety of techniques have been employed to bond the two surfaces together, the methods being distinguished by the characteristics of the bonded interface. Some of the common wafer-bonding techniques and their associated properties have reported.[30–34]

6.5.2 Epifilm-transferred technology

III-nitride semiconductors are promising materials for producing optoelectronic devices working in the ultraviolet to visible spectrum. Due to the lack of a substrate with a good lattice match, the majority of III-nitride devices are grown onto a sapphire substrate, which provides a hexagonal template for growing wurtzite GaN. However, the poor electrical conductivity and low thermal conductivity of the sapphire substrates causes the poor characteristics of the GaN electronic devices. Recently, GaN epifilm-transferred technology has been widely used to produce HB-LEDs, such as TFLEDs.[35,36] Epifilm-transferred technology combined with wafer bonding and laser lift-off (LLO) techniques may be a direct approach for eliminating the sapphire growth substrate. In this approach, the GaN epifilm is transferred to a substrate with better thermal and electrical conductivity

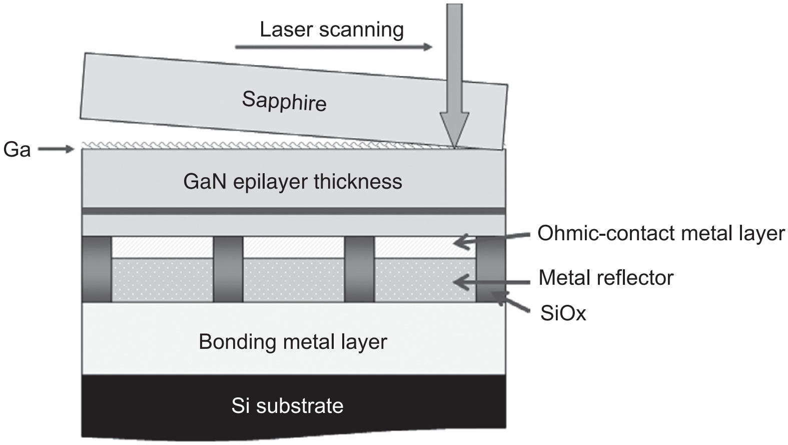

6.19 Laser lift-off process.

to improve the light extraction efficiency and drooping characteristics of GaN-based TFLED devices.

A GaN epifilm grown on a substrate can be separated from the substrate by a laser illumination process.[37,38] LLO techniques[39–41] use a KrF excimer pulsed laser. Sapphire is transparent to the beam ($\lambda_{ex}=248\,\text{nm}$), which is absorbed by the interfacial GaN. The temperature increases at the interface, inducing the decomposition of the interfacial GaN into gaseous nitrogen and gallium droplets, as shown in Fig. 6.19. This process is termed laser-assisted film debonding and has considerable potential for fabricating devices when used in conjunction with wafer-bonding techniques. However, a GaN TFLED structure is actually a GaN microcavity LED composed of a GaN epifilm placed between the top air/GaN interface and the bottom metallic reflector mirror.

6.6 PC nano-structures and PC LEDs

A photonic crystal (PC) nano-structure is any structure with a periodic variation in its refractive index and these structures provide exciting new ways to manipulate photons.[42–44] The periodicity can be in one, two or three spatial dimensions and can introduce a photonic bandgap (PBG) (a range of frequencies for which electromagnetic radiation is non-propagating) with the same dimensionality. A PBG arises due to Bragg's reflection and occurs when the spatial periodicity has a length approximately one half that of the wavelength of the incident electromagnetic radiation. The same phenomenon gives rise to the electronic bandgap in semiconducting materials.[45] Examples of PC structures with periodicity in different spatial dimensions are shown in Fig. 6.20. Recently, novel optical properties that are tunable by the period of the PC and the size of the nano-objects

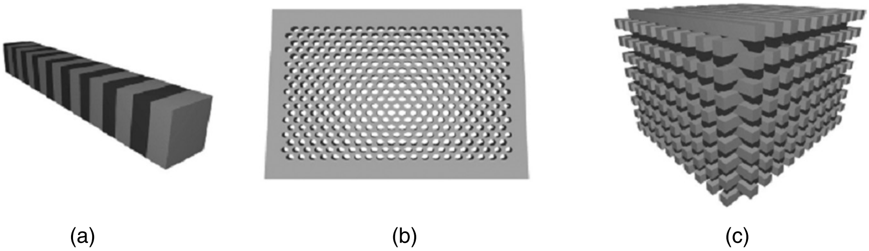
(a) (b) (c)

6.20 Photonic crystals with periodicity in (a) one, (b) two and (c) three dimensions. The different colors represent materials with different dielectric crystals.

have been the subject of much research work. One-dimensional (1D) PCs are used as Bragg reflectors, which are part of the optical feedback mechanism in distributed feedback lasers[46–47] and vertical cavity surface-emitting lasers.[48] In addition, two- and three-dimensional (2D and 3D) PCs have been the subject of intense research in areas related to sensing,[49–51] telecommunications,[52–54] slow light[55–58] and quantum optics.[59–61]

As mentioned above, PCs exhibit unique dispersion properties (e.g. such as a PBG[42]) and can be used to manipulate light emission. There are several schemes to obtain light extraction through PC nano-structures on GaN-based LEDs, as shown in Fig. 6.21,[62] such as

- *Inhibition of emission of guided modes by PBG.* Light can only escape using out-of-plane leakage modes. The emission region is etched with a deep pattern to forbid the propagation of guided modes, and thus force the emitted light to be redirected toward the outside, as shown in Fig. 6.21(a). This method needs high radiative efficiency. Etching through the active layer can cause troublesome current injection and large non-radiative recombination rates due to induced surface states.
- *Enhancement of spontaneous emission in a small 3D PC cavity by the Purcell effect*. Defects in PCs behave as microcavities, as shown in Fig. 6.21(b), such that the Purcell effect can be used to enhance spontaneous emission.
- *Emission extraction over the whole surface by leaky mode coupling.* PCs can be used as 2D diffraction gratings in slabs or as waveguides to extract the guided modes into the air and redirect the emission, so that light can only escape through leaky mode couplings, as shown in Fig. 6.21(c). Because the extraction and generation regions are not separated, the active layer is efficiently used as the total emitting surface.

In this study, the extraction of waveguide light from GaN PC sapphire-based and microcavity LED structures was studied using 2D PCs as diffractive elements. A light wave propagating in a GaN PC LED waveguide structure, with propagation partially confined by TIR, can interact with the reciprocal lattice vectors of the 2D

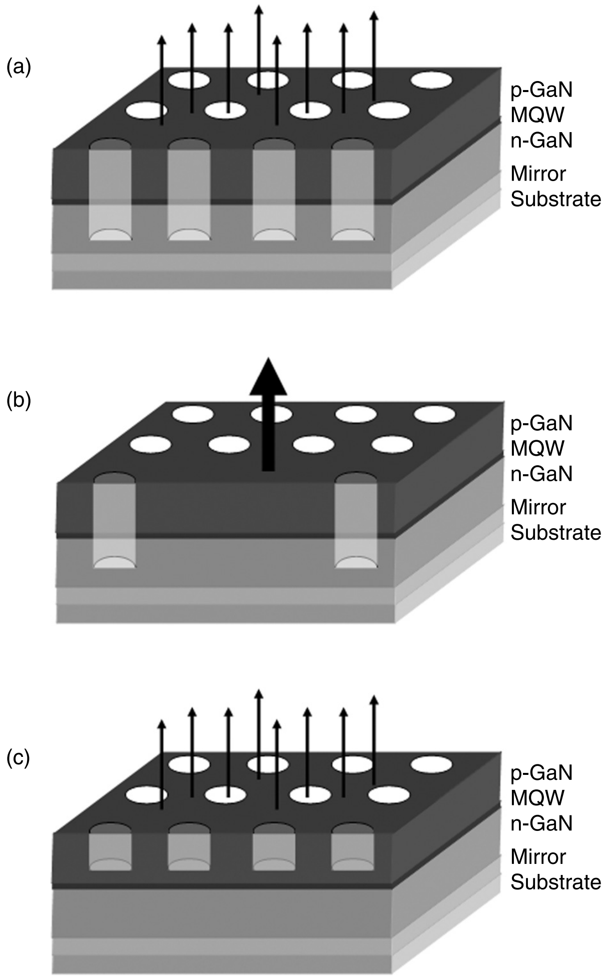
(a)
p-GaN
MQW
n-GaN
Mirror
Substrate
(b)
p-GaN
MQW
n-GaN
Mirror
Substrate
(c)
p-GaN
MQW
n-GaN
Mirror
Substrate

6.21 Various extraction methods using PCs: (a) PBG, (b) Purcell effect, (c) leaky mode coupling.

PC lattice to exhibit a variety of novel behaviors due to light localization.[63] On the other hand, GaN PC LEDs can use Bragg diffraction to scatter the guided light into the escape cone to circumvent the deleterious effect of TIR, which traps most of the light emitted in LED chips.[64]

Figure 6.21(c) is a schematic of a surface grating device showing light extraction from a PC lattice, which will be described using the Ewald construction of Bragg's diffraction theorem. According to Bragg's diffraction law: $k_g \sin\theta_1 + mG = k_0 \sin\theta_2$. Phase-matching diagrams in the wave number space are shown in Fig. 6.22(a). The two semicircles in Fig. 6.22(a) correspond to: (1) the waveguide mode

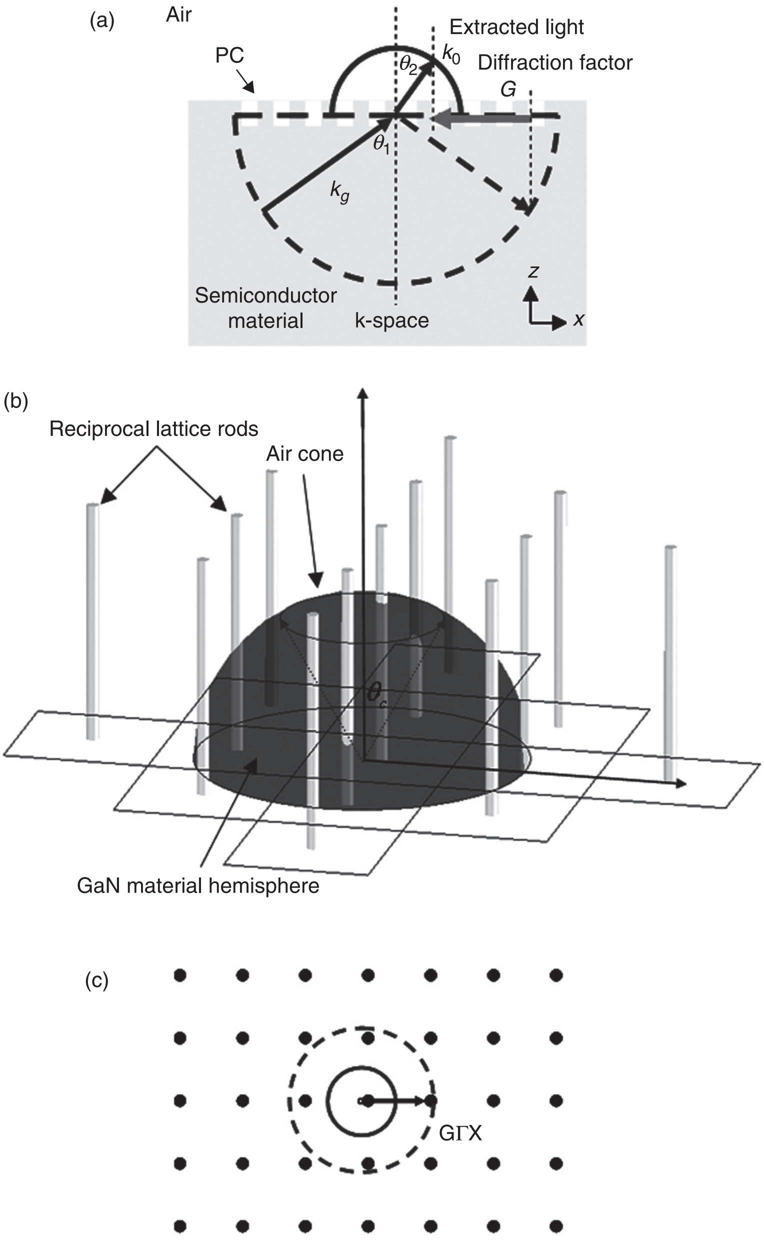
(a)
Air
Extracted light
PC
θ_2
k_0
Diffraction factor
G
θ_1
k_g
z
x
Semiconductor material
k-space
(b)
Reciprocal lattice rods
Air cone
θ_c
GaN material hemisphere
(c)
GΓX

6.22 (a) 2D PC structure with Bragg diffraction phase-matching diagrams. (b) Ewald construction for a square PC lattice. (c) Projection of the Ewald sphere construction onto the waveguide plane. The thick circle is the air cone and the dashed circle is the waveguide mode cone.

semicircle with radius $k_g = 2n\pi/\lambda$ where n is the effective refractive index of the guided mode and (2) the air cone with radius $k_0 = 2\pi/\lambda$. The light extraction from PC can be quantitatively analyzed using the Ewald construction in the reciprocal space. The extraction of waveguide light into air can be described by the relation $|k_g + G| < k_0$, where G is the diffraction vector. This relation can be represented graphically with the Ewald construction commonly used in X-ray crystallography. In the present case, for simplicity, the PC is treated as 2D in an overall 3D structure as is commonly done. In this case, the reciprocal lattice of the 2D PC will be represented as rods protruding perpendicular to the waveguide plane. Figure 6.22(b) depicts an Ewald sphere for a square PC lattice with the k vector of the incident light pointing directly at a reciprocal lattice point. The center of the sphere is at the end of the vector and the radius is the magnitude of k_g. The intersection points of the sphere with the protruding rods define the extraction direction of the diffracted light. For simplicity, only in-plane propagation needs to be considered and the projection onto the waveguide plane is sufficient. When the in-plane component of the resultant wave vector, after coupling to a reciprocal lattice vector, falls inside the air circle, the diffracted light can escape into the air, as shown in Fig. 6.22(c).

For example, in an actual 2D square PC lattice used as a grating, the diffraction vector exhibits anisotropy. Figure 6.23 shows the diffraction vector for various values of the lattice constant a, and dispersion circles for the in-plane wave vector in air, k_0, and in the semiconductor material, k_g. In the square lattice of the PC, $G_{\Gamma X}$ and $G_{\Gamma M}$ are $2\pi/a$ and $2\sqrt{2}\pi/a$, respectively. When $G_{\Gamma X} > k_0 + k_g$ $[a/\lambda < 1/(n+1)]$, the zone-folded curve does not enter the air curve, so diffraction does not occur, as

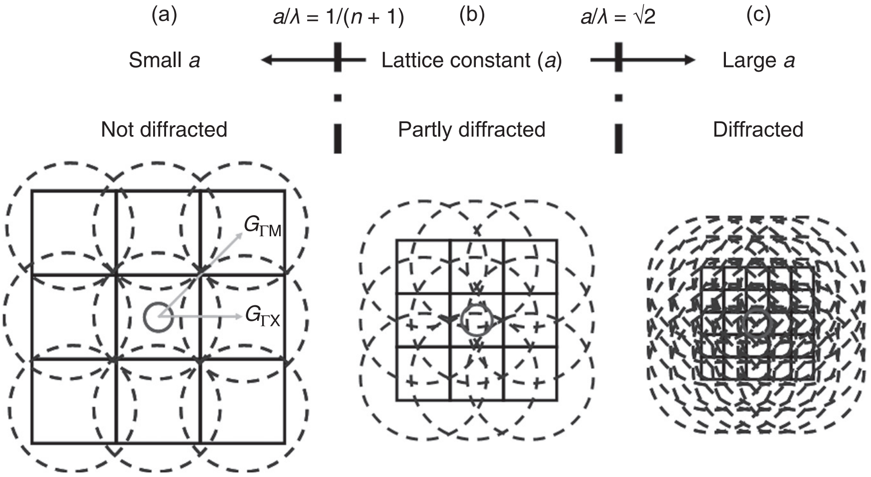

6.23 Brillouin zones for 2D square PC lattices showing the dispersion curves for k_0 (center thick circle) and k_g (dashed circles).

shown in Fig. 6.23(a). When *a* is larger than this value, some diffraction occurs, as shown in Fig. 6.23(b). When *a* is large enough to satisfy $G_{\Gamma M} < k_0$ ($a/\lambda > \sqrt{2}$), the diffraction vector is wholly included in the air curve, and this gives the maximum light diffraction efficiency. However, the diffraction efficiency cannot be unity for large *a*, since the light not only enters the extraction light cone but also another solid angle not extracted by the diffraction. Even when diffracted into the extraction light cone, half of the light will go downward.

6.7 Light emission characteristics of GaN PC TFLEDs

The blue GaN LED structure used consists of a 30-nm-thick GaN nucleation layer, a 4-μm-thick undoped GaN buffer layer, a 3-μm-thick silicon-doped n-GaN layer, which consists of a 150-nm $In_{0.05}Ga_{0.95}N$/GaN superlattice (SL) with ten periods and a 120-nm $In_{0.15}Ga_{0.85}N$/GaN MQW active region (dominant wavelength $\lambda_0 = 470$ nm) with eight periods, a 20-nm-thick Mg-doped p-AlGaN electron blocking layer and a 300-nm-thick Mg-doped p-GaN contact layer. The detailed wafer processing for the GaN TFLEDs with PC used the LLO technique to remove the growth substrate as described above and as shown in Fig. 6.24. The resulting structure was then thinned by chemical-mechanical polishing (CMP) to obtain a GaN cavity thickness $T \sim 1500$ nm. The PC with a square lattice of circular holes was then defined by holographic lithography. Holes were etched into the top n-GaN surface to a depth $t = 150$ nm. Figure 6.25(a) is a transmission electron micrograph (TEM) showing the cross section of the GaN PC TFLED structure. The lattice constant, *a*, of the PC used for the far-field study was 290 nm, 350 nm and 400 nm, and the hole diameter *d* was fixed with the ratio $d/a = 0.7$. A SEM image of a square PC lattice structure is shown in Fig. 6.25(b). Finally, a patterned Cr/Pt/Au (30/70/2000 nm) electrode was deposited onto the n-GaN as the n-type contact layer and Cr/Au metal (30/2000 nm) was deposited onto the backside of the silicon substrate.

A prepared sample structure is shown in Fig. 6.26. The light extraction characteristics of GaN PC TFLEDs with various values of the PC lattice constant *a* were measured and compared. The light-current-voltage (*L-I-V*) characteristics were measured using an integration sphere with a silicon photodiode. The turn-on voltage was about 2.7 V. The light output power of the GaN PC TFLEDs with PC lattice constant *a* values of 290 nm, 350 nm and 400 nm at a driving current of 200 mA is shown in Fig. 6.27. The output power was enhanced by 45%, 68% and 77%, respectively, compared to a GaN TFLED without PC. At 200 mA driving current, the forward voltages of the GaN PC TFLEDs with PC lattice constant *a* values of 290 nm, 350 nm and 400 nm were 6.2 V, 6.4 V and 6.5 V, respectively. The high forward voltages could be attributed to the high series resistance in this thin PC device.

Angular-resolved spectra were measured under electrical current injection for the far-field distribution. A continuous current of 20 mA was injected into a TO-mounted device at room temperature. Plate IV(a–c) (in colour section between pages 330 and 331) shows spectra taken along the ΓX and ΓM directions for PC

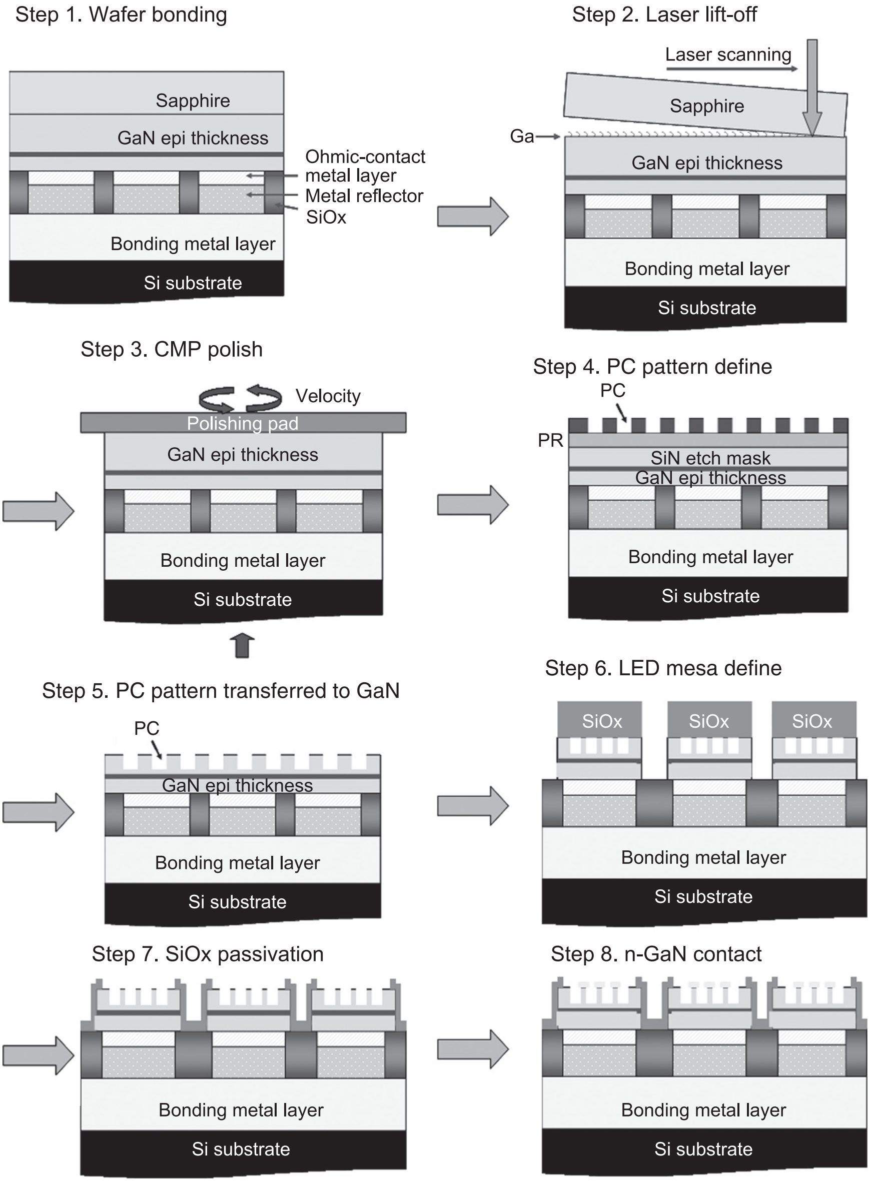
Step 1. Wafer bonding
Sapphire
GaN epi thickness
Ohmic-contact metal layer
Metal reflector
SiOx
Bonding metal layer
Si substrate
Step 2. Laser lift-off
Laser scanning
Sapphire
Ga
GaN epi thickness
Bonding metal layer
Si substrate
Step 3. CMP polish
Velocity
Polishing pad
GaN epi thickness
Bonding metal layer
Si substrate
Step 4. PC pattern define
PC
PR
SiN etch mask
GaN epi thickness
Bonding metal layer
Si substrate
Step 5. PC pattern transferred to GaN
PC
GaN epi thickness
Bonding metal layer
Si substrate
Step 6. LED mesa define
SiOx
SiOx
SiOx
Bonding metal layer
Si substrate
Step 7. SiOx passivation
Bonding metal layer
Si substrate
Step 8. n-GaN contact
Bonding metal layer
Si substrate

6.24 Fabrication steps for GaN-based TFLEDs with PC lattice structures. (PR: photoresist)

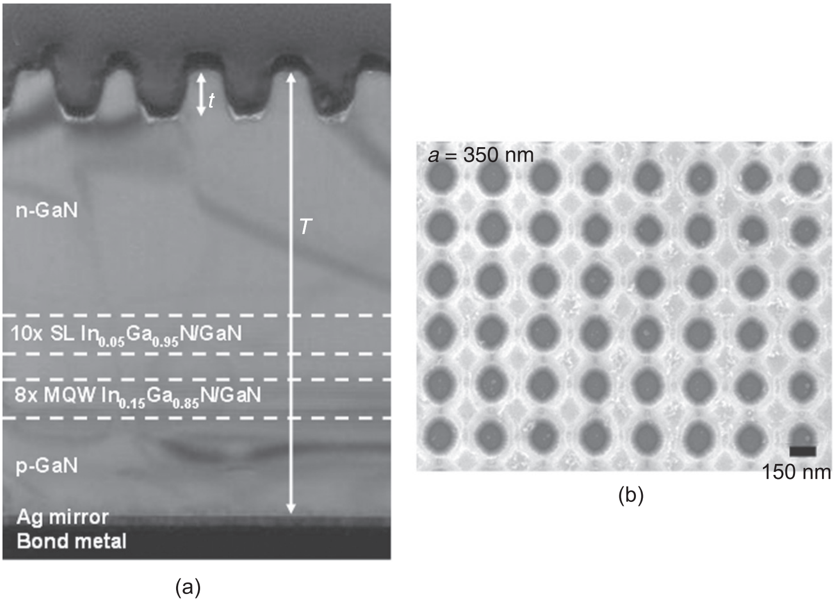
t
T
n-GaN
10x SL $In_{0.05}Ga_{0.95}N/GaN$
8x MQW $In_{0.15}Ga_{0.85}N/GaN$
p-GaN
Ag mirror
Bond metal
(a)
a = 350 nm
150 nm
(b)

6.25 (a) TEM showing a cross section of a GaN PC TFLED structure with etch depth $t = 150$ nm and GaN cavity thickness $T = 1500$ nm. (b) SEM image of top of PCs on a TFLED with lattice constant $a = 350$ nm and the diameter of air holes $d = 200$ nm, fabricated using holographic lithography.

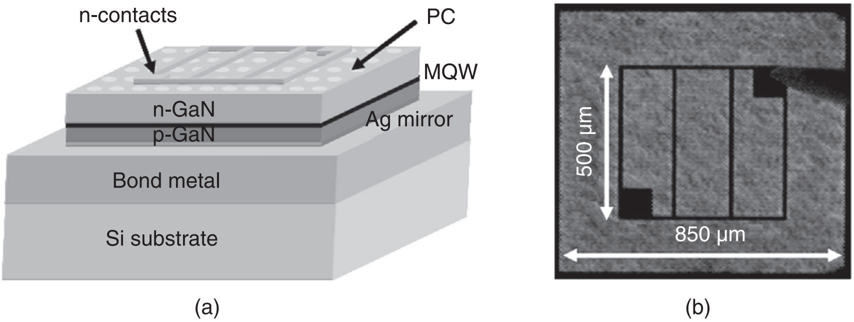
n-contacts
PC
MQW
n-GaN
p-GaN
Ag mirror
Bond metal
Si substrate
(a)
500 μm
850 μm
(b)

6.26 (a) GaN TFLED structure with PC. (b) Optical micrograph showing the blue light distribution across the die operated at a low injection current of 5 mA.

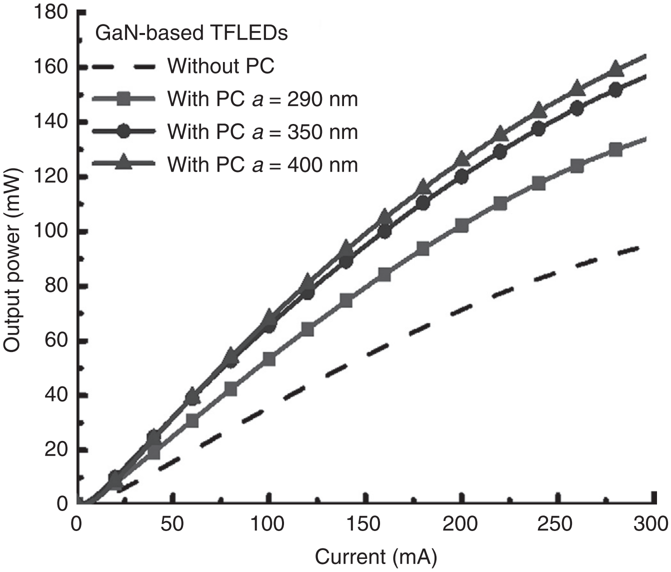

6.27 Light output power-current (*L-I*) curve characteristic of the GaN TFLED with PC and without PC.

lattice constant $a = 290$ nm, 350 nm and 400 nm. The light emission spectra were taken for every zenithal angle with 0.2° resolution from −90° to 90°. The plate shows the spectra on a wavelength versus angular plot with the color of a pixel representing the intensity of the light. Using this angular-resolved spectral technique, most of the states can be investigated efficiently. In a GaN PC TFLED, the far-field distribution will be significantly modified by PC lattice diffraction. The waveguide light traveling in the plane will be diffracted by the reciprocal wave vectors associated with the PC. Plate IV(d) shows the 2D free-photon band structure for the transverse electric (TE) modes with average refractive index $n = 2.42$. The three different PC lattice constant values created a range of $a/\lambda = 0.52$ to 0.91 for experimental investigation as enclosed in the boxes shown in Plate IV(d). These data were transformed into guided mode dispersion curves, which can be compared with the calculated band structures shown in the insets in Plate IV(d). This serves as a useful framework for understanding the experimental results. Plate IV(d) shows the normalized dispersion curves for each mode line in the ΓX and ΓM directions. Above the air lines, the band structure has an abundance of resonant states that are involved in the PC-assisted light extraction. Due to the shallow etching of the samples, which resulted in a negligible narrow bandgap, the observed dispersion in this study was in good agreement with the calculated 2D free-photon band structure. Only the guided modes of effective refractive index $n_{eff} = 2.414$ to 2.15 from our sample are visible. We can accurately fit the lowest-order mode with the free-photon band structure. The other modes are shifted higher than our red line because each mode has a different PC-induced effective index. Additionally, the extracted guided mode corresponds with the high symmetry point along the Γ axis of Γ_1 and Γ_2, which shows the light collimation profile. A detailed analysis of the angular-resolved emission patterns can determine the PC dispersion curves as well as the extraction efficiency for the various waveguide modes.

Furthermore, due to the discrete nature of the guided modes, this diffracted light will exhibit anisotropy in the far-field pattern in both in the zenith direction and the azimuthal direction.[65] The far-field emission patterns in the zenith direction were measured at a driving current of 50 mA, as shown in Fig. 6.28. The samples

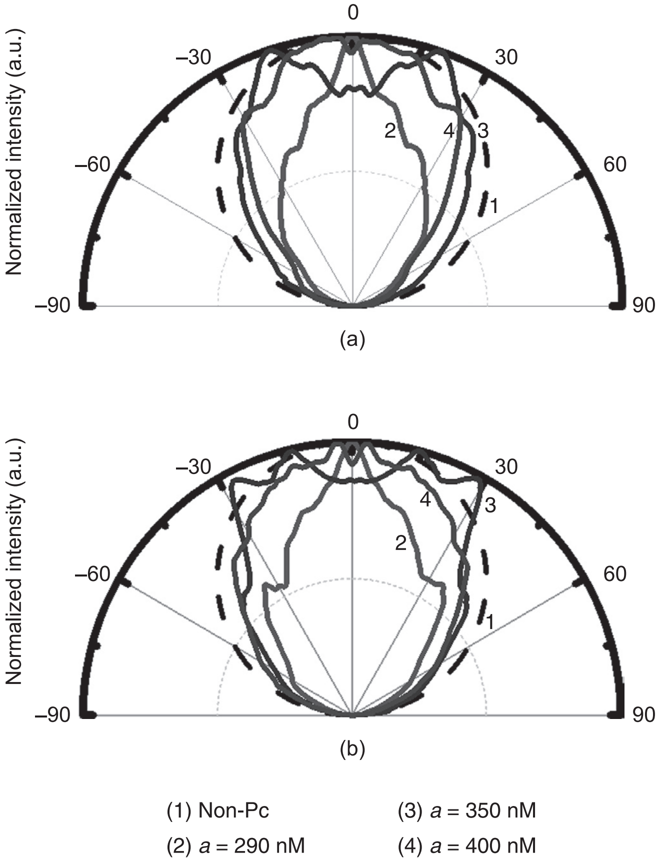

6.28 Far-field pattern normalized with the peak intensity in (a) the ΓX direction and (b) the ΓM direction for a PC at a driving current of 50 mA. The far-field pattern shows the different direction (a) ΓX and (b) ΓM with PhC at driving current of 50 mA (solid line for non-PC, dash line for *a*=290 nm, dot line for *a*=350 nm and dash dot line for *a*=400 nm).

with a PC lattice constant *a* of 290 nm and 400 nm both have collimated far-field patterns that peak near the normal to the GaN TFLED surface and have a small far-field angle at half intensity of ±31.7° (±41.05°) and ±42.45° (±49.7°) in the ΓX (ΓM) orientation of the PC lattice, respectively, which are much smaller than for a typical Lambertian cone, ±60°. The measured far-field emission pattern of the GaN non-PC TFLED was nearly Lambertian. In addition, the sample with PC lattice constant $a = 350$ nm has lobes at around ±17° (±15°, ±30°) in the ΓX (ΓM) orientation. Therefore, for a GaN PC TFLED, the far-field emission distribution is significantly modified by the PC structure, i.e. the lattice constant *a*. Furthermore, the far-field emission pattern remained unchanged when the current was varied from 20 mA to 200 mA. This invariance of the far-field pattern indicates the temperature stability of the device since the junction temperature of the device can vary significantly over this current range. We found that an encapsulated PC TFLED had similar far-field characteristics. Hence, GaN PC TFLEDs can be encapsulated to increase light enhancement while retaining the directional patterns.

In addition, the azimuthal anisotropy of the far-field distribution was measured as a function of the azimuthal angles using the angular-resolved spectra.[66] Plate V(a–c) plots the far-field distributions monochromatically in the azimuthal direction at a fixed wavelength of $\lambda_0 = 470$ nm with PC lattice constant *a* values of 290 nm, 350 nm and 400 nm. Different guided modes with different indexes will trace out an arc with the radius corresponding to the respective waveguide circle, which is well fitted by Ewald's construction of Bragg's diffraction theory.[67] Several lower guided modes are extracted by the PC lattice, as shown in Plate V (see colour section between pages 330 and 331). Additionally, we measured the top view of the 3D far-field patterns for the three different PC lattice constant values, which reveal PC diffraction patterns with fourfold symmetry due to the square lattice, as shown in colour Plate V(d–f).

The light enhancement of the GaN PC TFLEDs compared to the GaN non-PC TFLED at a driving current of 50 mA is shown in Fig. 6.29. The light enhancement is defined as the ratio of the light output of a GaN PC TFLED divided by that of the GaN non-PC TFLED, and the power was collected from angles ±0° to ±90°. The light enhancement by collection angle strongly depends on the far-field patterns of the GaN PC TFLEDs. For the collimated GaN PC TFLEDs the light enhancement was ~2.4 for a ±20° collection cone. For collimated patterns, the light enhancement increases with smaller collection angles. The differing profile of the PC with $a = 350$ nm had only slight light enhancement at small collection angles. Therefore, the collimation profile of the far-field pattern could contribute to strengthening the directional light enhancement in many applications, especially for etendue-limited applications. However, the extraction enhancement is not only a function of the PC parameters, but also other variables such as the GaN thickness and MQW placement.[68]

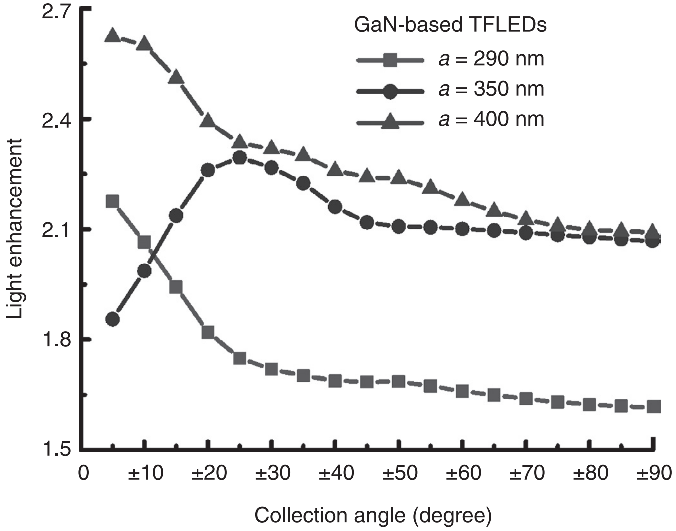

6.29 Light enhancement recorded at various output collection angles for GaN PC TFLEDs with three different values of *a*.

6.8 Conclusion

In this chapter we studied the FC- and TF-types of GaN-based LEDs, including their fabrication and electrical and optical characteristics. First, two types of GaN-based FCLEDs with an MPA structure and an oblique geometric sapphire shaping (SS) structure were demonstrated. For the MPA-FCLEDs, we used ICP to etch an MPA on the backside surface of the sapphire substrate to enhance light extraction. The light output power of the MPA-FCLEDs increased by 68% for a 3.2 μm textured MPA on the bottom side of the sapphire substrate. This enhancement can be attributed to the top surface roughness and the fact that photons are more likely to be emitted from the surface-roughened device, resulting in an increase of the light output power of the MPA-FCLED. For the SS-FCLEDs, FCLEDs with an oblique sapphire geometric structure and much thicker sapphire window layer were fabricated. A H_2SO_4:H_3PO_4 (3:1) solution was used to etch the backside surface of the sapphire substrate. The enhancement of the light extraction efficiency for 100 μm SS-FCLEDs was 55% under a current injection of 350 mA compared to C-FCLEDs. The novel FCLED structure not only reduced the TIR effect but facilitated light emission from the edges of the thicker sapphire window layer, resulting in an increase in the light extraction efficiency of the FCLEDs.

In the second part of the chapter we studied the combination of TF-types of GaN-based LEDs with PC nano-structures, including their fabrication and optical and electronic phenomena. The enhancement of the directional light extraction of the GaN PC TFLEDs with blue light emission was experimentally investigated. Angular-resolved spectra measurements revealed the directional profile and azimuthal anisotropy in the far-field distribution, with the guided modes extraction due to Bragg diffraction. Due to the shallow etching, the dispersion curve of the mode lines observed in the angular-resolved spectra closely resembled the band structures of the 2D free-photon band with the index corresponding to the average index for the slab waveguides. The extracted guided mode corresponds with the high symmetry point along the Γ axis of Γ_1 and Γ_2, which shows the light collimation profile. The enhancement of the light from the GaN PC TFLEDs within the collection cone angle depended on the measured 3D far-field patterns. In a ±20° collection cone, the collected light was enhanced by a factor of ~2.4 for a collimated PC TFLED compared to the GaN non-PC TFLED. This anisotropy and collimation of the PC slabs could be used for the light propagation extraction of etendue-limited applications. This research provides important information for designing LEDs for projection displays that take full advantage of what a PC can offer.

6.9 References

1 E. F. Schubert and J. K. Kim, Solid-state light sources getting smart, *Science*, Vol. 308, pp. 1274–1278, 2005.

2 E. F. Schubert, *Light-Emitting Diodes*, Cambridge University Press, Cambridge, UK, 2003.

3 M. R. Krames, O. B. Shchekin, R. Mueller-Mach, G. O. Mueller, L. Zhou, *et al.*, Status and future of high-power light-emitting diodes for solid-state lighting, *J. Disp. Technol.*, Vol. 3, p. 160, 2007.

4 C. Huh, K. S. Lee, E. J. Kang and S. J. Park, Improved light-output and electrical performance of InGaN-based light emitting diode by microroughening of the p-GaN surface, *J. Appl. Phys.*, Vol. 93, pp. 9383–9385, 2003.

5 S. J. Chang, C. S. Chang, Y. K. Su, C. T. Lee, W. S. Chen, *et al.*, Nitride-based flip-chip ITO LEDs, *IEEE Trans. Adv. Packag.*, Vol. 28, no. 2, p. 273, 2005.

6 D. L. Hibbard, S. P. Jung, C. Wang, D. Ullery, Y. S. Zhao, *et al.*, Low resistance high reflectance contacts to p-GaN using oxidized Ni/Au and Al or Ag, *Appl. Phys. Lett.*, Vol. 83, pp. 311–313, 2003.

7 D. L. Hibbard, S. P. Jung, C. Wang, D. Ullery, Y. S. Zhao, *et al.*, Al-based Ohmic reflectors with low leakage currents and high reflectance for p-GaN flip-chip processes, *Appl. Phys. Lett.*, Vol. 83, p. 311, 2003.

8 Y. Kondoh, S. Wantanabe, Y. Kaneko, S. Nakagawa, and N. Yamada, Nitride semiconductor light emitting device having a silver p-contact, US Patent 6,194,743.

9 T. Fujii, Y. Gao, R. Sharma, E. L. Hu, S. P. DenBaars, *et al.*, Increase in the extraction efficiency of GaN-based light-emitting diodes via surface roughening, *Appl. Phys. Lett.*, Vol. 84–86, p. 855, 2004.

10 R. Windisch, C. Rooman, S. Meinlschmidt, P. Kiesel, D. Zipperer, *et al.*, Impact of texture-enhanced transmission on high-efficiency surface-textured light-emitting diodes, *Appl. Phys. Lett.*, Vol. 79, p. 2315, 2001.

11 H. W. Huang, C. C. Kao, J. T. Chu, H. C. Kuo, S. C. Wang and C. C. Yu, Improvement of InGaN-GaN light-emitting diode performance with a nano-roughened p-GaN surface, *IEEE Photon. Technol. Lett.*, Vol. 17, no. 5, p. 983, 2005.

12 C.-E. Lee, Y.-J. Lee, H.-C. Kuo, M.-R. Tsai, B. S. Cheng, *et al.*, Enhancement of flip-chip light-emitting diodes with omni-directional reflector and textured micropillar arrays, *IEEE Photon. Technol. Lett.*, Vol. 19, p. 1200, 2007.

13 J. K. Kim, T. Gessmann, E. F. Schubert, J. Q. Xi, H. Luo, *et al.*, GaInN light-emitting diode with conductive omnidirectional reflector having a low-refractive-index indium-tin oxide layer, *Appl. Phys. Lett.*, Vol. 88, p. 013501, 2006.

14 T. Gessmann, H. Luo, J.-Q. Xi, K. P. Streubel and E. F. Schubert, Light-emitting diodes with integrated omnidirectionally reflective contacts, *Proc. SPIE*, Vol. 5366, p. 53, 2004.

15 Y. J. Lee, H. C. Kuo, T. C. Lu and S. C. Wang, High light-extraction GaN-based vertical LEDs with double diffuse surfaces, *IEEE J. Quantum Electron.*, Vol. 42, no. 12, p. 1196, 2006.

16 C. H. Lin, C. F. Lai, H. W. Huang, H. C. Kuo, Y. Y. Hung, *et al.*, Enhancement of InGaN–GaN indium–tin–oxide flip-chip light-emitting diodes with TiO_2–SiO_2 multilayer stack omnidirectional reflector, *IEEE Photon. Tech. Lett.*, Vol. 18, pp. 2050–2052, 2006.

17 J. H. Lau, *Flip Chip Technologies*, McGraw-Hill, 1995.

18 M. R. Krames, *et al.*, High-power truncated inverted pyramid $(Al_xGa_{1-x})_{0.5}In_{0.5}P$/GaP light-emitting diodes exhibiting >50% external quantum efficiency, *Appl. Phys. Lett.*, Vol. 75, p. 2365, 1999.

19 D. Eisert and V. Harle, International Conference on Numerical Simulation of Semiconductor Optoelectronic Devices, Session 3: Photonic Devices, invited paper, 2002.

20 C. S. Chang, S. J. Chang, Y. K. Su, C. T. Lee, Y. C. Lin, *et al.*, Nitride-based LEDs with textured side walls, *IEEE Photon. Technol. Lett.*, Vol. 16, p. 750, 2005.

21 C. C. Kao, H. C. Kuo, H. W. Huang, J. T. Chu, Y. C. Peng, *et al.*, Light-output enhancement in a nitride based light-emitting diode with 22 undercut side walls, *IEEE Photon. Technol. Lett.*, Vol. 17, p. 19, 2005.

22 C.-E. Lee, Y.-J. Lee, H.-C. Kuo, M.-R. Tsai, T.-C. Lu, *et al.*, Luminance enhancement of flip-chip light-emitting diodes by geometric sapphire shaping structure, *IEEE Photon. Technol. Lett.*, Vol. 20, p. 184, 2008.

23 C. E. Lee, Y. C. Lee, H. C. Kuo, M. R. Tsai, T. C. Lu, *et al.*, High brightness GaN-based flip-chip light-emitting diodes by adopting geometric sapphire shaping structure, *Semicond. Sci. Technol.*, Vol. 23, p. 1, 2008.

24 A. David, T. Fujii, B. Moran, S. Nakamura, S. P. DenBaars, *et al.*, Photonic crystal laser lift-off GaN light-emitting diodes, *Appl. Phys. Lett.*, Vol. 88, p. 133514, 2006.

25 H. K. Cho, S. K. Kim, D. K. Bae, B. C. Kang, J. S. Lee, *et al.*, Laser liftoff GaN thin-film photonic crystal GaN-based light-emitting diodes, *IEEE Photon. Technol. Lett.*, Vol. 20, p. 2096, 2008.

26 C. F. Lai, C. H. Chao, H. C. Kuo, C. E. Lee and W. Y. Yeh, Directional light extraction enhancement from GaN-based film-transferred photonic crystal light-emitting diodes, *Appl. Phys. Lett.*, Vol. 94, p. 123106, 2009.

27 K. Bergenek, Ch. Wiesmann, H. Zull, R. Wirth, P. Sundgren, *et al.*, Directional light extraction from thin-film resonant cavity light-emitting diodes with a photonic crystal, *Appl. Phys. Lett.*, Vol. 93, p. 231109, 2008.

28 Q. Y. Tong and U. Gosele, *Semiconductor Wafer Bonding Science and Technology*, John Wiley & Sons, Inc, New York, 1999.

29 Lord Raleigh, A study of glass surface in optical contact, *Proc. Phys. Soc. A*, Vol. 156, pp. 326–349, 1936.

30 S. H. Christiansen, R. Singh and U. Gosele, Wafer direct bonding: from advanced substrate engineering to future applications in micro/nanoelectronics, *Proc. IEEE*, Vol. 94, pp. 2060–2106, 2006.
31 C. Christensen and S. Bouwstra, Eutectic bonds on wafer scale by thin film multilayers, *Proc. SPIE, Int. Soc. Opt. Engineering*, Vol. 2879, p. 288, 1996.
32 C. den Besten, R. E. G. van Hal, J. Munoz and P. Bergveld, Polymer bonding of micro-machined silicon structures, *MEMS' 92*, 1992, p. 104.
33 G. Wallis and D. I. Pomerantz, Field assisted glass-metal sealing, *J. Appl. Phys.*, Vol. 40, pp. 3946–3949, 1969.
34 R. Stengl, K. Y. Ahn and U. Gosele, Bubble-free silicon wafer bonding in a non-cleanroom environment, *Jpn. J. Appl. Phys.*, Vol. 27, pp. L2364–L2366, 1988.
35 D. Sparks, G. Queen, R. Weston, G. Woodward, M. Putty, *et al.*, Wafer-to-wafer bonding of nonplanarized MEMS surfaces using solder, *J. Micromech. Microeng.*, Vol. 11, p. 630, 2001.
36 F. Niklaus, P. Enoksson, E. Kalvesten and G. Stemme, Low-temperature full wafer adhesive bonding, *J. Micromech. Microeng.*, Vol. 11, pp. 100–107, 2001.
37 M. K. Kelly, O. Ambacher, B. Dahlheimer, G. Groos, R. Dimitrov, *et al.*, Optical patterning of GaN films, *Appl. Phys. Lett.*, Vol. 69, pp. 1749–1751, 1996.
38 M. K. Kelly, O. Ambacher, R. Dimitrov, R. Handschuh and M. Stutzmann, Optical process for liftoff of Group III-nitride films, *Phys. Status Solidi A*, Vol. 159, p. R3, 1997.
39 W. S. Wong, T. Sands and N. W. Cheung, Damage-free separation of GaN thin films from sapphire substrates, *Appl. Phys. Lett.*, Vol. 72, pp. 599–601, 1998.
40 E. Yablonovitch, T. Gmitter, J. P. Harbison and R. Bhat, Extreme selectivity in the lift-off of epitaxial GaAs films, *Appl. Phys. Lett.*, Vol. 51, p. 2222, 1987.
41 E. Yablonovitch, T. Sands, D. M. Hwang, I. Schnitzer, T. J. Gmitter, *et al.*, Van der Waals bonding of GaAs on Pd leads to a permanent, solid-phase-topotaxial, metallurgical bond, *Appl. Phys. Lett.*, Vol. 59, pp. 3159–3161, 1991.
42 S. John, Strong localization of photons in certain disordered dielectric superlattices, *Phys. Rev. Lett.*, Vol. 58, pp. 2486–2489, 1987.
43 E. Yablonovitch, T. J. Gmitter and K. M. Leung, Photonic band structure: the face-centered-cubic case employing nonspherical atoms, *Phys. Rev. Lett.*, Vol. 67, pp. 2295–2298, 1991.
44 J. D. Joannopoulos, R. D. Meade and J. N. Winn, *Photonic Crystals: Molding the Flow of Light*, Princeton, 1995.
45 C. Hamaguchi, *Basic Semiconductor Physics*, Springer, 2001.
46 H. Kogelnik and C. V. Shank, Stimulated emission in a periodic structure, *Appl. Phys. Lett.*, Vol. 18, pp. 152–154, 1971.
47 M. Nakamura, A. Yariv, H. W. Yen, S. Somekh and H. L. Garvin, Optically pumped GaAs surface laser with corrugation feedback, *Appl. Phys. Lett.*, Vol. 22, pp. 515–517, 1973.
48 H. Soda, K. Iga, C. Kitahara and Y. Suematsu, GaInAsP/InP surface emitting injection lasers, *Jap. J. Appl. Phys.*, Vol. 18, pp. 2329–2330, 1979.
49 M. Loncar, A. Scherer and Y. Qiu, Photonic crystal laser sources for chemical detection, *Appl. Phys. Lett.*, Vol. 82, pp. 4648–4650, 2003.
50 E. Chow, A. Grot, L. W. Mirkarimi, M. Sigalas and G. Girolami, Ultracompact biochemical sensor built with two-dimensional photonic crystal microcavity, *Opt. Lett.*, Vol. 29, pp. 1093–1095, 2004.
51 C. L. C. Smith, D. K. C. Wu, M. W. Lee, C. Monat, S. T. Hanic, *et al.*, Microfluidic photonic crystal double heterostructures, *Appl. Phys. Lett.*, Vol. 91, pp. 121103, 2007.

52 S. Noda, K. Tomoda, N. Yamamoto and A. Chutinan, Full three-dimensional photonic bandgap crystals at near-infrared wavelengths, *Science*, Vol. 289, pp. 604–606, 2000.

53 Y. Jiang, W. Jiang, L. Gu, X. Chen and R. T. Chen, 80-micron interaction length silicon photonic crystal waveguide modulator, *Appl. Phys. Lett.*, Vol. 87, p. 221105, 2005.

54 K. Aoki, D. Guimard, M. Nishioka, M. Nomura, S. Iwamoto, *et al.*, Coupling of quantum-dot light emission with a three-dimensional photonic-crystal nanocavity, *Nat. Photon.*, Vol. 2, pp. 688–692, 2008.

55 Y. A. Vlasov, M. O'Boyle, H. F. Hamann and S. J. McNab, Electromagnetically induced transparency with tunable single-photon pulses, *Nature*, Vol. 438, p. 65, 2005.

56 T. F. Krauss, Slow light in photonic crystal waveguides, *J. Phys. D*, Vol. 40, p. 2666, 2007.

57 T. Baba, Slow light in photonic crystals, *Nat. Photon.*, Vol. 2, pp. 465–473, 2008.

58 T. Baba and D. Mori, Slow light engineering in photonic crystals, *J. Phys. D*, Vol. 40, p. 2659, 2007.

59 T. Yoshie, A. Scherer, J. Hendrickson, G. Khitrova, H. M. Gibbs, *et al.*, Vacuum Rabi splitting with a single quantum dot in a photonic crystal nanocavity, *Nature*, Vol. 432, pp. 200–203, 2004.

60 P. Lodahl, A. F. Driel, I. S. Nikolaev, A. Irman, K. Overgaag, *et al.*, Controlling the dynamics of spontaneous emission from quantum dots by photonic crystals, *Nature*, Vol. 430, pp. 654–657, 2004.

61 D. Englund, D. Fattal, E. Waks, G. Solomon, B. Zhang, *et al.*, Controlling the spontaneous emission rate of single quantum dots in a two-dimensional photonic crystal, *Phys. Rev. Lett.*, Vol. 95, p. 013904, 2005.

62 M. Rattier, H. Benisty, R. P. Stanley, J.-F. Carlin, R. Houdre, *et al.*, Toward ultrahigh-efficiency aluminum oxide microcavity light-emitting diodes: guided mode extraction by photonic crystals, *IEEE J. Sel. Top. Quant. Electron.*, Vol. 8, p. 238, 2002.

63 C. F. Lai, H. C. Kuo, C. H. Chao, H. T. Hsueh, J.-F. T. Wang, *et al.*, Anisotropy of light extraction from two-dimensional photonic crystal light-emitting diodes, *Appl. Phys. Lett.*, Vol. 91, p. 123117, 2007.

64 H. Ichikawa and T. Baba, Efficiency enhancement in surface grating type two-dimensional photonic crystal light emitting diode, *Appl. Phys. Lett.*, Vol. 84, pp. 457–459, 2004.

65 C. F. Lai, J. Y. Chi, H. H. Yen, H. C. Kuo, C. H. Chao, *et al.*, Polarized light emission from photonic crystal light-emitting diodes, *Appl. Phys. Lett.*, Vol. 92, p. 243118, 2008.

66 C. F. Lai, J. Y. Chi, H. C. Kuo, C. H. Chao, H. T. Hsueh, *et al.*, Anisotropy of light extraction from GaN two-dimensional photonic crystals, *Optics Express*, Vol. 16, p. 7285, 2008.

67 A. David, H. Benisty and C. Weisbuch, Optimization of light-diffracting photonic-crystals for high extraction efficiency LEDs, *IEEE J. Display Technol.*, Vol. 3, pp. 133–148, 2007.

68 J. J. Wierer, A. David and M. M. Megens, III-nitride photonic-crystal light-emitting diodes with high extraction efficiency, *Nat. Photonics*, Vol. 3, p. 163, 2009.

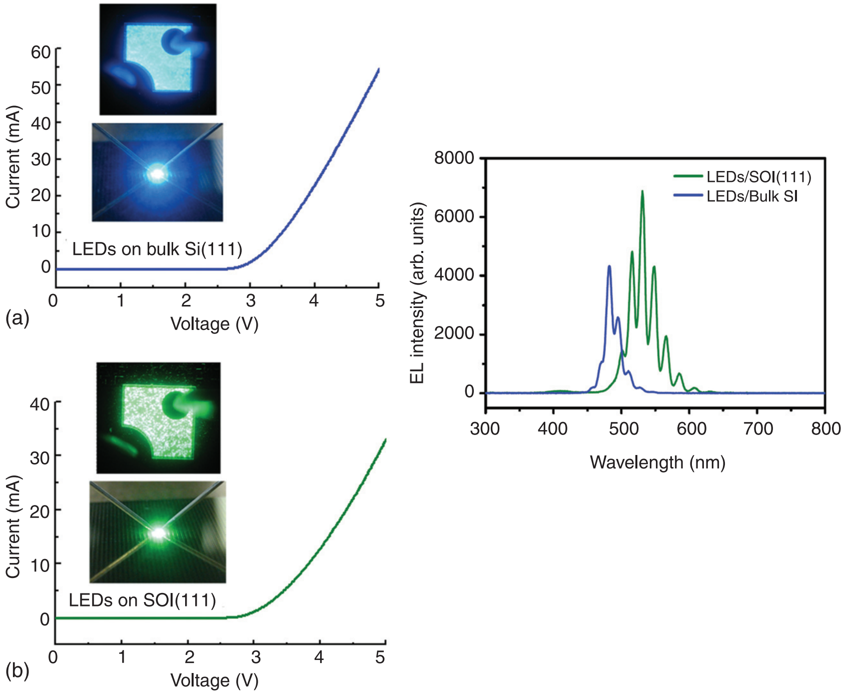

Plate I (Chapter 4) (a) Optical microscope image of green LEDs grown on SOI (111) under electrical probing and the *I-V* curve of an LED; (b) EL spectra of LEDs grown on Si (111) and SOI (111) under 100 mA current injection (Tripathy *et al.*, 2007).

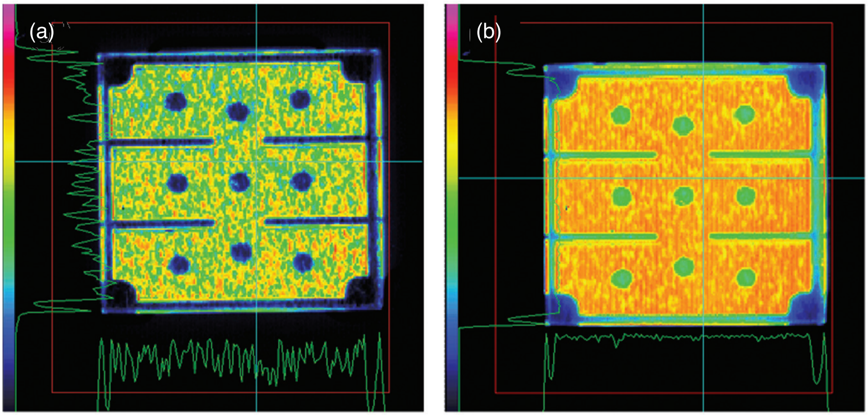

Plate II (Chapter 6) Photons from (a) a conventional flat-surface FCLED and (b) a MPA-FCLED for a dc injection current of 350 mA.

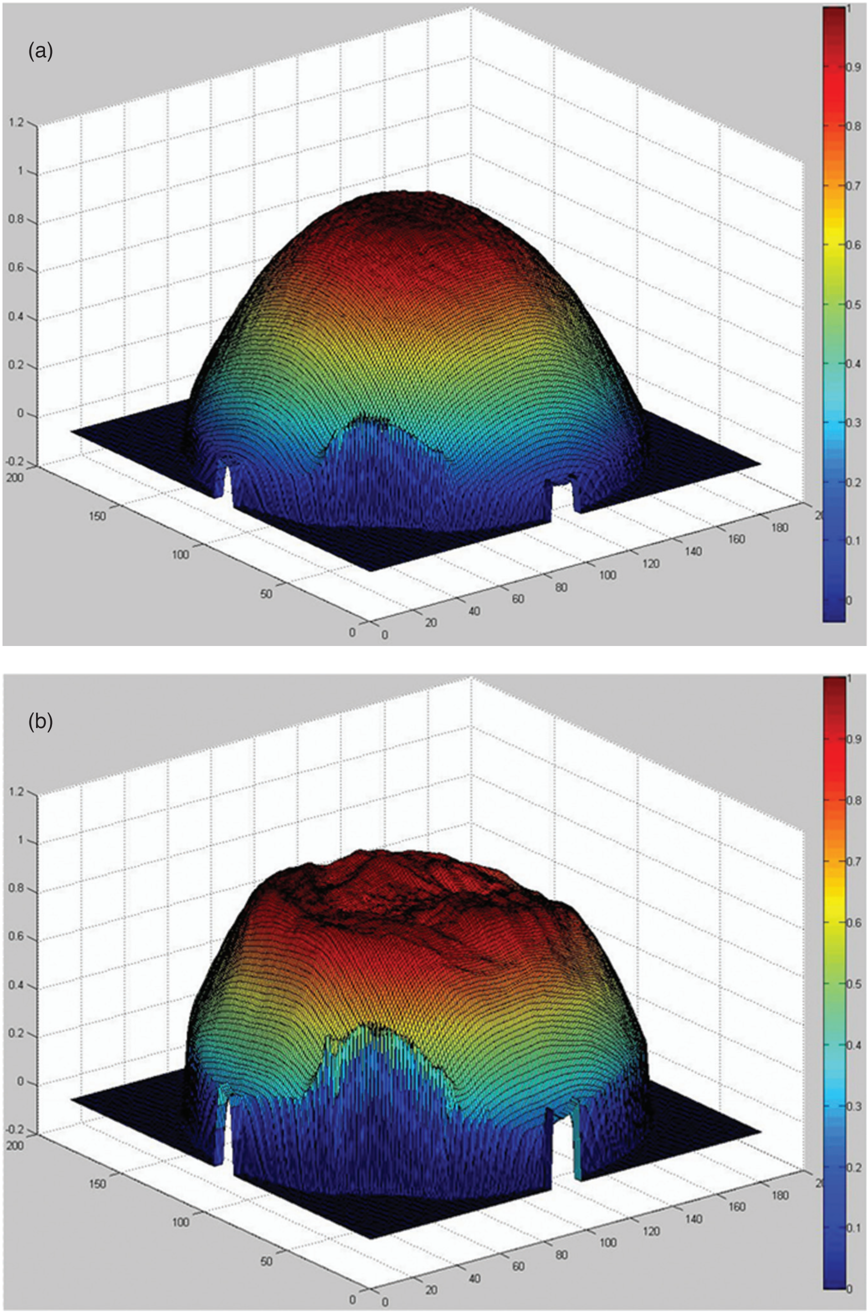

Plate III (Chapter 6) Normalized three-dimensional far-field patterns for (a) C-FCLEDs and (b) SS-FCLEDs.

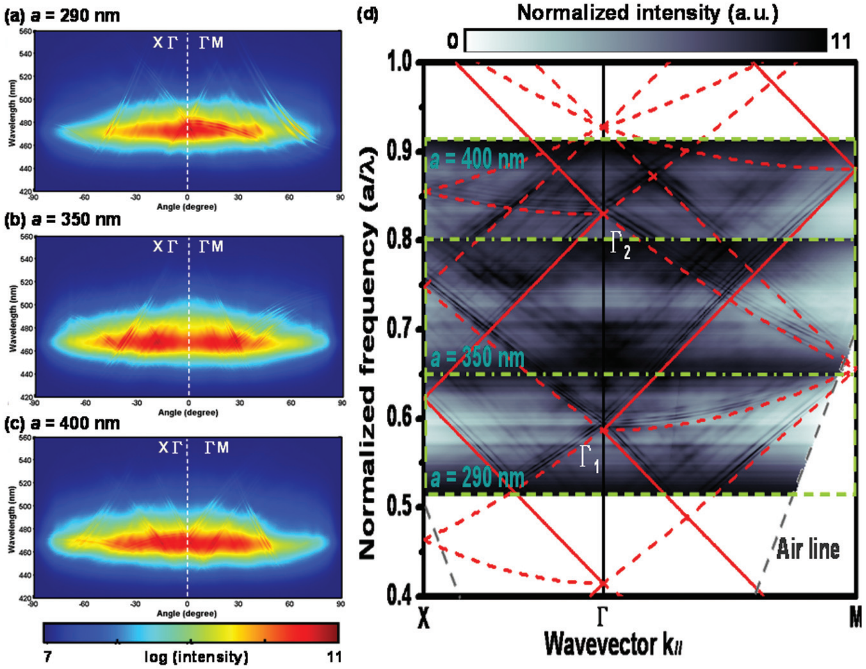

Plate IV (Chapter 6) Angular-resolved spectra for lattice constant (a) a = 290 nm, (b) a = 350 nm and (c) a = 400 nm, where ΓX direction points to the left and the ΓM direction points to the right. (d) Free-photon band structure calculated with n = 2.42 for the transverse electric modes. The red thick lines are the collinear coupled modes. The red dashed lines are the non-collinear coupled bands. The boxes show the experimental regions for a = 290 nm, 350 nm and 400 nm. The insets in the boxes are the calculated band structures.

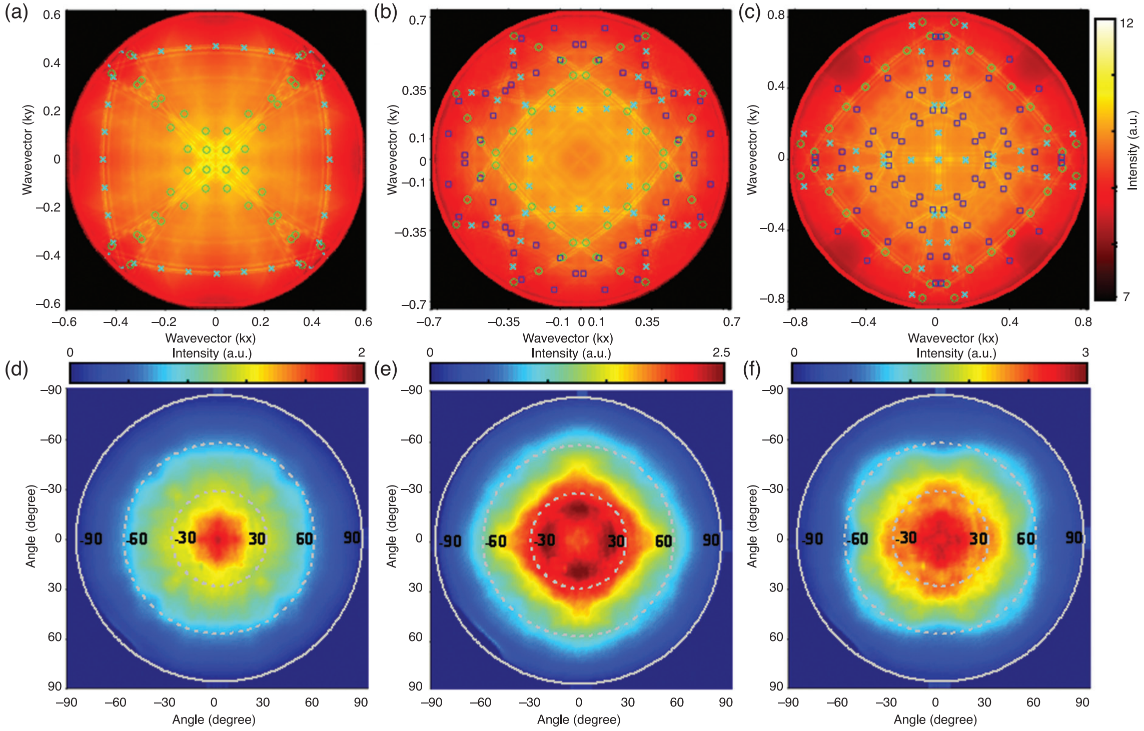

Plate V (Chapter 6) Intensity map of the extracted light at a fixed wavelength λ = 470 nm for (a) *a* = 290 nm, (b) *a* = 350 nm and (c) *a* = 400 nm. Symbols show values calculated using Bragg's diffraction theory fitted with effective refractive index $n_{\mathrm{eff}} = 2.414$ (cyan crosses for the ΓX direction, green circles for the ΓM direction and blue squares for the ΓXΓM direction). Top view of 3D far-field pattern for (d) *a* = 290 nm, (e) *a* = 350 nm and (f) *a* = 400 nm.

7

Nanostructured LEDs

C.-C. LIN, D. W. LIN, C.-H. CHIU, Z. Y. LI and
Y. P. LAN, National Chiao Tung University, Taiwan,
J. J. HUANG, National Taiwan University, Taiwan and
H.-C. KUO, National Chiao Tung University, Taiwan

DOI: 10.1533/9780857099303.1.216

Abstract: This chapter describes how, in order to achieve high efficiency light-emitting diodes (LEDs) and enhance the crystal quality of the epitaxial layer, we investigated the following nanotechnologies to enhance our LED devices: SiO_2-based nanorod-array patterned sapphire substrates (NAPSSs), native-grown GaN nanopillars (NPs) and etched nanopillars using embedded SiO_2 nanomasks. Our studies showed these approaches can achieve high-quality nanocrystalline growth and robust fabrication to produce high-performance LEDs. These novel nanotechnologies could be effective for improving GaN-based optoelectronic device performance in the future.

Key words: Gallium nitride, GaN, light-emitting diodes, nanotechnology.

7.1 Introduction

To address the next generation of applications in projectors, automobile headlights and high-end general lighting, further improvements in the optical output power and the external quantum efficiency (EQE) of LEDs are required. Due to the difficulties and high cost of preparing native GaN substrates, sapphire substrates have had a major role in nitride-based LED production. The development of GaN-based LEDs has shown significant progress over the past decade, in particular for the growth of GaN on lattice-mismatched sapphire substrates using metal-organic chemical vapor deposition (MOCVD).[1,2] It has been shown that epitaxial lateral overgrowth (ELO) using a microscale SiN_x or SiO_x patterned mask on as-grown GaN seed layers can effectively reduce the threading dislocation density (TDD).[3–5] However, the two-step growth procedure and the need for a sufficient thickness for GaN coalescence are costly and time-consuming. Meanwhile, high-quality GaN-based LEDs have been produced on a microscale patterned sapphire substrate (PSS) by wet-etching,[6] where the patterns served as a template for the ELO of the GaN buffer as well as acting as scattering centers for the emitted photons. Both the epitaxial crystal quality and the light extraction efficiency were improved by utilizing the PSS. With advances in fabrication processes, nanoscale patterned substrates have become available and the improvements in LED performance are more significant than microscale ones. The benefits of the reduced pattern size are: (i) the nanoscale patterns can reduce the strain caused by lattice mismatch, (ii) the nanoscale substrate can redirect the threading dislocation more efficiently and thus improve the crystal quality of epitaxial layers grown above this type of substrate and (iii) the enhanced scattering of light from voids formed during ELO growth can further improve the light extraction efficiency, which in turn increases the power output density.[7] LEDs grown on a nanoscale PSS showed a greater enhancement in output power than those grown on a microscale PSS. However, the fabrication of a nanoscale PSS generally requires electron-beam lithography[8] or nano-imprinting techniques,[9,10] making it unfavorable for mass production. In this chapter, we will review several techniques for fabricating a SiO_2 nanorod-array PSS (NAPSS), which serves as a template for the nanoscale ELO (NELO) of GaN by MOCVD to produce high-efficiency GaN-based LEDs. The further development of these nanoscale substrates will be for nano-sized (or core-shell type) LEDs, which can greatly reduce the volume of a device and have the maximum efficiency and flexibility. Some of the characterization methods for nanostructured LEDs in this chapter can be found in many other publications.[11–14] The strain relaxation of the grown GaN and InGaN layers was analyzed by the peak position of the Raman spectrum. The enhancement of the photon-scattering effect can be either calculated by a finite-difference time-domain (FDTD) simulation tool or measured by reflectivity in the specialized template. The TDD reduction can be verified from transmission electron microscopy (TEM) results and finally the measured power-current-voltage (*L-I-V*) curves can reveal the actual improvement in the devices under study.

In the following sections, we will discuss two major methods for fabricating nanostructured/patterned LEDs: the top-down technique and the bottom-up technique. The top-down method is the most widely used in forming a nanostructure because of its simplicity. The key process challenges are nano-patterning and how to avoid the formation of defects during crystalline coalescence. However, dry-etching, which is usually used in this processing step, could greatly degrade film quality.

The second method (the bottom-up approach) is more difficult in terms of fabrication implementation, mainly due to the difficulty in controlling epitaxial layer growth. The nanostructure is grown from a native substrate with or without pre-deposited patterns and the LED structure is grown on top of this nanorod array. Many parameters, such as III/V ratio, chamber pressure, carrier gas composition, etc., need to be carefully adjusted in order to create suitable nanorods.[10] Once the nanorod structure has formed, the subsequent LED growth is expected to have fewer defects and higher luminescent efficiency. A molecular beam epitaxy (MBE) technique will be discussed in this context, for which a 71% increase of output power has been demonstrated.[15]

7.2 General mechanisms for growth of gallium nitride (GaN) related materials

In this section, we will discuss some general aspects of the nanostructure growth of GaN-related materials. Creating a 2D uniform thin-film GaN has been the focus for researchers in the past two decades. As the planar growth technology became mature,[16–18] researchers began to turn their attentions to the nanostructure growth of this material. In this chapter, the low-pressure MOCVD system, EMCORE D75, was employed for generic GaN/InGaN device growth. The general recipe for bulk GaN on a planar substrate was: 300 mbar pressure, 2000–2500 V/III ratio and 1040–1060 °C temperature.

During the growth, trimethylgallium (TMGa), trimethylindium (TMIn) and ammonia (NH_3) were used as the gallium, indium and nitrogen sources, respectively. Silane (SiH_4) and bis-cyclopentadienyl magnesium (CP2Mg) were used as the *n*-dopant and *p*-dopant sources. The general epitaxial structure of the GaN-based LED grown on a *c*-plane sapphire substrate consisted of: a 30-nm GaN nucleation layer (GaN NL), 1-μm undoped GaN (u-GaN), 3-μm *n*-doped GaN (n-GaN), ten periods of 3-nm InGaN quantum wells and 12-nm GaN barriers, a 20-nm *p*-$Al_{0.1}Ga_{0.9}N$ electron-blocking layer (EBL) and a 0.2-μm *p*-doped GaN (p-GaN) cap layer. The *n*-type and *p*-type doping concentrations were 3×10^{18} cm^{-3} and 1×10^{18} cm^{-3}, respectively. Uniform thin-film growth is important, especially for the top-down nanostructure discussed in the next paragraph. In self-organized GaN nanorod growth, however, the conditions are different as we will discuss later in this chapter.

7.2.1 Top-down method

One of the simplest methods of producing a nano-patterned substrate is to use a nanoscale SiO_2 mask for lateral overgrowth. Researchers focusing on microscale masks[19,20] produced a robust technology, which is widely used in the current LED industry. It is natural to shrink the size of the mask as the fabrication technique matures. To form a nano-pattern, a self-assembled metal layer was considered as the masking material as this method has been used extensively in nanotechnology.[13,21]

The preparation of the SiO_2 NAPSS template started with the deposition of a 200-nm-thick SiO_2 layer on a *c*-face (0001) sapphire substrate by plasma-enhanced chemical vapor deposition, followed by the deposition of a 10-nm-thick nickel layer, and the subsequent rapid thermal annealing with flowing nitrogen gas at 850 °C for 1 min. The resulting self-assembled nickel clusters then served as the etch mask for a SiO_2 nanorod array by etching the semiconductor layers in a reactive ion etch system for 3 min. Finally, the sample was dipped in a heated nitric acid solution (HNO_3) at 100 °C for 5 min to remove the residual nickel masks. As shown in Fig. 7.1(a), the field-emission scanning electron micrograph

(FESEM) indicates that the fabricated SiO_2 nanorods were approximately 100–150 nm in diameter with a pillar density of 3×10^9 cm^{-2}. The spacing between the nanorods was about 100–200 nm in Fig. 7.1(a). As the deposition process began, localized and hexagonal island-like GaN nuclei were first formed from the sapphire surface to initiate GaN overgrowth, as shown in Fig. 7.1(b). Figure 7.1(c) shows the cross section of the GaN epilayer, where voids with a size varying from 150 to 200 nm can be seen between the highlighted SiO_2 nanorods. The voids between the nanorods on the micrographs suggest that not all the exposed surfaces exhibit the same growth rate. Hence, only the regions with higher growth rates, which might have originated from a larger exposed surface, could act as a seeding layer, facilitating the lateral coalescence of GaN during epitaxial growth. The *p*-GaN layer of the NAPSS LED was grown at a relatively low temperature (800 °C),

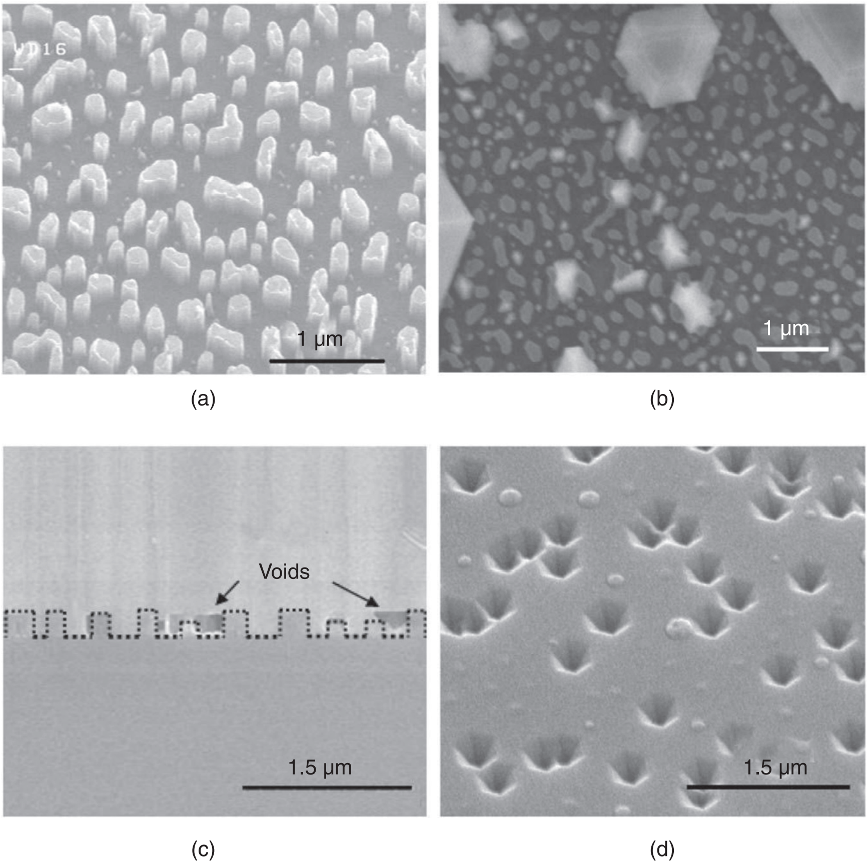

(a) (b)

(c) (d)

7.1 FESEMs of (a) the fabricated SiO_2 nanorod array, (b) GaN nuclei on the SiO_2 NAPSS as growth seeds, (c) cross section of the GaN epilayer on the NAPSS and (d) epitaxial pits on the *p*-GaN surface.[14]

leading to the formation of hexagonal pits due to the insufficient migration length of gallium atoms.[22] A FESEM image of the roughened *p*-GaN surface with randomly distributed pits is shown in Fig. 7.1(d).

As shown in Fig. 7.2(a), the threading dislocations (TDs) originated from the sapphire surface during the initial formation of GaN growth seeds on the NAPSS. The presence of voids confirmed the lateral coalescence of GaN, leading to the bending of dislocations near the edge of SiO_2 nanorods. The bent TDs eventually developed into stacking faults,[6] depicted by Type 1 in Fig. 7.2(b). Moreover, the coalescence fronts of GaN seeds provided a strain release layer where stacking faults could occur. These stacking faults were found mostly above the voids or the small GaN seeds,[23] blocking TD propagation, and this is known as the Type 2 mechanism. Occasionally, a blocked dislocation might also bend and form stacking faults.[24] If the growth rate is too slow to form a GaN seed, a dislocation can be blocked by the formation of voids (the Type 3 mechanism). Finally, we believe that the residual SiO_2 between nanorods can prohibit GaN growth and further reduce the formation of dislocations from the sapphire surface, shown as the Type 4 mechanism. It is also worth noting that the density of voids in the SiO_2 NAPSS was higher than for a microscale PSS. Therefore, we believe that the formation of stacking faults and voids was involved in the reduction and bending of dislocations.

The resulting self-assembled nickel clusters then served as etch masks to form SiO_2 nanorod arrays in a reactive ion etching (RIE) system for 20 min, which etched down to the sapphire surface. Finally, the sample was dipped in a heated nitric acid solution (HNO_3) at 100 °C for 5 min to remove the residual nickel. The 2-μm-tall GaN nanorods (NRs) with the SiO_2 nanomask were fabricated as shown

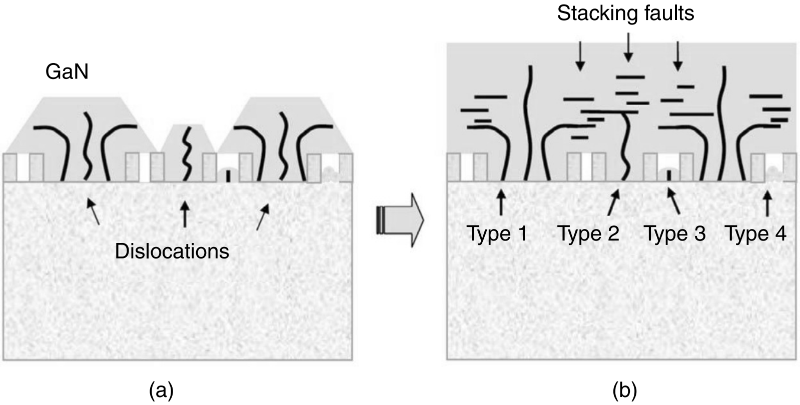

7.2 (a) Overgrowth process and the formation of dislocations, stacking faults and voids during the initial stage of epitaxy. (b) Four potential mechanisms for the reduction of the TDD.[14]

in Fig. 7.3(a). The GaN NRs have an average diameter of about 250–500 nm. It was also found that the GaN NR density was around 3.3×10^8 cm^{-2} as shown in Fig. 7.3(b). Figure 7.3(c) shows a scanning electron microscopy (SEM) cross section of GaN/InGaN epitaxial layers with voids and SiO_2 nanomasks after all the growth was complete. The estimated diameter of these voids ranges from 0.5 µm to 1 µm. These embedded voids and SiO_2 nanomasks (as shown in Fig. 7.3(d)) can increase the light extraction efficiency (LEE) due to extra light scattering.[25]

7.2.2 Bottom-up method

In this section, we introduce the growth mechanisms for GaN nanopillars on native sapphire or other types of substrate. The bottom-up growth of GaN nanopillars has been achieved by a number of groups using molecular beam epitaxy (MBE).[10,15,27–32] This growth mechanism does not necessarily require a catalyst or nanoscale masks, but only the right growth conditions, namely the III/V ratio, the gas flows and the growth temperature. Moreover, it is noticeable

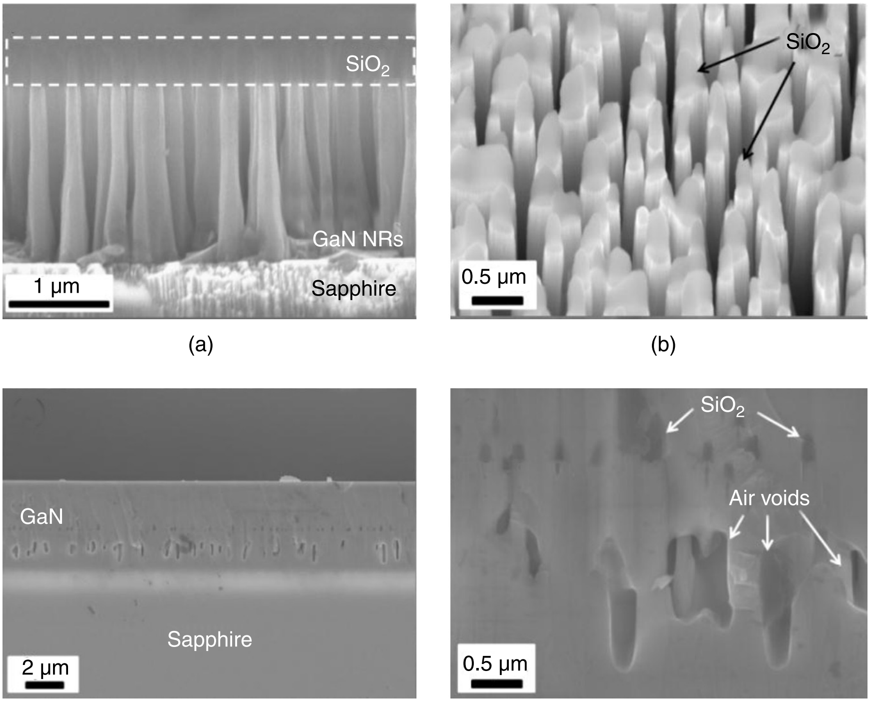

(a) (b)

(c) (d)

7.3 (a) SEM cross section of GaN NR template. (b) Tilted SEM image of GaN NR template. (c) and (d) SEM cross sections of GaN epilayer.[26]

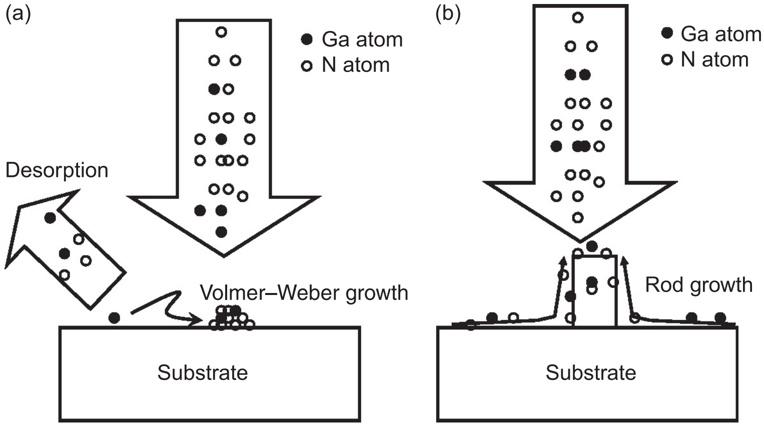

7.4 (a) Nucleation process and (b) growth process for GaN nanopillars. The distance d_{CR} is the average (critical) distance from where gallium ad-atoms can reach the nanopillar base; it depends strongly on the growth temperature.[27]

that the nanopillar diameter, density and distribution can be controlled by the growth conditions. The growth mechanisms can be categorized as (i) the nucleation process and (ii) the growth process.[27] The former determines the average nanopillar size and density, while the latter produces nanopillars with constant diameter. Figure 7.4(a) and (b) are schematic drawings for these two processes.

During the growth, there are abundant constituent atoms with high energies in the system. These atoms, both group III and group V, can reach the surface of the substrate and start to diffuse on the surface. The temperature of the surface provides the required kinetic energy for the particles to move around. However, unlike a lattice-matched material system (like GaAs-AlAs), the lattice mismatch between GaN and the native substrate (such as sapphire, silicon carbide or silicon) can favor 3D growth under strain build-up.[27] This phenomenon can even be enhanced by the high group V pressure in the system.[27,33] From Zywietz *et al.*, an excess of the group V element can set up a barrier that hinders the diffusion of gallium ad-atoms, and, in turn, roughens the surface and forms nuclei.[33] Once enough ad-atoms (gallium and nitrogen) gather at a nucleus site, by the capillary theory developed by Volmer and Weber the packet of nanoparticles can either keep on growing or later dissolve depending on whether it exceeds the critical size or not.[34] This critical size or radius increases with the substrate temperature.

Once the seed nuclei have formed, the growth direction is determined by the ratio of III/V species. For a given substrate temperature, a very small III/V ratio (a nitrogen-rich condition) will form a good array of nanopillars because the arriving gallium ad-atoms always try to stay on the top of the nuclei.[10,27] In contrast, if the

III/V ratio is large (a gallium-rich condition), lateral overgrowth will start and coalescence of GaN will eventually form a uniform 2D film.

If the conditions are right, nanorod growth can be expected. There will be a constant flow of gallium to the wafer, arriving either on the top of a nucleus to develop the pillar or reaching the surface of the wafer and diffusing toward the base of a nucleus, where the gallium ad-atoms climb up the rod to form the GaN composite, as shown in Fig. 7.4(b). Migration-enhanced epitaxy (MEE) occurs and the gallium diffusivity can be high even under a high nitrogen partial pressure.[10,35–37] The density of the rods can be controlled by the initial III/V ratio and the substrate temperature.[10,27] The underlying substrate morphology can also affect the density of the nucleation sites and thus the rod density.[38] Also, due to the nature of the growth, it takes time for gallium atoms to climb up to the top of a rod. The size of the nuclei can affect the growth rate of the nanorods and lead to a variation in the final height distribution. Usually, wider or larger rods grow more slowly.[36]

In this chapter, our GaN nanopillar structures were grown on an AlN buffer layer with a sapphire substrate using a radio-frequency (RF) plasma MBE system (known as ULVAC MBE).[15,39] A nitrogen-rich environment was created using a gallium flux one-fourth of the regular value, and the RF power was 900 W. The substrate temperature was kept at 900 °C during the growth. At the end of the growth, if the gallium flux is increased intentionally, lateral growth is enhanced and the final shape of the rods is funnel-like, which might be beneficial for subsequent LED growth.

7.3 General characterization method

7.3.1 Transmission electron microscopy and threading dislocation counting

One of the very first questions is how to characterize the dislocation density. In practice, we use TEM to examine the cross section of the material. The TDD is estimated directly from these images, as shown later in this chapter. First, we count the number of dislocations in a horizontal line on the GaN epilayer. The dislocation density per unit length is the number of dislocations divided by the length in the TEM image. Finally, the dislocation density per unit area is the square of the dislocation density per unit length (the unit is $\#/\mathrm{cm}^2$).

7.3.2 Raman spectroscopy

A frequently used technology to test the quality of a film is Raman spectroscopy. The inelastic scattering of incident photons provides detailed information about the phonon vibration in various modes. From the frequencies of these modes, information about the film stress and lattice mismatch can be deduced. This is important for the induced quantum-confined Stark effect (QCSE), which is common in polarized InGaN/GaN/AlN films.[11,12,40]

In a GaN unit cell, there are four modes of phonon oscillation: A1, B1, E1 and E2. The E2 mode is the most active in Raman scattering.[40,41] By measuring and comparing the native GaN substrate and a hetero-epitaxial substrate (i.e. sapphire, SiC, silicon, etc.), the difference in the E2 peaks can be calculated using the following equations:

$$\Delta\omega_\gamma = \omega_\gamma - \omega_0 = \mathrm{K}_\gamma \cdot \sigma_{xx}, \qquad [7.1]$$

where ω_γ and ω_0 are the Raman peaks of GaN from flat surface and nanorod-array templates, respectively. The stress σ_{xx} can be estimated by adopting a theoretical K_γ value of 2.56 cm^{-1}/GPa, as reported by Wagner and Bechstedt.[42] The E_2-high peak for a stress-free GaN substrate is about 567.1 ± 0.1 cm^{-1}.[43] The residual stress of the film can be calculated using Eq. 7.1 by comparing E_2 peaks.

7.3.3 Photoluminescence (PL) and internal quantum efficiency (IQE) measurements

The active region of an ideal LED emits one photon when one electron is injected. Each charged quantum particle (an electron) produces one light quantum particle (a photon). Thus the ideal active region of an LED has a quantum efficiency of unity. The internal quantum efficiency (IQE) is defined as:

$$\eta_{\text{int}} = \frac{\text{number of photons emitted from active region per second}}{\text{number of electrons injected into LED per second}} = \frac{P_{\text{int}} / h\nu}{I / e} \qquad [7.2]$$

where P_{int} is the optical power emitted from the active region and I is the injection current. Photons emitted by the active region should escape from the LED die. In an ideal LED, all photons emitted by the active region are also emitted into free space. Such an LED has an extraction efficiency of one. However, in a real LED, not all the power emitted from the active region is emitted into free space. However, it is difficult to measure the IQE accurately most of the time.

One of the methods to evaluate the IQE is to use a power-dependent photoluminescence (PL) measurement at high/low temperature. PL is a non-destructive method for understanding the internal material quality, and provides useful information about emission wavelength, light intensity and other optical properties. We can reasonably assume that there is no non-radiative recombination at very low temperatures (several kelvins) and the IQE will approach 100% at some point during the measurement. Moreover, we assume that the extraction efficiency (η_{ext}) does not change with increasing temperature. Therefore, the IQE can be defined as:[44]

$$\eta_{\text{int}}(T) = \frac{I(T)}{I(0)} \qquad [7.3]$$

where $I(0)$ is the PL intensity at 0 K and $I(T)$ is the PL intensity at temperature T. This method ignores the influence of the injected laser power density, which is not valid for a blue GaN-based LED material system. Since the absolute value at each measurement might not be accurate enough to determine the internal quantum efficiency, an alternative method was proposed to estimate the efficiency.[44] In this method, the power-dependent PL is measured at low temperature and at room temperature and, and the corresponding efficiency, η_{PL}, can be calculated as:[44]

$$\eta_{\text{PL}} = C\frac{I_{\text{PL}} / E_{\text{PL}}}{I_{\text{inj}} / E_{\text{inj}}} \Rightarrow \eta_{\text{int}} \qquad [7.4]$$

where I_{PL} is the collected PL intensity, I_{inj} is the injected laser intensity, E_{PL} is the measured light photon energy, E_{inj} is the injected photon energy and C is a constant related to the carrier injection efficiency, light extraction efficiency and correction efficiency of the PL. This power-dependent η_{PL} can be graphed and the maximum found at low temperature. At this maximum point, the internal quantum efficiency is assumed to be 100% and the low and room-temperature efficiency is normalized according to this value.[44] In this way, a simple but still accurate internal quantum efficiency of an LED can be found.

In PL measurement, the first thing to determine is the injected laser power. Then the actual spot size on the wafer has to be measured. The general formula for the equivalent carrier density generated by the injected laser power can be expressed by:[45]

$$\text{Carrier density} = \frac{P}{(h\nu)\times\phi\times d_{\text{active}}\times f}\times\exp(-\alpha_{\text{GaN}}d_{\text{GaN}})$$
$$\times[1-\exp(\alpha_{\text{InGaN}}d_{\text{active}})]\times(1-R) \qquad [7.5]$$

The injected carrier density is determined primarily by the power of the pumping laser (P), the energy of an injected photon (hv), the spot size of the pumping laser (φ), the thickness of the GaN and the active region (d_{GaN}, d_{active}), the repetition rate of the pumping laser (f), the absorption efficiency of GaN and InGaN (α_{GaN}, α_{InGaN}) and the reflectance of the pumping laser (R). These values can be found from the experimental set-up or standard references. In our lab, we have $\varphi = 50\,\mu\text{m}$, $d_{\text{GaN}} = 200\,\text{nm}$, $d_{\text{active}} = 156\,\text{nm}$, $\alpha_{\text{GaN}} = 0$, $\alpha_{\text{InGaN}} = 10^5\,\text{cm}^{-1}$, repetition rate of the laser = 76 MHz and R = 0.17, and these were used to calculate the injected carrier density for our samples.

7.4 Top-down technique for nanostructured LEDs

7.4.1 Free-standing GaN substrate on a nanorod template

The first direction application of this nanorod structure template was to create a free-standing GaN substrate using hydride vapor-phase epitaxy (HVPE).[46] Currently the most commonly used substrate for GaN-based optoelectronic devices is sapphire, which is not lattice matched nor thermal-expansion matched to GaN. Other material systems that are frequently considered are silicon and silicon carbide. However, these two materials also have the same problems as sapphire.

Silicon carbide substrates are also expensive. Native GaN is still the best candidate for device fabrication and previous research has demonstrated encouraging results.[47] However, difficulties in raw material growth hinder progress for this type of free-standing GaN substrate. Traditional high-pressure growth requires high temperature (>2800 K) and high equilibrium N_2 pressure (>45 kbar). These conditions are not very practical for industrial use.[48] Other methods, such as ammonothermal growth, have been proposed and are currently under intense study. Meanwhile, HVPE is still the most practical and favorable method for fabricating free-standing GaN substrates. Usui *et al.* used ELO and a thin MOCVD-grown GaN as a seed layer and achieved a dislocation density as low as 6×10^7 cm^{-2}.[20] A MOCVD-grown nanoscale GaN seed layer has also been used successfully in HVPE technology to prepare a high-quality substrate (or template).[46]

Figure 7.5(a) shows the process for fabricating the GaN substrate. As in the previous section, an undoped 1.8-μm-thick GaN layer was grown on a 2″ *c*-plane

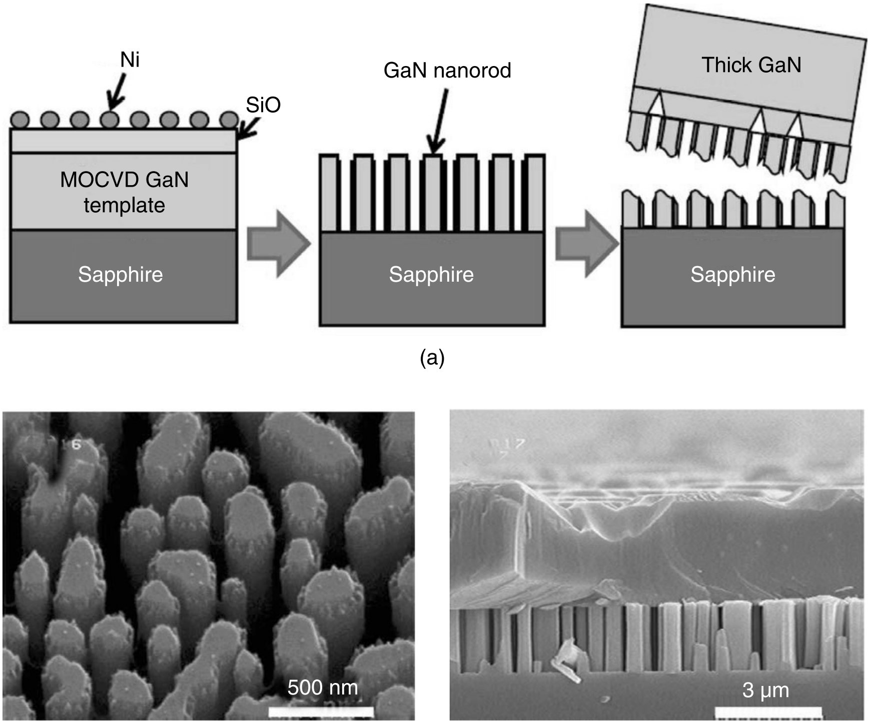

(a)

(b)

(c)

7.5 (a) Flowchart for producing GaN nanorods. (b) SEM image of a GaN nanorod array with SiO_2 passivated sidewalls. (c) SEM cross section of the a sample after the initial stage of HVPE regrowth with a growth time of 2 min.[46]

sapphire substrate by MOCVD. A standard top-down procedure was followed to create the nanostructure. The diameter and the etched depth of the nanorods were 200–500 nm and 1.8 μm, respectively. Afterward, we again deposited a 200-nm-thick SiO_2 layer on the nanorod template and utilized RIE to remove the SiO_2 layer on the top surfaces of the GaN nanorods, as shown in Fig. 7.5(b). This figure clearly shows that the sidewalls of the GaN nanorods were surrounded by a thin SiO_2 layer with a thickness of ~40 nm. Finally, HVPE was used to regrow a 300-μm-thick GaN layer; the details of the HVPE process are described in Chao *et al.*[49] During the HVPE cooling process, the 300-μm-thick GaN substrate separates from the underlying host sapphire substrate as a result of the release of the thermal strain. For comparison, a conventional as-grown GaN substrate was also prepared by HVPE on a sapphire substrate. Figure 7.5(c) is a cross section of the sample after the initial regrowth stage of HVPE. In this figure, the thickness of the GaN layer is approximately 3.3 μm and the surface is quite rough. The rough surface is believed to be due to the different growth rates of the GaN seeds in the initial stage of HVPE growth. This problem can be solved by increasing the growth time. Unlike the growth of GaN on microscale patterned substrates,[50] no voids were observed in this work because the GaN rod-to-rod intervals were small enough (200–400 nm).

Figure 7.6(a) and (b) show as-grown 300-μm-thick GaN films separated from a GaN nanorod-array template and a flat GaN template, respectively. Figure 7.6(a) shows a complete 2″ self-separated free-standing GaN substrate. In Fig. 7.5(c), we can observe that the GaN regrowth layer was suspended on the nanorod-array template because of the SiO_2 sidewall passivation. In general, during the HVPE cooling process, a large thermal stress will be induced by the quite different thermal expansion coefficients of GaN and Al_2O_3. In releasing the thermal

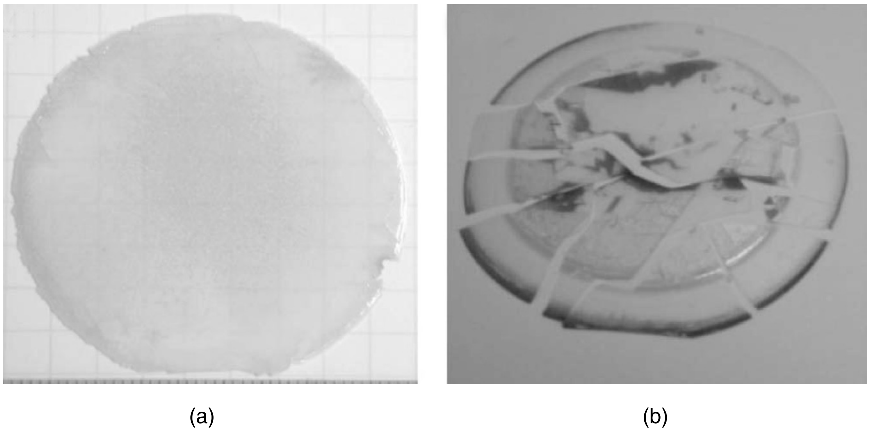
(a) (b)

7.6 GaN thick films obtained from (a) a GaN nanorod array and (b) a flat GaN surface.[46]

stress during the HVPE cooling process, the GaN nanorods became broken, which resulted in the self-separation of GaN from the sapphire substrate. In contrast, as shown in Fig. 7.6(b), GaN grown on a flat surface broke into several pieces because the thermal stress could not be released in the HVPE cooling process.

Figure 7.7 shows the typical PL spectra and bright-field TEM cross sections of GaN substrates obtained from the nanorod array and a flat GaN template. In

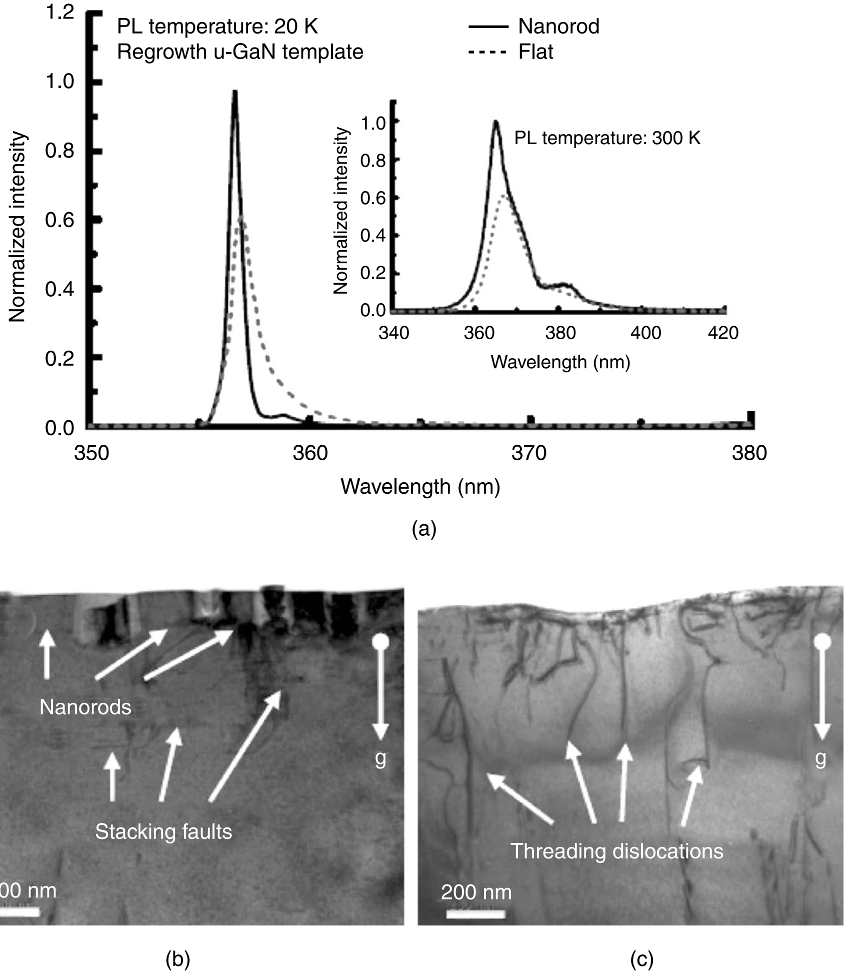

(a)

(b)

(c)

7.7 (a) PL spectra of GaN substrates separated from GaN nanorods and a flat GaN surface at 20 K. Inset shows the spectra at room temperature. TEM cross sections of the GaN substrates grown on (b) GaN nanorods and (c) a flat GaN surface.[46]

contrast with Fig. 7.7(c), we found that a number of stacking faults often occurred above the GaN nanorods, as shown in Fig. 7.7(b), but visible TDs were rarely observed in the vicinity. It is believed that the presence of stacking faults could block the propagation of TDs.[51] From the TEM images, the TDDs in the substrates obtained from a nanorod array and a flat GaN template were estimated to be ~10^7 cm^{-2} and ~5×10^9 cm^{-2}, respectively.

7.4.2 SiO_2 nanorod-array patterned sapphire template

In Section 7.4.1, it was shown that a nanorod template can effectively reduce the strain inside the film caused by the lattice and thermal expansion mismatch. The immediate thought was to apply this kind of method to LED growth by using SiO_2 nanomasks. Using a layout similar to that in Fig. 7.2, SiO_2 nanomasks can block GaN growth locally and lateral coalescence can happen in the areas not covered by the oxide. The resultant film has fewer TDDs and thus has a better quality of light emission. The patterning of the SiO_2 layer follows the procedures described in Section 7.2, and the subsequent LED growth is standard like those in Section 7.2.

GaN layers were grown on a planar sapphire substrate and on a NAPSS. After the devices were produced, TEM was employed to investigate the crystalline quality of the layers. As shown in Fig. 7.8(a), the TDD of GaN on the planar sapphire substrate was greater than 10^{10} cm^{-2} due to both the large lattice mismatch

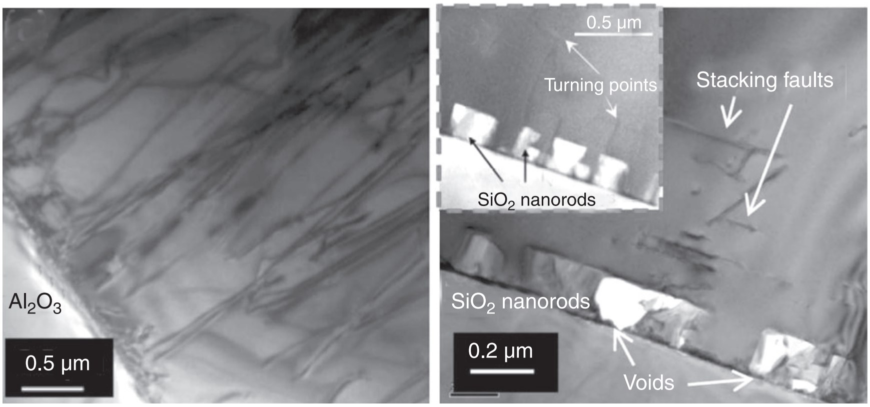

(a) (b)

7.8 (Color online) TEM images of the GaN/sapphire interface for GaN epilayers grown on (a) a planar sapphire substrate and (b) on a NAPSS. The inset of (b) shows the dislocation bending phenomenon with visible turning points.[14]

(13%) and the high thermal coefficient mismatch (62%) between sapphire and GaN. The crystalline quality of the GaN epilayer on a NAPSS was drastically improved from that grown on a planar sapphire substrate, as shown in Fig. 7.8(b). We found that there were often a number of stacking faults above the voids between the SiO_2 nanorods and visible TDs were rarely observed in the vicinity. It is believed that the presence of stacking faults could block the propagation of TDs.[51] Moreover, the TDs of the GaN layer on a NAPSS mainly originated from the exposed sapphire surface, and they could have bent due to the lateral growth of the GaN. The inset of Fig. 7.8(b) shows the dislocation bending with visible turning points. We considered that four potential mechanisms were involved in the reduction of the TDD, denoted Types 1 to 4 and illustrated in Fig. 7.2.

The finished epitaxial structures then underwent a standard four-mask LED fabrication process with a chip size of $350 \times 350\,\mu m^2$ and packaged into TO-18 with epoxy resin on top. The current-voltage (*I-V*) characteristics of the NAPSS LED and a conventional LED (C-LED) with the same chip size were measured at room temperature, as shown in Fig. 7.9(a). The forward voltages at 20 mA were 3.27 V for the conventional LED and 3.31 V for the NAPSS LED. The nearly identical *I-V* curves indicate that the nanoscale roughness on the *p*-GaN surface had little impact on the *I-V* characteristics.

Figure 7.9 shows the measured diode voltage and light output power versus the forward continuous dc current for the NAPSS and conventional LEDs. At an injection current of 20 mA, the light output power was approximately 22 mW and 14 mW for the NAPSS and conventional LEDs, respectively. The output power of the NAPSS LED was enhanced by a factor of 57% compared to that of the conventional LED. The inset shows the normalized electroluminescence (EL) spectra for both devices at an injection current of 20 mA. A minor wavelength blue-shift of ~2 nm was observed for the NAPSS LED, which was attributed to the partial release of the strain because of the NELO scheme.[52] The EQE of the NAPSS LED was calculated to be ~40.2%, which is an increase of 56% compared to that of the conventional LED (~25.7%). We believe that the 56% enhancement in EQE originates from the improved internal quantum efficiency and the enhanced extraction efficiency. The SiO_2 NAPSS-assisted NELO method effectively reduces the dislocation density in GaN-based LEDs, which increases the internal quantum efficiency. Moreover, the embedded SiO_2 nanorods in the GaN epilayer contribute to the enhanced light extraction efficiency due to the scattering at the interfaces of different refractive indices. Ueda *et al.*[53] reported that the output power linearly increases with the surface coverage ratio of nanosilica spheres. Similarly, the extraction efficiency was enhanced by the SiO_2 nanorod array.

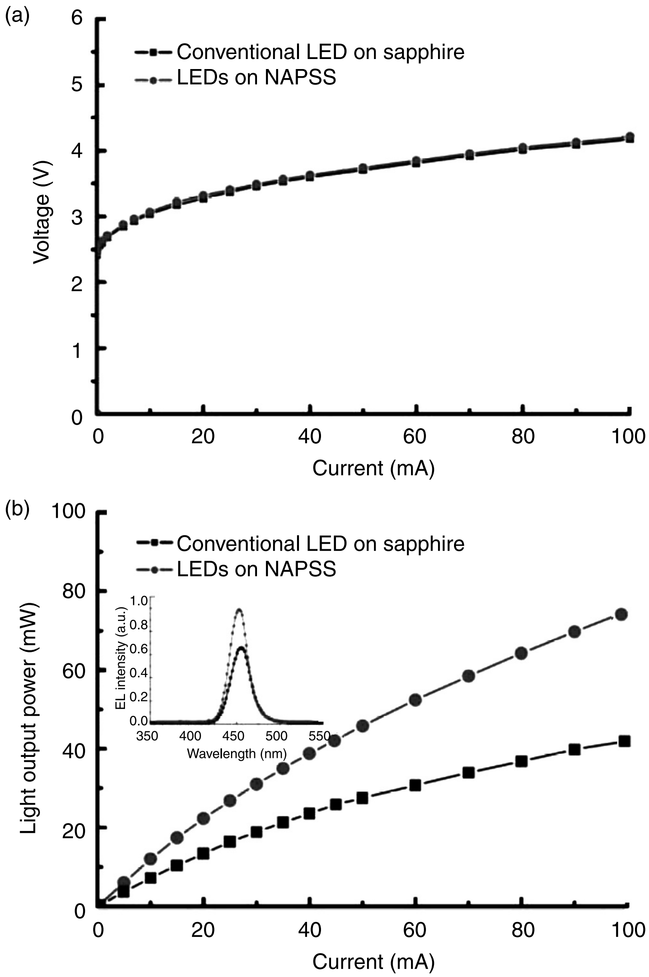

7.9 (Color online) Electrical and optical properties of a NAPSS and a conventional LED: (a) the current-voltage (*I*-*V*) curves, where the inset shows a schematic of a NAPSS LED, and (b) the output power-current (*L*-*I*) curves, where the inset shows the electroluminescence spectra for both devices at a driving current of 20 mA.[14]

7.4.3 Nanoscale patterned sapphire substrate with embedded photonic quasi-crystal

Once the SiO_2 nanomask has been built, further improvements can be made to this template. One of them is to use a photonic quasi-crystal (PQC). We utilized a nano-imprint technique to fabricate a nanoscale patterned sapphire substrate (NPSS) and a SiO_2 PQC on an *n*-GaN layer suitable for mass production. This

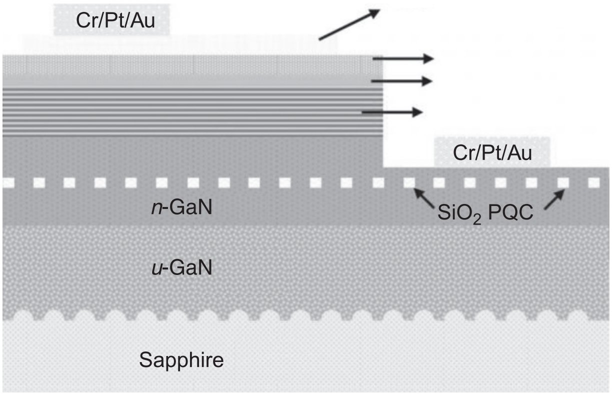

7.10 LED with a NPSS and a SiO_2 PQC structure.[54]

idea is similar to Section 7.2.2, except the patterns were fabricated using a nanoscale master. Experimental results revealed that the light output power of an LED with a NPSS and a SiO_2 PQC pattern on an *n*-GaN layer was significantly greater than that of a conventional LED.

Figure 7.10 is a schematic diagram of a GaN-based LED with a NPSS and a SiO_2 PQC structure on an *n*-GaN layer. This SiO_2 PQC pattern on an *n*-GaN layer was fabricated by nano-imprint lithography (NIL). Three patterned LEDs were fabricated in order to investigate the influence of the NPSS and the SiO_2 PQC on an *n*-GaN layer on the LED light output power and beam profile performance. For convenience, an LED with a SiO_2 PQC, an LED with a NPSS and an LED with a NPSS and a SiO_2 PQC structure were denoted as LED A, LED B and LED C, respectively.

The following details the process flow for producing a NPSS using the NIL technique on a flat sapphire substrate. First, we spin-coated a 200-nm polymer layer onto the sapphire substrate surface. Second, we placed a patterned mold onto the dried polymer film. By applying high pressure, we can heat the sapphire substrates to above the glass transition temperature of the polymer. After that, the sapphire substrates and the mold are cooled down to room temperature to release the mold. Finally, we used inductively coupled plasma reactive ion etching (ICP-RIE) with BCl_3 plasma to transfer the pattern onto the sapphire substrate and we removed the polymer layer with O_2 plasma etching gas in a RIE system.

Figure 7.11(a) shows the top view of a GaN epitaxial layer with a NPSS. The SEM image shows the characteristic NPSS nanolens pattern. The lattice constant (a) of the NPSS structure is 750 nm and the nanolens diameter (d) is 455 nm. The etching depth for the NPSS was approximately 182 nm. Figure 7.11(b) shows a cross section of the GaN epitaxial layer with a SiO_2 PQC pattern.

Unlike photonic crystals (PhCs), which have high natural lattice symmetry, PQCs appear random at first glance; however, closer inspection reveals them to

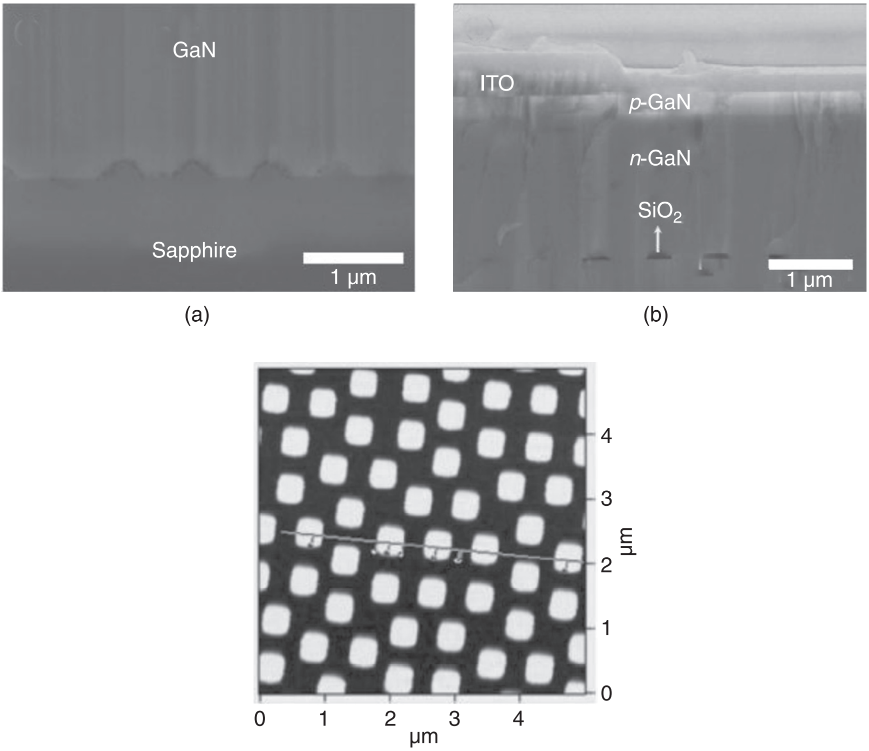

(a) (b)

(c)

7.11 SEM images of a sapphire surface with an NPSS: (a) top view and (b) cross section. ITO: indium-tin-oxide. (c) AFM top-view image of an *n*-GaN surface with a SiO$_2$ PQC.[54]

possess long-range order but short-range disorder. Figure 7.11(c) shows the top view of a 12-fold PQC pattern based on a square-triangular lattice. We choose the 12-fold PQC pattern because it gives better enhancement of the surface emission.[55] It was obtained from a PhC with a dodecagonal symmetric quasi-crystal lattice, as opposed to a regular PhC with a triangular lattice and eightfold PQC.[55] The recursive tiling of offspring dodecagons packed with random ensembles of squares and triangles in dilated parent cells forms the lattice. The lattice constant and rod diameter were 750 nm and 500 nm, respectively.

All LED samples were fabricated using the following standard processes with a mesa area of $300 \times 300\ \mu\text{m}^2$. Figure 7.12(a) shows the characteristics of a typical current-voltage (*I-V*) measurement. The measured forward-biased voltage under an injection current of 20 mA at room temperature for the conventional LED, LED A, LED B and LED C was 3.16 V, 3.15 V, 3.15 V and 3.23 V, respectively. In addition, the dynamic resistance of the conventional LED, LED A, LED B and LED C was 14.7 Ω, 14.8 Ω, 15.3 Ω and 15.4 Ω, respectively. Therefore, in terms of dynamic resistance, there was no effect on these devices of incorporating a NPSS and a SiO_2 PQC structure using the NIL process. The devices were mounted on a TO-can package. The light output was detected by an integrating sphere with a calibrated silicon photodiode so that the light emitted in all directions from the LED was collected. The intensity-current (*L-I*) characteristics of the conventional LED, LED A, LED B and LED C are shown in Fig. 7.12(b). At an injection current

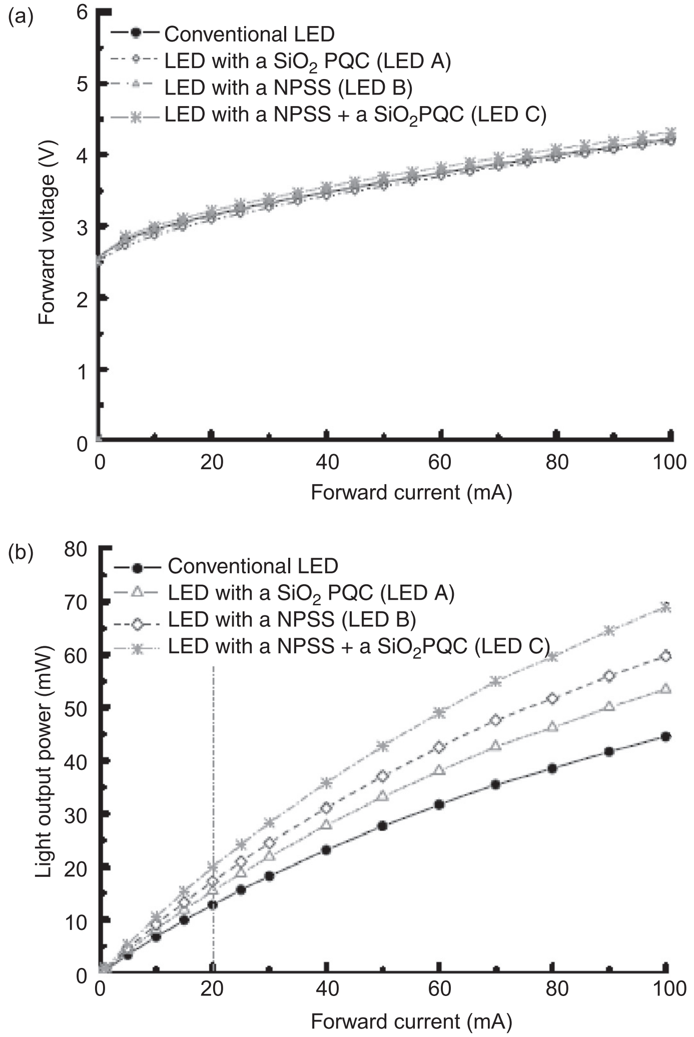

7.12 (a) Current-voltage (*I-V*) and (b) intensity-current (*L-I*) characteristics of a conventional LED, an LED with a SiO_2 PQC structure on an *n*-GaN layer, an LED with a NPSS and an LED with a NPSS and a SiO_2 PQC structure on an *n*-GaN layer.[54]

of 20 mA and peak wavelength of 460 nm, the light output powers of the conventional LED, LED A, LED B and LED C with the TO-can package are 12.8 mW, 15.4 mW, 17.3 mW and 18.9 mW, respectively. Hence, the percentage enhancement for LED A, LED B and LED C was 20%, 35% and 48%, respectively, compared to the conventional LED. The enhancement of output power was due to the better crystal quality and increased reflection at the GaN/sapphire interface. Using a NPSS is regarded as an effective way to reduce threading dislocations between GaN and the underlying sapphire substrate, and the method allows more light to reflect upward from the sapphire substrate. In addition, the use of a 12-fold SiO_2 PQC pattern also results in higher epitaxial crystal quality, which increases the light output power.[7,14,56]

To confirm the speculations above, TEM images were employed to investigate the crystalline quality of GaN layers epitaxially grown on a flat sapphire substrate and a NPSS. As shown in Fig. 7.13(a) and (b), it is obvious that the TDD of the GaN grown on a NPSS and a SiO_2 PQC structure was drastically reduced from that grown on a flat sapphire substrate. From Fig. 7.13(c), we found that a number of stacking faults often occurred above the nanolens patterns but visible TDs were rarely observed in the vicinity. It is believed that the presence of stacking faults could block the propagation of TDs.[14] Moreover, the TDs of the GaN layer on a NPSS and a SiO_2 PQC structure mainly originated from the exposed sapphire surface, and they could have bent due to the lateral growth of the GaN. Figure 7.13(c) shows the LED with a NPSS and a SiO_2 PQC structure with dislocation bending and visible turning points.[14]

7.4.4 Highly efficient and bright LEDs overgrown on GaN nanopillar substrates

While nanoscale masks can improve the quality of LEDs, a more elaborated method based on this technology can be used, i.e. the GaN nanopillar-array substrate. The formation of a nanopillar requires one more step than the previous two methods: dry-etching of the sapphire surface. This method maximizes the dislocation bending because of enhanced lateral growth and the larger air-void array embedded in the substrate scatters the light and increases the light extraction efficiency.

Figure 7.14(a–c) shows how the air gap was formed by nanoscale epitaxial lateral overgrowth (NELO) techniques on top of a SiO_2 nanomask. First, GaN NRs with an SiO_2 nanomask were formed on a sapphire substrate by top-down methods, as shown in Fig. 7.14(a). As the GaN NRs grow upwards, there is also lateral growth on the sidewall of individual NRs. This lateral growth eventually narrows the gaps between columns and forms holes with embedded air pockets, as shown in Fig. 7.14(b). Our previous study showed that this growth process adds extra *m*-plane (1010) GaN on the sidewalls of the etched pillars and inclined *r*-plane facets (1102) close to the top of the nanopillars.[57] Frajtag *et al.* also

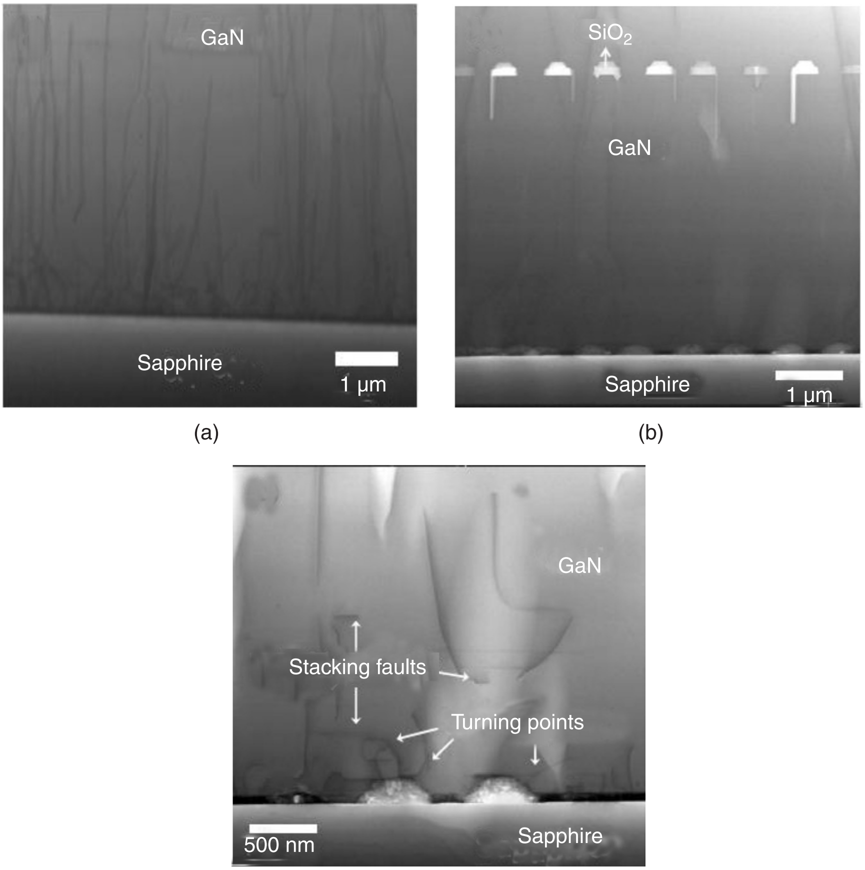

(a) (b)

(c)

7.13 TEM images of the GaN/sapphire interface for the GaN epilayer grown on (a) a flat sapphire substrate and (b) a NPSS and a SiO_2 PQC structure on an *n*-GaN layer. (c) GaN epilayer with a NPSS and a SiO_2 PQC structure on an *n*-GaN layer showing dislocation bending phenomenon with visible turning points.[54]

reported that the semi-polar planes coalesce, first due to their higher growth rates relative to the growth rates on the non-polar side faces of nanowires.[58] All of these growth mechanisms help the formation of voids in between the nanorods. The final step was planar epitaxial GaN overgrowth, and the air voids and SiO_2 nanomasks were encapsulated, as show in Fig. 7.14(c). To analyze the quality of the epitaxial layer in detail, we took TEM pictures of the GaN epilayers overgrown on GaN NRs, Fig. 7.14(d), and calculated the dislocation density. Fewer TDDs were observed within the range in view. The dislocation density on the top of the u-GaN was calculated to be around 5×10^7 cm^{-2}. Furthermore, we found the TDs were bent near the SiO_2 nanomasks. This behavior is similar to that seen with the NELO method for a SiO_2 NAPSS.[13] The reduction of the TDD can be attributed to the misfit (mainly perpendicular to the *c*-axis) and because dislocation bending occurred just above the voids, as shown in Fig. 7.14(e).

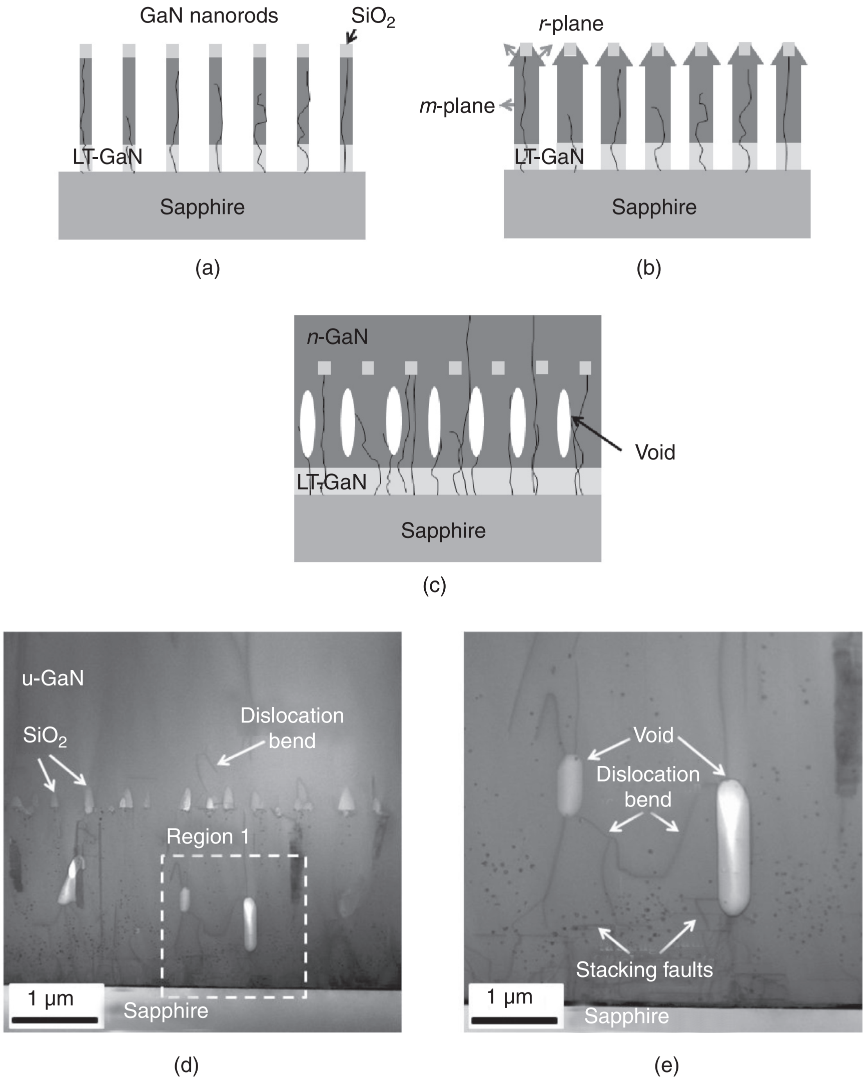
GaN nanorods
SiO2
LT-GaN
Sapphire
(a)
r-plane
m-plane
LT-GaN
Sapphire
(b)
n-GaN
Void
LT-GaN
Sapphire
(c)
u-GaN
SiO2
Dislocation bend
Region 1
1 μm
Sapphire
(d)
Void
Dislocation bend
Stacking faults
1 μm
Sapphire
(e)

7.14 (a), (b) and (c) Formation of air voids between GaN NRs and the u-GaN epitaxial layer. (d) TEM image of GaN epilayer overgrowth on GaN NRs. (e) High-resolution TEM image of region 1 in (d). The diffraction condition was $g=0002$.[26] (LT-GaN: low-temperature GaN)

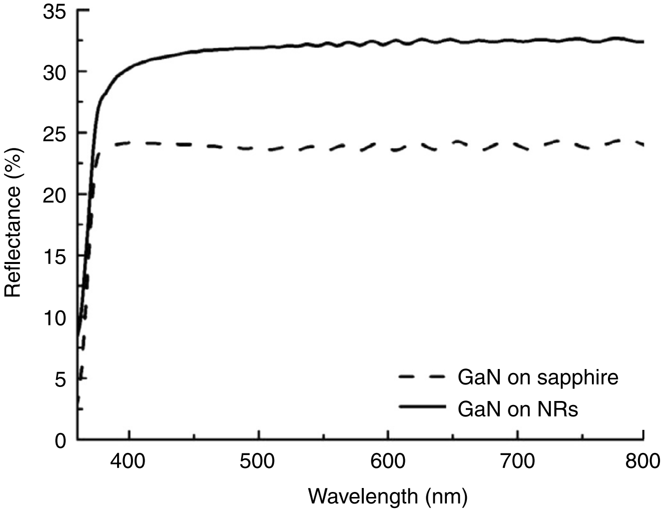

7.15 Diffuse reflectance spectra for both samples.[26]

To investigate the optical properties of the microscale air voids and SiO_2 nanomask in the GaN epilayers, reflectance spectra were measured for different samples, as shown in Fig. 7.15. The samples were grown with a single GaN layer on different substrates (planar and air void/nanomask) and coated with SiO_2 as the anti-reflection layer. The reflectance spectra have interference fringes due to the substrate interfaces, and have an abrupt cut-off at the wavelength around the GaN absorption edge at 379 nm. At the blue emission wavelengths, we found that the reflectance for the microscale voids and SiO_2 nanomask in the GaN epilayer was 1.32 times higher than for the GaN epilayer on planar sapphire. This result indicates that the reflectance increases significantly due to the microscale voids and SiO_2 nanomasks. This clearly demonstrates the light-scattering capability of the void/nanomask design, and the extra reflected light from this layer can be harvested in the front side.

Figure 7.16(a) displays the typical power-current-voltage (*L-I-V*) characteristics of NR-LEDs and C-LEDs. With an injection current of 20 mA, the forward voltage was 3.37 V and 3.47 V, and the output power was 21.6 mW and 13.1 mW, for the NR-LEDs and C-LEDs, respectively. The enhanced *L-I-V* characteristics can be attributed to the following factors. First, the reduction in TDD for the epitaxial layers leads to much fewer non-radiative recombination events and increases the photon generation efficiency. Second, more light can be extracted from the LED because of the light scattering effect from the embedded micro/nanoscale voids and SiO_2. In addition, at the reverse bias, the leakage current of the NR-LEDs is smaller than for the C-LEDs, as shown in Fig. 7.16(b). Several types of dislocation can contribute to the reverse-bias leakage current, and one of the dominant types

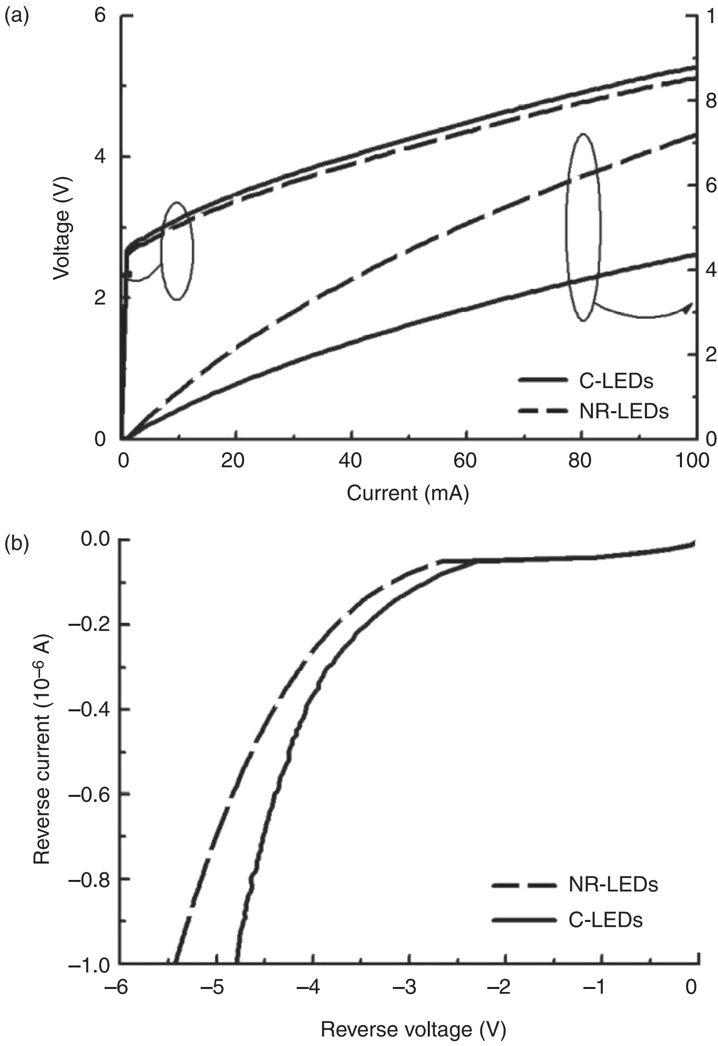

7.16 (a) Forward *L-I-V* characteristics for both fabricated LEDs. (b) Reverse *I-V* characteristics for both fabricated LEDs.[26]

is the screw dislocation.[59] The reduction of screw dislocations can certainly help to reduce the reverse-bias current,[59] and our measurement indicates the NR-LEDs had a better crystal quality, which was confirmed by the TEM results.

We still needed to quantify how much the improvement of the *L-I-V* is because of the better light extraction scheme due to the voids. A 3D FDTD simulation was used to calculate the LEE of the LEDs using the FullWAVE™ simulation program.[60] An array of 5 × 5 random nanorods with a height of 2 μm were used in the simulation. The unit cell had an area of ~7.56 μm^2, corresponding to a density of ~3 × 10^8 cm^{-2}. The structural dimensions were extracted from SEM images. The light sources were 15 dipole illuminators placed 0.32 μm below the surface and the detector was at top of the simulated device. The calculated electric-field distribution with an air void and SiO_2 period of 0.5 μm is shown in Plate VI(a). As can be seen in the plate, the light intensity from the NR-LEDs is higher than from the C-LEDs at the detector, which is a clear indicator of the higher photon extraction efficiency in NR-LEDs compared to C-LEDs. The corresponding normalized light output as a function of time was calculated and is plotted in Plate VI(b). The enhancement of light scattering can be calculated as the ratio of the steady-state light output from the NR-LEDs and the C-LEDs. From the simulated results, the light output from the NR-LEDs was around 1.447 times higher than from the C-LEDs. Since the external quantum efficiency is the extraction efficiency (η_{ext}) multiplied by the IQE (η_{int}), the enhancement of the NR-LED's IQE can thus be estimated as 14% compared to C-LEDs.

7.5 Bottom-up technique for GaN nanopillar substrates prepared by molecular beam epitaxy

The nanostructures discussed in Section 7.4 were generally fabricated by top-down methods,[61–63] such as an etching process. The dry-etching procedure normally generates defect states on the column surfaces, reducing the IQE. In this section, we will discuss the NELO of a high-quality GaN layer on a bottom-up nanostructure (self-assembled GaN nanopillars) grown by MBE.[64] Detailed analyses of the grown InGaN/GaN films and the electro-optical properties of LEDs based on such GaN NP templates will be discussed.

Following the process parameters and procedures described in the previous section, a RF-plasma MBE system was used to grow the nanostructure. As mentioned before,[39] a nitrogen-rich environment is necessary for rod formation. In our case, the first seeding layer was grown with a higher gallium flux (about 1.31 × 10^{-6} Torr) to produce a gallium-polar surface. Then the group III flux was reduced by a factor of four to 3.2 × 10^{-7} Torr to facilitate the growth of rods. Under this condition, with a substrate temperature of 900 °C, the nanorods were grown vertically for one hour. The gallium flux was changed in two steps (one at 7.3 × 10^{-7} Torr and the second at 1.31 × 10^{-6} Torr) to create a gradual change in the rod shape. Coalescence of the GaN film is expected with an increase in the amount of the group III element. Then 2D uniform thin-film growth was resumed to add the normal LED epitaxial structure.

Figure 7.17(a)–(c) shows the steps in the formation of air voids. First, the overall structure was started on a sapphire substrate using MBE at a substrate temperature of 740 °C (Fig. 7.17(a)). The growth sequence was scheduled such that it starts with regular GaN nanorods, but at the end of growth, we doubled the

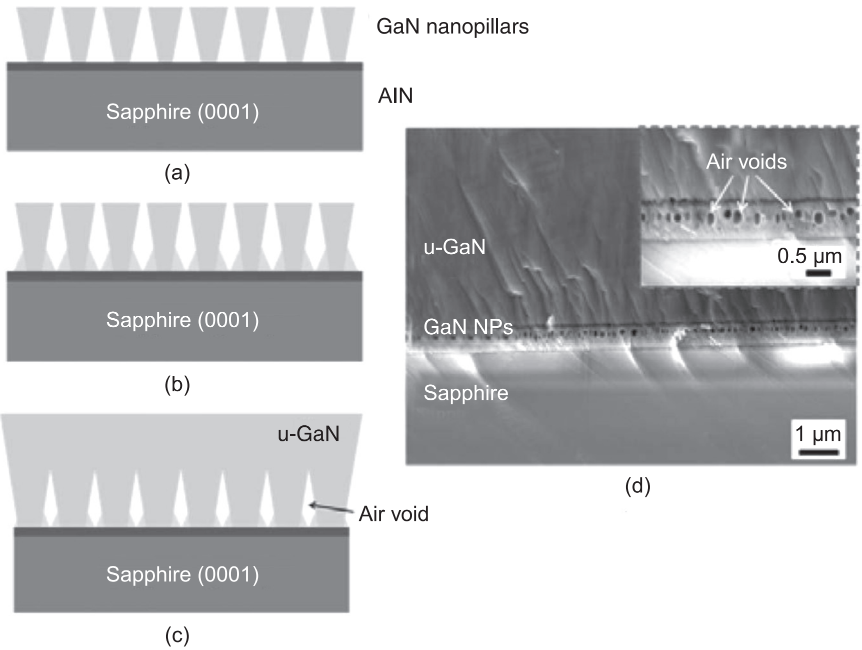

7.17 (a)–(c) Formation of air voids between the GaN NPs and u-GaN epitaxial layer. (d) SEM cross section. The inset shows air voids.[15]

gallium flux to enhance the lateral growth and the final shape of the rods was funnel-like. Figure 7.17(d) is an SEM image of the grown GaN NPs. It can clearly be seen that the GaN NPs have a funnel-like form on the inset in Fig. 7.17. The lateral growth eventually narrows the gap between columns and forms holes 0.2–0.25 μm in size, shown in Fig. 7.17(d). The density, diameter and the height were estimated to be around 1.15×10^{10} cm^{-2}, 50 nm and 0.8 μm, respectively.

The quality of the film can be evaluated from its surface roughness. After the u-GaN layer was deposited, without growing the remaining LED layers, the surface morphology was measured with an atomic force microscope (AFM), as shown in Plate VII (see colour plate section between pages 330 and 331). The root mean square (rms) value of the surface roughness was about 1.4 nm, indicating high surface quality and excellent coalescence overgrown on the GaN NP template. To analyze the quality of the epitaxial layer in detail, we used TEM to compare the cross sections of two types of device (NP-LEDs and C-LEDs). As we can see from Fig. 7.18(a), for the GaN epitaxial layer grown on sapphire without GaN NPs, several TDs propagate vertically from the GaN/sapphire interface, all the way to the upper layers of the device. As a result, the TDD in a conventional GaN layer can be as high as 10^9 cm^{-2}. For the GaN epitaxial layer grown on sapphire with GaN NPs, Fig. 7.18(b), it can be clearly seen that the crystallography is drastically different from that of the conventional LEDs. Fewer TDs are

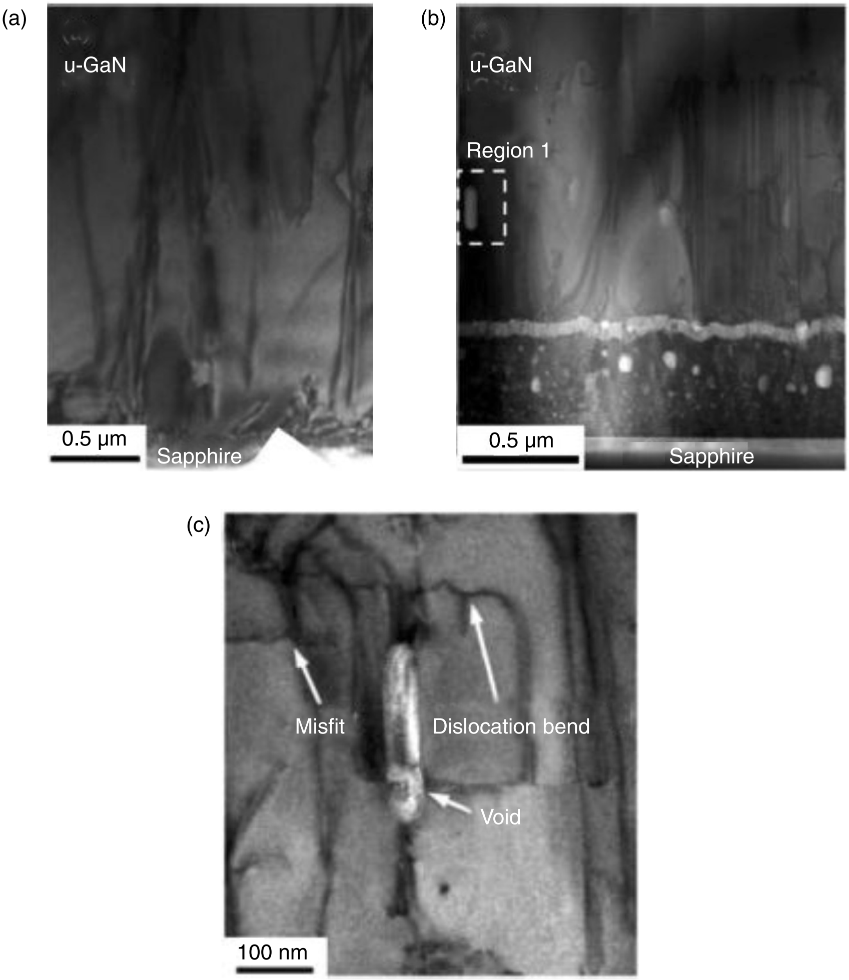

7.18 TEM images of (a) C-LEDs, (b) NP-LEDs and (c) a high-resolution TEM image of region 1 in (b). The diffraction condition was *g*=0002.[15]

observable within the range in view. The dislocation density on the top of the *n*-GaN MQWs was calculated to be around 7×10^7 cm^{-2}. The reduction of the TDD can be attributed to the misfit (mainly perpendicular to the *c*-axis) and the dislocation bending, which occurred just above the voids, as shown in Fig. 7.18(c). Such behavior is similar to that seen for the NELO method in Section 7.4.2.[13]

LED devices with a chip size of $350 \times 350\,\text{mm}^2$ were then fabricated from the completed epitaxial structures grown on sapphire with and without GaN NPs. Figure 7.19(a) shows the EL emission peak wavelength as a function of injection current for NP-LEDs and C-LEDs. The emission peak wavelength for the NP-LED

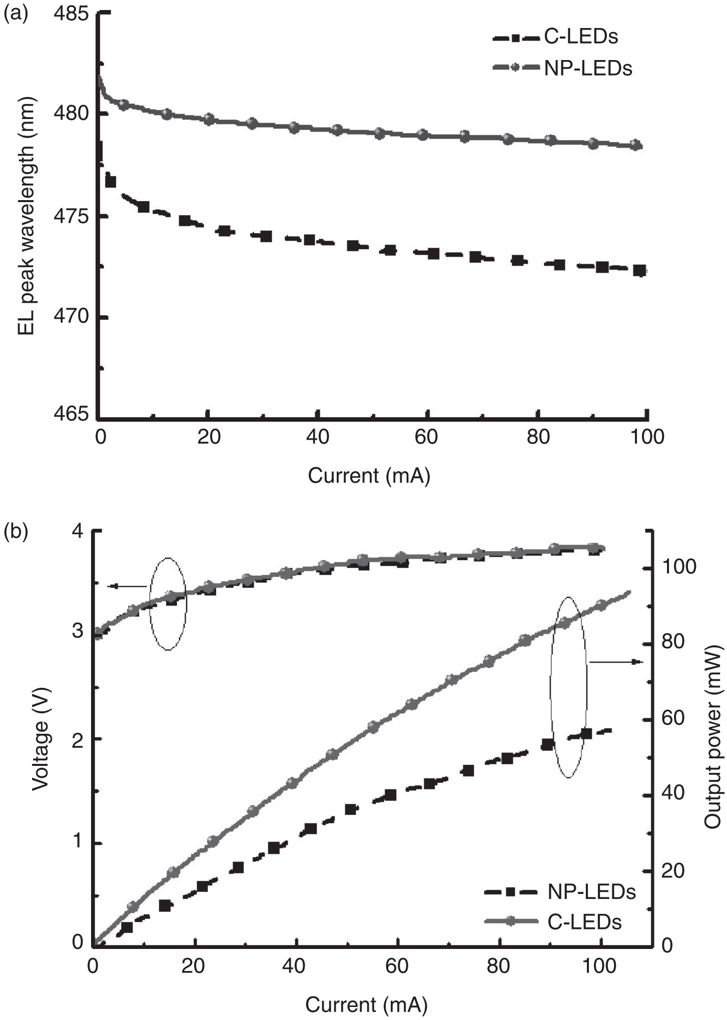

7.19 (a) EL peak wavelength as a function of injection current for the two fabricated LEDs. (b) *L-I-V* characteristics for the two fabricated LEDs.[15]

was slightly red-shifted (about 3.4 nm) from that of the C-LED, and this is reasonable since lateral strain relaxation favors higher indium incorporation.[65–67] More importantly, as we increased the injection current, the emission peak wavelength for the NP-LEDs had a smaller blue-shift (around 2.9 nm) compared with that of the C-LEDs (around 5.6 nm). This result indicates that the QCSE becomes weaker due to strain relaxation in the epitaxial layer overgrown on the GaN NP template, as we expected. Figure 7.19(b) displays the typical power–current–voltage (*L–I–V*) characteristics of the NP-LEDs and C-LEDs. With an injection current of 20 mA, the forward voltages are 3.38 V and 3.40 V, and the output powers are 25.3 mW and 14.8 mW, for the NP-LEDs and C-LEDs, respectively. The enhancement of the light part of the *L–I–V* characteristics can be attributed to the following factors: first, there is the reduction in the TDD in the epitaxial layers. This reduction leads to much fewer non-radiative recombination events in the NP devices and increases the photon generation efficiency. Second, more light can be extracted from the LED because of the light-scattering effect from the embedded nanoscale air voids.

To confirm the efficiency improvement of our NP-LED, the PL internal quantum efficiency was measured. A general approach for evaluating the IQE of LEDs is to compare the PL integrated intensity at a low temperature and at room temperature, as we mentioned in Section 7.3.[44] Figure 7.20 shows the measured IQE as a function of excitation power at 15 K and 300 K for NP-LEDs and C-LEDs. The efficiency is defined as the number of collected photons divided by the number of injected photons and normalized to the maximum efficiency at low temperature.[45] At 20 mW of excitation power, the IQE had increased from 58% (for C-LEDs) to 72% (for NP-LEDs), which corresponds to 1.24 times enhancement of efficiency. At this excitation level, we calculated the corresponding generated carrier density to be 2×10^{17} cm^{-3} by Eq. 7.5, and we calculated approximately the same level with 20 mA at room temperature. Thus, part of the efficiency improvement for

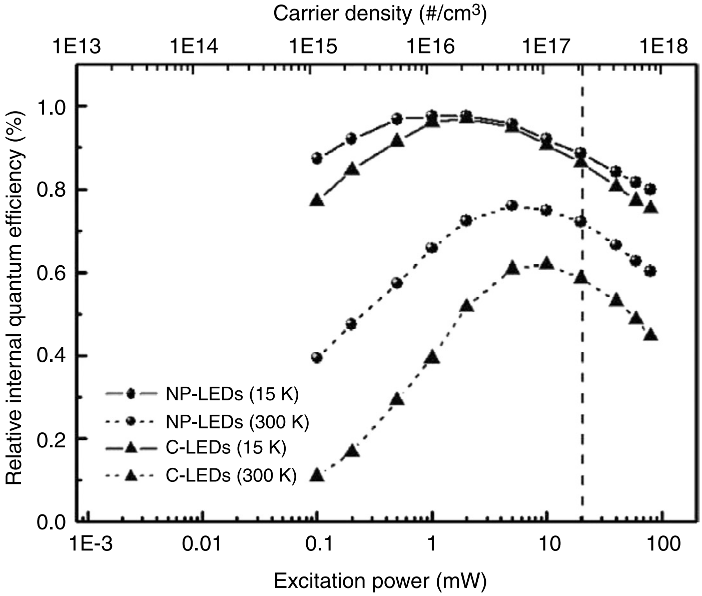

7.20 Relative IQE as a function of excitation power for C-LEDs and NP-LEDs.[15]

GaN NP-LEDs can be linked directly to the improvement of IQE due to the better crystal quality.

Again, we needed to quantify how much improvement of the *L–I–V* is because of the better light extraction scheme due to the air voids. A 2D FDTD simulation was using to calculate the LEE of the LEDs using the FullWAVE program.[60] The calculated electric-field distribution for an air-void period of 0.25 μm is shown in Plate VIII(a) (see colour section between pages 330 and 331), where an array of air-filled rectangular holes represents the air voids in our devices. The size of each rectangular hole was 0.2 μm × 0.1 μm. We set single dipole illumination sources at 0.5 μm below the top of the surface structures and the detector around the simulated device.[68] As can be seen in the plate, the electric-field intensity for NP-LEDs is higher than for C-LEDs at the detector, and this means the generated photons have a larger chance of escaping from inside the GaN to the air. The corresponding normalized light output as a function of the simulation time was calculated and is plotted in Plate VIII(b). From the simulated results, the light output from the NP-LEDs was around 1.48 times higher than from the C-LEDs. Combining this with the PL IQE measurement, there was a total enhancement of 82% (48% from LEE and 24% from IQE) compared with a conventional LED structure. The actual increase in the power output of the LED, 70%, was lower than predicted. This was possibly due to the randomness of the formation of air voids, which made our FDTD analysis overestimate the light-scattering effect.

7.6 Conclusion

In this chapter, we reviewed several designs for nanoscale patterned substrates to produce high-quality LEDs. High-quality GaN-based LED structures were successfully fabricated onto nanorod templates using these nanotechnologies. Both the top-down and bottom-up methods have advantages for device performance and should be considered. The ease of fabrication and growth for top-down devices should be beneficial for initial commercialization. However, the bottom-up method can potentially reduce the dislocations and defects caused by *in situ* processes and thus produce more powerful nanoscale devices.

7.7 References

1 Y. Narukawa, I. Niki, K. Izuno, M. Yamada, Y. Murazki, *et al.*, ‘Phosphor-conversion white light emitting diode using InGaN near-ultraviolet chip,’ *Jpn. J. Appl. Phys.*, *Part 2* 41, L371 (2002).

2 E. F. Schubert, *Light Emitting Diodes*, 1st ed., Cambridge University Press, Cambridge, England (2003).

3 A. Sakai, H. Sunakawa and A. Usui, ‘Defect structure in selectively grown GaN films with low threading dislocation density,’ *Appl. Phys. Lett.* 71, 2259 (1997).

4 T. S. Zheleva, O. H. Nam, M. D. Bremser and R. F. Davis, ‘Dislocation density reduction via lateral epitaxy in selectively grown GaN structures,’ *Appl. Phys. Lett.* 71, 2472 (1997).

5 D. S. Wuu, W. K. Wang, K. S. Wen, S. C. Huang, S. H. Lin, *et al.*, 'Defect reduction and efficiency improvement of near-ultraviolet emitters via laterally overgrown GaN on a GaN/patterned sapphire template,' *Appl. Phys. Lett.* 89, 161105 (2006).

6 D. S. Wuu, W. K. Wang, K. S. Wen, S. C. Huang, S. H. Lin, *et al.*, 'Fabrication of pyramidal patterned sapphire substrates for high-efficiency InGaN-based light emitting diodes,' *J. Electrochem. Soc.* 153, G765 (2006).

7 H. Gao, F. Yan, Y. Zhang, J. Li, Y. Zeng and G. Wang, 'Enhancement of the light output power of InGaN/GaN light-emitting diodes grown on pyramidal patterned sapphire substrates in the micro- and nanoscale,' *J. Appl. Phys.* 103, 014314 (2008).

8 A. Xing, M. Davanco, D. J. Blumenthal and E. L. Hu, 'Fabrication of 2-D photonic crystal membrane structure,' *J. Vac. Sci. Technol. B* 22, 70 (2004).

9 H. W. Huang, C. H. Lin, C. C. Yu, B. D. Lee, C. H. Chiu, *et al.*, 'Enhanced light output from a nitride-based power chip of green light-emitting diodes with nano-rough surface using nanoimprint lithography,' *Nanotechnol.* 19, 185301(2008).

10 S. Li and A. Waag, 'GaN based nanorods for solid state lighting,' *J. Appl. Phys.* 111, 071101 (2012).

11 C. Kisielowski, J. Krüger, S. Ruvimov, T. Suski, J. W. Ager III, *et al.*, 'Strain-related phenomena in GaN thin films,' *Phys. Rev. B* 54, 24, 17745–17753 (1996).

12 A. P. Jephcoat, R. J. Hemley, H. K. Mao, R. E. Cohen and M. J. Mehl, 'Raman spectroscopy and theoretical modeling of BeO at high pressure,' *Phys. Rev. B* 37, 9, 4727–4734 (1988).

13 C. H. Chiu, M. H. Lo, T. C. Lu, P. Yu, H. W. Huang, *et al.*, 'Nano-processing techniques applied in GaN-based light-emitting devices with self-assembly Ni nano-masks,' *IEEE J. Lightwave Technol.* 26, 1445 (2008).

14 C. H. Chiu, H. H. Yen, C. L. Chao, Z. Y. Li, P. C. Yu, *et al.*, 'Nanoscale epitaxial lateral overgrowth of GaN-based light-emitting diodes on a SiO_2 nanorod-array patterned sapphire template,' *Appl. Phys. Lett.* 93, 081108 (2008).

15 C.-H. Chiu, P.-M. Tu, C.-C. Lin, D.-W. Lin, Z.-Y. Li, *et al.*, 'Highly efficient and bright LEDs overgrown on GaN nanopillar substrates,' *IEEE J. Sel. Topics Quantum Electron.* 17, 4, 971–978 (2011).

16 H. Amano, N. Sawaki, I. Akasaki and Y. Toyoda, 'Metalorganic vapor phase epitaxial growth of a high quality GaN film using an AlN buffer layer,' *Appl. Phys. Lett.* 48, 353 (1986).

17 S. Nakamura, 'GaN growth using GaN buffer layer,' *Jpn. J. Appl. Phys.* 30 L1705 (1991).

18 S. Nakamura, T. Mukai and M. Senoh, 'Candela-class high-brightness InGaN/AlGaN double-heterostructure blue-light-emitting diodes,' *Appl. Phys. Lett.* 64, 1687 (1994).

19 T. S. Zheleva, O. Nam, W. M. Ashmawi, J. D. Grin and R. F. Davis, 'Lateral epitaxy and dislocation density reduction in selectively grown GaN structures,' *J. Cryst. Growth* 222, 706–718 (2001).

20 A. Usui, H. Sunakawa, A. Saki and A. A. Yamaguchi, 'Thick GaN epitaxial growth with low dislocation density by hydride vapor phase epitaxy,' *Jpn. J. Appl. Phys., Part 2* 36, 7B, L899–L902 (1997).

21 C.-H. Chiu, C.-C. Lin, D.-M. Deng, D.-W. Lin, J.-C. Li, *et al.*, 'Optical and electrical properties of GaN-based light emitting diodes grown on micro- and nano-scale patterned Si substrate,' *IEEE J. Quantum Electron.* 47, 7, 899–906 (2011).

22 Y. J. Lee, H. C. Kuo, T. C. Lu and S. C. Wang, 'High light-extraction GaN-based LEDs with double diffuse surfaces,' *IEEE J. Quantum Electron.* 42, 1196 (2006).

23 T. Nagai, T. Kawashima, M. Imura, M. Iwaya, S. Kamiyama, *et al.*, 'Microstructure in nonpolar *m*-plane GaN and AlGaN films,' *J. Cryst. Growth* 298, 288 (2007).

24 H. K. Cho, J. Y. Lee, K. S. Kim, G. M. Yang, J. H. Song, *et al.*, 'Effect of buffer layers and stacking faults on the reduction of threading dislocation density in GaN overlayers grown by metalorganic chemical vapor deposition,' *J. Appl. Phys.* 89, 2617 (2001).

25 E. H. Park, J. Jang, S. Gupta, I. Ferguson, C. H. Kim, *et al.*, 'Air-voids embedded high efficiency InGaN-light emitting diode,' *Appl. Phys. Lett.* 93, 191103 (2008).

26 C.-H. Chiu, C.-C. Lin, H.-V. Han, C.-Y. Liu, Y.-H. Chen, *et al.*, 'High efficiency GaN-based light-emitting diodes with embedded air voids/SiO2 nanomasks,' *Nanotechnol.* 23, 045303 (2012).

27 J. Ristic, E. Calleja, S. Fernández-Garrido, L. Cerutti, A. Trampert, *et al.*, 'On the mechanisms of spontaneous growth of III-nitride nanocolumns by plasma-assisted molecular beam epitaxy,' *J. Cryst. Growth* 310, 4035–4045 (2008).

28 M. A. Sanchez-Garca, E. Calleja, E. Monroy, F. J. Sanchez, F. Calle, *et al.*, 'The effect of the III/V ratio and substrate temperature on the morphology and properties of GaN- and AlN-layers grown by molecular beam epitaxy on Si (1 1 1),' *J. Cryst. Growth* 183, 23 (1998).

29 M. Yoshizawa, A. Kikuchi, M. Mori, N. Fujita, K. Kushi, *et al.*, 'Growth of self-organized GaN nanostructures on Al_2O_3(0001) by RF-radical source molecular beam epitaxy,' *Jpn. J. Appl. Phys.* 36, L459 (1997).

30 S. Guha, N. Bojarczuk, M. Johnson and J. Schetzina, 'Selective area metalorganic molecular-beam epitaxy of GaN and the growth of luminescent microcolumns on Si/SiO_2,' *Appl. Phys. Lett.* 75, 463 (1999).

31 R. Calarco, M. Marso, T. Richter, A. I. Aykanat, R. Meijers, *et al.*, 'Size-dependent photoconductivity in MBE-grown GaN-nanowires,' *Nanolett.* 5, 981 (2005).

32 K. A. Bertness, A. Roshko, N. A. Sanford, J. M. Barker and A. V. Davydov, 'Spontaneously grown GaN and AlGaN nanowires,' *J. Cryst. Growth* 287, 522 (2006).

33 T. Zywietz, J. Neugebauer and M. Sheffler, 'Adatom diffusion at GaN (0001) and (0001) surfaces,' *Appl. Phys. Lett.* 73, 487 (1998).

34 K. Chopra, *Thin Film Phenomena*, McGraw-Hill, New York (1969).

35 C. T. Foxon, S. V. Novikov, J. L. Hall, R. P. Campion, D. Cherns, *et al.*, 'A complementary geometric model for the growth of GaN nanocolumns prepared by plasma-assisted molecular beam epitaxy,' *J. Cryst. Growth* 311, 13, 3423–3427 (2009).

36 R. K. Debnath, R. Meijers, T. Richter, T. Stoica, R. Calarco, *et al.*, 'Mechanism of molecular beam epitaxy growth of GaN nanowires on Si (111),' *Appl. Phys. Lett.* 90, 123117 (2007).

37 K. A. Bertness, A. Roshko, L. M. Mansfield, T. E. Harvey and N. A. Sanford, 'Nucleation conditions for catalyst-free GaN nanowires,' *J. Cryst. Growth* 300, 94 (2007).

38 O. Landré, C. Bougerol, H. Renevier and B. Daudin, 'Nucleation mechanism of GaN nanowires grown on (111) Si by molecular beam epitaxy,' *Nanotechnol.* 20, 415602 (2009).

39 T. H. Yang, J. T. Ku, J.-R. Chang, S.-G. Shen, Y.-C. Chen, *et al.*, 'Growth of free-standing GaN layer on Si (1 1 1) substrate,' *J. Cryst. Growth.* 311, 7, 1997 (2009).

40 P. Perlin, J. Jauberthie-Carillon, J. P. Itie, A. San Miguel, I. Grzegory, *et al.*, 'Raman scattering and x-ray-absorption spectroscopy in gallium nitride under high pressure,' *Phys. Rev. B* 45, 1, 83–89 (1992).

41 C. A. Arguello, D. L. Rousseau and S. P. S. Porto, 'First-order Raman effect in wurtzite-type crystals,' *Phys. Rev.* 181, 3, 1351–1363 (1969).

42 J. M. Wagner and F. Bechstedt, 'Phonon deformation potentials of α-GaN and -AlN: An ab initio calculation,' *Appl. Phys. Lett.* 77, 346 (2000).
43 A. R. Goni, H. Siegle, K. Syassen, C. Thomsen and J. M. Wagner, 'Effect of pressure on optical phonon modes and transverse effective charges in GaN and AlN,' *Phys. Rev. B* 64, 035205 (2001).
44 S. Watanabe, N. Yamada, M. Nagashima, Y. Ueki, C. Sasaki, *et al.*, 'Internal quantum efficiency of highly-efficient $In_xGa_{1-x}N$-based near-ultraviolet light-emitting diodes,' *Appl. Phys. Lett.* 83, 24, 4906 (2003).
45 Y.-J. Lee, C.-H. Chiu, C. C. Ke, P. C. Lin, T.-C. Lu, *et al.*, 'Study of the excitation power dependent internal quantum efficiency in InGaN/GaN LEDs grown on patterned sapphire substrate,' *IEEE J. Sel. Topics Quantum Electron.* 15, 4, 1137–1143 (2009).
46 C. L. Chao, C. H. Chiu, Y. J. Lee, H. C. Kuo and P.-C. Liu, 'Freestanding high quality GaN substrate by associated GaN nanorods self-separated hydride vapor-phase epitaxy,' *Appl. Phys. Lett.* 95, 051905 (2009).
47 T. B. Wei, K. Wu, Y. Chen, J. Yu, Q. Yan, *et al.*, 'Improving light output of vertical-stand-type in GaN light-emitting diodes grown on a free-standing GaN substrate with self-assembled conical arrays,' *IEEE Electron Device Lett.* 33, 6, 857 (2012).
48 T. Paskova and K. R. Evans, 'GaN substrates – progress, status, and prospects,' *IEEE J. Sel. Topics Quantum Electron.* 15, 4, 1041 (2009).
49 C. L. Chao, P. C. Liu, T. W. Chi, H. H. Huang and J. D. Tsay, *Proceedings of the International Workshop on Nitride Semiconductors*, Montreux, Switzerland, 6–10 October 2008.
50 Y. J. Lee, J. M. Hwang, T. C. Hsu, M. H. Hsieh, M. J. Jou, *et al.*, 'Enhancing the output power of GaN-based LEDs grown on wet-etched patterned sapphire substrates,' *IEEE Photonics Technol. Lett.* 18, 1152 (2006).
51 Z. H. Feng, Y. D. Qi, Z. D. Lu and K. M. Lau, 'GaN-based blue light-emitting diodes grown and fabricated on patterned sapphire substrates by metalorganic vapor-phase epitaxy,' *J. Cryst. Growth* 272, 327 (2004).
52 K. Kusakabe, A. Kikuchi and K. Kishino, 'Characterization of overgrown GaN layers on nano-columns grown by rf-molecular beam epitaxy,' *Jpn. J. Appl. Phys., Part 2* 40, L192 (2001).
53 K. Ueda, Y. Tsuchida, N. Hagura, F. Iskandar, K. Okuyama, *et al.*, 'High performance of GaN thin films grown on sapphire substrates coated with a silica-submicron-sphere monolayer film,' *Appl. Phys. Lett.* 92, 101101 (2008).
54 H.-W. Huang, J.-K. Huang, S.-Y. Kuo, K.-Y. Lee and H.-C. Kuo, 'High extraction efficiency GaN-based light-emitting diodes on embedded SiO_2 nanorod array and nanoscale patterned sapphire substrate,' *Appl. Phys. Lett.* 96, 263115 (2010).
55 Z. S. Zhang, B. Zhang, J. Xu, K. Xu, Z. J. Yang, *et al.*, 'Effects of symmetry of GaN-based two-dimensional photonic crystal with quasicrystal lattices on enhancement of surface light extraction,' *Appl. Phys. Lett.* 88, 171103 (2006).
56 J. J. Chen, Y. K. Su, C. L. Lin, S. M. Chen, W. L. Li, *et al.*, 'Enhanced output power of GaN-based LEDs with nano-patterned sapphire substrates,' *IEEE Photonics Technol. Lett.* 20, 1193 (2008).
57 M. H. Lo, Y. J. Cheng, H. C. Kuo and S. C. Wang, 'Enhanced electron-hole plasma stimulated emission in optically pumped gallium nitride nanopillars,' *Appl. Phys. Lett.* 98, 121101 (2011).
58 P. Frajtag, J. P. Samberg, N. A. El-Masry, N. Nepal and S. M. Bedair, 'Embedded voids formation by overgrowth on GaN nanowires for high-quality GaN films,' *J. Cryst. Growth* 322, 27 (2011).

59 P. Puech, F. Demangeot, J. Frandon, C. Pinquier, M. Kuball, *et al.*, 'GaN nanoindentation: a micro-Raman spectroscopy study of local strain fields,' *J. Appl. Phys.* 96, 2853 (2004).

60 M. A. Tsai, Y. Peichen, C. H. Chiu, H. C. Kuo, T. C. Lu, *et al.*, 'Efficiency enhancement and beam shaping of GaN–InGaN vertical-injection light-emitting diodes via high-aspect-ratio nanorod arrays,' *IEEE Photon. Technol. Lett.* 21, 257 (2009).

61 H. S. Chen, D. M. Yeh, Y. C. Lu, C. Y. Chen, C. F. Huang, *et al.*, 'Strain relaxation and quantum confinement in InGaN/GaN nanoposts,' *Nanotechnol.* 17, 5, 1454 (2006).

62 C. H. Chiu, T. C. Lu, H. W. Huang, C. F. Lai, C. C. Kao, *et al.*, 'Fabrication of InGaN/GaN nanorod light-emitting diodes with self-assembled Ni metal islands,' *Nanotechnol.* 18, 44, 445201 (2007).

63 H. W. Huang, C. C. Kao, T. H. Hsueh, C. C. Yu, C. F. Lin, *et al.*, 'Fabrication of GaN-based nanorod light emitting diodes using self-assemble nickel nano-mask and inductively coupled plasma reactive ion etching,' *Mater. Sci. Eng. B* 113, 2, 125 (2004).

64 T. Kouno, K. Kishino, K. Yamano and A. Kikuch, 'Two-dimensional light confinement in periodic InGaN/GaN nanocolumn arrays and optically pumped blue stimulated emission,' *Opt. Expr.* 17, 22, 0440 (2009).

65 K. Y. Zang, Y. D. Wang, H. F. Liu and S. J. Chua, 'Structural and optical properties of InGaN/GaN multiple quantum wells grown on nano-air-bridged GaN template,' *Appl. Phys. Lett.* 89, 17, 171921 (2006).

66 A. Kikuchi, M. Kawai, M. Tada and K. Kishino, 'InGaN/GaN multiple quantum disk nanocolumn light-emitting diodes grown on (111) Si substrate,' *Jpn. J. Appl. Phys.* 43, 12A, L1524 (2004).

67 A. Kikuchi, M. Tada, K. Miwa and K. Kishino, 'Growth and characterization of InGaN/GaN nanocolumn LED,' *Proc. Int. Soc. Opt. Eng. (SPIE)* 6129, 36 (2006).

68 *FullWAVE 6.1*, RSoft Design Group Inc, Ossining, NY, 2008.

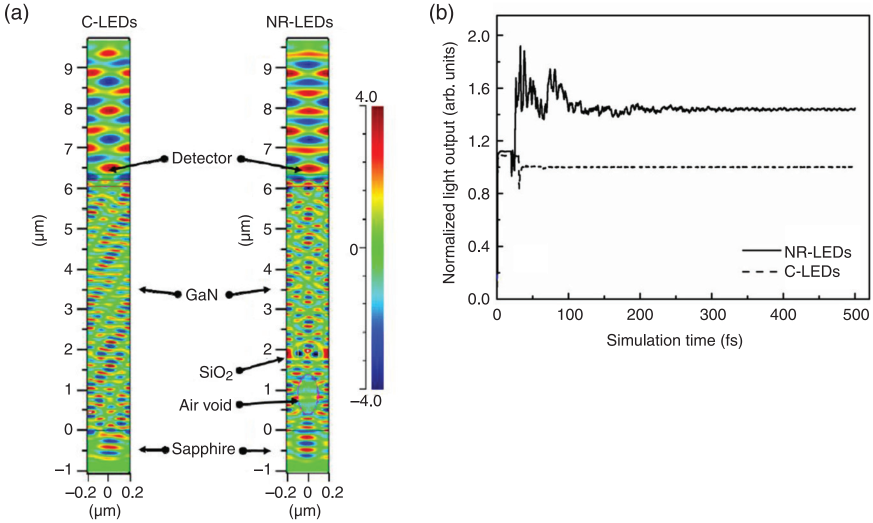

Plate VI (Chapter 7) (a) 3D FDTD of the calculated electric-field distribution for NR-LEDs and C-LEDs. (b) Normalized light output power as a function of the simulation time for C-LEDs and NR-LEDs.[26]

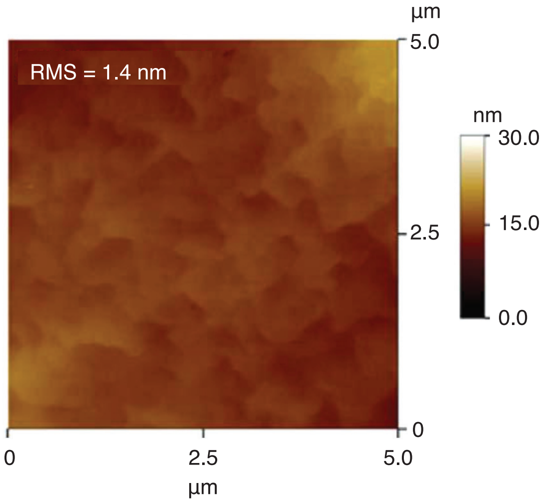
µm
5.0
2.5
0
RMS = 1.4 nm
nm
30.0
15.0
0.0
0
2.5
5.0
µm

Plate VII (Chapter 7) Surface morphology of overgrown GaN NP template as scanned by AFM.[15]

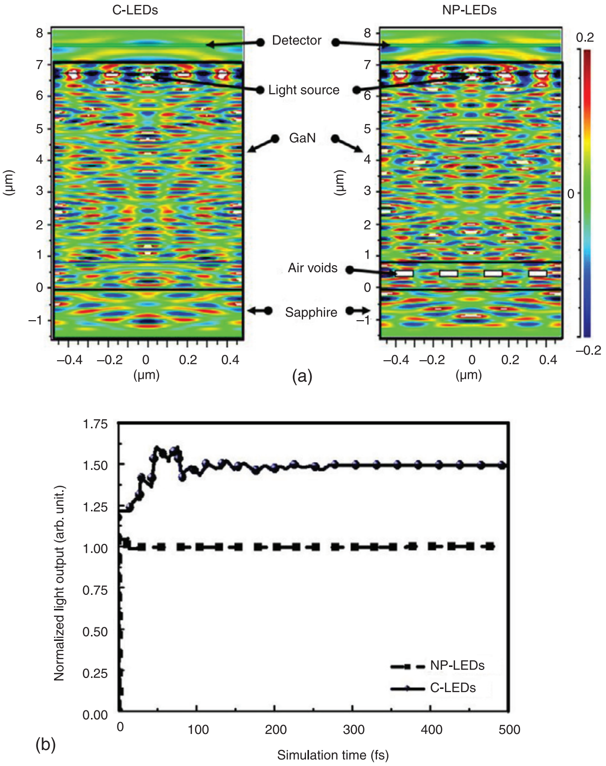

Plate VIII (Chapter 7) (a) 2D FDTD of the calculated electric-field distribution for NP-LEDs and C-LEDs. (b) Normalized light output power as a function of the simulation time for C-LEDs and NP-LEDs.[15]

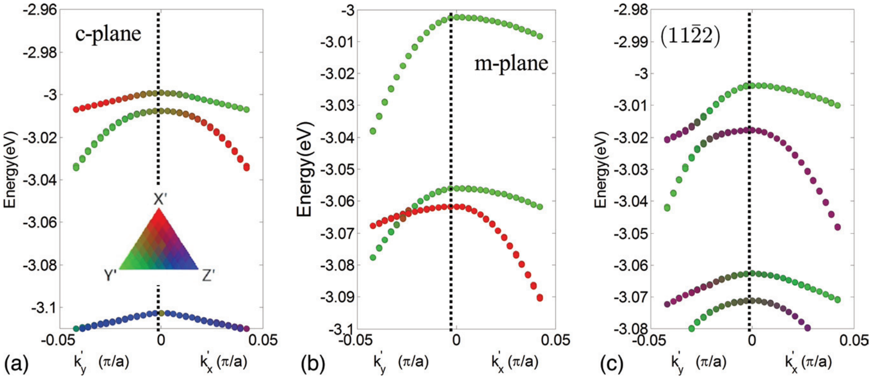

Plate IX (Chapter 8) Calculated valence E-k diagrams for (a) the c-plane, (b) the m-plane and (c) the semipolar plane (11$\bar{2}$2) $In_{0.2}Ga_{0.8}N$ QWs. The zero potential is referred to the conduction band of GaN. The bandgap of $In_{0.2}Ga_{0.8}N$ is about 2.72 eV.

8

Nonpolar and semipolar LEDs

Y.-R. WU, National Taiwan University, Taiwan, C.-Y. HUANG, TSMC Solid State Lighting, Ltd, Taiwan, and Y. ZHAO and J. S. SPECK, University of California, Santa Barbara, USA

DOI: 10.1533/9780857099303.1.250

Abstract: A polarization-induced electric field fundamentally limits nitride-based LEDs grown on the c-plane. Nonpolar and semipolar LEDs have potential for superior performance through high internal quantum efficiency over a wide spectral region and low efficiency droop due to improved carrier transport and high compositional homogeneity. Nonpolar and semipolar LEDs possess unique electroluminescent characteristics such as polarized light emission and reduced wavelength shift due to the lift of degeneracy in the conduction band and mitigated quantum-confined Stark effect. In epitaxial growth, the surface morphology and defect generation mechanism on nonpolar and semipolar planes differ from those on the c-plane due to the anisotropic surface geometry and tilted slip systems. LED chips are designed to enhance the light extraction efficiency of nonpolar and semipolar LEDs grown on free-standing GaN substrates.

Key words: nonpolar, semipolar, LED, nitride, GaN, InGaN, AlGaN, QCSE, droop, carrier transport, MOCVD, epitaxy.

8.1 Motivation: limitations of conventional c-plane LEDs

8.1.1 Quantum-confined Stark effect (QCSE)

In the 1990s, breakthroughs in GaN epitaxial growth techniques[1–3] and p-type GaN activation[4–5] led to the development of violet and blue light-emitting diodes (LEDs). High-quality nitride materials were grown with a GaN buffer layer on c-plane sapphire substrates along the [0001] direction of wurtzite unit cells, i.e., on the gallium polar (0001) surface.[2–3] In 1994, Nakamura *et al*. produced the first candela-class blue LED with a zinc-doped InGaN/AlGaN active region.[6] Today, high-brightness LEDs with efficacy greater than 100 lm/W are commercially available.

However, due to the absence of inversion symmetry in the wurtzite crystal structure, nitride-based materials are piezoelectric.[7–9] The biaxial plane stress in (0001) InGaN quantum wells (QWs) results in internal electrical fields along the c-axis. The discontinuity of polarization between a QW and the barrier results in a sheet charge in the interfaces. In the band profile for (0001)-oriented

GaN/InGaN (QW)/GaN, the polarization-induced charge separation results in a triangle-shaped potential profile, resulting in a reduced energy separation between the eigenstates in the conduction band and valence band. Therefore, the internal electric field causes a built-in red shift of the emission wavelengths in c-plane LEDs. With increasing injection current, the sheet charges at the QW/barrier interfaces are screened by injected carriers, which flattens the QWs' potential profile.[10, 11] As a result, conventional c-plane LEDs suffer from a blueshift of the emission wavelengths with increasing injection current. This wavelength shift with applied bias in a confined heterostructure is known as the quantum-confined Stark effect (QCSE).

Due to the triangular QW potential profile, the electron and hole wave functions in the QWs are spatially separated, which reduces the radiative recombination rate and in turn likely reduces the internal quantum efficiency (IQE). Therefore, to maintain a decent wave function overlap and IQE, the QW thickness in conventional c-plane LEDs is usually between 2–3 nm. However, thin QWs are regarded as one of the major causes of carrier transport and droop issues of LEDs under a high injection current.

8.1.2 The green gap

In the AlGaInP system, high IQE LED can be realized for the red spectral region ($\lambda = 630$–650 nm). However, the peak IQE is significantly lower in the yellow-green spectral region due to the direct-indirect bandgap transition. InGaN materials have a direct bandgap all over the visible spectral region. InGaN/GaN-based blue LEDs ($\lambda = 440$–460 nm) with high IQE have been demonstrated and are commercially available.[12] However, the efficiency of nitride-based LEDs also drops significantly toward the green spectral region. The low efficiency of green to yellow LEDs, whatever the material system, is known as the 'green gap' in the LED community.[13]

The low efficiency of nitride-based LEDs is attributed to two major causes: difficulties in epitaxial growth and strong QCSE. The lattice mismatch between InN and GaN is around 10%. To increase an LED's emission wavelengths, the indium content in the QWs has to be increased. For emissions in the green spectral region, the indium content in the QW has to be around 30%, which gives a ~3% lattice mismatch between the QW and the unstrained GaN underlayer. With high strain in the active regions, the strain energy is prone to being relaxed by the generation of new defects, such as pits, dislocations and stacking faults. Therefore, the epitaxial growth of nitride-based LEDs with high indium content is an area of significant interest.

Furthermore, QCSE also limits the performance of LEDs in the green spectral region. Since the polarization discontinuity between InGaN and GaN is proportional to the lattice mismatch strain, c-plane LEDs with a higher indium content in the QWs suffer more from QCSE. Therefore, green LEDs have a stronger wavelength shift and lower IQE compared to blue LEDs. The challenges in epitaxial growth might be dealt with by strain management[14] and further optimization of growth conditions.[15–18] However, the limitation due to QCSE originates from the nature of the materials, which is difficult to solve or alleviate by engineering. Hence, there is significant motivation for growing devices along crystal orientations with no or reduced internal polarization, to give further improvements in device performance in the green gap.

8.1.3 Carrier transport problems in multiple-quantum-well (MQW) LEDs

As mentioned above, the QW thickness of c-plane LEDs is kept thin to maintain a decent IQE. Therefore, increasing the number of QWs is a common method for increasing the total active volume. However, the achievable effective active volume of multiple-quantum-well (MQW) LEDs is limited by carrier transport between QWs. Electrons traveling in the conduction band have a smaller effective mass and higher mobility than holes in the valence band, resulting in an unbalanced carrier distribution among the QWs.[18–22]

For InGaN/GaN QWs, the band offset in the conduction band ΔE_c is higher than that in the valence band ΔE_v ($\Delta E_c = 0.6–0.7\Delta E_g$, where ΔE_g is the full bandgap difference). Thus, the electrons should have a higher barrier for escaping the QW by thermionic emission. However, experimental data show that hole transport is the major limiting factor in c-plane MQW LEDs.[23,24] Highly p-doped AlGaN layers are grown as electron-blocking layers (EBLs) above the active region to alleviate electron leakage problems.[25,26] Schubert attributed the electron leakage problem to the short dwell time of electrons after being injected into the QW.[27] The deep conduction offset and small effective mass give a high initial velocity to electrons injected into QWs. In a thin QW, the injected electrons have a high probability of coherently traveling through the QW without being captured by phonon relaxation. Sizov *et al.* proposed that ballistic transport is the dominant transport mechanism in long wavelength LEDs and laser diodes (LDs) instead of the commonly used drift-diffusion transport models.[28] Both of the above studies suggested that the polarization-related electric fields in QWs favor ballistic transport. The sheet charge on the QW/barrier interface accelerates the injected electrons and significantly reduces their dwell time. For holes injected into the QW, the initial velocity is much lower because of the smaller offset in the conduction band and their large effective mass. The probability of a hole experiencing ballistic transport through a QW is much lower. For those holes escaping from a QW via thermionic emission or via interacting with phonons, the strong polarization-related electric fields in the barrier forbid hole injection between adjacent QWs, causing most injected holes to populate the QWs that are nearest to the p-side.

Many barrier structures have been proposed to improve the hole injection efficiency in c-plane MQW LEDs, for example, the magnesium-doped barrier,[29,30] InGaN barrier,[31,32] compositionally graded InGaN barriers,[33,34] etc. However, introducing magnesium into the barrier causes magnesium to diffuse into the QWs and lowers the IQE of the devices, while using InGaN as a barrier causes strain management issues. Since nonpolar and semipolar LEDs have no or reduced polarization-induced electric fields, the hole injection efficiencies are improved compared to c-plane LEDs.[28,35]

8.1.4 Efficiency droop

Although LEDs with a high peak IQE under a low injection current are commercially available, their efficiency drops quickly with increasing current injection. The phenomenon of IQE deterioration with increasing injection current density is known as ‘droop’. To increase the total radiation flux of commercial LED bulbs, the total chip area was increased instead of driving up the current density. Therefore, the efficiency was retained though with increased fabrication costs. Hence, overcoming droop in LEDs for general illumination became a major focus of research .

To date, the physical origin of droop is still inconclusive. Some droop mechanisms have been proposed with potential solutions. Lumileds suggested that Auger recombination is the major cause of efficiency droop.[36,37] Auger recombination is a nonradiative recombination process in which the rate is proportional to the cube of the carrier density n ($\sim n^3$) in the materials. Lumileds observed an efficiency droop in the photoluminescence (PL) of an InGaN layer with increasing excitation power. The experiment was done under zero bias to exclude the effects of carrier dynamics in the active region. They concluded that droop is an inherent property in materials regardless of the design of a device. Kioupakis *et al.* from UCSB supported this conclusion with a first principles calculation of the Auger recombination coefficient (C) in InGaN.[38] It was argued that the phonon-assisted hole-hole-electron (h-h-e or $C_{p'}$ phonon) Auger recombination process dominates under a high carrier density especially for long wavelength emitters. The solution proposed by Lumileds’ theory was to use a thick InGaN QW to reduce the carrier density in the active region.[39] Li *et al.* at the National Taiwan University observed that the peak efficiency of c-plane LEDs was pushed from 10 A/cm^2 to 200 A/cm^2 by increasing the QW thickness from 2.5 nm to 13 nm, which is in agreement with Lumileds’ argument.[40]

However, researchers at Rensselaer Polytechnic Institute have an alternative view on the origin of droop. Instead of Auger recombination, they suggested that electron leakage under a high injection current is the dominant factor for efficiency droop.[41] It was proposed that the electrons are swept through the active region due to their small effective mass and the existence of a sheet carrier at QW/barrier interfaces. Those electrons that are not captured by QWs eventually vanish outside the active region, resulting in the low efficiency under high injection. In this point of view, droop can be alleviated by designing epilayer structures to balance the electron and hole transport in the active region. Samsung used a quaternary (Al, In, Ga)N alloy as barriers to match the polarization between barriers and QWs.[42] Using a quaternary alloy provides another degree of freedom when designing the polarization and bandgap of nitride materials. With the same polarization in the barriers and QWs, the sheet charge at the interface can be eliminated. Researchers at Virginia Commonwealth University designed QWs with a stepped potential to mitigate the effects of hot electrons. They observed an improvement in droop performance.[26,43] Wang *et al.* from National Chiao-Tung University used a graded InGaN barrier in MQW c-plane LEDs to improve hole transport. Droop is improved when there is a more uniform carrier distribution among the QWs.[33] Most recently studies using atom probe tomography (APT)[154] show that fluctuations in indium composition in a QW might be the reason for spectrum broadening. Later numerical studies that included indium alloy fluctuations[154] showed that the alloy fluctuation causes a carrier to become localized in the QW, which will increase the peak IQE. However, the much higher local carrier density will enhance Auger recombination. At the same time, the smaller active volume will also increase the chances of an overflow. The unstable alloy fluctuation in a QW also explains the variation in device characterization.

8.1.5 Advantages of nonpolar and semipolar LEDs

The QCSE imposes a limit on device performance for c-plane LEDs. To circumvent the detrimental effects of the internal polarization, growing devices along orientations that have zero or minimal polarization has been proposed as the solution for many unsolved issues. When there are no polarization-induced electric fields in the QW, the IQE is enhanced and there is an improved overlap between carrier wave functions. The QWs can be grown thicker without much reduction of the IQE as long as the defect density is not significantly increased. Therefore, the unbalanced carrier transport in MQW devices resulting from the over-thin QWs can be mitigated. Additionally, lower polarization reduces the energy barrier for hole injection into MQW devices. Kawaguchi *et al.* observed superior hole injection efficiency in semipolar MQW LEDs in dichromatic LED experiments with a simple GaN barrier structure.[35] Recently, improved droop was observed in nonpolar and semipolar LEDs with similar QW/barrier structures in c-plane LEDs.[44–46] Pan *et al.* from UCSB produced semipolar $(20\bar{2}\bar{1})$ single-quantum-well blue LEDs with a uniform planar emission and low droop.[46] Further theoretical calculations and experimental data for nonpolar and semipolar LEDs will be presented in other sections of this chapter.

8.2 Introduction to selected nonpolar and semipolar planes

8.2.1 Crystallography of wurtzite nitride

The Miller indices of nonpolar and semipolar planes are $(hk\bar{i}l)$ or (hkl), where $i=h+k$ and either h or k has a nonzero value, for example, $(10\bar{1}0)$ and $(11\bar{2}2)$. The plane of hkl is perpendicular to the vector (h, k, l) in the reciprocal lattice of wurtzite nitride. ϑ is defined as the angle between the surface normal vectors of the (0001) plane and an arbitrary $(hk\bar{i}l)$ plane and is given as:

$$\theta = \arccos\left(\frac{\sqrt{3}al}{\sqrt{4c^2(h^2+k^2+hk)+3a^2l^2}}\right) \tag{8.1}$$

Planes with $l=0$ are called nonpolar planes and those with $h=k=0$ are polar planes or the c-plane. All other non-c-planes with a nonzero l are all called semipolar planes. Selected planes are schematically illustrated in Table 8.1 and Fig. 8.1.

8.2.2 Changes in piezoelectric polarization charge with orientation

GaN has a wurtzite structure (space group $P6_3mc$ and point group 6 mm) and as a result it is polar and piezoelectric. The polarization in the unstrained state is referred to as spontaneous polarization and additional polarization is referred to as piezoelectric polarization; the c-axis is the polar axis. For the c-plane, semipolar and nonpolar structures, a crystal can be rotated through angles θ and ϕ, which are the angles of rotation from the z-axis (c-axis) to the x-axis and from the x-axis to the y-axis, respectively (Fig. 8.2).

In a semipolar or nonpolar quantum well, the crystal growth direction is different from the traditional c-axis. If an InGaN quantum well is grown in a different

Table 8.1 Selected wurtzite crystal planes

Plane	θ	Polarity
$(10\bar{1}3)$	32°	Semipolar
$(10\bar{1}2)$/r-plane	43°	Semipolar
$(11\bar{2}2)$	58°	Semipolar
$(10\bar{1}1)$	62°	Semipolar
$(20\bar{2}1)$	75°	Semipolar
$(11\bar{2}0)$/a-plane	90°	Nonpolar
$(10\bar{1}0)$/m-plane	90°	Nonpolar
$(20\bar{2}\bar{1})$	105°	Semipolar

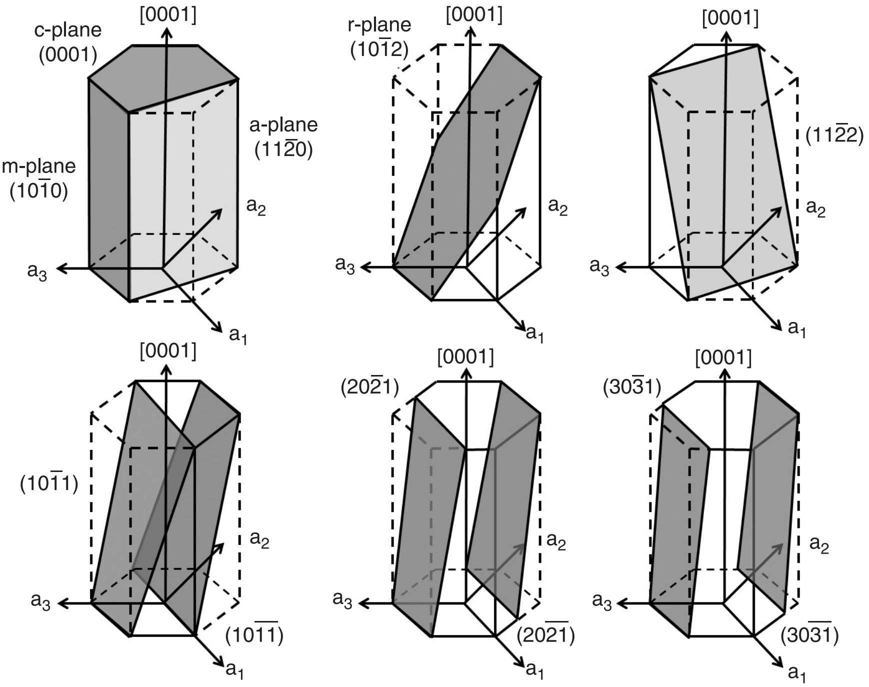
[0001]
c-plane
(0001)
a-plane
(11$\bar{2}$0)
m-plane
(10$\bar{1}$0)
a$_2$
a$_3$
a$_1$
r-plane
(10$\bar{1}$2)
(11$\bar{2}$2)
(10$\bar{1}$1)
(10$\bar{1}\bar{1}$)
(20$\bar{2}$1)
(20$\bar{2}\bar{1}$)
(30$\bar{3}$1)
(30$\bar{3}\bar{1}$)

8.1 Polar, nonpolar and semipolar planes in wurtzite crystal structures.

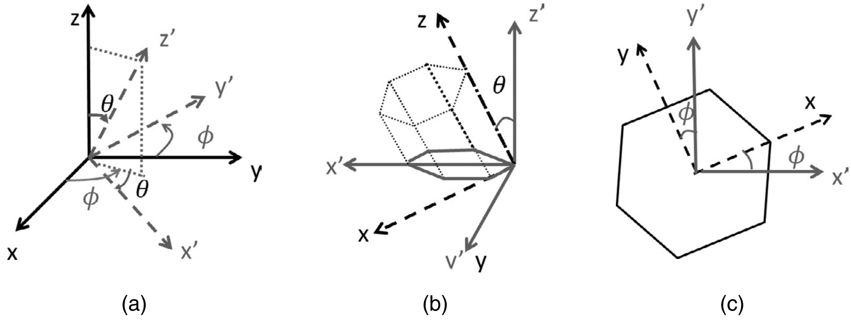
z
z′
y′
y
x
x′
θ
ϕ
(a)
(b)
(c)

8.2 New and old coordinates.

direction, the lateral strain and vertical strain are in the new growth direction. But all equations use the old coordinate system. Therefore, we need to rotate the coordinates back to the regular plane to get the strain components. The relation between the new coordinates and the old coordinates is defined by the equations:

$$P_{x'} = U_{x'x}P_x + U_{x'y}P_y + U_{x'z}P_z$$

$$P_{y'} = U_{y'x}P_x + U_{y'y}P_y + U_{y'z}P_z$$

$$P_{z'} = U_{z'x}P_x + U_{z'y}P_y + U_{z'z}P_z$$

P_x, P_y and P_z are some physical property, such as strain or the elastic tensor. $U_{x'x}$ is the cosine of the angle between the x' and x axes. U_{xz} is the cosine of the angle between x' and z axes. Note that $U_{x'z} \neq U_{z'x}$. If we rotate the coordinates by θ and φ, we can derive U as:

$$\mathrm{U} = \begin{pmatrix} \cos\theta\cos\varphi & \cos\theta\sin\varphi & -\sin\theta \\ -\sin\varphi & \cos\varphi & 0 \\ \sin\theta\cos\varphi & \sin\theta\sin\varphi & \cos\theta \end{pmatrix}. \qquad [8.2]$$

We rotate the crystal growth axis (defined as the z'-axis) from the (x, y, z) coordinates to the (x', y', z') coordinates. The relations between the wave vectors, strain tensors and elastic stiffness constants in the original coordinate system and the rotated coordinate system are:

$$\mathrm{k}'_\mathrm{i} = \sum_\alpha \mathrm{U}_{\mathrm{i}\alpha}\mathrm{k}_\alpha,$$

$$\varepsilon_\mathrm{ij} = \textstyle\sum_{\alpha\beta} \mathrm{U}_{\mathrm{i}\alpha}\mathrm{U}_{\mathrm{j}\beta}\varepsilon_{\alpha\beta},$$

$$\mathrm{C}'_\mathrm{ijkl} = \textstyle\sum_{\alpha\beta\gamma\delta} \mathrm{U}_{\mathrm{i}\alpha}\mathrm{U}_{\mathrm{j}\beta}\mathrm{U}_{\mathrm{k}\gamma}\mathrm{U}_{\mathrm{l}\delta}\mathrm{C}_{\alpha\beta\gamma\delta}. \qquad [8.3]$$

From Eq. 8.3 we can obtain the rotated elastic stiffness constants, which are defined through Hooke's law. The parameters for the elastic stiffness constants we used are also listed in Huang and Wu.[47]

According to Romanov *et al.*,[48] the lateral strain of a rotated semipolar plane InGaN layer grown on a GaN substrate is:

$$\epsilon_{\mathrm{m1}} = \frac{\mathrm{a_S} - \mathrm{a_L}}{\mathrm{a_L}} = \epsilon_{\mathrm{y'y'}} \qquad [8.4]$$

$$\epsilon_{\mathrm{m2}} = \frac{\mathrm{a_S c_S} - \sqrt{((\mathrm{a_L c_S})^2\ \cos^2\theta + (a_S c_L)^2\ \sin^2\theta)}}{\sqrt{((a_L c_S)^2\ \cos^2\theta + (a_T c_L)^2\ \sin^2\theta}} = \epsilon_{x'x'} \qquad [8.5]$$

where ($\mathrm{c_S}$, $\mathrm{a_S}$) and ($\mathrm{c_L}$, $\mathrm{a_L}$) are the lattice constants for the substrate and InGaN layer, respectively. θ is the rotation angle from the z-axis to the x-axis. The strain in the original coordinates can be obtained using the rotation matrix U as shown in Eq. 8.3. To calculate the piezoelectric polarization $\mathrm{P^{pz}}$, we use:

$$P^{pz} = \begin{pmatrix} 0 & 0 & 0 & 0 & e_{15} & 0 \\ 0 & 0 & 0 & e_{15} & 0 & 0 \\ e_{31} & e_{31} & e_{33} & 0 & 0 & 0 \end{pmatrix} \begin{pmatrix} \epsilon_{xx} \\ \epsilon_{yy} \\ \epsilon_{zz} \\ \epsilon_{yz} \\ \epsilon_{zx} \\ \epsilon_{xy} \end{pmatrix} = \begin{pmatrix} e_{15}\epsilon_{xz} \\ e_{15}\epsilon_{yz} \\ e_{31}\left(\epsilon_{xx} + \epsilon_{yy}\right) + e_{33}\epsilon_{zz} \end{pmatrix}, \qquad [8.6]$$

where e_{ij} is the piezoelectric tensor in Voigt notation.[48] When the plane is rotated to the nonpolar or the semipolar plane, the strength of polarization changes as well. According to Romanov *et al.*,[48] the polarization strength of an InGaN semipolar quantum well becomes:

$$\Delta P'_z = P^{pz}_{Lz'} + (P^{sp}_L - P^{sp}_S) \cos \theta \qquad [8.7]$$

where P^{sp}_L and P^{sp}_T are the spontaneous polarizations for the layer and the substrate, respectively. $P^{sp}_{Lz'}$ can be calculated from:

$$P^{sp}_{Lz'} = P^{sp} \cos\theta.$$

With some mathematical algebra,[48] the strain-induced piezoelectric polarization, $P^{pz}_{Lz'}$, can be expressed as:

$$\begin{aligned} P^{pz}_{L_{z'}} &= e_{31} \cos \theta \epsilon_{x'x'} + \left(e_{31} \cos^3 \theta + \frac{e_{33} - e_{15}}{2} \sin \theta \sin 2\theta \right) \epsilon_{y'y'} \\ &+ \left(\frac{(e_{31} + e_{15})}{2} \sin \theta \sin 2\theta + e_{33} \cos^3\theta \right) \epsilon_{z'z'} \\ &+ [(e_{31} - e_{33}) \cos \theta \sin 2\theta + e_{15} \sin \theta \cos 2\theta] \epsilon_{z'z'}. \end{aligned} \qquad [8.8]$$

The simplified polarization strength of an InGaN quantum well under a c-plane grown on a GaN substrate can be found in Kawaguchi *et al.*:[35]

$$P^{pz}_{InGaN-GaN}(x) = [0.148x - 0.0424x(1-x)] \text{C m}^{-2}$$

The polarization strength for different rotation angles can be plotted as shown in Fig. 8.3.

8.2.3 Influence of polarization on band bending, QCSE and carrier transport

As mentioned in the previous section, the polarization strength will change as the growth plane is rotated. When θ is larger than 45°, the polarization direction will even become switched. This makes the transport behavior of electrons and holes relatively complicated. For a nonpolar plane, such as the m-plane or a-plane, the

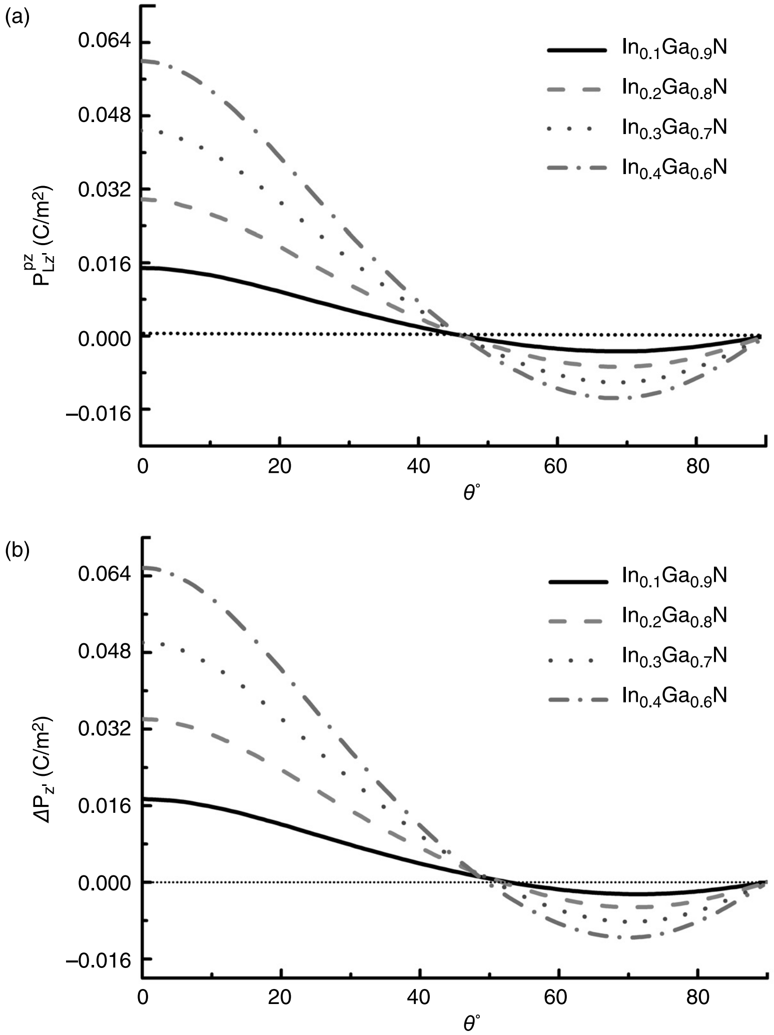

8.3 Calculated polarization charge density as a function of inclination angle for an InGaN quantum well.[48]

polarization strength is zero, and there are no polarization-related electric fields or polarization-related QCSE. For a rotation angle between 0° and 45°, the polarization direction is the same as for the c-plane with a gallium face but with a smaller electric field. When $\theta > 45°$, the band bending direction will change and this is similar to the nitrogen faces, which might significantly affect carrier transport. Figure 8.4 shows the band bending profile for the c-plane, the nonpolar m-plane, $(10\bar{1}3)$ and $(20\bar{2}1)$. As shown in Fig. 8.3, the nonpolar plane ($\theta = 90°$)

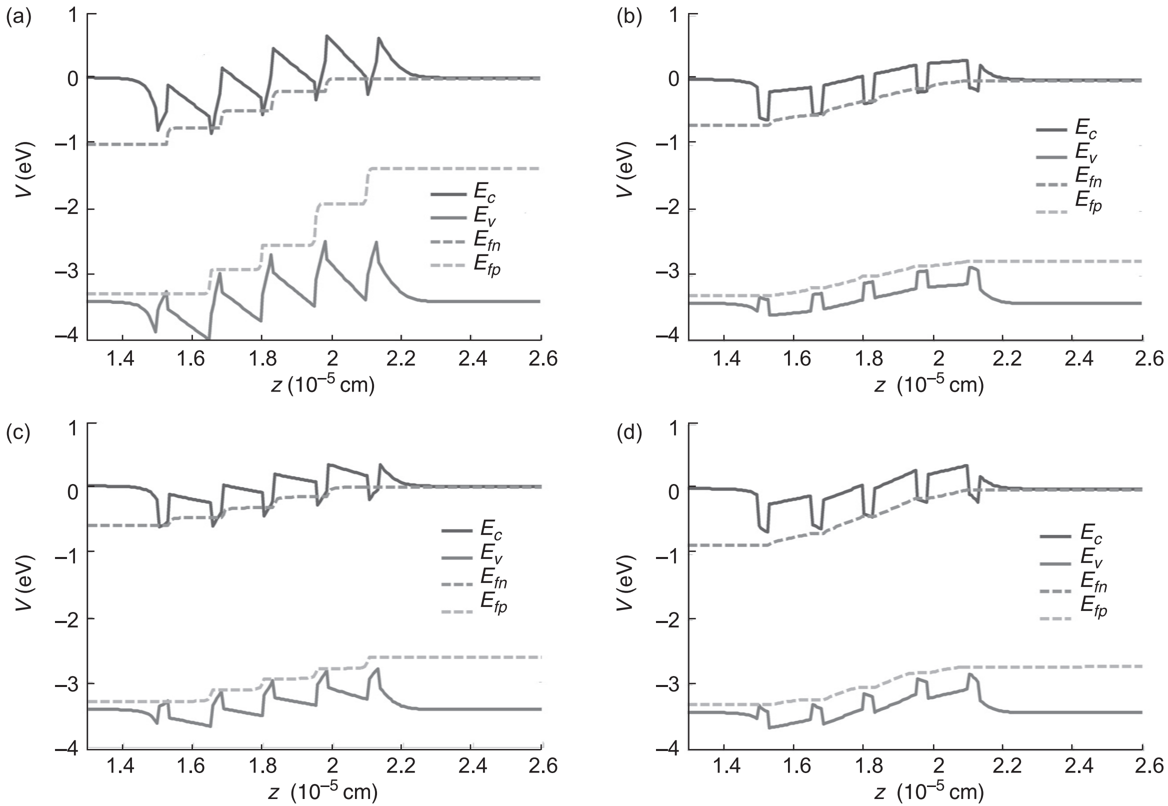

8.4 Calculated band profiles of InGaN MQWs for different growth orientations: (a) c-plane, (b) m-plane, (c) (10$\bar{1}$3), (d) (20$\bar{2}$1). E_c is the conduction band potential, E_v the valance band potential, E_{fn} the electron quasi-Fermi level and E_{fp} the hole quasi-Fermi level.

and the r-plane $(10\bar{1}2)$ ($\theta=45°$), where the polarization is close to zero, are like a normal QW. For the $(10\bar{1}3)$ plane, the polarization direction is close to that of the c-plane but with less band bending. For $(20\bar{2}1)$, the polarization has switched. This will cause an additional potential barrier when the carrier wants to escape from the first quantum well to the next quantum well, which has been observed experimentally by Kawaguchi *et al.*[35] The result showed that the direction of the polarization field will affect carrier transport significantly, especially for an MQW. The extra potential barrier caused by the polarization field in the case like a nitrogen face will increase the forward voltage of an LED significantly. Hence, the choice of semipolar plane will affect the power efficiency, which is a critical issue for energy applications.

8.2.4 Influence of anisotropic strain on E-k relaxation, band state mixing and optical polarization emission of light

To understand the light emission polarization of a semipolar quantum well system, we need to address the following issues: (1) the valence band state mixing, (2) the energy separation of the first valence band (CH1) and the second valence band (CH2) and (3) the effective mass ratio of the CH1 to CH2 bands, which will strongly affect the strength of the quantum confinement. The 6×6 $k\cdot p$ method can be used to calculate the influence of the valence band mixing and the strain. The 6×6 Hamiltonian can be expressed as:

$$H^{v}=\begin{array}{cc}\begin{pmatrix} F & 0 & -H^{*} & 0 & K^{*} & 0 \\ 0 & G & \Delta & -H^{*} & 0 & K^{*} \\ -H & \Delta & \lambda & 0 & I^{*} & 0 \\ 0 & -H & 0 & \lambda & \Delta & I^{*} \\ K & 0 & I & \Delta & G & 0 \\ 0 & K & 0 & I & 0 & F \end{pmatrix} & \begin{array}{c} |u_1\rangle \\ |u_2\rangle \\ |u_3\rangle \\ |u_4\rangle \\ |u_5\rangle \\ |u\rangle \end{array}\end{array} \qquad [8.9]$$

where

$$\mathrm{F}=\Delta_1+\Delta_2+\lambda+\theta$$

$$\mathrm{G}=\Delta_1-\Delta_2+\lambda+\theta$$

$$\lambda=\left(\frac{\hbar^2}{2\mathrm{m}_0}\right)[\mathrm{A}_1\mathrm{k}_z^2+\mathrm{A}_2(\mathrm{k}_x^2+\mathrm{k}_y^2)]+\mathrm{D}_1\epsilon_{zz}+\mathrm{D}_2(\epsilon_{xx}+\epsilon_{yy})$$

$$\theta=\frac{\hbar^2}{2\mathrm{m}_0}[\mathrm{A}_3\mathrm{k}_z^2+\mathrm{A}_4(\mathrm{k}_x^2+\mathrm{k}_y^2)]+\mathrm{D}_3\epsilon_{zz}+\mathrm{D}_4(\epsilon_{xx}+\epsilon_{yy})$$

$$K = \frac{\hbar^2}{2m_0} A_5 (k_x + ik_y)^2 + D_5(\epsilon_{xx} - \epsilon_{yy} + 2i\epsilon_{xy})$$

$$H = \frac{\hbar^2}{2m_0}\ i\,[A_6 k_z (k_x + ik_y) + A_7 (k_x + ik_y)] + i\,D_6(\epsilon_{xz} + i\epsilon_{yz})$$

$$I = \frac{\hbar^2}{2m_0}\ i\,[A_6 k_z (k_x + ik_y) - A_7 (k_x + ik_y)] + i\,D_6(\epsilon_{xz} + i\epsilon_{yz})$$

$$\Delta = \sqrt{2}\Delta_3$$

D_1 to D_6 are the deformation potentials and A_1 and A_7 are the fitting parameters to the valence band structure. k_i and ϵ_{ij} (i, j = x, y, z) are the wave vector and the strain tensor. Δ_1 is the crystal-field energy. Δ_2 and Δ_3 are the spin-orbit energy parameters. The parameters can be found in Huang and Wu.[47]

For the Hamiltonian of the crystal growth orientation z'-axis, $k_{z'}$ will be transformed into the differential forms $-i\partial/\partial z'$. The bases of the Hamiltonian $|u_1\rangle$ to $|u_6\rangle$ are $\frac{1}{\sqrt{2}}|X + iY, \uparrow\rangle, \frac{1}{\sqrt{2}}|X + iY, \downarrow\rangle, |Z\uparrow\rangle, |Z, \downarrow\rangle \frac{1}{\sqrt{2}}|X - iY, \uparrow\rangle$, and $\frac{1}{\sqrt{2}}|X - iY, \downarrow\rangle$. The polarization of the emission light is strongly affected by these bases.

Plate IX (see colour section between pages 330 and 331) shows the valence band E-k diagrams of an InGaN quantum well for the c-plane, the m-plane and the semipolar $(11\bar{2}2)$ plane. Red, green and blue represent the states of $|X'\rangle$, $|Y'\rangle$ and $|Z'\rangle$. If a state is mixed, it will have a mixed color as shown in the triangle in Plate IX(a).

In a c-plane InGaN/GaN strained QW, the basis of the valence band is mainly dominated by the $|X \pm iY\rangle$ states. Therefore, for the interband transition, the emitting strength for different polarized light is mainly given by the momentum matrix element:

$$|\langle f_e(z)\,|\,f_h(z)\rangle\,|\,\langle s|\Big|_a \cdot (-i\hbar\vec{\nabla})\Big|X \pm iY\rangle\,|^2, \qquad [8.10]$$

where $\langle f_e(z)|f_h(z)\rangle$ denotes the overlap between the z-dependent envelope function of the conduction and valence bands, which determines the dipole strength. â is the polarization of the generated light or the incident light. Since the bases are mainly dominated by the $|X\rangle$-like and $|Y\rangle$-like states for the c-plane case, the radiating dipoles are oriented along the plane of the QW. For a nonpolar plane, such as an m-plane quantum well (grown along the y direction), the $|X\rangle$-like (X') (defined as the a-axis here) state will become the first subband due to the anisotropy. The $|Z\rangle$-like (Y') state will become the second or even third subband and the $|Y\rangle$-like (Z') state will be the final one due to the anisotropic strain and quantum-confined effect. Therefore, the radiating dipole will be oriented along the a-axis, which will be a linearly polarized light source along the plane of the QW. For the semipolar plane, the situation is relatively more complicated. From the literature,[47,50,51] due to the anisotropic strain and shear strain in the semipolar QW, the valence band will be mixed with $|X\rangle$-, $|Y\rangle$- and $|Z\rangle$-like states depending on the rotation angle and the strain (or indium composition). For example, for the $(11\bar{2}2)$ plane shown in Plate IX(c), which is rotated by ~58° with respect to the (0001) plane, the first subband is mainly dominated by $|Y'\rangle$-like states for a low indium composition (<30%). Note that here we use rotated coordinate x', y' and z' axis for ease of comparison. The second subband is mixed with $m|X'\rangle + n|Z'\rangle$ like states. However, as the indium composition increases, the $m|X'\rangle + n|Z'\rangle$ subband will rise to the first subband due to the increase of the anisotropic strain. Therefore, the out-of-plane polarization will be observed for the higher indium cases.[52] From Huang and Wu,[47] we know that if the indium composition is less than 20%, the emitting dipole is mainly oriented along the in-plane of the QW for most rotating angles. When the indium composition continues to increase, the out-of-plane dipole will rise, especially for the angles around 20° to 60°.

8.3 Challenges in nonpolar and semipolar epitaxial growth

8.3.1 Heteroepitaxy of nonpolar and semipolar planes

In the early stages when bulk GaN substrates were not available, researchers tried to grow nonpolar and semipolar GaN templates on foreign templates. As in c-plane GaN heteroepitaxy, sapphire and SiC substrates were chosen because of their acceptable lattice mismatch and availability. $(11\bar{2}0)$ plane GaN, i.e. a-plane GaN, has been grown on an r-plane sapphire substrate.[53–57] Although a-plane GaN on r-plane sapphire is cost effective, the template suffered from a high density of facetted surface pits,[47,49] basal plane stacking faults and associated terminating partial threading dislocations.[55] GaN templates grown on m-plane sapphire have been reported for various planes with different pretreatments, such as the $(10\bar{1}0)$, $(10\bar{1}\bar{3})$ and $(11\bar{2}2)$ planes.[58–61] To produce an m-plane GaN template, γ-$LiAlO_2$[62,63] and m-SiC[64–66] substrates are better candidates because of their smaller lattice mismatch. However, $LiAlO_2$ substrates are chemically unstable and large m-SiC substrates are still expensive – and, in any case, m-plane GaN on either substrate had high densities of basal plane stacking faults and partial threading dislocations. For semipolar GaN templates, a $(11\bar{2}2)$ GaN template has been reported on m-plane sapphire,[53,54,67,68] patterned r-plane sapphire[69,70] and patterned Si substrates[71]. $(10\bar{1}1)$ or $(10\bar{1}\bar{1})$ GaN templates have been reported on (100) $MgAl_2O_4$ spinel[72,73] and patterned (001) silicon substrates.[74] A $(20\bar{2}1)$ GaN template has been prepared on a patterned $(22\bar{4}3)$ sapphire substrate.[75]

However, the crystal quality of nonpolar and semipolar GaN heteroepitaxy is still unsatisfactory. There is a high density of extended effects such as basal plane stacking faults (BPSFs) and pits. Although the defect density can be significantly reduced by coalescence growth on a patterned substrate,[69,70,74,75] high-quality large-area (e.g., 2″) nonpolar and semipolar GaN templates are still unavailable. To date, there are still no materials that can be used as substrates for GaN heteroepitaxy in an arbitrary orientation.

8.3.2 Homoepitaxy and the need for bulk GaN substrates

Instead of overcoming all the challenges of nonpolar and semipolar heteroepitaxy, homoepitaxy on free-standing bulk GaN substrates is widely regarded as the ultimate solution for nonpolar and semipolar epitaxy. Strain-free homoepitaxy greatly reduces the challenges in metal organic chemical vapor deposition (MOCVD) growth with a lower defect density. Substrates with arbitrary orientation are also easily available by cutting and polishing the free-standing bulk GaN. Therefore, the availability of high-quality bulk GaN is the key issue in the development of nonpolar and semipolar devices.

Because nitride materials decompose before they melt under atmosphere pressure, conventional liquid-phase bulk crystal growth techniques used in silicon and conventional III-V arsenide and phosphide systems are nearly impossible for nitrides. Free-standing bulk GaN can be grown by hydride vapor-phase epitaxy (HVPE). The GaN is synthesized from gas-phase gallium chloride (GaCl) and ammonia (NH_3) on a heated foreign substrate such as sapphire or SiC under atmosphere pressure.[76] Free-standing GaN is then obtained by a subsequent lift-off process from the substrate.[77–79] Smooth surfaces are obtained after several lapping and polishing steps.

To fabricate bulk nonpolar and semipolar substrates, two approaches are possible: (1) directly grow GaN along a nonpolar or semipolar direction via HVPE[80–82] or (2) slice the bulk GaN grown along the c-direction to expose the desired nonpolar or semipolar surface.[83] Issues similar to those for nonpolar and semipolar heteroepitaxy by MOCVD have also been encountered in HVPE growth. The high extended defect density and limited selection of planes impose strong challenges on nonpolar and semipolar HVPE growth. In addition, HVPE GaN grown along the c-direction has much better crystal quality.[76, 83] High-quality substrates with an arbitrary surface can be obtained by cutting HVPE GaN grown along the c-direction.

The scalability of the HVPE technique is limited by undesired gas-phase parasitic reactions.[84] Alternatively, the ammonothermal method has attracted significant attention because of its high scalability for mass production. The ammonothermal method uses supercritical ammonia to dissolve poly-crystalline GaN with mineralizers (for example, KNH_2 and NH_4X) under high pressure and high temperature.[85–87] The supercritical ammonia carries the dissolved GaN to seeds, which are at a lower temperature. The dissolved GaN crystallizes onto the seeds because of the lower solubility. The ammonothermal method can be scaled up by simply increasing the autoclave size and the number of seeds. The challenges for the ammonothermal method come from the high pressure (>100 MPa) and corrosive environment. Safety issues would raise the cost, despite its potential for high scalability. Growing Bulk GaN with high quality and low cost is still under development.[88]

8.3.3 Indium incorporation in nonpolar and semipolar planes

The $In_xGa_{1-x}N$ alloy plays an important role in nitride-based optoelectronics because its bandgap spans from UV to IR. However, the growth of the InGaN alloy is generally regarded as difficult even on free-standing GaN. Besides the large lattice mismatch between InN and GaN, the volatile indium adatoms impose challenges on InGaN epitaxial growth. To attain a high indium composition in MOCVD growth, the temperature has to be low to reduce indium desorption. However, poor adatom diffusion at low temperatures causes difficulties in the growth of high-quality InGaN with a high indium composition. The incorporation of indium is influenced by growth conditions such as chamber pressure and growth rates, but mostly it is determined by the atomic configuration at the surface. Therefore, a plane surface that favors indium incorporation is highly desirable.

The incorporation of indium varies for the different surfaces in a wurtzite nitride structure. For example, the m-plane showed relatively low indium incorporation compared to semipolar planes.[89] A theoretical calculation attributed the low indium incorporation to repulsive interactions between indium adatoms.[90,91] Durnev *et al.* suggested that semipolar planes with a 60° inclination angle to the c-plane ($\vartheta \sim 60°$) have the highest indium incorporation due to the minimal strain effects, which is consistent with data from co-loaded growth experiments.[91] The $(11\bar{2}2)$ plane ($\vartheta \sim 58°$) had the highest incorporation of indium among various nonpolar and semipolar planes with θ ranging from 58° to 90°.[92] Besides the strain-induced repulsive effects, the surface polarity also has a strong influence on indium incorporation. Zhao *et al.* showed that the $(20\bar{2}\bar{1})$ surface has a higher indium incorporation than the $(20\bar{2}1)$ surface.[92] These two planes have the same strain scheme with reversed polarities. A similar phenomenon was also observed between gallium-polar and nitrogen-polar surfaces.[93] A first principles calculation suggested that a higher binding energy between indium and the nitrogen-polar surface reduces the probability of indium desorption on the surface.[94] Therefore, a surface with a nitrogen-polar surface component has higher indium incorporation.

High-efficiency green LEDs have been produced on the $(20\bar{2}1)$ and $(11\bar{2}2)$ planes.[95,96] The high quality of the InGaN QWs was attributed to the high indium incorporation on the these surfaces. However, green $(20\bar{2}\bar{1})$ LEDs have not yet been produced due to other challenges in MOCVD growth.

8.3.4 Morphology of nonpolar and semipolar epitaxy

The morphology of nonpolar and semipolar epitaxy varies because of the unique atomic structure near the surface. A rough surface morphology causes a deterioration in the quality of epilayers and limits device performance. For nonpolar planes, striated morphologies have been observed for (Al, In, Ga)N epitaxy.[97–100] Atomic force microscope images showed that the striations on the a-plane are along the c-axis and those on the m-plane are along the a-axis. A first principles calculation suggested that the anisotropic adatom diffusion causes striation morphologies along a direction with a lower diffusion kinetic barrier.[101] For semipolar planes, striated morphologies were seen to be similar to their vicinal nonpolar planes. For example, striations were parallel to the c-axis projection for $(11\bar{2}2)$ GaN epitaxy[100,102] and striations were also observed along the a-axis on $(20\bar{2}1)$ and $(20\bar{2}\bar{1})$ epilayers.[103,104]

Threading dislocations (TDs) also influence the surface morphology for nonpolar and semipolar epitaxy. TDs with a screw dislocation component enhance the spiral growth centered at the TDs. The spiral growth creates pyramidal hillocks several microns high on the surface.[100,105–108] Hillock morphologies cause a non-uniform growth rate and indium incorporation across the surface. Lin *et al.* observed non-uniform photoluminescence in an m-plane laser diode structure with hillock morphologies.[108] To suppress the spiral growth centered at the TDs, an intentional miscut was introduced onto nonpolar and semipolar substrates. The right miscut on a substrate enhances terrace growth by introducing free steps on the surface, which interrupt the spiral growth by an interaction with the terrace growth. With a 1° miscut toward the nitrogen-polar surface, a planar surface morphology was achieved on m-plane LEDs and LDs.[108,109]

8.3.5 Strain-induced defect generation in nonpolar and semipolar epitaxy

The large lattice misfit between InN and GaN causes the growth of QWs with a high indium content challenging. The misfit stresses in the QWs are likely to be reduced by extended defect generation. Basal plane stacking faults (BPSFs) are commonly observed in nonpolar and some semipolar green emitters.[89, 110] Wu *et al.* found that the BPSFs in m-plane InGaN QWs (indium ~ 26%) were bounded by a half loop of partial dislocations extending to the surface.[89] Similar defect structures were also found in $(20\bar{2}1)$ and $(20\bar{2}\bar{1})$ green QWs. Black triangles observed using a fluorescence microscope in semipolar green emitters were also expected to be related to the formation of BPSFs.[104,108] The radiative efficiency of long wavelength nonpolar and semipolar LEDs is therefore limited due to the high defect densities.

Beside the formation of BPSFs, strain relaxation also generates misfit dislocations (MDs) in semipolar and nonpolar epitaxy. MDs along the m-axis can be formed by a basal plane slip in semipolar $(11\bar{2}2)$ InGaN/GaN heteroepitaxy.[112–115] MDs along the a-direction have also been observed in $(20\bar{2}1)$ InGaN/GaN heteroepitaxy and were produced by a similar mechanism.[116] For the semipolar $(30\bar{3}1)$ plane and the m-plane, the relaxation is initiated through a prismatic m-plane slip instead of a basal plane slip due to the high shear stress.[114–116] The formation of MDs could introduce surface morphologies and facilitate the nucleation of new defects. Romanov *et al.* calculated the critical thicknesses for the formation of MDs in nonpolar and semipolar heteroepitaxy with the Matthew–Blakeslee equilibrium model.[120] The critical thickness calculation can be used a reference in epilayer structure design to avoid the generation of defects from strain relaxation.[118–120]

8.4 Light extraction for nonpolar and semipolar LEDs

8.4.1 Light extraction efficiency as a limiting factor

Despite the many advantages of nonpolar and semipolar LEDs (e.g., reduced polarization-related effect, higher optical gain, etc.),[121–128] the output power and efficiency of current semipolar and nonpolar LEDs are still lower than those of the best reported c-plane devices, mainly due to the poor light extraction efficiency (η_{extr}) compared with their polar counterparts.[129–133] Light extraction efficiency has become the most important limiting factor for the efficiency of LEDs, since the IQE of nitride-based LEDs has been greatly improved (by more than 80%)[134] by the availability of low-dislocation GaN substrates and advances in MOCVD techniques. The low η_{extr} is primarily caused by the low critical angle (23°) of the light escape cone, due to the large difference between the refractive indices of GaN ($n \sim 2.5$) and air ($n = 1$).[135] For c-plane devices, both η_{extr} and the corresponding output power have been greatly improved by surface roughening methods such as patterned sapphire substrate (PSS) and photoelectrochemical (PEC) etching techniques.[135–139] Semipolar and nonpolar devices, however, still suffer from low light extraction efficiency due to the lack of proper roughening techniques, which have hindered their performance. In this section, we review several popular approaches in processing techniques, device structures and packing methods to increase the η_{extr} of InGaN-based LEDs.

8.4.2 Increasing η_{extr} via surface roughening

There have been many reports of advanced surface roughening techniques through the periodic patterning of the semiconductor material or an overlying dielectric layer, with micro or nano features to increase the η_{extr} of LEDs. For c-plane devices, PSS and PEC etching techniques have been widely implemented for commercial devices.[135–139] For semipolar and nonpolar devices, however, there are very few reports. Recently, Zhong *et al.* and Zhao *et al.* at UCSB demonstrated that surface patterning with conical features by inductively coupled plasma (ICP) etching could have the potential to achieve relatively high power and high efficiency semipolar devices.[140,141] The backsides of the LED devices were polished and patterned with conical features by conventional contact lithography,

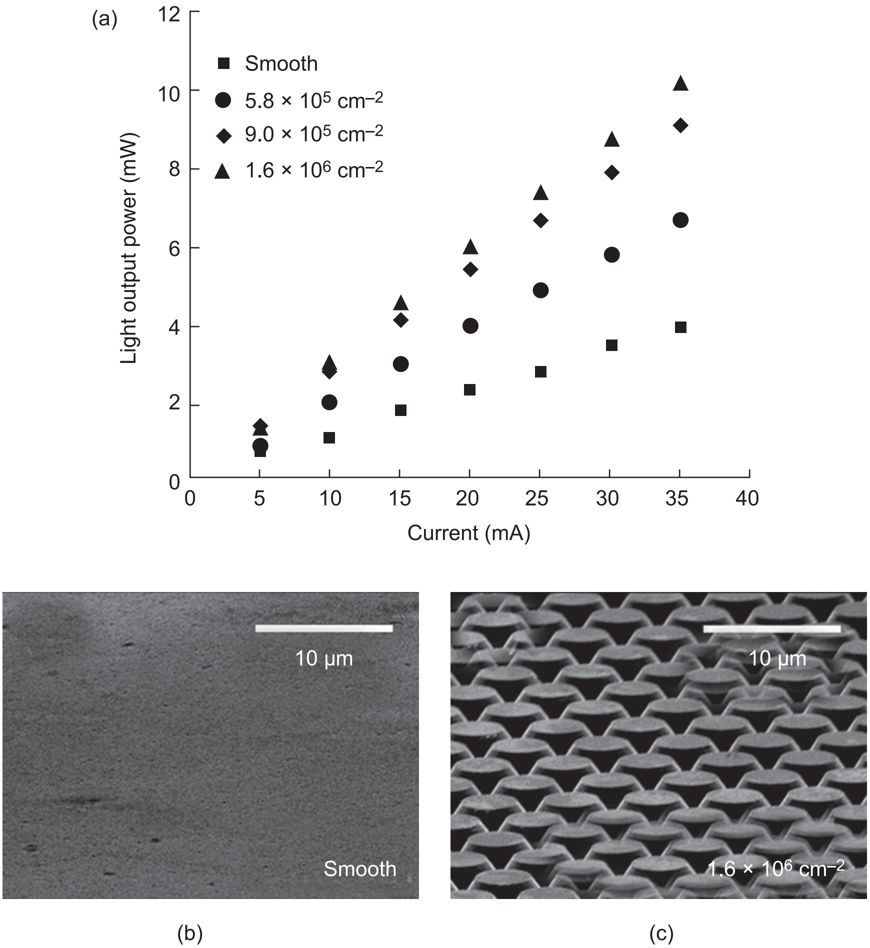

8.5 (a) Dependence of light output power on the density of conical features patterned on the backside of the devices. Scanning electron microscopy (SEM) images of the backside of the device with (b) a smooth surface and (c) a high density ($\rho = 1.6 \times 10^6 \text{cm}^{-2}$) of conical features (upper diameter Ø = 3 μm).[141]

followed by ICP etching. It was discovered that the η_{extr} of the LEDs increased dramatically as the density of the patterns increased, compared with a reference device with a smooth surface. Figure 8.5 demonstrates the dependence of light output power (corresponding to η_{extr}) on the density of the conical features. The experimental finding was also consistent with theoretical Monte Carlo ray tracing simulations on c-plane devices. This patterning technique resulted in semipolar blue LEDs with over 50% external quantum efficiency (EQE), which is comparable to the best c-plane devices. It is also noteworthy that nonpolar and semipolar LEDs are usually characterized by a high degree of polarized emission, which is of significant interest for laser and display applications.[142,143] Novel surface patterning design, such as with photonic crystal structures, to control or manage this optical polarization is a very interesting topic of research.[144]

8.4.3 Thin-film flip-chip LEDs

One of the most popular chip designs adopted by the LED industry to increase η_{extr} is the thin-film flip-chip (TFFC) LED.[145] The fabrication process for a TFFC LED typically includes a substrate removal step (sapphire or SiC substrate for a c-plane LED). After that, the LED chips are flipped and mounted. The thinness of the LEDs greatly reduces the modes that are trapped in the LED chip due to total internal reflection. Furthermore, the n-GaN surfaces are roughened using the process techniques described in Section 8.4.2 to further increase η_{extr}.[146] To date, Lumileds and Osram have successfully produced TFFC or thin-GaN device structures on InGaN-based LEDs.[147,148] A high light extraction efficiency of 80% has been reported for these TFFC LEDs.[149] However, up to now, most of the TFFC LEDs have been fabricated on c-plane devices. There are very few reports of TFFC LEDs on nonpolar or semipolar devices.

8.4.4 High light extraction packaging

Current conventional LED packaging structures suffer significantly from the backcoating effect, where a fraction of the light in an LED die is absorbed by the active layer, semi-transparent contacts (e.g., indium-tin-oxide or ITO) or reflective surfaces in the package (e.g., silver header coatings) due to the lead frames or the reflectors on the back surface of the LED dies. As a result, only a fraction of light is able to escape to the free space and the overall efficiency of the LEDs is reduced. To circumvent this problem, advanced LED package architectures, such as the suspended LED package, in which an LED die is suspended from gold wire-bonding leads, have been proposed.[150,151] However, this type of packaging has caused several heat dissipation problems, which greatly reduced the light output power of the LEDs at high current injections. More recently, Pan *et al.* at UCSB used a novel vertical-stand LED architecture based on a transparent submount (ZnO).[152] This package structure allows light to be extracted from all faces of an LED die, in particular from the backside surface, which is enhanced by the high refractive index and roughened surface of the vertical ZnO stand. In addition, using a ZnO submount helped to improve the heat dissipation from the LEDs. This packaging architecture has been successfully demonstrated for semipolar blue LEDs, which had a high EQE of over 50%.[45] The estimated η_{extr} is around 75%, which is much higher than for the conventional packaging.[153]

8.5 References

1. H. Amano, N. Sawaki, I. Akasaki and Y. Toyoda, *Appl. Phys. Lett.* **48**, 353 (1986).
2. S. Nakamura, *Jpn. J. Appl. Phys.* **30**, L1-705 (1991).
3. S. Nakamura, M. Senoh and T. Mukai, *Jpn. J. Appl. Phys.* **30**, L1-708 (1991).
4. H. Amano, M. Kito, K. Hiramatsu and I. Akasaki, *Jpn. J. Appl. Phys.* **28**, L2-112 (1989).
5. S. Nakamura, T. Mukai, M. Senoh and N. Iwasa, *Jpn. J. Appl. Phys.* **31**, L1-39 (1992).
6. S. Nakamura, T. Mukai and M. Senoh, *Appl. Phys. Lett.* **64**, 1687 (1994).
7. F. Bernardini and V. Fiorentini, *Phys. Stat. Sol. (b)* **216**, 391 (1999).
8. T. Takeuchi, C. Wetzel, S. Yamaguchi, H. Sakai, H. Amano, *et al.*, *Appl. Phys. Lett.* **73**, 1691 (1998).
9. T. Takeuchi, S. Sota, M. Katsuragawa, M. Komori, H. Takeuchi, *et al.*, *Jpn. J. Appl. Phys.* **36**, L382 (1997).
10. T. Kuroda and A. Tackeuchi, *J. Appl. Phys.* **92**, 3071 (1999).
11. S. Chichibu, T. Azuhata, T. Sota and S. Nakamura, *Appl. Phys. Lett.*, **69**, 4188 (1996).
12. Y. Narukawa, M. Ichikawa, D. Sanga, M. Sano and T. Mukai, *J. Phys. D: Appl. Phys.* **43**, 354002 (2010).
13. M. R. Krames, O. B. Shchekin, R. Mueller-Mach, G. O. Mueller, L. Zhou, *et al.*, *J. Display Technology* **3**, 160 (2007).
14. D. C. Houghton, M. Davies and M. Dion, *Appl. Phys. Lett.* **64**, 505 (1994).
15. M. S. Oh, M. K. Kwon, I. K. Park, S. H. Baek, S. J. Park, *et al.*, *J. Cryst. Growth* **289**, 107 (2006).
16. C. Wetzel, P. Li, T. Detchprohm and J. S. Nelson, *Phys. Stat. Sol. (c)* **2**, 2871 (2005).
17. T. Detchprohm, M. Zhu, W. Zhao, Y. Wang, Y. Li, *et al.*, *Phys. Stat. Sol. (c)* **6**, 840 (2009).
18. T. Shioda, H. Yoshida, K. Tachibana, N. Sugiyama and S. Nunoue, *Phys. Stat. Sol. (a)* **209**, 473 (2012).
19. A. David, M. J. Grundmann, J. F. Kaeding, N. F. Gardner, T. G. Mihopoulos, *et al.*, *Appl. Phys. Lett.* **92**, 053502 (2008).
20. J. P. Liu, J. H. Ryou, R. D. Dupuis, J. Han, G. D. Shen, *et al.*, *Appl. Phys. Lett.* **93**, 021102 (2008).
21. Y. L. Li, T. Gessmann, E. F. Schubert and J. K. Sheu, *J. Appl. Phys.* **94**, 2167 (2003).
22. M. Peter, A. Laubsch, P. Stauss, A. Walter, J. Baur, *et al.*, *Phys. Stat. Sol. (c)* **5**, 2050 (2008).
23. B. Galler, A. Laubsch, A. Wojcik, H. Lugauer, A. Gomez-Iglesias, *et al.*, *Phys. Stat. Sol. (c)* **8**, 2372 (2011).
24. J. H. Zhu, S. M. Zhang, H. Wang, D. G. Zhao, J. J. Zhu, *et al.*, *Appl. Phys. Lett.* **109**, 093117 (2011).
25. S. H. Han, D. Y. Lee, S. J. Lee, C. Y. Cho, M. K. Kwon, *et al.*, *Appl. Phys. Lett.* **94**, 231123 (2009).
26. X. Ni, X. Li, J. Lee, S. Liu, V. Avrutin, *et al.*, *J. Appl. Phys.* **108**, 033112 (2010).
27. M. F. Schubert and E. F. Schubert, *Appl. Phys. Lett.* **96**, 131102 (2010).
28. D. S. Sizov, R. Bhat, A. Zakharian, K. Song, D. E. Allen, *et al.*, *IEEE J. Sel. Top. Quantum Electron.* **17**, 1390 (2011).
29. J. Xie, X. Ni, Q. Fan, R. Shimada, Ü. Özgür, *et al.*, *Appl. Phys. Lett.* **93**, 121107 (2008).
30. S. H. Han, C. Y. Cho, S. J. Lee, T. Y. Park, T. H. Kim, *et al.*, *Appl. Phys. Lett.* **96**, 051113 (2010).

31. Y.-K. Kuo, J.-Y. Chang, M.-C. Tsai and S.-H. Yen, *Appl. Phys. Lett.* **95**, 011116 (2009).
32. R. M. Lin, S. F. Yu, S. J. Chang, T. H. Chiang, S. P. Chang, *et al.*, *Appl. Phys. Lett.* 101, 081120 (2012).
33. C. H. Wang, S. P. Chang, P. H. Ku, J. C. Li, Y. P. Lan, *et al.*, *Appl. Phys. Lett.* **99**, 171106 (2011).
34. C. S. Xia, Z. M. Simon Li, W. Lu, Z. H. Zhang, Y. Sheng, *et al.*, *Appl. Phys. Lett.* **99**, 233501 (2011).
35. Y. Kawaguchi, C. Y. Huang, Y. R. Wu, Q. Yan, C. C. Pan, *et al.*, *Appl. Phys. Lett.* **100**, 231110 (2012).
36. Y. C. Shen, G. O. Mueller, S. Watanabe, N. F. Gardner, A. Munkholm, *et al.*, *Appl. Phys. Lett.* **91**, 141101 (2007).
37. A. David and M. J. Grundmann, *Appl. Phys. Lett.* **96**, 103504 (2010).
38. E. Kioupakis, P. Rinke, K. T. Delaney and C. G. V. de Walle, *Appl. Phys. Lett.* **98**, 161107 (2011).
39. N. F. Gardner, G. O. Müller, Y. C. Shen, G. Chen, S. Watanabe, *et al.*, *Appl. Phys. Lett.* **91**, 243506 (2007).
40. Y.-L. Li, Y. R. Huang and Y. H. Lai, *Appl. Phys. Lett.* **91**, 181113 (2007).
41. M. H. Kim. M. F. Schubert, Q. Dai, J. K. Kim, E. F. Schubert, *et al.*, *Appl. Phys. Lett.* **91**, 183507 (2011).
42. M. F. Schubert, J. Xu, J. K. Kim, E. F. Schubert, M. H. Kim, *et al.*, *Appl. Phys. Lett.* **93**, 041102 (2008).
43. X. Ni, X. Li, J. Lee, S. Liu, V. Avrutin, *et al.*, *Appl. Phys. Lett.* **97**, 031110 (2010).
44. S. C. Ling, T. C. Lu, S. P. Chang, J. R. Chen, H. C. Kuo, *et al.*, *Appl. Phys. Lett.* **96**, 231101 (2010).
45. Y. Zhao, S. Tanaka, C. C. Pan, K. Fujito, D. Feezell, *et al.*, *Appl. Phys. Express* **4**, 082104 (2011).
46. C. C. Pan, S. Tanaka, F. Wu, Y. Zhao, J. S. Speck, *et al.*, *Appl. Phys. Express* **5**, 062103 (2012).
47. H.-H. Huang and Y.-R. Wu, *J. Appl. Phys*. **107**, 053112 (2010).
48. A. E. Romanov, T. J. Baker, S. Nakamura and J. S. Speck, *J. Appl. Phys.* **100**, 023522 (2006).
49. O. Ambacher, J. Majewski, C. Miskys, A. Link, M Hermann, *et al.*, *J. Phys.: Condens. Matter* **14**, 3399 (2002).
50. S. H. Park, D. Ahn and S. L. Chuang, *IEEE J. Quantum Electron*. **43**, 1175 (2007).
51. A. A. Yamaguchi, *Jap. J. Appl. Phys.* **46**, L789 (2007).
52. I. L. Koslow, M. T. Hardy, P. S. Hsu, P. Y. Dang, F. Wu, *et al.*, *Appl. Phys. Lett.* **101**, 121106 (2012)
53. M. D. Craven, S. H. Lim, F. Wu, J. S. Speck and S. P. DenBaars, *Appl. Phys. Lett.* **81**, 469 (2002).
54. J. L. Hollander, M. J. Kappers, C. McAleese and C. J. Humphreys, *Appl. Phys. Lett.* **92**, 101104 (2008).
55. Q. Sun, B. H. Kong, C. D. Yerino, T. S. Ko, B. Leung, *et al.*, *J. Appl. Phys.* **106**, 123519 (2009).
56. X. Ni, Y. Fu, Y. T. Moon, N. Biyikli and H. Morko, *J. Cryst. Growth* **290**, 166 (2006).
57. T. S. Ko, T. C. Wang, R. C. Gao, H. G. Chen, G. S. Huang, *et al.*, *J. Cryst. Growth* **300**, 308 (2007).
58. R. Sharma, P. M. Pattison, H. Masui, R. M. Farrell, T. J. Baker, *et al.*, *Appl. Phys. Lett.* **87**, 231110 (2005).

59. T. J. Baker, B. A. Haskell, F. Wu, J. S. Speck and S. Nakamura, *Jpn. J. Appl. Phys.* **45**, L154 (2006).
60. H. Masui, T. J. Baker, M. Iza, H. Zhong, S. Nakamura, *et al.*, *J. Appl. Phys.* **100**, 113109 (2006).
61. H. Jonen, H. Bremers, T. Langer, U. Rossow and A. Hangleiter, *Appl. Phys. Lett.* **100**, 151905 (2012).
62. P. Waltereit, O. Brandt, A. Trampert, H. T. Grahn, J. Menniger, *et al.*, *Nature* **406**, 865 (2000).
63. S. Ghosh, P. Waltereit, O. Brandt, H. T. Grahn and K. H. Ploog, *Phys. Rev. B* **65**, 075202 (2002).
64. Q. Sun, S. Y. Kwon, Z. Y. Ren, J. Han, T. Onuma, *et al.*, *Appl. Phys. Lett.* **92**, 051112 (2008).
65. Y. S. Cho, Q. Sun, I. H. Lee, T. S. Ko, C. D. Yerino, *et al.*, *Appl. Phys. Lett.* **93**, 111904 (2008).
66. Q. Sun, C. D. Yerino, Y. Zhang, Y. S. Cho, S. Y. Kwon, *et al.*, *J. Cryst. Growth* **311**, 3824 (2009).
67. Q. Sun, B. Leung, C.D. Yerino, Y. Zhang and J. Han, *Appl. Phys. Lett.* **95**, 231904 (2009).
68. P. Vennegues, T. Zhu, D. Martin and N. Grandjean, *J. Appl. Phys.* **108**, 113521 (2010).
69. N. Okada, A. Kurisu, K. Murakami and K. Tadatomo, *Appl. Phys. Express* **2**, 091001 (2009).
70. P. Mierry, N. Kriouche, M. Nemoz, S. Chenot and G. Nataf, *Appl. Phys. Lett.* **96**, 231918 (2010).
71. T. Hikosaka, T. Tanikawa, Y. Honda, M. Yamaguchi and N. Sawaki, *Phys. Stat. Sol. (c)* **5**, 2234 (2008).
72. J. F. Kaeding, M. Iza, H. Sato, S. P. DenBaars, J. S. Speck, *et al.*, *Jpn. J. Appl. Phys.* **45**, L536 (2006).
73. T. J. Baker, B. A. Haskell, F. Wu, P. T. Fini, J. S. Speck, *et al.*, *Jpn. J. Appl. Phys.* **44**, L920 (2005).
74. G. T. Chen, S. P. Chang, J. I. Chyi and M. N. Chang, *Appl. Phys. Lett.* **92**, 241904 (2008).
75. N. Okada, H. Oshita, K. Yamane and K. Tadatomo, *Appl. Phys. Lett.* **99**, 242103 (2011).
76. K. Fujito, S. Kubo and I. Fujimura, *MRS Bulletin*, **34**, 313 (2009).
77. S. S. Park, I. Park and S. H. Choh, *Jpn. J. Appl. Phys.* **39**, L1141 (2000).
78. A. D. Williams and T. D. Moustakas, *J. Cryst. Growth* **300**, 37 (2007).
79. H. Ashraf, R. Kudrawiec, J. L. Weyher, J. Serafinczuk, J. Misiewicz, *et al.*, *J. Cryst. Growth*, **312**, 2398 (2010).
80. B. A. Haskell, F. Wu, S. Matsuda, M. D. Craven, P. T. Fini, *et al.*, *Appl. Phys. Lett.* **83**, 1554 (2003).
81. B. A. Haskell, A. Chakaraborty, F. Wu, H. Sasano, P. T. Fini, *et al.*, *J. Electron. Mater.* **34**, 357 (2005).
82. B. A. Haskell, F. Wu, M. D. Craven, S. Matsuda, P. T. Fini, *et al.*, *Appl. Phys. Lett.* **83**, 644 (2003).
83. H. Ashraf, J. L. Weyher, G. W. G. van Dreumel, A. Gzregorzyck and P. R. Hageman, *J. Cryst. Growth* **310**, 3957 (2008).
84. B. Lucznik, B. Pastuszka, I. Grzegory, M. Boćkowski, G. Kamler, *et al.*, *J. Cryst. Growth* **281**, 38 (2005).
85. T. Hashimoto, F. Wu, J. S. Speck and S. Nakamura, *Nature Materials* **6**, 568 (2007).

86. R. Dwilinski, R. Doradzinski, J. Garczynski, L. P. Sierzputowski, A. Puchalski, *et al.*, *J. Cryst. Growth* **311**, 3015 (2009).
87. D. Ehrentraut and T. Fukuda, *Proc. IEEE* **98**, 7 (2010).
88. V. Avrutin,, D. J. Silversmith, Y. Mori, F. Kawamura, Y. Kitaoka, *et al.*, *Proc. IEEE* **98**, 1302 (2010).
89. F. Wu, Y. D. Lin, A. Chakraborty, H. Ohta, S. P. DenBaars, *et al.*, *Appl. Phys. Lett.* **96**, 231912 (2010).
90. J. E. Northrup, *Appl. Phys. Lett.* **95**, 133107 (2009).
91. M. V. Durnev, A. V. Omelchenko, E. V. Yakovlev, I. Yu. Evstratov and S. Yu. Karpov, *App. Phys. Lett.* **97**, 051904 (2010).
92. Y. Zhao, Q. Yan, C. Y. Huang, S. C. Huang, P. S. Hsu, *et al.*, *Appl. Phys. Lett.* **100**, 201108 (2012).
93. S. Keller, N. A. Fichtenbaum, M. Furukawa, J. S. Speck, S. P. DenBaars, *et al.*, *Appl. Phys. Lett.* **90**, 191908 (2007).
94. T. Zywietz, J. Neugebauer and M. Scheffler, *Appl. Phys. Lett.* **73**, 487 (1998).
95. H. Sato, H. Hirasawa, H. Asamizu, N. Fellows, A. Tyagi, *et al.*, *J. Light Visual Environ.* **32**, 107 (2008).
96. S. Yamamoto, Y. Zhao, C. C. Pan, R. B. Chung, K. Fujito, *et al.*, *Appl. Phys. Express* **3**, 122102 (2010).
97. C. Q. Chen, M. E. Gaevski, W. H. Sun, E. Kuokstis, J. P. Zhang, *et al.*, *Appl. Phys. Lett.* **81**, 3194 (2002).
98. H. Wang, C. Q. Chen, Z. Gong, J. Zhang, M. Gaevski, *et al.*, *Appl. Phys. Lett.* **84**, 499 (2004).
99. D. S. Li, H. Chen, H. B. Yu, X. H. Zheng, Q. Huang, *et al.*, *J. Cryst. Growth* **265**, 107 (2004).
100. T. Wernicke, S. Ploch, V. Hoffmann, A. Knauer, M. Weyers, *et al.*, *Phys. Stat. Sol (b)* **248**, 574 (2011).
101. L. Lymperakis and J. Neugebauer, *Phys. Rev. B* **79**, 241308 (2009).
102. M. J. Kappers, J. L. Hollander, C. McAleese, C. F. Johnston, R. F. Broom, *et al.*, *J. Cryst. Growth* **300**, 155 (2007).
103. S. Ploch, T. Wernicke, J. Thalmair, M. Lohr, M. Pristovsek, *et al.*, *J. Cryst. Growth* **356**, 70 (2012).
104. Y. Zhao, C. Y. Huang, F. Wu, K. Fujito, S. P. DenBaars, *et al.*, *Appl. Phys. Lett.* **102**, 091905 (2013).
105. A. Hirai, Z. Jia, M. C. Schmidt, R. M. Farrell, S. P. DenBaars, *et al.*, *Appl. Phys. Lett.* **91**, 191906 (2007).
106. H. Yamada, K. Iso, H. Masui, M. Saito, K. Fujito, *et al.*, *J. Cryst. Growth* **310**, 4968 (2008).
107. R. M. Farrell, D. A. Haeger, X. Chen, C. S. Gallinat, R. W. Davis, *et al.*, *Appl. Phys. Lett.* **96**, 231907 (2010).
108. Y. D. Lin, M. T. Hardy, P. S. Hsu, K. M. Kelchner, C. Y. Huang, *et al.*, *Appl. Phys. Express* **2**, 082102 (2009).
109. K. M. Kelchner, Y. D. Lin, M. T. Hardy, C. Y. Huang, P. S. Hsu, *et al.*, *Appl. Phys. Express* **2**, 071003 (2009).
110. A. M. Fischer, Z. Wu, K. Sun, Q. Wei, Y. Huang, *et al.*, *Appl. Phys. Express* **2**, 041002 (2009).
111. F. Wu *et al.* (to be submitted).
112. A. Tyagi, F. Wu, E. C. Young, A. Chakraborty, H. Ohta, *et al.*, *Appl. Phys. Lett.* **95**, 251905 (2009).

113. F. Wu, A. Tyagi, E. C. Young, A. E. Romanov, K. Fujito, *et al.*, *J. Appl. Phys.* **109**, 033505 (2011).
114. E. C. Young, F. Wu, A. E. Romanov, A. Tyagi, C. S. Gallinat, *et al.*, *Appl. Phys. Express* **3**, 011004 (2010).
115. P. S. Hsu, E. C. Young, A. E. Romanov, K. Fujito, S. P. DenBaars, *et al.*, *Appl. Phys. Lett.* **99**, 081912 (2011).
116. M. T. Hardy, P. S. Hsu, F. Wu, I. L. Koslow, E. C. Young, *et al.*, *Appl. Phys. Lett.* **100**, 202103 (2012).
117. S. Yoshida, T. Yokogawa, Y. Imai, S. Kimura and O. Sakata, *Appl. Phys. Lett.* **99**, 131909 (2011).
118. F. Wu, E. C. Young, I. Koslow, M. T. Hardy, P. S. Hsu, *et al.*, *Appl. Phys. Lett.* **99**, 251909 (2011).
119. P. S. Hsu, M. T. Hardy, E. C. Young, A. E. Romanov, S. P. DenBaars, *et al.*, *Appl. Phys. Lett.* **100**, 171917 (2012).
120. A. E. Romanov, E. C. Young, F. Wu, A. Tyagi, C. S. Gallinat, *et al.*, *J. Appl. Phys.* **109**, 103522 (2011).
121. A. Hangleiter, J. S. Im, H. Kollmer, S. Heppel, J. Off, *et al.*, *MRS Internet J. Nitride Semicond. Res.* **3**, 15 (1998).
122. A. Chitnis, C. Chen, V. Adivarahan, M. Shatalov, E. Kuokstis, *et al.*, *Appl. Phys. Lett.* **84**, 3663 (2004).
123. A. Chakraborty, B. A. Haskell, S. Keller, J. S. Speck, S. P. DenBaars, *et al.*, *Appl. Phys. Lett.* **85**, 5143 (2004).
124. A. Chakraborty, B. A. Haskell, H. Masui, S. Keller, J. S. Speck, *et al.*, *Jpn. J. Appl. Phys.* **45**, 739 (2006).
125. M. Schmidt, K. Kim, H. Sato, N. Fellows, H. Masui, *et al.*, *Jpn. J. Appl. Phys.* **46**, L126 (2007).
126. H. Masui, T. J. Baker, R. Sharma, P. M. Pattison, M. Iza, *et al.*, *Jpn. J. Appl. Phys.* **45**, L904 (2006).
127. K. Okamoto, H. Ohta, D. Nakagawa, M. Sonobe, J. Ichihara, *et al.*, *Jpn. J. Appl. Phys.* **45**, L1197 (2006).
128. S. H. Park and D. Ahn, *Appl. Phys. Lett.* **90**, 013505 (2007).
129. H. Sato, R. B. Chung, H. Hirasawa, N. Fellows, H. Masui, *et al.*, *Appl. Phys. Lett.* **92**, 221110 (2008).
130. H. Zhong, A. Tyagi, N. Fellows, F. Wu, R. B. Chung, *et al.*, *Appl. Phys. Lett.* **90**, 233504 (2007).
131. M. Funato, M. Ueda, Y. Kawakami, Y. Narukawa, T. Kosugi, *et al.*, *Jpn. J. Appl. Phys.* **45**, L659 (2006).
132. Y. Zhao, J. Sonoda, I. Koslow, J. S. Ha, H. Ohta, *et al.*, *Jpn. J. Appl. Phys.* **49**, 070206 (2010).
133. I. L. Koslow, J. Sonoda, R. B. Chung, C. C. Pan, S. Brinkley, *et al.*, *Jpn. J. Appl. Phys.* **49**, 080203 (2010).
134. T. Nishida, H. Saito and N. Kobayashi, *Appl. Phys. Lett.* **79**, 711 (2001).
135. T. Fuji, Y. Gao, R. Sharma, E. L. Hu, S. P. DenBaars, *et al.*, *Appl. Phys. Lett.* **84**, 855 (2004).
136. M. Yamada, T. Mitani, Y. Narukawa, S. Shijoji, I. Niki, *et al.*, *Jpn. J. Appl. Phys.* **41**, L1431 (2002).
137. D. Morita, M. Sano, M. Yamamoto, M. Nonaka, K. Yasutomo, *et al.*, *Phys. Stat. Sol. (a)* **200**, 114 (2003).
138. C. Huh, K. Lee, E. Kang and S. Park, *J. Appl. Phys.* **93**, 9383 (2003).

139. H. Kasugai, T. Miyake, A. Honshio, S. Mishima, T. Kawashima, *et al.*, *Jpn. J. Appl. Phys.* **44**, 7414 (2005).
140. H. Zhong, A. Tyagi, N. Pfaff, M. Saito, K. Fujito, *et al.*, *Jpn. J. Appl. Phys.* **48**, 030201 (2009).
141. Y. Zhao, J. Sonoda, C. C. Pan, S. Brinkley, I. Koslow, *et al.*, *Appl. Phys. Express* **3**, 102101 (2010).
142. Y. Zhao, S. Tanaka, Q. Yan, C. Y. Huang, R. B. Chung, *et al.*, *Appl. Phys. Lett.* **99**, 051109 (2011).
143. Y. Zhao, Q. Yan, D. Feezell, K. Fujito, C. G. Van de Walle, *et al.*, *Opt. Express* **21**, A53 (2013).
144. E. Matioli, S. Brinkley, K. M. Kelchner, S. Nakamura, S. P. DenBaars, *et al.*, *Appl. Phys. Lett.* **98**, 251112 (2011).
145. M. H. Crawford, *IEEE J. Sel. Top. Quantum Electron.* **15**, 1028 (2009).
146. I. Schnitzner, E. Yablonovitch, C. Caneau, T. J. Gmitter and A. Scherer, *Appl. Phys. Lett.* **63**, 2174 (1993).
147. O. B. Shchekin, J. E. Epler, T. A. Trottier, T. Margalith, D. A. Steigerwald, *et al.*, *Appl. Phys. Lett.* **89**, 071109-1 (2006).
148. V. Haerle, B. Hahn, S. Kaiser, A. Weimar, S. Bader, *et al.*, *Phys. Status Solidi A* **201**, 2736 (2004).
149. M. R. Krames, O. B. Shchekin, R. Mueller-Mach, G. O. Mueller, L. Zhou, *et al.*, *J. Disp. Technol.* **3**, 160 (2007).
150. H. Masui, N. N. Fellows, H. Sato, H. Asamizu, S. Nakamura, *et al.*, *Appl. Opt.* **46**, 5974 (2007).
151. N. Fellows, H. Masui, H. Sato, H. Asamizu, M. Iza, *et al.*, *Phys. Stat. Sol. (c)* **5**, 2216 (2008).
152. C. C. Pan, I. Koslow, J. Sonoda, H. Ohta, J. S. Ha, *et al.*, *Jpn. J. Appl. Phys.* **49**, 080210 (2010).
153. C. C. Pan, PhD Dissertation UCSB (2012).
154. Y.-R. Wu, R. Shivaraman, K.-C. Wang and J. S. Speck, *Appl. Phys. Lett.* **101**, 083505 (2012).

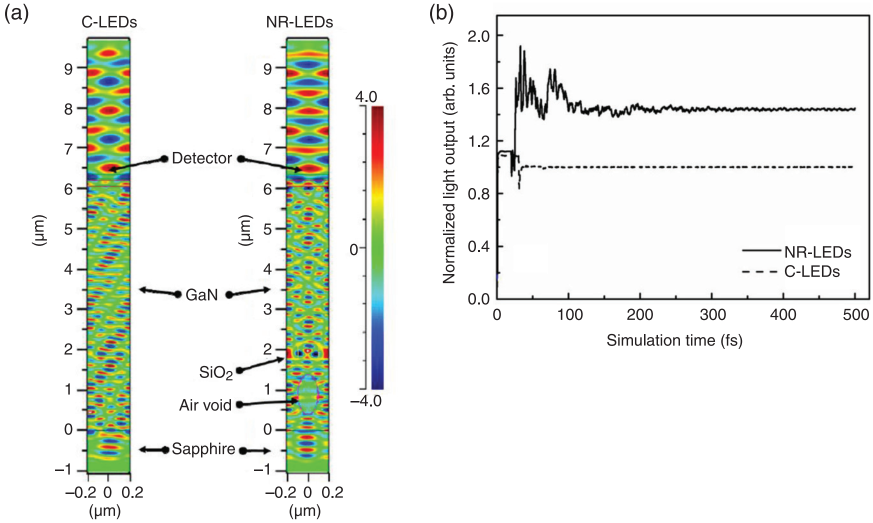

Plate VI (Chapter 7) (a) 3D FDTD of the calculated electric-field distribution for NR-LEDs and C-LEDs. (b) Normalized light output power as a function of the simulation time for C-LEDs and NR-LEDs.[26]

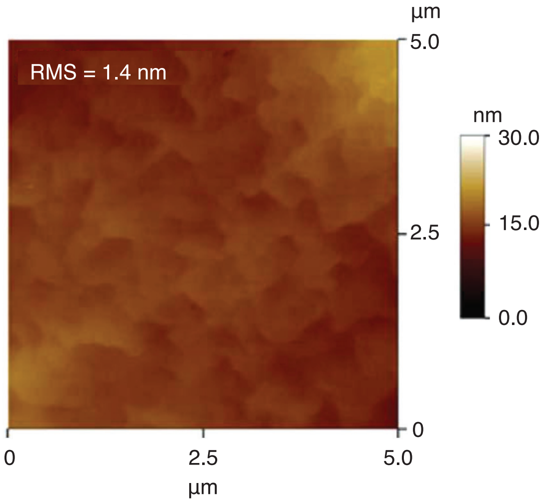
μm
5.0
2.5
0
RMS = 1.4 nm
nm
30.0
15.0
0.0
0
2.5
5.0
μm

Plate VII (Chapter 7) Surface morphology of overgrown GaN NP template as scanned by AFM.[15]

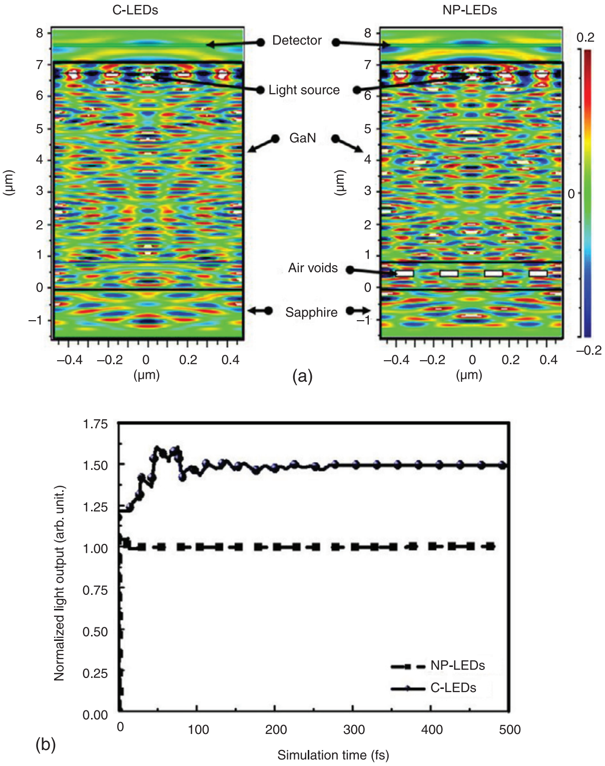

Plate VIII (Chapter 7) (a) 2D FDTD of the calculated electric-field distribution for NP-LEDs and C-LEDs. (b) Normalized light output power as a function of the simulation time for C-LEDs and NP-LEDs.[15]

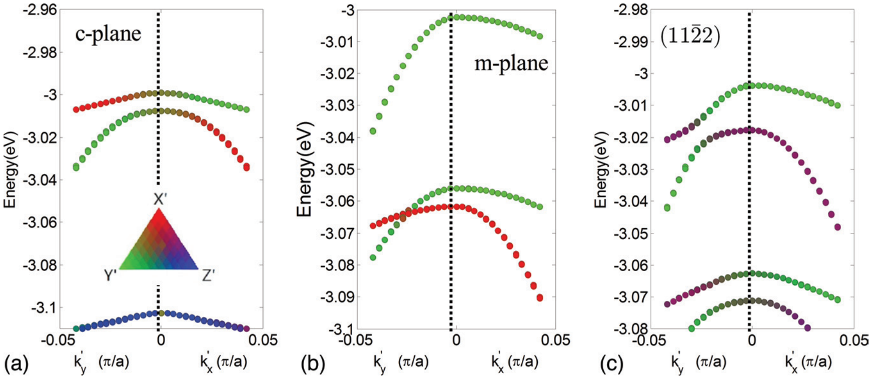

Plate IX (Chapter 8) Calculated valence E-k diagrams for (a) the c-plane, (b) the m-plane and (c) the semipolar plane $(11\bar{2}2)$ $In_{0.2}Ga_{0.8}N$ QWs. The zero potential is referred to the conduction band of GaN. The bandgap of $In_{0.2}Ga_{0.8}N$ is about 2.72 eV.

9

Efficiency droop in gallium indium nitride (GaInN)/gallium nitride (GaN) LEDs

D. S. MEYAARD, G.-B. LIN, J. CHO and
E. F. SCHUBERT, Rensselaer Polytechnic Institute, USA

DOI: 10.1533/9780857099303.2.279

Abstract: The decrease in efficiency at high current densities, i.e. the efficiency droop, is introduced in the context of GaInN/GaN light-emitting diodes (LEDs). We begin with an overview of the ABC model for the recombination of carriers in GaInN/GaN LEDs. The weaknesses of this model are described, and the model is reformulated by including a carrier leakage term. Several explanations for droop are presented and analyzed, including their strengths and weaknesses. Particular emphasis is given to high-level injection and the associated drift-induced electron leakage out of the active region. Finally, several proposed solutions to overcome efficiency droop are presented.

Key words: light-emitting diode, efficiency droop, compound semiconductor, carrier asymmetry.

9.1 Introduction

In an ideal light-emitting diode (LED), every electron supplied electrically would result in a photon of light output. In this case, the optical output power would vary linearly with injected current. The optical power of such an ideal diode is shown in Fig. 9.1(a) by the dashed curve. Experimentally, however, a linear curve for light versus current is not attained, due to non-radiative recombination at both low and high currents. The behavior at low currents is explained well by Shockley–Read–Hall (SRH) recombination: non-radiative recombination is stronger than radiative recombination at very small current densities, resulting in the measured behavior shown near the origin of the coordinate system of Fig. 9.1(a). A *linear* relation between light and current would result in a *flat* (constant) efficiency curve, as shown by the dashed line in Fig. 9.1(b). However, when viewing experimental curves for external quantum efficiency versus current, there exists a peak efficiency point located at relatively low currents. Typical high-quality GaN-based LEDs have a peak efficiency at current densities at more than 1 A/cm^2 but less than 10 A/cm^2. As the injected current increases, the efficiency gradually decreases, or droops, giving the phenomenon its name. Efficiency droop is a particular problem for high-power LEDs, for which the desired current of operation is significantly higher than the current at the peak-efficiency point.

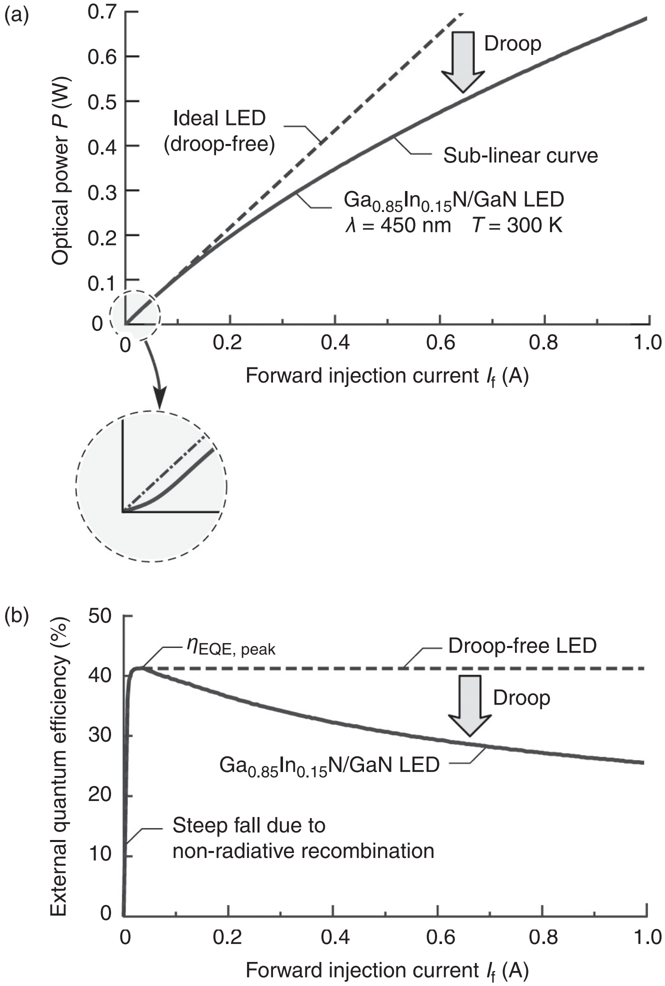

9.1 (a) Sub-linear increase of emitted optical power versus current typically exhibited by GaInN blue and green LEDs. (b) Efficiency versus current for the same device. The efficiency droops as the current increases. The dashed curve is for a droop-free device.

The magnitude of the efficiency droop can be quantified for a current I by the following equation:

$$\text{Droop} = \frac{\eta_{\text{EQE, peak}} - \eta_{\text{EQE}, I}}{\eta_{\text{EQE, peak}}} \qquad [9.1]$$

where $\eta_{\text{EQE}, I}$ is the external quantum efficiency (EQE) at the operating current I. Although this equation gives a quantitative value for droop, it is highly dependent on the peak EQE. Typically if a device has many defects or has poor material quality, it will have a low peak EQE, and will exhibit a smaller droop than a device with high material quality.

9.2 Recombination models in LEDs

Electron-hole recombination in LEDs is often modeled by the ABC model. This model assumes the equal injection of carriers into the active region ($J_n = J_p$). The recombination rate for this case can be written as:

$$R = An + Bn^2 + Cn^3 \qquad [9.2]$$

where n is the carrier concentration and A, B and C are the Shockley–Read–Hall, radiative and Auger coefficients, respectively. As observed from the equation above, SRH recombination is represented by the A coefficient, and has linear dependence on n. The ABC model correctly predicts a low-current region in the light output power (LOP) versus current curve where the LOP increases super-linearly with current (as shown in Fig. 9.1(a)). The linear dependence of SRH recombination (n) and the square dependence of radiative recombination (n^2), result in radiative recombination becoming the dominant recombination mechanism at higher current levels. At very high current levels, this model predicts that the Auger process will dominate recombination. The strength of Auger recombination in GaInN/GaN-based LEDs is still a controversial topic and will be discussed in detail later in this chapter.

The standard ABC model only considers the recombination of carriers inside the active region. This is not necessarily the case in real LEDs, due to carrier escape or non-capture by the active region. The exact mathematical description of carrier escape may be LED structure dependent or have a complex relation with the carrier concentration. It is therefore natural to use a general polynomial function, $f(n)$, to describe the carriers that recombine outside the active region. In order to make the ABC model more robust and complete, the $f(n)$ term, which describes carrier leakage, can be added to this model:

$$R = An + Bn^2 + Cn^3 + f(n) \qquad [9.3]$$

Figure 9.2 is a schematic diagram of recombination in the ABC$+f(n)$ model. Although the $f(n)$ term may be very important in describing recombination in an LED, the exact dependence of $f(n)$ on carrier concentration has, until recently, not been known.

Due to the wide bandgap in a GaN material system, it is likely that $f(n)$ has a weak effect at low currents but a stronger effect at very high currents. It therefore makes sense for $f(n)$ to contain terms with a higher-order dependence on n, such as n^3 or n^4. However, in order to keep $f(n)$ as general as possible, it can be expressed as a power series:

$$f(n) = an + bn^2 + cn^3 + dn^4 + \ldots \qquad [9.4]$$

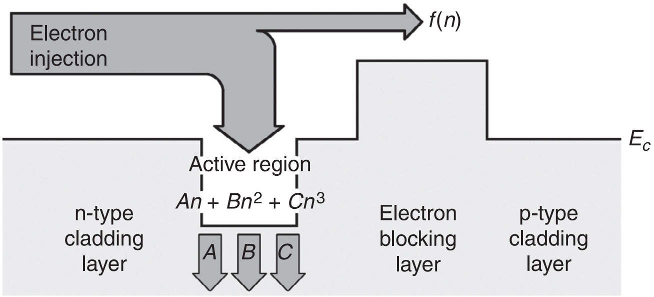

9.2 Illustration of electrons injected into the active region where they recombine, as expressed by recombination terms $An+Bn^2+Cn^3$, and electrons leaking out of the active region, as described by the function $f(n)$.

One of the features lacking in the ABC model when its predictions are compared to experimental data, is the shape of the EQE versus current curve. Phase-space filling has been used to explain this effect. This adds a carrier dependence to each coefficient, adding complexity to the model. However, the ABC model, even with phase-space filling, is still unable to explain the experimental results, particularly if the current is shown on a logarithmic scale encompassing several orders of magnitude. If there were only three recombination mechanisms (as assumed by the ABC model), plotting the EQE versus carrier concentration curve using a logarithmic abscissa would result in a curve that is symmetric about the point of peak efficiency. This would hold true, even when accounting for phase-space filling (Dai *et al.*, 2011). This is illustrated in Fig. 9.3(a), which shows a simulated internal quantum efficiency (IQE) versus n curve based on the ABC theory. Figure 9.3(b) shows examples of measurements using two different GaInN LEDs with different light-output characteristics. The abscissa is the square root of the LOP, which for high-efficiency devices, should be proportional to n. What is observed experimentally is not a symmetric curve but a heavily skewed curve, indicating that higher order terms are indeed necessary to describe the experimental results fully. This behavior of real devices can be fully explained using the ABC$+f(n)$ model, i.e. by adding a term, $f(n)$, to account for a limited injection efficiency.

9.3 Thermal roll-over in gallium indium nitride (GaInN) LEDs

In other material systems, such as III-V phosphides and arsenides, thermal heating has been observed to cause efficiency droop. This is an effect known as thermal roll-over, and occurs when the heat generated in the chip is so large that the light output power decreases at high current levels. This is typically observed under direct current (DC) injection conditions, because the self-heating effect is stronger

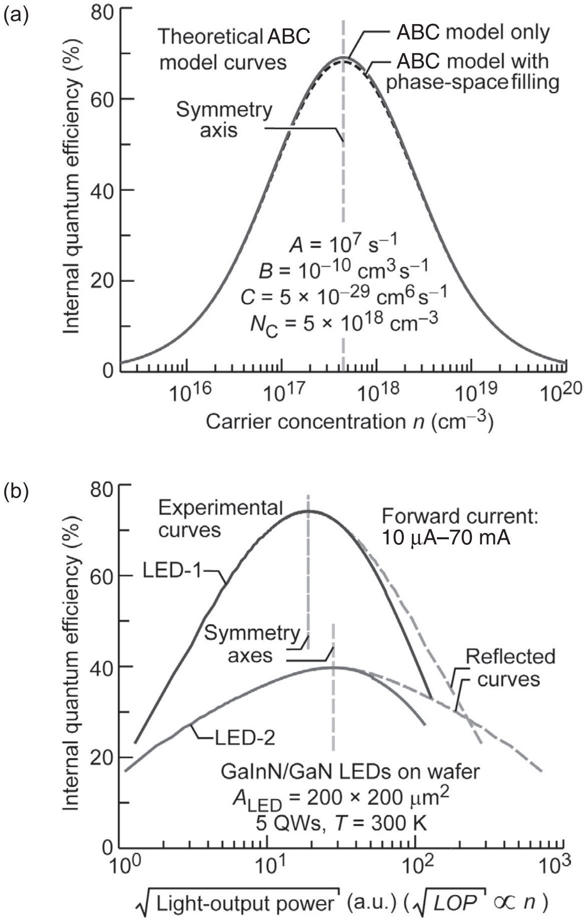

9.3 (a) Theoretical curves for IQE versus *n* based on the ABC model (without and with phase-space filling) showing symmetry. (b) Experimental curves for IQE versus square root of LOP showing asymmetry.

under DC conditions than under pulsed injection conditions. The thermal roll-over effect can be somewhat mitigated by employing efficient heat sinking in the packaging of an LED. Figure 9.4 shows the LOP versus current for a red AlGaInP/GaP LED. At room temperature, under pulsed injection biasing, the curve is almost linear. However, under DC injection biasing, thermal roll-over occurs, leading to a drop in efficiency.

At high currents, the increased temperature leads to increased SRH recombination, as well as carrier escape from the active region (Kish *et al.*, 1994). Because this effect is prominent in III-V phosphides and arsenides, it should occur in III-V nitrides as well. However, in GaInN/GaN LEDs, a comparison

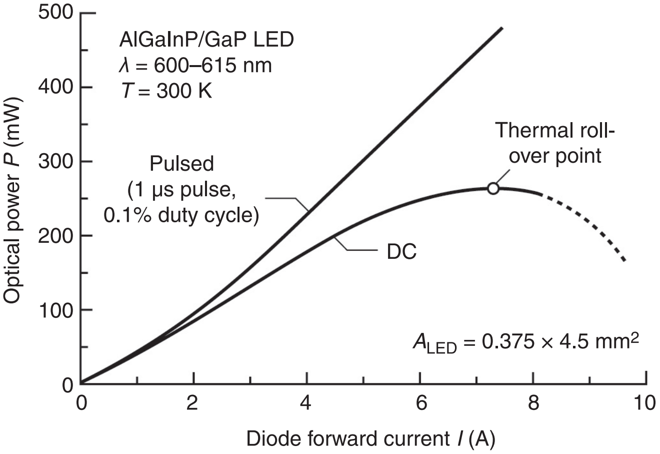

9.4 Optical power as a function of injection current for an AlGaInP/GaP LED for DC and pulsed injection conditions. The device has a large area of 1.69 mm^2. Under DC injection at a current of 7.3 A, the optical power reaches a maximum (the thermal roll-over point). Increasing the injection current beyond this point results in a decrease of the optical power (after Kish *et al.*, 1994).

between pulsed and DC performance indicates that thermal effects only play a small role in causing efficiency droop.

9.4 Auger recombination

Auger recombination is a non-radiative process involving three carriers. Direct Auger recombination occurs when an electron and hole recombine, but instead of producing light, either an electron is raised higher into the conduction band or a hole is pushed deeper into the valence band, as shown in Fig. 9.5(a). The direct Auger rate is related to carrier concentration by $R_{\text{Auger}} = C_{\text{eeh}} n^2 p$ and $R_{\text{Auger}} = C_{\text{ehh}} p^2 n$. Under typical operating conditions, it can be assumed that $n = p$. This is one of the assumptions of the ABC model. Therefore, the total rate of Auger recombination can be written as $R_{\text{Auger}} = C_{\text{Auger}} n^3$, where $C_{\text{Auger}} = C_{\text{eeh}} + C_{\text{ehh}}$. Auger recombination is a well-known effect in smaller bandgap semiconductors, but the effect of Auger recombination decreases strongly with increasing bandgap (Hader *et al.*, 2008). Experimentally, the accounts of the needed third-order non-radiative recombination coefficient vary. Some researchers state that the Auger coefficient would need to be of the order of $10^{-30}\,\text{cm}^6\cdot\text{s}^{-1}$ (Shen *et al.*, 2007), while others indicate that the value must be significantly higher, 10^{-27}–$10^{-24}\,\text{cm}^6\cdot\text{s}^{-1}$ (Ryu *et al.*, 2009), to account for droop. Auger recombination has been suggested as the cause of droop based on results of resonant optical excitation experiments on double heterostructure GaInN layers with GaN cladding (Shen *et al.*, 2007). These experiments found the third-order coefficient (which the authors associated with the Auger coefficient) to be in the range 1.4×10^{-30} to $2.0 \times 10^{-30}\,\text{cm}^6 \cdot \text{s}^{-1}$, using the recombination rate model.

Resonant optical excitation is designed to ensure that carriers are only generated in the active region, so that concerns such as carrier transport properties can be neglected. This is not necessarily true, however, as it has been demonstrated that even with excitation lower than the energy of the barriers (for a 405 nm laser), carriers escape the active region (Schubert *et al.*, 2009). Conflicting reports also exist on whether there is or is not significant droop during these photoluminescence measurements. Auger recombination will occur at some excitation level, so the question is how various groups calculated the actual carrier concentration in the active region, and if this is comparable to the carrier density during electroluminescence. On the theoretical side, the direct Auger coefficient has been calculated using first-principle calculations, yielding a value of $C = 3.5 \times 10^{-34}\,\text{cm}^6 \cdot \text{s}^{-1}$ (Hader *et al.*, 2008). Auger recombination has been one of the most controversial theories for explaining the efficiency droop in GaInN LEDs, but the actual effect of Auger recombination on the efficiency droop is still under debate.

Due to the low theoretical value for direct Auger recombination, several different variations have been proposed, as shown in Fig. 9.5. The first of these is interband Auger recombination. Using density-functional theory and many-body perturbation theory, the band structure for GaN can be calculated. This includes not only the lowest valley of the conduction band, but a second higher-lying band above it, as schematically shown in Fig. 9.5(b). This drastically increases the probability of Auger recombination occurring for GaN, yielding a coefficient of $2 \times 10^{-30}\,\text{cm}^6 \cdot \text{s}^{-1}$ (Delaney *et al.*, 2009). Others suggest that direct interband Auger

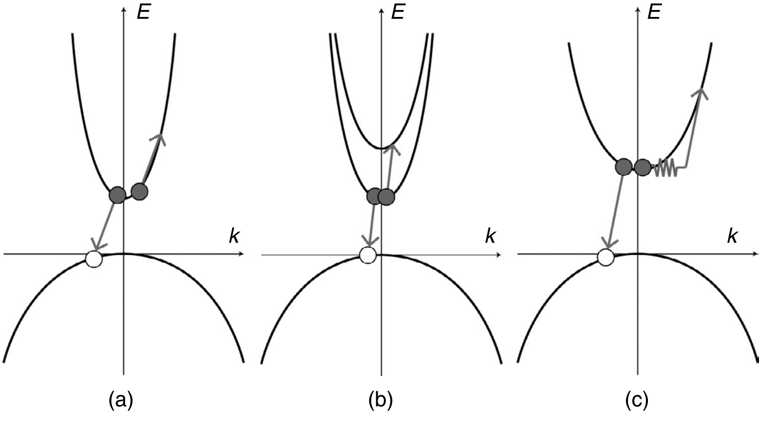

9.5 (a) Direct, (b) interband and (c) indirect Auger recombination. The significance of the effect of Auger recombination in GaN/GaInN LEDs is unclear.

recombination is only relevant for certain indium mole fractions, and therefore cannot explain the efficiency droop observed in GaN-based LEDs with a wide range of alloy compositions (Kioupakis *et al.*, 2011). To rectify this disconnect between theory and experimental data, indirect Auger recombination has also been proposed (shown in Fig. 9.5(c)). This process involves a carrier-phonon interaction, increasing the probability for Auger recombination to occur. A theoretical calculation of this coefficient yielded values between $1 \times 10^{-31}\,\mathrm{cm^6 \cdot s^{-1}}$ and $2 \times 10^{-31}\,\mathrm{cm^6 \cdot s^{-1}}$ (Kioupakis *et al.*, 2011), i.e. a range still not high enough to explain experimentally recorded values (Brendel *et al.*, 2011). Table 9.1 summarizes the theoretical and experimental reports of the Auger coefficient in the GaInN/GaN material system.

9.5 High-level injection and the asymmetry of carrier concentration and mobility

Over the entire history of the GaN-based material system, realizing p-type doping has been a significant hurdle. Even today, achieving a high hole concentration in GaN is a goal of both companies and academia. Even if a very large magnesium concentration is attained, it may severely degrade the hole mobility. For this reason, the conductivity in an n-type GaN region is typically much larger than the conductivity in a p-type GaN region. Electron blocking layers (EBLs) are commonly implemented using AlGaN; in this case, there are no shallow acceptors available. Therefore, the efficiency of p-type doping in AlGaN is very low. This leaves the likely possibility of the EBL blocking not only electrons but also impeding hole transport to the active region. This effect is illustrated in Fig. 9.6,

Table 9.1 Theoretical and experimental reports of the Auger and *C* coefficients in the GaInN/GaN material system

Method of calculation	Author	Room temperature Auger coefficient ($\mathrm{cm^6 \cdot s^{-1}}$)
Direct Auger recombination	Hader *et al.* (2008)	3.5×10^{-34}
Indirect Auger recombination	Kioupakis *et al.* (2011)	$0.5 \times 10^{-31} - 2.0 \times 10^{-31}$
Interband Auger recombination	Delaney *et al.* (2009)	2.0×10^{-30}
	Bertazzi *et al.* (2010)	1.0×10^{-32}
Experimental reports of Auger coefficient or *C* coefficient	Brendel *et al.* (2011)	1.8×10^{-31}
	Shen *et al.* (2007)	$1.4 \times 10^{-30} - 2.0 \times 10^{-30}$
	Zhang *et al.* (2009)	1.5×10^{-30}
	David and Grundmann (2010)	1.0×10^{-29}
	Dai *et al.* (2011)	8.0×10^{-29}
	Ryu *et al.* (2009)	$1.0 \times 10^{-27} - 1.0 \times 10^{-24}$

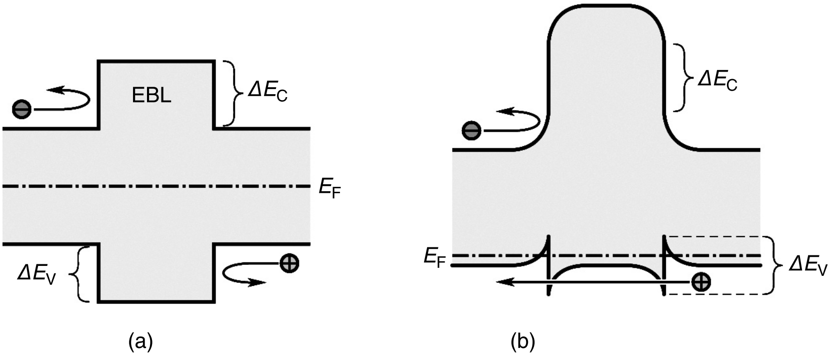

9.6 (a) Undoped and (b) p-doped EBL. An undoped EBL blocks electrons as well as holes. A p-doped EBL blocks electrons but not holes.

showing that high p-type doping in this region is very important in order to have good hole injection.

Taking a broader view of recombination in a diode, we can further analyze the effects due to the asymmetry of the carrier concentration. Simple diode theory is only valid under low-level injection conditions, when all of the applied voltage drops over the depletion region. In an n^+p junction, we can define the injected electron concentration at the edge of the p-type neutral layer as $\Delta n_p(0)$. The equilibrium hole concentration in the p-type region is p_{p0}. In this example, the standard well-known low-level injection condition is:

$$\Delta n_p(0) \ll p_{p0} \qquad [9.5]$$

This condition ensures that the conductivity of the depletion region is much lower than that of the p-type neutral layer, so that any incremental voltage applied to the diode drops over the depletion region. However, this condition does not take into account the difference in mobility between electrons and holes in GaN. In GaN, electron mobility may be in the range 200–300 cm^2/Vs, whereas hole mobility may be much lower, around 5 cm^2/Vs. For such extreme asymmetry, the low-level condition of Eq. 9.5 must be generalized to include mobility (Meyaard *et al.*, 2011):

$$\Delta n_p(0)\,\mu_n \ll p_{p0}\,\mu_p \qquad [9.6]$$

This generalized condition takes into account the strong asymmetry in both carrier concentration and mobility. If this condition, at some bias, is no longer valid, the applied diode voltage will begin to drop over the low-conductivity p-type region, causing band bending and increased electron spillover into that region. This has been proposed as an explanation for efficiency droop in GaInN LEDs (Meyaard *et al.*, 2011; Lin *et al.*, 2012).

Droop has been shown to increase dramatically at cryogenic temperatures, corresponding to a significant freeze-out of the holes. Experimental evidence for this is shown in Fig. 9.7. At very low temperatures, SRH recombination is minimized, leading to high efficiency. Due to the high activation energy of holes, the asymmetry in carrier concentration is enhanced, leading to increased electron leakage.

First, we estimate the transition from the low-injection to the high-injection regime. This occurs when the resistance of the depletion region ($R_{\text{depletion}}$) is equal to the resistance of the p-type region ($R_{\text{p-type}}$). $R_{\text{p-type}} = L_{\text{p-layer}}/(e\ \mu_{\text{p}}\ p_{\text{p0}}\ A)$, where $L_{\text{p-layer}}$, e and A are the p-type layer thickness, the elementary charge and the junction area, respectively. An upper limit for the deletion layer resistance is approximately given by $R_{\text{Depletion}} \approx W_{\text{Depletion}}/(2e\ \Delta n_{\text{p}}(0)\ \mu_{\text{n}}\ A)$. Equating $R_{\text{p-type}}$ and $R_{\text{Depletion}}$ yields the following relation:

$$\Delta n_p(0)\mu_n \approx \frac{W_{\text{Depletion}}}{2L_{\text{p-layer}}} p_{p0}\mu_p \tag{9.7}$$

Using parameters typical for GaN, this equation is satisfied when $\Delta n_{\text{p}}(0)\mu_{\text{n}}$ is about 1% to 10% of $p_{\text{p0}}\mu_{\text{p}}$. Using this simple case as a guide for a typical GaInN/GaN LED, we expect that if there is significant asymmetry, such as in GaN, electron leakage into the p-type region is likely. Once electrons reach the p-type region, they will likely recombine non-radiatively.

Another way of describing the onset of high injection is that it occurs when the drift current in an LED becomes comparable to the diffusion current. In a GaInN heterojunction (or quantum well) LED, the thickness of the p-type GaN is

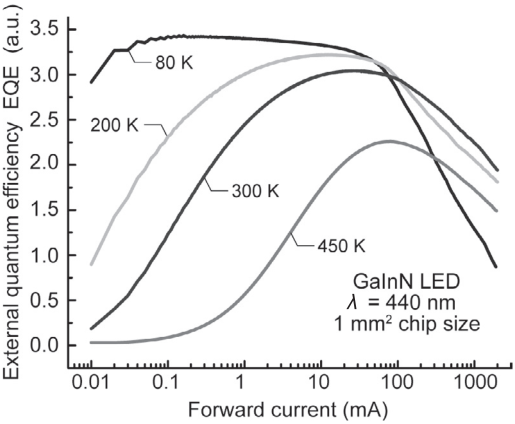

9.7 Measured external quantum efficiency of a GaInN LED for several temperatures ranging from 80 K to 450 K.

generally smaller than the electron diffusion length, so that the electron diffusion current leaking out of the active region of a heterojunction LED can be described as:

$$J_{\text{Diffusion}} = \frac{eD_n \Delta n_p(0)}{L_{\text{p-layer}}} \qquad [9.8]$$

where $L_{\text{p-layer}}$ is the thickness of the p-type layer and D_n is the electron diffusion coefficient for the p-type layer. As mentioned above, when the diode enters high-level injection, the applied diode voltage begins to drop over the p-type region, causing drift to occur. Using the Einstein relation, we can express the drift current at the edge of the p-type neutral region by:

$$J_{\text{Drift}} = e\mu_n \Delta n_p(0)E = eD_n \frac{e}{kT} \Delta n_p(0) \frac{J_{\text{total}}}{\sigma_p} \qquad [9.9]$$

where σ_p is the conductivity in the p-type layer. As the total current increases, so does the drift-induced leakage current. At some point, the drift current will become significant, and the injection efficiency into the LED's active region will be reduced. When this electric field develops, the I-V characteristics will deviate from the ideal exponential behavior, showing a series resistance. As seen in Fig. 9.8, it has indeed been found experimentally that the onset of droop occurs near the point of deviation of the experimental I-V curve from the ideal (exponential) I-V curve. The drift current is dependent on $\Delta n_p(0)$, which is expected to be low based on the low thermal excitation of carriers from quantum-well (QW) states and cladding-layer states. If n_{QW} is the electron concentration in the active region, then

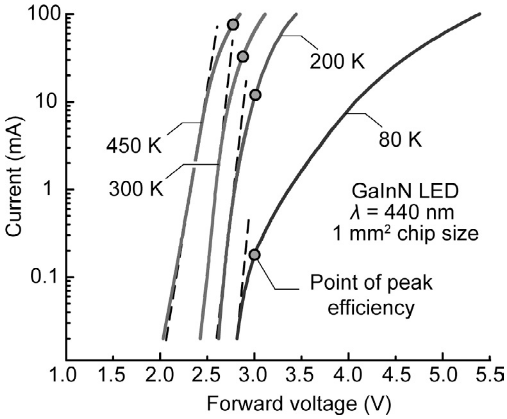

9.8 Measured I-V on a logarithmic scale, showing the onset of high-level injection and series resistance as well as the current at which the efficiency is maximal.

$\Delta n_p(0) = n_{\text{QW}} \exp\left(\frac{\Delta E_{\text{barrier}}}{kT}\right)$. The estimated $\Delta E_{\text{barrier}}$ of about 300 meV is quite high so that one may conclude that $\Delta n_p(0)$ would be insignificant. However, electrons typically have higher thermal energy than the lattice thermal energy, so if the lattice is at room temperature (300 K), it is expected that the electron temperature can be much higher than 300 K. This has indeed been observed by extracting the high energy slope of a GaInN/GaN LED optical emission spectrum under pulsed measurement conditions, which shows a carrier temperature 125 K higher than the lattice temperature (Lin *et al.*, 2012). Another factor for overcoming this barrier is the tunneling effect. In general, due to the participation of defects, experimental tunneling currents are larger than calculated tunneling currents. Finally the polarization fields in the device presumably play a significant role in lowering the energy barrier for electron escape. The polarization fields will be discussed in greater detail in the next section. For a comprehensive analytic discussion of electron leakage in the high-injection regime, the reader is referred to Lin *et al.* (2012).

As in GaN-based LEDs, droop has also been observed in LEDs made from the AlGaInP material system, particularly at cryogenic temperatures (Shim *et al.*, 2012). Poor hole concentration and poor hole mobility affect AlGaInP as well, yet, due to the smaller difference in electron and hole mobility, to a lesser degree than GaN. This explains why droop in AlGaInP-based LEDs is only observed at very low temperatures (Shim *et al.*, 2012).

9.6 Non-capture of carriers

There are several ways for electrons to reach the p-type region; one mechanism is electron leakage enhanced by carrier asymmetry or polarization fields. Another possibility is that the carriers are never captured by the active region. For a carrier to fall into a quantum well, it must emit an optical phonon or undergo an acoustic-phonon-mediated or impurity-mediated scattering event in order to lose its energy. If such carrier-phonon interaction does not occur, the carrier energy will remain high, and the carrier could, without falling into the quantum well, be carried into the p-type region by the polarization electric fields occurring in GaN and related materials. The transport of electrons without losing energy by phonon emission is known as ballistic transport. Quasi-ballistic transport occurs when the carrier interacts with one or more phonons but still does not lose enough energy to fall into a quantum well in the active region. This effect is illustrated in Fig. 9.9, where, due to band bending or polarization charges, the carrier needs to lose even more energy in order to be captured.

Although ballistic transport is a well-known phenomenon in electronic devices such as high-electron-mobility transistors, this phenomenon is not usually considered in LEDs. Typical commercially available LED simulation programs do not include ballistic transport and, thus, do not include non-capture in their physical foundation.

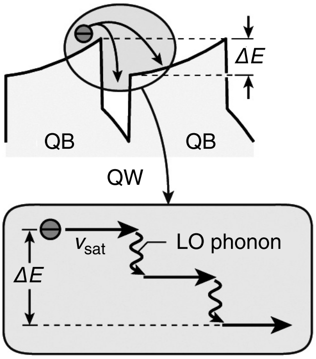

9.9 Non-capture of electron by QW and capture of electron into QW by emission of phonons. (LO: longitudinal optical)

9.7 Polarization fields

GaInN/GaN LEDs are typically grown on c-plane (0001) sapphire substrates by metal-organic vapor-phase epitaxy. In this plane, a significant spontaneous and piezoelectric polarization sheet charge exists. III-V nitrides have wurtzite crystal structure, with a basal hexagonal edge length *a* and a hexagonal prism height of *c*. The physical geometry of the lattice in the equilibrium atomic structure does not form a perfect tetrahedron, thereby causing spontaneous polarization in the direction of the c-plane surface-normal vector (Feneberg *et al.*, 2006). Piezoelectric polarization occurs when mechanical stress is added to the system, for example, by growing a lattice mismatched material, such as GaInN, on top of GaN. In LEDs, this mismatch occurs in both the GaInN QWs and the AlGaN electron blocking layer. This effect causes some amount of bound charge to appear at every heterointerface, causing band bending. The interface between the QW and quantum barrier (QB) on the p-side features a positive sheet charge, attracting electrons and lowering the conduction band edge. The interface between the QW and QB on the n-side has a negative sheet charge, attracting holes and raising the valence band edge. The band bending causes the quantum barriers to become triangular in shape, making carrier non-capture even more likely to occur, as well as making the QBs and EBL easier for carriers to overcome. This is illustrated in the simulated band diagram shown in Fig. 9.10. Due to the asymmetry in hole concentration, it has been shown that most of the recombinations in an LED occur in the QW closest to the p-type region (the last-grown QW). The positive sheet charge at the spacer/EBL interface pulls electrons away from and out of the last-grown QW.

9.8 Carrier delocalization

If GaInN were a random alloy, the gallium and indium atoms would be randomly distributed on the group-III lattice sites of the wurtzite crystal leading to regions

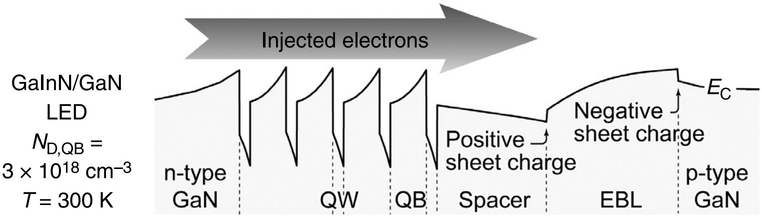

9.10 Simulated conduction-band diagram of a GaInN/GaN LED. Due to the positive space charge at the spacer/EBL interface, the electric field in the spacer layer makes electrons drift away from the QWs.

that are indium-rich or gallium-rich. The regions that have a high indium concentration have a lower bandgap energy, so carriers would tend to stay in these regions. Conversely, gallium-rich regions have a higher bandgap energy, repelling carriers.

In addition to random alloy fluctuations, additional indium fluctuations, indium clustering effects, have been described in the literature (Chichibu *et al.*, 1996, 2006; Mukai *et al.*, 1999). These indium clustering effects have been attributed to phase separation and spinodal decomposition. Micro-luminescence measurements have revealed non-uniform light emission, providing support for this claim. However, the non-uniformity could come from either random alloy variations or actual indium clustering effects. Three-dimensional atom probing experiments have produced spatially resolved maps of indium concentration. Although several groups have performed this experiment, it is still an open question whether these variations in indium are more significant than just random alloy fluctuations. Some reports show no statistically significant clustering of indium, diminishing the prospects for delocalization as the cause of droop (Galtrey *et al.*, 2007).

As stated above, carriers prefer to stay in regions of low energy, and thus regions of high indium content. Such localization of carriers prevents carriers from diffusing to regions where they may recombine non-radiatively through a defect or dislocation; this is illustrated in Fig. 9.11. At high carrier densities, it has been suggested that the small fluctuations are no longer sufficient to prevent carriers from reaching non-radiative recombination centers. However, this model suggests that as the dislocation density decreases, the efficiency droop also decreases. In experiments, the opposite trend is found: when the dislocation density is low, efficiency droop increases (Schubert *et al.*, 2007).

Density-activated defect recombination has been proposed as the primary cause for droop (Hader *et al.*, 2011). This model is somewhat similar to carrier delocalization, but with some differences. In this model, there are two types of non-radiative recombination centers: one homogeneously distributed in the QWs and the other separated by potential barriers. The centers homogeneously distributed are assumed to have a low recombination lifetime, of the order of tens

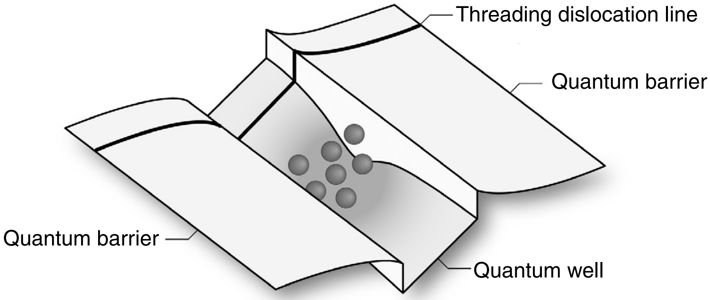

9.11 Electrons localized in a low-energy indium-rich domain of a GaInN quantum well. It has been postulated that the low-energy regions attract electrons and keep them from reaching non-radiative centers such as dislocation lines.

of nanoseconds. The other recombination centers are assumed to have much faster recombination lifetimes (of the order of 1 ns), but they only affect carrier recombination above a specific carrier density, when the carriers can overcome the potential barriers.

9.9 Discussion and comparison of droop mechanisms

Of the proposed mechanisms summarized above, although temperature effects can reduce the efficiency, they are certainly not the primary cause for efficiency droop.

Auger recombination has many factors that lessen the likelihood of its relevance for efficiency droop. This includes the small predicted theoretical Auger C coefficient, compared to the much larger experimental C coefficients. Auger recombination can be significant in small bandgap semiconductors, but is expected to have a small role in GaInN/GaN LEDs. The asymmetry of curves of experimental EQE versus n remains unexplained by any of the Auger models.

Indium fluctuations may cause a minor wavelength shift in LEDs, but they are unlikely to be the primary reason for the efficiency droop. A fundamental problem for this model remains that the efficiency droop does not decrease when the dislocation density is reduced.

The asymmetry of carrier transport properties and poor injection of holes are likely to play a significant role in causing the efficiency droop. These effects lead to electron spillover at high current densities, reducing the efficiency of a device. The strong asymmetry in electron and hole transport properties is a key difference between GaInN and other LED material systems. Furthermore, in support of this model, it has been shown that droop exists not only in the GaN material system but also in the AlGaInP material system, though at cryogenic temperatures. The effect of polarization fields may also be important in causing electron spillover, by reducing the current at which droop first occurs thereby exacerbating the droop problem.

9.10 Methods for overcoming droop

9.10.1 Good heat sinking

Good heat sinking is vital in high-power LEDs. Although thermal effects are not the primary cause of droop, heating effects can cause thermal roll-over and significantly reduce performance at high current densities. Good heat sinking also reduces non-radiative recombination in general, leading to improved performance at all currents. Flip-chip mounting or removing the growth substrate, e.g. with laser lift-off, can reduce the thermal resistance of an LED chip, making heat sinking more efficient.

9.10.2 Uniform current injection

Ensuring uniform current injection is another way to reduce the effect of droop in GaInN/GaN-based LEDs. This can be accomplished by ensuring good p-type and n-type conductivity in the neutral regions or changing the injection geometry of the LED. Lateral LEDs are still common for many applications, such as the backlights in LCD displays. Current through an LED will always take the path of least resistance, so if the n-type layer is resistive, current will crowd near the n-contact. This increases the current density locally, making the effects of droop more prominent. By creating a more conductive n-type current spreading layer, the current density is reduced, so that droop is relegated to a higher current. An example of LEDs with and without current crowding is shown in Fig. 9.12.

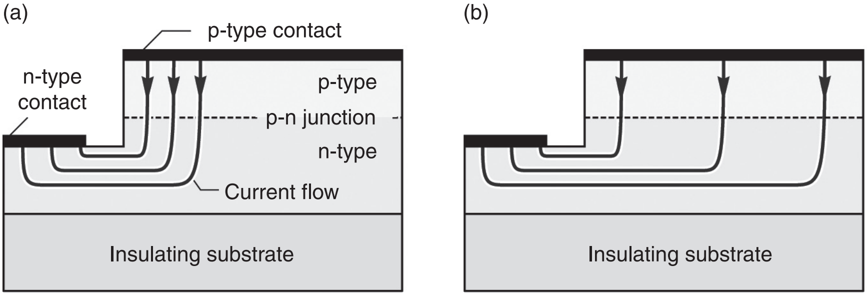

9.12 Lateral GaN-based LEDs grown on an insulating substrate (a) with and (b) without current crowding.

Another method of ensuring uniform current injection is to use laser lift-off to remove the sapphire substrate. This allows for contacts to be placed more uniformly over the n-type backside, creating a geometry where current flows vertically instead of laterally. Current crowding in this case is strongly reduced.

9.10.3 Larger LED chips

Simply making an LED chip larger results in a lower current density for a given optical output power. This means that the efficiency droop will be smaller at a given optical power. Figure 9.13(a) provides a clear picture of this: as the device area is increased, the current density is reduced, leading to less efficiency droop. Figure 9.13(b) shows the effect of adding more quantum wells to the active region.

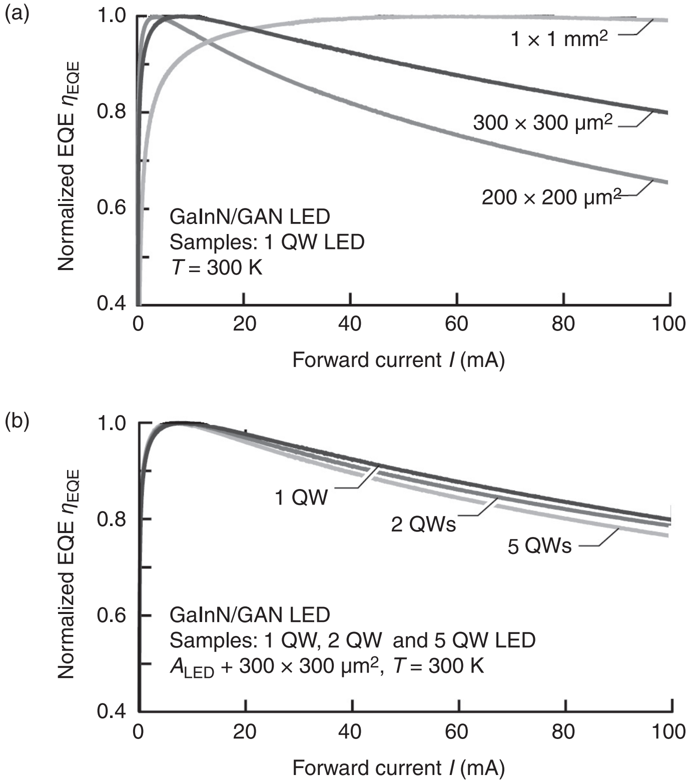

9.13 (a) External quantum efficiency (EQE) versus current for devices with different chip areas. (b) EQE versus current for devices with one, two or five quantum wells (after Zhu, 2011).

As previously mentioned, recombination occurs mostly in the quantum well closest to the p-side, and additional quantum wells do not change this fact. They may, however, affect other aspects of the device, such as the quality of the active region or strain.

9.10.4 Polarization matching

Polarization matching can make a large difference to the carrier dynamics in an LED. Because the polarization charge can increase carrier non-capture and carrier escape from the active region, there is strong motivation to reduce or eliminate the polarization fields. One method for eliminating the polarization fields is to grow the LED on a non-polar substrate. Although GaN grown on c-plane sapphire has strong polarization fields, other substrate-orientation options include the semi-polar and non-polar GaN bulk substrates. Examples of semi- and non-polar GaN include *m*-plane (1100) and *a*-plane (1120) GaN. These GaN substrates can be sliced from thicker GaN bulk material and are certainly more expensive. It has been shown that LEDs grown on non-polar substrates have significantly reduced efficiency droop. However, growth on non-polar substrates is typically more difficult than growth in the c-direction, resulting in narrower growth windows for producing high-quality LEDs. Another way to reduce the polarization fields in a GaN-based LED is to grow alloys, including quaternary alloys, that are lattice-matched and polarization-matched to the layer beneath them (Schubert *et al.*, 2008). This may include ternary or quaternary AlGaInN layers. By using AlGaInN as the quantum barrier instead of GaN, the same energy bandgap can be maintained while preventing any lattice mismatch. The same quaternary material system can be used to create an EBL with reduced lattice mismatch, rather than growing a lattice-mismatched AlGaN EBL. To reduce droop, appropriate compositions of $Al_xGa_{1-x-y}In_yN$ need to be selected, with both an appropriate bandgap and lattice constant (Kim *et al.*, 2007).

9.10.5 Tailored doping in the active region

Tailored doping in the active region is another method for reducing droop. Because of the poor hole transport characteristics, control of doping in the active region can help make recombination more uniform across all quantum wells. Quantum barriers are often n-type doped in order to improve device performance and reduce the shift in peak wavelength caused by screening the quantum-confined Stark effect (QCSE). By reducing, or eliminating this n-type doping, electron transport is hindered and hole transport may be improved, decreasing electron overflow. Some studies performed with p-type doping in the middle of a quantum barrier showed improved droop performance. Achieving p-type doping in the active region without deteriorating LED properties is difficult, however, because magnesium is a known luminescence killer.

Advanced electron blocking layers are sometimes used to reduce electron overflow and improve hole injection. Conventional EBLs are made out of AlGaN, but this material system has several problems, including, firstly, poor p-type doping characteristics. Secondly, the polarization charges hinder carrier confinement in the active layers. Several different methods can be used to improve these characteristics, such as using AlGaN/GaN superlattice EBLs to improve p-type doping and increase hole injection into the active region. Using a lattice-matched EBL can also improve performance by reducing electron leakage. Composition-graded EBLs can be used to improve hole transport and have little impact on electron transport. An example of this would be grading the aluminum content of an AlGaN EBL so that the barrier for holes becomes composition-graded, while maintaining the abrupt interface for electrons.

9.10.6 Thin quantum barriers

Thin quantum barriers can reduce the polarization field in a multiple quantum well (MQW) structure. For a periodic MQW structure, the following formula can be derived (Leroux *et al.*, 1999; Xu, 2011):

$$E_{\mathrm{QW}} = \sigma \frac{L_{\mathrm{QB}}}{\varepsilon_{\mathrm{QB}} L_{\mathrm{QW}} + \varepsilon_{\mathrm{QW}} L_{\mathrm{QB}}} \approx \frac{\sigma}{\varepsilon_r \varepsilon_0} \frac{L_{\mathrm{QB}}}{L_{\mathrm{QW}} + L_{\mathrm{QB}}}$$

where σ is the polarization-sheet-charge density occurring at the interfaces of the MQW structure, L_{QW} and L_{QB} are the thicknesses of the quantum well and quantum barrier, ε_{QW} and ε_{QB} are the dielectric constants of the quantum well and quantum barrier, ε_r is the relative dielectric constant of GaN ($\varepsilon_r = 8.9$) and ε_0 is the absolute dielectric constant. This formula illustrates how the electric field in a QW has a dependence on both the quantum well and quantum barrier thicknesses. For a single quantum well, $L_{\mathrm{QB}} \rightarrow \infty$, so the electric field in the quantum well is maximal. For this reason, even though recombination may take place mostly in the QW closest to the p-side, having a MQW structure clearly is advantageous over a single quantum well structure because it reduces the QCSE. Simply having thin barriers also reduces the electric field in the QWs, making radiative recombination more efficient. The reduction in the electric field also can reduce the probability of carrier non-capture by the active region. By making the barriers thin enough, carriers may be able to tunnel through the QBs instead of being transported over them. This reduces the likelihood of carrier escape from non-capture by a well, because carriers are more likely to propagate and stay at lower energy QW states. That is, electrons, rather than being transported over the thick barriers, propagate through the thin barriers by tunneling, thereby reducing the likelihood of non-capture. State-of-the-art GaInN MQW LEDs do in fact use thin quantum barriers, of the order of 3–5 nm, whereas traditional quantum barriers were much thicker, of the order of 8–12 nm.

9.10.7 Strain control

Strain control is important for GaInN/GaN LEDs. By growing GaInN underlayers, it is possible to alleviate the strain caused by the lattice mismatch in the active region. This reduces the QCSE, improves carrier capture and reduces electron leakage. Reducing this strain allows thicker QWs to be grown, improves carrier capture and reduces efficiency droop.

9.10.8 Increasing p-type doping

Increasing p-type doping is vital for decreasing the asymmetry in an GaInN/GaN LED in order to reduce efficiency droop. This is especially important for the EBL. If the doping is too high, however, defects may be generated in the p-type material, leading to an increase in non-radiative recombination. Very high doping concentrations ($N_A > 10^{19}\,\text{cm}^{-3}$) are known to create point defects, thereby decreasing the radiative efficiency in the LED. Other methods to increase the whole concentration are being explored, such as co-doping. An EBL having a superlattice structure can also help to improve the hole concentration and lead to less droop.

9.10.9 Unique active layer engineering

Unique active layer engineering can potentially improve LED performance. By changing the band profiles of the QWs, the QCSE can be minimized, leading to less droop. This could be done using a stepwise compositional grading of the structure to reduce the energy of carriers entering the well, thus reducing carrier non-capture. It could also be done using a graded growth-temperature profile (Zhao *et al.*, 2009).

9.10.10 Double heterostructure

Double heterostructure LEDs and LEDs with thicker QWs have been proposed as a solution to droop. Because recombination at high injection has a strong Cn^3 and Dn^4 dependence (Lin *et al.*, 2012), doubling the QW thickness reduces the Cn^3 recombination term by a factor of eight. Initial experiments indeed show higher light output at high currents for LEDs with thicker QWs compared to conventional LEDs (Gardner *et al.*, 2007). Since the efficiency droop is generally agreed to be a high-density effect, increasing the thickness of the quantum wells will reduce the carrier concentration and the efficiency droop, irrespective of the physical origin of the droop.

9.11 References

Bertazzi F., Goano M. and Bellotti E. ‘A numerical study of Auger recombination in bulk InGaN,’ *Applied Physics Letters* **97**, 231118 (2010).

Brendel M., Kruse A., Jönen H., Hoffmann L., Bremers H., *et al.* 'Auger recombination in GaInN/GaN quantum well laser structures,' *Applied Physics Letters* **99**, 031106 (2011).

Chichibu S., Azuhata T., Sota T. and Nakamura S. 'Spontaneous emission of localized excitons in InGaN single and multiquantum well structures,' *Applied Physics Letters* **69**, 30 (1996).

Chichibu S. F., Uedono A., Onuma T., Haskell B. A., Chakraborty A., *et al.* 'Origin of defect-insensitive emission probability in In-containing (Al, In, Ga)N alloy semiconductors,' *Nature Materials* **5**, 810 (2006).

Dai Q., Shan Q., Cho J., Schubert E. F., Crawford M. H., *et al.* 'On the symmetry of efficiency-versus-carrier-concentration curves in GaInN/GaN light-emitting diodes and relation to droop-causing mechanisms,' *Applied Physics Letters* **98**, 033506 (2011).

David A and Grundmann M. J. 'Droop in InGaN light-emitting diodes: A differential carrier lifetime analysis,' *Applied Physics Letters* **96**, 10, 103504-103504 (2010).

Delaney K. T., Rinke P. and Van de Walle C. G. 'Auger recombination rates in nitrides from first principles,' *Applied Physics Letters* **94**, 191109 (2009).

Feneberg M., *et al.* 'Piezoelectric fields in GaInN/GaN quantum wells on different crystal facets,' *Applied Physics Letters* **89**, 242112 (2006).

Galtrey M. J., Oliver R. A., Kappers M. J., Humphreys C. J., Stokes D. J., *et al.* 'Three-dimensional atom probe studies of an $In_xGa_{1-x}N$/GaN multiple quantum well structure: assessment of possible indium clustering,' *Applied Physics Letters* **90**, 061903 (2007).

Gardner N. F., Müller G. O., Shen Y. C., Chen G., Watanabe S., *et al.* 'Blue-emitting InGaN-GaN double-heterostructure light-emitting diodes reaching maximum quantum efficiency above 200 A/cm^2,' *Applied Physics Letters* **91**, 243506 (2007).

Hader J., Moloney J. V., Pasenow B., Koch S. W., Sabathil M., *et al.* 'On the importance of radiative and Auger losses in GaN-based quantum wells,' *Applied Physics Letters* **92**, 261103 (2008).

Hader J., Moloney J. V. and Koch S. W. 'Temperature-dependence of the internal efficiency droop in GaN-based diodes,' *Applied Physics Letters* **99**, 181127 (2011).

Kim M.-H., Schubert M. F., Dai Q., Kim J. K., Schubert E. F., *et al.* 'Origin of efficiency droop in GaN-based light-emitting diodes,' *Applied Physics Letters* **91**, 183507 (2007).

Kioupakis E., Rinke P., Delaney K. T. and Van de Walle C. G. 'Indirect Auger recombination as a cause of efficiency droop in nitride light-emitting diodes,' *Applied Physics Letters* **98**, 161107 (2011).

Kish F. A., DeFevere D. A., Vanderwater D. A., Trott G. R., Weiss R. J., *et al.* 'High luminous flux semiconductor wafer-bonded AlGaInP/GaP large-area emitters,' *Electronics Letters* **30**, 1790 (1994).

Leroux M., Grandjean N., Massies J., Gil B., Lefebvre P., *et al.* 'Barrier-width dependence of group-III nitrides quantum-well transition energies,' *Physical Review B* **60**, 1496 (1999).

Lin G.-B., Meyaard D. S., Cho J., Schubert E. F., Shim, H., *et al.* 'Analytic model for the efficiency droop in semiconductors with asymmetric carrier-transport properties based on drift-induced reduction of injection efficiency,' *Applied Physics Letters* **100**, 161106 (2012).

Meyaard D. S., Lin G.-B., Shan Q., Cho J., Schubert E. F., *et al.* 'Asymmetry of carrier transport leading to efficiency droop in GaInN based light-emitting diodes,' *Applied Physics Letters* **99**, 251115 (2011).

Mukai T., Yamada M. and Nakamura S. 'Characteristics of InGaN-based UV/blue/green/amber/red light-emitting diodes,' *Japanese Journal of Applied Physics* **38**, 3976 (1999).

Ryu H.-Y., Kim H.-S. and Shim J.-I. ‘Rate equation analysis of efficiency droop in InGaN light-emitting diodes,’ *Applied Physics Letters* **95**, 081114 (2009).

Schubert M. F., Chhajed S., Kim J. K., Schubert E. F., Koleske D. D., *et al.* ‘Effect of dislocation density on efficiency droop in GaInN/GaN light-emitting diodes,’ *Applied Physics Letters* **91**, 231114 (2007).

Schubert M. F., Xu J., Kim J. K., Schubert E. F., Kim M. H., *et al.* ‘Polarization-matched GaInN/AlGaInN multi-quantum-well light-emitting diodes with reduced efficiency droop,’ *Applied Physics Letters* **93**, 041102 (2008).

Schubert M. F., Xu J., Dai Q., Mont F. W., Kim J. K., *et al.* ‘On resonant optical excitation and carrier escape in GaInN/GaN quantum wells,’ *Applied Physics Letters* **94**, 081114 (2009).

Shen Y. C., Mueller G. O., Watanabe S., Gardner N. F., Munkholm A., *et al.* ‘Auger recombination in InGaN measured by photoluminescence,’ *Applied Physics Letters* **91**, 141101 (2007).

Shim J.-I., Han D.-P., Kim H., Shin D.-S., Lin G.-B., *et al.* ‘Efficiency droop in AlGaInP and GaInN light-emitting diodes,’ *Applied Physics Letters* **100**, 111106 (2012).

Xu J. ‘Efficiency and carrier transport in polarization-matched GaInN-based light-emitting diodes,’ dissertation, Rensselaer Polytechnic Institute, Troy, NY (2011).

Zhang M., Bhattacharya P., Singh J. and Hinckley J. ‘Direct measurement of Auger recombination in $In_{0.1}Ga_{0.9}N$/GaN quantum wells and its impact on the efficiency of $In_{0.1}Ga_{0.9}N$/GaN multiple quantum well light emitting diodes,’ *Applied Physics Letters* **95**, 201108 (2009).

Zhao H., Liu G., Li X.-H., Huang G. S., Poplawsky J. D., *et al.* ‘Growths of staggered InGaN quantum wells light-emitting diodes emitting at 520–525 nm employing graded growth-temperature profile,’ *Applied Physics Letters* **95**, 061104 (2009).

Zhu D. ‘Investigating and optimizing carrier transport, carrier distribution, and efficiency droop in GaN-based light-emitting diodes,’ dissertation, Rensselaer Polytechnic Institute, Troy, NY (2011).

10

Photonic crystal nitride LEDs

M. D. B. CHARLTON, University of Southampton, UK

DOI: 10.1533/9780857099303.2.301

Abstract: This chapter discusses the use of nanoscale surface texturing to improve the wall-plug efficiency of LEDs. We describe the use of photonic crystal surface texturing to improve efficiency by improving light extraction and controlling far-field beam shape. We discuss the underlying physical mechanisms and how to model light extraction and beam-shaping accurately using finite difference time domain (FDTD) methods. Attainable performance enhancement figures for the most common varieties of LEDs are given. The benefits of using high-dimensional lattice arrangements known as photonic quasi-crystals over conventional photonic crystal lattice arrangements are discussed. Finally we give an overview of common methods for mass-producing photonic crystal patterned LEDs and their limitations.

Key words: light-emitting diode (LED), photonic crystal (PC), photonic quasi-crystal (PQC), surface-patterned LED, patterned sapphire substrate (PSS), far-field beam profile, light extraction, beam-shaping, beam-steering, solar cell.

10.1 Introduction

In view of raised global awareness of the depletion of non-renewable energy sources and the associated impact on the environment, there is intense interest and highly focused efforts to develop green, renewable energy technologies and to increase the wall-plug efficiency of existing technologies where possible. Approximately 19% of the world's energy consumption is currently attributed to lighting. Present lighting technologies include incandescent lamps, fluorescent lamps, light-emitting diodes (LEDs) and organic light-emitting diodes (OLEDs). Various factors affect wall-plug efficiency.

10.1.1 Epitaxial materials

LEDs are based on a semiconductor heterostructure grown on a planar substrate. On application of a voltage across the heterostructure, electron-hole pairs (excitons) are generated in the junction regions of the epitaxial heterostructure, which then recombine after a short time delay (known as the relaxation time) generating a photon with energy equal to the electronic band gap energy associated with the heterostructure.

LEDs can be fabricated from a number of different semiconductor materials. Due to the dependence upon the intrinsic band gap energy, the wavelength of emission is primarily related to the choice of this material. Common epitaxial materials for conventional LEDs include: InGaN/GaN for blue, GaIn/GaN for green, AlGa/InP for red and InGaAsP/InP for infrared LEDs. To some degree, the wavelength of emission can be adjusted by inducing and controlling the strain in the epitaxial heterostructure, since this induces a change in relative energy levels of the band structure either side of the junction region. This technique has, for example, been employed in GaN-based LEDs to obtain green emission whereas the natural band gap energy would lie in the blue part of the spectrum.

Factors affecting internal quantum efficiency (IQE)

In a conventional LED, radiative emission resulting from recombination of exciton pairs in the multiple quantum well (MQW) layers must be maximised. This is achieved by optimising the internal quantum efficiency (IQE) of the epitaxy structure. IQE is therefore a measure of the efficiency of conversion of electrons to photons. To obtain high IQE, the epitaxial heterostructure must be substantially monocrystalline and have a low epitaxial defect density. Other factors affecting electrical efficiency include the layout and resistivity of the electrical contacts, and any change in strain due to localised heating of the layers, which in turn is dependent upon methods of heat extraction.

Base substrate material

In order to reduce the defect density the epitaxial layers must have a lattice constant that is well matched to that of the underlying substrate material. This determines the choice of underlying substrate. Sapphire is very well matched to GaN and so is the substrate of choice. However, sapphire is electrically insulating, is not a good heat conductor and is expensive to produce. Requirements for substrate materials place constraints on LED design and cost. Considerable efforts have been made to relieve substrate-dependent growth issues resulting in a variety of LED epitaxial configurations.

10.1.2 Types of LED

LEDs have evolved over the years into a variety of types, which can be grouped according to the epitaxial substrate structure.

P-side up lateral current spreading LEDs

The most conventional LED design, which is often used for blue GaN LEDs, is the P-side up lateral current spreading design (Fig. 10.1). This comprises a GaN

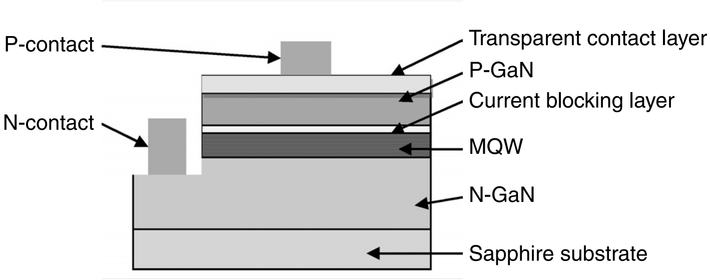

10.1 P-side up lateral current spreading LED.

layer grown directly onto a sapphire substrate with the N-doped layer at the bottom of the stack and P-doped layer at the top. Since sapphire is electrically insulating, the backside (N) contact must be off to the side of the LED, meaning that the injected current must spread to the sides of the contact (via the N-doped layer), hence the name – lateral current spreading design.

A thick undoped seed layer is first deposited onto the substrate to improve lattice matching to the sapphire. After some distance, the growth conditions are changed to create successive N- and P-doped layers with multiple quantum wells sandwiched in-between to form the junction regions. The N-doped layer is usually thick due to the need for efficient lateral current spreading from the side contact.

As the conductivity of the top P-side layer is relatively poor, an additional transparent conductive layer (TCL) is deposited on top of the device to improve electrical conductivity and allow uniform charge injection to the top P-GaN layer. The TCL material of choice is indium tin oxide (ITO); however, ITO is far from perfectly transparent, hence the TCL introduces optical and electrical losses through light-trapping and increased resistivity. ITO also degrades through absorption of moisture, so the overall device must be encapsulated in silicon dioxide with windows for the electrical contacts.

Non-transparent metal contact stacks are then deposited onto the TCL. The current spreads laterally via the contacts and TCL to the P-type layer. The top contact arrangement for P-side up LEDs is non-ideal since the non-transparent contacts mask part of the light-emitting area reducing the efficiency of the device.

Sapphire (which is well lattice matched to GaN) is a poor heat conductor. P-side up devices suffer reduced lifetimes if driven at the very high current densities required for general lighting applications. The need for a thin optically transparent top current spreading layer also places constraints on the achievable contact resistance, and therefore on electrical efficiency of the device.

Finally, the underlying sapphire substrate is often thinned by chemical mechanical polishing (CMP) and a reflective metal layer applied to the underside to reflect more of the light out of the top of the LED.

N-side up LEDs

A much more sophisticated configuration, which is used for high-power blue LEDs, is known as the vertical current spreading design. This overcomes lattice mismatch issues and provides improved heat extraction and reduced electrical contact resistance, but at the expense of complex fabrication. Figure 10.2 shows an N-side up vertical current spreading LED.

In this case the epitaxial layers are initially grown on a sacrificial sapphire substrate (similar to a conventional P-side up LED), but once grown, the P-side of the epistructure is bonded onto a highly conductive silicon or metallic (usually copper) carrier substrate. It is then released from the sacrificial growth substrate by laser lift-off. Finally, CMP is used to thin down the top surface of the N-GaN layer.

In this configuration, electrical injection to the MQWs is via the silicon or metal substrate and the underlying P-GaN layer, across the MQWs to the highly conductive N-GaN layer. In this case, as the entire substrate acts as the back contact, current is spread uniformly across the entire area of the P-GaN and travels vertically through the epitaxial layer stack, hence the configuration is known as vertical current spreading.

A key advantage of this configuration is that the epilayers can be grown much more thinly, which is important for light extraction. As the silicon or metal substrate has high thermal conductivity, heat extraction is much more efficient. In addition the metal interface layer between the substrate and GaN provides a highly reflective mirror, greatly improving light extraction efficiency by radiating light initially emitted towards the substrate (which would otherwise be absorbed by the substrate in a P-side up GaN on sapphire LED), back towards the surface. The best (vertical) GaN-based LEDs achieve an internal quantum efficiency of 80%.[1]

Patterned substrate LEDs

Another method for improving light extraction efficiency is to grow the epitaxial layers over patterned substrates. In this case, the underlying sapphire growth

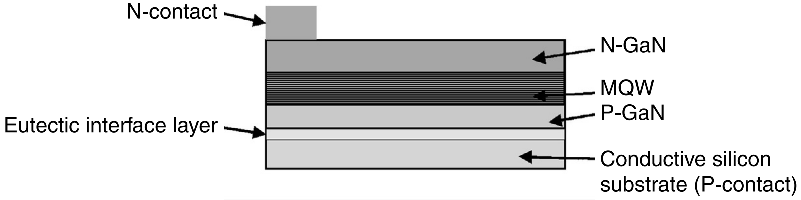

10.2 N-side up vertical current spreading LED.

substrate is pre-patterned with arrays of truncated cones, straight-sided pillars or curved structures by photolithography and chemical etching. The initial epitaxial growth position is pre-seeded by the pattern arrangement. Epitaxial strain can be relaxed at the substrate/semiconductor interface. The main benefit of the underlying patterning is to scatter light, which would otherwise be absorbed by the substrate, back in the vertical direction.

10.1.3 Light-trapping in LEDs

One of the limiting factors for LED efficiency is the issue of light being trapped inside the epitaxial heterostructure. At a smooth GaN/air interface the critical angle for total internal reflection (TIR), α_c, is given by:

$$\alpha_c = \sin^{-1}\left(\frac{n_1}{n_{GaN}}\right) \qquad [10.1]$$

Hence, α_c is just 24.1°. Although light is initially emitted in all directions by dipoles in the quantum wells (e.g. over a spherical solid angle of 4π steradians) only light emitted within a reduced solid angle given by a cone with an apex angle of 24.1° has any possibility of escaping (Fig. 10.3).

By calculating the ratio of the solid angle of the escape cone to the solid angle of emission given by:

$$(1-\cos(\alpha_c))/2 \qquad [10.2]$$

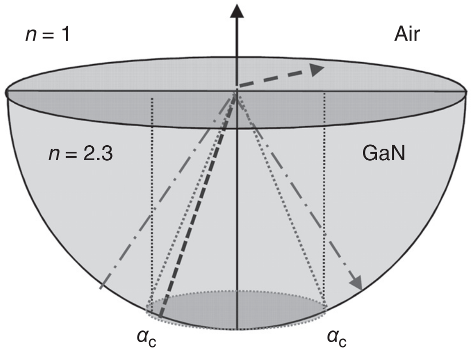

10.3 Light extraction cone. Dotted lines indicate the critical angle for total internal reflection and define the angular extent of the light extraction cone. The thick black dashed line is an example of a ray emitted within the extraction cone. It is refracted at the top surface and radiated at a glancing angle from the surface. The dash-dot line indicates a ray emitted at an angle above the critical angle. It is reflected at the top interface and trapped in the device.

we can calculate the percentage of light that has any chance of escaping. We find that at a GaN/air boundary only about 4.4% of the total light emitted has any possibility of escaping directly from the LED surface. The remaining light is reflected back and recycled within the LED heterostructure and substrate layers.

Light emitted within the light extraction cone is subject to Fresnel reflection loss at the GaN/air interface. Fresnel loss is highly dependent on angle of incidence (α) to the boundary and the polarisation state with respect to the plane of incidence to the boundary. Amplitude reflection coefficients for the S and P polarisation states are given by Eq. 10.3 below. The intensity reflection coefficients are given simply by the squares of these equations.

$$\rho_{\perp} = \frac{\cos\alpha - \sqrt{\left(\frac{n_2}{n_1}\right)^2 - \sin^2\alpha}}{\cos\alpha + \sqrt{\left(\frac{n_2}{n_1}\right)^2 - \sin^2\alpha}} \qquad \rho_{//} = \frac{\sqrt{\left(\frac{n_2}{n_1}\right)^2 - \sin^2\alpha} - \left(\frac{n_2}{n_1}\right)^2 \cos\alpha}{\sqrt{\left(\frac{n_2}{n_1}\right)^2 - \sin^2\alpha} + \left(\frac{n_2}{n_1}\right)^2 \cos\alpha} \qquad [10.3]$$

Substituting refractive index values into Eq. 10.3, we find that Fresnel loss increases from a minimum value of 18% at normal incidence to the interface to 100% at perpendicular incidence (along the boundary).

Taking all of this into account and assuming a random polarisation of emitted light, overall only around 3.4% of light emitted from the quantum wells is emitted immediately from the surface of a smooth unencapsulated LED. We must also remember that half the light emitted from the quantum wells radiates downwards towards the substrate. At the GaN/sapphire substrate boundary the critical angle is 46.6° and about 14.4% of emitted light becomes coupled into the substrate and is lost. The remainder of the light (82%) remains trapped inside the GaN layer (Fig. 10.4).

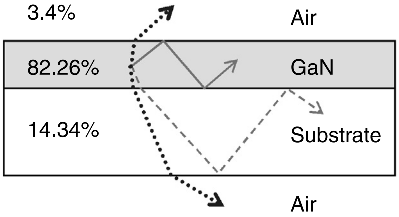

10.4 Example ray paths inside an LED. The dotted line is for a ray radiating incident to the boundaries at angles above the critical angles. The dashed line shows a ray trapped in the substrate layer. The solid line shows a ray trapped in the GaN layer. The percentages are for the optical power trapped in the GaN and substrate layers, and radiated to air.

Of course, some of the trapped light reflected back into the epitaxial layers is scattered from epitaxial defect sites to an angle lying within the allowed extraction cone. Some of the recycled light is also emitted from the edges of the LED chip so the actual light extraction figure will be slightly higher.

We can now appreciate that due to the relatively high refractive index of LED semiconductor materials combined with the fact that light is generated deep within the epitaxial structure, Fresnel reflection at the semiconductor/air interface causes confinement of a large proportion of the radiated energy. Hence, most of the light generated in the structure gets recycled internally. This factor severely limits the wall-plug efficiency for conventional LEDs. We can see from Fig. 10.4 that a small increase in critical angle for TIR can greatly increase the amount of light radiated from the LED. To improve wall-plug efficiency we need to defeat two key light-trapping processes: light recycling due to the small critical angle for total internal reflection and the Fresnel loss.

Radiometry and discussion of solid angle

We now take a closer look at the light recycling problem in relation to the direction of light emission from the quantum wells. Consider a radiative dipole positioned on one of the quantum wells inside an LED. If for the moment we take a simple 2D cross section through an LED structure then this dipole radiates over a flat 360° disc of angles. Light radiated at angles up to the critical angle for total internal reflection is radiated from the top surface; however, it is also refracted at the GaN/air interface. Due to refraction, light emitted at the critical angle for total internal reflection is actually emitted from the top of the LED in a direction parallel to the interface (e.g. at a glancing angle along the surface). Only light emitted at angles up to the critical angle for TIR actually contributes to the radiated power. For a simple unroughened smooth-surface LED, there is a direct relation between the direction of light emission within the LED and the angle at which it emerges from the top surface. Ignoring Fresnel reflection for the moment, in this simplified case there is an equal contribution to radiated power for all angles of emission from the radiative dipole up to the critical angle for total internal reflection.

However, if we now consider that in reality light is actually emitted from the dipole into a 3D solid angle, the contribution to total radiative power is no longer equal for all angles of emission up to the critical angle. Intuitively you might expect that most of the power radiated from the LED would have originated from light initially emitted at (or close to) normal incidence to the boundary, and you might expect the contribution to emitted power from rays emitted at the critical angle (which are radiated from the surface at a glancing angle nearly parallel to the boundary) to be far less than the contribution from those rays emitted at normal incidence.

However, in reality the situation is exactly the opposite way around.

Figure 10.5 plots the (relative) solid angle (equivalent to radiative surface area) subtended by a 1° wide annular extraction ring (the shaded annular surface area A in Fig. 10.6) as a function of launch angle (β) measured with respect to the surface normal. This is equivalent to the total power radiated from the dipole within a 1° angle, at a predetermined azimuth angle. We see from Fig. 10.5 that as the launch angle (β) increases from normal incidence (0°) to perpendicular to the interface (90°), the relative solid area subtended increases from 0 to 100. As a Lambertian source radiates equal power in all directions (i.e. uniform illumination per solid angle), this means that more optical power is actually emitted within a 1° annular ring at glancing angles (β=90°) than within a 1° ring close to normal incidence (β=0°), as the solid angle (corresponding to the relative area of a sphere) subtended is not actually the same in both cases, but in fact is very much larger at glancing angles.

This illustrates that in order to improve light extraction efficiency it is more useful to try to redirect rays of light initially emitted from the quantum wells at large angles to the normal that radiate nearly parallel to the interface (dotted ray in Fig. 10.7) rather than rays emitted at shallow angles to the normal that radiate nearly perpendicular to the boundary (dash-dot ray in Fig. 10.7).

Alternatively, increasing the critical angle for total internal reflection by even a small amount will increase the total emitted power from the LED by a large amount. Hence strategies that slightly shift the critical angle for total internal

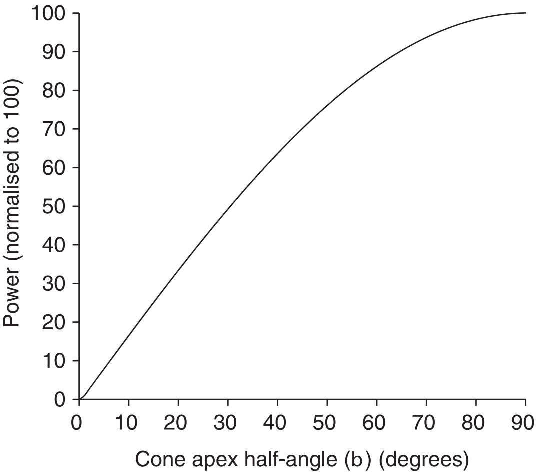

10.5 Relative power emitted into a 1° annular emission cone as a function of cone apex (polar) half-angle. 0° corresponds to emission in a vertical direction perpendicular to the top surface of the LED in which case there is no radial (sideways) emission. 90° corresponds to emission parallel to the surface of the LED (sideways). For non-zero polar cone angles, the LED emits power uniformly in all radial (azimuth) directions.

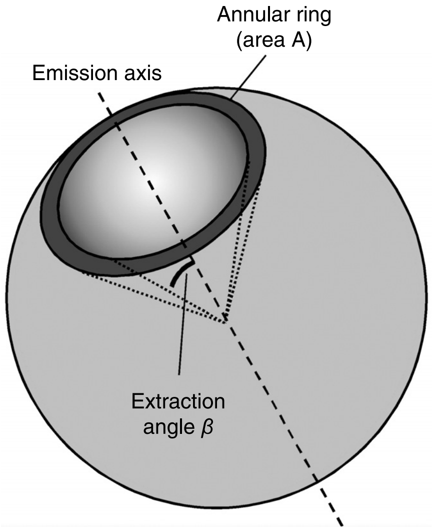

10.6 Annular emission cone and polar angle (*β*).

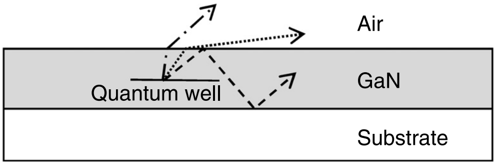

10.7 Examples of emitted ray paths. The dashed line is for a ray emitted at an angle above the critical angle; it does not escape and no power is transferred from the LED. The dotted line is for a ray emitted at an angle just below the critical angle; it radiates along the surface of the device. When summed over all azimuth angles, these rays actually transmit most of the radiated power. The dash-dot line is for a ray emitted at angle of emission close to the normal. When summed over all azimuth angles these rays actually transmit very little power.

reflection effectively can have a big impact on overall light extraction efficiency. This is a very important point, which we will return to in discussions later about the effect of surface patterning. We will now look in turn at several different methods for doing this.

10.1.4 Methods of improving light extraction from LEDs

Several methods can be employed to improve light extraction from conventional LEDs. All attempt to overcome Fresnel reflection loss at the surface/air interface.

The most common technique is to utilise random surface texturing to provide random scattering centres for trapped light such that photons eventually become directed into rays propagating within the normal extraction cone of the structure. In effect, roughening introduces sets of angled facets. This changes the conditions for total internal reflection in a highly localised way close to the angled facet, such that light emitted (or recycled) at an angle below the critical angle for TIR will be radiated from the surface.

Random texturing can be induced either during epitaxial growth or by subsequent electro-chemical etching of the surface layer. In both cases the positions of the random structures are seeded by epitaxial defect sites, and hence this technique is not compatible with or beneficial to very high-quality low defect density epitaxy. In addition, random roughening is very difficult to control, giving rise to large chip-to-chip and wafer-to-wafer performance variability, and the consequent need for performance binning. Overall, random surface texturing can improve light extraction efficiency for a P-side up LED by around 30–35%. However, that is the maximum performance benefit. The vast majority of devices within a wafer will be improved by a significantly smaller factor. Surface roughening for P-side up LED devices requires a very lengthy epitaxial overgrowth step, which is highly undesirable in terms of throughput of wafers through an LED production line.

Patterning the underlying substrate with large, widely spaced, curved (dome-shaped) structures (as is the case for a patterned sapphire substrate (PSS) device) works in a similar way – by redirecting recycled rays to angles lying within the normal extraction cone, but has the added benefit of changing the conditions for TIR at the GaN/substrate boundary, thereby reducing substrate absorption as well.

An alternative method (which is the real subject of this chapter) is to use small-scale periodic pattering in the form of a photonic crystal lattice etched some way into the heterostructure. In this case the photonic crystal provides a far more precisely engineered leakage mechanism for confined photons (which still reside in the high index material surrounding the holes) by redirecting confined modes to leaky radiating modes and actually reshaping the extraction light cone, for example by changing the Fresnel reflection conditions at the top surface in a complex way.

For surface patterning of any kind, it is extremely important that the etched structures do not puncture the quantum wells otherwise an electrical conduction path will be created. This can cause short-circuiting (shunting) of the device upon application of the current spreading layers. Alternatively, the leakage current is increased, which is undesirable since it reduces IQE.

10.2 Photonic crystal (PC) technology

Photonic crystals (PCs) are structured materials formed by etching 2D or 3D arrays of shaped structures into a dielectric medium. When fabricated with submicron dimensions, the arrays form the optical equivalent of a semiconductor material. That is, photons can only travel across the material if they are localised into distinct energy states and obey strict rules relating to direction of travel, polarisation state and energy (wavelength). An energy range can also exist for which there are no allowed states for propagation. This energy range is known as a photonic band gap. Before looking at photonic crystals in more detail, we will first expand on this concept and put it into clearer perspective using an analogy familiar to solid-state physicists.

10.2.1 The workings of PCs

Consider the motion of electrons through silicon. Single-crystal silicon is made of atoms arranged in a diamond lattice. Electrons moving through the silicon lattice experience the presence of the silicon nuclei through Coulomb interactions. As an electron travels through a silicon crystal, its interactions with the periodic potential of the atomic nuclei results in the formation of allowed and forbidden energy states. An energy range can exist for which electrons cannot travel through the lattice. This is called the electronic band gap. At other energies, electrons can travel across the silicon crystal, but only if they follow very special rules and conditions. For example, an electron must travel in a particular direction and must have a very specific energy state.

A photonic crystal is very similar. However, in this case, instead of electrons travelling in a silicon crystal, we now consider photons travelling in a block of dielectric material. For a photonic crystal, instead of having a periodic arrangement of atomic nuclei, we instead have arrays of tiny air holes placed carefully in a lattice arrangement. If we consider a truly 3D photonic crystal analogous to silicon, then the lattice would have a diamond (hexagonal close-packed) arrangement, and the air holes would be spherical. But a photonic crystal can be simplified to a 2D arrangement, in which case it could take a different shape – such as triangular or square, and the air holes could be cylindrical air tubes (Fig 10.8). A photon passing through this patterned dielectric will see regions of high refractive index (the dielectric material itself) interspersed with regions of low refractive index (the air holes). To a photon this contrast in refractive index is equivalent to the periodic potential an electron experiences in travelling through single-crystal silicon, and we find that there are allowed and forbidden photon energies.

As photon energy is inversely proportional to photon wavelength, this means the patterned dielectric block has certain allowed and forbidden wavelength states for photons. As illustrated in Fig. 10.9, the patterned dielectric will not allow passage of photons whose wavelength or energy lies in the photonic band gap, but allows free passage of photons with allowed wavelengths, but only provided they obey strict rules in terms of direction of propagation, polarisation state and energy. Of course the dielectric material must also be inherently transparent to the

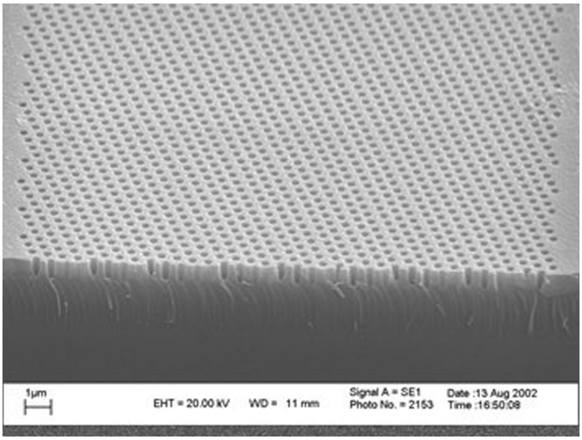

10.8 Photonic crystal with triangular symmetry etched into the surface of a dielectric slab waveguide structure. Light couples into (and out from) the device from the slab waveguides either side of the porous region. The lattice is designed and fabricated such that it is slightly angled with respect to this facet to allow propagation along a certain direction within the crystal.

operating wavelength band (otherwise the light would simply be absorbed by the material).

The permitted states of transmission of an optical device (such as a waveguide, for example) are known as modes. For photonic crystals the transmitted states are periodic in nature and are known as Bloch modes. Ranges of energy (or wavelength) with no permitted transmission states are known as photonic band gaps.

This is a highly simplified description of how a photonic crystal works. In reality the useful properties of a photonic crystal are due to partial reflection of the travelling waves at the interface of each and every etched hole, giving rise to a huge number of plane waves within the photonic crystal. The plane waves interfere with one another, either constructively or destructively depending on the direction of travel and wavelength. Overall the spatial modulation of the refractive index causes the localisation of photons into distinct energy states.

10.2.2 Classes of PC device

Photonic crystal devices can be grouped into two generic classes: those which make use of photonic band gaps and those which make use of dispersion properties. The first class of device includes spectral filters, microscale optical interconnects[2] and microcavity laser devices.[3] All of these applications make use of the reflective properties of a photonic band gap either to confine light within a microcavity

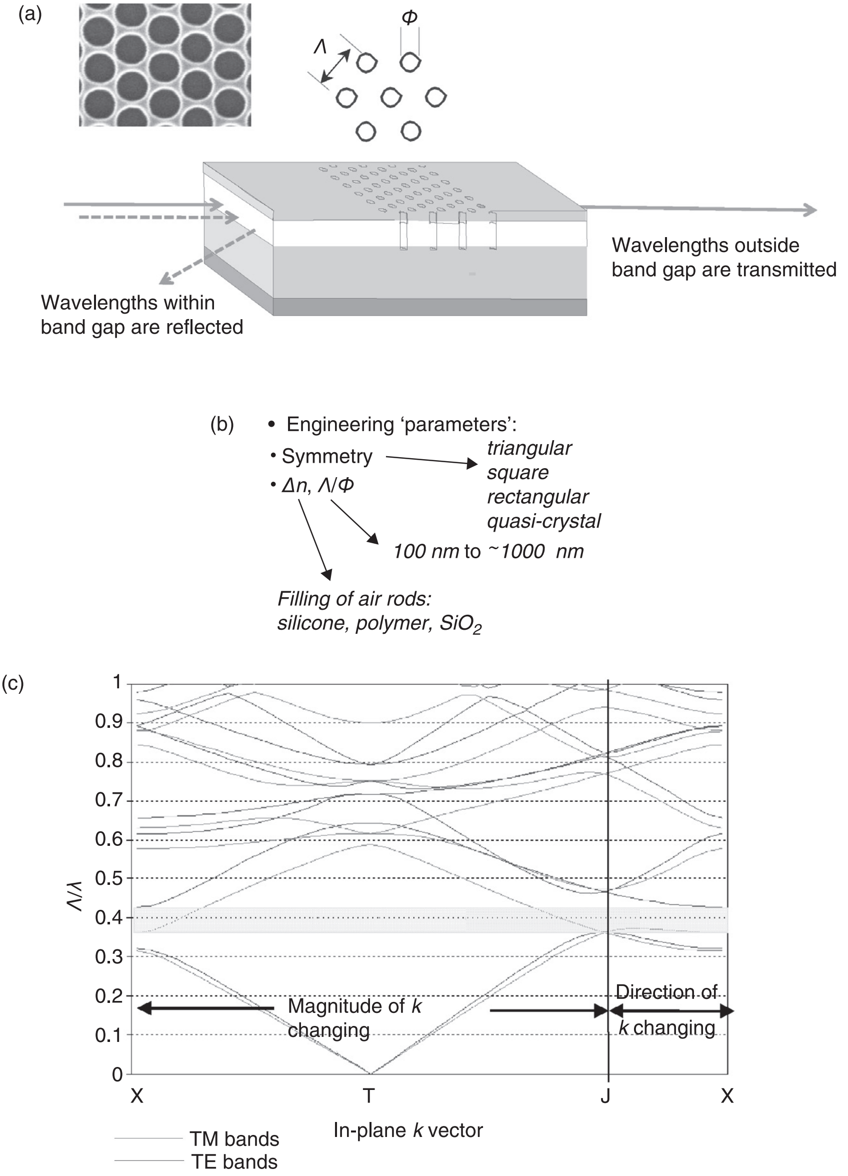
(a)
Φ
Λ
Wavelengths within band gap are reflected
Wavelengths outside band gap are transmitted
(b)
• Engineering 'parameters':
• Symmetry
triangular
square
rectangular
quasi-crystal
• Δn, Λ/Φ
100 nm to ~1000 nm
Filling of air rods: silicone, polymer, SiO₂
(c)
Λ/λ
1
0.9
0.8
0.7
0.6
0.5
0.4
0.3
0.2
0.1
0
Magnitude of k changing
Direction of k changing
X
T
J
X
In-plane k vector
TM bands
TE bands

10.9 (a) Simple illustration of a photonic crystal. (b) Key parameters that determine its operation. (c) Example band diagram showing dispersion curves and band gaps (explained in detail later). Wavelengths within the band gap (shaded area) are reflected (there is no dispersion curve for these wavelengths on the band diagram), whereas all others are partially transmitted. The engineering parameters determine what happens to the light as it travels through the device. (TE: transverse electric polarization; TM: transverse magnetic polarization) region or a line-defect waveguide, or to provide back reflection over a certain wavelength range.

The second set of generic applications includes spatial beam-steering, polarisation control and light extraction from LEDs. These applications do not require the existence of a photonic band gap but instead require transmission of light directly across the lattice. In these applications light must couple from the external environment (such as an input waveguide for an integrated optical device or quantum well for an LED) into guided modes, which exist and are allowed to travel across the photonic crystal.

For a given wavelength of light incident to the lattice, there is either partial transmission plus partial reflection or perfect reflection. Consider the first scenario (partial transmission plus partial reflection). Permitted states of transmission across a photonic crystal can be represented by an energy versus *k*-vector diagram – as for electrical semiconductors (Plate X, see colour section between pages 330 and 331).

Lines on the band diagram (known as dispersion relations to the solid-state physicist) provide vital information about exactly how photons of a given wavelength travel within the lattice. As travelling waves in a photonic crystal are known as Bloch modes, the lines on the band diagram show the properties of the guided Bloch modes. The position and shape of the dispersion curves encodes considerable useful information about how light travels through the lattice.

Most importantly the *y*-axis (scaled as frequency) tells us the wavelength (colour) of the light that can travel across the PC lattice. The *x*-axis (*k*-vector) tells us the direction in which light of that wavelength must travel in order to go across the PC lattice. For photonic crystals, direction is defined with respect to irreducible lattice symmetry directions as shown on the top right of Plate X. We see from the diagram that light of a given wavelength can often travel in multiple directions across the PC (for example, the T-J and T-X directions). The gradient of the lines is the group velocity of the light as it travels across the photonic crystal and so curvature of the lines (the second derivative) relates to changes in group velocity (group velocity dispersion). Strangely enough, it is possible for photonic crystals effectively to slow down and trap light.

The relation between the *x*-axis and *y*-axis of the band diagram (showing the position of the bands) gives the connection between the wavelength of permitted transmission modes in free space, and the effective wavelength as they travel within the lattice (we will discuss this in more detail in the next section). It also gives information about the effective refractive index that a wave sees as it travels across the lattice. The lower right of Plate X plots the effective index of the corresponding modes (this example is for the case of air holes on a triangular lattice in a glass material with refractive index 1.55; the actual geometry and relative size of the holes is shown on the top right). As we shall see later, all of these factors are very relevant to the problem of light extraction from LEDs.

Consider the second scenario for a photonic crystal – perfect reflection. In this case light within the lattice is effectively forbidden because of the existence of a photonic band gap. The existence of photonic band gaps is predominantly determined by the contrast in the index of refraction between the materials used in constructing the physical lattice. Band gaps can be non-polarisation-dependent and non-directional (known as complete and absolute band gaps), polarisation-dependent and non-directional (shaded orange in Plate X and known as polarisation-dependent band gaps) or directional and polarisation-dependent (shaded green in Plate X and known as partial directional polarisation-dependent band gaps).

The transmission of light through a photonic crystal is illustrated more clearly in Plate XI (see colour section between pages 330 and 331). In this figure, an example band diagram for a triangular lattice photonic crystal etched into a silicon nitride slab is shown, and the transmission properties of the crystal (calculated using the finite difference time domain method) are superimposed. The dotted black lines are the photon dispersion relations (which as we have just seen illustrates allowed modes of propagation for TE polarised waves as a function of frequency (y-axis) and k-vector (x-axis)). The red trace shows the corresponding transmission spectrum as a function of frequency (y-axis) and amplitude (x-axis). We clearly see that at frequencies where allowed Bloch modes (indicated by the dotted black curves) exist, transmission occurs. The solid grey curve shows reflection from the front of the crystal as a function of frequency and amplitude. At frequencies where Bloch modes do not exist (the gaps between the dotted black dispersion curves) there is strong reflection from the crystal. It is clear that the red and grey traces are exactly complementary over the normalised frequency range 0 to 0.5. At higher frequencies (shorter wavelengths) above 0.5 we find that light is still transmitted where allowed Bloch modes exist, but the transmitted light is subject to other optical effects such as diffraction (shown by the green curve in Plate XI), hence the red and grey curves (transmission and reflection) are no longer exactly complementary above that value. In practice, this means that incident light will split into multiple beams at frequencies lying above the diffraction limit, and the light will be partially transmitted and diffracted at the same time.

10.2.3 Regular PCs versus photonic quasi-crystals (PQCs): effect of lattice symmetry

Photonic crystals have traditionally emulated natural atomic lattice structures, and the most popular lattice shapes are 1D gratings (this is the simplest form of a photonic crystal) and 2D square or triangular lattices (these are the most common forms of photonic crystals). These lattices have, respectively, twofold, fourfold or sixfold symmetry. As the level of symmetry increases, the properties of the photonic crystals become less directional. The highest degree of symmetry found in nature is for the triangular lattice, which has sixfold symmetry.

For laser or LED applications the choice of lattice shape is very important because this in turn affects the far-field properties of the emitted light. (We will come back to this and look at it in much more detail later in this chapter.) Since photonic crystals are man-made structures defined by photolithographic techniques, lattice patterns do not have to be constrained to the limited set of arrangements commonly found in nature. More complex geometrical arrangements can be used instead.

A completely different class of artificial lattice shapes are known as photonic quasi-crystals (PQCs). Some example PQC structures are shown in Plate XII (see colour plate section between pages 330 and 331). On first sight PQCs appear random; however, on closer inspection PQCs they can be seen to possess long-range order but short-range disorder.[4]

PQCs are generated by simple geometrical algorithms. For example, the square-triangular lattice of Plate XII(c) was grown using the random Stampfli inflation method. The lattice was generated by recursive shrinking and tiling of a parent cell. The parent cell is shown as the red dashed lines in Plate XII(c). The lines show that the parent cell is composed of an arrangement of squares and triangles in a dodecagon shape. The corner points of intersection of the lines then become the positions for the holes. This class of PQC has orders of symmetry relating to the original parent cell shape. The sunflower lattice of Plate XII(b) was constructed using a different algorithm based on the Fibonacci series. This lattice has the unusual property of providing maximal packing of holes around a central region of space.

Analysis of the far-field diffraction pattern of a lattice reveals the true nature of its symmetry. The far-field diffraction pattern can be obtained simply by applying a Fourier transform (FT) to the arrangement of holes. Regular lattices and those with finite levels of symmetry, such as square-triangular, Penrose and Archimedean tilings,[5] reveal their symmetry by way of a few distinctly defined Bragg spots. There is a direct relationship between the number of Bragg spots, the number of lattice symmetry planes and the corresponding number of directions for light propagation within a PC lattice. For an LED it is desirable for there to be very many possible directions of propagation for light within the PC lattice as this results in a more uniform far-field illumination pattern (we will come back to this shortly).

Plate XII(d,e) shows the Fourier transform corresponding to some example quasi-crystal lattices. The far-field transform of the Fibonacci lattice (Plate XII(e)) has a well-defined circular ring with no sharply defined artefacts in the space immediately surrounding the central Bragg spot (e.g. there is a clear dark disc surrounding the central spot). Hence, the Fourier transform shows near perfect circular symmetry. Devices with a Fibonacci lattice are expected to have extremely isotropic dispersion properties, meaning that light can travel equally well in any direction.

The far-field pattern of an LED will show structural artefacts similar to those of the far-field diffraction pattern (the Fourier transform of the lattice shape). Simulated PC-LED beam patterns are shown in Plate XII(f,g). The far-field beam profile for the triangular lattice clearly shows triangular artefacts, whereas the Fibonacci lattice shows a circularly symmetric far-field beam profile.

Figure 10.10 shows actual measured far-field emission patterns for commercial PC-enhanced LEDs (the contrast range has been greatly enhanced in these images to bring out the features). Triangular artefacts are clearly visible for the blue LED

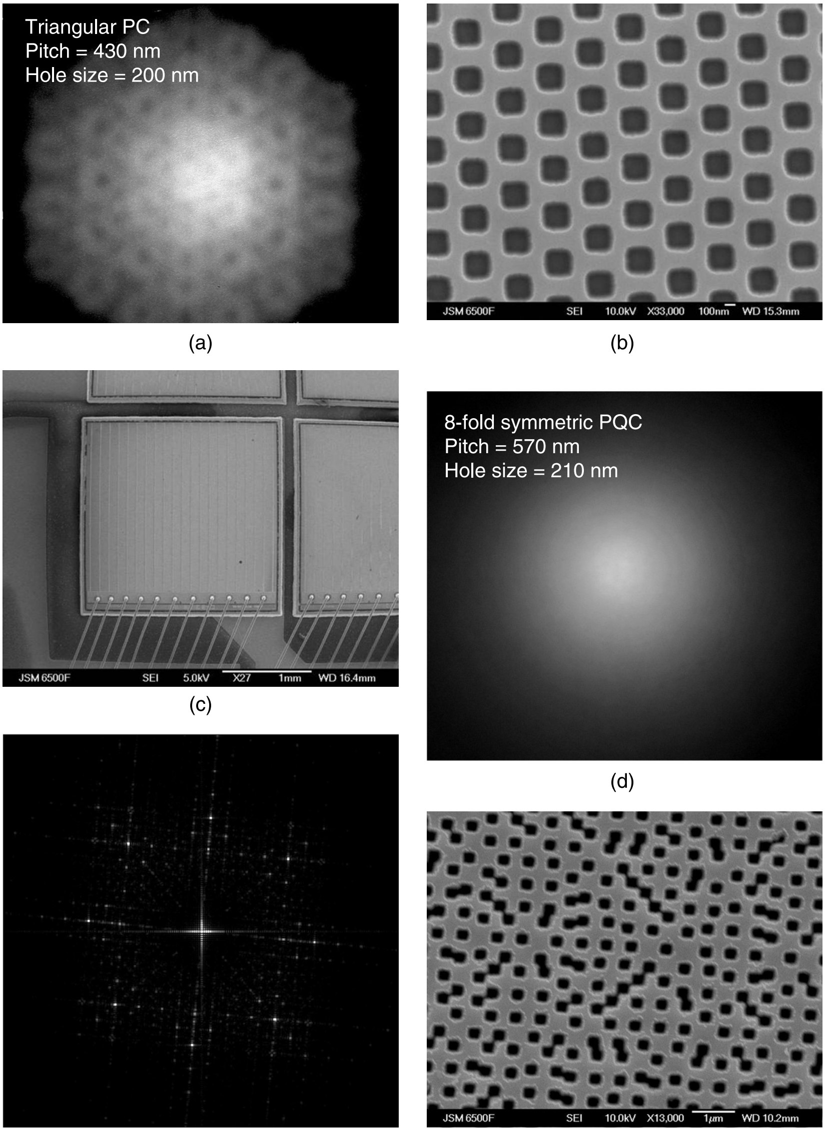
Triangular PC
Pitch = 430 nm
Hole size = 200 nm
JSM 6500F SEI 10.0kV X33,000 100nm WD 15.3mm
JSM 6500F SEI 5.0kV X27 1mm WD 16.4mm
8-fold symmetric PQC
Pitch = 570 nm
Hole size = 210 nm
JSM 6500F SEI 10.0kV X13,000 1μm WD 10.2mm

(a) (b)

(c) (d)

(e) (f)

10.10 Contrast enhanced images of far-field beam intensity for (a) a blue LED with a triangular PC lattice and (d) a red LED with an eightfold symmetric PQC lattice. Angular changes in intensity relate to the underlying PC lattice shape. A PQC lattice (d) gives a circularly symmetric beam profile with respect to azimuth angle whereas a triangular lattice (a) has triangular artefacts. (b, c) Scanning electron micrographs (SEMs) of the surface of the triangular lattice. (e) Fourier transform of the PQC lattice arrangement reveals eightfold symmetry. (f) SEM of the surface of the PQC lattice.

based on a triangular lattice, whereas the red LED based on a quasi-crystal has a much more uniform, circularly symmetric far-field pattern.

Artefacts such as these will affect the efficiency of phosphor colour-conversion coatings applied to the surface of an LED. For example, since there is a triangular arrangement of periodic dark and bright spots in the far-field illumination of the triangular lattice shape, the phosphor coating will not be uniformly illuminated, slightly reducing the overall wall-plug efficiency of the device.

10.3 Improving LED extraction efficiency through PC surface patterning

Moving back to the main topic of this book – LED light extraction – typical P-side up surface-emitting LEDs consist of a GaN slab layer several microns thick with a high refractive index and embedded MQWs positioned a small distance from the surface.[6] In a conventional unpatterned surface-emitting LED, the majority of the light emitted from the quantum wells becomes trapped in the high index GaN slab layer through TIR at the GaN/air and GaN/substrate boundaries. Since only a small fraction of emitted light radiates away from the top surface to free space, unroughened LEDs suffer from poor wall-plug efficiency.[7]

In the first section of this chapter we used a very simple model to estimate light-trapping, taking into account the solid angle of emission and the solid angle subtended by the extraction cone, at the critical angle for total internal reflection. This gives a ballpark figure for how much light becomes trapped inside the LED epitaxial layers. We now look in more detail at exactly how the back-reflected light becomes arranged into sets of trapped modes within a GaN epitaxy structure, and how surface patterning enables interaction with these modes.

In effect the GaN epistructure and substrate form a very thick, highly multi-mode slab waveguide. Light emitted at angles above the critical angle for TIR is localised into a multitude of distinct slab waveguide modes. By introducing periodic patterning, light trapped in some of these modes will become disrupted by scattering from the sidewalls of the patterned holes. In order to improve light extraction, we ideally want the patterning (of a photonic crystal) to interact with as many of the confined modes as possible. To extract all of the trapped light, the photonic crystal would need to interact (at least partially) with all of the trapped modes. (In practice this is very difficult for a normal P-side up LED, which has very thick epitaxial layers and may support 50 or more trapped modes.) Even better, we would ideally like to redirect light confined in trapped modes to specific emission angles inside the extraction cone, depending on the application for the LED.

Extending the analogy between photonic crystals and semiconductor materials further, we can borrow a concept generally used in solid-state semiconductor theory to illustrate the behaviour of electrons inside a semiconductor material. The physical process of light confinement in an LED can be explained (as before) diagrammatically by the energy versus *k*-vector (E-K) diagram. Figure 10.11

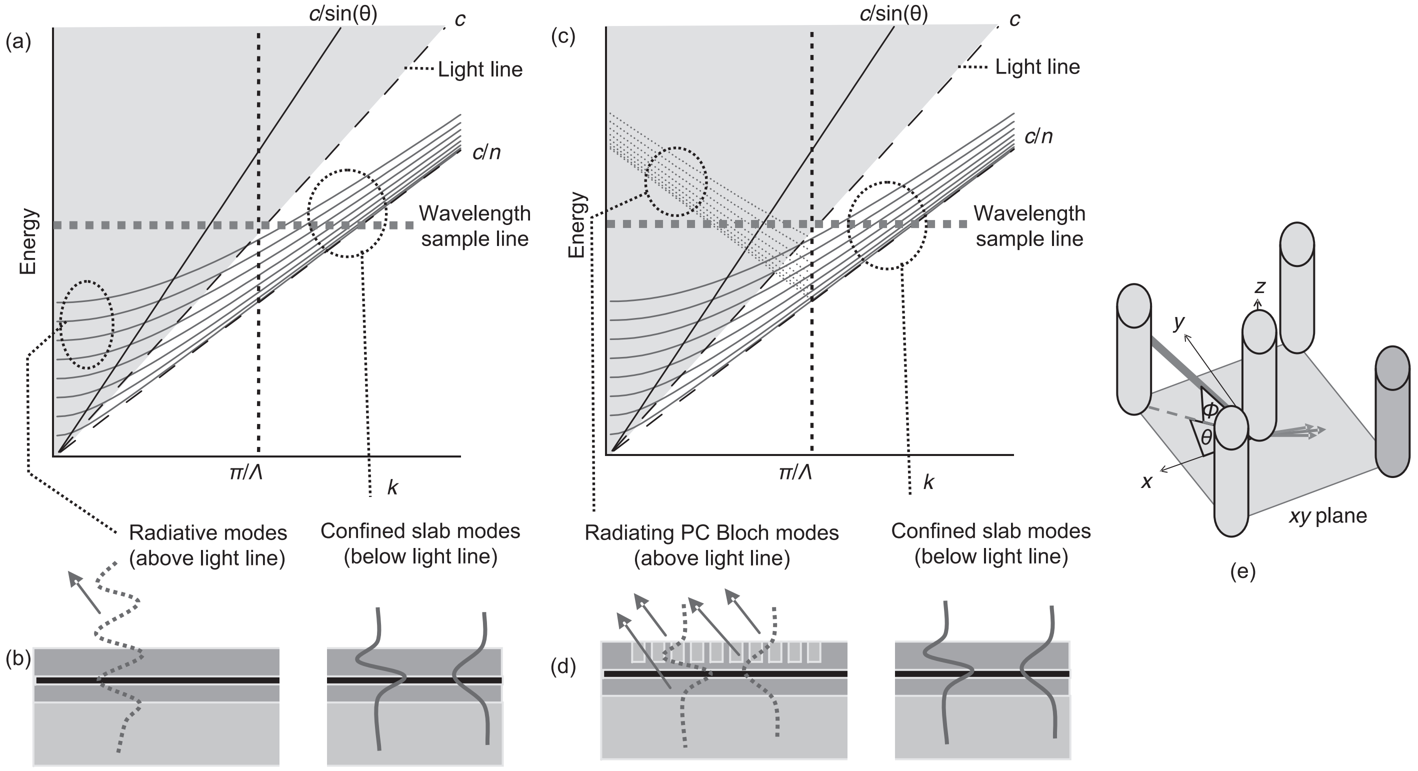
(a)
c/sin(θ)
c
Light line
c/n
Energy
Wavelength sample line
π/Λ
k
Radiative modes (above light line)
Confined slab modes (below light line)
(b)
(c)
c/sin(θ)
c
Light line
c/n
Energy
Wavelength sample line
π/Λ
k
Radiating PC Bloch modes (above light line)
Confined slab modes (below light line)
(d)
z
y
Φ
θ
x
xy plane
(e)

10.11 (a) Energy versus *k*-vector diagram for an unpatterned LED device. Solid curved lines: confined slab modes, shaded area: extent of light extraction cone, vertical dashed line: Brillouin zone boundary. (b) Trapped and radiating modes for an unpatterned LED. (c) Energy versus *k*-vector diagram showing modes in a PC-LED. Dashed lines: band-folded PC Bloch modes. (d) Modes for a PC-patterned LED. (e) Definition of angles: θ is the azimuth angle and φ the polar angle.

shows a much simplified illustrative example of a photonic band diagram for a thick slab waveguide with (Fig. 10.11(b)) and without (Fig. 10.11(a)) surface patterning. Figure 10.11 is a bit different to Plate X shown earlier, which we recall showed the full band structure corresponding to several directions of travel across a thin photonic crystal slab supporting just one set of waveguide modes. In the previous example (Plate X) we considered the case where light travels directly across the photonic crystal, exactly perpendicular to the sidewalls of the etched holes (e.g. from side to side across the PC lattice).

In this more realistic example (Fig. 10.11) we consider light travelling within a thick LED, which has very many trapped modes. The light travels at a set of distinct angles with respect to the rods and vertical direction. To simplify the discussion we only consider one direction of travel across the device (e.g. one azimuthal direction defined with respect to the symmetry directions of the photonic crystal patterning), and we look in detail at what would correspond to just one section of the first dispersion curve in Plate X (equivalent to the Γ-J direction in Plate X, for example). Hence in the following illustrative example, we completely disregard the higher dispersion bands and other directions of travel (Γ-X).

As before, the y-axis (energy) of Fig. 10.11 is related to the free space wavelength of the emitted light and the x-axis (k-vector) is related to the effective wavelength of the emitted light as it travels inside the patterned LED. The wavelength of the light will be significantly smaller when it travels inside the LED than the wavelength actually radiated from the top to the free space because it becomes reduced in proportion to the refractive index of the GaN material. In fact, for a patterned (photonic crystal) LED the situation is more complicated because the light sees an effective refractive index rather than the actual material refractive index. The effective refractive index is less than the material refractive index because some of the light will travel through the region with the air holes (an example of this was shown earlier at the top right of Plate X). Hence the effective refractive index for a mode of the photonic crystal could be anything between 1 (air) and 2.45 (GaN). Luckily the k-vector (x-axis of the band diagram) takes this into account.

We saw earlier that the k-vector is also related to the direction of propagation of a radiated wave. For an LED, the direction relates to both the azimuth angle of emission from the quantum well (θ as illustrated in Fig. 10.11(e)), which is defined with respect to the symmetry directions of the surface patterning (we saw earlier that directions of travel across the photonic crystal are denoted by symmetry directions such as Γ-X and Γ-J, as indicated on the top right Plate X) and the polar emission angle (φ as illustrated in Fig. 10.11(e)). In this case we can consider that the photonic crystal behaves equivalently to a simple slab waveguide for some of the Bloch modes (those which are trapped), and for those modes that are trapped, the polar angle φ is equivalent to the slab waveguide mode angle. For modes that are not trapped (which leak out of the top of the device), the polar angle φ is related to the radiation direction (it is not actually the radiation direction as refraction will occur at the surface).

For an unpatterned device the azimuth angle of emission is essentially irrelevant as all properties should be circularly symmetrical about any chosen point. This is not necessarily the case for a patterned device, where we need to consider both the azimuthal direction of emission with respect to the symmetry directions of the surface patterning as well as the transverse angle of emission (waveguide mode angle).

In Fig. 10.11, the curved solid lines (dispersion curves) represent the confined modes of the LED and indicate the permitted energy states for emitted light (y-axis). There should be one dispersion curve associated with each and every confined waveguide mode of the LED epistructure. For a typical 4.5-μm-thick LED emitting at 450 nm, we would expect around 50 trapped modes in A GaN layer (note Fig. 10.11(a,c) are just representative and only a few modes are shown). Each of the trapped modes has an associated angle of propagation (φ as illustrated in Fig. 10.11(e)). Light emitted from a radiative dipole positioned on the quantum well at an angle above the critical angle for TIR will couple into the mode with the closest matching mode angle (φ) at the wavelength of emission (in effect the k-vector of the emitted dipoles will couple to the most closely matched k-vector of the available confined modes). The dashed line running at an angle (called the light line) represents the condition for total internal reflection. Modes lying diagonally below the light line will be confined within the LED GaN layer by TIR, whereas those lying in the shaded region diagonally above the light line are free to radiate to free space.

In reality LEDs emit over a narrow range of wavelengths (about 25 nm). On Fig. 10.11, this is approximated by a broad horizontal (dashed) sample wavelength line (dashed blue line). Points of intersection between the sample wavelength line and the dispersion curves are the permitted modes of emission for the LED structure. From Fig. 10.11(a) we see that for an unpatterned LED, the majority of the modes lie below the light line and so are strongly trapped within the GaN slab.

Figure 10.11(c) shows the equivalent situation for the case where periodic patterning is applied to the top surface of the LED. This causes the dispersion curves to become folded at the Brillouin zone boundary (represented by the vertical dashed line in Fig. 10.11(c)). In this case the sample wavelength line (dashed horizontal blue line) then intersects not only a number of trapped modes lying below the light line, but also a set of new band-folded photonic crystal Bloch modes lying above the light line. In this case scattering events within the structure (originating from multiple reflections of photons from the dielectric interfaces of the holes etched into the surface) allow emitted photons to switch freely between confined slab modes and radiating leaky photonic crystal Bloch modes. Hence by etching a photonic crystal some distance into the top surface of a conventional LED structure, an engineered leakage mechanism can be introduced into the LED, which can significantly improve extraction efficiency.

For a surface-patterned LED, there is no longer any direct relation between the original direction of photon emission from a dipole on a quantum well, and the final direction of radiation from the top surface of the LED, whereas for an unroughened (or unpatterned) smooth-surface LED the original direction of emission from the dipole can be deduced directly from the angle of emission from the surface.

Geometric factors such as lattice shape, hole size and the dielectric constants of the materials used play an important role in determining the efficiency and directionality of the resultant leaky modes. Other key factors include etch depth and lattice symmetry.

10.3.1 Effect of etch depth

Etch depth plays an important role in determining the efficiency of cross-coupling between trapped waveguide modes associated with a thick LED slab structure and leaky Bloch modes associated with the 2D surface patterning. Typical P-side up LEDs support over 50 trapped slab waveguide modes. For maximum extraction efficiency, there must be strong coupling between trapped slab waveguide modes and leaky PC Bloch modes. Shallow etched PC structures only allow cross-coupling between a few higher-order trapped slab modes whereas PCs etched within close proximity to the MQWs allow extraction of more trapped slab modes. For maximum light extraction, the photonic crystal should ideally penetrate through the quantum wells and through the entire thickness of the epitaxial structure. However, this is not possible in practice since holes that puncture the quantum wells create electrical short circuits or current leakage paths. For P-side up LEDs, the top P-layer is usually very thin (just a few hundred nanometres), which means that the patterned holes can only go a small percentage distance through the thickness of the epitaxial layers. Top side patterning can only interact strongly with a few trapped modes, and weakly with a small number of others. Simple top side patterning (or roughening) for P-side up LEDs yields limited gains in terms of improvement in overall light extraction efficiency.

The situation is better for N-side up LEDs, as the epitaxial layers are usually much thinner thus supporting fewer modes to start with. Furthermore, the top N-GaN layer is relatively thick meaning that the quantum wells are positioned further below the surface of the LED. The PC patterning can penetrate a larger percentage of the distance to the MQWs, in which case it interacts with a larger number of the trapped modes.

10.4 PC-enhanced light extraction in P-side up LEDs

10.4.1 Fabrication of P-side up LEDs

One of the key advantages of photonic crystal light extraction technology is that it can be applied to a standard LED chip fabrication process. That is, photonic crystals can be applied to most types of commercial LED epitaxy to provide the benefits of improved light extraction efficiency and production yield, with small changes in production procedure.

Key requirements for PC-LEDs are that the epitaxy should produce a smooth surface and a low defect density. A high defect density is undesirable as it reduces internal quantum efficiency (IQE); however, it is actually beneficial in standard LED production where epitaxial or chemical surface roughening is used to improve light extraction since epitaxial defects seed surface roughness features. The additional process steps required for PC-LED fabrication are epitaxial process tuning to obtain a smooth surface and low defect density, surface patterning and etching.

Starting from pre-grown epitaxial GaN on a sapphire substrate with a smooth (rather than rough) surface, a thin (50–100 nm) SiO_2 layer is deposited by plasma-enhanced chemical vapour deposition (PECVD). This is later used as a hard mask for PC etching.

PC patterning options

For R&D prototyping and design development, a photonic crystal can be patterned by direct-write electron-beam lithography. In production, patterning is performed by nano-imprint lithography.

Ultraviolet (UV) lithography

In principle, deep UV (DUV) lithography could be an alternative patterning process; however, it is problematic in practice as even the highest quality GaN substrates have significant surface roughness due to drop-down particulates becoming embedded in the layers during epitaxial growth and have significant wafer bow due to the strain induced during growth. Both of these factors pose a serious problem for DUV lithography as these systems have very limited depth of focus at the required dimensions, making it extremely difficult to get high yield across a full 2″ (or larger) wafer. In addition DUV lithography is primarily intended for silicon-patterning and requires a carefully designed anti-reflective coating to achieve maximum resolution. Silicon is highly reflective to DUV light and has a very smooth surface. Hence a simple anti-reflective coating consisting of a quarter-wave stack is sufficient. GaN and sapphire, on the other hand, are both quite transparent to UV and so exposure light interacts strongly with the underlying substrate and epitaxial layers creating multiple back-reflections, blurring the edges of the features. This greatly reduces the fidelity of the surface-patterned features. This problem could be reduced by use of an anti-reflective coating but this may require multiple layers to make any significant difference and so is far harder to design. Furthermore, accurately applying a removable multi-layer coating to a rough and bowed GaN surface is very difficult.

Nano-imprint lithography (UV-NIL)

Currently for production, nano-imprint lithography (NIL) is the preferred solution. As there are many other texts dedicated to this subject, NIL will not be described in full detail here, but a brief description follows. In NIL, patterned features are transferred from a pre-fabricated stamp by a physical print process. The pattern is transferred to a thin polymer resist-like layer, which is applied to the top surface of the wafer. As this is a direct transfer method, the stamp is required to have features produced on a 1:1 basis with the final required design. The two primary methods of NIL are thermal and UV NIL.

Thermal nano-imprint lithography

In thermal imprinting, the substrate is heated to the glass transition temperature of the polymer layer whilst applying high pressure to a hard imprint stamp. The combination of heat, pressure and capillary action force the polymer into the features of the stamp. The substrate then cools down and the pressure is released solidifying the polymer layer. Due to the thermal mismatch of the substrate, stamp and polymer materials the final imprint may not have the same dimensions as the original stamp, and stamp life expectancy is low due to the stresses involved in releasing the stamp from the mould. Thermal imprinting is very problematic for photonic crystal structures due to the small dimensions of the structures and the high physical forces and temperatures required. Also the yield is extremely poor as an inflexible hard stamp must be used, which does not work well in combination with the rough surface topology due to embedded drop-down surface particulates typical for GaN wafers.

UV-nano-imprint lithography (UV-NIL)

UV-NIL imprints into a semi-liquid polymer layer, which flows easily around the features of the stamp by capillary action. The polymer is instantly hardened by applying UV light after application of the stamp to the surface under reduced pressure compared to thermal imprinting. The stamp is then withdrawn leaving a patterned surface. UV-NIL requires either a transparent stamp or an intermediate hard-mask layer. An intermediate hard mask is preferred since it can be a flexible membrane, and the process is more immune to wafer bow or surface particulates, increasing the yield per wafer to acceptable levels for production.

Electron-beam lithography

Electron-beam lithography (EBL) is the preferred patterning method for product development and is also the preferred method for producing the stamps used for nano-imprint lithography. In EBL, a resist layer is directly patterned by scanning with an electron beam electronically. Modern EBL systems have very good depth of focus (several hundred nanometres) and are able to correct for large-scale height variations of the wafer (of several hundred microns), and so are able to cope well with the rough surface topology of typical GaN wafers and associated wafer bow. EBL also has the advantage of allowing multiple designs to be fabricated together on one wafer. EBL is, however, a slow and expensive process, which is not practical for production. Substrate charging and proximity error effects must be taken into account to get good quality devices. Charging effects can be overcome by application of a sub-nanoscale removable conductive layer on top of the resist. Proximity error correction effects are overcome using specialised design correction software.

Photonic crystal etching

After pattering, the top SiO_2 hard mask is etched using inductively couple plasma (ICP) reactive ion etching (RIE) using a CHF_3/Ar gas mixture. The GaN layers are then etched to the required depth – being very careful not to penetrate through the quantum wells – using ICP-RIE with a Cl_2/O_2 gas mixture. The SiO_2 hard mask layer is removed by a simple wet chemical etch in a buffered oxide etchant (dilute hydrofluoric acid). Following removal of the sacrificial hard mask layer, the process resumes as per the regular production cycle.

Current spreading layer

Standard P-side up GaN on sapphire LED devices require efficient current spreading as the top P-doped GaN has low conductivity. This is usually an ITO coating with a typical thickness of 200–300 nm. The ITO current spreading layer (CSL) is deposited on top of the patterned LED either by reactive sputtering or electron gun evaporation. During deposition, oxygen is introduced into the chamber and the substrate is heated to around 150–200 °C. Alternatively (mainly for R&D) a thin (10 nm thick) nickel-gold bi-layer can be used instead of the ITO. This has the advantage that under highly directional deposition conditions the metal does not completely fill up the holes of the photonic crystal or coat the internal sidewalls of the holes and so preserves the high refractive index contrast required for efficient operation of a photonic crystal. After deposition of the current spreading layer, the devices are annealed in oxygen to increase the transparency of the current spreading layer further.

MESAs and contacts

The remainder of the chip process proceeds as for a normal P-side up LED. To isolate neighbouring chips electrically and to expose the underlying N-GaN layer in the region of the contact pad, MESA trenches are defined by optical contact lithography and ICP-RIE. The devices are then encapsulated in a thin SiO_2 overcoat layer using a combination of PECVD, optical contact lithography and wet chemical etching to define windows for the N- and P-side contacts. The SiO_2 encapsulation layer is mainly required to protect the ITO current spreading layer from the ingress of air as it degrades in moisture and air.

N and P contact stacks are then deposited by a metal lift-off process consisting of bi-layer resist patterning followed by directional e-gun evaporation and metal lift-off. The entire wafer is then backside polished by CMP and a metal mirror may be applied to the rear surface of the sapphire layer by e-gun evaporation. Finally the chip dice are defined by laser dicing.

Figure 10.12 shows an unencapsulated P-side up photonic quasi-crystal LED at various stages of fabrication. Figure 10.12(c–e) shows the top view of the device at different magnifications both before and after deposition of contact stacks and wire bonding. Figure 10.12(f) is a cross section through an etched photonic crystal LED. It shows relatively vertical sidewalls with an angle of 5–10°.

10.5 Modelling PC-LEDs

As LEDs are highly multi-mode incoherent optical systems, accurate modelling of light emission from photonic crystal LEDs is extremely tricky. Most conventional modelling tools for analysis of photonic crystals (such as plane wave and conventional finite difference time domain (FDTD) methods) are not easily able to take either of these factors into account. FDTD methods can, however, be adapted to investigate the emission properties of PC-LEDs. Properly adapted FDTD simulations can return useful and accurate information about the far-field beam profile, angular power distribution, and internal beam-steering efficiency of a photonic crystal. It is well beyond the scope of this chapter to give a full review of modelling methods or how they work (this is a very broad and complex subject), but in the next few pages I aim to give a very rough overview discussing some of the key problems involved.

10.5.1 Finite difference time domain (FDTD) simulation methods

FDTD is a very powerful simulation tool but requires detailed understanding of how it actually works for it to be used effectively and to obtain meaningful results. In the FDTD simulation method, an initial electro-magnetic field is stepwise propagated across a simulation space, which has been divided into a grid. The grid is initially set up to include a spatial representation of the dielectric function of the components to be analysed. Maxwell's equations for the E and H fields are discretised across the grid and the boundary conditions are solved at the interfaces between each grid cell on each iteration of the simulation. Each iteration of the

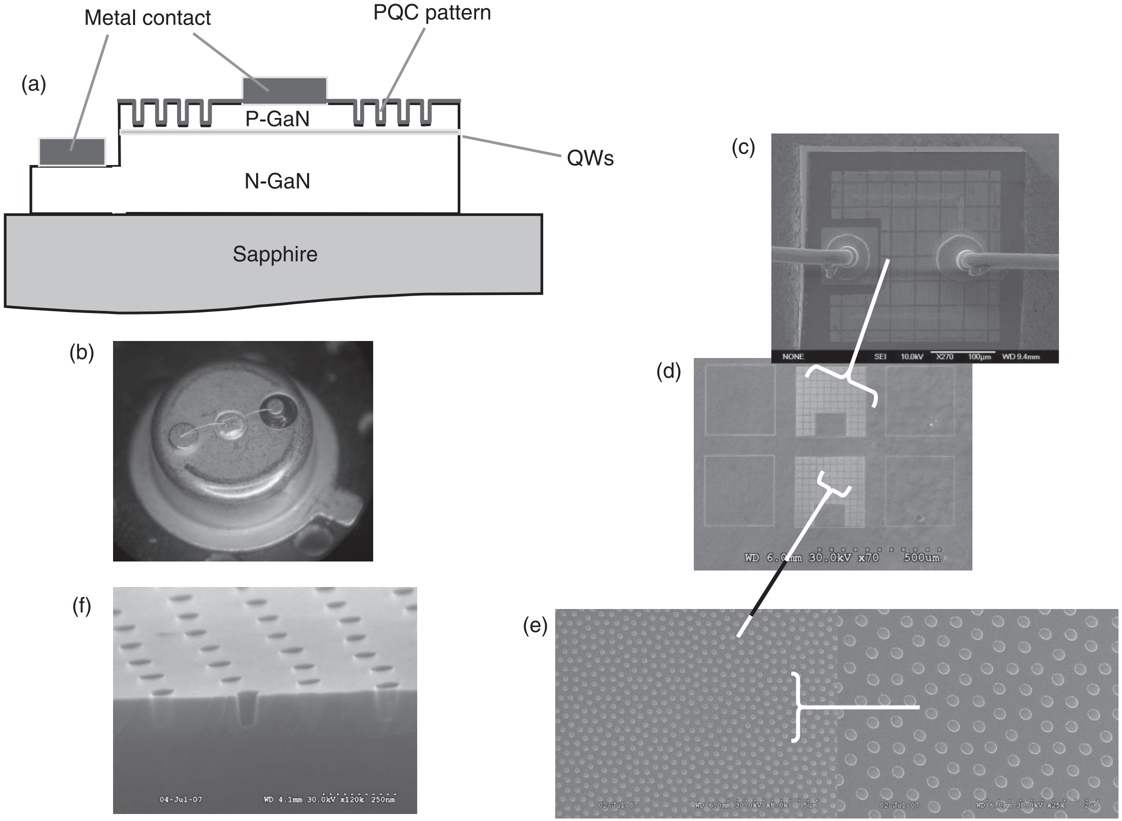
(a)
Metal contact
PQC pattern
P-GaN
N-GaN
QWs
Sapphire
(b)
(c)
NONE SEI 10.0kV X270 100μm WD 9.4mm
(d)
WD 6.0mm 30.0kV x70 500um
(e)
(f)
04-Jul-07
WD 4.1mm 30.0kV x120k 250nm

10.12 Fabricated PQC LED. (a) Diagram of the PQC LED, (b) photograph of a fully packaged LED, (c) SEM of a packaged LED, (d) SEM of undiced LEDs before mesa-etching and contact deposition, (e) high magnification SEMs of the PQC pattern, (f) cross section of the PQC pattern.

simulation corresponds to a small time step, and so initial waves gradually propagate across the simulation space as the simulation progresses.

FDTD calculations require both spatial and time-dependent derivatives of the field functions at the grid cell boundaries. Spatial derivatives are easily computed by sampling the field across two or more consecutive grid points and applying simple differencing equations. To calculate the temporal derivatives, snapshots of the field distribution across the entire simulation grid are kept from one time step to the next to allow time-dependent information to be passed forward through the calculation. Better accuracy can be obtained by using higher-order differencing schemes, which require even more grid snapshots to be kept. Whilst it is relatively easy to implement high-order spatial derivative calculation schemes, there is a large computational overhead in terms of the size of the data-set that must be kept to implement a high-order temporal derivative calculation, as many snapshots of the computational grid must be kept in memory. High-order temporal differencing schemes also require complex leapfrogging differencing schemes, which are again tricky to implement.

Boundary conditions must be applied at the edges of the simulation space as appropriate for the type of simulation and position within the device. For example, perfectly matched layer (PML) absorbing boundary conditions are needed for parts of the device where light radiates to free space (for example, at the top surface of an LED or the exit facet of a waveguide). Periodic boundary conditions are required at the sides if the structure is periodic. Provided the structure is symmetric, reflective boundary conditions can be used in conjunction with periodic or PML boundary conditions to reduce the overall simulation space.

Virtual sampling planes are placed within the simulation space. A set of consecutive grid cells (arranged in a line) are sampled periodically (every few simulation time steps). By applying a computational near-to-far-field transform to the field sampled across the sample plane, the angle of propagation and intensity of a wavefront can be derived. In fact, scattered beams propagating at several different angles can be resolved simultaneously.

10.5.2 Limitations of FDTD for modelling PC/PQC LEDs

Light launch considerations

Conventional FDTD simulation tools are designed to analyse coherent optical systems such as laser and optical waveguide devices, which support very few modes and are excited by coherent monochromatic light sources. Even if these devices have multi-modes, the number of modes is usually very small (<10) and the correct light launch conditions can be accurately represented by carefully positioning a single dipole emitter or a single plane-wave launch field. This rapidly couples coherently to the available modes allowing interference between them. For lasers and optical waveguides this is representative of the real situation.

LEDs on the other hand are very highly multi-mode systems (often supporting over 50 modes). The light launch is far more complicated as emission occurs simultaneously across the entire area of several different quantum wells. The emission processes in an LED are also non-coherent, and so light launch conditions cannot be represented by a single dipole or plane-wave emitter. To model LEDs correctly, a vast number (ideally an infinite number) of dipole emitters must be incorporated in the calculation. These should be distributed randomly across a number of spatial planes within the structure corresponding to the positions of each quantum well, and the dipoles should emit randomly in time.

Boundary condition considerations

Conventional FDTD software is normally used to model devices that naturally confine the light to a region of space in very close proximity to the boundaries of the device. Consider a simple rib waveguide (Fig. 10.13). An evanescent wave propagates exactly perpendicular to the waveguide surface decaying exponentially with distance from the waveguide walls. Light that escapes from the sidewalls of the waveguide has a very well controlled and narrow range of angles (exactly 0°). These are ideal conditions for the correct operation of the perfectly matched boundary conditions at the sides of the simulation space.

In fact, virtually no field energy actually impinges upon the simulation space side boundaries at wavelengths of 400 nm and 700 nm, so the type of boundary condition is almost irrelevant in this case up to the position of the exit from the waveguide. In other words, the side boundaries actually do virtually no work at all. At the end of the waveguide, things become more complicated as waves become diffracted and so diverge over a range of angles. They subsequently impinge upon the top boundary over a limited range of angles (as shown in the far-field angular plot in Fig. 10.13). Very little field energy impinges on the corners of the simulation space and the top boundary does not need to be particularly well tuned or non-directional for reasonable results to be obtained over the narrow angular range of projection from the guide facet. Usually when modelling conventional integrated optical devices, the collection plane is placed somewhere within the confined region of the waveguide, in which case the top boundary does not need to be very good at absorbing waves incident at shallow angles.

The situation is very different for LEDs. In this case the aim is to examine the angular scattering properties of the surface patterning to free space accurately. In order to model the angular properties of light emission from an LED we must rely on perfectly matched boundary layers to absorb the radiated light. In this case, the PML boundary conditions need to be extremely well tuned to ensure they do not reflect any power back into the simulation space at any angle, and they must work well up to large glancing angles. PML boundary conditions normally work very well for near-normal wave incidence. However, even well-tuned PMLs become imperfect absorbers for waves incident at large glancing angles (e.g. travelling

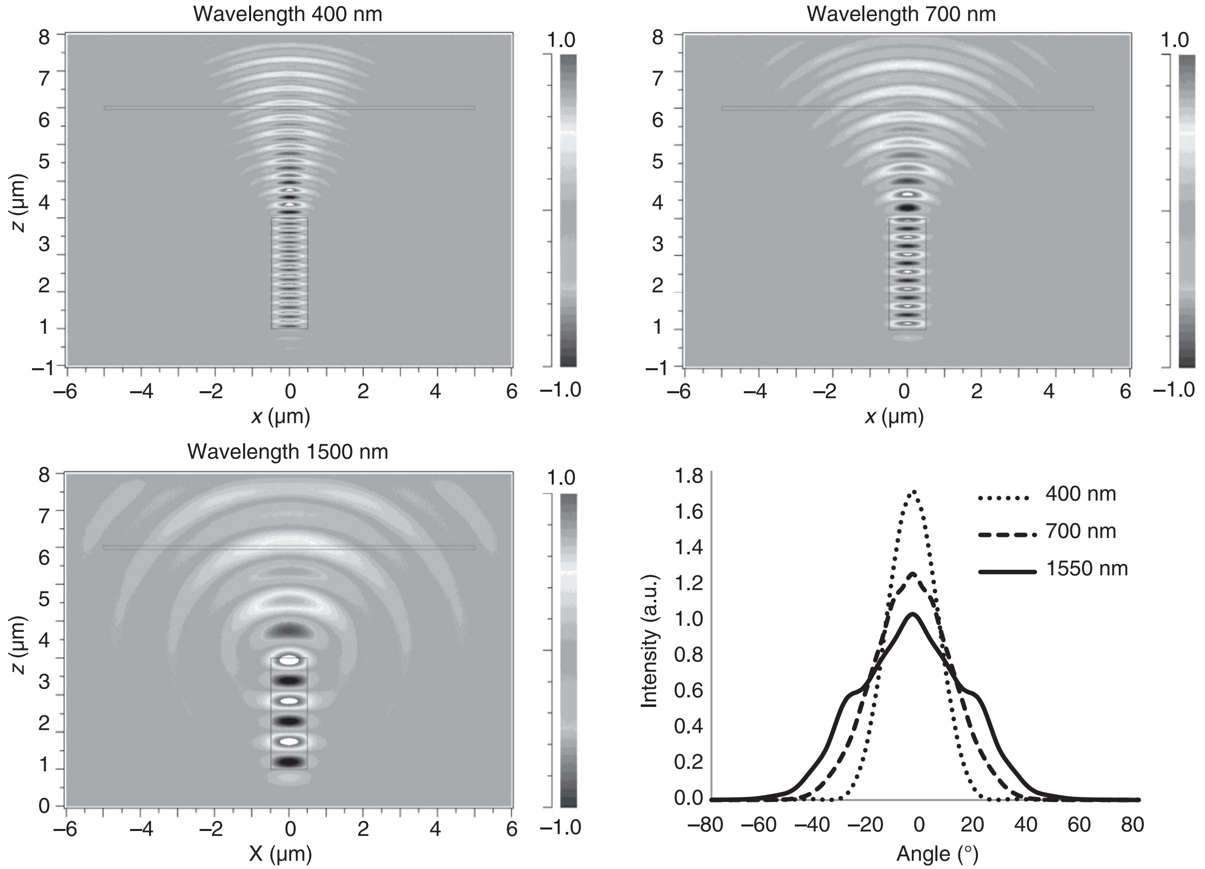

10.13 FDTD simulation for a rib waveguide with PML boundaries at all edges of the simulation space for wavelengths of 400 nm, 700 nm and 1500 nm. The graph shows the corresponding far-field beam scattering angles.

nearly parallel to the surface). In particular problems arise at the corners where the PML side and top boundaries meet.

Considerations for collection plane placement

For accurate analysis of far-field angular emission profiles, great care must be taken in positioning and calibrating the sampling (collection) planes to ensure that spurious errors are not introduced due to the imperfect behaviour of the boundary conditions. As even small amplitude back-reflected waves can have an adverse effect on the simulation results (particularly for a far-field profile) it is extremely important that the simulation space is very well set up and the boundary conditions finely tuned.

For example, there will be a partially bound evanescent wave for light incident close to the critical angle for total internal reflection to a high/low index dielectric interface. If the sampling plane is placed too close to the top surface of the LED, it will continuously capture part of this bound wave giving spurious results. On the other hand, if the sampling plane is placed too far away from the surface of the LED then it becomes incapable of receiving light travelling at shallow glancing angles and incapable of resolving the large angular spread of light at steep angles giving false results. Going back to the examples shown earlier in Fig. 10.13, narrow sampling planes are placed close to the exit of (or even within) the waveguide, in which case they are well away from the corners of the simulation space and are unlikely to sample back-reflected waves from the corners between boundaries.

Requirements for the extent of a cross-sectional profile

To take into account resonant interactions, which occur via light recycling within an LED, a full cross-sectional profile of the LED heterostructure must be incorporated into the simulation space. Hence the full epitaxial layer structure (including the underlying substrate) should form the basis for the simulation. The FDTD simulation must incorporate a broad emission bandwidth and emission from multiple quantum wells. The latter requires either very long computational times or distributed or cluster computing techniques.

Comparative normalisation of results

Most of the problems associated with the fine calibration of the simulation space and boundaries can be overcome by making comparisons (or normalisations) between simulations for a completely empty simulation space, an unpatterned smooth-surface LED and a surface-patterned (PC) LED. This provides a good sanity test by confirming that the simulation set-up is good, and allows small errors to be deconvolved from the final simulation results.

Modelling tools

As no suitable commercial modelling tools existed when the field of PC/PQC LED light extraction emerged, we (the authors of this chapter) developed our own FDTD software for modelling LEDs. This software takes all of the factors above into account and the simulations make a realistic representation of LEDs. The software runs on a multi-processor system in a Microsoft high-performance computing cluster (MS HPC) environment. All results presented in the following sections of this chapter arise from these calculations.

10.5.3 Unpatterned P-side up LED simulation example.

By way of a worked example we now look in detail at a simple sanity test simulation for an unpackaged, smooth-surface P-side up LED. Figure 10.14 is a schematic cross section through the device (not to scale) and Fig. 10.15 shows the corresponding simulation results. As discussed in the previous section, to derive the angular far-field profile accurately and deconvolve any errors or inefficiencies associated with the boundary conditions and corner points of the simulation space, comparisons are made between simulations for an unpatterned LED and simulations for a blank (air-filled) simulation space, with the collection (sampling) plane placed in the same position for both. In this case, the empty air-filled simulation provides a reference.

Simulation set-up

We recall (from the previous section) that the collection (observation) plane must be placed a small distance above the top surface of the LED, but ideally should not inadvertently oversample evanescent waves associated with partly trapped modes. We need to be even more careful about the position of the

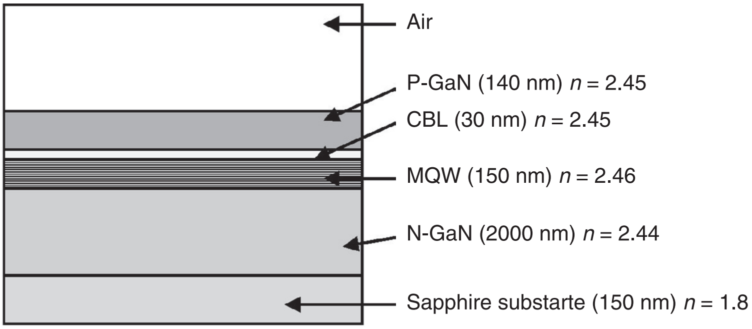
Air
P-GaN (140 nm) $n = 2.45$
CBL (30 nm) $n = 2.45$
MQW (150 nm) $n = 2.46$
N-GaN (2000 nm) $n = 2.44$
Sapphire substarte (150 nm) $n = 1.8$

10.14 Cross section through a P-side up LED showing physical dimensions and refractive index values. (CB: current blocking layer)

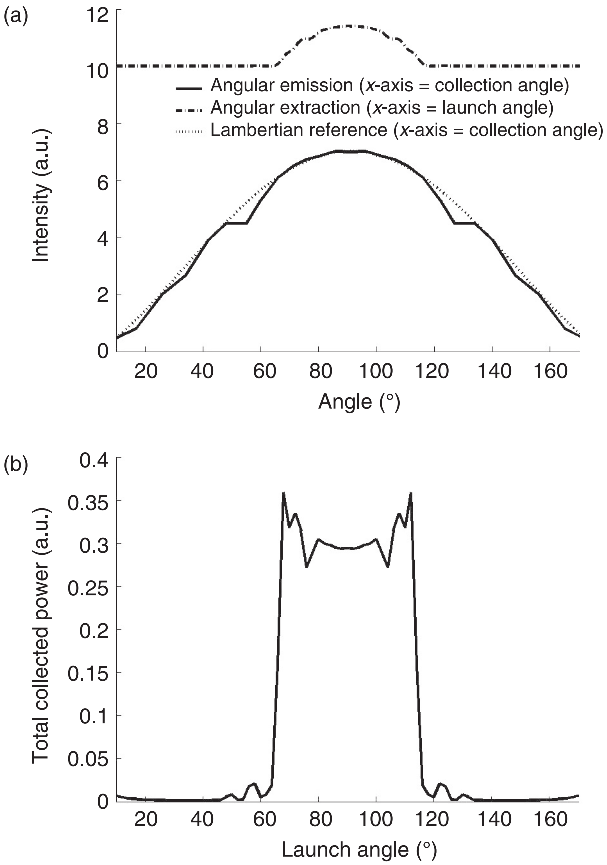

10.15 FDTD simulation for an unpatterned, P-side up LED device. (a) Angular intensity. (b) Total emitted power as a function of dipole emission angle.

light injection (launch) plane for the two simulations as the correct relative positions are not actually the same. For the LED there are multiple launch (light injection) planes corresponding to the position of each quantum well layer positioned just below the surface of the LED. In this simulation, dipoles are placed along the positions of the individual quantum wells. The collection plane, however, observes what goes on at the top surface of the LED since it acts as the radiant surface as far as the external observer is concerned (in this case the collection plane) and not the quantum wells. Hence, the launch plane for the empty air-filled reference simulation should be at a position equivalent to the top surface of the LED. The dipoles are therefore placed along the position of the surface of the LED, not the positions of the multiple quantum wells.

Although this is a small and subtle point it is very important for accurate calibration of the simulations for the following reason. If for the reference simulation the launch plane were placed at the positions of the quantum wells, the distance between the radiative surface (the launch plane for an empty simulation space) and the collection plane would be unrealistically large. The reference simulation would then not mimic oversampling of waves emitted at glancing angles for the case when the collection plane is very close to the LED surface, whereas with the launch plane at the LED surface it would and this allows these effects to be deconvolved from the results. Overall, this strategy simulates the far-field angular profile accurately up to a much larger angle than would otherwise be the case, since the collection plane can be placed closer to the LED surface (actually within the distance of near-field effects).

Finally by normalising the results of the LED simulation with the results from the reference simulation, the inherent response of the simulation space (e.g. the angular performance of the boundary conditions) can be decoupled from the measurement data.

Simulation results

The dot-dash curve in Fig. 10.15(a) plots the intensity of the extracted (radiated) light from the top surface of the unpatterned LED as a function of the original dipole launch angle within the quantum wells of the LED. Note in this and the following plots, angles are measured with respect to the interface (rather than the normal to the interface as is usually the case). Hence 90° corresponds to emission normal to the surface of the LED. The solid curve in Fig. 10.15(a) shows the corresponding angular intensity of light actually radiated from the top surface. The results show that the angular intensity follows a Lambertian profile (dotted curve) as would be expected for an unpatterned LED. Comparing the angular intensity extraction curve (dot-dash curve) over the angular range above the critical angle for total internal reflection (e.g. 65–90°) to the angular far-field intensity curve (over the full angular illumination range (0–90°), we see that the shape and fine features are the same for both. However, the angular range is different.

As discussed earlier, the FDTD simulations presented in Fig. 10.15(a) confirm that there is a direct relation between the original angle of emission from dipoles in the quantum wells and the final angle of emission from the top surface of the LED, corresponding to Snell's law of refraction. For an unpatterned smooth-surface LED, Snell's law of refraction simply applies at the interface between the top surface and air for angles of emission above the critical angle for TIR. In other words, we can see from the simulation results that there is no diffuse light scattering at the surface, as would be the case for a randomly roughened LED.

Figure 10.15(b) shows the corresponding total collected power as observed by the collection plane, but integrated across all collection angles as a function of original angle of emission (launch angle) from within the quantum wells. The power extraction curve gives a clear picture of how much light remains trapped inside the LED, and provides an insight into the light extraction mechanisms at work. From the power extraction plot we can clearly see that there is no light extracted for launch angles lying below the critical angle for total internal reflection (0–65°). For launch angles above the critical angle of TIR (65–90°) we see a near continuous amount of total collected power – as would be expected from a Lambertian source.

In the final sections of this chapter we shall see that the situation is much more complicated for a photonic crystal LED, where there is a large amount of diffuse light scattering at the surface. The key difference between photonic crystal patterning and random surface roughening is the ability of the photonic crystal to provide directional rather than diffuse scattering of trapped light. This mechanism provides a means to redirect trapped beams to specific useful angles of emission.

10.6 P-side up PC-LED performance

So far we have looked at the physical principles utilised by PC patterning to improve light extraction from LEDs, and touched on some of the pitfalls involved in simulating real devices, and performed a sanity test simulation for a conventional LED.

We now take a look at what happens if we introduce surface patterning to a P-side up LED. Figure 10.16 shows a cross section through a device (this diagram does not show all of the epitaxial layers, but is simplified to the most important ones). The only difference to the previous example is the introduction of a set of holes into the top surface penetrating some distance through the top P-GaN layer but stopping short of the quantum wells and current blocking layer (CBL). (Fabrication of this type of device was described earlier and images are shown in Fig. 10.12.)

Figure 10.17(a–c) shows the calculated (solid traces) and experimentally measured (dot-dash traces) angular far-field intensity profiles of radiated light as polar plots. (The same methods as described above are used for the simulation.)

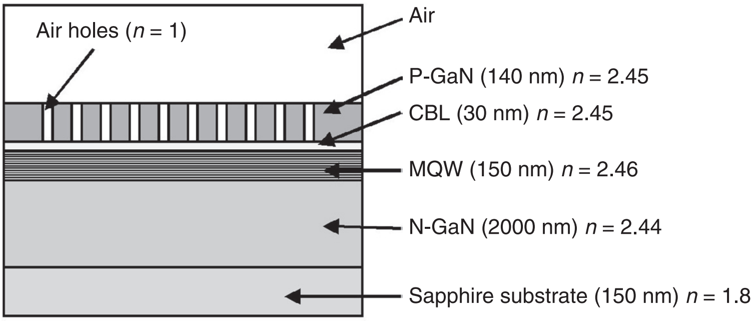
Air holes (n = 1)
Air
P-GaN (140 nm) n = 2.45
CBL (30 nm) n = 2.45
MQW (150 nm) n = 2.46
N-GaN (2000 nm) n = 2.44
Sapphire substrate (150 nm) n = 1.8

10.16 Cross section through a surface-patterned P-side up LED showing physical dimensions and refractive index values.

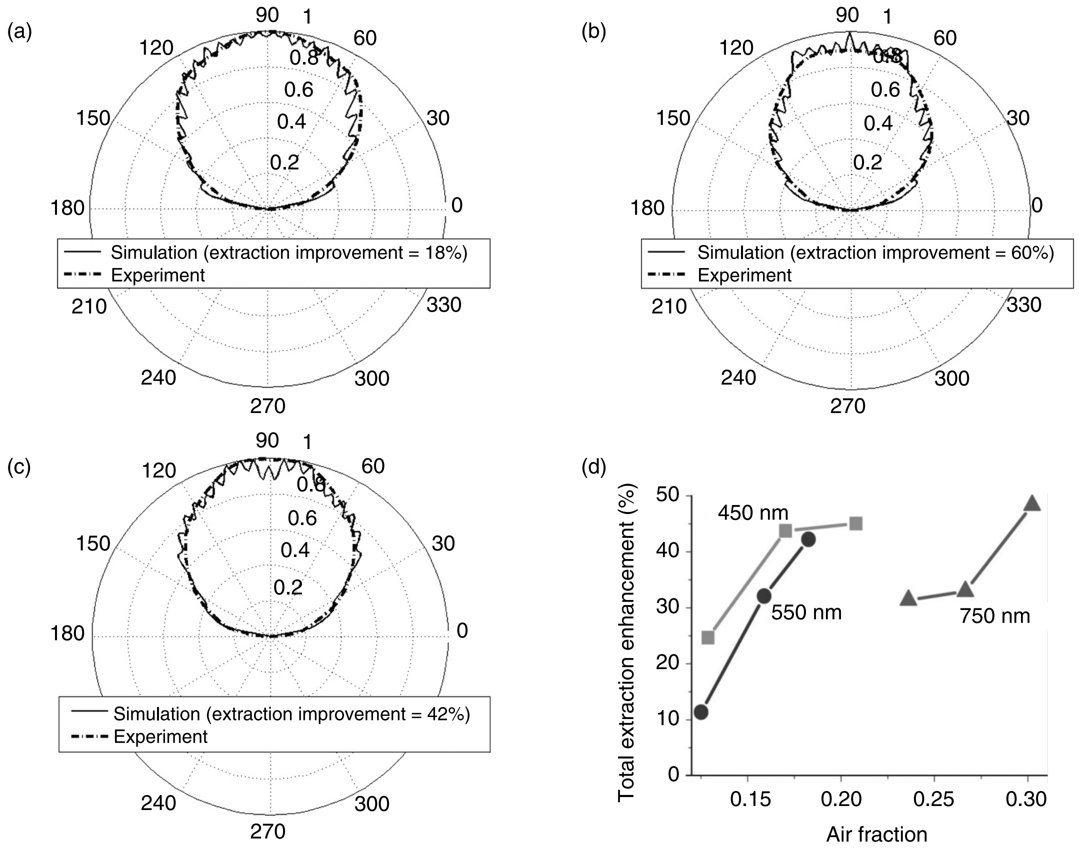

10.17 Comparison between experimentally measured and simulated angular far-field projection for PQC LED devices: (a) 750 nm pitch, (b) 450 nm pitch, (c) 550 nm pitch (130 nm etch depth for all). (d) Experimentally measured power extraction improvement values for surface-patterned P-side up LED.

In this case the surface patterning consists of a 12-fold symmetry photonic quasi-crystal lattice, based on square triangular tiling. Results are shown for three different lattice constants (450 nm, 550 nm and 750 nm), but the same etch depth and air-filling fraction of 0.22. This means that in each case the holes have the same diameter relative to the lattice pitch, and so results for different lattice pitch are directly comparable to each other in these plots

The oscillations on the simulation curves are due to the limited number of dipole launch angles used for the simulation (5° angular steps were used in this case). These oscillations would diminish if more dipole launch angles were used but at the expense of longer calculation time. It is the average envelope of the simulation curves which is of interest.

The legends on each sub-figure of Fig. 15.17(a–c) show the expected improvement in total extracted power compared to a smooth-surface LED. Firstly there is very good agreement between the measured and simulated directional far-field emission profiles. Comparing plots for the different lattice pitches, we see that there is a small but definite change in angular emission behaviour. The 450-nm pitch gives a slightly narrower beam than is the case for the 750-nm, pitch which has a divergent beam. More importantly there is a large improvement in predicted total power extraction for each of these designs compared to a reference unroughened LED. The extraction improvement varies from +18% for the 750-nm pitch device to +60% for the 450-nm pitch device, as shown by the legends.

Figure 10.17(d) shows the actual power extraction enhancement for a set of real LED devices measured experimentally using an integrating sphere set-up. The experimental data is in line with the theoretical predictions. From the experimental data we see that extraction enhancement of up to 50% is easily possible for a P-side up PC patterned LED. An equivalent conventionally roughened P-side up LED, taken from the top power bin, would be expected to show about 30% improvement in power extraction efficiency compared to an unroughened LED (remember this is from the top power bin). So photonic crystal patterning provides a definite improvement (20%) in power extraction compared to top bin conventional surface-roughened devices. More importantly, perhaps, there is far more control of PC surface roughening across the full area of the epitaxial wafer and so all PC devices should fall into the top power bin giving a benefit in terms of improved product yield per wafer.

10.6.1 Effect of etch depth on extracted power

Figure 10.18(a) shows the simulated far-field emission intensity for P-side up 300-nm and 400-nm pitch 12-fold symmetric PQC LEDs with etch depths of 110 nm and 130 nm. We see that there is very little change in far-field directionality with etch depth (the dashed and solid traces overlap) but there is a definite increase in total extracted power for both 300-nm and 400-nm lattice pitch devices (5% and 10% respectively) for just a 20-nm increase in etch depth (as shown by the legend).

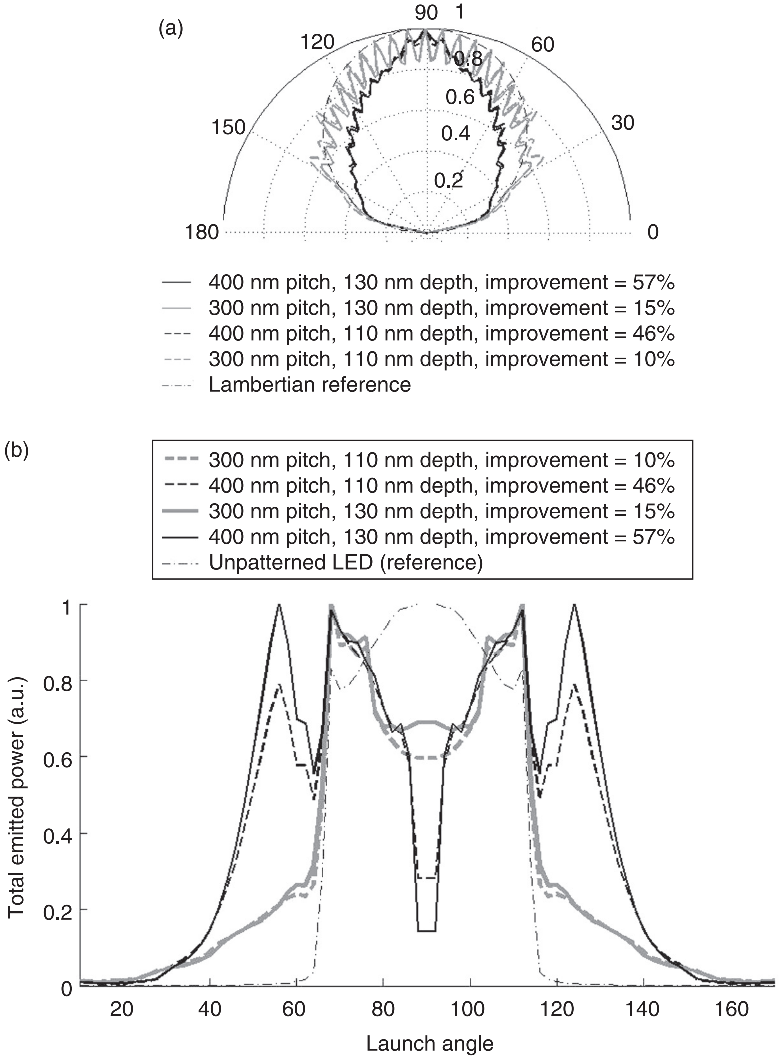

10.18 (a) Angular emission profile of radiated beam, (b) total emitted power as a function of dipole emission angle for 300 nm and 400 nm pitch 12-fold symmetric PQC P-side up LEDs with etch depths of 110 nm and 130 nm (as shown in the legend).

10.6.2 Beam-steering effects

Figure 10.18(b) shows the corresponding angular power extraction as a function of original emission direction from the quantum wells. Power extraction from an unpatterned reference device is also shown (dot-dash grey trace). As before the critical angle for TIR is clearly visible for the reference device at 65°.

By analysing the angular power extraction behaviour of emitting dipoles within the quantum wells of an LED (as shown in Fig. 10.18(b)), we can gain a clearer understanding of how the photonic crystal patterning works in terms of the underlying physical mechanisms. There are clear differences in angular power extraction between the PC devices and the unpatterned reference device. We see that in this particular case the PQC surface patterning actually reduces power extraction over the angular range 65–90°, which is the normal light extraction range for an unpatterned LED, proving that the surface patterning interacts with light radiated within the normal extraction cone – in this case in a detrimental way. However, the PC also scatters power radiated at angles far below the critical angle (30–40°) in a beneficial way to radiative modes, so overall we observe a net increase in total extracted power from the LED.

Looking more closely at the plots (Fig. 10.18(b)) for the 300-nm lattice pitch (110 nm and 130 nm etch depth), we see that like the unpatterned reference device there is a sharp drop in extracted power for dipole emission at the critical angle, but in this case instead of dropping straight to zero (as is the case for the unpatterned LED) power extraction drops to about 30%, and continues to reduce linearly to around 30° (note the gradual slope of the emission power curve). Hence, a small amount of additional power is extracted at angles far below the critical angle. This tells us that the surface patterning interacts with a very large number of higher-order trapped modes (as shown earlier in Fig. 10.11), but not very efficiently, so overall we obtain a small improvement in total power extraction efficiency (10–15%). Looking back at the angular intensity profile (Fig. 10.18(a)), the emission profile is Lambertian.

The 400-nm pitch device on the other hand extracts significantly more power over the range 40–60° (Fig. 10.18(b)) peaking at 100% extraction efficiency for the 130-nm etch depth at a dipole emission angle of 55°. If the etch depth is reduced to 110-nm the height of this new power extraction peak decreases, but the peak wavelength remains the same. This tells us that the extra power extracted by making a small (20 nm) increase in etch depth originates from a stronger interaction between the surface patterning and the same (previously trapped) mode. If the etch depth were increased further (which would in this case penetrate our quantum wells and so is not sensible in practice), then the surface patterning may interact with an additional higher-order trapped mode, but we would expect the shape and/or wavelength of the peak to change. Looking at the angular intensity profile (Fig. 10.18(a)) we also find that the device has a substantially reduced angular emission cone. Overall, although light extraction is greatly improved by the surface patterning compared to an unpatterned device, PC surface patterning is still very inefficient at extracting light radiated from the quantum wells at very shallow angles (0–30°).

Going back to the highly multi-mode waveguide analogy made earlier (presented in Fig. 10.11), this shows that the shallow surface-patterned PC only interacts with a few trapped modes, and in fact the surface patterning interacts most strongly with the higher-order modes. In an ideal case, the surface pattering would scatter light equally efficiently over the entire angular emission range (0–90°). In practice this is very difficult to achieve.

An analysis of the dipole angle power extraction behaviour therefore allows us to gain a strong physical insight into the mechanisms altering the far-field profile and improving power extraction, and so provides a powerful tool when analysing surface-patterned LEDs.

10.6.3 P-side up PQC LED electro-optical performance

Figure 10.19 shows actual measured electro-optical performance data comparing an unpatterned smooth-surface P-side up LED to a 12-fold symmetric PQC patterned P- side up LED. Both devices were fabricated from neighbouring areas of the same wafer to eliminate inaccuracies due to variation in IQE (which can change dramatically across the area of 2″ of GaN on a sapphire wafer).

Figure 10.19(a) is a schematic diagram of the experimental set-up used to measure the far-field angular beam profiles. Figure 10.19(b) shows the measured far-field profiles for the PQC patterned LED and the expected profile for a Lambertian emitter. The full width at half maximum of the unpatterned device is 120° compared to 60° for the PQC LED, demonstrating the beam-shaping capability of the technology. Figure 10.19(c) compares the emission spectra of the patterned and unpatterned devices. Both show a centre wavelength of 450 nm and very similar spectrum confirming that the PQC does not degrade the LED's spectral performance. Figure 10.19(d) compares the on-axis power versus electrical input power for the patterned and unpatterned LEDs. The PQC patterning increases the on-axis extraction power by over 20%.

Figure 10.19(e) shows the I-V characteristic. The LED was pulsed to avoid heating, which would otherwise distort the results. There is a relatively high forward resistance for both the unpatterned LED and the PQC LED due to the thin nickel-gold current spreading layer applied to the surface of these test devices (ITO was not used as the transparent current spreading layer to preserve the refractive index contrast between the GaN and the air inside the holes). Nonetheless the I-V curve confirms that the inclusion of the PQC into the GaN layer does not adversely degrade the electrical characteristics.

10.6.4 Effect of transparent current spreading and passivation layers on PQC performance

The final ITO transparent current spreading layer (TCSL) and oxide passivation layers have a dramatic effect on the performance of a PC/PQC LED. For a conventional (unpatterned) LED, the transparency of the transparent contact layer

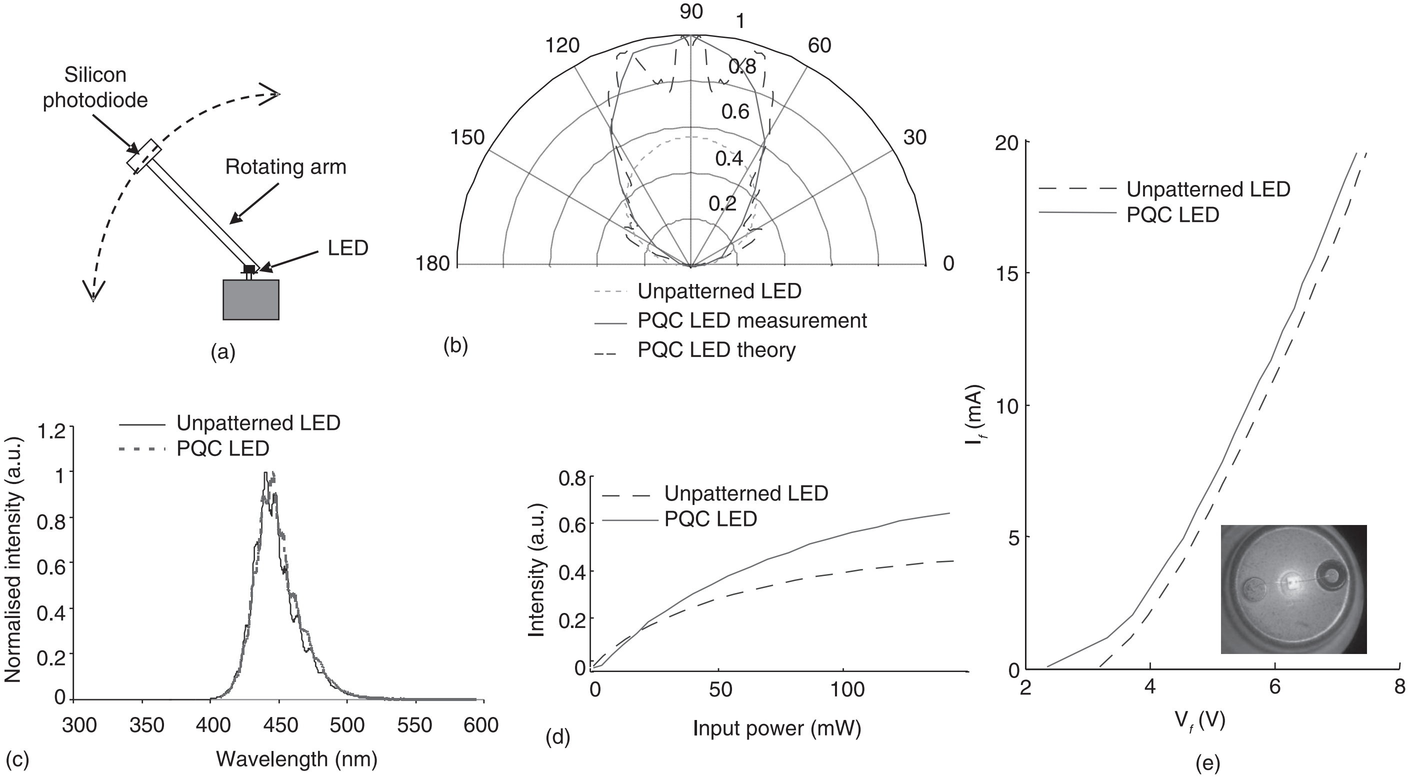

10.19 Electro-optical performance data comparing an unpatterned smooth-surface P-side up LED to a 12-fold symmetric PQC patterned P- side up LED. (a) Far-field measurement set-up. (b) Measured and simulated angular beam profiles. (c) Emission spectra. (d) On-axis intensity as a function of electrical input power (PQC patterning provides an increase in on-axis extraction power of over 20%). (e) I-V characteristic (high forward resistance is due to a nickel-gold current spreading layer applied to the surface of these test devices). Inset is a zoomed in photograph of the LED in operation. The glowing LED chip is mounted on a metal can and bond wires can be seen.

can be improved by optimising the optical thicknesses of the layers so that they are a quarter wavelength at the emission wavelength. In this case the TCL forms an anti-reflective coating and reduces the angle-dependent loss due to Fresnel reflections at the top surface of an LED over a wide range of angles within the normal extraction cone.

Applying ITO CSL layers to a PC-LED can, however, reduce the performance of the device by around 15%. This is due to the fact that the ITO will fill up the holes of the photonic crystal during deposition, greatly reducing the refractive index contrast between the holes and the GaN, which in turn reduces the efficiency of the PQC.

A Ni-Au CSL on the other hand has virtually no effect on the efficiency of the PQC, even if it penetrates the holes, since its thickness is a small fraction of the wavelength (just a few nanometres, typically <10 nm total). However, a Ni-Au current spreading layer has the disadvantage of poor optical transparency. The typical optical transmission of Ni-Au is in the region of 65% at a wavelength of 450 nm while the transmission of a thick ITO layer can reach 90% at a wavelength of 450 nm.

Assuming the conductivity of ITO is similar to that of Ni-Au, an ITO CSL can increase the efficiency by 38% over a Ni-Au CSL as the slight loss of efficiency in the PQC due to the ITO is compensated by reduced light absorption. The use of ITO as a current spreading layer is also highly preferable for production.

There are also possibilities for using more exotic materials as the TCL for PC/PQC LEDs, such as carbon nanotubes and graphene, both of which have very high conductivity, but very small layer thickness and low optical absorption (for the required layer thickness) in the visible region.

10.7 PC-enhanced light extraction in N-side up LEDs

10.7.1 Advantages of N-side up over P-side up device configuration for light extraction

Photonic crystals can also be etched into the top surface of N-side up vertical current spreading LEDs (power chips). As we shall see, in this case they can improve light extraction efficiency far more than for a P-side up LED. Figure 10.20 shows a schematic cross section through an N-side up PC-LED. There are several very important differences in comparison to a conventional P-side up device. There is an underlying metal mirror layer at the interface with the substrate and the quantum wells are placed just a couple of hundred nanometres from it. For a vertical LED the N-GaN layer can be polished back to create a thin GaN device, so that the overall thickness of the epistructure is usually very much thinner than is the case for a P-side up LED. The reduced overall device thickness greatly reduces the number of trapped optical modes within the epistructure, making the job of extracting light from the remaining trapped modes far easier.

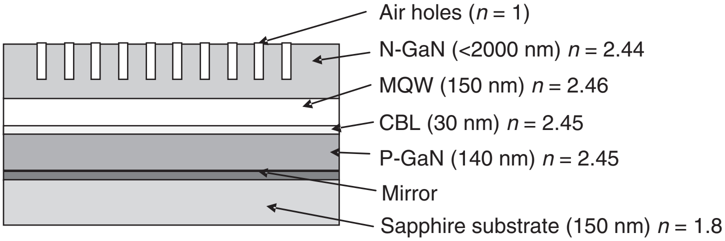
Air holes ($n = 1$)
N-GaN (<2000 nm) $n = 2.44$
MQW (150 nm) $n = 2.46$
CBL (30 nm) $n = 2.45$
P-GaN (140 nm) $n = 2.45$
Mirror
Sapphire substrate (150 nm) $n = 1.8$

10.20 Cross section through a surface-patterned N-side up LED showing typical physical dimensions and refractive index values.

Even after CMP, the top N-GaN layer is still significantly thicker (~2 μm) than the top P-GaN layer (130 nm) for P-side up LEDs. Consequently the quantum wells are buried further below the top surface of the device. PC holes are etched into the top surface of the N-GaN layer of a N-side up LED and it is possible to etch the surface-patterned PC a more significant distance (depth) into the epistructure (82% instead of just 6% of total device thickness). As discussed earlier, this has a big impact on the way in which the surface patterning interacts with trapped modes, and has a big impact in increasing the efficiency of light extraction.

10.7.2 Utilisation of microcavity effect in N-side up LEDs to improve power extraction

Another key difference between N- and P-side up LED configurations is the underlying metal mirror close to the quantum wells in N-side up devices. This creates a weak microcavity effect for light emitted in the downwards direction transverse to the quantum well. The thickness of the epistructure and the position of the quantum wells relative to the mirror can be optimised such that the radiative rate of emission from the quantum wells is slightly enhanced by optical feedback between the backside mirror and the quantum wells.[8] In addition, the microcavity effect changes the angular far-field intensity profile of the LED. When properly optimised, the microcavity effect can direct more energy into the forward emission direction. Figure 10.21 illustrates schematically how this works. Microcavity LEDs can be described by a simple analytical model, which has been validated against experimental measurements on fabricated devices. Figure 10.22 shows extraction efficiency as a function of distance between the mirror and the quantum wells, calculated using both rigorous FDTD and simple analytical methods (d is the distance between the mirror and the most central quantum well). In Fig. 10.22, a value of two corresponds to the benchmark figure for a simple thick LED with a backside mirror placed a large distance from the quantum wells (in which case microcavity effects do not contribute); a value of one corresponds to the benchmark

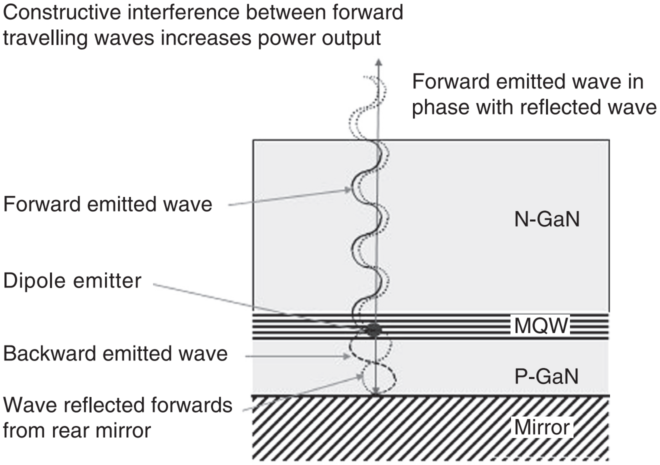
Constructive interference between forward travelling waves increases power output
Forward emitted wave in phase with reflected wave
Forward emitted wave
N-GaN
Dipole emitter
MQW
Backward emitted wave
P-GaN
Wave reflected forwards from rear mirror
Mirror

10.21 Microcavity effect in an N-side up vertical LED.

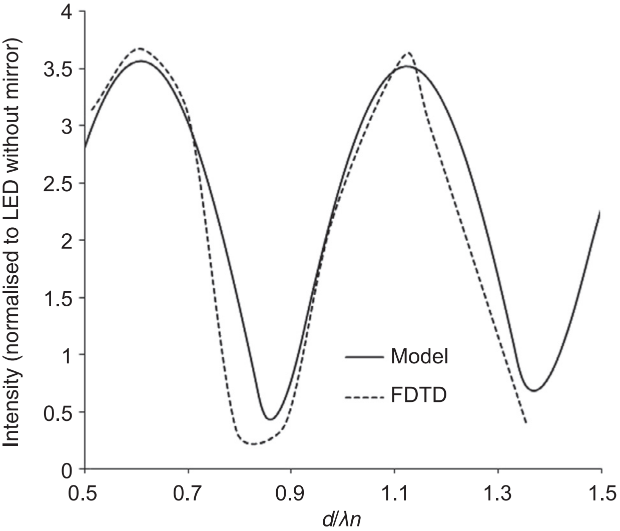

10.22 Comparison of FDTD and analytical models for cavity-enhanced thin GaN LED designs in comparison to conventional thick LEDs.

figure for an LED without a backside mirror (such as a simple P-side up LED). Both methods show that if properly tuned, a 75% improvement in light extraction can be obtained in comparison to a standard LED with a perfect lossless mirror placed a large distance behind the quantum wells.

10.7.3 N-side up PC-LED performance

We now take a look at what happens if surface patterning is introduced to an N-side up LED. To determine the performance benefit of PQC patterning, 4″ of N-side up GaN on a silicon wafer (provided by Luxtaltek Corp, Taiwan) was patterned with a number of different 12-fold symmetric PQC designs by direct-write electron-beam lithography (EBL) and reactive ion etching (Southampton University, UK). The lattice pitch and air-filling fraction were varied across the devices on the wafer. Plate XIII(a) (see colour plate section between pages 330 and 331) shows a photograph of the fully patterned 4″ flip-chip bonded GaN on a silicon wafer after etching to a depth of 600 nm (note there are no metal contacts or MESA isolation trenches at this stage). Under white light illumination the PQC areas show a variety of colours due to the different lattice pitch and air-filling fraction. Each square patterned area is $3 \times 3\,\text{mm}^2$ in size. Blank areas are deliberately left between the PQC patterned areas to provide control (reference) chips. It is important that the reference chips are positioned close to the PQC device areas as the IQE can change significantly across a wafer. Devices placed in close proximity to each other on the wafer will have very similar IQE and so are more comparable. In the photograph we also see a superimposed square grid pattern (1 mm spacing). This is an artefact of the laser lift-off process used earlier in the fabrication of the devices. Many other defects can be seen across the wafer – this is due to imperfections in the laser lift-off and the wafer bonding process. Plate XIII(b) shows SEM images of one of the surface-patterned areas showing the high uniformity of the pattern (note that the holes are not intended to be completely circular).

To determine optical light extraction performance, the photoluminescence (PL) was measured. This enables a relative comparison to be made between different devices, and has the advantage that it can be used at wafer level on devices that are only part fabricated and do not have electrical contacts. Wafer-level measurement has a further advantage as light emitted from the side edges of the chips is not collected and the effects of the PQC can easily be derived by comparison with unpatterned wafer areas.

Light at a shorter wavelength than the LED emission is shone onto the device. The quantum wells absorb the energy, and then give out light (luminescence) at a new wavelength corresponding to the band gap energy of the quantum wells. The experimental configuration used for PL measurement is shown in Fig. 10.23. A collimated 405.5-nm laser diode was focused to a wide (250 μm) spot on the LED surface. Incident light was filtered with a bandpass filter with transmission peaks centred at 400 nm. Reflected light was filtered with a bandpass filter otherwise the photodetector becomes saturated by the very strong pump reflection, and is unable to discriminate the luminescence from the excitation power. The GaN wafer had a peak emission wavelength of 456 nm. Measurements were recorded using a luminance camera placed 0.52 m away from the sample giving a collection angle of 0.5°. The camera rotated about the focus to record angular emission spectra.

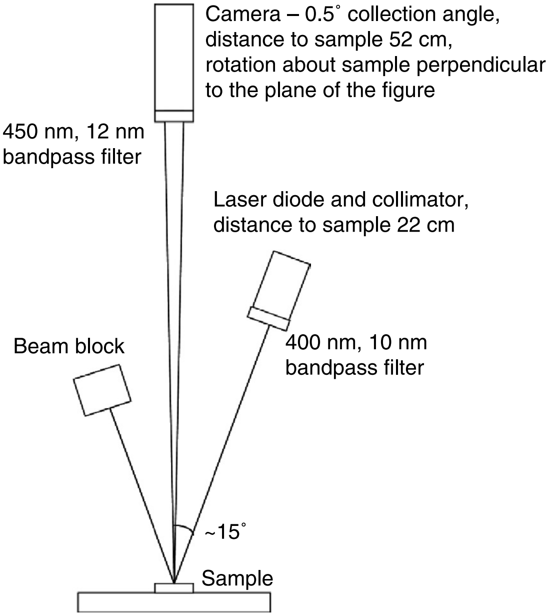
Camera – 0.5° collection angle, distance to sample 52 cm, rotation about sample perpendicular to the plane of the figure
450 nm, 12 nm bandpass filter
Laser diode and collimator, distance to sample 22 cm
Beam block
400 nm, 10 nm bandpass filter
~15°
Sample

10.23 Measurement system for recording photoluminescence from PQC samples.

Demonstration of microcavity effect in practice for an unpatterned N-side up LED

Figure 10.24 shows FDTD simulations and experimental measurements of the angular emission profile and angular dipole extraction profiles for an unpatterned vertical LED with N-GaN layer thickness of 2 μm. The solid black line shows the simulated far-field angular intensity profile into air (in this case the *x*-axis corresponds to the collection angle) and the solid grey line shows power extracted to air as a function of internal launch angle for the device (in this case the *x*-axis corresponds to the dipole emission angle within the GaN). The solid grey line shows a clear cut-off in extraction for launch angles below −26° or above +26° corresponding to the critical angle for total internal reflection and so shows the limit of the extraction cone for an unpatterned device.

Comparing features between the two traces, the angular intensity profile (solid black line) has two prominent peaks at ±66° (±5°) and ±36° (±5°) with smaller modulations between ±30°. Features in the angular extraction curve (solid grey line) follow exactly the same profile, but over a restricted angular range of ±26°, with prominent peaks at ±21.5° (±1°) and ±13° (±1°). This data indicates a direct correspondence between the internal angle of emission and far-field extraction angle, and so emission follows conventional refraction at the air/GaN interface

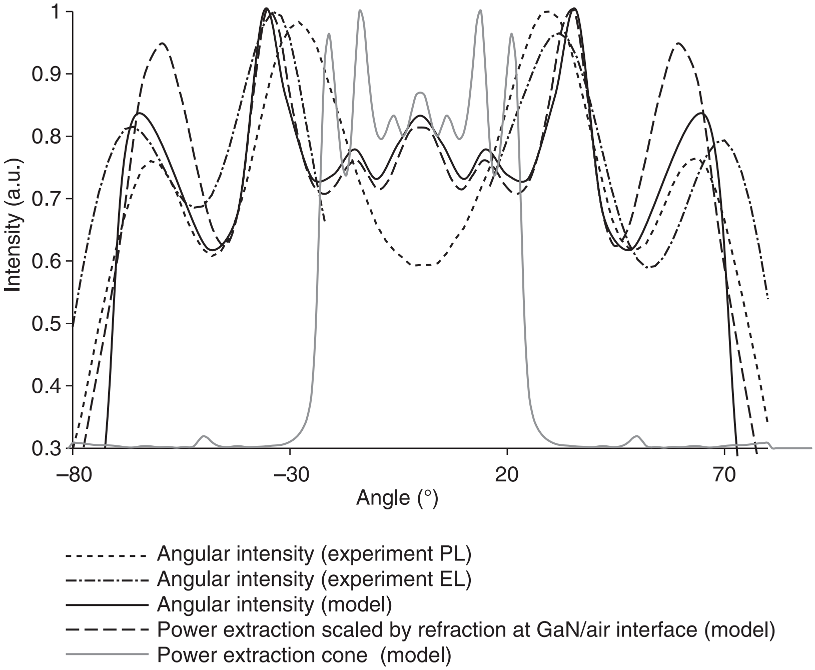

10.24 Measured and simulated angular emission (intensity) profiles of the radiated beam, and corresponding (computed) dipole extraction angles for an unpatterned vertical LED with N-GaN layer thickness of 2 μm. Overlap of rescaled power extraction curve with actual emitted angular intensity curves proves that simple refraction occurs at the surface of this device and there is little diffuse scattering.

(recall from the previous section that this was also the case for an unpatterned P-side up LED). To confirm this, the angular range for power extraction (solid grey line) was rescaled by the refraction condition at an air/GaN boundary according to Snell's law and a new trace (dashed black line) is superimposed onto the plot. This shows the expected angular power emission into air. There is excellent agreement between the solid black line and the dashed black line confirming that this is the case. The expected corresponding peak intensity angles would be at ±59° (±5°) and ±36° (±5°), which is in good agreement with the simulated angular intensity profile.

Modulations in the angular intensity (emission) profile for an unpatterned LED are purely due to weak microcavity resonance effects occurring in the back-plane of the LED between the quantum wells and the rear contact/mirror (as discussed in the previous section). Hence it is possible to modify the emission profile to some degree through microcavity effects and careful tuning of the epitaxial layer thickness.

Figure 10.24 also shows the measured photoluminescence (thin dotted line) and electroluminescence (EL) (thin dash-dot line) angular far-field profiles for a fabricated reference device with N-GaN thickness in the range 1.9–2.6 μm. The experimental photoluminescence has two smooth peaks at ±62° and ±28°, whereas the electroluminescence has two smooth peaks slightly shifted to shallower angles of ±66° and ±32°. These values are in excellent agreement with the peak angles predicted from the angular extraction curve (±66° and ±36°). The offset between the EL and PL values can be explained by the large variation in thickness of the N-GaN layer across the area of the wafer (the CMP process used was not very precise). PL and EL measurements were made on different positions across the wafer.

These results confirm that rigorous FDTD simulation correctly predicts: angular intensity profile, refractive confinement effects within the underlying epitaxy and power extraction enhancement for an unpatterned microcavity LED.

10.7.4 Performance improvement for N-side up PQC patterned LEDs

Far-field beam-shaping

Figure 10.25(a) shows the angle-dependent PL measured under the same excitation conditions for three different devices: an unpatterned control (reference) device and two 12-fold symmetric PQC patterns with pitch of 300 nm and 400 nm. There is a very significant (8×) improvement in on-axis intensity for both 300-nm and 400-nm pitch PQC designs compared to the unpatterned reference device, demonstrating the ability of the PQC to interact with and scatter power efficiently from the trapped modes of the device.

Figure 10.25(b) shows the PL normalised to the maximum value and compared with a Lambertian emission profile. The 300-nm pitch device shows broadening of the angular emission profile, whereas the 400-nm pitch shows narrowing of the emission profile. We also see that the unpatterned control device has a far from Lambertian emission profile due to the microcavity effect discussed earlier.

Enhanced power extraction

Figure 10.26 shows the simulated angular dipole extraction profile for a PQC patterned LED device. The dotted trace shows the predicted angular extraction cone for an unpatterned device revealing strong emission over the central angular range above the angle for total internal reflection (64°). The other lines show the angular extraction profile for various PQC patterned devices.

In stark contrast to the extraction profile for the unpatterned device the patterned device radiates light into air at emission angles well below the critical angle for TIR. In particular there is a new angular range of emission between 30–50°, and also for glancing angles below 20°.

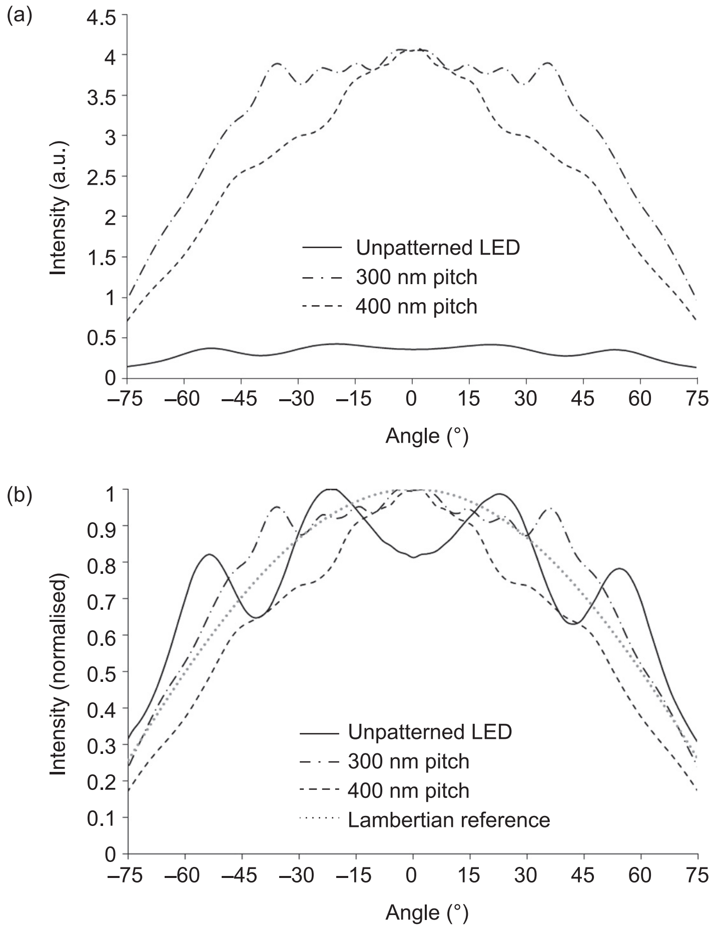

10.25 Angle-dependent photoluminescence for N-side up PQC patterned microcavity LEDs. (a) Raw PL measurement data showing 8× increase in power extraction over a 40° angular range for a 300-nm pitch PQC patterned device compared to an unpatterned reference device. (b) Normalised PL measurement data showing changes in angular beam profile due to PQC patterning. The unpatterned control device has a non-Lambertian emission profile due to weak microcavity effects between the quantum wells and rear mirror.

As explained in previous sections of this chapter, the angular dipole emission plot (Fig. 10.26) gives a physical insight into the mechanisms that give rise to increased extraction efficiency. Specifically, it demonstrates that the patterning causes scattering between strongly confined guided modes and radiative modes. For this to occur the photonic crystal must interact with a number of lower-order trapped modes inside the LED heterostructure.

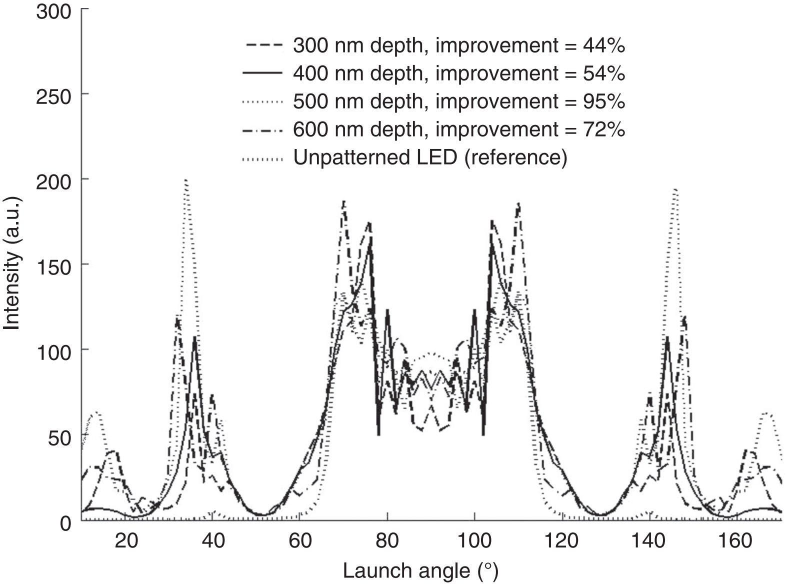

10.26 Simulated angular extraction profile for a PQC patterned device with 300 nm pitch for various etch depths.

This is very different to an average index effect, which could alternatively be induced by the surface patterning. A reduction in average index of the surface layer would be expected simply to shift the critical angle for total internal reflection to a smaller angle, thereby increasing extraction efficiency. From Fig. 10.26 we see that this is not the case. Looking closely at the angular range between 50–66° we see that extraction is increased a little and over this range the cut-off condition for TIR is less sharp (now sloped) indicating that there is a partial contribution to improved extraction efficiency, which can be attributed to a reduction in effective refractive index of the surface layers.

We also see that large angular ranges remain where no PC scattering occurs (20–30° and 45–50°), hence, for this design a large proportion of emitted radiation still remains trapped in the heterostructure. The theoretical modelling indicates a maximum improvement in total power extraction efficiency of 72% (relative to an unpatterned device with a smooth-surface condition and no encapsulation) could be achieved for this structure, assuming that introduction of the PQC does not compromise electrical performance, induce further damage to the quantum wells or introduce non-radiative surface states.

10.8 Summary

In this chapter we reviewed factors affecting wall-plug efficiency for LEDs, focussing on issues that affect light extraction from the epitaxial layers. We discussed the possibility of using photonic crystals to help improve light extraction and looked in detail at the physical means by which this can be done. The first half of the chapter was intended to give an understanding of the physical principles utilised by PC-LEDs. The second half of the chapter discussed the practical implementation of PC-LEDs and levels of performance enhancement attainable for P- and N-side up LEDs.

In Section 10.1, we briefly reviewed the most common configurations for LEDs and discussed factors that affect wall-plug efficiency for each type. We used simple radiometry to calculate ballpark figures for light-trapping in specific layers of a smooth-surface GaN on sapphire LED, and discussed general methods for improving light extraction.

In Section 10.2 a general overview of how photonic crystals work was presented. Photonic crystals are very complicated devices to understand. The properties of photonic crystals are normally represented or analysed using photonic band diagrams. These can be confusing and difficult to understand by the non-physicist. I tried to explain clearly why these tools are useful and how they can be interpreted and used effectively. A very simplistic PC device that supports only one trapped mode was used as an example to introduce the basic concepts. Some strange properties of photonic crystals that are utilised in other fields (for example, silicon photonics), such as slow light and multi-directional diffraction, were mentioned. Photonic quasi-crystals were also introduced and connections between LED far-field beam profile, lattice patterning and beam symmetry and choice of patterned lattice shape were discussed.

In Section 10.3 we discussed the physical mechanism for enhancing light extraction invoked by PC patterning, using a more realistic example of a thick P-side up LED supporting many trapped modes. Comparisons were made between a thick slab waveguide and an LED. We then discussed the effect of etch depth and epitaxial layer thickness on expected light extraction efficiency.

In Section 10.4 we looked at general issues affecting fabrication and mass production of PC and PQC LEDs. A step-by-step overview as to how PCs can be incorporated into P-side up LEDs was given and potential methods of patterning the photonic crystal that are scalable for mass production were discussed.

In Section 10.5 we discussed issues in modelling PC-LEDs using the FDTD method, limitations of conventional FDTD software and ways of improving simulation accuracy. In particular LEDs require very complicated light launch conditions, which are difficult to implement using conventional FDTD tools. Careful fine tuning of PML boundary conditions and calibration of the overall simulation space response along with careful placement of collection planes are absolutely critical for obtaining meaningful results. To obtain high accuracy, the full cross-sectional profile of the device, including the substrate, should be included in the simulation space, and comparisons made to unpatterned devices to ensure the simulation set-up is good. An example simulation for an unpatterned P-side up LED was used to describe more clearly subtle issues in setting up the simulations and to discuss simple internal beam-steering effects.

There are already a number of very different device configurations for commercial LEDs. In particular the two main configurations are P-side up lateral current spreading with and without a patterned substrate, and N-side up vertical current spreading. Not all configurations for LEDs lend themselves well to incorporation of PCs and performance benefits can vary greatly dependent on the type of LED.

In Section 10.6, example simulation and experimental measurements for PQC patterned P-side up LEDs were presented. We showed that an improvement in light extraction up to around 50% in comparison to a smooth-surface LED with an identical design is easily possible, but it is very difficult to change the far-field LED beam profile significantly. We discussed the origin of light extraction improvement in terms of trapped modes. Despite the surface patterning, the level of improvement provided by the PC/PQC patterning is relatively small, and a large amount of light still remains trapped within a P-side up device.

In Section 10.7, example simulation and experimental measurements for PQC patterned N-side up LEDs were presented. We showed that improvements in light extraction well beyond 100% are easily possible, and that there is scope to dramatically change the far-field beam profile as well.

The key difference in performance benefits between N- and P-side up patterned devices lies in the thickness of the underlying epitaxial layers and the relative percentage depth to which the patterned holes can be etched.

10.9 Conclusions

We have seen that photonic crystal surface patterning can provide significant improvement for light extraction for both N- and P-side up LEDs, with improvements of 50% compared to a smooth-surface P-side up LED easily possible. Conventional LEDs are surface roughened and so there is considerable device-to-device performance variation. This introduces the requirement to sort finished devices into power bins. The very best P-side up devices taken from the top power bin would have an efficiency improvement of up to 35% compared to smooth-surface LEDs. Overall, PCs provide an improvement of around 15% over top bin devices. Apart from improved overall light extraction there are secondary gains from the PC technology when applied to P-side up LEDs. As the nano-imprint process is more reproducible than random roughening, PC surface patterning can greatly improve the overall production yield, as all devices should effectively fall into the top power bin. In addition, fabrication becomes slightly easier as there is no longer a requirement for the final epitaxial overgrowth process used to create the surface roughening. The overgrowth step takes a considerable length of time and so reduces overall production throughput for the reactors. Application of PC patterning to patterned substrate P-side up LEDs provides smaller gains as PSS LEDs already have greatly improved performance over conventional surface-roughened LEDs.

For N-side up LEDs, the performance gains are far greater and improvements in extraction efficiency greater than 100% in comparison to a smooth-surface LED are easily possible. It is also more practical to change the shape of the emitted beam to suit a given application. However, the overall fabrication process for the final power chip is still very complex and costly compared to the simple P-side up configuration. For all types of LEDs improvement in device performance is still relative to the quality of the initial epitaxial material. PC patterning does nothing to improve the IQE of a poor quality epitaxial wafer.

Although this chapter has specifically discussed photonic crystal surface patterning for improving light extraction and beam-shaping for LEDs, all the techniques and background theory described are equally applicable to solar cells, photodetectors and OLEDs. In the case of solar cells, PCs can improve overall efficiency by improving light-trapping. Application of PCs to the surface of photodetectors can improve sensitivity and directionality of detection. OLEDs have an inherently very thin device layer construction and so are ideal for incorporation of photonic crystals. However, the refractive index of the polymer layers is low compared to GaN and the amount of light trapped within these layers is relatively small, and so the overall gain in terms of improvement in light extraction by utilising a PC is smaller than is the case for conventional LEDs but nonetheless not insignificant.

Photonic crystal light extraction methods have only recently been applied to commercial LEDs and currently there are very few commercial companies that have adopted the technology – most notable are Luminus Devices (US) and Luxtaltek Corp (Taiwan). PC-enhanced LEDs are finding their way already into mainstream consumer devices such as flat-screen televisions. The slow take-up of the technology is in part due to the need to scale up the patterning technology to mass production, which has involved a huge amount of effort and technical development in nano-imprint lithography. These processes are now becoming more mainstream. Over the next few years we can expect to see greater market penetration for devices utilising photonic crystal surface-patterning technology.

10.10 References

1. T. Nishida, H. Saito and N. Kobayashi, Efficient and high-power AlGaN-based ultraviolet light-emitting diode grown on bulk GaN, *Appl. Phys. Lett.*, **79**, 6, 711–712 (2001).
2. J.D. Joannopoulos, P.R. Villleneuve and S. Fan, Photonic crystals: putting a new twist on light, *Nature*, **386**, 143 (1997).
3. O.J. Painter, A. Husain, A. Scherer, J.D. O'Brien, I. Kim, *et al.*, Room temperature photonic crystal defect lasers at near-infrared wavelengths in InGaAsP, *J. Lightwave Technol.*, **17**, 2082–2088 (1999).

4. M.E. Zoorob, M.D.B. Charlton, G.J. Parker, J.J. Baumberg, M.C. Netti, Complete photonic bandgaps in 12-fold symmetric quasicrystals, *Nature*, **404**, 740–743 (2000).
5. M. Rattier, H. Benisty, E. Schwoob, C. Weisbuch, T.F. Krauss, *et al.*, Omnidirectional and compact guided light extraction from Archimedean photonic lattices, *App. Phys. Lett.*, **83**, 1283 (2003).
6. E.F. Shubert, *Light Emitting Diodes*, Cambridge University Press, 2003.
7. I. Schnitzer, E. Yablonovitch, C. Caneau and A. Scherer, 30% external quantum efficiency from surface textured, thin-film light-emitting diodes, *Appl. Phys. Lett.*, **63**, 2174 (1993).
8. Y.C. Shen, J.J. Wierer, M.R. Krames, M.J. Ludowise, M.S. Misra, *et al.*, Optical cavity effects in InGaN/GaN quantum-well-heterostructure flip-chip light-emitting diodes, *Appl. Phys. Lett.* **82**, 14 (2003).

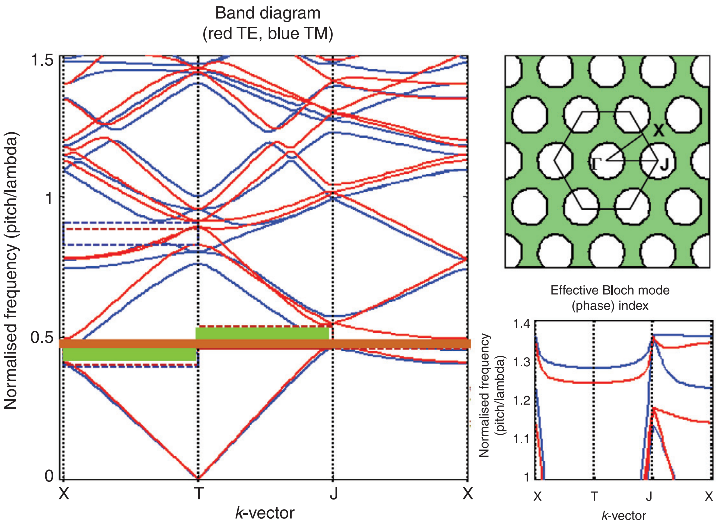

Plate X (Chapter 10) Left: Example *k*-vector (band) diagram. Red and blue lines are dispersion curves for TE and TM polarised modes. Green shaded areas indicate directional and polarisation-dependent band gaps. The orange shaded area is a non-directional but polarisation-dependent band gap. Top right: Lattice geometry and definition of symmetry directions. Bottom right: Effective phase index for modes transmitted by the photonic crystal.

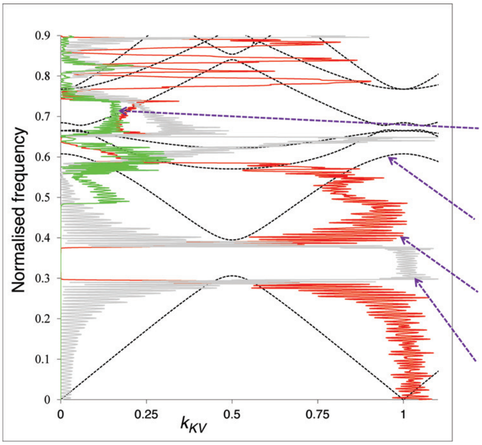

Green line shows diffraction as fn of frequency

Dotted lines show dispersion relations (allowed modes as fn of k-vector and frequency) as per the photonic band diagram

Red line shows transmission as fn of frequency

Grey line shows reflection as fn of frequency

Plate XI (Chapter 10) Example *k*-vector (band) diagram for a photonic crystal with superimposed transmission and reflection properties (calculated using a finite difference time domain method). The plot shows TE polarised waves propagating in a triangular photonic crystal composed of a silicon nitride slab with air cylinders (lattice pitch = 260 nm, rod radius = 150 nm) travelling along the Γ-X symmetry direction, within the plane of the lattice (there is no transverse *k*-vector component).

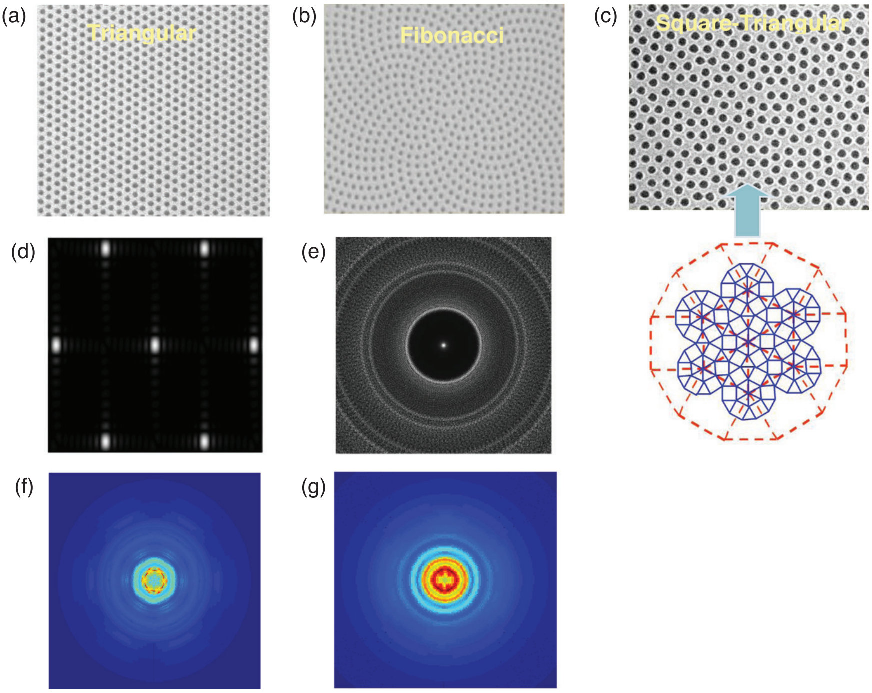
(a)
Triangular
(b)
Fibonacci
(c)
Square-Triangular
(d)
(e)
(f)
(g)

Plate XII (Chapter 10) Various PC and PQC lattice tiling schemes: (a) PC triangular lattice, (b) PQC Fibonacci lattice and (c) PQC square-triangular lattice. Diffraction patterns: (d) for a triangular lattice and (e) for a Fibonacci lattice. Far-field beam profiles: (f) for a triangular lattice and (g) for a Fibonacci lattice.

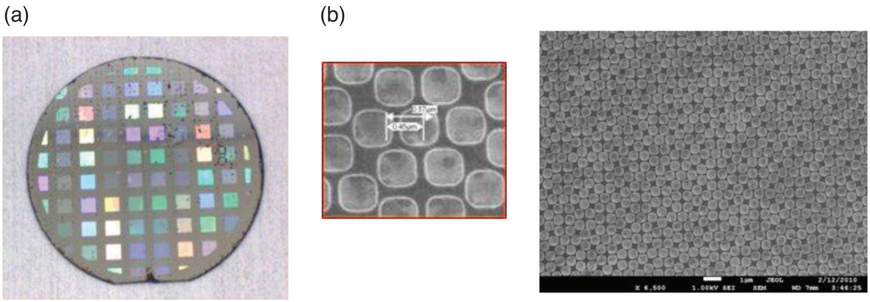

Plate XIII (Chapter 10) (a) Optical photograph of 4″ of flip-chip bonded GaN on a silicon wafer patterned by direct-write electron-beam lithography and reactive ion etching. Each device area is 3 × 3 mm^2 and there is a 2 mm gap between neighbouring devices. The PC parameters are different for each device and they scatter light differently to give a different colour. (b) SEM images of one of the surface-patterned areas.

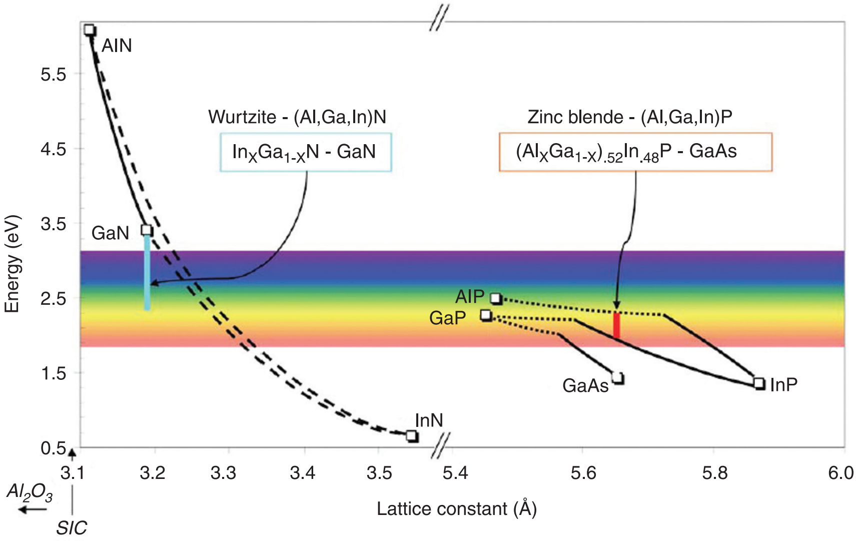

Plate XIV (Chapter 12) Energy bandgap versus lattice constant for wurtzite III-nitride and zinc-blende III-phosphide/arsenide semiconductor alloy systems employing aluminum, indium and gallium (Vurgaftman *et al.*, 2001; Yu *et al.*, 2005). Solid lines indicate direct-bandgap alloys, dotted lines indicate indirect-bandgap alloys and dashed lines are estimates (due to relative uncertainty in bowing parameters for high InN-fraction alloys). The (AlGa)InP system is lattice-matched to GaAs and emission is tunable from red (~650 nm) to yellow (~580 nm). The AlInGaN system is grown pseudomorphically on AlN (deep UV LEDs) or GaN (visible LEDs). (Reprinted with permission from Krames *et al.* (2007). Copyright 2007, IEEE.)

11

Surface plasmon enhanced LEDs

Q. HAO and T. QIU, Southeast University, China and
P. K. CHU, City University of Hong Kong, China

DOI: 10.1533/9780857099303.2.355

Abstract: Surface plasmon resonance is a nascent technique to improve the efficiency and intensity of LEDs with inorganic emitting materials such as GaN. The LEDs are known as surface plasmon enhanced LEDs. The mechanism is based on the energy coupling effect between the photons emitted from a semiconductor and metallic nanoparticles, which are fabricated by nanotechnology. This technique offers a unique way to obtain tunable optical properties by altering the type, size, geometry or interparticle distance of the metallic nanoparticles. The nanostructure can be optimized to yield the best enhancement. Next-generation super-bright solid-state light sources can be produced cheaply and easily by this technique.

Key words: surface plasmon resonance, surface plasmon enhanced LEDs, nanofabrication.

11.1 Introduction

LEDs have attracted considerable scientific and commercial interest since the realization of a practical LED device with emission frequencies in the visible region of the electromagnetic (EM) spectrum. Research activities have focused on how to produce economical LEDs with the desired color as well as white-light sources. The strong demand has also driven materials technology, and new types of emitting materials and configurations have been proposed to enhance performance. For example, low-dimensional emitting devices incorporating quantum wells (QWs) have been extensively investigated to achieve desirable emission colors and enhance device efficiency. However, conventional LEDs with an InGaN/GaN QW structure suffer from low internal quantum efficiency (IQE) due to non-radiative electron/hole pair recombination. Surface plasmons (SPs) have been exploited to enhance the efficiency of nitride LEDs to produce SP-enhanced LEDs. By using nano-scale metallic particles, the SP method provides strong enhancement in quantum efficiency when the extinction band of the SP is close to the bandgap emission energy of the LED. This coupling technique can significantly improve the performance of LEDs by providing economical materials emitting the desired color. The SP-based method offers two unique advantages. The first is tunability. The optical properties resulting from using SPs can be easily varied by altering the type, size, geometry and interparticle distance of the metallic nanoparticles (NPs). The second advantage is energy efficiency. The induced electromagnetic wave is locally confined and cannot propagate along the metal surface. Consequently, the energy loss is small. Furthermore, light extraction from the metal side is possible as the metal layer is transparent, and so it is possible to enhance the performance of LEDs by enhancing the efficiency together with IQE by fabricating plasmon-enhanced photonic crystals. This new technology has found many applications in general lighting for flat-panel displays. Recent improvements in reducing production costs and simplifying the fabrication process have made SP-enhanced LEDs very attractive commercially (Gu *et al.*, 2011).

11.2 Mechanism for plasmon-coupled emission

11.2.1 Surface plasmon

A SP is a quasi-particle arising from quantization of plasma oscillations confined to the surface. SPs interact strongly with light near a metallic surface resulting in another quasi-particle called a SP polariton, which propagates along the surface of the metal. Sometimes SP polaritons are also called SPs for convenience and we also use this abbreviation for SP polaritons in this chapter. SPs at the interface between a metal and a dielectric material have combined EM wave and surface charge characteristics. An EM wave has a transverse magnetic characteristic and the generation of surface charge requires an electric field normal to the surface. These two effects enhance the field component perpendicular to the surface near the surface, which decays exponentially with distance away from it (Chance *et al.*, 1978). The perpendicular field is evanescent or near-field in nature being a consequence of the bound, non-radiative nature of SPs because the wave vector of a polariton is normally larger than that of a free photon at the same frequency and prevents power from propagating away from the surface. Another important effect arising from the interaction between the surface charge density and EM field is the momentum of the SP mode, $\hbar k_{SP}$. Solving Maxwell's equations using the appropriate boundary conditions yields the SP dispersion relation (Sambles *et al.*, 1991), that is, the frequency-dependent SP wave-vector, k_{SP}, is:

$$k_{SP} = k_0 \sqrt{\frac{\varepsilon_d \varepsilon_m}{\varepsilon_d + \varepsilon_m}} \qquad [11.1]$$

The frequency-dependent permittivity of the metal, ε_m, and dielectric material, ε_d, must have opposite signs for SPs to be possible at the interface. This condition is satisfied on metals because ε_m is both negative and complex (the latter corresponding to absorption by the metal). The increase in momentum is associated with binding of the SPs to the surface, and the resulting momentum mismatch between the light and SPs with the same frequency must be bridged if light is to be used to generate SPs. To provide the missing momentum, we can use scattering from sub-wavelength protrusions or holes on the surface to generate SPs locally (Ditlbacher *et al.*, 2002).

We now discuss how SPs propagate on the metal surface. After light has been converted into an SP mode on a flat metal surface, it will propagate but be gradually attenuated due to losses from absorption by the metal. The degree of attenuation depends on the dielectric function of the metal at the oscillation frequency of the SPs. However, if the flat metal surface is rough or corrugated, then absorption by the metal will be overcome when the surface is periodically textured on the scale of the light wavelength. This is important for surface enhancement because it provides an effective way to maximize radiative relaxation as all relaxation channels compete with each other. Moreover, the most commonly used metal materials, silver and gold, have the smallest losses in the visible spectrum, which can lead to enhancement. When the frequency of light photons matches the natural frequency of oscillating surface electrons, resonance is established; this resonance in a nanometer-sized structure is called SP resonance. Simultaneously, the electric and magnetic fields can be localized thereby giving rise to an inhomogeneous EM field distribution, which can be exploited for local EM enhancement. This localization of the EM field near metal nanostructures and coupling to propagating modes can increase emission intensity by several orders of magnitude (Fort and Grésillon, 2008). Plasmons are the result of the quantization of classical plasma oscillations, and so most of their properties can be derived from Maxwell's equations. Thus it is possible to design specific surfaces with a matching optical spectrum utilizing calculated results since the surface morphology of the materials determines the type of SP. Hence, the main challenge in producing surface-enhanced LEDs is to control and design surface structures that maximize the enhancement of the fluorophore by adjusting the local electric field.

11.2.2 Plasmon-enhanced LEDs

SPs have attracted significant interest because optical efficiency in LEDs can be greatly enhanced by coupling the SPs with QWs. The efficiency of current LEDs with an InGaN/GaN QW structure is directly determined by the IQE, which is strongly influenced by non-radiative recombination induced by dislocations and other defects and by separation of the electron and hole wave functions by spontaneous polarization and strain-induced piezoelectric polarization (Kwon *et al*, 2008). IQE can be strongly enhanced by building SP-enhanced InGaN/GaN multiple QW LEDs with a metallic NP layer. As mentioned, the surface of the metallic layer must be rough and it should be well patterned to generate uniform luminance. The NPs on the rough surface cause resonant coupling between the semiconductor bandgap emission and SPs, resulting in significant improvement in the radiative decay rate and spontaneous emission rate of the light emitters. In the presence of SP particles, the local electric field and magnitude of the extinction spectrum are significantly enhanced at the SP resonance frequency. With regard to the efficiency improvement rendered by SP resonance, the enhanced electric field interacts with the emitting materials thereby increasing the spontaneous emission rate and consequently enhancing the IQE of the device.

The coupling of spontaneous emission from the QW into the SP mode can be observed due to the increased absorption at the SP resonance frequency. Time-resolved photoluminescence measurements show that the photoluminescence decay time in the presence of silver NPs is significantly reduced. As a result, the spontaneous emission rate and IQE are better. The effect of varying the distance between the active emitting region and metallic NPs on overall device efficiency also reveals that the larger local field is important. Coupling and enhancing vanish as the distance is increased above a certain threshold, and the distance should not be too small or too large. If it is too small, non-radiative quenching dominates and most of the energy is dissipated. In contrast, if the distance is too large, the coupling effect vanishes since only the electron/hole pairs near the metallic NPs can effectively couple to increase the IQE. This confirms the importance of the higher local field and demonstrates that the IQE can indeed be enhanced by SP via the electric field/emitter interaction. Normally, using NPs to enhance the IQE of LEDs is effective when the original IQE is very low (<1%). For example, this was verified with two InGaN/GaN QW-based LEDs emitting different colors. The one emitting green, which had a lower original IQE corresponding to a lower crystal quality, was enhanced more effectively than the one emitting blue (Yeh *et al.*, 2008a). The enhancement is affected by the type, shape, height and density of the metallic NPs. Ag/Au is the most common material for the NP metallic layer. However, fabrication of the ideal metal surfaces to achieve an enhancement is still difficult as the internal mechanism is very complicated and not clearly understood so far. In the next section, we will describe the fabrication techniques and how to improve the optical properties of LEDs.

11.3 Fabrication of plasmon-coupled nanostructures

11.3.1 Vacuum deposition

At present, vacuum deposition is the most successful method for fabricating electroluminescent LEDs. Under ultrahigh vacuum conditions, a thin metal film will form on the LED structure via condensation of atoms produced by evaporation. The film thickness is governed by factors such as substrate type, ambient pressure and sputtering time. One advantage of the technique is that it does not require chemical processing, and so chemical damage to the emitting region can be avoided. This method has been employed to produce silver NP arrays on silicon quantum dot LEDs (Kim *et al.*, 2008). Post thermal processing is often used to alter optical properties, such as the extinction spectrum of the materials, to increase the enhancement. NPs with the required sizes and heights can be produced by annealing at different temperatures and for different times on metal films with different thicknesses, to achieve the best coupling effect with the light emitters.

Yeh *et al.* (2007) annealed three samples with initial film thicknesses of 5 nm, 10 nm and 15 nm at 200 °C for 30 min and they observed that the size and heights of silver NPs were significantly increased. Annealing enhances the photoluminescence intensity of the SP light emitters due to enhanced SP/QW coupling. Kwon *et al.* (2008) successfully fabricated a SP-enhanced InGaN/GaN multiple QW blue LED with a silver NP layer inserted between the n-GaN layer and the multiple QW layer. The blue LED was deposited on a sapphire substrate using a low-pressure metal-organic chemical vapor deposition (MOCVD) system. Vacuum deposition together with post thermal processing was adopted due to the ease of implementation and reasonable cost of fabricating LEDs containing metallic NPs. After annealing at 750 °C for 10 min in a MOCVD chamber, the size and height of the NPs increased from 275 ± 50 nm and 8 ± 4 nm to 450 ± 50 nm and 15 ± 5 nm, respectively. Afterwards, a 20-nm-thick layer of undoped GaN, a 22-nm-thick InGaN/GaN multiple QW and a 0.2-μm p-type GaN layer were deposited onto the silver NPs and two electrodes were added to the LED structure. The LED was fabricated by the following process. The surface region of the p-GaN layer was partially etched using an inductively coupled plasma-etching process with gases to expose the n-GaN layer. An indium tin oxide layer with a thickness of 200 nm as a transparent current-spreading layer was deposited onto the p-GaN layer. Time-resolved photoluminescence measurements showed that the photoluminescence decay time of LEDs containing silver NPs was significantly lower compared to the photoluminescence decay time of LEDs without silver NPs, indicating that the spontaneous emission rate was increased by energy transfer between the QW light emitter and SPs of the silver NPs. These findings show that silver NPs can be used effectively to increase the IQE of InGaN/GaN blue LEDs due to the strong coupling of QWs with SPs from the silver NPs. The output optical power increased by 32.2% at an input current of 100 mA due to the enhancement of the IQE. Moreover, other InGaN/GaN multiple QW LEDs with different structures have been produced by the sputtering-annealing process (Sung *et al.*, 2007; Cho *et al.*, 2010).

11.3.2 Lithographic metallic layer

Lithography is a common method for producing materials with a feature size of less than 100 nm. A typical lithographic system consists of the following components: (1) a mask that contains the patterns to be transferred and tools to ensure precise pattern transfer, (2) an energy source (for example, a light source) to transfer the pattern from the mask to substrate, (3) a photoresist or resist to record the patterns on the substrate during exposure and (4) procedures that reliably detect pattern defects, which clearly become more challenging as the critical dimensions diminish. However, most optical lithographic techniques do not have the resolution to produce sufficiently small, tightly spaced plasmonic geometries. In comparison, electron-beam lithography, which utilizes electrons in lieu of photons, has been successfully used to produce sub-100 nm structures due to the better spatial resolution and larger depth of focus compared to conventional photolithography. Yu *et al.* (2008) systematically studied the surface-enhanced spectroscopy of gold nanohole arrays with diameters between 40 nm and 520 nm and edge-to-edge distances between 60 and 120 nm. The materials were fabricated by electron-beam lithography and the results compared to those obtained from gold nanodisk arrays with comparable geometric parameters. Figure 11.1 shows the scanning electron microscopy (SEM) images of three gold nanodisks with diameters of 60 nm, 100 nm and 200 nm and gratings with sizes of 100 nm, 150 nm and 250 nm. The height of the nanodisks was 50 nm. The tunable optical properties originate from the difference in the SP resonance modes that are most efficiently excited in the nanohole and nanodisk arrays. The large tolerance for the dimensions and empty space confined by the nanoholes suggest that they can be used as a functional component in SP-enhanced LEDs. Although there have been few reports on its application for SP-enhanced LEDs, electron-beam lithography has been utilized to produce metallic NPs exhibiting enhanced light emission efficiency. For example, metal-enhanced fluorescence has been reported by Pompa *et al.* (2006). Here, electron-beam lithography was used to fabricate highly ordered triangular gold prisms, 100–200 nm wide, on planar substrates. Uniform CdSe/ZnS core/shell nanocrystals dispersed in a polymethylmethacrylate matrix to control the distance between the nanocrystals and gold NPs were spin-coated onto the substrate, and the resulting enhancement was as high as 30-fold, as demonstrated by a comparison of the fluorescence with and without gold NPs.

Although electron-beam lithography has high resolution and can delineate extraordinarily fine patterns, it has a small sample throughput. The NPs produced are only two-dimensional and the equipment is expensive. Therefore, alternative techniques have been proposed. One is nanosphere lithography, which has many desirable characteristics as a laboratory-scale nanofabrication tool. Nanosphere lithography is relatively inexpensive while offering parallel processing and high throughput. It can produce two-dimensional periodic arrays of many types of NPs on a variety of substrates. In traditional nanosphere lithography, a suspension of nanospheres is dropped onto a substrate, where they self-assemble into a hexagonal closely packed two-dimensional colloidal crystal, which serves as a deposition mask. This is followed by vacuum/electron-beam deposition and, finally, removal of the nanosphere mask by ultrasonic treatment in an organic solution (Hulteen and Van Duyne, 1995). Unlike electron-beam lithography, patterning is based on self-assembly rather than electron-beam irradiation. Hence, production costs are reduced because only a small amount of nanosphere solution is needed. In addition, using copper instead of gold, silver and platinum does not cause a degradation of NP properties and can further pare production costs (Chan *et al.*, 2007). Other nanosphere lithography-based techniques, for example, double-layer mask-based and angle-resolved nanosphere lithography, allow more flexible tuning of the metallic NP optical response (Haynes *et al.*, 2002). Consequently,

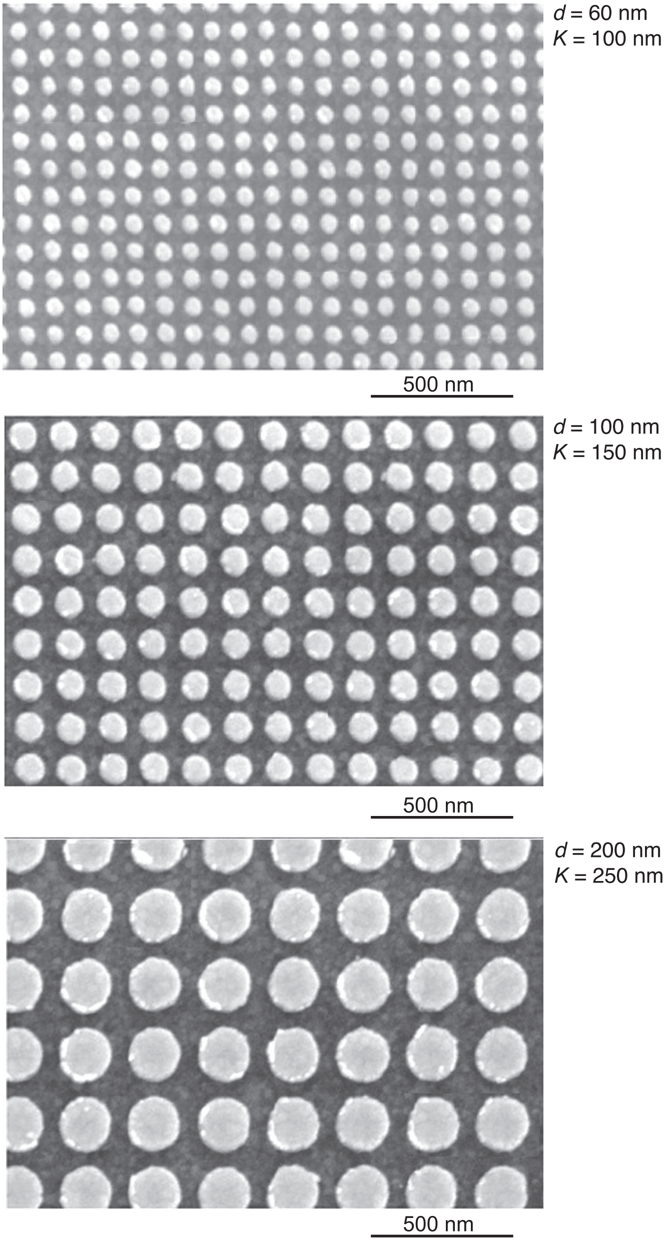
d = 60 nm
K = 100 nm
500 nm
d = 100 nm
K = 150 nm
500 nm
d = 200 nm
K = 250 nm
500 nm

11.1 SEM images of three gold nanodisks with diameters of 60 nm, 100 nm and 200 nm and gratings of 100 nm, 150 nm and 250 nm, respectively. The heights of all nanodisks were 50 nm. (Reprinted with permission from Yu *et al*. (2008). Copyright 2008, American Chemical Society.)

enhanced light emission is achieved. Nanosphere lithography has been utilized to fabricate metallic NPs to increase the photoluminescence from silicon nanocrystals and GaN light emitters (Mochizuki *et al.*, 2009; Mak *et al.*, 2009). It can produce size-tunable periodic silver NP arrays that are plasmonically active nanostructures by selecting the appropriate nanosphere diameter and/or thickness (Hulteen *et al.*, 1999; Jensen *et al.*, 2000; Haynes and Van Duyne, 2001). However, on account of inherent restrictions such as the difficulty of fabricating structures other than triangles or quasi-triangles, this method has not been extended to produce LEDs.

11.3.3 Template methods

In comparison with conventional lithographic techniques, using templates to fabricate electroluminescent LEDs has still to be explored. The template method is promising because of the ease of fabrication, excellent reproducibility, modest costs and capability of producing large areas. Moreover, the technique has the following advantages: (1) the ability to optimize periodic plasmonic geometries and tune the hot junction in the sub-10 nm regime and (2) the creation of long-range uniform plasmonic structures with centimeter dimensions. Common templates are often produced from porous anodic alumina (PAA) or by lithography techniques. At present, only PAA-based templates have been used to fabricate photoluminescent light emitters (Qiu *et al.*, 2009a).

PAA membranes form by self-organization when an aluminum foil is used as an anode in an electrolytic cell. This convenient nanotechnique has recently been used to fabricate highly ordered hemispherical silver nanocap arrays templated by PAA membranes as optical nanoantenna systems to support SP resonance at optical frequencies (Qiu *et al.*, 2009b). A typical method of preparing PAA involves two-step anodization. First, aluminum foils (99.99% pure), 0.2 mm thick, are degreased with acetone and electro-polished in a mixture of ethanol and perchloric acid with a volume ratio of 5:1 under a constant direct-current voltage of 15 V for 3 min to further remove surface impurities. After rinsing in distilled water and drying, the aluminum foils are anodized separately in a 0.5 M oxalic acid solution at a constant direct-current voltage of 40 V at 10 °C. The aluminum foils are then anodized for 2 h, which is followed by immersion in a mixture of chromic acid (1.8 wt%) and phosphoric acid (6 wt%) at 75 °C (1:1 in volume). After several hours, the alumina layer that grew in the first step is removed and the surface of the foil becomes bright. The PAA templates are obtained after a second anodizing step lasting 2 h.

PAA membranes with highly ordered nanopore arrays have many advantages from both the commercial and technical viewpoints. The densely packed nanopores in the array have diameters varying from several to hundreds of nanometers. The array has a periodic hexagonal arrangement. Precise control of the gap between the nanostructures in the sub-10 nm regime is possible, meaning that a high density of hot spots can be produced to yield enhanced photoluminescence. In addition to experimental conditions such as temperature, electrolyte concentration and applied anodic voltage, different pre-texturing processes have been developed to initiate pore growth on the aluminum surface and enhance the order of the resulting patterns (Asoh *et al.*, 2001). With careful optimization, a defect-free region with an area of several square centimeters has been produced (Masuda *et al.*, 1997). In fact, the use of PAA membranes as templates has been studied extensively and they can be used to fabricate various types of low-dimensional nanostructures including nanodots (Masuda and Fukuda, 1995), nanowires (Liu *et al.*, 2003) and nanotubes (Kim and Jin, 2001).

These different structures have been applied to Raman and fluorescence fields to enhance plasmon resonance. For example, Qiu *et al.* (2010) reported that they can be used in cell imaging. They fabricated a nanocap silver array using a direct-current magnetron sputtering system. The silver coatings were prepared on the PAA templates at room temperature under argon (20 sccm) in a conventional direct-current magnetron sputtering system. A 50-mm-diameter silver plate (99.99% pure) was used as the target. The sputtering chamber was initially evacuated to a base pressure below 2.5×10^{-3} Pa and then pre-sputtering was carried out at an argon gas pressure of 1.0 Pa for 5 min to clean the target surface. The power of the magnetron was ~40 W (voltage of 410 V and current of 100 mA). During deposition, the pressure in the magnetron chamber was 3.8×10^{-1} Pa and the distance between the target and the substrate was 20 cm. The sputtering time was 10 min. After deposition, the samples were protected from contamination and oxidation in a vacuum desiccator until they were used in further experiments. The results show that the fluorescence signals from fluorophores bound onto cell cytoskeletons were enhanced eightfold compared to the glass used in conventional experiments, demonstrating the potential of this PAA method in generating plasmon resonance.

11.4 Performance and outlook

In the past decade, advances in LEDs have enabled the widespread replacement of traditional lighting with solid-state light sources. However, as mentioned, typical inorganic blue light emitters based on GaN/InGaN QWs usually have a low IQE due to the relatively poor crystal quality. Since SPs can enhance efficiency when the original IQE is low, there is significant interest in using SPs to increase the overall efficiency of short-wavelength blue and green LEDs. The use of SPs in fabricating white LEDs has been described by Yeh *et al.* (2008b). Here, mixing the red light converted from blue/green photons and residual blue light leads to white-light emission. Instead of enhancing the IQE of a device, this configuration enhances light absorption by the CdSe/ZnS QWs via coupling between the QWs and SPs generated by the gold NPs. The advantages of this method are spectral tunability, high quantum efficiency and photo-stability. Another possible but seldom reported method for increasing the efficiency of white-light emitters is to incorporate NPs of different geometries into a device; a combination of NPs with various geometries results in several transmission dips corresponding to the type of NP (Bingham *et al.*, 2008). Hence, if different NPs with properly designed geometries are introduced into a white-light emitter, the various light components can be enhanced selectively, thereby producing light emitters with a required spectrum.

However, solid-state lighting applications require electrically injected devices and this adds challenges in producing the enhancing structures. When a metal layer is etched into a semiconductor, the LED's performance may degrade due to current leakage, surface recombination or damage to the QW layers. A photonic crystal is often added on to the top of an LED structure to improve the light extraction efficiency (Orita *et al.*, 2004), which is another limitation hampering the development of LEDs besides IQE. If it can be achieved, a perfectly designed structure combining the functions of photonic crystal and plasmon-enhanced material would be useful. This ideal three-dimensional structure would control light propagation in all directions. This functional structure may have the following advantages:

- Enhanced light extraction through scattering of waveguided light into radiation modes and inhibition of the emission of particular waveguided modes through the creation of a photonic bandgap.
- Enhanced spontaneous recombination rates (and the related IQE).
- Control of light emission patterns and, especially, enhancement of forward-directed light for LED applications that require high radiance.
- No degradation of LED performance and QW efficiency.

These dramatic efficiency improvements have not yet been realized by plasmon-mediated emission. There are many opportunities for demonstrating a greater enhancement of efficiency by improving QW/SP coupling, reducing SP losses and extracting light more effectively from the SP mode (Crawford, 2009).

The SP coupling technique can be applied to not only III-V materials, but also other materials that suffer from low quantum efficiency including indirect semiconductors (silicon, germanium, SiC, etc.). Usually, the emission efficiency of indirect semiconductors is quite low, but it is possible to enhance the efficiency using direct compound semiconductors by taking advantage of SP enhancement. This technique can produce super-bright solid-state light sources. They are expected to be cheap and easy to produce and become common light sources. In order to develop LED device structures based on this technique, we need to make very thin (10 nm) p- or n-doping layers and ohmic contact with layers of this size. These techniques are now being studied. SP coupling is a powerful method for developing efficient solid-state light emitters. When designing and fabricating even more efficient SP-enhanced optical devices with a wider spectral range, tuning of the SP mode is very important for achieving the matching condition of the energy coupling. SPs can be geometrically tuned by fabricating nanograting structures. It is predicted that using this technique, high-efficiency and high-speed light emission will be possible from optically as well as electrically pumped light emitters. Super-bright plasmonic light emitters are expected to become the dominant white-light sources for replacing conventional fluorescent tubes. The biggest challenges lie in the fabrication techniques. That is, even though the structures can be designed, it may not be possible to produce them using current technology. With regard to the fabrication challenges, it is expected that efforts will be made to extend existing methods that have proven useful for creating ordered metallic arrays, such as nano-imprinting and chemical synthesis, to LED fabrication. The key is to protect the LED structures during chemical processing (Gu, *et al.*, 2011).

11.5 Acknowledgements

This work was jointly supported by the National Natural Science Foundation of China under grants 51071045 and 51271057, the Program for New Century Excellent Talents in the University of the Ministry of Education of China under grant NCET-11-0096, the Natural Science Foundation of Jiangsu Province, China, under grant BK2012757, the open research fund of the Key Laboratory for MEMS of the Ministry of Education, Southeast University, Hong Kong Research Grants Council (RGC) General Research Funds (GRF) numbers CityU 112510 and 112212, as well as City University of Hong Kong research grants 9360110 and 9220061.

11.6 References

Asoh H, Nishio K, Nakao M, Tamamura T and Masuda H (2001) ‘Conditions for fabrication of ideally ordered anodic porous alumina using pretextured Al’, *J Electrochem Soc*, 148, B152–B156.

Bingham C M, Tao H, Liu X, Averitt R D and Zhang X, *et al.* (2008) ‘Planar wallpaper group metamaterials for novel terahertz applications’, *Opt Express*, 16, 18565.

Chan G H, Zhao J, Hicks E M, Schatz G C and Van Duyne R P (2007) ‘Plasmonic properties of copper nanoparticles fabricated by nanosphere lithography’, *Nano Lett*, 7, 1947–1952.

Chance P R, Prock A and Silbey R (1978) ‘Molecular fluorescence and energy transfer near interfaces’, *Adv Chem Phys*, 37, 1–65.

Cho C Y, Kwon M K, Lee S J, Han S H, Kang J W, *et al.* (2010) ‘Surface plasmon-enhanced light-emitting diodes using silver nanoparticles embedded in p-GaN’, *Nanotechnology*, 21, 205201.

Crawford M H (2009) ‘LEDs for solid-state lighting: performance challenges and recent advances’, *IEEE J Sel Top Quant*, 15, 1028–1040.

Ditlbacher H, Krenn J R, Felidj N, Lamprecht B, Schider G, *et al.* (2002) ‘Fluorescence imaging of surface plasmon fields’, *Appl Phys Lett*, 80, 404–406.

Fort E and Grésillon S (2008) ‘Surface enhanced fluorescence’, *J Phys D Appl Phys*, 41, 1–31.

Gu X, Qiu T, Zhang W and Chu P K (2011) ‘Light-emitting diodes enhanced by localized surface plasmon resonance’, *Nanoscale Res Lett*, 6,199.

Haynes C L and Van Duyne P R (2001) ‘Nanosphere lithography: a versatile nanofabrication tool for studies of size-dependent nanoparticle optics’, *J Phys Chem B*, 105, 5599–5611.

Haynes C L, McFarland A D, Smith M T, Hulteen J C and Van Duyne R P (2002) 'Angle-resolved nanosphere lithography: manipulation of nanoparticle size, shape, and interparticle spacing', *J Phys Chem B*, 106, 1898.

Hulteen J C and Van Duyne R P (1995) 'Nanosphere lithography: a materials general fabrication process for periodic particle array surfaces', *J Vac Sci Technol A*, 13, 1553.

Hulteen J C, Treichel D A, Smith M T, Duval M L, Jensen T R, *et al.* (1999) 'Nanosphere lithography: size-tunable silver nanoparticle and surface cluster arrays', *J Phys Chem B*, 103, 3854–3863.

Jensen T R, Malinsky M D, Haynes C L and Van Duyne P R (2000) 'Nanosphere lithography: tunable localized surface plasmon resonance spectra of silver nanoparticles', *J Phys Chem B*, 104, 10549–10556.

Kim K K and Jin J I (2001) 'Preparation of PPV nanotubes and nanorods and carbonized products derived therefrom', *Nano Lett*, 1, 631–636.

Kim B H, Cho C H, Mun J S, Kwon M K, Park T Y, *et al.* (2008) 'Enhancement of the external quantum efficiency of a silicon quantum dot light-emitting diode by localized surface plasmons', *Adv Mater*, 20, 3100–3104.

Kwon M K, Kim J Y, Kim B H, Park L K, Cho C Y, *et al.* (2008) 'Surface-plasmon-enhanced light-emitting diodes', *Adv Mater*, 20, 1253–1257.

Liu C H, Zapien J A, Yao Y, Meng X M, Lee C S, *et al.* (2003) 'High-density, ordered ultraviolet light-emitting ZnO nanowire arrays', *Adv Mater*, 15, 838–841.

Mak G Y, Fu W Y, Lam E Y and Choi H W (2009) 'Metallic nanoparticle array on GaN by microsphere lithography', *Phys Status Solidi C*, 6, S654.

Masuda H and Fukuda K (1995) 'Ordered metal nanohole arrays made by a two-step replication of honeycomb structures of anodic alumina', *Science*, 268, 1466–1468.

Masuda H, Yamada H, Satoh M, Asoh H, Nakao M *et al.* (1997) 'Highly ordered nanochannel-array architecture in anodic alumina', *Appl Phys Lett*, 71, 2770–2772.

Mochizuki Y, Fujii M, Hayashi S, Tsuruoka T and Akamatsu K (2009) 'Enhancement of photoluminescence from silicon nanocrystals by metal nanostructures made by nanosphere lithography', *J Appl Phys*, 106, 013517.

Orita K, Tamura S, Takizawa T, Ueda T, Yuri M, *et al.* (2004) 'High-extraction-efficiency blue light-emitting diode using extended-pitch photonic crystal', *Jpn J Appl Phys*, 43, 5809–5813.

Pompa P P, Martiradonna L, Della T A, Della S F, Manna L, *et al.* (2006) 'Metal-enhanced fluorescence of colloidal nanocrystals with nanoscale control', *Nat Nanotechnol*, 1, 126.

Qiu T, Kong F, Yu X Q, Zhang W J, Lang X Z, *et al.* (2009a) 'Tailoring light emission properties of organic emitter by coupling to resonance-tuned silver nanoantenna arrays', *Appl Phys Lett*, 95, 213104.

Qiu T, Zhang W L, Lang X Z, Zhou Y J, Cui T J, *et al.* (2009b) 'Controlled assembly of highly Raman-enhancing silver nanocap arrays templated by porous anodic alumina membranes', *Small*, 5, 2333–2337.

Qiu T, Jiang J, Zhang W J, Lang X Z, Yu X Q and Chu P K (2010), 'High-sensitivity and stable cellular fluorescence imaging by patterned silver nanocap arrays', *ACS Appl Mater Interfaces*, 2, 2465–2470.

Sambles J R, Bradbery G W and Yang F Z (1991) 'Optical-excitation of surface-plasmons: an introduction', *Contemp Phys*, 32, 173–183.

Sung J H, Kim B S, Choi C H, Lee M W, Lee S G, *et al.* (2009) 'Enhanced luminescence of GaN-based light-emitting diode with a localized surface plasmon resonance', *Microelectronic Engineering*, 86, 1120–1123.

Yeh D M, Chen C Y, Lu Y C, Huang C F and Yang C C (2007) 'Formation of various metal nanostructures with thermal annealing to control the effective coupling energy between a surface plasmon and an InGaN/GaN quantum well', *Nanotechnology*, 18, 265402.

Yeh D M, Huang C F, Chen C Y, Lu Y C and Yang C C (2008a) 'Localized surface plasmon-induced emission enhancement of a green light-emitting diode', *Nanotechnology*, 19, 345201.

Yeh D M, Huang C F, Lu Y C and Yang C C (2008b) 'White-light light-emitting device based on surface plasmon-enhanced CdSe/ZnS nanocrystal wavelength conversion on a blue/green two-color light-emitting diode', *Appl Phys Lett*, 92, 091112.

Yu Q M, Guan P, Qin D, Golden G and Wallace P M (2008), 'Inverted size-dependence of surface-enhanced Raman scattering on gold nanohole and nanodisk arrays', *Nano Lett*, 8, 1923–1928.

12

Nitride LEDs based on quantum wells and quantum dots

J. VERMA, A. VERMA, V. PROTASENKO,
S. M. ISLAM and D. JENA, University of Notre Dame, USA

DOI: 10.1533/9780857099303.2.368

Abstract: Tremendous progress has been made in the field of III-nitride light-emitting diodes from Schottky diodes to p-n junctions to heterostructures and structures based on quantum wells and quantum dots. The built-in polarization-induced electric field along {0001} reduces the oscillator strength in quantum well structures. However, this has been used to improve p-type doping in AlGaN alloys. InGaN-based high-efficiency blue LEDs have been developed and efforts are under way to fill the green gap in visible light emission from LEDs. On the other hand, wide bandgap III-nitrides are being developed for high-efficiency ultraviolet LEDs. Novel structures incorporating nanowires and photonic crystals are also being investigated.

Key words: p-n junction diode, polarization, dislocation, green gap, ultraviolet light-emitting diode.

12.1 Light-emitting diodes (LEDS)

Light-emitting diodes (LEDs) are used in a multitude of applications. Large-area displays and solid-state lighting stand to benefit immensely from high-efficiency light emitters. The availability of efficient solid-state light sources covering the entire visible spectrum has enabled a number of new applications that were previously not possible. Unlike inefficient incandescent light bulbs producing heat-induced radiation, solid-state light sources are designed to be efficient sources of photons at the quantum-mechanical level. Semiconductors form the basic fabric of LEDs. The operating mechanism of semiconductor LEDs involves the transition of electrons in a conduction band into an empty state in the valence band. If the process produces photons, it is called radiative recombination and results in useful light output. If the transition process is mediated by emission of phonons, it is non-radiative and results in loss of useful energy. The essence of LED design is to maximize the radiative transitions and reduce the non-radiative ones, under the constraints of the semiconductor material system used to realize them. We start the discussion with an introduction to the physics of electron motion in a p-n junction.

12.1.1 p-n junction diodes

Light emission was first observed from a semiconductor device in 1907 (Round, 1907). Unlike current LEDs, which use p-n junctions, the first semiconductor LEDs were metal-semiconductor Schottky diodes (Schubert, 2003). Later p-n homojunction LEDs were found to be more efficient light emitters than Schottky diodes. A p-n junction comprises an electron-rich n-type layer and an electron-deficient p-type layer in metallurgical contact. Chemical doping is typically achieved either during crystal growth or subsequently by ion implantation or thermally driven diffusion. An n-type semiconductor layer is formed when a donor atom provides an extra electron to the conduction band. This electron can move around freely through the crystal in response to electric fields or concentration gradients. Similarly, a p-type layer is formed when an acceptor atom captures an electron from the valence band creating a vacancy (hole), which can then move inside the crystal. From basic semiconductor physics, the electron and hole concentrations in a semiconductor in equilibrium are given by

$$n = N_c e \frac{(E_f - E_c)}{kT}, \qquad [12.1]$$

and

$$p = N_v e \frac{(E_v - E_f)}{kT}, \qquad [12.2]$$

where n and p are the volume concentrations (cm^{-3}) of electrons and holes, respectively, N_c is the conduction band-edge density of states, N_v is the valence band-edge density of states, E_f is the Fermi energy, E_c is the conduction band energy minimum, E_v is the valence band energy maximum, k is the Boltzmann constant and T is the ambient temperature. When the n- and p-regions are in contact, the free carriers in the p-n junction diffuse into regions of lower concentration. Holes diffuse from the p-layer into the n-layer, and electrons diffuse into the p-type layer. Thus a depletion region is created, which contains ionized acceptor and donor atoms and is devoid of free carriers. Carrier diffusion is constrained by the electric field produced due to the ionized charge dipole in the depletion region. This field creates a built-in potential, which is an energy barrier for carrier motion. Using the above equations along with Poisson's equation and assuming complete ionization of donor and acceptor atoms ($n=N_D$, $p=N_A$) and applying charge neutrality, the built-in potential is:

$$V_{bi} = \frac{q}{2\epsilon_s} \frac{N_A N_D}{N_A + N_D} W^2 \qquad [12.3]$$

or

$$V_{bi} = \frac{kT}{q} \ln\left(\frac{N_A N_D}{n_i^2}\right) \qquad [12.4]$$

where V_{bi} is the built-in potential, W is the depletion region width, N_A is the acceptor concentration, N_D is the donor concentration, n_i is the intrinsic carrier concentration, q is the electron charge and ϵ_s is the semiconductor dielectric constant. Under equilibrium conditions, the electron and hole Fermi levels are the same throughout the junction. Application of an external voltage across the junction, or optical excitation, creates a non-equilibrium situation. Under non-equilibrium conditions, the electron distribution and the hole distribution are considered to be in 'equilibrium amongst themselves', but not in equilibrium with each other. This non-equilibrium feature is quantitatively captured by the quasi-Fermi levels for electrons (E_{fn}) and holes (E_{fp}). The difference between the quasi-Fermi levels is a measure of how far from equilibrium the electron/hole system has been driven, with $E_{fn} - E_{fp} = 0$ signifying equilibrium. The quasi-Fermi levels are used to analyze current transport and the resulting optical phenomena in p-n junction LEDs.

The electron and hole current components in a p-n junction diode are given by the sum of the drift and diffusion currents:

$$J_n = qn\mu_n F + qD_n \frac{dn}{dx}, \qquad [12.5]$$

$$J_p = qn\mu_p F - qD_p \frac{dp}{dx}, \qquad [12.6]$$

where J_n and J_p are the electron and hole currents, respectively, F is the electric field, D_n is the electron diffusion constant, D_p is the hole diffusion constant and q is the unit electron charge. On applying a voltage bias, the minority carrier concentrations at the depletion region boundaries change from their equilibrium values; the new concentrations are given by the Shockley boundary conditions:

$$p_n(x_n) = p_{no} e^{\frac{qV_a}{kT}}, \qquad [12.7]$$

and

$$n_p(x_p) = n_{po} e^{\frac{qV_a}{kT}} \qquad [12.8]$$

where $p_n(x_n)$ is the hole concentration at the depletion region edge x_n in the n-type layer, $n_p(x_p)$ is the hole concentration at the depletion region edge x_p in the p-type layer, p_{no} is the equilibrium hole concentration in the n-type region, n_{po} is the equilibrium electron concentration in the p-type region and V_a is the applied bias. The minority carrier concentration near the depletion edge changes exponentially with the applied bias. The minority carrier concentration decreases exponentially away from the depletion region due to recombination of excess minority carriers with majority carriers. The minority carrier concentration thus drops exponentially from the depletion edge till it reaches the equilibrium concentration as shown in Fig. 12.1. The spatial variation of minority carriers in

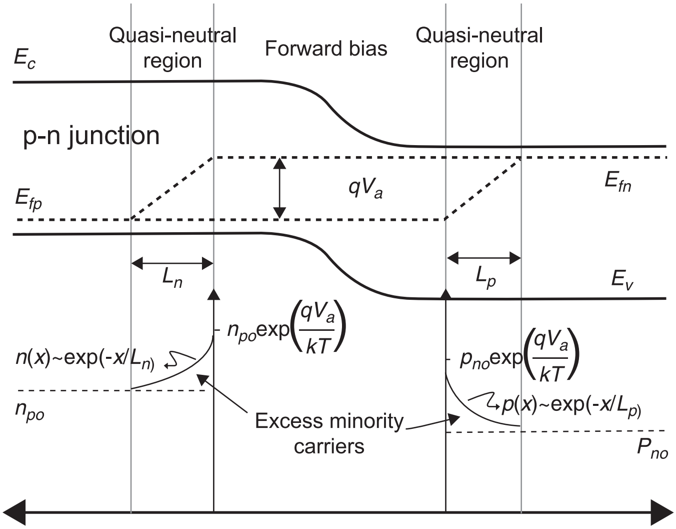
Quasi-neutral region
Forward bias
Quasi-neutral region
E_c
p-n junction
E_{fp}
qV_a
E_{fn}
L_n
L_p
E_v
$n_{po}\exp\left(\frac{qV_a}{kT}\right)$
$p_{no}\exp\left(\frac{qV_a}{kT}\right)$
$n(x)$~exp(-x/L_n)
$p(x)$~exp(-x/L_p)
n_{po}
Excess minority carriers
P_{no}

12.1 Band diagram and minority carrier distribution in a forward-biased p-n junction.

the quasi-neutral regions is obtained by solving the continuity equations in the region outside the depletion region:

$$p_n(x) = p_{no} + [p_n(x_n) - p_{no}]e^{-\frac{x}{L_p}}, \qquad [12.9]$$

and

$$n_p(x) = n_{po} + [n_p(x_p) - n_{po}]e^{-\frac{x}{L_n}} \qquad [12.10]$$

where L_n is the electron diffusion length and L_p is the hole diffusion length.

In the depletion region the current is carried primarily through diffusion, since the Fermi levels are approximately constant. The total current is the sum of electron diffusion current in the p-depletion edge, and the hole diffusion current at the n-depletion edge:

$$J_{total} = q\left(\frac{D_n}{L_n}n_{po} + \frac{D_p}{L_p}p_{no}\right)\left(e^{\frac{aV_a}{kT}} - 1\right) \qquad [12.11]$$

which can be written as

$$J_{total} = J_s\left(e^{\frac{qV_a}{kT}} - 1\right). \qquad [12.12]$$

This is the celebrated diode equation. The current increases exponentially with bias. In a p-n junction LED, electrons are injected into the depletion region from the n-side and holes are injected from the p-side. Thus, the depletion region, which was almost devoid of mobile carriers under equilibrium ($V_a = 0$), is flooded with excess electrons and holes under the application of a forward bias. If the situation in the depletion region is conducive to radiative recombination, the electrons recombine with holes to produce light. If not, then they either recombine non-radiatively producing heat, or overshoot to the other side contributing to recombination in the quasi-neutral n- and p-regions. Recombination in the quasi-neutral regions again may be radiative or non-radiative depending upon which process dominates.

12.1.2 Recombination mechanisms

The carriers injected into a diode undergo competitive radiative and non-radiative recombination processes. The generation rate is equal to the recombination rate at equilibrium. The photon absorption rate per unit volume, R_o, from the van Roosbroeck–Shockley model is the equilibrium recombination rate and is given by:

$$R_o = 8\pi c n'^2 \alpha_o \left(\frac{kT}{ch}\right)^3 \sqrt{\left(\frac{kT}{E_g}\right)} \int_{x_g}^{\infty} \frac{x^2\sqrt{x - x_g}}{e^x - 1}\,dx \qquad [12.13]$$

where c is the speed of light, n' is the refractive index of the material, k is the Boltzmann constant, T is the ambient temperature, α_o is the absorption constant at $E = 2E_g$ (E_g is the bandgap), $x = E/kT$ and $x_g = E_g/kT$. The radiative recombination rate in a semiconductor is given by:

$$R^* = Bnp, \qquad [12.14]$$

where B is the bimolecular recombination coefficient, n is the electron concentration and p the hole concentration. At equilibrium the rate is:

$$R_o = Bn_o p_o = Bn_i^2. \qquad [12.15]$$

Using 12.13 and 12.15 we can calculate B for different materials.

In a crystal, the carriers can undergo non-radiative recombination processes through defects, traps or by many-particle processes such as Auger recombination. Shockley, Read and Hall developed the theory for the non-radiative recombination of carriers due to traps that act as deep energy levels in the bandgap. The net recombination rate from the SRH theory is given by

$$R_{SRH} = \frac{np - n_i^2}{\tau_p(n + n_t) + \tau_n(p + p_t)}, \qquad [12.16]$$

where n is the electron concentration, p the hole concentration, n_i the intrinsic carrier concentration, τ_n the electron lifetime, τ_p the hole lifetime, n_t the electron density and p_t the hole density if the Fermi level is at the trap energy level. Thus,

$$n_t = n_i e^{\frac{E_t - E_i}{kT}}, \qquad [12.17]$$

and

$$p_t = n_i e^{\frac{E_i - E_t}{kT}}, \qquad [12.18]$$

where E_t is the trap energy level and E_i is the intrinsic Fermi energy level. At equilibrium, we have $np = n_i^2$ and thus there is no net recombination and generation – meaning that the two processes still occur but exactly cancel each other out. On the other hand, $np < n_i^2$ results in negative recombination, which is the same as generation, and $np > n_i^2$ results in recombination. The first case is achieved in a p-n junction under reverse bias conditions and is useful for the photovoltaic effect, which capitalizes on generation processes. The second case $np > n_i^2$ occurs under forward bias conditions: this non-radiative process competes for carriers with radiative processes.

In a defect-free intrinsic semiconductor, the non-radiative lifetime decreases with an increase in temperature, and it is a minimum when $E_t = E_i$. Therefore at high temperatures the radiative efficiency becomes low due to the high non-radiative recombination rate. Though here we have considered non-radiative recombination due to traps, in some cases deep level traps can lead to radiative recombination. An example is nitrogen-doped GaP, where nitrogen forms spatially localized states that are extended in momentum space allowing direct optical transitions in GaP, which is actually an indirect-bandgap semiconductor.

The other major non-radiative process is Auger recombination. In this process an electron scatters from the conduction band to a hole state in the valence band. But instead of the energy being released radiatively to a photon, it is spent in exciting another conduction band electron to a higher energy level in the conduction band (or a hole to the relevant higher energy level in the valence band). The excited electron (or hole) then relaxes back to the band minimum and releases the excess energy in the form of phonons, so the Auger processes are non-radiative. Since this process requires the presence of three carrier particles, the Auger recombination rate is given by

$$R_{Aug} = C_n n^2 p, \qquad [12.19]$$

for n-type semiconductors and

$$R_{Aug} = C_p p^2 n, \qquad [12.20]$$

for p-type semiconductors, where n is the electron concentration, p the hole concentration, and C_n and C_p are the Auger recombination coefficients. Under high-level injection conditions, the Auger recombination rate is proportional to the third power of the carrier density:

$$R_{Aug} = Cn^3. \qquad [12.21]$$

For III-V semiconductors (the group V elements used are arsenic or phosphorus),

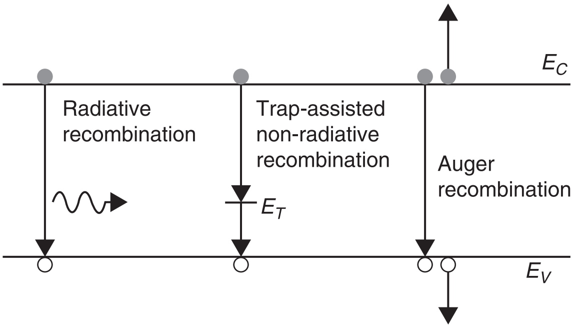

12.2 Band diagram showing different recombination processes.

C has been reported to be 10^{-29} cm^6.s^{-1} and for III-nitrides the value has been found to be close to 10^{-30} cm^6.s^{-1} (Shen *et al.*, 2007). Thus, due to the low value of *C*, Auger recombination becomes dominant only at high injection currents.

The various recombination mechanisms that occur in p-n junction LEDs described earlier are shown schematically in Fig. 12.2. The simplified total recombination rate in a semiconductor is given by:

$$R = An + Bn^2 + Cn^3, \tag{12.22}$$

where *A* is the monomolecular non-radiative recombination coefficient, *B* is the bimolecular radiative recombination coefficient, *C* is the Auger recombination coefficient and *n* is the electron carrier concentration.

While deriving the diode current equation, recombination processes in the quasi-neutral regions were considered, but those occurring inside the depletion region were neglected. If we consider this component, an additional recombination current term adds to the ideal diode current equation when the diode is operated in forward bias:

$$J_{net} = J_s\left(e^{\frac{qV_a}{kT}} - 1\right) + J_{rec} \tag{12.23}$$

where

$$J_{rec} = J_{SRH} + J_{rad} + J_{Aug} = q\int R\,dx \tag{12.24}$$

where *x* is the distance along the length, *R* is the net recombination rate given by 12.22 and the integral is taken over the active region.

12.1.3 LED efficiency

The wall-plug efficiency of a p-n junction LED is the watts of light produced divided by the watts spent in injecting current into the device. However, the overall conversion efficiency of an LED is given by

$$\eta_{tot} = \eta_{inj} \times \eta_{rad} \times \eta_{extr}, \qquad [12.25]$$

where the η_{tot} is the total efficiency, η_{inj} is the injection efficiency, η_{rad} is the radiative efficiency and η_{extr} is the extraction efficiency. The injection efficiency is the ratio of the number of carriers injected into the active region to the number of carriers injected into the LED structure from the contacts. The radiative efficiency is the fraction of the carriers injected into the active region that recombine radiatively. The extraction efficiency is the ratio of the photons that make it out of the LED to the photons generated in the active region. The radiative recombination efficiency is given by:

$$\eta_{rad} = \frac{Bn^2}{An + Bn^2 + Cn^3}, \qquad [12.26]$$

which can be written in terms of the carrier lifetime as:

$$\eta_{rad} = \frac{\dfrac{1}{\tau_{rad}}}{\dfrac{1}{\tau_{rad}} + \dfrac{1}{\tau_{nr}}}, \qquad [12.27]$$

where τ_{rad} is the radiative recombination lifetime and τ_{nr} is the non-radiative recombination lifetime. Identifying and minimizing the non-radiative loss processes and maximizing the radiative processes boost the efficiency of LEDs.

12.1.4 Homojunctions and heterojunctions, quantum wells and dots

The active region of a LED can be:

- a depletion region of a p-n junction structure (a homojunction)
- a quantum well (QW) or quantum dot (QD) region embedded in the depletion region surrounded by barriers (a heterojunction)
- a small bandgap depletion region in a double heterostructure p-n junction (a heterojunction).

To achieve a higher radiative recombination rate, the excess injected carrier concentration should be high in the layers where optical recombination is desired. For this reason, a double heterostructure design was adopted in which a low bandgap material is sandwiched between n-type and p-type layers of a high bandgap material. Thus the electron and holes are trapped in the low bandgap layer rather than being distributed along the whole diffusion length (Fig. 12.3). This results in an increased carrier concentration in the active region leading to higher radiative recombination efficiency.

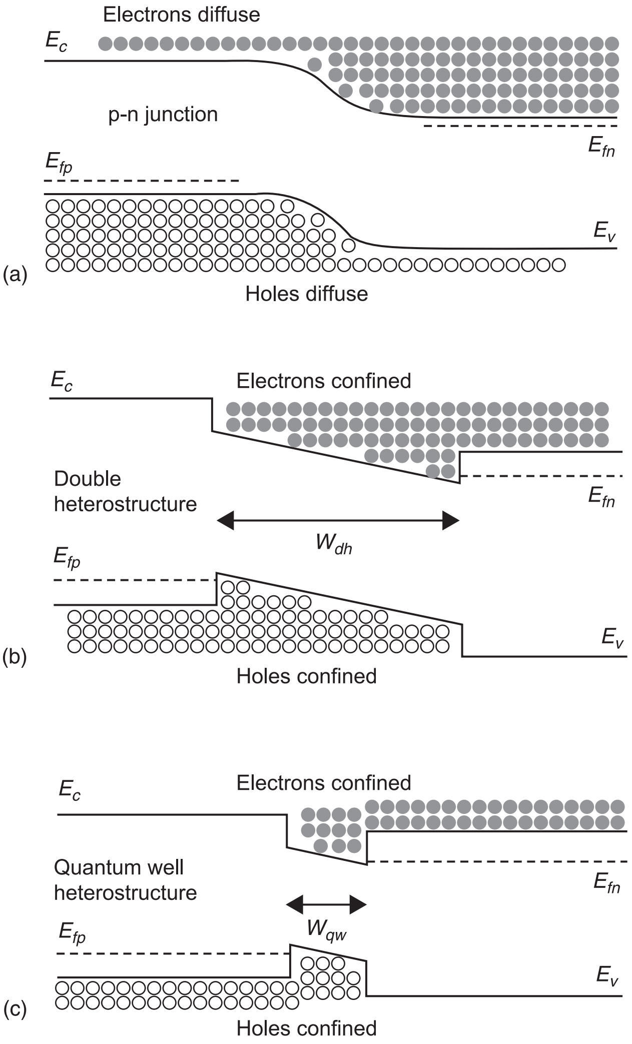
Electrons diffuse
E_c
p-n junction
E_{fn}
E_{fp}
E_v
(a)
Holes diffuse
E_c
Electrons confined
Double heterostructure
E_{fn}
W_{dh}
E_{fp}
E_v
(b)
Holes confined
E_c
Electrons confined
Quantum well heterostructure
E_{fn}
W_{qw}
E_{fp}
E_v
(c)
Holes confined

12.3 Conduction band diagrams showing carrier diffusion and confinement in: (a) a p-n junction (homojunction), (b) a double heterostructure (heterojunction) and (c) a quantum well heterostructure (heterojunction). As $W_{qw} < W_{dh}$, carrier confinement is higher in a quantum well than a double heterostructure resulting in a higher carrier concentration in a quantum well.

Another way to solve the problem of carrier diffusion is to utilize quantum well (QW) or quantum dot (QD) heterostructures. These are equivalent to a double heterostructure except that the width of the low bandgap region is much smaller (of the order of a few nanometers). One can use these as a single QW or multiple QWs (MQWs). The advantage of a low bandgap active region is that the quasi-Fermi levels can be pushed into the bands at low voltages, implying higher carrier injection for the same voltage. This is essential in lasers, but also useful in LEDs.

The carriers in an energy band in all semiconductor structures have a Fermi–Dirac distribution, so the carrier concentration has an exponential tail extending over the Fermi level at finite temperatures. A fraction of the excess carriers injected into the active region leaks out of the active region into the contact layers by surmounting any barriers in the way. This leakage current reduces η_{inj}. To reduce carrier leakage, electron-blocking layers (EBLs) are used in LEDs (Schubert, 2003). A higher bandgap layer, the EBL, is inserted between the p-type layer and the active region. The layer is heavily p-type doped to give a flat valence band profile to allow efficient hole injection. The bandgap difference is then completely reflected in the conduction band as shown in Fig. 12.4. Recently, graded electron-blocking layers (GEBL) have been employed to obtain the same effect (Wang *et al.*, 2010). The EBL blocks the electrons from leaking into the contact layer and thus increases recombination in the quantum well.

It took a long time for the mechanism of photon emission from semiconductors and the working of LEDs to be understood after the first experimental report. The first report of light emission from a semiconductor was in 1907 by Henry Joseph Round, a British engineer (Round, 1907). He observed yellow light

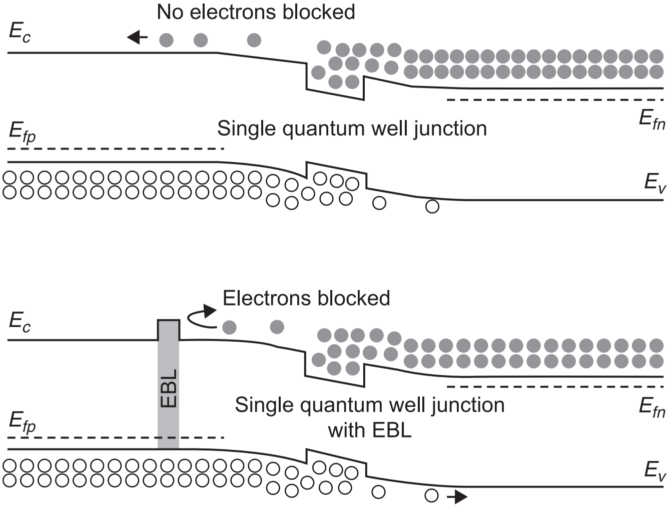

12.4 Band diagram of a single quantum well heterostructure, at forward bias, with and without an electron-blocking layer (EBL). The EBL blocks the electrons from leaking into the contact layer and thus increases recombination in the quantum well.

emission from SiC by applying a potential across two points of a crystal and reported the observation in *Electrical World*. In the latter half of the twentieth century, rapid progress was made in growing semiconductors, and methods such as liquid phase epitaxy (LPE), vapor phase epitaxy (VPE) and molecular beam epitaxy (MBE) were increasingly used for compound semiconductor growth.

The wavelength (or energy) of light emitted from semiconductor active regions is determined by the energy bandgap. The bandgaps of the III-nitride/arsenide/phosphide alloy system and the lattice constants are shown in Plate XIV (see colour section between pages 330 and 331). These alloys are predominantly used for fabricating LEDs covering the electromagnetic spectrum from the ultraviolet to the infrared.

12.1.5 LED development

The first LED was a Schottky diode, but subsequently p-n junctions were fabricated using GaAs, which emitted coherent infrared light at 842 nm (Hall *et al.*, 1962). Later Holonyak and Bevacqua (1962) demonstrated visible light emission at 710 nm from a GaAsP p-n junction. The realization of visible light emission was groundbreaking for solid-state lighting. LEDs became a component of displays. The GaAsP alloy system doped with nitrogen was used to fabricate green, yellow and amber LEDs (Krames *et al.*, 2007). But the efficiency of such LEDs was low due to the indirect bandgap of GaAsP alloys. The direct-gap AlGaInP alloy system was used to produce high-brightness visible LEDs ranging from 560 nm to 650 nm (Kuo *et al.*, 1990; Sugawara *et al.*, 1991; Huang *et al.*, 1992; Kish *et al.*, 1994; Krames *et al.*, 1999; Streubel *et al.*, 2002). Yellow, orange, red and green color emission could be obtained by using arsenide and phosphide based III-V semiconductors, but blue light emission was needed to complete the color spectrum in order to produce white light for lighting and displays.

Pankove *et al.* (1971) produced the first GaN LED at RCA in 1971. The structure comprised insulating GaN (zinc doped) and an unintentionally n-type doped GaN layer. Magnesium was thought to be a better p-type dopant for GaN films, but this doping was not realized till Amano *et al.* (1989) were able to obtain p-type GaN by low-energy electron-beam irradiation (LEEBI) of magnesium-doped GaN films. The electron beam was able to dissociate the Mg-H bonds, activating the magnesium and resulting in p-type doping. Nakamura *et al.* (1991a), working at Nichia (Japan), used thermal annealing to obtain the same effect in HVPE-grown magnesium-doped GaN films. Building on the success of obtaining p-type GaN layers, Nakamura *et al.* (1991b) produced the first GaN p-n junction light-emitting diode with emission at 430 nm. The GaN p-n junction LED was already more efficient than the then-commercial blue SiC LEDs.

Thereafter Nakamura *et al.* (1995) produced InGaN-based green and yellow LEDs emitting at 525 nm and 590 nm, respectively. The work on III-nitride visible

LEDs was carried forward into III-nitride ultraviolet LEDs, which utilized GaN/AlGaN heterostructures. Han *et al.* (1998) produced an AlGaN/GaN multiple quantum well (MQW) LED emitting at 353 nm. Employing AlN and AlGaN as the buffer layers for growing high-composition AlGaN active regions, the emission wavelength could be decreased further. AlN/AlGaN superlattice structures were utilized to reduce the dislocation density and defects in high-composition AlGaN layers grown on sapphire (Zhang *et al.*, 2002). Adivarahan *et al.* (2002) obtained emission at 285 nm from an AlGaN/AlGaN single quantum well (SQW) structure. Taniyasu *et al.* (2006) obtained emission at 210 nm from an AlN-based active region. However, the external quantum efficiencies (η_{tot}) achieved for the UV LEDs were low (Plate XV) (see colour section between pages 330 and 331). η_{tot} also decreases when the InGaN and AlInGaP composition is changed to obtain green LEDs (Plate XV). A variety of factors affect the external quantum efficiency (EQE) of III-nitride UV LEDs and green LEDs. Of these, defects and built-in polarization fields are the most prominent.

12.2 Polarization effects in III-nitride LEDs

III-nitrides are unique among semiconductors because of their large polarization values. In the following discussion we discuss the origin of polarization in III-nitrides and its pros and cons in optical devices such as LEDs.

12.2.1 Origin of spontaneous and piezoelectric polarization

The nitride family of semiconductors are formed from group III metals (aluminum, gallium and indium) and nitrogen from group V of the periodic table. In GaN, the nitrogen atom has much higher electronegativity than gallium. Therefore the electrons in a Ga-N bond are not equally shared between the two atoms, but pulled more towards the nitrogen atom. The bond is like an electric dipole with a dipole moment. As shown in Fig. 12.5, each gallium atom bonds to four nitrogen atoms and vice versa forming a tetrahedron. Other III-V semiconductors (III-As/P) crystallize to the zinc-blende crystal structure and the tetrahedron formed is almost perfectly symmetric so the four bonds forming the tetrahedron cancel each other's dipole moment, making the material non-polar. On the other hand, III-nitrides crystallize to a wurtzite crystal structure (non-centrosymmetric) forming an imperfect tetrahedron. Therefore, there is a net polarization along the c-axis <0 0 0 1>. This equilibrium polarization is called spontaneous polarization P_{sp}, and it exists even in the absence of strain in the material. It is similar to ferroelectricity, but the direction of the dipoles is frozen and cannot be altered by an external field.

Figure 12.6 shows bandgap versus lattice constant for the III-nitride family of semiconductors. It is evident that the lattice constants vary over a wide range. During epitaxial growth, lattice mismatch leads to strain, which further distorts

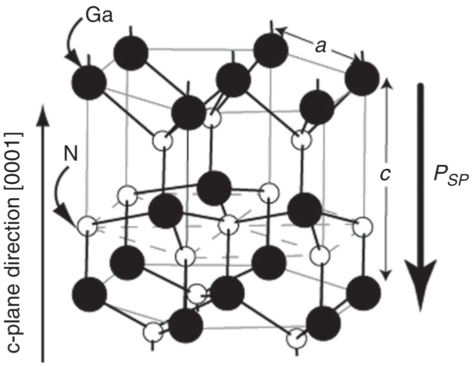

12.5 GaN wurtzite crystal structure (Simon, 2009).

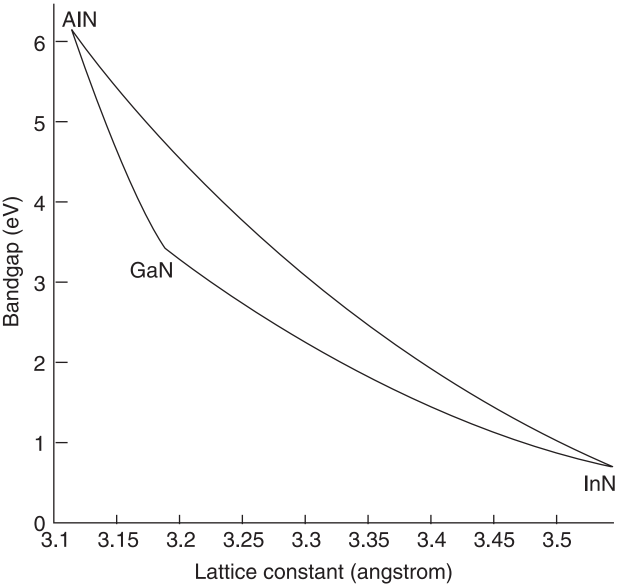

12.6 Bandgap vs lattice constant for the III-nitride semiconductor family.

the tetrahedron of bonds causing additional polarization known as piezoelectric polarization P_{pz}. The total polarization of a III-nitride film is the sum of spontaneous and piezoelectric components ($P_{tot}=P_{sp}+P_{pz}$).

The spontaneous and piezoelectric polarization, lattice constants and bandgap as a function of composition for III-nitride semiconductors are summarized in Table 12.1. Figure 12.7 shows the spontaneous, piezoelectric and total

Table 12.1 III-nitride properties as a function of composition

Spontaneous polarization (C/m^2) (Butte and Grandjean, 2007; Fiorentini *et al.*, 2002)	$P^{sp}_{Al_xGa_{1-x}N} = -0.090x - 0.034(1-x) + 0.019x(1-x)$ $P^{sp}_{In_xGa_{1-x}N} = -0.042x - 0.034(1-x) + 0.038x(1-x)$ $P^{sp}_{Al_xIn_{1-x}N} = -0.090x - 0.042(1-x) + 0.071x(1-x)$
Lattice constants (Å) (Butte and Grandjean, 2007) (using Vegard's law)	$a_{AlGaN}(x) = 3.189 - 0.077x$ $a_{InGaN}(x) = 3.189 + 0.356x$ $a_{AlInN}(x) = 3.545 - 0.433x$ $c_{AlGaN}(x) = 5.188 - 0.208x$ $c_{InGaN}(x) = 5.188 + 0.512x$ $c_{AlInN}(x) = 5.70 - 0.72x$
Piezoelectric polarization (C/m^2) (Butte and Grandjean, 2007; Fiorentini *et. al.*, 2002)	$P^{pz}_{GaN} = -0.918\varepsilon + 9.541\varepsilon^2$ $P^{pz}_{AlN} = -1.808\varepsilon + 5.624\varepsilon^2; \varepsilon < 0$ $P^{pz}_{AlN} = -1.808\varepsilon - 7.888\varepsilon^2; \varepsilon > 0$ $P^{pz}_{InN} = -1.373\varepsilon + 7.559\varepsilon^2$ $P^{pz}_{AlxInyGa1\text{-}x\text{-}yN} = xP^{pz}_{AlN} + yP^{pz}_{InN} + (1-x-y)P^{pz}_{GaN}$ where basal strain $\varepsilon(x,y) = [a_{sub} - a(x,y)]/a(x,y)$
Bandgap (eV) (Piprek, 2007) (unstrained, 300 K)	$E_g^{AlxGa_{1-x}N} = 6.2x + 3.4(1-x) - 0.7x(1-x)$ $E_g^{InxGa_{1-x}N} = 0.7x + 3.4(1-x) - 1.4x(1-x)$ $E_g^{Al_xIn_{1-x}N} = 6.2x + 0.7(1-x) - 2.5x(1-x)$

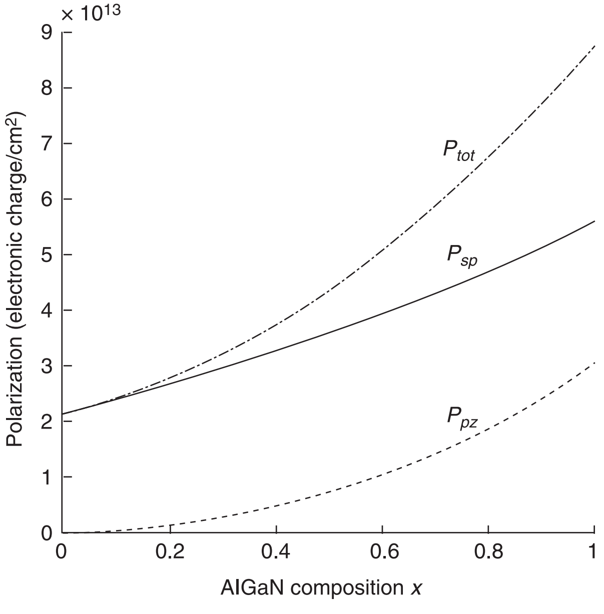

12.7 Spontaneous P_{sp}, piezoelectric P_{pz} and total polarization P_{tot} (electronic charge $q = -1.6 \times 10^{-19}$ C) for pseudomorphic AlGaN on GaN.

polarization of AlGaN strained to a GaN substrate, as calculated from the above formulas.

12.2.2 Polarization-induced electric fields

A schematic layer structure of a III-nitride LED is shown in Fig. 12.8. A lower bandgap InGaN quantum well (QW) is sandwiched between higher bandgap GaN barriers. Using a low bandgap active region helps in carrier confinement, improving the internal quantum efficiency (IQE) as discussed above. Usually the barrier and QW regions have different P_{tot} values, producing a polarization discontinuity at the heterointerface. From Maxwell's boundary condition equations, we know that the polarization discontinuity manifests as a bound sheet charge given by $P_1 - P_2 = \sigma_\pi$. This bound interface charge of density σ_π is shown in Fig. 12.8: it occurs as a dipole across the InGaN layer. The interface charge density is usually of the order of 10^{13} cm^{-2} resulting in large electric fields in the quantum well of the order of~MV/cm as shown in Fig. 12.9 for InGaN LEDs with a GaN barrier.

The large polarization-induced electric field bends the energy bands in the QW, forcing the electrons to one side and the holes to the other. The different effects of this large field on LED performance are discussed below.

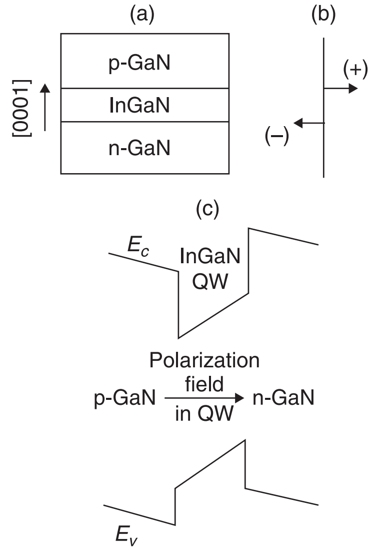

12.8 (a) Basic metal-polar nitride LED, (b) interface charges and (c) band diagram showing polarization field.

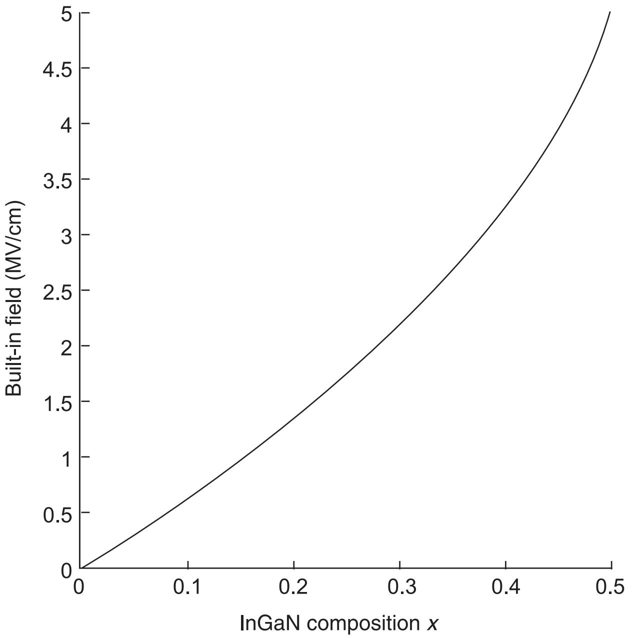

12.9 Polarization-induced electric field in an GaN/InGaN/GaN QW as a function of InGaN composition. The field points in the –c direction.

Red-shifted photon emission (quantum-confined Stark effect: QCSE)

As shown in Fig. 12.10, the polarization-induced field in the QW reduces the transition energy from the first electron subband to the first hole subband resulting in a red-shift of the emission from the LED, which is known as the quantum-confined Stark effect (Takeuchi *et. al.*, 1997; Deguchi *et. al.*, 1999). Upon application of forward bias, excess carriers are injected into the QW, which screen part of the polarization field, leading to blue-shifting of the spectrum with increasing current density (Takeuchi *et. al.*, 1997).

Decrease in oscillator strength

The rate at which an electron in the conduction band state $|c\rangle$ relaxes to an empty state (hole) in the valence band $|v\rangle$ by emitting a photon is given by Fermi's golden rule for optical transitions (Davies, 1998):

$$R_{rad} = \frac{2\pi}{\hbar} |V_{cv}|^2 \, \delta(\varepsilon_c - \varepsilon_v - \hbar\omega), \qquad [12.28]$$

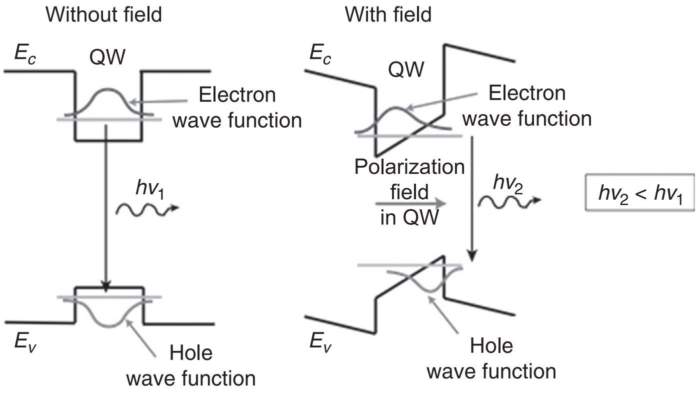

12.10 Quantum-confined Stark effect in nitride LEDs.

where ε_c and ε_v are the energy of an electron in the initial (CB) and final (VB) states, respectively, $\hbar\omega$ is the energy of the emitted photon and the Dirac δ function ensures energy conservation in the transition process. From Eq. 12.28, the radiative transition rate is proportional to the square of the matrix element V_{cv}, which quantifies the strength of the interaction between the electron and photon systems. Quite often in calculations, instead of using the matrix element directly, an equivalent quantity proportional to $|V_{cv}|^2$ called the oscillator strength is used. In a QW, the oscillator strength f_{osc} of an interband transition is (Butte and Grandjean, 2007; Davies, 1998):

$$f_{osc} = \frac{2}{m_e \hbar\omega_{cv}} \left|\left\langle u_c \middle| e.p \middle| u_v \right\rangle\right|^2 \left| \int f_e(z) f_h(z)\, dz \right|^2, \qquad [12.29]$$

where m_e is the mass of an electron, $\hbar$ is Planck's constant, ω_{cv} is the transition angular frequency, $\langle u_c \mid e.p \mid u_v \rangle$ is the momentum matrix element with u_c and u_v being the conduction band and valence band periodic Bloch functions, respectively. $\int f_e(z) f_h(z) dz$ is the overlap integral of the electron and hole envelope wave functions. The effect of large fields in the QW on the envelope functions is shown in Fig. 12.11.

The spatial separation of electron and hole envelope functions due to the field in the QW reduces the overlap integral (Im *et al.*, 1998). This reduces the radiative recombination rate, thus allowing non-radiative processes an upper hand in the competition for carrier recombination, leading to reduced IQE of light-emitting devices.

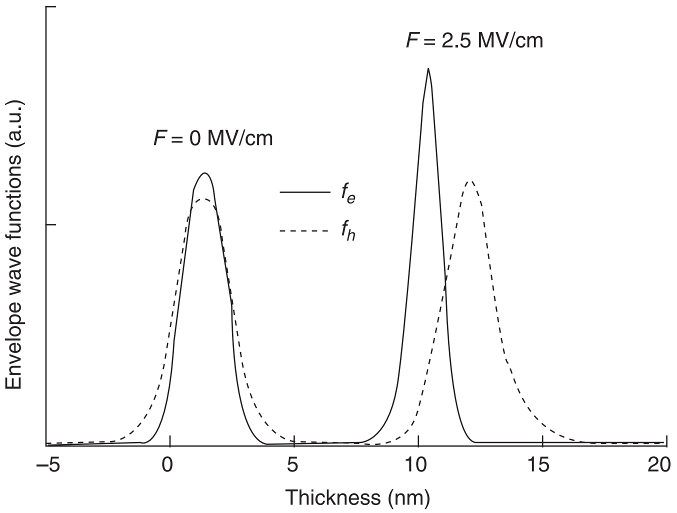

12.11 Reduction in overlap of electron and hole envelope wave functions with an increase in polarization field (Butte and Grandjean, 2007, with kind permission from Springer Science+Business Media BV).

12.2.3 Methods for improving internal quantum efficiency

Increasing the overlap by using thin quantum wells (QWs) and quantum dots (QDs)

The radiative decay time of carriers in an AlGaN/GaN QW and peak energy of emission as a function of well width are shown in Fig. 12.12 (Im *et al.*, 1998). Increasing the width of a QW leads to a red-shift in emission due to the QCSE and a corresponding decrease in the radiative decay rate due to the smaller electron/hole overlap. A similar trend is seen in GaN/AlN QDs (Renard *et al.*, 2009). By increasing the height of the dots, the photoluminescence decay time increases. This effect is due to the presence of polarization-induced electric fields in the active region.

On the other hand, when the QW width or QD size is decreased, the electron/hole subband energies increase because of size quantization effects. Since the energy band-offset confining the carriers in a well is finite, using very thin QWs or small QDs leads to poor confinement of carriers. This suggests that a careful design trade-off is necessary to determine the optimal QW and QD sizes for improving the overlap of carriers without compromising carrier confinement.

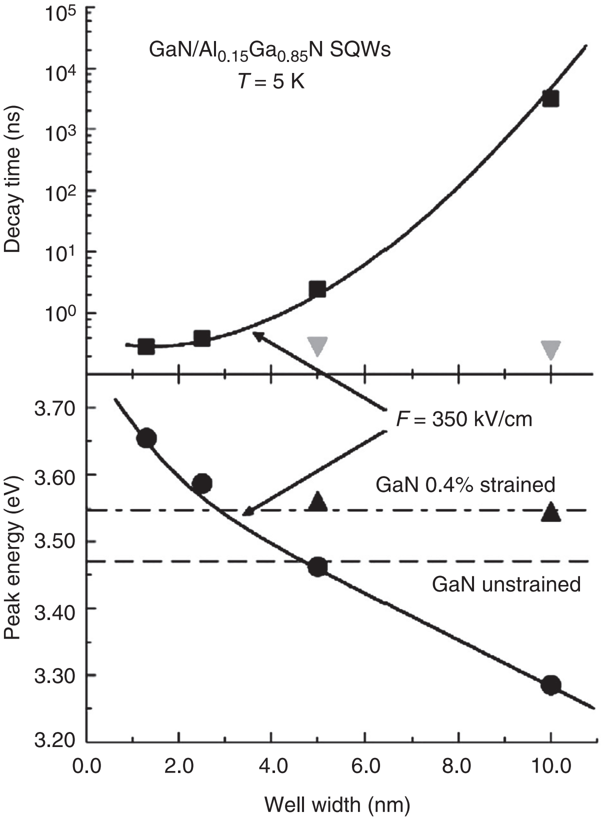

12.12 Comparison of the measured energy positions (circles) and decay times (squares) of the low-energy lines in GaN/AlGaN QWs calculated based on piezoelectric fields. (Reprinted with permission from Im *et al.* (1998). Copyright 1998, American Physical Society.)

Use of semipolar/non-polar substrates

An attractive way to increase the electron/hole overlap is to reduce or completely eliminate the polarization-induced electric field in the QW active region. This is achieved by growing III-nitride LED heterostructures in semipolar or non-polar crystallographic orientations (Waltereit *et al.*, 2000). Various crystallographic planes of III-nitrides are shown in Fig. 12.13 (Konar *et al.*, 2012). Since the polarization vector is along the c-axis [0 0 0 1] of the crystal, all the crystal orientations perpendicular to it of the form (h k l 0) have no polarization and are called non-polar planes (i.e., the m-plane: {1 −1 0 0} and the a-plane: {1 1 −2 0}). A plane oriented at an angle with the c-plane other than 90° is called a semipolar plane (e.g. the r-plane). LEDs grown along semipolar crystal orientations can retain the polarization-

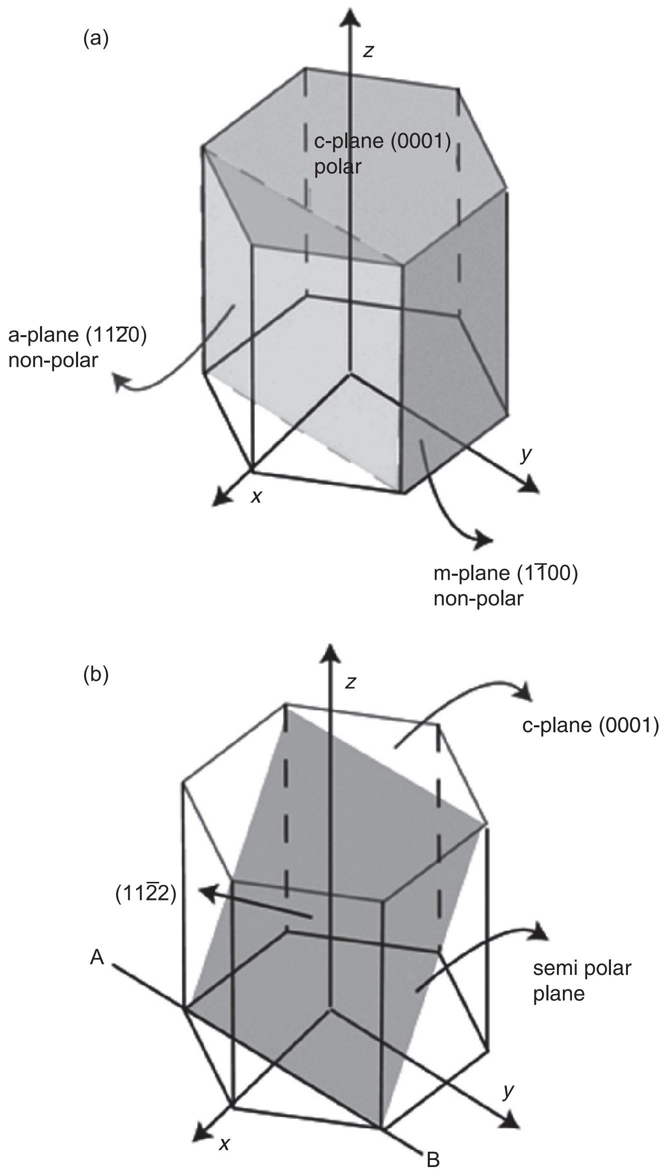
(a)
z
c-plane (0001)
polar
a-plane $(11\bar{2}0)$
non-polar
y
x
m-plane $(1\bar{1}00)$
non-polar
(b)
z
c-plane (0001)
$(11\bar{2}2)$
A
semi polar
plane
y
x
B

12.13 (a) Non-polar and (b) semipolar planes in III-nitrides. (Reproduced with permission from Konar *et al.* (2012). Copyright 2012, IOP Publishing. All rights reserved.)

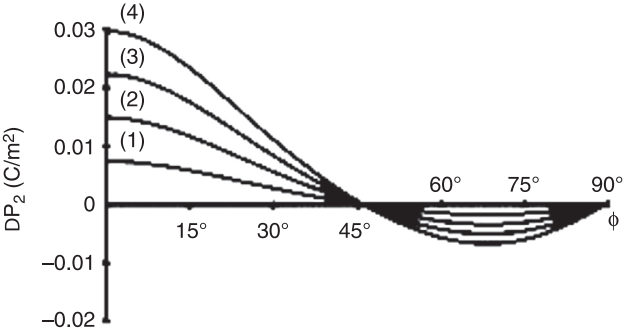

12.14 Computed polarization charge density in an InGaN/GaN QW as a function of tilt angle of the growth plane with respect to the c-plane. (Reprinted with permission from Romanov *et al.* (2006). Copyright 2006, AIP Publishing LLC.)

induced electric field in the QWs, but with a much smaller magnitude compared to those grown in the polar direction (Fig. 12.14) (Romanov *et al.*, 2006).

LEDs with very high efficiency have already been realized using the non-polar and semipolar orientations (Feezell *et al.*, 2007; Masui *et al.*, 2010; Nakamura, 2009). When large-area semipolar and non-polar GaN substrates become available, the efficiencies of LEDs are expected to improve across the entire spectrum due to reduced polarization-induced fields.

The largest volume application of III-nitride LEDs is in solid-state lighting. One hurdle in the development of efficient white light sources is the problem of efficiency droop (Piprek, 2010). Efficiency droop is the reduction in the LED electricity-to-light conversion efficiency at high injection current densities. The reasons for this behavior are still a topic of vigorous debate (Piprek, 2010). Semipolar and non-polar orientations are expected to reduce the efficiency droop, making the realization of efficient solid-state lighting possible (Pan *et al.*, 2012).

Polarization-matched LEDs

A method for reducing the fields inside a quantum well while retaining the polar orientation of growth is to reduce the polarization discontinuity at the well/barrier interface. This can be achieved by careful choice of quaternary AlInGaN barrier layers (Schubert *et al.*, 2008). Polarization-matching gives flexibility in retaining a band offset of the barrier and simultaneously in tuning the polarization. With the right material combination, the barrier and well layers become polarization-matched but have different bandgaps. This is shown in Fig. 12.15 (Schubert *et al.*, 2008). Polarization-matching has been shown to reduce the efficiency droop in InGaN LEDs and to decrease the blue-shift in spectrum with increasing current density (Schubert *et al.*, 2008; Xu *et al.*, 2009). The epitaxial growth of the

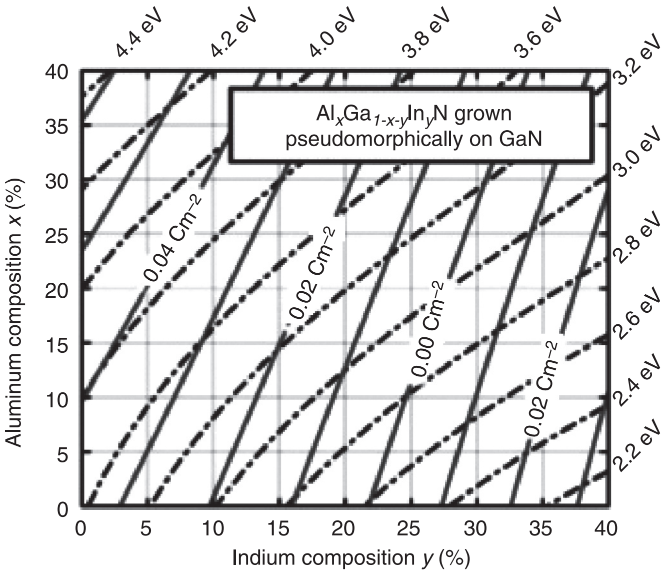

12.15 Polarization charge and bandgap contours for quaternary $Al_xGa_{1-x-y}In_yN$ grown pseudomorphically on GaN (Reprinted with permission from Schubert *et al.* (2008). Copyright 2008, AIP Publishing LLC.)

required material combinations are currently difficult, but are expected to improve in the future.

12.2.4 Problem of p-type doping in nitride LEDs and polarization-induced doping

p-type doping in III-nitrides remained elusive for a long time till the breakthrough by Amano *et al.* (1989). High-performance optoelectronic devices followed soon after it was realized that magnesium acceptors in GaN grown by chemical vapor deposition processes require activation (Nakamura *et al.*, 1993, 1995). However, even today, obtaining high hole concentrations in III-nitrides is difficult due to the large activation energy (E_A=200 meV) (Simon *et al.*, 2010) of magnesium in GaN. The situation becomes worse in high aluminum composition AlGaN alloys, since the magnesium activation energy in AlN is even higher (E_A=630 meV) (Simon *et al.*, 2010). Low hole concentrations combined with low hole mobility make the p-side of LEDs highly resistive, causing high I^2R losses. For ultraviolet (UV) LEDs fabricated using AlGaN alloys, it has remained difficult to fabricate low-resistance ohmic contacts to p-AlGaN because of the low hole concentration. A p-GaN cap layer is often used to lower the ohmic contact resistance, but this layer absorbs a portion of the UV light emitted in the active region, leading to reduced extraction efficiency of the LED.

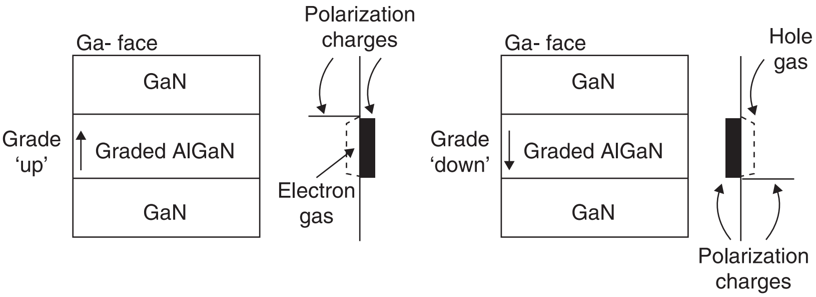

12.16 Three-dimensional polarization-induced n- and p-type doping (Jena, 2003).

In this section some disadvantages of polarization-induced fields in GaN LEDs were described. But just like any physical feature in semiconductors, if used judiciously, polarization also offers various advantages. It can be used to improve the p-type doping in III-nitrides. At a sharp heterojunction, the polarization discontinuity manifests as a bound sheet charge. Similarly, in a graded heterojunction, polarization manifests as a fixed bulk charge $\nabla.P=\rho_\pi$. If, instead of making an abrupt heterojunction, we continuously grade the material from one composition to another, the polarization charge is spread over the graded layer as shown in Fig. 12.16 (Jena, 2003). This fixed bulk polarization charge attracts oppositely charged mobile carriers to satisfy local charge neutrality. The creation of mobile charges is tantamount to doping. Since the polarization-induced doping process is purely electrostatic, it has no thermal activation energy, and the mobile carriers do not freeze out at low temperatures (Simon *et al.*, 2010). p-type polarization-induced doping has been demonstrated to improve light emission compared to magnesium-doped p-layers (Simon *et al.*, 2010).

12.3 Current status of III-nitride LEDs

High-efficiency red LEDs had been developed using $(Al_xIn_{1-x})_{1-y}Ga_yP$ alloys. However, there is a crossover from a direct gap to an indirect gap in $(Al_xIn_{1-x})_{1-y}Ga_yP$ alloys as x approaches 0.53, which results in decreased LED efficiency as the wavelength is reduced from 650 nm to the green part of the spectrum at 560 nm. Moreover, a lack of a suitable higher bandgap material leads to poor carrier confinement resulting in increased electron leakage. This further reduces the EQE of AlInGaP LEDs as they inch towards emission in the green region of the visible spectrum. As mentioned in Section 12.1.5, once the problems of growth and p-type doping were figured out, the field of III-nitride LEDs developed rapidly. The successful demonstration of metal-organic chemical vapor deposition (MOCVD)-grown InGaN/AlGaN double heterostructure violet LEDs and laser diodes by Nakamura *et al.* (1994), Fig. 12.17, further brought the

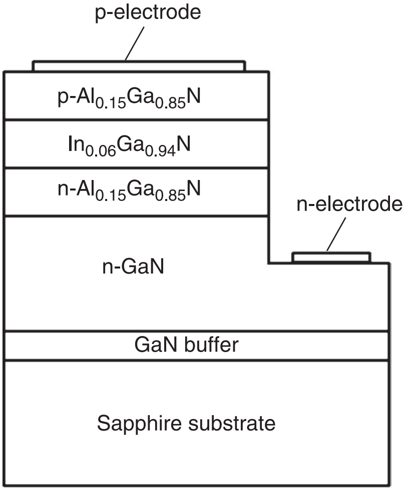

12.17 InGaN-AlGaN double heterostructure LED. The structure came to form the basis for future LED work with III-nitrides. (Reprinted with permission from Nakamura *et al*. (1994). Copyright 1994, American Institute of Physics.)

III-nitrides, and specifically the InGaN alloy system, into the limelight. Additionally, the InGaN alloy system spanned the entire visible spectrum. As a result, InGaN emerged as the front-runner for producing high-efficiency LEDs emitting from blue to green.

12.3.1 III-nitride visible LEDs

Nakamura *et al.* (1994) utilized single quantum well (SQW) InGaN LED structures to improve the EQE of InGaN-based blue LEDs from 2.7% (Nakamura *et al.*, 1994) to 7.3% (Nakamura *et al.*, 1995). The pre-strained growth technique in which low indium content InGaN/GaN quantum wells are inserted before the growth of the InGaN/GaN MQW active area has also proved to be useful in boosting the IQE of InGaN LEDs (Huang *et al.*, 2008). The IQE, photoluminescence (PL) intensity and electroluminescence (EL) intensity at 20 mA injection current were improved by 167%, 140% and 182%, respectively. This achievement was thought to be due to a weaker QCSE and weaker localization effect for carriers.

The growth of InGaN LEDs has been performed predominantly along the [0001] or gallium-polar direction by MOCVD. As discussed before, the large polarization field separates the electron and hole wave functions in the quantum well active regions. Recently a number of methods have been employed to improve the wave function overlap. Growth along non-polar/semipolar directions reduces the polarization-induced field and enhances the radiative recombination efficiency (Feezell *et al.*, 2009; Park *et al.*, 2007a; Schmidt *et al.*, 2007; Farrell *et al.*, 2007; Koslow *et al.*, 2010). Koslow *et al.* (2010) obtained 26.5% EQE InGaN LEDs at 452 nm whereas Zhao *et al.* (2011) achieved 52% EQE for blue-violet InGaN LEDs on semipolar free-standing GaN (FS-GaN). Additionally, incorporation of a δ-AlGaN layer or δ-InN in an InGaN QW and staggered QWs improves the wave function overlap resulting in increased radiative recombination (Arif *et al.*, 2007; Zhao *et al.*, 2009a, 2009b, 2009c, 2010a, 2010b; Park *et al.*, 2007b, 2009a, 2009b; Liao *et al.*, 2010; Park and Kawakami, 2006; Zhao and Tansu, 2010). Modifying the QWs into a triangular shape has also been found to enhance the radiative recombination efficiency (Yang *et al.*, 2009).

By increasing the indium fraction in an InGaN alloy, green and yellow LEDs with EQE of 2.1% and 1.2% (Nakamura *et al.*, 1995), respectively, were successfully produced. The decrease in EQE (Fig. 12.18) with increasing indium fraction in InGaN has been attributed to deteriorating material quality. The miscibility problem of indium and gallium leads to phase separation in high-composition InGaN, and the large lattice mismatch with the underlying GaN substrate induces more defects and dislocations compared to moderate indium

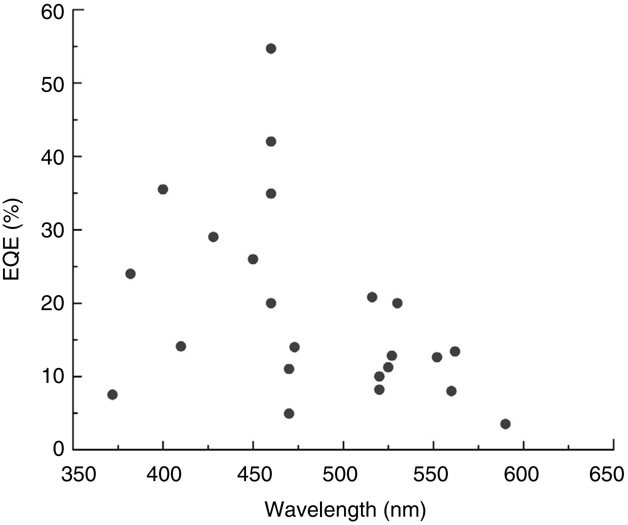

12.18 EQE variation with peak emission wavelength. A change in indium fraction in InGaN results in variation of IQE (Akita *et al.*, 2007; Chang *et al.*, 2003, 2010; Chen *et al.*, 2002; Guo *et al.*, 2010; Kim *et al.*, 2001; Leea *et al.*, 2011; Liu *et al.*, 2011; Lundin *et al.*, 2010; Nakamura and Chichibu, 2000; Nguyen *et al.*, 2011; Pan *et al.*, 2004; Sato *et al.*, 2008; Sheu *et al.*, 2001; Tadatomo *et al.*, 2001; Wuu *et al.*, 2005a, 2005b; Yamada *et al.*, 2002; Yamamoto *et al.*, 2010; Zhang *et al.*, 2010, 2012; Zhao *et al.*, 2011).

composition (Ho and Stringfellow, 1996; Teles *et al.*, 2000). Insertion of a low indium content InGaN layer prior to the QWs can also boost the performance of green LEDs, but the physics behind the increase in efficiency is different from that for blue InGaN LEDs. The energy transfer between donor-acceptor levels of GaN toward InGaN/GaN quantum wells was mediated with an underlying layer of $In_{0.063}Ga_{0.937}N$ (Xia *et al.*, 2010). The energy transfer stimulates light emission from the QWs and therefore the LED emitted 85% more light.

The EQE of InGaN LEDs increases for low injection current densities and then decreases gradually as the current density is increased (Fig. 12.19). The drop in efficiency with increasing current is termed the efficiency droop. Droop is observed universally in InGaN LEDs irrespective of the InGaN composition. Even non-polar and semipolar plane grown LED structures show degrees of efficiency droop at all temperatures. A number of possible physical reasons for droop have been investigated. Among them, non-radiative Auger recombination, electron leakage due to built-in polarization, high dislocation density, and poor hole concentration and mobility have been argued as the causes of efficiency droop (Shen *et al.*, 2007; Hader *et al.*, 2008; Delaney *et al.*, 2009; Pope *et al.*, 2003; Kim *et al.*, 2007; Schubert *et al.*, 2007, 2008; Hangleiter *et al.*, 2005; Monemar and Sernelius, 2007; van der Laak *et al.*, 2007; Laubsch *et al.*, 2007; Zhao *et al.*, 2010a). At this time, there is no clear verdict for the primary factor and it is likely there are various mechanisms at play. Polarization-matched active region and electron-blocking layers have been shown to mitigate the droop. Zhao *et al.* (2010a) recently employed thin AlInN barriers in place of AlGaN to decrease the carrier leakage and improve the drop in IQE with increasing current density. Moreover, a reduction in dislocation density (Fig. 12.20) in the structure also increases the efficiency and thus improves the efficiency droop (Fig. 12.21).

The radiative recombination efficiency of LEDs can also be improved by using QDs in place of QWs. QDs are zero-dimensional structures providing three-dimensional confinement of carriers. QD LEDs have been produced with III-arsenic semiconductors and the large lattice mismatch helped the growth of QDs in Stranski–Krastanov (SK) mode. Tanaka *et al.* (1996) were the first to grow GaN QDs. They used an anti-surfactant methodology and the GaN QDs showed stimulated emission under optical excitation. Adelmann *et al.* (2004) systematically studied GaN QD nucleation on AlN and recorded the QD height dependence on the substrate temperature during growth. Due to the QCSE, the peak emission wavelength from GaN QDs embedded in AlN increased as the QD height was increased. It was also found that the decay time increased with QD height in accordance with the QCSE (Renard *et al.*, 2009). Brown *et al.* (2006) studied the formation of GaN QDs under a varying gallium flux. They showed that high energy peaks in the PL spectrum from GaN/AlN QD structures were obtained from the QW formed by the GaN wetting layer and corroborated this with a theoretical model.

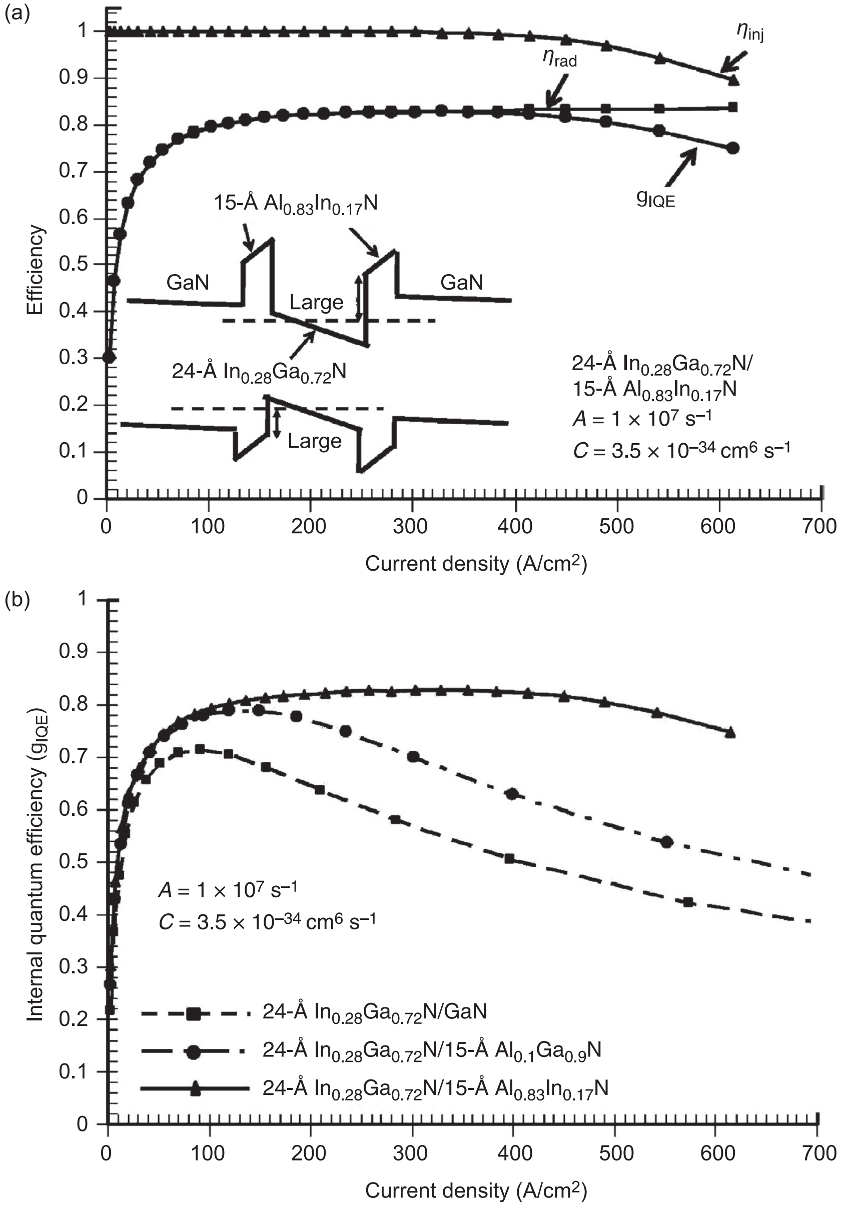

12.19 (a) IQE (η_{IQE}) of a 24-Å $In_{0.28}Ga_{0.72}N$/15-Å $Al_{0.83}In_{0.17}N$ QW (λ~480 nm) at 300 K. IQE (η_{IQE}), radiative efficiency (η_{rad}) and current injection efficiency (η_{inj}) are plotted as a function of total current density. (b) IQE (η_{IQE}) as a function of total current density for a 24-Å $In_{0.28}Ga_{0.72}N$/GaN QW, a 24-Å $In_{0.28}Ga_{0.72}N$/15-Å $Al_{0.1}Ga_{0.9}N$ QW and a 24-Å $In_{0.28}Ga_{0.72}N$/15-Å $Al_{0.83}In_{0.17}N$ QW. (Reprinted from Zhao *et al.* (2010b) with permission from Elsevier.)

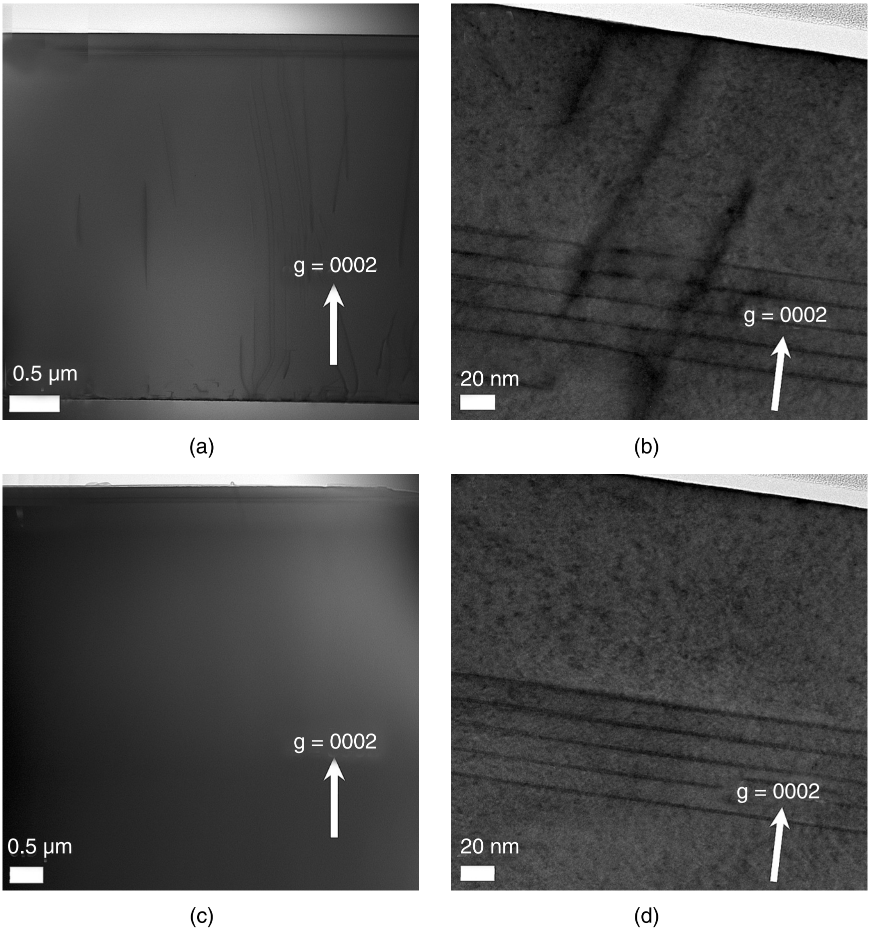

(a) (b)

(c) (d)

12.20 High-resolution transmission electron micrographs (HR-TEM) showing the defect distribution in LEDs. Cross section of full thickness of LEDs: (a) on sapphire and (c) on a FS-GaN substrate; top region including the MQWs of LEDs (b) on sapphire and (d) on a FS-GaN substrate. (Reprinted with permission from Chao *et al.* (2011). Copyright, 2011 IEEE.)

InGaN has a large lattice mismatch with GaN and therefore the alloy system is a suitable candidate for forming QDs on GaN through the Stranski–Krastanov (SK) mode. It has long been suspected that indium segregation in InGaN QWs leads to the formation of QDs. It is believed that such dots help in radiative recombination in InGaN LEDs in spite of the high density of dislocations (Narukawa *et al.*, 1997, 1999; O'Donnell *et al.*, 1999; Martin *et al.*, 1999; Chichibu *et al.*, 1996, 2001; Lai *et al.*, 2005, 2006). To investigate further, InGaN QDs were intentionally grown by MOCVD using silicon as an anti-surfactant

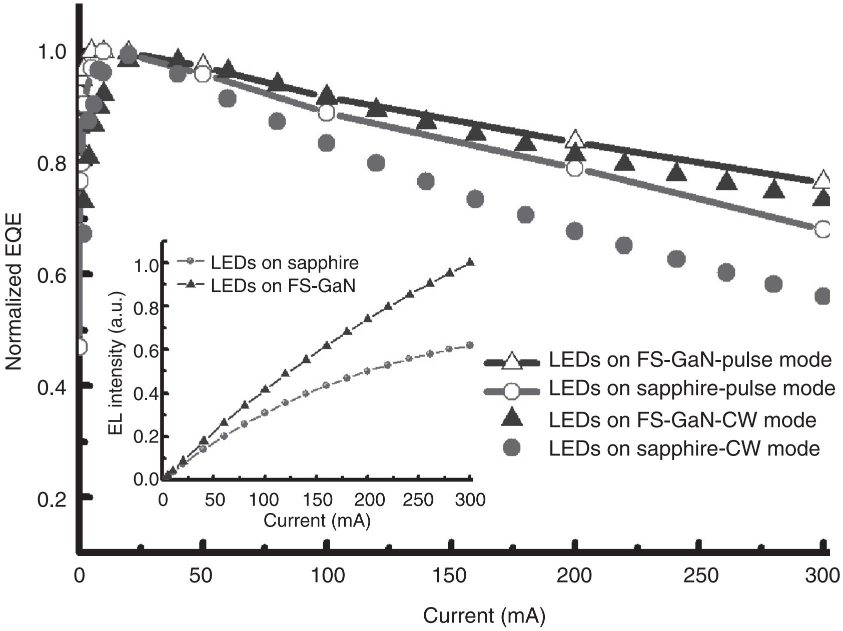

12.21 Normalized external quantum efficiency as a function of forward current for LEDs on sapphire and FS-GaN under continuous wave (CW) and pulse operations. The inserted plot is the output power versus current under CW mode. (Reprinted with permission from Chao *et al.* (2011). Copyright 2011, IEEE.)

(Hirayama *et al.*, 1998), and by MBE in the SK growth mode (Adelmann *et al.*, 2000). Xu *et al.* (2007) produced red, green and blue LEDs using InGaN QDs. Moustakas *et al.* (2008) showed that InGaN QD active region LEDs emit blue and green light. It was found that larger QDs nucleate near dislocations while small QDs nucleate in dislocation-free areas. Therefore the QDs mitigate non-radiative recombination at dislocations. InGaN QD green LEDs using tunnel injection were found to exhibit reduced efficiency droop at high current densities compared to similar InGaN QW LEDs (Bhattacharya *et al.*, 2010). Based on initial findings, III-nitride quantum dots are attracting increasing interest for enhancing the EQE of InGaN LEDs and potentially overcoming the efficiency droop problem.

12.3.2 III-nitride UV LEDs

Mukai *et al.* (1998) found that by decreasing the indium composition in the InGaN active region the emission wavelength could be decreased and 7.5% efficient 371-nm InGaN/AlGaN double heterostructure LEDs were fabricated. However, the InGaN alloy system cannot emit light at wavelengths less than 365 nm (the GaN bandgap). Moreover, the poor carrier confinement in the QWs of low indium composition InGaN/GaN LEDs reduces the efficiency. Thus, the AlGaN alloy system has been explored in order to achieve shorter wavelength emission in the UV region. Since AlN is a direct-bandgap semiconductor with a bandgap of ~6.2 eV, light emitters down to ~200 nm are feasible in the AlGaN material system. Visible LEDs are used in displays and solid-state lighting and UV LEDs are candidates for sterilization, as lithography tools, in water decontamination and as novel bio-sensors.

Khan *et al.* (1990) obtained the first optical emission from an AlGaN/GaN MQW structure. An AlGaN/GaN MQW structure LED was produced and emitted light at an energy above the GaN bandgap at 353 nm (Han *et al.*, 1998). The confining effects of the QW led to energy emission above the GaN bandgap. Figure 12.22(a) shows a typical UV LED structure, which consists of $Al_xGa_{1-x}N$/$Al_yGa_{1-y}N$ QW/barrier active region.

Initially III-nitride UV LED structures were grown on GaN buffer layers on sapphire. To achieve higher energy emission with increased efficiency, UV-transparent substrates are essential. With advances in growth techniques, AlN-on-sapphire became the substrate of choice for UV LEDs. High-composition AlGaN layers have a low lattice mismatch with the AlN buffer layer leading to reduced defect and dislocation density. Mukai *et al.* (2001) and Akita *et al.* (2007) showed that a decrease in dislocation density enhances the EQE of III-nitride LEDs. The AlN layer is effectively transparent to photons emitted from the $Al_xGa_{1-x}N$/$Al_yGa_{1-y}N$ active region. With advances in epitaxial growth methods,

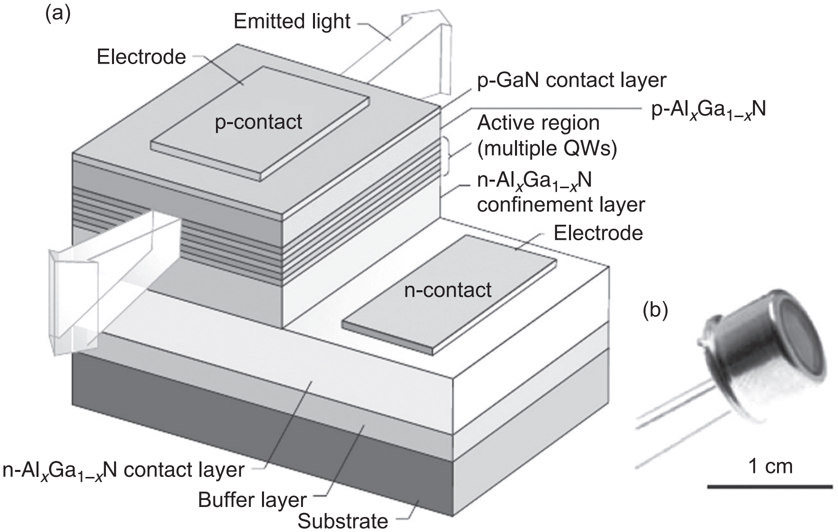
(a)
Emitted light
Electrode
p-contact
p-GaN contact layer
p-Al$_x$Ga$_{1-x}$N
Active region (multiple QWs)
n-Al$_x$Ga$_{1-x}$N confinement layer
Electrode
n-contact
(b)
n-Al$_x$Ga$_{1-x}$N contact layer
Buffer layer
Substrate
1 cm

12.22 (a) Typical UV LED. (b) Packaged UV LED. (Reprinted from Khan *et al.* (2008) with permission from Macmillan Publishers Ltd, copyright 2008.)

light emission was obtained at further short wavelengths (215–340 nm) (Khan *et al.*, 2008). Yoshida *et al.* (2008) produced a UV laser diode emitting at 342 nm based on an AlGaN active region. Shatalov *et al.* (2006) obtained stimulated emission from AlN at 214 nm through optical excitation.

As discussed earlier, mobile hole concentrations are rather low in high-composition magnesium-doped AlGaN layers. This increases the resistive losses in the diode. It is difficult to form ohmic contacts with increasing AlGaN composition. Therefore magnesium-doped GaN layers have been used for deep UV LEDs. The p-GaN layer also reduces current crowding in the top layer. Since the bandgap of GaN is smaller than the energy of photons emitted, this contact layer absorbs some of the emitted light and decreases the overall efficiency of the device. To overcome the p-type deficiency in wide bandgap III-nitrides, short-period AlGaN/AlGaN superlattices have been used. The built-in polarization of III-nitrides ionizes the magnesium in the GaN/Al(Ga)N superlattice leading to efficient doping through miniband formation (Kozodoy *et al.*, 1999; Goepfert *et al.*, 1999). AlN/AlGaN superlattices have also been used to achieve thick crack-free n-type AlGaN layers on AlN buffer layers (Zhang *et al.*, 2002). Polarization-induced doping by compositional grading of AlGaN in wide bandgap semiconductors has been shown to improve the hole concentration in p-AlGaN layers (Simon *et al.*, 2010).

Sapphire is insulating in nature and AlN is also a poor conductor. Thus lateral current crowding in UV LEDs grown on sapphire poses a major problem. Interdigitated finger structures and micropixel designs have been utilized successfully to facilitate the uniform injection of carriers. As a result an improvement in UV LED power output has been obtained (Khan *et al.*, 2005; Guo and Schubert, 2001; Adivarahan *et al.*, 2004).

The built-in polarization also affects the performance of UV LEDs. Polarization-matched active regions, electron blocking and low-resistance contact layers have improved the efficiency droop in InGaN visible LEDs. For UV LEDs, too, the AlInGaN alloy system and similar techniques can help in increasing their efficiencies.

III-nitride quantum dot UV LEDs have been produced using GaN QDs grown by the anti-surfactant method (Tanaka *et al.*, 1996). Self-assembled GaN QDs were grown by MBE in the SK and modified-SK growth modes (Adelmann *et al.*, 2000; Brown *et al.*, 2006; Renard *et al.*, 2009). InAlGaN QDs grown by the anti-surfactant method have shown promising results with emission at 335 nm (Hirayama and Fujikawa, 2008). By increasing the QD density, the emission intensity was increased. By varying the height of the GaN QDs, the emission energy could be tweaked from 310 nm to 440 nm (Renard *et al.*, 2009). Recently, Verma *et al.* (2013) demonstrated 261 nm emission from GaN QDs that had two monolayers. The QDs were grown in an AlN matrix and tunneling transport of carriers was employed in the LED structure.

The AlInGaN alloy system has a large parameter space with regard to bandgap, polarization fields and band offset, allowing the design of the most effective LED structures over a wide spectral range. It can be used to grow different quantum-confined structures in the form of QDs and QWs, and with the various techniques for improving the extraction efficiency, high-efficiency UV LEDs are expected in the near future.

12.4 Modern LED designs and enhancements

In addition to the LED structures described above, novel designs are being explored to improve the efficiency of III-nitride LEDs. We briefly review some of the ideas in this section.

12.4.1 Resonant-cavity light-emitting diodes (RCLEDs)

In an LED, light is emitted by the spontaneous recombination of electrons and holes in the active region. The efficiency depends on how fast this process occurs, which is proportional to the optical density of states at the frequency of emission. In an RCLED the active region is placed inside a resonant cavity (RC) whose resonant frequency matches the desired emission frequency (or wavelength) of the LED. This increases the optical density of states near the emission frequency speeding up the spontaneous emission rate. Thus, RCLEDs have higher optical intensities, improved LED efficiency, higher spectral purity because of the cavity and a much more directed far-field emission pattern (Schubert, 2003). RCLEDs were first realized with the III-arsenide system (Schubert *et al.*, 1992) but they have also been realized with III-nitrides (Song *et al.*, 2000; Calle *et al.*, 2002; Dorsaz *et al.*, 2004; Mastro *et al.*, 2008).

12.4.2 Super-luminescent light-emitting diodes (SLEDs)

SLEDs are edge-emitting p-n junctions with optical gain. When the injection current in the diode is increased to the extent that there is population inversion, the light emitted from the active region is amplified by stimulated emission as it propagates in the active region, which is also a gain medium. In this way high optical power output, compared to normal LEDs, can be obtained. Even though SLEDs have an active region with gain, they do not lase because there is no feedback mechanism available. As a consequence, SLEDs have high optical powers. Their spectrum is broader compared to lasers, but narrower than LEDs (Schubert, 2003). High-power blue SLEDs have been produced using III-nitrides (Feltin *et al.*, 2009; Rossetti *et al.*, 2010; Kafar *et al.*, 2012).

12.4.3 Nanowire LEDs

High-composition InGaN QW active regions are susceptible to strain-related degradation. However, if the InGaN active regions are grown in a nanowire geometry, the stress can be relaxed without generating dislocations. For this reason, InGaN nanowires hold great promise for realizing high-efficiency LEDs emitting in different parts of the visible spectrum (Kuykendall *et al.*, 2007; Guo *et al.*, 2010). Core/shell nanowire LEDs can also enable multicolor emitters (Qian *et al.*, 2005).

12.4.4 Polariton LEDs

A polariton is a quasi-particle formed when photons couple strongly with excitons (Pledran, 2008). They are half-light (photon) and half-matter (excitons), and are formed when excitons are created in a high-finesse optical cavity. Polaritons are bosons with an integral spin but very small mass. Therefore they can form a Bose–Einstein condensate at much higher temperatures, leading to highly efficient light-emitting devices with very low lasing thresholds (Deng *et al.*, 2003; Christopoulos *et al.*, 2007; Das *et al.*, 2011). Electrically injected polariton LEDs have been realized based on both III-arsenides (Tsintzos *et al.*, 2008) and III-nitrides (Lu *et al.*, 2011). Such devices are attracting attention because they could be used for semiconductor optoelectronics in the strong coupling regime, where light and matter behave as one.

12.5 References

Adelmann, C., Simon, J., Feuillet, G., Pelekanos, N. T., Daudin, B., *et al.* (2000). 'Self-assembled InGaN quantum dots grown by molecular-beam epitaxy', *Appl. Phys. Lett.*, 76, 1570–1572.

Adelmann, C., Daudin, B., Oliver, R. A., Briggs, G. A. D. and Rudd, R. E. (2004). 'Nucleation and growth of GaN/AlN quantum dots', *Phys. Rev. B*, 70, 125427-1–125427-8.

Adivarahan, V., Wu, S., Chitnis, A., Pachipulusu, R., Mandavilli, V., *et al.* (2002). 'AlGaN single-quantum-well light-emitting diodes with emission at 285 nm', *Appl. Phys. Lett.*, 81, 3666–3668.

Adivarahan, V., Wu, S., Sun, W. H., Mandavilli, V., Shatalov, M. S., *et al.* (2004). 'High-power deep ultraviolet light-emitting diodes based on a micro-pixel design', *Appl. Phys. Lett.*, 85, 1838–1840.

Akita, K., Kyono, T., Yoshizumi, Y., Kitabayashi, H. and Katayama, K. (2007). 'Characteristics of InGaN light emitting diodes on GaN substrates with low threading dislocation densities', *Phys. Status Solidi (a)*, 204, 246–250.

Amano, H., Kito, M., Hiramatsu, K. and Akasaki, I. (1989). 'P-type conduction in Mg-doped GaN treated with low-energy electron beam irradiation (LEEBI)', *Jpn. J. Appl. Phys.*, 28, L2112–L2114.

Arif, R. A., Ee, Y. K. and Tansu, N. (2007). 'Polarization engineering via staggered InGaN quantum wells for radiative efficiency enhancement of light emitting diodes', *Appl. Phys. Lett.*, 91, 091110–091112.

Bhattacharya, P., Zhang, M. and Hinckley, J. (2010). 'Tunnel injection $In_{0.25}Ga_{0.75}N$/GaN quantum dot light-emitting diodes', *Appl. Phys. Lett.*, 97, 251107.

Brown, J. S., Petroff, P. M., Wu, F. and Speck, J. S. (2006). 'Optical properties of GaN/AlN(0001) quantum dots grown by plasma-assisted molecular beam epitaxy', *Jpn. J. Appl. Phys.*, 45, L669–L672.

Butte, R. and Grandjean, N. (2007). 'Effects of polarization in optoelectronic quantum structures', in Wood, C. and Jena, D., *Polarization Effects in Semiconductors: From Ab Initio Theory to Device Applications*. Springer, Berlin, 1st edition, p. 487.

Calle, F., Naranjo, F. B., Fernandez, S., Sanchez-Garcia, A., Calleja, E., *et al.* (2002). 'Nitride RCLEDs grown by MBE for POF applications', *Phys. Stat. Sol. A* 192, 2, 277–285.

Chang, C. S., Chang, S. J., Su, Y. K., Kuo, C. H., Lai, W. C., *et al.* (2003). 'High brightness InGaN green LEDs with an ITO on n^{++}-SPS upper contact', *IEEE Trans. Elect. Devices*, 50, 2208–2212.

Chang, Y.-L., Wang, J. L., Li, F. and Mi, Z. (2010). 'High efficiency green, yellow, and amber emission from InGaN/GaN dot-in-a-wire heterostructures on Si(111)', *Appl. Phys. Lett.*, 96, 013106–013108.

Chao, C.-L., Xuan, R., Yen, H.-H., Chiu, C.-H., Fang, Y.-H., *et al.* (2011). 'Reduction of efficiency droop in InGaN light-emitting diode grown on self-separated freestanding GaN substrates', *IEEE Photonics Technol. Lett.*, 23, 798–800.

Chen, C. H., Chang, S. J., Su, Y. K., Chi, G. C., Sheu, J. K., *et al.* (2002). 'High-efficiency InGaN-GaN MQW green light-emitting diodes with CART and DBR structures', *IEEE J. Sel. Topics Q. Elect.*, 8, 284–288.

Chichibu, S., Azuhata, T., Sota, T. and Nakamura, S. (1996). 'Spontaneous emission of delocalized excitons in InGaN single and multiquantum well structures', *Appl. Phys. Lett.*, 69, 4188–4190.

Chichibu, F., Azuhata, T., Sugiyama, M., Kitamura, T., Ishida, Y., *et al.* (2001). 'Optical and structural studies in InGaN quantum well structure laser diodes', *J. Vac. Sci. Technol. B*, 19, 2177–2183.

Christopoulos, S., Hogersthal, G. B. H., Grundy, A. J. D., Lagoudakis, P. G., Kavokin, A. V., *et al.* (2007). 'Room-temperature polariton lasing in semiconductor microcavities', *Phys. Rev. Lett.*, 98, 126405.

Das, A., Heo, J., Jankowski, M., Guo W., Zhang, L., *et al.* (2011). 'Room temperature ultralow threshold GaN nanowire polariton laser', *Phys. Rev. Lett.*, 107, 066405.

Davies, J. H. (1998), *The Physics of Low-Dimensional Semiconductors*, Cambridge University Press.

Deguchi, T., Sekiguchi, K., Nakamura, A., Sota, T., Matsuo, R., *et al.* (1999). 'Quantum-confined Stark effect in an AlGaN/GaN/AlGaN single quantum well structure', *Jpn. J. App. Phys.*, 38, L914–L916.

Delaney, K. T., Rinke, P. and Van de Walle, C. G. (2009). 'Auger recombination rates in nitrides from first principles', *Appl. Phys. Lett.*, 94, 191109–191111.

Deng, H., Welhs, G., Snoke, D., Bloch, J. and Yamamoto, Y. (2003). 'Polariton lasing vs. photon lasing in a semiconductor microcavity', *PNAS 100*, 26, 15318–15323.

Dorsaz, J., Carlin, J. F., Zellweger, C. M., Gradecak, S. and Ilegems, M. (2004). 'InGaN/GaN resonant-cavity LED including an AlInN/GaN Bragg mirror', *Phys. Stat. Sol. (a)*, 201, 2675–2678.

Farrell, R. M., Feezell, D. F., Schmidt, M. C., Haeger, D. A., Kelchner, K. M., *et al.* (2007). 'Continuous-wave operation of AlGaN cladding-free nonpolar *m*-plane InGaN/GaN laser diodes', *Jpn. J. Appl. Phys.*, 46, L761–L763.

Feezell, D. F., DenBaars, S. P., Speck, J. S. and Nakamura, S. (2007). 'Recent performance of nonpolar and semipolar GaN-based light emitting diodes and laser diodes', *Compound Semiconductor Integrated Circuit Symposium 2007*, IEEE.

Feezell, D. F., Schmidt, M. C., DenBaars, S. P. and Nakamura, S. (2009). 'Development of nonpolar and semipolar InGaN/GaN visible light-emitting diodes', *MRS Bulletin*, 34, 318–323.

Feltin, E., Castiglia, A., Cosendey, G., Sulmoni, L., Carlin, J. F., *et al.* (2009). ‘Broadband blue superluminescent light-emitting diodes based on GaN’, *Appl. Phys. Lett.*, 95, 081107.

Fiorentini, V., Bernardini, F. and Ambacher, O. (2002). ‘Evidence for nonlinear macroscopic polarization in III–V nitride alloyheterostructures’, *Appl. Phys. Lett.*, 80, 1204–1206.

Goepfert, I. D., Schubert, E. F., Osinsky, A. and Norris, P. E. (1999). ‘Demonstration of efficient *p*-type doping in AlxGa$_{1-x}$N/GaN superlattice structures’, *Electron. Lett.*, 35, 1109–1111.

Guo, X. and Schubert, E. F. (2001). ‘Current crowding in GaN/InGaN light emitting diodes on insulating substrates’, *J. Appl. Phys.*, 90, 4191–4195.

Guo, W., Zhang, M., Banerjee, A. and Bhattacharya, P. (2010). ‘Catalyst-free InGaN/GaN nanowire light emitting diodes grown on (001) silicon by molecular beam epitaxy’, *Nano Lett.*, 10, 3355–3359.

Hader, J., Moloney, J. V., Pasenow, B., Koch, S. W., Sabathil, *et al.* (2008). ‘On the importance of radiative and Auger losses in GaN based quantum wells’, *Appl. Phys. Lett.*, 92, 261103–261105.

Hall, R. N., Carlson, R. O., Soltys, T. J., Fenner, G. E. and Kingsley, J. D. (1962). ‘Coherent light emission from GaAs junctions’, *Phys. Rev. Lett.*, 9, 366–369.

Han, J., Crawford, M. H., Shul, R. J., Figiel, J. J., Banas, M., *et al.* (1998). ‘AlGaN/GaN quantum well ultraviolet light emitting diodes’, *Appl. Phys. Lett.*, 73, 1688–1690.

Hangleiter, A., Hitzel, F., Netzel, C., Fuhrmann, D., Rossow, U., *et al.* (2005). ‘Suppression of nonradiative recombination by V-shaped pits in GaInN/GaN quantum wells produces a large increase in the light emission efficiency’, *Phys. Rev. Lett.*, 95, 127402-1–127402-4.

Hirayama, H. and Fujikawa, S. (2008). ‘Quaternary InAlGaN quantum-dot ultraviolet light-emitting diode emitting at 335 nm fabricated by anti-surfactant method’, *Phys. Stat. Sol. (c)*, 5, 2312–2315.

Hirayama, H., Tanaka, S., Ramvall, P. and Aoyagi, Y. (1998). ‘Intense photoluminescence from self-assembling InGaN quantum dots artificially fabricated on AlGaN surfaces’, *Appl. Phys. Lett.*, 72, 1736–1738.

Ho, I.-H. and Stringfellow, G. B. (1996), ‘Solid phase immiscibility in InGaN’, *Appl. Phys. Lett.*, 69, 2701–2703.

Holonyak, N. and Bevacqua, S. F. (1962). ‘Coherent (visible) light emission from Ga(As$_{1-x}$P$_x$) junctions’, *Appl. Phys. Lett.*, 1, 82–83.

Huang, K. H., Yu, J. G., Kuo, C. P., Fletcher, R. M., Osentowski, *et al.* (1992). ‘Twofold efficiency improvement in high performance AlGaInP light-emitting diodes in the 555–620 nm spectral region using a thick GaP window layer’, *Appl. Phys. Lett.*, 61, 1045–1047.

Huang, C.-F., Liu, T.-C., Lu, Y.-C., Shiao, W.-Y., Chen, Y.-S., *et al.* (2008). ‘Enhanced efficiency and reduced spectral shift of green light-emitting-diode epitaxial structure with prestrained growth’, *J. Appl. Phys.*, 104, 123106-1–123106-7.

Im, J. S., Kollmer, H., Off, J., Sohmer, A., Scholz, F. *et al.* (1998). ‘Reduction of oscillator strength due to piezoelectric fields in GaN/Al$_x$Ga$_{1-x}$N quantum wells’, *Phys. Rev. B*, 57, R9435–R9438.

Jena, D. (2003). Polarization induced electron populations in III-V nitride semiconductors: transport, growth and device applications, PhD thesis, UCSB.

Kafar, A., Stanczyk, S., Grzanka, S., Czernecki R., Leszczynski, M., *et al.* (2012). ‘Cavity suppression in nitride based superluminescent diodes’, *J. App. Phys.*, 111, 083106.

Khan M. A., Skogman, R. A., Van Hove, G. M., Krishnankutty, S. and Kolbas, R. M. (1990). 'Photoluminescence characteristics of AlGaN-GaN-AlGaN quantum wells', *Appl. Phys. Lett.*, 56, 1257–1259.

Khan, M. A., Shatalov, M., Maruska, H. P., Wang, H. M. and Kuokstis, E. (2005). 'III–nitride UV devices', *Jpn. J. Appl. Phys.*, 44, 7191–7206.

Khan, A., Balakrishnan, K. and Katona, T. (2008). 'Ultraviolet light-emitting diodes based on group three nitrides', *Nature Photonics*, 2, 77–84.

Kim, A. Y., Gotz, W., Steigerwald, D. A., Wierer, J. J., Gardner, N. F., *et al.* (2001). 'Performance of high-power AlInGaN light emitting diodes', *Phys. Stat. Sol. (a)*, 188, 15–21.

Kim, M.-H., Schubert, M. F., Dai, Q., Kim, J. K., Schubert, E. F., *et al.* (2007). 'Origin of efficiency droop in GaN-based light-emitting diodes', *Appl. Phys. Lett.*, 91, 183507–183509.

Kish, F. A., Steranka, F. M., DeFevere, D. C., Vanderwater, D. A., Park, K. G., *et al.* (1994). 'Very high-efficiency semiconductor wafer-bonded transparent-substrate (Al Ga) In P/GaP light-emitting diodes', *Appl. Phys. Lett.*, 64, 2839–2841.

Kneissl, M., Kolbe, T., Chua, C., Kueller, V., Lobo, N., *et al.* (2011). 'Advances in group III-nitride-based deep UV light-emitting diode technology', *Semicond. Sci. Technol.*, 26, 014036–014041.

Konar, A., Verma, A., Fang, T., Zhao, P., Jana, R., *et al.* (2012). 'Charge transport in non-polar and semi-polar III-V nitride heterostructures', *Semicond. Sci. Technol.*, 27, 024018.

Koslow, I. L., Sonoda, J., Chung, R. B., Pan, C., Brinkley, S., *et al.* (2010). 'High power and high efficiency blue InGaN light emitting diodes on (30-3-1) free-standing semipolar bulk GaN substrate', *Jpn. J. Appl. Phys.*, 49, 080203–080205.

Kozodoy, P., Hansen, M., DenBaars, S.P. and Mishra, U.K. (1999). 'Enhanced Mg doping efficiency in $Al_{0.2}Ga_{0.8}N$/GaN superlattices', *Appl. Phys. Lett.*, 74, 3681–3683.

Krames, M. R., Ochiai-Holcomb, M., Höfler, G. E., Carter-Coman, C., Chen, E. I., *et al.* (1999). 'High-power truncated-inverted-pyramid (Al Ga) In P/GaP light-emitting diodes exhibiting >50% external quantum efficiency', *Appl. Phys. Lett.*, 75, 2365–2367.

Krames, M. R., Shchekin, O. B., Mueller-Mach, R., Mueller, G. O., Zhou, L., *et al.* (2007). 'Status and future of high-power light-emitting diodes for solid-state lighting', *J. Disp. Tech.*, 3, 160–175.

Kuo, C. P., Fletcher, R. M., Osentowski, T. D., Lardizabal, M. C., Craford, M. G., *et al.* (1990). 'High performance AlGaInP visible light-emitting diodes', *Appl. Phys. Lett.*, 57, 2937–2939.

Kuykendall, T., Ulrich, P., Aloni, S. and Yang, P. (2007). 'Complete composition tunability of InGaN nanowires using a combinatorial approach', *Nature Materials*, 6, 951–956.

Lai, Y.-L., Liu, C.-P. and Chen, Z.-Q. (2005). 'Study of the dominant luminescence mechanism in InGaN/GaN multiple quantum wells comprised of ultrasmall InGaN quasiquantum dots', *Appl. Phys. Lett.*, 86, 121915–121917.

Lai, Y.-L., Liu, C.-P., Hsuen, T.-H., Lin, Y.-H., Chung, H.-C., *et al.* (2006). 'The influence of quasi-quantum dots on physical properties of blue InGaN/GaN multiple quantum wells', *Nanotechnol.*, 17, 4300–4306.

Laubsch, A., Sabathil, M., Bruederl, G., Wagner, J., Strassburg, M., *et al.* (2007). 'Measurement of the internal quantum efficiency of InGaN quantum wells', *Proc. SPIE*, 6486, 64860J-1–64860J-10.

Leea, J. W., Taka, Y., Kima, J.-Y., Honga, H.-G., Chaea, S., *et al.* (2011). 'Growth of high-quality InGaN/GaN LED structures on (111) Si substrates with internal quantum efficiency exceeding 50%', *J. Crystal Growth*, 315, 263–266.

Liao, C. T., Tsai, M. C., Liou, B. T., Yen, S. H. and Kuo, Y. K. (2010). 'Improvement in output power of a 460 nm InGaN light-emitting diode using staggered quantum well', *J. Appl. Phys.*, 108, 063107-1–063107-6.

Liu, Z., Wei, T., Guo, E., Yi, X., Wang, L., *et al.* (2011). 'Efficiency droop in InGaN/GaN multiple-quantum-well blue light-emitting diodes grown on free-standing GaN substrate', *Appl. Phys. Lett.*, 99, 091104–091106.

Lu, T. C., Chen, J. R., Lin, S. C., Huang, S. W., Wang, S. C., *et al.* (2011), 'Room temperature current injection polariton light emitting diode with a hybrid microcavity', *Nano Lett.*, 11, 2791–2795.

Lundin, W. V., Nikolaev, A. E., Sakharov, A. V., Zavarin, E. E., Usov, S. O., *et al.* (2010). 'High-efficiency InGaN/GaN/AlGaN light-emitting diodes with short-period InGaN/GaN superlattice for 530–560 nm range', *Tech. Phys. Lett.*, 36, 1066–1068.

Martin, R. W., Middleton, P. G., O'Donnell, K. P. and Van der Stricht, W. (1999). 'Exciton localization and the Stokes' shift in InGaN epilayers', *Appl. Phys. Lett.*, 74, 263.

Mastro, M. A., Caldwell, J. D., Holm, R. T., Henry, R. L. and Eddy, C. R. (2008). 'Design of gallium nitride resonant cavity light-emitting diodes on Si substrates', *Adv. Mater.*, 20, 115–118.

Masui, H., Nakamura, S., DenBaars, S. P. and Mishra, U. K. (2010). 'Nonpolar and semipolar III-nitride light-emitting diodes: achievements and challenges', *IEEE TED*, 57, 88–100.

Monemar, B. and Sernelius, B. E. (2007). 'Defect related issues in the 'current roll-off' in InGaN based light emitting diodes', *Appl. Phys. Lett.*, 91, 181103–181105.

Moustakas, T. D., Xu, T., Thomidis, C., Nikiforov, A. Y., Zhou, L., *et al.* (2008). 'Growth of III-nitride quantum dots and their applications to blue-green LEDs', *Phys. Stat. Sol. (a)*, 205, 2560–2565.

Mukai, T., Morita, D. and Nakamura, S. (1998). 'High-power UV InGaN/AlGaN double-heterostructure LEDs', *J. Crystal Growth*, 189–190, 778–781.

Mukai, T., Nagahama, S., Iwasa, N., Senoh, M. and Yamada, T. (2001). 'Nitride light-emitting diodes', *J. Phys. Condens. Matter*, 13, 7089–7098.

Nakamura, S. (2009). 'Current status of GaN-based solid-state lighting', *MRS Bulletin*, 34, 101–107.

Nakamura, S. and Chichibu, S. F. (2000). *Introduction to Nitride Semiconductor Blue Lasers and Light Emitting Diodes*, London and New York, CRC Press.

Nakamura, S., Mukai, T. and Senoh, M. (1991a). 'High-power GaN P-N junction blue-light-emitting diodes', *Jpn. J. Appl. Phys.*, 30, L1998–L2001.

Nakamura, S., Senoh, M. and Mukai, T. (1991b). 'Highly P-typed Mg-doped GaN films grown with GaN buffer layers', *Jpn. J. Appl. Phys.*, 30, L1708–L1711.

Nakamura, S., Senoh, M. and Mukai, T. (1993). 'High power InGaN/GaN double heterostructure violet light emitting diodes', *Appl. Phys. Lett.*, 62, 2390–2392.

Nakamura, S., Mukai, T. and Senoh, M. (1994). 'Candela-class high-brightness InGaN/AlGaN double-heterostructure blue-light-emitting diodes', *Appl. Phys. Lett.*, 64, 1687.

Nakamura, S., Senoh, M., Iwasa, N. and Nagahama, S. (1995). 'High-brightness InGaN blue, green and yellow light-emitting diodes with quantum well structures', *Jpn. J. Appl. Phys.*, 34, L797–L799.

Narukawa, Y., Kawakami, Y., Funato, M., Fujita, S., Fujita, S., *et al.* (1997). 'Role of self-formed InGaN quantum dots for exciton localization in the purple laser diode emitting at 420 nm', *Appl. Phys. Lett.*, 70, 981–983.

Narukawa, Y., Kawakami, Y., Fujita, S. and Makamura, S. (1999). 'Dimensionality of excitons in laser-diode structures composed of $In_xGa_{1-x}N$ multiple quantum wells', *Phys. Rev. B*, 59, 10283–10288.

Nguyen, H. P. T., Zhang, S., Cui, K., Han, X., Fathololoumi, S., *et al.* (2011). 'p-type modulation doped InGaN/GaN dot-in-a-wire white-light-emitting diodes monolithically grown on Si(111)', *Nano Lett.*, 11, 1919–1924.

O'Donnell, K. P., Martin, R. W. and Middleton, P. G. (1999). 'Origin of luminescence from InGaN diodes', *Phys. Rev. Lett.*, 82, 237–240.

Pan, C.-C., Lee, C.-M., Liu, J.-W., Chen, G.-T. and Chyi, J.-I. (2004). 'Luminescence efficiency of InGaN multiple-quantum-well ultraviolet light-emitting diodes', *Appl. Phys. Lett.*, 84, 5249–5251.

Pan, C. C., Tanaka, S., Wu, F., Zhao, Y., Speck, J. S., *et al.* (2012). 'High-power, low-efficiency-droop semipolar (20-2-1) single-quantum-well blue light-emitting diodes', *Appl. Phys. Expr.*, 5, 062103.

Pankove, J. I., Miller, E. A., Richman, D. and Berkeyheiser, J. E. (1971). 'Electroluminescence in GaN', *J. Luminescence*, 4, 63.

Park, J. and Kawakami, Y. (2006). 'Photoluminescence property of InGaN single quantum well with embedded AlGaN δ layer', *Appl. Phys. Lett.*, 88, 202107–202109.

Park, S. H., Ahn, D. and Chuang, S. L. (2007a). 'Electronic and optical properties of *a*- and *m*-plane wurtzite InGaN/GaN quantum wells', *IEEE J. Quantum Electron.*, 43, 1175–1182.

Park, S. H., Park, J. and Yoon, E. (2007b). 'Optical gain in InGaN/GaN quantum well structures with embedded AlGaN delta layer', *Appl. Phys. Lett.*, 90, 023508–023510.

Park, S. H., Ahn, D. and Kim, J. W. (2009a). 'High-efficiency staggered 530 nm InGaN/InGaN/GaN quantum-well light-emitting diodes', *Appl. Phys. Lett.*, 94, 041109–041111.

Park, S. H., Ahn, D., Koo, B. H. and Kim, J. W. (2009b). 'Electronic and optical properties of staggered InGaN/InGaN quantum-well light-emitting diodes', *Phys. Status Solidi, A Appl. Mater. Sci.*, 206, 2637–2640.

Piprek, J. (2007). *Nitride Semiconductor Devices: Principles and Simulation*, Wiley-VCH, 1st edition.

Piprek, J. (2010). 'Efficiency droop in nitride-based light-emitting diodes', *Phys. Status Solidi (a)*, 207, 2217–2225.

Pledran, B. D. (2008). 'Polaritronics in view', *Nature*, 453, 297–298.

Pope, I. A., Smowton, P. M., Blood, P., Thomson, J. D., Kappers, M. J., *et al.* (2003). 'Carrier leakage in InGaN quantum well light-emitting diodes emitting at 480 nm', *Appl. Phys. Lett.*, 82, 2755–2757.

Qian, F., Gradecak, S., Li, Y., Wen, C. Y. and Lieber, C. M. P. (2005). 'Core/multishell nanowire heterostructures as multicolor, high-efficiency light-emitting diodes', *Nano Lett.*, 5, 2287–2291.

Renard, J., Kandaswamy, P., Monroy, E. and Gayral, B. (2009). 'Suppression of nonradiative processes in long-lived polar GaN/AlN quantum dots', *Appl. Phys. Lett.*, 71, 131903–131905.

Romanov, A. E., Baker, T. J., Nakamura, S. and Speck, J. S. (2006), 'Strain-induced polarization in wurtzite III-nitride semipolar layers', *J. Appl. Phys.* 100, 023522.

Rossetti, M., Dorsaz, J., Rezzonico, R., Duelk, M., Velez, C., *et al.* (2010), 'High power blue-violet superluminescent light emitting diodes with InGaN quantum wells', *Appl. Phys. Exp.* 3, 061002–061004.

Round, H. J. (1907), ‘A note on carborundum’, *Electrical World*, 49, 308.

Sato, H., Chung, R. B., Hirasawa, H., Fellows, N., Masui, H., *et al.* (2008). ‘Optical properties of yellow light-emitting diodes grown on semipolar (1122) bulk GaN substrates’, *Appl. Phys. Lett.*, 92, 221110–221112.

Schmidt, M. C., Kim, K.-C., Farrell, R. M., Feezell, D. F., Cohen, D. A., *et al.* (2007). ‘Demonstration of nonpolar *m*-plane InGaN/GaN laser diodes’, *Jpn. J. Appl. Phys.* 46, L190–L191.

Schubert, E. F. (2003). *Light Emitting Diodes*, Cambridge University Press.

Schubert, E. F., Wang, Y. H., Cho, A. Y., Tu, L. W. and Zydzik, G. J. (1992). ‘Resonant cavity light emitting diode’, *Appl. Phys. Lett.*, 60, 921–923.

Schubert, M. F., Chhajed, S., Kim, J. K., Schubert, E. F., Koleske, D. D., *et al.* (2007). ‘Effect of dislocation density on efficiency droop in GaInN/GaN light-emitting diodes’, *Appl. Phys. Lett.*, 91, 231114–231116.

Schubert, M. F., Xu, J., Kim, J. K., Schubert, E. F., Kim, M. H., *et al.* (2008). ‘Polarization-matched GaInN/AlGaInN multi-quantum-well light-emitting diodes with reduced efficiency droop’, *Appl. Phys. Lett.*, 93, 041102–041104.

Shatalov, M., Gaevski, M., Adivarahan, V. and Khan, A. (2006). ‘Room-temperature stimulated emission from AlN at 214 nm’, *Jpn J. Appl. Phys.*, 45, L1286–L1288.

Shen, Y.-C., Mueller, G. O., Watanabe, S., Gardner, N. F., Munkholm, A. and Krames, M. R. (2007). ‘Auger recombination in InGaN measured by photoluminescence’, *Appl. Phys. Lett.*, 91, 141101–141103.

Sheu, J. K., Chi, G. C. and Jou, M. J. (2001). ‘Enhanced output power in an InGaN-GaN multiquantum-well light-emitting diode with an InGaN current-spreading layer’, *IEEE Photonics Tech. Lett.*, 13, 1164–1166.

Simon, J. (2009). Polarization engineered III-V nitride heterostructure devices by molecular beam epitaxy, PhD thesis, University of Notre Dame.

Simon, J., Protasenko, V., Lian, C., Xing, H. and Jena, D. (2010). ‘Polarization-induced hole doping in wide-band-gap uniaxial semiconductor heterostructures’, *Science*, 327, 60–64.

Song, Y. K., Diagne, M., Zhou, H., Nurmikko, A. V., Schneider, R. P., *et al.* (2000). ‘Resonant-cavity InGaN quantum-well blue light-emitting diodes’, *Appl. Phys. Lett.*, 77, 1744–1746.

Streubel, K., Linder, N., Wirth, R. and Jaeger, A. (2002). ‘High brightness AlGaInP light-emitting diodes’, *IEEE J. Sel. Topics Quantum Electron.*, 8, 321–332.

Sugawara, H., Ishikawa, M. and Hatakoshi, G. (1991). ‘High-efficiency In-GaAlP/GaAs visible light-emitting diodes’, *Appl. Phys. Lett.*, 58, 1010–1012.

Tadatomo, K., Okagawa, H., Ohuchi, Y., Tsunekawa, T., Jyouichi, T., *et al.* (2001). ‘High output power InGaN ultraviolet light-emitting diodes fabricated on patterned substrates using metalorganic vapor phase epitaxy’, *Phys. Stat. Sol. (a)*, 188, 121–125.

Takeuchi, T., Sota, S., Katsuragawa, M., Komori, M., Takeuchi, H., *et al.* (1997), ‘Quantum-confined Stark effect due to piezoelectric fields in GaInN strained quantum wells’, *Jpn. J. Appl. Phys.*, 36, L382–L385.

Tanaka, S., Iwai, S. and Aoyagi, Y. (1996). ‘Self-assembling GaN quantum dots on $Al_xGa_{1-x}N$ surfaces using a surfactant’, *Appl. Phys. Lett.*, 69, 4096–4098.

Taniyasu, Y., Kasu, M. and Makimoto, T. (2006). ‘An aluminium nitride light-emitting diode with a wavelength of 210 nanometres’, *Nature*, 441, 325–328.

Teles, L. K., Furthmüller, J., Scolfaro, L. M. R., Leite, J. R. and Bechstedt, F. (2000). ‘First-principles calculations of the thermodynamic and structural properties of strained $InxGa_{1-x}N$ and $AlxGa_{1-x}N$ alloys’, *Phys. Rev. B*, 62, 2475–2585.

Tsintzos, S. I., Pelekanos, N. T., Konstantinidis, G., Hatzopoulos, Z. and Savvidis, P. G. (2008). 'A GaAs polariton light-emitting diode operating near room temperature', *Nature*, 453, 372–375.

van der Laak, N. K., Oliver, R. A., Kappers, M. J. and Humphreys, C. J. (2007). 'Role of gross well-width fluctuations in bright, green-emitting single InGaN/GaN quantum well structures', *Appl. Phys. Lett.*, 90, 121911–121913.

Verma, J., Kandaswamy, P., Protasenko, V., Verma, A., Xing, H., *et al.* (2013). 'Tunnel-injection GaN quantum dot ultraviolet light-emitting diodes, *Appl. Phys. Lett.*, 102, 041103-1–041103-4.

Vurgaftman, I., Meyer, J. R. and Ram-Mohan, L. R. (2001). 'Band parameters for III-V compound semiconductors and their alloys', *J. Appl. Phys.*, 89, 5815–5875.

Waltereit, P., Brandt, O., Trampert, A., Grahn, H. T., Menniger, J., *et al.* (2000). 'Nitride semiconductors free of electrostatic fields for efficient white light-emitting diodes', *Nature*, 406, 865–868.

Wang, C. H., Ke, C. C., Lee, C. Y., Chang, S. P., Chang, W. T., *et al.* (2010). 'Hole injection and efficiency droop improvement in InGaN/GaN light-emitting diodes by band-engineered electron blocking layer', *Appl. Phys. Lett.*, 97, 261103–261105.

Wuu, D. S., Lin, S.-H., Han, P., Horng, R.-H., Hsu, T.-C., *et al.* (2005a). 'Efficiency improvement of near-ultraviolet InGaN LEDs using patterned sapphire substrates', *IEEE J. Quantum Electron.*, 41, 1403–1409.

Wuu, D. S., Wang, W. K., Shih, W. C., Horng, R. H., Lee, C. E., *et al.* (2005b). 'Enhanced output power of near-ultraviolet InGaN-GaN LEDs grown on patterned sapphire substrates', *IEEE Photonics Tech. Lett.*, 17, 288–290.

Xia, Y., Hou, W., Zhao, L., Zhu, M., Detchprohm, T., *et al.* (2010). 'Boosting green GaInN/GaN light-emitting diode performance by a GaInN underlying layer', *IEEE Trans. Electron. Devices*, 57, 2639–2643.

Xu, T., Nikiforov, A. Y., France, R., Thomidis, C., Williams, A. and Moustakas, T. D. (2007). 'Blue–green–red LEDs based on InGaN quantum dots grown by plasma-assisted molecular beam epitaxy', *Phys. Stat. Sol. (a)*, 204, 2098–2102.

Xu, J., Schubert, M. F., Noemaun, A. N., Zhu, D., Kim, J. K., *et al.* (2009). 'Reduction in efficiency droop, forward voltage, ideality factor, and wavelength shift in polarization-matched GaInN/GaInN multi-quantum-well light-emitting diodes', *Appl. Phys. Lett.*, 94, 011113.

Yamada, M., Mitani, T., Narukawa, Y., Shioji, S., Niki, I., *et al.* (2002). 'InGaN-based near-ultraviolet and blue-light-emitting diodes with high external quantum efficiency using a patterned sapphire substrate and a mesh electrode', *Jpn. J. Appl. Phys.*, 41, L1431–L1433.

Yamamoto, S., Zhao, Y., Pan, C.-C., Chung, R. B., Fujito, K., *et al.* (2010). 'High-efficiency single-quantum-well green and yellow-green light-emitting diodes on semipolar (20 21) GaN substrates', *Appl. Phys. Express*, 3, 122102–122104.

Yang, Z., Li, R., Wei, Q., Yu, T., Zhang, Y., *et al.* (2009). 'Analysis of optical gain property in the InGaN/GaN triangular shaped quantum well under the piezoelectric field', *Appl. Phys. Lett.*, 94, 061120–061122.

Yoshida, H., Yamashita, Y., Kuwabara, M. and Kan, H. (2008). 'A 342-nm ultraviolet AlGaN multiple quantum-well laser diode', *Nature Photonics*, 2, 551–554.

Yu, K. M., Liliental-Weber, Z., Walukiewicz, W., Shan, W., Ager, J. W., *et al.* (2005). 'On the crystalline structure, stoichiometry and band gap of InN thin films', *Appl. Phys. Lett.*, 86, 071910–071912.

Zhang, J. P., Wang, H. M., Gaevski, M. E., Chen, C. Q., Fareed, Q., *et al.* (2002). 'Crack-free thick AlGaN grown on sapphire using AlN/AlGaN superlattices for strain management', *Appl. Phys. Lett.*, 80, 3542–3544.

Zhang, M., Bhattacharya, P. and Guo, W. (2010). 'InGaN/GaN self-organized quantum dot green light emitting diodes with reduced efficiency droop', *Appl. Phys. Lett.*, 97, 011103–011105.

Zhang, S., Cui, K., Korinek, A., Botton, G. A. and Zetian, M. (2012). 'High-efficiency InGaN/GaN dot-in-a-wire red light-emitting diodes', *IEEE Photonics Tech. Lett.*, 24, 321–323.

Zhao, H. and Tansu, N. (2010). 'Optical gain characteristics of staggered InGaN quantum well lasers', *J. Appl. Phys.*, 107, 113110-1–113110-12.

Zhao, H. P., Liu, G. Y., Li, X. H., Arif, R. A., Huang, G. S., *et al.* (2009a). 'Design and characteristics of staggered InGaN quantum wells light-emitting diodes in the green spectral regimes', *IET Optoelectron.*, 3, 283–295.

Zhao, H., Arif, R. A. and Tansu, N. (2009b). 'Design analysis of staggered InGaN quantum wells light-emitting diodes at 500-540 nm', *IEEE J. Sel. Top. Quantum Electron.*, 15, 1104–1114.

Zhao, H., Liu, G., Li, X.-H., Huang, G. S., Poplawsky, J. D., *et al.* (2009c). 'Growths of staggered InGaN quantum wells light-emitting diodes emitting at 520–525 nm employing graded growth temperature profile', *Appl. Phys. Lett.*, 95, 061104–061106.

Zhao, H., Liu, G. and Tansu, N. (2010a). 'Analysis of InGaN-delta-InN quantum wells for light-emitting diodes', *Appl. Phys. Lett.*, 97, 131114–131116.

Zhao, H., Liu, G., Arif, R. A. and Tansu, N. (2010b). 'Current injection efficiency induced efficiency-droop in InGaN quantum well light-emitting diodes', *Solid State Electron.*, 54, 1119–1124.

Zhao, Y., Tanaka, S., Pan, C.-C., Fujito, K., Feezell, D., *et al.* (2011). 'High-power blue-violet semipolar (2021) InGaN/GaN light-emitting diodes with low efficiency droop at 200 A/cm^2, *Appl. Phys. Express*, 4, 082104-1–082104-3.

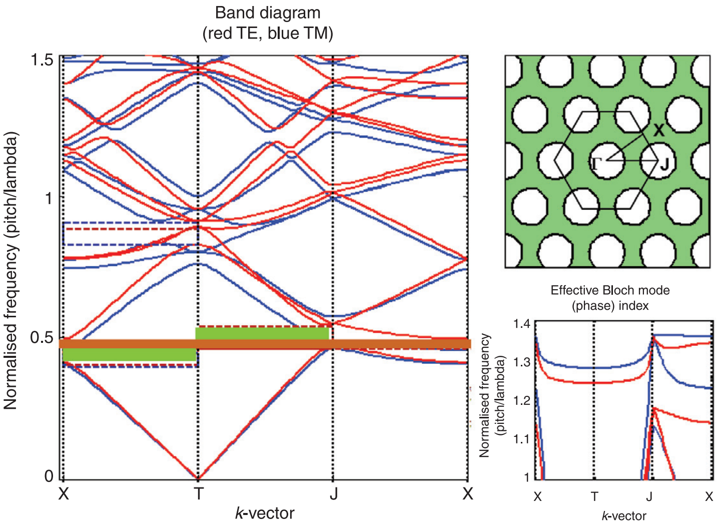

Plate X (Chapter 10) Left: Example *k*-vector (band) diagram. Red and blue lines are dispersion curves for TE and TM polarised modes. Green shaded areas indicate directional and polarisation-dependent band gaps. The orange shaded area is a non-directional but polarisation-dependent band gap. Top right: Lattice geometry and definition of symmetry directions. Bottom right: Effective phase index for modes transmitted by the photonic crystal.

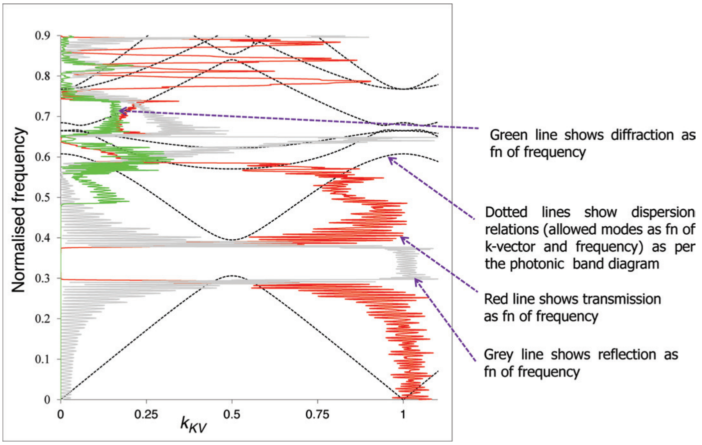

Green line shows diffraction as fn of frequency

Dotted lines show dispersion relations (allowed modes as fn of k-vector and frequency) as per the photonic band diagram

Red line shows transmission as fn of frequency

Grey line shows reflection as fn of frequency

Plate XI (Chapter 10) Example *k*-vector (band) diagram for a photonic crystal with superimposed transmission and reflection properties (calculated using a finite difference time domain method). The plot shows TE polarised waves propagating in a triangular photonic crystal composed of a silicon nitride slab with air cylinders (lattice pitch = 260 nm, rod radius = 150 nm) travelling along the Γ-X symmetry direction, within the plane of the lattice (there is no transverse *k*-vector component).

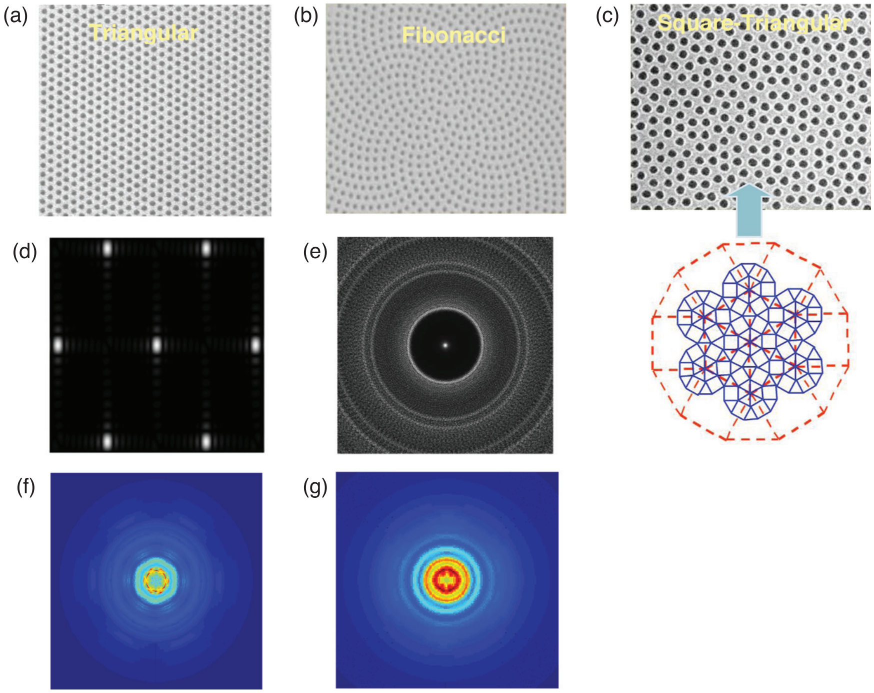
(a)
Triangular
(b)
Fibonacci
(c)
Square-Triangular
(d)
(e)
(f)
(g)

Plate XII (Chapter 10) Various PC and PQC lattice tiling schemes: (a) PC triangular lattice, (b) PQC Fibonacci lattice and (c) PQC square-triangular lattice. Diffraction patterns: (d) for a triangular lattice and (e) for a Fibonacci lattice. Far-field beam profiles: (f) for a triangular lattice and (g) for a Fibonacci lattice.

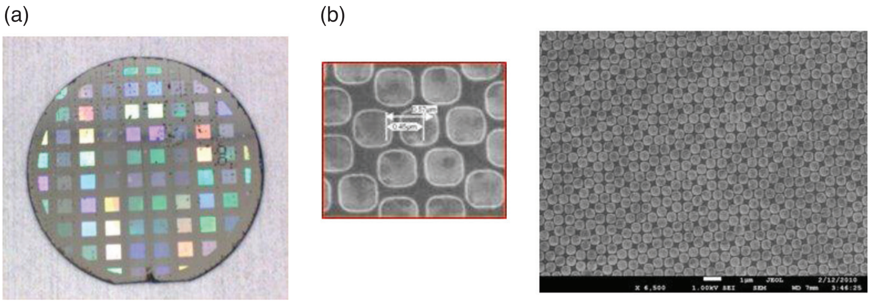

Plate XIII (Chapter 10) (a) Optical photograph of 4″ of flip-chip bonded GaN on a silicon wafer patterned by direct-write electron-beam lithography and reactive ion etching. Each device area is 3 × 3 mm^2 and there is a 2 mm gap between neighbouring devices. The PC parameters are different for each device and they scatter light differently to give a different colour. (b) SEM images of one of the surface-patterned areas.

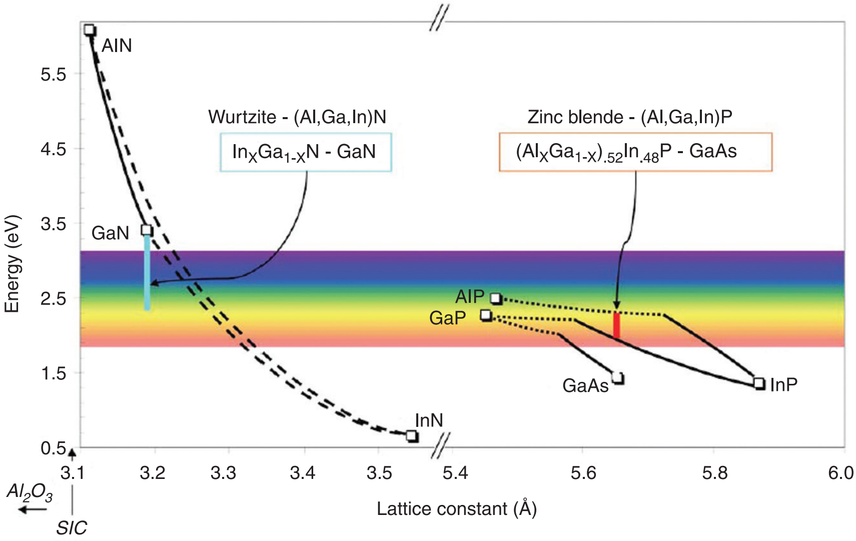

Plate XIV (Chapter 12) Energy bandgap versus lattice constant for wurtzite III-nitride and zinc-blende III-phosphide/arsenide semiconductor alloy systems employing aluminum, indium and gallium (Vurgaftman *et al.*, 2001; Yu *et al.*, 2005). Solid lines indicate direct-bandgap alloys, dotted lines indicate indirect-bandgap alloys and dashed lines are estimates (due to relative uncertainty in bowing parameters for high InN-fraction alloys). The (AlGa)InP system is lattice-matched to GaAs and emission is tunable from red (~650 nm) to yellow (~580 nm). The AlInGaN system is grown pseudomorphically on AlN (deep UV LEDs) or GaN (visible LEDs). (Reprinted with permission from Krames *et al.* (2007). Copyright 2007, IEEE.)

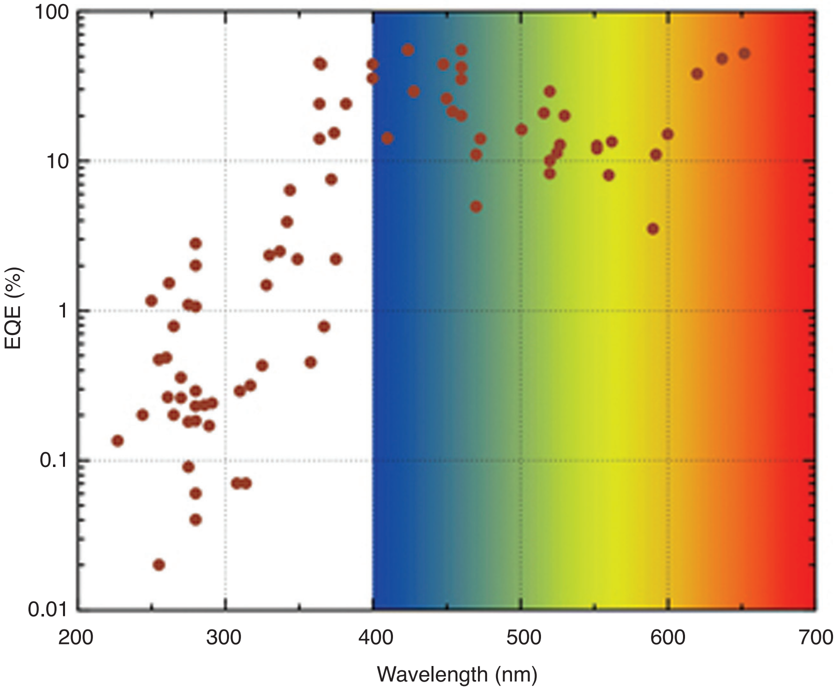

Plate XV (Chapter 12) EQE for LEDs based on the AlInGaN and AlInGaP alloy systems. As the peak emission wavelength decreases the EQE is observed to decrease. The green gap is easily discernible (Akita *et al.*, 2007; Chang *et al.*, 2003, 2010; Chen *et al.*, 2002; Guo *et al.*, 2010; Kim *et al.*, 2001; Kneissl *et al.*, 2011; Leea *et al.*, 2011; Liu *et al.*, 2011; Lundin *et al.*, 2010; Nakamura and Chichibu, 2000; Nguyen et al., 2011; Pan *et al.*, 2004; Sato *et al.*, 2008; Sheu *et al.*, 2001; Tadatomo *et al.*, 2001; Wuu *et al.*, 2005a, 2005b; Yamada *et al.*, 2002; Yamamoto *et al.*, 2010; Zhang *et al.*, 2010, 2012; Zhao *et al.*, 2011).

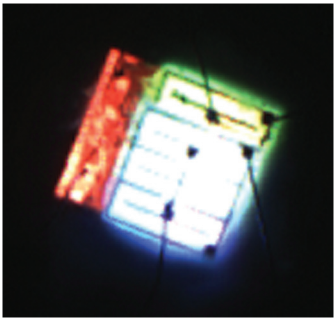

Plate XVI (Chapter 13) An initial version of an LED stack; sidewall emissions contribute to inhomogeneous color-mixing.

13

Color tunable LEDs

Y. F. CHEUNG, Z. MA and H. W. CHOI,
The University of Hong Kong, People's Republic of China

DOI: 10.1533/9780857099303.2.409

Abstract: Light-emitting diodes are inherently monochromatic light sources. However, owing to their miniature footprints, color-mixing using these devices is much more feasible compared to conventional light sources, which are many times larger in size. The ability to mix colors offers the capability of color-tuning in real time without the use of color filters. Two types are color-tunable LEDs are described in this chapter: red-green-blue stacked LEDs suitable for high-power applications and group-addressable micro-LED arrays with jet-printed red-green blue micro-pixels, suitable for monolithic integration.

Key words: light-emitting diodes, color-tuning, chip-stacking, micro-LED, jet-printing.

13.1 Introduction

13.1.1 Motivation for color tuning and review of existing technologies

Over the past decade light-emitting diodes (LEDs) based on the III-nitride material system have been extensively developed with the aim of replacing incandescent and gas discharge lamps as energy-efficient solid-state light sources. Tremendous progress has indeed been achieved, owing to intensive efforts carried out at research laboratories in institutions and in industry alike. Major advances in material epitaxy, device processing and chip packaging have contributed to the significant success of LEDs in display backlighting, traffic lights, street lighting and general lighting, as the efficiencies of these emitters have moved closer to their full potential. This is particularly encouraging in the midst of concerns over depletion of energy resources, not to mention the long list of advantages offered by LEDs over older technologies.

One major difference between LEDs and incandescent and fluorescent lighting is the emission spectrum. The monochromatic spectrum of an LED means that color conversion or combination is always necessary for the generation of broadband light. This is not required for incandescence because of its broadband emission; however, its spectrum is excessively broadband with most of the spectral components in the infrared so that wasteful filtering is necessary. Similarly, the discrete wavelength emission from a gas discharge calls for additional fluorescent materials to produce useful emission in the visible region.

The monochromatic nature of LED emission creates the potential for producing energy-efficient color-tunable light emitters. Colors can be varied by tuning the wavelength of the light source, or by addition or mixing of different colors. An emissive light source that is wavelength tunable across the visible spectrum is not yet available; therefore, color-mixing based on the additive principle is often used. For instance, colors can be mixed by projecting beams of the primary colors onto a surface. On the other hand, devices such as liquid crystal displays (LCDs) rely on the filtering of light through a mosaic of color filters from a rear broadband light source.

Unlike conventional light sources based on incandescence or fluorescence, light-emitting diodes are fixed wavelength monochromatic miniature light emitters, making them highly suited for additive color-mixing. Many applications, such as panel displays, mood lighting or even the biological excitation of cells, need light sources that are color-tunable across the visible spectrum and beyond. Solutions based on this concept, in the form of RGB LEDs where chips emitting the primary colors are bonded onto the same package adjacent to each other, are now available and have been adopted for LED panel displays.[1] A major drawback of this approach are spatial color variations, which cause non-ideal color-mixing when emission cones from the discrete devices do not overlap with each other completely.[2] Diffusers are often used to overcome this problem, although optical losses of ~20% are inevitable,[3] together with a loss of color sharpness and richness.

There have been several demonstrations of LEDs with color-tuning capabilities, including devices based on multiple junctions, quantum dots or nanocolumns, albeit with limited tuning ranges. To overcome the limitations, two different strategies for providing color-tuning capabilities in LEDs have been designed and implemented.

The first approach involves three separate RGB emitters vertically stacked on top of each other. LED chips emitting the primary colors can be physically stacked on top of each other to produce a color-tunable LED. In such an arrangement, light rays emitted by each LED can be combined and mixed naturally as rays from the lower LEDs pass through the upper LEDs and mix with rays emitted by the latter.

The second approach involves creating an array of interconnected micrometer-scale emitters of different colors. A true single-chip solution employing a group-addressable micro-pixelated emitter, in conjunction with jet-printed color-conversion pixels can be realized. Being a single-chip solution, these group-addressable micro-LED emitters are readily scalable for integration into full-color emissive micro-displays, which certainly would be a breakthrough in emissive display technology.

13.2 Initial idea for stacked LEDs

This approach is based upon optimization of the optical pathways of the LED emissions. Optical mixing requires that the radiation patterns from the discrete

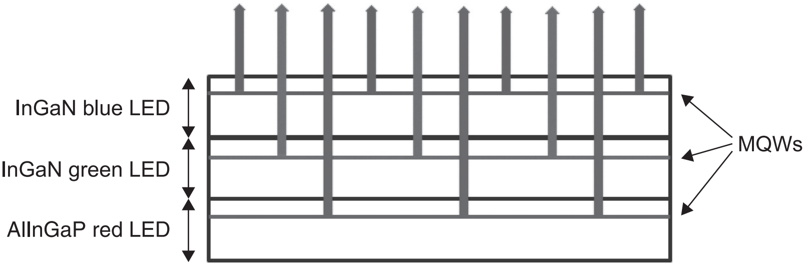

13.1 Color-mixing through RGB chip-stacking. (MQW: multiple quantum well)

LEDs overlap with each other. Instead of attempting to mix the beams using external optics, RGB devices are physically placed such that their optical paths are aligned. The schematic diagram of Fig. 13.1 illustrates this idea. The emissions from the three LEDs are naturally mixed without the need for additional optics.

This idea can be realized by stacking the RGB chips on top of each other, in a stacking topography. This is possible by virtue of the fact that GaN LED chips are grown on transparent sapphire substrates; light can pass through the chip without absorption or significant attenuation. The AlInGaP red LED, with a non-transparent (to visible light) GaAs substrate, must be placed at the bottom of the stack (which happens to be the necessary sequence as explained shortly). An InGaN green LED is placed on top of the red LED, and a blue InGaN LED is subsequently placed at the top of the stack. This stacking strategy ensures optimal color-mixing. Adopting this stacking sequence also ensures that light emitted from the lower devices (with a narrower bandgap) will pass through the upper devices (with wider bandgaps). The sapphire substrates of InGaN LEDs are also transparent to visible light. A schematic diagram of the proposed device is illustrated in Fig. 13.2. The three

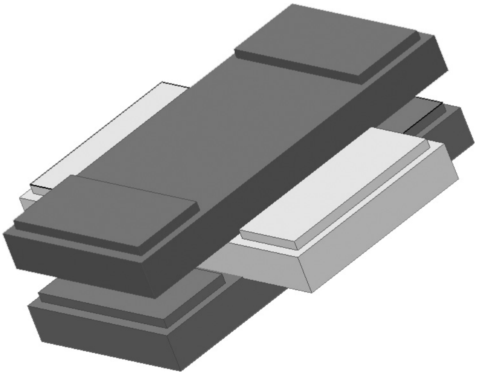

13.2 LED chip stacking.

devices are either connected in parallel or are individually controllable electrically. When connected in parallel, the cathodes and anodes are interconnected, with the insertion of appropriate resistors for adjusting the required bias voltages of each device (depending on the required proportions of red, green and blue spectral components). Such a two-terminal device acts as an all-semiconductor white-light LED.

Another implementation gives user-access to the individual cathodes, while interconnecting their anodes, resulting in a four-terminal device. When all three devices are illuminated, the optically mixed output is polychromatic light with three spectral peaks, or white light with the right proportions of red, green and blue. Varying the proportions of the primary colors can be used to produce white light of different color temperatures. Monochromatic light can be obtained by turning on a single device. Other colors can be tuned by lighting up two or three devices simultaneously and adjusting the appropriate bias voltages. This proposed stacked design does not require color conversion for generating polychromatic light and is thus conversion-loss free.

The red, green and blue LED chips used in this study emit with center wavelengths of 640 nm, 510 nm and 470 nm respectively. They were fabricated from AlInGaP on GaAs and InGaN on sapphire wafers grown by metal-organic chemical-vapor deposition (MOCVD). The sapphire substrates of the nitride wafers were thinned down to ~150 μm, followed by fabrication of devices via standard micro-fabrication.

Assembly of the stack began by attaching a red LED die to a TO-can using electrically conductive adhesive. A small volume of UV-curing optical adhesive was dispensed onto the surface of the red LED chip, just enough to cover the emissive region, before the green LED chip was mounted on top using a manual die bonder. The bonding pads must not be covered by the epoxy. The blue LED chip was mounted on the top in the same manner. Once the chips were aligned in place, the stack was exposed to UV light under a deuterium lamp. The adhesive hardened and the stack became fixed in place. Finally, the pads were wire-bonded to the package. Bias voltages were applied to the terminals to test the functionality of the assembled device. Although the LEDs lit up, the optical output was not as homogeneous as expected, as shown in Plate XVI (in colour section between pages 330 and 331), although it is much improved compared with conventional RGB devices. As observed, the contribution of light emission from the sidewalls of the chips was neglected in the design, prompting further improvements.

13.3 Second-generation LED stack with inclined sidewalls

A seemingly simple solution to this problem would be to block sidewall emission; however, this would significantly reduce light extraction, defeating the motivation of maximizing efficiency for our stack design. A solution is needed to channel

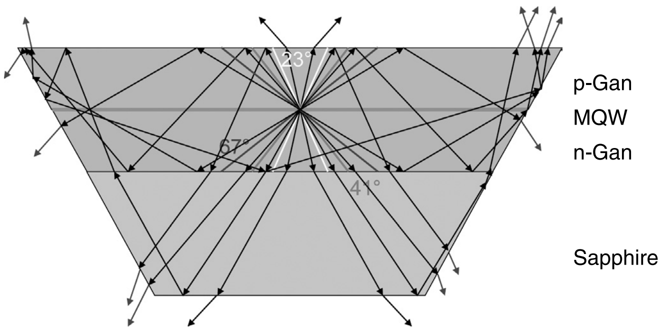

13.3 Typical light rays propagating in a TP-LED.

laterally propagating light into the vertical direction for emission through the top window; this can be achieved by an LED with an inverted truncated pyramid (TP) geometry and a mirror coating on its inclined sidewalls. The inclined sidewalls can serve as a reflector, redirecting light rays that would be trapped in a cuboid LED, for extraction through the top emitting area; examples of such rays are indicated in blue in Fig. 13.3. Krames *et al.* prepared AlInGaP devices with this type of geometry using the beveled dicing technique.[4] This would be difficult for GaN chips with hard sapphire substrates. Instead, a single-step laser-micromachining approach was adopted to form the angled facets.

In traditional laser micromachining, a focused beam is directed onto the wafer orthogonally. Using a modified set-up, in which a laser-turning mirror is inserted between the focusing objective and the wafer, the beam is redirected to strike the wafer at an oblique angle.[5] This oblique incident beam is used to dice the green and blue GaN LED chips, and it shapes the chips into inverted pyramids as it cuts. The set-up for laser micromachining consists of a UV laser source, beam-focusing optics and an x-y motorized translation stage. The laser source is a third harmonic ND:YLF diode-pumped solid-state (DPSS) laser manufactured by Spectra Physics. The laser emits at 349 nm, while the pulse repetition rate ranges from single pulse to 5 kHz. At a reference diode current of 3.2 A, the pulse energy is 120 μJ at a repetition rate of 1 kHz, with a pulse width of around 4 ns. The TEM_{00} beam can be tightly focused to give high spatial resolution. After beam expansion and collimation through a beam expander, the laser beam is reflected 90° by a dielectric laser line mirror and focused onto the horizontal machining plane to a very tiny spot several micrometers in diameter with a focusing triplet. All optics used are made of UV fused silica and are anti-reflection (AR) coated. The additional feature of our set-up, as illustrated in the schematic diagram of Fig. 13.4, is the insertion of a UV mirror at an oblique angle within the optical path between the focusing optics and the machining plane, which serves to deflect the convergent beam so that it strikes the sample at an oblique angle with respect to the horizontal

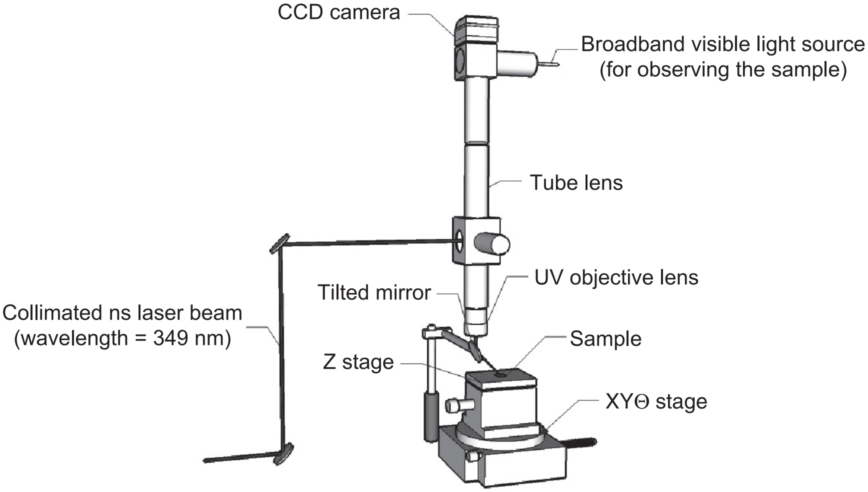

13.4 Laser micromachining set-up, incorporating a tilted mirror for controlling the angle of incidence of the laser beam at the sample surface.

working plane. The size of the beam at the focal point is not only limited by the capability of the UV objective lens but is also sensitive to the coaxiality of the optics. With this modified set-up, it is relatively easy to optimize and monitor the beam through the tube lens using the CCD camera. The optical set-up is optimized before insertion of the tilting mirror, and then the mirror can be inserted without affecting the coaxiality of the laser beam, so that the dimension of the beam spot remains unaffected.

The beam can be effectively used for micro-sectioning to produce non-vertical sidewall profiles. The angle of incidence of the deflected laser beam on the wafer is 2θ, where θ is the angle between the plane of the mirror and the normal. This angle is readily and precisely controlled by mounting the mirror onto a rotation stage: the incident angle can be varied over a wide range. We used a UV objective with a focal length of 75 mm, based on two considerations. Firstly, the focal length should be long enough to accommodate the mirror in the optical path. Secondly, the ideal tool for the fabrication of microstructures should have a very long penetration depth and negligible lateral dispersion. Nevertheless, an objective lens with a longer focal length also produces a larger focused beam spot. The two parameters are related via the following equation:

$$d = \frac{4\lambda M^2 f}{\pi D}$$

where M^2 quantifies the beam quality, λ is the wavelength of the laser beam, f the focal length and D the diameter of the incident beam.

Chips of TP geometry were diced and shaped by applying four successive oblique laser cuts onto the four sides of an LED fabricated using standard micro-fabrication procedures. A scanning electron microscope (SEM) image of a TP-LED is shown in Plate XVII(a), while Plate XVII(b) shows the TP-LED lit up (see color section between pages 330 and 331). A layer of silver was selectively coated onto the angled sidewalls by electron-beam evaporation (by covering the top face with a photoresist), which served as a mirror to redirect light into the vertical direction.

A ray-tracing simulation coded in MATLAB was used to predict the extraction efficiencies of the TP- LEDs,[6] taking into account light refraction based on Snell's law (in vector form):

$$\mathbf{r}_r = \mathbf{r}_{in} + [2(\mathbf{n} \cdot -\mathbf{r}_r)]\mathbf{n} \tag{13.1}$$

$$\begin{aligned}\mathbf{r}_t = {} & (n_1 / n_2)\mathbf{r}_m + \{(n_1 / n_2)(\mathbf{n} \cdot -\mathbf{r}_r) \\ & + \sqrt{1 - (n_1 / n_2)^2[1 - (\mathbf{n} \cdot -\mathbf{r}_r)^2]}\}\mathbf{n}\end{aligned} \tag{13.2}$$

where $\mathbf{r}_{in}$, $\mathbf{r}_r$ and $\mathbf{r}_t$ are the normalized vectors of the incident ray, reflected ray and transmitted ray, respectively, n_1 and n_2 are the refractive indices, and $\mathbf{n}$ is the normalized normal vector of the interface. Light reflectivity and transmissivity were evaluated using the Fresnel equations:

$$R_s = \left\{ \frac{n_1 \cos(\theta_i) - n_2 \sqrt{1 - [(n_1 / n_2)\sin(\theta_i)]^2}}{n_1 \cos(\theta_i) + n_2 \sqrt{1 - [(n_1 / n_2)\sin(\theta_i)]^2}} \right\}^2 \tag{13.3}$$

$$R_p = \left\{ \frac{n_1 \sqrt{1 - [(n_1 / n_2)\sin(\theta_i)]^2} - n_2 \cos(\theta_i)}{n_1 \sqrt{1 - [(n_1 / n_2)\sin(\theta_i)]^2} + n_2 \cos(\theta_i)} \right\}^2 \tag{13.4}$$

where R_s and R_p are the reflection coefficients of the s-polarized and p-polarized light rays and θ_i is the incident angle. $\cos(\theta_i)$ can be obtained from the term $(\mathbf{n} \cdot -\mathbf{r}_r)$ used in Eqs 13.1 and 13.2. The absorption rule is:

$$I = I_o \exp(-\alpha L) \tag{13.5}$$

where I_o and I are the intensities at the initial and final points of the light path, α the absorption coefficient ($\alpha_{\mathrm{GaN}} = 150\,\mathrm{cm}^{-1}$ was used in the simulation) and L the distance travelled by each light ray.

The active region of an LED was modeled by a 50 × 50 array of point sources. The light extraction efficiency was evaluated by summing the intensities of light rays escaping from the LED divided by the total intensity of the light rays emitted:

$$\eta = \sum_{\theta,\phi} f(I_{\theta,\phi}) \Big/ \sum_{\theta,\phi} I_{\theta,\phi} \tag{13.6}$$

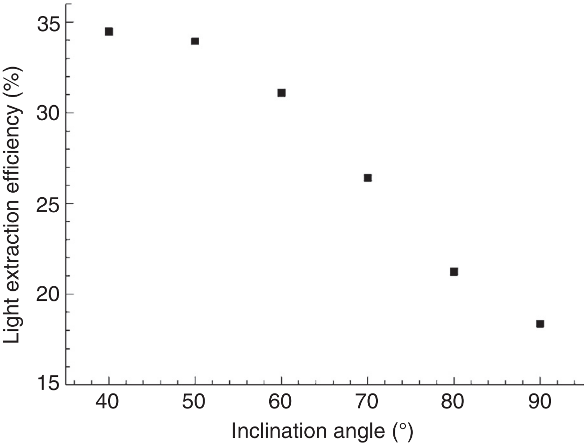

13.5 Light extraction efficiency as a function of inclination angle.

where I is the light intensity emitted at a specific angle (θ, ϕ), and $f(I)$ the light intensity extracted at that angle. Figure 13.5 is a plot of light extraction efficiency as a function of inclination angle. As observed from the graph, the light extraction efficiency for a cuboid structure (90°) is 18.3%, rising to 33.9% for an inclination angle of 50°. A further increase in inclination angle results in little further improvement, while the cutting efficiency is reduced. Therefore, 50° was deemed to be the optimal choice.

A stack was assembled using these modified chips following an identical procedure as before. Plate XVIII(a) (see color section between pages 330 and 331) is an SEM image of the assembled device, showing the tri-layer topology. The contact pads of each chip are exposed for wire-bonding. Plate XVIII(b) shows emission from the current injected device. For illustration, the chips in the device of Plate XVIII have not been thinned down; in the final version, the chips were thinned down to ~100 μm. The color-mixing capability of the stacked device is improved, with optically mixed output through its top output aperture. For a fair and objective comparison, both the stacked LED and the RGB LED were biased to emit with identical CIE coordinates of (0.31, 0.31) at a total current of 20 mA. Due to slight dissimilarities in the component chips, the bias voltages are slightly different. Optical micrographs of both devices operated under these conditions are shown in Plate XIX (see color section). It is immediately apparent that color homogeneity has been improved, with single-spot color-mixed emission, in stark contrast to the three spots of spatially separated light from the RGB device. However, monochromatic emission was still observed at the edges of the chips, corresponding to the locations of the planar electrodes, leaving room for further improvements.

13.4 Third-generation tightly integrated chip-stacking approach

It is apparent that in order to solve the color homogeneity problem completely, chips in a stack have to be of identical dimensions and overlap with each other completely. So a new chip stacking architecture was designed to overcome these limitations. The RGB chips have identical dimensions, eliminating possibilities for optical leakage. This was achieved by forming channels on the sapphire substrates by laser micromachining,[7] which were designed to fit the wire bonds snugly. When assembled, the bond wires appear to protrude from the stacked chip tower, while the tower maintains a planar facet. Figure 13.6 is a schematic diagram of the updated design.

As before, red, green and blue LED chips were used. The sapphire substrates of the nitride wafers were thinned down to ~150 μm, followed by fabrication of devices via standard micro-fabrication. These were diced into 1 mm^2 chips by laser micromachining using a nanosecond diode-pumped solid-state ultraviolet (349 nm) laser source. Channels were formed at the locations needed for the wire bonds of the underlying chip; they were micromachined with the same laser used for dicing. The chips to be machined were placed on an XY motorized platform with the sapphire surface facing up. The laser beam, expanded and collimated by a beam expander, moves across the surface to form a 2-D channel of the desired dimensions. Figure 13.7 shows an SEM image of one such channel formed on the backside sapphire face of an LED chip.

The stack was assembled by adhering the bottom n-contact of a red AlInGaP vertical LED chip to a TO-can using electrically conductive epoxy; the top p-electrode was wire-bonded to a lead on the TO-can. The green InGaN LED chip with a laser micromachined bottom channel was aligned to cover the red LED in its entirety so that the wire bonds of the red LED fitted snugly into the trench; the snap-in action automatically aligned the chips. Between the chips, optical epoxy was applied to secure them in position. The p-electrodes on the green LED were then wire-bonded to the package. Similarly, the blue InGaN LED chip was piled

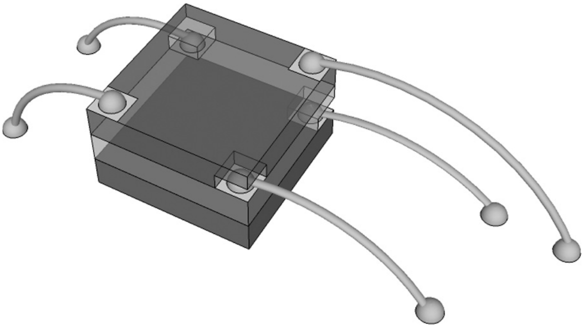

13.6 Tightly integrated stacked LED with embedded wire bonds.

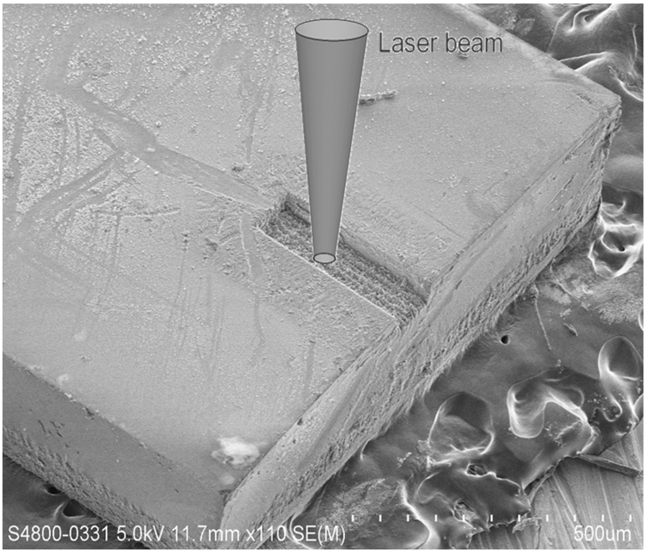

13.7 SEM image of a laser micromachined channel on the backside sapphire face of a 1 mm^2 InGaN LED chip.

on top of the green LED; the stacking procedure is illustrated in the schematic diagram of Fig. 13.8(a). The resultant tri-layer tower structure is shown in the optical microphotograph of Fig. 13.8(b). Optical measurements were made by mounting packaged LEDs onto the input port of a 2-inch integrating sphere, fiber coupled to a radiometrically calibrated optical spectrometer.

The color homogeneity of the stacked device was evaluated, this being the primary goal of this design. The red, green and blue chips in a stack were biased at currents of 79 mA, 109 mA and 38 mA in order to emit white light with CIE coordinates of (0.3, 0.3) when measured in the normal direction. Angular emission profiles are used to assess color homogeneity. For comparison, the same set of measurements was performed on a commercial RGB LED (Avago ASMT-QTC0-0AA02). An optical fiber, coupled to a spectrometer, was rotated about the central axis of the device being tested. The blue, green and red chips in the stack tower were turned on sequentially, and the optical intensity at each angle between 0° and 180° in steps of 1° was recorded (90° being the normal direction). The data collected from the stacked LED and conventional RGB LED are plotted on the hemispheres of polar graphs (Fig. 13.9). The shapes of the angular plots are self-explanatory: the emission graphs of the stacked tower overlap each other, as if they are emitted from the same chip. On the other hand, the emission from individual chips in the conventional RGB LED exhibits distinct directionality, giving rise to an overall non-homogeneous appearance.

While the quantitative measurements presented should be convincing enough, the visual appearances of the emission from the devices paint an even clearer

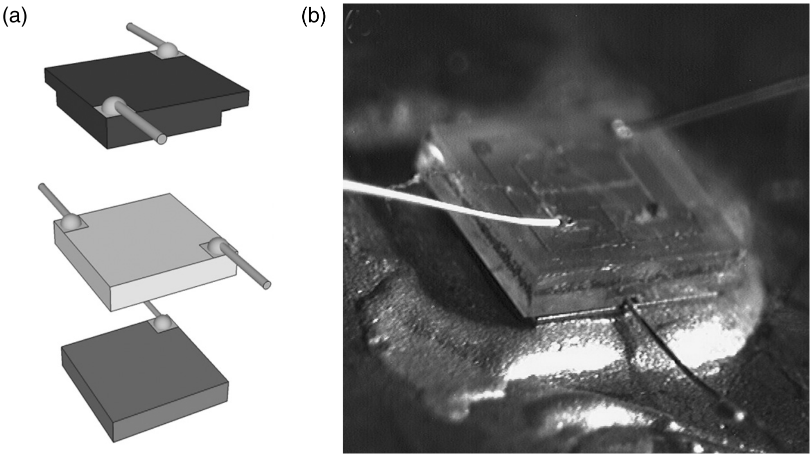

13.8 (a) Layer sequence and chip structure. (b) Optical microphotograph of the assembled stacked LED.

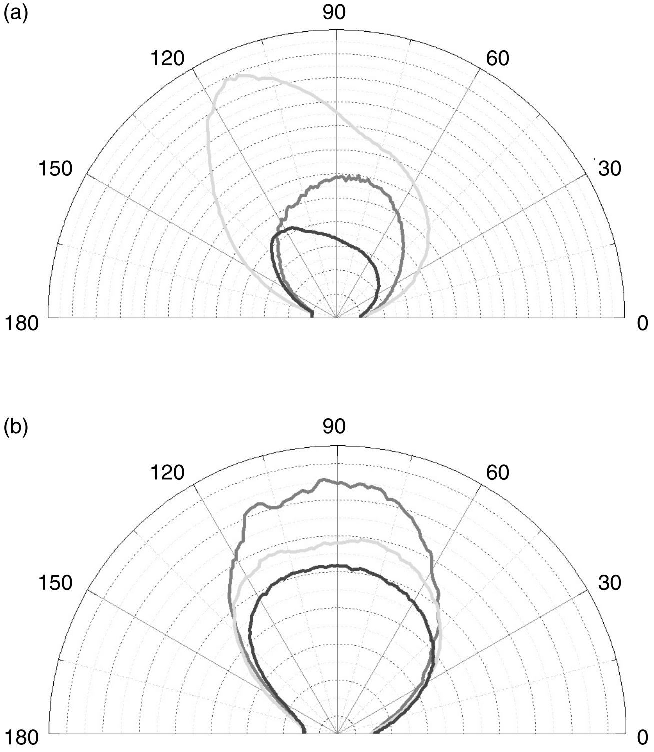

13.9 Polar emission plots for the red, green and blue spectral components of (a) the commercial RGB LED and (b) the stacked RGB LED.

picture. Plate XX(a) and (b) (see color section between pages 330 and 331) are optical photographs of the stacked LED and the conventional RGB LED, respectively, captured in the normal direction using a color CCD camera. Both devices were biased to emit a range of different polychromatic colors by mixing appropriate proportions of red, green and blue light. Emission from the stacked tower always appears as a single color, visual proof of satisfactory internal color-mixing. On the other hand, red, green and blue spots of light remain clearly visible from the RGB LED.

To understand the consequences of stacking on optical performance, the L-I characteristics of the chips on different layers of the stack were measured. For the LED chips in the stack, only one of the three chips was turned on for each set of measurements. For a fair comparison, identical RGB chips were mounted side-by-side onto an identical package, equivalent to the conventional planar RGB LED configuration. The measured L-I data for the blue, green and red devices are plotted in Fig. 13.10; the curves formed by square symbols are data points

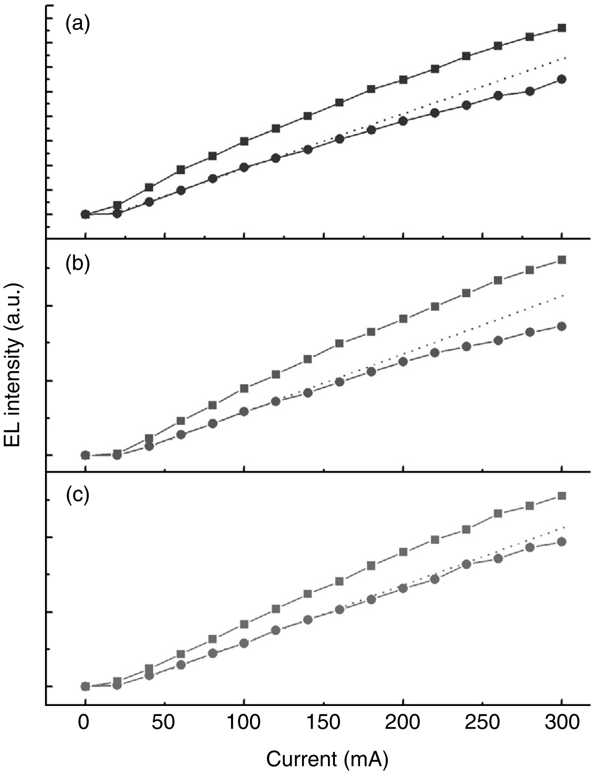

13.10 L-I characteristics of (a) blue (b) green and (c) red LEDs in a stack (circle symbols) and in a planar configuration (square symbols). Dotted line is a linear extrapolation.

for the planar RGB devices, while those with circular symbols are the stacked devices.

For all measured currents, the emitted light intensity from the LED chips mounted in a planar configuration was higher than for chips integrated into the stacked structure, although to varying extents, due to a combination of thermal, absorption and reflection effects. For the red LED at the lowest layer of the stack structure, the emitted power dropped by ~24% at 300 mA (all subsequent comparisons are based on a bias current of 300 mA); this is attributed to a combination of thermal loading and interface reflections. The extent of the optical reduction due to thermal effects for chips in the stack can be estimated from the deviation of the L-I curves from the linearly extrapolated dotted curves in Fig. 13.10. As expected, thermal effects for the red LED were minimal since the chip is attached directly to the package, allowing efficient conductive heat-sinking. The remaining optical reductions were due to optical losses along the red light optical path, mainly in the form of interface reflection losses. Red light will pass through the green and blue quantum wells (QWs), and the sapphire substrates, with minimal absorption. For the green LED sandwiched between the red and blue LED chips, the reduction in optical power was the most severe of the three at ~34%; thermal effects were more severe as the generated heat has to be channeled away through the red LED chip. Light emitted downward from the green chip is almost completely absorbed by the red QWs, while light emitted upward suffers from interface reflection losses. This is exacerbated by partial absorption of the green light by the blue QWs in the chip above, due to spectral overlap between the blue and green QWs. Fortunately, such losses can easily be avoided by picking blue and green LED chips with a larger separation of central wavelengths. The blue LED, being at the top, suffers an optical reduction of ~27%; this is due to a combination of thermal effects and absorption of downward emitted blue light by the green QWs. Being exposed at the top, convective heat dissipation is possible, reducing the heat burden. The measured data provide insight into the major optical loss mechanisms, so that suitable remedies can be applied. In particular, absorption of downward propagating light from the blue and green chips may be eliminated by using a coating of a wavelength-selective distributed Bragg reflector on the bottoms of the chips, which would selectively reflect and transmit light.

Phosphor-free white-light emission is a challenging yet important topic in LED technology, promising to take solid-state lighting to the next level. In the literature there have been several reports of broadband emission using various methods, as summarized below:

- Dual wavelength InGaN/GaN multiple quantum well (MQW) LEDs were described by Qi *et al.*[8] The dual QWs had different well widths and barrier widths, with designed emission in the blue and green regions.
- Sekiguchi *et al.* grew nanocolumn arrays with diameters ranging from 137 nm to 270 nm using radio-frequency molecular beam epitaxy (rf-MBE) on top of

a patterned titanium mask.[9] Each device emitted a single wavelength, although theoretically the idea could be extended by growing nanocolumns with different diameters within the same wafer, which may be a challenging growth problem.

- Lin *et al.*[10] described a similar approach, although the nanorods were self-aligned during the plasma-assisted MBE (PAMBE) growth, so that the diameters were beyond dimensional control, and thus the emission spectrum was unpredictable.
- The use of quantum dots is yet another approach for modifying emission wavelengths. MQWs incorporating indium-rich InGaN connected-dot nanostructures with a height of ~1.0 nm were described by Soh *et al.*[11] Cool-white phosphor-free emission was produced by a single chip.

The stacked tower can also function as a conversion-free white-light LED and a correlated color temperature (CCT)-variable white-light LED. Figure 13.11 shows emission spectra of a stacked LED operated as a cool white light source (CCT of 7332 K, driven at currents of 79 mA, 120 mA and 45 mA for the red, green and blue LEDs, respectively), a neutral white light source (5999 K at 79 mA, 110 mA and 38 mA) and a warm white light source (2362 K at 150 mA, 121 mA and 29 mA). The luminous efficiency of the device operated at these three CCTs was 19.23 lumens per watt, 20.19 lumens per watt and 20.70 lumens per watt, respectively, which are respectable figures for a prototypic device. For comparison, the planar RGB LED assembled using identical chips performed as follows: 32.02 lumens per watt, 32.78 lumens per watt and 37.22 lumens per watt at CCTs of

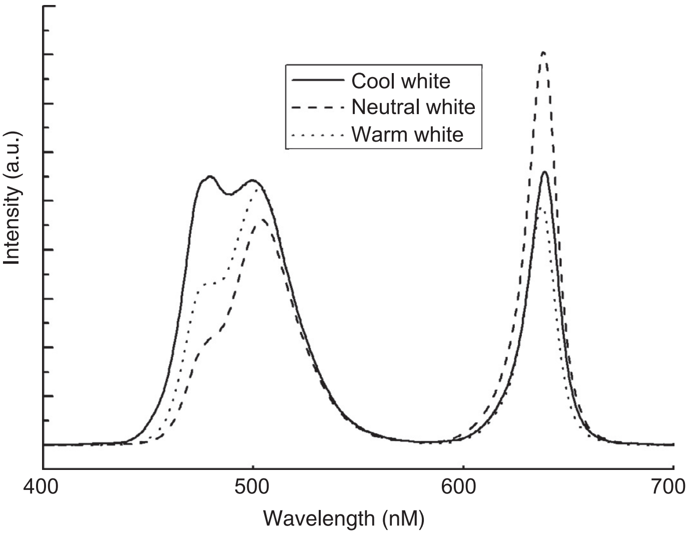

13.11 Optical emission spectra of a stacked LED functioning as a phosphor-free LED emitting cool, neutral and warm white.

7141, 6104 and 2401 K, respectively. In other words, the efficacy of the stacked LED was approximately 38% lower than its planar counterpart; however, the additional functionalities far overweigh the losses. It is also worth noting that the luminous efficacy is nearly independent of CCT, allowing efficient operation at low CCTs, which is desirable for indoor lighting; the characteristics are obviously superior to those of phosphor-converted white LEDs at low CCT due to the low efficiencies of longer wavelength phosphors.

13.5 Group-addressable pixelated micro-LED arrays

13.5.1 Natural color-mixing using miniature RGB pixels

An alternative way of color-mixing red, green and blue is to have an array of miniaturized RGB emitters, each of which is so small that it cannot be resolved by the human eye. The major advantage of this approach is the ability to integrate multiple color-tunable emitters into a single wafer and there is the possibility of building single-chip full-color displays. In this section, the ongoing development for the realization of such a display is described. Implementation can be achieved using a micro-LED, where the active region of the LED is sectioned into multiple micrometer-sized regions called pixels.[12] Color conversion elements are introduced into each of these pixels, as depicted in Plate XXI (see color section between pages 330 and 331). As a result, each pixel will emit at a different wavelength according to the fluorescent material coating.

Since each pixel is of micrometer scale, the overall output appears optically mixed as the dimensions of the pixels are beyond the resolution limit of the unaided human eye, as illustrated in Plate XXII (see color section). Pixels with the same emission color are interconnected via metal lines. The intensity of the blue-, green- and red-emitting regions is varied by varying the bias voltage to the three cathodes of the device, and so the output wavelength (color) can be continuously tuned. For example, if we apply a bias voltage to the red cathode only, the red pixels will light up and the overall device will appear red, as shown in Plate XXIII(a) (see color section). However, if both the red and blue cathodes are connected to a supply voltage as shown in Plate XXIII(b), both the blue and red elements will be illuminated and the overall device will appear purple due to color-mixing at the micro-scale level.

13.5.2 Implementation of group-addressable micro-LED arrays

A group-addressable blue LED forms the basis of a color-tunable LED. The active region of the device is micro-sectioned into multiple individual emitters, each of which should be have dimensions in the vicinity of tens of microns. Pixels of like colors are interconnected via metallization, so that they can be addressed as a group. There are three groups of pixels, one for each of the primary colors. Since the starting wafer emits blue light, the pixels designated for blue emission do not

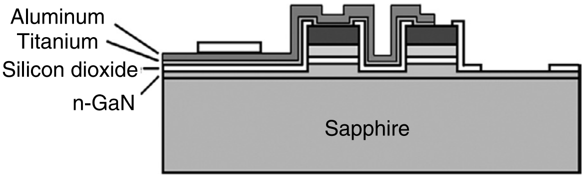

13.12 Cross section of two adjacent micro-LED pixels.

require an additional coating of fluorescent materials. Green and red fluorescent materials are coated onto the other groups of pixels, which are pumped by the high-energy blue-light emitter beneath to generate the respective color.

A group-addressable micro-LED has an architecture similar to that of a regular parallel-addressed[13] or matrix-addressed[14] micro-LED, where individual pixels are patterned by photolithography and etched by a plasma. Figure 13.12 shows a cross-sectional view of a typical micro-LED structure. To maximize the packing density, the emitters are hexagonal shaped and closely packed. The dimensions of individual pixels are in the range 50–100 μm. Pixels emitting the same color should not be directly adjacent to each other. Metal interconnects are deposited between pixels of like colors, terminating at the edge of the chip as a bond pad. Due to the complexity of the interconnect routing, multi-layer metallization is required. Plate XXIV(a) (see color section between pages 330 and 331) is a schematic diagram of the device layout, where regions shaded in red are the individual micro-pixels, green is for the the metallic interconnects and bond pads, while an isolation oxide layer is deposited in the grey region to allow dual-layer interconnections. A fabricated device is shown in Plate XXIV(b). The group-addressable behavior of the fabricated LEDs is illustrated in Fig. 13.13. When an electrical bias voltage is applied between the common cathode and one set of anodes, one-third of the micro-LED pixels light up.

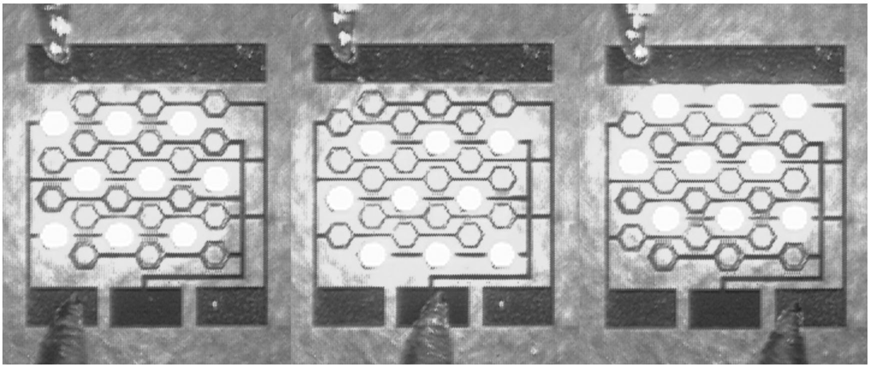

13.13 A group-addressable micro-LED in action: one of the three groups of pixels lights up at a time.

13.5.3 Forming RGB pixels by jet-printing

The final, yet most challenging step, is the selective deposition of fluorescent materials onto individual pixels. Having explored photolithographic methods without success, it became apparent that direct deposition of fluorescent materials is a potential solution. Inkjet-printing was thus adopted, based on its ability to dispense liquids with volumes as low as picoliters.[15] To be compatible with inkjet-printing, the fluorescent particles must be soluble in a solvent, much smaller than the nozzle and of spherical shape to prevent clogging of the printhead. In our experiments, fluorescent microspheres with diameters of about 0.39 μm were used. Two types of fluorescent microspheres were used to produce green and orange-red emissions.[16,17] The internally dyed green nanospheres were maximally excited at 468 nm and produced broadband green emission with two spectral peaks at 525 nm and 560 nm. The internally dyed orange-red nanospheres absorbed maximally at 558 nm and fluoresced in a longer wavelength region with spectral peaks at 570 nm and 610 nm. The top left of Plate XXV (see color section between pages 330 and 331) shows the fluorescence from a close-packed array containing green and orange-red microspheres.

Microspheres suspended in de-ionized water were printed onto a group-addressable micro-LED using a Jetlab 4 printer from Microfab. During the printing process, the inkjet nozzle was driven by an AC-voltage waveform to eject stable and reproducible micro-drops in the drop-on-demand (DOD) mode. After the micro-drops were deposited onto assigned pixels according to a CAD pattern corresponding to the micro-pixel layout, the de-ionized water evaporates, leaving behind fluorescent microspheres sitting on the top of the pixels, as illustrated in the bottom right of Plate XXV. The formation of micro-drops from the nozzle could be observed via an integrated stroboscopic camera system, as shown in Fig. 13.14. Typically the radii of the drops were approximately equal to the radius of the

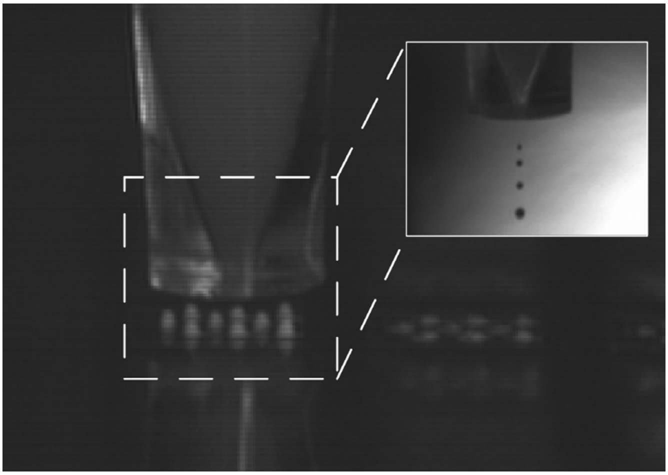

13.14 Close-up of jet-printing of fluorescent microspheres onto pixels.

nozzle that ejected them. The operating parameters for ejecting an optimal micro-drop were experimentally determined; they included the nature of the particles and fluid (viscosity, surface tension and concentration), the sizes of the particles, the nozzle aperture and the working environment (pressure, temperature and humidity).

13.5.4 Preliminary results

Plate XXVI (see color section between pages 330 and 331) shows a completed monolithic color-tunable LED with jet-printed red and green pixels. To deliver sufficient levels of red or green light emission, drops were repeatedly deposited over the same pixel to form a microsphere stack more than 100 μm thick; this requires hundreds of drops to be deposited on nearly the same spot. Inevitably, deposited microspheres may become displaced from their intended locations and affect adjacent ones. Such occurrences may be minimized by heating the substrate to accelerate evaporation. However, since the nozzle is in close proximity to the substrate with a separation of about 200 μm to ensure precise landing, substrate heating may cause the solvent inside the tip of the nozzle to dry out quickly, so that fluorescent microspheres aggregate near the tip of the nozzle, impeding the bursting of micro-drops.

The group-addressable pixels can be controlled independently by adjusting suitable bias voltages or currents to generate different colors or color temperatures, as shown in Plate XXVII (see color section). When all three groups of RGB pixels were turned on and viewed without magnification, the individual pixels were no longer be resolvable and appear as a single point source, producing a natural color-mixing effect.

Development of this technology is still in progress in our laboratory. As the color-tunable LEDs are monolithic, there is the possibility of integrating multiple emitters onto a single wafer and thus the possibility of producing a full-color emissive micro-display on a single-chip.

13.6 Conclusions

The prospect of having color-tunable emitters is exciting, and would expland the functionalities of LEDs beyond conventional lighting applications. To fully implement this idea, new forms of LED must be developed. Two designs for color-tunable LEDs were proposed and described in this chapter. A vertically stacked LED, based on aligning the optical paths of three RGB chips so that the paths are on top of each other, is a solution for individual high-power color-tunable emitters. Such devices can be used to assemble large-area LED display panels. The micro-pixelated design, on the other hand, enables monolithic integration of multiple devices and is thus an ideal platform for single-chip full-color emissive micro-displays, promising to challenge similar devices produced by OLED technologies.

13.7 References

1 N. Shlayan, R. Venkat, P. Ginobbi and A. K. Singh, ‘Energy Efficient RGBW Pixel Configuration for Light-Emitting Displays’ *J. Display Tech.* 5, 418 (2009).

2 H. Wu, N. Narendran, Y. Gu, and A. Bierman, ‘Improving the performance of mixed-color white LED systems by using scattered photon extraction technique’ *Proc. SPIE* 6669, 666905 (2007).

3 C.-C. Sun, W.-T. Chien, I. Moreno, C. T. Hsieh, M.-C. Lin, *et al.*, ‘Calculating model of light transmission efficiency of diffusers attached to a lighting cavity’ *OSA Optics Express* 18, 6137 (2010).

4 M. R. Krames, M. Ochiai-Holcomb, G. E. Hofler, C. Carter-Coman, E. I. Chen, *et al.*, ‘High-power truncated-inverted-pyramid $(Al_xGa_{1-x})_{0.5}In_{0.5}P/GaP$ light-emitting diodes exhibiting >50% external quantum efficiency’ *App. Phys. Lett.* 75, 2365–2367 (1999).

5 X. H. Wang, P. T. Lai and H. W. Choi, ‘Laser-micromachining of optical microstructures with inclined sidewall profile’ *J. Vacuum Sci. Tech. B* 72, 1048–1052 (2009).

6 W. Y. Fu, K. N. Hui, X. H. Wang, K. K. Y. Wong, P. T. Lai *et al.*, ‘Geometrical shaping of InGaN light-emitting diodes by laser micromachining’ *IEEE Photonics Tech. Lett.* 21, 1078 (2009).

7 G. Y. Mak, E. Y. Lam and H. W. Choi, ‘Liquid-immersion laser micromachining of GaN grown on sapphire’ *Appl. Phys. A* 102, 441 (2011).

8 Y. D. Qi, H. Liang, W. Tang, Z. D. Lu, K. M. Lau, ‘Dual wavelength InGaN/GaN multi-quantum well LEDs grown by metalorganic vapor phase epitaxy’ *J. Cry. Growth* 272, 333 (2004).

9 H. Sekigucki, K. Kishino and A. Kikuchi, ‘Emission color control from blue to red with nanocolumn diameter of InGaN/GaN nanocolumn arrays grown on same substrate’ *Appl. Phys. Lett.* 96, 231104 (2010).

10 H.-W. Lin, Y.-J. Lu, H.-Y. Chen, H.-M. Lee and S. Gwo, ‘InGaN/GaN nanorod array white light-emitting diode’ *Appl. Phys. Lett.* 97, 073101 (2010).

11 C. B. Soh, W. Liu, J. H. Teng, S. Y. Chow, S. S. Ang, *et al.*, ‘Cool white III-nitride light emitting diodes based on phosphor-free indium-rich InGaN nanostructures’ *Appl. Phys. Lett.* 92, 261909 (2008).

12 C. W. Jeon, H. W. Choi, E. Gu and M. D. Dawson, ‘High-density, matrix-addressable AlInGaN-based 368 nm micro-array light-emitting diodes’ *IEEE Photonics Tech. Lett.* 16, 2421 (2004).

13 H. W. Choi, C. W. Jeon, M. D. Martin, P. R. Edwards and R. W. Martin, ‘Fabrication and performance of parallel-addressed InGaN micro-LED arrays’ *IEEE Photonics Tech. Lett.* 15, 510 (2003).

14 C. W. Jeon, H. W. Choi and M. D. Dawson, ‘Fabrication of matrix-addressable InGaN-based microdisplays of high array density’ *IEEE Photonics Tech. Lett.* 15, 1516 (2003).

15 I. Amemiya, Y. Nomura, K. Mori, M. Yoda, I. Takasu, *et al.*, ‘LED packaging by ink-jet microdeposition of high-viscosity resin and phosphor dispersion’ *J. Soc. Information Display* 16, 475 (2008).

16 K. N. Hui, P. T. Lai and H. W. Choi, ‘Spectral conversion with fluorescent microspheres for light emitting diodes’ *OSA Optics Express* 16, 13 (2008).

17 K. N. Hui, Y. F. Fu, W. N. Ng, C. H. Leung, P. T. Lai, *et al.*, ‘Polychromatic light-emitting diodes with a fluorescent nanosphere opal coating’ *Nanotech.* 19, 355203 (2008).

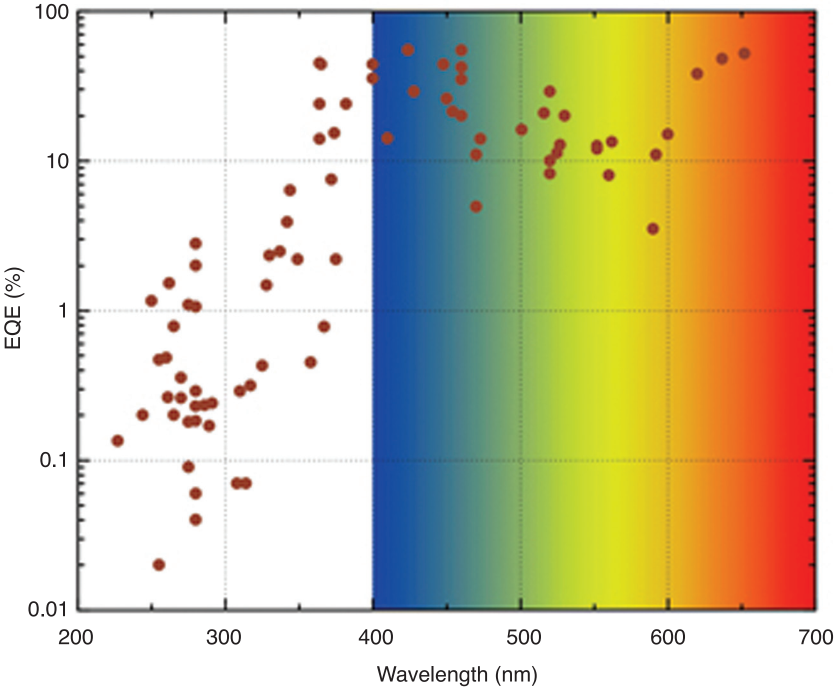

Plate XV (Chapter 12) EQE for LEDs based on the AlInGaN and AlInGaP alloy systems. As the peak emission wavelength decreases the EQE is observed to decrease. The green gap is easily discernible (Akita *et al.*, 2007; Chang *et al.*, 2003, 2010; Chen *et al.*, 2002; Guo *et al.*, 2010; Kim *et al.*, 2001; Kneissl *et al.*, 2011; Leea *et al.*, 2011; Liu *et al.*, 2011; Lundin *et al.*, 2010; Nakamura and Chichibu, 2000; Nguyen et al., 2011; Pan *et al.*, 2004; Sato *et al.*, 2008; Sheu *et al.*, 2001; Tadatomo *et al.*, 2001; Wuu *et al.*, 2005a, 2005b; Yamada *et al.*, 2002; Yamamoto *et al.*, 2010; Zhang *et al.*, 2010, 2012; Zhao *et al.*, 2011).

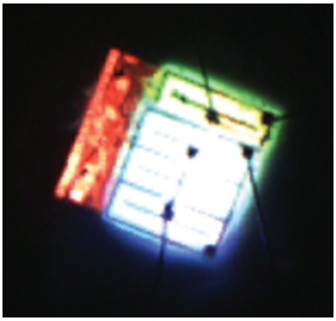

Plate XVI (Chapter 13) An initial version of an LED stack; sidewall emissions contribute to inhomogeneous color-mixing.

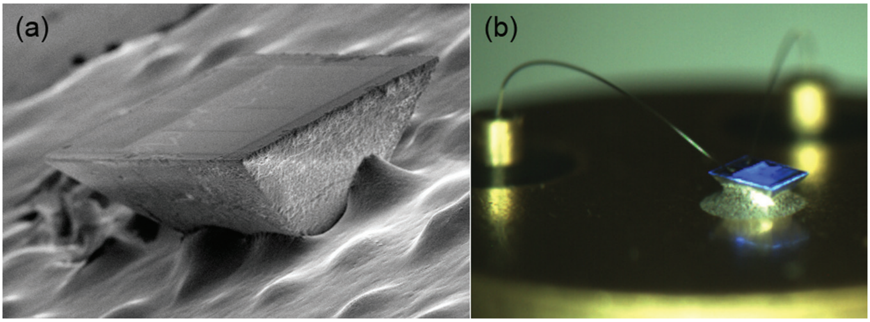

Plate XVII (Chapter 13) (a) SEM image showing a TP-LED. (b) The same device turned on.

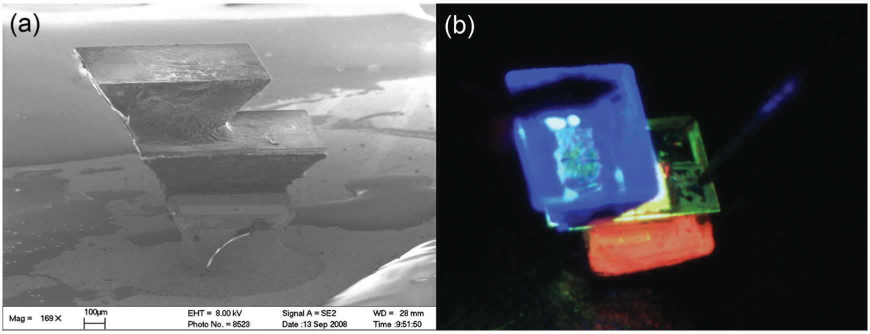
(a)
(b)
Mag = 169 X
100µm
EHT = 8.00 kV
Photo No. = 8523
Signal A = SE2
Date :13 Sep 2008
WD = 28 mm
Time :9:51:50

Plate XVIII (Chapter 13) (a) SEM image showing an LED stack assembled from LED chips of inverted-pyramidal geometry. (b) The same LED stack with all the devices turned on.

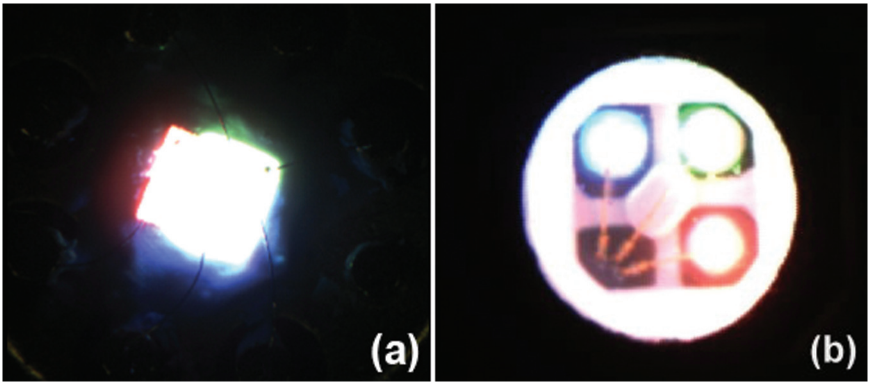

Plate XIX (Chapter 13) Sidewall light leakage is still evident from the stacked LED with inclined sidewalls as shown in (a), but it has significantly better optical mixing compared with a conventional RGB LED as shown in (b).

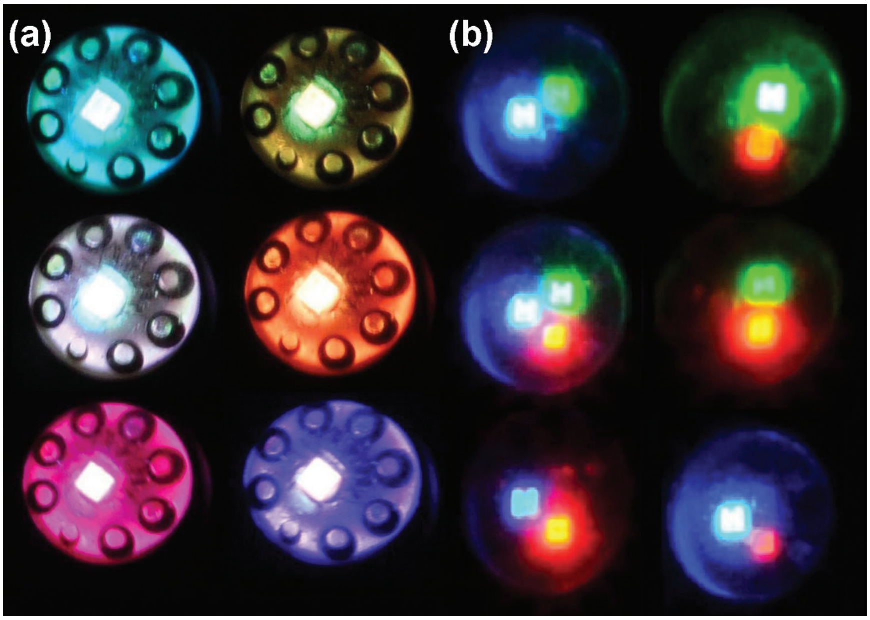

Plate XX (Chapter 13) Optical microphotographs showing the (a) stacked LED and (b) planar RGB LED emitting different colors, highlighting the effectiveness of color-mixing versus chip-stacking.

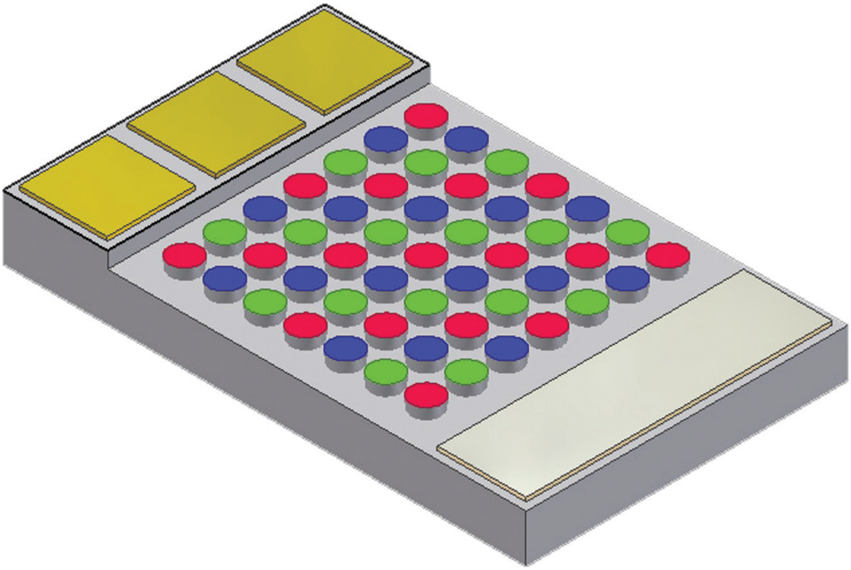

Plate XXI (Chapter 13) Micro-pixelated RGB LED.

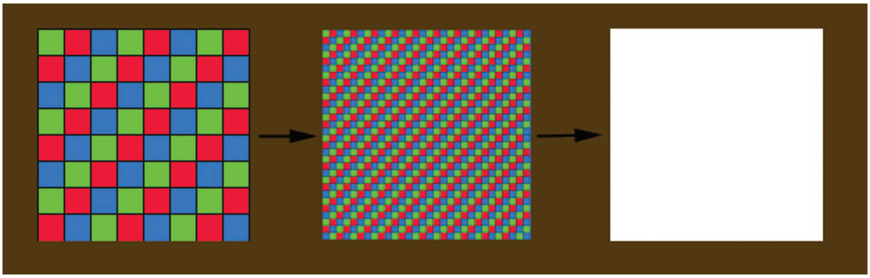

Plate XXII (Chapter 13) Color-mixing using micron-sized pixels. As the dimensions of the pixels shrink, the pixels become unresolvable to the unaided eye and the device appears white.

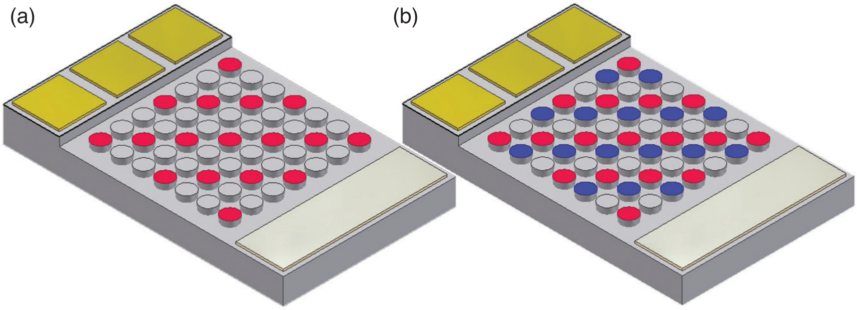

Plate XXIII (Chapter 13) The device with (a) red pixels and (b) both red and blue pixels turned on.

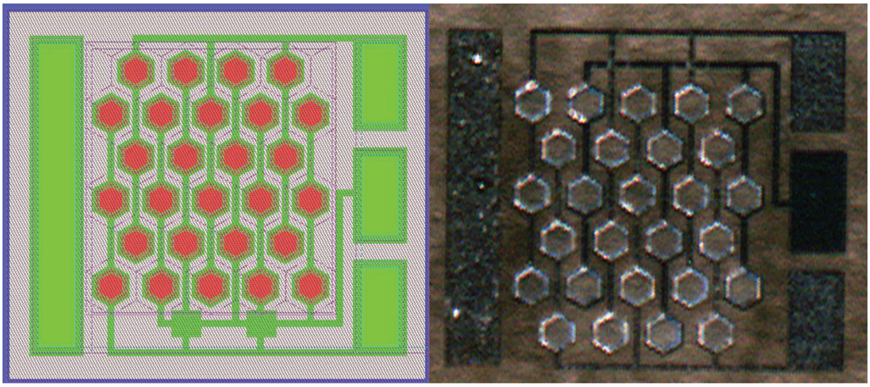

(a)

(b)

Plate XXIV (Chapter 13) (a) Layout of a group-addressable micro-LED and (b) optical microphotograph of a fabricated device.

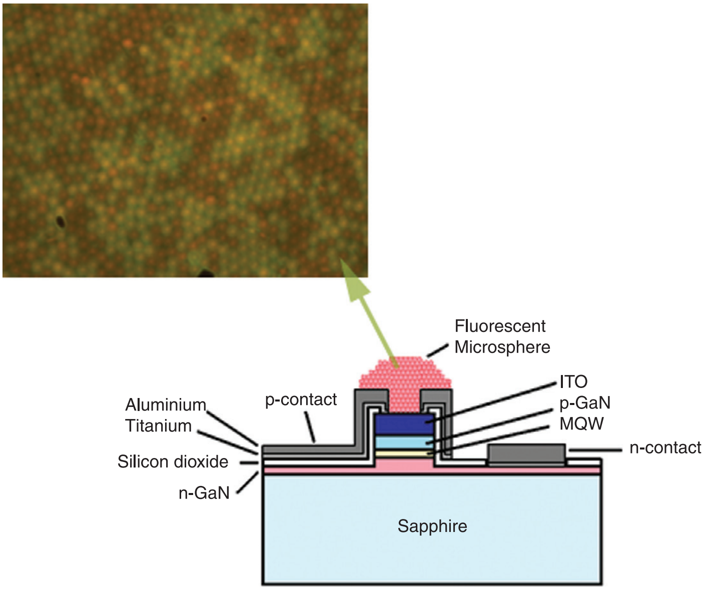
Fluorescent Microsphere
ITO
p-GaN
MQW
n-contact
Aluminium
Titanium
p-contact
Silicon dioxide
n-GaN
Sapphire

Plate XXV (Chapter 13) Top left: Optical micrograph of a close-packed array of green and orange-red fluorescent microspheres. Bottom right: Cross section of a single pixel with a fluorescent microsphere coating, which contains a close-packed array of green and orange-red fluorescent microspheres.

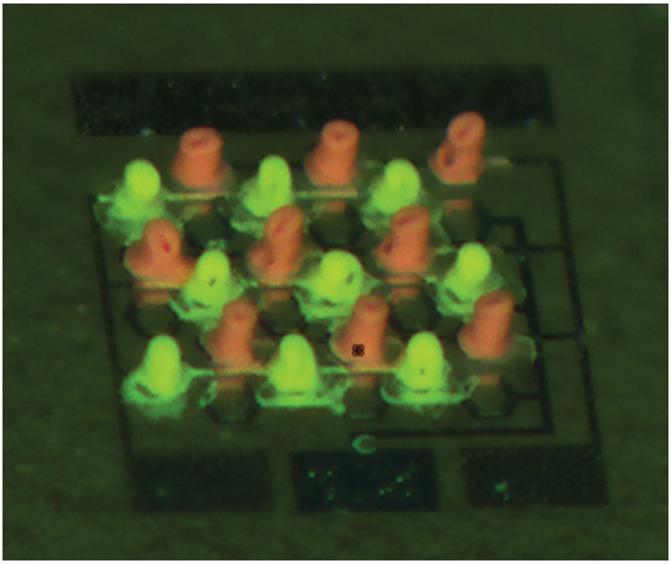

Plate XXVI (Chapter 13) Micrograph of a completed micro-pixelated color-tunable device with deposited red and green fluorescent microsphere stacks.

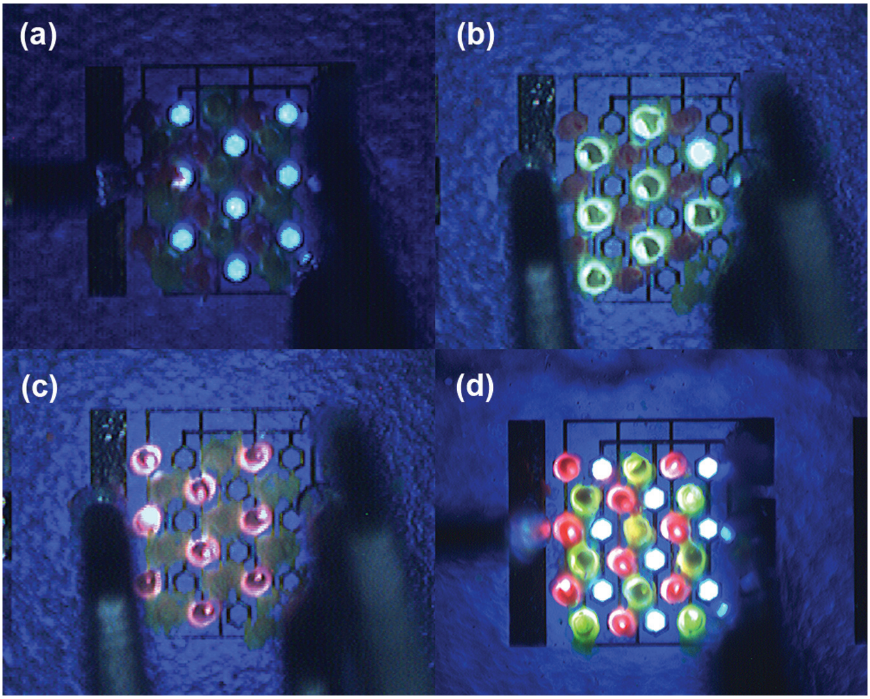

Plate XXVII (Chapter 13) (a) Blue, (b) green and (c) red pixels illuminated. In (d), all pixels are turned on.

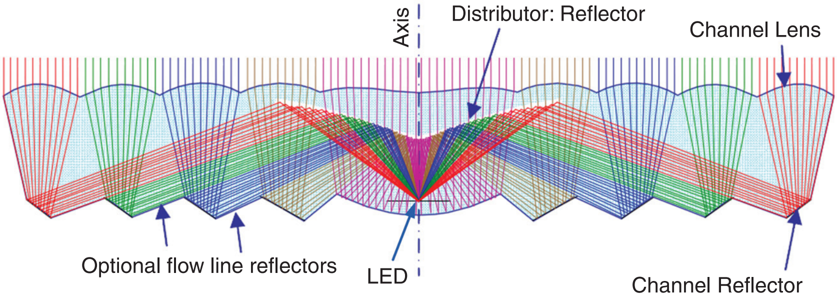
Axis
Distributor: Reflector
Channel Lens
Optional flow line reflectors
LED
Channel Reflector

Plate XXVIII (Chapter 15) Multichannel optics designed for an LED. (Reproduced with permission from Minano *et al.*[57] Copyright 2010, SPIE.)

14

Reliability of nitride LEDs

T.-T. CHEN, C.-F. DAI, C.-P. WANG, H.-K. FU,
P.-T. CHOU and W. Y. YEH,
Industrial Technology Research Institute (ITRI), Taiwan

DOI: 10.1533/9780857099303.2.428

Abstract: In this chapter, we introduce the relevant standards for commonly used LED reliability tests, LED failure analysis techniques and a failure analysis flow chart for LEDs. Finally, we discuss the underlying physical mechanisms behind LED failure based on failure analysis results.

Key words: life test, ESD test, failure evaluation, degradation mechanism.

14.1 Introduction

With the widespread application of nitride-based white LEDs in fields such as lighting and display, the evaluation of the reliability of LED products has taken on increasing importance. Common LED reliability issues include the methodologies of LED lifetime and reliability tests, characterization of LED failure phenomena and analysis of LED failure mechanisms. The objective is to enhance the reliability of LEDs by reducing the possible causes of failure. In comparison to other reliability testing methods in the semiconductor industry, which focus mainly on electrical characteristics, reliability tests for LEDs involve characterizing the electrical and optical properties. Monitoring the decay of an LED's light output with respect to time is the most rigorous basis for assessing the reliability and lifetime of LEDs. In addition, unlike other semiconductor devices, the characterization of LED luminescence properties can also yield numerous insights for failure analysis. In this chapter, we will discuss and offer recommendations on these issues.

14.2 Reliability testing of nitride LEDs

Reliability tests for nitride LEDs generally include the power and temperature cycling test (JESD22-A105), the salt atmosphere test (JESD22-A107), the mechanical shock test (JESD22-B110, JESD22-B104), the thermal shock test (JESD22-A106), the vibration test (JESD22-B103), the temperature cycling test (JESD22-A104), the high and low temperature storage test (JESD22-A119, JESD22-A103), the high temperature and humidity operating lifetime test (JESD22-A110), the moisture resistance test (JESD22-A118), the electrostatic discharge (ESD) robustness test (JESD22-A114) and the LED lumen maintenance test (IES LM-80-08). The lifetime test also encompasses the estimation of the lifetime. These are the most commonly used tests by LED manufacturers for evaluating the reliability of LED devices. Since these tests are destructive and can result in damaging the LED device, sampling is commonly used during testing.

In this chapter, we focus on the ESD robustness and LED lumen maintenance tests, which are the main reliability tests for nitride LEDs. In 2008, the Illuminating Engineering Society (IES) published the standard 'IES LM-80-08: Measuring Lumen Maintenance of LED Light Sources', which specified the measurements for the lumen maintenance testing of LED light sources, including LED packages, arrays and modules. The standard 'IES TM-21-11: Projecting Long Term Lumen Maintenance of LED Light Sources' was subsequently published in 2011, and most LED manufacturers now employ these two standards as the benchmark for testing LEDs. It should be noted that: (1) the standards mentioned so far are only for the output luminous flux through a lumen maintenance test, but lumen maintenance is not entirely representative of the lifetime of an LED. However, lumen maintenance is commonly used to determine the lifetime of an LED device. (2) There are no separate lifetime testing standards for LED dies or the packaging materials; therefore, the lifetime test of an LED die can only be conducted with its simplest packaged form.

The ESD robustness tests for LEDs include the human body model (HBM), the machine model (MM) and the charged device model (CDM). The HBM and MM simulate the discharge of static electricity from a human or machine to an LED device, whereas in the CDM test, the LED itself carries the static charge and discharges to the surrounding environment. For most current LED products (including the die itself and the packaged components), HBM damage is the most commonly observed and, therefore, the HBM is the primary test employed to evaluate ESD robustness at the level of the LED die and the finished LED products.

14.2.1 Methods for life testing and lifetime estimation

The life testing methods for LEDs adhere primarily to the LM-80-08 standard. The LM-80-08 standard stipulates that the driving current employed in LED life tests must be representative of commonly used applications, with three case temperatures: 55 °C, 85 °C and a manufacturer-specified temperature. In order to acquire sufficient testing data to estimate the lifetime of an LED accurately, the life test must be performed for at least 6000 hours. Furthermore, at intervals of at least once every 1000 hours during the LED life test, variations in the light output, chromaticity coordinates, forward voltage, etc. must be measured. The LM-80-08 standard does not specify the percentage to which the lumen has decayed before an LED is deemed to have failed, and define the lumen maintenance life to be the time for the LED lumen to decay to 70% or 50% of its initial value.

The LM-80-08 standard also does not provide any guideline for how to estimate the lifetime based on the 6000 hours of test data. According to the TM-21-11 standard, the lifetime estimation is based on a projection of the LED lumen maintenance rate from data obtained through the LM-80-08 tests. For an LED, the lumen decay typically follows a simple exponential model, because the LED component materials undergo diffusion over time and the rate of diffusion increases with operating temperature.[1] Based on this model, the lifetime estimate for LED lumen decay is given by the TM-21-11 standard as:

$$\Phi(t) = B \cdot e^{-\alpha \cdot t}, \tag{14.1}$$

where Φ is the lumen output at time t, B is an initial constant and α is the lumen decay rate constant. From this exponential decay equation, one can estimate the LED lifetime for a fixed temperature. If one wishes to estimate the LED lifetime at different temperatures, it is necessary to introduce the Arrhenius equation,[1] which describes how the component materials of an LED and chemical reactions at different temperatures affect the lumen decay rate:

$$\alpha = A \cdot e^{-\frac{E_a}{kT}}, \tag{14.2}$$

where E_a is the activation energy, k the Boltzmann constant, T the temperature and A a constant related to the properties of the material. In particular, one can obtain E_a/k by plugging in the empirical lifetimes at two different temperatures:

$$\frac{E_a}{k} = \frac{\ln(\alpha_1) - \ln(\alpha_2)}{\frac{1}{T_2} - \frac{1}{T_1}} \tag{14.3}$$

where α_1 and α_2 are the lumen decay rate constants at temperatures T_1 and T_2, respectively. Substituting the E_a/k obtained from Eq. 14.3 back into Eq. 14.2, the Arrhenius equation, one can obtain the lumen decay rate constants at different temperatures. From Eq. 14.1, one can obtain the relation between lumen decay and time at intermediate temperatures, i.e. the lifetime estimates at intermediate temperatures. The lifetime estimation as defined by the LM-80-08 and TM-21-11 standards has enabled LED manufacturers to adopt a universal set of criteria for lifetime testing and evaluation.

14.2.2 Methods for electrostatic discharge (ESD) testing

An ESD takes place between two objects at different electrostatic potentials, with a transfer of energy. Figure 14.1 depicts the equivalent circuit used to simulate the ESD process. In addition to the device under test (DUT), the ESD configuration consists of a power supply, capacitors and resistors. The power supply provides the testing voltage for the ESD, and typically for LED samples this ranges from 0

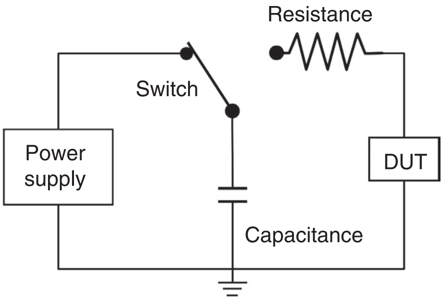

14.1 Equivalent circuit for ESD.

to 4000 V. When the capacitor is fully charged and has attained electrostatic balance, instantaneous switching of the circuit via the switch will lead to a discharge of current from the capacitor through the resistance to the DUT to simulate an actual ESD scenario. Of the three most commonly used discharge modes, namely HBM, MM and CDM, HBM damage is the most commonly observed in LED devices. Therefore, LED manufacturers in general begin with the HBM ESD robustness level test as the basis for classifying products according to their reliability. There are two main sets of specifications adopted in HBM tests. In the MIL-STD-883G and JEDEC JESD22-A114 series, the equivalent capacitance of the human body is set at 100 pF and the corresponding equivalent discharge resistance is set at 1.5 kΩ. In the IEC-61000-4-2 specifications, the equivalent capacitance of the human body is set at 150 pF and the corresponding equivalent discharge resistance is set at 330 Ω. Other commonly adopted specifications include the JESD22-A115 series for the MM mode and the JESD22-C101 series for the CDM mode.

14.3 Evaluation of LED degradation

Due to factors such as the intrinsic defects in an LED die and the uneven distribution of current and temperature, the degradation of an LED die tends to be concentrated in specific regions rather than being evenly distributed. Since some of these degraded regions are only a few tens or hundreds of nanometers across, many of the analytical techniques need to be coupled with a microscope when used for characterization, such as emission microscopy (EMMI) and electroluminescence (EL) mapping in combination with optical microscopy (OM), energy dispersive spectroscopy (EDS) and electron energy loss spectroscopy (EELS) in combination with scanning electron microscopy (SEM) and transmission electron microscopy (TEM), etc. These characterization techniques are typically employed to ascertain the degradation regions as well as to analyze the failure mechanisms of the LED die. In this chapter, we will not explain in detail the principles underpinning the various failure characterization techniques, and will merely introduce the application of several commonly used characterization techniques in LED failure analysis. Further, a general LED failure analysis flow chart is included for reference in Section 14.3.2.

14.3.1 Failure evaluation techniques

Since the failure criteria for LEDs are not specified in the LM-80-08 standards, LED manufacturers typically define the failure of an LED as the point when the light output of an LED at its operating voltage drops under 70% of the initial value, or when the leakage current exceeds 1 μA at −5 V reverse voltage. The characterized regions and detectable signals for the various characterization techniques used during LED failure evaluation are listed in Table 14.1. Failure analysis characterization can be broadly divided into three categories. The first category is morphology characterization (e.g. OM images, X-ray images, SEM

Table 14.1 Detectable signals and characterization regions for various characterization techniques

Characterization technique	Characterization region	Detectable signals
OM	Surface Die/wire bonding	Strength of reflected visible light
X-ray image	Surface Die/wire bonding	Strength of transmitted X-ray
EL mapping	Surface Active region Electrode	Forward-biased emission
EMMI	Surface Leakage path Sidewall	Reverse-biased emission
SEM	Die structure Electrode Transparent conductive layer	Secondary electrons
EDS	Die structure Electrode Transparent conductive layer	Characteristic X-ray spectrum
TEM	Die structure Quantum well (QW) structure Interface quality	Transmission electrons
EELS	Die structure Quantum well (QW) structure Interface quality	Transmission electrons
Secondary ion mass spectroscopy (SIMS)	Die structure Quantum well (QW) structure Interface quality	Secondary ions

images, TEM images, etc.) where external structural damage is observed with incident visible light, X-rays or electrons. The second category uses electrical and optical imaging, such as EL mapping and EMMI, to obtain luminescence images of the LED under forward and reverse bias, respectively, to characterize failure regions that exhibit no external structural damage (e.g. the active layer, the surface leakage pathway, etc.). The third category uses composition mapping and chemical bond imaging (e.g. EDS and EELS coupled with SEM or TEM) to verify the failure of the LED. If the cross section of an LED die is to be observed then the necessary vertical cuts are made using the focused ion beam (FIB) method. The FIB method is also used to prepare TEM samples. The FIB method must be used before some of the other failure analysis techniques described above.

14.3.2 Failure evaluation flow chart

In Fig. 14.2, we have reorganized the contents of Table 14.1 into a failure evaluation flow chart for a typical LED die. The flow chart progresses from the top to the bottom, and in principle, non-destructive characterization procedures are performed before destructive characterization procedures. Likewise, macroscopic characterization procedures are performed before microscopic characterization procedures. Non-destructive characterization mainly entails the use of techniques such as EL mapping and EMMI to inspect the electrodes and transparent conductive layer (TCL) for damage, and to perform detailed characterization of regions with weaker luminescence or current leakage. When using EL mapping or EMMI for macroscopic characterization of the surface of an LED die, it may be necessary to remove the encapsulated cap on the die if the silicon or phosphor on the surface of the die is found to be interfering with the characterization. However, this procedure is likely to damage the die or wire bonding, thereby rendering EL mapping and EMMI next to impossible. When performing SEM and EDS analyses of the structure and composition of an LED die surface, there should be no encapsulated material on the surface of the die. For destructive characterization, FIB can be used, based on surface images obtained with EMMI or SEM, to make longitudinal cuts in regions with obvious current leakage or sites with apparent surface defects, followed by EDS and SEM observations of the failure conditions in the cross section of the sample. Finally, FIB can be used to produce a TEM sample of a specific region for further characterization. When using TEM to observe defect-related causes of failure, such as threading dislocation and defect generation, measurements should also be made of the initial sample to verify the variations before and after the appearance of the defects that resulted in the failure of the LED. After the encapsulated material on the surface of the LED die has been removed, secondary ion mass spectroscopy (SIMS) can be directly used to obtain the composition distribution of the LED sample at different depths.

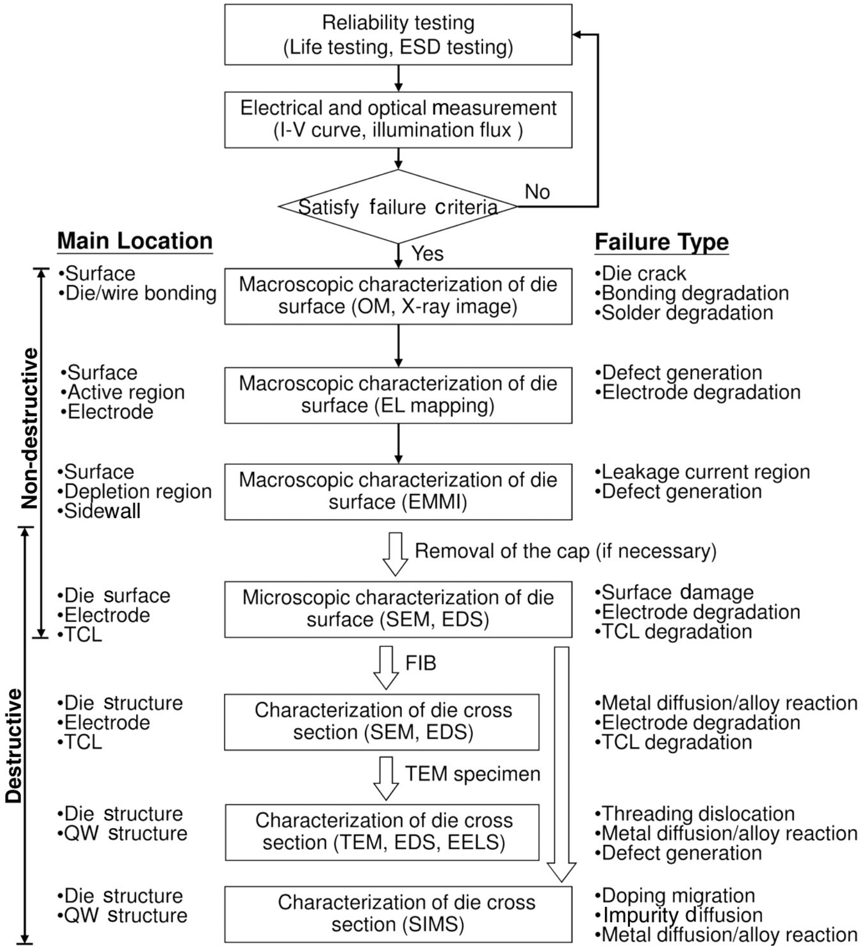
Reliability testing
(Life testing, ESD testing)
Electrical and optical measurement
(I-V curve, illumination flux)
Satisfy failure criteria
No
Yes
Main Location
Failure Type
Non-destructive
Destructive
•Surface
•Die/wire bonding
Macroscopic characterization of die surface (OM, X-ray image)
•Die crack
•Bonding degradation
•Solder degradation
•Surface
•Active region
•Electrode
Macroscopic characterization of die surface (EL mapping)
•Defect generation
•Electrode degradation
•Surface
•Depletion region
•Sidewall
Macroscopic characterization of die surface (EMMI)
•Leakage current region
•Defect generation
Removal of the cap (if necessary)
•Die surface
•Electrode
•TCL
Microscopic characterization of die surface (SEM, EDS)
•Surface damage
•Electrode degradation
•TCL degradation
FIB
•Die structure
•Electrode
•TCL
Characterization of die cross section (SEM, EDS)
•Metal diffusion/alloy reaction
•Electrode degradation
•TCL degradation
TEM specimen
•Die structure
•QW structure
Characterization of die cross section (TEM, EDS, EELS)
•Threading dislocation
•Metal diffusion/alloy reaction
•Defect generation
•Die structure
•QW structure
Characterization of die cross section (SIMS)
•Doping migration
•Impurity diffusion
•Metal diffusion/alloy reaction

14.2 LED failure evaluation flow chart.[2]

14.4 Degradation mechanisms

The degradation mechanisms for most nitride LEDs are intimately related to intrinsic defects as well as the current density and junction temperature. During extended LED lifetime tests, the defect density will increase with time and render the LED degradation all the more apparent. When an LED suffers from an ESD stress fracture, there will be instantaneous failure and different forms of degradation. In general, around 1–3 W of electrical power (in other words, an operating current for a 1 mm^2 LED die of 350–1000 mA) is injected into a high-power LED over the course of operation, and the junction temperature follows the corresponding equation:

Junction temperature = Ambient temperature + Thermal resistance × Electrical power,

with the thermal resistance being dependent on the packaging. However, during actual operation, due to factors such as the structure or design, the current is unevenly distributed throughout the LED die, and the regional current density and junction temperature can often vastly exceed the averages across the entire LED die. Therefore, degradation tends to be concentrated in specific regions, shortening an LED's lifetime. Building on the discussions on reliability testing in Section 14.2 and reliability analysis techniques in Section 14.3, we now discuss degradation mechanisms.

14.4.1 Degradation mechanisms found in LED life testing

Various failure mechanisms resulting from extended use can affect an LED's lifetime and luminescence efficiency. As described in Section 14.2.1, most LED life testing methods currently in use adhere to the specifications of the LM-80-08 standards published by the Illuminating Engineering Society. Testing is conducted under specific conditions to gauge the reliability of LEDs through extended aging tests and to analyze the physics behind the various types of failure stemming from the aging process. However, the composition of an LED is extremely complex, and includes components such as conductors, semiconductors and non-conductive materials. The failure mechanisms of an LED, in addition to the electrical and thermal stress failures commonly observed in diode elements, also include failures due to light emission. For example, deterioration of the plastic encapsulation material can result in a drop in the optical transmittance. A drop in the conversion efficiency of the phosphor can render the physics behind LED failure even more complex. The most common manifestation of LED failure is a drop in the output power, usually quantified by luminous efficacy (lm/W). Most of the common failure phenomena will vary with changes in the leakage current and forward bias, as shown in Fig. 14.3 and Fig. 14.4.

The current versus voltage of a diode is given by:

$$I_{junction} = I - \frac{V - IR_s}{R_p} = I_s \exp\left[\frac{e(V - IR_s)}{n_{ideal}KT}\right], \tag{14.4}$$

where $I_{junction}$ is the current across the p-n junction, I is the total input current, R_p is the parallel resistance, R_s is the series resistance and n_{ideal} is the ideality factor. As shown in Fig. 14.3, Zone I is where the carrier recombination effect occurs, Zone II is where the ideality factor influences the ideal diode equation and Zone III is the series resistance range, which is a result of the ohmic contact.[4] From variations of the diode current versus voltage curve as well as the corresponding influencing factors during the aging test, one can make a rough guess of the failure mechanism.

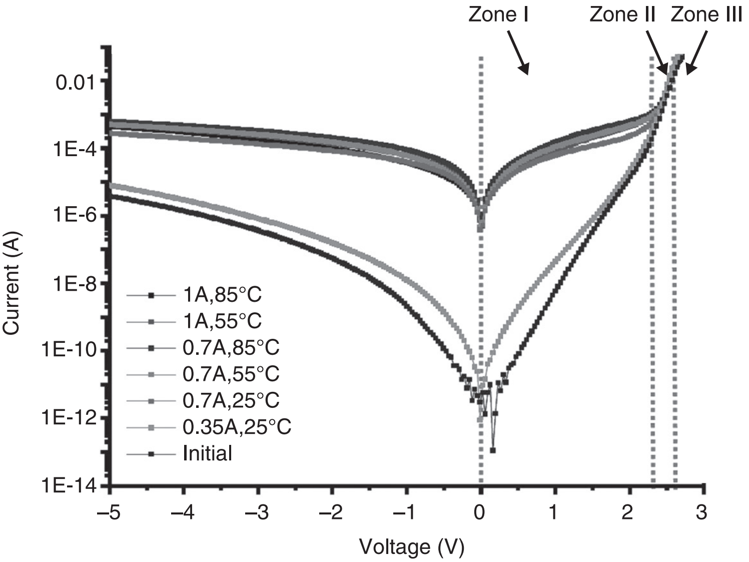

14.3 Semi-log current–voltage curve measured after long-term aging tests.[3] (Copyright 2011, Japan Society of Applied Physics.)

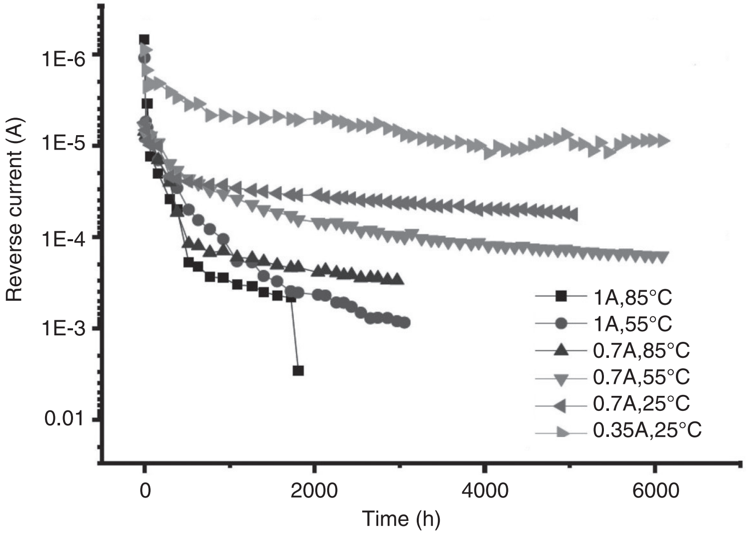

14.4 Reverse current as a function of aging time under various conditions.[3] (Copyright 2011, Japan Society of Applied Physics.)

Many related studies have shown that factors causing a decay of LED luminous efficacy include the reduction of the internal quantum efficiency, which occurs as a result of an increase in the density of non-radiative recombination defects, an increase in the ohmic contact resistance due to aging of the materials, the formation of point defects by hydrogen and magnesium ions, etc.[5]

The concentration of electrical stress or heat stress as a result of uneven current density may accelerate or exacerbate the aforementioned causes of failure. For example, the reverse current of an LED increases by several orders with increasingly harsh aging conditions (greater voltage and current) and longer operating times, as shown in Fig. 14.4. Possible causes include an increase in the dislocation density across the p-n junction[6] or surface damage caused by the etching process.

In general, LED failure physics can be classified as: (1) rapid degradation in the initial stage, (2) gradual degradation and (3) catastrophic degradation.

Rapid degradation in the initial stage

The underlying causes of rapid degradation are line defects of the die, which are usually caused by lattice mismatches. Most of the common line defects arise from surface defects of the die. They grow along the surface defects after the application of external electrical or thermal stress.

Gradual degradation

As described in Section 14.2.1, most LED efficiency decay models exhibit gradual degradation, with the rate of decay dependent on the activation energy and temperature.

Catastrophic degradation

Catastrophic degradation is usually the result of electrical damage, which can take place during the operation or installation of the device. The majority of such failures can be discerned from the dark spots or dark regions in the p-n junction as observed by EL mapping. Another possible cause is short-circuiting of the p-n junction, which can be observed from the current versus voltage relation in the low-bias range.

14.4.2 Degradation mechanisms found in LED ESD testing

During an electrostatic discharge, most of the damage that leads to failure of an LED die is the result of a transient peak discharge and a transient high temperature. A relatively large peak current is accompanied by a large energy release, which will result in damage to the components and thus lead to failure. In view of the destructive effects of ESD on LED components, a better understanding of the sources and mechanisms of failure, as well as the prevention and remedial steps to be taken, will vastly enhance the application value of LED devices.

The main causes of ESD failure are defect density, electrical conductivity and thermal dissipation. However, under different ESD stresses, the causes of ESD-induced LED component failures can be classified as:[7]

- Hard failure: When an LED die is subjected to large transient currents or voltage pulses, it will rupture internally throughout the epitaxial layers, leading to the creation of a conduction pathway. The generation of defects will enhance the leakage pathways for the leakage current, and the temperature and current crowding effects will cause melting at the interface of the metal and semiconductor, indirectly contributing to the diffusion of dopant atoms and metal atoms and causing a short-circuit of the component, which culminates in permanent failure.[7]
- Soft failure: When an LED die is subjected to a small transient current or voltage pulse, the annihilation of some of the defective pathways[7] or the unstable conductivity of the leakage pathways[8] can lead to instability in the leakage current. During this time, the LED will still function normally, but its performance will gradually deteriorate with frequent use.

When ESD stresses of different polarity are applied to an LED device, a reverse bias voltage will have a greater impact than a forward bias voltage on the leakage current. There are different mechanisms for the current flow in LED devices for forward and reverse bias. Under a forward bias, the current flows in the conduction band. Therefore, when an external forward ESD bias is applied to an LED device, the ESD transient discharge current is also carried in the conduction band of the device, and no associated defects are created. Under a reverse bias, most of the current is concentrated in the leakage pathways, and the electrons in the p-GaN valence band will be driven by the large potential difference and will cross over into the GaN conduction band via the defect energy levels in the p-n junction, a process that will create more defect energy levels in the p-n junction and thus greater leakage currents. However, as mentioned for soft failure, when the applied ESD stress is relatively low, there will be instability in the size of the leakage current.

In addition to the aforementioned size and polarity effects of ESD stress on LED reliability, the ESD robustness of an LED is also related to its structure. Current conduction in most LED devices assumes a horizontal structure, since most LEDs currently in use employ a sapphire substrate, which is non-conductive and has poor thermal conductivity. As shown in Fig. 14.5, the p-pad electrode and the n-pad electrode are located on the left and right, respectively, on the same side of the sapphire substrate. Therefore, when an LED device is subjected to an ESD stress, the current crowding effect will lead to a mix of thermal, potential difference and light emission phenomena. This will render the die prone to local fixed-point

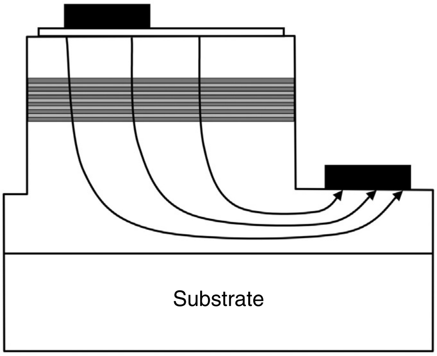

14.5 Horizontal structure of an LED device.[10]

failures,[9, 10] and this is the most common cause of failure during a transient electrostatic discharge.

Therefore, optimization of the location of the electrodes and the design of the structure will reduce current crowding in the conduction pathways.[7] When the separation between the two electrodes is large, the differences in the resistance of the various current conduction pathways will render some of the local regions prone to the current crowding effect. Energy will be dissipated in the form of heat, making it more likely for the LED to experience regional failure under the application of an ESD stress.[9] According to the current conduction pathways depicted in Fig. 14.5, the active region, the n-GaN area and the contact area between the contact layer and the p-GaN are the three main areas in the LED device where the heat from the current crowding effect originates. The poor thermal conductivity (35 W/mK) of the sapphire substrate will result in the accumulation of heat within the device, leading to diffusion of the internal doping ions. At the same time, melting of the metallic points of contact may also occur, creating a short-circuit that will cause permanent failure of the LED die.

14.5 Conclusion

In this chapter, we described the two characterization methods most commonly adopted by LED manufacturers to evaluate the reliability of LEDs, and outlined the standards for comparing different products. Among the tests employed are the lifetime test and ESD robustness test after extended operation at different temperatures and currents. During the failure analysis phase, we follow the failure analysis flow chart outlined in Section 14.3.2, and perform non-destructive failure analysis before destructive failure analysis. We can further supplement our results with luminescence images under forward and reverse bias, high-resolution electron microscope images, EDS composition images, EELS binding energy images, etc. to ascertain the failure regions and causes. LED failure mechanisms are often related to intrinsic defects, current density, junction temperature, etc. Factors such as current crowding and regional hot spots tend to shorten the operating lifetime of an LED, with failure usually concentrated in specific regions.

The main indicators for LED reliability have traditionally been based on criteria such as light output, operating voltage, size of the reverse leakage current, etc. In the future, monitoring of the junction temperature should be added to the list of criteria for reliability evaluation, and as with the measurement of other criteria (e.g. light output or luminous flux, operating voltage, etc.), a means of quickly establishing the junction temperature should be incorporated to aid comprehensive inspection and grading of LED products. For long-term lifetime testing, consider using large currents or high temperatures to shorten the duration of the tests significantly, and formulate lifetime estimation methods for quickly evaluating an LED's lifetime and reliability. Regarding the ESD robustness test, the development of comprehensive non-destructive ESD characterization technologies to replace the current destructive testing methods should become the focus of future research aimed at enhancing LED reliability. In addition, due to the diversification and rapid development of LED products, the establishment of testing and evaluation criteria that extend current standards and cater for such disparate products as AC LEDs, high voltage LEDs, micro-LED arrays, etc. is yet another area that deserves attention.

14.6 References

1 Lanza, C. *et al.* (1967) 'Aging effects in GaAs electroluminescent diodes', *Solid-St. Electron.*, 10, 21–31.

2 Osamu Ueda (1996) *Reliability and Degradation of III-V Optical Devices*, Boston, Artech House.

3 Yang, S. C. *et al.* (2011) 'Accelerated degradation of high power light-emitting diode resulted from inhomogeneous current distribution', *Jpn. J. Appl. Phys.*, 50, 034301-1–034301-6.

4 Meneghesso, G. *et al.* (2003) 'Reliability of visible GaN LEDs in plastic package', *Microelectronics Reliability*, 43, 1737–1742.

5 Kozodoy, P. *et al.* (2000) 'Depletion region effects in Mg-doped GaN', *J. Appl. Phys.*, 87, 770–775.

6 Yang, S. C. *et al.* (2010) 'Failure and degradation mechanisms of high-power white light emitting diodes', *Microelectronics Reliability*, 50, 959–964.

7 Matteo, M. *et al.* (2010) 'Soft and hard failures of InGaN-based LEDs submitted to electrostatic discharge testing', *IEEE Elec. Dev. Lett.*, 31, 579–581.

8 Chen, N. C. *et al.* (2009) 'Damage of light-emitting diodes induced by high reverse-bias stress', *J. Crystal Growth*, 311, 994–997.

9 Shim, J.-I. (2008) 'Design and characterization issues in GaN-based light emitting diodes', *Proc. of SPIE*, 7135, 71350C-1–71350C-9.

10 Meneghesso, G. *et al.* (2001) 'Electrostatic discharge and electrical overstress on GaN/InGaN light emitting diodes', *Electrical Overstress/Electrostatic Discharge Symposium*, 247–252.

15

Chip packaging: encapsulation of nitride LEDs

X. LUO and R. HU, Huazhong University of
Science and Technology, People's Republic of China

DOI: 10.1533/9780857099303.2.441

Abstract: Nitride light-emitting diodes (LEDs), from nitride chips to devices, must be packaged. The chip packaging processes have an important role in determining the final optical and thermal characteristics of the LEDs, and the packaging processes should be well designed from the perspectives of heat dissipation and illumination. In this chapter, we introduce chip packaging for nitride LEDs so that the readers will gain a comprehensive understanding of LED packaging. This chapter starts by describing the functions and the structures of nitride LED chip packaging, and then emphasizes the optical and thermal designs for LED packaging coupled with particular processes.

Key words: light-emitting diode (LED), chip packaging, wire bonding, phosphor coating, freeform lens, thermal resistance.

15.1 Functions of LED chip packaging

Considered to be the next generation of light sources, light-emitting diodes (LEDs) are widely used because of their extraordinary features compared to traditional light sources, such as high luminous efficiency, high reliability, long lifetime, environmentally friendly, low-power consumption, etc. A bare LED chip may light up but it cannot be used due to its poor long-term reliability. LED chip packaging not only ensures good performance of LED devices by enhancing reliability and optical characteristics, but it is used to control and adjust the final performance. As a prerequisite of LED use, LED chip packaging plays an important role in determining the final optical and thermal performance of LED devices. Like electronic packaging, LED chip packaging has six main functions, as shown in Fig. 15.1.

15.1.1 Encapsulation and protection

One of the purposes of LED chip packaging is to provide a physical housing to protect the LED chip and bonding wires from the hostile environment. A nitride LED chip is vulnerable to its environment, especially the real working conditions include moisture and dust in the air, vibration, shock (mechanical shock and thermal shock), thermal cycling, etc. Moisture and dust in the air are the two main direct causes of LED device failure.[1–3] Moisture can invade the

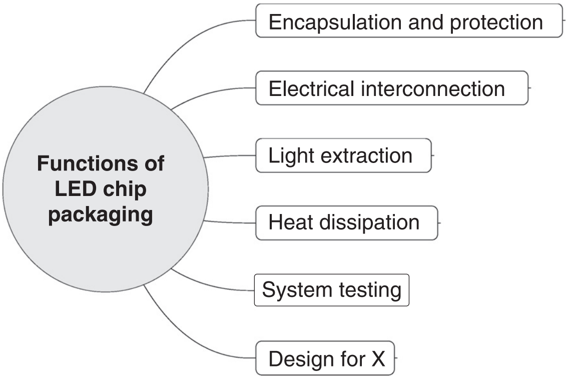
Functions of LED chip packaging
Encapsulation and protection
Electrical interconnection
Light extraction
Heat dissipation
System testing
Design for X

15.1 Functions of LED chip packaging.

interfaces of the packaging and induce delamination, which will increase contact thermal resistance and degrade reliability significantly. Dust can block light output and also increase the thermal resistance of an LED package. Other hostile mechanical or thermal conditions may cause the failure of solder joints, delamination, degradation of packaging materials, etc. With LED chip packaging, most of the interconnections and the chip are protected, and failure tends to be more usually attributed to the packaging of the devices rather than to the devices themselves. The encapsulant material needs to have chemical inertness, rigidity, high-temperature stability, high optical transparency and a high refractive index.

15.1.2 Electrical interconnection

With LED chip packaging, an LED chip is usually bonded onto a copper heat sink or lead frame structure using solder or a conductive die adhesive. Various LED chip structures are shown in Fig. 15.2. Chip bonding is dependent on the position of the electrodes. With wire bonding between the chip and lead frame, as shown in Fig. 15.3, electrical power is input to the chip through the lead frame, which acts as secondary electrodes, providing electrical paths for power and signal distribution.

15.1.3 Light extraction

Light extraction is very important in high-brightness LED packaging. A high luminous efficiency requires high light extraction from an LED package. When blue light emanates from the multi-quantum wells of an LED chip and reaches the interface between the chip and the air, the total internal reflection (TIR) phenomenon would happen. The consequence of TIR is that some of the blue light

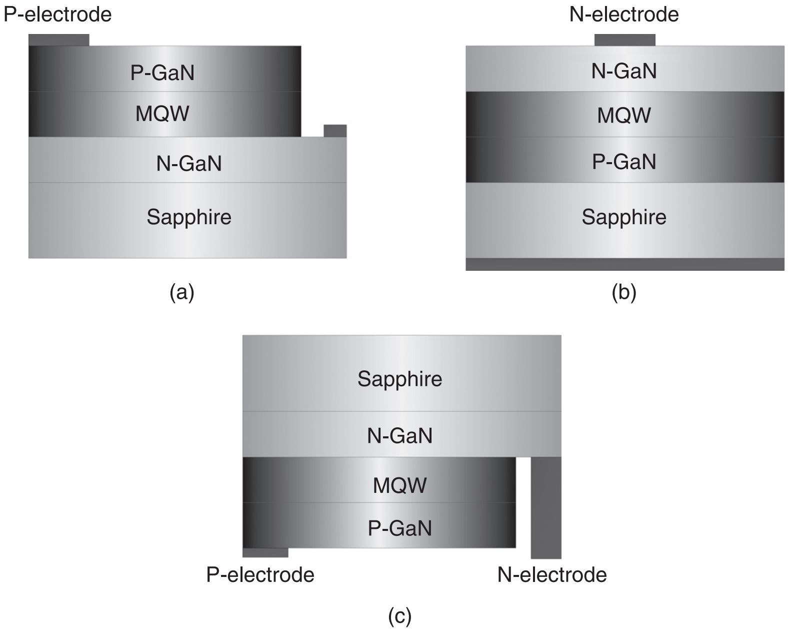
P-electrode
P-GaN
MQW
N-GaN
Sapphire
(a)
N-electrode
N-GaN
MQW
P-GaN
Sapphire
(b)
Sapphire
N-GaN
MQW
P-GaN
P-electrode
N-electrode
(c)

15.2 Three types of high-power LED chip: (a) a conventional chip, (b) a vertical injection chip and (c) a flip chip. (MQW: multi-quantum well)

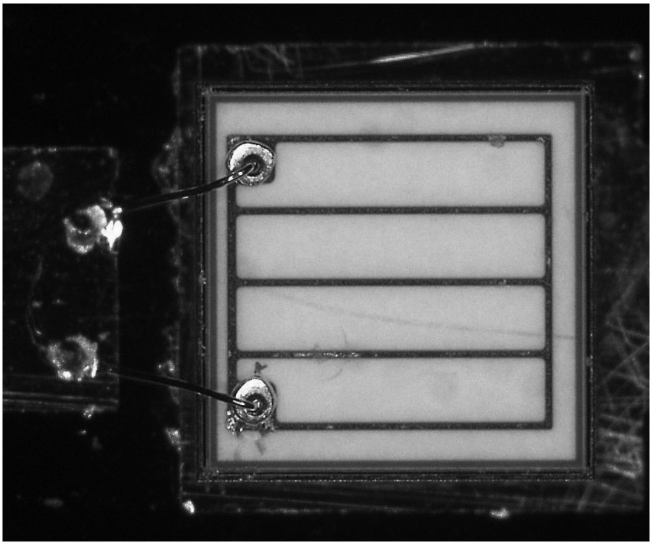

15.3 Wire bonding for electrical interconnection.

cannot escape from the chip structure, but instead it oscillates inside the chip structure until it is absorbed by the chip materials.

According to Snell's law, at the interface:

$$n_{chip}\sin\theta_{chip}=n_{air}\sin\theta_{air} \qquad [15.1]$$

where n_{chip} and n_{air} are the refractive indices of the LED chip and air, respectively. θ_{chip} and θ_{air} are shown in Fig. 15.4. The refractive index of GaN material n_{chip} is normally around 2.4 and n_{air} usually equals 1.0. With total internal reflection, when θ_{air} equals 90° θ_{chip} is the half angle of the escape cone and it can be calculated as:

$$\theta_{chip} = \arcsin\left(\frac{n_{air}}{n_{chip}}\sin\theta_{air}\right) = \arcsin\left(\frac{1}{2.4}\right) \approx 24.6° \qquad [15.2]$$

However, when an LED chip is packaged, there is a thin layer of silicone between the LED chip and the air. The refractive index of the silicone layer is 1.5. Therefore with total internal reflection, when $\theta_{silicone}$ equals 90°, θ_{chip} is calculated as

$$\theta_{chip} = \arcsin\left(\frac{n_{silicone}}{n_{chip}}\sin\theta_{silicone}\right) = \arcsin\left(\frac{1.5}{2.4}\right) \approx 38.7° \qquad [15.3]$$

Compared with Eq. 15.2, it can be seen that θ_{chip} has increased, which means more light can escape from the chip structure and light extraction is enhanced. In short, LED chip packaging can enhance light extraction.

15.1.4 Heat dissipation

Although LEDs are considered as cold light sources compared with conventional light sources, this does not mean that heat dissipation for LEDs is unnecessary. Due to the low photoelectric conversion efficiency of current LED devices, most

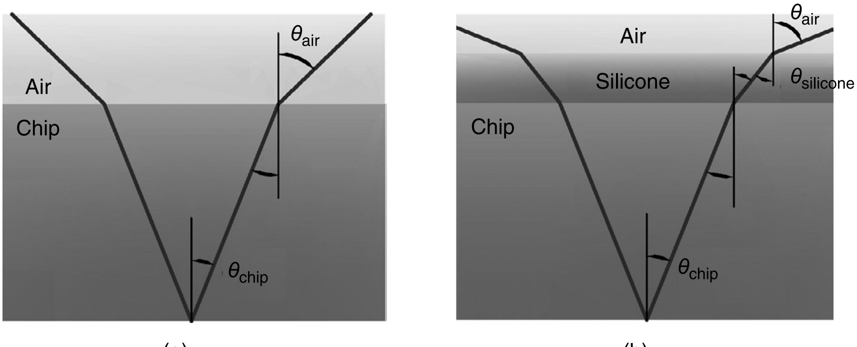

15.4 Refraction at the (a) chip and air interface and (b) chip, silicone and air interfaces.

of the input electrical power is converted into heat, thus good solutions for heat dissipation in LED applications are of great importance.

Since the dimensions of a 1 W LED chip are usually very small compared to the substrate, the heat flux is almost 70 W/cm^2, which is much higher than a conventional microprocessor chip.[4] The high-power density can generate significant heat inside the small chip, which may lead to a high junction temperature, thus increasing non-radiative recombination of holes and electrons, decreasing luminous efficiency, degrading packaging materials, etc.[5–7] Therefore, the junction temperature of an LED usually should not exceed 120 °C. Thermal management is a critical consideration for overall LED device performance, reliability and lifetime.

The thermal resistance of the package from the junction to the lead frame is the most common parameter for evaluating the heat dissipation of LED packages. The essence of heat management is to make the heat dissipation path as short as possible with a surface as large as possible. In other words, the purpose of thermal management is to reduce the thermal resistance of an LED package. Currently, a typical efficient design may have a thermal resistance of 8 °C/W, which means that the LED junction will be 8 °C hotter than the lead frame. To reduce thermal resistance, some LED chip packaging designs have a copper heat sink.

15.1.5 System testing

The fast development of the LED industry has resulted in higher demands on thermal designs, optical illumination designs, manufacturing testing, etc. A feedback mechanism that can provide accurate and effective information based on the overall performance of LED products is necessary in the development of holistic designs and manufacturing processes for LEDs. Once LED chips are packaged, the system as a whole needs to be rigorously tested to check performance and quality. System testing LEDs can comprehensively provide all of the performance parameters. The system test results can be used to determine the locations that are inconsistent with overall requirements and to find solutions for improving the packaging processes, device design, material selection, etc. This can further improve the overall characteristics of LEDs and decrease the cost of manufacturing and mass production.

15.1.6 Design for X

One of the main functions of LED chip packaging is that it can help to realize a range of performance characteristics and functions. Design for X, where X is a variable with many values, is a widely used method in industry, and it mainly includes:[8]

- design for performance (high brightness, uniform illumination, specific light intensity distribution, etc.)

- design for reliability
- design for cost
- design for manufacturability
- design for assembly
- design for testing
- design for the environment.

Consider the light intensity distribution designs shown in Fig. 15.5 as an example. The light intensity distribution of a typical LED chip is usually of the Lambertian type, but we can realize batwing and side-emitting types using different packages (more specifically, using different lens designs) according to the different requirements of the LED applications.[9,10] A Lambertian lens is the configuration mostly widely adopted in LED packaging. Lambertian radiation can be used in applications such as road lights and MR16 lamps. Batwing lenses and side-emitting lenses are suitable for applications such as backlighting and cell phones.

15.2 Basic structure of LED packaging modules

To realize the different requirements for heat dissipation and luminescence efficiency of LEDs in different applications, a large variety of types of LED packaging structures have been proposed. LED packages can be divided into four types: lamp LEDs, surface-mounted devices (SMDs), power LEDs and high-power LEDs.[11] Figure 15.6 shows the development of packaging structures for LED modules. Although there are very many different LED packages and technologies, basically an LED module has either a low-power or a high-power packaging structure.

15.2.1 Low-power LED packaging

Figure 15.6 is a schematic of a low-power LED package. Currently, a low-power LED is an LED packaged with epoxy resin. The chip is bonded onto the lead frame with solder or silver paste, and the top of the chip is bonded on the other part of the lead frame with bonding wires. The whole lead frame is immersed into a mold filled with epoxy resin. The size of the metal lead frame for a low-power LED is small and the thermal conductivity of epoxy resin is also small, thus the heat dissipation ability is limited. As a result, the maximum driving current is limited to ~20 mA and the typical forward voltage is ~3.2 V. These characteristics limit the LED power to 0.1 W and the light output rarely exceeds 2–3 lm. Consequently, low-power LEDs are mostly used as indicators.

15.2.2 High-power LED packaging

Since low-power LEDs cannot satisfy all application requirements, high-power LEDs were produced with the development of semiconductor material and

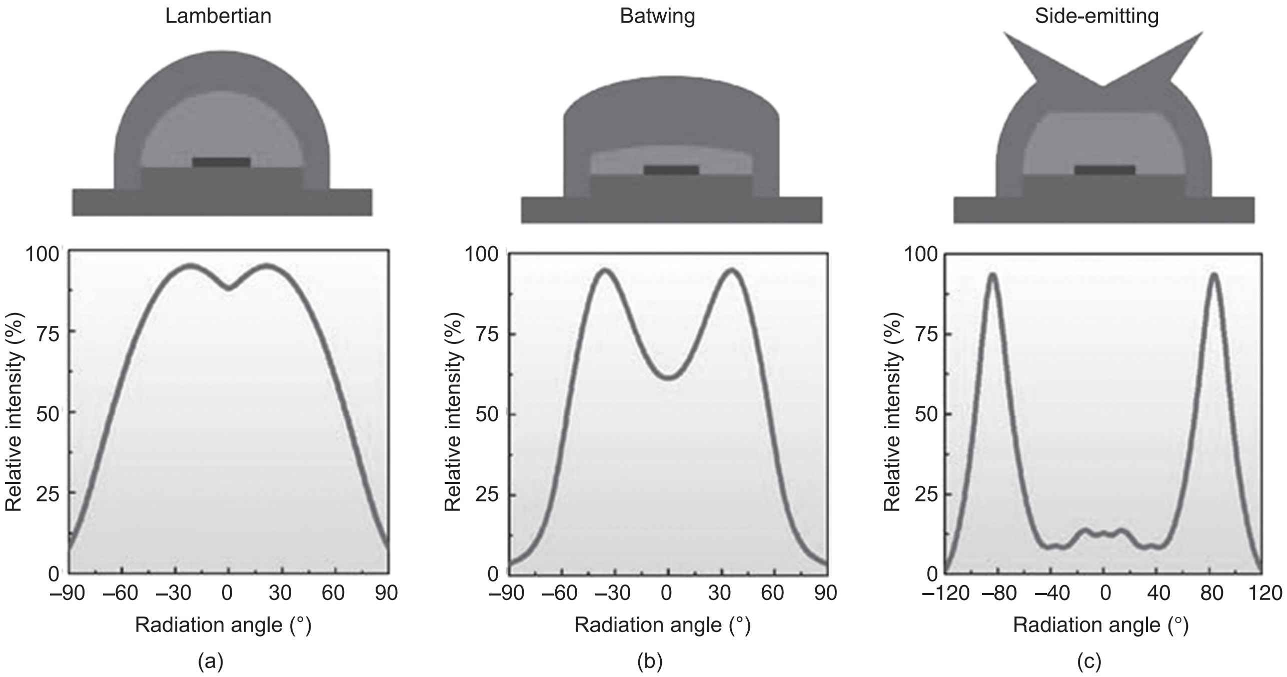

(a)

(b)

(c)

15.5 Light intensity distribution of three different packages: (a) Lambertian, (b) batwing and (c) side-emitting.

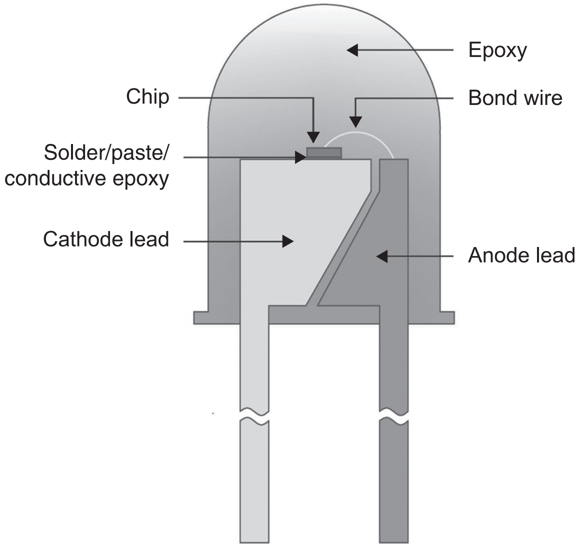

15.6 Low-power LED package.

packaging technologies. As well as the electrical and optical paths, high-power LED packages should also have a thermal dissipation path. There are many kinds of high-power LED packaging structures, including lead frame LEDs, silicon packaging LEDs, printed circuit board (PCB) packaging LEDs and ceramic packaging LEDs. These structures are almost the same and the only difference lies in the substrate materials. Therefore, we will use the lead frame LED as an example for describing the basic structure of LED packaging modules. Luxeon, which was proposed by Lumileds Co in 1998 and is widely used, is a typical lead frame LED (Fig. 15.7). In the Luxeon structure, the chip is bonded onto the heat sink with solder or silver paste. The material for the heat sink is usually copper, which has high thermal conductivity. The electrodes of the chip are connected to the lead frame by the bonding wires. Silicone gel phosphor of a specific concentration is dispersed onto the chip surface to form a phosphor layer. The lens is embedded into the molding compound using a mechanical structure. Silicone gel fills the interspace between the lens and the molding compound to protect the chip and bonding wires. High-power LED packaging has better heat dissipation, thus the power can be more than ten times that of low-power LED packaging. Normally, a high-power LED is driven at a much higher current, typically 350 mA, 700 mA or 1000 mA. The power can be increased to 1–5 W and commercially available 1 W LED packages can produce up to 231 lm of light.[12]

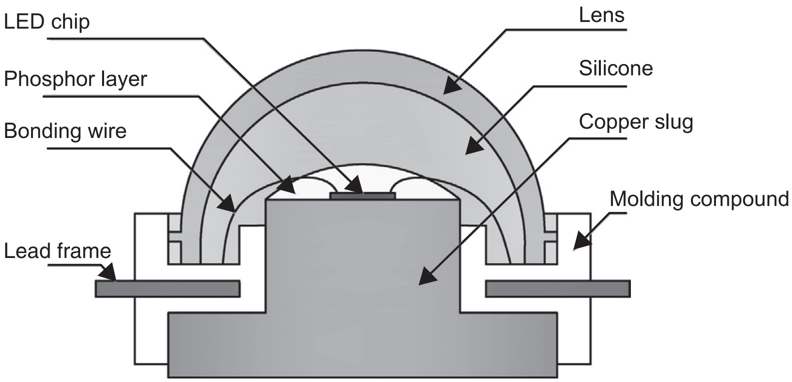
LED chip
Phosphor layer
Bonding wire
Lead frame
Lens
Silicone
Copper slug
Molding compound

15.7 Typical high-power LED package.

15.3 Processes used in LED packaging

Production of an LED starts from an LED chip and progresses to an LED package, an LED module and then to a system. It is obvious that LED packaging is necessary before the applications of LEDs. The LED packaging processes affect the final optical performance and reliability of LED devices, thus they are critical. The typical packaging processes for a high-power LED are shown in Fig. 15.8 and are described briefly below.

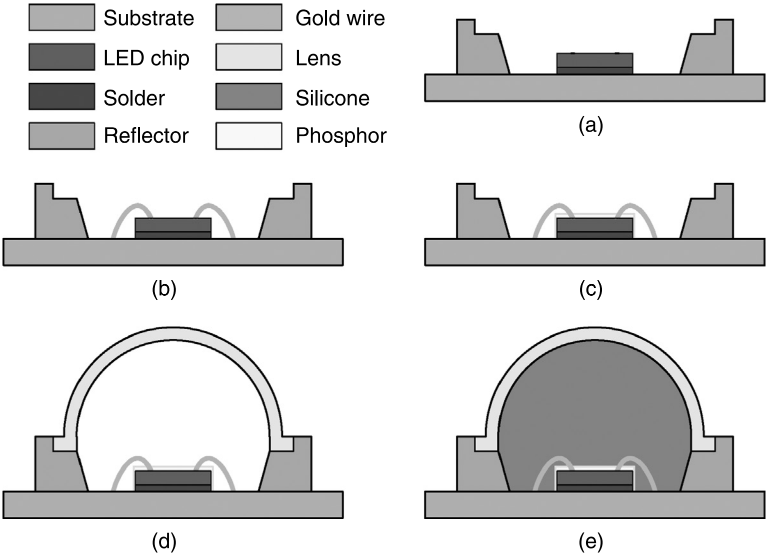
Substrate
LED chip
Solder
Reflector
Gold wire
Lens
Silicone
Phosphor
(a)
(b)
(c)
(d)
(e)

15.8 LED packaging processes: (a) chip bonding, (b) wire bonding, (c) phosphor coating, (d) lens laying, (e) silicone injection and curing.

15.3.1 Chip bonding

The chip is bonded onto the substrate with solder or silver paste. The solder or silver paste is pre-coated onto the substrate and then the chip is mounted onto the solder or pasted with slight pressure. The solder is melted and cooled by reflow soldering, or the silver paste is cured at high temperature.

15.3.2 Wire bonding

The electrodes of the chip are connected to the lead frame by the wire bonding. The wire bonding process should be very careful, otherwise bonding failure may occur due to bond pad cratering, peeling or cracking below the bond pad.[13] The wire bonding processes depend on how the electrodes are situated on the chips. The materials of the bonding wires for LEDs are usually gold or copper.

Gold wire

Gold wire bonding is widely used for LEDs since gold wire can be bonded easily by heat, pressure and ultrasonic energy, which is referred to as thermosonic bonding. In addition, the junction size, bond strength and electrical and thermal conductivity of gold wire are also suitable for LED applications.

Copper wire

Compared with gold wire, copper wire can achieve greater mechanical stability. Standard bond strength tests, such as the wire pull test and the ball shear test, have demonstrated that copper wire bonds are 25–30% stronger than comparable gold wire bonds. However, copper wires have significant disadvantages compared with gold wires, and the copper wire bonding process is not yet well understood and it is immature. Copper can oxidize at a relatively low temperature and the bonding parameters are harsher (a higher bond force and more ultrasonic energy are required). Therefore, copper wire bonding is still being studied and optimized.[14]

15.3.3 Phosphor coating

A phosphor layer is dispersed onto the chip surface manually or with a dispenser. The phosphor layer will absorb some of the blue light emanating from a blue LED chip and re-emit yellow light, so that white light is produced as a mix of the blue light and yellow light. The white-light quality is sensitive to the thickness, concentration and location of the phosphor layer. As shown in Fig. 15.9, there are three phosphor coating methods.

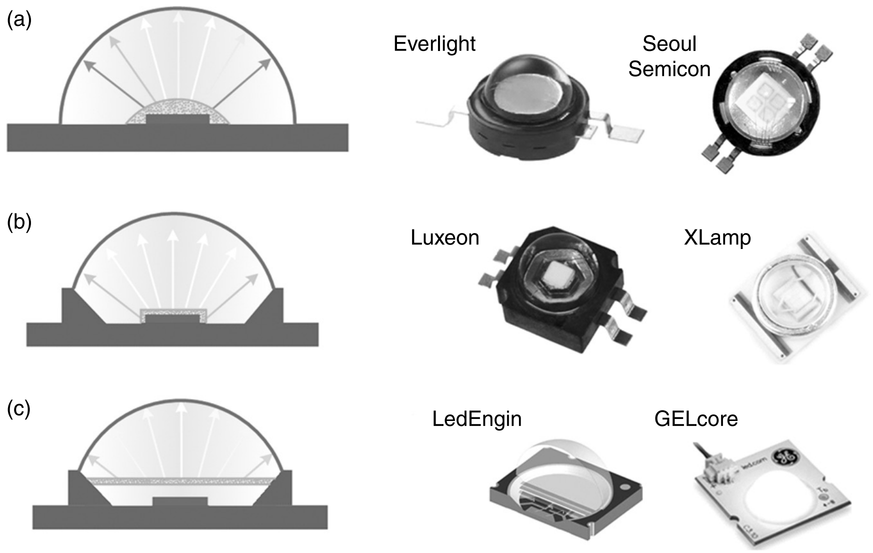

15.9 Phosphor coating technologies: (a) freely dispersed coating and representative products (Everlight and Seoul Semicon), (b) conformal coating and representative products (Luxeon from Lumileds and XLamp from Cree), (c) remote coating and representative products (LedEngin and GELcore).

Freely dispersed coating

The freely dispersed coating method is the simplest one that is massively applied in the traditional LED packaging industry. A phosphor embedded silicone matrix is dispensed onto a chip without a mold to restrict the flow until a surface force balance is achieved. The phosphor layer is normally convex and the thickness of the central zone on a chip is larger than that of the edge zone. This variation in thickness may cause spatially non-uniform distribution of the transmitted blue and yellow light, resulting in the final white light of poor angular color uniformity (ACU). Colored rings may appear in the edge of the final white light pattern. In addition, due to the variation of the mixture volume in the dispensing process, the average correlated color temperature (CCT) may vary from package to package. This results in a low yield and an increased cost.

Conformal coating

A conformal coating is produced by a progressive packaging process, which can realize an extraordinarily thin phosphor layer. To control the final color output, the concentration of the phosphor layer is usually high due to its thinness. This method overcomes the problem with the non-uniform thickness of the phosphor layer produced by the freely dispersed method, and the angular color uniformity of the white light can be greatly enhanced. The conformal coating method was first developed by Lumileds, which used an electrophoretic method[15,16] to deposit charged phosphor particles onto the chip surface. The thickness of the phosphor film can be adjusted by controlling the voltage and deposition time. Therefore, a conformal coating can easily have micron precision. Other approaches, such as slurry, settling,[17] evaporating solvent,[18] wafer-level coating,[19] capillary-assisted coating[20] and direct white light,[21] can also be used to conformally coat a phosphor. As shown in Fig. 15.9, representative products with a conformal coating of phosphor are Luxeon from Lumileds and XLamp from Cree. However, it has been confirmed experimentally that approximately 50–60% of the light is back-scattered by the phosphor layer.[22,23] The back-scattered light rays are re-absorbed by the chip and some of the energy is lost due to absorption by the packaging materials. In addition, localized heating caused by a high-power chip can induce thermal quenching and reduce the quantum efficiency of the phosphor.[24]

Remote coating

Remote phosphor coating, in which the phosphor layer is some distance above the LED chip, was proposed for reducing the amount of light trapped in LED chips and improving the luminous efficiency of white LEDs.[25–27] This LED structure can lower the temperature of the phosphor layer and enhance the stability of the color, because less heat is transferred from the LED chip to the phosphor layer.[28] As shown in Fig. 15.9, representative products with a remote coating of phosphor include LedEngin and GELcore. The main disadvantage of remote coating is that the shape of the thin phosphor layer is not easy to control and realize. Due to surface tension of the liquid, the pre-cured encapsulant materials and phosphor layer normally have concave surfaces. The curvature of these surfaces is dependent on the dimensions and surface roughness of the reflector, the viscosity of the silicone phosphor, operating temperature, etc. Since the remote phosphor layer is away from the LED chip, its area is usually much larger than the area of the LED chip. The large phosphor layer will disorder the propagating light and disrupt the pattern of light re-emission significantly since the optics is usually designed for chips or small light sources.

15.3.4 Lens laying

The lens is embedded into the substrate using a mechanical structure. The lenses, as the dominant optics, are the key components for realizing the different optical requirements of applications. A conventional lens is a hemisphere, but its optical performance is poor. Freeform lenses have better optical performance and they can be designed to suit various illumination requirements. A detailed introduction to the optical design of freeform lenses will be given in section 15.6.

15.3.5 Silicone injection and curing

Silicone gel is injected into the interspace between the lens and molding compound to protect the chip and bonding wires. The whole module is put into an oven to cure the silicone at a relatively high temperature for a short time. After curing, the silicone will adhere to the lens and the molding compound and keep moisture and dust away.

15.4 Optical effects of gold wire bonding

As an optoelectronic device, an LED can be optically designed for many different applications, such as backlighting, displays, projectors, automotive lighting, road lighting, landscape lighting and indoor lighting. The quality of the light from an LED is important for applications, and includes the light pattern, light uniformity and light color. Since the packaging processes will affect the light output of an LED, their optical design must be optimized.

Due to the wetting effect, the phosphor gel spreads along the gold wire surfaces. As shown in Fig. 15.10, the gold wires influence the geometry of the phosphor layer. Figure 15.11 shows how the profiles of phosphor layers are influenced by the gold wires based on experimental results. Compared with the phosphor layer

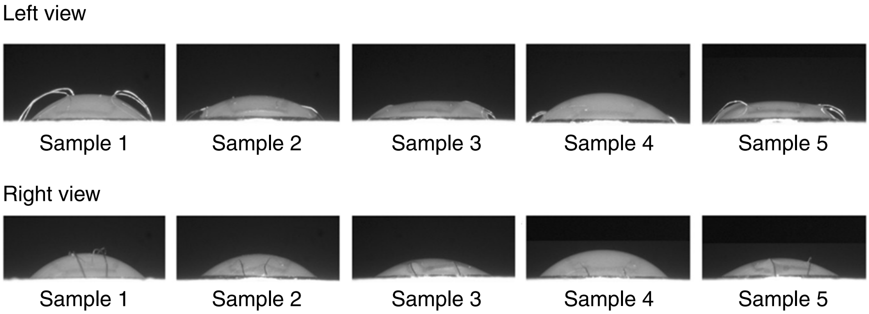
Left view
Sample 1
Sample 2
Sample 3
Sample 4
Sample 5
Right view
Sample 1
Sample 2
Sample 3
Sample 4
Sample 5

15.10 Left and front views of phosphor layers in LED module samples.

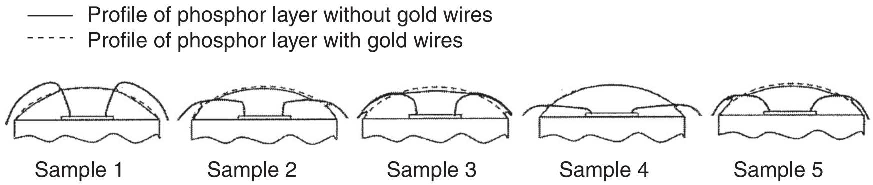
Profile of phosphor layer without gold wires
Profile of phosphor layer with gold wires
Sample 1
Sample 2
Sample 3
Sample 4
Sample 5

15.11 Shape and height of the gold wires of the five samples and their phosphor profiles.

without gold wires, it is clear that the shapes of the phosphor layers for Sample 2, Sample 3 and Sample 5 were significantly influenced by the gold wires, in particular, near the gold wires. In Sample 3, the gold wires are lower than in Sample 1, and the external parts of the wires are closer to the surface of the phosphor, hence more phosphor gel spreads along the gold wire surfaces until the surface energy for the air, phosphor gel and gold wire becomes balanced. Obviously, this reduces the height of the phosphor layer and change its curvature. For Sample 1 and Sample 4, the effect of the gold wires on the phosphor layer geometry is tiny, and the left and front views of the phosphor layers are nearly the same.

As shown in Fig. 15.12, to quantify the optical effect of the gold wire, the angular CCT of the five samples at points (r, θ, ϕ) on plane C$\theta-(\theta+180°)$ of the top hemisphere is recorded. Points are defined by (r, θ, ϕ) in the coordinate system, where the origin is fixed at the center of the top surface of the copper heat sink. r is the radial distance. Inclination angle ϕ is measured from the fixed zenith direction Z. Azimuth angle θ is measured from the azimuth axis A. Plane C$\theta-(\theta+180°)$ is defined as the plane passing through the origin and zenith direction Z, and where the azimuth angle of points on that plane is θ.

Figure 15.13 shows the results of measuring the spatial angular CCT distributions of different samples, using a CCT recorder. For all samples, the angular CCT fluctuation for plane C0° – 180° is smaller than for plane C90° – 270° in the package. The reason may be that the geometries of the phosphor layers for plane C90° – 270° in all samples are affected by the gold wires more than for plane C0° – 180°. Taking Sample 5 for instance, the angular CCT decreases dramatically from 7512 K (at $\phi=-90°$) to 5050 K (at $\phi=-40°$) for plane C90° – 270°, while it decreases from 5719 K (at $\phi=-90°$) to 5125 K (at $\phi=-40°$) for plane C0° – 180°. For Sample 1 and Sample 4, the angular CCT distributions for plane C0° – 180° and plane C90° – 270° are similar, whereas, for Sample 2,

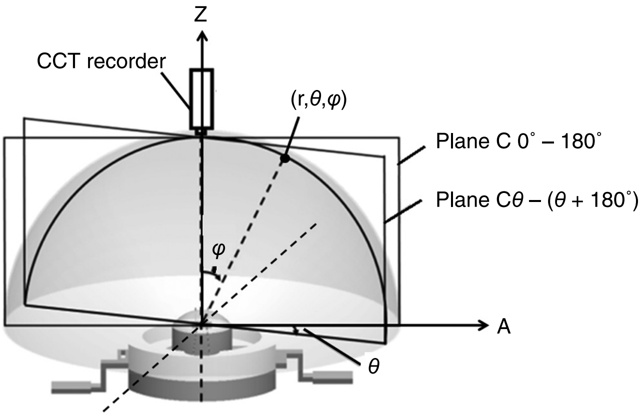

15.12 Angular CCT measurement.

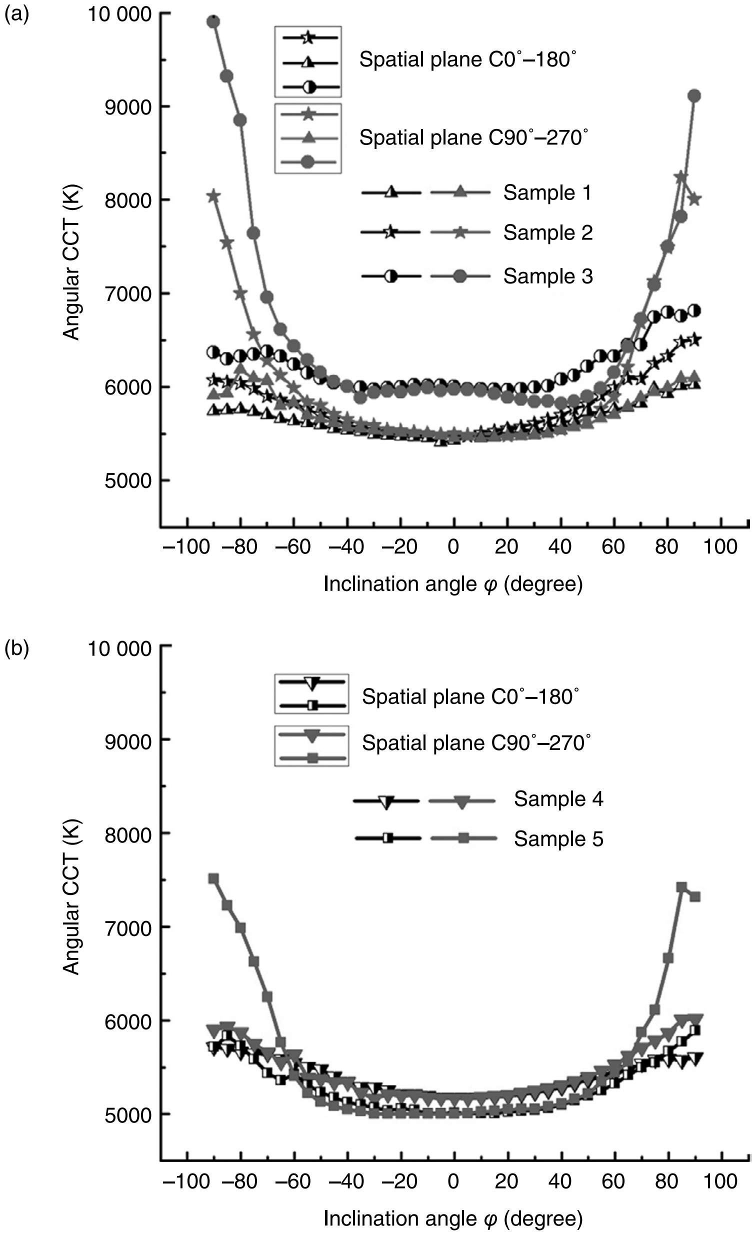

15.13 Angular CCT distributions for plane C0° – 180° and plane C90° – 270°: (a) Sample 1, Sample 2 and Sample 3; (b) Sample 4 and Sample 5.

Sample 3 and Sample 5, the angular CCT deviates sharply as the inclination angle ϕ changes from 0° to ±90° for the two planes. This is because the shape of the phosphor gel for the two planes varies less for Sample 1 and Sample 4, as we mentioned for Fig. 15.11.

These experimental results for the angular CCT distributions correspond well with the geometries of the phosphor layers. CCT distributions of LED modules, encapsulated with silicone gel and with a lens, also show a similar trend. The results show that the gold wire bonding process has an important effect on the angular CCT distribution of an LED package. Thus, when manufacturing LED products, the shape of the gold wire should be well designed and optimized to improve the optical performance of the products.[29]

15.5 Optical effects of phosphor coating

As a bulk scattering material, the phosphor absorbs short-wavelength emissions from the primary LED chip and down-converts them to long-wavelength emissions. For instance, the most widely used white LEDs have a blue GaN LED pumping a YAG:Ce^{3+} yellow phosphor. Mixing the yellow phosphorescence and the escaped blue emission produces white light. The phosphor layer plays an important role in determining the final optical performance of LED devices. Many studies have investigated the effect of phosphor properties on packaging performance.[30–38] The location, thickness, concentration and geometry of the phosphor layer are the most important factors affecting an LED's optical performance.

15.5.1 Phosphor location

The location of the phosphor is the primary consideration for LED packaging. As mentioned above, there are three main ways to realize the phosphor layer, i.e. a freely dispersed coating, conformal coating and remote coating. It is obvious that the phosphor locations realized by these three methods are different. By changing the phosphor layer from being close to the chip to away from the chip, the propagation path and light energy will be affected by scattering and absorption by the phosphor, reflection from the substrates, absorption in the chip, refraction by the lens, etc. Absorption in the phosphor and chip will influence the output optical power. Scattering by the phosphor will disorder the propagating light. The rays could converge to central zones through reflection from the reflector and refraction by the lens or diverge to edge zones. These will induce variations in light extraction and CCT.[35]

Kim *et al.*[38] compared the light extraction efficiency of four different placements and arrangements for the phosphor as shown in Fig. 15.14(a). They used a new packaging method with a diffuse reflector cup and the remote phosphor configuration to enhance light extraction, as shown in Fig. 15.14(a4). The light

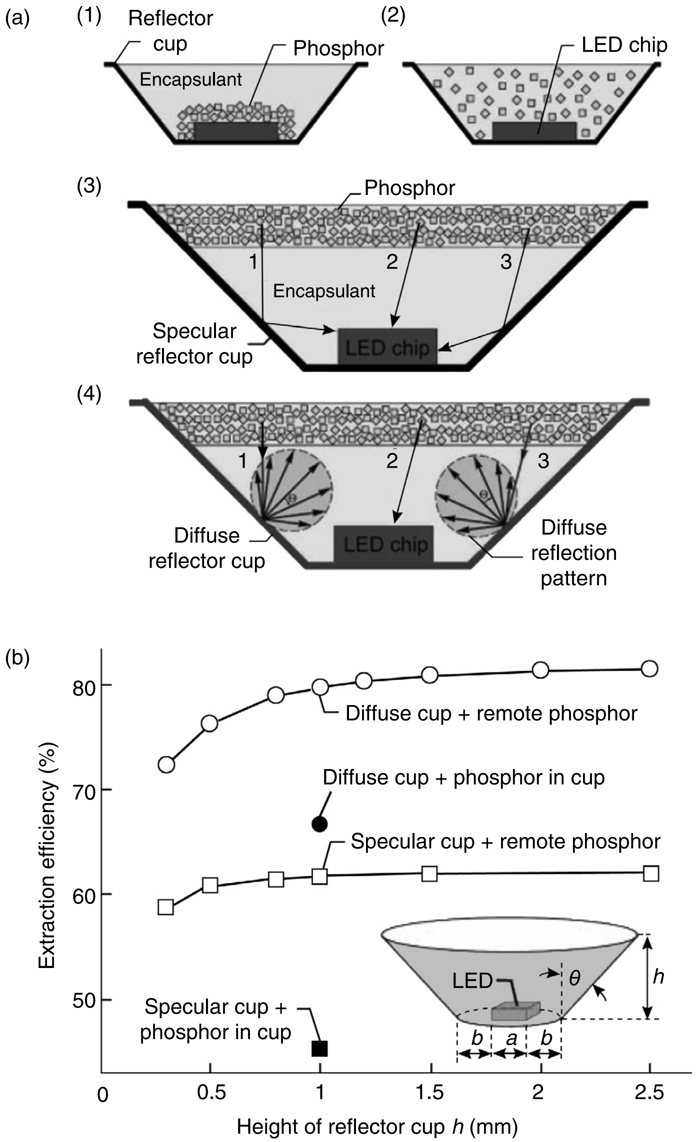

15.14 (a) Arrangement of phosphor in white LEDs: (1) Conformal distribution directly on LED chip; (2) uniform distribution in reflector cup (phosphor-in-cup); (3) uniform distribution in thin layer above LED chip (remote phosphor); (4) remote phosphor distribution in diffuse reflector cup. (b) Calculated light extraction efficiency as a function of the height of the reflector cup, obtained from ray-tracing simulations. (Reproduced with permission from Kim *et al.*[38] Copyright 2005, Japan Society of Applied Physics.)

extraction efficiency of the four configurations was compared. The surface of the reflector is specular in Fig. 15.14(a3), and diffuse in Fig. 15.14(a4). They conducted ray-tracing simulations to confirm the benefits of the proposed methods and the results are shown in Fig. 15.14(b). The light extraction efficiency was improved by using the remote phosphor arrangement by 36% for a specular reflector cup, and 75% for a diffuse reflector cup, compared with the phosphor-in-cup arrangement for a specular reflector cup. For the phosphor-in-cup arrangement, the use of a diffuse reflector cup results in a 47% improvement over the specular reflector cup.

15.5.2 Phosphor thickness and concentration

The thickness and concentration of the phosphor are secondary considerations for white LED packaging. This is because the luminous flux and the color of an LED are adjusted mainly through changing the phosphor thickness and concentration after the phosphor converters have been chosen. The phosphor thickness and concentration can be varied during manufacturing and they affect the optical consistency of white LEDs.[39–45] The optical consistency depends on the ability to control fluctuations in optical performance so that the luminous efficiency, CCT and color rendering index (CRI) remain within the desired range. The optical consistency is an important parameter for the quality of the light from an LED.

Sommer *et al.*[42] found that changing the phosphor thickness and concentration can affect the spatial color distribution. Tran *et al.*[43] experimentally studied the effects of phosphor thickness and concentration on LED luminous flux and correlated color temperature. Their results showed that a package with a lower phosphor concentration and a higher phosphor thickness had a lower trapping efficiency and caused less backscattering of the light, and thus had higher luminous efficacy. When the CCT value was around 4000 K, the experimental results showed that the lumen output for a 1.8 mm thick phosphor package was 23% higher than for a 0.8 mm thick phosphor package. Hence, they also found that the brightness or luminous efficiency of white LEDs highly depends on the phosphor thickness and concentration.

Our group systematically analyzed the effects of YAG:Ce phosphor thickness and concentration on the optical performance of phosphor-converted white LEDs, considering light extraction, luminous efficiency and CCT.[44–46] Five LED packaging methods with different phosphor locations are presented for comparison, as shown in Fig. 15.15. In Methods I, II and III we conformally coated the phosphor to replicate the shape of the chip. The difference is that there was a small gap between the phosphor and the chip in Methods II and III whereas the phosphor was directly dispensed onto the chip surface in Method I. In Method IV, the phosphor had a planar shape but the location was farther than that for Methods II and III. In all methods, the surfaces of the board and reflector were coated with

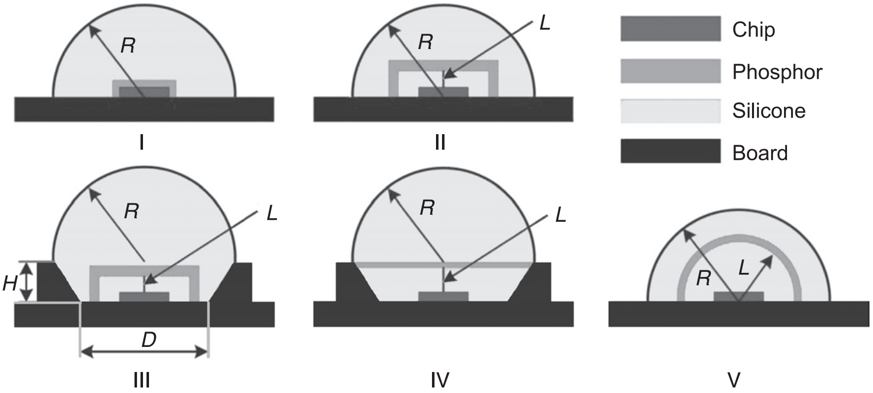

15.15 Five packaging methods used in the analysis. *L* gives the location of the phosphor. In Methods II, III and IV, *L* is the gap between the phosphor and the chip. In Method V, *L* is the radius of the phosphor. The radius (*R*) of the lens was 4 mm. The baseline diameter (*D*) of the reflector was 3 mm and the height (*H*) was 2 mm.

silver to provide high reflection. For each method, the phosphor thickness and concentration were varied and the five cases are listed in Table 15.1.

The results of the Monte Carlo ray-tracing simulations are shown in Fig. 15.16 and Fig. 15.17. To explain the results, we have to define the luminous efficiency (η) and color mixing fraction (f) as:

$$\eta = 683\ \mathrm{lm/W} \times \frac{P_{pc-B}V_{pc-B} + P_{pc-Y}V_{pc-Y}}{P_{elec}} \qquad [15.4]$$

$$f = P_{pc-Y}/(P_{pc-B} + P_{pc-Y}) \qquad [15.5]$$

where P_{elec} is the consumed electrical power, and $V_{pc\text{-}B}$ and $V_{pc\text{-}Y}$ are eye sensitivity coefficients for blue light spectra and converted-yellow light spectra, respectively. $P_{pc\text{-}B}$ and $P_{pc\text{-}Y}$ are the extracted optical power of the blue light and converted-yellow light, respectively.

From Fig. 15.16 and Fig. 15.17, we can see that the brightness and the light color of the five packaging methods change as the phosphor thickness and concentration varies. Generally, for each case, that is for fixed phosphor thickness and concentration, the luminous efficiency and the color mixing fraction of

Table 15.1 Phosphor thickness and concentration for the five cases

Case	1	2	3	4	5
Phosphor thickness (μm)	60	100	140	40–200	
Phosphor concentration (g/cm^3)		0.4–1.4		0.6	1

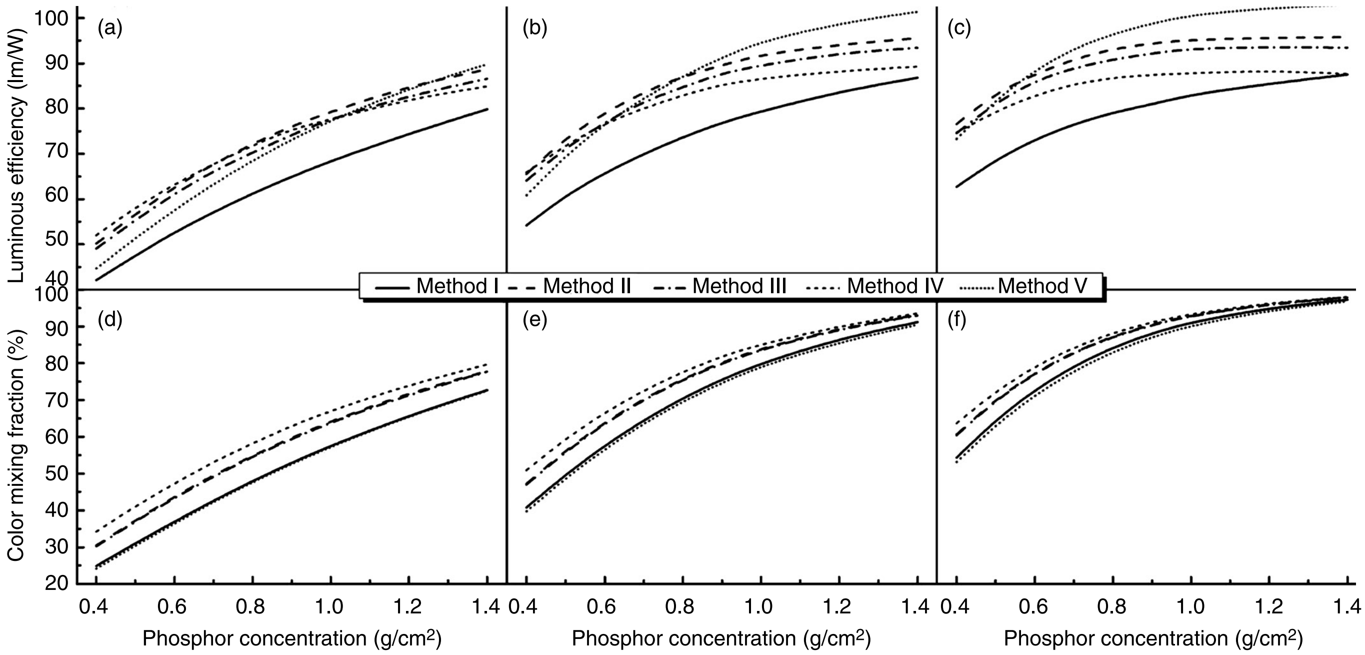

15.16 Dependencies of luminous efficiency and color mixing fraction of the five packaging methods on phosphor concentration for (a) and (d) Case 1, (b) and (e) Case 2, and (c) and (f) Case 3.

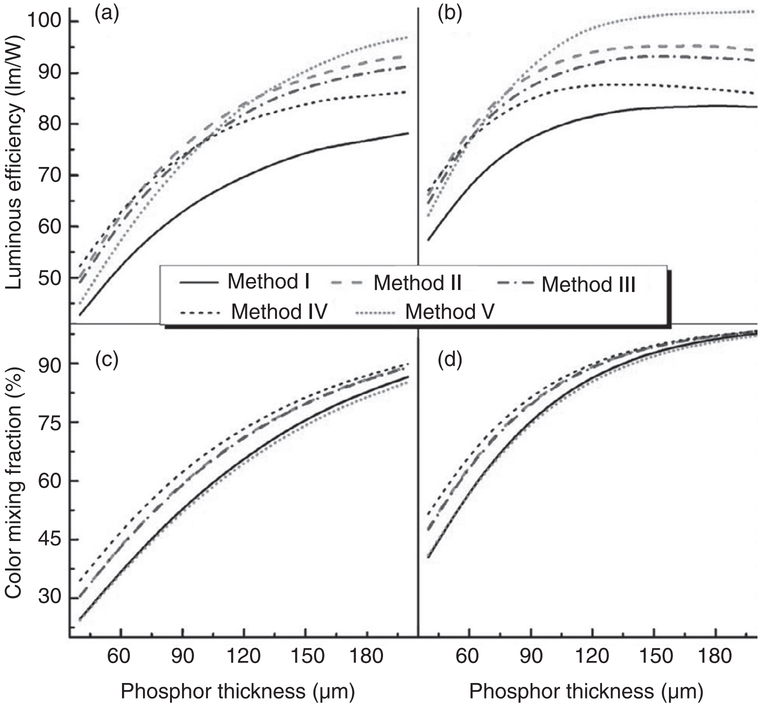

15.17 Dependencies of luminous efficiency and color mixing fractions of the five packaging methods on the phosphor thickness for (a) and (c) Case 4, and (b) and (d) Case 5.

Method IV increase more slowly than for the other methods. The luminous efficiencies of Method I and Method V increase more rapidly than the others, and the luminous efficiency of Method V is higher than that of Method I. The color mixing fractions of Method I and V are always close, indicating similar variations of their light color. The luminous efficiencies and color mixing fractions of Methods II and III vary similarly and their variations are moderate among the five packaging methods.

15.5.3 Phosphor geometry

The above discussions cover the phosphor location, thickness and concentration, but for specific cases, which are not sufficient to give an understanding of the influence of phosphor geometry on the luminous flux. Yu *et al.*[47] investigated the effect of changing phosphor geometry using Monte Carlo ray-tracing simulations. Figure 15.18 shows the five phosphor geometries: dispersed-coating geometry (the conventional coating method), two-flat geometry (planar layer), top-convex geometry (top interface has a convex shape), bottom-convex geometry (bottom

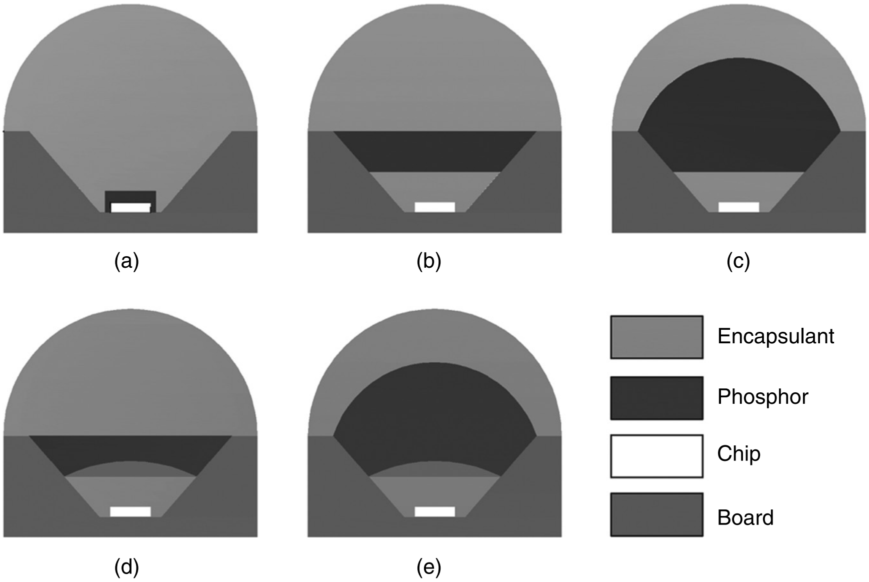

15.18 Cross sections of phosphor-converted LEDs with (a) dispersed-coating phosphor geometry, (b) two-flat phosphor geometry, (c) top-convex phosphor geometry, (d) bottom-convex phosphor geometry and (e) two-convex phosphor geometry.

interface has a convex shape) and two-convex geometry (both top and bottom interfaces have a convex shape). In the simulations, they used the mean free path (MFP), which is the average distance that photons travel between collisions with phosphor particles, for the analysis instead of the phosphor concentration because the MFP is inversely proportional to the phosphor concentration.[48] They normalized the luminous fluxes of the phosphor-converted LEDs with different phosphor geometries with respect to the dispersed-coating case. They confirmed that the remote phosphor configuration has a higher luminous flux than conventional dispersed-coating LEDs. The remote-phosphor LED having a phosphor layer with a hemispherical top surface improved by more than 12% compared with the conventional dispersed-coating case, and a 5% improvement compared with the two-flat cases. Won *et al.*[49] fabricated high-power white LEDs by combining blue LEDs and green $(Ba, Sr)_2SiO_4:Eu^{2+}$ and red $CaAlSiN_3:Eu^{2+}$ phosphors with various phosphor geometries. The results showed that the luminous efficiency improved because of a decrease in the reabsorption of green light by the red phosphor owing to a difference of refractive indices. The white LED had a very high luminous efficiency of 51 lm/W and a high color rendering index of 95 under 350 mA.

15.6 Optical effects of freeform lenses

The direct output of an LED chip is usually a circular spot with non-uniform illumination, which struggles to meet the illumination requirements. Appropriate optics including primary lenses or secondary lenses are essential for obtaining high-quality LED illumination.[50–54] Many solid-state lighting (SSL) applications use a secondary optic to couple light from the LED into a desired beam shape. There has been a trend for using freeform lenses in LED optical design because of advantages such as high design freedom, small size and precise light irradiation control.[51] Many different methods have been proposed for freeform lens design, such as the tailored freeform lens surface design method, the simultaneous multiple-surface lens design method, the discontinuous freeform lens design method and the continuous freeform lens design method.

15.6.1 Tailored freeform surface design method

In 2002, Harald Ries and Julius Muschaweck[55] proposed the tailored freeform surface design method, where a freeform surface is constructed through numerical solution of partial differential equations. The method uses wavefronts, which are surfaces of constant phase in the electromagnetic field. The local normal to the wavefront is the propagation direction of the field, which is the connection between wave optics and ray or geometrical optics.[56] For a given wavefront, a set of rays can be defined using the local surface normals. In a similar way, a set of rays can be used to construct the equivalent wavefronts. This method can be used to obtain an optical surface by solving a series of non-linear partial differential equations. It can ensure the local smoothness of the surface by adopting the continuous Gaussian curvature of surface, and it can obtain an ideal distribution of illumination in an area with small angles.

However, it still has limitations:

- The calculations are complex and difficult for light sources with arbitrary light intensity distribution.
- It is only suitable for light sources with a small volume and does not consider rays with large emerging angles.
- It has low utilization efficiency.

Therefore, the theory and design need further development. Figure 15.19 shows a freeform lens designed by the tailored method and its performance. A detailed description of this method can be found in Ries and Muschaweck.[55]

15.6.2 Simultaneous multiple surfaces (SMS) method

This method can be used for the simultaneous design of multiple optical surfaces. The original idea came from Minano and it was further developed by Benitez,

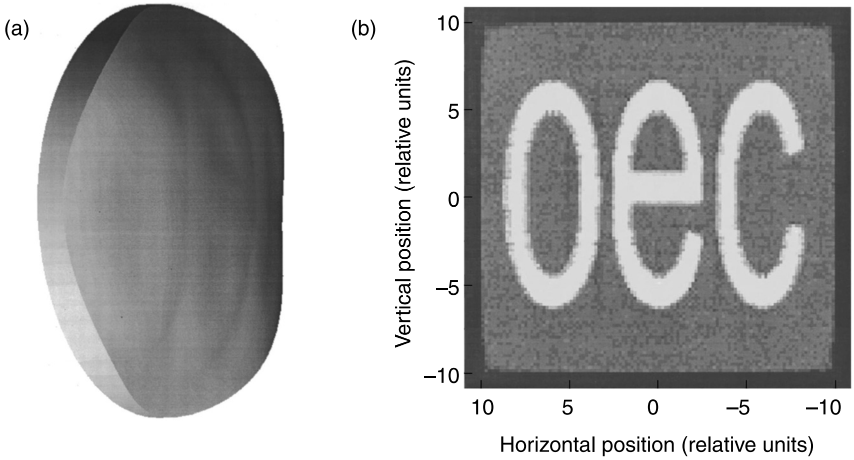

15.19 (a) Freeform lens designed based on the tailored method and (b) its numerical illumination performance. (Reproduced with permission from Ries and Muschaweck.[55] Copyright 2002, Optical Society of America.)

therefore the SMS method is also called the Minano–Benitez design method.[57–59] The SMS method is a procedure for designing two optical surfaces such that two given normal congruencies W_{i1} and W_{i2} are transformed (by a combination of refractions and/or reflections at these surfaces) into another two given normal congruencies W_{o1} and W_{o2}, as shown in Fig. 15.20. The SMS method generates an

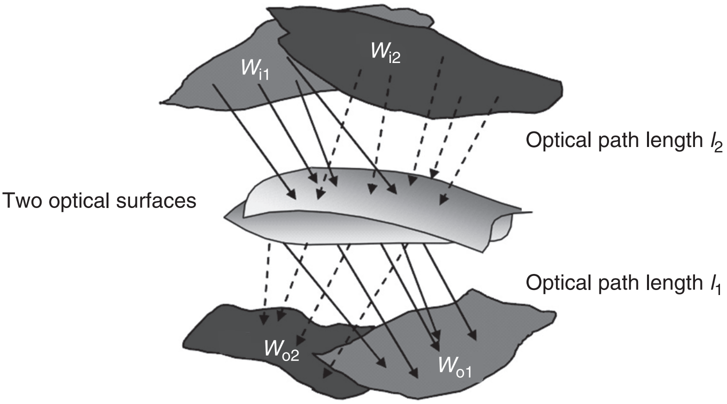

15.20 The simplest version of the SMS 3D method generates two surfaces that transform two input congruencies onto two output ones. (Reproduced with permission from Minano *et al.*[57] Copyright 2010, SPIE.)

optical system with two freeform surfaces that deflect the rays of the input bundles into the rays of the corresponding output bundles and vice versa. At present, only the SMS method can deal with an extended light source effectively. The SMS method can be used to produce LED lighting using the effective design method of freeform lenses. Plate XXVIII (see color plate section between pages 330 and 331) show the multichannel optics for an LED designed using the SMS method.[57]

The advantages of the SMS method are:

- It can be used to design more than one optical surface simultaneously.
- It is suitable for designing an optical system with an extended source.
- It is applicable for rays with large emerging angles.
- It makes greater utilization of the light source.

However, in this method the given illumination distributions need to be converted into wavefronts. It also needs to solve second-order non-linear Monge–Ampère equations through a complicated and lengthy calculation.

15.6.3 Discontinuous freeform lens method

Both the SMS method and the tailored method mentioned above are based on the coupling of input wavefronts and output wavefronts. A practical design method is to establish light energy mapping relations between the light source and the target. The strategy for designing a freeform lens based on energy mapping is as follows. Firstly, it is assumed that all of the light emitted from the light source radiates onto the target plane, which means the energy of the light source is equal to that of the target plane. Both the light source and target plane are divided into many cells, where the light energy is constant over a cell. According to the edge ray principle, the corresponding relation between each energy cell of the light source and the target plane is established by solving the energy conservation-based differential/integral equation or through direct correspondence. Finally, according to Snell's law and methods for constructing curved surfaces, points on the freeform surface can be calculated and an integrated optical surface can be constructed. This surface has to be validated and modified through numerical simulation.

The introduction of discontinuities into a lens surface can effectively reduce the normal deviation, but there is no guarantee that all light rays will be transmitted to corresponding positions on the irradiance plane. The cliffs between the discontinuous surfaces will distort a small portion of the light.[60] The total energy transmission ratio from the point light source to the target plane is as high as 95%. Figure 15.21 shows an example of a discontinuous freeform lens and the simulation results of its irradiance on the target plane.[61]

A discontinuous freeform lens was designed, fabricated and tested by us.[62] We found that during mass production of the lens (i.e. injection molding), many manufacturing factors, such as the surface morphology of the mold, the injection molding temperature and pressure, and the viscosity of the liquid, affect the

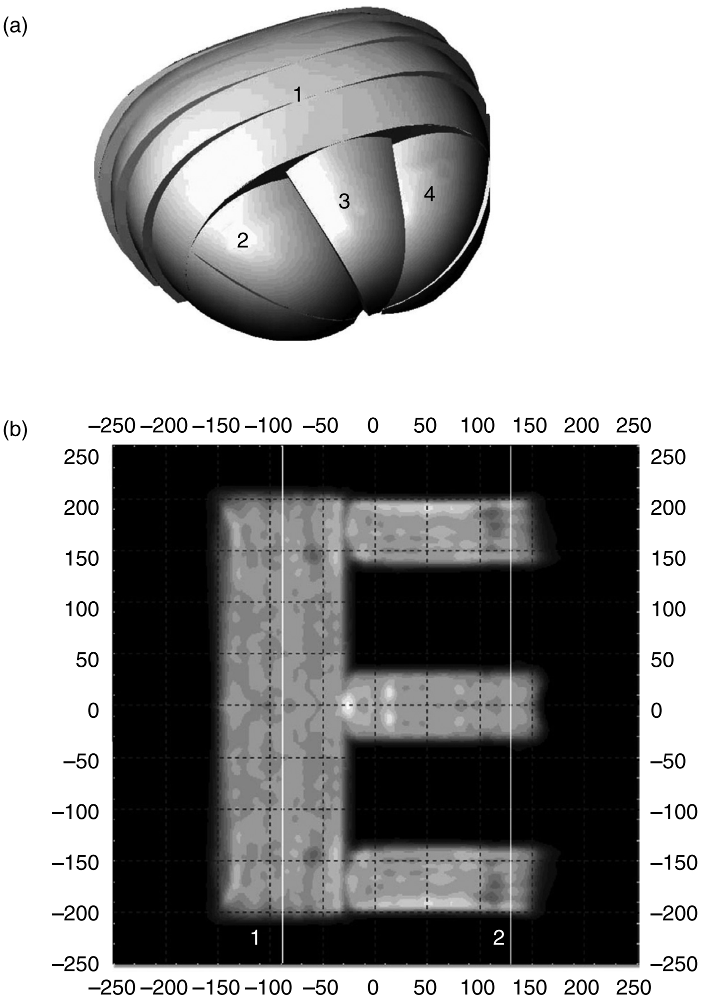

15.21 (a) Discontinuous freeform lens used to form an 'E' light pattern and (b) a simulation of its illumination. (Reproduced with permission from Wang *et al.*[61] Copyright 2007, Optical Society of America.)

surface morphology of the discontinuous freeform lens and thereby affect its optical performance. As shown in Fig. 15.22, the surface roughness and smooth transitions between the discrete sub-surfaces are two of the most common manufacturing defects found in discontinuous freeform lenses. The light pattern for a lens made from BK7 optical glass at 70 cm away from the LED is shown in Fig. 15.23. It is obvious that the illumination is poor: the distribution of light energy on the target plane is non-uniform and the shape of the light pattern is not

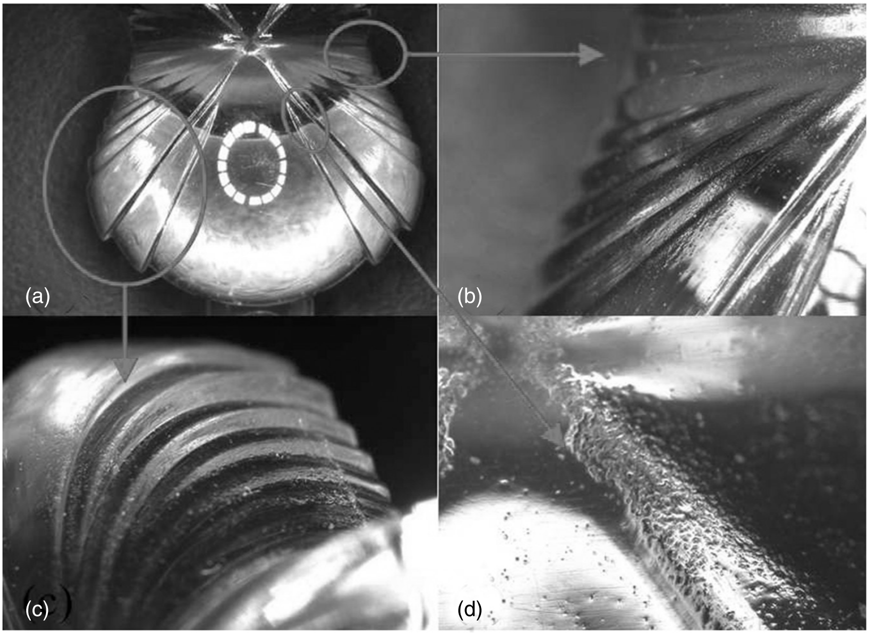

15.22 Micrographs of different parts of a PMMA discontinuous freeform lens.

rectangular. There are obvious dark and bright stripes on the light pattern, especially in the center and along the diagonals. Therefore, when designing a discontinuous freeform lens, we have to pay attention to the manufacturing defects and add feedback to the initial designs.

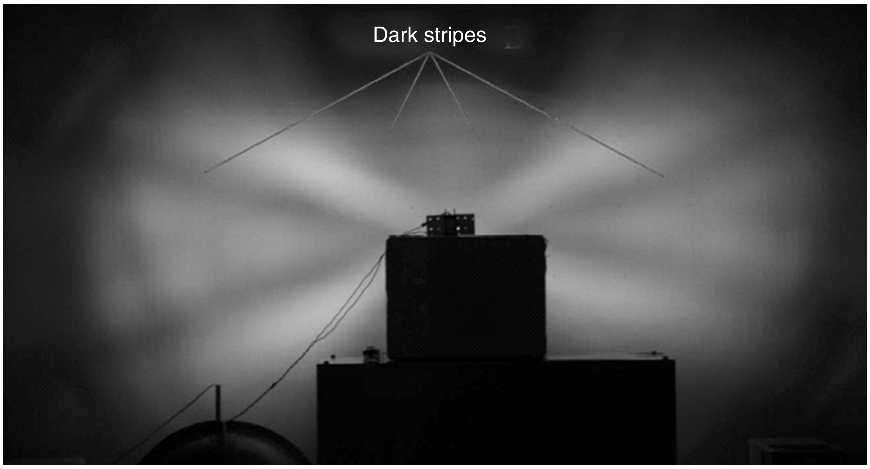

15.23 Light pattern for a BK7 optical glass lens at 70 cm away from LED.

15.6.4 Continuous freeform lens method

It is difficult to fabricate discontinuous freeform lenses. A continuous freeform lens has high illumination quality and is easy to fabricate. A continuous freeform lens is designed by a similar method as a discontinuous freeform lens. The only difference lies in the error control in the normal directions of the refracted rays through the lens surface. The details of the design method are presented in the references.[63–65] Using the method, we designed freeform lenses for road lighting, automotive headlamps, MR16 lamps, etc. Figure 15.24 shows a continuous freeform lens for LED road lighting and its illumination performance. From Fig. 15.24, we can see that surface of the lens is quite smooth and the light pattern is better than that shown in Fig. 15.23. The comparison demonstrates that the continuous freeform lens method is an effective way to design a freeform lens for LED lighting. Plate XXX (see color section between pages 330 and 331) shows a freeform lens for an MR16 lamp and its lighting performance. The illumination uniformity is good but there is obvious light deterioration at the edge of the light pattern, which needs further optimization.

15.7 Thermal design and processing of LED packaging

As mentioned above, temperature plays a crucial role in the reliability of LED packages; therefore it is necessary to consider thermal aspects during design. The primary goal of thermal design is to maintain the junction temperature of the LED device below the critical temperature. Exceeding the critical temperature can lead to accelerated light output degradation and even to catastrophic failure. The critical temperature is essential for basic semiconducting properties, including non-radiative recombination via deep levels, surface combination and carrier loss over heterostructure barriers. Light output decreases with an increase of junction temperature.[66] High temperatures reduce the internal quantum efficiency of an LED chip and the quantum efficiency of the phosphor. The lifetime of LEDs decreases with an increase of junction temperature.[67] The wavelength of the

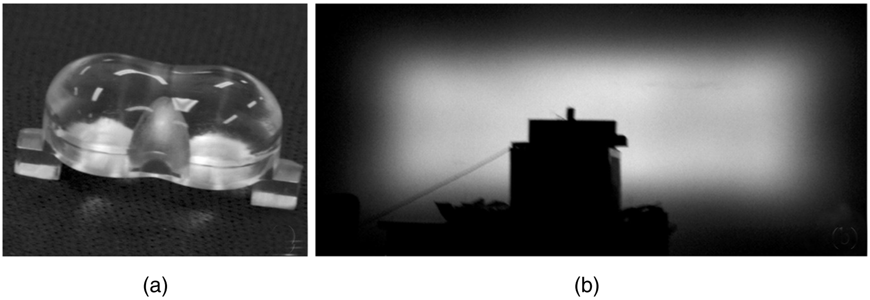
(a) (b)

15.24 (a) Continuous freeform lens for LED road lighting and (b) its illumination performance in the laboratory.

emitted light shifts with an increase of junction temperature,[68] which leads to variations in the correlated color temperature and color rendering index. Another goal of thermal design is to minimize the temperature throughout the assembly during operation. Because of the mismatch of the coefficients of thermal expansion (CTE), an elevated temperature induces thermal stresses in the packaging components, leading to cracks, delamination and other failures. The reliability of LED applications decreases with an increase of junction temperature. An increase of phosphor temperature may lead to degradation of phosphor efficiency, which is known as phosphor thermal quenching.[69] Phosphor thermal quenching will decrease light output through an increase of the non-radiative transition probability. Therefore, it is of great importance to conduct thermal design for LED packaging.

15.7.1 Thermal design of packaging

Because of the small area and relatively low temperature of LEDs, only a small amount of heat is dissipated by radiation. Conduction and convection are the dominating heat transfer modes in LED packaging products. Since LED chips are encapsulated, there are two paths for heat dissipation in LED packages. The first is the upper path through the encapsulant to the ambient air, and the other is the lower path through the substrate to the ambient air. Since encapsulants are usually polymers with low thermal conductivities, most of the heat is conducted through the substrate and then dissipated to the ambient air. In this case, the lower path is the main heat dissipation path. Figure 15.25(a) shows the thermal resistance network of the lower path for a complete Luxeon LED module. From this thermal resistance network, it can be seen that there are many interfaces in LED packages and the total thermal resistance is the sum of the series thermal resistances, which is called the system thermal resistance. A thermal resistance network is a good way to evaluate heat dissipation. A low system thermal resistance implies that heat can be conducted to the environment efficiently and therefore the junction temperature will be low at the ambient temperature.

Instead of using separate heat sink/lead frame assembly packaging as shown in Fig. 15.25(a), another approach for high-power LED solutions is the chip-on-board (CoB) technology, in which the chip is directly mounted onto the board with an appropriately designed circuit. Figure 15.25(b) shows the thermal resistance network of a CoB package. From Fig. 15.25(b), it can be seen that the one of the thermal interfaces between the chip and the heat sink has been eliminated in CoB packaging and the size is more compact, therefore the packaging density when using CoB can be significantly higher. The direct contact between the LED and the board allows for optimal thermal management with a high packaging density and results in long-lasting and high-performance LEDs. CoB technology can be used to produce LED arrays for different applications. The advantages of CoB LEDs include:

- compactness
- high intensity, particularly at close distances
- high uniformity even at a close working distance
- better thermal performance (long lifetime, high stability, etc.)
- clustering of LEDs on a circuit board
- reduction of manufacturing cost for the same power

Following the analysis of the heat dissipation paths of LED packages, we will discuss thermal problems inside LED packages from top to bottom as shown in Fig. 15.25. The LED chip is not the only heat source – there is also self-heating of the phosphor layer. Hence, we will discuss the self-heating of phosphor layer first, and then contact thermal resistance, spreading thermal resistance and cooling solutions in turn.

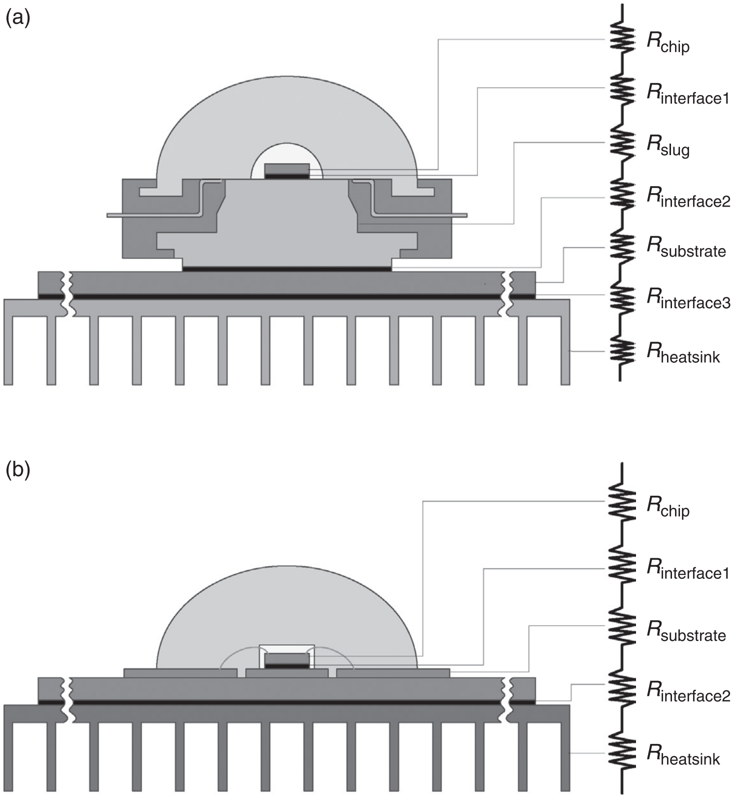
(a)
R_{chip}
$R_{interface1}$
R_{slug}
$R_{interface2}$
$R_{substrate}$
$R_{interface3}$
$R_{heatsink}$
(b)
R_{chip}
$R_{interface1}$
$R_{substrate}$
$R_{interface2}$
$R_{heatsink}$

15.25 Thermal resistance network of: (a) a Luxeon LED; (b) a chip-on-board (CoB) package.

15.7.2 Self-heating of the phosphor coating

Since not all of the absorbed blue light is converted to yellow light by the phosphor layer, some of the absorbed light must turn into heat. Therefore, there is local heating of the phosphor particles, which also contributes to heat generation inside an LED package. Arik *et al.*[70] studied the effects of localized heat generation in particles and layers using the finite element technique. They found that 3 mW of heat generated in a 20 μm diameter spherical phosphor particle might lead to excessive temperatures, which could be a major source of light output degradation and reliability problems for high-power LEDs. Yan *et al.*[71] found that the junction temperature, which characterizes the thermal behavior of monotonic color LED emitters, cannot be used on its own to characterize the thermal behavior of white LEDs. They also found that the phosphor temperature is critical in determining the lumen performance and reliability of white LEDs.

Studying the heat generated in a phosphor layer is a complex coupled problem involving both photonics and thermal aspects. A combination of optical simulation and finite element simulation was used to investigate this problem.[72] In the Monte Carlo optical simulation, the heat accumulated through optical absorption by the packaging materials was calculated. The heat was loaded into the finite element model and the temperature field of the LED package was simulated. The location of hotspots in a phosphor-converted white LED package for two different kinds of phosphor coating (a direct coating and a remote coating) were compared, while the phosphor concentration was changed. Plates XXXI and XXXII (see color section between pages 330 and 331) show the results. From Plate XXXI, it can be seen that on increasing the phosphor concentration from 0.05 g/cm^3 to 0.35 g/cm^3, the temperature of the LED packages increased and the hotspot was more obvious. The hotspot was close to the phosphor layer in Plate XXXI regardless of the phosphor concentration. As shown in Plate XXXII, for the remote coating, the location of the hotspot had shifted. When the phosphor concentration was low (0.05 g/cm^3), the hotspot was located at the chip; when the phosphor concentration increased, the hotspot shifted to the phosphor layer. It was concluded that the location of hotspots in remote phosphor coating packages depends on the phosphor concentration, while there was no dependence for direct phosphor coating packages. In summary, the location of hotspots depends on phosphor concentration as well as the packaging method.

15.7.3 Contact thermal resistance and the thermal interface material

LEDs are composed of many components, which are mounted on top of each other as layers. There are many interfaces between the layers, such as the chip-to-copper slug interface, the copper slug-to-substrate interface and the substrate-to-heat sink interface. Basically, there are two kinds of interface:

- a permanent interface, such as a solder or die adhesive
- a non-permanent interface, e.g. where a component is mounted onto a heat sink or between an assembled module and a chassis.

No real surface is perfectly smooth, and surface roughness is believed to play a critical role in determining the contact thermal resistance. In an interface, only a small area mechanically makes contact between the two surfaces, thus the contact thermal resistance is an important part of the overall thermal resistance. Figure 15.26 is a basic schematic of heat transfer between two materials. There are two principal contributions to the heat transfer at the joint:

- solid-to-solid conduction at the points of contact
- conduction through entrapped air in the void spaces created by the contact.

The second contribution is believed to be the major cause of resistance to heat flow, since the thermal conductivity of air is quite small in comparison to that of solids.[73] The total contact thermal resistance is therefore the two contributions taken in parallel, as shown in Fig. 15.26, where R_c is the thermal resistance of the solid-to-solid conduction and R_g is the thermal resistance of the entrapped air or an infilling thermal interface material (TIM). The TIM is used to expel the air and fill in the void at the interface to reduce the contact thermal resistance.[74, 75] Compared with the other packaging materials along the heat flow path, the TIM has the lowest thermal conductivity. Consequently, the TIM acts as a bottleneck in the heat flow path and thus affects the heat flow rate. Categories and general properties of TIMs are listed in Table 15.2.

15.7.4 Spreading thermal resistance and packaging substrate

Generally, LED devices are mounted on a broad substrate. Heat generated by an LED die conducts through the package and transfers to the substrate. As LED dies

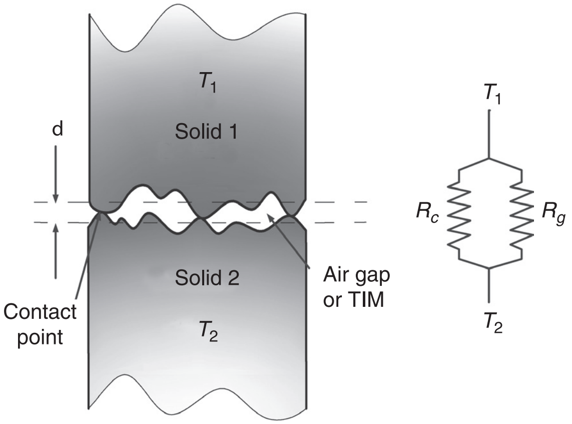

15.26 Contact face of an interface. (TIM: thermal interface material)

Table 15.2 Categories and general properties of TIMs

Category	General properties
Thermal grease	• Usually consists of two primary components, i.e. a polymer base and a ceramic or metallic filler. Silicone is usually used as the polymer base material • Typical fillers: alumina, AlN, ZnO, SiO_2, BN, silver, aluminum powders, etc.
Phase change materials (PCMs)	• Low-temperature thermoplastic adhesive • All-metal phase change materials based on low melting alloys and shape memory alloys • Typical PCMs: thermal pads, low melting alloys, shape memory alloys, exfoliated clay, fusible/non-fusible fillers
Thermally conductive elastomers (gels)	• Generally consist of a silicone elastomer filled with thermally conductive ceramic particles • Thermal resistance depends on thickness, clamping pressure and bulk thermal conductivity
Adhesives	• Typically silver particles in a cured epoxy matrix • Low thermal conductivity
Solders	• High thermal conductivity • High processing temperature • Challenge: voids underneath the chips
Carbon-based TIMs	• Unique thermal and rheological properties • Typical materials: carbon fibers/nano-fibers, graphite flakes, carbon nanotubes

and packages are usually much smaller than the substrate, the heat dissipation processes can be treated as a heat flux from a surface conducting into a larger plate. When an LED comes into contact with the base of a large heat sink, the hotspot phenomenon appears. A large spreading thermal resistance contributes to this phenomenon. Spreading thermal resistance is the main contributor to the overall thermal resistance when heat is conducted from a small area into a large plate, especially for LEDs. Therefore it is very important to reduce the spreading thermal resistance for LED packaging.

For many LED applications, to meet the demands for illumination and reduce costs, several chips are packaged into one module. For these multi-chip packages, the spreading thermal resistance is large. The heat from different chips interacts and since the locations of the chips affects the spreading thermal resistance, it is essential to optimize the design. By changing the arrangement of the chips on the substrate, the spreading resistance can be reduced and the temperature distribution can be made uniform. Plate XXXIII (see color plate section between pages 330 and 331) shows the temperature before and after the optimization of the position of LED chips.[76]

Another method for reducing spreading thermal resistance is to use a heat pipe type substrate such as a flat-plate vapor chamber. Figure 15.27 shows how a flat-plate vapor chamber works. A flat-plate vapor chamber is a vacuum vessel

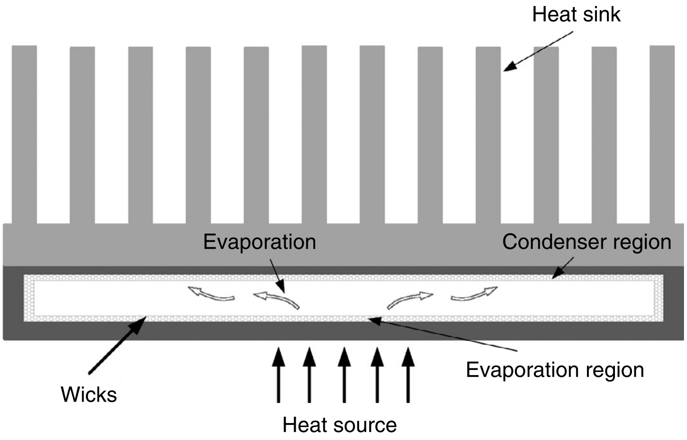

15.27 Working mechanism of flat-plate vapor chambers.

with a wick structure on the inside walls. The chamber is partly filled with a working liquid. As heat is applied, the liquid in the evaporation region absorbs the heat from the heat source and evaporates, and the resulting vapor flows to fill the empty part of the cavity. Whenever the vapor comes into contact with a cooler wall surface, it will condense and release the latent heat of vaporization to the heat sink. Finally the condensed liquid returns to the evaporation region via the capillary force of the wick. The area of the heat sink is usually several-fold or several tenfold that of the heat source. The net effect of a flat-plate vapor chamber is to transport heat from the evaporation region to the condenser region so the heat generated by the heat source is diffused to the heat sink where the heat flux density decreases considerably. Because of the flowing vapor inside the chamber, the temperature of the top surface of the chamber is uniform in theory, thus the spreading thermal resistance can be reduced significantly. Moreover, the dissipation efficiency of a heat sink coupled with a flat-plate vapor chamber can be increased. Huang *et al.*[77] experimentally studied the thermal performance of a vapor chamber module applied to high-power LEDs and found that the spreading thermal resistance of a flat-plate vapor chamber at 30 W was lower than that of a copper plate by 34%. We fabricated a flat-plate vapor chamber coupled to a fin heat sink and used it to cool a 20 W LED light source. We found that the flat-plate vapor chamber was a good way to alleviate the hotspots and decrease the spreading thermal resistance.[78]

15.7.5 Cooling solutions for LED applications

Cooling solutions for LED applications either use passive or active cooling. Passive cooling occurs when heat is transferred without any artificially imposed force and extra energy consumption, such as free air convection. Active cooling needs an imposed force or input power, such as forced air cooling, liquid cooling (microchannel cooling or micro-jet cooling), semiconductor refrigeration, ultrasonic heat dissipation and superconducting cooling.

Generally speaking, the heat dissipation ability of passive cooling is limited since the convection heat-transfer coefficient h for air is usually less than 10 W/(m^{2}K). Because of the small h, according to Newton's law of cooling, a large heat exchange area A is needed for sufficient heat transfer. As a result, engineers usually improve the heat dissipation performance of a plate fin heat sink by increasing the number of fins to increase the heat exchange area A or designing the space between the fins and increasing the height of the fins to increase the heat transfer coefficient h. So far, plate fin heat sinks have worked quite well with general LED lighting products.[79]

Compared with passive cooling, active cooling can enhance the heat transfer ability significantly, but its application to LED products is limited because of reliability and cost requirements. When the total power of an LED is very high, passive cooling is inadequate and active cooling must be used. There are many kinds of active cooling solutions; here we only consider forced convection and micro-jet cooling as examples to demonstrate active cooling solutions. Forced convection is driven by an artificial force or power, such as a fan or pump, which accelerates the air flow and substantially increases the heat transfer coefficient. Forced convection can improve the heat exchange rate significantly compared with free convection. Another kind of active liquid cooling technology is the micro-jet.[80–82] Figure 15.28 shows a closed-loop LED micro-jet array cooling system. It has three parts: a micro-jet array device, a micro-pump and a mini fluid container with a heat sink. In the closed-loop system, water or another fluid is driven into the micro-jet array device through an inlet by a micro-pump. There are many micro-jets inside the jet device, which directly impinge onto the bottom plate of the LED array. Since an impinging jet has a very high heat transfer coefficient, the heat created by the LEDs is easily removed by the fluid recycling

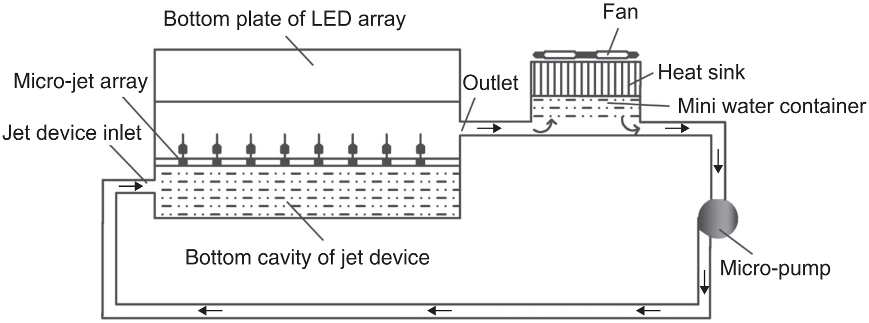

15.28 Closed-loop micro-jet array cooling system.

in the system. The fluid heats up and its temperature increases after it flows out of the jet device, and the heated fluid enters the mini fluid container. The heat sink, which has a fan, cools the fluid and the heat dissipates into the external environment. The cooled fluid is delivered back to the jet device to cool the LED array, again driven by the force of the micro-pump in the system.

15.8 Conclusion

In this chapter, issues with the chip packaging for nitride LEDs were reviewed, including the functions, structures, processes, and the optical and thermal design of LEDs. Packaging processes have an important role in determining the final optical and thermal performance of LEDs, thus they should be well designed optically and thermally. The effects of the gold wire bonding process, the phosphor coating process and lenses on optical performance were discussed. Heat dissipation for high-power LEDs is a big challenge and the LED packages should be thermally well designed. A thermal design should take into account the packaging structure and phosphor self-heating. The effects of contact thermal resistance, spreading thermal resistance and external cooling solutions were also discussed.

15.9 References

1 J. Z. Hu, L. Q. Yang and M. W. Shin, Thermal effects of moisture-inducing delamination in light-emitting diode packages, *Electronic Components Technology Conference*, pp. 1957–1962, 2006.

2 X. B. Luo, B. L. Wu and S. Liu, Effects of moist environments on LED module reliability, *IEEE Transactions on Device and Materials Reliability*, Vol. 10, No. 2, pp. 182–186, June 2010.

3 J. Z. Hu, L. Q. Yang and M. W. Shin, Mechanism and thermal effect of delamination in light-emitting diode packages, *Microelectronics Journal*, Vol. 38, No. 2, pp. 157–163, 2007.

4 M. Arik and S. Weaver, Chip scale thermal management of high brightness LED packages, *Proceedings of SPIE*, Vol. 5530, pp. 214–223.

5 Q. Chen, X. B. Luo, S. Zhou and S. Liu, Dynamic junction temperature measurement for high power light emitting diodes, *Review of Scientific Instruments*, Vol. 82, p. 084904, 2011.

6 Y. M. Gu and N. Narendran, A non-contact method for determining junction temperature of phosphor converted white LEDs, *Proceedings of SPIE*, Vol. 5187, pp. 107–114, 2004.

7 Y. Xi, J. Q. Xi, T. Gessmann, J. M. Shah, J. K. Kim, *et al.*, Junction and carrier temperature measurements in deep-ultraviolet light-emitting diodes using three different methods, *Applied Physics Letters*, Vol. 86, p. 031907, 2005.

8 S. Liu and X. B. Luo, *LED Packaging for Lighting Applications: Design, Manufacturing and Testing*, John Wiley & Sons, USA, 2011.

9 J. B. Jiang, S. To, W. B. Lee and B. Cheung, Optical design of a freeform TIR lens for LED streetlight, *Optik*, Vol. 121, pp. 1761–1765, 2010.

10 J. G. Chang, L. D. Liao and C. C. Hwang, Enhancement of the optical performances for the LED backlight systems with a novel lens-cap, *Proceedings of SPIE*, Vol. 6289, p. 62890X, 2006.

11 D. A. Steigerwald, J. C. Bhat and D. Collins, Illumination with solid state lighting technology, *IEEE Journal of Selected Topic in Quantum Electronics*, Vol. 18, No. 2, pp. 310–320, 2002.

12 http://www.cree.com/press/press_detail.asp?i=1304945651119

13 G. Harman, *Wire Bonding in Microelectronics*, 3rd ed., McGraw Hill, 2010.

14 K. Toyozawa, K. Fujita, S. Minamide and T. Maeda, Development of copper wire bonding application technology, *IEEE Transactions on Components, Hybrids, and Manufacturing Technology*, Vol. 13, No. 4, pp. 667–672, 1990.

15 W. D. Collins, M. R. Krames, G. J. Verhoeckx and N. J. M. Leth, Using electrophoresis to produce a conformal coated phosphor-converted light emitting semiconductor, US Patent, Lumileds Lighting, US 6576488, 2001.

16 W. D. Collins, M. R. Krames, G. J. Verhoeckx and N. V. Leth, Method for conformally coating a light emitting semiconductor structure with a phosphor by electrophoresis, European Patent Application, Lumileds Lighting, EP 1267424A2, 2002.

17 J. H. Yum, S. Y. Seo, S. Lee and Y. E. Sung, Comparison of Y3Al4O12:Ce0.05 phosphor coating methods for white light-emitting diode on gallium nitride, *Solid State Lighting and Displays, Proceedings of SPIE*, San Diego, CA, USA, pp. 60–69, 2001.

18 B. P. Loh, N. W. Medendorp Jr, P. Andrews, Y. Fu, M. Laughner, *et al.*, Method of uniform phosphor chip coating and LED package fabricated using method, US Patent, Cree Inc, 20080079017 A1, 2008.

19 B. Braune, K. Peterson, J. Strauss, P. Kromotis and M. Kaempf, A new wafer level coating technique to reduce the color distribution of LEDs, *Light-Emitting Diode: Research, Manufacturing, and Applications XI, Proceedings of SPIE*, San Jose, CA, USA, p. 64860X, 2007.

20 H. Zheng, X. B. Luo, R. Hu, B. Cao, X. Fu, *et al.*, Conformal phosphor coating using capillary microchannel for controlling color deviation of phosphor-converted white light-emitting diodes, *Optics Express*, Vol. 20, No. 5, pp. 5092–5098, 2012.

21 S. Liu, Method to fabricate white light-emitting diode, Chinese Patent Application, 200610029858.6, 2006.

22 K. Yamada, Y. Imai and K. Ishii, Optical simulation of light source devices composed of blue LEDs and YAG phosphor, *Journal of Light and Visual Environment*, Vol. 27, No. 2, pp. 70–74, 2003.

23 Y. Zhu, N. Narendran and Y. Gu, Investigation of the optical properties of YAG:Ce phosphor, *Sixth International Conference on Solid State Lighting, San Diego, CA, USA, Proceedings of SPIE*, p. 63370S, 2007.

24 M. Arik, A. Seltur, S. Weaver, D. Haitko and J. Petroski, Chip to system thermal needs and alternative thermal technologies for high brightness LEDs, *Journal of Electronic Packaging*, Vol. 129, No. 3, pp. 328–338, 2007.

25 J. K. Kim, H. Luo, E. F. Schubert, J. Cho, C. Sone, *et al.*, Strongly enhanced phosphor efficiency in GaInN white light-emitting diodes using remote phosphor configuration and diffuse reflector cup, *Japanese Journal of Applied Physics*, Vol. 44, pp. L649–L651, 2005.

26 H. Luo, J. K. Kim, E. F. Schubert, J. Cho, C. Sone, *et al.*, Analysis of high-power packages for phosphor-based white-light-emitting diodes, *Applied Physics Letters*, Vol. 86, No. 24, p. 243505, 2005.

27 H. Luo, J. K. Kim, Y. Xi, E. F. Schubert, J. Cho, *et al.*, Analysis of high-power packages for white-light-emitting diode lamps with remote phosphor, *Materials Research Society*, Vol. 892, p. FF09-07, 2006.

28 B. F. Fan, H. Wu, Y. Zhao, Y. L. Xian and G. Wang, Study of phosphor thermal-isolated packaging technologies for high-power white light-emitting diodes, *IEEE Photonics Technology Letters*, Vol. 19, No. 15, pp. 1121–1123, 2007.

29 B. L. Wu, X. B. Luo, H. Zheng and S. Liu, Effect of gold wire bonding process on angular correlated color temperature uniformity of white light-emitting diode, *Optics Express*, Vol. 19, No. 24, pp. 24115–24121, 2011.

30 Z. Y. Liu, C. Li, B. H. Yu, Y. H. Wang, S. Liu, *et al.*, Effects of YAG:Ce phosphor particle size on optical performance of white LEDs, *12th International Conference on Electronic Packaging Technology and High Density Packaging*, pp. 1066–1071, 2011.

31 R. Hu, X. B. Luo and S. Liu, Effect of the amount of phosphor silicone gel on optical property of white light-emitting diodes packaging, *12th International Conference on Electronic Packaging Technology and High Density Packaging*, pp. 1081–1084, 2011.

32 R. Hu, X. B. Luo, H. Feng and S. Liu, Effect of phosphor settling on the optical performance of phosphor-converted white light-emitting diodes, *Journal of Luminescence*, Vol. 132, pp. 1252–1256, 2012.

33 C. Sommer, F. Reil, J. R. Krenn, P. Hartmann, P. Pachler, *et al.*, The impact of light scattering on the radiant flux of phosphor-converted high power white light-emitting diodes, *Journal of Lightwave Technology*, Vol. 29, No. 15, pp. 2285–2291, 2011.

34 C. Sommer, F. P. Wenzl, F. Reil, J. R. Krenn, P. Pachler, *et al.*, A comprehensive study on the parameters effecting color conversion in phosphor converted white light-emitting diodes, *Tenth International Conference on Solid State Lighting, Proceedings of SPIE*, Vol. 7784, p. 77840D, 2010.

35 C. Sommer, P. Hartmann, P. Pachler, M. Schweighart, S. Tasch, *et al.*, A detailed study on the requirements for angular homogeneity of phosphor converted high power white LED light sources, *Optical Materials*, Vol. 31, pp. 837–848, 2009.

36 Y. Uchida and T. Taguchi, Lighting theory and luminous characteristics of white light-emitting diodes, *Optical Engineering*, Vol. 44, No. 12, p. 124003, 2005.

37 A. Keppesn, S. Denijs, S. Wouters, W. R. Rychaert, G. Deconinck, *et al.*, Modelling the spatial colour distribution of phosphor-white high power light-emitting diodes, *Proceedings of SPIE*, Vol. 7717, p. 77170J, 2010.

38 J. K. Kim, H. Luo, E. F. Schubert, J. H. Cho, C. S. Sone, *et al.*, Strongly enhanced phosphor efficiency in GaInN white light-emitting diodes using remote phosphor configuration and diffuse reflector cup, *Japanese Journal of Applied Physics*, Vol. 44, No. 21, pp. 649–651, 2005.

39 Z. Y. Liu, S. Liu, K. Wang and X. B. Luo, Effects of phosphor's location on LED packaging performance, *International Conference on Electronic Packaging Technology and High Density Packaging*, Shanghai, China, p. 4606982-1-7, 2008.

40 Z. Y. Liu, S. Liu, K. Wang and X. B. Luo, Status and prospects for phosphor-based white LED packaging, *Frontiers of Optoelectronics in China*, Vol. 2, No. 2, pp. 119–140, 2009.

41 Z. Y. Liu, S. Liu, K. Wang and X. B. Luo, Studies on optical consistency of white LEDs affected by phosphor thickness and concentration using optical simulation, *IEEE Transactions on Components and Packaging Technology*, Vol. 33, No. 4, pp. 680–687, 2010.

42 C. Sommer, F. P. Wenzl, P. Hartmann, P. Pachler, M. Schweighart, *et al.*, Tailoring of the color conversion elements in phosphor-converted high-power LEDs by

optical simulations, *IEEE Photonics Technology Letters*, Vol. 20, No. 5, pp. 739–741, 2008.

43 N. T. Tran and F. G. Shi, Studies of phosphor concentration and thickness for phosphor-based white light-emitting-diodes, *Journal of Lightwave Technology*, Vol. 26, No. 21, pp. 3556–3559, 2008.

44 Z. Y. Liu, S. Liu, K. Wang and X. B. Luo, Optical analysis of color distribution in white LEDs with various packaging methods, *IEEE Photonics Technology Letters*, Vol. 20, No. 24, pp. 2027–2029, 2008.

45 Z. Y. Liu, S. Liu, K. Wang and X. B. Luo, Measurement and numerical studies of optical properties of YAG:Ce phosphor for white light-emitting diode packaging, *Applied Optics*, Vol. 49, No. 2, pp. 247–257, 2010.

46 R. Hu, X. B. Luo and S. Liu, Study on the optical properties of conformal coating light-emitting diode by Monte Carlo simulation, *IEEE Photonics Technology Letters*, Vol. 23, No. 20, pp. 1673–1675, 2011.

47 R. Y. Yu, S. Z. Jin, S. Y. Cen and P. Liang, Effect of the phosphor geometry on the luminous flux of phosphor-converted light-emitting diodes, *IEEE Photonics Technology Letters*, Vol. 22, No. 23, pp. 1765–1767, 2010.

48 Y. Zhu and N. Narendran, Optimizing the performance of remote phosphor LEDs, *Japanese Journal of Light Visual Environment*, Vol. 32, No. 2, pp. 115–119, 2008.

49 Y. H. Won, H. S. Jang, K. W. Cho, Y. S. Song, D. Y. Jeon, *et al.*, Effect of phosphor geometry on the luminous efficiency of high-power white light-emitting diodes with excellent color rendering property, *Optics Letters*, Vol. 34, No. 1, pp. 1–3, 2009.

50 Z. X. Feng, Y. Luo and Y. J. Han, Design of LED freeform optical system for road lighting with high luminance/illuminance ratio, *Optics Express*, Vol. 18, No. 21, pp. 22020–22031, 2010.

51 Y. Ding, X. Liu, Z. R. Zheng and P. F. Gu, Freeform LED lens for uniform illumination, *Optics Express*, Vol. 16, No. 17, pp. 12958–12966, 2008.

52 W. A. Parkyn, The design of illumination lenses via extrinsic differential geometry, *Proceedings of SPIE*, Vol. 3428, pp. 154–162, 1998.

53 K. Wang, D. Wu, F. Chen, Z. Y. Liu, X. B. Luo, *et al.*, Angular color uniformity enhancement of white light-emitting diodes integrated with freeform lenses, *Optics Letters*, Vol. 35, No. 11, pp. 1860–1862, 2010.

54 K. Wang, D. Wu, Z. Qin, F. Chen, X. B. Luo, *et al.*, New reversing design method for LED uniform illumination, *Optics Express*, Vol. 19, No. S4, pp. A830–A840, 2011.

55 H. Ries and J. Muschaweck, Tailored freeform optical surfaces, *Journal of the Optical Society of America A*, Vol. 19, No. 3, pp. 590–595, 2002.

56 J. Chaves, *Introduction to Nonimaging Optics*, CRC press, Taylor & Francis Group, 2008.

57 J. C. Minano, P. Benitez, J. Y. Liu, J. Infante, J. Chaves, *et al.*, Applications of the SMS method to design of compact optics, *Proceedings of SPIE*, Vol. 7717, p. 771701, 2010.

58 P. Benitez, J. C. Minano, J. Blen, R. Mohedano, J. Chaves, *et al.*, Simultaneous multiple surface optical design method in three dimensions, *Optics Engineering*, Vol. 43, No. 7, pp. 1489–1502, 2004.

59 O. Dross, A. Cvetkovic, J. Chaves, P. Benitez and J. C. Minano, LED headlight architecture that creates a high quality beam pattern independent of LED shortcomings, *Proceeding of SPIE*, Vol. 5942, p. 59420D, 2005.

60 K. Wang, S. Liu, F. Chen, Z. Qin, Z. Y. Liu, *et al.*, Freeform LED lens for rectangularly prescribed illumination, *Journal of Optics A: Pure and Applied Optics*, Vol. 11, p. 105501, 2009.

61 L. Wang, K. Y. Qian and Y. Luo, Discontinuous free-form lens design for prescribed irradiance, *Applied Optics*, Vol. 46, No. 18, pp. 3716–3723, 2007.

62 K. Wang, S. Liu, F. Chen, Z. Y. Liu and X. B. Luo, Effect of manufacturing defects on optical performance of discontinuous freeform lenses, *Optics Express*, Vol. 17, No. 7, pp. 5457–5465, 2009.

63 K. Wang, F. Chen, Z. Y. Liu, X. B. Luo and S. Liu, Design of compact freeform lens for application specific light-emitting diode packaging, *Optics Express*, Vol. 18, No. 2, pp. 413–425, 2010.

64 S. Wang, K. Wang, F. Chen and S. Liu, Design of primary optics for LED chip array in road lighting applications, *Optics Express*, Vol. 19, No. S4, pp. A716–A724, 2011.

65 F. Chen, S. Liu, K. Wang, Z. Y. Liu and X. B. Luo, Free-form lenses for high illumination quality light-emitting diode MR16 lamps, *Optical Engineering*, Vol. 48, No. 12, p. 123002, 2009.

66 Y. S. Tang, S. F. Hu, C. C. Lin, N. C. Bagkar and R. S. Liu, Thermal stable luminescence of $KSrPO_4$:Eu phosphor for white light UV light-emitting diodes, *Applied Physics Letters*, Vol. 90, No. 15, p. 151108, 2007.

67 M. P. Arik and J. Weaver, Thermal challenges in the future generation solid state lighting applications: light emitting diodes, *International Society Conference on Thermal Phenomena*, San Diego, USA, pp. 113–120, 2002.

68 J. Y. Tsao, Solid state lighting-lamps-chips and materials for tomorrow, *IEEE Circuits and Devices Magazine*, Vol. 20, No. 3, pp. 28–37, 2004.

69 J. A. DeLuca, An introduction to luminescence in inorganic solids, *Journal of Chemical Education*, Vol. 57, No. 8, pp. 541–548, 1980.

70 M. Arik, S. Weaver, C. Becker, M. Hsing and A. Srivastava, Effects of localized heat generation due to the color conversion in phosphor particles and layers of high brightness light emitting diodes, *Proceedings of International Electronic Packaging Technical Conference and Exhibition*, Maui, Hawaii, USA, pp. 611–619, 6–11 July 2003.

71 B. Yan, N. T. Tran, J. P. You and F. G. Shi, Can junction temperature alone characterize thermal performance of white LED emitters?, *IEEE Photonics Technology Letters*, Vol. 23, No. 9, pp. 555–557, 1 May 2011.

72 R. Hu and X. B. Luo, Will the hotspot location in the high power phosphor converted white light-emitting diode package shift?, *International Conference on Advanced Electromaterials*, Jeju, Korea, 7–10 Nov. 2011.

73 J. P. Holman, *Heat Transfer*, McGraw-Hill Inc and China Machine Press, Beijing, China, 2005.

74 R. Prasher, Thermal interface materials: historical perspective, status, and future directions, *Proceedings of the IEEE*, Vol. 94, No. 8, pp. 1571–1586, 2006.

75 F. Sarvar, D. C. Whalley and P. P. Conway, Thermal interface materials – a review of the state of the art, *Electronics System Integration Technology Conference*, Dresden, Germany, pp. 1292–1302, 2006.

76 T. Cheng, X. B. Luo, S. Y. Huang and S. Liu, Thermal analysis and optimization of multiple LED packaging based on a general analytical solution, *International Journal of Thermal Science*, Vol. 49, No. 1, pp. 96–201, 2010.

77 H. S. Huang, Y. C. Chiang, C. K. Huang and S. L Chen, Experimental investigation of vapor chamber module applied to high-power light-emitting diodes, *Experimental Heat Transfer*, Vol. 22, pp. 26–38, 2009.

78 X. B. Luo, R. Hu, T. H. Guo, X. L. Zhu, W. Chen, *et al.*, Low thermal resistance LED light source with vapor chamber coupled fin heat sink, *Electronic Components and Technology Conference*, pp. 1347–1352, 2010.

79 X. B. Luo, W. Xiong, T. Cheng and S. Liu, Design and optimization of horizontally-located plate fin heat sink for high power LED street lamps, *Electronic Components and Technology Conference*, San Diego, CA, USA, pp. 854–859, 2009.

80 X. B. Luo and S. Liu, A microjet array cooling system for thermal management of high-brightness LEDs, *IEEE Transactions on Advanced Packaging*, Vol. 30, No. 3, pp. 475–484, August 2007.

81 X. B. Luo, W. Chen, R. X. Sun and S. Liu, Experimental and numerical investigation of a microjet-based cooling system for high power LEDs, *Heat Transfer Engineering*, Vol. 29, No. 9, pp. 774–781, 2008.

82 X. B. Luo, S. Liu, X. P. Jiang and T. Cheng, Experimental and numerical study on a micro jet cooling solution for high power LEDs, *Science in China Series E: Technological Science*, Vol. 50, No. 4, pp. 478–489, 2007.

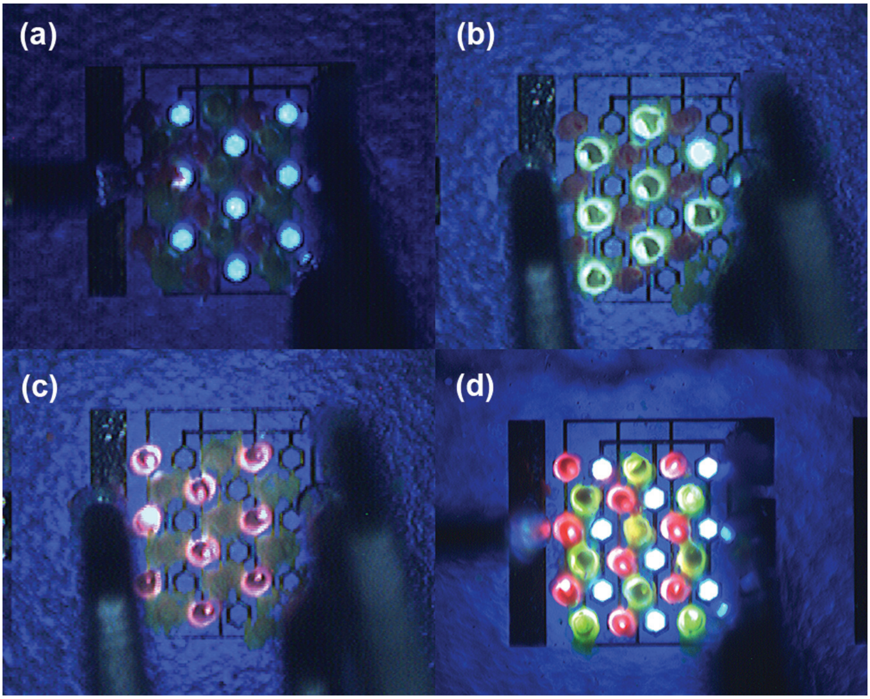

Plate XXVII (Chapter 13) (a) Blue, (b) green and (c) red pixels illuminated. In (d), all pixels are turned on.

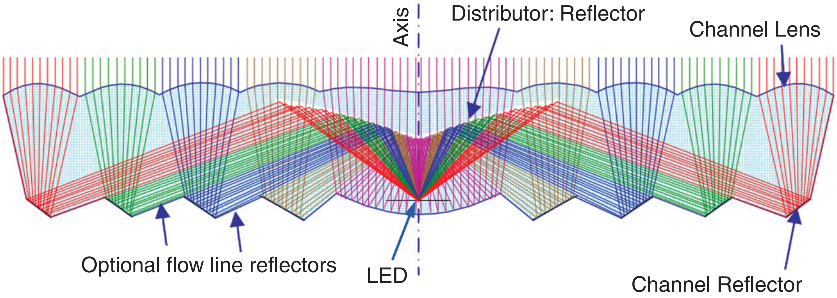
Axis
Distributor: Reflector
Channel Lens
Optional flow line reflectors
LED
Channel Reflector

Plate XXVIII (Chapter 15) Multichannel optics designed for an LED. (Reproduced with permission from Minano *et al.*[57] Copyright 2010, SPIE.)

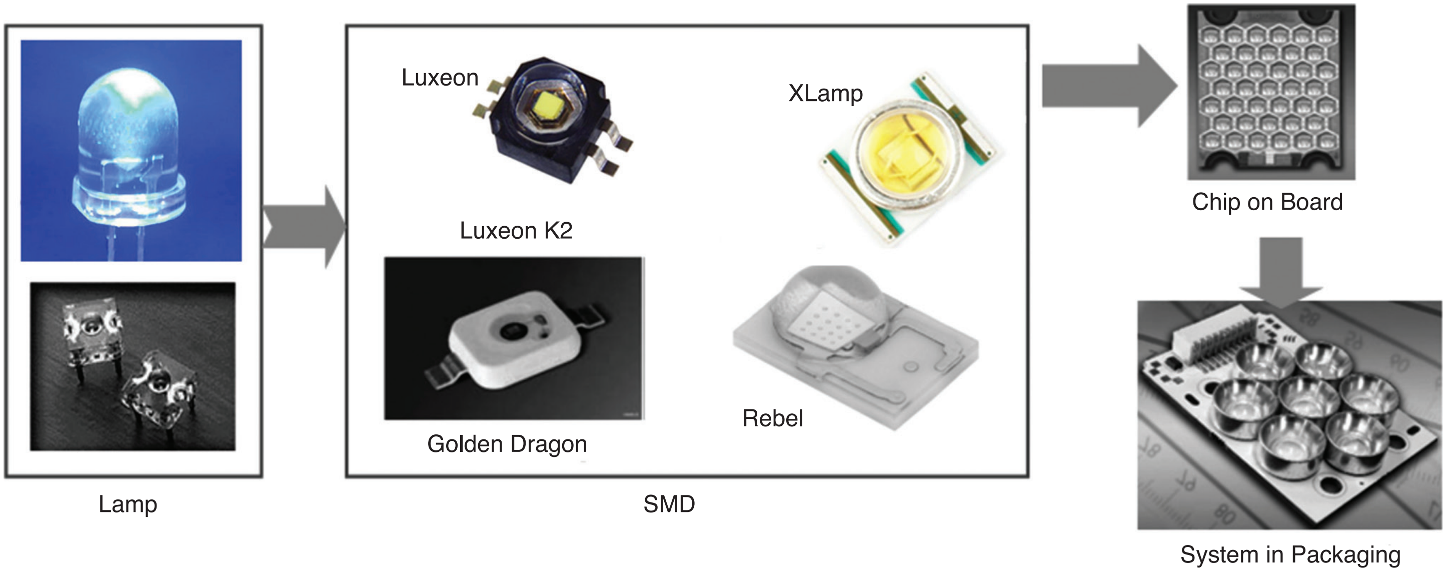
Lamp
Luxeon
Luxeon K2
Golden Dragon
XLamp
Rebel
SMD
Chip on Board
System in Packaging

Plate XXIX (Chapter 15) Development of LED packaging technology and structures.

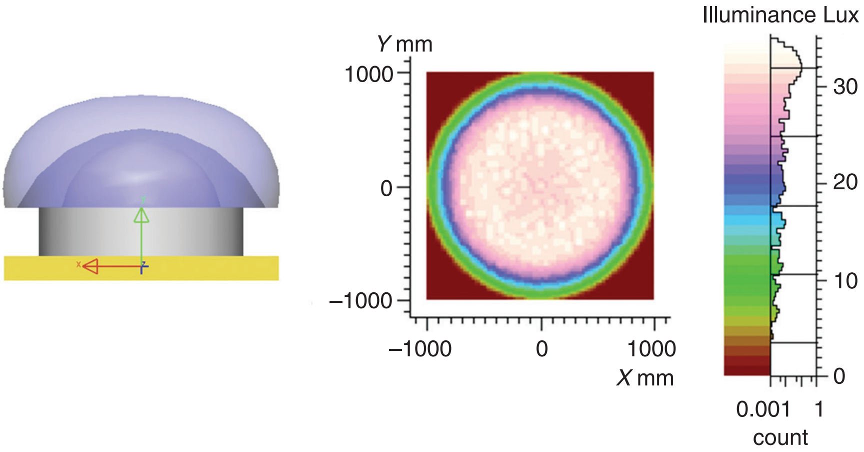

Plate XXX (Chapter 15) MR16 freeform lens and its lighting performance.

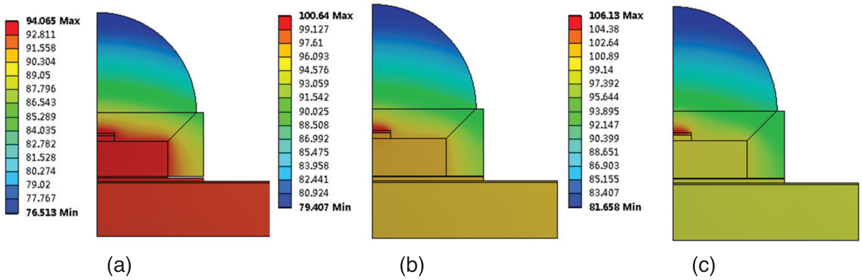

Plate XXXI (Chapter 15) Hotspot locations for different phosphor concentrations for an LED package with a direct phosphor coating: (a) 0.05 g/cm^3, (b) 0.2 g/cm^3 and (c) 0.35 g/cm^3.

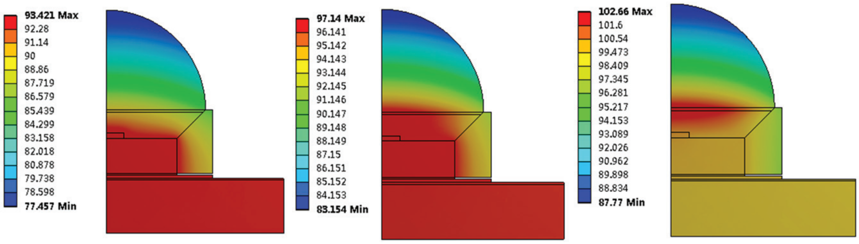
93.421 Max
92.28
91.14
90
88.86
87.719
86.579
85.439
84.299
83.158
82.018
80.878
79.738
78.598
77.457 Min
97.14 Max
96.141
95.142
94.143
93.144
92.145
91.146
90.147
89.148
88.149
87.15
86.151
85.152
84.153
83.154 Min
102.66 Max
101.6
100.54
99.473
98.409
97.345
96.281
95.217
94.153
93.089
92.026
90.962
89.898
88.834
87.77 Min

(a) (b) (c)

Plate XXXII (Chapter 15) Hotspot locations for different phosphor concentrations for an LED package with a remote phosphor coating: (a) 0.05 g/cm^3, (b) 0.2 g/cm^3 and (c) 0.35 g/cm^3.

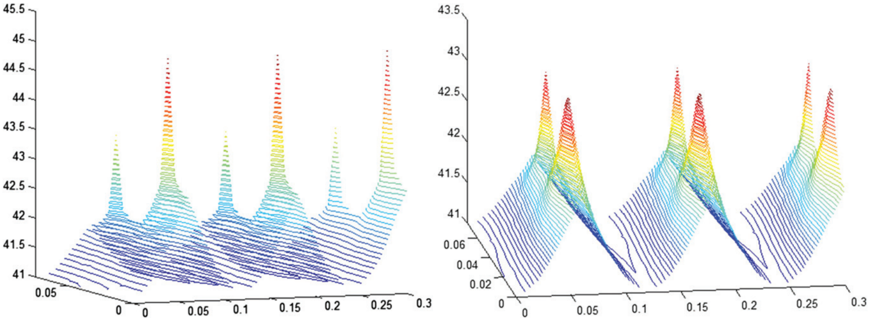

(a) (b)

Plate XXXIII (Chapter 15) Three-dimensional temperature field for a quarter of a street lamp heat sink plate (a) before position optimization and (b) after position optimization.

16

White LEDs for lighting applications: the role of standards

R. KOTSCHENREUTHER, OSRAM GmbH, Germany

DOI: 10.1533/9780857099303.3.485

Abstract: The revolution in the world of lighting needs a solid basis. That basis consists of standards that specify the safety and performance requirements of LED products. The present use of LEDs is described and they are compared with traditional light sources, and an outlook for possible future LED applications is provided.

Key words: LED (package, module, lamp), standards (terms, safety, performance), non-visual effects of light.

16.1 General lighting applications

There are different types of lighting application. A simple view divides the market into general lighting and specialty lighting, and this division is used all over the lighting business and is shared by manufacturers, wholesalers, light planners, architects and other professional users.

What is the criterion for this division? It is based on the purpose or location of the application. In most cases, general lighting is characterised by having a large sales volume. The locations where applications are used are, for example:

- General lighting: factories, offices, streets, shops, houses, warehouses, conference rooms, restaurants, car parks
- Specialty lighting: cars, backlighting, stadia, stages, televisions, greenhouses.

Table 16.1 shows which kind of light source is used in which application and where LED light sources are used. However, the real functional substitution depends on the specific requirements, like colour (correlated colour temperature, CCT), brightness (luminous flux), colour rendering (CRI), light distribution, lifetime and stability of parameters over lifetime, homogeneity, climatic conditions, colour and luminous flux control, dimmability, efficiency, photobiological safety, geometry, sensitivity of objects to heat and UV radiation and last but not least the non-visual effects of light on human beings.

At present, LED products can replace non-LED products in many general lighting applications. In the specialty lighting application in greenhouses, LED modules have an advantage because they can emit at the optimum wavelengths for the cultivation of vegetables. Also for television studio lighting, LEDs can

Table 16.1 Application of non-LED light sources and LED light sources (not exhaustive)

Type		Non-LED light source	LED light source
General lighting	Architectural illumination	High-pressure mercury High-pressure sodium	LED modules
General lighting	Conference room	Compact fluorescent integral (CFLi) Halogen incandescent Single-capped fluorescent	LED modules Single-capped LED lamps
General lighting	Factory hall	High-pressure mercury High-pressure sodium Linear fluorescent Metal halide	Double-capped LED lamps LED modules
General lighting	Residential	Compact fluorescent integral (CFLi) Halogen incandescent	Single-capped LED lamps
General lighting	Office	Halogen incandescent Linear fluorescent Metal halide	Double-capped LED lamps LED modules Single-capped LED lamps
General lighting	Hospitality	Compact fluorescent integral (CFLi) Halogen incandescent Single-capped fluorescent	LED modules Single-capped LED lamps
General lighting	Shop, boutique	Compact fluorescent integral (CFLi) Halogen incandescent Metal halide (low power)	LED modules Single-capped LED lamps
General lighting	Retail	Halogen incandescent Linear fluorescent	Double-capped LED lamps LED modules Single-capped LED lamps
General lighting	Outdoor, street	High-pressure mercury High-pressure sodium Low pressure sodium Metal halide	LED modules Double-capped LED lamps
General lighting	Warehouse, stock	High-pressure mercury Linear fluorescent Metal halide	–
Specialty lighting	Automotive	Halogen incandescent Incandescent Metal halide (low power)	LED lamps, special cap LED modules
Specialty lighting	Backlighting	–	LED modules
Specialty lighting	Greenhouse	High-pressure sodium	LED modules

Specialty lighting	Stadium	Metal halide	–
Specialty lighting	Stage	Metal halide High-pressure xenon	LED modules
Specialty lighting	Television studio lighting	High-pressure xenon Metal halide	LED modules

produce exactly the required colour. LED cannot be used where high luminous flux packages are needed, e.g. for stadium lighting. The present LED module power limit meanwhile passes 100 W. Across both general and specialty lighting, the first uses of LEDs were for automotive lighting and architectural lighting, and in backlighting, LEDs have a long application history.

16.2 LED terminology

16.2.1 History and recent changes

Before the features of LED lighting products, whether designed for a specific lighting solution or as replacements for existing light sources, can be discussed, the terms 'LED package', 'LED module', 'LED replacement', 'retrofit', 'conversion kit', 'single-capped LED lamp', 'double-capped LED lamp', 'LED luminaire', etc. need to be defined.

On the one hand, LED lighting uses the traditional combination of devices for illumination, from the generator or transformer to the installed luminaire. On the other hand, intermediate components between the light source and luminaire, e.g. the lamp cap and the lampholder, may be different. LED modules can be directly built into a luminaire and may not require a lamp cap and lampholder. Even if these component parts are present, their functionality might be different. The inherent process of non-active heat transport, associated with the heat sensitivity of LEDs, requires a new constructional awareness and sometimes new components – and new terms. Above all, the creativity of the developers of LED light solutions is unlimited, and the presently defined terms may not be suitable for the next generation of technical innovation and it may be necessary to make changes.

The lighting industry and related businesses recognised the need for a worldwide LED language. In 2001, the first draft of a vocabulary was made available (it was published in 2004[1]). It was based on the technical literature produced by LED manufacturers and the standards for LEDs for non-lighting applications. The draft was offered to the International Electrotechnical Commission (IEC) in Geneva, but at that time it did not attract much attention because little effort was being made to produce common standards for LED lighting. Predominantly, the terms in the draft were temperature and construction related, but also a few of them were linked to photometry and colorimetry with reference to the International Electrotechnical Vocabulary (IEV).[2] In the following years, it became clearer which terms the dictionary should focus on, and finally in 2011 it was published by the IEC as technical specification IEC/TS 62504.[3] The development of the technical specification (TS) triggered other bodies outside the IEC to begin similar work. In the USA a standard was drafted and published in 2010;[4] in Japan, JELMA produced a document[5] that was the basis for national LED standards. Also the Commission Internationale de l'Éclairage (CIE) decided to form a new body, CIE TC 2-66, to define LED terms within the scope of the CIE. These publications and the simultaneous development of LED products required an update of IEC/TS 62504. This update will gather all LED terms, spread over the different LED product standards that have been published. The aim of the review is to separate out terms that naturally fall within the remit of the IEV or CIE or are of such common nature that an explanation is not required. The guiding principle is the usefulness for end users, LED product manufacturers, testing laboratories and, if possible, government bodies.

16.2.2 Definitions and their implications

The definition of terms is strongly connected to the test requirements. For example, if an LED module is designated as a type 1 module, the testing laboratory will automatically also test the control gear which is on board. IEC TC 34 concluded that the LED package was the lowest and most detailed level requiring a definition, because of the commercial interests of module and luminaire manufacturers. Definitions of lower levels – chips or dies – were not deemed to be helpful. An LED package is understood as an LED die plus the attached terminals (Plate XXXIV (see colour section between pages 330 and 331)).

Currently, the IEC defines an LED package as:

> One single electrical component encapsulating principally one or more LED dies, possibly with optical elements and thermal, mechanical, and electrical interfaces
>
> NOTE 1 The component does not include the control unit of the control gear, does not include a cap, and is not connected directly to the supply voltage.
>
> NOTE 2 A LED package is a discrete component and part of the LED module. For a schematic built-up of a LED package, see Annex A
>
> [IEC/PAS 62717 Ed.1, 3.24 modified][6]

After defining an LED package, the question is: what is an 'LED module'?

The latest IEC definition of that term is (second edition of IEC/TS 62504 in preparation)

> **LED module**
>
> Light source having no cap, incorporating one or more LED package(s) on a printed circuit board which may have one or more of the following:
>
> Electrical, optical, mechanical, and thermal components, interfaces and control gear
>
> NOTE 1 A LED module may be integrated (LEDi module, Type 1) or semi-integrated (LEDsi module, Type 2) or non-integrated (LEDni-module, Type 3).
>
> NOTE 2 The LED module usually is designed to be part of a lamp or luminaire.

The reason for the definition is to make a sharp distinction between an LED module and an LED lamp. The difference between them is the cap (Plate XXXV (see colour section)). An LED lamp is equipped with a cap, whereas an LED module does not have a cap. However, if an LED module is combined with a cap, it becomes an LED lamp. Caps can be, for example, Edison screw or bayonet caps, or new types of caps. Caps allow heat transfer and are used for mechanical fixation. Also, an electrical connection can be provided. The new types of caps fall under the remit of the Zhaga consortium;[7] transition of their results to the IEC is being considered.

An LED module can be integrated with the luminaire in three ways:

- Independent: The module is tested for safety in the same way as a luminaire.
- Built-in: Accessibility testing is not required since it is enclosed in the luminaire.
- Integrated: This module cannot be tested separately from the luminaire.

The complete control gear can be on board the module (type 1), it may be split into a supply part and a control part with only the control part on board (type 2), or the complete control gear may be outside the module (type 3).

For comparison, in the Underwriters Laboratories' standard[8] an LED array or module is defined as: 'An assembly of one or more LED discrete electronic components on a printed circuit board, typically with optics and additional thermal, mechanical, and electrical interfaces.' JEL 311[5] defines an LED module as: 'A unit of one or more LEDs mounted on a board, arranged horizontally or spatially to configure an unit mechanically, electrically and optically, or aggregation of them including arrangements of LEDs in an array and in a cluster.' These module definitions are not basically different to the IEC definition. Recently, the IEC addressed the non-availability of the cap and the different types of control gear integration. Ideally, all definitions should be identical. However, national or regional regulations may deviate.

16.3 Copying traditional lamps?

The installed luminaire base, mainly with traditional lamps, cannot be ignored for LED products entering the market. Although, the aim of industry and politicians is to promote LED light sources with their unique features, we are just beginning to introduce them into private households and professional applications. A century of incandescent, fluorescent and high-intensity lighting will not be easy to replace in reality and in people's emotions. However, the prediction[9] is that the introduction of LED modules will progress rapidly.

At present, and apart from the use of LED modules, two possible solutions are feasible and can be found in the market. First, an interim solution is to replace traditional light sources in installed luminaires. The LED lamps could be single-capped LED lamps with an Edison screw cap, bayonet cap or compact fluorescent lamp (CFL)-stick cap. Other applications require double-capped LED lamps, such as in the well-known linear fluorescent configuration (Fig. 16.1).

In many cases an old low-efficiency fluorescent lamp will be equipped with old electromagnetic control gear. The replacement can be a retrofit or a conversion. A retrofit LED simply replaces a fluorescent lamp and the conventional starter is replaced with an LED starter[10] (Fig. 16.2). The existing control gear is not touched. In contrast, a conversion LED will require some rewiring of the luminaire. In both cases, retrofit and conversion, the re-insertion of a fluorescent lamp will be possible without any risk.

A second possible solution is to develop new luminaires for LED lamps. These could have traditional caps or even new cap-lampholder fits, which would not replace existing lighting installations. The 'fluorescent world' would be served by LED light sources, similar in shape, but with better performance, e.g. with a better light distribution through adapting the luminaire elements, compared with a retrofit or conversion LED.

As well as replacement of incandescent, halogen incandescent, compact fluorescent, self-ballasted compact fluorescent and linear fluorescent lamps, there are ways to replace some of the high-intensity discharge (HID) lamps. These lamps have cap-lampholder systems some of them are different from those used for non-HID lamps.

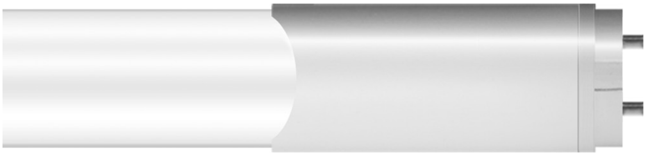

16.1 Double-capped LED lamp (retrofit).

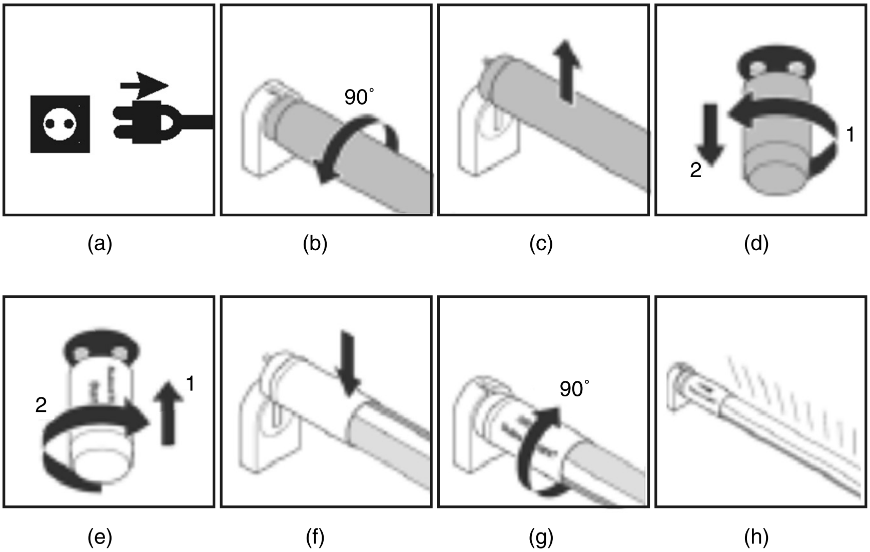

16.2 Replacing a fluorescent lamp with an LED lamp.[10]

16.4 Freedom of choice

16.4.1 Colour

The range of white LED chips has many more colours, or more accurately, the chromaticity coordinates, than those specified for traditional lamps. In this context, the term ‘bin’ is used;[11] a bin is like a basket that can be made bigger or smaller in order to include LEDs from different parts of the colour space. Binning usually encompasses luminous flux and forward voltage. Unlike, for example, halogen incandescent lamps where the filament temperature determines the colour and binning is not needed, a sorting procedure for LED chips is unavoidable at present. So, the ‘freedom’ of LED colour choice is also the economic necessity of selling those chips whose colour lies outside the tolerance range.

The terms ‘warm white’, ‘neutral white’ and ‘cold white’ describe three areas in the colour space. They are expressed by the correlated colour temperatures (CCTs), which are close to the target chromaticity coordinates and are well established for different lighting scenarios. For fluorescent lamps, people have been accustomed to choose CCTs between 2700 K and 6500 K, and the Planckian curve is cut by the Judd lines into pieces, all of the pieces being a kind of white (Table 16.2). Around these coordinates, ellipses of different sizes can be drawn, the bigger the ellipse, the greater the probability that variations in colour are perceived. Since, however, these are non-overlapping ellipses, there is always some place in between them (compared with the circumscribing rectangles) where

Table 16.2 Colour and chromaticity coordinates for fluorescent lamps[12]

Colour	Colour temperature, T_c (°C)	x	y
F 6500	6400	0.313	0.337
F 5000	5000	0.346	0.359
F 4000	4040	0.380	0.380
F 3500	3450	0.409	0.394
F 3000	2940	0.440	0.403
F 2700	2720	0.463	0.420

no colour is defined (Fig. 16.3). Will this choice of colours be followed by LED light sources? What is the criterion for following the traditional approach or using another approach?

LED products – lamps with traditional caps and modules – meet different customer requirements. For example, LED lamps with Edison caps are used in houses and the expectations of the end users are for lamps that provide a similar atmosphere as the traditional lamps. Therefore, the relevant standard for LED lamp performance, IEC 62612,[14] has the same CCTs and chromaticity coordinates as for fluorescent lamps.

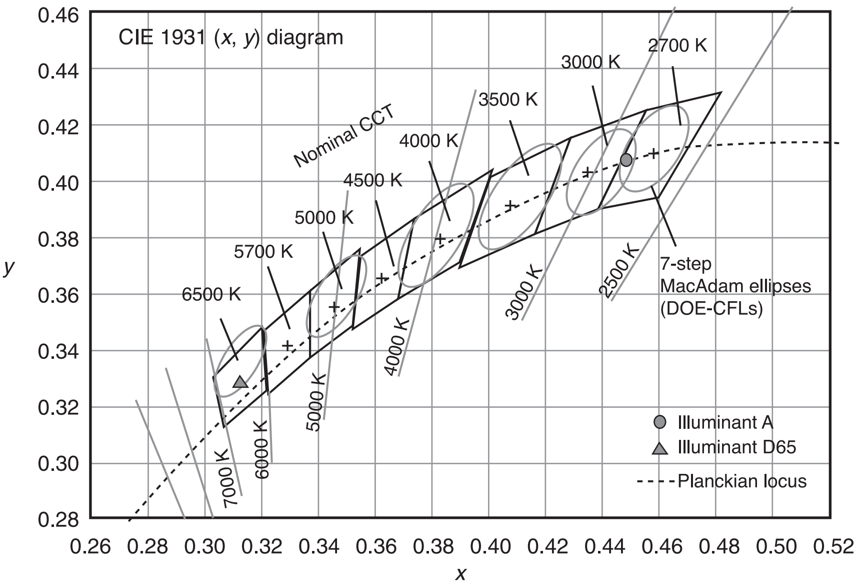

16.3 Tolerance areas in the colour space.[13]

LED modules can be used in many different luminaires and the purchase of a new luminaire comes with an expectation that the CCT may have changed. Therefore, the LED module standard[6] is not bound to the CCTs of CFLs and fluorescent lamps: 'This PAS applies to LED modules for which it is in most cases possible to choose a CCT value that best fulfils the requirement of a particular application. Standardised colour points are under consideration.' Nevertheless, the production, storage, logistics, advertising and sale of thousands of different LED modules with different CCTs is not economic. In the medium term, a consolidation of CCT variety is expected.

16.4.2 Lumen maintenance and t_p temperature

Claims for the lifetimes of LEDs are often of the order of 50 000 h or more. Nobody can verify this claim, since 50 000 h of continuous operation is equal to about 5 years. This span is longer than the development time of new LED products, which is of the order of 6 to 9 months. The LED standards therefore provide an approach that is different to whole LED lifetime tests. The IEC has accepted that instead of whole lifetime testing, the manufacturer's claim after a maximum of 6000 h or 25% of lifetime is tested. This is not a substitute for real lifetime testing, but the only way available to obtain reliable quality (if you do not want to make predictions). The idea is that the manufacturers know the behaviour of their products with regard to light emission over time. Depending on the material used for the LED, the lumen maintenance curve may not show a continuous decrease of light output; therefore, a simple linear extrapolation during the first 6000 h is not always feasible. The IEC LED standards classify the lumen maintenance of an LED based on its non-linear behaviour, without assigning 'good' or 'bad' to any class. An LED module may, for example, be in a low class at 6000 h, which means a relatively low luminous flux at that time, but subsequently there may be a significant increase in the lumen output. The lifetime of an incandescent lamp is limited by the thickness of the filament wire because tungsten is transported away from the filament, which in the end causes the filament to break; a similar steady lifetime-determining process over the whole lifetime has not yet been described for LEDs.

An LED's luminous flux and its development over time depend on the temperature at the junction and on the operating current. For determining an LED's lifetime, it is impractical to measure the junction temperature, t_c; instead the performance temperature, t_p, is used (the t_p point may be identical to the t_c point). At a fixed operating current, the lifetime varies with the temperature at the t_p point. The same LED product can be qualified for different t_p and lifetime pairs and manufacturers can choose to provide this data (Table 16.3). IECPAS 62717 takes this into account. The expectation is that a low t_p will correspond to a long lifetime and a high t_p to a short lifetime. This has been observed for different applications. For hot ambient conditions – such as in a tight luminaire or in a hot

Table 16.3 Template performance temperature and lifetime table[6]

Performance temperature, t_p (°C) measured at the t_p point	XX[a]	XX[a]	XX[a]
Rated lifetime (h)	XX XXX[a]	XX XXX[a]	XX XXX[a]

Note:[a] The values are provided by the LED module manufacturer.

climate – the lifetime indication will be short whereas for cold ambient conditions a long lifetime will be indicated.

16.5 Current and future trends

Forecasts on when and to what extent LED products will replace traditional light sources mostly show a sharply increasing trend – for example see the McKinsey report (Fig. 16.4).[9] Licht.de also provides a commercial and technical outlook.[15]

The realisation of this expectation is related to the speed and quality of LED development. New concepts for developing light sources have been supported by

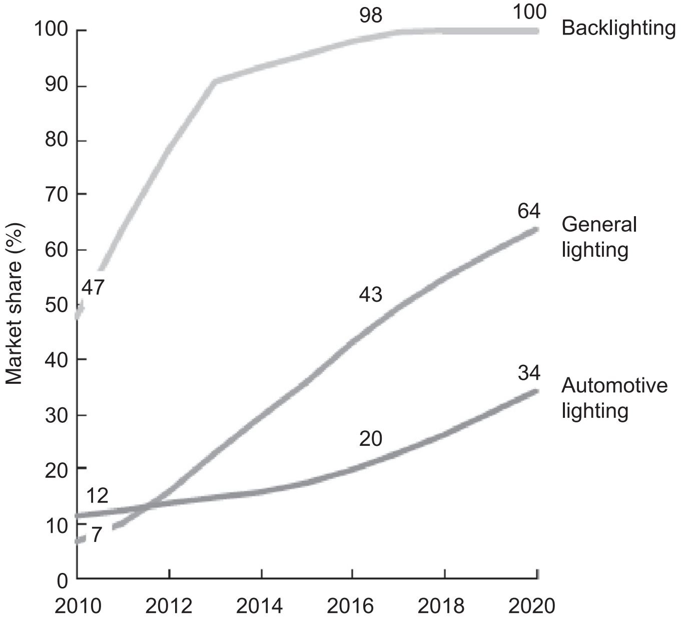

16.4 Value-based predictions of LED market share by sector.[9]

industry, in some respects by copying the electronics industry. The Zhaga consortium[7] brings together the traditional lighting industry with new players from the electronics sector. The rapid changes in LED production techniques often requires that some parts of a product are changed while other parts stay the same in order to minimise production effort and cost.

For the products developed by Zhaga, some parts of the light engine (which is roughly what the IEC calls the LED module) are kept constant while the tailored parts are connected via interfaces. The interfaces are described by electrical, mechanical, optical, geometrical and thermal requirements. By defining the interfaces, quick changes of the products carrying these interfaces are possible in the factory: the interfaces are kept constant, while the components behind change.

As well as the future technical solutions described above, which aim to make production smart, there is a biological view. Much effort is currently being expended to make efficient light sources, control gears and luminaires, though this is purely about efficiency, saving energy and reducing CO_2 emissions. However, the human factor is missing. Some years ago, a third type of photoreceptor was found in the human eye: these photoreceptors are not involved in using the eye as an instrument for seeing the world. Their function is to set the biological clock for the diurnal sleep pattern, along with the relevant physio-chemical activators. The actions of humans are determined by light, especially the effective part of the spectrum. Light solutions should take into account this non-visible effect of light.[16]

16.6 References

1 ZVEI, 2004, *Begriffe für LED – LED Definitions*. Available at: http://www.zvei.org/de/publikationen_veranstaltungen/publikationen_downloads/publikationen_der_fachverbaende/?no_cache=1&tx_ZVEIpubFachverbaende_pi1%5BrealId%5D=566.

2 IEC 60050-845/CIE 17.4, 1987, *International Electrotechnical Vocabulary – Lighting/International Lighting Vocabulary*.

3 IEC/TS 62504, 2011, *General Lighting – LEDs and LED Modules – Terms and Definitions*.

4 IESNA RP-16-10, *Nomenclature and Definitions for Illuminating Engineering*.

5 JELMA standard JEL 311, 2004, *General Requirements for Photometric Methods of White LEDs for General Lighting*.

6 IEC/PAS 62717, 2011, *LED Modules for General Lighting – Performance Requirements*.

7 Available at: www.zhagastandard.org.

8 UL 8750:2009, *Light Emitting Diode (LED) Equipment for Use in Lighting Products*.

9 McKinsey, 2011, *Lighting the Way – Perspectives on the Global Lighting Market*.

10 IEC 62776 (in preparation), *Double-Capped LED Lamps Designed to Retrofit Linear Fluorescent Lamps – Safety Specification*.

11 IEC/PAS 62707-1, 2011, *LED – Binning – Part 1: General Requirements and White Grid*.

12 IEC 60081, 1997, *Double-Capped Fluorescent Lamps – Performance Specifications*.

13 ANSI C78.377, 2008, *Specifications for the Chromaticity of Solid State Lighting Products*.

14 IEC/PAS 62612, 2009, *Self-Ballasted LED Lamps for General Lighting Services – Performance Requirements*.

15 licht.de, licht.wissen 17, *LED: The Light of the Future*. Available at: http://www.licht.de/fileadmin/shop-downloads/lichtwissen17_LED_Light_of_the_Future.pdf

16 licht.de:licht.wissen 19, *Impact of Light on Human Beings*. Available at: http://www.licht.de/fileadmin/shop-downloads/lichtwissen19_Impact_Light.pdf

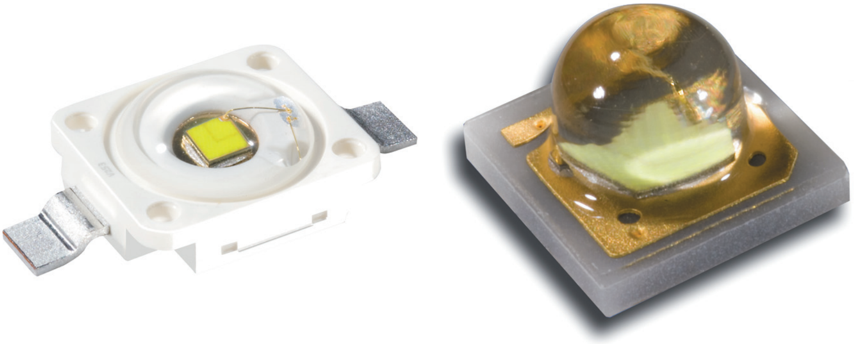

Plate XXXIV (Chapter 16) LED packages from OSRAM.

24V=
+
Tc
OSRAM
526
CM01E
<RoHS>
−
OSRAM
OSRAM
PARATH
230V · 6

Plate XXXV (Chapter 16) LED module versus LED lamp. Top: LED modules COINLight and Backlight from OSRAM. Bottom: LED lamp from OSRAM.

17

Ultraviolet LEDs

H. HIRAYAMA, RIKEN, Japan

DOI: 10.1533/9780857099303.3.497

Abstract: Advances in deep ultraviolet (DUV) light-emitting diodes (LEDs) fabricated using wide-bandgap AlGaN-based semiconductors are described. Crystal growth techniques for wide-bandgap AlN- and AlGaN-based semiconductors have been developed and used to produce 220–350 nm-band DUV-LEDs. Significant increases in internal quantum efficacy (IQE) have been achieved for AlGaN DUV emissions by developing low threading dislocation density (TDD) AlN buffer layers on sapphire substrates. The electron injection efficiency (EIE) of the LEDs was significantly increased by introducing a multi-quantum barrier (MQB). We discuss the increase in external quantum efficiency (EQE) of AlGaN DUV-LEDs achieved by improving the IQE, as well as the EIE and light extraction efficiency (LEE).

Key words: AlN, AlGaN, deep UV-LED, threading dislocation density, external quantum efficiency.

17.1 Research background of deep ultraviolet (DUV) LEDs

The development of semiconductor light sources operating in the deep ultraviolet (DUV) region, such as DUV light-emitting diodes (LEDs) and laser diodes (LDs), is quite an important subject because they are required for a wide variety of applications. Figure 17.1 summarizes the potential applications of high-efficiency DUV-LEDs and LDs. DUV-LEDs and DUV-LDs with emission wavelengths in the range of 230–350 nm are expected to be used in applications such as sterilization, water purification, medicine and biochemistry, and as light sources for high-density optical recording, white-light illumination, fluorescence analytical systems and related information sensing fields. They are also very important for air purification equipment and for zero-emission automobiles.[1,2]

The wavelength range between 260–280 nm is most suitable for sterilization or water purification with direct UV light. For UV purification using a titanium oxide (TiO_2) catalyst, the wavelength range between 320–380 nm is also useful. For white LED illumination using UV-LEDs with a mixture of RGB phosphors, wavelengths around 340 nm are considered to be most suitable, taking into account both the efficient absorption by the phosphors (<350 nm) and the high-efficiency wavelength range of AlGaN UV-LEDs. For sterilization and several kinds of optical sensing, DUV-LEDs can be useful even though the process efficiency is

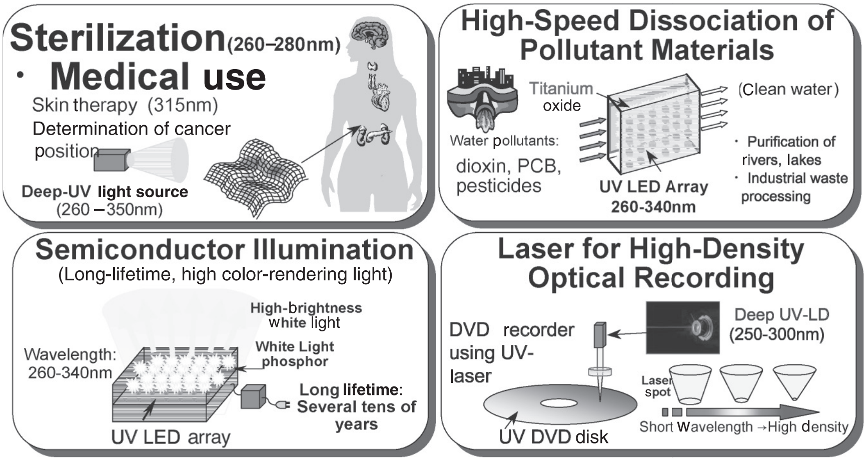
Sterilization(260–280nm)
· Medical use
Skin therapy (315nm)
Determination of cancer position
Deep-UV light source
(260 –350nm)
High-Speed Dissociation of Pollutant Materials
Titanium oxide
(Clean water)
Water pollutants:
dioxin, PCB, pesticides
UV LED Array
260-340nm
· Purification of rivers, lakes
· Industrial waste processing
Semiconductor Illumination
(Long-lifetime, high color-rendering light)
High-brightness white light
White Light phosphor
Wavelength:
260-340nm
Long lifetime:
Several tens of years
UV LED array
Laser for High-Density Optical Recording
DVD recorder using UV-laser
Deep UV-LD
(250-300nm)
Laser spot
UV DVD disk
Short Wavelength →High density

Other application fields:
- Sterilization, household air cleaners
- High speed purification of automobile exhaust gasses
- Optical sensing (luminescence analysis, surface analysis, UV sensing)
- Chemical and biochemical industry

17.1 Potential applications of deep ultraviolet (DUV) LEDs and LDs.

not very high. On the other hand, for LED lamps, the efficiency and output power are required to be quite high.

Because of their wide direct transition energy range in the UV, covering the region between 6.2 eV (AlN) and 3.4 eV, AlGaN and quaternary InAlGaN are attracting considerable attention as candidate materials for the realization of DUV-LEDs and DUV-LDs.[2] Figure 17.2 shows the relation between the direct transition bandgap energy and the lattice constant for the wurtzite (WZ) InAlGaN material system and the lasing wavelengths of various gas lasers. The main advantages of using AlGaN or InAlGaN for DUV light sources are: (1) the possibility of obtaining high-efficiency optical emission from quantum wells (QWs), (2) the possibility of producing both p- and n-type semiconductors in the wide-bandgap spectral region, (3) their physical properties, i.e. nitrides are mechanically hard and the devices have long lifetimes and (4) the fact that the materials are free from harmful arsenic, mercury and lead.[2]

Figure 17.3 shows the current status of the external quantum efficiency (EQE) of nitride UV-LEDs measured at room temperature (RT). Research into AlGaN-based UV-LEDs for wavelengths shorter than 360 nm, i.e., wavelengths of 330–355 nm,[3–5] was initiated by several research groups between 1996 and 1999. In the US, work on deep UV light sources is coordinated by DARPA's Semiconductor Ultraviolet Optical Sources (SUVOS) program. The group at the

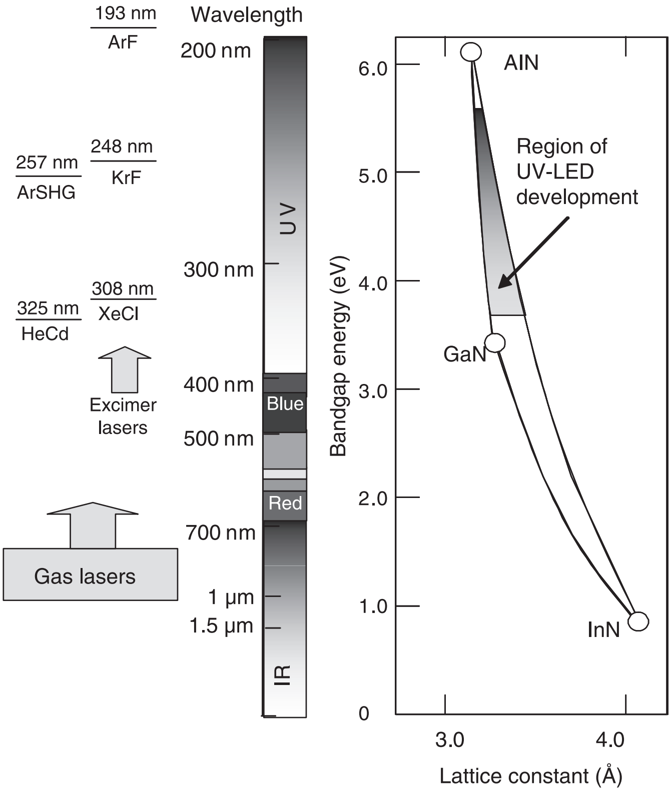

17.2 Relation between the direct transition bandgap energy and the lattice constant for the wurtzite (WZ) InAlGaN material system and the lasing wavelengths of various gas lasers.

University of South Carolina (USC) produced the first 250–280-nm AlGaN-based DUV-LEDs between 2002 and 2006.[6–8] In 2006, the group at NTT produced the shortest wavelength (210 nm) LED to date using an AlN emitting layer; however, the EQE was quite low (of the order of $2 \times 10^{-6}\%$) because they did not obtain sufficient electron-hole confinement or efficient carrier injection due to using the highest bandgap AlN emitter.[9]

We commenced research into AlGaN-based deep UV-LEDs in 1997. We produced the first efficient DUV (230 nm) photoluminescence (PL) from AlGaN QWs,[10] and a 333 nm AlGaN-QW UV-LED on SiC in 1999.[4] We have also developed high-efficiency UV-LEDs using quaternary InAlGaN-based QWs.[2,11,12] We have achieved a high internal quantum efficiency (IQE) of 47% for 338 nm quaternary InAlGaN QWs and demonstrated several milliwatts of continuous-wave (CW) operation with 340–350 nm InAlGaN-based UV-LEDs on GaN single-crystal substrates[13] and sapphire substrates.[14–15]

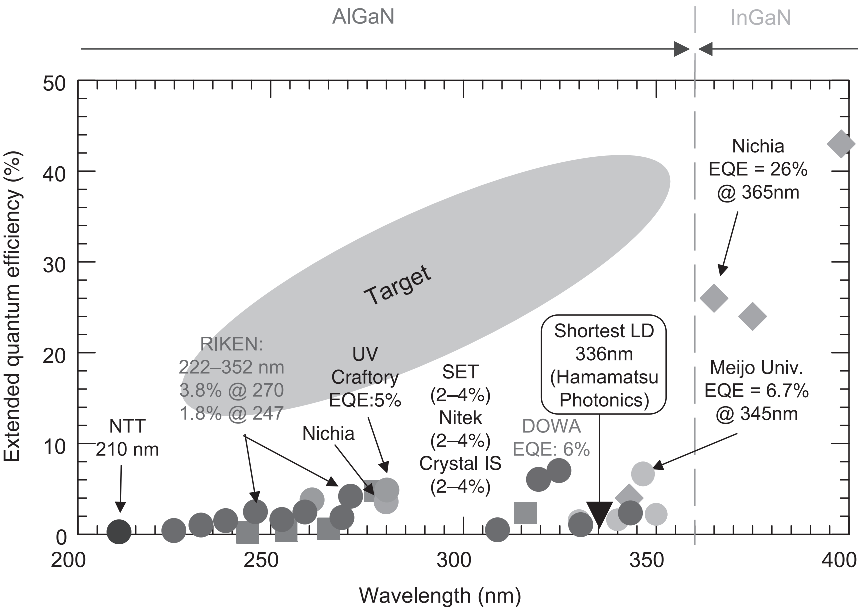

17.3 Current status of the external quantum efficiency (EQE) of nitride UV-LEDs measured at room temperature.

The development of AlGaN-based LEDs to obtain higher efficiency has recently become extremely competitive. We developed a new method for obtaining low threading dislocation density (TDD) AlN templates on sapphire substrates,[16] and achieved high IQE values (>60%) for AlGaN-QW DUV emission.[17] We also achieved high electron injection efficiencies (EIEs) using a multi-quantum barrier (MQB) design[18] and produced AlGaN- and InAlGaN-based DUV-LEDs with a wide emission range (222–351 nm) and high EQE (a maximum of 3.8%).[19–22] Sensor Electronic Technology (SET) have developed commercial DUV-LEDs with wavelengths of 240–360 nm.[23] Crystal IS have developed DUV-LEDs on AlN single-crystal substrates fabricated by a sublimation method.[24] The US companies, SET, Crystal IS and Nitek, developed high EQE (2–4%) DUV-LEDs with wavelengths of 260–280 nm during the period between 2009 and 2011.[23–26] Also, the Japanese companies, UV Craftory and Nichia, demonstrated EQEs of about 5% and 3% for DUV-LEDs in 2010.[27,28] The shortest wavelength achieved for a DUV-LD is 336 nm,[29] which was achieved by Hamamatsu Photonics.

The next targets in deep UV device research are to develop EQEs of several tens of percent for 220–350 nm DUV-LEDs and to achieve 250–330 nm DUV-LDs. However, the realization of high-EQE DUV-LEDs with wavelengths below 360 nm is still challenging, as shown in Fig. 17.3, because of some major problems.

The sudden drop in efficiency of DUV-LEDs below 360 nm is mainly due to the following three factors:

- The IQE of AlGaN is quite sensitive to the TDD.
- The hole concentration of p-AlGaN is quite low and the electron injection efficiency (EIE) is low.
- The light extraction efficiency (LEE) is low because of the absorption of UV light in p-GaN contact layers and in p-electrodes.

The development of low TDD AlN templates on sapphire substrates is very important, because the IQE of AlGaN QWs is as low as 1% if the QWs are fabricated on conventional AlGaN/AlN templates with a high TDD ($>2 \times 10^{10}$ cm^{-2}). We found that the IQE of an AlGaN QW can be increased to several tens of percent by reducing the TDD below 5×10^{8} cm^{-2}. In order to fabricate such a low TDD AlN template, innovative crystal growth techniques must be used. We achieved low TDD AlN templates by using an ammonia (NH_3) pulse-flow multilayer (ML) growth technique.[16] Using low TDD AlN templates, we obtained high-IQE (>60%) emission from AlGaN QWs.

To realize high-efficiency UV-LEDs and UV-LDs, quaternary InAlGaN with a few percent of indium is considered to be quite effective because efficient DUV emission can be obtained due to the indium-segregation effect.[11,12] The emission from a localized electron-hole pair in the indium-segregation region of quaternary InAlGaN is quite effective for obtaining a high IQE. Due to this effect, quaternary InAlGaN is very promising as the active layer of 200–350 nm band LDs and LEDs. The advantage of InAlGaN is that the emission efficiency of quaternary InAlGaN is less sensitive to the TDD due to the effect of localized carriers in the indium-segregation area.

The device properties of AlGaN DUV-LEDs strongly depend on the properties of the p-AlGaN. The hole concentration of p-AlGaN with high aluminum content (aluminum > 60%) is quite low (as low as 10^{14} cm^{-3}) due to its very deep acceptor level, which is reported to be 240 meV (GaN) to 670 meV (AlN). As a result, the EIE of a DUV-LED is reduced due to the leakage of electrons to the p-side layers. The high series resistance of p-type layers is also a problem for the device properties. We demonstrated that the leakage of electrons can be dramatically suppressed by reflecting the electrons using an MQB design.

Due to the lack of high-hole-density p-type AlGaN, we must use p-GaN contact layers. A p-GaN contact layer causes a significant reduction in LEE due to the strong absorption of UV light by the p-GaN layer. The value of LEE for a DUV-LED is typically below 10% due to absorption through the p-GaN contact layer, as well as the lack of a transparent p-type electrode or a highly reflective electrode that can be used in the DUV spectral region.

The current value of EQE for 270 nm DUV-LEDs from our group is approximately 4%, which is determined by 60% IQE, 80% EIE and 8% LEE. Further improvements in EQE are expected as we move toward the production of commercial DUV-LEDs. Techniques for increasing each of these efficiencies are described in the following sections.

17.2 Growth of low threading dislocation density (TDD) AlN layers on sapphire

In order to realize high-efficiency DUV-LEDs, it is necessary to develop a low TDD AlGaN/AlN template. The TDD of a conventional AlN buffer layer on a sapphire substrate, fabricated using a low-temperature (LT)-AlN buffer, was greater than 2×10^{10} cm^{-2}. On the other hand, a TDD of 10^8–10^9 cm^{-2} is required in order to obtain high IQE values of several tens of percent from AlGaN QWs. Several fabrication methods have been used to obtain high-quality AlN buffers; for example, the use of AlN/AlGaN superlattices (SLs) grown with alternating gas feeds,[6] AlGaN buffer layers deposited by epitaxial lateral overgrowth (ELO)[30] and a combination of GaN/AlN SLs and AlGaN produced by alternate source-feeding epitaxy (ASFE) on SiC.[31]

We grew AlN layers directly onto sapphire substrates at a high growth temperature after initial nitridation with NH_3. The growth temperature was around 1300 °C, and the V/III ratio was relatively low. Figure 17.4 shows the relation between the full width at half-maximum (FWHM) of X-ray diffraction (10–12) and (0002) ω-scan rocking curves (XRCs) and the nitridation time of AlN layers grown on sapphire

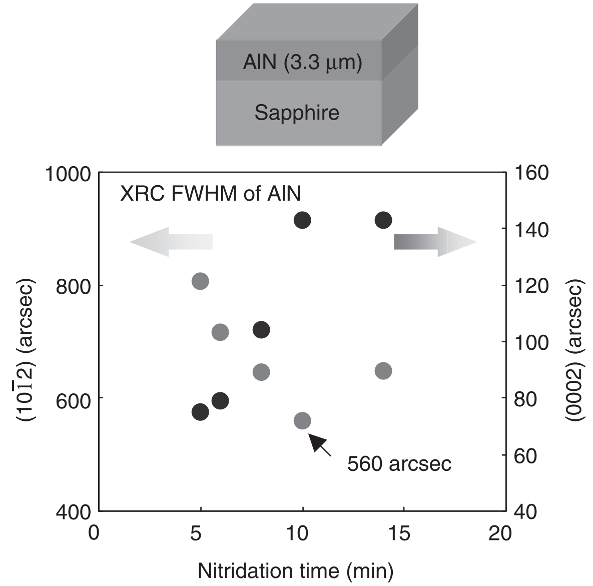

17.4 Full width at half maximum (FWHM) of X-ray diffraction (10-12) ω-scan rocking curves (XRC) for AlN layers grown on sapphire substrates as a function of initial nitridation time.

substrates. As the nitridation time increased from 5 to 10 min, the FWHM of (10–12) XRC reduced to 560 arcsec. The value of the FWHM of (10–12) XRC corresponds to the edge-type threading dislocation density. We found that larger AlN nuclei formed in the initial stages of the growth process with longer nitridation times, and that edge dislocations were reduced by embedding them in a thick AlN layer. However, heavy nitridation on sapphire caused an inversion from aluminum to nitrogen polarity, which led to the generation of abnormally large nuclei on the AlN surface. We also found that a long nitridation time led to cracks on the AlN surface.

It is necessary to satisfy several conditions to achieve high-quality AlGaN/AlN templates that can be used for DUV emitters, i.e., a low TDD, crack-free, atomically flat surfaces and stable aluminum (+c) polarity. We used an ammonia (NH_3) pulsed-flow multilayer (ML) growth method to fabricate AlN layers on sapphire. Figure 17.5 shows the gas flow sequence and a schematic view of the growth control method with pulsed- and continuous-flow gas feeding.

The samples were grown on sapphire (0001) substrates by low-pressure metal-organic chemical vapor deposition (LP-MOCVD). First, an AlN nucleation layer and a 'burying' AlN layer were deposited, both by NH_3 pulsed-flow growth. The trimethylaluminum (TMAl) flow was continuous during the NH_3 pulsed-flow sequence, as shown in Fig. 17.5. Low-TDD AlN can be achieved by promoting coalescence in the AlN nucleation layer. After the growth of the first AlN layer, the surface is still rough because of the low growth rate during the pulsed-flow mode. We added a high-growth-rate continuous-flow mode to reduce the surface roughness. By repeating the pulsed- and continuous-flow modes, we obtained a crack-free, thick AlN layer with an atomically flat surface. NH_3 pulsed-flow growth is effective for obtaining high-quality AlN because of the enhancement of precursor migration. Furthermore, it is effective for obtaining stable aluminum (+c) polarity, which is necessary for suppressing polarity inversion from aluminum to nitrogen, by maintaining aluminum-rich growth conditions.

As described above, we used three growth modes. The initial deposition, which fabricated an AlN nucleation layer, was through NH_3 pulsed-flow growth with a growth pressure of 200 Torr and a temperature of 1300 °C, with an average V/III ratio of approximately 60. Following this, migration enhancement epitaxy, which was used for the coalescence process, was performed using NH_3 pulsed-flow growth at 76 Torr and 1200 °C with an average V/III ratio of approximately 750. An AlN layer was then grown at a high rate using a conventional continuous flow process at 76 Torr and 1200 °C with a V/III ratio of approximately 25. The growth rates in the pulsed- and continuous-flow modes were approximately 0.6 and 6 μm/h, respectively.

The advantage of using ML-AlN for a DUV-LED is that a low TDD AlN can be obtained without the need for AlGaN layers, yielding a device structure with minimal DUV absorption. An AlGaN-free buffer is believed to be important for realizing sub-250 nm-band high-efficiency LEDs.

Figure 17.6 shows the FWHM of the X-ray diffraction (10–12) ω-scan rocking curves (XRC) for various stages of ML-AlN growth. The FWHM of XRC

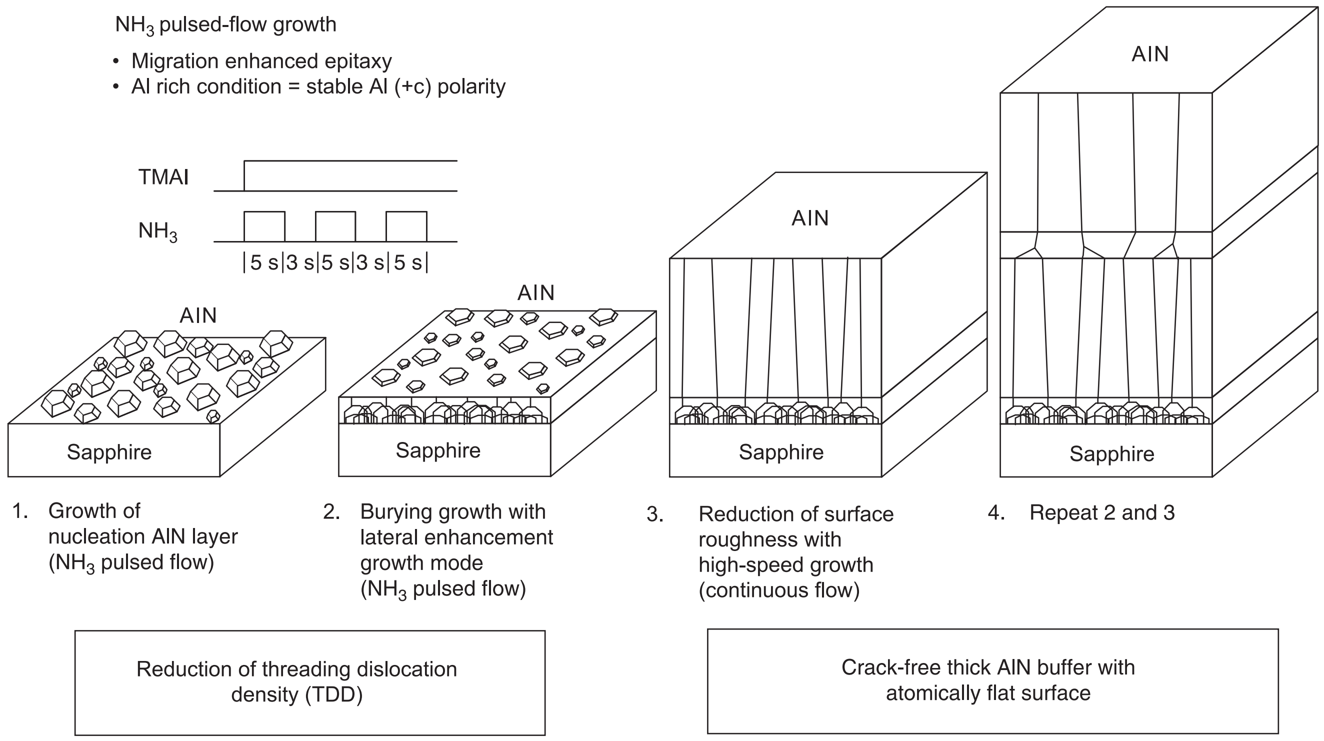
NH3 pulsed-flow growth
• Migration enhanced epitaxy
• Al rich condition = stable Al (+c) polarity
TMAl
NH3
|5 s|3 s|5 s|3 s|5 s|
AlN
Sapphire
AlN
Sapphire
AlN
Sapphire
AlN
Sapphire
1. Growth of nucleation AlN layer (NH3 pulsed flow)
2. Burying growth with lateral enhancement growth mode (NH3 pulsed flow)
3. Reduction of surface roughness with high-speed growth (continuous flow)
4. Repeat 2 and 3
Reduction of threading dislocation density (TDD)
Crack-free thick AlN buffer with atomically flat surface

17.5 Gas flow sequence and the growth control method used for an NH_3 pulsed-flow multilayer (ML)-AlN growth technique.

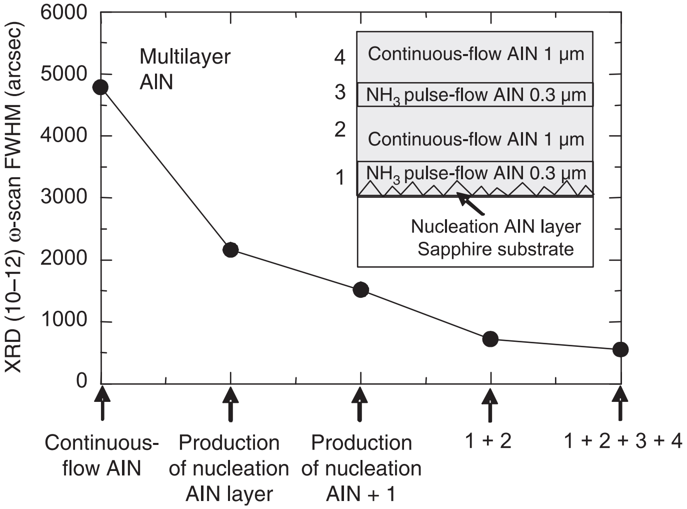

17.6 Reduction in the FWHM of the X-ray diffraction (10-12) ω-scan rocking curve (XRC) for various stages of ML-AlN growth.

(10–12) for AlN reduced from 2160 to 550 arcsec with two repetitions of the NH_3 pulsed-flow ML-AlN growth. Figure 17.7 shows atomic-force microscope (AFM) images of the surface of ML-AlN on sapphire after various stages of ML-AlN growth. We can observe that the surface was improved by growing multilayers of AlN and we can confirm that there was an atomically flat surface. The root mean square (RMS) of the surface roughness of the ML-AlN layer obtained from the AFM image was 0.16 nm.

Figure 17.8 shows (a) the schematic structure and (b) the cross-sectional transmission electron microscope (TEM) image of an AlGaN/AlN template with

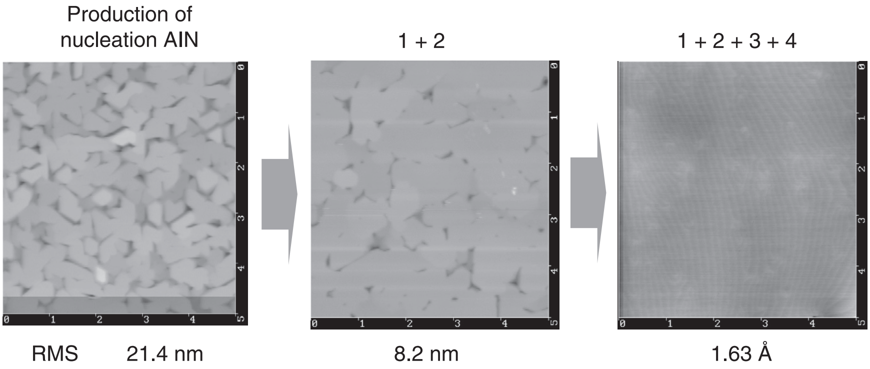

17.7 AFM images of the surface of ML-AlN with an area of $5 \times 5\,\mu m^2$ square after various stages of growth.

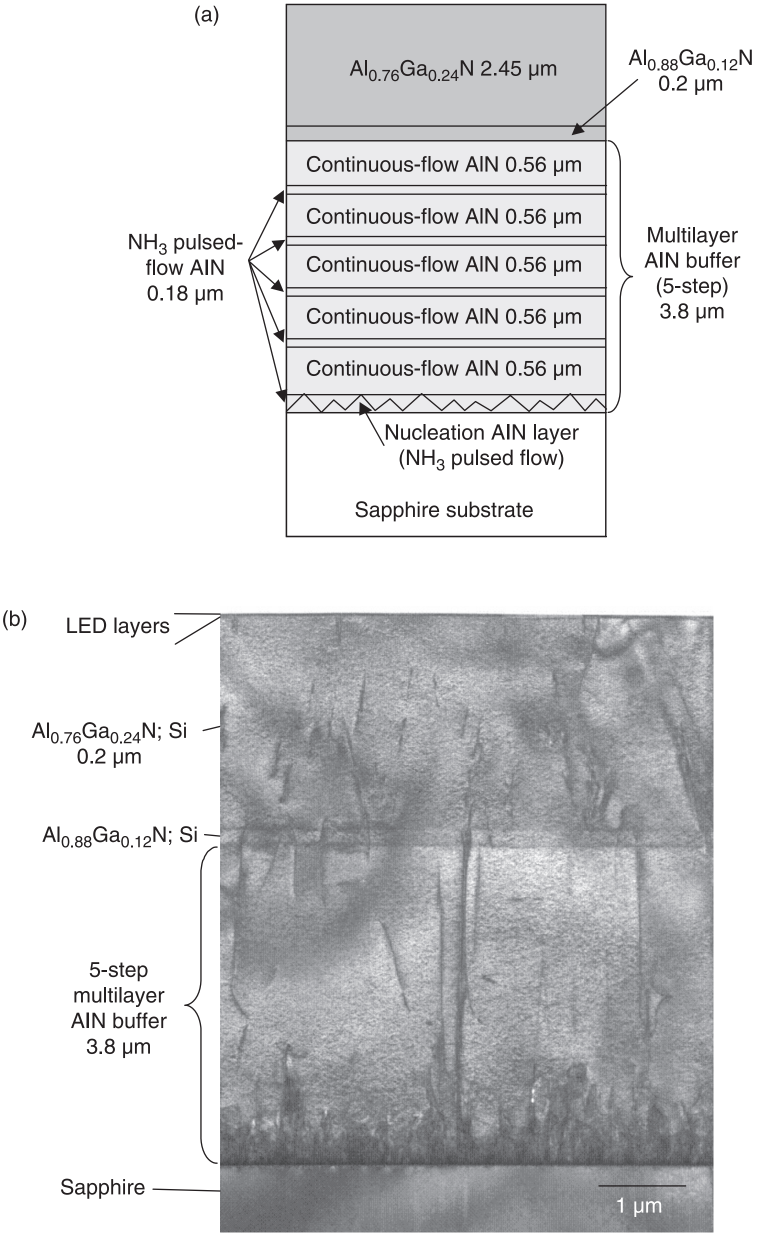
(a)
Al0.76Ga0.24N 2.45 μm
Al0.88Ga0.12N
0.2 μm
Continuous-flow AlN 0.56 μm
Continuous-flow AlN 0.56 μm
Continuous-flow AlN 0.56 μm
Continuous-flow AlN 0.56 μm
Continuous-flow AlN 0.56 μm
NH3 pulsed-
flow AlN
0.18 μm
Multilayer
AlN buffer
(5-step)
3.8 μm
Nucleation AlN layer
(NH3 pulsed flow)
Sapphire substrate
(b)
LED layers
Al0.76Ga0.24N; Si
0.2 μm
Al0.88Ga0.12N; Si
5-step
multilayer
AlN buffer
3.8 μm
Sapphire
1 μm

17.8 (a) Structure and (b) cross-sectional TEM image of an AlGaN/AlN template with a five-step ML-AlN buffer layer grown on a sapphire substrate.

a five-step ML-AlN buffer layer grown on a sapphire substrate. The total thickness of the ML-AlN buffer was typically 4 μm. The minimum values of the FWHM of the (0002) and (10–12) XRCs of the ML-AlN were approximately 150 and 250 arcsec, respectively. The minimum values of the edge- and screw-type dislocation densities of the ML-AlN were approximately 3×10^8 and 4×10^7 cm^{-2}, respectively, as measured from the cross-sectional TEM image.

17.3 Marked increases in internal quantum efficiency (IQE)

We observed a remarkable enhancement of the DUV emission of AlGaN QWs by fabricating them on low TDD AlN templates.[17] Figure 17.9 shows a cross-sectional TEM image of the quantum-well region of an AlGaN multi-quantum well (MQW) DUV-LED with an emission wavelength of 227 nm fabricated on a ML-AlN buffer. We used a thin quantum well to obtain a high IQE because it suppressed the effects of the polarization field in the well. This is believed to be particularly important for obtaining the atomically smooth hetero-interfaces that are necessary for a high IQE from such a thin QW. The atomically flat hetero-interfaces of the 1.3 nm-thick three-layer QWs are shown in the cross-sectional TEM image.

Figure 17.10 shows photoluminescence (PL) spectra of AlGaN QWs fabricated on ML-AlN templates with various values of XRC (10–12) FWHM, as measured at room temperature (RT). The peak emission wavelengths of the QWs were around 254 nm. The QWs were excited with a 244 nm argon-ion second harmonics

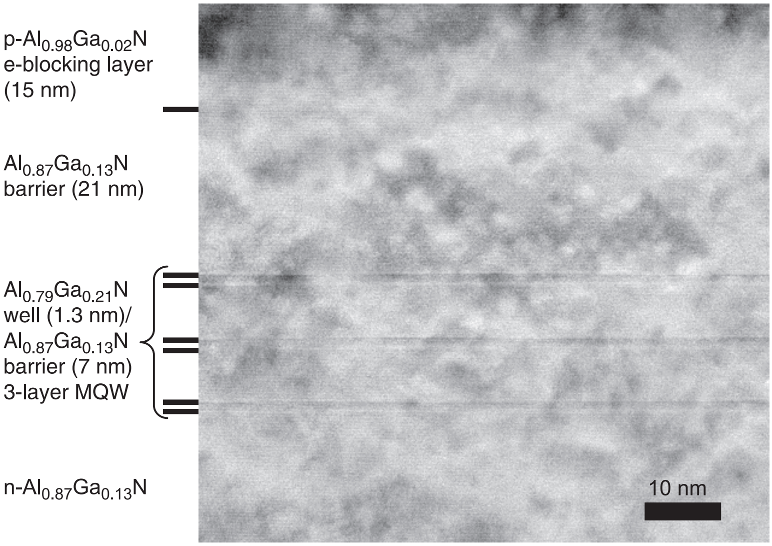
p-$Al_{0.98}Ga_{0.02}N$ e-blocking layer (15 nm)
$Al_{0.87}Ga_{0.13}N$ barrier (21 nm)
$Al_{0.79}Ga_{0.21}N$ well (1.3 nm)/ $Al_{0.87}Ga_{0.13}N$ barrier (7 nm) 3-layer MQW
n-$Al_{0.87}Ga_{0.13}N$
10 nm

17.9 Cross-sectional TEM image of the quantum well region of an AlGaN MQW DUV-LED.

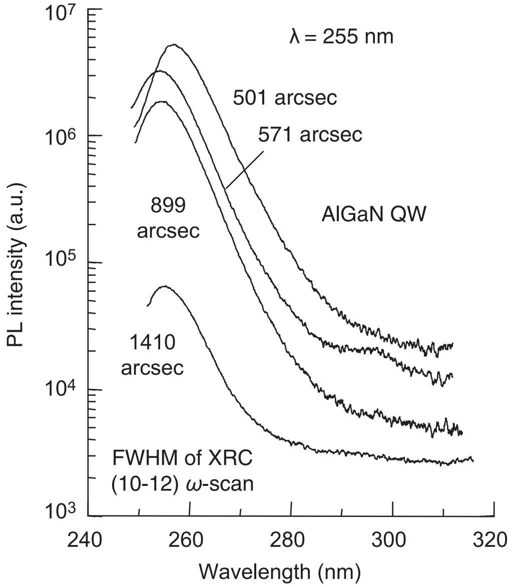

17.10 Photoluminescence (PL) spectra of AlGaN QWs on multilayer (ML) AlN templates with various values of XRC (10-12) FWHM.

generation (SHG) laser. The excitation power density was fixed at 200 W/cm^2. The PL emission intensity of the AlGaN QWs was significantly increased by improving the XRC (10–12) FWHM, as shown in Fig. 17.10. We can see from Fig. 17.10 that the emission efficiency of AlGaN depends strongly on the edge-type TDD.

Figure 17.11 shows the PL peak intensity as measured at RT for 254-nm-emission AlGaN QWs as a function of XRC (10–12) FWHM. The PL intensity increased by approximately 100 times by reducing the XRC (10–12) FWHM from 1400 to 500 arcsec. The PL intensity increased rapidly when the FWHM of the XRC was reduced to 500–800 arcsec. The rapid increase in the PL intensity can be explained by a reduction of the non-radiative recombination rate as the distance between threading dislocations becomes greater compared with the carrier diffusion length in the QW. We obtained a similar enhancement of the emission from AlGaN QWs with QWs of various wavelengths.

Figure 17.12 shows the temperature dependence of the integrated PL intensity measured for an AlGaN MQW with an emission wavelength at 288 nm fabricated on a ML-AlN template. The IQE can be roughly estimated from the temperature dependence of the integrated PL intensity if we assume that the non-radiative recombination rate is quite low at low temperature. The estimated IQE for the 288-nm-emission AlGaN QW was approximately 30% at RT.

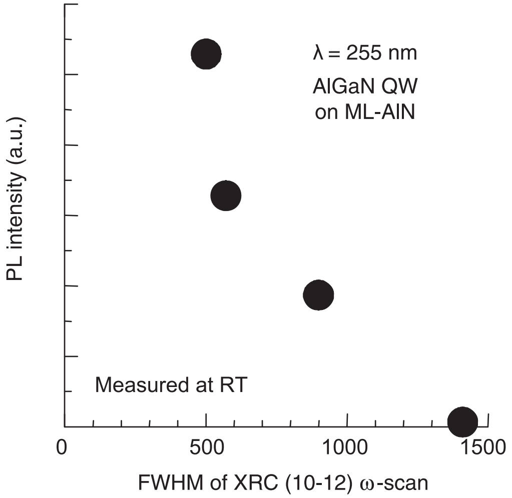

17.11 PL intensity of AlGaN QWs as a function of XRC (10-12) FWHM of AlGaN buffers.

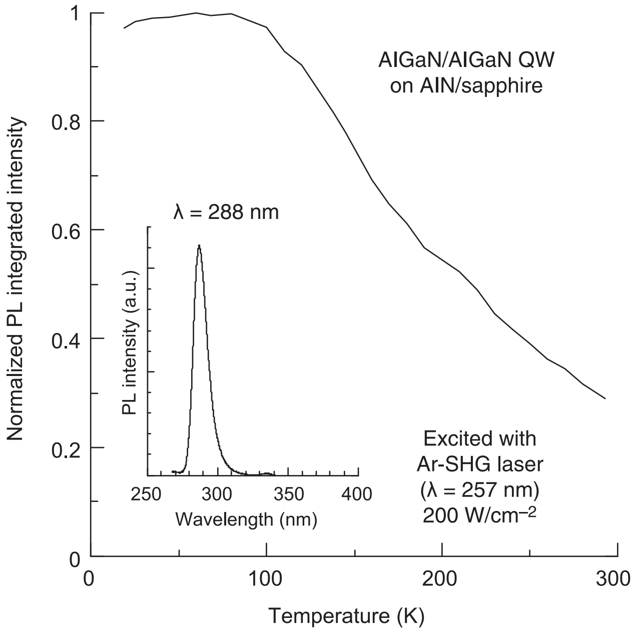

17.12 Temperature dependence of integrated PL intensity for an AlGaN three-layer MQW grown on a ML-AlN template.

The quaternary alloy InAlGaN is attracting considerable attention as a candidate material for realizing DUV-LEDs, since efficient UV emission as well as higher hole concentrations can be realized[2] due to indium-incorporation effects. The incorporation of a few percent of indium into AlGaN is considered to be quite effective for obtaining a high IQE, because efficient DUV emission can be obtained due to the indium-segregation effect,[11,12] which has already been investigated for the ternary InGaN alloy.

Figure 17.13 show a schematic image of a band diagram of a quaternary InAlGaN alloy with radiative recombination by localized carriers into the indium-segregation region, and a surface cathodoluminescence (CL) image obtained from a quaternary InAlGaN layer.[2] Emission fluctuations in the submicron region are clearly visible in the surface CL image. The dark spots in the bright area of the surface CL image were confirmed to correspond to the position of threading dislocations (TDs). The fluctuations in the emission are considered to be due to

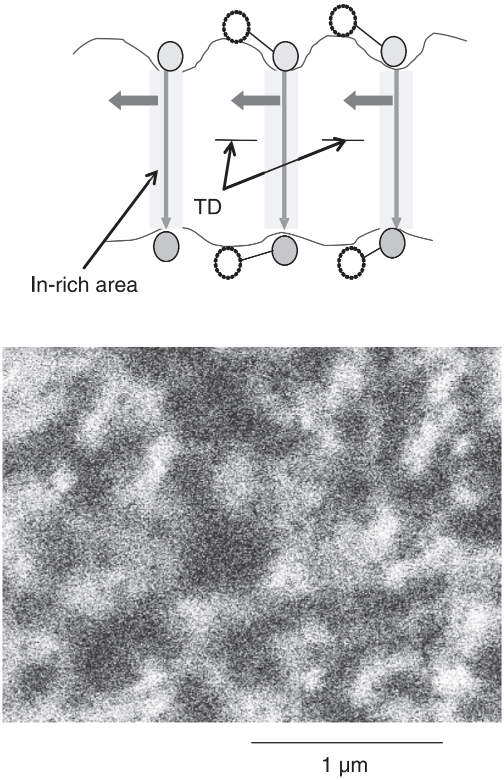

17.13 Band diagram of a quaternary InAlGaN alloy and radiative recombination by localized carriers into the indium-segregation region, and a surface cathodoluminescence (CL) image obtained from a quaternary InAlGaN layer.

carrier localization in the indium-segregation area. Surface CL images obtained for quaternary InAlGaN were very similar to those obtained for InGaN films. Electron-hole pairs localized in the low-potential valley emit before they are trapped in non-radiative centers induced by dislocations. Therefore, the advantage of indium incorporation is that the emission efficiency is less sensitive to the TDD.

Figure 17.14 shows the temperature dependence of the integrated PL intensity measured for an InAlGaN/InAlGaN MQW with an emission wavelength of

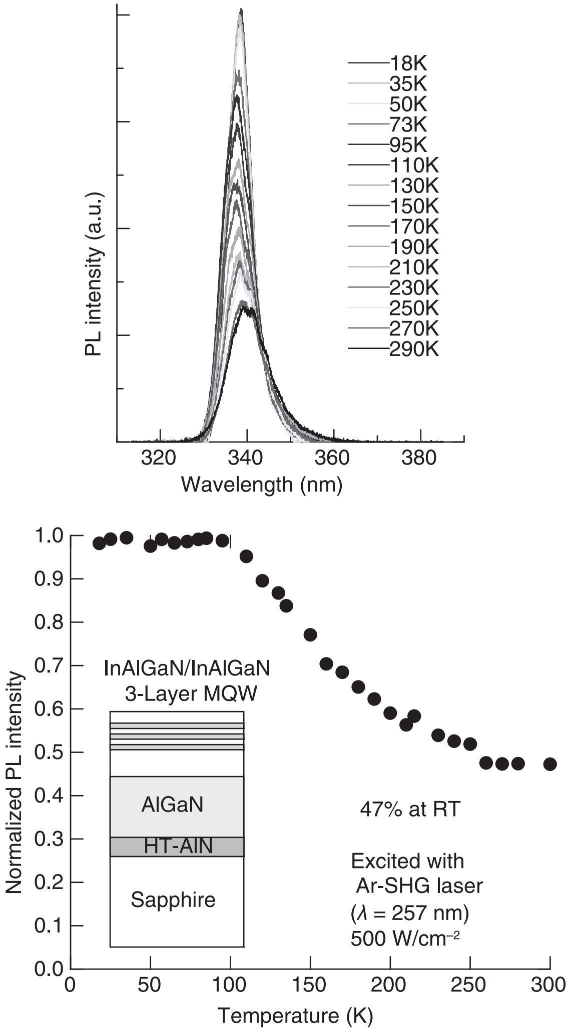

17.14 Temperature dependence of integrated PL intensity measured for an InAlGaN/InAlGaN MQW with an emission wavelength of 338 nm fabricated on a high-temperature (HT)-AlN buffer on sapphire.

338 nm fabricated on a high-temperature (HT)-AlN buffer on sapphire. The TDD of the HT-AlN was approximately $2 \times 10^{10}\,\mathrm{cm}^{-2}$. The estimated IQE from Fig. 17.14 was approximately 47% at RT. We found that a high IQE can be obtained for InAlGaN QWs in the wavelength range 310–380 nm, even when using a high TDD template.[2,11,12]

Then we took up the challenge of developing crystal growth to produce high-quality InAlGaN alloys emitting at the 'sterilization' wavelength (280 nm).[21] The crystal growth of high-aluminum-composition quaternary InAlGaN is relatively difficult, because indium incorporation becomes more difficult with increasing growth temperature, which is required to maintain the crystal quality of high-aluminum-content AlGaN. We achieved high-quality quaternary InAlGaN layers with high-aluminum-content (>45%) using epitaxy with a relatively low growth rate, i.e., 0.03 μm/h. The emission intensity of a 280 nm-band quaternary InAlGaN QW at RT increased by five times on reducing the growth rate from 0.05 to 0.03 μm/h.

Figure 17.15 shows the PL spectra of a quaternary InAlGaN QW measured at 77 K and at RT. We obtained extremely high intensity PL emission at RT. The ratio of the integrated intensity of the RT PL against the 77 K PL was 86%. Thus, high IQE was obtained from the quaternary InAlGaN-QW at RT. Figure 17.16 summarizes the wavelength dependence of the ratio of the integrated PL intensity (PL measured at RT against PL measured at low temperature – usually 10 K), which is directly related to the IQE. The IQE of 340 nm-band InAlGaN QWs is 30–50%, even with a high TDD template ($2 \times 10^{10}\,\mathrm{cm}^{-2}$). However, the IQE was

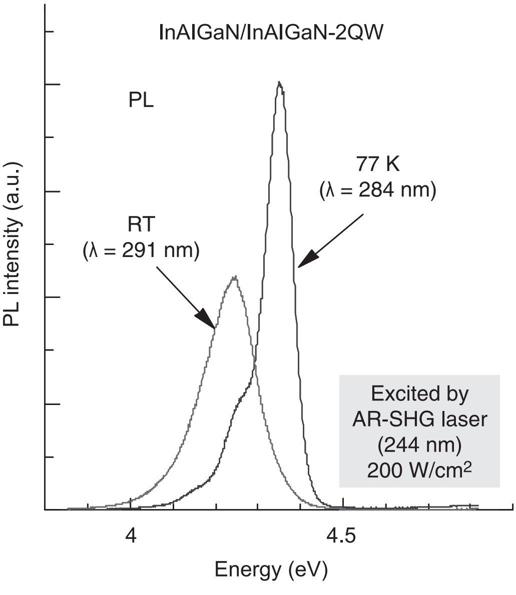

17.15 PL spectra of a quaternary InAlGaN QW measured at 77 K and at RT.

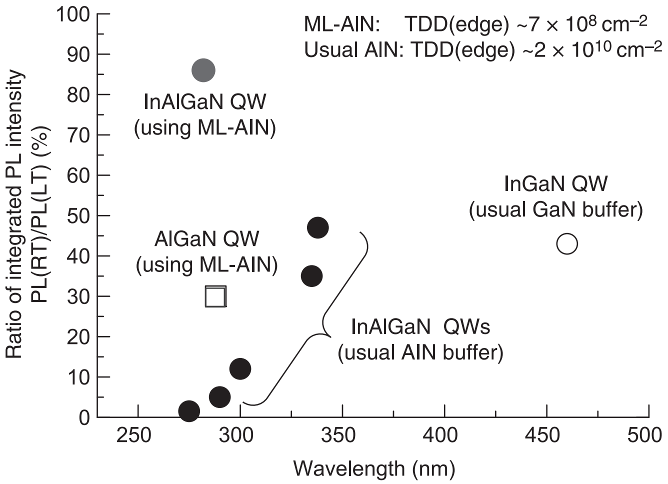

17.16 Wavelength dependence of the ratio of the integrated PL intensity (PL measured at RT against PL measured at low temperature).

below 2% for short-wavelength (280 nm) QWs. On the other hand, we achieved high values of IQE by fabricating QWs on low TDD ML-AlN templates. The ratios of the integrated PL intensity for 280 nm-band QWs were approximately 30% and 86% for an AlGaN QW and an InAlGaN QW, respectively.

17.4 Aluminum gallium nitride (AlGaN)-based DUV-LEDs fabricated on high-quality aluminum nitride (AlN)

AlGaN and quaternary InAlGaN DUV-LEDs were fabricated on low TDD ML-AlN templates.[16–22] Figure 17.17 shows a schematic of the structure and emission of an AlGaN-based DUV-LED fabricated on a sapphire substrate. Table 17.1 shows typical design values for the aluminum composition (x) in the $Al_xGa_{1-x}N$ wells, the buffer and barrier layers, and the electron-blocking layers (EBLs) that were used for the 222–273 nm AlGaN-MQW LEDs. High-aluminum-composition AlGaN layers were used to obtain short-wavelength DUV emissions. A typical LED structure consisted of an approximately 4-μm-thick undoped ML-AlN buffer layer grown on sapphire, a 2-μm-thick silicon-doped AlGaN buffer layer, followed by a three-layer undoped MQW region consisting of 1.3-nm-thick AlGaN wells and 7-nm-thick AlGaN barriers, a 20-nm-thick undoped AlGaN barrier, a 15-nm-thick magnesium-doped AlGaN EBL, a 10-nm-thick magnesium-doped AlGaN p-layer and an approximately 20-nm-thick magnesium-doped GaN contact layer. The quantum well thickness varied within the range 1.3–2 nm. Thin quantum wells are preferable for AlGaN QWs to suppress the effect of the large piezoelectric fields in

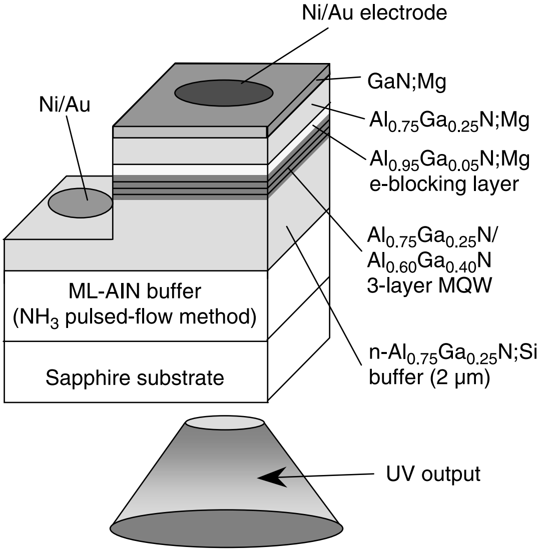
Ni/Au electrode
Ni/Au
GaN;Mg
$Al_{0.75}Ga_{0.25}N$;Mg
$Al_{0.95}Ga_{0.05}N$;Mg
e-blocking layer
$Al_{0.75}Ga_{0.25}N$/
$Al_{0.60}Ga_{0.40}N$
3-layer MQW
ML-AlN buffer
(NH_3 pulsed-flow method)
Sapphire substrate
n-$Al_{0.75}Ga_{0.25}N$;Si
buffer (2 µm)
UV output

17.17 AlGaN-based DUV LED fabricated on a sapphire substrate and UV emission.

Table 17.1 Typical design values for the aluminum composition (*x*) in $Al_xGa_{1-x}N$ wells, and buffer, barrier and electron-blocking layers (EBLs) for 222-273 nm AlGaN MQW LEDs

Wavelength (nm)	Well (*x*)	Barrier and buffer layers (*x*)	Electron blocking layer (*x*)
222	0.83	0.89	0.98
227	0.79	0.87	0.98
234	0.74	0.84	0.97
248	0.64	0.78	0.96
255	0.60	0.75	0.95
261	0.55	0.72	0.94
273	0.47	0.67	0.93

the well. Ni/Au electrodes were used for both the n-type and p-type electrodes. The typical size of the p-type electrode was $300 \times 300\,\mu m^2$. The output power that radiated into the back of the LED was measured using a silicon photodetector located behind the LED sample, which was calibrated to measure the luminous flux from LED sources using an integrated-spheres system. The LEDs were measured under bare wafer or flip-chip conditions. The forward voltages of the bare wafer and the flip-chip samples were 20–30 V and 7–10 V, respectively.

Figure 17.18 shows the electroluminescence (EL) spectra of the fabricated AlGaN and InAlGaN MQW LEDs with emission wavelengths of 222–351, all measured at room temperature (RT) with an injection current of around 50 mA. As

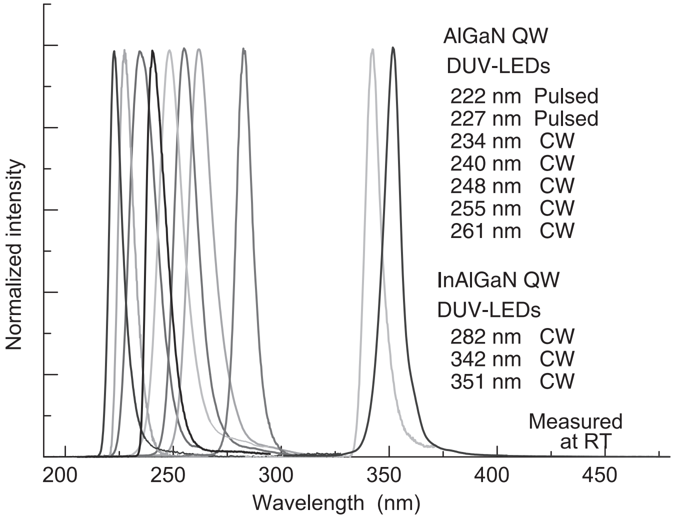

17.18 Electroluminescence (EL) spectra of fabricated AlGaN and InAlGaN MQW LEDs with emission wavelengths of 222–351 nm, all measured at room temperature (RT) with injection currents of around 50 mA.

can be seen, single-peak operation was obtained for each sample. The deep level emission was negligible for every LED.

Figure 17.19 shows the EL spectra of a 227 nm AlGaN LED on a log scale. We obtained single-peaked EL spectra, even for sub-230 nm wavelength LEDs. The

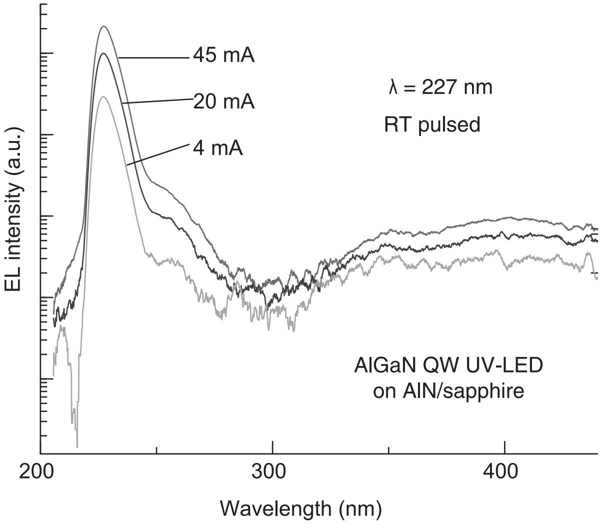

17.19 EL spectra on a log scale of a 227 nm AlGaN LED.

deep level emissions with wavelengths at around 255 and 330–450 nm were more than two orders of magnitude smaller than the main peak. These peaks may correspond to deep level emissions associated with magnesium-acceptors or other impurities. The output power of the 227 nm LED was 0.15 mW at an injection current of 30 mA, and the maximum EQE was 0.2% under RT pulsed operation. The pulse width and the repetition frequency were 3 μs and 10 kHz, respectively.

Figure 17.20 shows the EL spectra for various injection currents, and the current versus output power (I-L) and EQE (η_{ext}) characteristics for a 222 nm AlGaN MQW LED measured under RT pulsed operation. Single-peaked operation was realized: this is the shortest reported wavelength for an AlGaN LED on a

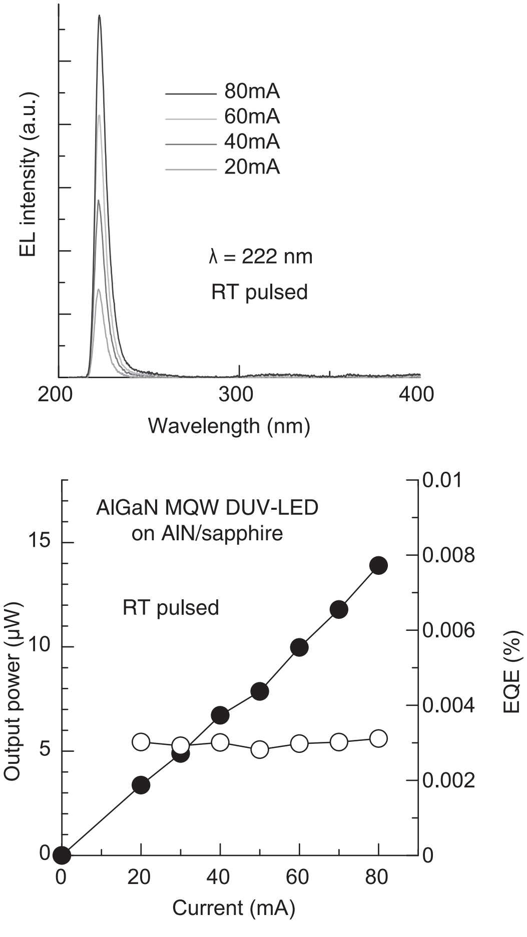

17.20 EL spectra for various injection currents, and current versus output power (I-L) and EQE (η_{ext}) characteristics for a 222 nm AlGaN MQW LED measured under RT pulsed operation.

sapphire substrate. The output power of the 222 nm LED was 14 μW at an injection current of 80 mA, and the maximum EQE was 0.003% under RT pulsed operation.

Figure 17.21 shows (a) current versus output power (I-L) and (b) current versus EQE (η_{ext}) for 250 nm-band AlGaN MQW LEDs under RT CW operation. We fabricated two types of samples with different aluminum compositions in the AlGaN EBLs, one at 90% and the other at 95%. The corresponding barrier heights of the EBLs in the conduction band were 280 meV and 420 meV, respectively. As seen in Fig. 17.21, the EQE of the LEDs was significantly increased with a higher electron-blocking height. This indicates that electron overflow is significantly reduced due to

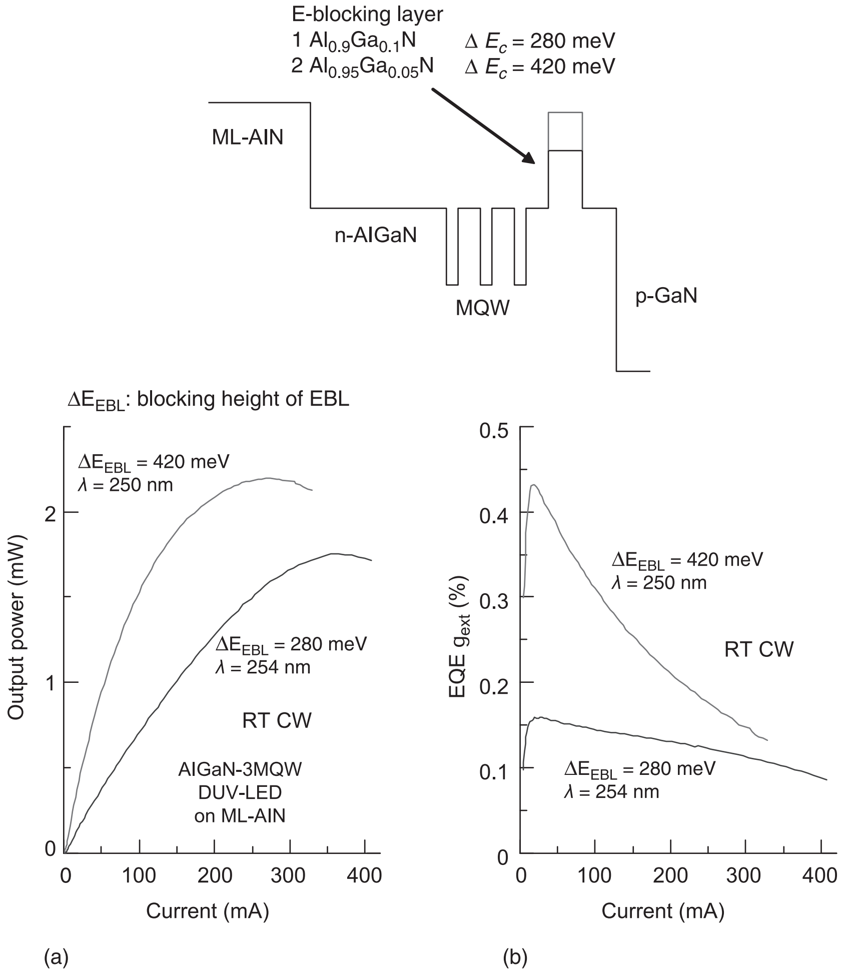

17.21 (a) Current versus output power (I-L) and (b) current versus EQE (η_{ext}) for 250 nm-band AlGaN-MQW LEDs under RT continuous-wave (CW) operation.

electron reflection by the EBL, and therefore the EIE into the QW is increased. The maximum output power and EQE were 2.2 mW and 0.43%, respectively, for an LED with an emission wavelength of 250 nm under RT CW operation.

Figure 17.22 shows the wavelength dependence of the output power of 245–260 nm AlGaN MQW LEDs, for various edge-type TDDs of the AlN templates and electron barrier heights of the EBLs. A marked increase in EQE was observed on reducing the TDD and increasing the EBL height. The EQE of the 250 nm-band LED increased from 0.02% to 0.4% and the output power increased by more than 30 times on reducing the TDD from 3×10^9 cm^{-2} to 7×10^8 cm^{-2}. We also found that a higher electron blocking height is effective for obtaining high output power.

Figure 17.23 shows the EL spectra of 225 nm-band AlGaN QW DUV-LEDs with various quantum well thicknesses, as measured under RT pulsed operation. The well thicknesses were in the range 1.6–4 nm. Intense emission was obtained for the thin QWs. From this experiment, we confirmed that thin quantum wells are suitable for AlGaN QWs because they suppress the effect of the large piezoelectric fields.

It has been reported that emission in the normal c-axis direction (vertical emission) is difficult to obtain from an AlN (0001) or a high-aluminum-content AlGaN surface, because the optical transition between the conduction band and the top of the valence band is mainly only allowed for light that has its electric

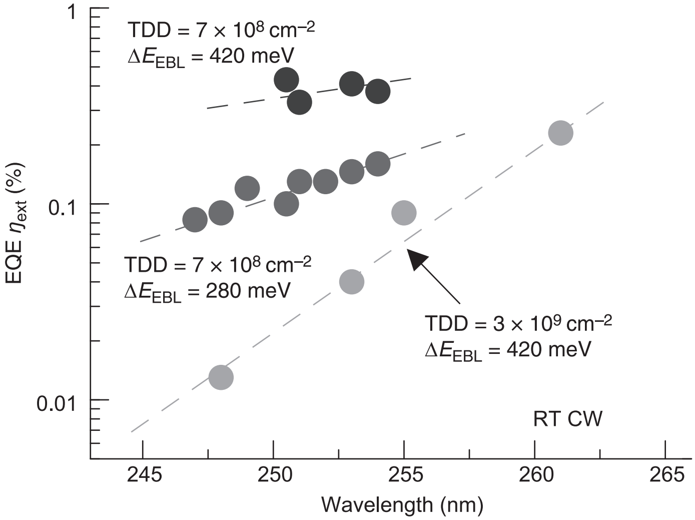

17.22 Wavelength dependence of EQE (η_{ext}) of 245–260 nm AlGaN MQW LEDs for various edge-type TDDs of the AlN template and electron barrier heights of the EBL.

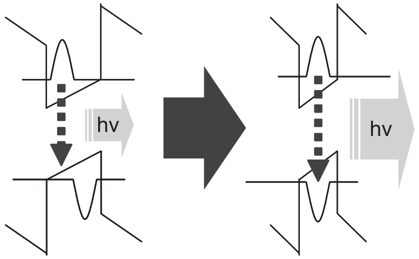

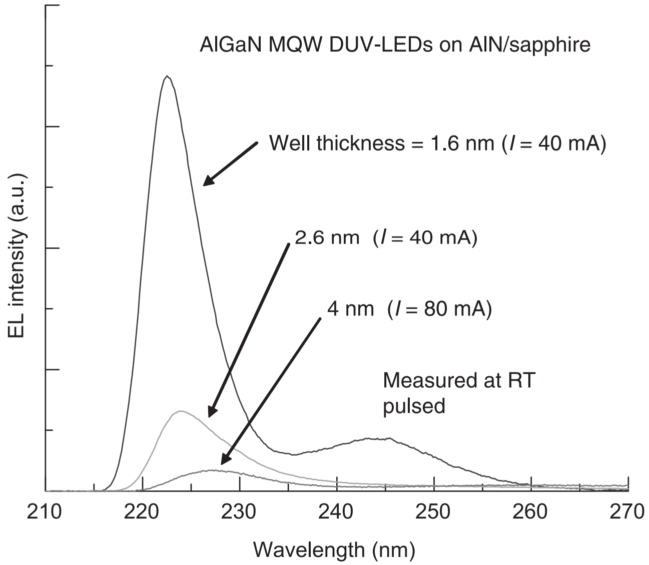

17.23 EL spectra of 225 nm-band AlGaN-QW DUV LEDs with various quantum well thicknesses, measured under RT pulsed operation.

field parallel to the c-axis direction of AlN (E//c).[7] The suppression of the vertical emission is a significant problem for AlGaN-based DUV-LEDs, because it results in a significant reduction in the light extraction efficiency. Several groups have reported that vertical c-axis emission is suppressed for high-aluminum content AlGaN QWs.[32,33] Banal *et al.* showed that the critical aluminum composition for polarization switching could be expanded to approximately 0.82 by using a very thin (1.3 nm) quantum well, when AlGaN-QW was fabricated on an AlN/sapphire template.[32]

Figure 17.24 shows the radiation angle dependence of the emission spectra of a 222 nm AlGaN QW LED on AlN/sapphire. We demonstrated that normal c-axis-direction emission (vertical emission) can be obtained for short-wavelength (222 nm) LEDs, even when the aluminum composition range of the AlGaN QW was as high as 83%.[20]

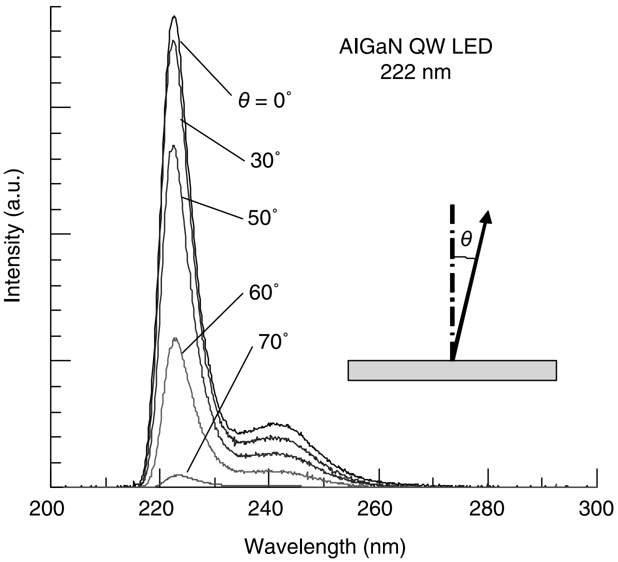

17.24 Radiation angle dependence of the emission spectra for a 222 nm AlGaN QW LED.

We fabricated quaternary InAlGaN-based DUV-LEDs to increase the IQE and EIE of DUV-LEDs. Figure 17.25 shows the schematic structure and a cross-sectional TEM image of an InAlGaN QW DUV-LED. We confirmed that the surface roughness of the InAlGaN layer was significantly improved by introducing

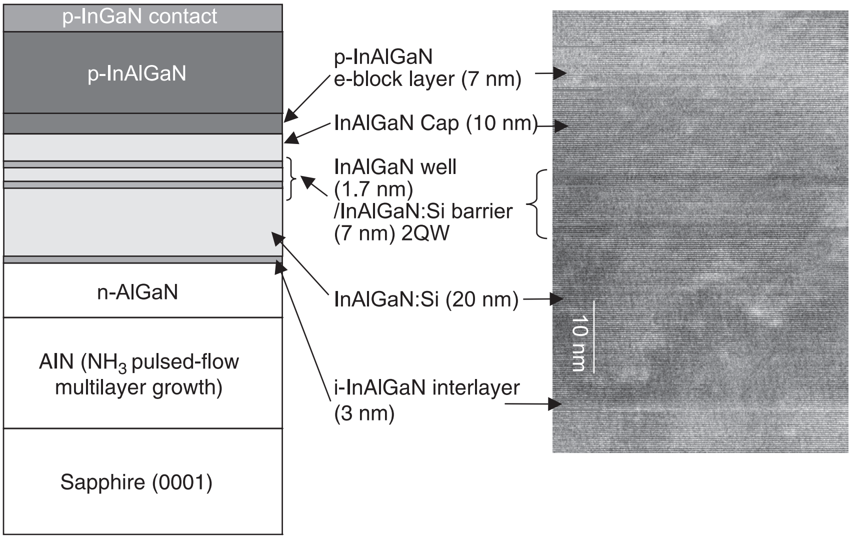
p-InGaN contact
p-InAlGaN
n-AlGaN
AlN (NH_3 pulsed-flow multilayer growth)
Sapphire (0001)
p-InAlGaN e-block layer (7 nm)
InAlGaN Cap (10 nm)
InAlGaN well (1.7 nm) /InAlGaN:Si barrier (7 nm) 2QW
InAlGaN:Si (20 nm)
i-InAlGaN interlayer (3 nm)
10 nm

17.25 Structure and cross-sectional TEM image of an InAlGaN QW DUV-LED.

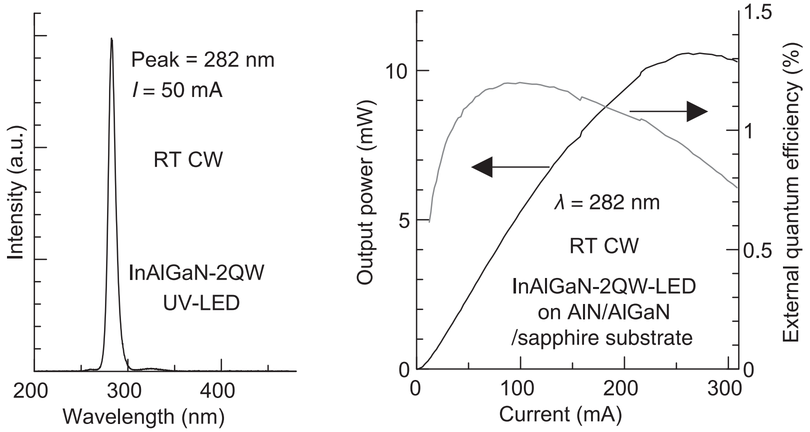

17.26 EL spectrum and current versus output power (I-L) and EQE of an InAlGaN-based QW DUV-LED with emission wavelength at 282 nm.

a silicon-doped InAlGaN buffer layer. The InAlGaN-based DUV-LED is considered to be attractive for achieving high EQE due to the higher IQE and higher hole concentration obtained by indium-segregation effects. Figure 17.26 shows the EL spectrum and the current versus output power (I-L) and EQE of an InAlGaN-based QW DUV-LED with an emission wavelength of 282 nm. The maximum output power and EQE were 10.6 mW and 1.2%, respectively, under RT CW operation. From these results, we found that quaternary InAlGaN QWs and p-type InAlGaN are quite useful for achieving high-efficiency DUV-LEDs.

17.5 Increase in electron injection efficiency (EIE) and light extraction efficiency (LEE)

High internal quantum efficiencies (IQEs) of 30–80% have been realized for AlGaN and InAlGaN quantum wells (QWs) with emission wavelengths of 220–350 nm.[17,21] The low EQE figures for AlGaN DUV-LEDs compared with those for InGaN blue LEDs are a result of low electron injection efficiency (EIE) into the QWs due to electron leakage caused by low hole concentrations in the p-type AlGaN layers, as well as inferior light extraction efficiencies (lower than 8%) due to strong UV absorption in the p-GaN contact layer and the p-side electrode. The EIEs for 250–280 nm-band AlGaN-based DUV-LEDs were roughly estimated to be 10–30% by numerical calculations.[2] We added a multi-quantum barrier (MQB) as an EBL in an AlGaN QW LED and consequently achieved a marked increase in EIE.[18]

Figure 17.27 shows a schematic image of the enhancement of electron injection efficiency caused by using an MQB in AlGaN DUV-LEDs. In order to obtain a high EIE, an EBL is effective for suppressing the overflow of electrons above the QW into the p-type AlGaN layers. A high barrier is required for an EBL in order

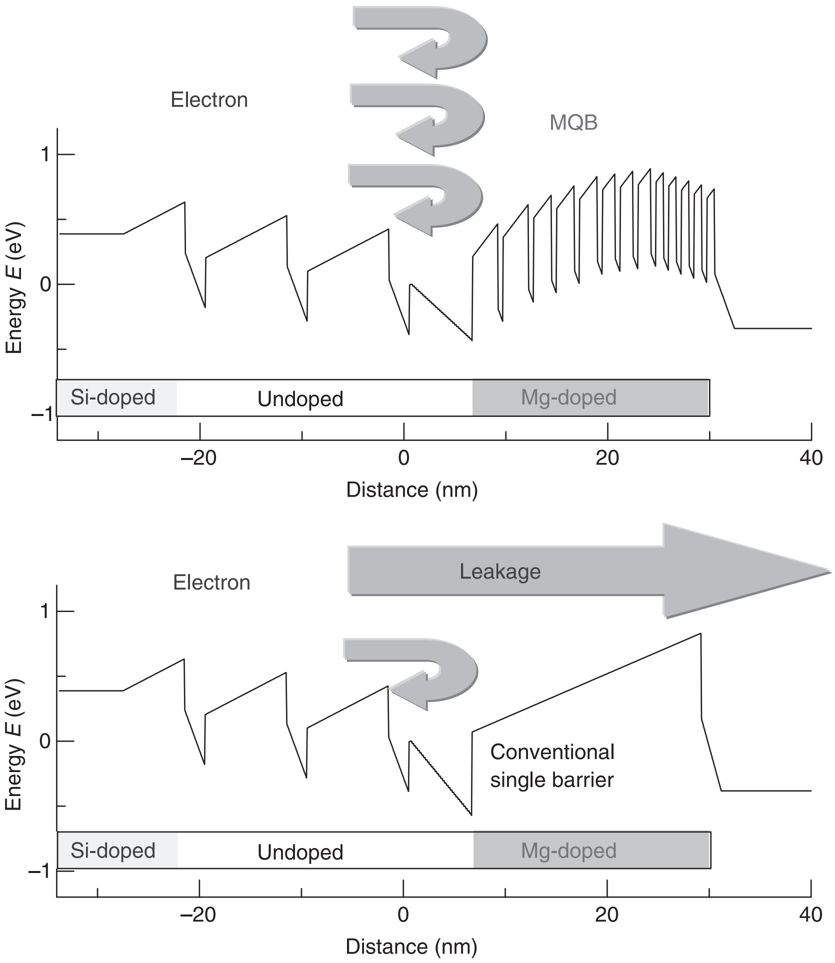
Electron
MQB
Energy E (eV)
1
0
−1
Si-doped
Undoped
Mg-doped
−20
0
20
40
Distance (nm)
Electron
Leakage
Energy E (eV)
1
0
−1
Conventional
single barrier
Si-doped
Undoped
Mg-doped
−20
0
20
40
Distance (nm)

17.27 Enhancement of electron injection efficiency by using an MQB in AlGaN DUV-LEDs.

to obtain a sufficiently high EIE. We tried using AlN or high-aluminum-composition (aluminum >0.95) AlGaN layers for the EBL;[18–21] however, the barrier height of these EBLs was still not sufficient to obtain the desired high EIE. Indeed, the EIE was particularly low for short-wavelength AlGaN LEDs (<250 nm), because the electron-barrier heights of the EBLs in these devices was low in relative terms. This material limitation can be overcome by enhancing the effective barrier height through the introduction of an MQB, which causes multi-reflection effects in the wave functions. The MQB was predicted theoretically by Iga *et al.* in 1986,[34] and the effects were demonstrated experimentally in GaInP/AlInP red laser diodes in 1991.[35] It has been reported that the effective electron barrier of an MQB in comparison with a bulk potential barrier is as much as 30% higher for GaAs/AlAs and 50% higher for GaInAs/InP MQBs. It is believed that AlN/AlGaN or AlGaN/AlGaN MQBs would be quite effective for increasing the effective barrier height of an EBL and, as a result, would contribute to the realization of high EQE AlGaN DUV-LEDs.

Figure 17.28 shows a conduction band diagram (right) and the electron transmittance (left) for an AlGaN/AlGaN MQB and a conventional single-barrier EBL calculated for a 250 nm-band AlGaN QW LED. The multi-reflection effects in the heterostructures were analyzed using a transfer-matrix method. It was shown that the effective electron barrier of an MQB in comparison with a conventional single-barrier EBL was as much as twice as high for an AlGaN/AlGaN MQB using barriers with thickness modulation.

Figure 17.29 shows the schematic structure and a cross-sectional TEM image of a fabricated 250 nm AlGaN QW DUV-LED with an MQB. We investigated an appropriate MQB structure experimentally for use with 250 nm-based DUV-LEDs. We found that the insertion of an initial thick barrier is important for reflecting lower-energy electrons. We also found that thin barriers contribute to the reflection of higher-energy electrons. The optimized MQB structure for a 250 nm AlGaN QW LED was a five-layer $Al_{0.95}Ga_{0.05}N/Al_{0.77}Ga_{0.23}N$ MQB with thicknesses of **7**/ 4/ **5.5**/ 4/ **4**/ 2.5/ **4**/ 2.5/ **4** nm, in which the bold letters are for the barriers and the normal letters are for valleys. The total thickness of the MQB should be less than 40 nm, because a coherent length exists for the multi-reflection effect of an MQB.

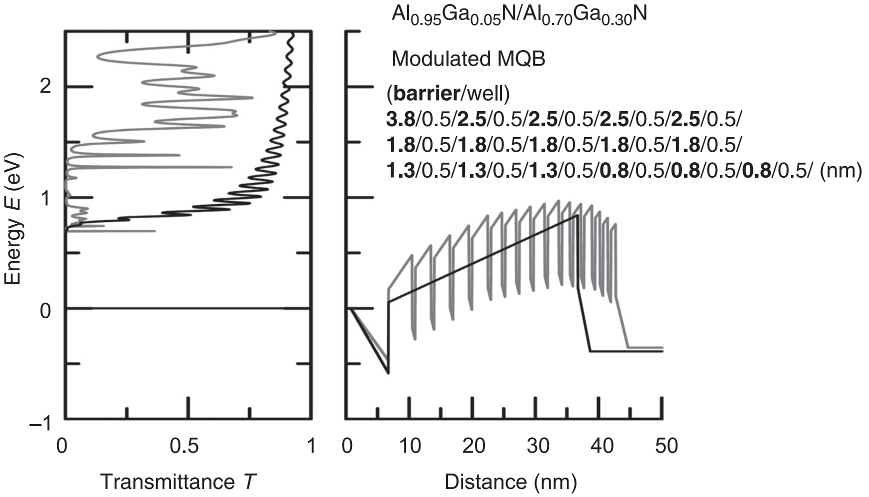

17.28 Conduction band diagram (right) and electron transmittance (left) of an AlGaN/AlGaN MQB and a conventional single-barrier EBL calculated for a 250 nm-band AlGaN QW LED.

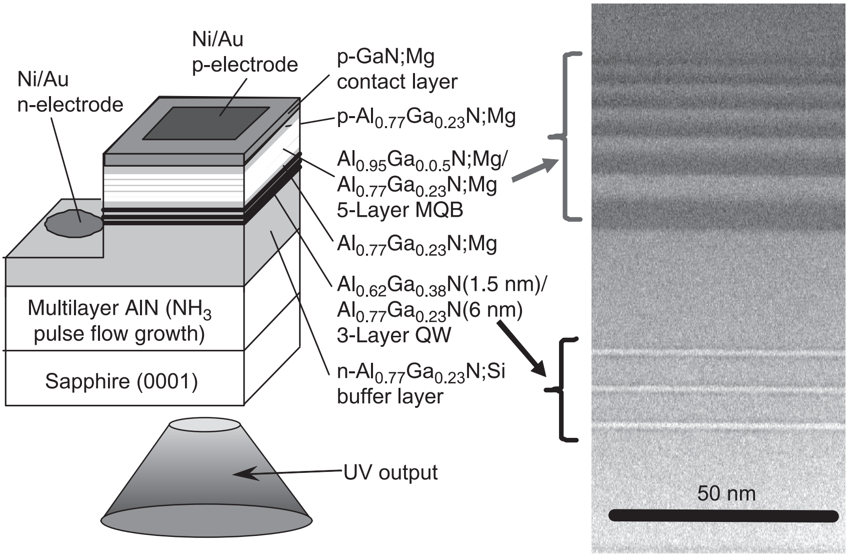
Ni/Au
p-electrode
Ni/Au
n-electrode
p-GaN;Mg
contact layer
p-$Al_{0.77}Ga_{0.23}N$;Mg
$Al_{0.95}Ga_{0.0.5}N$;Mg/
$Al_{0.77}Ga_{0.23}N$;Mg
5-Layer MQB
$Al_{0.77}Ga_{0.23}N$;Mg
$Al_{0.62}Ga_{0.38}N$(1.5 nm)/
$Al_{0.77}Ga_{0.23}N$(6 nm)
3-Layer QW
n-$Al_{0.77}Ga_{0.23}N$;Si
buffer layer
Multilayer AlN (NH_3
pulse flow growth)
Sapphire (0001)
UV output
50 nm

17.29 Structure and cross-sectional TEM image of 250 nm AlGaN DUV-LED with an MQB.

Figure 17.30 shows the current versus output power (I-L) and current versus EQE (η_{ext}) for a 250 nm AlGaN MQW LED with an MQB or a single EBL, both measured under RT CW operation. Significant increases in output power and EQE were observed when the single EBL was replaced by the MQB. The maximum

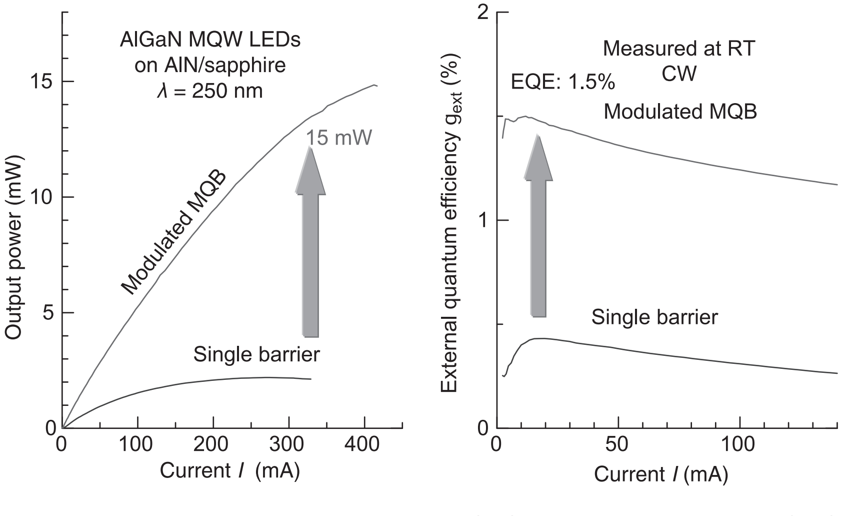

17.30 Current versus output power (I-L) and current versus EQE (η_{ext}) for 250 nm AlGaN MQW LEDs with an MQB and with a single EBL.

output powers of the 250 nm LED with the MQB and the single EBL were 15 mW and 2.2 mW, respectively. The EQE of a 250 nm LED increased by approximately four times with the introduction of the MQB. From Fig. 17.30, we estimated that the EIE of the 250 nm LED improved from approximately 25% to more than 80% by using the MQB.

Figure 17.31 shows the current versus output power (I-L) for a 237 nm AlGaN-MQW LED with an MQB or a single EBL, both measured under RT CW operation. The enhancement of the EIE with the MQW was found to be extremely high for short-wavelength DUV-LEDs. The output power of the LED increased by approximately 12 times when the single EBL was replaced by the MQB.

Figure 17.32 summarizes the wavelength dependence of the EQE of AlGaN DUV-LEDs with MQBs and single EBLs. The enhancement factors of the EQE by introducing the MQB are approximately 10, 4 and 3 times for 235, 250 and 270 nm AlGaN LEDs, respectively. Figure 17.33 shows the current versus output power (I-L) and the EQE (η_{ext}) for a high-output-power 270 nm AlGaN MQW LED with an MQB, as measured under RT CW operation. An output power of 33 mW was obtained for a bare-chip sample, which is the highest reported value to date. A much higher output power can be obtained with heat dissipation through a flip-chip geometry. The highest value of the EQE for a 270 nm AlGaN DUV-LED was 3.8% using a similar LED structure.[22]

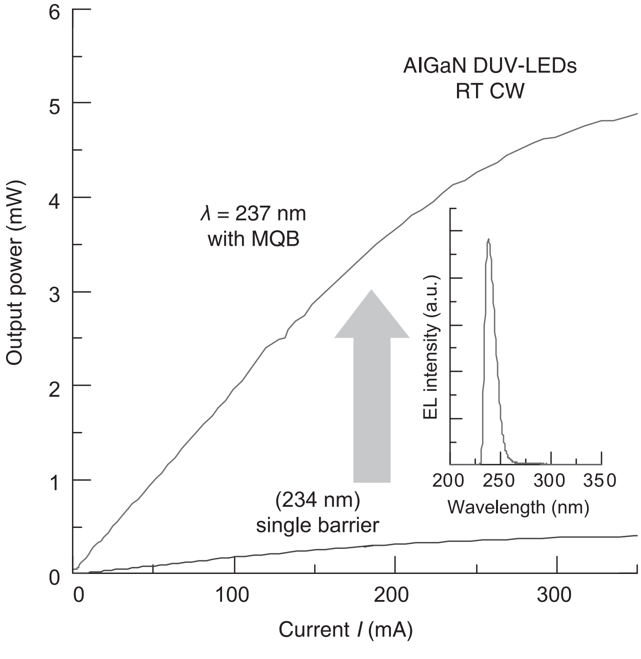

17.31 Current versus output power (I-L) for 237 nm AlGaN MQW LEDs with an MQB and with a single EBL.

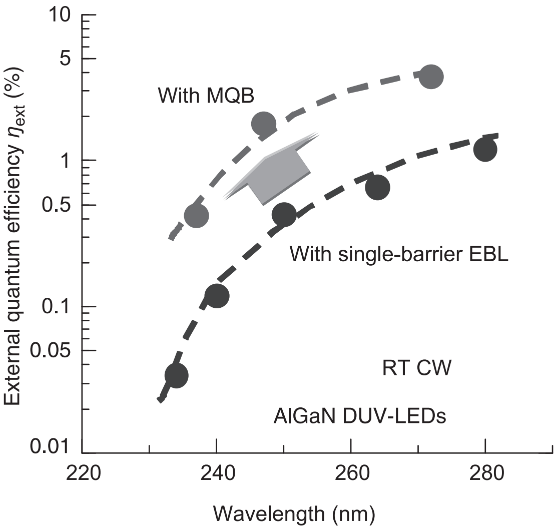

17.32 Wavelength dependence of EQE of AlGaN DUV-LEDs with MQBs and single EBLs.

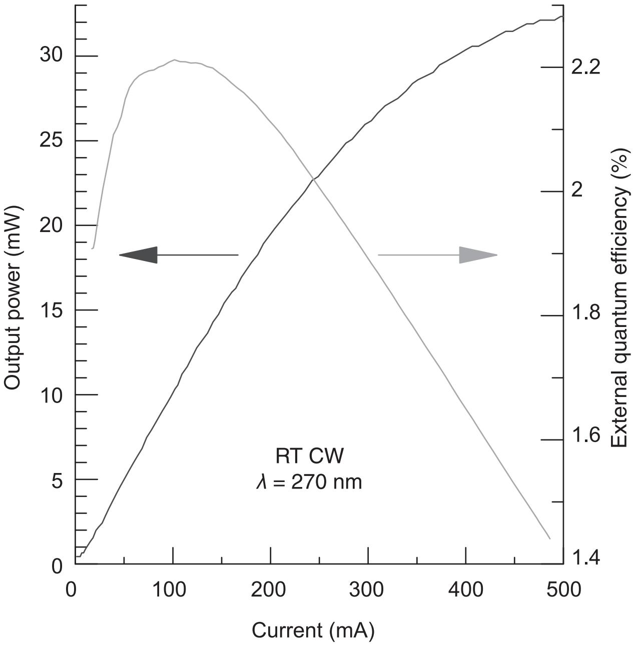

17.33 Current versus output power (I-L) and EQE (η_{ext}) for a high-output-power 270 nm AlGaN MQW LED with an MQB, measured under RT CW operation.

The improvement in the LEE of a DUV-LED is particularly important for the next research subject, because LEE is less than 10% for conventional AlGaN DUV-LEDs. The low LEE for AlGaN LEDs is caused by strong DUV absorption in the p-GaN contact layers and the p-side electrodes. A p-type AlGaN layer, which is expected to be a transparent contact layer, is not yet useful because the hole concentration of magnesium-doped AlGaN is quite low. The reflectance of Ni/Au p-electrodes is also low (approximately 25%). The reflectance of DUV by aluminum is 92%, but ohmic contacts are hard to obtain. Additionally, a transparent p-type electrode for AlGaN is yet to be developed. For these reasons, improvements in LEE for AlGaN DUV-LEDs are relatively difficult to obtain, although they have already been achieved for InGaN/GaN-based blue LEDs.

The LEE can be improved by using a thin p-GaN contact layer, which absorbs less DUV, as well as by using highly reflective aluminum-based electrodes. The LEE can also be enhanced by using photonic nano-structures, fabricated on the backside of the sapphire substrate or on the interface of the substrate and the AlN buffer layer.

Figure 17.34 is a schematic image of the improvement in the LEE of an AlGaN DUV-LED by using a thin p-GaN contact layer and an aluminum-based highly

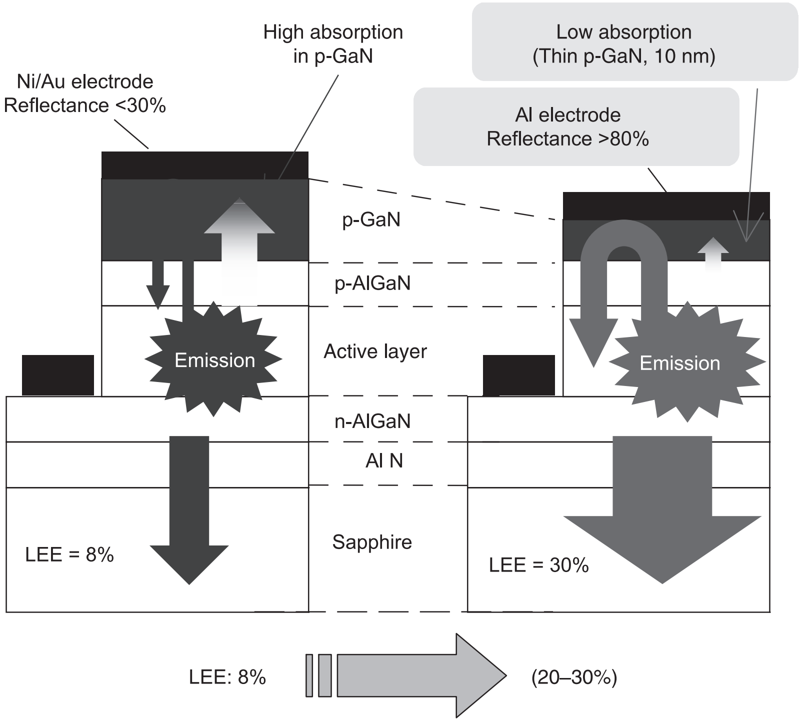
High absorption in p-GaN
Low absorption (Thin p-GaN, 10 nm)
Ni/Au electrode Reflectance <30%
Al electrode Reflectance >80%
p-GaN
p-AlGaN
Active layer
Emission
Emission
n-AlGaN
Al N
Sapphire
LEE = 8%
LEE = 30%
LEE: 8%
(20–30%)

17.34 Improvement of the LEE in an AlGaN DUV-LED using a thin p-GaN contact layer and an aluminum-based highly-reflective p-electrode.

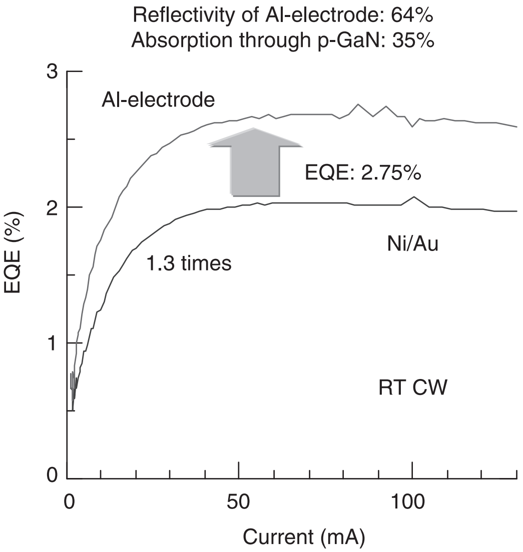

17.35 Enhancement of EQE for a 270 nm AlGaN LED by using thin p-GaN and a Ni/Al electrode.

reflective p-electrode. The LEE can be improved from 8% up to 20–30% by thinning the p-GaN contact layer to approximately 10 nm and by fabricating a highly reflective Ni/Al p-electrode. Ohmic contacts can be obtained by inserting a very thin (< 1 nm) nickel layer between the aluminum and the p-AlGaN. In the actual experiment, the reflectance of the p-type electrode was increased from 25% to 64% by replacing the usual Ni/Au by a Ni (1 nm)/Al (150 nm) electrode. Light absorption was reduced to about 50% by using a thin (about 30 nm) p-GaN contact layer. We obtained an ohmic contact on a p-electrode by using 33 nm of p-GaN and inserting about 1 nm of nickel. Figure 17.35 shows the enhancement of EQE for a 270 nm AlGaN LED by using thin p-GaN and a Ni/Al electrode. The EQE was approximately 1.3 times higher due to the enhancement of the LEE.

17.6 Conclusions and future trends

Figure 17.36 summarizes the maximum output power of AlGaN- and InAlGaN-based DUV-LEDs fabricated on low TDD ML-AlN templates by the RIKEN group[16–22] in the past five years. Between 2007 and 2011 we achieved significant increases in the EQE and output power of AlGaN and InAlGaN DUV-LEDs with emission wavelengths ranging from 222 nm to 351 nm by introducing low TDD AlN templates, InAlGaN emitting and p-type layers, and MQB electron-blocking layers. The maximum output power increased to 15–33 mW for 245–270 nm LEDs. We also obtained approximately 5 mW CW power for a 237 nm short

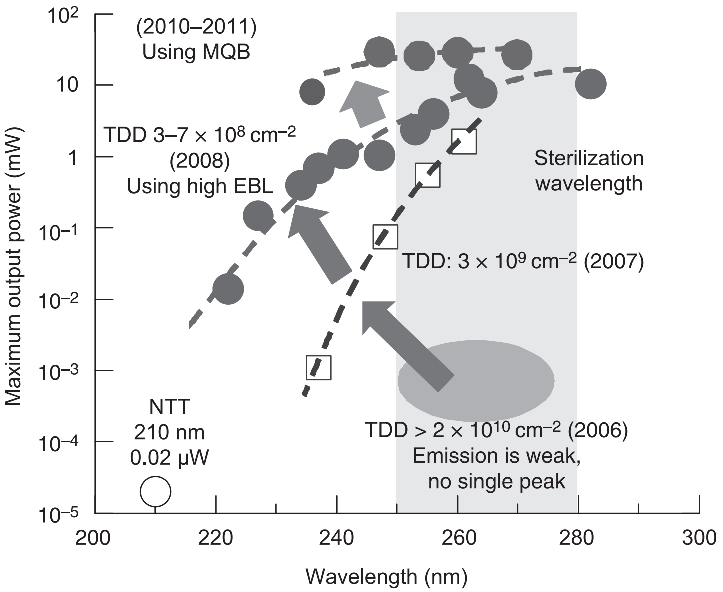

17.36 Maximum output power of AlGaN- and InAlGaN-based DUV-LEDs fabricated on low TDD ML-AlN templates by the RIKEN group[16–22] in the last five years.

wavelength LED. These achievements will contribute to accelerating the practical application of DUV-LEDs and to expanding them for a wide range of applications.

The EQE of AlGaN DUV-LEDs will be significantly increased by improving the IQE, EIE and LEE in the near future. The IQE for AlGaN QW DUV emission is expected to increase from 50% to more than 90% by reducing the TDD of the AlN templates from the current 3×10^8 cm^{-2} to 1×10^7 cm^{-2} by using an epitaxial lateral overgrowth (ELO) method or by using AlN single-crystal wafers. Quaternary InAlGaN emitting layers are also effective for increasing the IQE, as mentioned in Section 17.4.

A high EIE can be obtained by using an optimized MQB structure in AlGaN DUV-LEDs, as mentioned in Section 17.5. Further improvements in EIE (>90%) could be realized by increasing the hole concentration of p-type AlGaN, which is considered to be relatively difficult by the usual method.

The LEE could be significantly increased by replacing the p-GaN contacts with a transparent p-AlGaN layer, as well as by introducing a transparent p-type electrode. The achievement of a high hole concentration for AlGaN is difficult because the magnesium-acceptor level is very deep in AlGaN. This difficulty could be solved by introducing a co-doping technique. Co-doping of Mg-O, Mg-Si or C-O is considered to be effective for obtaining shallow acceptor levels, even in AlGaN semiconductors. If shallow acceptor levels are realized by using a co-doping technique, then the LEE could be improved to more than 60%, which has already been achieved for blue LEDs. Through these developments, the EQE of AlGaN DUV-LEDs is expected to improve by several tens of percent in the near future.

17.7 References

1 A. Zukauskas, M. S. Shue and R. Gaska, *Introduction to Solid-State Lighting*, Wiley and Sons Publishers, New York (2002).

2 H. Hirayama, 'Quaternary InAlGaN-based high-efficiency ultraviolet light-emitting diodes', *J. Appl. Phys.* **97**, 091101 1-19 (2005).

3 J. Han, M. H. Crawford, R. J. Shul, J. J. Figiel, M. Banas, *et al.*, 'AlGaN/GaN quantum well ultraviolet light emitting diodes', *Appl. Phys. Lett.* **73**, 1688–1690 (1998).

4 A. Kinoshita, H. Hirayama, M. Ainoya, A. Hirata and Y. Aoyagi, 'Room-temperature operation at 333 nm of $Al_{0.03}Ga_{0.97}N/Al_{0.25}Ga_{0.75}N$ quantum-well light emitting diodes with Mg-doped superlattice layers', *Appl. Phys. Lett.* **77**, 175–177 (2000).

5 T. Nishida, H. Saito and N. Kobayashi, 'Efficient and high-power AlGaN-based ultraviolet light-emitting diode grown on bulk GaN', *Appl. Phys. Lett.* **78**, 711–713 (2001).

6 W. H. Sun, V. Adivarahan, M. Shatalov, Y. Lee, S. Wu, J. W. Yang, *et al.*, 'Continuous wave milliwatt power AlGaN light emitting diodes as 280 nm', *Jpn. J. Appl. Phys.* **43**, L1419–L1421 (2004).

7 V. Adivarahan, S. Wu, J. P. Zhang, A. Chitnis, M. Shatalov, *et al.*, 'High-efficiency 269 nm emission deep ultraviolet light-emitting diodes', *Appl. Phys. Lett.* **84**, 4762–4764 (2004).

8 M. A. Khan, 'MOVPE of nitride UV emitters and detectors', *13th International Conference on Metal Organic Vapor Phase Epitaxy (ICMOVPE-XIII)*, 3, (2006).

9 Y. Taniyasu, M. Kasu and T. Makimoto, 'An aluminum nitride light-emitting diode with a wavelength of 210 nanometers', *Nature*, 444, 325–328 (2006).

10 H. Hirayama, Y. Enomoto, A. Kinoshita, A. Hirata and Y. Aoyagi, 'Efficient 230–280 nm emission from high-Al-content AlGaN-based multi-quantum wells', *Appl. Phys. Lett.* **80**, 37–39 (2002).

11 H. Hirayama, A. Kinoshita, T. Yamabi, Y. Enomoto, A. Hirata, *et al.*, 'Marked enhancement of 320–360 nm UV emission in quaternary $In_xAl_yGa_{1-x-y}N$ with In-segregation effect', *Appl. Phys. Lett.* **80**, 207–209 (2002).

12 H. Hirayama, Y. Enomoto, A. Kinoshita, A. Hirata and Y. Aoyagi, 'Room-temperature intense 320 nm-band UV emission from quaternary InAlGaN-based multi-quantum wells', *Appl. Phys. Lett.* **80**, 1589–1591 (2002).

13 H. Hirayama, K. Akita, T. Kyono, T. Nakamura and K. Ishibashi, 'High-efficiency 352 nm quaternary InAlGaN-based ultraviolet light-emitting diodes grown on GaN substrates', *Jpn. J. Appl. Phys.* **43**, L1241–L1243 (2004).

14 S. Fujikawa, T. Takano, Y. Kondo and H. Hirayama, 'Realization of 340-nm-band high-output-power (7 mW) InAlGaN quantum well ultraviolet light-emitting diode with p-type InAlGaN', *Jpn. J. Appl. Phys.* **47**, 2941–2944 (2008).

15 S. Fujikawa, T. Takano, Y. Kondo and H. Hirayama, '340 nm-band high-power InAlGaN quantum well ultraviolet light-emitting diode using p-type InAlGaN layers', *Phys. Stat. Sol. (c)* **5**, 2280–2282 (2008).

16 H. Hirayama, T. Yatabe, N. Noguchi, T. Ohashi and N. Kamata, '231–261 nm AlGaN

deep-ultraviolet light-emitting diodes fabricated on AlN multilayer buffers grown by ammonia pulse-flow method on sapphire', *Appl. Phys. Lett.* **91**, 071901 1–3 (2007).

17 H. Hirayama, T. Yatabe, T. Ohashi and N. Kamata, 'Remarkable enhancement of 254–280 nm deep ultraviolet emission from AlGaN quantum wells by using high-quality AlN buffer on sapphire', *Phys. Stat. Sol. (c)* **5**, 2283–2285 (2008).

18 H. Hirayama, Y. Tsukada, T. Maeda and N. Kamata, 'Marked enhancement in the efficiency of deep-ultraviolet AlGaN light-emitting diodes by using a multiquantum-barrier electron blocking layer', *Appl. Phys. Express* **3**, 031002 (2010).

19 H. Hirayama, N. Noguchi, T. Yatabe and N. Kamata, '227 nm AlGaN light-emitting diode with 0.15 mW output power realized using thin quantum well and AlN buffer with reduced threading dislocation density', *Appl. Phys. Express*, **1**, 051101 1–3 (2008).

20 H. Hirayama, N. Noguchi and N. Kamata, '222 nm deep-ultraviolet AlGaN quantum well light-emitting diode with vertical emission properties', *Appl. Phys. Express*, **3**, 032102 (2010).

21 H. Hirayama, N. Noguchi, S. Fujikawa, J. Norimatsu, T. Takano, *et al.*, '222–282 nm AlGaN and InAlGaN based high-efficiency deep-UV-LEDs fabricated on high-quality AlN on sapphire', *Phys. Status Solidi (a)*, **206**, 1176–1182 (2009).

22 S. Fujikawa, H. Hirayama and N. Maeda, 'High-efficiency AlGaN deep-UV LEDs fabricated on a- and m-axis oriented c-plane sapphire substrates', *Phys. Status Solidi (c)*, **9**, 3–4, 790–793 (2012).

23 M. Shatalov, W. Sun, Y. Bilenko, A. Sattu, X. Hu, *et al.*, 'Large chip high power deep ultraviolet light-emitting diodes', *Appl. Phys. Express* **3**, 062101 (2010).

24 J. R. Grandusky, S. R. Gibb, M. C. Mendrick, C. Moe, M. Wraback, *et al.*, 'High output power from 260 nm pseudomorphic ultraviolet light emitting diodes with improved thermal performance', *Appl. Phys. Express* **4**, 082101 (2011).

25 V. Adivarahan, A. Heidari, B. Zhang, Q. Fareed, S. Hwang, *et al.*, '280 nm deep ultraviolet light emitting diode lamp with an AlGaN multiple quantum well active region', *Appl. Phys. Express* **2**, 102101 (2009).

26 S. Hwang, D. Morgan, A. Keslar, M. Lachab. B. Zhang, *et al.*, '276 nm substrate-free flip-chip AlGaN light-emitting diodes', *Appl. Phys. Express* **4**, 032102 (2011).

27 C. Pernot, M. Kim, S. Fukahori, T. Inazu, T. Fujita, *et al.*, 'Improved efficiency of 255–280 nm AlGaN-based light-emitting diodes', *Appl. Phys. Express* **3**, 061004 (2010).

28 A. Fujioka, T. Misaki, T. Murayama, Y. Narukawa and T. Mukai, 'Improvement in output power of 280-nm deep ultraviolet light-emitting diode by using AlGaN multi quantum wells', *Appl. Phys. Express* **3**, 041001 (2010).

29 H. Yoshida, Y. Yamashita, M. Kuwabara and H. Kan, 'Demonstration of an ultraviolet 336 nm AlGaN multiple-quantum-well laser diode', *Appl. Phys. Lett.* **93**, 241106 1–3 (2008).

30 K. Iida, T. Kawashima, A. Miyazaki, H. Kasugai, A. Mishima, *et al.*, '350.9 nm UV laser diode grown on low-dislocation-density AlGaN', *Jpn. J. Appl. Phys.* **43**, 4A, L499–L451 (2004).

31 T. Takano, Y. Narita, A. Horiuchi and H. Kawanishi, 'Room-temperature deep-ultraviolet lasing at 241.5 nm of AlGaN multi-quantum-well laser', *Appl. Phys. Lett.*, **84**, 3567–3569 (2004).

32 R. G. Banal, M. Funato and Y. Kawakami, 'Optical anisotropy in [0001]-oriented AlGaN/AlN quantum well ($x > 0.69$)', *Phys. Rev. B* **79** (2009) 121308(R).

33 H. Kawanishi, M. Senuma, M. Yamamoto, E. Niikura, and T. Nukui, 'Extremely weak

surface emission from (0001) c-plane AlGaN multiple quantum well structure in deep-ultraviolet spectral region', *Appl. Phys. Lett.* **89** (2006) 081121.

34 K. Iga, H. Uenohara and F. Koyama, 'Electron reflectance of multiquantum barrier (MQB)', *Electron. Lett.* **22** (1986) 1008.

35 K. Kishino, A. Kikuchi, Y. Kaneko and I. Nomura, 'Enhanced carrier confinement effect by the multiquantum barrier in 660 nm GaInP/AlInP visible lasers', *Appl. Phys. Lett.* **58** (1991) 1822.

18

Infrared emitters made from III-nitride semiconductors

Y. KOTSAR and E. MONROY,
CEA-Grenoble, INAC/SP2M/NPSC, France

DOI: 10.1533/9780857099303.3.533

Abstract: III-nitride semiconductors are the materials of choice for green-to-ultraviolet optoelectronics, and there has been worldwide research into wide bandgap GaN and gallium-rich InGaN alloys in the last two decades. Less effort has been devoted to explore their potential for infrared (IR) wavelengths, where they compete with the well-established arsenide and phosphide technologies. This chapter summarizes the progress and challenges in the various approaches for III-nitride IR technology. We first describe light-emitting diodes based on InN and indium-rich InGaN alloys. Then we introduce the fabrication of IR optoelectronic devices using intra-atomic transitions in the 4*f* electronic shell of lanthanide ions incorporated in a GaN-based active region. Finally, we summarize nitride-based intersubband technology, where IR transitions occur between confined electronic states in the conduction band of GaN/Al(Ga)N nanostructures, either quantum wells or quantum dots.

Key words: nitride, infrared, rare earth, intersubband, quantum well.

18.1 Introduction

III-nitride semiconductors launched the first optoelectronic revolution of the twenty-first century with the advent of solid-state blue lasers (Blu-ray) and light-emitting diodes (LEDs) for lighting (mercury-free lamps, outdoor full-color screens and LED television screens). LEDs based on the III-nitride material system have a large spectral range from green to ultraviolet using InGaN/GaN and AlGaN/GaN quantum wells (QWs) as active media. Much less research effort has been devoted to InN and indium-rich alloys, which are the natural nitride-based choice for red optoelectronics. A major breakthrough in 2002, stemming from the much improved quality of InN films grown using molecular beam epitaxy (MBE), resulted in the bandgap of InN being revised from 1.9 eV to a much narrower value of 0.64 eV (~1.9 μm wavelength) (Davydov *et al.*, 2002). This extended the interband optoelectronic capabilities of III-nitrides into the infrared (IR) spectrum. However, this IR technology is penalized by high residual doping, poor thermal stability and surface effects characteristic of InN (Wu, 2009). Thus, alternative approaches have been proposed for III-nitride IR technology. First, a number of research groups have developed LEDs by incorporating rare-earth (RE) elements, such as erbium (Er), thulium (Tm) and praseodymium (Pr), into GaN in order to achieve luminescence via intra-atomic transitions in the 4*f* electronic shell of these lanthanide ions (Steckl *et al.*, 2002; O'Donnell and Hourahine, 2006; Dahal *et al.*, 2010). Another approach is the intersubband (ISB) technology, where the IR transition occurs between confined electronic states in the conduction or in the valence band of semiconductor nanostructures (Hofstetter *et al.*, 2010a; Kotsar *et al.*, 2011a; Beeler *et al.*, 2013). In this chapter, we summarize the state of the art of the various III-nitride IR technologies, namely high-indium-content interband optoelectronics, rare-earth doping and ISB technology.

18.2 High indium (In) content alloys for infrared emitters

The external quantum efficiency of InGaN LEDs, which is as high as 75% for blue devices, drops below 25% in the green spectral range and even lower for longer wavelengths. This efficiency drop stems from a combination of multiple degradation mechanisms including spinodal decomposition of InGaN at high indium content, non-radiative recombination associated with native defects and the piezoelectricity-induced quantum-confined Stark effect (QCSE), which reduces the electron-hole wave function overlap (Barletta *et al.*, 2007). Non-polar and semipolar crystallographic orientations have been investigated for enhancing indium incorporation and addressing the charge separation issue (Speck and Chichibu, 2009). The development of a (11-22)-oriented material has led to the production of amber LEDs with a performance comparable to those of phosphide alloys (Sato *et al.*, 2008).

Intense InGaN photoluminescence (PL) occurs over the entire spectral range from the bandgap of InN to that of GaN (Franssen *et al.*, 2008). However, electrically driven InGaN LEDs require the formation of a *p-n* junction, which at long wavelengths implies either overcoming the challenge of *p*-type doping and contacting high-indium-content InGaN layers or dealing with the huge lattice mismatch between the *p*-GaN contact layer and the high-indium-content active region (the plane lattice mismatch between GaN and InN is 11%). LEDs based on the latter approach have been reported by Wu *et al.* (2012), who described an *n*-InN/*p*-GaN structure displaying rectifying I-V characteristics with a turn-on voltage around 0.8 V. IR emission peaking at 1573 nm was observed under forward bias.

An approach for circumventing the problems associated with the lattice mismatch consists in nanostructuring the active region, either by incorporating InGaN quantum dots (QDs), which can be synthesized defect-free in a GaN matrix (Xu *et al.*, 2007), or by growing nanocolumn arrays, which can either be self-assembled and deposited by tuning the growth conditions (Kikuchi *et al.*, 2004) or are spatially localized via selective area growth (Sekiguchi, 2010; Albert *et al.*, 2013). The elastic relaxation of the misfit strain via surface deformation in these nanostructures enables the fabrication of InGaN-based red LEDs (Kikuchi *et al.*, 2004), although their efficiency and reliability is still far from commercial values. Regarding the near-IR spectral range, 1.55 μm (0.8 eV) light emission can be readily achieved by quantum confining InN or alloying with GaN (Che *et al.*, 2007; Grandal *et al.*, 2011; Naranjo *et al.*, 2011), but the challenge for device fabrication lies again in electron injection. A first demonstration of IR (1.46 µm wavelength) LEDs was recently reported with an active region consisting of a GaN:Si/$In_{0.87}Ga_{0.13}N$/$In_{0.3}Ga_{0.7}N$:Mg nanocolumn array, as illustrated in Fig. 18.1 (Kishino *et al.*, 2012).

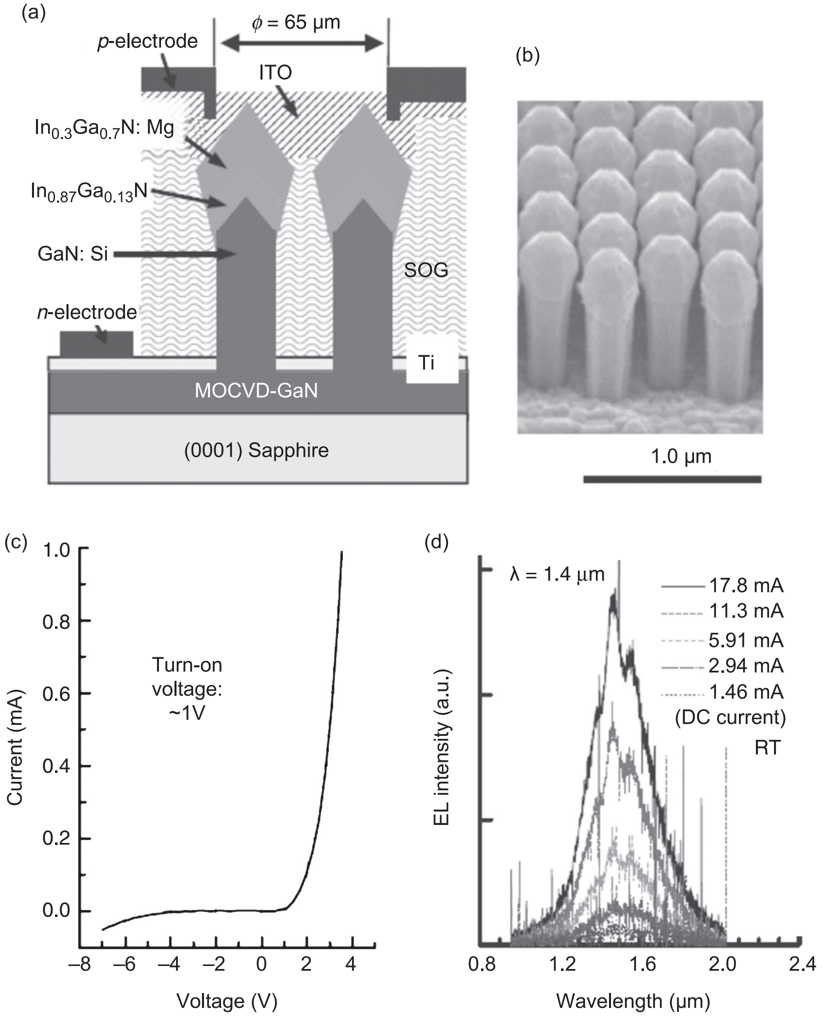

18.1 (a) Cross-sectional schematic structure of a near-IR nanocolumn LED. (b) Scanning electron microscopy (SEM) image of an LED crystal taken at an angle of 55° to the normal. (c) Current versus voltage characteristics under DC current injection. (d) Electroluminescence (EL) spectra under DC current injection at room temperature (RT). (ITO: indium tin oxide; MOCVD: metal-organic chemical vapor deposition; SOG: spin-on-glass) (Reprinted with permission from Kishino *et al.* (2012). Copyright 2012, Japan Society of Applied Physics.)

The quest for brighter far-IR sources has made InN the focus of investigation for terahertz emission. Irradiated with ultrafast laser pulses, semiconductor surfaces can be used to generate broad terahertz pulses efficiently (Yang *et al.*, 1971). InN is a promising candidate for this application due to its high mobility, the large difference between the diffusion length of electrons and holes and the very low probability of inter-valley scattering. Several groups have reported terahertz generation from InN films and nanostructures (Ascazubi *et al.*, 2004; Chern *et al.*, 2006; Ahn *et al.*, 2007; Wang *et al.*, 2010; Shubina *et al.*, 2010; Polyakov *et al.*, 2010; Xu *et al.*, 2011; Sun *et al.*, 2011); however, the underlying physical mechanisms are still under debate. Terahertz generation in InN has been attributed to the photo-Dember effect (Lin *et al.*, 2008; Matthaus *et al.*, 2008). Mu *et al.* (2007) thought that the terahertz emission in InN was due to resonance-enhanced optical rectification. More recently, Xu *et al.* (2010) explained the terahertz generation from InN by the destructive interference between optical rectification and a photocurrent surge. The role of the polarization fields in InN in enhancing the terahertz emission is also under discussion (Ahn *et al.*, 2008; Sun *et al.*, 2011).

18.3 Rare-earth (RE) doped gallium nitride (GaN) emitters

Luminescence from RE ions in solid hosts involves transitions within the 4*f* electronic shell that are parity forbidden in a free ion by the Laporte selection rule, but are allowed through the admixture of states of opposite parity induced by the crystal field in solids. These intra-4*f* transitions are still not fully allowed, resulting in excited state lifetimes of ~1 μs to 1 ms for RE-doped systems. The energy of the emission lines is relatively independent of the host material; however, the matrix has a very strong effect on the radiative transition probability, and hence on the photoemission intensity. The study of luminescence from RE ions embedded in semiconductors has quite a long history, especially for the 1.54 μm IR band emitted by Er^{3+} (Ennen, 1983), which is suitable for transmission through silica fibers over long distances. Favennec *et al.* (1989) established that the thermal quenching in erbium-doped semiconductors decreases with increasing bandgap, which has driven research on RE-doped GaN.

The RE doping of GaN can be accomplished by ion implantation (Wilson *et al.*, 1994) or by *in situ* doping during growth (Mackenzie *et al.*, 1997; Hori *et al.*, 2004, 2006; Ugolini *et al.*, 2006; Feng, 2013). Ion implantation has the advantage of simplicity and it has good control of the dopant location and density independent of the growth conditions. However, implantation induces structural damage, which cannot be completely removed by annealing. On the other hand, *in situ* doping requires a good understanding and control of the growth process, since the RE flux interacts with the other species and modifies the GaN growth kinetics. *In situ* RE-doped layers do not suffer from the damage effects of ion implantation and therefore have a significantly higher radiative efficiency.

Light emission from GaN:RE has been demonstrated via photoluminescence, cathodoluminescence and electroluminescence. The energy from excited carriers is transferred to the RE dopants by the impact excitation of hot carriers or as a result of nearby electron-hole recombination. The RE then relaxes either radiatively or non-radiatively (by multiphonon emission or the Auger mechanism). Radiative emission in the near-IR from RE-doped GaN occurs at 801 nm using thulium (Steckl *et al.*, 1999), at 1000 nm and 1540 nm with erbium (Wilson *et al.*, 1994; Garter *et al.*, 1999; Ugolini *et al.*, 2007), and at 956 nm, 1303 nm and 1914 nm with praseodymium (Birkhahn *et al.*, 1999a), as summarized in Fig. 18.2.

The emission intensity can be optimized using the RE concentration. As the RE ion density is increased, the average distance between ions is reduced proportional to the cube root of the RE concentration. When RE ions are located sufficiently close to each other, the excitation residing in one ion can migrate to a neighboring RE ion as a result of resonant energy transfer (cross-relaxation), which increases the non-radiative relaxation probability. A GaN lattice allows unusually high substitutional RE doping concentrations (up to ~3–5 at.%), while preserving the optical activation of RE dopants (Birkhahn *et al.*, 1999b). However, the optimum RE concentration in terms of radiative efficiency is around 0.5–1% (Steckl *et al.*, 2002).

Visible electroluminescent devices consisting of thin GaN:RE films operating under high voltage (>100 V) have been demonstrated using the red, green and blue emission lines of europium, erbium and thulium ions in GaN (Steckl *et al.*, 2002). Devices incorporating erbium as a dopant exhibit equally intense visible (537/558 nm) and IR (1.55 μm) emissions.

GaN-based *p-i-n* structures incorporating GaN:Er in the active region have been demonstrated by Feng *et al.* (2012). A schematic of a device structure together with IR electroluminescence spectra are shown in Fig. 18.3. IR electroluminescence was detected at 20 mA current injection. The observed emission consisted of a band at 1.00 μm originating from the intra-4*f* transition from the $^4\mathrm{I}_{1\ 1/2}$ to the $^4\mathrm{I}_{1\ 5/2}$ state of Er^{3+}, and a band at 1.54 μm due to the transition

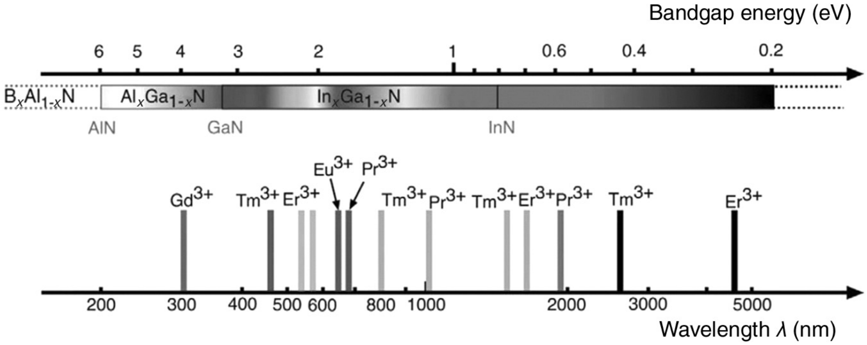

18.2 Emission wavelengths from selected transitions in rare-earth ions and associated bandgap energies of alloys of III-N compound semiconductors. (Reprinted with permission from Steckl *et al.* (2007). Copyright 2007, Elsevier.)

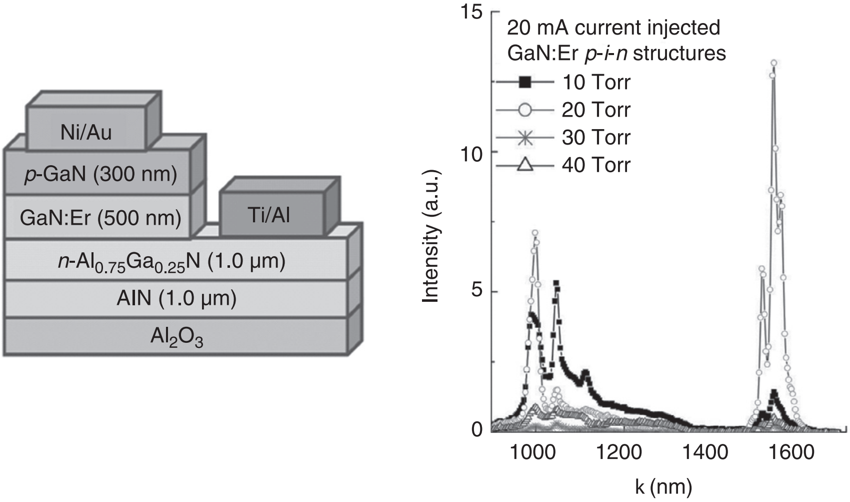

18.3 Left: MOVPE-grown GaN:Er *p-i-n* structure. Right: Infrared electroluminescence spectra detected at 20 mA from GaN:Er *p-i-n* structures grown at different pressures. (MOVPE: Metal-organic vapor phase epitaxy) (Reprinted with permission from Feng *et al.* (2012). Copyright 2012, Optical Society of America.)

from the $^4I_{13/2}$ to the $^4I_{15/2}$ state. The intensity ratio between these two luminescence bands depended on the growth conditions, particularly on the growth pressure.

18.4 III-nitride materials for intersubband (ISB) optoelectronics

An alternative approach for producing nitride devices for IR optoelectronics consists in using ISB transitions in QWs or QDs. ISB devices have several interesting features such as intrinsic wavelength tailorability, high-speed modulation, thermal stability of the operating wavelength and innovative design potential. The capability of ISB devices operating in the mid-IR and far-IR spectral range has been demonstrated using arsenic-based systems like GaAs/AlGaAs and InGaAs/AlInAs-InP with applications in night-vision cameras, gas sensing, medicine and the chemical industry. The shortest operational ISB wavelength is limited by the conduction band offset, which is 1.75 eV for the GaN/AlN system and is large enough to reach the optical fiber transmission windows at 1.3 and 1.55 μm. In the near-IR, a specific advantage of ISB transitions in III-N materials is the ultra-short electron recovery time of about a few hundreds of femtoseconds (Iizuka *et al.*, 2000; Hamazaki *et al.*, 2004), which is used in all-optical switches in the 0.1–1 Tbit/s regime. In the far-IR domain, due to the large longitudinal-optical (LO) phonon energy (92 meV), ISB lasers based on III-nitrides have the potential to operate above room temperature, overcoming the thermal limitations of arsenic-based terahertz lasers, which is attributed to thermally activated LO-phonon scattering.

18.4.1 Physics of ISB transitions

ISB transitions were observed for the first time in 1982 in a transistor structure (Ando *et al.*, 1982), but it was one decade later that the first ISB device appeared: the QW infrared photodetector (Levine, 1993). In 1994, Faist *et al.* (1994) made a major breakthrough in ISB technology: an alternative to the laser diode with a novel operating principle – the quantum cascade laser (QCL). This was the beginning of a period of tremendous development of ISB technology, which resulted in commercially available devices operating in the mid- and far-IR.

To illustrate basic ISB physics, we will consider a QW with two confinement states in a single-particle approach (Liu and Capasso, 2000; Bastard, 1988). Any transition from a state i to a state f, interband or ISB, follows Fermi's golden rule:

$$W_{fi} = \frac{2\pi}{\hbar}\left|\left\langle \psi_f \middle| H' \middle| \psi_i \right\rangle\right|^2 \delta(E_f - E_i - \hbar\omega) \qquad [18.1]$$

where H' is the interaction Hamiltonian, ψ and E are the wave function and energy of the confinement levels of the initial and final states, and $\hbar\omega$ is the radiation energy. As the radiation wavelength is much longer than the lattice periodicity for an interband transition, and longer than the QW width for an ISB transition, it is possible to apply the dipole approximation:

$$H' = \frac{q^2 E_0^2}{4m^{*2}\omega^2}(\vec{e}\cdot\vec{p}) \qquad [18.2]$$

where q is the elementary charge, E_0 is the electric field amplitude, m^* is the effective mass, and $\vec{e}$ and $\vec{p}$ are the polarization vector and momentum operator, respectively. Substituting Eq. 18.2 in Eq. 18.1 we obtain:

$$W_{fi} = \frac{2\pi}{\hbar}\frac{q^2 E_0^2}{4m^{*2}\omega^2}\left|\left\langle \psi_f \middle| \vec{e}\cdot\vec{p} \middle| \psi_i \right\rangle\right|^2 \delta(E_f - E_i - \hbar\omega) \qquad [18.3]$$

Applying the envelop function formalism, the wave function of an electron ψ can be expressed as a product of a periodic Bloch function, u, and a slowly varying envelope function, f. Therefore, the matrix element $\langle \psi_f|\vec{e}\cdot\vec{p}|\psi_i\rangle$ splits into:

$$\langle \psi_f|\vec{e}\cdot\vec{p}|\psi_i\rangle = \vec{e}\cdot\langle u_v|\vec{p}|u_{v'}\rangle\langle f_n|f_{n'}\rangle + \vec{e}\cdot\langle u_v|u_{v'}\rangle\langle f_n|\vec{p}|f_{n'}\rangle \qquad [18.4]$$

where v and v' and n and n' are the band and subband indices of the final and initial states, respectively. The first term describes the selection rules for the interband transitions and it vanishes for transitions within the same band. The second term is related to the ISB processes, and it consists of an overlap integral of envelop functions, which is nonzero when considering the same subbands, and a dipole matrix element of the envelope functions. Introducing the envelop function expression in a QW:

$$f_n(\vec{r}) = \frac{1}{\sqrt{S}} \exp\left(i\vec{k}_\perp \cdot \vec{r}_\perp\right)\chi(z) \qquad [18.5]$$

where S is the sample area, $\chi(z)$ is the envelop function component along the growth axis, and $\vec{k}_\perp$ and $\vec{r}_\perp$ denotes the 2D vectors (k_x, k_y) and (x, y), we can write the dipole matrix element of the envelop functions as:

$$\left\langle f_n \middle| \vec{\varepsilon} \cdot \vec{p} \middle| f_{n'} \right\rangle = \frac{1}{S} \varepsilon_z \delta(k_\perp^i - k_\perp^f) \int dz \chi_n^*(z) p_z \chi_{n'}(z) \qquad [18.6]$$

Thus, only an electric field with a component perpendicular to the semiconductor layers is involved in ISB transitions (polarization selection rule). Moreover, due to the inversion symmetry of the potential, only transitions with opposite parities of the envelope wave functions are allowed in symmetric QWs. This last rule can be overcome by breaking the QW symmetry either by design or with an electric field. However, the polarization selection rule imposes a certain additional geometrical complexity when performing experiments and realizing devices. Structures respond only to transverse magnetic (TM)-polarized light, which implies that surface gratings or waveguide configurations have to be used to couple the light into the active region.

18.4.2 Electronic structure

The optical properties of nitride QWs are strongly affected by the internal electric field inherent to wurtzite-phase nitride heterostructures grown along the <0001> axis. This field arises from the piezoelectric and spontaneous polarization discontinuity between the well and barrier materials (Bernardini *et al.*, 1997). Modeling of the quantum confinement in nitride QWs should therefore go beyond the flat-band approximation and account for the internal electric field in the QW and in the barriers. As an example, Fig. 18.4(a) is the band diagram of GaN/AlN (2 nm/3 nm) superlattices (SLs) calculated using the nextnano^3 8-band k.p Schrödinger–Poisson solver (Birner *et al.*, 2007) with the material parameters described in Kandaswamy *et al.* (2008). The structures were considered to be strained on the AlN substrate. The potential has a characteristic sawtooth profile due to the internal electric field. The electron wave functions of the ground hole state, h_1, the ground electron state, e_1, and the excited electron states, e_2 and e_3, are shown. In narrow QWs (~1 nm) the energy difference between e_1 and e_2 is mostly determined by the confinement in the QW, whereas for larger QWs (>2 nm) this difference is mostly determined by the QCSE, since both electronic levels lie in the triangular part of the QW potential profile.

A detailed graph of the evolution of the ISB transitions e_2–e_1 and e_3–e_1 with the QW thickness and strain state is shown in Fig. 18.4(b), in comparison with the experimental data from GaN/AlN SLs. The increase in the e_2–e_1 ISB energy difference in the superlattice strained on GaN is because of the enhancement of the electric field in the QW, due to the larger piezoelectric coefficients of the AlN barrier in comparison to the GaN QW (Kandaswamy *et al.*, 2008).

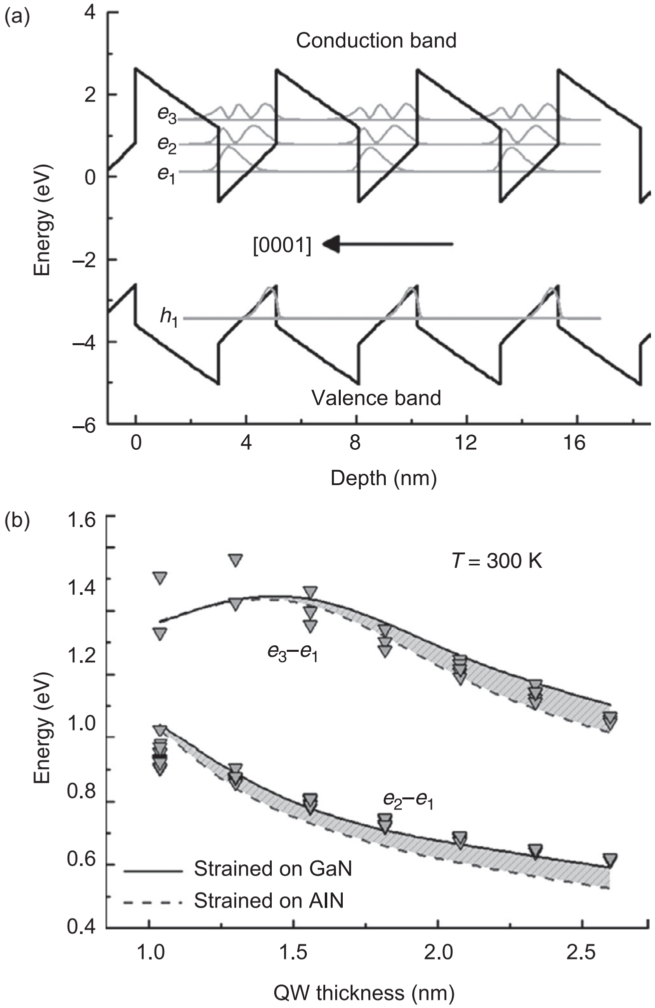

18.4 (a) Band diagram of GaN/AlN QWs in a superlattice with 3-nm-thick AlN barriers and 2-nm-thick GaN QWs. (b) Variation of the e_2–e_1 and e_3–e_1 ISB transition energy as a function of QW thickness. Triangles indicate experimental data and solid and dashed lines correspond to theoretical calculations assuming the structure is fully strained on AlN and on GaN, respectively. (Reprinted with permission from Kandaswamy *et al.* (2008). Copyright 2008, American Institute of Physics.)

18.4.3 Growth and structural properties

An important requirement in the growth of III-nitride nanostructures for ISB devices is the precise control of the thickness and interfaces. Plasma-assisted molecular-beam epitaxy (PAMBE) seems to be the most suitable technique thanks to its low growth temperature, which hinders GaN-AlN interdiffusion (Sarigiannidou *et al.*, 2006). The growth of GaN (0001) by PAMBE is extensively discussed in the literature (Adelmann *et al.*, 2003; Neugebauer *et al.*, 2003; Heying *et al.*, 2000). The deposition of two-dimensional (2D) GaN layers requires precise control over the III/V ratio during growth, in particular gallium-rich conditions are required, and hence growth optimization translates into a determination of an adequate metal excess and the growth temperature. At a substrate temperature higher than 700 °C and for a specific range of gallium fluxes corresponding to slightly gallium-rich conditions, the gallium excess remains on the growing surface in a state of dynamic equilibrium, i.e. the gallium coverage is independent of the gallium exposure time. It is possible to stabilize the amount of gallium from less than 1 monolayer (ML) up to 2.5 ML. However, smooth surfaces can only be achieved with a gallium coverage of 2.5 ± 0.1 ML, where the gallium excess is arranged into a so-called laterally contracted gallium bilayer, which consists of two gallium layers adsorbed on the gallium-terminated (0001) GaN surface (Adelmann *et al.*, 2003; Neugebauer *et al.*, 2003). For AlN, the deposition of layers with an atomically flat surface morphology also requires metal-rich conditions. However, aluminum does not desorb from the surface at the standard growth temperature for GaN. Therefore, to eliminate the aluminum excess at the surface, it is necessary to interrupt the growth periodically under nitrogen. An alternative approach for the 2D growth of AlN and low aluminum content (<50%) Al(Ga)N layers is to use gallium as a surfactant, with the aluminum flux corresponding to the required aluminum mole fraction (Iliopoulos and Moustakas, 2002; Kandaswamy, 2009a).

GaN/AlN is a lattice mismatched system (the in-plane lattice mismatch is 2.5%), which results in strain. The strain relaxation mechanism can be elastic (through undulation of the surface) or plastic (through the introduction of misfit dislocations or stacking faults, crack propagation or decohesion of the layer). These defects can affect the device properties and cause non-radiative recombination, carrier scattering or enhanced diffusion of dopants and impurities. For nitride heterostructures grown along the [0001] axis, which is the predominant growth orientation in commercial devices, the formation of regular networks of misfit dislocations is hindered since the most crystallographically favorable slip system, the (0001) basal plane with <11–20> {0002} slip directions, lies parallel to the heterointerfaces. In PAMBE growth, the metal-to-nitrogen ratio and the growth temperature are key parameters: they define the mechanisms of strain relaxation during growth. Indeed, gallium-rich conditions hinder crack formation and minimize strain relaxation (Kandaswamy, 2009a). For GaN/AlN superlattices, a periodic misfit relaxation causes the formation of stacking fault loops that initiate at the beginning of the AlN deposition, propagate through the barrier and close within the following QW (Kandaswamy, 2009a). In contrast, transmission electron microscopy (TEM) images from GaN/AlGaN superlattices reveal sharp interfaces free of stacking faults or other periodic defect (Kotsar *et al.*, 2011b). Figure 18.5(a) and (b) are high-resolution TEM images of GaN/AlN and GaN/$Al_{0.44}Ga_{0.56}N$ superlattices, respectively, showing abrupt interfaces at the atomic layer scale. The misfit stress between the superlattice and the underlayer is relaxed mainly by the generation of 60° $\frac{1}{3}(11-20)$ dislocations (Sugiura, 1997; Kandaswamy, 2009a; Kotsar *et al.*, 2011b), which fold towards the growth direction giving rise to edge-type threading dislocations. The density of edge-type dislocations should be kept as low as possible since the dislocations cause the loss of transverse magnetic polarization, which adversely affects the performance of ISB devices (Iizuka *et al.*, 2006a).

GaN/AlN QWs with ISB transitions in the near-IR can also be synthesized by metal-organic vapor phase epitaxy (MOVPE) (Baumann *et al.*, 2006; Bayram *et al.*, 2009; Sodabanlu *et al.*, 2009). In this case, it is critical that the growth temperature is reduced from the 1050–1100 °C required for 2D GaN layers to 900–950 °C (or even to 770 °C according to Yang *et al.* (2009)), to minimize GaN-AlN interdiffusion. Furthermore, deposition under compressive strain (e.g. using AlN substrates) is recommended at these growth temperatures to prevent the red shift of the ISB transition due to instabilities of the GaN/AlN interface (Nicolay *et al.*, 2007).

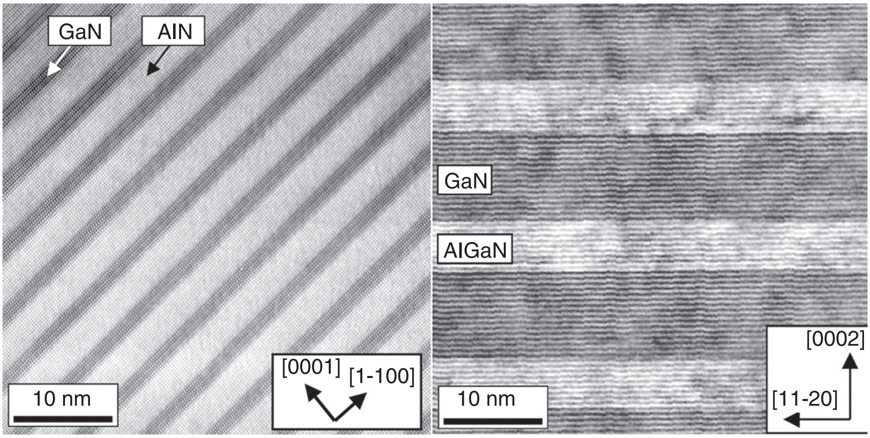

(a) (b)

18.5 High-resolution cross-sectional TEM images of: (a) a GaN/AlN (1.5 nm/3 nm) superlattice taken along the <11$\bar{2}$0> zone axis (reprinted with permission from (Kandaswamy, 2009a), copyright 2009, American Institute of Physics); (b) a GaN/$Al_{0.44}Ga_{0.56}N$ superlattice viewed along the <1–100> zone axis (reprinted with permission from Kotsar (2011b), copyright 2011, American Institute of Physics).

18.4.4 Optical characterization

Figure 18.6(a) shows the room-temperature photo-induced IR absorption spectra of GaN/Al(Ga)N superlattices with different dimensions and aluminum contents

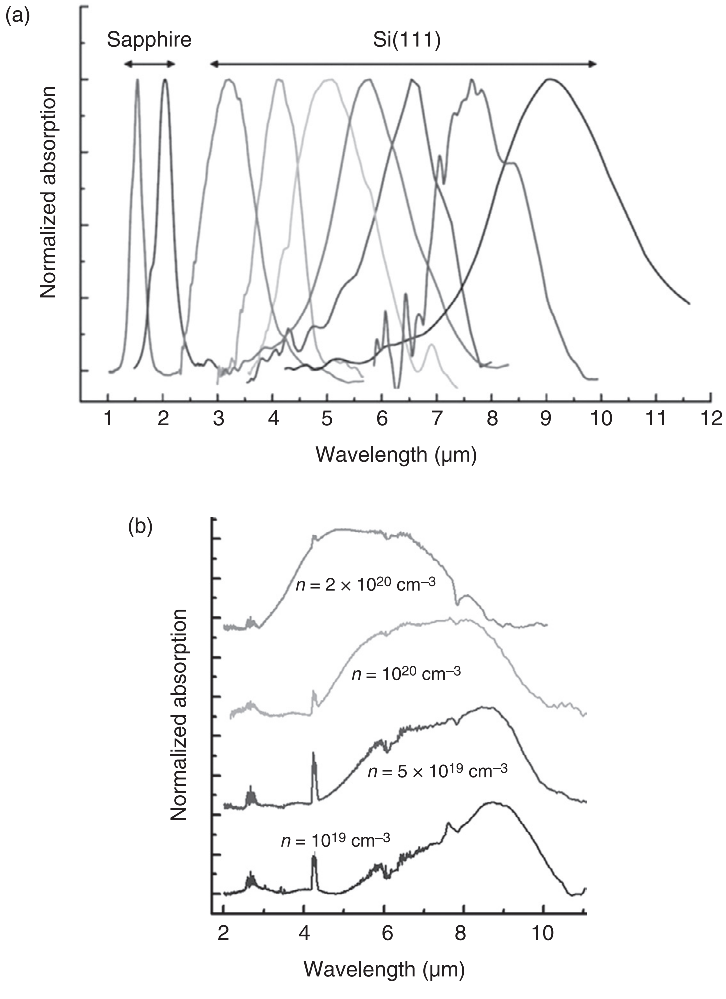

18.6 (a) Room-temperature TM-polarized IR photo-induced absorption spectra for GaN/AlGaN SLs with different barrier aluminum contents and QW widths, grown either on sapphire or Si(111) templates. (Reprinted with permission from Kandaswamy *et al.* (2009b). Copyright 2009, American Institute of Physics.) (b) IR absorption spectra for TM-polarized light for GaN/Al$_{0.1}$Ga$_{0.9}$N (7 nm/4 nm) QWs grown on GaN-on-Si(111) with different doping levels. Spectra are vertically shifted for clarity. (Reprinted with permission from Kandaswamy *et al.* (2010). Copyright 2010, American Institute of Physics.)

in the barriers. The samples show pronounced TM-polarized absorption, attributed to the transition from the first to the second electronic levels in the QW ($e_1 \rightarrow e_2$), while no absorption was observed for transverse electric (TE) polarized light within experimental sensitivity. By changing the geometry and composition, the ISB absorption can be tailored to cover the near-IR range from 1.0 μm and the mid-IR region up to 10 μm (Suzuki and Iizuka, 1999; Gmachl *et al.*, 2000, 2001; Ng *et al.*, 2001, 2002; Kishino *et al.*, 2002; Iizuka *et al.*, 2002; Helman *et al.*, 2003; Tchernycheva *et al.*, 2006; Sherliker *et al.*, 2007; Liu *et al.*, 2007; Kandaswamy *et al.*, 2008, 2009b; Bayram *et al.*, 2009; Péré-Laperne *et al.*, 2009; Andersson *et al.*, 2009; Berland *et al.*, 2010; Tian *et al.*, 2012; Chen *et al.*, 2013). To observe ISB absorption, it is necessary to control the carrier concentration in the QWs to guarantee that the first electronic level is populated. Doping is a critical parameter for reaching the targeted operating wavelength, since the ISB absorption energy blue-shifts markedly with increasing doping level due to many-body effects (Kandaswamy *et al.*, 2010), as illustrated in Fig. 18.6(b). Furthermore, the influence of doping on the interface roughness results in a variation of the absorption line width as a function of the doping location (Edmunds *et al.*, 2012).

When integrating III-nitride nanostructures into a complete device, it is necessary to keep in mind that the magnitude of the carrier distribution depends not only on the silicon doping level in the QWs, but also on the presence of unintentional dopants and on the carrier redistribution due to the internal electric field. The large polarization discontinuities in a III-N material system can result in a significant (even dominant) contribution to the infrared absorption in GaN/AlN superlattices (Kandaswamy *et al.*, 2008).

To further reduce the ISB transition energy, Machhadani *et al.* (2010) proposed an alternative strategy for producing a flat potential in the QW layers by engineering the internal electric field. They investigated structures with 40 periods of step QWs, comprising a GaN well, an $Al_{0.05}Ga_{0.95}N$ step barrier and an $Al_{0.1}Ga_{0.9}N$ barrier. Transmission measurements performed at 4 K reveal TM-polarized ISB absorption at 4.2 THz, in good agreement with simulations, as illustrated in Fig. 18.7.

18.4.5 The AlInN/(In)GaN system

The lattice mismatch between GaN and AlN can lead to high defect densities and cracking in GaN/AlN superlattices. An alternative materials approach to overcome this problem is the use of AlInN alloys. AlInN with an indium composition around 17–18% is lattice matched to GaN and has a refractive index contrast equivalent to AlGaN with 46% aluminum content (6% contrast with GaN at a wavelength of 1.55 μm). Therefore, AlInN is a promising material for distributed Bragg reflectors and thick waveguide layers. However, we must keep in mind that lattice-matched AlInN/GaN heterostructures can have an electric field as large as 3 MV/cm, solely generated by the spontaneous polarization discontinuity.

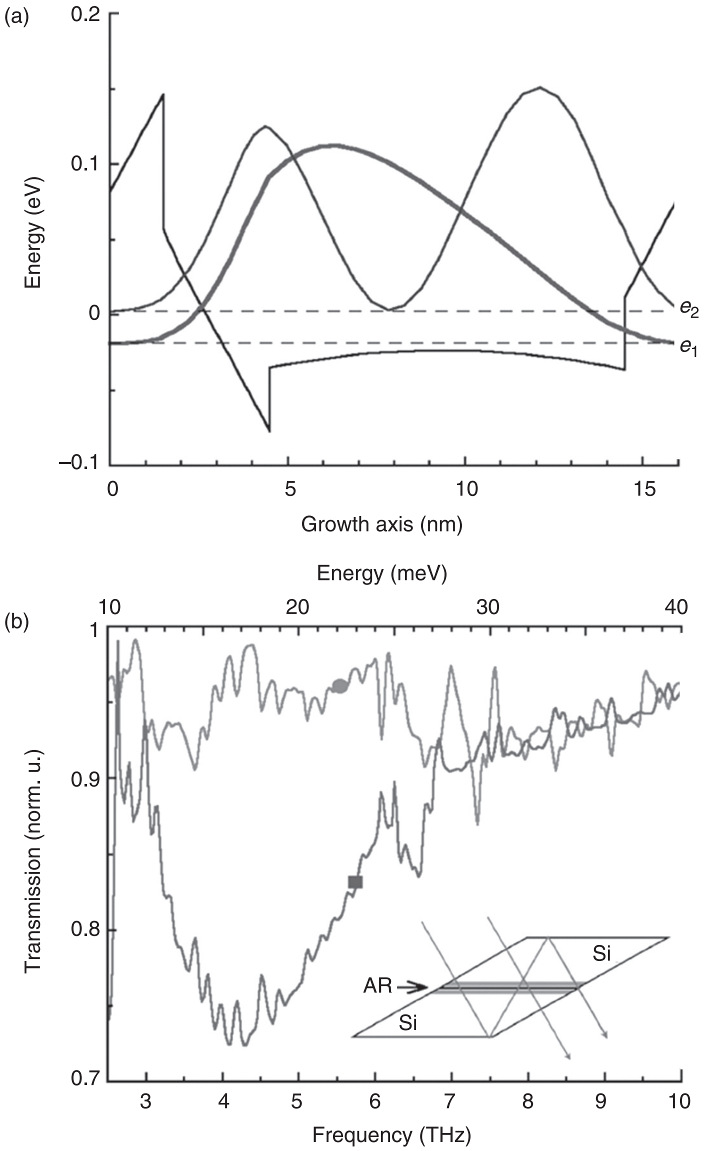

18.7 (a) Conduction band profile and squared envelope functions of the first two electronic levels (e_1, e_2) for a step QW sample with a 15-nm-thick step barrier. (b) Transmission spectra for TM polarized light (marked with a square) and TE polarized light (circle) at T=4.7 K. (Reprinted with permission from Machhadani *et al.* (2010). Copyright 2010, American Institute of Physics.)

The potential of AlInN/GaN lattice-matched systems for use in ISB technology has been explored (Nicolay *et al.*, 2005, 2006). However, this material system has not been adapted for ISB optoelectronics for telecommunication applications since the conduction band offset is in the range of ~1 eV (Gonschorek *et al.*, 2008). ISB absorption in the near-IR spectral region has been reported at 2.3–2.9 μm in GaN/$Al_{0.85}In_{0.15}N$ superlattices (Nicolay *et al.*, 2005; Malis *et al.*, 2009).

An alternative approach for managing the strain in the structure while retaining access to shorter wavelengths is to add a small amount of indium (below 5%) both to the barrier and to the QW, to form an AlInN/GaInN superlattice (Cywiński *et al.*, 2006). This material combination reduces the probability of crack propagation in comparison to GaN/AlN, although it retains a certain degree of strain. However, it is difficult to control the indium mole fraction precisely, and the simulation of the electronic structure remains a challenging task.

18.4.6 Alternative crystallographic orientations

The already high design complexity in terms of modeling IR QCLs further increases in materials with an internal electric field like polar III-nitrides. A simple solution to this problem is to use non-polar crystallographic orientations like the *m*-plane {1–100} or *a*-plane {11–20}, but the epitaxy of these orientations is an arduous task, due to the strong anisotropy of the surface properties, resulting in a high density of crystalline defects. An alternative approach is the growth on semipolar planes, which are those (*hkil*) planes that have at least two non-zero *h*, *k* or *i* Miller indices and a non-zero *l* Miller index. For non-polar materials, ISB optical absorption at $\lambda \sim 2.1$ μm with a full width at half maximum (FWHM) of 120 meV has been reported in silicon-doped 1.75-nm-thick GaN QWs with 5.1-nm-thick AlN barriers grown by PAMBE on *r*-plane sapphire. The materials had a pure *a*-plane orientation (Gmachl and Ng, 2003).

Near-IR ISB absorption has been reported for semipolar (11-22)-oriented GaN/AlN superlattices (Lahourcade *et al.*, 2008; Machhadani *et al.*, 2013). In comparison to polar QWs, semipolar structures have quasi-square potential band profiles with symmetric wave functions due to the reduced electric field of 0.5–0.6 MV/cm in the QWs. The evolution of ISB transition energy with QW thickness is shown in Fig. 18.8. In semipolar structures, the reduction in the internal electric field results in a red shift of the ISB energy. The experimental data was obtained from identical polar and semipolar samples consisting of 40 periods of GaN/AlN with 3 nm AlN barriers. The absorption FWHM (~80–110 meV) is comparable to that measured in polar structures (Tchernycheva *et al.*, 2006).

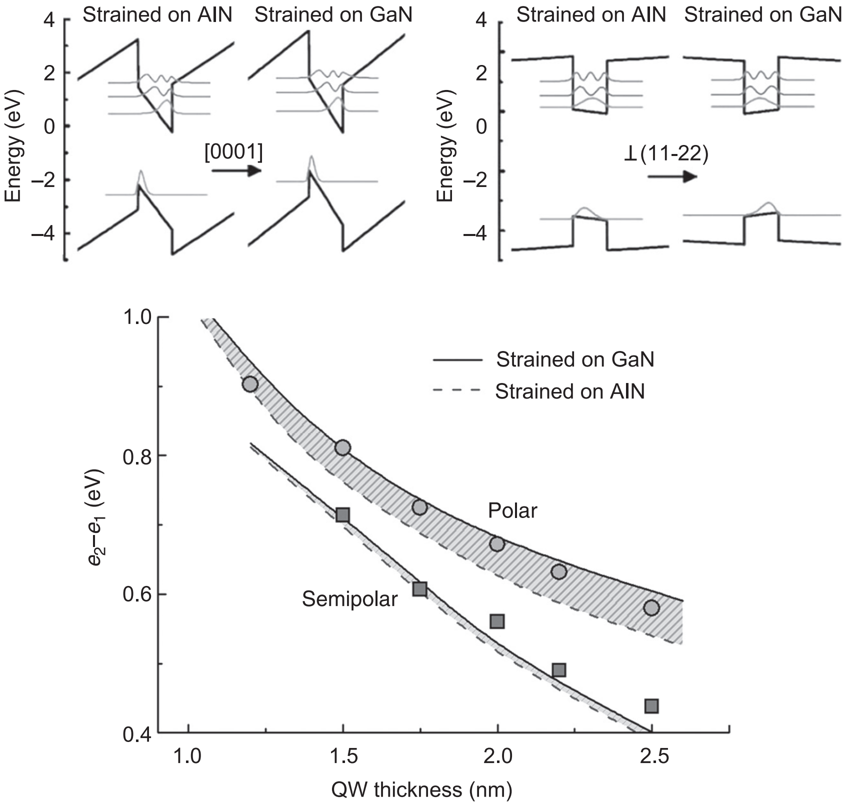

18.8 Top: band diagram of (0001)- and (112-2)-oriented GaN/AlN (2.5 nm/5 nm) superlattices assuming the structure is fully strained on AlN or GaN. Bottom: Variation of e_2–e_1 energy as a function of well width in polar and semipolar QWs strained on GaN and AlN. (Reprinted with permission from Lahourcade *et al.* (2008). Copyright 2008, American Institute of Physics.)

18.4.7 Cubic III-nitrides

Another approach to eliminate the internal electrical field in III-nitride heterostructures is to crystallize III-nitride semiconductors in a zinc-blend structure. Furthermore, the LO phonon energy in cubic GaN is almost the same as in wurtzite GaN (92.7 meV (Brazis and Raguotis, 2006)) whereas the effective mass is much smaller ($m^* = 0.11$–$0.17m_0$ (Pugh *et al.*, 1999; Suzuki and Uenoyama, 1996)) than in wurtzite GaN ($m^* = 0.2m_0$), which should result in higher gain and a lower threshold current in QCLs. The cubic orientation can be selected by PAMBE using 3C-SiC substrates. However, due to their thermodynamically unstable nature, cubic films have low structural quality with a high density of stacking faults. ISB absorption in the 1.40–4.0 μm spectral range has been reported for cubic GaN/AlN

SLs (DeCuir *et al.*, 2007; Machhadani *et al.*, 2011), in agreement with theoretical calculations assuming a conduction band offset of 1.2 eV and an effective mass $m^* = 0.11 m_0$. ISB terahertz absorption at 4.7 THz has also been observed in cubic GaN/$Al_{0.05}Ga_{0.95}N$ (12 nm/15 nm) QWs (Machhadani *et al.*, 2011).

18.5 ISB devices

18.5.1 All-optical switches

Thanks to the ultrafast ISB recovery time, which is in the 150–400 fs range (Iizuka *et al.*, 2000; Heber *et al.*, 2002) and is due to the strong interaction of electrons with LO phonons, GaN/AlN QWs and QDs have been proposed active media for all-optical switches (saturable absorbers) operating at a Tbit/s data rate at telecommunication wavelengths. These ultrafast all-optical devices are of great interest for optical time-division multiplexed systems. The switching is based on the bleaching of the intersubband absorption by an intense control pulse. All-optical switching at 1.55 μm with a sub-picosecond commutation time has been demonstrated by several groups (Rapaport *et al.*, 2003; Iizuka *et al.*, 2004, 2005, 2006b, 2009; Li *et al.*, 2007; Nevou *et al.*, 2009; Sodabanlu *et al.*, 2011). Control switching energies as low as 38 pJ for 10 dB modulation depth (Li *et al.*, 2007) and 25 pJ for 5 dB contrast (Iizuka *et al.*, 2009) have been demonstrated.

The intraband absorption saturation of GaN/AlN QDs has been probed by Nevou *et al.* (2009), who obtained values in the range 15–137 MW/cm^2 (0.03–0.27 pJ/μm^2). The large error bar was a consequence of the focusing uncertainty in the sample. However, even the upper estimate of the saturation intensity for QDs is smaller than the corresponding value for GaN/AlN QWs (Li *et al.*, 2007).

18.5.2 Infrared photodetectors

The room-temperature operation of photoconductive QW infrared photodetectors (QWIPs) has been demonstrated (Hofstetter *et al.*, 2003). However, these devices have a low yield due to the large dark current originating from the high density of threading dislocations in heteroepitaxial III-nitrides (~10^9 cm^{-2}). An alternative for bypassing the leakage problem is to fabricate photovoltaic devices, where zero-bias operation guarantees a minimum dark current (Hofstetter *et al.*, 2006, 2007; Baumann *et al.*, 2006). Photovoltaic ISB detectors use non-linear optical rectification processes in asymmetric QWs (Hofstetter *et al.*, 2007). Recently, a strong performance enhancement (the responsivity increased by a factor of 60) for these detectors was achieved by using QDs instead of QWs in the active region (Hofstetter *et al.*, 2010b). The improvement is attributed to the longer electron lifetime in the upper QD states and the increased lateral electron displacement.

Lateral quantum dot infrared photoconductors (QDIPs) have been fabricated in samples consisting of 20 periods of silicon-doped GaN/AlN QDs. The devices had a photocurrent that was only observed for TM-polarized light, following the intraband s–p_z selections rules (Doyennette *et al.*, 2005; Vardi *et al.*, 2006). The photocurrent, which was due to bound-to-bound intraband transitions within the QDs, is attributed to lateral hopping conductivity (Vardi *et al.*, 2009).

Finally, IR photodetectors based on cubic GaN/AlN QW superlattices have also been reported (DeCuir *et al.*, 2008). These devices exhibit a photovoltaic effect that is overtaken by the dark current for temperatures above 215 K. The photoresponse was consistent with ISB transition phenomena, but the mechanism behind the photovoltaic behavior remains unknown.

18.5.3 Quantum cascade detectors

Quantum cascade detectors (QCDs) are photovoltaic devices consisting of several periods of an active QW coupled to a short-period superlattice, which serves as an extractor (Giorgetta *et al.*, 2009). Under illumination, electrons from the ground state are excited to the upper state of the active QW and then transferred to the extractor region where they experience multiple relaxations towards the next active QW. This results in a macroscopic photovoltage in an open circuit configuration, or in a photocurrent if the device is loaded on a resistor. A major advantage is that the the dark current is extremely low and the capacitance can be reduced by increasing the number of periods, which gives a high frequency response.

GaN/AlGaN QCDs operating in the near-IR have been reported (Vardi *et al.*, 2008a; Sakr *et al.*, 2010), with the structure illustrated in Fig. 18.9. These devices take advantage of the polarization-induced internal electric field in the heterostructure. They have an efficient AlGaN/AlN electron extractor where the energy levels are separated by approximately 90 meV to form a phonon ladder. The peak responsivity of a GaN/AlGaN QCD at room temperature is ~10 mA/W (~1000 V/W) (Vardi *et al.*, 2008a). Detectors with 40 periods of the active region with a size $17 \times 17\,\mu\text{m}^2$ had a -3 dB cut-off frequency at 11.4 GHz (Vardi *et al.*, 2008b). However, the speed of these QCDs was governed by the RC constant of the device and not by an intrinsic mechanism. Pump and probe measurements of these devices showed relaxation times ~1 ps, as shown in Fig. 18.9(d), which indicates that the available bandwidth exceeds 200 GHz (Vardi *et al.*, 2011). Sakr *et al.* (2013) produced GaN/AlGaN QCDs, which showed a significant improvement in terms of responsivity and bandwidth, reaching at least 9.5 ± 2 mA/W for $10 \times 10\,\mu\text{m}^2$ devices at a 1.5 μm peak detection wavelength at room temperature, with a -3 dB cut-off frequency at ~40 GHz. The enhanced responsivity was achieved by illuminating the side facet of the QCDs (the illumination was perpendicular to the growth axis), as a result of the good coupling between TM-polarized waveguide-propagated light and ISB transitions. The frequency bandwidth was improved by reducing the top contact resistance and the contact layer resistivity, as well as the device capacitance through increasing the number of periods.

Because of the internal field in III-nitride QWs, symmetry breaking of the potential permits ISB transitions not only between the ground electronic state and

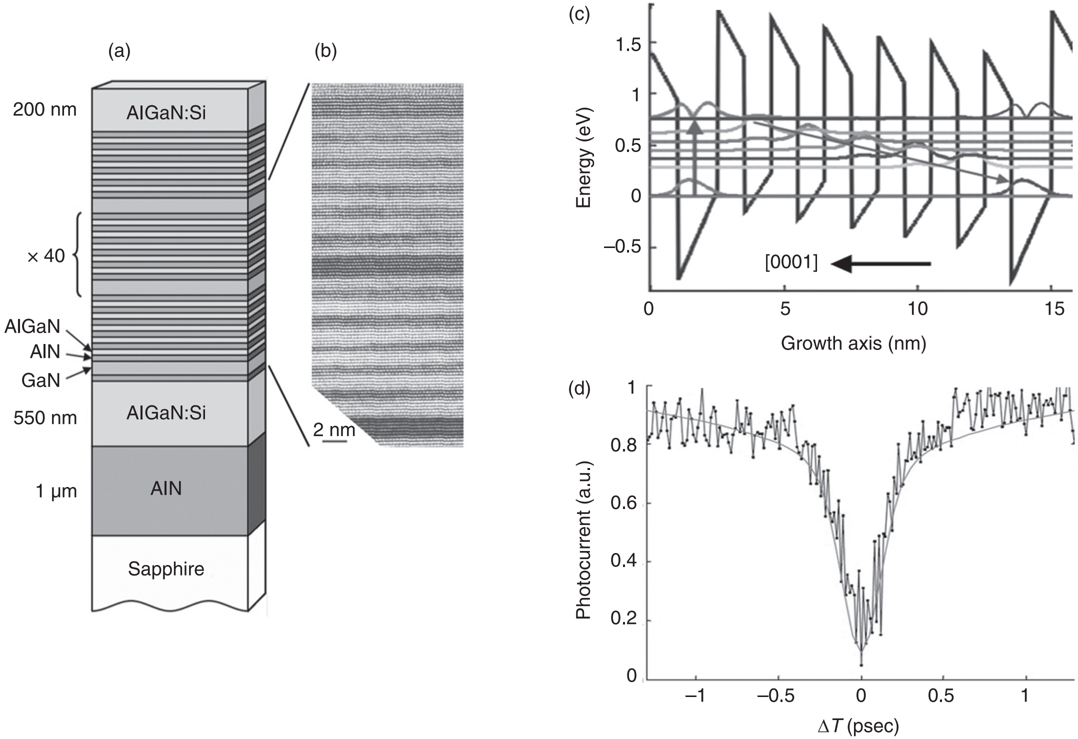

18.9 (a) GaN/AlN/AlGaN QCD. (b) High-resolution transmission electron micrograph of a period of the structure (active GaN QW followed by a five-period AlGaN/AlN extractor), viewed along the <11–20> axis. (Reprinted with permission from Vardi (2008a). Copyright 2008, American Institute of Physics.) (c) Band diagram and energy levels in one stage of the structure. (Reprinted with permission from Vardi (2008a). Copyright 2008, American Institute of Physics.) (d) QCD photocurrent as a function of pump-probe delay at room temperature under zero bias conditions. Full line: simulation fit based on rate equations and phonon scattering theory. (Reprinted with permission from Vardi *et al.* (2011). Copyright 2011, American Institute of Physics.)

the first excited state, $e_1 \rightarrow e_2$, but also between e_1 and the second excited state, e_3, a transition forbidden in symmetric QWs. This feature was exploited in the fabrication of a two-color GaN-based QCD operating at 1.7 µm and 1 µm at room temperature (Sakr, 2012a).

Finally, a simplified QCD design where the extractor superlattice is replaced by an AlGaN layer has been proposed (Sakr, 2012b). The thickness and composition of the extractor alloy were chosen so that the energy separation between the ground state of the extractor and the ground state of the active QW is close to the LO-phonon energy. An alloy-extractor device with a peak photovoltaic response at 1.9 µm has been demonstrated (Sakr, 2012b).

18.5.4 Light emitters

ISB luminescence has been observed both in GaN/AlN QWs and QDs under optical pumping (Nevou *et al.*, 2006, 2007, 2008; Driscoll *et al.*, 2009). Figure 18.10 shows the emission at a wavelength of 2.1 µm obtained from GaN/AlN (2 nm/3 nm) QWs. It is important to recall that ISB PL is a very inefficient process because of the very short non-radiative ISB relaxation lifetime. However, this does not prevent the realization of high performance ISB lasers because large stimulated gains can be achieved thanks to the high oscillator strength associated

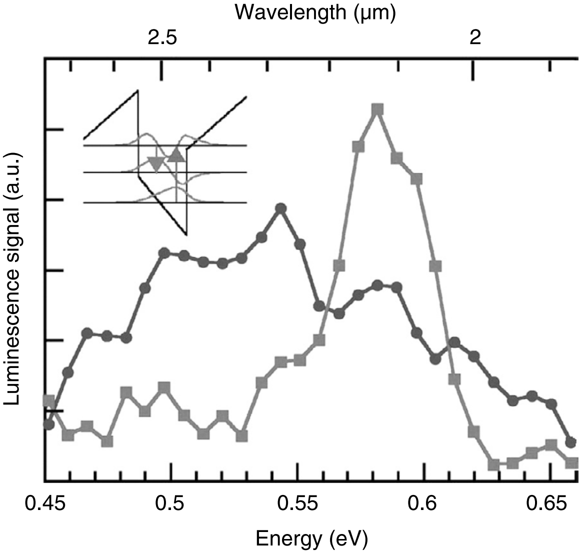

18.10 Room temperature ISB PL spectra from 2-nm-thick GaN/AlN QWs, undoped (circles) and doped with [Si] = 5×10^{19} cm^{-3} (squares). The inset illustrates the conduction band energy levels. (Reprinted with permission from Nevou *et al.* (2007). Copyright 2007, American Institute of Physics.)

with ISB transitions. The observation of ISB luminescence proves the feasibility of optically pumped ISB emitting devices in the near-IR. However, in order to develop quantum fountain lasers, further work is required on growth optimization, processing and the dedicated laser active region and cavity design.

There is interest in pushing the operation of ISB nitride devices to longer wavelengths, particularly to the terahertz frequency range. The terahertz spectral region is subject to intensive research because of its potential in a number of application domains such as medical diagnostics, security screening and quality control. In terms of sources, QCLs based on GaAs/AlGaAs QWs have emerged as excellent candidates for applications requiring a few tens of milliwatts power in the 1.2–5 THz spectral range (Köhler *et al.*, 2002). Although much progress has been accomplished in terms of QCL performance, the maximum operating temperatures reported so far – 186 K and 120 K for pulsed and continuous wave operation – are still too low for widespread application (Kumar *et al.*, 2009; Williams *et al.*, 2005). There are two major processes that cause the degradation of population inversion (and thus the gain) in terahertz QCLs at high temperature: thermal backfilling and thermally activated phonon scattering. Backfilling of the lower radiative state with electrons from the heavily populated injector occurs either by thermal excitation (following a Boltzmann distribution) or by reabsorption of non-equilibrium LO-phonons (the hot-phonon effect) (Lü and Cao, 2006). The other main degradation mechanism is the onset of thermally activated LO-phonon scattering, as electrons in the upper radiative state acquire sufficient in-plane kinetic energy to emit an LO-phonon and relax non-radiatively to the lower radiative state. Both of these mechanisms depend to a large extent on the electron gas temperature, which is 50–100 K higher than the lattice temperature during device operation.

The best temperature performances are obtained with so-called resonant-phonon QCL designs (Williams *et al.*, 2003). In this scheme, the injector states are designed so that the lower radiative state is resonantly coupled into the upper injector level, which is separated by approximately the LO-phonon energy from the second injector level, providing efficient depopulation of the lower lasing state and a fast relaxation path towards the upper radiative state. The explicit inclusion of an LO-phonon scattering event for depopulation means that resonant-phonon designs have a relatively large energetic barrier (about one LO phonon) to thermal backfilling. However, the low LO-phonon energy in arsenide compounds (36 meV for GaAs) constitutes a major bottleneck for operation at higher temperatures. Wide bandgap semiconductor materials such as GaN, with an LO-phonon energy of 92 meV (22.3 THz), should pave the way for terahertz QCLs operating above room temperature. Furthermore, the large LO-phonon energy of GaN opens the possibility of QCLs operating at wavelengths inaccessible to GaAs-based devices due to Reststrahlen absorption. There are a number of theoretical proposals for nitride QCLs operating in the far-IR region (Jovanovic *et al.*, 2004; Sun *et al.*, 2005; Vukmirovic *et al.*, 2005; Bellotti *et al.*, 2008, 2009), as illustrated in Fig. 18.11. All these designs follow the resonant-phonon scheme.

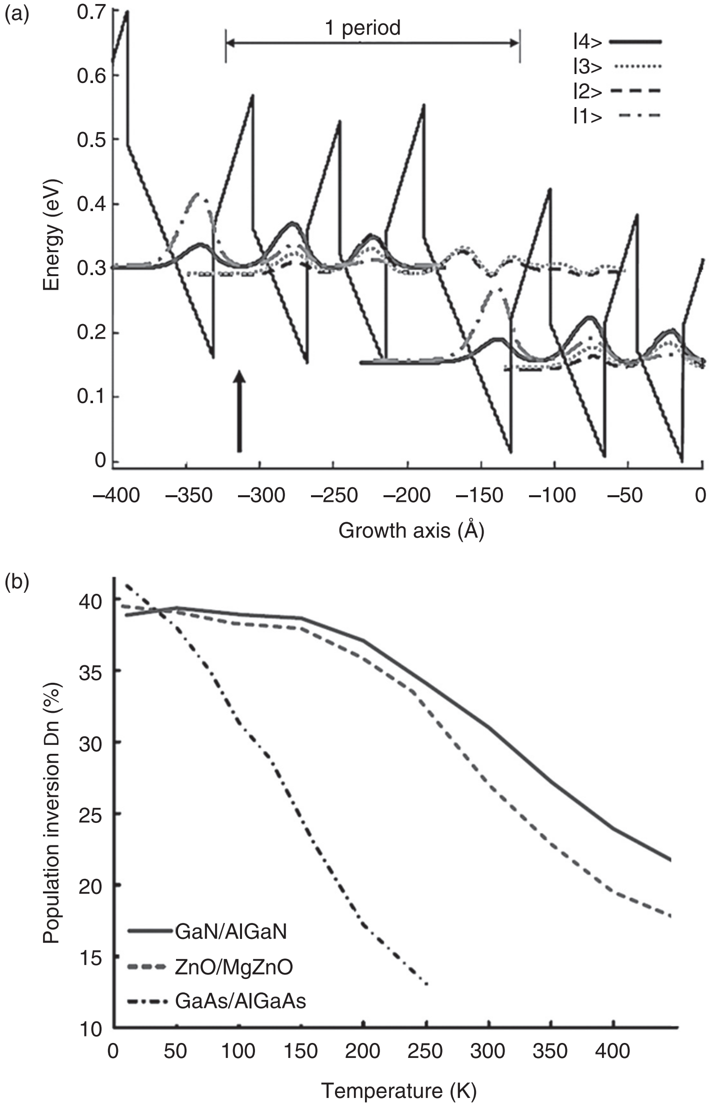

18.11 (a) Conduction-band profile and squared envelope functions of a GaN/$Al_{0.15}Ga_{0.85}N$ terahertz QCL design. (b) Calculated fractional population inversion of terahertz QCL structures based on various material families, as a function of temperature. (Reprinted with permission from Bellotti *et al.* (2009). Copyright 2009, American Institute of Physics.)

Researchers from the University of Leeds (UK) have engineered one of the first designs for GaN-based QCLs (Jovanovic *et al.*, 2004), a 34-µm-wavelength QCL design in both the *a*- and *c*-planes. Population inversions in active laser states up to 19% for the *a*-plane design and up to 40% for the *c*-plane design were predicted and, based on estimated modal gain and waveguide/mirror losses, the researchers concluded that the observation of laser action in GaN/AlGaN cascades should be feasible in both planes.

Terashima and Hirayama (RIKEN, Japan) produced terahertz QCL designs based on four-well resonant-phonon GaN/AlGaN structures (Terashima and Hirayama, 2009, 2011). The structures were synthesized by PAMBE. They have a single-metal plasmon waveguide geometry. Electroluminescence at 1.37 THz has been reported (Terashima and Hirayama, 2011). Paiella and Moustakas's group at Boston University proposed a QCL design emitting at 2 THz (Belloti *et al.*, 2008). They conducted a rigorous comparison between a GaAs/AlGaAs QCL and the GaN/AlGaN terahertz QCLs emitting at the same wavelength using a microscopic model of carrier dynamics in QCL gain media based on a set of Boltzmann-like equations solved with a Monte Carlo technique (Belloti *et al.*, 2008, 2009). Their results showed that the population inversion within GaN lasers is much less dependent on temperature than conventional GaAs designs.

Mirzaei *et al.* (2012) proposed a dual-wavelength QCL that emits at both 33 µm and 52 µm with the output optical powers having a similar behavior for both wavelengths. The design uses LO-phonon resonance to extract electrons from the lower radiative levels, and incorporates a miniband injector, theorized via rate equation analysis to operate properly up to 265 K.

Chou *et al.* (2011) modeled GaN-based resonant-phonon terahertz lasers using a transfer matrix method, paying particular attention to the effect of the strain state. They predicted higher terahertz powers in GaN/AlGaN heterostructures compared to heterostructures incorporating indium (Chou *et al.*, 2012).

Finally, Yasuda *et al.* (2011) used the non-equilibrium Green's function to model GaN terahertz QCL devices, namely a four-well resonant-phonon InAlGaN/GaN structure on (0001)-oriented GaN, and a two-well non-polar GaN/AlGaN structure (Yasuda, 2012).

Overall, many different designs from various simulation models have been presented. However, the production of nitride-based terahertz QCLs still has two major challenges: a more robust design of the active QWs to obtain ISB transitions in the far-IR is required and the leakage currents associated with threading dislocations arising from the heteroepitaxial growth of GaN must be dealt with. Recently single-crystal GaN substrates with various crystallographic orientations have been made commercially available. They can be used to grow low-defect nitride structures, bringing new possibilities for the development of a nitride-based QCL in the near future.

18.6 Conclusions

In this chapter, we reviewed recent research on III-nitride IR technologies, namely high indium-content InGaN optoelectronics, RE incorporation and the GaN/Al(Ga)N ISB approach. Driving the InGaN LED technology from blue towards longer wavelengths results in a significant drop in internal quantum efficiency due to problems with the large lattice mismatch between InN and GaN, and the challenges with *p*-type doping and contacting high-indium-content InGaN layers. Approaches to circumvent these problems use a nanostructured active region via the introduction of QDs or nanocolumn arrays. Devices operating in the near IR, with a wavelength around 1.5 μm, have been demonstrated, but their reliability and performance is not yet competitive with other IR technologies. Nonetheless, research on InN has revealed the potential of this semiconductor for the development of far-IR sources. Broad terahertz pulses are efficiently generated by irradiation of an InN surface with femtosecond laser pulses.

Several groups have produced IR LEDs by incorporating RE elements into GaN in order to achieve luminescence via 4*f* intra-atomic transitions in these ions. Electroluminescent devices operating at the technologically important 1.55 μm wavelength have been demonstrated, but they require a high bias voltage (>100 V) and have relatively low efficiency.

Finally, ISB optoelectronics has emerged recently as a potential application field for III-nitride materials. III-nitride heterostructures are excellent candidates for high-speed ISB devices in the near-IR thanks to their large conduction band offset (~1.8 eV for the GaN/AlN system) and sub-picosecond ISB scattering rates. However, bandgap engineering requires the precise control of material growth and modeling that are notoriously difficult in GaN/AlGaN. The first prototypes of nitride-based ISB devices were room-temperature multi-Tbit/s all-optical switches operating at 1.5 μm, photovoltaic and photoconductive quantum well infrared photodetectors, quantum dot infrared photodetectors and ISB electro-optical modulators. Near-IR ISB luminescence from GaN/AlN QWs and QDs has been reported. The concept of quantum cascade applied to III-nitrides has been demonstrated by the development of QCDs operating in the 1.5–2.0 μm spectral range.

An emerging field for GaN-based ISB devices is the extension towards the far-IR spectral range, and several theoretical designs for a GaN-based terahertz QCL have recently been reported. At far-IR wavelengths, the large GaN LO-phonon energy (92 meV) is useful in achieving ISB operation at relatively high temperatures, and also in covering IR wavelengths that are not accessible by other III-V semiconductors due to Reststrahlen absorption. However, the extension of this ISB technology towards longer wavelengths requires a reduction of the polarization-induced internal electric field, which poses new material challenges.

18.7 Acknowledgements

The authors acknowledge support from the EU ERC-StG TeraGaN (#278428) project.

18.8 References

Adelmann, C., Brault, J., Mula, G., Daudin, B., Lymperakis, L., *et al.* (2003) 'Allium adsorption on (0001) GaN surface', *Phys. Rev. B*, 67, 165419.

Ahn, H., Ku, Y.-P., Wang, Y.-C., Chuang, C.-H., Gwo, S., *et al.* (2007) 'Terahertz spectroscopic study of vertically aligned InN nanorods', *Appl. Phys. Lett.*, 91, 163105.

Ahn, H., Ku, Y. P., Chuang, C. H., Pan, C. L., Lin, H. W., *et al.* (2008) 'Intense terahertz emission from *a*-plane InN surface', *Appl. Phys. Lett.*, 92, 102103.

Albert, S., Bengoechea-Encabo, A., Sanchez-Garcia, M. A., Kong, X., Trampert, A., *et al.* (2013) 'Selective area growth of In(Ga)N/GaN nanocolumns by molecular beam epitaxy on GaN-buffered Si(111): from ultraviolet to infrared emission', *Nanotechnology*, 24, 174303.

Andersson, T. G., Liu, X. Y., Aggerstam, T., Holmström, P., Lourdudoss, S., *et al.* (2009) 'Macroscopic defects in GaN/AlN multiple quantum well structures grown by MBE on GaN templates', *Microelectronics J.*, 40, 360–362.

Ando, T., Fowler. A. B. and Stern, F. (1982) 'Electronic properties of two-dimensional electronic systems', *Rev. Mod. Phys.*, 54, 437–672.

Ascazubi, R., Wilke, I., Denniston, K., Lu, H. and Schaff, W. (2004) 'Terahertz emission by InN', *Appl. Phys. Lett.*, 84, 4810.

Barletta, P. T., Berkman E. A., Moody B. F., El-Masry N. A., Emara A. M., *et al.* (2007) 'Development of green, yellow, and amber light emitting diodes using InGaN multiple quantum well structures', *Appl. Phys. Lett.*, 90, 151109.

Bastard, G. (1988) *Wave Mechanics Applied to Semiconductor Heterostructures*, Halsted Press.

Baumann, E., Giorgetta, F., Hofstetter, D., Golka, S., Schrenk, W., *et al.* (2006) 'Near infrared absorption and room temperature photovoltaic response in AlN/GaN superlattices grown by metal-organic vapour-phase epitaxy', *Appl. Phys. Lett.*, 89, 041106.

Bayram, C., Péré-Laperne, N. and Razeghi, M. (2009) 'Effects of well width and growth temperature on optical and structural characteristics of AlN/GaN superlattices grown by metal-organic chemical vapour deposition', *Appl. Phys. Lett.*, 95, 201906.

Beeler, M., Trichas, E. and Monroy, E. (2013) 'III-nitride semiconductors for intersubband optoelectronics: a review', *Semicond. Sci. Technol.*, 28, 074022.

Bellotti, E., Driscoll, K., Moustakas, T. D. and Paiella, R. (2008) 'Monte Carlo study of GaN versus GaAs terahertz quantum cascade structures', *Appl. Phys. Lett.*, 92, 101112.

Bellotti, E., Driscoll, K., Moustakas, T. D. and Paiella, R. (2009) 'Monte Carlo simulation of terahertz quantum cascade laser structures based on wide-bandgap', *J. Appl. Phys.*, 105, 113103.

Berland, K., Stattin, M., Farivar, R., Sultan, D. M. S., Hyldgaard, P., *et al.* (2010) 'Temperature stability of intersubband transitions in AlN/GaN quantum wells', *Appl. Phys. Lett.*, 97, 043507.

Bernardini, F., Fiorentini, V. and Venderbilt, D. (1997) 'Spontaneous polarization and piezoelectric constants of III-V nitrides', *Phys. Rev. B*, 56, R10024–R10027.

Birkhahn, R. H., Garter, M. J. and Steckl, A. J. (1999a) 'Red light emission by photoluminescence and electroluminescence from Pr-doped GaN on Si substrates', *Appl. Phys. Lett.*, 74, 2161.

Birkhahn, R. H., Hudgins, R. A., Lee, D. S., Steckl, A. J., Molnar, R. J., *et al.* (1999b) 'Growth and morphology of Er-doped GaN on sapphire and HVPE substrates', *J. Vac. Sci. Technol. B*, 17, 1195.

Birner, S., Zibold, T., Andlauer, T., Kubis, T., Sabathil, M., *et al.* (2007) 'Nextnano: general purpose 3-D simulations', *IEEE Trans. Electron Dev.*, 54, 2137.

Brazis, R. and Raguotis, R. (2006) 'Monte Carlo modelling of phonon-assisted carrier transport in cubic and hexagonal gallium nitride', *Optical Quantum Electronics*, 38, 339.

Che, S. B., Mizuno, T., Wang, X., Ishitani, Y. and Yoshikawa, A. (2007) 'Fabrication and properties of coherent-structure In-polarity InN/$In_{0.7}Ga_{0.3}N$ multiquantum wells emitting at around 1.55 μm', *J. Appl. Phys.*, 102, 083539.

Chen, G., Li, Z. L., Wang, X. Q., Huang, C. C., Rong, X., *et al.* (2013) 'Effect of polarization on intersubband transition in AlGaN/GaN multiple quantum wells', *Appl. Phys. Lett.*, 102, 192109.

Chern, G. D., Readinger, E. D., Shen, H., Wraback, M., Gallinat, C. S., *et al.* (2006) 'Excitation wavelength dependence of terahertz emission from InN and InAs', *Appl. Phys. Lett.*, 89, 141115.

Chou, H., Manzur, T. and Anwar, M. (2011) 'Active layer design of THz GaN quantum cascade lasers', *SPIE Proc.*, 8023, 802309.

Chou, H., Anwar, M. and Manzur, T. (2012) 'Active layer design and power calculation of nitride-based THz quantum cascade lasers', *SPIE Proc.*, 8268, 82680O.

Cywiński, G., Skierbiszewski, C., Fedunieiwcz-Żmuda, A., Siekacz, M., Nevou, L., *et al.* (2006) 'Growth of thin AlInN/GaInN quantum wells for applications to high-speed intersubband devices at telecommunication wavelength', *J. Vac. Sci. Technol. B*, 24, 1505–1509.

Dahal, R., Ugolini, C., Lin, J. Y., Jiang, H. X. and Zavada, J. M. (2010) '1.54 μm emitters based on erbium doped InGaN p-i-n junction', *Appl. Phys. Lett.*, 97, 141109.

Davydov, V. Y., Klochikhin, A. A., Seisyan R. P., Emtsev, V. V., Ivanov, S. V., *et al.* (2002) 'Absorption and emission of hexagonal InN. Evidence of narrow fundamental band gap', *Phys. Stat. Sol. B*, 229, R1–R3.

DeCuir, E. A., Fred, E., Manasreh, M. O., Schörmann, J., As, D. J., *et al.* (2007) 'Near-infrared intersubband absorption in nonpolar cubic GaN/AlN superlattices', *Appl. Phys. Lett.*, 91, 041911.

DeCuir, E. A., Manasreh, M. O., Tschumak, E., Schörmann, J., As, D. J., *et al.* (2008) 'Cubic GaN/AlN multiple quantum well photodetector', *Appl. Phys. Lett.*, 92, 201910.

Doyennette, L., Nevou, L., Tchernycheva, M., Lupu, A., Guillot, F., *et al.* (2005) 'GaN-based quantum dot infrared photodetector operating at 1.38 μm', *Electron. Lett.*, 41, 1077–1078.

Driscoll, K., Liao, Y., Bhattacharyya, A., Zhou, L., Smith, D. J., *et al.* (2009) 'Optically pumped intersubband emission of short-wave infrared radiation with GaN/AlN quantum wells', *Appl. Phys. Lett.*, 94, 081120.

Edmunds, C., Tang, L., Shao, J., Li, D., Cervantes, M., *et al.* (2012) 'Improvement of near-infrared absorption linewidth in AlGaN/GaN superlattices by optimization of delta-doping location', *Appl. Phys. Lett.*, 101, 102104.

Ennen, H., Kaufmann, U., Pomrenke, G., Schneider, J., Windscheif, J., *et al.* (1983) 'Rare earth activated luminescence in InP, GaP and GaAs', *J. Cryst. Growth*, 64, 165.

Faist, J., Capasso, F., Sivco, D. L., Sirtori, C., Hutchinson, A. L., *et al.* (1994) 'Quantum cascade laser', *Science*, 264, 553.

Favennec P. N., L'Haridon, H., Salvi, M., Moutonnet, D. and Le Guillou, Y. (1989) 'Luminescence of erbium implanted in various semiconductors: IV, III-V and II-VI materials', *Electron. Lett.*, 25, 718.

Feng, I.-W., Li, J., Lin, J., Jiang, H. and Zavada, J. (2012) 'Effects of growth pressure on erbium doped GaN infrared emitters synthesized by metal organic chemical vapor deposition', *Optical Materials Express*, 2, 1095–1100.

Feng, I.-W., Li, J., Lin, J., Jiang, H. and Zavada, J. (2013) 'Optical excitation cross section of erbium in GaN', *Applied Optics* 52, 1132–1135.

Franssen, G., Gorczyca, I., Suski, T., Kaminska A., Pereiro, J., *et al.* (2008) 'Bowing of the band gap pressure coefficient in $In_xGa_{1-x}N$ alloys', *Appl. Phys. Lett.*, 103, 033514.

Garter, M. J., Scofield, J. D., Birkhahn, R. H. and Steckl, A. J. (1999) 'Visible and infrared emission from ITO/GaN:Er/Si Schottky diodes', *Appl. Phys. Lett.*, 74, 182.

Giorgetta, F. R., Baumann, E., Graf, M., Quankui, Y., Manz, C., *et al.* (2009) 'Quantum cascade detectors', *IEEE. J. Quantum Electron.*, 45, 1039.

Gmachl, C. and Ng, H. M. (2003) 'Intersubband absorption at ~2.1 μm in *a*-plane GaN/AlN multiple quantum wells', *Electron. Lett.*, 39, 567–569.

Gmachl, C., Ng, H. M., Chu, S. N. G. and Cho, A. Y. (2000) 'Intersubband absorption at λ~1.55 μm in well- and modulation-doped GaN/AlGaN multiple quantum wells with superlattice barriers', *Appl. Phys. Lett.*, 77, 3722–3724.

Gmachl, C., Ng, H. M. and Cho, A. Y. (2001) 'Intersubband absorption in degenerately doped GaN/$Al_xGa_{1-x}N$ coupled double quantum wells', *Appl. Phys. Lett.*, 79, 1590–1592.

Gonschorek, M., Carlin, J.-F., Feltin, E., Py, M. A., Grandjean, N., *et al.* (2008) 'Two-dimensional electron gas density in $Al_{1-x}In_xN$/AlN/GaN heterostructures ($0.03 \leq x \leq 0.23$)', *J. Appl. Phys.*, 103, 093714.

Grandal, J., Pereiro, J., Bengoechea-Encabo, A., Fernández-Garrido, S., Sánchez-García, M. A., *et al.* (2011) 'InN/InGaN multiple quantum wells emitting at 1.5 μm grown by molecular beam epitaxy', *Appl. Phys. Lett.*, 98, 061901.

Hamazaki, J., Matsui, S., Kunugita, H., Ema, K., Kanazawa, H., *et al.* (2004) 'Ultrafast intersubband relaxation and nonlinear susceptibility at 1.55 μm in GaN/AlN multiple-quantum wells', *Appl. Phys. Lett.*, 84, 1102.

Heber, J., Gmachl, C., Ng, H. and Cho, A. (2002) 'Comparative study of ultrafast intersubband electron scattering times at 1.55 μm wavelength in GaN/AlGaN heterostructures', *Appl. Phys. Lett.*, 81, 1237.

Helman, A., Tchernycheva, M., Lusson, A., Warde, E., Julien, F. H., *et al.* (2003) 'Intersubband spectroscopy of doped and undoped GaN/AlN quantum wells grown by molecular-beam epitaxy', *Appl. Phys. Lett.*, 83, 5196–5198.

Heying, B., Averbeck, R., Chen, L. F., Haus, E., Riechert, H., *et al.* (2000) 'Control of GaN surface morphologies using plasma-assisted molecular beam epitaxy', *J. Appl. Phys.*, 88, 1855.

Hofstetter, D., Schad, S.-S., Wu, H., Schaff, W. J. and Eastman, L. F. (2003) 'GaN/AlN-based quantum-well infrared photodetector for 1.55 μm', *Appl. Phys. Lett.*, 83, 572.

Hofstetter, D., Baumann, E., Giorgetta, F. R., Graf, M., Maier, M., *et al.* (2006) 'High-quality AlN/GaN-superlattice structures for the fabrication of narrow-band 1.4 μm photovoltaic intersubband detectors', *Appl. Phys. Lett.*, 88, 121112.

Hofstetter, D., Baumann, E., Giorgetta, F. R., Guillot, F., Leconte, S., *et al.* (2007) 'Optically nonlinear effects in intersubband transitions of GaN/AlN-based superlattice structures', *Appl. Phys. Lett.*, 91, 131115.

Hofstetter, D., Baumann, E., Giorgetta, F. R., Theron, R., Wu, H., *et al.* (2010a) ‘Intersubband transition based processes and devices in GaN/AlN-based heterostructures’, *IEEE Proc.*, 98, 1234–1248.

Hofstetter, D., Di Francesco, J., Kandaswamy, P. K., Das, A., Valdueza-Felip, S., *et al.* (2010b) ‘Performance improvement of AlN–GaN-based intersubband detectors by using quantum dots’, *IEEE Photonics Technol. Lett.*, 22, 1087.

Hori, Y., Biquard, X., Monroy, E., Jalabert, D., Enjalbert, F., *et al.* (2004) ‘GaN quantum dots doped with Eu’, *Appl. Phys. Lett.*, 84, 206.

Hori, Y., Andreev, T., Jalabert, D., Monroy, E., Le Si Dang, *et al.* (2006) ‘GaN quantum dots doped with Tb’, *Appl. Phys. Lett.*, 88, 053102.

Iizuka, N., Kaneko, K., Suzuki, N., Asano, T., Noda, S., *et al.* (2000) ‘Ultrafast intersubband relaxation (150 fs) in AlGaN/GaN multiple quantum wells’, *Appl. Phys. Lett.*, 77, 648.

Iizuka, N., Kaneko, K. and Suzuki, N. (2002) ‘Near-infrared intersubband absorption in GaN/AlN quantum wells grown by molecular beam epitaxy’, *Appl. Phys. Lett.*, 81, 1803–1805.

Iizuka, N., Kaneko, K. and Suzuki, N. (2004) ‘Sub-picosecond modulation by intersubband transition in ridge waveguide with GaN/AlN quantum wells’, *Electron. Lett.*, 40, 962963.

Iizuka, N., Kaneko, K. and Suzuki, N. (2005) ‘Sub-picosecond all-optical gate utilizing an intersubband transition’, *Optics Express*, 13, 3835.

Iizuka, N., Kaneko, K. and Suzuki, N. (2006a) ‘Polarization dependent loss in III-nitride optical waveguides for telecommunication devices’, *J. Appl. Phys.*, 99, 093107.

Iizuka, N., Kaneko, K. and Suzuki, N. (2006b) ‘All-optical switch utilizing intersubband transition in GaN quantum wells’, *IEEE J. Quantum Electron*, 42, 765.

Iizuka, N., Yoshida, H., Managaki, N., Shimizu, T., Hassanet, S., *et al.* (2009) ‘Integration of GaN/AlN all-optical switch with SiN/AlN waveguide utilizing spot-size conversion’, *Optics Express*, 17, 23247.

Iliopoulos, E. and Moustakas, T. D. (2002) ‘Growth kinetics of AlGaN films by plasma-assisted molecular-beam epitaxy’, *Appl. Phys. Lett.*, 81, 295.

Jovanovic, V. D., Indjin, D., Ikonic, Z. and Harrison, P. (2004) ‘Simulation and design of GaN/AlGaN far-infrared (γ=34 μm) quantum-cascade laser’, *Appl. Phys. Lett.*, 84, 2995.

Kandaswamy, P. K., Guillot, F., Bellet-Amalric, E., Monroy, E., Nevou, L., *et al.* (2008) ‘GaN/AlN short-period superlattices for intersubband optoelectronics: a systematic study of their epitaxial growth, design, and performance’, *J. Appl. Phys.*, 104, 093501.

Kandaswamy, P. K., Bougerol, C., Jalabert, D., Ruterana, P. and Monroy, E. (2009a) ‘Strain relaxation in short-period polar GaN/AlN superlattices’, *J. Appl. Phys.*, 106, 013526.

Kandaswamy, P. K., Machhadani, H., Bougerol, C., Sakr, S., Tchernycheva, M., *et al.* (2009b) ‘Midinfrared intersubband absorption in GaN/AlGaN superlattices on Si(111) templates’, *Appl. Phys. Lett.*, 95, 141911.

Kandaswamy, P. K., Machhadani, H., Kotsar, Y., Sakr, S., Das, A., *et al.* (2010) ‘Effect of doping on the mid-infrared intersubband absorption in GaN/AlGaN superlattices grown on Si(111) templates’, *Appl. Phys. Lett.*, 96, 141903.

Kikuchi, A., Kawai, M., Tada, M. and Kishino, K. (2004) ‘InGaN/GaN multiple quantum disk nanocolumn light-emitting diodes grown on (111) Si substrate’, *Jpn. J. Appl. Phys.*, 43, L1524–L1526.

Kishino, K., Kikuchi, A., Kanazawa, H. and Tachibana, T. (2002) ‘Intersubband transition in (GaN)[sub *m*]/(AlN)[sub *n*] superlattices in the wavelength range from 1.08 to 1.61 μm’, *Appl. Phys. Lett.*, 81, 1234–1236.

Kishino, K., Kamimura, J. and Kamiyama, K. (2012) 'Near-infrared InGaN nanocolumn light-emitting diodes operated at 1.46 μm', *Appl. Phys. Express*, 5, 031001.

Köhler, R., Tredicucci, A., Beltram, F., Beere, H. E., Linfield, E. H., *et al.* (2002) 'Terahertz semiconductor-heterostructure laser', *Nature*, 417, 156.

Kotsar, Y., Machhadani, H., Sakr, S., Kandaswamy, P. K., Tchernycheva, M., *et al.* (2011a) 'III-nitride semiconductors for intersubband devices', *Proc. SPIE*, 7945, 79451D.

Kotsar, Y., Doisneau, B., Bellet-Amalric, E., Das, A., Sarigiannidou, E., *et al.* (2011b) 'Strain relaxation in GaN/$Al_xGa_{1-x}N$ superlattices grown by plasma-assisted molecular-beam epitaxy', *J. Appl. Phys.*, 110, 033501.

Kumar, S., Hu, Q. and Reno, J. L. (2009) '186 K operation of terahertz quantum-cascade lasers based on a diagonal design', *Appl. Phys. Lett.*, 94, 131105.

Lahourcade, L., Kandaswamy, P. K., Renard, J., Ruterana, P., Machhadani, H., *et al.* (2008) 'Interband and intersubband optical characterization of semipolar (11-22)-oriented GaN/AlN multiple-quantum-well structures', *Appl. Phys. Lett.*, 93, 111906.

Levine, B. F. (1993) 'Device physics of quantum well infrared photodetectors', *J. Appl. Phys.*, 74, R1–R81.

Li, Y., Bhattacharyya, A., Thomidis, C., Moustakas, T. D. and Paiella, R. (2007) 'Ultrafast all-optical switching with low saturation energy via intersubband transitions in GaN/AlN quantum-well waveguides', *Optics Express*, 15, 17922.

Lin, K. I., Tsai, J. T., Wang, T. S., Hwang, J. S., Chen, M. C., *et al.* (2008) 'Drift current dominated terahertz radiation from InN at low-density excitation', *Appl. Phys. Lett.*, 93, 262102.

Liu, H. C. and Capasso, F. (eds) (2000) *Intersubband Transitions in Quantum Wells*, Academic.

Liu, X. Y., Holmström P., Jänes, P., Thylén, L. and Andersson, T. G. (2007) 'Intersubband absorption at 1.5–3.5 μm in GaN/AlN multiple quantum wells grown by molecular beam epitaxy on sapphire', *Phys. Stat. Sol. B*, 244, 2892–2905.

Lü, J. T. and Cao, J. C. (2006) 'Monte Carlo simulation of hot phonon effects in resonant-phonon-assisted terahertz quantum-cascade lasers', *Appl. Phys. Lett.*, 88, 061119.

Machhadani, H., Kotsar, Y., Sakr, S., Tchernycheva, M., Colombelli, R., *et al.* (2010) 'Terahertz intersubband absorption in GaN/AlGaN step quantum wells', *Appl. Phys. Lett.*, 97, 191101.

Machhadani, H., Tchernycheva, M., Rigutti, L., Sakr, S., Colombelli, R., *et al.* (2011) 'Intersubband absorption of cubic GaN/Al(Ga)N quantum wells in the near-infrared to terahertz spectral range', *Phys. Rev. B*, 83, 075313.

Machhadani, H., Beeler, M., Sakr, S., Warde, E., Tchernycheva, M., *et al.* (2013) 'Systematic study of near-infrared intersubband absorption of polar and semipolar GaN/AlN quantum wells', *J. Appl. Phys.*, 113, 143109.

Mackenzie, J. D., Abernathy, C. R., Pearton, S. J., Hommerich, U., Wu, X., *et al.* (1997) 'Er doping of III-nitrides during growth by metalorganic molecular beam epitaxy', *J. Cryst. Growth*, 175/176, 84.

Malis, O., Edmunds, C., Li, D., Manfra, M. J. and Sivco, D. L. (2009) 'Near-infrared intersubband absorption in molecular-beam epitaxy-grown lattice-matched InAlN/GaN superlattices', *Appl. Phys. Lett.*, 94, 161111.

Matthaus, G., Cimalla, V., Pradarutti, B., Riehemann, S., Notni, G., *et al.* (2008) 'Highly effcient THz emission from differently grown InN at 800 nm and 1060 nm excitation', *Opt. Commun.*, 281, 3776.

Mirzaei, B., Rostami, A. and Baghban, H. (2012) 'Terahertz dual-wavelength quantum cascade laser based on GaN active region', *Optics Laser Technol.*, 44, 378–383.

Mu, X., Ding, Y., Wang, K., Jena, D. and Zotova, Y. B. (2007) 'Resonant terahertz generation from InN thin films', *Opt. Lett.*, 32, 1423.

Naranjo, F. B., Kandaswamy, P. K., Valdueza-Felip, S., Calvo, V., González-Herráez, M., *et al.* (2011) 'Non-linear absorption of InN/InGaN multiple-quantum-well structures at optical telecommunication wavelengths', *Appl. Phys. Lett.*, 98, 031902.

Neugebauer, J., Zywietz, T. K., Scheffler, M., Northrup, J. E., Chen, H., *et al.* (2003) 'Adatom kinetics on and below the surface: the existence of a new diffusion channel', *Phys. Rev. Lett.*, 90, 056101.

Nevou, L., Julien, F. H., Colombelli, R., Guillot, F. and Monroy, E. (2006) 'Room-temperature intersubband emission of GaN/AlN quantum wells at $\lambda = 2.3\,\mu$m', *Electronics Lett.*, 42, 1308–1309.

Nevou, L., Tchernycheva, M., Julien, F. H., Guillot, F. and Monroy, E. (2007) 'Short wavelength ($\lambda = 2.13\,\mu$m) intersubband luminescence from GaN/AlN quantum wells at room temperature', *Appl. Phys. Lett.*, 90, 121106.

Nevou, L., Julien, F. H., Tchernycheva, M., Guillot, F., Monroy, E., *et al.* (2008) 'Intraband emission at $\lambda \approx 1.48\,\mu$m from GaN/AlN quantum dots at room temperature', *Appl. Phys. Lett.*, 92, 161105.

Nevou, L., Mangeney, J., Tchernycheva, M., Julien, F. H., Guillot, F., *et al.* (2009) 'Ultrafast relaxation and optical saturation of intraband absorption of GaN/AlN quantum dots', *Appl. Phys. Lett.*, 94, 132104.

Ng, H. M., Gmachl, C., Siegrist, T., Chu, S. N. G. and Cho, A. Y. (2001) 'Growth and characterization of GaN/AlGaN superlattices for near-infrared intersubband transitions', *Phys. Stat. Sol. A*, 188, 825–831.

Ng, H. M., Gmachl, C., Heber, J. D., Hsu, J. W. P., Chu, S. N. G., *et al.* (2002) 'Recent progress in GaN-based superlattices for near-infrared intersubband transitions', *Phys. Stat. Sol. B*, 234, 817–821.

Nicolay, S., Carlin, J. F., Feltin, E., Butte, R., Mosca, M., *et al.* (2005) 'Midinfrared intersubband absorption in lattice-matched AlInN/GaN multiple quantum wells', *Appl. Phys. Lett.*, 87, 111106.

Nicolay, S., Feltin, E., Carlin, J.-F., Mosca, M., Nevou, L., *et al.* (2006) 'Indium surfactant effect on AlN/GaN heterostructures grown by metal-organic vapor-phase epitaxy: applications to intersubband transitions', *Appl. Phys. Lett.*, 88, 151902.

Nicolay, S., Feltin, E., Carlin, J.-F., Grandjean, N., *et al.* (2007) 'Strain-induced interface instability in GaN/AlN multiple quantum wells', *Appl. Phys. Lett.*, 91, 061927.

O'Donnell, K. P. and Hourahine, B. (2006) 'Rare earth III-nitrides for optoelectronics', *Eur. Phys. J. Appl. Phys.*, 36, 91–103.

Péré-Laperne, N., Bayram, C., Nguyen-Thê, L., McClintock, R. and Razeghi, M. (2009) 'Tunability of intersubband absorption from 4.5 to 5.3 μm in a GaN/$Al_{0.2}Ga_{0.8}N$ superlattices grown by metalorganic chemical vapor deposition', *Appl. Phys. Lett.*, 95, 131109.

Polyakov, V. M., Cimalla, V., Lebedev, V. and Schwierz, F. (2010) 'Impact of *n*-type doping on the terahertz surface emission from *c*-plane InN', *Phys. Stat. Sol. A*, 207, 1353–1355.

Pugh, S. K., Dugdale, D. J., Brand, S. and Abram, R. A. (1999) 'Electronic structure calculations on nitride semiconductors', *Semicond. Sci. Technol.*, 14, 23.

Rapaport, R., Chen, G., Mitrofanov, O., Gmachl, C., Ng, H. M., *et al.* (2003) 'Resonant optical nonlinearities from intersubband transitions in GaN/AlN quantum wells', *Appl. Phys. Lett.*, 83, 263–265.

Sakr, S., Kotsar, Y., Haddadi, S., Tchernycheva, M., Vivien, L., *et al.* (2010) 'GaN-based quantum cascade photodetector with 1.5 μm peak detection wavelength', *Electron. Lett.*, 46, 1685.

Sakr, S., Giraud, E., Dussaigne, A., Tchernycheva, M., Grandjean, N., *et al.* (2012a) 'Two-color GaN/AlGaN quantum cascade detector at short infrared wavelengths of 1 and 1.7 μm', *Appl. Phys. Lett.*, 100, 181103.

Sakr, S., Giraud, E., Tchernycheva, M., Isac, N., Quach, P., *et al.* (2012b) 'A simplified GaN/AlGaN quantum cascade detector with an alloy extractor', *Appl. Phys. Lett.*, 101, 251101.

Sakr, S., Crozat, P., Gacemi, D., Kotsar, Y., Pesach, A., *et al.* (2013) 'GaN/AlGaN waveguide quantum cascade photodetectors at $\lambda \approx 1.55$ μm with enhanced responsivity and ~40 GHz frequency bandwidth', *Appl. Phys. Lett.*, 102, 011135.

Sarigiannidou, E., Monroy, E., Gogneau, N., Radtke, G., Bayle-Guillemaud, P., *et al.* (2006) 'Comparison of the quality in Ga-face and N-face polarity GaN/AlN multiple-quantum well structures', *Semicond. Sci. Technol.*, 21, 612.

Sato, H., Chung, R. B., Hirasawa, H., Fellows, N., Masui, H., *et al.* (2008) 'Optical properties of yellow light-emitting diodes grown on semipolar (11–22) bulk GaN substrates', *Appl. Phys. Lett.*, 92, 221110.

Sekiguchi, H., Kishino, K. and Kikuchi, A. (2010) 'Emission color control from blue to red with nanocolumn diameter of InGaN/GaN nanocolumn arrays grown on same substrate', *Appl. Phys. Lett.* 96, 231104.

Sherliker, B., Halsall, M., Kasalynas, I., Seliuta, D., Valusis, G., *et al.* (2007) 'Room temperature operation of AlGaN/GaN quantum well infrared photodetectors at a 3–4 μm wavelength range', *Semicond. Sci. Technol.*, 22, 1240.

Shubina, T. V., Andrianov, A. V., Zakhar'in, A. O., Jmerik, V. N., Soshnikov, I. P., *et al.* (2010) 'Terahertz electroluminescence of surface plasmons from nanostructured InN layers', *Appl. Phys. Lett.*, 96, 183106.

Sodabanlu, H., Yang, J.-S., Sugiyama, M., Shimogaki, Y. and Nakano, Y. (2009) 'Strain effects on the intersubband transitions in GaN/AlN multiple quantum wells grown by low-temperature metal organic vapor phase epitaxy with AlGaN interlayer', *Appl. Phys. Lett.*, 95, 161908.

Sodabanlu, H., Yang, J.-S., Tanemura, T., Sugiyama, M., Shimogaki, Y., *et al.* (2011) 'Intersubband absorption saturation in AlN-based waveguide with GaN/AlN multiple quantum wells grown by metalorganic vapor phase epitaxy', *Appl. Phys. Lett.*, 99, 151102.

Speck, J. S. and Chichibu S. F. (2009) 'Nonpolar and semipolar group III nitride-based materials', *MRS Bulletin*, 34, 304–312.

Steckl, A. J., Garter, M. J., Lee, D. S., Heikenfeld, J. and Birkhahn, R. H. (1999) 'Blue electroluminescence from Tm-doped GaN light emitting devices', *Appl. Phys. Lett.*, 75, 2184.

Steckl, A. J., Heikenfeld, J. C., Lee, D. S., Garter, M. J., Baker, C. C., *et al.* (2002) 'Rare-earth-doped GaN: growth, properties, and fabrication of electroluminescent devices', *IEEE J. Sel. Topics Quantum Electron.*, 8, 749–766.

Steckl, A. J., Park, J. H. and Zavada, J. M. (2007) 'Prospects for rare earth doped GaN lasers on Si', *Materials Today*, 10(7–8), 20.

Sugiura, L. (1997) 'Dislocation motion in GaN light-emitting devices and its effect on device lifetime', *J. Appl. Phys.*, 81, 1633–1638.

Sun, G., Soref, R. A. and Khurgin, J. B. (2005) 'Active region design of a terahertz GaN/$Al_{0.15}Ga_{0.85}N$ quantum cascade laser', *Superlattices Microstructures*, 37, 107.

Sun, G., Xu, G., Ding, Y. J., Zhao, H., Liu, G., *et al.* (2011) 'Efficient terahertz generation within InGaN/GaN multiple quantum wells', *IEEE J. Sel. Topics Quantum Electron.*, 17, 48–53.

Suzuki, N. and Iizuka, N. (1999) 'Effect of polarization field on intersubband transition in AlGaN/GaN quantum wells', *Jpn. J. Appl. Phys.*, 38 (Part 2, No. 4A), L363–L365.

Suzuki, M. and Uenoyama, T. (1996) 'Optical gain and symmetry in III-V nitride lasers', *Appl. Phys. Lett.*, 69, 3378.

Tchernycheva, M., Nevou, L., Doyennette, L., Julien, F. H., Warde, E., *et al.* (2006) 'Systematic experimental and theoretical investigation of intersubband absorption in GaN/AlN quantum wells', *Phys. Rev. B*, 73, 125347.

Terashima, W. and Hirayama, H. (2009) 'Design and fabrication of terahertz quantum cascade laser structure based on III-nitride semiconductors', *Phys. Stat. Sol. C*, 6, S615–S618.

Terashima, W. and Hirayama, H. (2011) 'Spontaneous emission from GaN/AlGaN terahertz quantum cascade laser grown on GaN substrate', *Phys. Stat. Sol. C*, 8, 2302–2304.

Tian, W., Yan, W. Y., Hui, X., Li, S. L., Ding, Y. Y., *et al.* (2012) 'Tunability of intersubband transition wavelength in the atmospheric window in AlGaN/GaN multi-quantum wells grown on different AlGaN templates by metalorganic chemical vapor deposition', *J. Appl. Phys.*, 112, 063526.

Ugolini, C., Nepal, N., Lin, J. Y., Jiang, H. X. and Zavada, J. M. (2006) 'Erbium-doped GaN epilayers synthesized by metal-organic chemical vapor deposition', *Appl. Phys. Lett.*, 89, 151903.

Ugolini, C., Nepal, N., Lin, J. Y., Jiang, H. X. and Zavada, J. M. (2007) 'Excitation dynamics of the 1.54 μm emission in Er doped GaN synthesized by metal organic chemical vapor deposition', *Appl. Phys. Lett.*, 90, 015110.

Vardi, A., Akopian, N., Bahir, G., Doyennette, L., Tchernycheva, M., *et al.*, (2006) 'Room temperature demonstration of GaN/AlN quantum dot intraband infrared photodetector at fiber-optics communication wavelength', *Appl. Phys. Lett.*, 88, 143101.

Vardi, A., Bahir, G., Guillot, F., Bougerol, C., Monroy, E., *et al.* (2008a) 'Near infrared quantum cascade detector in GaN/AlGaN/AlN heterostructures', *Appl. Phys. Lett.*, 92, 011112.

Vardi, A., Kheirodin, N., Nevou, L., Machhadani, H., Vivien, L., *et al.* (2008b) 'High-speed operation of GaN/AlGaN quantum cascade detectors at $\lambda \approx 1.55\,\mu m$', *Appl. Phys. Lett.*, 93, 193509.

Vardi, A., Bahir, G., Sachacham, S., Kandaswamy, P. K. and Monroy, E. (2009) 'Photocurrent spectroscopy of bound-to-bound intraband transitions in GaN/AlN quantum dots', *Phys. Rev. B*, 80, 155439.

Vardi, A., Sakr, S., Mangeney, J., Kandaswamy, P. K., Monroy, E., *et al.* (2011) 'Femto-second electron transit time characterization in GaN/AlGaN quantum cascade detector at 1.5 micron', *Appl. Phys. Lett.*, 99, 202111.

Vukmirovic, N., Jovanovic, V. D., Indjin, D., Ikonic, Z., Harrison, P., *et al.* (2005) 'Optically pumped terahertz laser based on intersubband transitions in a GaN/AlGaN double quantum well', *J. Appl. Phys.*, 97, 103106.

Wang, X. Q., Zhao, G. Z., Zhang, Q., Ishitani, Y., Yoshikawa, A., *et al.* (2010) 'Effect of Mg doping on enhancement of terahertz emission from InN with different lattice polarities', *Appl. Phys. Lett.*, 96, 061907.

Williams, B. S., Callebaut, H., Kumar, S., Hu, Q. and Reno, J. L. (2003) '3.4-THz quantum cascade laser based on longitudinal-optical-phonon scattering for depopulation', *Appl. Phys. Lett.*, 82, 1015–1017.

Williams, B. S, Kumar, S., Hu, Q. and Reno, J. L. (2005) 'Operation of terahertz quantum-cascade lasers at 164 K in pulsed mode and at 117 K in continuous-wave mode', *Opt. Expr.*, 13, 3331.

Wilson, R. G., Schwartz, R. N., Abernathy, C. R., Pearton, S. J., *et al.* (1994) '1.54 μm photoluminescence from erbium and oxygen co-implanted GaN', *Appl. Phys. Lett.*, 65, 992.

Wu, J. (2009) 'When group-III nitrides go infrared: new properties and perspectives', *J. Appl. Phys.*, 106, 011101.

Wu, G.-G., Li, W.-C., Shen, C.-S., Gao, F.-B., Liang, H.-W., *et al.* (2012) 'Near infrared electroluminescence from *n*-InN/*p*-GaN light-emitting diodes', *Appl. Phys. Lett.*, 100, 103504.

Xu T., Nikiforov, A. Y., France, R., Thomidis, C., Williams, A., *et al.* (2007) 'Blue–green–red LEDs based on InGaN quantum dots grown by plasma-assisted molecular beam epitaxy', *Phys. Stat. Sol. A*, 204, 2098–2102.

Xu, G., Ding, Y. J., Zhao, H., Liu, G., Jamil, M., *et al.* (2010) 'THz generation from InN films due to destructive interference between optical rectification and photocurrent surge', *Semicond. Sci. Technol.*, 25, 015004.

Xu, G., Sun, G., Ding, Y. J., Zotova, I. B., Jamil, M., *et al.* (2011) 'Mechanism for THz generation from InN micropyramid emitters', *J. Appl. Phys.*, 109, 093111.

Yang, K. H., Richards, P. L. and Shen, Y. R. (1971) 'Generation of far-infrared radiation by picosecond light pulses in $LiNbO_3$', *Appl. Phys. Lett.*, 19, 320.

Yang, J.-S., Sodabanlu, H., Sugiyama, M., Nakano, Y. and Shimogaki, Y. (2009) 'Blueshift of intersubband transition wavelength in AlN/GaN multiple quantum wells by low temperature metal organic vapor phase epitaxy using pulse injection method', *Appl. Phys. Lett.*, 95, 162111.

Yasuda, H., Kubis, T. and Hirakawa, K. (2011) 'Non-equilibrium Green's function calculation for GaN-based terahertz quantum cascade laser structures', *2011 36th International Conference on Infrared, Millimeter and Terahertz Waves (IRMMW-THz)*.

Yasuda, H., Hosako, I. and Hirakawa, K. (2012) 'Designs of GaN-based terahertz quantum cascade lasers for higher temperature operations', *2012 Conference on Lasers and Electro-Optics (CLEO). THz)*.

19

LEDs for liquid crystal display (LCD) backlighting

C.-F. CHEN, National Central University, Taiwan

DOI: 10.1533/9780857099303.3.566

Abstract: Over the past decade, light-emitting diodes (LEDs) have been adopted for use in various liquid crystal display (LCD) devices, from mobile phones to LCD televisions. LCDs with LED backlight units have become a popular choice for display purposes. For LCD devices, the quality and features of the light source affect or even directly determine the optical quality and market competitiveness of the LCD products. Several advantages of LEDs solve a few outstanding problems with LCDs. LEDs inside LCDs have solidified the mainstream status of LCDs. We describe the types and structures of LED LCD backlight units, the market trends and technological developments, the advantages and key technologies of LED LCD televisions, and the key points in the optical design of LED backlights.

Key words: LED LCD backlight, LCD backlight, backlight unit, LED backlight.

19.1 Introduction

With the rapid increase of modern multimedia requirements, a wide range of display devices have become available. Thin-film-transistor liquid crystal displays (TFT-LCDs) are one of the most popular display devices. They range from small to large[1–3] in devices such as mobile phones, notebooks and netbooks (NBs), car navigation systems and televisions. Because an LCD cannot radiate by itself, it has to rely on an external source to provide the illumination. Generally, a backlight unit (BLU) positioned on the back of an LCD cell is used to supply sufficient and uniform brightness and light for transmissive and transflective LCDs. Around 2004, LCD technology became suitable for televisions. Due to the strong market demand for thin flat-panel televisions and the limits on other display technology from technological bottlenecks, LCD televisions have gradually penetrated the television market. The penetration rate of LCD televisions exceeded 50% for the first time in 2008 and they have substantially replaced the cathode ray tube (CRT). However, LCD televisions still have many shortcomings, such as poor viewing angles, response times, contrast ratios and color gamut compared to plasma televisions. Therefore some people have always thought that the LCD television would just be a transitional product, unless its shortcomings could be overcome or its features improved. Currently, everyone agrees that the LED light source has

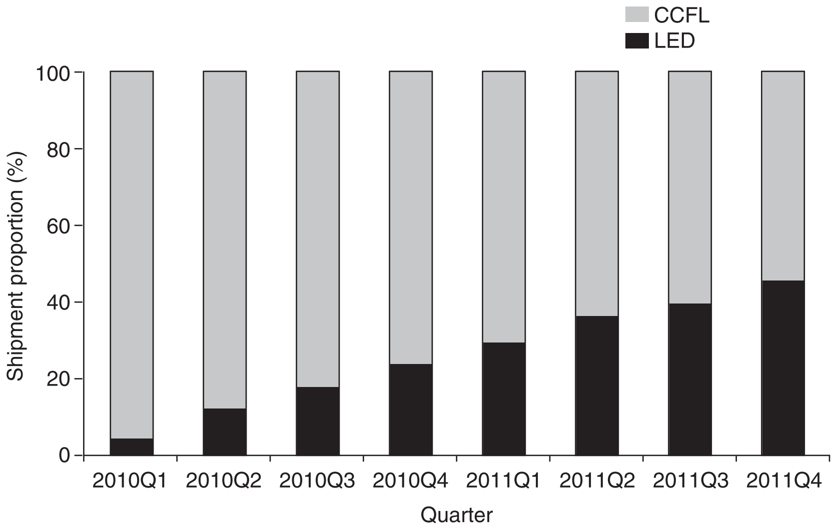

19.1 Shipment proportion of LED and CCFL LCD televisions.[4]

been the savior of LCD technology. LEDs can effectively overcome the shortcomings of LCDs and enhance their quality. Thus LCDs have successfully consolidated their mainstream status, especially in LCD televisions. The shipment proportion of LED and cold cathode fluorescent lamp (CCFL) LCD televisions based on a survey by Displaybank in February 2012 is shown in Figure 19.1.[4] For LCD televisions, the LED penetration rate is increasing and it exceeded 50% in the last quarter of 2011.

Over the last decade, organic light-emitting diode (OLED) display technology has been the biggest threat to LCD technology. Although the LCD technology using LEDs has improved and can be further enhanced in the future, as long as the OLED display technology manufacturing costs decline, LCD technology is still in danger of being replaced by OLED technology. This is because OLEDs are self-emissive and have many other advantages over LED LCD technology, such as wider viewing angles, faster response times, slim body, light weight and they can flex.

19.2 Types of LED LCD backlighting units (BLUs)

19.2.1 Technical considerations for the light source

The most significant part of a BLU is the light source. The best light source for a specific BLU is determined by factors such as spectral content, luminous flux and efficiency, operating temperature range and stability over that range, and dimmability. The types of light source used in BLUs include: LEDs, CCFLs, hot

Table 19.1 General characteristics of light sources for BLUs[5]

Characteristics	CCFL	White LED	RGB LED	FFL	EEFL	HCFL
Typical efficiency (lm/W)	80	>100	>60	30	80	65
Color gamut (% of NTSC specification)	72–80%	>65%	>100%	80%	72%	92%
Mercury	~4 mg	0 mg	0 mg	0 mg	<4 mg	>5 mg
Produced heat	Moderate	Moderate	Moderate	High	Low	Moderate
Gas composition	Hg, Ar, Ne	None	None	Xe, Ar, Ne	Hg	Ar

cathode fluorescent lamps (HCFLs), external electrode fluorescent lamps (EEFLs), flat fluorescent lamps (FFLs) and electroluminescent (EL) devices.[3] The general properties of these light sources for BLUs are listed in Table 19.1.[5] CCFLs were once considered the best light sources for LCDs, even though they have many shortcomings. The advantageous properties of LEDs and FFLs make them more suitable than CCFLs for use in a BLU.

In recent years, with the rapid development of LED technology, especially the advances in luminous flux and efficiency, LEDs have gradually replaced CCFLs and they are used in all LCD products. Further, the rate of incorporation of LEDs into each type of LCD product has begun to gradually increase. Their use in LCD backlights has always been the main driving force behind the LED market.

The applications of LED BLUs to LCDs roughly fall into three categories depending on how the white light is generated:

- The multi-color type of LED is composed of multiple-colored LEDs or LED chips and can be controlled to produce different colors at different temperatures. The most common are RGB LEDs consisting of red (R), green (G) and blue (B) LEDs. The cell of an RGB LED has one red LED, one green LED and one blue LED or one red LED, two green LEDs and one blue LED. Recently, two kinds of six-color LED solutions have been proposed: either red, green, blue, cyan (C), yellow (Y) and magenta (M) or red, green, blue, cyan yellow and purple (P).
- A typical phosphor type of LED comprises a blue LED chip closely packaged with a yellow phosphor or red and green phosphors. Another phosphor type used to produce white light is the UV LED chip or LED packaged with blue and yellow phosphors or packaged with red, green and blue phosphors. A similar type of LED to the phosphor type is where the blue LED chip is based on a homoepitaxially grown zinc selenide (ZnSe) substrate. The function of the ZnSe substrate is the same as that of the phosphor in the typical phosphor type.
- A typical remote phosphor type of LED has the same working principle as the phosphor type, except that the phosphor and LED chip or LED are not adjacent.[6]

Within the above categories, the main types of LEDs used include: side-view white LEDs, top-view white LEDs, RGB multi-chip LEDs and single-color LEDs.

19.2.2 BLU classification

In general, there are four LED BLU structures for LCDs differentiated by the position of the light source and by their structural characteristics: edge-type, direct-type, hollow-type and folded-mixing-light guide plate (LGP)-type. Schematic diagrams of each type are shown in Fig. 19.2 (a–d).

Edge-type structure

An edge-type structure has at least one LED light bar located at an edge of the LGP of the LCD device, as shown in Fig. 19.2(a). Light is transmitted through a light guide by means of total internal reflection. The key components of an edge-type structure include: LEDs, an LGP with a micro-structure or dots, a back reflector and diffusers.[7] To meet the requirement for low power consumption, a brightness enhancement film (BEF) or dual brightness enhancement film (DBEF) needs to be used in the BLU.[8]

Direct-type structure

A direct-type structure has LEDs positioned below the LCD panel, as shown in Fig. 19.2(b). A typical direct-type backlight device includes: several LEDs placed above a metal core printed circuit board (MCPCB), a reflector, a diffusion plate and some optical function films.[9] This structure has the advantages of a large backlight, high brightness and light weight and is also easier for local dimming. However, to maintain a uniform brightness, a light-mixed cavity is necessary between the light sources and the diffusion plate. For this reason, a direct-type BLU is thicker than an edge-type BLU.

Hollow-type structure

Hollow-type structures have two directional LED light bars located at the two edges of the hollow cavity of the BLU, as shown in Fig. 19.2(c). A hollow-type structure BLU is composed of at least two LED light bars, a hollow cavity, a patterned reflector placed at the bottom of the cavity, a structural diffusion plate and some optical films.[10] The poor brightness uniformity is generally a serious drawback of this type.

Folded-mixing-LGP-type structure

A folded-mixing-LGP-type structure has at least one folded mixing color LGP and several multiple-color LEDs, typically RGB LEDs, positioned below the

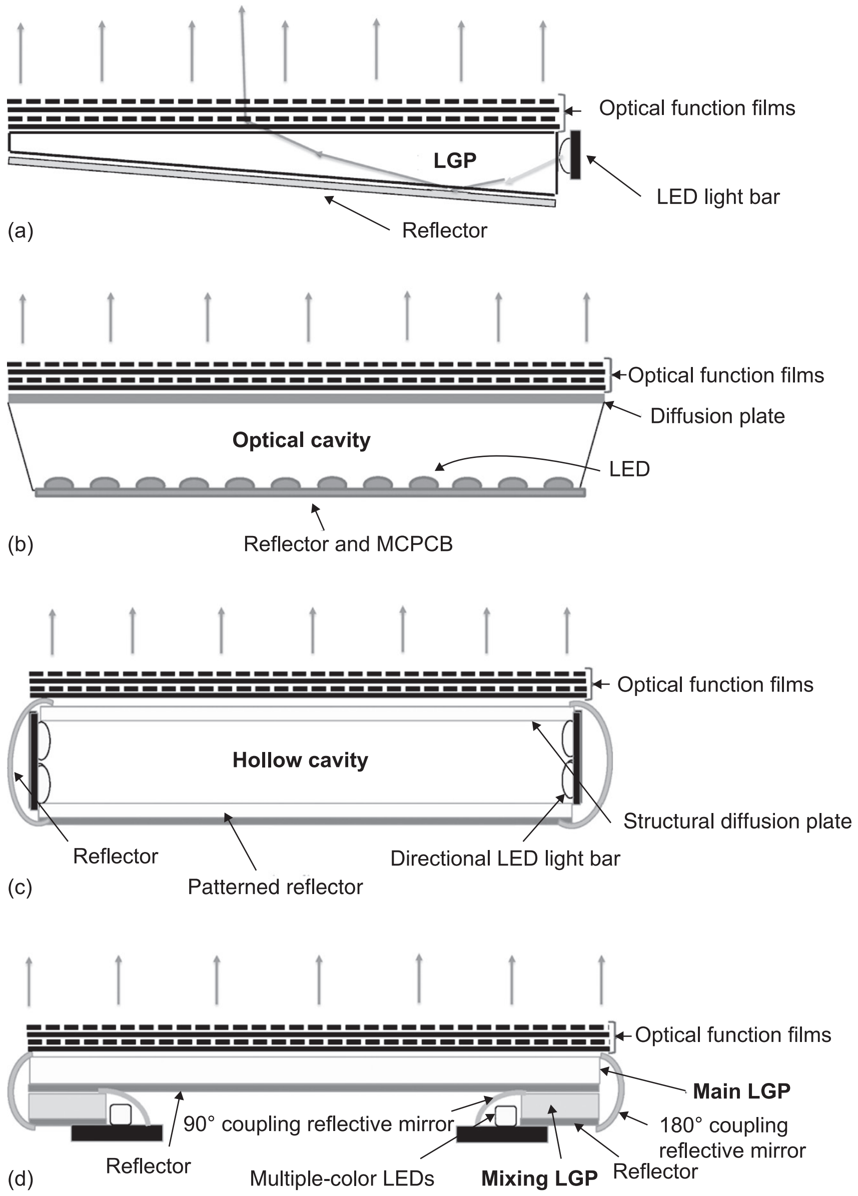
Optical function films
LGP
LED light bar
Reflector
(a)
Optical function films
Diffusion plate
Optical cavity
LED
Reflector and MCPCB
(b)
Optical function films
Hollow cavity
Structural diffusion plate
Reflector
Directional LED light bar
Patterned reflector
(c)
Optical function films
Main LGP
180° coupling reflective mirror
90° coupling reflective mirror
Reflector
Multiple-color LEDs
Mixing LGP
Reflector
(d)

19.2 Schematic diagrams of (a) edge-type, (b) direct-type, (c) hollow-type and (d) folded-mixing-LGP-type LED backlight structures for LCDs.

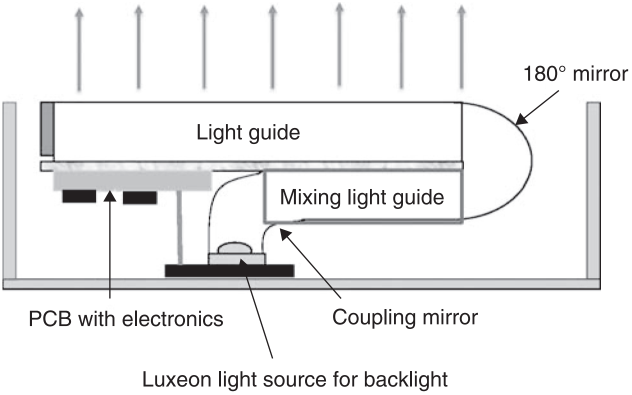

19.3 BLU assembly using a Luxeon DCC as a light source of.[12]

main LGP, as shown in Fig. 19.2(d). Its main components comprise: high-power multiple-color LEDs, a folded mixing LGP, a main LGP placed behind the LCD panel, a 90° coupling reflective mirror and a 180° coupling reflective mirror.[11, 12] Philips Lumileds Lighting Company has presented a typical structure for a BLU assembly. This uses a Luxeon DCC as a light source, which is based on RGB LEDs with a Lambertian radiation pattern, as shown in Fig. 19.3.[12] The multicolored light emitted from the multiple-color LEDs is coupled into the mixing light guide with a 90° mirror. This light is propagated, diffused and mixed in the mixing light guide. Uniform white light can be obtained from the folded mixing LGP. The 180° mirror then directs this white light into the main light guide. This type of structure has the advantages of high brightness, wider color gamut, compact shape and good thermal dissipation.

19.3 Technical considerations for optical films and plates

The optical qualities of a BLU depend on the optical films or plates used, such as an LGP, a diffusion film, a prismatic BEF, a micro-lens BEF, a reflective polarizer BEF and a diffusion plate. LGPs are usually made of optical grade materials such as polymethyl-methacrylate (PMMA), ZEONOR® or polycarbonate (PC). Table 19.2 lists the general characteristics of these three materials. The materials used for LGPs in the current market are still based on PMMA. An LGP can be either wedge-shaped or flat. In general, because of space considerations, mobile phones, car satellite navigation devices, notebooks, and small and medium-sized products commonly use a wedge-shaped LGP such as that shown in Fig. 19.2(a).

Table 19.2 General characteristics of three materials used for LGPs

Characteristics	PMMA	ZEONOR	PC
Proportion	1.2	1.01	1.20
Water absorption (%)	0.3	<0.01	0.2
Transmittance at 3 mm	92	92	88
Index of refraction	1.49	1.53	1.59
Hardness	2H	H	B
Glass transition temperature, T_g (°C)	105	140	145

Structured BEFs and reflective polarizer BEFs can recycle some of the wasted light energy, increasing the effective area of the luminance. The 3M Company manufactures BEFs, named the Vikuiti™ BEF II[13] and BEF III,[14] which can direct diffused light into the backlight and through the LCD. This increases the brightness for an on-axis viewer. Typically, two orthogonally aligned BEFs are used in the BLU of mobile products while the BLU of monitors and televisions uses a single BEF. In comparison, the Vikuiti™ DBEF, a very common reflective polarizer BEF, uses 3M's multi-layer optical film technology.[15] The DBEF increases the amount of light available for illuminating LCD displays by making use of light that would normally be absorbed by the rear polarizer of the LCD panel. The backlight efficiency is increased while maintaining the viewing angle. It can increase on-axis brightness by up to 60% in NB displays with a slab LGP and up to 97% in NB displays with a wedge LGP. The brightness gains of the Vikuiti™ BEF II and BEF III are listed in Table 19.3.

The main aim in the development of optical films and plates is multi-functional integration, to produce a so-called integrated optical film or plate. Examples are a BEF with a diffusion function, a diffusion film with a brightness enhancement function (usually called a gain diffusion film) and an LGP with a diffusion and/or brightness enhancement function.

Table 19.3 Brightness gains of Vikuiti™ BEF II[13] and BEF III[14]

	Single sheet	Two sheets crossed at 90°
BEF II	60%	120%
BEF III	59%	111%

19.4 Requirements for LCD BLUs

19.4.1 Features of LCD BLUs

An ideal BLU needs to have features such as good uniformity of the brightness, ultra-slim, light weight, ultra-narrow bezel, low power consumption, long life, wide color gamut (good white spectrum), short response time, large brightness adjustment range, fast modulation, temperature insensitivity, color that is adjustable according to the temperature, support for field sequential color technology, flexibility, support for two-dimensional (2D) and three-dimensional (3D) convertible displays, user friendly, environmentally friendly and low cost. Therefore, the light source itself should be slim, light and user and environmentally friendly and have low power consumption, a long life, quick response time, fast modulation, wide color gamut and a color adjustable according to temperature.

19.4.2 Environmental requirements

There are both legal environmental requirements and optional energy saving programs that can affect the development and use of electronic equipment. In July 2006, the European Union (EU) began the formal implementation of the RoHS Directive: the restriction of the use of certain substances in electrical and electronic equipment that are potentially hazardous to us. One of these controlled substances is mercury. However, as there is an exclusion clause for it, CCFLs can still continue to use mercury for now.

The Official Journal of the EU published Commission Regulation (EC) No. 642/2009 on 22 July 2009. This implemented Directive 2005/32/EC of the European Parliament and of the Council with regard to ecodesign requirements for televisions. The first phase of the regulations was implemented from 20 August 2010.

Energy Star is an international standard for energy-saving consumer products and programs. The project was initiated in the United States in the 1990s and has become multi-national. Manufacturers can choose of their own accord to affix the Energy Star label to qualified products. The first products included in the project were mainly computers and other information appliances. It was then gradually extended to motors, office equipment, lighting, appliances and so on. Table 19.4 lists the calculations for the maximum power requirements in the on mode.[16]

Table 19.4 Calculation of maximum on mode power requirements (P_{ON_MAX})[16]

Product type diagonal screen size, d (inches)	P_{ON_MAX} (watts) (r is the screen resolution in megapixels and A is the viewable screen area, rounded to the nearest 0.1 square inches)
$d < 12.0$	$(6.0 \times r) + (0.05 \times A) + 3.0$
$12.0 < d < 25.0$	$(6.0 \times r) + (0.0145 \times A) + 4.0$
$25.0 < d < 30.0$	$(6.0 \times r) + (0.18 \times A) - 40.0$
$30.0 < d < 60.0$	$(0.27 \times A) + 8.0$

19.5 Advantages and history of LED BLUs

19.5.1 Advantages of LEDs for LCD BLUs

LEDs provide numerous options and advantages for LCD BLUs. Generally the advantages of an LED BLU are the following.

Low operating DC voltage

LEDs use a low-voltage power-driven supply, unlike the high voltage power needed for a CCFL. Therefore, they do not need an inverter. This significantly helps to make an LED safer and reduces electronic noise. Not only that, an LED circuit can use less space, costs and energy consumption are reduced and the heat that would be generated by the inverter is not lost. The design of the power supply module is also relatively simple.

Wide operating temperature range

LEDs can work instantly at all temperatures without the need for heaters. The operating temperature range of an LED is between about −40 °C to +85 °C. LEDs can start promptly at −40 °C unlike CCFLs, which do not work properly in such environments. As LEDs are functional over a wide temperature range, they are favored by the military and in aviation, exploration and similar fields.

High luminous efficiency (low power consumption)

At present, the luminous efficiency of a white LED for use in a BLU is over about 130 lm/W. This is nearly twice as efficient as a CCFL. As LED technology progresses further, this luminous efficiency will continue to improve.

Package size and chroma selection flexibility

The optical design and use of LEDs is flexible. They are scalable and the chroma selection is flexible.

Wide color gamut

For the RGB LEDs used in LCDs, the National Television System Committee (NTSC) color gamut can be over 100% and can even achieve 150%.

Longer operating life

An LED has a specific lifespan. The lifetime is 60 000 to 100 000 hours, for a suitable current and voltage, which is far longer than a CCFL. Using LEDs can greatly extend the life of an LCD television and has overwhelming advantages compared with plasma technology.

Rapid switching speed

The response time of an LED is as short as a nanosecond, which is about one millionth that of a CCFL. The screen on an LCD device can appear blurry because of the slow response time of the liquid crystal. This is caused by screen persistence of fast moving objects. This drawback can be solved to some extent by using an LED BLU. An LED can support instant backlight blinking technology and dynamic scanning backlight technology. This technique effectively reduces motion blur and the display quality will be significantly improved. An LED can support the field sequential color technology. The color filter, which accounts for 30% of the cost of an LCD device, can be replaced by quick scanning RGB LEDs. An LED can also support local dimming technology. This technique can achieve high contrast and enhance the color saturation for low power consumption.

Wide adjustment range for brightness, contrast and chromaticity

LED power control is simple and the brightness adjustment range is large, unlike CCFLs, which have a threshold for the minimum brightness. Therefore, in the bright outdoors or dark indoors, it is simple for users to adjust the brightness of the display device for ease of viewing. This is particularly useful in automotive, avionic and marine electronics, where the product display must be able to deal with lighting conditions ranging from bright sunlight to the moon at night. In addition, when the video display source switches between computers and DVD players, it can be easily adjusted between a 9600 K and 6500 K white balance, without sacrificing the brightness and contrast.

Environmentally friendly

LEDs are made of non-toxic materials. Unlike incandescent lamps, they cause no mercury pollution, and there is no UV or IR radiation in their spectra.

Quicker illumination to stable brightness

LEDs require no warm-up time or general heating.

Robustness

LEDs have a high resistance to mechanical shock as they do not have glass tubes. LEDs are slim, light, safe and quiet: they are a solid-state solution without an inverter.

The above advantages significantly promote the use of LEDs in BLUs. Moreover, for specialized products such as military, avionics, marine and automotive displays, LCDs based on CCFLs are unable to meet user requirements.

However, there are still challenges in using LEDs. In particular, these include cost, system design complexity and performance with temperature. For a high-power LED BLU, it is very difficult to use the edge-type structure with a narrow bezel and the direct-type with high brightness uniformity and slim body. For a high-power RGB LED model, the optical design makes it difficult to obtain good color control and high color uniformity. Some of the time there will be an uneven color because the decay rate of each one of the LED colors is inconsistent. The heat produced by the LED will lead to LED color variation, LED brightness variation, shortened lifetime, deformation and LGP aging.

19.5.2 Development history of LED BLUs

LED BLUs were first used in mobile phones. This application of LEDs was also the fastest to penetrate the market for LCD products. Since edge-type BLUs with a side-view-type white LED do not require much packaging or high operating power, they have proven to be the best choice. From about 2006, the market began to use LEDS in the BLUs of notebooks. In 2006, computer manufacturers produced only 11.3-inch and 12.1-inch notebooks using LEDs. At the beginning of 2007, several computer manufacturers launched a 13.3-inch and even a larger 15.4-inch product using an LED backlight. The most common choice is a wedge-shaped LGP with a white top-view-type LED bar.

The LED industry and LCD industry intended to use LEDs in televisions. An RGB LED BLU was first used by Sony Corporation in August 2004 for its 40-inch and 46-inch QUALIA 005 LCD televisions. The power consumption for the 40-inch and 46-inch models is 470 W and 550 W, respectively. To solve the problem of how hot these become, the models use fans, heat pipes and heat sinks. The heat pipes are horizontally arranged and there are large heat sinks on both sides of the back of the BLU. The heat passes through the heat pipes to the heat sinks on both sides, which are cooled by fans. Using this particular design, the color gamut can be extended up to 105%. This elaborate design is expensive and uses a thick backlight unit (up to 10 cm). South Korea's Samsung Electronics demonstrated 46-inch and 40-inch LCD televisions without additional thermal design at the 2005 CES show. They used direct-type BLUs with a medium-power (0.3–0.5 W) LED and color sensor.

In 2006 there were crucial developments for LCD televisions. There were several technological advances and solutions to problems. Larger LCDs were successfully developed, such as LG Display's 100-inch model and Samsung Electronics' 82-inch model. A double frame rate (or higher) became possible, which can effectively solve the dynamic image blur. Local dimming (also known as high dynamic range) technology using an LED backlight can make the contrast quality up to 10 000 or more, and greatly reduce energy consumption. Further, eight-domain multi-domain vertical alignment (MVA) technology can reduce the color washout problem of the previous MVA technology, solving the problem of the LCD viewing angle.

The main focus of research for LCD LED BLUs is still to achieve high color saturation (or wide color gamut). Ultra-slim LCD televisions are realized by using a direct-type BLU with low-power LEDs or an edge-type BLU with medium-power LEDs. The field sequential color method works without a color filter. It uses direct fast-switching R-, G- and B-LEDs to produce the respective R-, G- and B-display pictures, through the persistence of vision to create full-color display effects.

The first large-screen LCD television with an edge-type LED BLU, the KLV-40ZX1M, was launched by Sony in September 2008. It was Sony's thinnest 40-inch LCD monitor measuring a mere 9.9 mm in width. However, it was expensive so demand for the product was poor. Samsung Electronics then launched a mid-priced LCD television with an edge-type BLU using medium-power LEDs. Due to a sales strategy highlighting the slim body, price and quality, Samsung Electronics successfully created the LED LCD television market. Thus, LED LCD televisions were a sought after commodity in 2009. Hence the market for LED LCD televisions was created.

According to a report by NPD DisplaySearch,[17] due to lower-than-expected consumer adoption of LED LCD televisions at the end of 2011, television makers changed their strategy for direct-type LED BLU televisions by developing products that use less power and cost less by reducing the number of LEDs per television set. Their aim is to develop an adaptation of the original LED BLU with a slim design and better picture quality.

19.6 Market trends and technological developments

19.6.1 Market trends

Over the past decade, LEDs have slowly been incorporated into various LCD devices, initially in mobile phones and recently in LCD televisions. Due to a combination of factors, including the fact that OLED development has made less progress than expected, that there has been no significant breakthrough in the technology of other light sources used in LCDs and that the quality of LEDs has been continuously improved, LCDs with an LED BLU have gradually become the best choice for displays. For LCD devices, the quality and features of the light source affect or even directly determine the optical quality and market competitiveness of the LCD products. Several advantages of LEDs solve a few of the outstanding problems with LCDs. It is clear that using an LED inside an LCD has increased the mainstream status of LCDs. A market forecast for large BLUs based on a survey by LEDinside published in August 2011 is shown in Fig. 19.4.

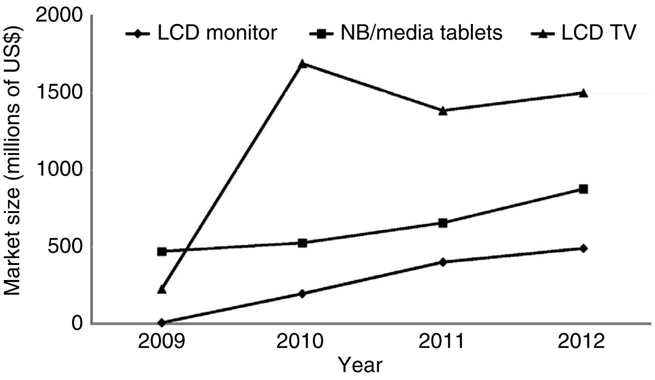

19.4 Market forecast for large BLUs based on a survey by LEDinside published in August 2011.

A cost forecast based on a survey produced by NPD DisplaySearch for different BLU types for 32-inch high-definition (HD) 60 Hz LCD televisions is shown in Fig. 19.5.[4] The high cost of LED BLUs obviously affects the commercial market penetration of LCDs based on LEDs. To reduce costs, television manufacturers have been adopting two-chip LEDs to reduce the number of LEDs. The number of LEDs used per set with a direct-type BLU is expected to be less than in a set with an edge-type BLU.[4] Figure 19.6 shows a forecast for the number of LED packages per television set.[17]

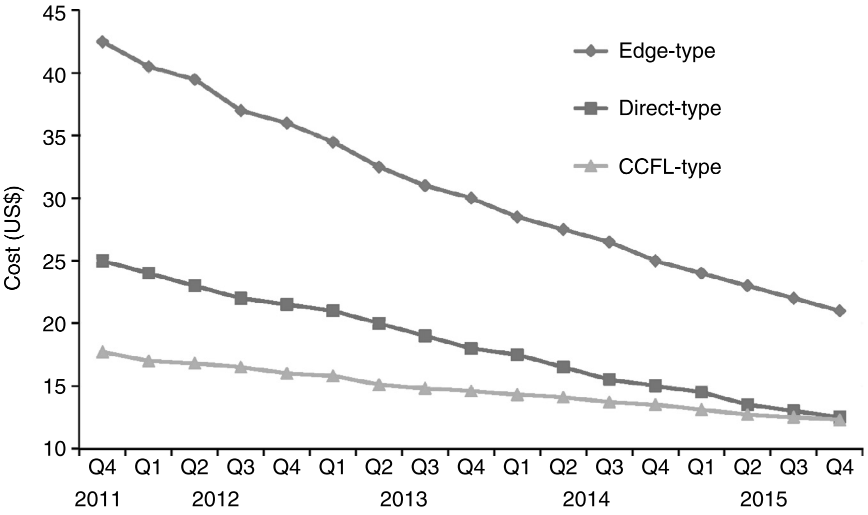

19.5 Cost forecast for different BLU types for 32-inch HD 60 Hz LCD televisions.[4]

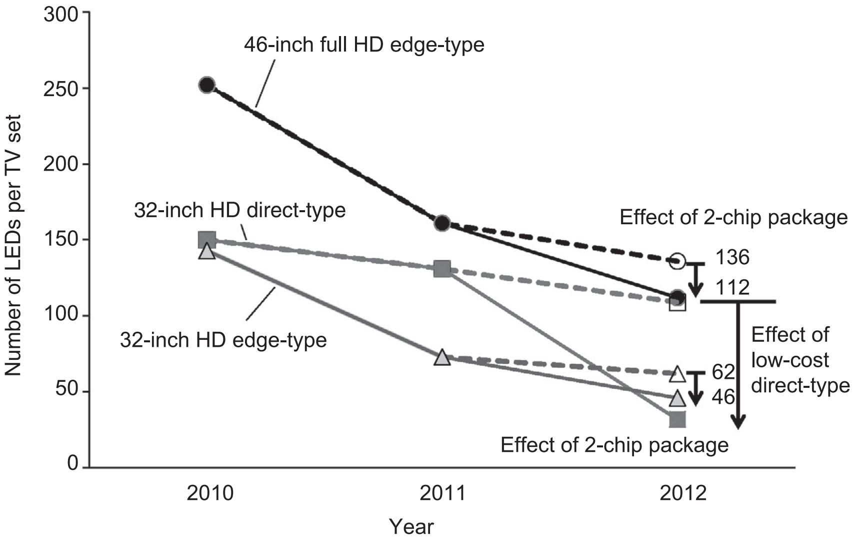

19.6 Forecast for number of LED packages per television set.[17]

Overall the focus of technological development is to produce devices with: a slimmer body; higher quality (in terms of better brightness uniformity, higher brightness, less unevenness, lower color washout and higher color saturation); lighter weight; lower cost; larger size; narrower bezel (for aesthetic reasons and ease of application, e.g. for an LCD video wall); better environmental factors (lower carbon emissions, lower power consumption and less use of non-toxic materials); rapid switching or rapid scanning; wide brightness and contrast adjustment ranges; finer local dimming and more smart functions, for example, auto-adjusting the brightness. However, many of these technologies are conflicting, for example, display size and power consumption or thickness and brightness uniformity for direct-type BLUs. Based on these desired qualities, an ideal BLU can almost be realized with LEDs and LEDs are able to meet the requirements of any application.

For different products and different product positioning, there are different trends in the technological developments. Tables 19.5 and 19.6 list these trends for the different products and product positioning, respectively.

The current status and the trends in development of LED LCD televisions are discussed below. Table 19.7 shows the status of the technology for LED LCD televisions. Recently, technological developments for LED LCD televisions using an edge-type structure have included:

- reducing the number of LED bars so that they are on one side instead of two sides to lower the cost
- reducing the thickness of the LGPs to reduce the cost, weight and module thickness

Table 19.5 Technological development trends for different products

Product	Common LED type		Common BLU type	Development trends
Mobile phone Netbook Notebook	B-LED chip+Y phosphor B-LED chip+RG phosphors	Low-power chip Medium-power chip	Edge-type	Slimmer Lighter weight Higher quality Narrower bezel Lower power consumption Wide brightness adjustment range Auto-adjust the brightness Environmentally friendly Lower cost
Monitor	B-LED chip+Y phosphor RGB chips LED RGB LED	Medium-power chip High-power chip	Edge-type Direct-type	Higher quality Narrower bezel Lower power consumption Auto-adjust the brightness Environmentally friendly Lower cost
Television	B-LED chip+Y phosphor	Low-power chip	Edge-type	All
Large announcement display	RGB LED	Medium-power chip High-power chip	Direct-type	

Table 19.6 Technological development trends for different product positioning

Product position	Common LED type		Common BLU type	Development trend
High-grade television	RGB LED B-LED chip+RG phosphors	Low-power chip Medium-power chip	Direct-type	All
Medium-grade television	B-LED chip+Y phosphor	Medium-power chip High-power chip	Edge-type	Slimmer Higher quality Environmentally friendly Lower cost
Low-grade television	B-LED chip+Y phosphor	Medium-power chip	Direct-type	Environmentally friendly
		High-power chip		Lower cost

Table 19.7 Status of technology for LED LCD televisions

	Direct-type			Edge-type
LED chip type	RGB LED Low-power chip Medium-power chip High-power chip	White LED[1] Low-power chip Medium-power chip	White LED High-power chip	White LED Medium-power chip High-power chip
Color gamut	>100%	70%	70%	70%
Local dimming	Yes	Yes	No	No
Thickness	Thicker	Slimmer	Thicker	Slimmer
Cost	Highest	Higher	Lowest	Lower
Power consumption	Lower	Lower	Higher	Higher
Chromaticity deviation	Larger	Smaller	Smaller	Larger
Image quality	Highest	Higher	Lower	Lower

Note:[1] B-LED chip+Y phosphor

- reducing the chromaticity deviation of the LGPs
- using micro-structures with higher efficiency for the LGPs
- using local dimming technology
- changing the packaging from the 5630 type to the longer 7030 type.

For edge-type structures, the technological development of LED LCD televisions mainly focuses on cost and quality.

19.6.2 Advantages and key technologies of LED LCD televisions

Compared with CCFL-type LCDs, LED-type LCDs:[18]

- produce images with greater dynamic contrast
- can be extremely slim with some screens less than half an inch (0.92 cm) thick[19]
- offer a wider color gamut when an RGB-LED BLU is used[20,21]
- produce less environmental pollution on disposal
- have typically 20–30% less power consumption
- are more robust and reliable
- have a non-linear, wider dimming range
- give full and flicker-free dimming at all temperatures down to 5% or lower
- can have a higher image quality
- can realize programmable chromaticity adjustments.

The key technologies used in LED LCD televisions that make them so advantageous include:

- LED spectral and LED light bar design
- good design potential
- thermal design
- optical design of modules
- integration and efficiency of the drive circuit
- local dimming technology.

19.6.3 New display technologies using LEDs: crystal LED displays

In early 2012, Sony Corporation announced that it had developed a next-generation self-luminous display technology called the crystal LED display, and unveiled a 55-inch crystal LED prototype at CES 2012.[22] Each pixel of an ultra-fine RGB color LED chip is directly connected to a light emitter. For 1080 full HD resolution, the total number of LED chips is about 6 million. So far, according to information from Sony Corporation, compared with existing LCDs, the prototype has about 3.5 times the contrast ratio, 1.4 times the color gamut and 10 times faster response time.

19.7 Optical design

19.7.1 Design factors

According to the specific application requirements, some of the design factors to be considered are:[23]

- diagonal display size
- panel thickness
- luminance
- color gamut
- thermal environment and associated constraints
- power limits
- dynamic contrast
- BLU cost.

19.7.2 Key design considerations

Compared to a CCFL-based BLU, the key design considerations include:

- designing the LED light guide bar to form line-shaped light, as in a CCFL
- for an edge-type structure, designing the micro-structure of the light injection surface of the LGP to diffuse light emitted from the LED chips fully
- for edge-type and direct-type structures, designing the secondary optical parts to diffuse light emitted from a middle- or high-LED chip array fully.

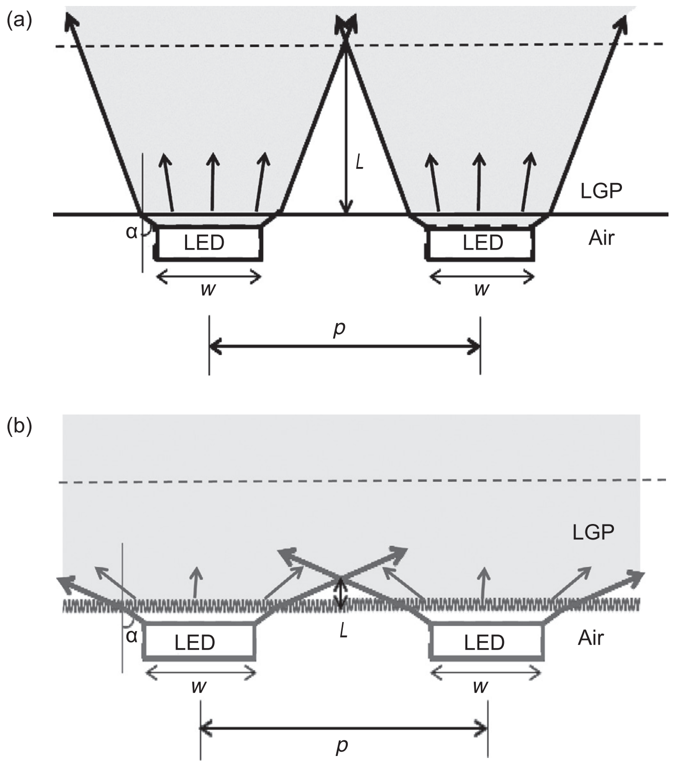

19.7 Light propagation from the light injection surface of an LGP (a) without and (b) with a micro-structure.

The effect of the micro-structure of the light injection surface of an LGP is shown in Fig. 19.7.

19.7.3 Edge-type BLUs

The optical design considerations for edge-type LED BLUs are listed in Table 19.8. When the white LED light is just coupled into the LGP, the light is more concentrated in front of the LED and then slowly spreads out. This unequal distribution of the light creates a hot spot. Using the estimated length of the color mixing area as a model,[24] the rough length of the hot spot area L for an injection surface without a micro-structure can be written as:

$$L = \frac{(p-w)/2}{\tan\left[\sin^{-1}\left(\frac{\sin\alpha}{n}\right)\right]}, \qquad [19.1]$$

Table 19.8 Optical design considerations for edge-type LED BLUs

Item	Description
Selection and configuration of LED type	1. Select the type of LEDs, such as side-view-type or top-view-type; white LED or multi-color LEDs. 2. Based on the features of the selected LED type, configure and design the relative position of all LEDs.
Diffusing light emitted from LED chips	To obtain a narrow bezel, select the micro-structure type and design the structure parameters of the light injection surface of the LGP. Because of the cost, some commercial products still do not use a micro-structure on the light injection surface of the LGP.
LGP geometry, physical properties and processing	1. Select a wedge-shaped or flat-shaped LGP. 2. Select the LGP material. 3. Select the processing method such as printing or injection molding.
Selection of the extraction patterns and design of the extraction pattern density on the bottom surface of the LGP	1. Select the extraction patterns for the up- and down-surfaces of the LGP. The light escape probability and escape angle are related to the geometry and optical features of the extraction patterns. 2. Consider manufacturing issues. 3. Based on the features of the selected LED type, design the extraction pattern (micro-structure) density on the bottom surface of the LGP to meet the requirements for uniformity, efficiency and manufacturability. 4. Based on cost, the extraction pattern is fabricated by etching and dot printing for most commercial products.
Injection molding or flat panel cutting	The LGP is fabricated by injection molding or flat panel cutting combining with dot printing or hot embossing.
Selection and disposition of optical films	The selection and disposition of the optical films will affect the viewing angle, efficiency, optical quality and cost.
Chromaticity uniformity and chromaticity shifting	1. The optical films, LGP material and manufacturing method will affect the chromaticity deviation. 2. Using laser direct processing and hot embossing to fabricate the extraction patterns can reduce the chromaticity deviation. 3. The LED chromaticity must be uniform.
With or without local dimming	LGP design is specific to the 1D local dimming technology used. Based on cost and technology maturity, most commercial products do not use local dimming.

where p is the LED pitch, w is the width of the LED emitting area, α is a half of the half-intensity angle and n is the LGP index. Schematic diagrams of these parameters and light propagation are shown in Fig. 19.7. This estimated result is very rough. If the selected LEDs are multi-color, the estimated length of the color mixing area is the same as in Eq. 19.1, except that p is modified to represent the maximum pitch between equal color LEDs.[24]

To meet the requirements for a narrow bezel and uniform brightness, the LED hot-spot problem needs to be eliminated, which can be achieved using microstructures such as prisms, pyramids, cylindrical lenses or lenses. These are used on the light injection surface of an LGP to couple and diffuse the light efficiently from the LEDs into the LGP.[7] The secondary optical element is also used to diffuse the light fully to form an approximately linear light source injecting into the LGP.[25] A total internal reflection lens has been designed and used to improve the brightness and uniformity of the backlight. The brightness and uniformity were improved by 40% and 83%, respectively, compared with a conventional backlight unit. Furthermore, the technologies used for the LGP and optical films are the same as for a CCFL-type device.

Listed below are some examples of applications of LED edge-type BLUs. A 19-inch LCD monitor with a six-lead MULTILED®, the LRTB G6SG, was developed by OSRAM Opto Semiconductors.[26] It uses a light bar with 77 LEDs and an LED pitch of 5 mm instead of some of the CCFLs. Only two of the CCFLs were replaced and the rest of the design (housing, light guide, optical films, etc.) remained unchanged. It only requires a passive cooling system of ventilation slots in the housing and the MCPCBs were mounted on thin heat sinks. Due to the continuous increasing LED brightness, a smaller number of LEDs are needed and the heat generated is relatively reduced.

Using high-power LEDs for larger LCD BLUs has clear advantages over small LEDs. Philips Lumileds Lighting Company developed an edge-type LED BLU with high-power side-emitting white Luxeon™ LEDs.[27,28] The schematic construction is shown in Fig. 19.8. The light from the side-emitting LEDs is

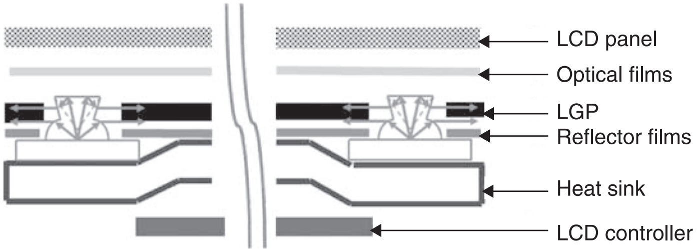

19.8 Edge-type LED BLU with high-power side-emitting white Luxeon™ LEDs.[27]

Table 19.9 Optical specifications for a commercial example of a 7-inch BLU

Item	Symbol	Unit	Condition	Minimum	Typical	Maximum	Remark
Center luminance	L	cd/m^2	25°C	5500	6400	–	Measured at the center of the lighting area
Luminance uniformity	ΔL	%	25°C	80	85	–	$L_{min}/L_{max} \times 100\%$
Chromaticity x	–	–	25°C	0.280	0.305	0.330	LEDs from different color bins are not allowed on the same MCPCB
Chromaticity y	–	–	25°C	0.280	0.305	0.330	

Table 19.10 Materials used in a commercial example of a 7-inch BLU

Part	Quantity	Part model (supplier)
LEDs	7 pieces × 2 strings	NSSW206 (NICHIA)
MCPCB	1	AL-5052 (CS Aluminium)
Reflector sheet	1	RW188 (Kimoto)
Light guide plate	1	Idemitsu LC-1500 (PC material) (Green Point)
Diffuser	1	BS-04(188) (Keiwa)
Prism sheet (horizontal)	1	BEF III-T 90/50 (3M)
Reflective polar	1	DBEF-D400 (3M)

coupled into an LGP with an optical incoupling efficiency of 82%. This BLU has the advantages of a thin design and high coupling efficiency.

Consider a commercial 7-inch BLU in which the lighting area is 145.8 mm × 82.2 mm and the LGP thickness is 0.6 mm. The optical specifications and materials used are listed in Tables 19.9 and 19.10, respectively. Here L_{min} and L_{max} are the measured minimum and maximum luminance for the nine points shown in Fig. 19.9. H and W are measured in the vertical and horizontal directions, respectively. To avoid the hot spot area, the lighting area begins at 3 mm away from the incident surface. The optical design considerations for this example are shown in Table 19.11.

Consider a commercial example of a 46-inch BLU. The requirements are specified in Table 19.12. The optical measured positions are shown in Fig. 19.10.

19.7.4 Direct-type BLUs

Compared with a CCFL-based BLU, the most important point of optical design for an LED-based BLU is designing the secondary optical parts to diffuse the light emitted from the medium- or high-power LED chip arrays fully.

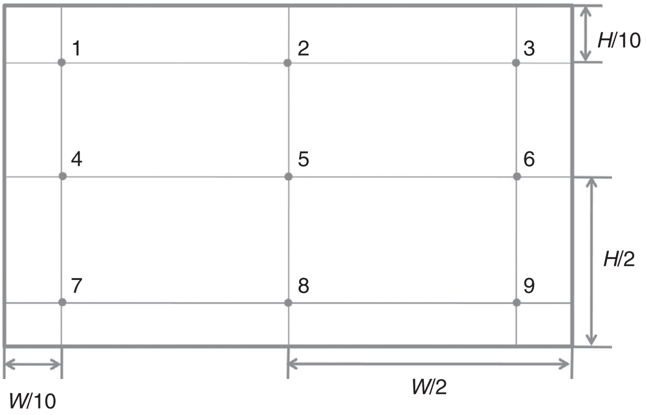

19.9 Measured positions for the 7-inch BLU.

Table 19.11 Optical design considerations for a commercial example of a 7-inch BLU

Item	Description
Selection and configuration of LED type	White top-view-type LED, NFSW036C, is used. Two strings of LED strips are arranged on the long side.
Diffusing light emitted from LED chips	There is no micro-structure on the light injection surface of the LGP.
LGP geometry, physical properties and process	A flat-shaped PMMA LGP is used and fabricated by injection molding.
Selection of the extraction patterns and design of the extraction pattern density on the bottom surface of the LGP	The extraction pattern structure is fabricated by etching. It is designed according to previous experience and software tools.
Injection molding or flat panel cutting	The LGP is fabricated by injection molding.
Selection and disposition of optical films	Selection and disposition of optical films will affect the viewing angle, efficiency, optical quality and cost.
Chromaticity uniformity	LEDs from different color bins cannot be used on the same MCPCB.
With or without local dimming	Local dimming is not used.

Table 19.12 Requirements specification for a commercial example of a 46-inch BLU

	Part	Description
LED	LED bar arrangement	Bottom (single side)
	Package type	top-view, 5630
	LED phosphor	RG or YAG
LGP	Thickness	3 mm
Optical films	Reflector sheet	1 piece
	Diffuser plate	1 piece
	Prism sheet	1 piece
Optical specification	Brightness	5900 cd/m^2
	Luminance uniformity	Minimum 75%, typical 80%
	Chromaticity uniformity	$\Delta x \leqq 0.015$, $\Delta y \leqq 0.015$
	Chromaticity shifting	$\Delta x \leqq 0.003$, $\Delta y \leqq 0.003$
Power	LED electric power	≦63 W

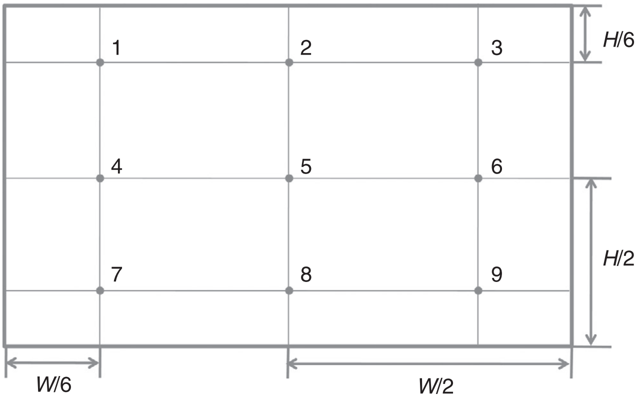

19.10 Measured positions for the 46-inch BLU.

If low-power LEDs are adopted, the structure is generally simple and does not have secondary optical parts. The estimated thickness of the light-mixed cavity H can be written as:

$$H = \frac{(p - w)/2}{\tan \alpha}, \qquad [19.2]$$

where p is the maximum pitch between equal color LEDs, w is the width of the LED emitting area and α is a half of the half-intensity angle. For the optical design of direct-type BLUs with medium- or high-power LEDs, the main considerations are listed in Table 19.13.

Some application examples of specific LED direct-type BLUs now follows. Consider a 23-inch direct-type BLU based on 72 high-power side-emitting RGB

Table 19.13 Optical design considerations for a direct-type LED BLU

Item	Description
Selection and configuration of LED type	Select the type of LEDs, such as RGB LEDs or a white LED. Based on the features of the selected LED type, configure and design the relative position of all LEDs.
Diffusing light emitted from LED chips with a side-emitting lens[29–32] or wide-distribution-radiating lens[28]	Several secondary optical elements are used to diffuse light emitted from LED chips. Side-emitting and wide-distribution-radiating lenses are commonly used. These lenses can reduce the thickness and increase the optical quality of the device. If a side-emitting lens is adopted, use local dimming.
Designing the shape of the light-mixing cavity	Design the inclination angle and shape of the four sides. Design the shape of the reflective bottom surface. Select and design the structure of the reflective bottom surface.
Selecting the diffusion plate	Select a suitable diffusion plate.
Selection and disposition of the optical films	Selection and disposition of the optical films will affect the viewing angle, efficiency, optical quality and cost.
Chromaticity uniformity	Selection of the optical films, LGP material and manufacturing methods will affect the chromaticity deviation. The LED chromaticity must be uniform.
With or without local dimming	LGP design is specific to the local dimming technology (0D, 1D or 2D) used.

Nichia
T = 0.8 mm:NINSW208B, C
T = 0.6 mm:NSSW206B, C
T = 0.4 mm:NSSW206B, C

Luxeon™ LEDs consisting of two strips of 36 LEDs each.[28] The LED pitch is 12 mm. The variance of the brightness profile of the resulting backlight as a function of the spacing between the two strips is shown in Fig. 19.11(b) with the spacing ranging from 50 mm to 120 mm. For RGB LED BLUs, the color uniformity is a relevant performance parameter. The measured color uniformity for this BLU as a function of LED pitch is shown in Fig. 19.12. The upper and lower curves show results for a random placement of LEDs from R, G and B batches of LEDs (called unselected LEDs) and individual LEDs selected based on optimizing the flux for color uniformity (called selected LEDs), respectively. Comparing with

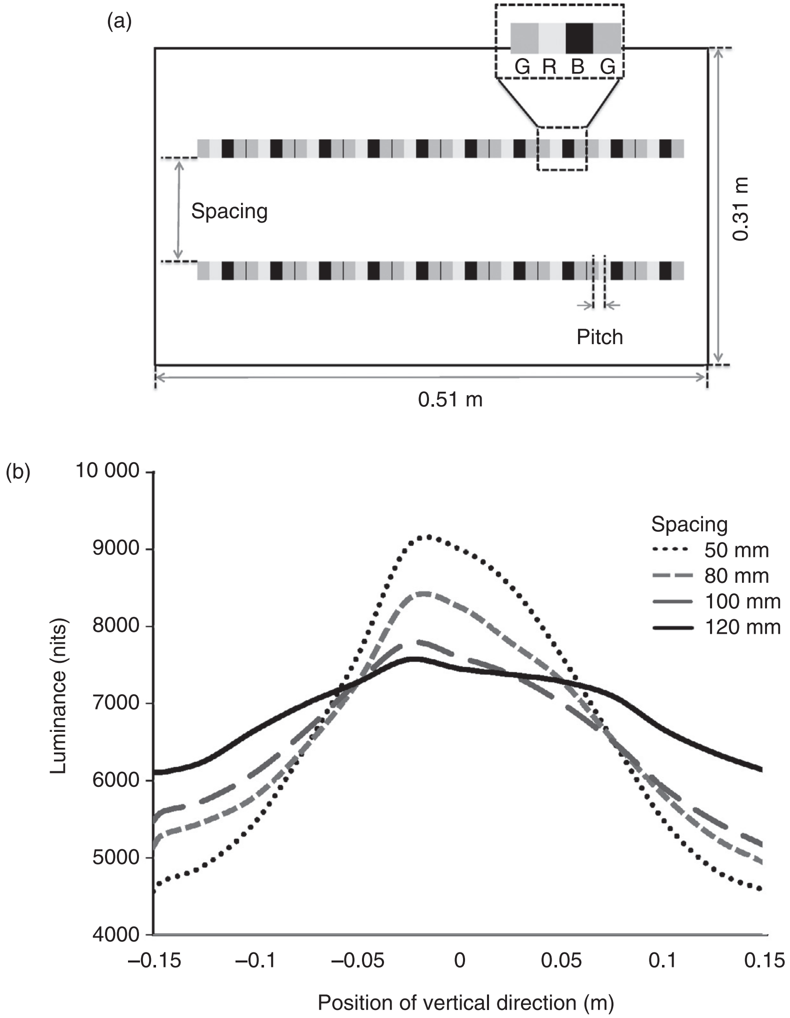

19.11 (a) Basic design parameters and (b) measured luminance profile as a function of light source spacing for a 23-inch BLU with side-emitting RGB Luxeon LEDs.[28]

the unselected LEDs, the color non-uniformity of the selected LEDs was reduced by approximately half. By using LED selection, RGB LED light sources can easily be used for a BLU with higher color uniformity.

A 32-inch LCD television based on high-power Golden DRAGON® ARGUS® LEDs, which are a Golden DRAGON® combined with a wide radiating ARGUS® lens, has been designed and manufactured.[9] Figure 19.13 shows the arrangement of the RGGB LED clusters with a reflector cover foil. The ARGUS® lens deflects

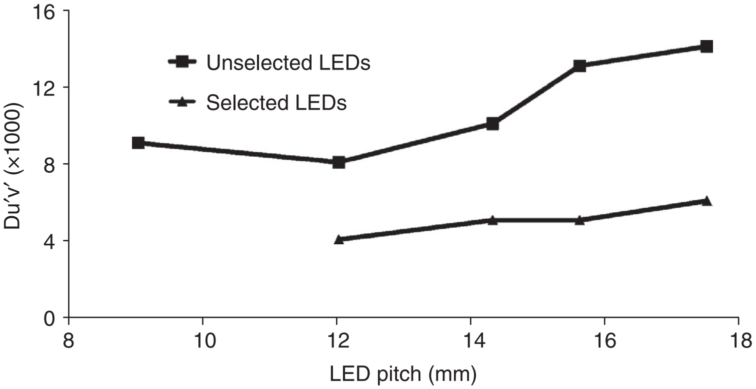

19.12 Measured color uniformity for a 23-inch BLU as a function of LED pitch.[28] (Du'v' is the deviation of chromaticity on the CIE 1976 (u', v') diagram.)

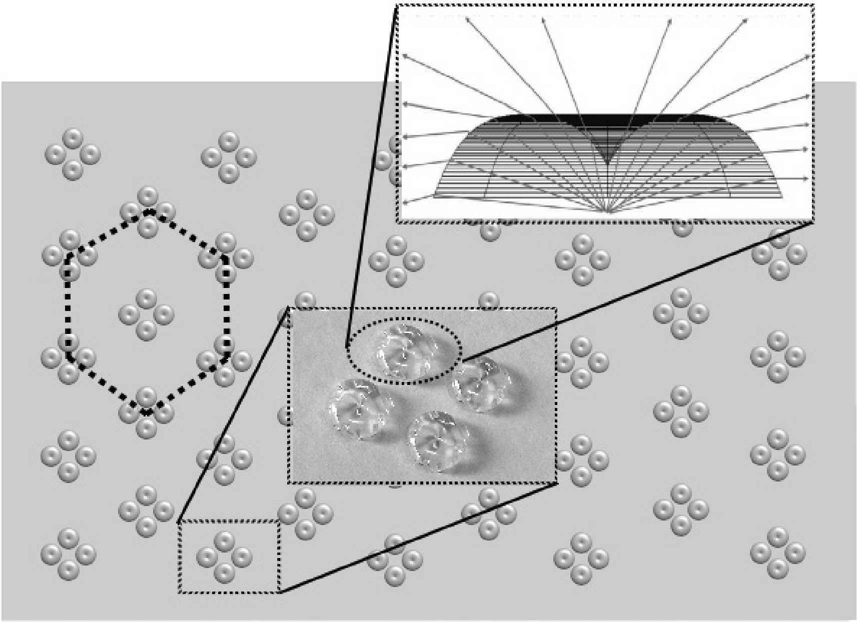

19.13 Arrangement of RGGB LED clusters with reflector cover foil.[9]

the light emitted from the chip to give a flat homogeneous distribution. For optimum color homogeneity, a compact cluster arrangement is adopted. This BLU, used with a reflector box with an inner height of 35 mm, consists of 41 RGGB LED clusters mounted on an MCPCB. A hexagonal arrangement of the clusters with a pitch of 82 mm between cluster centers was used. For the thermal design, the RGGB LED clusters were mounted on a 2-mm-thick metal plate, without active cooling. The NTSC color gamut of the complete LCD television was up to 105%.

19.8 References

1 Hunt, R. (2004) ‘Displays: past, present, and future,’ *11th Int. Display Workshop 04*, pp. 3–6.

2 Boer, W. (2005) *Active Matrix Liquid Crystal Displays: Fundamentals and Applications*, London, Newnes.

3 Insight Media (2008) *LCD Backlight Report*, May 2008, Insight Media.

4 Uno, T. and Kim, J. (2012) *Quarterly LED and CCFL Backlight Cost Report*, Santa Clara, NPD DisplaySearch.

5 Delphi Display Systems, Inc. (2008) *Comparison of LCD Backlight Technology for Outdoor Applications*, Delphi Display Systems whitepapers.

6 Ito, Y., Tsukahara, T., Masuda, S., Yoshida, T., Nada, N., *et al.* (2008) ‘Optical design of phosphor sheet structure in LED backlight system,’ *SID Symposium Digest of Technical Papers*, 39, 866–869.

7 Käläntär, K., Okada, M. and Ishiko, H. (2009) ‘Monolithic block-wised light guide with controlled optical crosstalk for field-sequential color/scanning LCD’, *SID Symposium Digest of Technical Papers*, 40, 1038–1041.

8 Anderson, J., Schardt, C., Yang, J., Koehler, B., Ostlie, B., *et al.* (2007) ‘New back reflector and front film for improved efficiency of direct-lit LED backlights for LCD TV’, *SID Symposium Digest of Technical Papers*, 38, 1236–1239.

9 Ploetz, L. and Stich, A. (2005) ‘LED display backlighting – large screen and TV application using Golden DRAGON® ARGUS®,’ *Osram Opto Semiconductors Application Note*, 11 March 2005, 1–8.

10 Tsuchiya, R., Kawasaki, Y., Ikebe, S., Shiba, T. and Kinoshita, J. (2008) ‘Thin side-lit, hollow-cavity flat LED lighting panel for ultra-uniform LCD backlight applications,’ *SID Symposium Digest of Technical Papers*, 39, 874–877.

11 Martynov, Y., Huub Konijn, H., Nicola Pfeffer, N., Simon Kuppens, S. and Wim Timmers, W. (2003) ‘High-efficiency slim LED backlight system with mixing light guide,’ *SID Symposium Digest of Technical Papers* 34, 1259–1261.

12 Philips Lumileds Lighting (2005) *SnapLED and SuperFlux Categories and Labels: Luxeon DCC for LCD backlighting, Application Brief AB27*. Available at: http://www.philipslumileds.com/support/documentation/application-briefsb [accessed on 10 February 2005].

13 3M Corporation (2012) *Vikuiti™ Brightness Enhancement Film II (BEF II)*. Available at: http://products3.3m.com/catalog/us/en001/electronics_mfg/vikuiti/node_QVCDZB50FVbe/root_GST1T4S9TCgv/vroot_S6Q2FD9X0Jge/gvel_GD378D0HGJgl/theme_us_vikuiti_3_0/command_AbcPageHandler/output_html.

14 3M Corporation (2012) *Vikuiti™ Brightness Enhancement Film III (BEF III)*. Available at: http://products3.3m.com/catalog/us/en001/electronics_mfg/vikuiti/node_Q2ZGN85GDRbe/root_GST1T4S9TCgv/vroot_S6Q2FD9X0Jge/gvel_GD378D0HGJgl/theme_us_vikuiti_3_0/command_AbcPageHandler/output_html.

15 3M Corporation (2012) *Vikuiti™ Dual Brightness Enhancement Multi-Functional Film (DBEF)*. Available at: http://products3.3m.com/catalog/us/en001/electronics_

mfg/vikuiti/node_DPGRHQ6199be/root_GST1T4S9TCgv/vroot_S6Q2FD9X0Jge/gvel_K6PCGS29T6gl/theme_us_vikuiti_3_0/command_AbcPageHandler/output_html.

16 Eligibility Criteria (2012) *ENERGY STAR® Program Requirements Product Specification for Displays*, draft 2, version 6.0.

17 Uno, T. and Liu, L. (2012) *Quarterly LED Backlight Report*, Santa Clara, NPD DisplaySearch.

18 LED TELE (2012) *LED vs LCD TV Comparison*. Available at: http://www.ledtele.co.uk/ledvslcd.html info@ledtele.co.uk.

19 AOC Corporate Website (2012) *23-inch Aire Pro i2353Ph Monitor*, Available at: http://us.aoc.com/monitor_display/i2353ph.

20 West, R., Konijn, H., Sillevis-Smitt, W., Kuppens, S., Pfeffer, N., *et al.* (2003) 'High brightness direct LED backlight for LCD-TV,' *SID Symposium Digest of Technical Papers*, 34, 1262–1265.

21 Hsieh, P. and Lin, H. (2009) 'Colorimetric transformation with two sets of LED backlight for multi-primary LCD,' *SID Symposium Digest of Technical Papers*, 40, 649–652.

22 Semenza, P. (2012) *Sony Unveils New TV Display Technology: Direct-Emission LED, Display Search*. Available at: http://www.displaysearchblog.com/2012/01/sony-unveils-new-tv-display-technology-direct-emission-led/ [accessed on 10 January 2012].

23 Smith-Gillespie, R. (2008) 'Advanced flat panel display backlighting techniques,' *Proc. of SPIE*, 6956, 69560K, 1–11.

24 Stich, A. (2004) 'LEDs, new light sources for display backlighting,' *Osram Opto Semiconductors Application Note*, 2 February 2004, 1–9.

25 Hwang, J., Shin, D., Gong, D., Park, C., Kang, W., *et al.* (2008) 'Enhancement of brightness and uniformity by LED backlight using a total internal reflection (TIR) lens,' *SID Symposium Digest of Technical Papers*, 39, 1645–1648.

26 Hüttner, J. (2003) 'LED display backlighting-monitor applications using 6-lead MULTILED®,' *Osram Opto Semiconductors Application Note*, 9 September 2003, 1–7.

27 Folkerts, W. and West, R. (2004) 'LED backlight designs using Luxeon high flux light source solutions,' *SID 2004 Seattle*, oral presentation file.

28 Folkerts, W. (2004) 'LED backlighting concepts with high flux LEDs,' *SID Symposium Digest of Technical Papers*, 35, 1226–1229.

29 West, R., Konijn, H., Kuppens, S., Pfeffer, N., Vader, Q., *et al.* (2003) 'LED backlight for large area LCD TV's', *Proceedings of the 10th International Display Workshops*, pp. 657–660.

30 West, R., Sasser, G. and Stewart, J. (Lumileds Lighting US, LLC) 2003. *Side Emitting Light Emitting Device*, US Patent 6598998, 29 July 2003.

31 West, R., Sasser, G. and Stewart, J. (Lumileds Lighting US, LLC) 2004, *Side Emitting LED and Lens*, US Patent 6679621, 20 January 2004.

32 Noh, J., Park, J., Kim, D., Wang, J. and Hwang, J. (Samsung Electronics Co., Ltd.) 2004, *Side Emitting Device, Backlight Unit Using the Same as Light Source and Liquid Crystal Display Employing the Backlight Unit*, US Patent 7322721, 29 January 2008.

20

LEDs in automotive lighting

J. D. BULLOUGH, Rensselaer Polytechnic Institute, USA

DOI: 10.1533/9780857099303.3.595

Abstract: This chapter discusses the use of light-emitting diode (LED) sources in vehicular lighting for illumination and signaling. Photometric requirements for automotive lighting are discussed, along with the key differences between LED and filament sources in terms of visual responses. Finally, the energy and environmental implications for LEDs in automobiles are discussed.

Key words: automotive headlamps, vehicular signals, forward illumination, vehicle emissions.

20.1 Introduction

The majority of roads in North America and much of the rest of the world are not illuminated by fixed pole-mounted roadway lighting systems (NHTSA, 2007). Because of this, automotive lighting is a key component for driving safely at night. The performance requirements for vehicle headlamps (such as those published in the United States as Federal Motor Vehicle Safety Standard 108) are based on standards and recommendations published by the Society of Automotive Engineers (SAE) and similar industry organizations. These requirements stipulate certain minimum or maximum luminous intensities toward different directions from the center of the vehicle lighting system. A similar set of photometric performance requirements exists for countries outside North America; these differ in the particulars but have the same objectives of specifying luminous intensities to ensure vehicle lighting systems provide sufficient light for drivers to see at night while minimizing glare to other drivers, and to ensure that vehicle signal lights can be detected promptly and without ambiguity.

The present chapter summarizes some of the performance requirements for vehicle lighting systems and includes a discussion of the impact of light-emitting diode (LED) sources on driver visual responses, compared to filament sources (such as incandescent and tungsten-halogen lamps), the traditional light source used in most automotive lighting applications.

20.2 Forward lighting

For automotive headlamps that provide illumination ahead of the vehicle, two headlamps are required, mounted as far apart as practical. Each headlamp must meet the same performance requirements. There are two primary types of beam patterns (beam patterns are the resulting distributions of luminous intensity produced by vehicle headlamps): the high (or driving) beam and the low (or passing) beam. North American requirements for several angular locations for high- and low-beam headlamps are given in Table 20.1 and Table 20.2.

Table 20.1 Selected photometric requirements for high-beam headlamps in the United States

Angular location (degrees left/right, up/down)	Maximum luminous intensity (cd)	Minimum luminous intensity (cd)
(0° right, 0° up)	75 000	40 000
(3° left, 1° up) and (3° right, 1° up)	–	5 000
(0° right, 2° up)	–	1 500
(3° left, 0° up) and (3° right, 0° up)	–	15 000
(6° left, 0° up) and (6° right, 0° up)	–	5 000
(9° left, 0° up) and (9° right, 0° up)	–	3 000
(12° left, 0° up) and (12° right, 0° up)	–	1 500
(0° right, 1.5° down)	–	5 000
(0° right, 2.5° down)	–	2 500
(9° left, 1.5° down) and (9° right, 1.5° down)	–	2 000
(12° left, 2.5° down) and (12° right, 2.5° down)	–	1 000
(0° right, 4° down)	12 000	–

Table 20.2 Selected photometric requirements for low-beam headlamps in the United States

Angular location (degrees left/right, up/down)	Maximum luminous intensity (cd)	Minimum luminous intensity (cd)
(8° left, 0° up) and (8° right, 0° up)	–	64
(8° left, 4° up) and (8° right, 4° up)	–	64
(4° left, 0° up) and (4° right, 0° up)	–	125
(4° left, 2° up) and (4° right, 2° up)	–	125
(1.5° right, 0.5° down)	20 000	8 000
(6° left, 1° down)	–	750
(2° right, 1.5° down)	–	15 000
(9° left, 1.5° down) and (9° right, 1.5° down)	–	750
(15° left, 2° down) and (15° right, 2° down)	–	700
(1.5° left, 1° up)	700	–
(1.5° left, 0.5° up)	1 000	–
(1.5° left, 0.5° down)	3 000	–
(1° right, 1.5° up)	1 400	–
(1° right, 0.5° up), (2° right, 0.5° up) and (3° right, 0.5° up)	2 700	–
(4° right, 4° down)	8 000	–

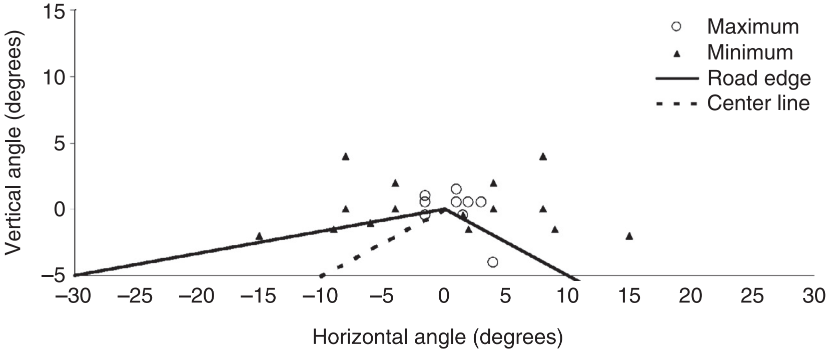

20.1 Photometric requirements for low-beam headlamp patterns in the United States, superimposed onto an image of a two-lane roadway.

As expected, the requirements for high beams have higher intensities and fewer maximum intensity values than low beams. Additionally, the high beam has a symmetrical beam pattern. In contrast, the low beam has an asymmetrical beam pattern, with more stringent maxima toward the left side (where oncoming traffic in North America is more likely to be found; beam patterns in countries with left-side traffic are reversed left-to-right). Figure 20.1 shows the intensity requirements for a low-beam headlamp pattern overlaid onto the angular locations of a straight, two-lane road. Using the inverse-square law, it is possible to convert the angular luminous intensity values to illuminances on the roadway and on objects located ahead of the vehicle; illuminances from each headlamp should be added together to obtain the total.

Figure 20.2 is a photograph of a low-beam headlamp pattern projected onto a wall in front of the headlamp. To reduce glare on oncoming and preceding drivers,

20.2 Photograph of a low-beam headlamp beam pattern projected onto a wall.

low-beam patterns usually have the sharp vertical gradients shown in Fig. 20.2. Above the so-called cutoff boundary between the light and dark portions of Fig. 20.2, the intensities are low and there is little light. The cutoff boundary makes it possible to check and adjust the vertical aim of the headlamp. Most North American headlamps require the location of the right-side cutoff boundary to be at the same height as the headlamp (Schoettle *et al.*, 2008). The left-side cutoff boundary is usually lower than the right-side boundary to reduce the amount of light entering oncoming drivers' eyes. The sharp cutoff boundary of low-beam headlamp patterns restricts the forward visibility of drivers. When driving speeds exceed 60–65 km/h, it can be difficult for a driver to detect some potential hazards and stop in time (Andre and Owens, 2001) when using low-beam headlamps. High beams are warranted for such conditions, except if approaching traffic is within 100 m or so. However, most drivers underutilize their high-beam headlamps (Sullivan *et al.*, 2004).

As a result of the sharp cutoff boundaries of low-beam headlamp patterns, the vertical aim is a very important factor for optimum performance. In the United States, for example, most states do not require headlamps to be properly aimed as part of a safety inspection (NHTSA, 2007). A recent study of vertical aim among vehicles (Skinner *et al.*, 2010) found that most vehicles had at least one poorly aimed headlamp. When the aim is too high, the headlamps can contribute to disability glare and discomfort glare (Perel, 1996; Sivak *et al.*, 1998). When the aim is too low, the driver's forward visibility can be compromised because of the sharp vertical cutoff.

Vehicle headlamp systems that can change or adapt in response to different driving conditions, called adaptive forward-lighting systems (AFSs), are starting to cause a re-evaluation of the fixed high- and low-beam headlamp patterns that have been used for many decades (Wördenweber *et al.*, 2007). Some vehicles have cornering and bending lights; bending lights sometimes use mechanical elements to swivel one or both headlamps toward roadway curves. Some European vehicles are equipped with a 'town' headlamp beam pattern that has lower maximum luminous intensities and a broader distribution than most low beams to help detect pedestrians while driving at low speeds in urban locations. AFS requirements for most nations are promulgated by the UN Economic Commission for Europe (ECE) in Vehicle Regulation No. 123. The Federal Motor Vehicle Safety Standard 108 in the United States is presently silent with respect to AFSs.

Presently, most automotive headlamps use filament sources (tungsten-halogen or more simply, halogen) with reflector or projector optical systems to produce the necessary beam pattern. A relatively small proportion of headlamps use high-intensity discharge (HID) lamps, which use a metal halide and xenon to allow the lamps to be switched on immediately. Headlamps using LEDs are just beginning to be used on a few vehicle models. Regardless of the light source used, all headlamps are required to meet the same photometric requirements.

20.3 Signal lighting

Vehicles need to have signal lights to allow drivers to communicate their actions with respect to braking and turning during both the day and night. An increasing proportion of vehicles use LEDs for signal lighting. Different signal lights have different requirements for both color and luminous intensity. The Federal requirements for vehicle signals in the United States are based on SAE standards and recommendations. Table 20.3 lists the color and permissible luminous intensity values for several vehicle signal light types.

Performance requirements for vehicle signal lights in Europe do not differ much from those in North America regarding color and luminous intensity (Bullough *et al.*, 2007), with an important exception. Turn signal lights at the back of a vehicle can be red or yellow in the United States with different intensity requirements depending upon which color they are. In most of the rest of the world, rear turn signals must be yellow. Allen (2009) reports that yellow rear turn signals tend to result in fewer crashes, possibly because of their higher luminous intensities than red rear turn signals, or because the yellow color makes them easier to tell apart from brake or tail lights. The National Highway Traffic Safety Administration (NHTSA) is considering whether yellow should be required for all rear-mounted automotive turn signals.

Table 20.3 Photometric and color requirements for vehicle signal lights in the United States

Signal function	Required color	Minimum–maximum luminous intensity (cd)
Tail (presence) light	Red	2–18
Stop light	Red	80–300
Center high-mounted stop light	Red	25–130
Rear turn light	Red or yellow	80–300 (if red), 130–750 (if yellow)
Front turn light	Yellow	130–750
Backup or reversing light	White	80–300 (if two), 80–500 (if one)

20.4 Human factor issues with LEDs

LED sources are substantially different from filament lamps used in most present-day automotive lighting applications in a number of important ways:

- LEDs have higher luminous efficacies (in lm/W) than filament sources, meaning they can produce higher intensities or broader beam patterns for the same amount of energy, or have a similar light output with lower energy requirements.

- The narrowband spectral output of colored LEDs produces a highly saturated color appearance, in contrast to broadband sources such as filament lamps, which require filters in order to produce colored illumination (Fig. 20.3).
- White phosphor-converted LEDs can be produced with a higher correlated color temperature (CCT) than filament lamps, which results in a more bluish color appearance.
- LEDs have very rapid onset and offset times: 10–20 ns, including the decay time of yttrium aluminum garnet (YAG) phosphors, compared to about 80–250 ms for filament lamps.

The photometric, colorimetric and temporal properties of LED sources can also influence drivers' ability to see and respond to potential hazards in and along the roadway. For vehicle headlamp systems, the spectral distribution of typical phosphor-converted white LEDs, based on blue InGaN devices in combination with YAG phosphors, has a larger proportion of short-wavelength (blue) light than the spectral distribution of filament sources like incandescent and halogen lamps (Fig. 20.4). This difference is relevant to visual performance while driving, because at light levels commonly experienced while driving at night, which result in asphalt pavement luminances between 0.1 cd/m^2 and 1 cd/m^2 (He *et al.*, 1997), the visual detection of hazards is supported by a combination of cone and rod visual receptors in the eye.

However, photometric quantities such as illuminance (in lx), luminance (in cd/m^2), luminous intensity (in cd) and luminous flux (in lm) are entirely based on the spectral response of the cone receptors in the eye. Cone receptors are used

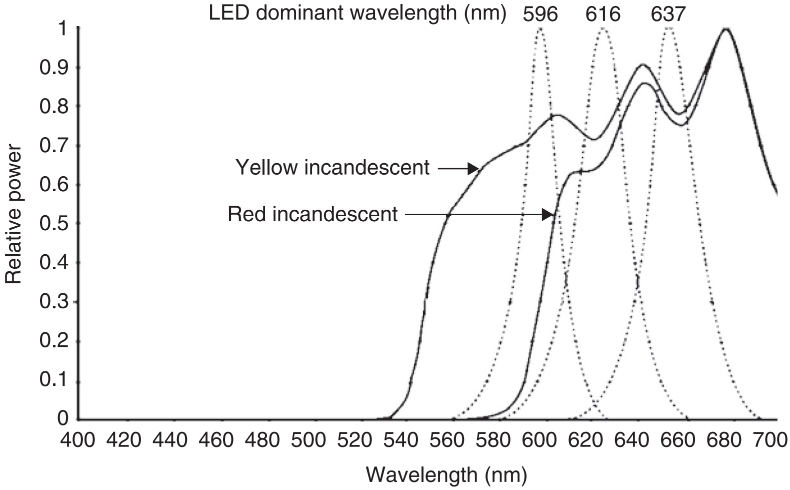

20.3 Spectral distributions of yellow and red LED and (filtered) filament sources.

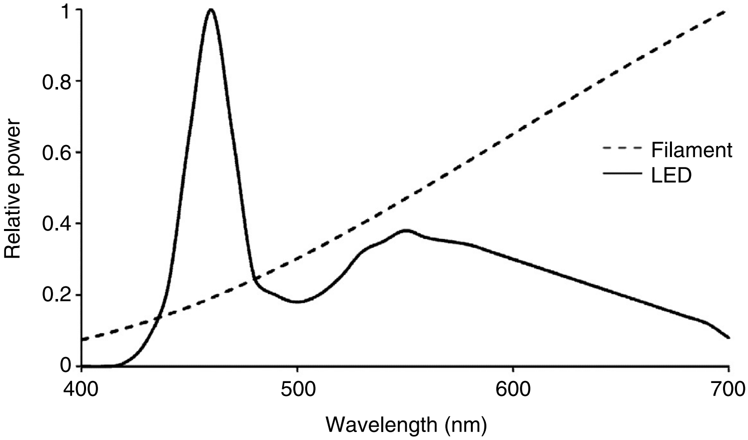

20.4 Spectral distributions of white LED and (unfiltered) filament sources.

exclusively for seeing at light levels typically experienced outdoors and indoors during the daytime, which is usually between 10 and 1000 cd/m^2. This apparent discrepancy between the way light is measured and how we see matters because, collectively, rod receptors are more sensitive to short visible wavelengths (such as blue and green light) than cone receptors (Rea *et al.*, 2004). Thus, the usual photometric quantities (lx, cd/m^2, cd and lm) can underestimate a driver's ability to see under LED sources at night, relative to his or her ability to see under filament lamps.

A unified photometric system has recently been published by the Commission internationale de L'Éclairage (CIE) to quantify the relative role of rods and cones (CIE, 2010) in seeing at night. As a consequence, it could be possible to obtain equivalent nighttime visual performance using LED sources that produce light levels that are 20% to 30% lower than those produced by filament lamps (Van Derlofske and Bullough, 2006). Another visual response that may favor LEDs over filament sources is the perception of roadway scene brightness, according to a brightness model developed by Rea *et al.* (2011). This response appears to have increased short-wavelength sensitivity. Figure 20.5 shows the predicted roadway scene brightness under headlamps using filament, HID and LED sources.

The relatively high amount of short-wavelength spectral power in white LED illumination might also have some possible negative impacts for vehicle lighting, however. When headlamps of different colors produce equivalent conventional photometric quantities, disability glare (a reduction in visual performance that is caused by scatter in the eyes from a bright light) is not influenced by the spectral content of the headlamp illumination (Schreuder, 1976). This is not the case for discomfort glare, which is defined as an annoying or painful sensation that is

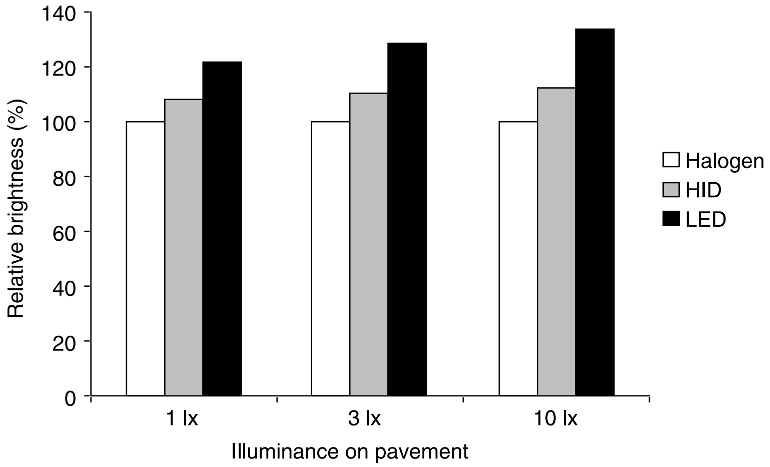

20.5 Relative brightness of roadway pavement surfaces illuminated by photometrically equated light sources (halogen, HID and LED).

experienced when viewing a bright light in the visual scene of interest. Like the perception of roadway scene brightness, discomfort glare also exhibits increased sensitivity to short-wavelength light (Bullough, 2009). It is not fully understood whether, or to what extent, increased discomfort glare affects driving safety. There is some evidence that shows that when drivers experience discomfort glare from oncoming headlamps, they are more likely to exhibit driving behaviors such as increases in head movements and increased throttle variability, which in turn have been found to be correlated with an increased crash risk (Bullough *et al.*, 2008).

Regarding the visual detection of vehicle signal lights, because LEDs have substantially shorter onset times than filament lamps, they can have some advantages, especially for vehicle brake lamps. Bullough (2005) demonstrated that visual reaction times to the onset of a colored light signal, such as a brake light or turn signal, could be predicted using a threshold quantity of light energy (in cd·s) received at drivers' eyes. When a tungsten filament lamp is first switched on there is a relatively gradual increase in illumination from the filament and it can take up to 250 ms to reach full brightness. LEDs have practically instantaneous rise times and can produce the threshold quantity of light energy more quickly. As a result, LEDs elicit shorter visual reaction times than filament sources of the same nominal color and peak luminous intensity (Bullough *et al.*, 2002).

Importantly, because the rate of deceleration of a braking vehicle is linked to the same action that turns on the brake light itself (pressing the brake pedal), shorter light source rise times can provide a stopping distance benefit of nearly 7 m for a driver following a braking vehicle (Sivak *et al.* 1994), a small but sometimes practically significant increase.

20.5 Energy and environmental issues

Because they have higher luminous efficacies compared to filament sources, automotive lighting systems using LED sources can have substantially reduced power requirements. In separate studies, Hamm (2009) and Schoettle *et al.* (2009) estimated the typical wattages for conventional filament source-based vehicle lighting systems and for LED lighting systems. The average of their estimates for different lighting and signaling functions are summarized in Table 20.4.

Also listed in Table 20.4 are estimated values for the total annual hours of use for each type of lighting system, based on driving patterns in the United States (Buonarosa *et al.*, 2008). Table 20.4 also includes the resulting total annual lighting energy use for filament- and LED-based automotive lighting systems. Under the assumption that each kWh of lighting energy use on a vehicle powered by gasoline corresponds to CO_2 emissions of 1.29 kg (Schoettle *et al.*, 2009), the total reduction in annual energy use that would be expected to accompany a shift from filament lamps to LEDs for automotive lighting would be 27.4 kWh/year, and would correspond to an annual reduction of CO_2 emissions of about 35 kg/year for each automobile.

Table 20.4 Estimated power and energy use of filament lamp and LED automotive lighting systems

	Power per vehicle (W/vehicle)			Annual energy use (kWh/year)	
Function	Filament source	LED source	Annual use (h/year)	Filament source	LED source
Low-beam headlamp	124	87	97	12.08	8.47
High-beam headlamp	132	64	10	1.29	0.63
Daytime running lamp	48	18	382	18.30	7.03
Position lamp	14	3	107	1.54	0.29
Front turn signal	52	14	22	1.15	0.31
Rear turn signal	52	10	22	1.15	0.22
License plate lamp	17	2	107	1.80	0.16
Reverse lamp	43	7	4	0.16	0.03
Center high-mounted stop lamp	34	4	81	2.73	0.28
Brake signal	52	11	81	4.16	0.86
Tail lamp	14	2	107	1.52	0.26
Total annual energy use (kWh/year)				**45.9**	**18.5**

20.6 Future trends

LED automotive lighting systems are already common for signal lighting applications, and have been introduced for forward headlamp systems. The rapid advances in luminous efficacy will continue to make them increasingly attractive for automotive use. The solid-state construction of LED systems, modular configurations and relative ease of intensity control through current modulation or pulse width modulation provide significant promise for energy-saving vehicle lighting systems that can adapt in real time to changing roadway, traffic and weather patterns using AFS technologies. These advantages of LEDs will likely make dynamic rear signal lighting systems practical as well.

20.7 Sources of further information and advice

For additional information about automotive lighting in general including the growing use of LED sources, consult Wördenweber *et al.* (2007). An overview of the components of the roadway transportation lighting system, including automotive lighting, roadway lighting and traffic signals, is provided by Bullough (2011). For an extensive discussion of the human factor aspects of lighting for transportation, Boyce (2009) is an excellent resource. Research from the National Highway Traffic Safety Administration on vehicle lighting systems can be found online at http://www.nhtsa.gov/Research/Human+Factors, and reports from the Lighting Research Center at Rensselaer Polytechnic Institute are available online at http://www.lrc.rpi.edu/programs/transportation/TLA/PublicInformation.asp.

20.8 Acknowledgments

The preparation of this chapter was supported by the members of the Transportation Lighting Alliance (www.lrc.rpi.edu/programs/transportation/tla): Audi, Automotive Lighting, Hella, OSRAM Sylvania, Philips Lighting and Varroc Lighting Sytems.

20.9 References

Allen, K. (2009) *The Effectiveness of Amber Rear Turn Signals for Reducing Rear Impacts*, Washington, US Department of Transportation.

Andre, J. and Owens, D. A. (2001) ‘The twilight envelope: a user-centered approach to describing roadway illumination at night,’ *Hum Factors*, 43, 620–630.

Boyce, P. R. (2009) *Lighting for Driving*, New York, CRC Press.

Bullough, J. D. (2005) ‘Onset times and the detection of colored signal lights,’ *Transp Res Rec*, 1918, 123–127.

Bullough, J. D. (2009) ‘Spectral sensitivity for extrafoveal discomfort glare,’ *J Mod Optics*, 56, 1518–1522.

Bullough, J. D. (2011) ‘Roadway transportation lighting,’ in Kutz, M., *Handbook of Transportation Engineering: Volume II*, New York, McGraw-Hill, pp. 8.1–8.24.

Bullough, J. D., Yan, H. and Van Derlofske, J. (2002) ‘Effects of sweeping, color and luminance distribution on response to automotive stop lamps,’ in *Advanced Lighting Technology for Vehicles*, Warrendale, Society of Automotive Engineers, pp. 179–183.

Bullough, J. D., Van Derlofske, J. and Kleinkes, M. (2007) 'Rear signal lighting: from research to standards, now and in the future,' in *Automotive Lighting Technology and Human Factors in Driver Vision and Lighting*, Warrendale, Society of Automotive Engineers, pp. 157–166.

Bullough, J. D., Skinner, N. P., Pysar, R. P., *et al.* (2008) *Nighttime Glare and Driving Performance: Research Findings*, Washington, National Highway Traffic Safety Administration.

Buonarosa, M. L., Sayer, J. R. and Flannagan, M. J. (2008) *Real-World Frequency of Use of Lighting Equipment*, Ann Arbor, University of Michigan.

CIE (2010) *Recommended System for Mesopic Photometry Based on Visual Performance*, Vienna, Commission Internationale de L'Éclairage.

Hamm, M. (2009) 'Green lighting: analysing the potential for reduction of CO_2 emissions in full-LED headlamps,' in *Automotive Lighting Technology*, Warrendale, Society of Automotive Engineers, pp. 9–14.

He, Y., Rea, M. S., Bierman, A. and Bullough, J. D. (1997) 'Evaluating light source efficacy under mesopic conditions using reaction times,' *J Illum Eng Soc*, 26, 125–138.

NHTSA (2007) *Nighttime Glare and Driving Performance: Report to Congress*, Washington, US Department of Transportation.

Perel, M. (1996) 'Evaluation of headlamp beam patterns using the Ford CHESS program,' in Gaudaen, G., *Motor Vehicle Lighting*, Warrendale, Society of Automotive Engineers, pp. 153–157.

Rea, M. S., Bullough, J. D., Freyssinier, J. P. and Bierman, A. (2004) 'A proposed unified system of photometry,' *Lighting Res Technol*, 36, 85–111.

Rea, M. S., Radetsky, L. C. and Bullough, J. D. (2011) 'Toward a model of outdoor lighting scene brightness,' *Lighting Res Technol*, 43, 7–30.

Schoettle, B., Sivak, M. and Takenobu, N. (2008) 'Market-weighted trends in the design attributes of headlamps in the US,' in *Automotive Lighting Technology*, Warrendale, Society of Automotive Engineers, pp. 85–93.

Schoettle, B., Sivak, M. and Fujiyama, Y. (2009) 'LEDs and power consumption of exterior automotive lighting: implications for gasoline and electric vehicles,' *8th International Symposium on Automotive Lighting*, Munich, Herbert Utz Verlag, pp. 11–20.

Schreuder, D. A. (1976) *White or Yellow Lights for Vehicle Head-lamps?* Voorburg, Institute for Road Safety Research.

Sivak, M., Flannagan, M., Sato, T., *et al.* (1994) 'Reaction times to neon, LED, and fast incandescent brake lamps,' *Ergonomics*, 37, 989–994.

Sivak, M., Flannagan, M. J. and Miyokawa, T. (1998) *Quantitative Comparisons of Factors Influencing the Performance of Low-Beam Headlamps*, Ann Arbor, University of Michigan.

Skinner, N. P., Bullough, J. D. and Smith, A. M. (2010) 'Survey of the present state of headlamp aim,' *Transportation Research Board 89th Annual Meeting*, Washington, Transportation Research Board.

Sullivan, J. M., Adachi, G., Mefford, M. L. and Flannagan, M. J. (2004) 'High-beam headlamp usage on unlighted rural roadways,' *Lighting Res Technol*, 36, 59–65.

Van Derlofske, J. and Bullough, J. D. (2006) 'Spectral effects of LED forward lighting: visibility and glare,' in *Automotive Lighting Technology and Human Factors in Driver Vision and Lighting*, Warrendale, Society of Automotive Engineers, pp. 11–18.

Wördenweber, B., Wallaschek, J., Boyce, P. and Hoffman, D. D. (2007) *Automotive Lighting and Human Vision*, New York, Springer.

Index

α-alumina, 70
active cooling, 475–6
adaptive forward-lighting systems (AFS), 598
adlayer-enhanced lateral diffusion (AELD), 4
AlInN/(In)GaN system, 545–7
all-optical switches, 549
'AlN-deposited' sapphire, 78
alternate source-feeding epitaxy (ASFE), 502
alternative crystallographic orientations, 547–8
aluminium gallium nitride (AlGaN) based on DUV-LEDs
  fabricated on high quality aluminium nitride (AlN), 513–21
    current vs output power and current vs EQE, 517
    EL spectra for various injection currents and current vs output power and EQE, 516
    EL spectra of 225 nm-band AlGaN-QW with various quantum well thickness, 519
    EL spectra on log scale of 227 nm AlGaN LED, 515
    EL spectrum and current vs output power and EQE with emission wavelength at 282 nm, 521
    electroluminescence (EL) spectra with emission wavelengths of 222–351 nm, 515
    fabricated on sapphire substrate and UV emission, 514
    radiation angle dependence of emission spectra for 222nm AlGaN QW LED, 520
    structure and cross-sectional TEM image of InAlGaN QW DUV-LED, 520
    typical design values for aluminium composition, 514
    wavelength dependence of EQE of 245–260 nm AlGaN MQW LEDs, 518
aluminium nitride (AlN), 513–21
ammonia MBE, 3
angle-resolved nanosphere lithography, 360–2
ARGUS LEDs, 591–2
Arrhenius equation, 430
atom probe tomography (APT), 254
atomic force microscopy (AFM), 110
Auger coefficient, 285
Auger mechanism, 537
Auger recombination, 253, 284–6, 293, 372
automotive lighting
  light-emitting diodes (LEDs), 595–604
    energy and environmental issues, 603
    forward lighting, 595–8
    future trends, 603–4
    human factor issues, 599–602
    signal lighting, 599

backlighting units (BLUs)
  classification, 569–71
    BLU assembly using Luxeon DCC as light source, 571
    direct-type structure, 569
    edge-type structure, 569
    folded-mixing-LGP-type structure, 569, 571
    hollow-type structure, 569
    schematic diagrams of different structure, 570
  technical considerations for light source, 567–9
    general characteristics of light sources, 568
  types of LED LCD, 567–71
ballistic transport, 290
basal plane stacking faults (BPSF), 263, 266
$Ba_3Si_6O_{12}N_2$:Eu^{2+}, 162
Batwing lens, 446
Bloch function, 539
Bloch modes, 314
Boltzman distribution, 553
Boltzmann constant, 369, 430
boron phosphide (BP), 106
Bragg reflector, 421
buried heterostructure, 81

c-plane, 255
catastrophic degradation, 437
cathodoluminescence (CL), 510–11, 537
ceiling temperature, 37
chemical doping, 369
chemical mechanical polishing (CMP), 303

chip bonding, 450
chip-on-board (CoB) technology, 469
chip packaging
  design for X, 445–6
    light intensity distribution of three different packages, 447
  encapsulation of nitride LEDs, 441–76
    basic structure of LED packaging modules, 446–9
    optical effects of freeform lenses, 463–8
    optical effects of gold wire bonding, 453–6
    optical effects of phosphor coating, 456–62
  functions, 441–6
    electrical interconnection, 442
    encapsulation and protection, 441–2
    heat dissipation, 444–5
    illustration, 442
    light extraction, 442, 444
    system testing, 445
  processes used, 449–53
    chip bonding, 450
    LED packaging processes, 449
    lens laying, 452
    phosphor coating, 450–2
    silicone injection and curing, 453
    wire bonding, 450
  thermal design, 469–70
    thermal resistance network, 470
  thermal design and processing of LED packaging, 468–76
    contact thermal resistance and thermal interface material, 471–2
    cooling solutions for LED applications, 474–6
    self-heating of phosphor coating, 471
    spreading thermal resistance and packaging substrate, 472–4
chroma selection flexibility, 574
close-coupled showerhead (CCS) reactors, 45–54
  calculated distribution of MMGa for different sizes of CCS reactor, 50
  cross section of a showerhead and its surface on the reactor side, 47
  design of a modern CCS reactor, 50–4
    GaN growth rate vs TMGa molar flow for elevated reactor pressures, 53
    heater for a 55″ × 2″ CCS reactor, 51
    n-GaN growth for different reactor heights, 52
    state-of-the-art 55″ × 2″ CCS reactor, 51
  distribution of TMGa and MMGa in CCS reactor, 49
  flow field in CCS reactor of height 11mm, 48
  illustration, 46
  introduction to principles, 45–50
  vertical flow reactor with showerhead to give uniform flow distribution, 45
co-doping technique, 529–30
coefficients of thermal expansion (CTE), 469
cold cathode fluorescent lamp (CCFL), 567
colour, 491–3
  colour and chromaticity coordinates for fluorescent lamps, 492
  tolerance areas in colour space, 492
colour rendering index (CRI), 458
colour tunable light-emitting diodes (LEDs), 409–26
  group-addressable pixelated micro-LED arrays, 423–6
    forming RGB pixels by jet printing, 425–6
    implementation of group-addresable micro-LED arrays, 423–4
    natural colour-mixing using miniature RGB pixels, 423
    preliminary results, 426
  initial idea for stacked LEDs, 410–12
    colour-mixing through RGB chip-stacking, 411
    LED chip stacking, 411
  motivation for colour tuning and review of existing technologies, 409–10
  second-generation LED stack with inclined sidewalls, 412–16
    laser micromachining set-up, 414
    light extraction efficiency as function of inclination angle, 416
    SEM image of TP-LED and TP-LED lit up, 415
    typical light rays propagating in TP-LED, 413
  third-generation tightly integrated chip-stacking approach, 417–23
    characteristics of blue, green and red LEDs in stack and planar configuration, 420
    embedded wire bonds, 417
    layer sequence and chip structure and optical microphotograph of assembled stacked LED, 419
    optical emission spectra of stacked LED functioning as phosphor-free, 422
    optical photographs of stacked LED and conventional RGB LED, 420
    polar emission plots for red, green and blue spectral components, 419
    SEM image of laser micromachined channel on backside sapphire face, 418
Commission Internationale de l'Eclairage (CIE), 488
compact fluorescent lamp (CFL), 490
conduction band diagram, 523
conformal coating, 451–2
contact thermal resistance, 471–2
  categories and general properties of TIMs, 473
  contact face of interface, 472
continuous freeform lens method, 468
  LED road lighting and its illumination performance in laboratory, 468

continuous wave (CW) operation, 498
cooling solutions
  LED applications, 474–6
    closed-loop LED micro-jet array cooling system, 475
copper wire, 450
correlated colour temperature (CCT), 422, 451, 485, 491–2, 600
corundum, 70
coupling, 357–8
crystal LED displays, 583
cubic III-nitrides, 548–9
curing, 453
current crowding, 295
current spreading layer, 325
Czochralski method, 100

deep ultraviolet lithography (DUV), 323
deep ultraviolet (UV) light-emitting diodes (LEDs), 497–502
degradation mechanisms, 434–39
  found in LED ESD testing, 437–9
    horizontal structure of an LED device, 439
  found in LED life testing, 435–7
    catastrophic degradation, 437
    gradual degradation, 437
    rapid degradation in initial stage, 437
    reverse current as function of ageing time under various conditions, 436
    semi-log current-voltage curve measured after long-term ageing tests, 436
design factors, 583
device under test (DUT), 430–1
diode current equation, 374
diode-pumped solid state (DPSS) laser, 413
direct-current magnetron sputtering system, 363
direct-type backlighting units (BLUs), 587
discontinuous freeform lens method, 465–7
  light pattern for BK7 optical glass at 70 cm away from LED, 467
  micrographs of different parts of PMMA, 467
  used to form an E light pattern and simulation of its illumination, 466
dispersion relations, 314
distributed Bragg reflector (DBR), 198
double heterostructure, 298
double-layer mask-based lithography, 360–2
drop-on-demand (DOD) mode, 425–6

Economic Commission for Europe (ECE), 598
edge-type backlighting units (BLUs), 584–7
efficiency droop, 280, 393
  Auger recombination, 284–6
    direct, interband and indirect Auger recombination, 285
    theoretical and experimental reports of the Auger and *C* coefficients in the GaInN/GaN material system, 286
  carrier delocalisation, 291–3
    electrons localised in low-energy indium-rich domain of a GaInN quantum well, 293
  discussion and comparison of droop mechanisms, 293–4
  gallium indium nitride /gallium nitride LEDs, 279–98
    sub-linear increase of emitted optical power vs current, 280
  high-level injection and the asymmetry of carrier concentration and mobility, 286–90
    measured external quantum efficiency of a GaInN LED, 288
    measured I-V on a logarithmic scale, 289
    undoped and p-doped EBL, 287
  methods for overcoming droop, 294–8
    double heterostructure, 298
    external quantum efficiency vs current for devices with different chip areas, 295
    good heat sinking, 294
    increasing p-type doping, 298
    larger LED chips, 295–6
    lateral GaN-based LEDs grown on insulating substrate, 294
    polarisation matching, 296
    strain control, 298
    tailored doping in the active region, 296–7
    thin quantum barriers, 297
    uniform current injection, 294–5
    unique active layer engineering, 298
  non-capture of carriers, 290–1
    non-capture of electron by QW and capture of electron into QW by emission of phonons, 291
  polarisation fields, 291, 292
    simulated conduction-band diagram of GaInN/GaN LED, 292
  recombination models in LEDs, 281–2
    electrons injected into the active region where they recombine, 282
  thermal roll-over in gallium indium nitride LEDs, 282–4
    optical power as function of injection current for an AlGaInP/GaP LED, 284
    theoretical curves for IQE vs *n* based on ABC model, 283
Einstein relation, 289
electrical interconnection, 442
  three types of high-power LED chip, 443
  wire bonding, 443
electrically conductive adhesive, 412
electroluminescence (EL), 391, 514–15, 537
  mapping, 431–2
electroluminescent devices, 568
electron-beam lithography, 324–5, 360–1
electron-blocking layers (EBL), 377, 513
electron-cyclotron resonance (ECR), 4
electron injection efficiency (EIE), 521–8

electron transmittance, 523
electronic band gap, 311
electronic structure, 540–1
electrostatic discharge (ESD), 428–9
  methods, 430–1
    equivalent circuit for ESD, 431
EMCORE D75, 218
emission microscopy (EMMI), 431–2
emissivity-corrected surface temperature, 59
encapsulation, 442
  nitride LEDs and chip packaging, 441–76
    basic structure of LED packaging modules, 446–9
    functions, 441–6
    optical effects of freeform lenses, 463–8
    optical effects of gold wire bonding, 453–6
    optical effects of phosphor coating, 456–62
    processes used, 449–53
    thermal design and processing, 468–76
energy dispersive spectroscopy (EDS), 431–2
Energy Star, 573
entroid shift, 148
environmentally friendly, 575
epitaxial lateral overgrowth (ELO), 82, 216, 502
Ewald construction of Bragg's diffraction theorem, 202, 210
external electrode fluorescent lamp (EEFL), 568
external quantum efficiency (EQE), 118, 216, 280, 378–9

failure evaluation flow chart, 433–4
  flow chart illustration, 434
failure evaluation techniques, 432–3
  detectable signals and characterisation regions for various characterisation techniques, 432
Federal Motor Vehicle Safety Standard 108, 598
Fermi-Dirac distribution, 377
Fermi's golden rule, 383
Fermi's rule, 539
field-emission scanning electron micrograph (FESEM), 218
film thickness, 358
flat fluorescent lamp (FFL), 568
flat-plate vapour chamber, 473–4
flip-chip LEDs (FCLEDs), 183
flip-chip technology, 184–5
  background to flip-chip LEDs, 183
  GaN-based flip-chip LEDs and, 183–5
  solder or Au stud bump, 185
  structure of conventional GaN-based LED, 184
flying height, 40
focused ion beam (FIB), 432–3
forward lighting, 595–8
  photograph of low-beam headlamp beam pattern projected onto wall, 597
  photometric requirements for low-beam headlamp patterns in United States, 597
  selected photometric requirements for high-beam headlamps in United States, 596
  selected photometric requirements for low-beam headlamps in United States, 596
'free-standing' substrates, 77
freeform lenses, 463–8
freely dispersed coating, 451
frequency-dependent permitivity, 356
Fresnel equations, 415
full width at half-maximum (FWHM), 502–3
FullWAVE simulation, 239

gallium indium nitride (GaInN) LEDs
  efficiency droop, 279–98
    Auger recombination, 284–6
    carrier delocalisation, 291–3
    discussion and comparison of droop mechanisms, 293–4
    high-level injection and the asymmetry of carrier concentration and mobility, 286–90
    methods for overcoming droop, 295–8
    non-capture of carriers, 290–1
    polarisation fields, 291
    recombination models in LEDs, 281–2
    thermal roll-over in gallium indium nitride LEDs, 282–4
gallium nitride
  buffer-layer strategies, 105–13
    aluminium nitride buffer layer, 107–8
    atomic layer deposition of Al_2O_3, 110
    dislocation density, 111
    IQE data for LEDs grown on sapphire and ALD-coated silicon substrates, 113
    PL spectra of GaN on an AlAs buffer on silicon, 106
    Raman spectra for GaN epilayers grown on Si (111) substrates, 109
    series of reactant and purge pulses used for single layer control in atomic layer deposition, 111
    superlattice structures, 108–10
    surface pits in GaN grown on 100nm ALDAl_2O_3, 112
    XRD patterns for HT-GaN, 108
    zinc oxide, aluminium arsenide and other materials, 105–7
  challenges for the growth of GaN on silicon substrates, 104–5
    GaN layer grown directly on Si (111) substrate showing cracking, 104
    thermal expansion mismatch between GaN and silicon, 104–5
    thermal management, 105
  device technologies, 113–38
    comparison of *L-l* characteristics of blue LEDs on sapphire and silicon substrates, 116
    cross section and top view of GaN on patterned Si (111), 127

    - early device efforts, 113–15
    - EL spectra for LEDs grown on sapphire and on Si/AlD-Al$_2$O$_3$, 114
    - FE-SEM and RT-PL spectra of 1.0 μm GaN nanorod sample, 136
    - GaN grown on structured Si (111) substrate with different stripe orientations, 126
    - GaN LEDs on patterned silicon substrates, 126–8
    - GaN nanowires and nanorods on silicon, 131–8
    - growth of selective area *m*-plane on GaN on patterned Si (112), 133
    - hexagonal prism representing a GaN crystal unit cell with nonpolar and polar planes, 130
    - HRXRD rocking curves for GaN (0002) and (10–12) ω-scans of samples, 119
    - InGaN/GaN nanorod LEDs on Si, 135
    - *l-V* and *L-l* curves for an InGaN/GaN MQW blue LED, 117
    - *l-V* characteristics, EL spectra and *L-l* characteristics of LEDs on silicon and copper wafer, 125
    - large-area AFM images of GaN films on Si (111), 121
    - layer transfer, 120–6
    - LED device structure, 132
    - MPLED and NPLED, 128
    - *n*-GaN PL spectra at room temperature, 124
    - PL intensity of MPLEDs, NPLEDs, 129
    - progress in large-area substrates, 115–20
    - QW structures on polar and nonpolar orientations and their band diagrams, 131
    - room-temperature CL spectrum of GaN LED structure, 138
    - room-temperature PL spectra for 6nm thick InGaN double heterostructure LED active layers, 134
    - selective lift-off process flow, 123
    - SEM images of Si (111) pillars after dry etching, 137
    - semipolar and nonpolar GaN LEDs on silicon, 128–31
    - weak-beam dark-field TEM images of GaN/SiN$_x$/AlGaN/AlN/Si structures, 120
  - epitaxial overgrowth of GaN on sapphire substrates, 81–6
    - evolution of selective area and lateral epitaxial overgrowth, 83
    - lateral epitaxial overgrowth and pendeo-epitaxy of GaN, 83
    - patterned sapphire substrates, 85–6
    - pendeo-epitaxy, 84–5
    - selective-area growth and epitaxial lateral overgrowth, 81–4
  - future trends, 88–9
  - growth on non-polar and semi-polar surfaces, 86–8
  - history of epitaxial GaN on sapphire substrates for device-quality materials, 67–9
    - device-quality GaN epitaxial growth, 69
    - early development, 67
    - powder GaN, 67–8
    - thin-film GaN, 68–9
  - overview of gallium nitride on silicon substrates, 100
  - possible substrates for the epitaxial growth of GaN, 101
  - sapphire substrates, 69–77
    - comparison of various foreign and native substrates for wurtsite III-N semiconductors, 76
    - comparison with other substrates, 72–7
    - material properties of sapphire and GaN, 72
    - properties of sapphire for substrates of III-N materials, 70–2
  - sapphire substrates for visible LEDs, 66–89
  - silicon overview, 101–3
    - advantages of silicon, 101–2
    - atomic orientation of AlN on Si (111) and Si (100) substrates, 103
    - crystallography, 102–3
  - on silicon substrates, 99–139
  - strained heteroepitaxial growth on sapphire substrates, 77–80
    - concept development and demonstration of strained heteroepitaxial growth, 78–9
    - growth mechanism in GaN strained heteroepitaxy, 79–80
    - strained heteroepitaxial growth of GaN on sapphire substrate, 80
- gallium nitride (GaN) LEDs
  - efficiency droop, 279–98
    - Auger recombination, 284–6
    - carrier delocalisation, 291–3
    - discussion and comparison of droop mechanisms, 293–4
    - high-level injection and the asymmetry of carrier concentration and mobility, 286–90
    - methods for overcoming droop, 295–8
    - non-capture of carriers, 290–1
    - polarisation fields, 291
    - recombination models in LEDs, 281–2
    - thermal roll-over in gallium indium nitride LEDs, 282–4
- Gaussian curvature, 463
- GELcore, 452
- gold wire bonding, 450, 453–6
- Golden DRAGON, 591–2
- good heat sinking, 294
- graded electron-blocking layers (GEBL), 377

gradual degradation, 437
Grashof number, 45, 46

Hamiltonian interaction, 539
hard failure, 438
heat dissipation, 444–5
heterojunctions, 375–8
heterostructure field-effect transistors (HFETs), 73
high angle annular dark field scanning electron microscopy (HAADF-STEM), 161
high-electron mobility transistors (HEMTs), 73
high-intensity discharge (HID), 598
  lamps, 490
high luminous efficiency, 574
high-power LED packaging, 448–9
  illustration, 449
high-resolution X-ray diffraction (HRXRD), 109
high temperature storage test, 428–9
Hillock morphologies, 266
homojunctions, 375–8
hot cathode fluorescent lamp (HCFL), 568
hot-phonon effect, 553
human body model (HBM), 429
humidity operating lifetime test, 428–9
hydride vapour-phase epitaxy (HVPE), 225, 264

III-nitride light-emitting diodes (LEDs)
  current status, 390–9
    InGaN-AlGaN double heterostructure LED, 391
    ultraviolet (UV), 396–9
    visible, 391–6
  polarisation effects, 379–90
    methods for improving internal quantum efficiency, 385–9
    origin of spontaneous and piezoelectric polarisation, 379–82
    polarisation-induced electric fields, 382–5
    problem of p-type doping in nitride LEDs and polarisation-induced doping, 389–90
III-nitride semiconductors
  infrared emitters, 533–56
    high indium (In) content alloys, 534–6
    intersubband (ISB) devices, 549–55
    rare-earth doped gallium-nitride (GaN) emitters, 536–8
  intersubband (ISB) optoelectronics, 538–49
    AlInN/(In)GaN system, 545–7
    alternative crystallographic orientations, 547–8
    cubic III-nitrides, 548–9
    electronic structure, 540–1
    growth and structural properties, 541–3
    optical characterisation, 544–5
    physics of ISB transitions, 539–40
III-nitride ultraviolet light-emitting diodes (LEDs), 396–9
  typical UV LED and packaged UV LED, 397
III-nitride visible light-emitting diodes (LEDs), 391–6
  EQE variation with peak emission wavelength, 392
  high-resolution transmission electron micrographs (HR-TEM) showing defect distribution, 395
  IQE graph, 394
  normalised external quantum efficiency as function of forward current, 396
Illuminating Engineering Society (IES), 429
indium tin oxide (ITO), 303
inductively coupled plasma (ICP), 267
inductively coupled plasma reactive ion etching (ICP-RIE), 232
infrared emitters
  high indium (In) content alloys, 534–6
    IR LED recently reported with active region consisting of nanocolumn array, 535
  III-nitride semiconductors, 533–56
    intersubband (ISB) devices, 549–55
    intersubband (ISB) optoelectronics, 538–49
    rare-earth doped gallium-nitride (GaN) emitters, 536–8
infrared photodetectors, 549–50
innovative crystal growth techniques, 501
integrated stroboscopic camera system, 425–6
inter-valley scattering, 536
internal quantum efficiency (IQE), 182, 224, 251, 282, 302, 323, 382
  marked increases, 507–13
    band diagram of quaternary InAlGaN alloy and radiative recombination, 510
    cross-sectional TEM image of quantum well region of AlGaN MQW DUV-LED, 507
    PL intensity of AlGaN QW as function of XRC FWHM, 509
    PL spectra of quaternary InAlGaN QW measured at 77K at RT, 512
    temperature dependence of integrated PL intensity, 511
    wavelength dependence of ratio of integrated PL intensity, 513
  methods for improvement, 385–9
    comparison of measured energy positions and decay times, 386
    increasing overlap by using thin quantum wells (QWs) and quantum dots (QD), 385–6
    polarisation-matched LEDs, 388–9
    use of semipolar/non-polar substrates, 386–8
International Electrotechnical Commission (IEC), 487–8
International Electrotechnical Vocabulary (IEV), 487–8
intersubband (ISB) devices, 549–55

  - all-optical switches, 549
  - infrared photodetectors, 549–50
  - light emitters, 552–5
    - condiuction-band profile and calculated fractional population inversion of terahertz QCL, 554
    - room temperature ISB PL spectra from 2-nm thick GaN/AlN QWs, 554
  - quantum cascade detectors, 550–2
    - GaN/AlGaN QCDs operating in near-IR structure illustration, 551
- intersubband (ISB) optoelectronics, 538–49
  - AlInN/(In)GaN system, 545–7
  - alternative crystallographic orientations, 547–8
    - band diagram and oriented GaN/AlN superlattices and variation of energy as function of well width, 548
  - cubic III-nitrides, 548–9
  - electronic structure, 540–1
    - band diagram of GaN/AlN QWs in superlattice and ISB transition energy, 541
    - high-resolution cross-sectional TEM images, 543
  - growth and structural properties, 541–3
  - optical characterisation, 544–5
    - conduction band profile and squared envelope functions and transmission spectra for TM and TE, 546
    - room temperature TM-polarised IR photo-induced absorption spectra, 544

- jet printing
  - forming RGB pixels, 425–6
    - close-up of jet-printing of fluorescent microspheres onto pixels, 425
- Jetlab 4 printer, 425–6

- Lambertian lens, 446
- Lambertian radiation pattern, 569, 571
- laser lift-off (LLO), 295
  - techniques, 199
- laser micromachining, 413
- lateral epitaxial growth (LEG), 82
- lateral epitaxial overgrowth (LEO), 82
- lateral overgrowth (LOG), 82
- lateral quantum dot infrared photoconductors, 549–50
- lattice mismatched system, 542–3
- LED lamps, 145
- LED lumen maintenance test, 428–9
- LED module, 489
- LED packaging modules
  - basic structure, 446–9
    - high-power LED packaging, 448–9
    - low-power LED packaging, 446
- LedEngin, 452
- lens laying, 452
- lifetime estimation, 429–30
- light emission, 537
- light emitters, 552–5
- light-emitting diodes (LEDs), 368–79
  - automotive lighting, 595–604
    - forward lighting, 595–8
    - future trends, 603–4
    - signal lighting, 599
  - development, 378–9
  - efficiency, 374–5
  - efficiency droop in gallium indium nitride/gallium nitride LEDs, 279–98
    - Auger recombination, 284–6
    - carrier delocalisation, 291–3
    - discussion and comparison of droop mechanisms, 293–4
    - high-level injection and the asymmetry of carrier concentration and mobility, 286–90
    - methods for overcoming droop, 295–8
    - non-capture of carriers, 290–1
    - polarisation fields, 291
    - recombination models in LEDs, 281–2
    - thermal roll-over in gallium indium nitride LEDs, 282–4
  - energy and environmental issues, 603
    - estimated power and energy use of filament lamp and LED automotive lighting systems, 603
  - gallium nitride on silicon substrates, 99–139
    - buffer-layer strategies, 105–13
    - challenges for the growth of GaN on silicon substrates, 104–5
    - device technologies, 113–38
    - overview of gallium nitride on silicon substrates, 100
    - silicon overview, 101–4
  - homojunctions and heterojunctions, quantum wells and dots, 375–8
    - band diagram of single quantum well heterostructure at forward bias with or without EBL, 377
    - conduction band diagrams showing carrier diffusion and confinement, 376
  - human factor issues, 599–602
    - relative brightness of roadway pavement surfaces illuminated by photometric, 602
    - spectral distributions of white LED and filament sources, 601
    - spectral distributions of yellow and red LED and filament sources, 600
  - liquid crystal display (LCD) backlighting, 566–93
    - advantages and history, 574–7
    - market trends and technological developments, 577–83
    - optical design, 583–93
    - requirements, 572–3
    - technical considerations for optical films and plates, 571–2

    - types of LED LCD backlighting units (BLUs), 567–71
  - nonpolar and semipolar, 250–69
    - challenges in epitaxial growth, 263–7
    - introduction to selected nonpolar and semipolar planes, 255–63
    - light extraction fro nonpolar and semipolar LEDs, 267–9
    - limitations and conventional c-plane LEDs, 250–4
  - p-n junction diodes, 369–72
    - band diagram and minority carrier distribution in forward-biased p-n junction, 371
  - recombination mechanisms, 372–4
    - band diagram showing different recombination processes, 374
- light extraction, 442, 444
  - refraction at the chip and air interface and chip, silicone and air interfaces, 444
- light extraction efficiency (LEE), 221, 521–8
  - increase in EIE, 521–8
    - conduction band diagram and electron transmittance of AlGaN/AlGaN MQB, 523
    - current vs output power and current vs EQE for 250 nm AlGaN MQW LEDs, 524
    - current vs output power and EQE for high-output power 270nm, 526
    - current vs output power for 237nm AlGaN MQW LEDs, 525
    - enhancement of EIE by using MQB in AlGaN DUV-LEDs, 522
    - enhancement of EQE for 270 nm AlGaN LED by using thin p-GaN and Ni/Al electrode, 528
    - improvement of LEE in an AlGaN DUV-LED using thin p-GaN contact layer, 527
    - structure and cross-sectional TEM image of 150 nm AlGaN DUV-LED with MQB, 524
    - wavelength dependence of EQE of AlGaN DUV-LEDs with MQB and single EBL, 526
- liquid crystal display (LCD) backlighting
  - advantages of light-emitting diodes (LEDs) for LCD BLUs, 574–6
    - environmentally friendly, 575
    - high luminous efficiency and low power consumption, 574
    - longer operating life, 574–5
    - low operating DC voltage, 574
    - package size and chroma selection flexibility, 574
    - quicker illumination to stable brightness, 575
    - rapid switching speed, 575
    - robustness, 575–6
    - wide adjustment range for brightness, contrast and chromaticity, 575
    - wide colour gamut, 574
    - wide operating temperature range, 574
  - development history of LED BLUs, 576–7
  - environmental requirements, 573
    - calculation of maximum on mode power requirements, 573
  - light-emitting diodes (LEDs), 566–93
    - optical design, 583–93
    - shipment proportion of LED and CCFL LCD televisions, 567
    - technical considerations for optical films and plates, 571–2
    - types of LED LCD backlighting units (BLUs), 567–71
  - market trends and technological developments, 577–83
    - advantages and key technologies of LED LCD televisions, 582–3
    - new display technologies using LEDs, 583
  - requirements, 572–3
    - features, 572–3
- liquid crystal displays (LCD), 410
- liquid-encapsulated Czochralski (LEC) technique, 77
- liquid phase epitaxy (LPE), 378
- lithographic metallic layer, 359–62
  - SEM image of three gold nanodisks with diameters of 60nm, 100nm and 200 nm, 361
- lithography, 359–60
- longer operating life, 574–5
- low-energy electron-beam irradiation (LEEBI), 378
- low operating DC voltage, 574
- low power consumption, 574
- low-power LED packaging, 446
  - illustration, 448
- low-pressure metal-organic chemical vapour deposition (LP-MOCVD), 503
- low temperature storage test, 428–9
- low threading dislocation density (TDD)
  - growth of AIN layers on sapphire, 502–7
    - AFM images of surfaces of ML-AIN after various stages of growth, 505
    - FWHM of X-ray diffraction XRC as function of initial nitridation time, 502
    - gas flow sequence and growth control method, 504
    - reduction in FWHM on XRC for various stages of ML-AIN growth, 505
    - structure and cross-sectional TEM image of AlGaN/AIN template, 506
- lumen maintenance
  - temperature, 493–4
    - template performance temperature and lifetime table, 494
- Luminus Devices (US), 353

Luxeon, 586
  structure, 448
Luxeon LED module, 469
Luxtaltek Corp (Taiwan), 353

machine model (MM), 429
market trends, 577–82
  cost forecast for different BLU types for 32-inch HD 60Hz LCD televisions, 578
  forecast for number of LED packages per television set, 579
  market forecast for large BLUs based on survey by LED inside published in August 2011, 578
  status of technology for LED LCD televisions, 582
  technological development trends for different product positioning, 581
  technological development trends for different products, 580
MATLAB, 415
Matthew-Blakeslee equilibrium model, 267
Maxwell's equation, 356, 382
mean free path (MFP), 462
mechanical shock test, 428–9
MESAs and contacts, 325–6
metal-organic chemical-vapour deposition (MOCVD), 3, 27–65, 67, 185, 216, 264, 359, 390–1, 412
  close-coupled showerhead reactors, 45–54
    calculated distribution of MMGa for different sizes of CCS reactor, 50
    cross section of a showerhead and its surface on the reactor side, 47
    design of a modern CCS reactor, 50–4
    distribution of TMGa and MMGa in CCS reactor, 49
    flow field in CCS reactor of height 11mm, 48
    GaN growth rate vs TMGa molar flow for elevated reactor pressures, 53
    heater for a 55″ × 2″ CCS reactor, 51
    illustration, 46
    introduction to principles, 45–50
    n-GaN growth for different reactor heights, 52
    state-of-the-art 55″ × 2″ CCS reactor, 51
    vertical flow reactor with showerhead to give uniform flow distribution, 45
  planetary reactors, 35–44
    ceiling temperature control, 38
    cross-section of state-of-the-art planetary reactor, 42
    depletion curve for planetary reactor, 37
    design of modern planetary reactor, 41–4
    gas-foil rotation of a satellite disc, 40
    growth rate vs TMGa molar flow rate for different reactor pressures, 43
    illustration of planetary reactor, 36
    introduction to the principles, 35–41
    laminar flow field of 56″ × 2″ planetary reactor, 43
    MQW photoluminescence wavelength and n-GaN thickness mapping of 6″ wafers, 44
    RF coil electrically heats the conductive graphite susceptor, 39
    state-of-the-art planetary reactor with 56″ × 2″ wafers, 41
  in situ monitoring systems and growing nitride-based materials, 54–65
    curvature measurement during an LED run, 64
    Fabry-Pérot oscillation of the reflectance signal during GaN growth on sapphire substrate, 55
    linear diode array for 2D mapping of surface temperature, 61
    material properties of III nitrides and substrates, 63
    measuring reflectance, 54–8
    measuring temperature, 58–62
    optical set-up for wafer curvature measurement, 63
    reflectance curve, reactor temperature and emissivity-corrected surface temperature of generic LED growth run, 57
    reflectance signal for three surface morphological of GaN layer grown on sapphire substrate, 56
    shape of reflectance curve correlates to surface morphology, 57
    spectra of black-body radiation, 59
    surface temperature and emissivity-corrected surface temperature, 60
    surface temperature of GaN on sapphire, 62
  systems, 28–35
    basic principles, 28–31
    comparison of gas properties of N_2 and H_2, 33
    gas concentration monitoring system, 30
    growth mechanisms of MOCVD, 31–5
    MOCVD system with gas blending system, 28
    modern MOCVD system, 31
    pathways for the gas phase reaction, 34
    simplified growth mechanism in GaN MOCVD system, 32
metal-organic vapour phase epitaxy (MOVPE), 107, 543
metal surface, 357
micro-LED arrays
  implementation of group-addressable, 423–4
    group-addressable micro LED in action, 424
  preliminary results, 426
micro-patterned silicon (MPSi), 128
Minano-Benitez design method, 463–4
miniature RGB pixels, 423

misfit dislocations (MDs), 266
modes, 312
modulation doping, 86
moisture resistance test, 428–9
molecular beam epitaxy (MBE), 27, 106, 217, 221, 378
  growth techniques, 4
  nitride nanocolumn materials, 12–17
    aluminium gallium nitride NCs, 15
    GaN NCs grown directly on Si (111) substrates, 13
    growth of NCs from stable nuclei, 14
    InN and InGaN NCs, 15–16
    InN grown at different temperatures, 16
    non-tapered InN NC and InN NC ensemble grown on Si (111) substrate, 16
    overgrown GaN on NCs on a sapphire substrate, 17
    overgrowth of nitride NCs, 17
    self-catalyst growth of GaN NCs using MBE, 12–15
  nitride nanostructures based on NCs, 17–21
    core-shell NCs, 19
    InGaN/GaN CSNC white light LED, 18
    low-excitation room-temperature spectra of eight-period InGaN/GaN MQWs, 20
    quantum disks embedded in NCs, 17–19
    selective area growth of NCs, 19–21
  nitride semiconductors growth, 3–21
  plasma-assisted MBE growth of nitride epilayers and quantum structures, 5–12
    activation energies of silicon-doped and nominally undoped $Al_xGa_{1-x}N$, 11
    AFM images of GaN grown within nitrogen-stable regime, intermediate regime and gallium-droplet regime, 8
    aluminium nitride epilayers, 8–9
    doping in nitride materials, 10–11
    gallium nitride epilayers, 5–8
    growth diagram showing gallium flux vs substrate temperature for the gallium-droplet, 7
    indium gallium nitride and indium nitride epilayers, 9
    key developments and milestones achieved during the development of MBE-grown LEDs and LDs, 12
    light emitters based on nitride MQWs, 11–12
    nitride-based InGaN/GaN multi-quantum wells, 9–10
    plot of Ga flux vs growth temperature, 6
    RHEED patterns for GaN epilayers, 5
monochromatic light, 412
monomethyl gallium (MMGa), 36
Monte Carlo, 555
  ray-tracing simulations, 459
MPLED, 128
multi-domain vertical alignment (MVA), 577
multi-quantum barrier (MQB) design, 500
multi-quantum well (MQW), 507
MULTILED, 586
multiphonon emission, 537
multiple quantum well (MQW), 297, 421

nano-imprint lithography, 324
nano-patterned silicon (NPSi), 128
nanoscale patterned sapphire substrate (NPSS), 231
nanosphere lithography, 360–1
nanostructured LEDs, 216–45
  bottom-up technique for nanopillar substrates properly by molecular beam epitaxy, 240–5
    C-LEDs, NP-LEDs and high-resolution TEM image of region 1, 242
    EL peak wavelength as function of injection current for two fabricated LEDs, 245
    formation of air voids between the GaN NPs and u-GaN epitaxial layer, 241
    relative IQE as function of excitation power for C-LEDs and NP-LEDs, 244
  general characterisation method, 223–5
    photoluminescence and internal quantum efficiency measurements, 224–5
    Raman spectroscopy, 223–4
    transmission electron microscopy and threading dislocation counting, 223
  general mechanisms for growth of GaN related materials, 218–23
    bottom-up method, 221–3
    FESEMs of fabricated SiO_2 nanorod array, 219
    GaN NR template, 221
    nucleation process and growth process for GaN nanopillars, 222
    overgrowth process and formation of dislocations, stacking faults and voids, 220
    top-down method, 218–21
  top-down technique for nanostructured LEDs, 225–40
    current-voltage and intensity-current characteristics of conventional LED and LED with SiO_2, 234
    diffuse reflectance spectra for both samples, 238
    electrical and optical properties of NAPSS and conventional LED, 231
    flowchart for producing GaN nanorods, 226
    formation of air voids between GaN NRs and u-GaN epitaxial layer, 237
    forward L-I-V characteristics for both fabricated LEDs, 239
    free-standing GaN substrate on nanorod template, 225–9

    - GaN/sapphire interface for GaN epilayer, 229, 236
    - GaN thick films from GaN nanorod array and flat GaN surface, 227
    - highly efficient and bright LEDs overgrown on GaN nanopillar substrates, 235
    - LED with NPSS and SiO_2PQC structure, 232
    - nanoscale patterned sapphire substrate with embedded photonic quasi-crystal, 231
    - PL spectra of GaN substrates separated from GaN nanorods and flat GaN surface, 228
    - sapphire surfaces with NPSS, 233
    - SiO_2 nanorod-array patterned sapphire template, 229–35
- nanowire light-emitting diodes (LEDs), 399–400
- National Highway Traffic Safety Administration (NHTSA), 599
- National Television System Committee (NTSC), 574
- natural colour-mixing
  - miniature RGB pixels, 423
- nitride light-emitting diodes (LEDs)
  - encapsulation and chip packaging, 441–76
    - basic structure of LED packaging modules, 446–9
    - functions, 441–6
    - optical effects of freeform lenses, 463–8
    - optical effects of gold wire bonding, 453–6
    - optical effects of phosphor coating, 456–62
    - processes used, 449
    - thermal design and processing, 468–76
  - evaluation of LED degradation, 431–4
    - failure evaluation flow chart, 433–4
    - failure evaluation techniques, 432–3
  - fabrication, 181–212
  - GaN-based flip-chip LEDs and flip-chip technology, 183–5
    - background to flip-chip LEDs, 183
    - flip-chip technology, 184–5
    - solder or Au stud bump, 185
    - structure of conventional GaN-based LED, 184
  - GaN FCLEDs with geometric sapphire shaping structure, 191–8
    - C-FCLED and SS-FCLED devices, 195
    - crystallography facets, 194
    - current-voltage characteristics of SS-FCLEDs and C-FCLEDs, 196
    - fabrication steps for SS-FCLEDs, 192
    - GaN SS-FCLED, 193
    - light output power and wall-plug efficiency as function of injection current, 197
    - normalised far-field patterns for SS-FCLEDs and C-FCLEDs for two directions, 198
    - photomicrographs of C-FCLED and SS-FCLED chips, 196
    - sapphire shaping structure, 193
  - GaN FCLEDs with textured micro-pillar array, 185–90
    - chip bonded to the silicon sub-mount, 187
    - current-voltage characteristics of flat-surface FCLEDs and MPA-FCLEDs, 189
    - fabrication steps for GaN FCLEDs with MPAs, 186
    - light extraction enhancement vs MPA depth, 190
    - light output power-current curves of flat-surface FCLEDs and MPA-FCLEDs, 190
    - MPA surfaces of sapphire backside with various depths and bevel angles, 188
    - silicon sub-mount before FC bonding, 187
  - GaN thin-film photonic crystal LEDs, 198–200
    - epifilm-transferred technology, 199–200
    - laser lift-off process, 200
    - semiconductor wafer bonding, 199
  - light emission characteristics of GaN PC TFLEDs, 205–11
    - cross section of GaN PC TFLED structure, 207
    - fabrication steps for GaN-based TFLEDs with PC lattice structures, 206
    - far-field pattern normalised with the peak intensity, 209
    - GaN TFLED structure PC, 207
    - light enhancement recorded at various output collection angles for GaN PC TFLEDs, 211
    - light output power-current curve characteristic of GaN TFLED, 208
  - PC nano-structures and PC LEDs, 200–5
    - Brillouin zones for the 2D square PC lattices showing the dispersions curves, 204
    - 2D PC structure with Bragg diffraction phase-matching diagrams, 203
    - photonic crystals with periodicity, 201
    - various extraction methods using PCs, 202
  - quantum wells and quantum dots, 368–400
    - current status of III-nitride LEDs, 390–9
    - light-emitting diodes (LEDs), 368–79
    - modern LED designs and enhancements, 399–400
    - polarisation effects in III-nitride LEDs, 379–90
  - reliability, 428–40
    - degradation mechanisms, 434–39
  - reliability testing, 428–31
    - methods for electrostatic discharge (ESD) testing, 430–1
    - methods for life testing and lifetime estimation, 429–30

nitride semiconductors
  molecular beam epitaxy growth, 3–21
    nitride nanocolumn materials, 12–17
    nitride nanostructures based on NCs, 17–21
    plasma-assisted MBE growth of nitride epilayers and quantum structures, 5–12
    techniques, 4
non-polar substrates, 386–8
  usage, 386–8
    computed polarisation charge density in an InGaN/GaN QW, 388
    non-polar and semipolar planes in III-nitrides, 387
nonpolar and semipolar LEDs, 250–69
  challenges in epitaxial growth, 263–7
    heteroepitaxy of nonpolar and semipolar planes, 263–4
    homoepitaxy and the need for bulk GaN substrates, 264–5
    indium incorporation in nonpolar and semipolar planes, 265
    morphology of nonpolar and semipolar epitaxy, 265–6
    strain-induced defect generation in nonpolar and semipolar epitaxy, 266–7
  introduction to selected nonpolar and semipolar planes, 255–63
    calculated band profiles of InGaN MQWs for different growth orientations, 260
    calculated polarisation charge density as function of inclination angle for an InGaN quantum well, 259
    changes in piezoelectric polarisation charge with orientation, 255–8
    crystallography of wurtzite nitride, 255
    influence of anisotropic strain on E-k relaxation, band state mixing and optical polarisation emission of light, 261–3
    influence of polarisation on band bending, QCSE and carrier transport, 258–61
    new and old coordinates, 256
    polar, nonpolar and semipolar planes in wurtzite crystal structures, 256
    selected wurtzite crystal planes, 255
  light extraction for nonpolar and semipolar LEDs, 267–9
    dependence of light output power on the density of conical features patterned on the backside of the devices, 268
    high light extraction packaging, 269
    increasing η_{extr} via surface roughening, 267–9
    light extraction efficiency as a limiting factor, 267
    thin-film thin-chip LEDs, 269
  limitations and conventional c-plane LEDs, 250–4
    advantages of nonpolar and semipolar LEDs, 254
    carrier transport problems in multiple-quantum-well LEDs, 252–3
    efficiency droop, 253–4
    green gap, 251–2
    quantum-confined Stark effect, 250–1
nonpolar planes, 255
NPLED, 128

ominidirectional reflectors (ODRs), 183
optical characterisation, 544–5
optical design, 583–93
  design factors, 583
  direct-type BLUs, 587, 589–93
    arrangement of RGGB LED clusters with reflector cover foil, 592
    basic design parameters and measured luminance profile, 591
    measured colour uniformity for 23-inch BLU as function of LED pitch, 592
    optical design considerations, 590
  edge-type BLUs, 584–7
    high-power side-emitting white Luxeon LEDs, 586
    materials used in commercial example of 7-inch BLU, 587
    measured positions for 7-inch BLU, 588
    measured positions for 46-inch BLU, 589
    optical considerations for commercial example of 7-inch BLU, 588
    optical design considerations, 585
    optical specifications for commercial example of 7-inch BLU, 587
    requirement specification for commercial example of 46-inch BLU, 589
  key design considerations, 583–4
    light propagation from light injection surface of an LGP and with or without micro-structure, 584
optical effects
  freeform lenses, 463–8
    continuous freeform lens method, 468
    discontinuous freeform lens method, 465–7
    simultaneous multiple surfaces (SMS) method, 463–5
    tailored freeform surface design method, 463
  gold wire bonding, 453–6
    angular CCT distribution for plane C0° – 180° and plane C90° –270°, 455
    angular CCT measurement, 454
    left and front views of phosphor layers in LED module samples, 453
    shape and weight of gold wires of five samples and their phosphor profiles, 453
  phosphor coating, 456–62
    geometry, 461–2
    location, 456–8
    thickness and concentration, 458–61
optical fibre, 418

optical films
  technical considerations for plates, 571–2
    brightness gains Vikuiti BEF II and BEF III, 572
    general characteristics of materials used LGP, 572
optical microscopy (OM), 431–2
optoelectronic device, 453
organic light-emitting diode (OLED), 567
oscillator strength, 383–5
(oxo)imido-silicate phosphors, 171, 175

p-n junction diodes, 369–72
package size, 574
packaging substrate, 472–4
Panasonic ultrasonic FC bonder, 192
partial directional polarisation-dependent band gaps, 315
passive cooling, 475–6
patterned sapphire substrate (PSS), 85–6, 216, 267, 310
patterning, 360–1
PC LEDs, 200–5
PC nano-structures, 200–5
PC patterning options, 323
pendeo-epitaxy, 84–5
perfectly matched layer (PML), 328
performance requirements, 599
phase-space filling, 282
phosphor coating, 450–2
  conformal coating, 451–2
  freely dispersed coating, 451
  geometry, 461–2
    cross sections of phosphor-converted LEDs, 462
  location, 456–8
    arrangement in white LEDs and calculated light extraction efficiency, 457
  optical effects, 456–62
  remote coating, 452
  self-heating, 471
  technologies, 451
  thickness and concentration, 458–61
    dependencies of luminous efficiency and colour mixing fraction of five packaging methods, 460, 461
    five cases, 459
    five packaging methods used in analysis, 459
phosphor-free white-light emission, 421
photo-Dember effect, 536
photoelectrochemical (PEC) etching, 267
photoionisation, 173
photoluminescence (PL), 391, 507–8, 534
  decay time, 359
photoluminescent light emitters, 362
photoluminiscence (PL), 224
photometric quantities, 600–1
photonic band gap, 311
photonic crystal etching, 325
photonic crystal nitride LEDs, 301–53
  epitaxial materials, 301–2
    base substrate material, 302
    factors affecting internal quantum efficiency, 302
  fabrication of P-side up LEDs, 322–6
    current spreading layer, 325
    electron-beam lithography, 324–5
    fabricated PQC LED, 327
    MESAs and contacts, 325–6
    nano-imprint lithography, 324
    PC patterning options, 323
    photonic crystal etching, 325
    thermal nano-imprint lithography, 324
    ultraviolet lithography, 323
    UV-nano-imprint lithography, 324
  improving LED extraction efficiency through PC surface patterning, 318–22
    effect of etch depth, 322
    energy vs *k*-vector diagram for an unpatterned LED device, 319
  light-trapping in LEDs, 305–9
    annular emission cone and polar angle, 309
    emitted ray paths, 309
    example ray paths inside an LED, 306
    light extraction cone, 305
    radiometry and discussion of solid angle, 307–9
    relative power emitted into a 1° annular emission cone as function of cone apex, 308
  limitations of FDTD for modelling PC/PQC LEDs, 328–32
    boundary condition considerations, 329–31
    comparative normalisation of results, 331
    considerations for collection plane placement, 331
    light launch considerations, 328–9
    modelling tools, 332
    requirements for the extent of cross-sectional profile, 331
  methods of improving light extraction from LEDs, 309–10
  modelling PC-LEDs, 326–35
    FDTD simulation for a rib waveguide with PML boundaries, 330
    finite difference time domain simulation methods, 326–8
  N-side up PC-LED performance, 345–8
    demonstration of microcavity effect in practice for an unpatterned N-side up LED, 346–8
    measured and simulated angular emission profiles, 347
  P-side up PC-LED performance, 335–42
    angular emission profile of radiated beam, 338
    beam-steering effects, 338–40

effect of etch depth on extracted power, 337–8
effect of transparent current spreading and passivation layers on PQC performance, 340–2
experimentally measured vs simulated angular far-field projection for PQC LED devices, 336
P-side up PQC LED electro-optical performance, 340
unpatterned smooth-surface P-side up LED vs 12-fold symmetric PQC patterned P-side up LED, 341
PC-enhanced light extraction in N-side up LEDs, 342–50
advantages of N-side up over P-side up device configuration for light extraction, 342–3
cross section through a surface-patterned N-side up LED, 343
FDTD vs analytical models for cavity-enhanced thin GaN LED designs, 344
measurement system for recording photoluminescence from PQC samples, 346
microcavity effect in N-side up vertical LED, 344
utilisation of microcavity effect in N-side up LEDs to improve power extraction, 343–4
PC-enhanced light extraction in P-side up LEDs, 322–6
performance improvement for N-side up PQC patterned LEDs, 348–50
angle-dependent photoluminescence, 349
enhanced power extraction, 348
far-field beam-shaping, 348
simulated angular extraction profile for PQC patterned device, 350
photonic crystal technology, 310–18
classes of PC device, 312–15
contrast enhanced images of far-field beam intensity, 317
illustration of photonic crystal, 313
photonic crystal with triangular symmetry etched into the surface of dielectric slab waveguide structure, 312
regular PCs vs photonic quasi-crystals, 315–18
workings of PCs, 311–12
summary, 350–2
types of LED, 302–5
illustration of P-side up lateral current spreading LED, 303
N-side up LEDs, 304
N-side up vertical current spreading LEDs, 304
P-side up lateral current spreading LEDs, 302–3
patterned substrate LEDs, 304–5
unpatterned P-side up LED simulation example, 332–5
cross section through P-side up LED showing physical dimensions and refractive index values, 332
cross section through surface-patterned P-side up LED showing physical dimensions and refractive index values, 335
FDTD simulation for unpatterned P-side up LED device, 333
simulation results, 334–5
simulation set-up, 332–4
photonic quasi-crystal (PQC), 231, 316
piezoelectric polarisation, 255
origin of spontaneous polarisation, 379–82
bandgap vs lattice constant for III-nitride semiconductor family, 380
GaN wurtzite crystal structure, 380
III-nitride properties as function of composition, 381
total polarisation for pseudomorphic AlGaN on GaN, 381
Planckian curve, 491–2
Planck's constant, 384
Planck's formula, 58
Planck's law, 58
planetary reactors, 35–44
ceiling temperature control, 38
depletion curve, 37
design of modern planetary reactor, 41–4
cross-section of state-of-the-art planetary reactor, 42
growth rate vs TMGa molar flow rate for different reactor pressures, 43
laminar flow field of 56″ × 2″ planetary reactor, 43
MQW photoluminescence wavelength and n-GaN thickness mapping of 6″ wafers, 44
state-of-the-art planetary reactor with 56″ × 2″ wafers, 41
gas-foil rotation of a satellite disc, 40
illustration, 36
introduction to the principles, 35–41
RF coil electrically heats the conductive graphite susceptor, 39
plasma-assisted molecular beam epitaxy (PAMBE), 3, 422, 541–2
aluminium nitride epilayers, 8–9
doping in nitride materials, 10–11
activation energies of silicon-doped and nominally undoped $Al_xGa_{1-x}N$, 11
gallium nitride epilayers growth, 5–8
AFM images of GaN grown within nitrogen-stable regime, intermediate regime and gallium-droplet regime, 8

    - growth diagram showing gallium flux vs substrate temperature for the gallium-droplet, 7
    - plot of Ga flux vs growth temperature, 6
    - RHEED patterns for GaN epilayers, 5
  - growth of nitride epilayers and quantum structures, 5–12
  - indium gallium nitride and indium nitride epilayers, 9
  - light emitters based on nitride MQWs, 11–12
    - key developments and milestones achieved during the development of MBE-grown LEDs and LDs, 12
  - nitride-based InGaN/GaN multi-quantum wells, 9–10
- plasmon-coupled emission
  - mechanism, 356–8
    - plasmon-enhanced LEDs, 357–8
    - surface plasmon, 356–7
- plasmon-coupled nanostructures
  - fabrication, 358–63
    - lithographic metallic layer, 359–62
    - template methods, 362–3
    - vacuum deposition, 358–9
- plasmon-enhanced LEDs, 357–8
- Poisson's equation, 369
- polar plane, 255
- polarisation-dependent band gaps, 315
- polarisation-induced doping
  - problem of p-type doping in nitride LEDs, 389–90
    - three-dimensional polarisation-induced n- and p-type doping, 390
- polarisation-induced electric fields, 382–5
  - basic metal-polar nitride LED and interface charges and polarisation field band diagram, 382
  - decrease in oscillator strength, 383–5
    - reduction in overlap of electron and hole envelope wave functions, 385
  - GaN/InGaN/GaN QW as function of InGaN composition, 383
  - red-shifted photon emission, 383
    - quantum-confined Starck effect in nitride LEDs, 384
- polarisation-matched light-emitting diodes (LEDs), 388–9
  - polarisation charge and bandgap contours, 389
- polarisation matching, 296
- polariton light-emitting diodes (LEDs), 400
- polycarbonate (PC), 571
- polymethyk-methacrylate (PMMA), 571
- porous anodic alumina (PAA), 362
- post thermal processing, 358
- power and temperature cycling test, 428–9
- pseudo-white, 145
- pulse-flow multilayer growth technique, 501
- Purcell effect, 201
- QUALIA 005 LCD, 576
- quantum barrier (QB), 291
- quantum cascade detectors, 550–2
- quantum cascade laser (QCL), 539
- quantum-confined Stark effect (QCSE), 86, 102, 128, 223, 296, 534
- quantum dots, 375–8
  - nitride light-emitting diodes (LEDs) based on quantum wells, 368–400
    - current status of III-nitride LEDs, 390–9
    - light-emitting diodes (LEDs), 368–79
    - modern LED designs and enhancements, 399–400
    - polarisation effects in III-nitride LEDs, 379–90
- quantum well infrared photodetectors (QWIP), 549
- quantum-well (QW), 289, 291, 375–8
  - nitride light-emitting diodes (LEDs) based on quantum dots, 368–400
    - current status of III-nitride LEDs, 390–9
    - light-emitting diodes (LEDs), 368–79
    - modern LED designs and enhancements, 399–400
    - polarisation effects in III-nitride LEDs, 379–90
- quantum wells (QW), 498
- quartz, 42
- quartz diffusion barrier, 42
- quasi-ballistic transport, 290
- quasi-Fermi levels, 369–70
- quaternary alloy, 510
- quicker illumination, 575

- radiative recombination efficiency, 393
- radio-frequency molecular beam epitaxy (rf-MBE), 421
- radio-frequency (RF) plasma, 4
- radio-frequency (RF) plasma-assisted MBE, 132
- random texturing, 310
- rapid degradation, 437
- rapid switching speed, 575
- rare-earth doped gallium-nitride (GaN) emitters, 536–8
  - emission wavelengths from selected transitions in rare-earth ions, 537
  - MOVPE-grown GaN:Er p-i-n structure and IR electroluminescence spectra, 538
- reactive ion etching (RIE), 122, 220
- recombination mechanisms, 372–4
- red-shifted photon emission, 383
- reflective high-energy electron diffraction (RHEED), 5
- remote coating, 452
- resonant-cavity light-emitting diodes (RCLEDs), 399
- Reynolds number, 48
- robustness, 428–9, 575–6
- root mean square (RMS), 110, 505

rotating disk reactor (RDR), 45–6
rotation speed, 40

salt atmosphere test, 428–9
sapphire, 303, 398
sapphire substrates, 69–77
  comparison with other substrates, 72–7
    comparison of various foreign and native substrates for wurtsite III-N semiconductors, 76
    native substrates, 75–7
    other foreign substrates based on oxides, sulfides and metals, 74–5
    silicon carbide substrates, 72–4
    silicon substrates, 74
  properties of sapphire for of III-N materials, 70–2
    chemical and thermal properties, 71–2
    material properties of sapphire and GaN, 72
    structural properties, 70–1
scanning electron microscopy (SEM), 106, 359–60, 431–2
Schrödinger-Poisson solver, 540
second harmonics generation (SHG) laser, 507–8
secondary ion mass spectrometry, 106
secondary ion mass spectroscopy, 433
selective-area epitaxial growth (SAEG), 82
selective-area growth (SAG), 81
selective-area lateral epitaxial overgrowth (SALEO), 82
selective epitaxial growth (SEG), 82
selective epitaxy (SE), 81
selective growth (SG), 81
'self-doping' effect, 86
Semiconductor Ultraviolet Optical Sources (SUVOS) program, 498–9
semipolar planes, 255
semipolar substrates, 386–8
Sensor Electronic Technology (SET), 500
separation by implantation of oxygen (SIMOX) process, 118
Shockley, Read and Hall theory, 280, 372
Shockley boundary conditions, 370
short-period superlattice (SPS), 185
signal lighting, 599
  photometric and colour requirements for vehicle signal lights in United States, 599
silicon nitride, 107
silicon-on-insulator (SOI) substrates, 118
silicon substrates
  overview of gallium nitride on, 100
silicone injection, 453
simple diode theory, 287
simultaneous multiple surfaces (SMS) method, 463–5
  simplest version of SMS 3D method generates two surfaces, 464
single quantum well (SQW), 378–9
Snell's law, 415, 443
  refraction, 334
soft failure, 438
solid-state lighting (SSL), 364, 463
spontaneous polarisation, 357–8, 379–82
Stark effect, 10
sterilisation, 497–8
strain-induced piezoelectric polarisation, 357–8
Stranski-Krastanov (SK) mode, 13, 393
super-bright solid-state light sources, 364
super-luminescent light-emitting diodes (SLEDs), 399
superlattice (SL), 108
surface-mounted devices (SMD), 446
surface phase diagrams, 5
surface plasmon, 356–7
surface plasmon enhanced light-emitting diodes (LEDs), 355–65
  fabrication of plasmon-coupled nanostructures, 358–63
  mechanism for plasmon-coupled emission, 356–8
  performance and outlook, 363–5
surface plasmon (SP) polariton, 356
susceptor, 29
system testing, 445

tailored freeform surface design method, 463
  lens designed based on tailored method and numerical illumination performance, 464
tape-automated bonding (TAB), 184
technical specification (TS), 487–8
temperature cycling test, 428–9
template methods, 362–3
thermal air conductivity, 472
thermal interface material, 471–2
thermal nano-imprint lithography, 324
thermal resistance spreading, 472–4
  working mechanism of flat-plate vapour chambers, 474
thermal roll-over, 282–4
thermal shock test, 428–9
thin-film film-chip (TFFC) LED, 269
thin-film LEDs (TFLED), 198
thin quantum barriers, 297
threading dislocation density (TDD), 216
threading dislocations (TDs), 266, 510–11
top surface metallurgy (TSM), 184
total internal reflection (TIR), 182, 305, 442
transmission electron microscope, 505–6
transmission electron microscopy, 431–2, 542–3
transmission electron microscopy-energy dispersion X-ray spectroscopy (TEM-EDS), 161
transparent conductive layer (TCL), 303, 433
transparent current spreading layer (TCSL), 340
transverse magnetic (TM)-polarised light, 540
transversed electric polarised light, 545

- triple gas injector, 42
- triple injector, 35
- ‘true bulk’ GaN substrates, 77
- tunnelling effect, 290
- two-step strained heteroepitaxy, 79

- ultraviolet lithography, 323
- ultraviolet (UV), 389
- ultraviolet (UV) light-emitting diodes (LEDs), 497–530
  - AlGaN-based on DUV-LEDs fabricated on high quality AIN, 513–21
  - future trends, 528–30
    - maximum output power of AlGaN and InAlGaN-based DUV-LEDs, 529
  - growth of low threading dislocation density (TDD) AIN layers on sapphire, 502–7
  - increase in electron injection efficiency (EIE) and light extraction efficiency (LEE), 521–8
  - marked increases in internal quantum efficiency (IQE), 507–13
  - research background of DUV LEDs, 497–502
    - current status of EQE of nitride UV-LEDs measured at room temperature, 500
    - potential applications, 498
    - relation between direct transition bandgap energy and lattice constant for wurtzite, 499
- ultraviolet (UV) mirror, 413
- ULVAC MBE, 223
- under bump metallurgy (UBM), 184
- uniform current injection, 294
- unique active layer engineering, 298
- UV-nano-imprint lithography (UV-NIL), 324

- vacuum deposition, 358–9
- van Roosbroeck-Shockley model, 372
- vapour-liquid-solid (VLS) mechanism, 12
- vapour phase epitaxy (VPE), 378
- vehicle headlamp systems, 598
- vertical gradient freeze (VGF) technique, 77
- vibration test, 428–9
- Vikuiti, 572
- visible electroluminescent devices, 537
- visible LEDs
  - gallium nitride on sapphire substrates, 66–89
    - epitaxial overgrowth of GaN on sapphire substrates, 81–6
    - future trends, 88–9
    - growth on non-polar and semi-polar surfaces, 86–8
    - history of epitaxial GaN on sapphire substrates for device-quality materials, 67–9
    - sapphire substrates, 69–77
    - strained heteroepitaxial growth on sapphire substrates, 77–80
- Volmer-Weber (VW) growth mode, 13

- ω-scan rocking curves, 502–3
- water purification, 497–8
- wetting, 453–4
- white light-emitting diodes (LEDs)
  - chemical composition of representative nitride and oxynitride phosphors, 149–50
  - compounds activated by Ce^{3+}, 165–8
    - excitation and luminescence spectra of Ce^{3+}-activated yttrium oxoimidosilicates, 168
    - excitation and luminescence spectra of $La_{2.94}Ce_{0.06}Si_6N_{11}$, 166
    - La-Si-N compounds, 165
    - Ln-Si-Al-O-N:Ce^{3+} (Ln=La, Ce) compounds, 167–8
    - Ln-Si-O-N:Ce^{3+} or Tb^{3+} (Ln=Y, La) compounds, 165–7
    - quaternary phases of Y_2O_3-YN-Si_3N_4-SiO_2 system, 166
  - compounds activated by Eu^{2+}, 150–65
    - AE-Al-Si-N (AE=Ca, Sr) compounds, 152–5
    - AE-Si-N (AE=Ca, Sr, Ba) compounds, 150–2
    - AE-Si-O-N (AE=Ca, Sr, Ba) compounds, 161–5
    - $AESi_2O_2N_2$ crystal structures, 162
    - $AESi_2O_2N_2$:Eu^{2+} excitation and luminescence spectra, 164
    - β-sialon crystal structure viewed along the c-axis, 157
    - β-sialon:Eu^{2+} excitation and luminescence spectra, 157
    - $Ba_3Si_6O_{12}N_2$:Eu^{2+} excitation and luminescence spectra, 163
    - Ca-A-sialon crystal structure viewed along the c-axis, 159
    - Ca-α-sialon:Eu^{2+} excitation and luminescence spectra of, 159
    - $CaAlSiN_3$ crystal structure, 153
    - CIE colour coordinates of $(Sr_{1-u}Ca_u)Si_2O_2N_2$:Eu^{2+} and $(Sr_{1-v}\ Ba_v)Si_2O_2N_2$:$Eu^{2+}$, 164
    - crystal structure of Sr-containing sialon, 160
    - crystal structures of $Ba_3Si_6O_9N_4$ and $Ba_3Si_6O_{12}N_2$, 162
    - green phosphors with narrow band width, 158
    - layered structures of $AESi_2O_2N_2$ (AE=Ca, Sr or Ba), 163
    - local coordination around calcium atom in $CaAlSiN_3$, 154
    - luminescence and excitation spectra of $AE_2Si_5N_8$:Eu^{2+}, 151
    - luminescence and excitation spectra of $CaAlSiN_3$:Eu^{2+} and $Sr_{0.8}Ca_{0.2}AlSiN_3$:Eu2+, 152
    - nitrogen atom coordinated with four silicon atoms in $SrYSi_4N_7$, 156

    reported phases in the Ca_3N_2-AlN-Si_3N_4 system, 155
    Si-Al-O-N compounds – Ca-α-sialon:Eu^{2+} and β-sialon:Eu^{2+}, 155–60
    Sr-sialon or $SrSi_{10-x}Al_{18+x}N_{32-x}O_x$ (x=0), 160–1
  copying traditional lamps, 490–1
    double-capped LED lamp, 490
    replacing a fluorescent lamp with LED lamp, 491
  cross section of typical white LED, 145
  current and future trends, 494–5
    value-based predictions of LED market share by sector, 494
  definitions and implications, 488–9
    LED package is understood as LED die plus attached terminals, 488
  features of crystal structure of nitride and oxynitride phosphors, 168–71
    condensation of $[(Al,Si)N_4]$ and $[(Al,Si)O_4]$ tetrahedra, 169–70
    lattice defects, 170–1
    location of the activator ion in host crystal, 169
  features of optical transitions of nitride and oxynitride phosphors, 171–5
    excitation and luminescence transitions at long wavelength, 171–2
    photoionisation (or autoionisation) processes, 173
    quantum efficiency, 174–5
    quantum efficiency of typical white LED phosphors, 174
    small thermal quenching, 171–4
    thermal quenching of luminescence intensity under 450 nm light excitation, 172
    variation of thermal quenching, 174
  freedom of choice, 491–4
    colour, 491–3
    lumen maintenance and temperature, 493–4
  general applications, 485–7
    non-LED light sources and LED light sources, 486–7
  impact on society, 144–5
  LED terminology, 487–9
    history and recent changes, 487–8
  lighting applications and role of standards, 485–95
  optical transitions of Ce^{3+} and Eu^{2+}, 146–9
    energy level diagram for Ce^{3+}, 147
    luminescence and excitation spectra of $(Sr_{0.75}Ba_{0.25})_2SiO_4$:$Eu^{2+}$ and $(Y_{0.75}Gd_{0.25})_3Al_6O_{12}$:$Ce^{3+}$, 149
    optical transitions of Eu^{2+}, 149
    physical factors in host crystal affecting the optical transition energies of Ce^{3+}, 147
  phosphors, 144–76
    future trends, 175–6
  requirements, 146
  structure, 145
wide adjustment range, 575
wide colour gamut, 574
wide operating temperature range, 574
wire bonding, 450
  copper wire, 450
  gold wire, 450

X-ray diffraction (XRD), 106, 502–3
X-ray photoelectron spectroscopy (XPS), 107

ZEONOR, 571
ZnS phosphors, 171